

# MICROBEAM ANALYSIS

# 1987

Roy H. Geiss, *Editor*

Proceedings of the 22nd Annual Conference  
of the  
Microbeam Analysis Society  
In association with the  
Japanese Society for the Promotion of Science  
Australian Microbeam Analysis Society  
Kona, Hawaii, 13-17 July 1987



*San Francisco Press, Inc.*

Box 6800, San Francisco, CA 94101-6800

*Printed in the U.S.A.*

#### PUBLISHER'S NOTICE

Microbeam Analysis Society (MAS) and its publisher, San Francisco Press, Inc., are not responsible for the information and views presented in this volume by the several contributors.

San Francisco Press, Inc., also publishes the Proceedings of the Annual Meeting of the Electron Microscopy Society of America (EMSA), the proceedings of the triennial workshop on Analytical Electron Microscopy (AEM), and the Electron Microscopy Safety Handbook. Information on back issues follows. *MAS and EMSA members prepaying by personal check get a 20% discount from the prices listed below.* Overseas orders must be prepaid. California purchasers please add sales tax.

##### **Microbeam Analysis**

1975, 1976 (spiral bound)	\$25 each
1977 (full-length papers, Boston meeting)	\$25
1979, 1980, 1981	\$25 each
1982	\$42.50
1984	\$30
1985	\$40
1986	\$55
1987	\$50

##### **EMSA Proceedings**

1983, 1984, 1985	\$45 each
1986	\$55
1987	\$65

##### **Analytical Electron Microscopy**

1981	\$25
1984, 1987*	\$40 each

<b>Electron Microscopy Safety Handbook</b>	<b>\$15</b>
--	-------------

\* The proceedings of the AEM-1987 workshop also contain the MAS-1987 papers on surface analysis.



# TABLE OF CONTENTS<sup>†</sup>

Note, vii

Officers of the Microbeam Analysis Society, vii

Sustaining Members' Information, viii

## 1. PRESIDENTIAL SYMPOSIUM (C. E. Fiori)

\*Wells, The history and future of the scanning electron microscope, 1

## 2A. EPMA: ANALYTICAL (J. T. Armstrong)

Nockolds, The use of background in the electron probe analysis of bulk samples, 9

Smith, Wynne, The prediction of background intensities in energy-dispersive EPMA, 12

Romig, Hlava, Chambers, A comparison of matrix correction procedures for the x-ray microanalysis of U-Nb alloys, 15

Small, Newbury, Myklebust, Test of a bremsstrahlung equation for energy-dispersive x-ray spectrometers, 20

Heinrich, A general correction for fluorescence from characteristic lines, 23

Heinrich, A simple correction procedure for continuum fluorescence, 24

## 2B. EPMA: MAPPING (R. L. Myklebust)

Myklebust, Newbury, Marinenko, Bright, Background correction in electron microprobe compositional mapping with wavelength-dispersive x-ray spectrometry, 25

Carpenter, Digital x-ray mapping at low magnification with the use of wavelength-dispersive techniques in EPMA, 29

Newbury, Applications of compositional mapping in materials science, 33

Kohara, Zenitani, Kajikawa, Soezima, High-speed mapping and data-processing system for EPMA, 37

Marinenko, Newbury, Myklebust, Bright, A statistical evaluation of wavelength-dispersive digital compositional mapping with the electron microprobe, 40

Konopka, An improved calculator for digital image calculation, 43

McCoy, Colorad system for mapping elemental composition determined by x-ray analysis, 46

## 2C. EPMA: INSTRUMENTATION AND ANALYSIS (D. B. Wittry)

Golijanin, Wittry, Alignment and characterization of doubly curved x-ray diffractors, 51

Wittry, Golijanin, Development of an x-ray microprobe for local spectrochemical analysis, 54

Nagatsuka, Miyokawa, Otsuki, Watanabe, Suzumi, Tagata, A new automated EPMA system with distributive processing capability, 57

Ware, Programming for keyboard-operated EDS-WDS microanalysis, 62

Sentner, Heitur, EPMA of Be in Cu-Be alloys with the use of a layered synthetic microstructure dispersion element, 65

Thompson, Walker, Hydrogen detectability in uranium by  $U N_{VI}O_{IV}$  peak shift, 69

## 3A. SEM: LOW VOLTAGE (J. B. Pawley)

\*Osumi, Nagatani, High-resolution low-voltage SEM of uncoated biological specimens fixed by the freeze substitution fixation method, 71

\*Wells, Low-loss electron images of uncoated nonconducting samples in the SEM, 76

Sugiyama, Ikeda, Uchikawa, Voltage contrast mechanism of SEM images over passivated devices, 79

\*Kinalidis, Wolfe, Low-voltage, high-current-density SEM, 82

\*Pawley, Low-voltage SEM, 83

## 3B. SEM: APPLICATIONS (Y. Uchikawa, G. Cleaver)

Reid, Nauka, Rosner, Laderman, Application of SEM cathodoluminescence to the study of GaAs/Si, 87

Ikuta, Mase, Shimizu, Line-sampling stroboscopy with SEM, 91

Konopka, Shinohara, Quantitative analysis with standards on a field-emission microscope, 96

Guilemany, Mellor, Miguel, Gil, Dynamic studies of martensitic transformation on copper shape-memory alloys with the SEM, 99

## 3C. SEM: IMAGE SIMULATION (D. E. Newbury)

Kotera, Suga, Monte Carlo modeling of keV electron scattering in a charged-up insulator, 102

\*Joy, Image simulation for the SEM, 105

\*Newbury, Monte Carlo electron trajectory simulations for scanning electron microscopy and microanalysis, 110

Thompson, Surface characterization by use of automated stereo analysis and fractals, 115

Joy, A note on charging in low-voltage SEM, 117

<sup>†</sup>An Author Index begins on p. 373.

\*Invited paper.

#### 4A. OPTICAL SPECTROSCOPY: MICRO-RAMAN (E. S. Etz, P. Dhamelincourt, F. Adar)

- \*Dhamelincourt, Delhay, Evolution and prospects of Raman microprobing techniques, 119
- Milanovich, Tomas Hirschfeld: Reflections on the life and work of a 'micro' pioneer, 121
- Archibald, Honigs, NIR FT-Raman of derivatized controlled pore glass, 123
- Exarhos, Donley, Real-time Raman detection of molecular changes in ceramics undergoing sliding friction, 125
- Schrader, Ozkan, Laser Raman microprobe analysis of selective oxidation catalysts, 128
- Gardiner, Littleton, Bowden, Raman microscopy mapping of high-temperature air corrosion products on iron chromium alloy, 131
- Sharma, Urmos, Micro-Raman spectroscopic studies of materials at ambient and high pressures with cw and pulsed lasers, 133
- \*Kiefer, Micro-Raman spectroscopy with laser light traps, 137
- Kerker, Bhandari, Absorption and scattering by heterogeneous particles, 138
- Dhamelincourt, Brémard, Laurey, Merlin, Turrell, Polarization measurements in Raman micro-spectroscopy, 139
- Adar, Lerner, Talmi, The signal-to-noise advantages of multichannel detectors on Raman micro-probes, 141
- Fauchet, High-spatial-resolution analysis of semiconductor thin films with a Raman micro-probe, 144
- Exarhos, Friedrich, Raman microprobe characterization of dielectric films following high-energy pulsed laser irradiation, 147
- Purcell, Characterization of quality and strain in GaAs semiconductors by micro-Raman spectroscopy, 151
- Magnotta, Observation of HSiCl by laser-induced microfluorescence during the direct-laser writing of silicon microstructures, 153
- \*Dovich, Burgi, Photothermal microscope, 155
- Etz, Tracking chemical transformations of particles in the Raman microprobe, 158
- Truchet, Delhay, TEM with Castaing's electron x-ray and laser Raman probes for simultaneous elemental and molecular analysis at submicrometric scale, 163
- Katzenberger, Adar, Lerner, An improved algorithm for linearizing in wavelength or wavenumber spectral data acquired with a diode array, 165
- Louden, Cook, Kelly, Phillipson, Concentration profiles of methyl centralite diffused into a nitrocellulose extruded mono-perforated small-arms propellant determined by Raman micro-spectroscopy, 166
- Dhamelincourt, Dhamelincourt, Wallart, In situ micro-Raman study of discharge products of LiSOCl<sub>2</sub> cells, 167

#### 4B. OPTICAL SPECTROSCOPY: MICRO-IR (B. Cook)

- \*Messerschmidt, Design and performance standards for IR microscopes in spectroscopy, 169
- Harthcock, Atkin, Compositional mapping with the use of functional group images obtained by IR microprobe spectroscopy, 173
- Smith, Welch, Graham, Chughtai, The effect of metal substrates on the photodegradation of polymer films, 177
- Reffner, Messerschmidt, Coates, IR microbeam analysis, 180
- Beauchaine, Rosenthal, Applications of FTIR microscopy in polymer analysis, 185
- Beauchaine, Kempfert, Fuller, Rosenthal, Applications of FTIR microscopy in forensic analysis, 187
- Ishida, Ozaki, Kamoto, Ishitani, Iriyama, Takagi, Tsukie, Shibata, Ishihara, Kameda, Raman microprobe and Fourier transform-IR microsampling studies of the microstructure of gall-stones: II. Calcium phosphate stone and fatty acid calcium-salt stone, 189

#### 4C. OPTICAL SPECTROSCOPY: MICRO-RAMAN FLUORESCENCE (F. Milanovich)

- \*Kohen, Hirschberg, Fried, Cohen, Santus, Reyftman, Morliere, Schachtschabel, Mangel, Shapiro, Prince, Microspectrofluorometric study of cell structure and function, 192
- Yu, Cai, Ho, Thompson, Kuck, Microbeam Raman/fluorescence analysis of eye lens, 197
- Mizuno, Takata-Kanematsu, Nozawa, Ozaki, Iriyama, Ikeda, Laser Raman optical dissection study of an intact lens: Comparison among horizontal axis profiles of lens water, sulfhydryl, and disulfide contents, 199
- Velapoldi, Gjelsvig, A fluorescence technique for determining the porosity of geologic core samples on a macro- and microscale, 202
- Pasteris, Wopenka, Use of a laser Raman microprobe to trace geological reactions, 205
- Barbillat, Dhamelincourt, Cornard, Lenain, Multichannel microfluorometer with laser excitation, 210
- Macklin, Brownlee, Chang, Bunch, Micro-Raman spectroscopic measurement of carbon in meteorites and interplanetary dust particles, 211
- Chen, Chang, Ma, Laser Raman spectroscopic study of ocular lens in rats, 213

## 5A. MATERIALS SCIENCE: CERAMICS (W. J. Clegg)

- \*Mitchell, Pirouz, Heuer, Electron microscopy studies of some metastable ceramic phases, 215
- Krishnan, Thomas, Microanalysis of polytypoid ceramics by imaging, diffraction, and spectroscopy, 222
- Heuer, Howitt, Oxygen bubble formation in nuclear waste glasses by gamma irradiation, 225
- Howitt, Heuer, Kelsey, Flynn, The microstructure of explosively deformed alumina, 227
- Chan, Howitt, Harker, Crystalline phases of the simulated ICPP nuclear wastes, 230
- Clegg, Horsfall, Briscoe, A microstructural study of aluminum- $\delta$ -alumina composites, 233
- Omlor, Lloyd, Brodecki, Jackson, Sample preparation of rapidly solidified powder particles for AEM, 237
- Elliott, Staudhammer, Johnson, Diffusion in shock-activated Be-Al interfaces, 239

## 5B. MATERIALS SCIENCE: THIN FILMS (A. B. Harker)

- DeNatale, Harker, Transformation behavior in amorphous thin films, 241
- Harker, DeNatale, Substrate effects in the microstructure and phase transformation of vanadium dioxide, 244
- DeNatale, Sankur, Gunning, Microstructure-property relations in optical thin films, 247
- Kitchen, McLaughlin, Omlor, Lloyd, Brodecki, Interface studies of AlGaAs/InGaAs pseudomorphic modulation doped field-effect transistors with p-doped surface layers, 250
- Fitzgerald, Moir, Storey, An investigation of the ferrite-magnesium oxide interface, 253
- Hosking, Semarge, Hills, Characterization of a graphite-OFHC copper braze joint, 257

## 6. BIOLOGICAL APPLICATIONS (Peter Ingram)

- Crooker, Sod, Myers, Baran, Morrison, Ion probe microanalysis of Li- and Be-treated hepatocyte cultures, 261
- Anderson, Brazal, Natividad, Lopez, Ultrastructural changes in the glomerulus of a hibernator by scanning and transmission electron microscopy, 264
- LeFurgey, Hawkey, Lieberman, Ingram, Na-Ca compartmentation in cultured heart cells, 267
- Marshall, Condron, Quantitative procedures for bulk frozen-hydrated biological samples based on  $\phi(\rho z)$  curves, 269
- Visscher, Robison, Argentieri, In vivo and in vitro analysis of a polymer drug-delivery system, 271
- Leapman, Swyt, Removal of plural inelastic scattering in EELS from organic samples: A new approach, 273

## 7. COMPUTER-AIDED IMAGING AND SIMULATION (M. Carr)

- \*Russ, Russ, Teaching computers to see, 277
- Mott, Computer comparison of digital images, 287
- Bright, An object finder based on multiple thresholds, connectivity, and internal structure, 290
- \*Kilaas, Interactive software for simulation of high-resolution TEM images, 293
- McCarthy, Christenson, Seymour, Techniques for computer-aided imaging in SEM and STEM, 301
- Lakshminarasimha, Johnson, Computer-generated three-dimensional microstructures, 307

## 8. GEOLOGICAL APPLICATIONS (P. F. Hlava)

- Jarosewich, The use of the electron microprobe in the Smithsonian Institution Museums, 312
- Knowles, Microprobe analysis of tetrahedrite in the Coeur d'Alene Mining District, Idaho, 313
- Wayne, Solberg, Sinha, Microprobe analysis of "reset" zircons from the Brevard Zone, near Rosman, N.C., 315
- Stockton, Color and chemistry of gem garnets, 317
- Hinthorne, Bentley, Electron and ion microprobe investigation of plagioclase phenocrysts in the Frenchman Springs and Roza members of the Columbia River basalts, 321
- Friel, Computer-aided imaging of basaltic glass, 325
- Stuart, Vavra, Levesque, Analysis of microporosity in reservoir rocks by combined SEM and digital image analysis, 327
- Minkin, Chao, Back, Chen, Use of microbeam methods in the study of disseminated gold deposits: Prospecting, 1980s style, 329
- Mackinnon, Kaser, Microanalysis of clays at low temperature, 332
- Blake, Mardinly, Bunch, AEM of extraterrestrial materials: Results from microtome sections of carbonaceous chondrites and interplanetary dust particles, 335
- Henry, Toney, Combined cathodoluminescence/backscattered electron imaging and trace element analysis with the electron microprobe: Applications to geologic materials, 339
- Storms, Artaxo, Bryunseels, Van Grieken, Individual particle analysis by automated EPMA for the improvement of source apportionment studies for remote aerosols, 343
- Recca, Lange, Grove, MINQUANT I: A quantitative analysis for Tracor Northern TASK5, 346
- Lange, Recca, MINQUANT II: A mineral code soft key program for Sandia TASK8, 348
- Calvo, Guilemany, Gómez de Salazar, Ureña, SEM-BSE microstructure of PbZn ore from Navalmedio, Ciudad Real, Spain, 349

## 9. LASER MICROPROBE ANALYSIS (R. A. Fletcher)

- \*Seydel, Lindner, LAMMA as a tool in microbiology, 353
- Artaxo, Storms, Van Grieken, LAMMA study of aerosol samples collected in the Amazon Basin, 356
- Schröder, Einerhand, Lauer, Eschweiler, Langner, Fain, Bauch, Multi-isotope multi-element labeling in microbeam analysis of biological tissues, 359
- Musselman, Rickman, Linton, Fingerprinting of chemical species in microparticles: Correlative laser and electron microprobe studies, 361
- Linton, Musselman, Bruynseels, Simons, Inorganic cluster ion formation in the laser microprobe, 365
- Fletcher, Curie, Observations derived from the application of principal-component analysis to the laser microprobe mass spectrometer, 369
- Author index, 372

## Note

This volume contains substantially all papers presented at the 22nd Annual Meeting of the Microbeam Analysis Society, except a group of papers on surface analysis, which will appear in the companion volume *Analytical Electron Microscopy—1987* scheduled for publication at the end of 1987.

### Officers of the Microbeam Analysis Society (1987)

#### *MAS Executive Council*

*President:* Charles E. Fiori, National Institutes of Health, Bethesda, Md.  
*President Elect:* W. F. Chambers, Sandia National Laboratories, Albuquerque, N.M.  
*Past President:* Gordon Cleaver, General Electric Co., Vallecitos Nuclear Center, Pleasanton, Calif.  
*Treasurer:* A. D. Romig Jr., Sandia National Laboratories, Albuquerque, N.M.  
*Secretary:* John T. Armstrong, California Institute of Technology, Pasadena, CA 91125, (818) 356-6253

#### *Directors*

Gary Aden, Kevex Corp., Foster City, Calif.  
Ron Gooley, Los Alamos Scientific Laboratory, Los Alamos, N.M.  
Tom Huber, JEOL (USA) Inc., Peabody, Mass.  
Peter Ingram, Research Triangle Institute, N.C.  
John Small, National Bureau of Standards, Gaithersburg, Md.  
David B. Williams, Lehigh University, Bethlehem, Pa.

#### *Honorary Members*

L. S. Birks, Naval Research Laboratory, USA  
I. B. Borovskii, Academy of Sciences, USSR  
Raymond Castaing, University of Paris (Orsay), France  
V. E. Cosslett, University of Cambridge, Great Britain  
Peter Duncumb, Tube Investments Research Laboratories, Great Britain  
T. A. Hall, University of Cambridge, Great Britain  
K. F. J. Heinrich, National Bureau of Standards, USA  
R. E. Ogilvie, Massachusetts Institute of Technology, USA  
Gunji Shinoda, Osaka University, Japan  
D. B. Wittry, University of Southern California, USA



### **Sustaining Members' Information**

AMRAY, INC.  
160 Middlesex Turnpike  
Bedford, MA 10730

Product Contact: Greg Cameron, Ken Benoit, (617) 275-1400

Product Line: Manufacturer of Scanning Electron Microscopes.

Regional Sales Offices:  
George Bruno, New England, (617) 275-8310  
Ed Griffith, Mid-Atlantic, (609) 662-3922  
Tom Richards, Mid-Atlantic-South, (609) 662-3922  
Ken Lindberg, Jr., South-East, (305) 767-4220  
Mark Reynolds, Mid-East, (216) 579-0035  
Fred Feuerstein, Mid-West, (312) 695-6117  
Don Brayton, West Coast, (408) 748-1300  
Gerry O'Loughlin, West Coast, (408) 748-1300

BIO-RAD POLARON INSTRUMENTS, INC.  
19 Blackstone Street  
Cambridge, MA 02139

Product Contact: Robert Schoonhoven, Fran Stubits (617) 864-5820

Product Line: Sputter coating and carbon evaporation systems; Laser Scanning Microscope; CryoTrans SEM systems; TEM and SEM specimen preparation equipment; Metallurgical standards and reagents for specimen preparation.

Regional Sales Offices:  
Jane Knoper, 780 Trimble Rd., Bldg. 1, Suite 201, San Jose, CA 95131

CAMBRIDGE INSTRUMENTS, INC.  
P.O. Box 123  
Buffalo, NY 14240

Product Contact: Peter W. Boutell (716) 891-3009

Product Line: Scanning Electron Microscopes - EDX and WDX x-ray systems.

Regional Sales Offices:  
W. Wuestenhoefer, 2840 San Tomas Expsrwy., Suite 16, Santa Clara, CA 95051  
M. Cohen, 40 Robert Pitt Drive, Monsey, NY 10952  
R. Kanishak, 9360 Chartwell Drive, Dallas, TX 75243

CAMECA INSTRUMENTS, INC.  
2001 West Main Street  
Stamford, CT 06902

Product Contact: Thomas C. Fisher (203) 348-5252

Product Line: SX-50 Scanning Electron Microscope; IMS-4F Ion Microanalyzer.

Regional Sales Offices:  
Robert P. Johnson, Western Regional Sales Manager (203) 348-5252

DAPPLE SYSTEMS  
355 West Olive, Suite 100  
SUNNYVALE, CA 94806

Product Contact: Bill Stewart (408) 733-3283

Product Line: Microcomputer-based analytical instrumentation including image analysis and energy-dispersive x-ray analysis.

DENTON VACUUM, INC.  
2 Pinoak Ave.  
Cherry Hill, NJ 08003

Product Contact: Robert Specht, Chris O'Connor (609) 424-1012

Product Line: Gold sputter coaters for SEM; High-vacuum carbon coaters for TEM;  
Laboratory research vacuum evaporators.

EDAX INTERNATIONAL, INC.  
P.O. Box 135  
Prairie View, IL 60069

Product Contacts: Ken Mason, Technical Data (312) 634-0600  
Marilyn Tillman, Delivery & Prices (312) 634-0600

Product Line: Energy-dispersive x-ray analysis systems for x-ray microanalysis and image  
collection, display, and processing in SEMs, TEMs, and electron microprobes.

Regional Sales Offices:  
Richard Feller, Bannockburn, IL (312) 634-0600  
Frank Gibson, Spring, TX (713) 350-8654  
Brad Lawrence, San Jose, CA (408) 729-6442  
Eugene Martin, Silver Spring, MD (301) 598-8881  
Larry Williams, Snellville, GA (404) 979-5441

EMTEK Corporation  
25574 Rye Canyon Rd., Suite D  
Valencia, CA 91355

Product Contact: Robert E. Matchett (805) 257-1215

Product Line: Sales and service, Scanning Electron and Ion Microprobe Analyzers.  
Upgrades and retrofits for the former Bausch and Lomb and Applied Research Laboratories  
Microanalyzers.

Regional Sales Offices:  
Donald P. Leshner, 7718 Castle Rock Dr., Warren, OH 44484  
EMTEK GmbH, Hans-Bockler-Strasse 7, D-6078 Neu-Isenburg, West Germany

GATAN, INC.  
6678 Owens Drive  
Pleasanton, CA 94566

Product Contact: Kevin Scudder (412) 776-5260

Product Line: Specimen preparation equipment for material science; Specialized TEM  
specimen holders; Parallel-detection electron energy loss spectrometers.

Regional Sales Offices:  
Kevin Scudder, 780 Commonwealth Dr., Warrendale, PA 15086 (412) 776-5260

GW ELECTRONICS, INC.  
Norcross, Georgia 30092

Product Contact: Bob Lewis (404) 449-0707

Product Line: Electronic accessories for scanning electron microscopes.

INSTRUMENTS S.A., INC.  
173 Essex Avenue  
Metuchen, NJ 08840

Product Contact: Bruce D. Perrulli (201) 494-8660

Product Line: MOLE/Raman Molecular Microprobe; ICP Spectrometers; Monochromators;  
Spectrographs



INTERNATIONAL SCIENTIFIC INSTRUMENTS, INC.  
1457 McCarthy Blvd.  
Milpitas, CA 95035

Product Contact: Michael McCarthy (408) 945-2233

Product Line: International Scientific Instruments, Inc. (ISI) markets a full range of scanning electron microscopes, electron beam testing systems, and electron optical line width measuring equipment.

Regional Sales Office:  
International Scientific Instruments, Inc., Avon Park South, 20 Tower Lane, Building 2,  
Avon, CA 06001

JEOL USA, INC.  
11 Dearborn Road  
Peabody, MA 01960

Product Contact: Charles Nielsen, Steve Hamilton (617) 535-5900

Product Line: Electron microscopes (TEM, SEM, TEMSCAN), microprobes (Auger, electron, x-ray), linewidth measurement systems, electron beam lithography systems.

Regional Sales Offices:  
Thayer Brickman, Jack Francis  
JEOL U.S.A., Inc., 3500 W. Bayshore Rd., Palo Alto, CA 94303, (415) 493-2600

KEVEX CORPORATION  
1101 Chess Drive  
Foster City, CA 94404

Telex: 760-7256 KEVEX UC  
Fax: 415-573-1539

Product Contact: Drew Isaacs (415) 573-5866

Product Line: Complete product line of materials analysis systems for qualitative and quantitative x-ray and digital image analysis. Product line includes instrumentation for energy-dispersive x-ray analysis, wavelength-dispersive analysis, Auger and electron energy loss spectrometry, and digital image acquisition and feature analysis. Also featured are systems for automated chemical and digital image analysis. Analyzers may be multitasked for simultaneous use by several operators and interfaced with VAX and other computers. X-ray detectors for all elements heavier than Be and digital beam control systems are available for all models of electron microprobes, SEM, TEM, and STEM.

Regional Sales Offices:  
9989 Windsor Way, San Ramon CA 94583 (415) 828-2188  
71 Rising Trail Drive, Middleton, CT 06457 (717) 639-2330  
16 Barberrry Hill Road, Gainesville, GA 30506 (404) 889-1363  
2617 N. Central Park, Chicago, IL 60647 (312) 384-1260  
109-F Corporate Blvd., S. Plainfield, NJ 07080 (201) 754-2277  
19635 Cottonwood Trail, Strongsville, OH 44136, (216) 238-8666  
107 Danbury Drive, Oak Ridge, TN 37380 (201) 754-2277  
6417 Glenmoor Avenue, Garland, TX 75043 (214) 699-1944  
PO Box 200, Mercer Island, WA 98040 (206) 232-3444  
P.O. Box 505, Thornhill, Ontario L3T 4A2 Canada (416) 731-2161

KRISEL CONTROL, INC.  
16 Farsta Court  
Rockville, MD 20850

Product Contact: Christos Hadidiacos (301) 762-1790

Product Line: Automation equipment for electron microprobe/microscope, featuring on-line data acquisition and reduction with Alpha and ZAF correction schemes. Single-crystal automation system for on-line data collection, centering, calculation of orientation matrix, and refinement of cell parameters for an x-ray diffractometer.

LINK ANALYTICAL  
240 Twin Dolphin Drive, Suite B  
Redwood City, CA 94065

Product Contact: Frank Brown, Dave Edwards (415) 595-5465

Product Line: Energy- dispersive x-ray microanalysis and x-ray fluorescence systems.

LOGETRONICS, INC.  
7001 Loisdale Road  
Springfield, VA 22150

Product Contact: Lynell D. Cameron (703) 971-1400, Telex 89-455

Product Line: Manufacturer of photographic enlargers and reducers which are used to produce enhanced prints from electron microscope films or similar imagery such as industrial x-ray films.

WALTER C. McCRONE ASSOCIATES, INC.  
850 Pasquinelli Drive  
Westmont, IL 60559

Product Contact: John Gavrilovic (312) 887-7100

Product Line: Analytical and consulting services -- ultramicroanalysis, small-particle analysis, light microscopy, analytical electron microscopy, scanning electron microscopy, electron microprobe analysis, secondary ion mass spectrometry, micro x-ray diffraction, organic microanalysis for small particles and subnanogram samples. Failure analysis on solid-state devices, bond failures, corrosion problems, thin-film analysis. Microscopy supplies and accessories, microscope sales (Olympus microscope dealer), light microscopy supplies. Asbestos consulting and testing, analysis of suspect materials for asbestos by light microscopy and/or electron microscopy, building surveys, air sampling, monitoring during abatement projects.

Regional Sales Offices:  
Ian M. Stewart/Bonnie L. Betty, McCrone Accessories and Components, 2508 S. Michigan Ave.  
Richard L. Hatfield, McCrone Environmental Services, 5500 Oakbrook Parkway, Suite 200  
Norcross, GA 30093, (404) 449-8474 or 8461

MICRON, INC.  
3815 Lancaster Pike  
Wilmington, DE 19805

Product Contact: James F. Ficca, Jr. (302) 998-1184

Product Line: Analytical service laboratory.

MICROSPEC CORPORATION  
45950 Hotchkiss Street  
Fremont, CA 94539

Product Contact: Richard C. Wolf, William D. Donnelly (415) 656-8820

Product Line: WDX-3PC Wavelength-dispersive x-ray spectrometer system.  
WDX-2A Wavelength-dispersive x-ray spectrometer system.

NISSEI SANGYO AMERICA, LTD.  
HITACHI SCIENTIFIC INSTRUMENT DIVISION  
460 Middlefield Road  
Mountain View, CA 94043

Product Contact: Hideo Naito (415) 961-0461

Product Line: Scanning electron microscopes, transmission electron microscopes.

Regional Sales Offices:  
Nissei Sangyo America, Ltd., 2096 Gaither Rd., Rockville, MD 20850  
Nissei Sangyo America, Ltd., 1701 Golf Rd., Suite 401, Rolling Meadows,  
IL 60008  
Nissei Sangyo America, Ltd., 89 Galaxy Blvd., Suite 14, Rexdale,  
Ontario M9W 6A4, Canada

PERKIN-ELMER  
PHYSICAL ELECTRONICS DIVISION  
6509 Flying Cloud Drive  
Eden Prairie, MN 55344

Product Contact: Marlin A. Braun (612) 828-6318

Product Line: Full line of analytical instruments for surface and thin film analysis, including scanning Auger microprobes, Auger, ESCA, and SIMS, and components including LEED and ion guns, for research and production applications. Contract services for all of these techniques.

Regional Sales Offices:

Guy R. Messenger, 7310 Ritchie Highway., Suite 520, Glen Burnie, MD 21061, (301) 761-3053  
Edward T. Grabey, 5 Progress St., Edison, NJ 08820, (201) 561-6730  
Tom J. Swanson, 564 Forbes Ave., Suite 1312, Pittsburgh, PA 15219, (412) 261-6760  
Christopher J. Macey, 2 Taunton St., Plainville, MA 02762, (617) 695-7181  
John J. Kadlec, 1011 S. Sherman St., Richardson, TX 75081, (214) 669-4419  
Jude H. Koenig, Meredith J. Bigley, 151 Bernal Rd., Suite 5, San Jose, CA 95119  
(408) 629-4343

Elm W. Sturkol, 325 Canyon Center, 1881 Ninth St., Boulder, CO 80302, (303) 449-4573  
Dave Harris, Bill Stickle, 1161-C San Antonio Rd., Mt. View, CA 94043, (415) 967-2600  
Europe: Bahnhofstrasse 30, D-8011 Vaterstetten, West Germany, Tel. 011-49-8106-3810

Hong Kong: 303 Fourseas Bldg., 208-212 Nathan Rd., Tsimshatsui, Kowloon,  
Hong Kong., Tel. 3-7210788, TLX 37753 HKPHIHX, Dr. John P. Chan

Japan: ULVAC PHI, Inc., 2500 Hagisono, Chigasaki-shi, Kanagawa-ken,  
Japan, Tel. 0467-85-6522, TLX. 3862157

India: Blue Star, Ltd., Sahas, 414/2 Vir Savarkar Marg., Probhadev 1,  
Bombay 400 025, India

PHILLIPS ELECTRONIC INSTRUMENTS, INC.  
85 Mckee Drive  
Mahwah, NJ 07430

Product Contact: John S. Fahy (201) 529-3800

Product Line: Transmission analytical electron microscopes, scanning analytical electron microscopes, and analytical accessories for electron microscopes.

Regional Sales Offices:

A. Hugo, 55 Virginia Ave., West Nyack, NY 10994  
D. Ahr, 6231 Executive Blvd., Rockville, MD 20852  
H. Ittner, 155 N.E. 100th St., Suite 403, Seattle, WA 98125  
T. Bates, 7094 Peachtree Industrial Blvd., Suite 220, Norcross GA 30071  
B. Smick, Suite D45, 2525 East Oakton, Arlington Heights, IL 60005  
Ms. Jo Long, 7302 Harwin Dr., Suite 106, Houston, TX 77036  
S. Spiers, 3000 Scott Blvd., Suite 113, Santa Clara, CA 95050

POLAROID CORPORATION  
575 Technology Square  
Cambridge, MA 02139

Product Contact: Elinor Solit (617) 577-4337

Product Line: Cameras, films, and associated equipment.

Regional Sales Offices:

Call 1-800-225-1618 for local dealers, contacts, and information.

PRINCETON GAMMA-TECH, INC.  
1200 State Road  
Princeton, NJ 08540

Product Contact: Mark Smith (609) 924-7310

Product Line: Princeton Gamma Tech's product line consists of the PGT System 4+ microanalysis system with complete EDS x-ray analysis capabilities for SEM, TEM, and STEM. Also highlighted in our product line is PGT Imagecraft, digital image processing, enhancement and quantitative image analysis for light microscopy as well as electron microscopy.

Regional Sales Offices:

PGT, 568 Weddell Drive, Suite 1, Sunnyvale, CA 94089 (408) 734-8124 Mr. Dan Berger

QBI INTERNATIONAL  
2034 Golden Gate Avenue  
San Francisco, CA 94115

Product Contact: Quentin A. Brown (415) 929-1622

Product Line: The SEMSCAN, a wavelength-dispersive spectrometer that excels in the analysis of light elements.

SPECTRA-TECH, INC.  
652 Glenbrook Road  
P.O. Box 2190G  
Stamford, CT 06906

Product Contact: Linda Finger (800) 243-9186, (in CT) (203) 357-7055

Spectra-Tech Europe, Ltd., Genisis Center, Science Park South, Birchwood,  
Warrington, WA3 7BH England, Tel. National Padgate (0925) 810 418,  
International +4492 581 0418  
Sanyo Shuppan Boeki Co., Inc., P.O. Box 5037, Tokyo International,  
100-31 Japan Tel. (02) (699) 3761

SPI SUPPLIES  
DIVISION OF STRUCTURE PROBE, INC.  
535 E. Gay Street  
PO Box 656  
West Chester, PA 19381-0656

Product Contact: Charles A. Garber, Ph.D. (215) 436-5400

Product Line: SPI Supplies: Small instruments and consumable supplies for electron microprobe and electron microscope laboratories including sputter coaters, table-top vacuum evaporators, and microprobe standards. Structure Probe: Independent laboratory providing SEM/EDS, TEM, probe, Auger, XPS, XRD, and other services for industry and government. Member of American Council of Independent Laboratories; accredited by American Association for Laboratory Accreditation.

Laboratories:  
230 Forrest St., Metuchen, NJ 08840, (201) 549-9350  
63 Unquowa Rd., Fairfield, CT 06430, (203) 254-0000  
1015 Merrick Rd., Copiague, L.I., NY, (516) 789-0100

Regional Sales Offices:  
SPI Supplies/Canada, PO Box 187, Station "T", Toronto, Ont.,  
Canada M6B 4A1, (416) 787-9193

C. M. TAYLOR CORPORATION  
289 Leota Avenue  
Sunnyvale, CA 94086

Product Contact: Dr. Charles M. Taylor (408) 245-4229

Product Line: Standards for microbeam analysis by SEM, microprobe, and ion probe using energy-dispersive, wavelength-dispersive, and mass spectrometers. Standards available exceed 175 different metals, alloys, glasses, and compounds or minerals. Bence-Albee standards are available. Manufacture many types of sample holders, polishing jigs, and other equipment for sample preparation. Also offer electron microprobe analytical services using a MAC-5 instrument, with FRAME B or Bence-Albee correction procedures.

M. E. TAYLOR ENGINEERING, INC.  
21604 Gentry Lane  
Brookville, MD 20833

Product Contact: M.E. (Gene) Taylor (301) 942-3418

Product Line: Scintillators, SEM supplies, secondary and backscatter electron detectors, vacuum foreline traps, specimen stubs, filaments and related items. Precision machine work and scientific glass blowing. Repair most EDS detectors.

Regional Sales Office:  
Dave Ballard, 15817 Crabbs Branch Way, Rockville, MD 20855, (301) 330-0077

TRACOR NORTHERN, INC.  
2551 West Beltline Highway  
Middleton, WI 53562

Product Line: Scanning electron microscopes.

Regional Sales Office:  
Vickers Instruments, Inc., 800 W. Cummings Park, Suite 1900, Woburn,  
MA 01801, (617) 932-3800

CARL ZEISS, INC.  
One Zeiss Drive  
Thornwood, NY 10594

Product Contact: William I. Miller, III (914) 747-1800

Product Line: Electron Microscopes, TEM/SEM

Regional Sales Offices:  
Dietrich Voss, PO Box 2025, Willis, TX 77378, (409) 856-7678



# 1. Presidential Symposium

## THE HISTORY AND FUTURE OF THE SCANNING ELECTRON MICROSCOPE

Oliver C. Wells

The scanning electron microscope (SEM) is 52 years old. Here, I shall describe the development so far and try to see how it will continue. The main points are, first, the development of the SEM was the work of many people; second, successful ideas are sometimes not immediately recognized as such even after being demonstrated in practice; and third, the progress that has led from an experiment in the laboratory to an extraordinarily successful commercial machine is likely to continue.

Unfortunately, the history must be kept brief. Accordingly, the bibliography has been cut off almost completely at 1965, which is when the earliest commercial SEM was announced. The present situation is then summarized briefly.

### *Historical Review*

Knoll (1935 and 1941) built an SEM in which the electron column was similar in many ways to a cathode-ray tube. The spot size was an appreciable fraction of a millimeter. He showed what can be done with simple apparatus. He demonstrated various "modern" ideas such as the television rate of scan; the use of low beam energy to avoid specimen charging; electron-channeling pattern (ECP) contrast in the secondary electron (SE) image to show the grains in a polycrystalline Si-Fe sheet; the use of the beam to induce a potential on a nonconducting particle and then to measure what this potential is; and so on.

Von Ardenne (1938 et seq.) added magnetic lenses to give a smaller beam diameter. He examined solid specimens before devoting his main effort to operation of the SEM in transmission. Oatley (1982) wrote: "Von Ardenne was the true father of the scanning electron microscope, who had all the right ideas. His misfortune was to have worked at a time when experimental techniques had not advanced quite far enough to enable him to bring those ideas to full practical fruition." (The very significant contributions that Prof. Oatley made to the development of the SEM are described below.)

V. K. Zworykin and his coworkers at RCA Laboratories made significant contributions to both the SEM and transmission electron microscope (TEM) in the 1940s. Zworykin, Hillier, and Snyder (1942) describe an SEM that had much in common with the modern form. Zworykin et al. (1945) discuss the theory of the SEM in some detail. The workers at RCA concluded

that the TEM was more valuable than the SEM because it was simpler and gave better resolution. (Some very good images of solid samples had been obtained using replicas.) In addition, there was work to be done in microanalysis (as described below). On this question, they may well have been right given the situation at that time. The concentration of their resources on the development of high-resolution techniques in the TEM and on microanalysis was generally regarded as being the most sensible thing to do. Work on the SEM was terminated.

In the late 1940s, the TEM was being established in many laboratories worldwide. Cambridge in England was no exception. V. E. Cosslett and his students were doing significant work at the Cavendish Laboratory.

This set C. W. Oatley a problem just down the road in the Engineering Laboratories. He was interested in electron microscopy as a method for training electrical engineers. It obviously did not make sense to compete directly against a group who were doing great things with microscopes that were at the forefront of what was available commercially.

Oatley decided that the wartime development of improved cathode-ray tubes and the more recent development of a demountable electron multiplier with Be-Cu dynodes by Baxter (1949) justified a renewed effort on the SEM. McMullan (1979) has said that the majority opinion was against it, but Gabor (1948) "took quite an optimistic view of its prospects."

Oatley (1972 et seq.) has described the way in which his students developed the SEM into its modern form. This work involved the development of the instrument, the theory of operation, and how it should be applied. He supervised the SEM work in detail until 1960, when he was elected Head of the Electrical Division in the Engineering Department. His place was taken by W. C. Nixon (1964 and 1968). It is quite clear that Prof. Oatley's contribution to the development of the SEM has not received the worldwide recognition it doubtless deserves.

A series of Ph.D. projects were started at that time. McMullan (1953) built an instrument with electrostatic lenses and obtained backscattered electron (BSE) images with a tilted specimen and with the BSE collector in the forward position. He was influenced in his choice of contrast mechanism by the development of the reflection electron microscope by Ruska (1933), von Borries (1940), and Menter (1952). His discussion of BSE image formation was of particular interest. The idea of the low-loss electron (LLE) image was proposed by him (1953a): "... the beam from the specimen could be restricted to the electrons which have lost only small amounts of energy and which have therefore travelled only short distances through the specimen." Oatley (1982) wrote: "A reading of his Ph.D. dissertation leaves one amazed at the amount of ground that he was able to cover." A replica of McMullan's SEM is in the Science Museum in London (McMullan

The author is at the IBM Thomas J. Watson Research Center, Box 218, Yorktown Heights, NY 10598.

### *Glossary*

BSE	backscattered electron(s)
EBIC	electron beam induced conductivity
ECP	electron channeling pattern
LLE	low-loss electron(s)
SE	secondary electron(s)
SEM	scanning electron microscope
TEM	transmission electron microscope

lan 1986).

(Later it was found that for topographic studies that used the LLE image, the collection solid angle as shown in Fig. 4(c) of McMullan (1953a) must include the plane of the specimen surface in the forward direction. I built an energy-filtering LLE detector in 1971.)

Smith and Oatley (1955) established the value of the secondary electron (SE) image for the study of rough samples, and studied dynamic processes in the SEM. The type of SE image that has become such a familiar sight in the popular press was first demonstrated by Ken Smith when he moved the electron multiplier in McMullan's SEM closer to the specimen. In the course of an investigation into the "forming" of point-junction contacts, Smith noticed that the entire image became brighter or darker when a few volts were applied to the specimen. This chance observation was the basis for Oatley's discovery of voltage contrast (see below). Smith also built a BSE detector in which an aluminized scintillator was mounted close to the sample to subtend a large solid angle, made a preliminary trial with a water vapor cell, and gave the signal-to-noise ratio condition for this type of detector. The idea of using a scintillator instead of a phosphor to collect electrons in the SEM was suggested by Oatley. In the 1950s this substitution gave a speed advantage. Nowadays, phosphors seem to be just as good.

Smith (1960) describes an SEM with magnetic lenses that he built and shipped to the Pulp and Paper Research Institute in Montreal. This was the first SEM to be applied to industrial problems on a routine basis. References are cited under Smith and under Buchanan. The paper by Smith (1959) is the first that contains SE images from rough samples of present-day quality. It has always been a mystery to me why this reference is cited so infrequently, considering how significant is the work that it contains.

I followed Smith, built an SEM, and in one of my experiments changed the position of the scintillator to see how this change affects the BSE image. The present status of this line of work is described elsewhere in these Proceedings. One of my scintillators had a hole in it for the beam to pass through on its way to the specimen, but here I must acknowledge that the general concept of symmetrical detection of BSE had been discussed by McMullan (1953). Concerning Oatley's research philosophy, on several occasions he said: "Why don't you put together something *simple* that *works*?"

The theory of SE imaging of topographic contrast at that time was as follows. Smith had demonstrated the value of the SE method from quite a wide range of samples. He had started to explain the underlying contrast mechanisms, and took part in many of the following discussions. In my thesis, I calculated the diameter of the escape area for SE excited by the beam as it *enters* the specimen, and argued that this figure will set an upper limit limit for the spatial resolution. (The situation at a sharp edge is different.) The references listed under Everhart et al.,

Thornley, and Pease et al. describe how the escaping BSE excites SE from a larger area, which provides useful signal at low magnification or a "background" at high magnification. What we all missed is that a fraction of the incoming beam remains remarkably compact during the early stages of the penetration into the sample, and this feature can sometimes show subsurface structures quite sharply by using the BSE-excited secondaries (i.e., the usual "bad guys" at high magnification) to give the signal.

By the early 1960s, research into the SEM was also taking place at Westinghouse, at Bell Laboratories (where an x-ray microanalyzer was used), in France, in Russia, and at some other locations also. Luminescent images were obtained by McMullan in 1953 (Smith and Oatley, 1955) and by Davoine et al. (1960). Tipper, Dagg, and Wells (1959) studied metal fractures. Everhart and Thornley (1960) described the SE detector that later became the standard in commercial SEMs. Thornley and Cartz (1962) used a low-beam energy to examine uncoated ceramics. Thornley, Brown, and Speth (1964) demonstrated the electron-beam storage of information. References to ion etching in the SEM are cited under Stewart, Boyde, and Broers. High-resolution studies were described by Pease and Nixon (1965a).

Work was also started with semiconductors. Oatley and Everhart (1957) obtained voltage contrast from a reverse-biased p-n junction. Time-resolved voltage contrast was demonstrated by Plows and Nixon (1968) and by MacDonald, Robinson, and White (1969). Semiconductors were also studied by Thornton et al. (1963), Spivak et al. (1964), and by the luminescent method of Wittry and Kyser (1964). Electron-beam fabrication was suggested by von Ardenne (1938) and was put into practice by Buck and Shoulders (1958), Möllenstedt and Speidel (1960), Shoulders (1960), Wells, Everhart, and Matta (1963 and 1965), Thornley and Sun (1965), and Broers (1965).

The electron voltaic effect was discovered by Ehrenberg, Lang, and West (1951). Everhart (1958) obtained a waveform as a finely focused electron beam was scanned across a p-n junction. Induced signal *images* (later called either *charge collection images* or *EBIC images*) were obtained by Wells, Everhart, and Matta (1963 and 1965), Everhart, Wells, and Matta (1963 and 1964), Lander et al. (1963), and Czaja et al. (1964 and 1965). So far as I know, the earliest demonstration of such images from a semiconductor device and of pattern registration during electron-beam fabrication by SEM techniques was in my two references above.

Stewart and Snelling (1965) describe the first commercial SEM, which was then marketed by the Cambridge Instrument Co. Kimoto and Hashimoto (1966) collected BSE using a pair of solid-state diodes, and described the "sum-or-difference" BSE imaging technique for showing either the compositional variations or the surface topography of the specimen. Shortly thereafter JEOL introduced a commercial SEM.

Microanalysis of thin films by the energy-loss method was demonstrated by Hillier (1943



et seq.). The x-ray microanalyzer with a static probe was proposed by Hillier (1947) and demonstrated by Castaing and Guinier (1949). The x-ray microanalyzer with a scanning electron beam was demonstrated by Cosslett and Duncumb (1956). The development of a commercial instrument took place slightly earlier than for the SEM. In view of what I say below, it is interesting to see that Cosslett and Duncumb (1957) mounted the sample for microanalysis in the high-field region of a condenser-objective lens.

I hope that I can be forgiven for not summarizing the development of the SEM after the announcement of commercial models in 1965. The number of people who have contributed significantly to the subject is far too large. Suffice to say that by 1987 commercial SEMs have reached such an advanced state of excellence that the researcher is forced either to apply them as they are, or to search (in the manner of Prof. Oatley, perhaps) for ideas that for some reason have become "unfashionable" in the hope that such a search will lead to something useful and new. A recent example is the reflection electron microscope, which fell into disuse in the 1950s but was restored to the forefront of microscopy by innovations introduced by Osakabe, Yagi, and Honjo (1980).

#### *The Next 50 Years*

The first step in foreseeing what will happen in the next 50 years is to look at Knoll's 1935 paper and realize that the most important component of the modern SEM that is missing is the computer. The way in which computers are increasingly being used to control the apparatus and to record, evaluate, process and replay the data is shown in Table 1.

One of the earliest uses of computers was in x-ray microanalysis, where a relatively small amount of "hard data" had to be processed in a fairly elaborate way. As often as not they were processed by being sent to the main computer. Use of a small, dedicated machine followed. The processing of images is taking much the same path. Soon every instrument will contain a computer as an essential component.

The first item shown in Table 1 is the use of a computer to adjust the apparatus, which is already being done in a partial way. One of the earliest examples is in the control program for the x-ray microanalyzer, in which the computer automatically adjusts a wavelength spectrometer to the maximum count rate for a chosen x-ray peak. Measurement of the beam current in the x-ray microanalyzer is another example. SEMs are sold with an optional feature to adjust the focus automatically. Perhaps one of the most comprehensive examples of the computer control of an instrument is in electron-beam lithography, where the computer centers the electron gun, aligns the column, moves the table, searches for the index marks, generates the exposure pattern, pulses and deflects the electron beam, and so on. It is to be expected that in the future this approach will be applied routinely even in the simplest of commercial SEMs.

Table 1 also shows the use of a computer to

record, manipulate, and replay data. The use of text-handling techniques to add comments to the data is also noteworthy.

An additional use of computers in scanning electron microscopy is in the modeling of image contrasts. Monte Carlo calculations of electron penetration in solid targets were carried out on a small computer by Curgenven and Duncumb (1971). This approach has been considerably extended by Joy (1984). It permits the calculation of edge effects, the imaging of subsurface structures, resolution limits, and so on.

The improvement in the quality and quantity of work that will be achieved by the use of computers to control apparatus is only just becoming evident. It will surely become even more important in the future.

One of the factors that has contributed greatly to the success of the SEM has been the growth of the microelectronics industry. A major factor here has been the trend to smaller devices, narrower lines, and thinner films. Advances can be expected in any aspect of the SEM that impacts upon this industry, such as linewidth measurement, profile measurement, improved resolution, improved measurement accuracy, reduced beam damage by low-voltage and low-dose techniques, systematic measurements of patterns that are repeated over a large area, searching for defects, automatic operation without the need of an operator, and analysis of a large mass of data.

In the biological field, a major part of the work is in specimen preparation. Ways are needed to examine nonconducting samples without a conducting surface layer. Low-dose techniques are needed to minimize damage to the specimen. (The possibilities offered by computer control are obvious.) Low-voltage operation gives good images of low-density samples; here, there is a need to obtain good resolution in spite of the difficulties in focusing of low energy beams. Cryotechniques are also useful.

A parallel line of development is in the discovery and development of new forms of image contrast. The first step is usually to examine the physical processes involved in existing methods of image formation more closely. Thus, in the case of the SE image, it will almost certainly be useful to take the SE one at a time and measure the energy, direction, number of SE emitted simultaneously, other types of coincidence effect, and so on. It seems likely that this goal can best be achieved in ultrahigh vacuum. Ideas must be stolen from surface science. Similar methods can be applied to BSE and x-ray microanalysis also.

An interesting present trend is the development of SEMs for the examination of solid specimens in the high-field region of a condenser-objective lens. The improvement that this approach gave in the TEM is described by Ruska (1965): "The specimen must lie in the position at which the axial field strength is a maximum. Such an imaging field, which simply decreases from a maximum, has a spherical aberration constant about 10 times smaller than the magnetic objectives hitherto used, where the specimen is generally situated in

front of the whole field; the chromatic aberration constant is half as small, and the resulting resolution limit is nearly twice as good." Images can be obtained by the collection of SE, BSE, or LLE; it is expected that all these methods will be considerably improved.

A further line of development, unspectacular perhaps but nonetheless significant, will be the steady improvement in all aspects of the apparatus. Better vacuum, smaller electron beams, and the further development of surface-sensitive techniques are all important.

Obviously it is not possible to predict the future development of a subject with total accuracy. However, in the case of the SEM the present widespread level of interest and rate of progress leaves one feeling confident that significant developments are sure to occur.

#### *Appendix*

Professor Oatley commented on a preliminary draft of this paper as follows:

"Would you consider putting in a mention of Les Peters? It was actually he and I who

first showed contrast at a p-n junction. Everhart arrived shortly afterward and publication was delayed until he had completed a more thorough investigation. . . . Les Peters . . . contributed so much that I would like to see his name somewhere.

". . . You draw a distinction between phosphors and scintillators. . . . The basic idea of electron-phosphor-photomultiplier came from the 1940 RCA work, though their arrangement was . . . inefficient. McMullan and I considered this possibility but thought the afterglow of phosphors then available was too long for a 1-second frame scan. When organic scintillators were developed by the nuclear people, I got hold of a piece and gave it to Ken Smith, who was nearing the end of his time as a research student. He used it for the detection of fast backscattered electrons. I think I probably made the rather obvious suggestion of using a light pipe. The basic ideas were then ready for the more detailed work of Everhart and Thornley. Nowadays P-47 phosphor is commonly used on the end of the light pipe, so why the distinction between scintillators and phosphors?"

TABLE 1.--Computer-aided imaging in the x-ray microanalyzer and SEM.

	<b>X-Ray Microanalyser</b> (usually a spectrum)	<b>SEM</b> (usually an image)
<b>Set up the system:</b>	Measure current Adjust spectrometers	Automatic focus
<b>While recording the data:</b>	Control apparatus Record parameters Calculate dead-time Move the specimen	Scan the beam Put data on photo Integrate noise Move the specimen
<b>Compute:</b>	Identify peaks Measure peaks Subtract background Deconvolute spectra Calculate ZAF Store data	Measure line-widths Measure inclusions Adjust levels Subtract images Process images Store image
<b>During the replay:</b>	Control format (Text handling)	Control format (Text handling)
<b>Model image contrasts:</b>	Monte Carlo	Monte Carlo

### Bibliography on the SEM and related subjects 1935-1965:

- Ahmed H, and Beck A H W, (1963): "Thermionic emission from dispenser cathodes." J. Appl. Phys. **34**, 997-998.
- Allen J W, and Smith K C A, (1956): "Electron microscopy of etched germanium surfaces." J. Electronics **1**, 439-443 and 2 plates.
- Ardenne M von (1938a): "The scanning electron microscope: practical construction" (in German). Z. Tech. Phys., **19**, 407-416.
- (1938b): "The scanning electron microscope: theoretical fundamentals" (in German). Z. Phys., **109**, 553-572.
- (1978): "The history of scanning electron microscopy and of the electron microprobe" (in German with English abstract). Optik **50**, 177-188.
- (1985): "On the history of scanning electron microscopy, of the electron microprobe, and of early contributions to transmission electron microscopy." Adv. El. El. Phys., Suppl. 16, 1-21, P.W. Hawkes, Ed., Academic Press.
- Atack D, and Smith K C A, (1956): "The scanning electron microscope. A new tool in fibre technology." Pulp Paper Mag. Canada (Convention issue) **57**, 245-251.
- Baxter A S, (1949): "Detection and analysis of low energy disintegration particles." Ph.D. Diss., Univ. Cambridge, England.
- Beck A H W, and Ahmed H, (1963): "The activation process in dispenser cathodes." J. Electron. Control **14**, 623-627.
- Borries B von (1940): "Sub-light-microscopical resolution when imaging surfaces in the electron microscope" (in German). Z. Physik, **116**, 370-378.
- Boyde A and Stewart A D G, (1962): "A study of the etching of dental tissues with argon ion beams." J. Ultrastruct. Res. **7**, 159-172.
- and Stewart A D G, (1963): "Scanning electron microscopy of the surface of developing mammalian dental enamel." Nature (London) **198**, 1102-1103.
- Brachet C, (1946): "Note on the resolution of the scanning electron microscope" (in French), Bull. L'Assoc. Tech. Mar. et Aero., No. 45, 369-378.
- Broers A N, (1965a): "Combined electron and ion beam processes for microcircuits." Microelectronics and Rel. **4**, 103-104 and 1 plate.
- (1965b): "Micromachining by sputtering through a mask of contamination laid down by an electron beam. First Int. Conf. Electron and Ion Beam Sci. and Tech., R.A. Bakish, Ed., 191-204.
- Buchanan J G, and Smith K C A, (1960): "Preliminary studies of damage in papermaking wood chips using the scanning electron microscope." pp. 547-550 in: Proc. Eur. Reg. Conf. El. Microsc.; Delft, Aug. 1960.
- Buck D A, and Shoulders K R, (1958): "An approach to microminiature printed systems." in Proc. Eastern Joint Computer Conference, Dec. 1958.
- Castaing R, and Guinier A (1949): "Application of electron probes to metallographic analysis" (in French). Pages 60-63 in: Proc. 1st Conf. El. Microsc., Delft.
- (1951): "Application of electron probes to local chemical and crystallographic analysis." Ph.D. Diss., Univ. Paris.
- Cosslett V E, and Duncumb P, (1956): "Micro-analysis by a flying-spot x-ray method." Nature (London) **177**, 1172-1173.
- and Duncumb P, (1957): "A scanning microscope with either electron or x-ray recording." Electron Microscopy. Proc. Stockholm Conf., Sept. 1956. Almquist and Wiksells, Uppsala; Academic Press, New York, U.S.A., 1957, 12-14.
- Curgenven L, and Duncumb P, (1971): Report 303 dated 28 July 1971, available from Tube Investments Research Laboratories, Hinxton Hall, Hinxton, Saffren Walden, Essex, England.
- Czaja W, and Wheatley G H (1964): "Simultaneous observation of diffusion-induced dislocation slip patterns in silicon with electron beam scanning and optical means." J. Appl. Phys **35**, 2782-2783.
- and Patel J R (1965): "Observations of individual dislocations and oxygen precipitates in silicon with a scanning electron beam method." J. Appl. Phys **36**, 1476-1482.
- Davoine F, Pinard P, and Martineau M, (1960): "Observation of cadmium sulphide bombarded with electrons of 5 kev energy" (in French). J. Phys. Radium **21**, 121-124.
- Ehrenberg W, Lang C S, and West R (1951): "The electron voltaic effect." Proc. Phys.

- Soc.(London) **A64**, p. 424 only.
- Everhart T E**, (1958): "Contrast formation in the scanning electron microscope." Ph. D. Diss., Cambridge Univ., England.
- , Wells O C, and Oatley C W, (1959): "Factors affecting contrast and resolution in the scanning electron microscope." *J. Electron. Control*, **7**, 97-111.
- (1960): "Simple theory concerning the reflection of electrons from solids." *J. Appl. Phys.* **31**, 1483-1490.
- , Smith K C A, Wells O C, and Oatley C W, (1960): "Recent developments in scanning electron microscopy." pp. 269-273 in: *Proc. Fourth Int. Conf. on Electron Microscopy*; Berlin Sept. 1958; Vol. 1. Physics, W. Bargmann et al, eds; Springer Verlag, Berlin, 1960.
- and Thornley R F M, (1960): "Wide-band detector for micro-microampere low-energy electron currents." *J. Sci. Instrum.*, **37**, 246-248.
- , Wells O C, and Matta R K (1963): "Evaluation of passivated integrated circuits using the scanning electron microscope." (Extended Abstract), *Electrochemical Society, Electronics Division* **12**, no. 2, 2-4. (New York meeting, Oct. 1963.)
- , Wells O C, and Matta R K (1964a): "Evaluation of passivated integrated circuits using the scanning electron microscope." *J. Electrochem. Soc.*, **111**, 929-936.
- , Wells O C, and Matta R K (1964b): "A novel method of semiconductor device measurements." *Proc. IEEE*, **52**, 1642-1647.
- Gabor D**, (1948): "The Electron Microscope," 2nd. Ed., Reinhold.
- Green D** and Nathanson H C (1965): "Observation of inversion layers under insulated-gate electrodes using a scanning electron microscope." *Proc. IEEE*, **53**, 183-184.
- , Sandor J E, O'Keeffe T W and Matta R K, (1965): "Reversible changes in transistor characteristics caused by scanning electron microscope examination." *Appl. Phys. Lett.* **61**, 3-4.
- Hillier J**, (1943): "On microanalysis by electrons." *Phys. Rev.* **64**, 318-319.
- and Baker R F, (1944): "Microanalysis by means of electrons." *J. Appl. Phys.* **15**, 663-675.
- (1947): "Electron probe analysis employing x-ray spectrography." U.S. Patent 2,418,029.
- Joy D C**, (1984): "Beam interactions, contrast, and resolution in the SEM." *J. Microsc.* **136**, 241-258.
- (1985): "Resolution in low voltage scanning electron microscopy." *J. Microsc.* **140**, 283-292.
- Kimoto S**, and Hashimoto H (1966): "Stereoscopic observation in scanning microscopy using multiple detectors." Pages 480-489 in: *The Electron Microprobe. Proc. Symp. held in Washington, D.C., Oct. 1964.* T.D. McKinley et al Eds., J. Wiley and Sons, New York, N.Y.
- Knoll M** (1936): "Static potential and secondary emission of bodies under electron irradiation" (in German). *Z. Tech. Phys.*, **11**, 467-475.
- (1941): "Deflecting action of a charged particle in the electric field of a secondary emitting cathode" (in German). *Naturwiss.*, **29**, 335-336.
- Lander J J**, Schreiber H, Buck T M, and Mathews J R (1963): "Microscopy of internal crystal imperfections in Si p-n junction diodes by use of electron beams." *Appl. Phys. Lett.*, **3**, 206-207.
- McAuslan J H L**, and Smith K C A, (1956): "The direct observation in the scanning electron microscope of chemical reactions." pp. 343-345 in: *Electron Microscopy. Proc Stockholm Conf.*; Sept. 1956. F.S. Sjostrand and J. Rhodin, Eds; Academic Press, N.Y. 1957.
- MacDonald N C**, Robinson G Y and White R M (1969): "Time-resolved scanning electron microscopy and its application to bulk-effect oscillators." *J. Appl. Phys.* **40**, 4516-4528.
- Mackintosh I M**, (1965): "Applications of the scanning electron microscope to solid-state devices." *Proc. IEEE*, **53**, 370-377.
- McMullan D** (1953a): "An improved scanning electron microscope for opaque specimens." *Proc. IEE* **100 Pt. II**, 245-259.
- (1953b): "The scanning electron microscope and the electron-optical examination of surfaces." *Electronic Eng.*, **25**, 46-50.
- (1979): Unpublished notes.
- (1985): "Recollections of the early days of SEM in the Cambridge University Engineering Department, 1948-53." *J. Microscopy* **139**, Pt. 2, Aug. 1985, 129-138.
- (1986): "Replica of the first Cambridge SEM for the Science Museum." *Proc. Roy. Microsc. Soc.* **21**, 203-206.
- Menter J W** (1952): "Direct examination of solid surfaces using a commercial electron microscope in reflection." *J. Inst. Metals*, **81**, 163-167 and 3 plates.

- Möllenstedt G**, and **Speidel R**, (1960): "Electron optical microrecorder with electron microscopic control" (in German), *Physik. Blatter* **16**, 192-198.
- Nixon W C** (1964): "Scanning electron microscopy." *J. Roy. Microsc. Soc.* **83**, 213-216 and 2 plates. Reprinted: *Microelectron. Rel.* **4**, 3889-3890.
- (1968): "Twenty years of scanning electron microscopy, 1948-1968, in the Engineering Department, Cambridge University, England." *SEM1968*, O. Johari, Ed., 55-62.
- Oatley C W** and **Everhart T E** (1957): "The examination of p-n junctions with the scanning electron microscope." *J. Electronics* **2**, 568-570 and 1 plate.
- , **Nixon W C**, and **Pease R F W**, (1965): "Scanning electron microscopy." *Advan. Electron. Electron Phys.*, **21**, 181-247.
- (1969): "Isolation of potential contrast in the scanning electron microscope." *J. Sci. Instrum. (J. Phys. E)*, **2**, 742-744.
- (1972): "The scanning electron microscope. Part I. The instrument." Cambridge Univ. Press, England.
- (1981): "Detectors for scanning electron microscope." *J. Phys. E: Sci. Instrum.*, **14**, 971-976.
- (1982): "The early history of the scanning electron microscope." *Appl. Phys. Rev.*, R1-R13 (published as a section of *J. Appl. Phys.* **53**(2), February 1982).
- , **McMullan D** and **Smith K C A** (1985): "The development of the scanning electron microscope." *Adv. El. El. Phys.*, Suppl. 16, 443-482, P.W. Hawkes, Ed., Academic Press.
- Osakabe N**, **Yagi K**, and **Honjo G** (1980): "Reflection electron microscope observations of dislocations and surface structure phase transition on clean (111) silicon surfaces." *Japan. J. Appl. Phys.* **19**, L309-L312.
- Pease R F W**, and **Nixon W C**, (1965a): "High resolution scanning electron microscopy." *J. Sci. Instrum.* **42**, 31-35.
- and **Nixon W C**, (1965b): "Microformation of filaments." Pages 220-230 in: *First Int. Conf. Electron and Ion Beam Sci. and Tech.*; Toronto, May 1964; R.A. Bakish, Ed.; John Wiley and Sons, N.Y.
- Plows G S**, and **Nixon W C** (1968): "Stroboscopic scanning electron microscopy." *J. Sci. Instrum. (J. Phys. E)*, **1**, 595-560. See also: *Microelectron. Rel.* **10**, 317-323 and 3 plates (1969).
- Ruska E** (1933): "Electron microscopic imaging of electron-irradiated surfaces" (in German). *Z. Physik*, **83**, 492-497.
- (1965): "Current efforts to attain the resolution limit of the transmission electron microscope." *J. Roy. Microsc. Soc.* **84**, Pt. 1, April 1965, 77-103.
- Shoulders K R**, (1960): "Research in microelectronics using electron-beam-activated machining techniques." Interim Scientific Report, Contract Nonr-2887(00), Office of Naval Research, Washington, DC (Sept. 1960).
- Smith K C A**, and **Oatley C W** (1955): "The scanning electron microscope and its fields of application." *Brit. J. Appl. Phys.*, **6**, 391-399.
- (1956): "The scanning electron microscope and its fields of application." Ph.D. Diss., Cambridge Univ., England.
- (1959): "Scanning electron microscopy in pulp and paper research." *Pulp Paper Mag. Canada* **60**, T366-T371.
- (1960): "A versatile scanning electron microscope." Pages 177-180 in: *Proc. Eur. Reg. Conf. on Electron Microsc.*; Delft 1960; Vol. 1; A.L. Houwink and B.J. Spit, Eds.; De Nederlandse Vereniging Voor Electronenmicroscopie, Delft; 1961.
- (1961): "Scanning." Pages 241-251 in: "Encyclopedia of Microscopy;" G.L. Clark, Ed.; Reinhold Publishing Corp., N.Y.
- Spivak G V**, **Saparin G V** and **Pereverzev N A**, (1962): "Potential distribution in a p-n junction as observed by electron-optical scanning." *Bull. Acad. Sci. USSR, Phys. Ser. (USA)* **26**, 1362-1365.
- , **Ivanov R D**, **Pavlyuchenko O P**, and **Sedov N N**, (1963): "Mechanism of contrast formation in mirror, emission and scanning electron-optical systems." *Bull. Acad. Sci. USSR, Phys. Ser. (USA)* **27**, 1120-1127.
- Stewart A D G**, and **Boyde A**, (1962): "Ion etching of dental tissues in a scanning electron microscope." *Nature (London)* **196**, 81-82.
- and **Snelling M A**, (1965): "A new scanning electron microscope." Pages 55-56 in: *Electron Microscopy. Proc. Third Eur. Reg. Conf.*; Prague, Sept. 1964; M. Titlebach, Ed.; Pub. House of Czechoslovak Academy of Sciences, Prague.

- Thornhill J W**, and Mackintosh I M, (1965): "Application of the scanning electron microscope to semiconductor device structures." *Microelectron. Rel.* **4**, 97-100.
- , **Matta R K**, and **Wood W H**, (1965): "Examining three-dimensional microstructures with the scanning electron microscope." *Grana Palynologica (Almqvist and Wiksells)*, **6**, 3-6 and 2 plates.
- Thornley R F M**, (1960a): "New applications of the scanning electron microscope." Ph.D. Diss., Cambridge Univ., Cambridge, England.
- (1960b): "Recent developments in scanning electron microscopy." Pages 173-176 in: *Proc. Eur. Reg. Conf on Electron Microsc.*; Delft 1960; Vol. 1; A.L. Houwink and B.J. Spit, Eds.; De Nederlandse Vereniging Voor Electronenmicroscopie, Delft; 1961.
- and **Cartz L**, (1962): "Direct examination of ceramic surfaces with the scanning electron microscope." *J. Amer. Ceramic Soc.*, **45**, 425-428.
- , **Brown A V**, and **Speth A J**, (1964): "Electron beam recording of digital information." *IEEE Trans. Electron Dev.* **ED-13**, 36-40.
- and **Sun T**, (1965): "Electron beam exposure of photoresist." *J. Electrochem. Soc.* **112**, 1151-1153.
- Thornton P R**, **Culpin M J**, and **Drummond I W**, (1963): "Direct observation of the high-field regions in GaAs." *Solid State Electron.* **6**, 532-533 and 2 plates.
- (1965): "The scanning electron microscope." *Sci. J.* **1**, 11, 66-71.
- Tipper C F**, **Dagg D I** and **Wells O C**, (1959): "Surface fracture markings on alpha iron crystals." *J. Iron Steel Inst. (London)*, **193**, 133-141.
- Wells O C**, (1957): "The construction of a scanning electron microscope and its application to the study of fibres." Ph.D. Diss., Cambridge Univ., Cambridge, England.
- (1959): "Examination of nylon spinneret holes by scanning electron microscopy." *J. Electronics and Control*, **7**, 373-376.
- (1960): "Correction of errors in stereomicroscopy." *Brit. J. Appl. Phys.* **11**, 199-201.
- , **Everhart T E**, and **Matta R K** (1963): "Automatic positioning of device electrodes using the scanning electron microscope." *Ext. Abstr. (Electrochem. Soc.), Electronics Div.*, **12**, no. 2, 5-12. (New York meeting, Oct. 1963.)
- , **T.E. Everhart** and **R.K. Matta** (1965). "Automatic positioning of device electrodes using the scanning electron microscope." *IEEE Trans. Electron Dev.* **ED-12**, 556-563.
- (1971): "Low-loss image for scanning electron microscope." *Appl. Phys. Lett.* **19**, 232-235.
- Wittry D B** and **Kyser D F**, (1964): "Use of electron probes in the study of recombination radiation." *J. Appl. Phys.* **35**, 2439-2442.
- and **Kyser D F**, (1965): "Cathodoluminescence at p-n junctions in GaAs." *J. Appl. Phys.* **36**, 1387-1389.
- Zworykin V K**, **Hillier J**, and **Snyder R L**, (1942): "A scanning electron microscope." *ASTM Bull.*, no. 117, 15-23.
- , **Morton G A**, **Ramberg E G**, **Hillier J**, and **Vance A W** (1945): "Electron optics and the electron microscope." *John Wiley and Sons*, New York, N.Y.

## 2A. EPMA: Analytical

### THE USE OF BACKGROUND IN THE ELECTRON PROBE ANALYSIS OF BULK SAMPLES

C. E. Nockolds

The information contained in the continuum radiation has been exploited in several areas of electron beam analysis. In thin-film analysis the Hall method<sup>1</sup> is used to compensate for variations in mass-thickness across a sample. For particles and rough bulk materials the P/B method<sup>2,3</sup> has been used to overcome the difficulties of calculating the matrix correction. In this paper the use of the background in the analysis of bulk samples with known geometry (i.e., flat polished samples) is explored.

The current generation of SEM/EDS analytical systems have the ability to carry out routine analysis, and in many cases to perform automatic analyses by moving the beam or the specimen stage. However, these systems usually have no convenient method of closely monitoring the beam current which means that the results have to be normalized to 100%. In conventional electron probe microanalyzers the non-normalized analysis total is a very useful indicator of some problem with the analysis (the beam down a hole in the sample), or the presence of an element not being analyzed. This study follows the work of Wendt and Schmidt,<sup>4</sup> who showed that an integrated region of background could be used as an alternative to directly measuring the beam current. Although the use of background under or close to the characteristic peaks has many advantages with respect to matrix corrections, the major disadvantages are that it is difficult to measure the background accurately under a large peak, and it requires long counting times to obtain good statistics. It seems sensible to follow Hall<sup>1</sup> and use a large region of background away from the characteristic peaks.

Kramers's equation for the continuum x rays, and the various modifications that have been proposed, suggest that there is a relationship between average atomic number ( $Z$ ) and background counts, in the form shown below.

$$B' = Ag(Z)$$

where  $B'$  is the background integrated over some range in energy, corrected for the effects of x-ray absorption and backscattered electrons in the sample;  $g(Z)$  is a function that expresses the relationship between  $B'$  and  $Z$ , which according to Kramer's law would be  $g(Z) = Z$ ; and  $A$  is a constant determined by the operating conditions (beam currents, accelerating voltage, etc.), the detector/specimen geometry, and the particular region used for the background integration. (Under typical conditions of analysis,  $A$  is essentially a measure of beam exposure.)

We define a peak-to-background ratio

$$PB = I/[B'/g(Z)] = 1/A$$

where  $I$  is the integrated intensity for a characteristic x-ray peak, and a  $k$ -ratio

The author is at the EM Unit, University of Sydney, N.S.W., 2006 Australia.

$$k^* = PB_u/PB_s$$

where the subscript  $u$  refers to the "unknown" sample and  $s$  refers to the standard. Then combining these two equations we obtain

$$k^* = (I/A)_u/(I/A)_s = I_u/I_s$$

This is the conventional  $k$ -ratio corrected for differences in beam current between the standard and the unknown. However, the correct value for  $A_u [= B'/g(Z)]$  cannot be calculated until the composition of the sample is known, and so the  $k$ -ratio  $k^*$  must be determined by iteration within the full matrix correction procedure. For example, if the preferred correction procedure is ZAF, then

$$C_u = (k^*C_s)ZAF_u/ZAF_s$$

#### Experimental

Because of the local requirements, and to simplify the process, the initial study was restricted to the range of compounds normally found in mineral silicates and oxides (essentially from  $MgO$  to  $Fe_2O_3$  or a range of average atomic number of 10 to 20). To insure adequate statistics and to avoid characteristic peaks, the integration range for the background was from 8 to 20 keV. The usual accelerating voltage for this range of samples is 15 kV; however, this voltage was increased to 20 kV to improve the count rate in the region above 8 keV.

We were able to simplify the correction of the integrated background  $B$  for absorption and backscatter greatly by calculating the factors at a single energy value within the energy range 8-20 keV, using a conventional ZAF algorithm. The data were collected by an EDAX 9900 Analyzer attached to a Philips 505 SEM. The specimen was tilted at  $18^\circ$  and the take-off angle to the detector was  $38^\circ$ . The total count rates were of the order of 4000 cps and the analysis time was set at 100 live seconds. Under these conditions the integrated background varied from approximately 24 000 counts for  $Al_2O_3$  to 50 000 counts for  $Fe_2O_3$ . The beam current was monitored by means of a Faraday cup mounted on the specimen stage.

Five well characterized, standard samples were used to determine the calibration curves shown in Figs. 1 and 2:  $Al_2O_3$ ,  $SiO_2$ ,  $TiO_2$ , and  $Fe_2O_3$ . Figure 1 shows the plot of  $B'$  versus  $Z$  for the five points and the least-squares fitted line. Figure 2 shows the plot of  $\log B'$  versus  $\log Z$ .

#### Results

As indicated by Figs. 1 and 2 there is an approximately straight-line relationship regardless of whether the plot is  $B'$  vs  $Z$  or  $\log B'$  vs  $\log Z$ , although the log plot gives a much closer fit to the least-squares line. The equations of the two fitted lines are

$$B' = 5095Z - 20598$$

$$\log B' = 1.388 \log Z + 7.154$$

For the linear plot the background is zero when  $Z = 4$ , which probably indicates that this straight-line function does not extend far beyond the present range. For the log plot,  $\log B'$  is zero when  $Z = 0.006$ . Consequently, it was decided to use the  $g(Z)$  derived from the log plot for subsequent calculations. The  $g(Z)$  function is

$$g(Z) = Z^{1.388}$$

To test the use of  $k^*$ , a series of measurements were made on the  $\text{CaSiO}_3$  standard. The beam current was varied from 0.5 to 0.63 nA and for three of the measurements (analyses 4, 5, 6 in Table 1) "bad" analysis points were chosen, as described at the bottom of Table 1. These points illustrate three of the many possible problems that might arise, for example during an automatic analysis run. In part (a) of Table 1, the  $k$ -ratios were derived from the ratio of characteristic intensities (with  $\text{CaSiO}_3$  used as the standard for both Ca and Si). These  $k$ -ratios were normalized and processed by a conventional ZAF procedure, and the final results normalized to 100% concentration by weight. In part (b)  $k^*$  was used as the  $k$ -ratio (once again with  $\text{CaSiO}_3$  used as the standard) and iterative refinement of  $k^*$  was added to the iteration process of the ZAF calculation. Since the standard and unknown are the same, it was not surprising to find that the convergence was reasonably quick. The calculations converged satisfactorily by simple iteration after 10 cycles. With a convergence routine such as the Wegstein procedure, the calculations converged after 5 cycles.

A further use of this method is that it allows for the determination of an element by difference (such as water in the silicate minerals). To test this feature a calculation was made using the raw data for analysis 3 in Table 1. In this calculation it was assumed that the compound contained CaO by difference and only the  $k$ -ratio for Si was included in the calculation (a rather extreme example of water by difference). Here it was necessary to assume initially that the compound was pure  $\text{SiO}_2$ . After convergence the final result was  $\text{SiO}_2$ , 52.16%; and CaO, 47.84%.

### Conclusions

This method of using the background to allow for beam-current fluctuations and to use the information about average atomic number seems to be promising. The work of Vander Wood et al.<sup>5</sup> indicates that a sensible curve may be obtained only within a well-defined set of compounds. If that is true, the method will still have application in areas such as the silicate minerals. The procedure can be easily incorporated into a Bence-Albee program, and the background from an EDS could be used in conjunction with peak intensities measured on a WDS.

### References

1. T. A. Hall, in K. F. J. Heinrich, Ed., *Quantitative Electron Probe Microanalysis*, NBS Special Publ. 298, 1968, 269.
2. J. A. Small et al., *SEM/1978* 1, 445.
3. P. J. Statham and J. B. Pawley, *ibid.*, 469.
4. M. Wendt and A. Schmidt, *Phys. Stat. Sol.* 46A: 179, 1978.
5. T. B. Vander Wood, J. G. Pearson, and P. R. Buseck, *Microbeam Analysis--1983*, 85.

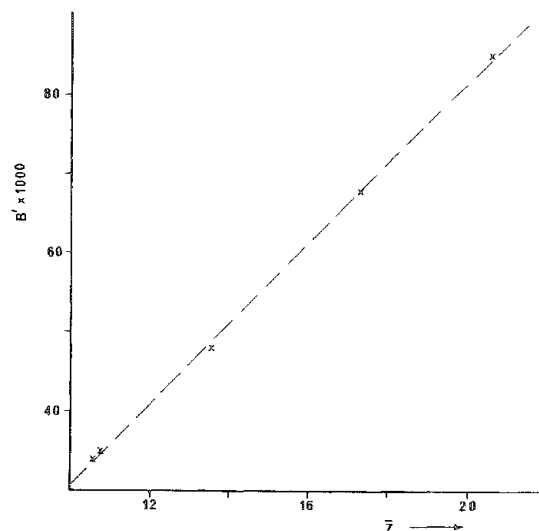


FIG. 1.--Corrected background  $B'$  vs average atomic number for  $\text{Al}_2\text{O}_3$ ,  $\text{SiO}_2$ ,  $\text{TiO}_2$ , and  $\text{Fe}_2\text{O}_3$ . Dashed line is fitted to the five points by least squares.

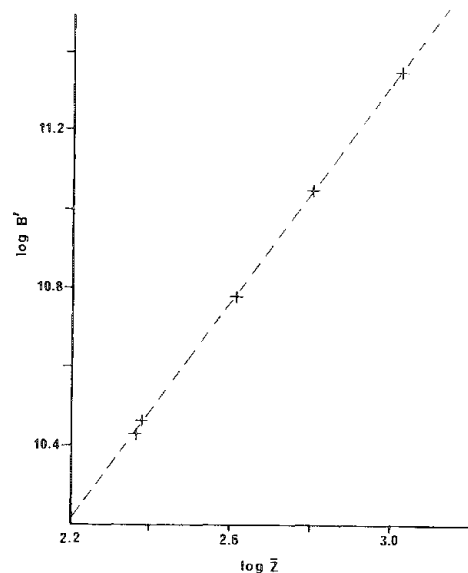


FIG. 2.--Graph of  $\log B'$  versus  $\log \bar{Z}$  for the same five compounds shown in Fig. 1.



TABLE 1.--Six analyses from Wollastonite sample ( $\text{CaSiO}_3$ ), comparing results from continuum correction procedure with those given by normalization to 100% oxide. Chemical composition (wt%) of  $\text{CaSiO}_3$  is 51.78%  $\text{SiO}_2$ , 48.22%  $\text{CaO}$ .

Analysis #	1	2	3	4 <sup>a</sup>	5 <sup>b</sup>	6 <sup>c</sup>
(a) Normalized to 100% oxide						
$\text{SiO}_2$	51.50	51.65	51.78	30.95	52.10	52.22
$\text{CaO}$	48.50	48.35	48.22	69.05	47.90	47.78
(b) Continuum correction						
$\text{SiO}_2$	51.46	51.06	52.72	24.80	44.96	35.96
$\text{CaO}$	48.49	47.55	48.94	54.18	40.36	31.35
Total	99.95	98.61	101.66	78.98	85.32	67.31

- a. Analysis over a crack in sample
- b. Analysis half on sample, half on resin
- c. Analysis over "fluff" on surface

## THE PREDICTION OF BACKGROUND INTENSITIES IN ENERGY-DISPERSIVE ELECTRON MICROPROBE ANALYSIS

D. G. W. Smith and D. A. Wynne

Accurate calculation of background intensities is fundamental to successful quantitative energy-dispersive electron microprobe analysis. Several expressions relating continuum intensity to atomic number, accelerating potential, and continuum energy have been proposed.<sup>1-9</sup> This paper compares three of them and suggests a possible explanation for discrepancies between two of the more recent expressions.

Before it is recorded, the generated x-ray continuum is modified by several processes, including absorption within the sample, absorption in detector components, the occurrence of escape events, incomplete charge collection in the detector, and any pulse pile-up not successfully eliminated by electronic means. The physical characteristics of the detector--the Be window, the Au contact surface layer, the Si dead-layer and the thickness of the active volume--are unique to each individual detector and are generally not known in any detail. It is therefore difficult to make accurate theoretical corrections for the effects of these components on emitted x-ray intensities. However, it has been shown that the actual effects can be modeled experimentally by use of the continuum recorded from substances such as Be, B, or C, which have no characteristic peaks in the range of energies normally recorded by a Si(Li) detector.<sup>6,7,9</sup> By taking into account the effects of the physical characteristics of a detector in this way, an expression that predicts the pattern of variation of continuum intensity for atomic numbers from 4 to 92, accelerating potentials from 5 to 30 kV, and continuum energies from 0.5 to 10 keV can be derived. In practical applications residual errors are generally better than  $\pm 5\%$  of the calculated intensity, even where absorption edges and other spectral artifacts are present. The same expression and approach can be used to calculate background intensities in wavelength dispersive analysis.<sup>9</sup>

Recent work by Small et al.<sup>8</sup> produced an alternative expression for continuum intensity based on a data set obtained with a different detector and spectrometer. Intensities recorded by an energy-dispersive spectrometer are controlled also by probe current, the size of the detector, and its position relative to the sample. Even if one ignores these factors, which produce only a change of scale and not of shape, surprisingly large discrepancies are apparent between intensities predicted by the expression of Small et al.<sup>8</sup> and the earlier

expression of Smith et al.<sup>6,7,9</sup> (Figs. 1-6). Comparisons have been restricted to the energy range 0.5-10 keV, the range for which the data of Smith et al. were fitted. However, at higher continuum energies ( $>15$  keV) it would be necessary to take into account the reduced detector efficiency due to partial transmission of high-energy photons. Again, the size of the effect will depend on the thickness characteristics of individual detectors. Small et al. corrected for the effects of anisotropy of x-ray generation, effects that were not taken into account by Smith et al., since they are irrelevant to the calculation of intensities for detectors in a fixed position. However, it seems unlikely that such anisotropy could account for the discrepancies observed.<sup>5</sup> A practical and necessary corollary of these differences is that neither expression satisfactorily predicts background values for the spectrometer on which the other data were gathered. For comparison, Kramers's expression<sup>1</sup> has also been plotted in Figs. 1-6, in which intensities have been arbitrarily normalized at 10 keV.

The expression of Smith et al.<sup>6,7</sup> has the form  $I = kZ^n[E_0 - E]/E^x$ , where  $I$  is the intensity,  $Z$  the average atomic number,  $E_0$  the accelerating potential, and  $E$  the continuum energy. Exponents  $n$  and  $x$  are defined below and  $k$  is an experimental constant. The expression was derived with data from a 1974 model Ortec energy-dispersive spectrometer fitted to an A.R.L. EMX microprobe. Later, when an attempt was made to use this same expression to predict intensities recorded by an Ortec EDS II energy-dispersive spectrometer fitted to an A.R.L. SEMQ instrument, small but distinct and repeatable discrepancies were apparent between calculated and observed backgrounds. To achieve the same high-quality background fit, it is necessary to modify the values of some terms in the expression slightly. The values of the exponents in the two expressions are shown below:

$$\begin{aligned} \text{EMX: } n &= E(0.0739 - 0.0051 \ln Z) + p; \\ p &= 1.6561 - 0.1150 \ln Z; \\ x &= a = 1.76 - 0.00145(Z/E) \end{aligned}$$

$$\begin{aligned} \text{SEMQ: } n &= E(0.0560 - 0.0033 \ln Z) + p; \\ p &= 1.6561 - 0.1150 \ln Z; \\ x &= a = 1.76 - 0.00080(Z/E) \end{aligned}$$

Figure 6 shows the ratios of intensities calculated for three different atomic numbers by both expressions at 15 kV, the accelerating potential used in routine analysis in the laboratory and the only potential at which the expression for the EDS II spectrometer was tested extensively. The principal differences are at low continuum energies, but clearly there are disparities throughout the spectra. For comparison, the corresponding ratios of intensities calculated by the expression of

D. G. W. Smith is at the Department of Geology, University of Alberta, Edmonton, Alberta, Canada T6G 2E3; D. A. Wynne is at the The Alberta Research Council, P.O. Box 8330, Postal Station F, Edmonton, Alberta, Canada T6H 5X2. This work has been supported by grant A4254 to the first author.

both Small et al. and Kramers to the intensities calculated by the EMX expression, are also shown.

Both detectors have windows with a manufacturer's nominal thickness of 7  $\mu\text{m}$ . The EEDS II detector was fitted with a custom-designed nose containing a range of different selectable apertures on a turntable. During calibration of this spectrometer it was noted that unless smaller collimating apertures were placed in exactly the same fixed position in front of the detector window, differences in intensity of recorded spectra could be clearly and repeatably observed. This result indicates a difference in the character of one or more of the detector components in different regions.

Statham addressed the possibility that backscattered electrons contribute to the observed background by exciting continuum in the Be detector window.<sup>5</sup> He concluded that the effect would be minor: about 2.3% of the observed background would be generated in this way. However, his calculations were based on a 13  $\mu\text{m}$  window (a thick window by today's standards), 20 keV backscattered electrons, and a sample of average atomic number 11. Substitution of an extreme value of 92 for the atomic number of the sample (and the concomitant significant increase in the fraction of electrons backscattered) increases this figure to about 5%. Furthermore, increase in the operating voltage, and hence in the energy of backscattered electrons impacting on the window, results in greater average depths of penetration and x-ray generation, which further reduces absorption suffered by window-generated continuum before it reaches the Si(Li) dead-layer. In particular, low-energy x rays, in the range 1-3 keV, which are normally most strongly attenuated by the Be window, are most enhanced by these mechanisms.

Finally, some of the observed intensity may result from electrons actually penetrating the Be window and impacting directly on the detector surface. This mechanism would be insignificant at accelerating potentials below 20 kV if the Be window was of constant 7  $\mu\text{m}$  thickness, but could be important if there are significant thin spots such as may be indicated by the aperturing experiments described earlier. Furthermore, above 20 kV an increasing number of electrons will penetrate the window to generate x rays in the thin Au layer and Si dead-layer.

Because the detector on the EMX probe is placed so far from the sample (-27 cm) and is surrounded on all sides by the grounded walls of the vacuum tank, it may suffer less severely from the effects of radiation generated within the window by backscattered electrons. The detector on the SEMQ instrument, about 10 cm from the sample (very close to and between the objective lens and the cone of the light optical system) may also receive a contribution of electrons scattered from these components. This possibility was also recognized by Statham<sup>5</sup> in the context of the desirability of having a well-collimated detector. Thus the expression derived by Smith et al.<sup>6,7</sup> using the spectrometer on the EMX instrument, should provide the more accurate estimate of

continuum intensity generated in the sample. That may explain why this expression works well with crystal spectrometers.<sup>9</sup> In Fig. 6, if it were assumed that the EMX instrument did not suffer at all from the effects of backscattered electron generated intensity, the deviation of this ratio from unity would give a measure of the size of the effect in the SEMQ instrument. As would be expected, differences appear to be largest at lower continuum energies and at highest atomic numbers, where the largest fraction of electrons are backscattered.

### Conclusions

Although they are at the same take-off angle (52.5°), the two Ortec detectors investigated show significant differences in the background shape observed for a given substance under fixed operating conditions. The expressions that have been derived to predict the background for the two spectrometers both differ from that of Small et al.<sup>8</sup> Neither of the Ortec detectors has been intentionally shielded from backscattered electrons, although one of them is very much more remote from the sample than the other and is partly buried in a cavity in the wall of the spectrometer. It is not clear whether the possibility of window excitation by backscattered electrons was either avoided or taken into account by Small et al. It is also not clear whether the authors considered the possibility of transmission of photons through the detector or the transmission of electrons through the Be window when modeling at higher continuum energies.

We therefore concluded that expressions developed to describe *generated* continuum intensity as a function of  $Z$ ,  $E$ , and  $E_0$  based on data from energy-dispersive spectra may be significantly in error due to backscattered electrons generating an intensity component in the detector window and even in the detector itself if the window is sufficiently thin in places to transmit the high-energy electrons. The use of such expressions to determine the background in energy-dispersive electron microprobe analysis may be practicable only if they are restricted to the spectrometers used to gather the data set from which the expressions were derived. This is indeed the principle used in the application of the expressions derived by Smith et al.<sup>6,7</sup>

Further experiments will be attempted to determine what changes in intensities are observed in the recorded energy-dispersive spectra when backscattered electrons are deliberately deflected away from the aperture of the detector.

### References

1. H. A. Kramers, "On the theory of x-ray absorption and the continuous x-ray spectrum," *Phil. Mag.* 46: 836-871, 1923.
2. N. Ware and S. J. B. Reed, "Background correction for quantitative electron microprobe analysis using a lithium drifted silicon detector," *J. Phys.* 6E: 286-288, 1973.
3. T. S. Rao Sahib and D. B. Wittry, "The x-ray continuum from thick targets," *Proc.*

6th Intern. Conf. X-ray Optics and Microanalysis, Osaka, 1971, 131-137.

4. E. Lifshin, M. F. Ciccarelli, and R. B. Bolon, "X-ray spectral measurement and interpretation," in J. I. Goldstein and H. Yakowitz, Eds., *Practical Scanning Electron Microscopy, Electron and Ion Microprobe Analysis*, New York: Plenum, 1975, 263-297.

5. P. J. Statham, "The generation and anisotropy of thick target bremsstrahlung and implications for quantitative energy dispersive analysis," *X-ray Spect.* 5: 154-168, 1976.

6. D. G. W. Smith, C. M. Gold, and D. A. Tomlinson, "The atomic number dependence of the X-ray continuum intensity and the practical calculation of background in energy dis-

persive electron microprobe analysis," *X-ray Spect.* 4: 14-17, 1975.

7. D. G. W. Smith and C. M. Gold, "EDATA2: A FORTRAN IV computer program for processing wavelength- and/or energy-dispersive electron microprobe analyses," *Microbeam Analysis--1979*, 273-278.

8. J. A. Small, S. D. Leigh, D. E. Newbury, and R. L. Myklebust, "Continuum radiation produced in pure-element targets by 10-40 keV electrons: An empirical model," *Microbeam Analysis--1986*, 289-291.

9. D. G. W. Smith and S. J. B. Reed, "The calculation of background in wavelength dispersive electron microprobe analysis," *X-ray Spect.* 10: 198-202, 1981.

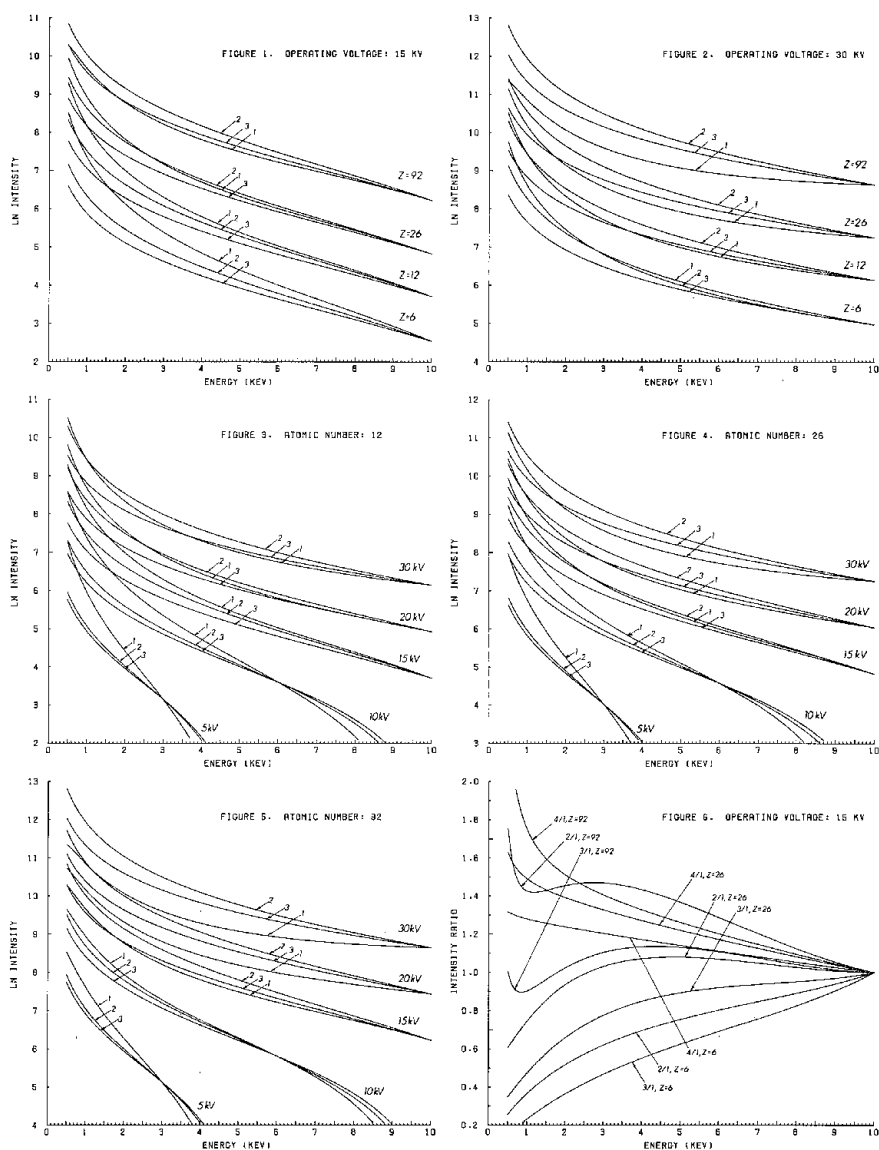


FIG. 1-6.--Calculated continuum intensities: 1. Smith et al. (EMX); 2. Small et al.; 3. Kramers; 4. Smith et al. (SEM). All spectra arbitrarily normalized at 10 keV (except Figs. 3-5 5kV and 10kV data normalized at 3 and 6 keV, respectively).

# A COMPARISON OF MATRIX CORRECTION PROCEDURES FOR THE X-RAY MICROANALYSIS OF U-Nb ALLOYS

A. D. Romig Jr., P. F. Hlava, and W. F. Chambers

Two different matrix correction procedures for the quantification of x-ray intensity data from bulk specimens are currently in use.<sup>1</sup> The realization that matrix corrections were required to quantify the x-ray data was made originally by Castaing.<sup>2</sup> The oldest procedure based on "first-principles calculations" rather than empirical calibration curves is ZAF,<sup>3</sup> where Z, A, and F indicate that to determine composition, the emitted x-ray intensity data are corrected for atomic number effects, absorption effects, and characteristic fluorescence effects, respectively. More recently, an alternate procedure referred to as  $\phi(\rho z)$ , has been developed to the point of practical applications in microanalysis.<sup>4-8</sup> In this procedure, empirical fits to the depth-dependent (depth  $z$  and mass depth  $\rho z$ , where  $\rho$  is density) x-ray generation function  $\phi(\rho z)$  are numerically integrated directly to obtain both the generated and emitted x-ray intensities. A characteristic fluorescence correction is then applied. Recently, a variation on  $\phi(\rho z)$  has been introduced in which "fundamental" expressions for the  $\phi(\rho z)$  function are used.<sup>9</sup> This procedure, although not yet widely available, is often referred to as the "PAP" correction algorithm.

The objective of this study is to evaluate the quantification accuracy of the two matrix correction procedures, ZAF and "empirical"  $\phi(\rho z)$ . A series of homogenous U-Nb alloys (1 to 12 wt% Nb) were analyzed at several accelerating voltages (10 to 40 kV) and their compositions were determined by the two corrections algorithms. Pure-element standards were used to make the comparison between the two correction procedures as rigorous as possible. The quantification results are compared to known compositions determined by wet chemical analytical techniques. The x-ray microanalysis results are then examined to evaluate the relative accuracy of the two techniques and any dependence of electron-beam energy.

## The Matrix Correction Procedure

The intensity of x rays generated in a pure element bulk solid target can be determined from integration of the depth dependent x-ray generation function  $\phi(\rho z)$  as

$$I_g = \int_0^\infty \phi(\rho z) d(\rho z) \quad (1)$$

One can determine the intensity of x-rays emitted from the target in the absence of characteristic and continuum fluorescence by including absorption in Eq. (1):

$$I_e = \int_0^\infty \phi(\rho z) [\exp(-\frac{\mu}{\rho} \rho z \csc \psi)] d(\rho z) \quad (2)$$

The authors are at Sandia National Laboratories, Albuquerque, NM 87185. The work was performed under U.S. Department of Energy contract DE-AC04-76DP00789.

where  $\frac{\mu}{\rho}$  is the mass absorption coefficient,  $z$  is depth, and  $\psi$  is the x-ray take-off angle ( $z \csc \psi$  is the x-ray path length through the specimen). To calculate the actual composition explicitly, Eq. (2) must be corrected for characteristic and continuum fluorescence effects. The  $\phi(\rho z)$  function implicitly includes the effects of electron backscatter and fluorescent yield.

Both the ZAF and  $\phi(\rho z)$  correction procedures require the use of standards of known composition. The characteristic x-ray intensity for each element in the unknown is ratioed against the characteristic x-ray intensity for each element in the standard(s) to determine a k-ratio,

$$k = I(\text{unknown})/I(\text{standard}) \quad (3)$$

One then calculates the composition by correcting the k-ratio by the matrix correction factors, using one of the two correction procedures. The matrix correction must be applied to both the standard and unknown, since the composition of the standards and the unknown are different. The concentration of component  $i$  in the unknown is then

$$C_i = k_i \frac{(\text{unknown matrix correction factor})}{(\text{standard matrix correction factor})} \quad (4)$$

Both matrix correction procedures, ZAF and  $\phi(\rho z)$ , are generally based on Eqs. (1) and (2). Since the composition of the specimen is unknown and the terms in Eqs. (1) and (2) are compositionally dependent, these equations must be solved iteratively until a convergent solution is obtained. The difference between the various procedures lies in the approximations used to calculate the characteristic x-ray emission and the absorption effect.

## ZAF Corrections

The ZAF matrix correction procedure is the oldest and the most commonly used. Many researchers have contributed to its development over the past 25 years. At the current time, work still continues to improve the correction.<sup>10-12</sup> The ZAF procedure splits Eq. (2) into two parts: the  $\int_0^\infty \phi(\rho z) d(\rho z)$  is effectively the atomic number correction Z and the  $\int_0^\infty \exp(-\frac{\mu}{\rho} \rho z \csc \psi) d(\rho z)$  is effectively the absorption correction. However, the Z and A corrections are not calculated by direct integration of  $\phi(\rho z)$ , but rather by other numerical approximations.

The atomic number effect in a pure element bulk specimen is given by

$$Z \text{ effect} = R \int_{E_c}^{E_0} \frac{Q(E)}{dE/d\lambda} dE \quad (5)$$

where  $R$  is the fraction of backscattered electrons,  $E_0$  is the incident beam energy,  $E_c$  is the ionization energy for the characteristic x ray of interest,  $Q(E)$  is the ionization cross section, and  $dE/d\lambda$  is the electron

loss/unit path length (stopping power).<sup>13</sup>

The absorption correction is considered to be the least accurate approximation in ZAF.<sup>10</sup> Various approximations for the absorption correction are available. Many are numerical fits to measured absorption data;<sup>14,15</sup> the most recent are simple geometric fits to measured ratios of Eq. (2) to Eq. (1).<sup>11</sup>

The characteristic fluorescence correction is also a result of empirical fits to experimental data. The correction most commonly used today is that of Reed.<sup>16</sup> The characteristic fluorescence effect is often small, and hence uncertainty in the correction usually has little effect on the final results.

The continuum fluorescence correction is very small and is typically ignored.<sup>17</sup> Corrections have been developed<sup>18</sup> but are not usually included in commercially available software.

#### *Empirical $\phi(\rho z)$ Correction*

The  $\phi(\rho z)$  correction procedure requires direct integration of the x-ray depth generation function. Equation (1) must be integrated for each element in the unknown and the standard and the ratio of results used in the correction. The resulting ratio is essentially an atomic-number correction. The generated intensity is also of value in that it is directly used in the correction for x-ray fluorescence. The integral of Eq. (2) divided by the integral of Eq. (1) for the standard and the unknown yields the absorption correction. Direct integration of Eq. (2) for the unknown and the standard gives the emitted x-ray intensities, and as such represents both the atomic number and absorption corrections. The  $\phi(\rho z)$  correction procedures available today all use direct integration of Eq. (2). The fluorescence correction is then applied to the  $\phi(\rho z)$  result in exactly the same manner as in ZAF. Perhaps a better name for this correction procedure would be  $\phi(\rho z) F$ .

In order to integrate  $\phi(\rho z)$ , a mathematical expression for its functionality is required. Much of the work to date involves exponential fits to  $\phi(\rho z)$ .<sup>4-8</sup> The most commonly used fit is a modified Gaussian function of the form

$$\phi(\rho z) = \gamma \left\{ 1 - \frac{\gamma - \phi(0)}{\gamma} \exp(-\beta \rho z) \right\} \exp[-\alpha^2 (\rho z)^2] \quad (6)$$

where  $\phi(0)$  is a parameter describing the generation of x rays at the surface ( $z = 0$ ), and  $\alpha$ ,  $\beta$ , and  $\gamma$  are fitting parameters.<sup>4-8</sup> The values of the four parameters are determined by fitting the  $\phi(\rho z)$  curves. The  $\phi(\rho z)$  curves are obtained either by experiment or by Monte Carlo modeling. The four parameters are not arbitrary power series fits, but rather expressions that depend on several physical factors including atomic number, atomic weight, overvoltage, backscatter coefficients, cross sections, mean free electron path length in the target, etc.<sup>4-8,15</sup> The two groups most active in the area of the development of this quantification procedure are the Brown and Packwood group in Canada<sup>4-6</sup> and the Bastin group in the Netherlands.<sup>7,8</sup> The principal difference between the quantification approach

taken by each group is the values and expressions used for the four fitting parameters.

#### *Experimental Procedure*

The following procedure was used to prepare and analyze the experimental alloys. A series of U-Nb alloys (1.32, 1.89, 4.06, 5.87, 7.41, 12.86 wt% Nb, as determined by wet chemical analysis) were homogenized at 850 °C for 185 days and water quenched. All the alloys were determined to be homogeneous to within 0.02 wt% (absolute) by the method described by Goldstein.<sup>18</sup> The samples were polished through 0.06  $\mu$ m alumina and carbon coated for analysis in a Cameca MBX electron probe micro-analyzer. The U  $M\alpha_1$  and Nb  $L\alpha_1$  lines were used in the analysis. PET diffracting crystals were used for each element. Pure-element standards were used to accentuate any error in the x-ray intensity data quantification. The analyses were performed at 10, 15, 20, 25, 30, 35, and 40 kV at a nominal beam current of 33 nA (88 nA for 10 kV). Uranium x rays were acquired until the total number of counts accumulated insured a relative counting error of less than 0.2%. The total number of U counts acquired was over 250 000. The total acquired Nb counts varied from approximately 5000 to 60 000 counts.

The quantitation was done on a TN2000 running Sandia TASK.<sup>19</sup> The k-ratio determined for each element from each analysis was input into the two matrix correction procedures, ZAF and  $\phi(\rho z)$ . Hence, any discrepancy between the results of the ZAF and  $\phi(\rho z)$  corrections would be due to the correction procedure and not statistical counting errors.

The ZAF procedure<sup>20</sup> incorporated into Sandia TASK uses the most current input data and accurate correction expressions available in the literature. The atomic number correction is that of Duncub and Reed.<sup>13</sup> The atomic-number correction uses the Duncumb polynomial expansion fit for the electron backscatter coefficient<sup>21</sup> and the Berger-Seltzer expression for stopping power.<sup>22</sup> The absorption correction is made by use of Heinrich's modification of the Philibert expression.<sup>23</sup> The absorption coefficients for atomic numbers  $\geq 10$  were obtained by a fourth-order curve fit to Heinrich's data.<sup>24</sup> The absorption coefficients for B, N, O, and F are from the tabulations of Henke and Ebisu.<sup>25</sup> The absorption coefficient for carbon is that of Bastin and Heijligen.<sup>26</sup> The characteristic fluorescence effect is corrected using the method of Reed.<sup>16</sup> The fluorescence correction uses the emission line and absorption edge data from Bearden<sup>27</sup> and Doyle.<sup>28</sup> Where tabulated data are unavailable, the emission lines and absorption edge fits are determined by a parameterization equation.<sup>29</sup> This ZAF correction procedure does not treat continuum fluorescence.

The  $\phi(\rho z)$  correction procedure is based on  $\phi(\rho z)$  expressions due to Bastin.<sup>7</sup> The same absorption coefficients are used in  $\phi(\rho z)$  as in ZAF. The  $\phi(\rho z)$  software corrects for characteristic fluorescence with exactly the same procedure that is used in ZAF, including the use of the same input parameters. Like ZAF,  $\phi(\rho z)$  does not correct for continuum fluorescence.

## Results and Discussion

Table 1 summarizes the results. The error shown represents only one standard deviation ( $\sigma$ ) of the total counts. Since these experiments were specifically designed to investigate U-Nb alloys, the decision was made to make the comparison on the basis of calculated composition. For more extensive studies, it is recommended that the method of Bastin be used, in which calculated and measured values of the  $k$ -ratio are compared with the use of histograms.<sup>9</sup>

In all cases, the ZAF procedure underestimated the actual Nb content. None of the analyses measured the correct composition within the one standard deviation ( $1\sigma$ ) error bars. The discrepancy between the composition calculated by ZAF and the actual composition always exceeded 6% (relative). The error in the composition determination increased with increasing accelerating voltage. This trend is reasonable since the electron penetration increases at higher beam energies, as does the effective absorption path length, so that more significant corrections are required. ZAF correction procedures have been used successfully for U-Nb alloys when the compositions of the standard and unknowns are approximately equal.<sup>30</sup> Similar compositions of the standard and unknown tend to minimize the quantification error, since any correction errors for the standard and unknown are almost identical.

The  $\phi(\rho z)$  correction procedure was far more successful at quantifying the data since the  $\phi(\rho z)$  correction simulates the physics of electron beam/solid interactions more completely and realistically than the ZAF correction. At 10, 20, 25, 30, 35, and 40 kV, most of the compositions calculated by  $\phi(\rho z)$  match the actual compositions within the  $1\sigma$  counting error. All match within twice the  $1\sigma$  counting error. However, the values measured at 15 kV are all consistently low in Nb content by approximately 5 to 6% (relative). The total compositions measured at 15 kV require that the composition errors should not be due to beam fluctuations or uncertainties in the beam energy. Currently, the source of the error at 15 kV is unknown. However, even under the worst condition (15 kV), the  $\phi(\rho z)$  correction is much more accurate than ZAF.

## Summary

Two matrix correction procedures, ZAF and  $\phi(\rho z)$ , have been evaluated for the analysis of U-Nb alloys (1.33 to 12.99 wt% Nb) at beam energies from 10 to 40 keV. For the use of pure-element standards,  $\phi(\rho z)$  correctly determine the composition under most conditions; compositions determined by ZAF consistently underestimate the Nb content. The ZAF procedure works adequately for U-Nb alloys only with the use of standards with composition similar to the compositions of the unknown.

## References

1. J. D. Brown, "Quantitative electron probe microanalysis: A review," *Microbeam Analysis--1982*, 151.
2. R. Castaing, *Applications of Electron Probes to Local Chemical and Crystallographic Analysis*, PhD. thesis, University of Paris, 1951.
3. J. Philibert and R. Tixier, in K. F. J. Heinrich, Ed., *Quantitative Electron Probe Microanalysis*, NBS Special Publication, Washington, D.C., 1968, 13.
4. J. D. Brown and J. L. Parobek, "X-ray production as a function of depth for low energy electrons," *X-ray Spectr.* 5: 36, 1976.
5. J. D. Brown and R. H. Packwood, "Quantitative electron probe microanalysis using Gaussian  $\phi(\rho z)$  curves," *X-ray Spectr.* 11: 187, 1982.
6. J. D. Brown and W. H. Robinson, "Quantitative analysis by  $\phi(\rho z)$  curves," *Microbeam Analysis--1979*, 238.
7. G. F. Bastin, F. J. J. van Loo, and H. J. M. Heijligers, "Evaluation of the use of Gaussian  $\phi(\rho z)$  curves in electron probe microanalysis: A new optimization," *X-ray Spectr.* 13: 91, 1984.
8. G. F. Bastin, H. J. M. Heijligers, and F. J. J. van Loo, "A further improvement in the Gaussian  $\phi(\rho z)$  approach for matrix correction in quantitative electron probe microanalysis," *Scanning* 8: 45, 1986.
9. J. L. Puchou and F. Pichoir, "'PAP'  $\phi(\rho z)$  procedure for improved quantitative microanalysis," *Microbeam Analysis--1985*, 104.
10. D. A. Sewell, G. Love, and V. D. Scott, "Universal correction procedure for electron-probe microanalysis: I. Measurement of x-ray depth distribution in solids," *J. Phys.* D18: 1233, 1985.
11. D. A. Sewell, G. Love, and V. D. Scott, "Universal correction procedure for electron-probe microanalysis: II. The absorption correction," *J. Phys.* D18: 1245, 1985.
12. D. A. Sewell, G. Love, and V. D. Scott, "Universal correction procedure for electron-probe microanalysis: III. Comparison with other recent correction procedures," *J. Phys.* D18: 1269, 1985.
13. P. Duncumb and S. J. B. Reed, "The calculation of stopping power and backscatter effects in electron probe microanalysis," in Ref. 3, p. 133.
14. J. Philibert, "A method for calculating the absorption correction in electron probe microanalysis," in H. H. Patee, V. E. Coslett and E. Engstrom, Eds., *3rd Int. Symp. on X-ray Optics and X-ray Microanalysis*, New York: Academic Press, 1963, 379.
15. G. Love and V. D. Scott, "Evaluation of a new correction procedure for quantitative electron probe microanalysis," *J. Phys.* D11: 106, 1978.
16. S. J. B. Reed, "Characteristic fluorescence correction in electron probe microanalysis," *Brit. J. Appl. Phys.* 16: 913, 1965.
17. R. L. Myklebust, C. E. Fiori, and K. F. J. Heinrich, *Frame C: A compact procedure for Quantitative Energy-dispersive Electron Probe Analysis*, NBS Technical Note 1106, Washington, D.C., 1979.
18. J. I. Goldstein et al., *Scanning Electron Microscopy and X-ray Microanalysis*, New York: Plenum Press, 1981, 432.
19. W. F. Chambers, "SANDIA TASK8: A sub-routined electron microprobe automation system," Sandia Report SAND85-2037, Albuquerque,

TABLE 1.--Comparison of ZAF and  $\phi(\rho z)$  quantification of U-Nb.

Alloy	10kV			15kV			20kV			25kV			30kV			35kV			40kV		
	$\phi(\rho z)$	ZAF		$\phi(\rho z)$	ZAF		$\phi(\rho z)$	ZAF		$\phi(\rho z)$	ZAF		$\phi(\rho z)$	ZAF		$\phi(\rho z)$	ZAF		$\phi(\rho z)$	ZAF	
U - 1.32 wt%Nb Nb(wt%) U(wt%) Total(Wt%)	1.33±0.03	1.24±0.02		1.27±0.03	1.17±0.03		1.32±0.03	1.18±0.03		1.33±0.03	1.16±0.03		1.31±0.03	1.11±0.03		1.36±0.03	1.13±0.03		1.36±0.03	1.11±0.03	
	98.18±0.26	98.21±0.28		98.20±0.28	98.15±0.28		98.39±0.28	98.25±0.28		99.39±0.28	99.13±0.28		98.25±0.28	97.99±0.28		98.93±0.28	98.46±0.28		99.27±0.28	98.70±0.28	
	99.51	99.45		99.47	99.32		99.71	99.43		100.72	100.29		99.56	99.10		100.29	99.59		100.62	99.81	
U - 1.89 wt%Nb Nb(wt%) U(wt%) Total(Wt%)	1.89±0.03	1.76±0.03		1.83±0.03	1.68±0.03		1.89±0.03	1.71±0.03		1.87±0.03	1.63±0.03		1.94±0.03	1.65±0.03		1.94±0.03	1.61±0.03		1.96±0.03	1.60±0.03	
	97.57±0.27	97.62±0.28		97.87±0.28	97.80±0.28		98.01±0.28	97.80±0.28		98.99±0.28	98.64±0.28		98.87±0.28	98.34±0.28		99.02±0.28	98.36±0.28		99.13±0.28	98.33±0.28	
	99.47	98.38		99.70	99.48		99.90	99.51		100.86	100.27		100.81	99.99		100.96	99.97		101.09	99.93	
U - 4.06 wt%Nb Nb(wt%) U(wt%) Total(Wt%)	4.07±0.04	3.80±0.04		3.84±0.05	3.56±0.05		4.04±0.04	3.65±0.04		4.10±0.04	3.59±0.04		4.08±0.04	3.48±0.04		4.14±0.04	3.46±0.04		4.11±0.04	3.38±0.04	
	94.79±0.27	94.85±0.27		95.25±0.27	95.11±0.27		96.08±0.27	95.66±0.27		96.78±0.27	96.06±0.27		96.13±0.27	95.11±0.27		97.12±0.27	95.80±0.27		97.04±0.27	95.50±0.27	
	98.87	98.65		99.09	98.67		100.12	99.31		100.88	99.65		100.21	98.59		101.26	99.26		101.15	98.88	
U - 5.87 wt%Nb Nb(wt%) U(wt%) Total(Wt%)	5.83±0.05	5.46±0.05		5.59±0.06	5.20±0.06		5.78±0.05	5.24±0.05		5.87±0.05	5.17±0.05		5.93±0.05	5.09±0.05		6.00±0.04	5.04±0.04		5.90±0.04	4.88±0.04	
	92.64±0.26	92.78±0.26		93.75±0.26	93.56±0.26		94.47±0.27	93.90±0.27		95.22±0.27	94.24±0.27		95.20±0.27	93.80±0.27		95.26±0.27	93.47±0.27		94.87±0.27	92.79±0.27	
	98.47	98.24		99.34	98.76		100.24	99.14		101.09	99.41		101.13	98.89		101.26	98.51		100.77	97.67	
U - 7.41 wt%Nb Nb(wt%) U(wt%) Total(Wt%)	7.60±0.06	7.12±0.06		7.01±0.07	6.53±0.07		7.35±0.05	6.69±0.05		7.42±0.06	6.55±0.06		7.79±0.06	6.42±0.06		7.55±0.05	6.37±0.05		7.47±0.05	6.21±0.05	
	93.29±0.26	93.48±0.26		91.54±0.26	91.31±0.26		92.72±0.26	92.03±0.26		93.68±0.26	92.64±0.26		93.36±0.29	91.73±0.29		93.41±0.26	91.48±0.26		93.39±0.26	90.91±0.26	
	100.88	100.60		98.55	97.84		100.07	98.71		101.10	99.19		101.15	98.15		100.96	97.85		100.86	97.12	
U - 12.86 wt%Nb Nb(wt%) U(wt%) Total(Wt%)	13.26±0.07	12.52±0.07		12.25±0.10	11.50±0.10		12.71±0.07	11.67±0.07		12.83±0.07	11.45±0.07		12.90±0.07	11.25±0.07		13.10±0.07	11.20±0.07		12.81±0.06	10.80±0.06	
	86.45±0.24	86.78±0.24		86.51±0.24	86.20±0.24		87.74±0.25	88.74±0.25		88.36±0.25	87.84±0.25		88.55±0.25	86.12±0.25		88.45±0.25	85.37±0.25		88.64±0.25	85.40±0.25	
	99.71	99.30		98.77	97.70		100.45	100.41		101.17	99.29		101.46	97.37		101.45	96.57		101.45	95.90	



N.M., 1985.

20. J. H. Doyle and W. F. Chambers, *ZAF80: An Improved Quantitative Analysis for the FLEXTRAN Language Systems*, Rocky Flats Report 3215, Golden, Co., 1981.

21. D. R. Beaman and J. A. Isasi, *Electron Beam Microanalysis*, ASTM Special Technical Publication 506, 1972.

22. S. J. B. Reed, *Electron Microprobe Analysis*, Cambridge: Cambridge University Press, 1975, 204.

23. K. F. J. Heinrich, "The absorption correction model for microprobe analysis," Paper 7 presented at the Second National Conference on Electron Microprobe Analysis, 1967.

24. K. F. J. Heinrich, "X-ray absorption uncertainty," in T. D. McKinely, K. F. J. Heinrich, and D. B. Wittry, Eds., *The Electron Microprobe*, New York: Wiley, 1966, 296.

25. B. L. Henke and E. S. Ebisu, "Low energy electron absorption in solids," *Adv. in X-ray Analysis* 17: 150, 1974.

26. G. F. Bastin and H. J. M. Heijligers, *Quantitative Electron Probe Microanalysis of Carbon in Binary Carbides*, Report, Eindhoven University of Technology, The Netherlands, 1984, 90.

27. J. A. Bearden, "X-ray wavelength," *Rev. Mod. Phys.* 39: 78, 1967.

28. B. L. Doyle et al., *Atomic Data and Nuclear Data Tables*, 24(No. 5), 1979.

29. F. Schamber, N. Wodke, and J. McCarthy, *ZAF Operation and Program Description Version 10*, Internal Report, Tracor Northern, 2551 W. Beltline Hwy., Middleton, WI 53562, 1977.

30. A. D. Romig Jr., "Phase stability and diffusion in U-Nb," *Metall. Trans.* (in preparation).

## TEST OF A BREMSSTRAHLUNG EQUATION FOR ENERGY-DISPERSIVE X-RAY SPECTROMETERS

J. A. Small, D. E. Newbury, and R. L. Myklebust

Recently we published an empirical model describing the generation of bremsstrahlung x radiation as a function of atomic number  $Z$  of the target, x-ray energy  $E_v$ , and electron energy  $E_0$ .<sup>1,2</sup> This model was developed for pure element targets excited by 10-40keV electrons, and was based on fitting a high-quality data set where great care was taken to insure that the detector was operating properly and that the spectra were free from artifacts.<sup>3</sup> The model was determined empirically from a large data set consisting of over 4100 x-ray intensity measurements which were accumulated on a Cameca Electron Probe with a 10mm<sup>2</sup> United Scientific Si-Li x-ray spectrometer. The basic formulation of the equation was that the log of the generated bremsstrahlung intensity  $I_v$ , is linear in the term  $\ln[Z(U - 1)]$ , where  $U = E_1/E_v$ ; and that the fitted line parameters slope  $M$  and intercept  $B$ , are themselves linear functions of the beam energy.

$$\ln(I_v) = M \ln[Z(U - 1)] + B \quad (1)$$

For the large data set, we found that

$$M = 0.00599E_0 + 1.05, \quad B = 0.0322E_0 + 5.80$$

The performance of Eq. (1) in predicting the experimental intensities over all ranges of  $E_v$  and  $E_0$  is shown in the histogram of the deviation between experimental and predicted intensities values, normalized to experimental values, in linear (i.e., nonlog) space (Fig. 1). This distribution is symmetrically centered around zero error with 63% of the values falling between  $\pm 10\%$ . This model was determined empirically from data collected on a single detector system.

It is the objective of this work to determine the applicability of Eq. (1) to other detector systems. The testing of the linearity in  $E_0$  of the slope and intercept requires the collection of large data sets at several  $E_0$  values on the various instruments. An important first step in the evaluation of this model, prior to the collection of several large data sets, is the testing of the assumptions and resulting corrections we used in the development of the model to convert measured x-ray intensities to generated intensities.<sup>1</sup> In this paper, we test the correction of experimental intensities to generated intensities by fitting the  $Z$  and  $E_v$  dependence, which are incorporated in the term containing the natural log of Kramers's variable,  $Z(U - 1)$ , for data

collected on an alternate detector system.

### Experimental

To evaluate the various corrections, we used a Cameca electron probe equipped with a 30mm<sup>2</sup> Tracor Northern Si(Li) detector mounted at 40° take-off angle. The database consisted of 87 intensity measurements which were collected at dead-times of less than 15%, on solid targets with atomic numbers of 22, 26, 33, 40, 42, and 79. The incident electron energy was 20 keV with bremsstrahlung x-ray energies selected in the range from 1.5 to 16 keV. The energy windows which were selected and the data reduction were identical to the procedures used in developing the model and are detailed in Ref. 1. We did not collect data on light-element targets with atomic numbers below 10 since the light elements showed anomalous behavior in the original modeling effort.

### Results

To compare the new database to the model, the slope  $M$  and the intercept  $B$  in Eq. (1) were determined from a fit of the experimental measurements. The predicted intensities from the model were then compared to the measured intensities by means of relative-error histograms. For this work, the relative error is defined as the difference between experimental and predicted intensities normalized to the experimental values. The results of the comparison (Fig. 2) indicate excellent agreement between the model in Eq. (1) and the new database. The distribution of the error histogram is symmetrical around zero error with 87% of the errors having values less than  $\pm 10\%$ . The performance of the model applied to this new set of data is actually superior to the fit obtained in the previous work. This result suggests that the model is independent of the choice of energy-dispersive spectrometer system.

### Sources of Error

Spectral quality must be considered very carefully in establishing experimental conditions for measuring data sets to test our model. The x-ray background is usually thought to consist of only x-ray bremsstrahlung, but there only can be two significant distortions to the background as measured on an electron column instrument with a Si-Li x-ray spectrometer: pulse pileup and backscattered electron penetration into the detector.

The first of these distortions arises because of the nature of the measurement process in an energy dispersive spectrometer (EDS) system. Because the x-ray photons are measured in a time serial fashion, the possibility of pulse coincidence exists. EDS systems include sophisticated circuitry to eliminate spurious pulses, which arise from two separate photon

The authors are at the Center for Analytical Chemistry, National Bureau of Standards, Gaithersburg, MD 20899. To describe adequately materials and experimental procedures, it is occasionally necessary to identify commercial products by manufacturer's name or label. In no instance does such identification imply NBS endorsement, nor does it imply that the particular product or equipment is necessarily the best for that purpose.

events arriving at the detector closely spaced in time. However, the time resolution of the pulse inspection circuitry inevitably has a limit, and pulses that arrive at the detector spaced closer than this time resolution are incorrectly measured. In most EDS measurements this effect is only readily noticeable for characteristic peaks as the so-called "double energy" peak located at twice the energy of the parent characteristic x-ray peak. However, distortions of the spectrum can arise because of coincidence of the characteristic peak photons with the bremsstrahlung photons and the coincidence of bremsstrahlung photons of various energies. Such an effect can be seen in the spectrum in Fig. 3, recorded with the Cameca/TN system at a dead time of approximately 20%, as a shelf, starting at point A, of apparent photons extending beyond the Duane-Hunt limit. Although the Gaussian energy-response function of the detector will displace some bremsstrahlung photon events that lie at or near  $E_0$  to an apparent energy above  $E_0$ , such anomalous events follow a Gaussian shape to zero intensity. The presence of a shelf indicates pulse coincidence. The fit of our model to a data set collected under these conditions produced a broader error distribution, with only 71% of the data points within  $\pm 10\%$  of the model.

The second effect, penetration of backscattered electrons into the detector, can produce severe distortions of the spectral background. In the electron microprobes used to collect our original data set and the data sets described above, the EDS detector is protected from the penetration of backscattered electrons by the strong magnetic field of the objective lens. In examining spectra from EDS detectors placed on conventional scanning electron microscopes, where the detector op-

erates in a low magnetic field that does not provide shielding, we have observed substantial background distortions. An example of this effect is shown in Fig. 4. The spectrum was first measured with the detector mounted in the conventional fashion (Fig. 4a). A magnetic deflector was then attached to the snout of the detector. A spectrum measured under identical beam and specimen conditions showed a significant reduction in the backscattered electron contribution to the spectrum (Fig. 4b).

### Conclusions

For accurate bremsstrahlung modeling and subsequent use of quantitation techniques based on peak-to-bremsstrahlung ratios, the spectra must be recorded with careful attention to the detector environment and operating conditions to insure that the background is predominantly due to x-ray bremsstrahlung. We have shown that when a data set is properly recorded, the  $Z$  and  $E_0$  dependence in Eq. (1) can be used accurately to predict bremsstrahlung x-ray intensities from a second experimental set-up. This finding suggests that Eq. (1) is independent of the energy-dispersive detector system used in the collection of the database.

### References

1. J. A. Small, S. D. Leigh, D. E. Newbury, and R. L. Myklebust, *J. Appl. Phys.* 61: 459-469, 1987.
2. J. A. Small, S. D. Leigh, D. E. Newbury, and R. L. Myklebust, *Microbeam Analysis* --1986, 289-291.
3. C. E. Fiori, R. L. Myklebust, and D. E. Newbury, in C. Lechene and R. Warner, Eds., *Microbeam Analysis in Biology*, New York: Academic Press, 1979, 225.

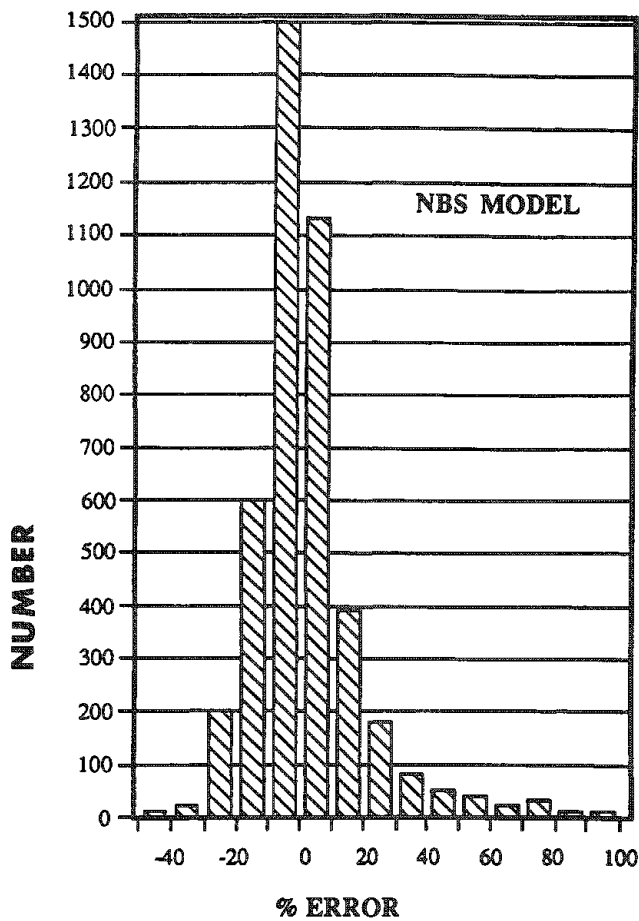


FIG. 1.--Error histogram for empirical model compared to original database.

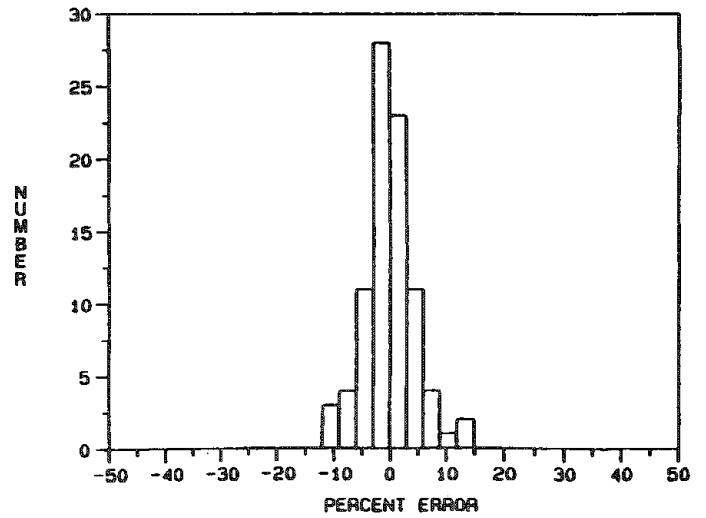


FIG. 2.--Error histogram comparing empirical model to database from Cameca/TN system.

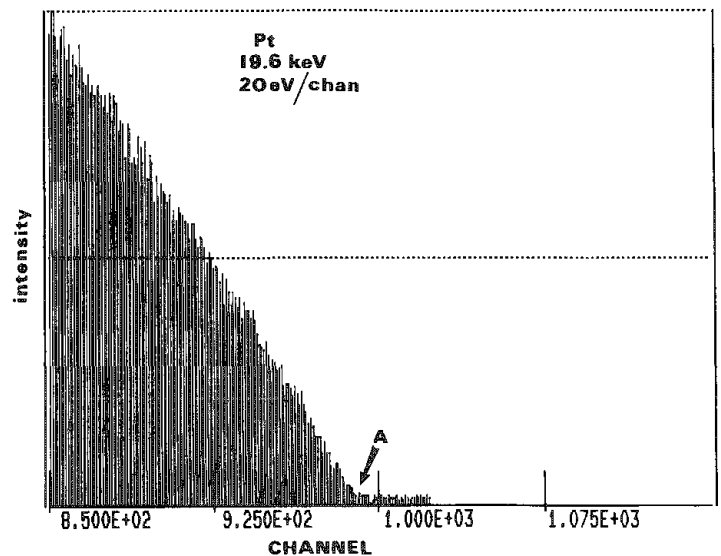


FIG. 3.--X-ray spectrum of Pt showing pile-up events past Duane-Hunt limit. Presence of shelf at channel 1024 is artifact of collection procedure. Last channel collected on spectrum was channel 1024; inclusion of channels out to 1100 is for display purposes only.

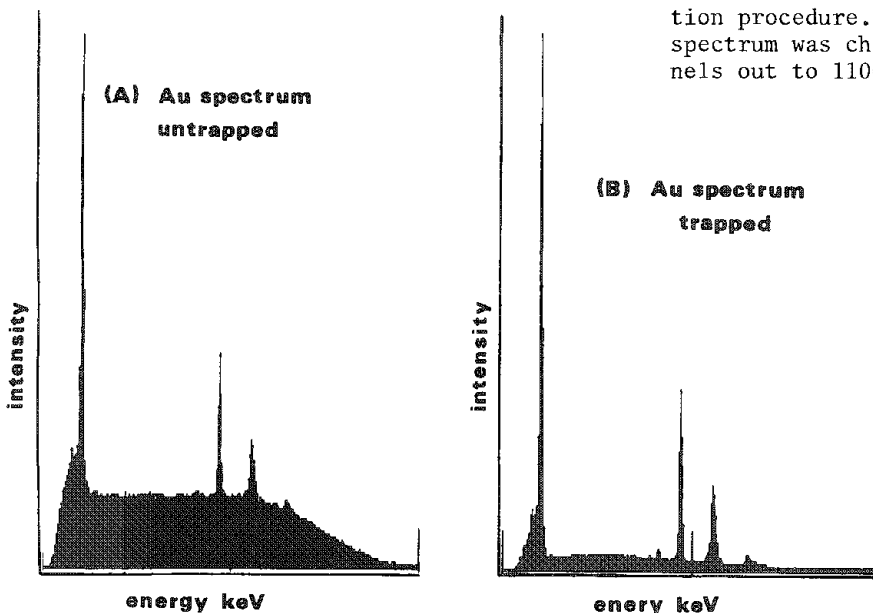


FIG. 4.--(a) X-ray spectrum of Au with no electron trap on detector; (b) x-ray spectrum of Au with electron trap on detector.

## A GENERAL CORRECTION FOR FLUORESCENCE FROM CHARACTERISTIC LINES

K. F. J. Heinrich

The fluorescence caused by characteristic lines was first described in Castaing's thesis;<sup>1</sup> it is applied in a complete form in the program COR,<sup>2</sup> but in most other procedures the abbreviated version due to Reed and Long<sup>3</sup> is used. Both versions describe the fraction of radiation absorbed by an element secondarily excited by means of the absorption jump ratios, for which expressions exist for some absorption edges only. The version by Reed and Long uses simplifications that further restrict the range of applicability. The algorithm described in this publication permits an automatic application of the exact fluorescent correction to all situations, without the use of the jump ratios.

In the versions in use at present, the following terms occur in the final equation:

$$[\mu(ab)/\mu(*b)] (r_a - 1)/r_a' \quad (1)$$

where  $\mu(ab)$  and  $\mu(*b)$  are the absorption coefficients for the exciting radiation of element b in element a and in the composite specimen. The jump ratio  $r_a$  for a given atomic level is the ratio of the mass absorption coefficients for element a across the absorption edge of reference. In the secondary excitation at the K level,  $r_a'$  is identical to  $r_a$ , but in the L and M levels it is the product of all jump ratios between the exciting line and the level that fluoresces. At the M level as many as five jump ratios may be involved, and normally there are no provisions for calculating them; hence, M lines are usually neglected in fluorescence calculations.

The use of the jump ratios dates from the time when mass absorption coefficients had to be entered manually. Now that every program contains algorithms for mass absorption coefficients, the use of jump ratios is unnecessary. Calling  $\mu^1$  and  $\mu^2$  the mass absorption coefficients of the absorbing element at the high- and low-energy sides of the edge of reference,  $E_b$  the energy of the exciting line of element b, and  $E_{da}$  the energy of the edge of reference of a, we can replace term (1) by

$$(\mu_1 - \mu_2)/[\mu(*b) \cdot (E_b/E_{da})^{2.7}] \quad (2)$$

as shown in Fig. 1. The power 2.7 is an average slope of the logarithms of  $\mu$  vs wavelength (or -2.7 for  $\log \mu$  vs  $\log E$ ). It can be seen that the presence or absence of edges between the exciting line and the edge emitting the line of interest is of no consequence, and that  $\mu(ab)$  has also cancelled. By means of a simple search program comparing the lines of element b with the edge of interest of element a, all fluorescence cases of interest can be determined and calculated by the usual formula modified as shown in (2). Cases such as that of a Ni-Co alloy in which only the Co K $\alpha$  line excites the Ni K level are automatically and

correctly treated.

### References

1. R. Castaing, doctoral thesis, University of Paris, 1951.
2. J. Henoc et al., NBS Tech. Note 769, National Bureau of Standards, Washington, D. C., 1973.
3. S. J. B. Reed and J. V. P. Long, in H. H. Pattee, V. E. Cosslett, and A. Engstrom, Eds., *Proc. 3d Intern. Conf. X-ray Optics and Microanalysis*, New York: Academic Press, 1963, 317.

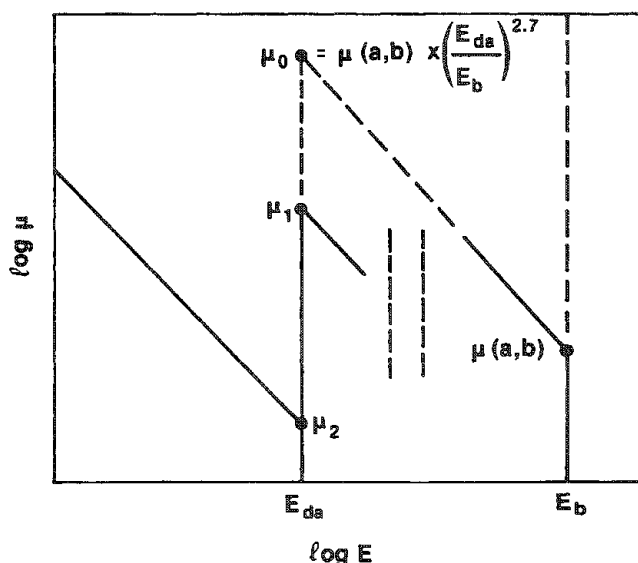


FIG. 1.--Energy  $E_b$  is that of exciting line (element b);  $E_{da}$  is absorption edge of excited line of element a; coefficients  $\mu^1$  and  $\mu^2$  are those at either side of edge  $E_{da}$ , for element a. If all absorptions of exciting radiation were taking place at energy  $E_{da}$ , absorption coefficient would be  $\mu_0 \approx \mu(ab) (E_{da}/E_b)^{2.7}$ .

# A SIMPLE CORRECTION PROCEDURE FOR CONTINUUM FLUORESCENCE

K. F. J. Heinrich

Corrective procedures for fluorescence excited by the continuum have been proposed by Henoc<sup>1,2</sup> and by Springer.<sup>3</sup> In most analyses the effect of continuum fluorescence does not exceed a few percent and tends to compensate between specimen and standard. However, in the case of high-energy primary radiation, particularly in a matrix of low average atomic number, such as Zn K $\alpha$  in soft biological tissues, its neglect in the data-reduction procedure, may lead to serious errors. By changing the integration procedure, eliminating the need for sorting edges and entering absorption edge jumps, one can simplify the system without sacrifice in accuracy and use it in routine data-reduction procedures.

The correction for continuum fluorescence requires a model for the emission of the continuum. Next, the fluorescent effect is calculated as in characteristic fluorescence. However, since the continuous radiation extends over a range of photon energies, the equation must be integrated over the range of the continuum energies that produce fluorescent emission.

The cited procedures require the sorting of all absorption edges above that of the emitting line, and separate integration for each interval between them. Because numerical integrations were considered too time-consuming in the past, algebraic models were developed for the integrations.<sup>1,3</sup> Their use makes it difficult to substitute alternate equations for the continuum generation, and may lead to simplifications that affect the accuracy of the procedure. In Henoc's program COR<sup>2</sup> a numerical integration replaced the formal integration.

The calculation can be simplified by means of a numeric integration over the energy region of interest, without consideration of the position of the absorption edges. The unit interval of the integration steps is a fixed fraction of the wavelength interval between the operating potential  $E_0$  and the energy  $E_c$  of the excited edge. The effects of the edges are implicit in the corresponding x-ray absorption coefficients. If the number of integration intervals is large enough, the positions of the absorption edges within any integration step do not introduce errors that are significant, or larger than those due to uncertainties in other parameters for continuum generation. As in the method proposed for characteristic fluorescence,<sup>4</sup> one can replace  $\mu(a,b)/\mu(*,b) \cdot (r_a - 1)/r_a'$ , where  $\mu(a,b)$  and  $\mu(*,b)$  are the absorption coefficients for the exciting radiation of element b in element a and in the composite specimen, by  $(\mu_1 - \mu_2)/[\mu(*b) \cdot (E_b/E_d)^{2.7}]$  (where  $\mu_1$  and  $\mu_2$  are the absorption coefficients for the emitting element on either side of the corresponding absorption edge), so that the jump ratios  $r_a$  and  $r_a'$  disappear.

The author is at the National Bureau of Standards, Gaithersburg, MD 20899.

In the proposed procedure we express wavelength in units of 1/eV and photon energy in units of eV (rather than keV). Calling N the number of steps in the numerical integration, we determine a constant wavelength interval for each step:

$$\Delta\lambda = [(1/E_c) - (1/E_0)]/N \quad (1)$$

where  $E_c$  is the critical excitation energy for the line of interest and  $E$  the operating energy (operating voltage). The mean energy  $E_T$  for step T of the integration is

$$1/[\Delta\lambda(T - \frac{1}{2}) + (1/E_0)] \quad (2)$$

and the energy interval for step T is equal to

$$\Delta E_T = 1/[(1/E_0) + (T - 1)\Delta\lambda] - 1/[(1/E_0) + T\Delta\lambda] \quad (3)$$

The parameters u and v used in the fluorescence correction are, as usual,

$$u = \mu(*E_a) \csc \psi / \mu(*, E_T) \quad (4)$$

$$v = [3.6 \times 10^{10} / E_0^{1.65} - E_c^{1.65}] / \mu(*, E_T)$$

where  $\psi$  is the x-ray emergence angle (energies in eV). We obtain for the emergent fluorescent intensity:

$$I_{fc} = (\pi/4) C_a \omega p_a (\mu_1 - \mu_2) (k/2) \bar{Z} \sum_{T=1}^N (E_T/E_c)^{-2.7}$$

$$\cdot \frac{f[E_T \chi(*a)]}{\mu(*E_T)} \left[ \frac{E_0}{E_T} - 1 \right] \left[ \frac{\ln(1+u)}{u} + \frac{\ln(1+v)}{v} \right] \Delta E_T \quad (5)$$

Here,  $C_a$ ,  $p_a$ , and  $\omega$  are the concentration, weight of line, and fluorescent yield of the emitting element and line,  $\bar{Z}$  the average atomic number of the specimen, and  $k/2$  is the constant in Kramers's equation. The term  $f[E_T \chi(*a)]$  is formally equal to the primary absorption factor corresponding to a critical excitation potential equal to  $E_T$ , with the absorption coefficient of the specimen for the emitted radiation  $\mu(*, E_a)$ . The following expression can be used for the constant  $k/2$ :

$$\frac{k}{2} = (2.1 - 0.047307Z + 3.9094 \times 10^{-4} Z^2) 10^{-9} \quad (6)$$

It is easy to replace Kramers's equation by other formulas such as that proposed by Small.<sup>5</sup> Ten integration steps in the integration are sufficient. Even a small personal computer can perform this calculation in a few seconds, so that there is no longer any reason to exclude the continuum fluorescence calculation from the correction procedures.

## References

1. J. Henoc, in K. F. J. Heinrich, Ed., NBS Spec. Publ. 298, Washington, D.C., 1968.
2. J. Henoc et al., NBS Tech. Note 769, Washington, D.C., 1973.
3. G. Springer, *Neues Jahrbuch f. Mineralogie, Abhandlungen* 106: 241, 1967.
4. K. F. J. Heinrich, these proceedings.
5. J. Small et al., *J. Appl. Phys.* 61(2): 1987.

## 2B. EPMA: Mapping

### BACKGROUND CORRECTION IN ELECTRON MICROPROBE COMPOSITIONAL MAPPING WITH WAVELENGTH-DISPERSIVE X-RAY SPECTROMETRY

R. L. Myklebust, D. E. Newbury, R. B. Marinenko, and D. S. Bright

Compositional mapping with the electron microprobe is the technique of creating quantitative images by carrying out complete quantitative analysis procedures at every point of a scan matrix.<sup>1</sup> A proper background correction is vital if accurate quantitation is to be achieved for minor and trace constituents. The background depends strongly on the composition, varying at a particular x-ray energy approximately with the average atomic number. In conventional single point analysis, background correction can be accomplished by several approaches.

1. The spectrometer(s) can be detuned from the characteristic peak to measure the background on either side of the peak while the beam continues to excite the same region of unknown composition that is being analyzed.

2. On a system with multiple spectrometers, the background can be measured on one spectrometer while the other spectrometers are tuned to characteristic x-ray peaks. A correction for efficiency is then used to adjust the measured background to these other spectrometers.

3. From an initial calculation of the composition of the unknown, the average atomic number can be calculated based on major constituents. The background can then be measured on a pure element with approximately this same atomic number, providing no characteristic peaks of this element occur at the wavelengths of interest. Alternately, a substantially different atomic number can be used for the background measurement with appropriate scaling based on the average atomic number and Kramers's equation, which gives the functional dependence of the x-ray bremsstrahlung on atomic number.<sup>2</sup>

For the analysis procedures of compositional mapping, the background problem is exacerbated by the sheer number of analytical data points involved, namely the  $n \times n$  product of the scan matrix, where the background may differ significantly from point to point. Swyt and Fiori,<sup>3</sup> Marinenko et al.<sup>1</sup> and Myklebust<sup>4</sup> have described instrumental methods for background correction in compositional mapping that make use of scanning a background matrix map in a manner analogous to the second of the three procedures described above. The difficulty with such methods is the time-intensive nature of such a process. Since most instruments have a small number of wavelength-dispersive spectrometers, e.g., three or fewer, the necessity of devoting a spectrometer to a background channel means a significant loss of analytical information or an increase in the

time spent in completing a compositional map.

#### *Background Correction Without Scanning*

When the situation is examined in detail, we can demonstrate that it is not in fact necessary to scan a background map. For characteristic x rays, the x-ray intensity at any point in the scan matrix on a flat specimen can vary for either of two reasons: the composition of the specimen may vary or the spectrometer may defocus because the beam has been scanned sufficiently far off the optic axis of the spectrometer. As the magnification is progressively reduced and the scanned area is made larger, the second of these effects predominates. For example, a 50% peak intensity loss is observed from the center to the edge of an  $0.5 \times 0.5$  mm scan field (200 $\times$ ) in a typical instrument. However, the spectral background, which consists mostly of the x-ray bremsstrahlung, is a slowly varying function with wavelength, except in the region of an absorption edge. The strong defocusing effect observed with characteristic x rays that are sharply peaked thus becomes negligible for the background. This observation is demonstrated in Fig. 1, which compares a standard map recorded with a scanned field of  $0.5 \times 0.5$  mm (200 $\times$ ) for a characteristic peak (Fig. 1a) and a background region (Fig. 1b) obtained by detuning the spectrometer off the peak to a nearby background wavelength. In order to be sure that sufficient background counts were recorded in the background map to observe any defocusing effects, the beam current and the pixel dwell time were increased to accumulate a total of approximately 500 counts per pixel. A line trace across this background map reveals that the defocusing effect is less than 2% across the image, compared to the peak map, where the defocusing results in a drop of more than 50% in the intensity.

#### *Background Correction in Images Based on Average Atomic Number*

Although spectrometer defocusing is not a significant problem when an image is corrected for the background, there remains the very important problem of correcting for the variation in the background with the average atomic number of the unknown. We propose that a suitable background correction for compositional images can be developed as follows, incorporating the compositional mapping procedure described previously.

1. A background reading is taken for each wavelength spectrometer (A,B,C, etc.) with the beam fixed on a particular element  $Z_1$  which is not found in the specimen.

2. The characteristic peak maps are then recorded for the unknown, with correction for defocusing by any of the four possible methods: stage scanning, crystal rocking, standard mapping, or peak modeling.

---

The authors are with the Center for Analytical Chemistry, National Bureau of Standards, Gaithersburg, MD 20899.

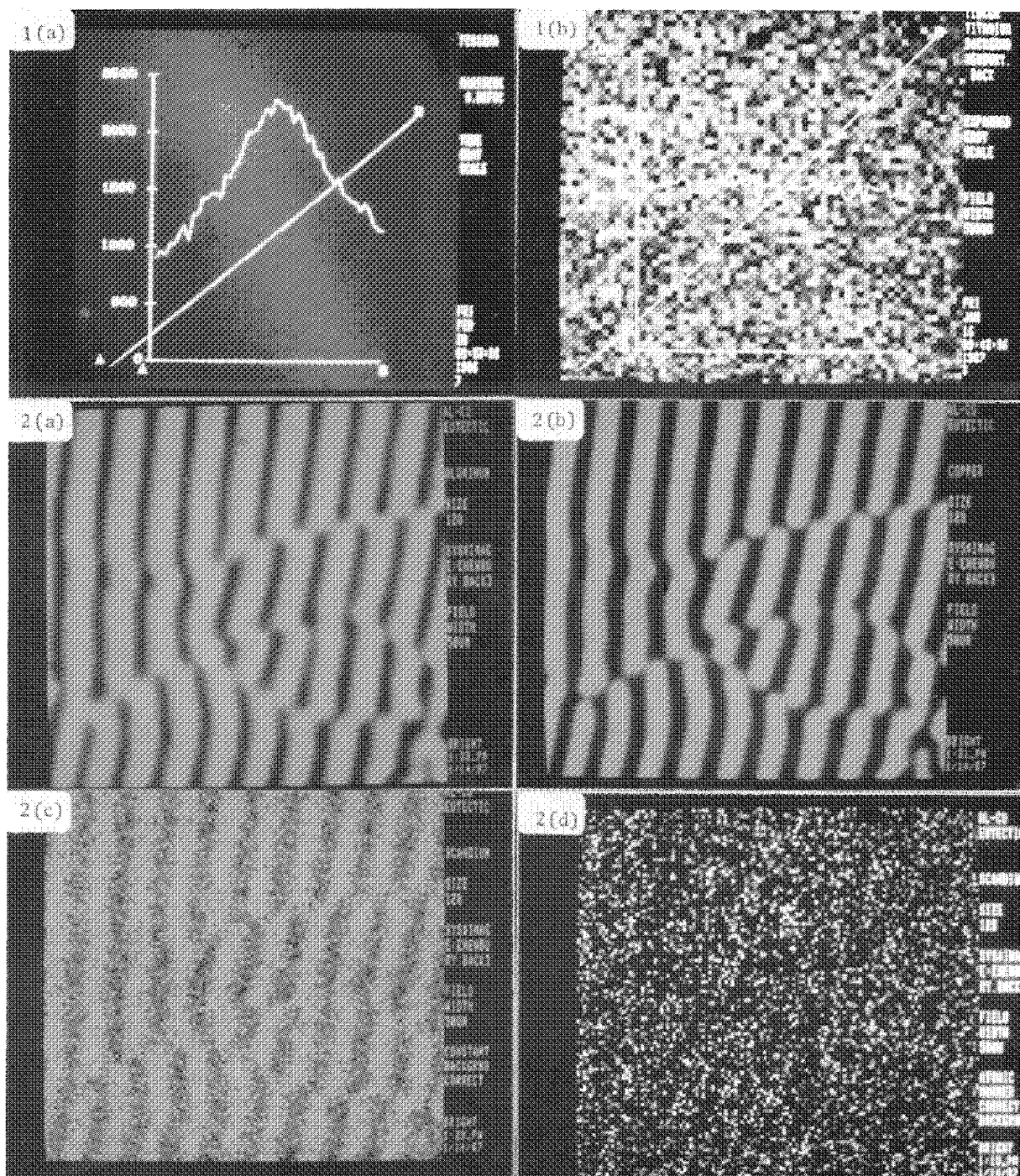


FIG. 1.--Defocusing effects for scan field of  $0.5 \times 0.5$  mm on (a) TiK characteristic peak and (b) nearby background channel; apparent contrast in background map has been enhanced. Line trace along vector A-B is shown for each intensity map. Vertical scale is in x-ray counts.

FIG. 2.--Compositional maps for aluminum-copper eutectic alloy: (a) aluminum; (b) copper; (c) scandium, with constant background correction based on measurements on carbon; (d) scandium, with variable background correction based on average atomic number calculated from principal constituents.



3. Quantitative analysis is performed at each pixel with ZAF matrix corrections or alpha coefficients. In this first quantitative calculation stage, the measured background on  $Z_1$  is used for background subtraction.

4. Based on the major constituents determined in this analysis, the average atomic number ("Z-bar") is calculated at each pixel (forming a "Z-bar map").

5. This Z-bar map is used to calculate a background map appropriate to each spectrometer, by use of the calculation  $(Z\text{-bar}/Z_1) \times BKGZ_1$  based on Kramers's relation, where  $BKGZ_1$  is the background measured with that spectrometer on element  $Z_1$ .<sup>2</sup>

6. The quantitation is now repeated with the background at each pixel taken from the background maps.

If necessary, this procedure could be repeated in an iterative fashion, but the initial estimate of the average atomic number from the quantitative analysis of the major constituents is sufficiently accurate to give an accurate background correction.

#### Testing and Application

As a test of the accuracy of this method, images were prepared for a eutectic alloy of aluminum and copper, which was characterized by a fine lamellar structure. Two spectrometers were assigned to the Al and Cu characteristic peaks; the third spectrometer recorded the signal at the wavelength for scandium, which is not present in the specimen. Background readings were taken for all three spectrometers on carbon. The initial quantitation was performed with the carbon background readings for the measured Al and Cu intensities. The quantitative compositional maps for Al and Cu are shown in Figs. 2(a) and (b). (In all the images in this paper, higher concentrations are indicated by gray levels on the white end of the scale.) Despite the lack of scandium in the specimen, the calculated scandium map (Fig. 2c) shows an apparent segregation of scandium in the copper-rich phase. A Z-bar map was then calculated from the concentrations for Al and Cu. From this Z-bar map, background maps were calculated for all three spectrometers. The calculated background map for the third spectrometer was then subtracted from the scandium signal map, and the quantitation was repeated, with the result shown in Fig. 2(d). The apparent compositional structure visible in the scandium map corrected with a constant background (Fig. 2c) is completely eliminated in the scandium map corrected with a variable background calculated from the average atomic number (Fig. 2d). The maximum concentration represented in Fig. 2(d) is 0.08%, which represents the limit of detection for scandium under the conditions used for this compositional map (20 keV, 17 nA, 2s integration time, 128 x 128 scan matrix, 2000 diameters magnification).

As an example of an application of the method to a practical problem, consider the compositional mapping of the aluminum wire-iron screw electrical junction that has undergone failure while in service.<sup>5</sup> Figures 3(a)

and (b) show the distribution of aluminum and iron at the reaction zone associated with the failure. A map for zinc with a constant background correction is shown in Fig. 3(c), with a high degree of contrast expansion applied. In addition to the zinc-rich region in the upper right of this image, there is apparently more zinc in the iron-rich region of the specimen (0.45 wt%) than in the aluminum-rich region (0.35 wt%). However, after correction with the variable background based on average atomic number (Fig. 3d), the true situation is found to be reversed, with zinc at 0.30 wt% in the aluminum-rich constituent and 0.05 wt% in the iron-rich region, which is at the detection limit.

For calculating compositional maps, the correction of background by the average atomic number method gives significantly improved performance and efficiency over the methods previously utilized. Further testing is needed to describe fully practical detection limits. Additional improvements in accuracy can be expected by incorporation of a more accurate background equation for better modeling of the atomic-number dependence of the background.<sup>6</sup>

#### References

1. R. B. Marinenko, R. L. Myklebust, D. S. Bright, and D. E. Newbury, "Digital x-ray compositional mapping and 'standard map' corrections for wavelength-dispersive spectrometer defocussing," *J. Microscopy* (in press).
2. H. A. Kramers, "On the theory of X-ray absorption and of the continuous X-ray spectrum," *Phil. Mag.* 48: 836, 1923.
3. C. R. Swyt and C. E. Fiori, "Large-field x-ray compositional mapping with multiple dynamically focused wavelength-dispersive spectrometers," *Microbeam Analysis--1986*, 482.
4. R. L. Myklebust, R. B. Marinenko, D. E. Newbury, and D. S. Bright, "Quantitative calculations for compositional mapping techniques in electron probe microanalysis," *Microbeam Analysis--1985*, 101.
5. D. E. Newbury and S. Greenwald, "Observations on the mechanisms of high resistance junction formation in aluminum wire connections," *NBS J. Research* 85: 429, 1980.
6. J. A. Small, S. D. Leigh, D. E. Newbury, and R. L. Myklebust, "Modeling of the bremsstrahlung radiation produced in pure-element targets by 10-40 keV electrons," *J. Appl. Phys.* 61: 459, 1987.

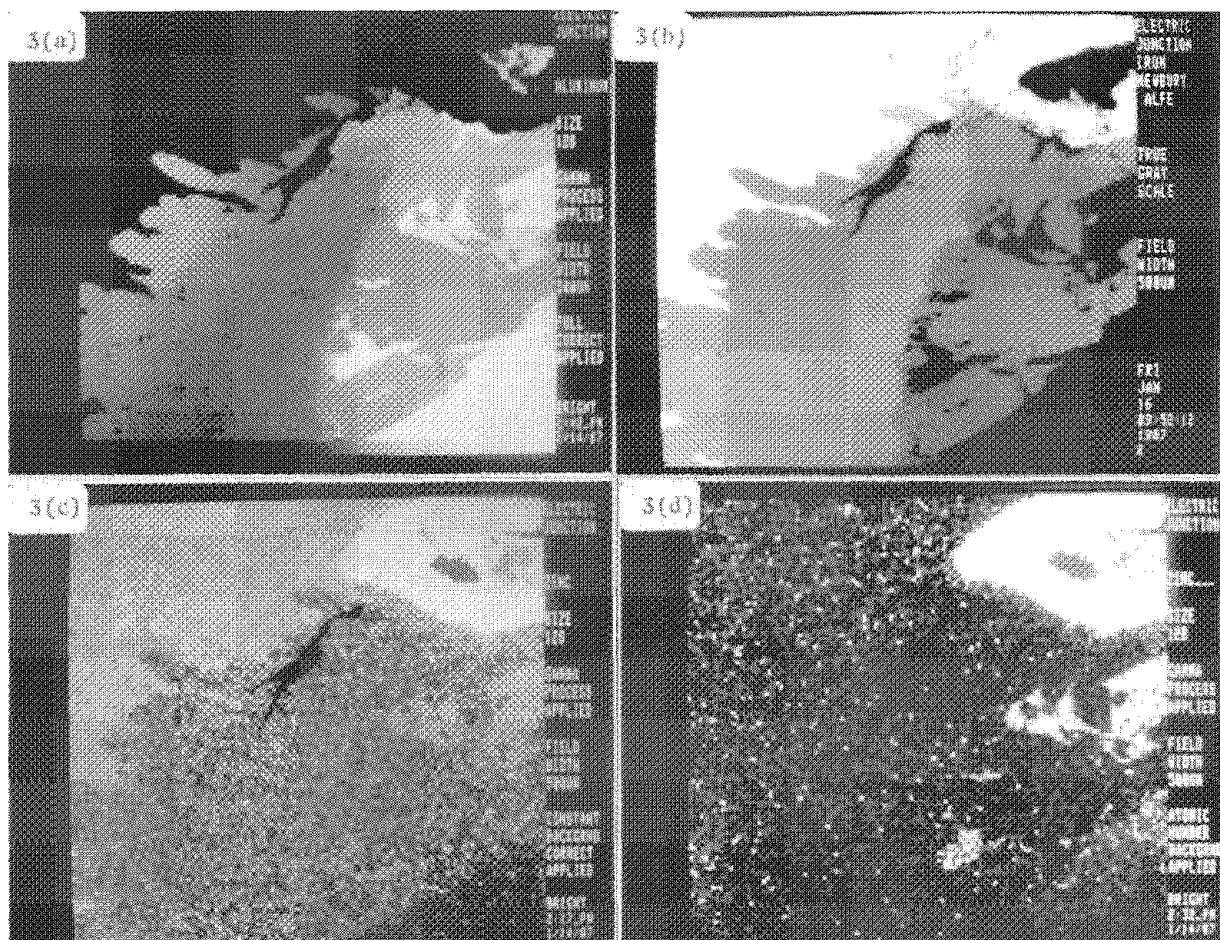


FIG. 3.-- Compositional maps for failed electrical junction between an aluminum wire and a steel screw: (a) aluminum; (b) iron; (c) zinc, with constant background correction based on measurements on carbon; contrast has been artificially enhanced to make low concentration levels visible; (d) zinc with variable background correction based on average atomic number calculated from principal constituents; contrast has been artificially enhanced.

## DIGITAL X-RAY MAPPING AT LOW MAGNIFICATION WITH THE USE OF WAVELENGTH-DISPERSIVE TECHNIQUES IN ELECTRON-PROBE MICROANALYSIS

P. K. Carpenter

Low-magnification compositional mapping by digital image-processing techniques has become an increasingly important tool in electron-probe microanalysis. Previously, energy-dispersive spectrometers (EDS) have been used to acquire digital x-ray maps because they can collect counts for many elements simultaneously and thus allow for rapid acquisition of data. EDS detectors also lack the serious defocusing problems that have prohibited the use of wavelength-dispersive spectrometers (WDS) at magnifications below about 1000 $\times$ , and as a consequence nearly all low-magnification mapping is done by EDS. However, WDS detectors have a higher peak-to-background ratio and are necessary for use in situations where one is studying samples in which compositional variations are small and/or concentration levels are low. Use of WDS for detailed mapping at magnifications as low as 100 $\times$  requires a technique that corrects for defocusing and allows quantitative calculations to be made at each pixel location in the digital image. The ultimate goal is to acquire digital compositional maps for both sample and standard, followed by calculation of k-ratios at each pixel and final correction of the k-ratios by ZAF (or other appropriate method) to concentration units. This procedure results in a complete chemical analysis at each pixel in the image and provides quantitative information about the spatial distribution of elements in a sample.

Wide-area compositional mapping can be accomplished in two ways. On microprobe systems equipped with stage automation, digital x-ray images can be acquired if the stage is positioned to each pixel position and all spectrometers are counted. This approach avoids the problem of WDS defocusing by moving the sample rather than rastering the electron beam, and has been used to produce detailed digital maps.<sup>1</sup> However, stage positioning errors can produce artifacts in the image, and commercially available software packages typically are not set up for stage mapping. The second method is digitally to position the electron beam on the sample, count all spectrometers at each pixel location, and make a correction for WDS defocusing. More recent attempts to acquire low-magnification x-ray maps have assumed that the WDS defocusing is identical for both sample and standard, so that images acquired on both could be used to obtain k-ratios for subsequent calculations.<sup>2,3</sup> This approach requires that the sample and standard have precisely the same x-ray peak shape, which may not be a valid assumption for low-atomic-number elements where variations in peak position and shape are observed among different

compounds containing the element of interest.<sup>4</sup> Also, because the count rate approaches zero away from the focused zone of the WDS detector, this method should be restricted to magnifications higher than 400 $\times$ , so that counts can be obtained throughout the image area. Because fewer counts are acquired on both the sample and standard away from the focused zone, there is an increase in the counting error which is propagated through subsequent calculations to produce a larger error in concentration. As will be shown, satellite lines and other x-ray peaks proximal to the line of interest are another problematic artifact that must be dealt with in image interpretation.

The technique discussed in this paper is designed to acquire digital x-ray maps by WDS at magnifications as low as 100 $\times$ . This goal is accomplished by simultaneous scanning of the WDS spectrometer over the x-ray peak to maintain spectrometer focus while the electron beam is digitally positioned during image acquisition. The images acquired by this technique are free of artifacts such as satellite lines.

### *Instrumentation and Techniques*

This work was performed on a JEOL JXA-733 Superprobe equipped with three WDS spectrometers, a Tracor Northern TN-5500 EDS x-ray analyzer, and a TN-5600 stage and spectrometer automation system. The microprobe is equipped with a TN-5700 image analysis system which controls digital beam positioning and is used for the acquisition, processing, and storage of video and x-ray images of up to 512  $\times$  512 pixel size. The 733 Superprobe is outfitted with a scan rotation module which is used to orient the electron beam scanning direction during digital mapping. The author modified the Tracor Northern IPA57 software package on the TN-5700 to control WDS spectrometer scanning by reference to the low-magnification x-ray photography subroutine from the Tracor Northern TASK microanalysis program.

Preliminary work was carried out on pure metal standards with the use of 128  $\times$  128 and 256  $\times$  256 pixel x-ray maps to evaluate the technique; several 512  $\times$  512 maps were used to study natural samples. An accelerating voltage of 15 kV, beam current of 10-20 nA, and pixel dwell times of 10-70 ms were used.

Each WDS spectrometer has a setting for the scan rotation of the electron beam that corresponds to the axis of curvature of the analyzing crystal. The operator determines the correct scan rotation setting by acquiring digital x-ray maps in which the focus band is oriented horizontally; this setting is used for all subsequent images. The next step is to calculate the total deviation from the normal spectrometer peak position that is required to keep the spectrometer in focus as the beam is rastered

---

The author is at the LSU Basin Research Institute, Baton Rouge, LA 70803-4101.

across the sample. The theoretical basis for this calculation has been previously described,<sup>5</sup> and the deviation is calculated from the following equation for a JEOL 733 Super-probe:

$$OF = Y(\sin \phi) \sqrt{1 - \sin^2 \theta} / \sin \theta$$

where OF is the deviation from the peak position in mm,  $Y = 50/M$  is the lateral offset on the sample in mm,  $M$  is the magnification, and  $\phi$  is the take-off angle. For the 733 Super-probe  $\sin \theta = P/280$ , where  $P$  is the peak position in mm. The spectrometer is scanned through the range  $20^\circ F$  during digital image acquisition, and through software control the peak scan and image acquisition are synchronized.

#### Discussion of Results

The true test of any method which attempts to correct WDS defocusing is to collect x-ray intensity maps on pure-element standards that are free of intensity variations. Maps were acquired on pure silicon and iron standards by use of WDS spectrometers equipped with TAP, PET, and LIF analyzing crystals (Figs. 1 and 2). No background correction was necessary due to the high peak-to-background ratio on these pure-element standards. The uncorrected intensity maps collected at  $100\times$  illustrate that intensities drop off to zero away from the focus zone (Figs. 1A, 1D, and 2A). These uncorrected images also show secondary intensity bands, especially developed on the spectrometers with TAP and LIF crystals, that are produced by satellite peaks and the  $\alpha_1 \alpha_2$  characteristic doublet. Such artifacts are undesirable, since they could be interpreted as enriched concentrations in uncorrected WDS maps.

The focus-corrected intensity maps collected by synchronous peak scanning during digital image acquisition indicate that there is a minimum variation in intensity at  $100\times$  magnification, and suggest that this approach should be successful for general mapping purposes. The absence of artifacts in the corrected intensity maps is especially desirable, and gray-level histograms of these images are characterized by a normal distribution resulting from random x-ray production alone, rather than the bimodal distributions seen on uncorrected maps having satellite bands of lower intensity.

This method was applied to investigate trace element variations of Hf in a zircon  $[(Zr,Hf)_2SiO_4]$  grain, which is characterized by oscillatory zoning. This zoning is known from previous work to result from variations in Hf concentration below the 1 wt% level, and is illustrated in a backscattered-electron image in Fig. 2(C). A focus-corrected Hf x-ray map was acquired over a 10h period to document variations in this element. The focus-corrected WDS map clearly illustrates the compositional variations in Hf, whereas a simultaneously acquired EDS map for Hf showed only background counts.

#### Sampling Considerations

Digital compositional maps acquired at low

magnification are subject to a sampling bias based on the relative sizes of the analytical volume where x-rays are produced and the pixel dimension at that magnification. The minimum x-ray production volume is probably no less than  $1 \mu m$  in diameter, so that the sample is overscanned if a digital image format of  $512 \times 512$  or  $1024 \times 1024$  pixels is used. The upper limit on the spatial resolution of digital x-ray images is thus about  $1 \mu m$  per pixel. Conversely, one should use a defocused beam when acquiring digital x-ray maps with a size format of  $64 \times 64$  pixels or smaller, because the pixel size may be considerably larger than the x-ray volume of the focused beam. One should estimate and set the x-ray volume by varying the beam diameter to match the pixel size in order completely to sample the material being investigated. For this reason one must use an optimum magnification that adequately samples the scale of chemical variations and covers as much area of the sample as to be comprehensive.

#### Conclusion

The problem of WDS defocusing can be solved by simultaneously scanning over the x-ray peak on the spectrometer during digital image acquisition. The electron-beam scan rotation setting is used to orient the scan direction for each WDS spectrometer. Focus-corrected intensity maps acquired by this method are free of artifacts and indicate that the method is desirable for investigation of samples for low-magnification compositional mapping. The relative sizes of the analytical volume and the image pixels must be closely matched during image acquisition for best sampling of the material being studied.

#### References

1. Y. Ono et al., "High-speed wide-area analysis by electron probe," *Microbeam Analysis--1985*, 145.
2. R. B. Marinenko et al., "Wavelength-dispersive techniques for compositional mapping in electron-probe microanalysis," *Microbeam Analysis--1985*, 159.
3. R. L. Myklebust et al., "Quantitative calculations for compositional mapping techniques in electron-probe microanalysis," *Microbeam Analysis--1985*, 101.
4. J. I. Goldstein et al., *Scanning Electron Microscopy and X-Ray Microanalysis*, New York: Plenum Press, 1981, 439-445.
5. W. F. Chambers, "Computer controlled photography on an electron microprobe," *Microbeam Analysis--1978*, 84.

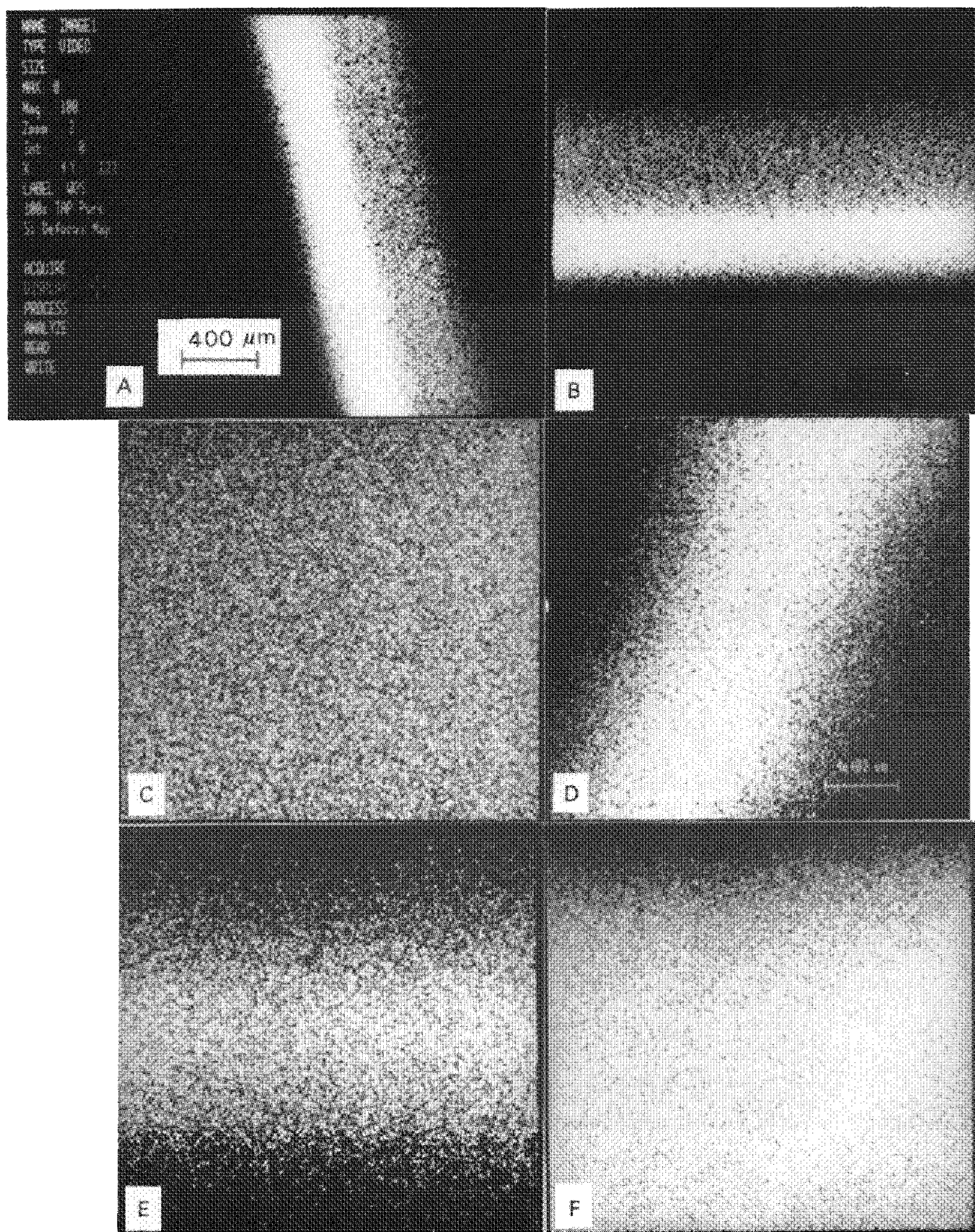


FIG. 1.--Digital x-ray maps ( $256 \times 256$  pixels) on TAP and PET spectrometers: (a) 100 $\times$  Si map on pure Si metal, TAP spectrometer; note defocused main and secondary satellite peak bands. (b) Scan rotation orientation for TAP spectrometer used for map acquisition. (c) Focus-corrected Si x-ray map taken on pure Si metal, TAP spectrometer at 100 $\times$  and 1000s accumulation time. (d) 100 $\times$  Si map on pure Si metal, PET spectrometer; note defocusing. (e) Scan rotation orientation for PET spectrometer. (f) Focus-corrected Si x-ray map taken on pure Si metal, PET spectrometer at 100 $\times$  and 1000s accumulation time.



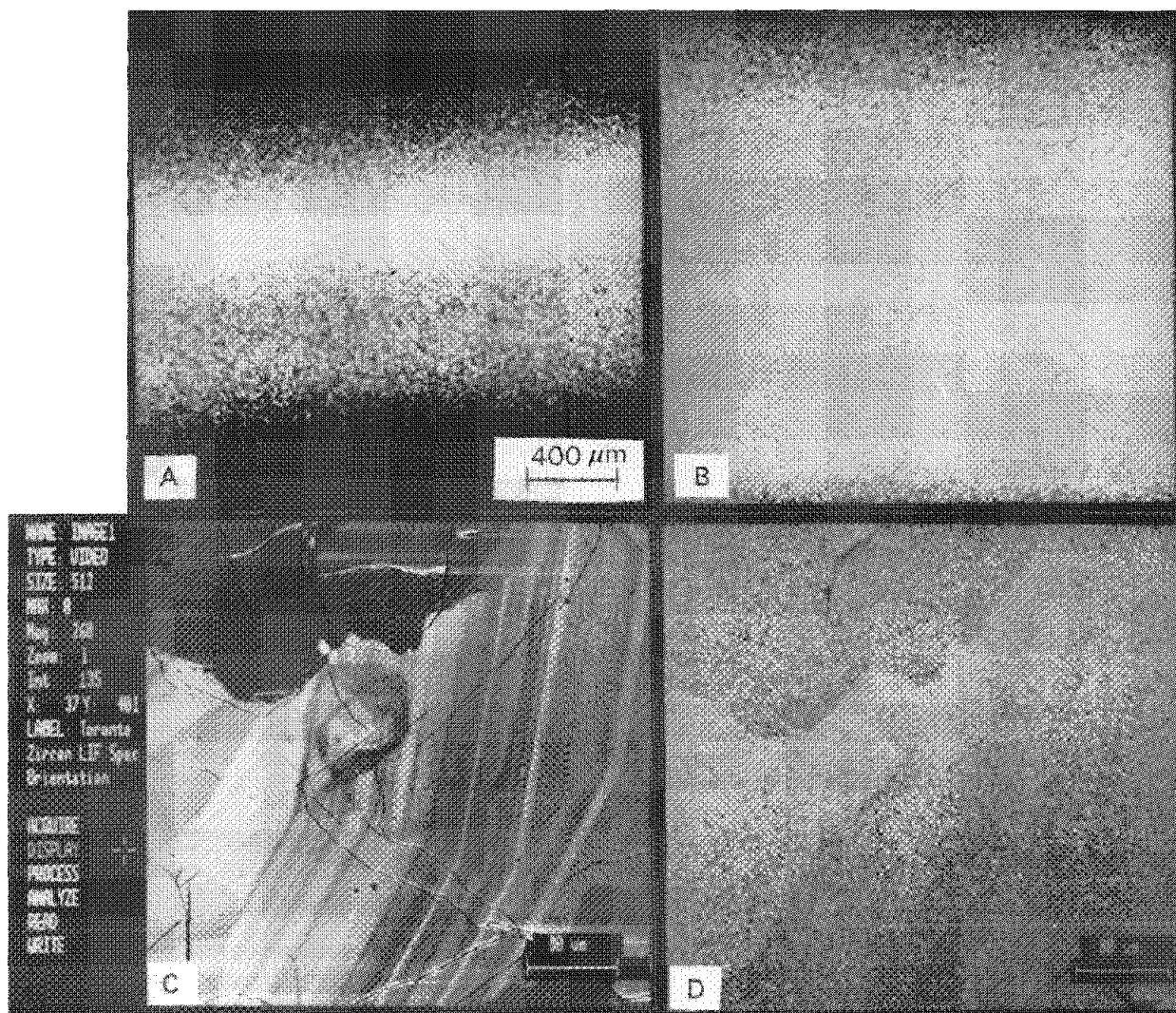


FIG. 2---Digital compositional maps: (a) WDS defocus image and scan rotation setting for LIF spectrometer on pure Fe at 100 $\times$  magnification (256  $\times$  256 pixels). Double band results from presence of  $\alpha_1\alpha_2$  doublet on x-ray peak. (b) Focus-corrected x-ray map for pure Fe on LIF spectrometer at 100 $\times$  with accumulation time 1000 s (256  $\times$  256 pixels). (c) Digital backscattered-electron image of zircon grain at 260 $\times$  (512  $\times$  512 pixels). Oscillatory zoning is due to Hf variations below the 1% level. (d) Focus-corrected Hf x-ray map on zircon grain using LIF spectrometer at 260 $\times$  accumulated over 10h period (map is 512  $\times$  512 pixels and pixel dwell time is 0.07 s/pixel).

## APPLICATIONS OF COMPOSITIONAL MAPPING IN MATERIALS SCIENCE

Dale E. Newbury

Electron probe microanalysis has been traditionally applied to the solution of problems in materials science through the combined use of several modes of operation. Quantitative analysis with full corrections for deadtime, background, standardization, and matrix corrections is performed at individual points selected by the analyst. These point analyses are supported by line scans of signal intensity across features, by x-ray area scans that produce images giving a qualitative impression of the lateral distribution of elemental constituents, and by scanning electron microscope (SEM) images prepared with the backscattered electron (BSE) signal, which is sensitive to compositional differences.

Over the past several years, the development of the technique of compositional mapping by electron probe microanalysis has resulted in new capabilities for the analyst.<sup>1-3</sup> Compositional mapping involves the use of advanced computer techniques for control of the electron probe to record the x-ray intensity over the scanned area for each constituent of interest. These intensity matrices can be converted to compositional matrices by application of the full calculation sequence of conventional quantitative analysis at each point in the scanned matrix. Signals from both energy-dispersive and wavelength-dispersive x-ray spectrometers can be used. Because of the greater peak-to-background and the higher characteristic x-ray count rates that can be obtained with wavelength-dispersive spectrometers, this type is preferred when minor (1-10 wt%) or trace (< 1 wt%) constituents are to be mapped. The numerical values of the composition that result from this procedure can be converted into a gray scale for display on a video monitor. With a sufficiently large digital scan density, 128 × 128 or more, the display of the compositional data with gray-scale or color encoding produces an image with an extraordinary amount of detail. These images, or compositional maps, are supported at every pixel location by stored values of the concentrations for all constituents measured. The analyst thus has available the powerful combination of an image that is much richer in detail than a conventional x-ray area scan and the quantitative analytical values available for interrogation at any desired point, along any vector, or over any specified area.

In this paper examples are given of applications of the technique of compositional map-

ping to problems in materials science. These problems have been selected to illustrate some of the new capabilities made possible by compositional mapping.

### *Detection of Compositional Contrast*

This first discussion concerns the most obvious application of compositional mapping, namely the detection of compositional contrast in images. We note at the outset that the objective is not to supplant SEM/BSE images for this purpose, but rather to augment the capability for compositional imaging. The signal strength of the electron image is approximately 10 000 times stronger than the x-ray mapping signal. However, the BSE image lacks the elemental specificity to determine what constituent is being imaged. Moreover, although BSE detectors are now available that claim contrast sensitivity to a level of 0.1 atomic number units, this sensitivity is only present for low-atomic-number targets. Even then, it is doubtful that variations in minor and trace elements would produce sufficient contrast to be detected.

An illustrative example (Fig. 1) shows compositional maps for (a) aluminum, (b) iron, and (c) copper at the interface of an aluminum wire/steel screw (brass coated) electrical junction from a household receptacle that has failed.<sup>4</sup> The several compositional regions visible include the nearly pure aluminum and iron end members of the couple, as well as two regions of intermetallic compound that have formed as part of the failure mechanism. To enhance the visibility of the intermetallic regions, the image contrast has been artificially enhanced in the iron image. Quantitative analysis revealed these intermetallic regions to be FeAl<sub>3</sub> and Fe<sub>2</sub>Al<sub>5</sub> at the maximum limit of aluminum solubility for these phases. The change in aluminum concentration between the phases is approximately 8 wt%, as shown in the quantitative line trace along the vector A-B in Fig. 1(a). The difference in average atomic number between these phases is approximately 1 unit, which should make the difference visible by BSE/SEM imaging. The trace copper constituent, which is easily seen in the compositional map shown in Fig. 1(c), is found to be segregated to the aluminum-rich region at a level of approximately 0.7 wt%. It would not be possible to detect the contrast produced by such a trace component in a BSE image, even if a pure-aluminum reference region were present in the field of view.

A second example of the utility of compositional mapping for imaging structures that would be difficult to observe by SEM/BSE is shown in Fig. 2. The structure here is a complex heavy-metal alloy containing gold and platinum family metals from a pre-Hispanic artifact found in the Pacific lowlands of Ecuador.<sup>5</sup> Compositional maps with traces along

---

The author is with the Center for Analytical Chemistry, National Bureau of Standards, Gaithersburg, MD 20899. The materials science problems which provided the stimulus for this work were kindly provided by his colleagues, S. Greenwald, D. B. Butrymowicz, and C. Handwerker (NBS), and H. Lechtman (MIT).

the vector A-B for (a) platinum, (b) osmium, and (c) iridium reveal that the platinum forms a discontinuous phase while the osmium is present in the continuous phase. Iridium is present in the discontinuous phase, but within this phase it has formed a discontinuous precipitate. The compositional maps directly reveal the complex nature of these structures. Conventional dot mapping would be of little use in this case because of the small changes in iridium concentration within the discontinuous phase and the high bremsstrahlung background that results from the high average atomic number of the phases.

#### *Mapping at Low Concentration Levels*

In conventional x-ray area scanning (dot mapping) with recording directly onto film, the lowest concentration levels that can be mapped are of the order of 5 wt%, and even then visibility is usually hampered by high background noise. With proper background correction, concentration levels below 0.1 wt% can be achieved by compositional mapping.<sup>6</sup> (For the specimen compositions that produce inherently low spectral background due to low atomic number, Fiori et al. have demonstrated mapping below 0.01 wt%.<sup>7</sup>) An example (Fig. 3) is the phenomenon of diffusion-induced grain boundary migration (DIGM) in the copper-zinc system.<sup>8</sup> The zinc constituent is mapped over the range 0-10 wt%; various portions of the boundary that migrated show concentrations above 2 wt%. A boundary in the lower portion of the image only accumulated approximately 0.2 wt% of zinc and did not undergo migration. This low level of concentration is easily seen against the background because of accurate background subtraction.

#### *Mapping Small Changes in Concentration*

Conventional dot mapping is severely limited in its sensitivity to small contrast changes relative to high fixed levels of the constituent being mapped, which would produce a high background level of dots. Compositional mapping techniques can accommodate this problem through the use of a variety of image-processing algorithms that can be applied to the compositional data after quantitative calculations to enhance the visibility of the concentration levels of interest. An example of this sort was encountered in a study of the DIGM phenomenon in the silver-gold system.<sup>9</sup> In this case, the boundary migration occurred with concentration changes in the silver of about 8% above a matrix level of 65%. In order to view this modulation in the composition, the image enhancement technique of "black-level processing" was applied. A static concentration level is first subtracted from the data, and then the remaining intensity above this level is enhanced to the full dynamic range of the display. The resulting image for the silver constituent, clearly shows the region in which DIGM has occurred (Fig. 4).

#### *Finding the Unexpected*

Probably the most exciting thing about compositional maps is the opportunity to recognize phenomena that might have been otherwise

missed with conventional analysis procedures. Although the quality of an analysis at a single pixel in a compositional map typically lacks the statistical significance and detection limit of a conventional single-point analysis, for which 10 to 100 times more counts can be accumulated, the juxtaposition of many analytical points to form an image nevertheless often reveals new information. The final example (Fig. 5) demonstrates this effect. The problem is again diffusion-induced grain boundary migration in the Cu-Zn system. Figure 5(a) shows a zinc compositional map for which the highest concentrations are approximately 2 wt%. The corresponding copper compositional map is shown in Fig. 5(b) after contrast expansion by the black-level processing procedure. A surprising effect is observed in the copper ahead of the region of zinc enrichment, as confirmed by the use of color overlay techniques for positional analysis. The copper is seen to be depleted below the level that exists in the DIGM region. This missing mass was eventually confirmed to be oxygen through the use of an ion microscope. The oxygen appears to be involved with the diffusional process ahead of the boundary where the zinc has migrated. Critical to this observation was the capability for contrast expansion of the x-ray compositional map.

Compositional mapping provides a useful new tool for the materials analyst, as these examples demonstrate. Further advances in the technique will probably be stimulated in great measure by the experience gained in applying compositional mapping to specific challenging problems from many fields.

#### *References*

1. R. L. Myklebust, R. B. Marinenko, D. E. Newbury, and D. S. Bright, "Quantitative calculations for compositional mapping techniques in electron probe microanalysis," *Microbeam Analysis--1985*, 101.
2. R. B. Marinenko, R. L. Myklebust, D. S. Bright, and D. E. Newbury, "Digital x-ray compositional mapping and 'standard map' corrections for wavelength-dispersive spectrometer defocusing," *J. Microscopy* 145: 207, 1987.
3. C. R. Swyt and C. E. Fiori, "Large-field x-ray compositional mapping with multiple dynamically focused wavelength-dispersive spectrometers," *Microbeam Analysis--1986*, 482.
4. D. E. Newbury and S. Greenwald, "Observations on the mechanisms of high resistance junction formation in aluminum wire connections," *NBS J. Res.* 85: 429, 1980.
5. T. Wolf, *Viajes científicos por la República del Ecuador*, Memoria sobre la geografia y geologia de la Provincia de Esmeraldas, Guayaquil: Imprenta del Comercio, 1879, vol. 3.
6. R. L. Myklebust, D. E. Newbury, R. B. Marinenko, and D. S. Bright, "Background correction in electron microprobe compositional mapping with wavelength-dispersive x-ray spectrometry," these proceedings.
7. C. E. Fiori, C. R. Swyt, and K. E. Gorten, "Continuum correction of x-ray images in scanning electron column instruments," *Microbeam Analysis--1984*, 179.



8. T. J. Piccone, D. B. Butrymowicz, D. E. Newbury, J. R. Manning, and J. W. Cahn, "Diffusion-induced grain boundary migration in the Cu-Zn system," *Scripta Met.* 16: 839, 1982.

9. D. B. Butrymowicz, D. E. Newbury, D. Turnbull, and J. W. Cahn, "Diffusion-induced grain boundary migration in the Au-Ag system," *Scripta Met.* 18: 1005, 1984.

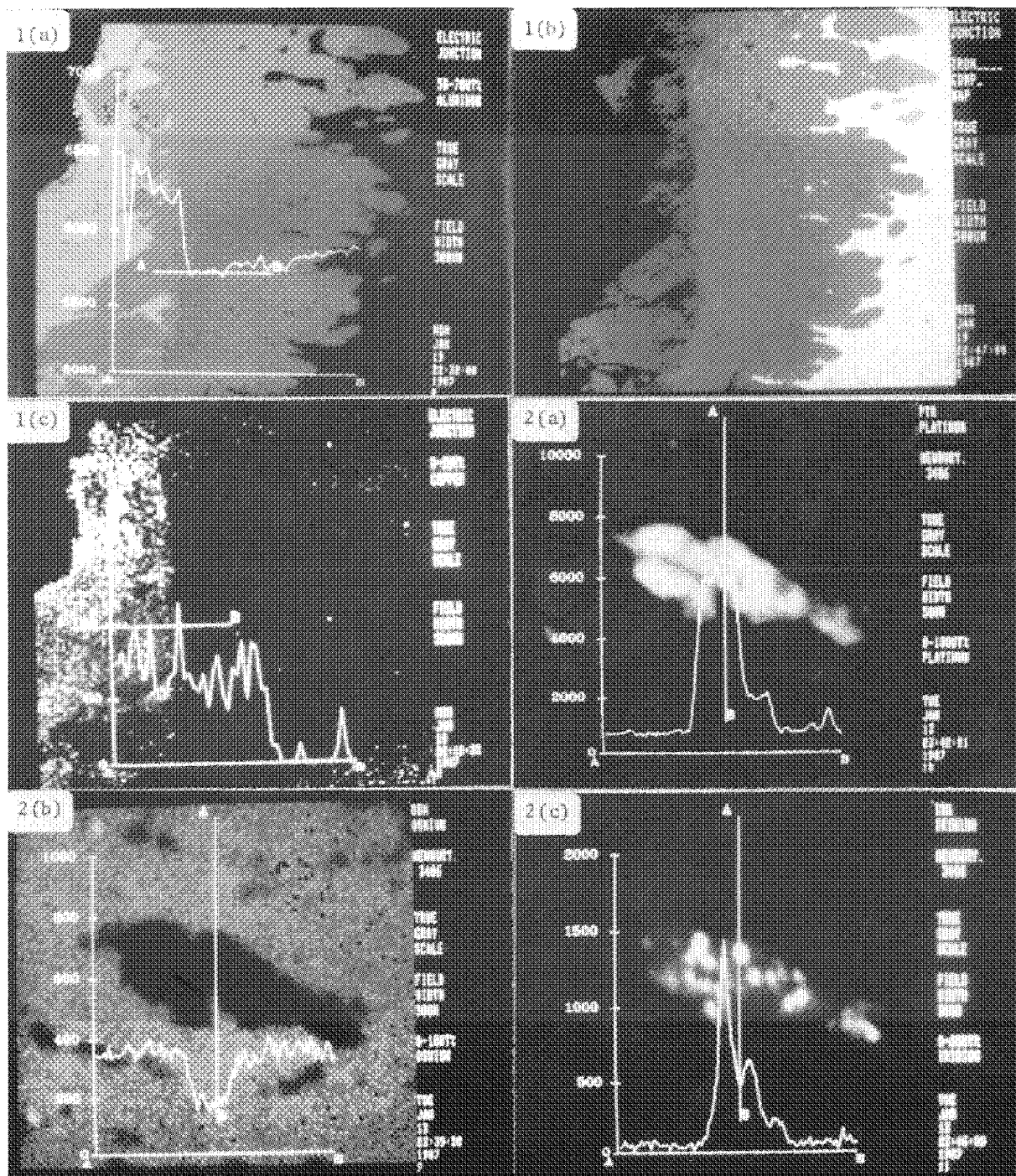


FIG. 1.--Compositional maps of failed electrical junction between aluminum wire and brass-coated steel screw: (a) aluminum, with compositional trace along vector A-B, 50-70 wt% Al; (b) iron, contrast-enhanced to emphasize different phases; (c) copper, with compositional trace along vector A-B, 0-2 wt% Cu. Field width for all images: 500  $\mu$ m

FIG. 2.--Compositional maps of pre-Hispanic gold/platinum alloy: (a) platinum, compositional trace A-B, 0-100 wt%; (b) osmium, compositional trace A-B, 0-10 wt%; and (c) iridium, compositional trace A-B, 0-20 wt%. Field width for all images: 50  $\mu$ m.

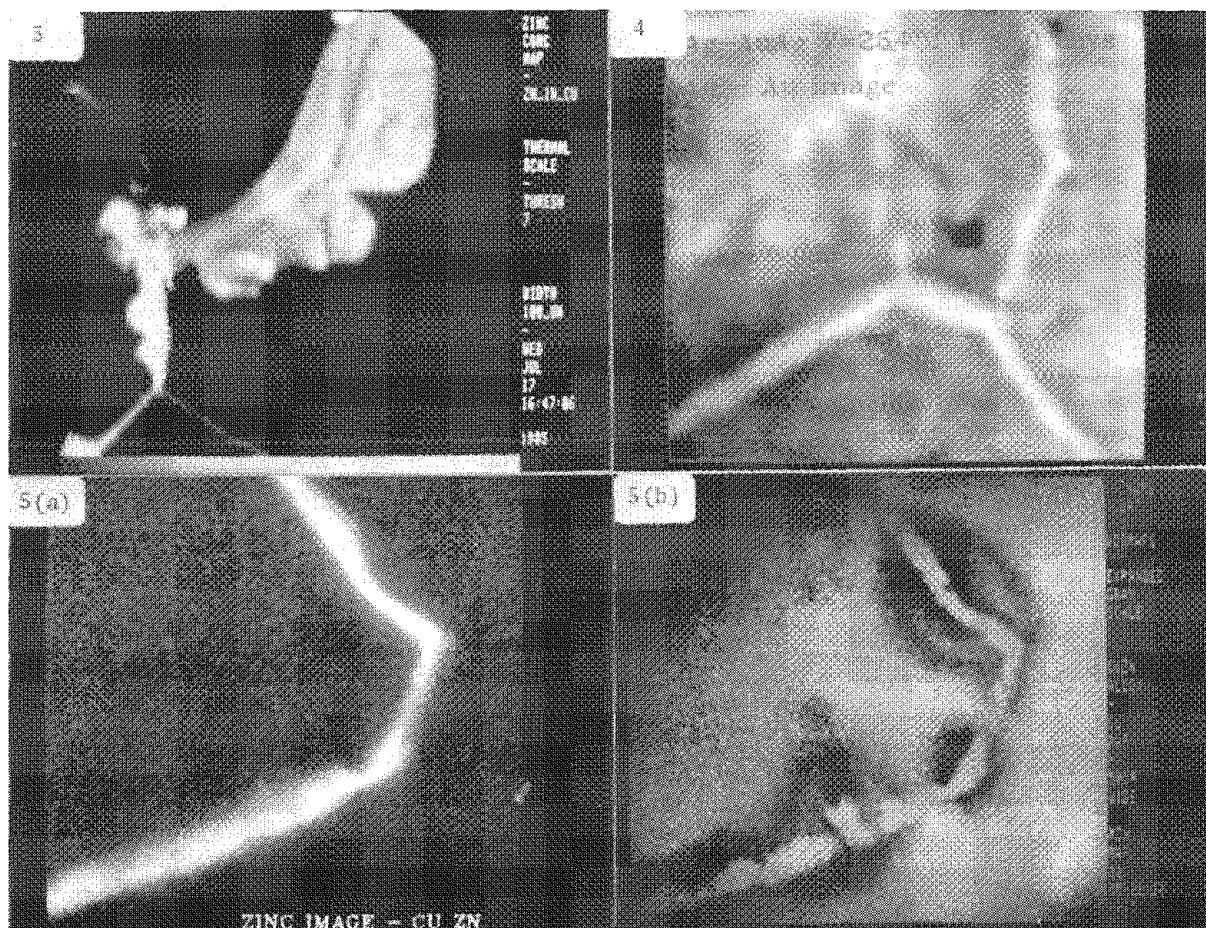


FIG. 3.--Compositional map of zinc at grain boundaries of polycrystalline copper after diffusion-induced grain boundary migration. Concentrations of zinc from 0-10 wt% are displayed (gray-scale bar). Field width: 100  $\mu\text{m}$ .

FIG. 4.--Compositional map of silver in silver-gold alloy. Image has been enhanced by black-level processing. Ag concentration in boundary, 73%; matrix, 65%. Field width: 50  $\mu\text{m}$ .

FIG. 5.--Compositional maps of (a) zinc, maximum concentration 2 wt%, and (b) copper, enhanced by black-level processing. Field width: 50  $\mu\text{m}$ .

## HIGH-SPEED MAPPING AND DATA-PROCESSING SYSTEM FOR EPMA

Kiyohiro Kohara, Fukuo Zenitani, Tetsuo Kajikawa, and Hiroyoshi Soezima

We have recently developed a high-speed mapping system (H-system) that dynamically controls an electron-probe microanalyzer (EPMA), collects various signals (such as secondary electrons, backscattering electrons, specimen current, x ray, cathode luminescence, and others) by means of either beam scanning or stage scanning in two dimensions at a very high speed, and displays processed data in real time. We have also developed a scanning image processing system (SIPS) that permits highly sophisticated image analysis of the area data transferred from this H system or directly from the EPMA unit on an on-line basis. Both the data collection and the real-time display for the H system are performed so rapidly that it only takes 10 s at the most for beam scanning of one frame of  $512 \times 512$  picture elements, at a rate of 10 mm/s for 1  $\mu$ m stepwise stage scanning. As to the processing contents of the SIPS, almost all the requirements for the scanning image and material are contained in the system. Moreover, the system can be connected to various types of scanning microanalyzers (Auger electron microanalyzer, ion microanalyzer, etc.) besides the EPMA without special modification.

### *System Configuration*

Figure 1 shows the overall configuration of the system; Fig. 2, an external view. Since the main EPMA unit incorporates microcomputers,<sup>1,2</sup> a simple control command via RS232C from the host computer can execute operation, signal detection, processing, and display for the electro-optical system, x-ray spectrometer, and specimen stage.

The H system comprises a digital scan converter (DSC),<sup>3,4</sup> a color controller, and a color CRT. The electron signals or x-ray signals are accumulated as image information in the DSC, and this information is displayed on the color CRT after real-time processing by the color controller.

The DSC consists of an image memory and a control unit, which is equipped with an image of  $512 \times 512 \times 16$  bits. In the data collection by primary beam scanning, the image signal from the EPMA synchronizes with this beam scanning and is written in the image memory after A/D conversion at a high speed. As to the x-ray signal, frame integration up to 1000 times can be made, since a 16-bit is allotted to each image element. In the x-ray signal collection by means of the specimen scanning, data are written in an image memory address corresponding to the position of the specimen stage. The contents of the image memory is being continuously output at a TV rate. The color controller, which contains a provision

for generating a color-monitor display in freely tinted pseudo color, comprises a conversion table used with a 16-bit microprocessor and a high-speed RAM. In the conversion table (64k words), each 16 color mixture comprising R (red), G (green), and B (blue) is converted into 4096 colors based on the digital output signal of the DSC, and output in the monitor CRT. The time consumption has been greatly improved by the adoption of the table system, compared with the system in which the contents of a display memory are modified.

The system is capable of freely combining the table contents; for example, discrimination of color by density can be easily performed. For the color CRT, a 60Hz noninterlaced CRT with a 31.25kHz horizontal deflection frequency and 521 total scanning lines is used.

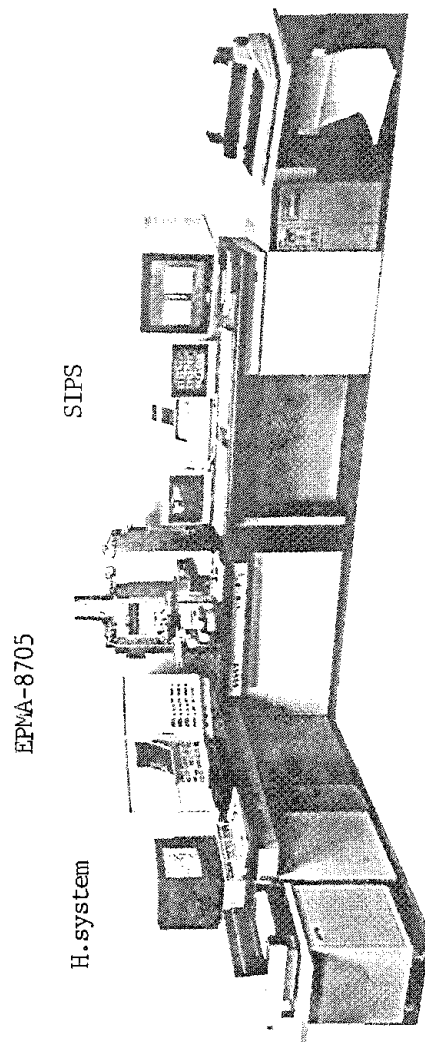
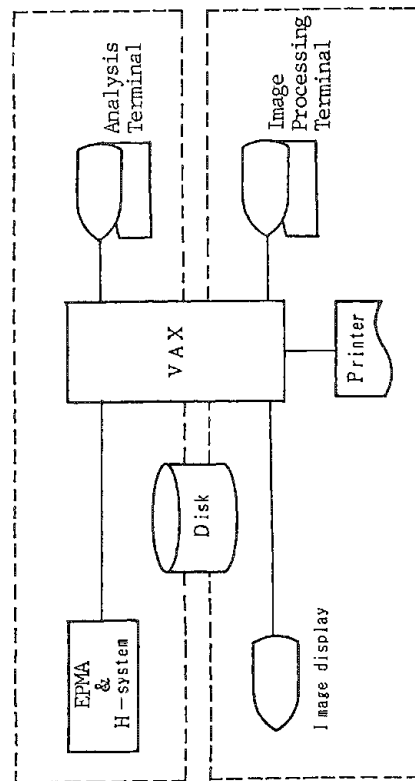
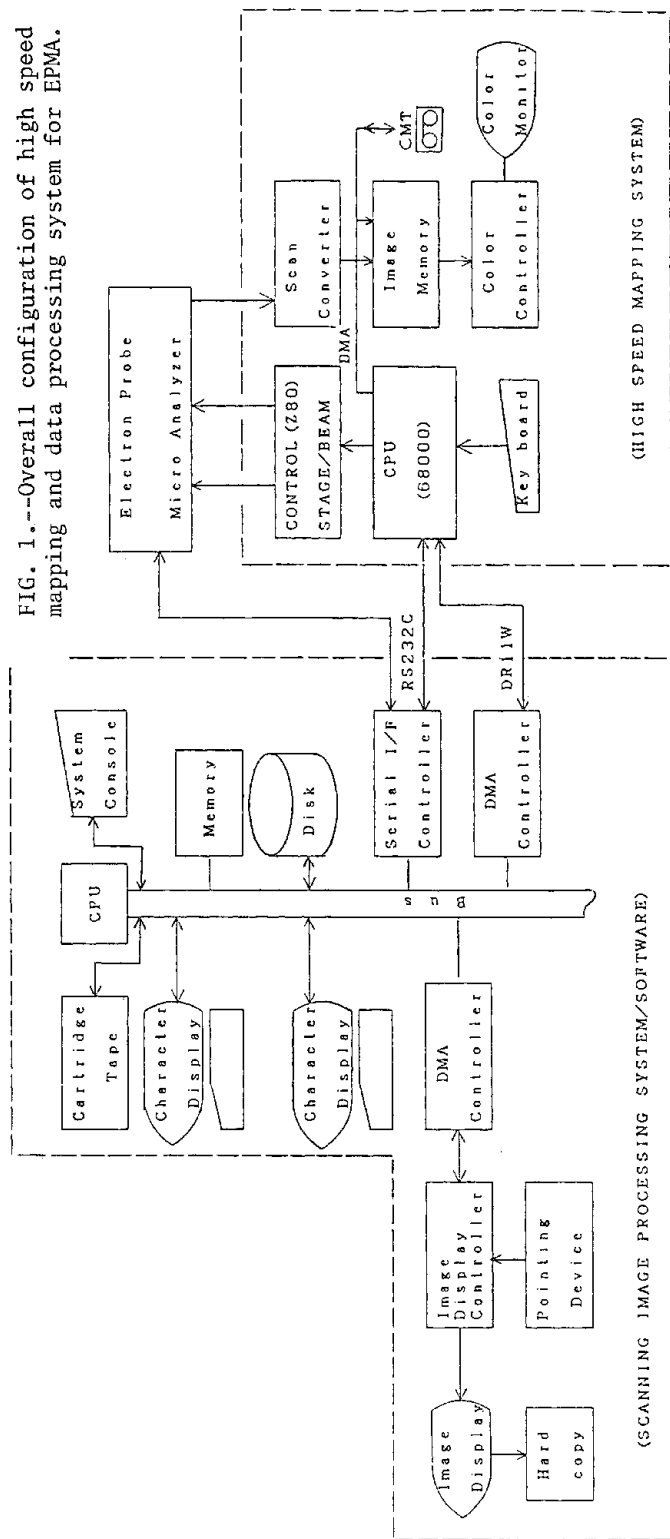
The stage controller drives the specimen stage and transfers measured data to the memory in a specified sampling time, scanning an analysis region. The time loss resulting from acceleration or deceleration is canceled because the driving speed is specified by the measuring range, overall data points, and integration time for all data in the case of the stage drive.

As for the data collection, image processing and display, the microprocessors, which are incorporated independently for performing each of these functions, engage in parallel operation; overall analyzing time is thus shortened, which enables the color mapping method to perform so easily as other analysis methods for EPMA in the routine analysis through the application of this system. In the case of highly sophisticated image processing, data are transferred to a host computer by means of DMA (direct memory access).

The SIPS,<sup>5,6</sup> is a computer system that dynamically controls EPMA by means of a 32-bit super minicomputer, Micro VAX II (DEC), immediately processes or analyzes the mapping image, and checks the diffusion of several elements or a specific quantity of an element in a specimen while collecting data, besides the conventional element analysis. The mapping data are directly filed in a magnetic disk of the computer which controls the main EPMA unit. In the application of the H system, the time required for data collection is considerably shortened, and the collected mapping data are filed in the magnetic disk at a high speed. The collected data can be also copied and stored in a compact magnetic tape with large capacity (90 Mb).

Two types of special terminals, one for analysis and the other for image processing, are available for the SIPS (Fig. 3). Qualitative analysis, line analysis, and ZAF calculation, as well as mapping data collection in several visual fields on several test samples can be performed on the analysis terminal,

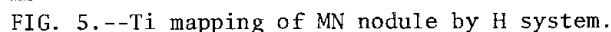
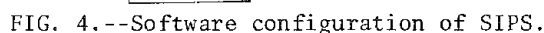
The authors are at Shimadzu Corp., 1 Nishinokyo-Kuwabaracho, Nakagyo-ku, Kyoto 604, Japan.



The image processing and image analysis functions are provided as independent commands (Fig. 4). Figure 5 shows an output example of an H system.

1. F. Zenitani, T. Hirai, M. Kawai, K. Ko-

- yanagi, Y. Mori, and H. Soezima, *29th Meeting of Japan Society of Appl. Phys.* 4a-A-10, 1982.
2. H. Hirai, K. Koyanagi, and H. Soezima, *38th Meeting of Japan Electron Microscopy Society* 26-A11-13, 1982.
3. F. Zenitani, M. Kawai, H. Hattori, and H. Soezima, *19th Meeting of Appl. Spectrometry* 3A13, 1983.
4. F. Zenitani, H. Komi, T. Hirai, and H. Soezima, *Proc. 11th Intern. Cong. Electron Microscopy*, Kyoto, 1986, 557-558.
5. K. Kohara, F. Zenitani, T. Kajikawa, Y. Hida, and T. Miyazaki, *47th Meeting of Japan Society of Appl. Phys.* 29-2G-1, 1986.
6. Y. Hida, M. Sasaki, T. Miyazaki, K. Ito, and T. Kajikawa, *112th Meeting of the Iron and Steel Institute of Japan*, 86-S829, 1986.



## A STATISTICAL EVALUATION OF WAVELENGTH-DISPERSIVE DIGITAL COMPOSITIONAL MAPPING WITH THE ELECTRON MICROPROBE

R. B. Marinenko, D. E. Newbury, R. L. Myklebust, and D. S. Bright

We previously reported on two different procedures to quantitate digital maps taken with wavelength-dispersive spectrometers (WDS) on the electron microprobe.<sup>1,2</sup> They are the Standard Map and the Defocus Modeling procedures, which are used to correct for spectrometer defocusing in low-magnification maps (a scanned area exceeding  $50 \times 50 \mu\text{m}$ ). When digital maps are taken, optional parameters such as the number of pixels and the x-ray accumulation time per pixel are left to the judgment of the experimentalist. The selection of these parameters is in turn related to the magnification, the extent of detail being studied, and the concentrations and resulting count rates observed for each element. We have begun a study of compositional mapping parameters to assist us in evaluating and optimizing the two procedures. The results of these initial experiments are described here.

### *Instrumentation and Data Acquisition*

The Cameca electron microprobe used in this work is equipped with three spectrometers, a standard Tracor Northern TN-2000 analyzer, and a TN-1310 automation system. The instrument automation includes a PDP-11/34 computer, which is configured with 48K words of memory including memory management.

The WDS digital x-ray maps were obtained with the Tracor Northern XIP program and the accompanying Tracor Northern WDS module, which were modified in our laboratory to take counts directly from the WDS scalars at each pixel in the map.<sup>1</sup> Maps from the three spectrometers can be acquired simultaneously and are then transferred from disk to a Digital Equipment Corp. VAX 11/780 computer, where the data are separated into individual maps for each spectrometer, quantitated with the NBS matrix correction procedure FRAME,<sup>3</sup> and displayed on an IP 8500 DeAnza Image Analysis System.

In the experiments described here, the Au Ma maps were obtained with the horizontal spectrometer and the PET crystal, and the Ag La and Au La maps with the vertical spectrometers and the PET and LIF crystals, respectively. An excitation potential of 20 kV and Faraday cup current of 65 nA were used. The magnification was  $400\times$  which corresponds to an area of  $250 \times 250 \mu\text{m}$ . The NBS Standard

Reference Material (SRM) 481 was used for this study. This SRM includes wires of pure gold, pure silver, and four gold-silver alloys which are homogeneous on the micrometer scale.<sup>4</sup>

The statistical program used in this work divides each map into nine equivalent regions. For a  $64 \times 64$  pixel map, each region is  $18 \times 18$  pixels located in a  $3 \times 3$  grid. The program calculates an average value and standard deviation for each region, and report the minimum and maximum pixel values in each region. In addition, an average value and standard deviation is reported for the entire map. From the tabulated information, a quick examination can be made to determine whether there are any pixels or regions in the map that grossly disagree with the rest of the map.

### *Discussion*

The first experiment compares the Standard Map procedure with the Defocus Modeling procedure. In the Standard Map procedure, a map of the standard elements (or compounds) is recorded under identical conditions of size, orientation, and spectrometer positions, as was done for the unknown specimen. After background and dead-time corrections, a k-ratio is calculated for each pixel from a pixel-to-pixel match of the two maps taken with the same spectrometer. Then a composition for each element of interest is calculated for each pixel from the k-ratio using the NBS matrix correction procedure FRAME.<sup>3</sup> In the Defocus Modeling procedure, a wavelength scan through the peak of the element being analyzed is used as a reference for the construction of a standard map, which is used for subsequent calculations as previously described.

A digital WDS map was taken from each alloy and pure element in SRM 481. Wavelength scans were taken from the pure elements. The map size for all maps was  $64 \times 64$  pixels. The time/pixel was adjusted for each map so that approximately 1000 counts/pixel were observed for the element with the lowest count rate. Each map was recorded in less than 1 h.

The results of the experiment appear in Table 1, where the concentrations calculated for each element from each mapping procedure are listed. The numbers listed here are average values taken from the concentrations of all pixels in the final concentration map for the analyzed element. Since two different gold lines were used, each was used in separate calculations to determine the total map. Therefore, the results for the Ag La map are listed twice. Next to each average concentration, the number (in parentheses) is a single relative standard deviation observed for the entire concentration map. It was

---

The authors are at the Center for Analytical Chemistry, National Bureau of Standards, Gaithersburg, MD 20899. Certain commercial equipment, instruments, or materials are identified in this paper to specify adequately the experimental procedure. Such identification does not imply NBS recommendation or endorsement; nor does it imply that the materials or equipment identified are necessarily the best available for the purpose.



included to give some measure of the variation observed throughout each map. Comparing the results from two procedures for the same elemental line of the same alloy, we find the relative standard deviations are similar in all but a very few cases. Both methods provide similar performance in regard to the achievable precision. The efficiency and flexibility of the Defocus Modeling procedure provide great advantages, as was discussed in detail previously.<sup>2</sup>

The accuracy of the calculated concentration can be evaluated by comparison of the average concentration with the certified values. For the Au L $\alpha$  and Au M $\alpha$  analyses, neither procedure demonstrates an obvious advantage. As the gold concentration decreases, the difference between the calculated concentration and the certified value does increase, with Au M $\alpha$  too low and Au L $\alpha$  too high. However, for the Ag L $\alpha$  analysis, the agreement between the results of the Standard Map procedure and the certified values is considerably better than the results from the Defocus Modeling procedure. This difference in the two methods is probably not due to a deficiency in the Defocus Modeling procedure, but more probably to a small error in the magnification value or the selection of the line of optimum focus used for constructing the synthetic element map. The Ag L $\alpha$  line is a sharper peak than either the Au M $\alpha$  line or the Au L $\alpha$  line; therefore, a small error in the magnification or in the line of optimum focus would result in a larger error for the Ag L $\alpha$  map than for the Au maps. This problem will be more fully investigated.

There was some concern that the results above, which are average values determined from the entire map, might not hold true for smaller areas of the map if there were serious inaccuracies in the defocus corrections that were location dependent. One could then make serious mistakes when interpreting multielement compositional maps with multiple phases. One needs to have confidence in the observations regardless of the location of the pixel in the map. Therefore, we have compared the average results from the entire map with results from a more remote region of each element map, which was selected to be as far from the line of focus as possible.

Figure 1 is a gray-scale display of the three original element maps of the alloy before any corrections were made. Since a different spectrometer was used to record each, the line of focus is different in each map. Figure 2 is one map (the Au M $\alpha$  map) with the nine regions used in the statistical program outlined. For each element, the region of lowest expected count rate, away from the optimum line of focus, was selected for evaluation. For Au M $\alpha$  this was the upper left corner; for Ag L $\alpha$ , the upper right corner; and for Au L $\alpha$ , the lower right corner. Table 2 shows the results from the statistical analysis of these remote regions. There is no significant difference between these values and the average values from the entire map. Examination of the tabulated data for each map also showed that the average value from an entire map was generally within 1-2% of the av-

erages observed for each of the nine regions. The precision for each of the nine regions was comparable to or better than that observed for the entire map. (This observation is expected, since there is more variation between counts/pixel over the entire map than within any single region of the map.) Both procedures, therefore, function as well for a portion of the map as for the entire map.

A second experiment was designed to compare the quantitative results obtained from different-size maps taken at different times per pixel. The Au<sub>80</sub>Ag<sub>20</sub> alloy of SRM 281 was used. The Defocus Modeling procedure was used to determine the concentrations, because this procedure is far more efficient in an experiment of this type than the Standard Map procedure would have been. Only one wavelength scan from each of the three spectrometers was needed to construct (calculate) a standard map for each element at each of four different pixel sizes used. The Standard Map procedure would have increased the data acquisition time three-fold in order to take all the needed standard maps. It took more than two days to acquire the data for this experiment.

Table 3 lists the average compositions for each element map and the calculated total maps. As for the previous table, the number in parentheses is a relative single standard deviation for the entire map. In addition to the accumulation time (in seconds) spent on each pixel for each map, the total accumulation time (in hours) is listed, to give an indication of how the size and time/pixel relationship help in deciding the practicality of an experiment. These total mapping times are not a simple multiple of the pixels and the time/pixel as there is a considerable amount of computer overhead time in our accumulation system.

Both the precision observed for the entire map and the accuracy of the average composition (comparison made with the certified values) are improved when longer times/pixel are used. These results are not surprising, since the statistics in the maps taken at shorter times, particularly the 0.1s maps, were not very good; the number of counts per pixel before background subtraction is only about 400 counts for the Au M $\alpha$  line and slightly less than 300 counts for the L $\alpha$  lines. The same systematic error described in the first experiment is present in the determination of the Ag L $\alpha$  concentration. Again, this error will be reduced with a more exact knowledge of the magnification and/or line of optimum focus.

The choice of the pixel size of a map and the time/pixel will ultimately depend upon many factors, such as the resolution required in the final map, the tolerable quantitative error in the final result, the amount of time available for mapping, the concentration levels in the specimen, and the x-ray count rates. The results of Table 3 show that even at very short times per pixel, with only a few hundred counts per pixel, both the accuracy and precision errors are less than 10%. Where resolution is not critical and lower quantitative errors are required, smaller maps taken at 64  $\times$  64 or 128  $\times$  128 pixels can provide errors of 2-3% or less by use of longer counting

times (1 s or more). Longer counting times per pixel can be used for larger maps as well, but the total accumulation time would become unreasonably long. Even with a beam current regulator, mapping beyond what can reasonably be done overnight could be risky as the current does drift slowly over long periods of time as the filament ages, and there is the risk of losing a filament.

### Conclusions

These preliminary experiments have shown that good quantitative analysis can be done on WDS digital maps. The accuracy and precision depend on the specimen being studied, the size of the error that can be tolerated, and the time factor. Some adjustments are required to make the Defocus Modeling procedure as accurate as the Standard Map procedure, and will be studied in detail.

### References

1. R. B. Marinenko et al., *J. Microsc.* February, 1987.
2. R. L. Myklebust et al. *Microbeam Analysis--1986*, 495.

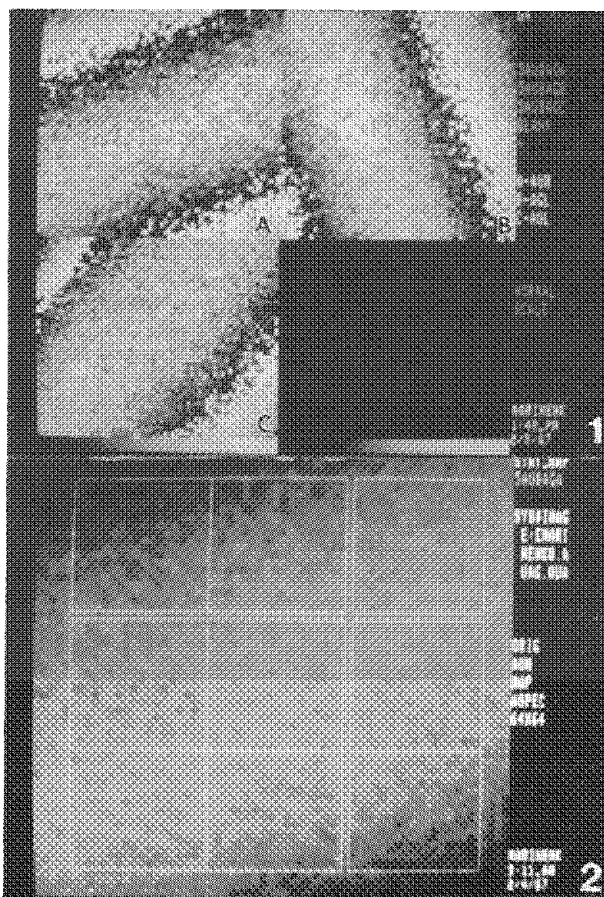


FIG. 1.--Gray-scale display of three original element maps of the Au80Ag20 alloy. Each gray-level change corresponds to 50% drop in x-ray intensity. (A) Au M $\alpha$ , (B) Ag L $\alpha$ , (C) Au L $\alpha$ .

FIG. 2.--Original Au M $\alpha$  map. The nine regions per map used in statistical analysis program are outlined.

3. H. Yakowitz, R. L. Myklebust, and K. F. J. Heinrich, *FRAME: An On-line Correction Procedure for Quantitative Electron Probe Microanalysis*, NBS Tech. Note 796, 1973.

4. K. F. J. Heinrich, R. L. Myklebust, and S. D. Rasberry, *Preparation and Evaluation of SRM's 481 and 482 Gold-silver and gold-copper Alloys for Microanalysis*, NBS Special Publication 260-28, 1971.

TABLE 1.--Quantitative analysis of Au-Ag alloys by digital mapping procedures.

Concentration in weight percent*					
ALLOY	PROCEDURE	AuM $\alpha$	ELEMENT/LINE AgL $\alpha$	AuL $\alpha$	TOTAL
Au80Ag20	Cert.Values	80.05	19.96	80.05	100.01
	Stand.Map	79.56(3.2)	19.86(5.5)		99.39(2.8)
	Defoc.Mod.	79.98(2.6)	19.86(5.5) 20.38(2.8) 20.38(2.8)	81.19(6.1) 101.02(5.3) 100.33(2.1)	101.02(5.3) 100.33(2.1) 103.00(2.8)
Au60Ag40	Cert.Values	60.05	39.92	60.05	99.97
	Stand.Map	58.68(3.4)	40.11(2.7)		98.75(2.3)
	Defoc.Mod.	58.99(2.7)	40.11(2.7) 41.13(3.2) 41.13(3.2)	60.08(4.5) 100.96(3.1) 100.07(2.0)	100.96(3.1) 100.07(2.0) 103.38(4.6)
Au40Ag60	Cert.Values	40.03	59.93	40.03	99.96
	Stand.Map	38.72(3.6)	60.21(2.1)		98.89(1.9)
	Defoc.Mod.	38.94(3.0)	60.21(2.1) 61.62(4.3) 61.62(4.3)	41.43(4.3) 101.60(2.2) 100.51(2.7)	101.60(2.2) 100.51(2.7) 102.44(3.7)
Au20Ag80	Cert.Values	22.43	77.58	22.43	100.01
	Stand.Map	21.63(4.1)	77.61(2.0)		99.19(1.8)
	Defoc.Mod.	21.75(3.9)	77.61(2.0) 79.24(2.6) 79.24(2.6)	23.61(5.7) 101.18(2.1) 100.95(2.0)	101.18(2.1) 100.95(2.0) 102.03(2.5)

\* A single average relative standard deviation for the entire map is in parentheses.

TABLE 2.--Quantitative results from one region of the Au-Ag alloy digital maps.

Concentration in weight percent*					
ALLOY	PROCEDURE	AuM $\alpha$	ELEMENT/LINE AgL $\alpha$	AuL $\alpha$	
Au80Ag20	Cert.Values	80.05	19.96	80.05	
	Stand.Map	79.79(3.1)	20.35(3.8)		80.06(3.7)
	Defoc.Mod.	78.98(1.9)	20.22(2.4) 20.22(2.4)	81.58(2.4)	
Au60Ag40	Cert.Values	60.05	39.92	60.05	
	Stand.Map	58.78(3.4)	40.42(2.5)		60.38(3.8)
	Defoc.Mod.	58.15(2.1)	40.42(2.5) 41.19(1.7) 41.19(1.7)	61.56(2.9)	
Au40Ag60	Cert.Values	40.03	59.93	40.03	
	Stand.Map	38.87(3.6)	60.03(2.1)		41.30(4.1)
	Defoc.Mod.	38.46(2.4)	60.03(2.1) 59.71(1.9) 59.71(1.9)	42.12(3.1)	
Au20Ag80	Cert.Values	22.43	77.58	22.43	
	Stand.Map	21.74(4.4)	78.05(1.9)		23.35(4.8)
	Defoc.Mod.	21.49(3.4)	78.05(1.9) 77.69(1.1) 77.69(1.1)	23.83(4.1)	

\* A single average relative standard deviation for the region is in parentheses.

TABLE 3.--Statistical study of a homogeneous Au80Ag20 NBS SRM alloy.

CONCENTRATIONS IN WEIGHT PER CENT CALCULATED FROM DEFOCUS MODELLING PROCEDURE*					
MAP DIM.	TIME/ Pixel Map (s) (h)	AuM $\alpha$	ELEMENT AgL $\alpha$	AuL $\alpha$	TOTAL
512	.1 15.5	83.27(5.9)	21.72(7.3) 21.72(7.3)		105.0(4.7) 106.7(6.9)
256	.4 9.3	82.17(4.3)	21.48(5.0) 21.48(5.0)		103.6(3.4) 103.6(2.7)
128	1.2 5.9	80.63(3.1)	21.88(3.2) 21.20(3.2)		101.8(2.4) 102.1(1.7)
256	.1 3.6	81.40(5.1)	21.36(6.6) 21.36(6.6)		102.7(4.3) 104.4(5.0)
128	.4 2.3	80.74(3.8)	21.40(3.9) 21.40(3.9)		102.1(3.1) 104.2(3.1)
64	1.2 1.5	81.21(2.2)	21.07(2.6) 21.07(2.6)		101.2(2.0) 102.3(1.8)
128	.1 1.0	81.15(5.1)	21.31(6.1) 21.31(6.1)		102.4(4.2) 104.0(4.9)
64	.4 0.6	80.10(3.2)	21.07(3.5) 21.07(3.5)		101.1(2.6) 102.3(2.6)
64	.1 0.3	80.05(5.0)	21.04(6.2) 21.04(6.2)		101.0(4.1) 102.3(4.7)
CERT.VALUES		80.05	19.96	80.05	100.01

\* A single average relative standard deviation for the entire map is in parentheses.



## AN IMPROVED CALCULATOR FOR DIGITAL IMAGE MANIPULATION

J. F. Konopka

The main purpose of this calculator is to allow the user to assign any available color to any measured range of x-ray intensities collected from one element or a combination of elements after suitable numeric processing. It also allows combining this information with digitized images from other sources of signals such as secondary or backscattered electrons, in an interactive and iterative fashion. This paper presents changes made since the first presentation of this calculator in 1984.<sup>1</sup>

The advantage of a calculator over other interfaces is that it allows the most freedom to try new algorithms and the most operations to be done in the least time. With less effort needed to accomplish a series of operations it becomes more likely that they get done and that new facts will be learned about a sample. Simple menu-driven approaches have the disadvantage that they generally allow only one operation at a time, which means multiple passes over the data and storage of intermediate results. For example, in a biological sample containing K, Ca, and P, if one wanted to correlate P and Ca abundance, one would first calculate a K K $\beta$  image from the K K $\alpha$  image by use of the known K $\alpha$ /K $\beta$  ratio, then subtract the K K $\beta$  from the Ca image, scale the resulting Ca image, scale the P image, and compare the resulting Ca and P processed images. With the interface described here, up to four input images may be simultaneously used as inputs and up to 200 operations may be performed in one pass through the data. In the example described above all the processing could be done in one pass. This style of interface puts the user in the driver's seat. Instead of being channeled along the path of available menus, users are limited in the range of what can be done only by their ingenuity and by the availability of published algorithms for combining images. In addition, the use of a calculator interface is relatively simple to use compared with other systems which require the user to learn BASIC or some other difficult to use programming language.

### *Changes*

Improvements were made in three areas. First, several new functions have been added. Table 1 lists all the available functions. Newly added math operators are a fast-integer square root (SQRT), a fast-integer base-two logarithm (ILOG2), and a special function called "times divide (\* /)," which multiplies two numbers and then divides the result by a third number. This procedure is faster than separate multiply and divide functions and the intermediate result is kept at 32-bit precision, which makes the result more precise. To make documentation easier, a comment command

has been included. When the backslash character is encountered, all text between it and the right edge of the screen are ignored by the calculator and thus may be used to explain what is being done. To make color selection easier, simple colors may now be keyed in by name (RED, GREEN, BLUE...). An implicit change was to implement TRUE flags as 16 bits on, which permits doing "arithmetic with truth values"<sup>2</sup> and reduces the need for bulky IF... ELSE... THEN construct. Fewer commands means faster operation and a command string that is easier to read.

The second improvement is that commands are now entered with an editor rather than serially. The obvious benefit is that the entire input command set may be reviewed before execution begins. On a sample screen (Fig. 1) shows commands in Post Fix notation (sometimes known as Reverse Polish). As an option the user may select algebraic or In Fix notation (sometimes known as "Obwrocony Angielski" which is Polish for "Reverse English"). If any word is unrecognized, the editor is automatically reentered and the unknown word is flagged in red, so that corrections can be easily made. Another feature is that all the text is saved in a special memory buffer. Each time the calculator is reentered all the previous commands are redisplayed. Thus, one can easily repeat a command sequence many times while making small changes. Finally, to make usage simpler, almost no syntax is required except that all words are separated by at least one space and the commands must be placed in the correct order. The users are otherwise free to put words in any columns or rows, to indent or not indent, etc., as they please.

Finally, an interactive histogram display of all files used as input is provided in the same display as the editor. The vertical scale is logarithmic and the horizontal scale adjusts automatically to the range of the data. Each histogram is provided with a cursor controlled by cursor keys and a numeric display of cursor position. This feature dramatically improves the utility of this interface, as the histogram of each input image may be minutely inspected while decisions are being made about a calculation sequence. The histogram data are also buffered to speed iterative use of the calculator.

### *Operation*

In operation, the user first specifies which files are to be used as input, where the result should be displayed, and (if desired) the name and size of a file in which the result are to be stored. As before, there are no restrictions on mixing files of different array sizes or different data types. For example, a 512  $\times$  512 secondary electron image may be combined with 256  $\times$  256 x-ray maps. At

---

The author is at Kevex Corp., 1101 Chess Drive, Foster City, CA 94404.

this point the software verifies that the files exist, reads in the histogram if they are not already in the memory, and presents the display shown in Fig. 1. The user now keys in the set of operations to be executed. During this time the text may be moved about and changed as desired, and the histograms may be inspected with the cursor. When editing is done the software interprets the commands, then steps through each point of the image, and the input commands are executed at each point. This is a stack based calculator. At the end of the calculations the last number at the top of the stack is written to graphics and, optionally, to a disk file. The stack is automatically reset at each pixel.

### Examples

Maps of alloys or mineral phases are created from logical combinations of elemental x-ray intensities. An intensity window is specified for each component of the phase. In the calculator a flag is set true or false at each pixel depending on the x-ray counts in that pixel. The results of all such tests are then ANDed together, which produces a color showing the distribution of the specified alloy or phase. Multiple phases may be displayed in one image if each phase is made a primary color (red, blue, green) and then ORed together. Combinations of colors appear as new colors. This use is demonstrated in the map of Fig. 1, which shows an MnS inclusion in steel surrounding some Al and Ca oxides. In the first two lines intense values of Al are set red and intense values of Ca are set green. The OR command joins these two conditions. Where the two elements occur together a yellow spot (red + green) appears. Next, a condition is specified which sets MnS to blue. This condition requires both elements to be present. Unlike in dot maps, if only one element is present the spot remains dark. The resultant image (Fig. 2) shows three distinct regions: one for MnS, one for Al, and one for Ca. A distinct Ca-rich region does not appear.

In a similar use, the resulting mask of elemental combinations can be used to mix colors with gray scale (secondary- or backscattered-electron) images to pinpoint the position of the isolated phase. If the desired combination of elements are present, the color is shown; otherwise, the gray-scale image is shown.

If background data as well as peak data are collected, peak-to-background images can be generated that will correct mapped intensities collected from rough surfaces, varying geometries, and varying beam current, and that may, at high overvoltages, be helpful on charging samples.<sup>3</sup> Similarly, one can correct thin-film samples collected with an STEM for small thickness variations by mapping element ratios.

Rudimentary quantitative maps may be generated in several ways. Dividing peak-to-background ratios in the sample image by peak-to-back-

ground ratios from standards yields fairly good numbers. The main problem is the poor precision due to the small number of background counts usually available. Interelement ratios yield better statistics but require some interpretation. Uncorrected k-ratios also yield quantitative information<sup>4</sup> that is often at least as accurate as the precision available from thenumber of x rays acquired. One byte of data (255 counts) is no more precise than 6%, and 1000 counts of data have a precision of about 3%. Filtering the images improves these numbers at the sacrifice of some spatial resolution.

Finally, simple spatial masks can be defined that allow position-dependent processing. This procedure can be used to mask out artifacts, to display only a portion of an image, or to make combined images. For example, in a cross section of a layered sample one half the image could be the backscatter-electron image and the other half could be digital x-ray images.

I have demonstrated an approach to digital-image manipulation which is flexible, interactive and iterative, and yields useful results. I hope that this will stimulate development of other, more sophisticated tools for analysts. The next extension may be to add the necessary capabilities to implement more precise quantitative mapping<sup>5</sup> with a minimum of fuss.

### References

1. J. Konopka, Joint EMSA and MAS Meeting, Detroit, 1984 (late breaking reports on Physical Science).
2. Leo Brodie, *Thinking Forth*, Englewood Cliffs, N. J.: Prentice-Hall, 1984, 244 (quote from C. Moore).
3. P. Rez and J. Konopka, "Accuracy of peak-to-background method for quantitative analysis," *Microbeam Analysis--1981*, 183.
4. K. A. Thompson and L. R. Walker, "Quantitative and low-magnification mapping by the electron microprobe," *Microbeam Analysis--1986*, 491.
5. C. E. Fiori, "Quantitative compositional mapping of biological cryosections," *Microbeam Analysis--1986*, 183.

TABLE 1.--List of calculator commands.

Command Set	
+ - * / */	arithmetic operators
OR AND NOT XOR	logical operators
NEG ABS	negation, absolute value
MIN MAX	minimum or maximum of two values
IF ... ELSE ... THEN	branching operators
SQRT	square root
ILOG	base two integer logarithm
X Y	row and column of current pixel
OVER DUP DROP	stack operators
= <>	comparisons; equal, not equal
< >	less than, greater than
RED GREEN BLUE	codes for primary colors
A B C D	symbols for image data
nnn	constants

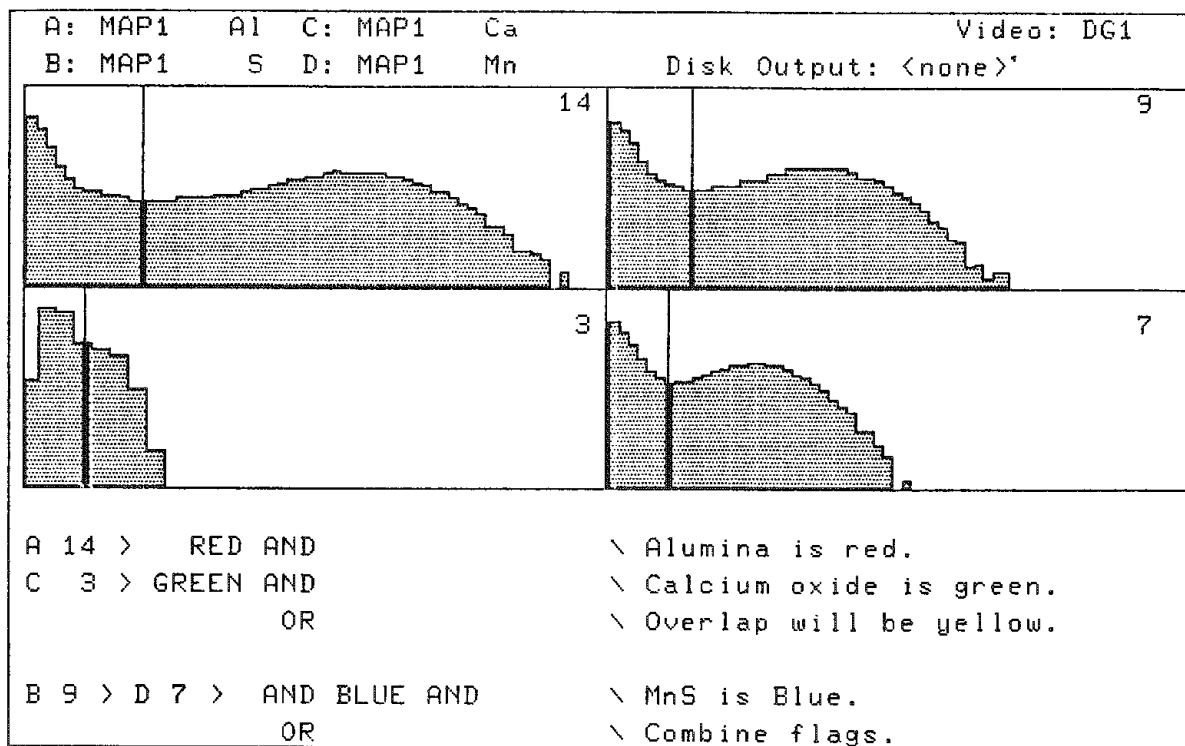


FIG. 1.--Example of calculator showing four files as input; text is commentary.

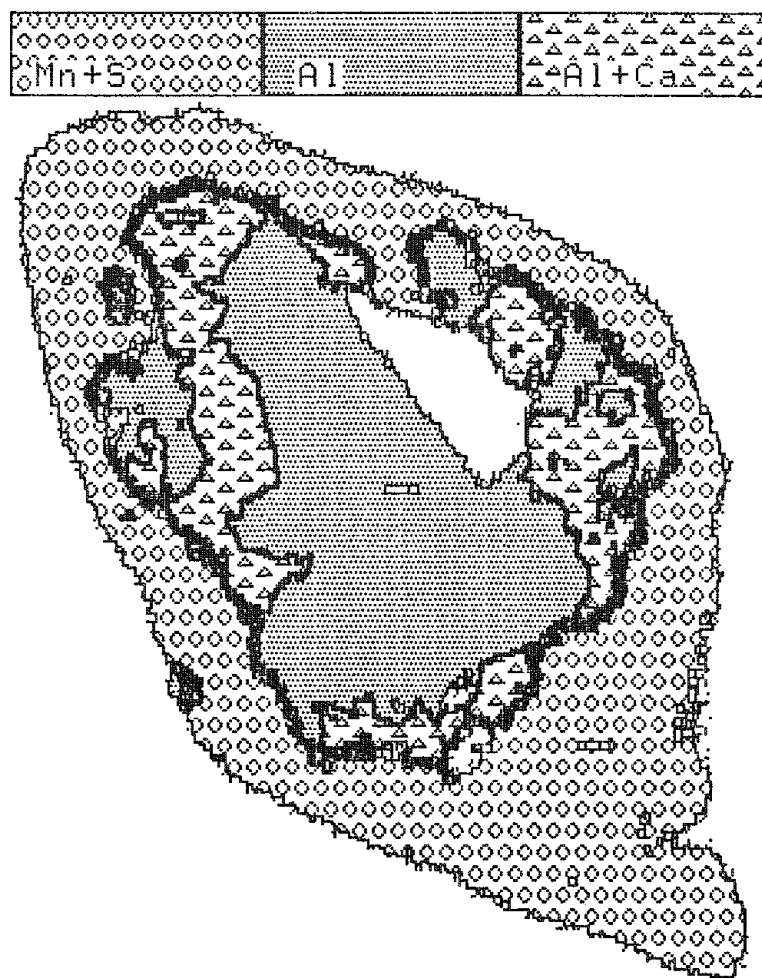


FIG. 2.--Image generated by commands shown in Fig. 1.

## COLORAD SYSTEM FOR MAPPING ELEMENTAL COMPOSITION DETERMINED BY X-RAY ANALYSIS

D. D. McCoy

Colorad is a color-imaging system that maps concentrations and phase distributions of elements in a designated region of a material by analysis of x-ray signals generated in the material by a scanning electron beam. Color variations show the amounts of various elements present and the composition of the phases. The instrument measures the intensity of each element's characteristic x-ray signal, then assigns a lightness to represent the concentration of a selected element, and a color (characterized by hue, value, and chrome) for a given combination of elements. The color display is unambiguously associated with concentration levels, which permits elemental analysis of concentrations as low as 0.5%. Because the brightness of the image is independent of signal strength, the instrument is particularly valuable for determining the composition of phases present. A typical use of Colorad is in analyzing the material in the vicinity of a braze joint to determine the quality of the braze.

Modern electron microprobes are equipped to be reasonably good scanning electron microscopes as well as x-ray microprobes. They can be used to make good images with both secondary electrons and backscattered electrons. In addition, one can use them to make an x-ray image of the characteristic radiation of a selected element by choosing either (1) an appropriate wavelength with a wavelength-dispersive spectrometer (WDS), or (2) an appropriate specific energy with an energy-dispersive spectrometer (EDS). To generate such images, the electron beam is continuously swept over the surface of the sample until enough x-ray information is generated to produce a photographable image on a cathode-ray tube. The resulting x-ray image shows the location of the selected element but provides very little reliable information on concentration.

Such x-ray images are difficult to interpret in terms of elemental concentrations for a number of reasons. Unwanted background information is present, which always leaves some doubt as to what part of the image represents real information and what part does not. This background information also causes poor image definition. Moreover, conditions for creating an image are never the same for any two elements or from one sample to another, which makes it difficult to establish a proper expo-

sure time for photographing the image. The relative brightness of any area in the image depends on the relative concentration in that area of the selected element in the sample matrix, which suggests that brightness might be calibrated to indicate concentration; however, the brightness is also strongly affected by a number of other factors, including the electron accelerating voltage, the beam current, the total number of times the beam is swept over the sample, the relative excitation efficiency of the element and the x-ray line chosen, and the peak-to-background ratio of that element in a given matrix.

Many of the above problems have been overcome by the Colorad system described here, which uses an imaging technique that combines up to four elements into one image and clearly displays phases present and changes in elemental composition within a phase.

### *The Colorad System*

The Colorad system includes three basic units: the Colorad chassis, a red-green-blue (RGB) monitor for displaying the color video image, and a color camera for photographing the image. The present version of Colorad is provided with eight x-ray input ports (up to four of which can be used at any one time) and one analog-signal input port (for secondary electrons, backscattered electrons, sample current, etc.). Input to the eight x-ray ports comes from four WDS units and four EDS units. Three types of output signals are provided: x-y sweep drivers, RGB video drivers, and an RS232 terminal port.

The Colorad chassis contains a microprocessor board, two graphics boards for storing the image, a board for the required color-lookup table, a sweep-driver board, an alphanumeric board, and the Colorad counter board. These seven boards perform the following six functions:

1. The microprocessor board controls the functions of the other boards with software and provides the clock pulses for the Colorad counter board.
2. Each of the two graphics boards stores one half of an image word in the form of a four-bit word. The two four-bit words are combined to make an eight-bit word that is used for addressing the color-lookup table. These boards also furnish the control signals for converting the data to a video signal.
3. The color-lookup table stores the colors that are addressed by the graphics boards and converts them to an RGB signal for driving the RGB monitor and the color camera.
4. The sweep-driver board converts digital x-y addresses for the electron beam position to an analog signal for driving the sweep coils of the electron microprobe.
5. The alphanumeric board provides the

---

The author is at the Lawrence Livermore National Laboratory, Livermore, CA 94550. He acknowledges the support and encouragement of Q. C. Johnson, R. G. Meisenheimer, and J. D. Balser during the development of Colorad. T. G. Allison gave helpful advice on preparation of the software, and E. L. Arnold contributed electronics support. This work was done under the auspices of the U.S. Department of Energy under Contract W-7405-ENG-48.

capability for overlaying element symbols on color-coded patches for identifying elemental compositions of the phases present and also for labeling the images.

6. The counter board selects the desired signals (both x-ray and analog), counts their pulses for a preset period, and presents them to be read by the microprocessor board for evaluation.

### *The Colored Image*

Before describing how Colorad is used, it is worthwhile to describe the image and what it conveys. Whereas spot analyses or line scans with the electron microprobe may reveal important information about the sample (subsequently, when the data have been analyzed), an image such as produced by Colorad can provide the observer--almost immediately--with an overview of an area that reveals unknown inclusions or other variables in the sample. A secondary-electron or backscattered-electron image may reveal topography and spatial distributions of phases or variations in average atomic number, but a Colorad x-ray image contains information that identifies elemental composition and concentrations of a material. In the Colorad system, color provides a vehicle for a dramatic increase in the visual information content of an x-ray image. By properly assigning colors, one can display both the elemental content and the variations in elemental concentration within a given combination of elements.

How does Colorad display both elemental composition and variations in elemental concentration? The answer to this question begins with a brief explanation of color parameters. According to the Munsell notation,<sup>1</sup> a color is tridimensional; the three dimensions are hue, value, and chroma. A color's *hue*, the name of the color or color family (e.g., red, yellow, green), is related to the wavelength of light of that color, as are the other color parameters. *Value* of a color is the lightness or darkness of the color (e.g., light green, medium green, dark green). *Chroma* of a color is the strength or intensity of the color (e.g., the degree to which one's sensation of the color differs from that of white or gray).

From the above it follows that we can assign the elements or any combination of elements in a composition (such as elements A, B, C, etc., or combinations AB, ABC, AC, ABCD, etc.) their own colors with their own unique properties of hue and chroma. It also follows that if, for example, the element B decreases in concentration in the elemental combination ABC, one can decrease the value of that color proportionally to its decrease in concentration. One can do so because changing the value of the color does not change one's ability to identify the color, since its hue and chroma remain unchanged.

Basic x-ray imaging, with a total of four x-ray signals at any one time, requires 15 color combinations that are different in hue and chroma. For showing concentration changes, it is statistically feasible in many cases to show at least five levels of concentration

or levels of color value. That makes a total of 75 possible combinations of color to select from. The color-lookup table is actually made up of 15 combinations of hue and chroma and 15 value levels for each hue and chroma, which makes a total of 225 colors to choose from. The reason is explained later in the paper.

### *Operation of Colorad*

Two basic types of image routines can be selected with Colorad. The first routine provides the ability to identify phases by hue and chroma and to show concentration changes of a selected element within any phase by changes in color value. There is also a variation of this routine that allows one to reject information from areas in the sample that contain plastic, which can produce incorrect x-ray information. The areas containing plastic can be identified by use of the back-scattered image from the microprobe, which is adjusted to show the plastic as black and the other areas as gray or white. This information is sent to the Colorad display and causes it to ignore data from the plastic zones.

The second routine allows one to make a color image by use of secondary electrons, with the hue and chroma of areas in the image determined by their elemental composition, and the shading of the image (which provides depth) shown by the value of the color. Fifteen value levels (similar to gray levels in black-and-white images) for each hue and chroma are used with this routine. (This method does not display elemental concentration changes because the secondary-electron signal controls the value of the color.) If there is any topography in the sample, entire x-ray signal should come from an energy-dispersive spectrometer to prevent the erroneous reading of data.

Other useful data routines have been developed for the Colorad software. One is the color-bar pattern, which is a display of the entire color-lookup table, showing all the hue and chroma combinations (15) and their respective value levels (either 5 or 15). This display is useful for checking whether the camera is reproducing the colors faithfully. It is also a good reference for selecting a color to substitute for another, or to check whether the color-lookup table is loaded properly.

Another useful routine provides for labeling, so that one can add an image identification, sample number, etc. to the image. One can also add a scale marker to the image (to indicate size). Selected color patches, representing different phases, can be added to the image, with corresponding elemental identifications superimposed on the patches. The correct identifications are automatically selected.

Still another useful routine provides the ability to exchange colors in the color-lookup table before or after an image is made. As an example, suppose two of the colors are too closely related and/or one of the colors has no eye appeal; the user can easily call up another color and substitute it for the undesired color. Also, the user can exchange the

values of the colors within a hue and chroma group if they are too bright or too dark, etc. There is even a provision that allows the user to define his own colors, or define the color-lookup table.

The software is easy to run, as we illustrate here with a step-by-step example of how an image is created, to show concentration changes in a parent phase. The program first offers an instruction menu to the user, and displays and/or prints out the menu if the user accepts. The user accesses the desired routine by entering a number or a letter. The program then provides the option of specifying a label, and asks for input of information on desired magnification, number of detectors, identifying number of each detector, and element symbols associated with each detector. The program then inquires whether count rates are to be measured; if they are, it measures the background and peak count rates for any selected phase(s) and provides the input settings for all the time periods the program is to execute. Alternatively, a count clock rate for a given time period can be input to cause the program to provide the proper input setting for, say, showing concentration differences. After selecting the time period and input parameters for each element, the user chooses for each elemental combination (e.g., compound, precipitate, alloy, etc.) the particular element for which he wishes to see concentration changes. Resolution or detail (and hence speed of acquisition, to some extent) is determined by the choice of either 250 or 125 pixels per line and whether the image is to be quarter-screen or full-screen size. Upon receiving the go-ahead signal (G) from the user, the program then produces the Colorad image. The image can be viewed, as it is being made, on the RGB monitor. (A typical image might require 20-40 min.) When the image is complete, all the area fractions for each phase are printed out by the computer and provide useful data for calculating volume fractions.

#### *Interpreting the Image*

The Colorad image has a number of significant properties. The most important one is that it identifies elemental combinations (up to four elements) and shows changes in concentrations of atomic species within any combination of elements. In most cases it is possible to display all phases present in a specified area at one time, so that the spatial distribution of phases is easily observed. Overlaying of images is not required in order to obtain elemental combinations, because the data for all the elements being analyzed are gathered simultaneously from the same spot. The beam is allowed to reside in one spot only once, for a time long enough to gather data that are statistically reliable. In that way any unwanted background information can be completely removed and color value levels of specific count rates assigned. Because of this ability, the resulting resolution of the x-ray images is significantly increased. Images have been produced with an apparent x-ray spatial resolution of the order of 0.1  $\mu\text{m}$ .

Because the majority of the x rays emitted from the sample come from the point where the electron beam strikes the sample, adjacent areas of the sample emit comparatively few x rays. By rejecting the lower count rates, areas across boundaries are not detected. That is the reason for Colorad's significant increase in image resolution, which allows the chemistry of much smaller areas to be observed than by other methods. Because the brightness of the image is controlled by preassigned color values, widely varying x-ray intensities (count rates) can be designated with the same color value, so that the brightness of the image becomes independent of count rate.

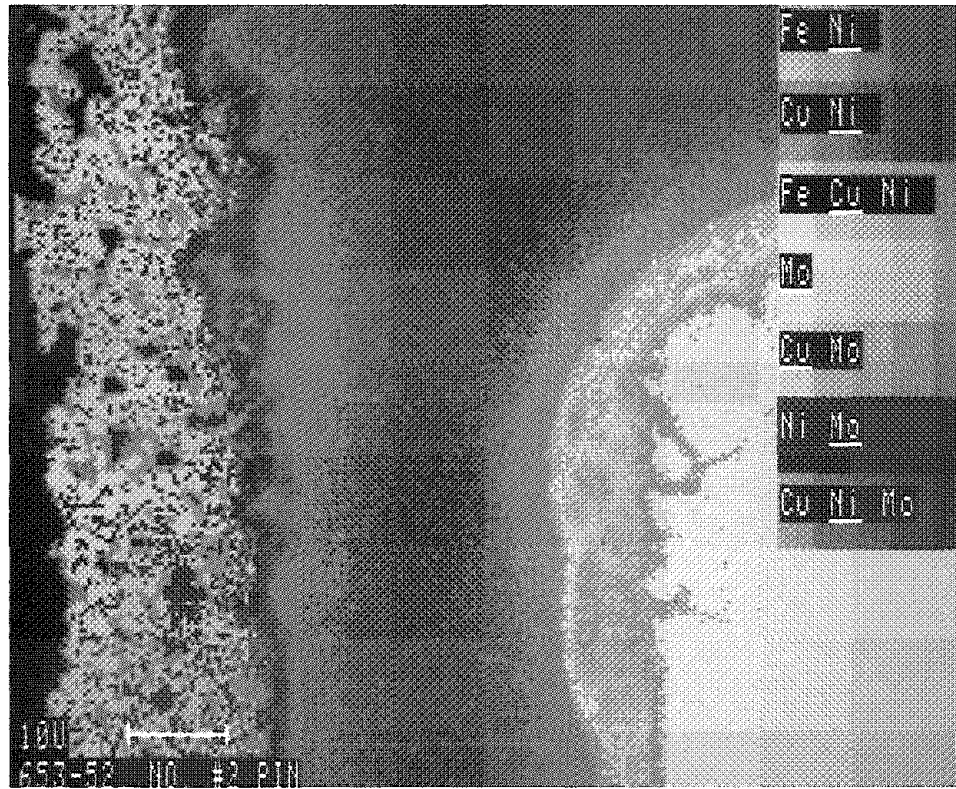
Because the image can be viewed as it is being made, one can determine immediately whether the desired results are being obtained. One can speed up the process and scan an area more quickly by selecting only the center quarter of the image and skipping every other pixel. This technique produces an image in 1/16 the usual time. However, this fast-scanning procedure is rarely necessary once the user has gained some experience in making Colorad images.

A Colorad image contains 50 000 pixels: 200 lines, each made up of 250 pixels. The 200 lines are interlaced (each line is repeated twice), which results in a 400-line image. Because only color addresses (and not pixels) are stored for each primary color, only 64K of eight-bit memory space is required. Some of the empty space is used to store labeling, magnification, and pixel counts for each phase.

Figure 1 is an example of a Colorad image of a good braze joint between alumina ceramic and Kovar for a glass-to-metal seal. A cross section of the braze joint is portrayed here; the alumina ceramic, not shown, lies just to the left of this image. When the braze joint is made, the alumina is first metallized by application of a paste of a mixture of 80% molybdenum metal, 10% manganese, and 10% silicon dioxide. Nickel is then plated onto the metallized surface layer and onto the Kovar in a Watts nickel bath. (Kovar is 29% nickel and 17% cobalt, with the remainder iron.) The two materials are then brazed with copper at a temperature above 1100 C.

The areas described in Fig. 1 can be identified from the labeled color patches on the right side of the picture. The element symbols on each color patch indicate which elements are selected to represent a phase. The underlined element symbol indicates which element is selected to show variations in relative concentration. If there is a decrease in concentration, the value of the color decreases (the color grows darker).

The color identified with the symbols Fe and Ni corresponds to Kovar. The Fe-Cu-Ni phase is green in the image; the light-green areas are richest in Cu, and the Cu concentration decreases progressively as the green becomes darker. This color change in the image shows how far the Cu diffusion has progressed into the Kovar metal. The purple area identified as Cu and Ni shows that there was sufficient Ni plating in this area, which has now reacted with the Cu to form Cu-Ni alloy. The lightest area (highest in value) repre-



Colorad image of good-quality brazed joint between alumina ceramic and Kovar metal. (See paper by D. D. McCoy.)

1. The first step in the process of creating a new product is to identify a market need. This involves conducting market research to understand what consumers want and what gaps exist in the current market. Once a need is identified, the next step is to develop a concept that addresses this need. This is often done through brainstorming sessions and the creation of a product prototype. The prototype is then tested with a small group of consumers to gather feedback and make necessary adjustments. After several iterations, a final product is developed and launched into the market. The success of the product is then monitored through sales data and customer feedback, leading to further refinements and marketing efforts.



sents a concentration of Ni of about 0.24, with a continually decreasing concentration down to the darkest area, which has a concentration of only about 0.02. The minimum detectable limit for the concentration of Ni in the Cu-Ni phase was set at 0.001.

Continuing across the Cu filler metal, we note a thin red-brown Cu-Ni-Mo strip between a purple-blue Ni-Mo area. This strip, which represents a zone of Cu, Ni, and Mo alloyed together, exists only where there is a wider band of the high-value, Ni-rich Cu-Ni phase (violet). This red-brown strip represents a zone of good bonding; when it is absent, the bond strength is weak. The purple-blue Cu-Mo area represents a Cu and Mo alloy formed during brazing. It shows that the Cu must have diffused beyond the Ni plating during the braze cycle. The yellow Mo represents the Mo in the metallizing paste, which lies on the

surface of the alumina ceramic part.

#### *Other Applications*

The Colorad system is adaptable to other scanning instruments. For example, it should be easily adaptable to a scanning electron microscope or to a scanning transmission electron microscope, either of which would merely have to be provided with an energy-dispersive spectrometer. It should also be adaptable to a scanning Auger microprobe. In a more general sense, Colorad should be adaptable, in principle, to any scanning instrument that generates a spectrum from which energy windows can be selected.

#### *References*

1. A. H. Munsell, *A Color Notation*, Baltimore: Munsell Color Co., 1971.



## 2C. EPMA: Instrumentation and Analysis

### ALIGNMENT AND CHARACTERIZATION OF DOUBLY CURVED X-RAY DIFFRACTORS

D. M. Golijanin and D. B. Wittry

The key element of a proposed instrument for microprobe x-ray fluorescence analysis (MXRF)<sup>1</sup> is a doubly bent single crystal with toroidally curved crystal planes. Such a crystal provides point-to-point focusing of a selected x-ray wavelength when the crystal has the Johansson geometry in radial planes. In order to achieve high x-ray photon intensity in the focused spot, a crystal of small dimensions must subtend a large solid angle, which can be done only by doubly bending the crystal to small radii of curvature.

If the crystal planes are properly oriented and if surface irregularities do not cause nonuniform bending of the planes, the minimum size of an x-ray microprobe should be limited by the width of the crystal's rocking curve and by the finite extinction depth.<sup>2</sup> In this paper we describe experiments to verify the crystal orientation and to test the diffraction properties of doubly bent crystals.

#### *Crystal Preparation*

The starting material for the doubly curved diffractor was a block of single crystal germanium Czochralski grown in the  $\langle 100 \rangle$  direction. It is mounted on a pivoted arm (cf. Fig. 2 in Ref. 1) with an orientation such that the surface of the cut crystal is as close as possible to the  $\langle 111 \rangle$  direction. Cutting is done with a wire saw of 40  $\mu\text{m}$  diamond impregnated steel wire 0.2 mm in diameter. Loading of the pivoted arm against the wire generates a circular arc of 100 mm radius and advancing the crystal by a micrometer screw before a second cut is made yields a cylindrically curved lamella. Lamellae thickness from 0.25 to 0.4 mm were used in the present experiments. A typical cut crystal lamella is shown in Fig. 1.

The damage produced by cutting is removed by chemical etching. A standard semiconductor etch, CP-4, normally produces a smooth and visually shiny surface.<sup>3</sup> The etching reaction is vigorous and requires agitation to prevent local overheating and assure uniform surface finish.

In our preliminary investigations we chose  $\text{CuK}\alpha$  radiation and the (333) reflection of Ge, which conveniently provides a Bragg angle of  $\sim 45^\circ$ . For this case, to obtain the Johansson geometry in radial planes and to have the same angle of incidence for all points on the surface, the crystal lamella must be bent to a sphere of radius of 50 mm (half the radius of

the cylindrical cut). To obtain plastic deformation of the crystal lamella, it was pressed uniformly over a spherical mold at 720 C. Since the slip planes in Ge are (111) planes it was hoped that slip would occur with a minimum of undesirable effect on the (333) reflection. After bending, the temperature is decreased rapidly in order to prevent crystal polygonization.

#### *Orientation Determination*

The crystallographic orientation of a cylindrically cut crystal lamella can be determined by one of the well known diffraction methods (Laue or Kossel). A Kossel diffraction pattern of a single crystal consists of a set of conics formed by a diverging beam of characteristic x-ray radiation.<sup>4</sup>

When a diverging beam of monochromatic x rays is intercepted by a single crystal, radiation diffracted from a set of planes forms a cone with its axis normal to the planes and a semi-angle which is the complement of the Bragg angle.<sup>5</sup> The pattern recorded on a photographic film consists of bright (reflection) and dark (absorption) conic sections superimposed on background due to incoherent scattering. In order to study the orientation of the crystal lamellae we used the standard stereographic projection because circles on the sphere appear as circles on the planes of projection. Unfortunately, since the positions of projected poles do not coincide with the center of the circles, and because the Kossel pattern is actually a gnomonic projection, the stereographic projection is not identical to the actual Kossel pattern.

Figure 2(a) shows the transmission Kossel pattern of the curved but unbent crystal lamella. The poor overall contrast<sup>6</sup> in the transmission mode is due to the  $1/r$  drop in intensity of the conics (coherent scattering) and  $1/r^2$  drop in background (incoherent scattering). Larger film-to-crystal distance would provide better contrast; however, we did not use it, in order to have as complete a pattern as possible on standard Polaroid film. The dark (absorption) conics are missing presumably because the lamella is too thin or "too perfect" for an appreciable absorption of copper  $\text{K}\alpha$  radiation to occur by extinction. The visible variation of background is caused by nonuniform thickness of the cut lamella.

It was found impossible to index the patterns with the assumption that the  $\langle 111 \rangle$  direction was normal to the crystal's surface at its center. On reexamining the position of the crystal for cutting it was found to be misoriented by  $45^\circ$  about the  $\langle 100 \rangle$  axis [the flats on the boule were assumed to be (100) faces instead of (110) faces]. Figure 2(b) shows the indexed pattern projected on a (64,45,0) plane. This pattern shows that the lamella orientation is close to the orienta-

Author Golijanin is at the USC Department of Materials Science, Los Angeles, CA 90089-0241; author Wittry is at the USC Department of Materials Science and of Electrical Engineering. This work was supported in part by a gift from KeveX International Corp. The authors thank Mr. Song-quan Sun for Technical assistance.



tion expected from the way it was cut.

The reflection Kossel pattern from an unbent crystal positioned as it would be if it were bent consists only of short conic segments (Fig. 3). The orientation is more difficult to determine than it is for the transmission pattern because of the ambiguity in the determination of the position of the portion of the crystal that gives rise to a given diffraction.

#### *Diffraction by Doubly Curved Crystals*

A doubly bent crystal was cemented onto a crystal holder by phenylsalicylate, which has a low melting point and is soluble in acetone. The alignment assembly has four degrees of freedom, which should provide for correct positioning of a crystal and source relative to the focal circle. The crystal, crystal holder, and the alignment assembly are shown in Fig. 4.

Our initial attempts to observe the focused x-ray spot on a fluorescent screen by using a TV camera proved to be unsuccessful owing to low sensitivity of the phosphor-camera system. Also, discrete exposures on a photographic film did not yield information about the position and intensity of the spot due to characteristic radiation because of the small width of a rocking curve and the fact that low-order planes with strong diffraction had an angle with respect to the surface. We tried raster-like scanning of two of the crystal alignment controls (1 and 4 on Fig. 4) during exposure, but it appeared that the time interval during which the spot due to characteristic radiation is diffracted was too short to leave a significant mark on the film.

Figure 5 shows the pattern of a doubly bent crystal. According to the system geometry of Fig. 4 and the indexing of Fig. 3, the brightest spot is the (440) reflection. When CuK $\alpha$  radiation is filtered through a thin brass foil, the (620) spot remains bright, which proves that the (440) spot was formed by continuous radiation and may be considered a "Laue" spot from the bent crystal.

#### *Conclusion*

Our preliminary results have shown that it is possible to doubly bend a thin crystal lamella to small radii of curvature. Also, diffraction patterns (Figs. 3 and 5) from unbent and bent crystal, respectively, prove that actual three-dimensional focusing is achieved and that the crystal retained its single-crystal diffraction characteristics even after severe plastic deformation.

The size of a focused x-ray spot as well as crystal thickness variations observable in Fig. 2(a) and the visual roughness of the etched crystal surfaces indicates that surface roughness may cause nonuniform crystal plane bending. A possible solution to this problem is to polish the cylindrically cut lamella mechanically before bending. More work still has to be done on crystal alignment by carefully monitoring changes in output of a solar cell used as a detector while the crystal orientation is changed. An alternative approach would be to use a very sensitive TV

camera for real-time monitoring of the diffraction patterns.

#### *References*

1. D. B. Wittry and D. M. Golijanin, "Development of an x-ray microprobe for local spectrochemical analysis" (this volume).
2. D. B. Wittry and D. M. Golijanin, "X-ray microprobes: A comparison of laboratory sources and synchrotron sources," *Proc. 11th Intern. Conf. X-ray Optics and Microanalysis* (in press).
3. F. J. Biondi, Ed., *Transistor Technology*, New York: Van Nostrand Reinhold, vol. 3, 1958, 156.
4. The term "Kossel pattern" usually denotes a diffraction pattern produced by diverging monochromatic x-ray radiation generated within or at the surface of a crystal. "Pseudo-Kossel" pattern is sometimes used to denote a diverging beam diffraction pattern formed by radiation that is not characteristic of an element in the crystal. For simplicity, we use "Kossel pattern" to denote the diverging-beam x-ray diffraction patterns obtained in the present work.
5. K. Lonsdale, *Phil. Trans. Roy. Soc. A240*: 219, 1947.
6. R. W. James, *The Optical Principles of the Diffraction of X-Rays*, London: G. Bell and Sons, 1958.

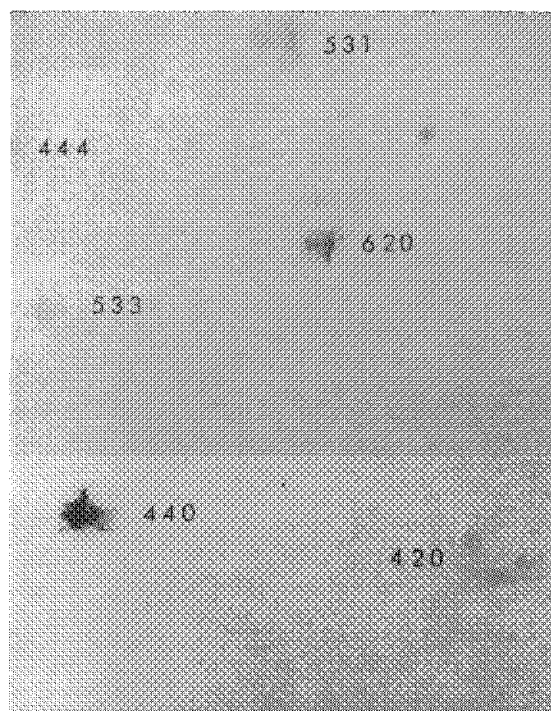


FIG. 5.--Diffraction pattern of doubly curved crystal. Film was located in plane P of Fig. 4. Electron beam conditions: 20 kV, 50  $\mu$ A. (Negative reproduction of original recorded on Polaroid 57 film, 30 min.)

## DEVELOPMENT OF AN X-RAY MICROPROBE FOR LOCAL SPECTROCHEMICAL ANALYSIS

D. B. Wittry and D. M. Golijanin

There is a need for an analytical technique for materials characterization that would have high sensitivity, provide quantitative measurements with high accuracy, provide information on local variations, and be applicable to volatile or radiation-sensitive materials. None of the presently available techniques can yield all these attributes. The most useful techniques at the present time include electron probe x-ray microanalysis (EPMA), Auger electron spectrometry (AES), x-ray photoelectron spectrometry (XPS), secondary ion mass spectrometry (SIMS), and x-ray fluorescence analysis (XRF). All except XRF require that the specimen be placed in vacuum and cannot be easily applied to nondestructive analysis of radiation-sensitive materials. EPMA, AES, SPX, and conventional XRF are limited in sensitivity. SIMS provides the high sensitivity desired but cannot be easily made quantitative. XPS and conventional XRF are difficult to use for obtaining information on small regions.

Microprobe x-ray fluorescence analysis (MXRF) could provide most of the features mentioned if one could use excitation by a focussed beam of monochromatic x-rays. For this reason, considerable effort has been devoted to the development of an x-ray microprobe based on the use of synchrotron radiation. However, if such a microprobe can be developed, it will not be a solution to the analytical problems encountered in most laboratories because of the need to do experiments in a remote location, the limited time available for experiments, and the need to schedule experiments a long time in advance.

An x-ray microprobe based on a laboratory x-ray source would be relatively inexpensive and readily available whenever required for as long a period as required. For MXRF, three diffractors would suffice to cover most of the periodic table<sup>1</sup> and these diffractors could be parfocal to facilitate analysis of the same microvolume when different diffractors are used.<sup>2</sup> The x-ray microprobe based on a laboratory x-ray source could be used as a means of excitation not only for MXRF but also for microprobe XPS and for fundamental investigation of x-ray physics.

### *Method of Forming the X-ray Microprobe*

In a previous paper<sup>3</sup> we have discussed the possibility of a high-intensity x-ray microprobe based on a microfocussing x-ray source and a doubly curved crystal. The geometry (Fig. 1)

corresponds to rotation of the Johansson geometry about a line joining the source and image. This transformation provides exact three-dimensional focusing of a point source to a point image. The intensity that could be obtained in a microprobe based on these principles can be comparable to the intensity predicted for x-ray microprobes based on bending radiation from storage rings,<sup>3</sup> i.e., about  $7.5 \times 10^8$  photons/s- $\mu\text{m}^2$ . The high intensity results from the use of characteristic x-ray lines from a source of high brightness and the use of a diffractor that collects and focuses x rays within a large solid angle. Because of the large solid angle used, the beam convergence is greater than that of microprobes based on synchrotron radiation; however, the effect on the spatial resolution is negligible if the fluorescence lines are strongly absorbed by the specimen or if thin specimens are used (i.e., 10-30  $\mu\text{m}$  as commonly used in optical microscopy of biological or petrological specimens).

The estimated intensity is based on 40kV electron beam for generating  $\text{CuK}\alpha$  x rays, x-ray production efficiency published by Green and Cosslett, the usual  $f(\chi)$  to take account of absorption, and an x-ray diffractor as shown in Fig. 1 with an efficiency of 0.33,  $\theta_1 = 30^\circ$ ,  $\theta_2 = 60^\circ$ , and  $\phi = 120^\circ$ . An electron focal spot size of 20  $\mu\text{m}$  with a current of 1 mA is assumed; this is a conservative value based on the electron optics and tungsten thermionic source. The minimum probe size is expected to be limited by the width of the crystal's rocking curve and by the extinction depth in the crystal, and is estimated to be about 25  $\mu\text{m}$  for a point source (32  $\mu\text{m}$  for a 20 $\mu\text{m}$  source).

In order to provide a large aperture with diffractors of a reasonable size, the radii of curvature must be much smaller than radii previously used for doubly curved crystals. In addition, the Johansson geometry must be obtained in all radial planes. In the present work, one meets these requirements by first cutting a thin cylindrically curved lamella from a single crystal (Fig. 2). The lamella is then plastically deformed by a special process<sup>4</sup> to shape the crystal over a convex mold, at a temperature at which slip can occur on the slip planes. The crystal orientation is selected so that one of the sets of slip planes utilized for diffraction.

In the initial tests we have utilized a germanium crystal and the (333) reflection, which corresponds to a Bragg angle of nearly  $45^\circ$  for  $\text{CuK}\alpha$  radiation. In this case, while the crystal planes will be toroidally curved, the mold is essentially spherical. For the crystals we used, the mold had a radius of curvature of about 5 cm. A crystal successfully bent over this mold is shown in Fig. 3.

The diffractors have been tested with a microfocussing x-ray source constructed from electron

Author Wittry is at the Departments of Materials Science and Electrical Engineering and author Golijanin is at the Department of Materials Science at the University of Southern California, Los Angeles, CA 90089-0241. This work was supported in part by a gift from Kevex International Corp.

probe microanalyzer components (ARL model EMX-SM). A schematic diagram of the microfocus x-ray source is shown in Fig. 4; experiments to study the diffracting properties of the doubly bent crystals are described in another paper in these proceedings.

#### *An Instrument for Microprobe X-ray Fluorescence Analysis*

An important advantage of the MXRF technique in addition to the small spot size is the use of focused monochromatic radiation for excitation. The background that occurs in conventional XRF due to Rayleigh scattering of the continuum is almost completely eliminated. An estimate of the principal remaining source of background, namely continuum produced by photoelectrons, indicates a signal-to-background ratio of about  $10^4$  to  $10^6$  for a pure specimen.

Because of the improved detection limits that can be obtained with a high signal-to-background ratio, it is anticipated that most analytical applications will involve x-ray fluorescence spectra with many lines due to trace impurities. Therefore, a practical instrument must include a wavelength-dispersive spectrometer as well as an energy-dispersive spectrometer. Other essential elements include an optical viewing system and a precision specimen stage.

An instrument for x-ray fluorescence analysis based on the x-ray microprobe described is currently under development at the University of Southern California. It consists of the microfocus x-ray source of Fig. 4, a germanium crystal diffractor, an x-y-z- $\theta$  specimen stage driven with stepping motors, an optical viewing system providing 50 $\times$  magnification on a TV screen, a computer-controlled wavelength-dispersive spectrometer (EMX-SM type) and an energy-dispersive spectrometer (Kevex 7000). A photograph of the instrument in its present state of development is shown in Fig. 5.

Future developments of this instrument will include the addition of other diffractors to provide for efficient excitation of a broader range of elements and an improved microfocus x-ray source with a rotating anode containing multiple elemental targets. With these improvements, it is anticipated that the MXRF technique will become another important analytical technique for the characterization of materials.

#### *References*

1. M. Kotera and D. B. Wittry, "X-ray fluorescence analysis with monochromatic x-rays," *J. de Physique* 45 (Colloque C2, Sup. 2): 281-284, 1984.
2. D. B. Wittry, "System for local excitation by monochromatic x-rays," U.S. Patent 4 599 741, 8 July 1986.
3. D. B. Wittry and D. M. Golijanin, "X-ray microprobes: A comparison of laboratory sources and synchrotron sources," *Proc. 11th Intern. Conf. X-ray Optics and Microanalysis*, (in press).
4. D. B. Wittry, patent application pending.

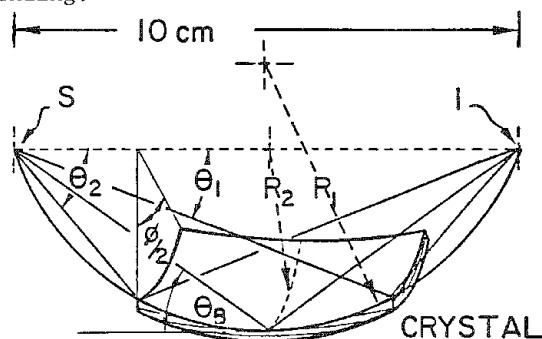


FIG. 1.--Geometry of doubly curved crystal diffractor for x-ray microprobe. Monochromatic x rays from source S are focused by crystal to image I.

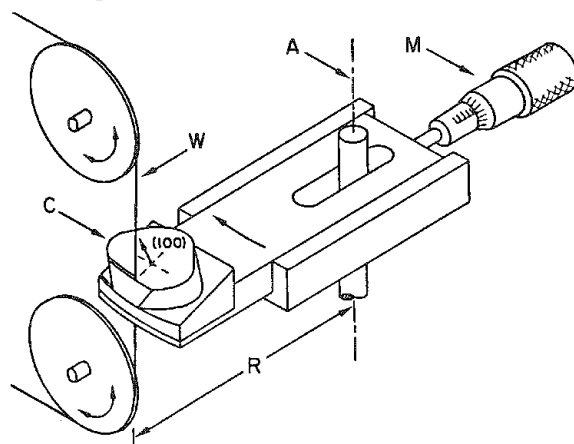


FIG. 2.--Diagram of diamond wire saw for cutting crystals. Crystal C is mounted on arm that rotates about axis A. Diamond-impregnated wire W cuts cylindrical lamella of radius R whose thickness is determined by advancing crystal after each cut by micrometer screw M.

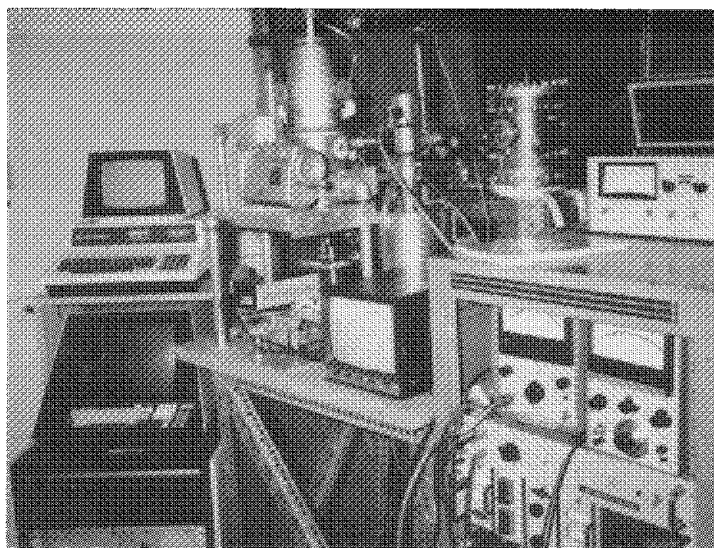
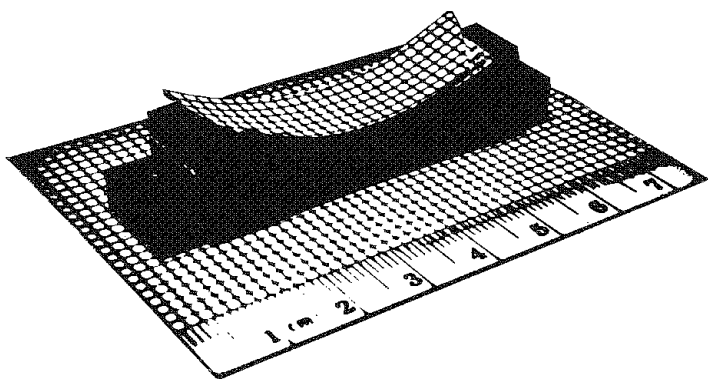


FIG. 3.--Doubly curved crystal attached to backing plate. To show double curvature, crystal was coated with white paint to make it diffusely reflecting and a grid was projected onto crystal by 35mm slide projector.

FIG. 5.--X-ray microprobe instrument. Console on right contains controls for microfocus x-ray source; console on left contains controls for EDS and WDS. Spectrometers have been removed for performing tests of crystal diffractors, but drive mechanism for WDS can be seen in front of electron-beam column. The y-y-z- $\theta$  stage and TV camera for viewing specimen can be seen below beam column.

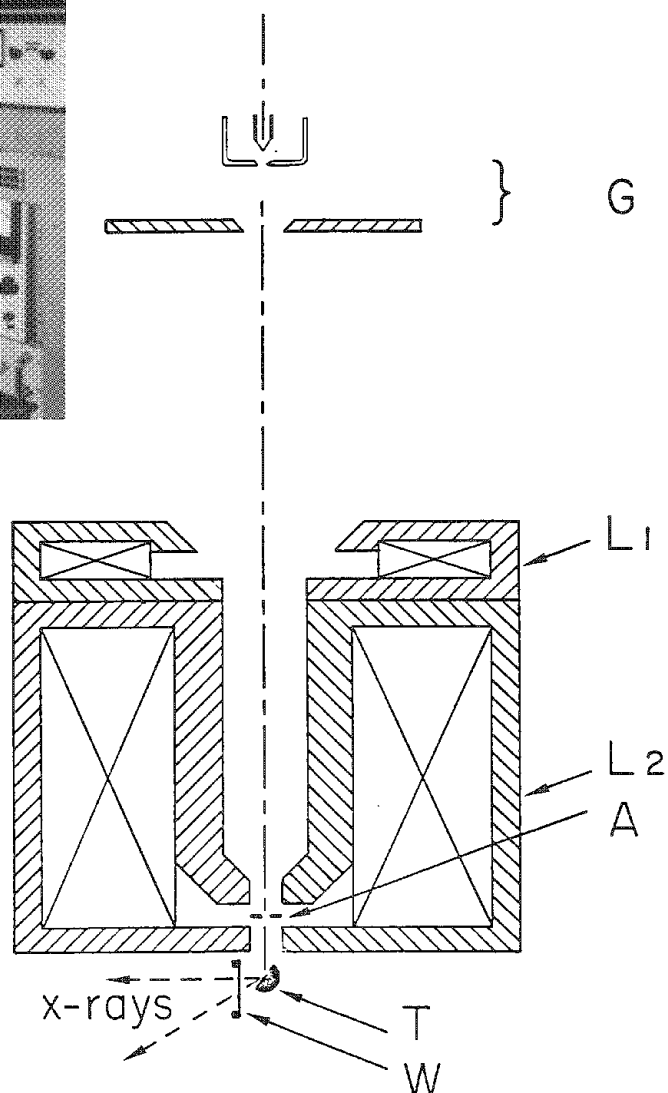


FIG. 4.--Microfocus x-ray source: Electron beam from gun G is focused onto a target T by two magnetic electron lenses adapted from an electron probe microanalyzer.  $L_1$  is modified objective lens,  $L_2$  is condenser lens from EMX-SM. Beam angular aperture is determined by fixed aperture A. Beam column enclosure (not shown) is evacuated by sputter ion pump; x rays emerge from this enclosure through window W.



## A NEW AUTOMATED EPMA SYSTEM WITH DISTRIBUTIVE PROCESSING CAPABILITY

Yoshitaka Nagatsuka, Toshiaki Miyokawa, Masayuki Otsuki,  
Tadashi Watanabe, Jun Suzumi, and Shojiro Tagata

Influenced by the rising demands of metallurgy, geology, and material science, research work with electron probe microanalysis (EPMA) has been significantly expanded in recent years. The modern EPMA system requires not only high-precision data with good reproducibility, as in qualitative or quantitative analysis, but also vast amounts of data and rapid image processing as in area analysis.<sup>1-3</sup> The system also needs to be fully automated and complete, including control of the electron optical and scanning system. Moreover, the latest analytical instrument should have the capability of multi-user, multi-job function. Because EPMA needs increasing analysis volume and time, it is now necessary to process the previously acquired data while acquiring the present data by one or more persons. And since analysis methods and techniques are continuously advancing, the analytical instrument must have a room for improvement or expansion, both in software and hardware.

In this paper, we introduce an approach to coping with these various requirements by taking a new automated EPMA system, the JEOL JXA-8600M, as an example.

### *Hardware*

The hardware configuration of the JXA-8600M with an image processor is shown in Fig. 1. In this system, three processors are used; the first (MPU) is used essentially to control the electron optical and scanning system; the second (APU), for data acquisition, including control of the stage, spectrometer, and MPU; and the third (HPU), for data reduction and total system management.

The electron optical and scanning system is provided with intelligent, self-adjusting functions by MPU and allows external control (accelerating voltage, magnification, probe current, probe diameter, etc.) from HPU via APU. Data transmission between HPU and APU is achieved by sharing of the same common dual ported memory (DPM) with which the concurrent measurement and data reduction in each processor is most efficiently executed.

HPU is fitted with a 40MB Winchester disk (30 MB fixed and 10 MB removable), color graphic display, graphic plotter, and a powerful image processor with a 4MB frame memory. High-speed image processing and particle analysis are done on this image processor via its pipeline processor after voluminous area data are received from HPU through the DMA line.

---

The authors are with JEOL Ltd., 1418 Nakagami, Akishima, Tokyo 196, Japan. They are grateful to Prof. Yoshibumi Naitoh of Yamaguchi Jewelry Academy for providing them with Cr-diopside samples.

### *Software*

Figure 2 shows the schematic memory arrangements for APU and HPU. Each processor shares the same memory region on DPM. At the stage of system start-up, the data-acquisition program of APU is downloaded through this DPM from HPU within a few seconds.

When the downloading for APU is completed, the APU is activated and made ready to accept commands from HPU. More than 60 commands are available, including the simple control commands and several macro commands. The simple control commands are written in the efficient Assembly language; the macro commands, such as spectrometer peak seeking, data acquisition by spectrometer scanning or by stage scanning, and low-magnitude x-ray image photography, are written in the FORTRAN language.

There are three regions--S, P, and D--in the shared memory. Region S holds system data on all present physical states of the system and a command buffer space to communicate between the two processors, APU and HPU. Region P holds the parameters necessary for running a macro command. The data acquired by the macro command are stored into region D. When the acquired data fill up region D, an interrupt signal is issued from APU to HPU. During this acquisition time, the HPU can also execute other tasks. Thus, the two processors work concurrently, except when transferring the interrupt signal, so that the total analysis speed is very high compared with other multi-processor systems based on the DMA or serial communication method.

Since the two processors only share the same common memory and exchange the interrupt signal, it is possible to improve or modify the software and/or hardware for each processor independently. It is thus possible to enhance the quality of an application program of HPU without changing the software of APU. It is also possible to implement a new function by modification of the software/hardware of APU or by addition of a new intelligent device to APU without modification of the software of HPU. Thus, the instrument has a great capacity to cope with any modification or future expansion of the system.

### *Analysis Program*

Based on the above-mentioned hardware and software, many analysis programs have been developed. Each analysis program written in FORTRAN-77 language has the following extremely powerful performance.

*Qualitative Analysis.* X-ray spectra (max. 20) of several unknown specimens are acquired and displayed in real time by use of several types of analyzing crystals and saved into disk. Peak positions are automatically determined by use of second-derivative data of

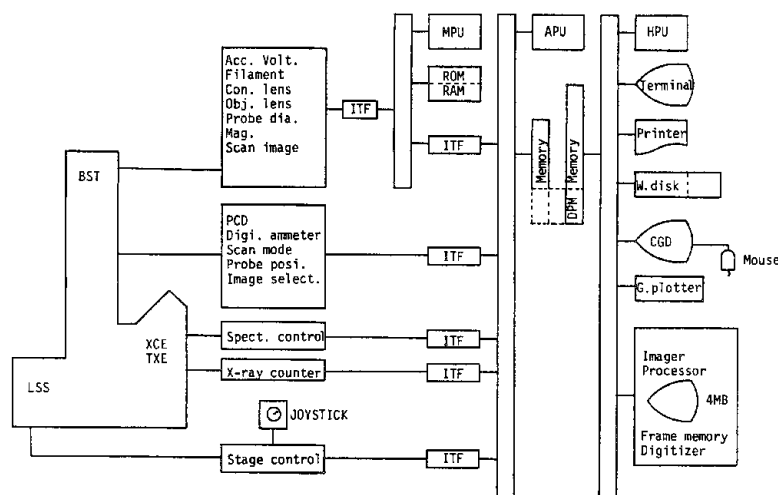


FIG. 1.--Block diagram of JXA-8600M.

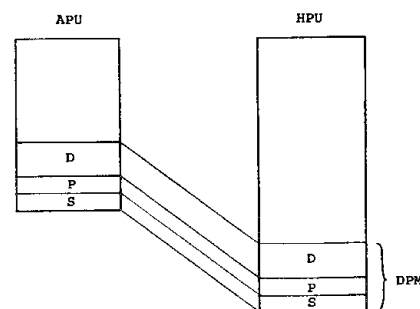


FIG. 2.--Schematic memory arrangements for APU and HPU.

acquired spectra. Element identification in three ranks is performed by comparison of the determined peak positions and intensities with the first-order characteristic x-ray lines ( $K\alpha$ ,  $K\beta$ ,  $L\alpha$ ,  $L\beta$ ,  $M\alpha$ ,  $M\beta$ ) of all elements. Peak assignment is made for up to 10th-order lines of all kinds of x rays for the identified elements. All the above work is automatically accomplished during the measurement. Acquired x-ray spectra can be output onto a color display or graphic plotter, together with the identified element names at the corresponding peak positions. Spectral expansion or contraction for the X or Y direction is possible by shift of the cursor with a mouse device attached to the display. One can also achieve manual element identification, by moving the KLM marker using the mouse.

**Quantitative Analysis.** This program is based on a databased analysis technique. The chemical composition of a standard sample necessary for quantitative correction needs to be input only once. By calling a condition file that includes standard intensities, one can directly analyze unknown specimens without any elaborate setup of the measurement conditions. The results of the unknown specimen can be saved in a separate file and can be listed at any time, together with mean values and their standard deviations. It is possible to store 1000 different measurement conditions, register 1000 different standard samples, and preset more than 32 000 analysis positions for unknown samples. This program can use several types of quantitative corrections, including ZAF, Bence & Albee, thin film (Philibert-Tixer or Reuter), and calibration curve methods.

**Line Analysis.** The specimen stage is driven stepwise in any direction from the preset start position to the preset destination position at any interval (minimum 1  $\mu\text{m}$ ) with any dwell time. X-ray intensities of up to 20 elements on several unknown samples are acquired by means of several types of analyzing crystals and are saved into disk. The acquired spectra can be output onto a printer, color display or graphic plotter.

**Area Analysis.** Two-dimensional intensities (up to 20, each consisting of  $1024 \times 1024$  pixels) of x rays and/or electron image signals (SEI or BEI) are acquired by stage scan or beam scan for up to 50 analysis areas by use of several types of analyzing crystals and/or an image signal digitizer, displayed in real time and stored into disk. The acquired intensities of x rays or electron image signals, or element concentrations converted from them, can be output onto a color display or graphic plotter. It is also possible to transfer the acquired data to the image processor through the DMA line and to make a super-rapid image display and particle analysis. The image on the color display or image processor can be easily and instantly changed by a mouse or digitizer attached to their respective devices.

**Manipulation Job Program.** This program is a collection of some 70 different fundamental functions of EPMA analysis. With this program, one can control EPMA through key input as if he controlled it manually. Also, this program offers some useful frequently used utilities such as "Set spectrometer to element peak," "Peak seeking," "Linescan," and "Low-magnitude x-ray photography." It is also possible to schedule the execution of each command by the programming facilities.

**Other Application Programs.** Several other programs are available, including standardless semiquantitative analysis, trace-element analysis, chemical-shift analysis and spectrum-deconvolution analysis, and various map display programs. With the standardless semiquantitative analysis program, one can obtain quantitative analysis data on an unknown sample from the qualitative analysis data without standard measurement. With the trace-element analysis program, one can determine the presence of some minor elements contained in a sample. With the spectrum-deconvolution analysis program, one can make quantitative spectrum separation by comparing the unknown spectrum with the standard spectrum.

## Some Applications

**Example of Qualitative Analysis.** Figure 3 shows acquired spectra of an optical glass sample. All elements contained in this sample whose concentrations are above 1% are given in the A-rank element list. Table 1 shows the result and a part of a peak assignment list of the identified elements.

**Examples of Area Analysis.** Figures 4-8 show the macro-area analysis of Mg, Fe distribution in Cr-diopside mineral. The analyzed area is 20 × 16 mm and consists of 500 × 400 pixels. In this analysis, characteristic x rays of Na, Al, Si, Ti, Cr, Mn, and Ca, as well as BEI signal, were measured. Detailed structure of compositional zoning of the mineral can be seen clearly, which was hardly imagined from point or line analysis.

## Conclusions

We have introduced an EPMA system with distributive processing capability and its application software. This kind of distributive processing will be more frequently used in the future EPMA system. In such a case, it will become a keypoint to determine the performance of the system, how properly the processors are arranged, and how effectively each processor communicates with others.

## References

1. Y. Ono et al., "High-speed wide-area analysis by electron probe," *Microbeam Analysis--1985*, 145.
2. Y. Nagatsuka et al., "A high speed macro area fine analysis and image processing system in EPMA," *Proc. 11th Intern. Cong. on Electron Microscopy*, 1986, 485.
3. T. Miyokawa et al., "A new rigorous identification method for constituent element in EPMA," *ibid.*, 555.

TABLE 1.--Analysis result of optical glass.

### Result

A-Rank : B C O Si Ca Sr Y La

B-Rank : Mn Zn Ga Rh Sm Lu Hf Re

C-Rank : U Pr Os

Spectrum no. = 1 Channel = 1 Crystal = NSTE

Peak no.	Peak (mm)	Peak-Back (counts)	Element Line (Order)
1	65.900	480.	O KA (1) U LA1,2 (1) Sr LL (3) Y LB3 (4) Ca SKA4 (7)
2	123.900	249.	C KA (1) La MA (3) Pr MG (4) Sr LB3 (7) Sr LB4 (7) Sr LB1 (7)
3	130.900	159.	Sr LL (6) Si KB (7) Si KB1 (7) O KA (2) La MB (4) Sr LB3 (9) Sr LB4 (9)
4	161.000	3.	Y LA1 (9) Y LA2 (9) Sr LB3 (10) Sr LB4 (10) Y LA1 (10) Y LA2 (10) Y LN (9)
5	178.600	17.	B KA (1) Sr LA1 (10) Sr LA2 (10) Sr LN (9) Si KB (10) La MA (5) Sr LN (10) Y LL (10) Zn LA1,2 (6) Rh MG (3)

Spectrum no. = 2 Channel = 5 Crystal = TAP

Peak no.	Peak (mm)	Peak-Back (counts)	Element Line (Order)
1	65.400	34.	La LL (2) Y LB4 (1) Re LB2 (5) Re LB15 (5) Sm LB1 (3) Y LB1 (1) Sr KB5 (8) Y LA1 (1) Os MA (1) Y LA2 (1) Zn KB1,3 (5) Lu LA1 (4) Sr LB1 (1) Pr LB3 (3) Y KB1 (9) Y KA1 (8) Y KA1,2 (8) Sr LA1 (1) Sr LA2 (1) Os LB7 (6) U KB1,3 (3) Re LN (5) Si KA1,2 (1) Si KA2 (1) Lu LG2 (6) Lu LB1 (5) Hf LL (4) La LB4 (3) La LB1 (3) Pr LA1 (3) Y LL (1) Rh LG2,3 (2) Pr LG3 (4) Pr LG2 (4) Sr LN (1) Y KA2 (9) U KA1 (3)
2	67.700	571.	
3	70.300	1480.	
4	72.200	703.	
5	74.800	1666.	
6	77.600	510.	
7	80.200	49.	
8	81.600	17.	

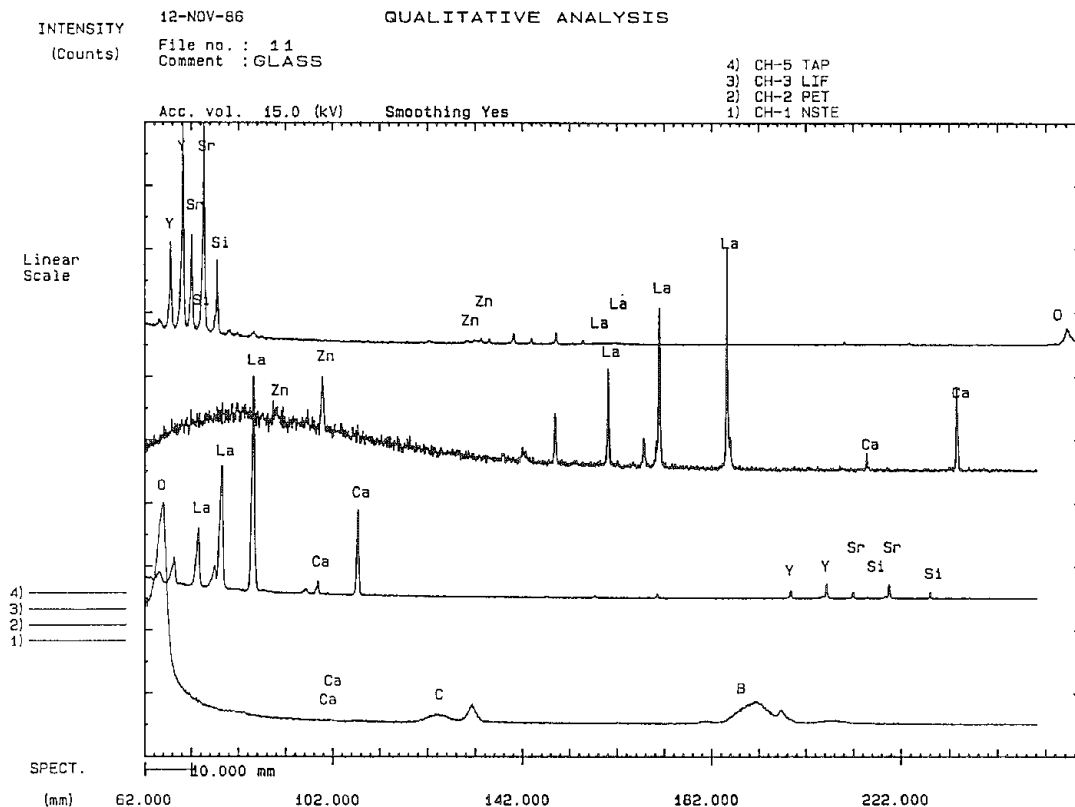


FIG. 3.--Acquired spectra with identified element label.

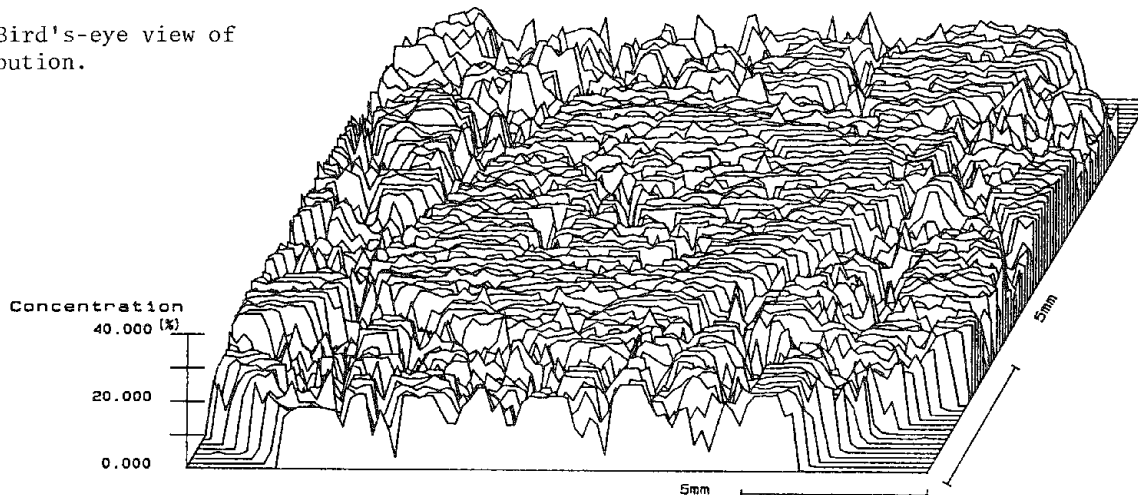
TABLE 2.--Particle analysis example of Mg distribution.

\*\*\*\*\* Summary \*\*\*\*\*

File no. : 102  
Report no. : 1  
Device name : DL3  
Comment : Particle analysis result for Mg  
Unit of length : millimeter  
Coupling : B

Name	Max	Min	Ave	S.D.
S	99.244	0.14240	7.7181	23.056
ML	14.568	0.63200	2.5331	3.2045
PM	46.268	1.7760	7.8578	10.289
FH	13.640	0.60000	2.2682	3.0177
FV	11.520	0.24000	2.0023	2.5387
CH	11.920	0.60000	2.0211	2.6548
CV	10.600	0.24000	1.8541	2.3519
BD	12.376	0.29600	1.8618	2.7449
TH	167.9	7.6	77.2	56.9
HD	11.241	0.42580	1.9136	2.4829
SF1	2.9043	1.2985	1.8375	0.4502
SF2	3.5786	1.0862	1.6775	0.5445
SF3	2.6378	1.0532	1.5305	0.3836
ND	8.3787	1.0807	4.7297	3.6489
LD	4.4407	2.2528	3.4712	0.91038

FIG. 4.--Bird's-eye view of Mg distribution.



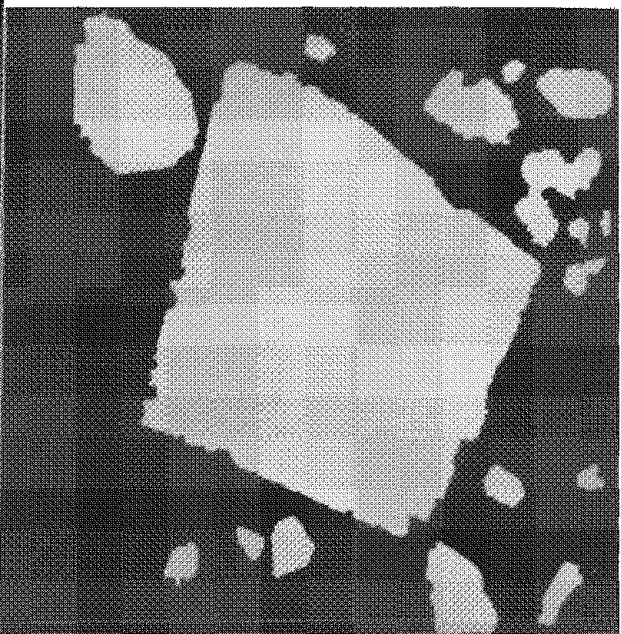
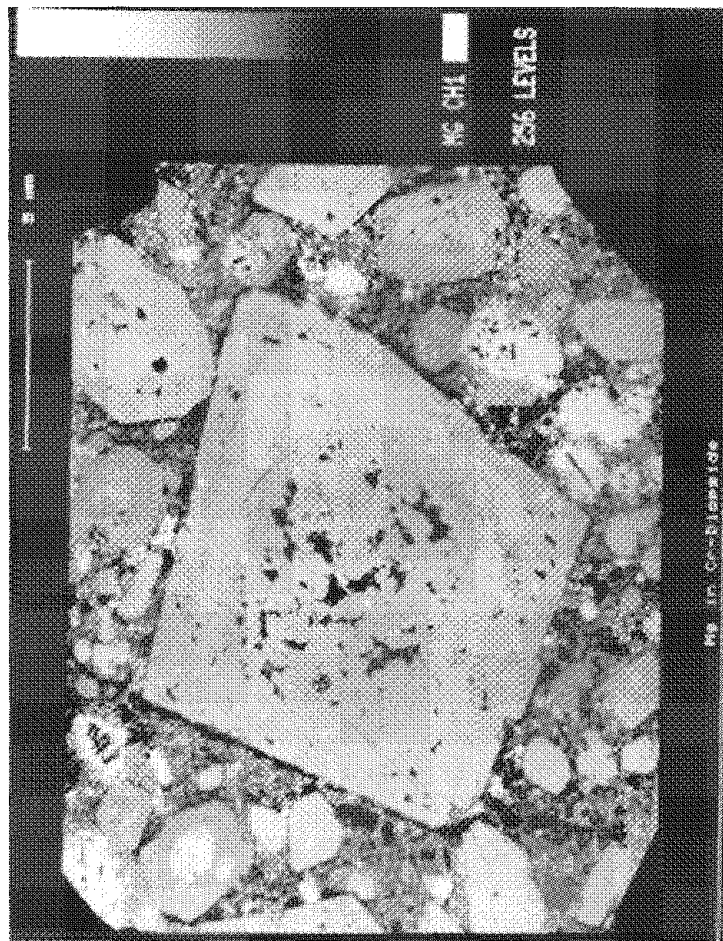
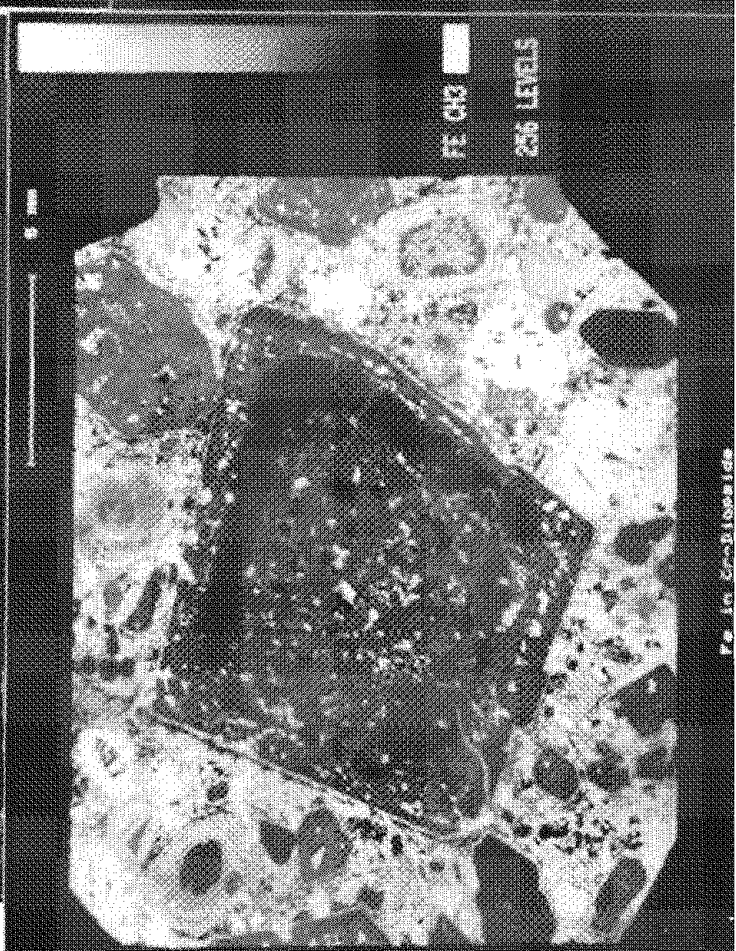
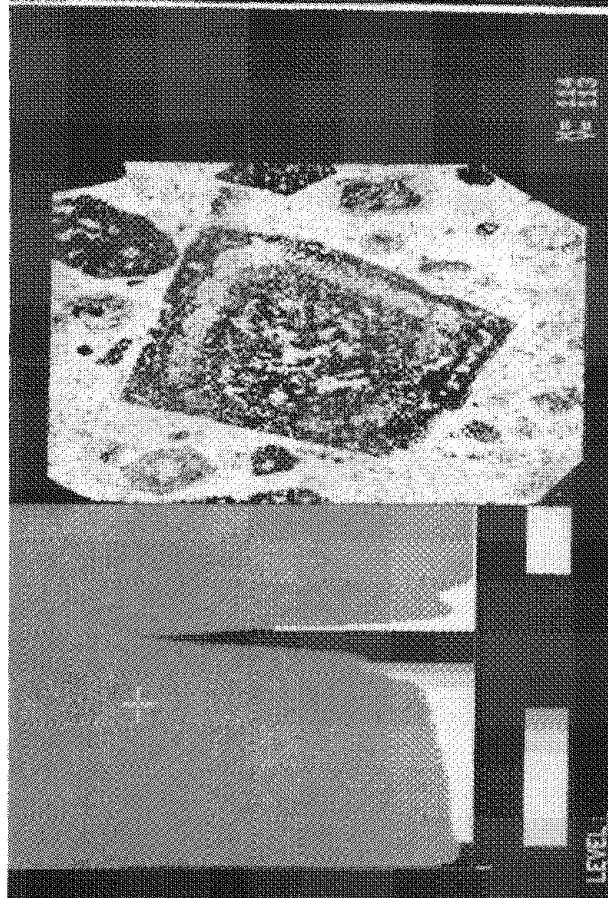


FIG. 5.--Mg distribution in Cr-diopside with concentration histogram.  
 FIG. 6.--Mg distribution in 256 gray-scale levels.  
 FIG. 7.--Fe distribution in 256 gray-scale levels.  
 FIG. 8.--Digitized and filtered image of Mg distribution.

## PROGRAMMING FOR KEYBOARD-OPERATED EDS-WDS MICROANALYSIS

N. G. Ware

The automated electronprobe has evolved into a machine operated entirely from the computer keyboard. The absence of knobs and dials, the functions of which must be replaced by computer peripherals, places extra responsibility on the computer programmer. The software must translate the intentions of the operator into action by the machine without either abusing the instrument or wasting the user's time. In addition, it is essential that the software correctly solves analytical problems, necessary that it monitors the performance of the instrument, and desirable that it carries out bookkeeping and managerial tasks. Electronprobe software requires much development before the potential of the current generation instrument is fulfilled. This paper describes the foundations on which a viable FORTRAN-based package may be constructed.

The computer is responsible for driving a formidable list of components: wavelength-dispersive (WD) spectrometers, the Si(Li) detector, the specimen stage, the electron optical column, the electron detectors, the optical microscope, the vacuum system, photographic equipment, assorted video terminals, printers, and plotters as well as owner-added gimmicks such as loudspeakers, voice synthesizers, and the room lights. Programming is simplified if it is limited to driving a particular installation and performing only the analyses likely to be demanded of it. However, the resulting software can then be used only with the individual instrument and cannot be tested or improved at other laboratories. The extra effort by the owner-programmer in designing a package usable by other laboratories is well worth while; allowance should be made for all combinations of crystals, spectrometers, and specimen stages and provision made for the widest range of operating conditions and analyzed chemical elements.

Quantitative x-ray microanalysis is the primary function of the electronmicroprobe, but the software package should be designed so that other tasks may be included such as x-ray spectroscopy, model analysis, compositional mapping, and image analysis. This goal is accomplished by the familiar expedient of having a number of programs performing different tasks but sharing data stored in data files. Furthermore, in a multi-user computer system, it is possible, first, to have programs spawn each other; and second, to activate a command file at log-on time that runs the main menu program. Thus the electronprobe user need know nothing about computer control languages and need only to be told to type a simple message such as HELLO PROBE/GDAY (account PROBE, password, GDAY, in the DEC RSX system) to gain

access to the main menu and subsequent user-friendly dialog. However, this low level of security would cause problems at many multi-operator laboratories. It is best that the initials of the operator be entered, together with a security code issued on passing a driver's test, before the main menu is displayed. Then all calibrations and changes to data files can be tagged with the date and initials of the operator. Since anything done to the machine may be recorded, accounts of machine usage may be made automatically. Only public files need be read by the main menu system; extra security, at the discretion of the probe manager, may be given to the laboratory accounts and certain instrumental parameter files.

The electronprobe may be driven by the keyboard in two ways. Instructions in the form of fairly lengthy mnemonics may be typed, or all the keys may be assigned functions and descriptions of the functions displayed on the terminal screen. It is not possible to display all possible functions simultaneously but the entire instrument may be covered by use of only four driving programs:

A. Specimen stage and simple scanning driver. This program is the most frequently used and allows the operator to position the beam at the required spot on the specimen. The specimen may be examined by optical or scanning electron microscopy (SEM) and the spot selected by moving the stage or deflecting the beam. The program may include a sample changing routine where the computer operates the vacuum system and displays instructions as to sample manipulation.

B. Electron column. This program allows selection of the accelerating voltage, beam current, spot size, and scanning raster. The actual lens currents may be displayed and the times of switching the filament heater recorded.

C. WDS spectrometers. Used for setting bias voltages and the pulse height analyzer, changing crystals, driving the spectrometers, and measuring count rates.

D. SEM and camera driver. Used for obtaining all images and for photography.

A fifth program may be required if the EDS system has no independent multichannel analyzer (MCA). Programs B, C, and D may be spawned in turn by program A.

The display and mode of operation of these programs should be designed to satisfy the preferences of the users. A display scheme that has proved satisfactory is exemplified in Figs. 1 through 4; a description of the program is given at the top of the screen, the functions of the command keys are in the middle, and a line of switching keys is displayed near the bottom of the screen. Data input and transient instructions and warnings would appear at the very bottom of the display. For



example, Fig. 1 shows a display for program A written for the CAMECA SX50. The functions of the instrument's thumbwheels are displayed at the top right corner; they move the stage in the X, Y, and Z directions. When the keyboard letter 'T' is touched, the message 'Stage' switches to 'Screen' and the thumbwheels then move a marker on the CRT displaying the electron image. The other switching keys work in a similar way; touching 'F' switches the Faraday cup IN or OUT; 'L' switches the microscope lamp 'ON' or 'OFF'; 'R' switches between reflected and transmitted light, and so on. Typing 'G' switches the scan generator on or off, typing 'P' switches the beam from point to area scan, and 'A' selects the area scanned between magnification  $\times 100$  and  $\times 80\,000$ . The operator may move the stage by a number of microns defined by Q and S by typing X, Y, or Z. 'S' may be switched between 1 and 1000  $\mu\text{m}$  and 'Q' is either plus or minus. Moving the stage in this way is useful if the thumbwheels are in use controlling the beam. Typing 1, 2, or 3 spawns the other driving programs. Some 25 keys are activated by this program, yet the whole display is assimilated at a glance and requires only a few minutes of operation for familiarity.

Figure 2 shows the terminal display of a program for selecting points for automatic quantitative analysis on a CAMEBAX MICROBEAM electronprobe. Here the whole procedure is run from a single screen display and the stage-driving protocol has been built into the main program. This program tends to be used in preference to the alternative sequential

dialog method.

A spectrometer handling routine that could be modified for use on any automated microprobe is illustrated in Figs. 3 and 4. Figure 3 shows the display for all spectrometers simultaneously (limit of 5 spectrometers); this feature is useful for manual x-ray spectrometry and for starting up and switching off the system. Figure 4 shows the display for controlling a single spectrometer, used as part of the WDS calibration procedure.

The role of the ED spectrometer when fitted to an automated microprobe is primarily that of phase identification. Frequently the operator is familiar with the spectra of the phases in the sample and can make a phase identification by a glance at the EDS spectrum after less than 1 s accumulation of x rays. The old-fashioned hardwired multichannel analyzer (MCA) coupled to the computer by a fast interface (e.g., IEEE) provides a cheap and very efficient EDS display device for the automated probe. KLM markers and color displays are not required. When the spectrum is unfamiliar and when x-ray peak identification is ambiguous, the fastest way to resolve the problem is by use of the WD spectrometers.

It is important that the MCA be controlled by the computer; the ED spectrometer then becomes part of the keyboard system and may be used by phase identification and quantitative analysis programs. Programming for combined ED and WD quantitative analysis is made easy when the two types of spectrometer share the same data files and are controlled by the same program.

+-----+   PROBE DRIVING PROGRAM     Stage and Screen   +-----+						----   *        Z   ----				
E = Exit B = Backlash on stage J = Set up Z movement U = Move Z one micron C = Enter coordinates X,Y or Z = move stage M = Change samples 1 = Column program 2 = Spectrometer prog 3 = Photography prog						----   X        Y   ----				
Q	S	F	L	R	T	A/P/G	I	D	K	H
+	100	OUT	OFF	REF	Stage	Point	BSE	SFS	6	7

FIG. 1

```

+-----+
| SELECT POINTS FOR ANALYSIS |
+-----+

E = Exit      B = Backlash    P = Reset display
J = Set up Z movement      V = Up 2 microns
C = Clear XYZPOS file      I = Include data in file
A = Align stage            W = Work through file
G = Go to X&Y positions entered through keyboard

```

Q	S	Cup F	Vert Y,U,D	Horiz X,R,L	Focus Z	Method M	Formula 0	Analysis number
+	100	IN	25432	41648	3115	SMITH4	12	43

FIG. 2

```

+-----+
| SPECTROMETER DRIVING |
|      ROUTINE         |
+-----+

```

	Sp 1	PET	Sp 2	LIF	Sp 3	TAP	Sp 4	ODPB
Bias	1287	INT	1752	INT	1313	DIF	1432	DIF

FIG. 3

```

+-----+
| SPECTROMETER DRIVING |
|      ROUTINE         |
+-----+

```

Q	S	K	B	I	L	W	X	P
+	200	PET	1782	DIF	125	150	OFF	37474

FIG. 4



# ELECTRON PROBE MICROANALYSIS OF Be IN Cu-Be ALLOYS WITH THE USE OF A LAYERED SYNTHETIC MICROSTRUCTURE DISPERSION ELEMENT

D. A. Sentner and H. I. Heitur

Beryllium analysis in the electron microprobe is possible with the use of synthetic lignoceric, cerotic, or melissic acid analyzing crystals.<sup>1</sup> The long-term stability and low peak reflectivity of the synthetic acid crystals limit their practical use and commercial availability. Layered Synthetic Microstructures (LSM) have been synthesized and used as analyzing crystals for the detection of boron, carbon, nitrogen, and oxygen in electron microprobes and x-ray fluorescence system.<sup>2,3</sup>

## Experimental Method

A boron carbide/molybdenum LSM with a spacing of  $2d = 198 \text{ \AA}$  was prepared (by Ovonic Synthetic materials, Inc.) and installed in a Cameca MBX electron microprobe. Stretched polypropylene was used for the column and detector windows. P-10 gas was used in the detector. Microanalysis was performed with an accelerating voltage of 10 kV and current of 0.1  $\mu\text{A}$ . Beryllium  $K\alpha$  intensity measurements were performed for 60 s. Analysis standards were prepared from pure beryllium metal and beryllium oxide. Beryllium carbides and copper cobalt beryllides were precipitated in a copper-beryllium alloy to test the ability of the LSM analyzer to detect beryllium in micron-size phases in a copper-rich matrix.

## Results

Limited-range spectral scans of the beryllium metal, beryllium oxide, beryllium carbide and cobalt beryllides are shown in Fig. 1. The beryllium  $K\alpha$  peaks in the oxide and carbide spectral scans show a measurable shift in wavelength relative to beryllium metal. The wavelength values have not been corrected to account for refraction.

The measured beryllium  $K\alpha$  peak intensities for pure beryllium metal, beryllium oxide, and precipitated beryllium carbide and cobalt beryllide are compared in Table 1. Background measurements were taken above and below Be  $K\alpha$  peaks and averaged.

A secondary-electron image of precipitated beryllium carbides in a copper-rich matrix and the corresponding beryllium, copper, and carbon elemental distribution images are shown in Fig. 2.

Beryllium levels in cobalt beryllides precipitated in a copper-rich matrix were documented by elemental line scans and distribution images. Figure 3 contains a secondary-electron image and the corresponding elemental line scans for beryllium, copper, and cobalt from a precipitated cobalt beryllide. Elemental distribution images of beryllium, copper, and cobalt from a stringer of cobalt beryl-

lides are shown in Fig. 4.

## Summary and Conclusions

An LSM analyzing crystal was used in an electron microprobe to detect beryllium. Beryllium peak locations and intensities were documented for beryllium metal, beryllium oxide, beryllium carbide, and copper-cobalt beryllide. The ability to detect beryllium in micro-size phases in a copper-rich matrix was illustrated with elemental distribution images and linescans of precipitated beryllium carbides and cobalt beryllides.

## References

1. S. Kimoto et al., "Beryllium detection in electron probe microanalysis," *JEOL News* 7M(no.1): 2-6, 1969.
2. K. Kavabe et al., "Coated multilayer dispersion element for x-ray microanalysis," *Proc. 11th Intern. Cong. on Electron Microscopy*, Kyoto, 1986, 569-570.
3. J. A. Nicolosi et al., "Layered synthetic microstructures for long wavelength x-ray spectrometry," *Optical Engineering* 25: 964-969, 1986.

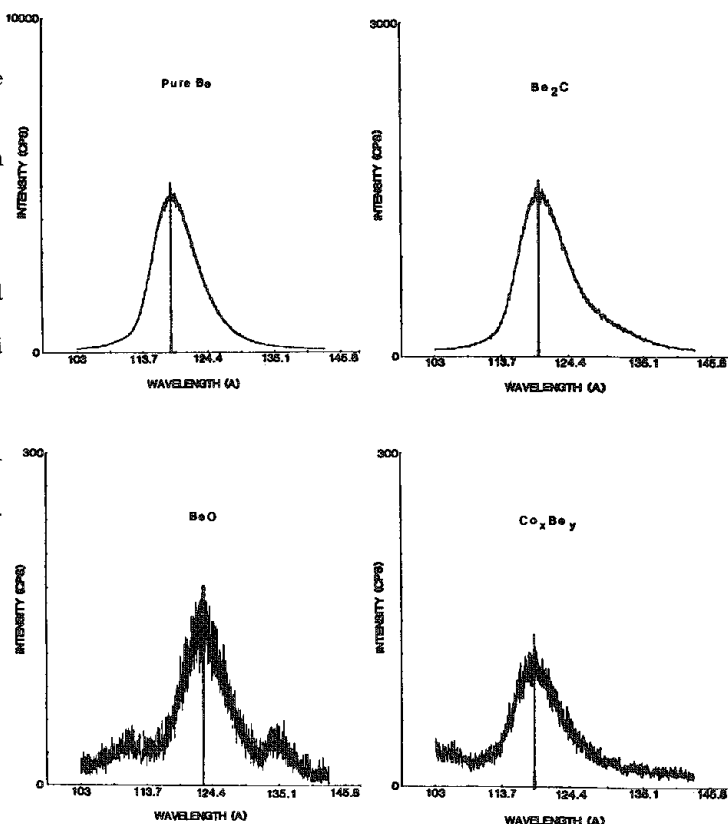


FIG. 1.--Beryllium  $K\alpha$  spectral scan for (a) beryllium metal, (b)  $\text{Be}_2\text{C}$ , (c)  $\text{BeO}$ , (d)  $\text{Co}_x\text{Be}_y$ .

Author Heitur is employed by Micron, Inc., Wilmington, Del.; author Sentner is employed by NGK Metals Corp., Reading, PA 19612-3367.

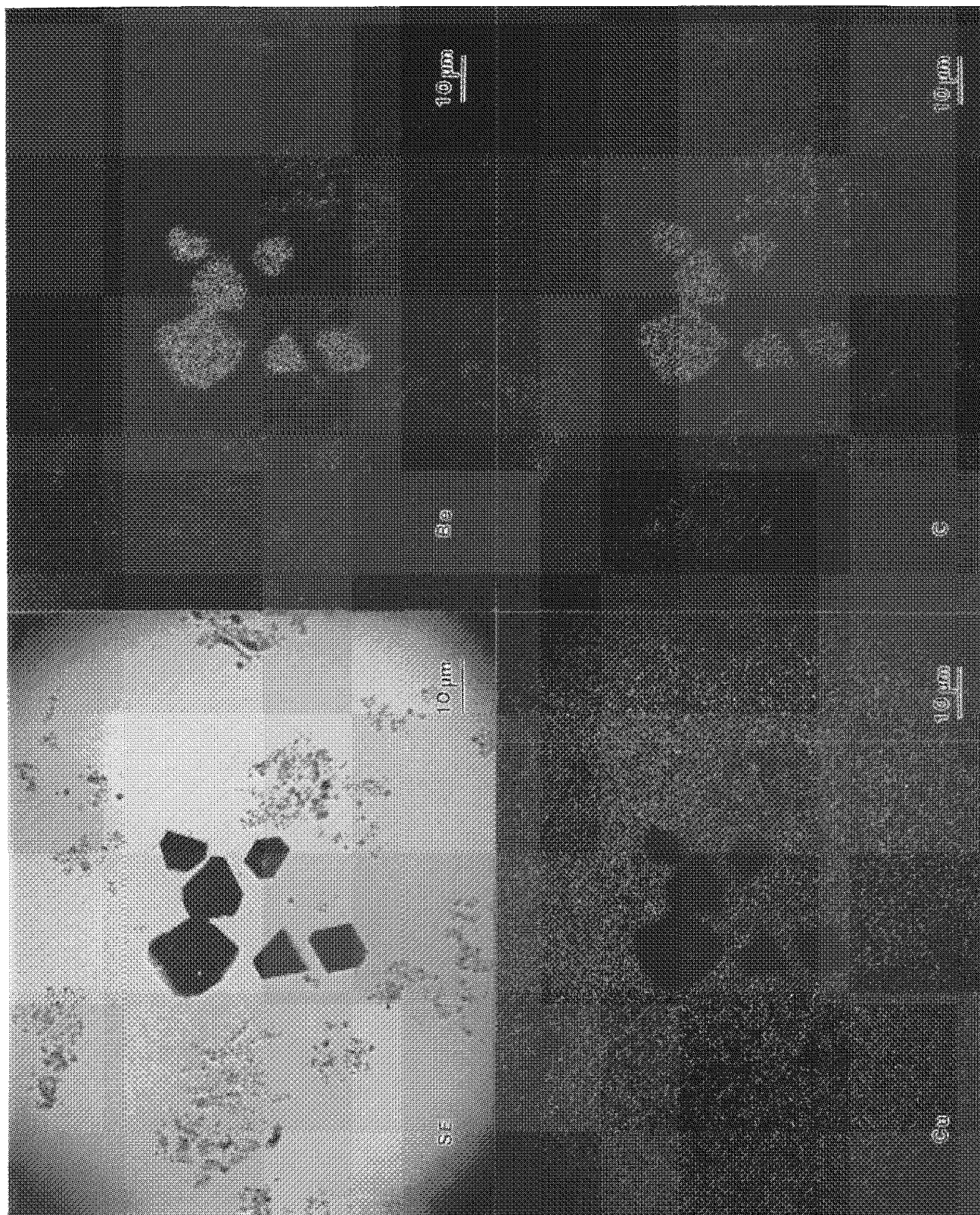


FIG. 2.--Secondary-electron image of precipitated beryllium carbide and corresponding beryllium, copper, and carbon elemental distribution images.

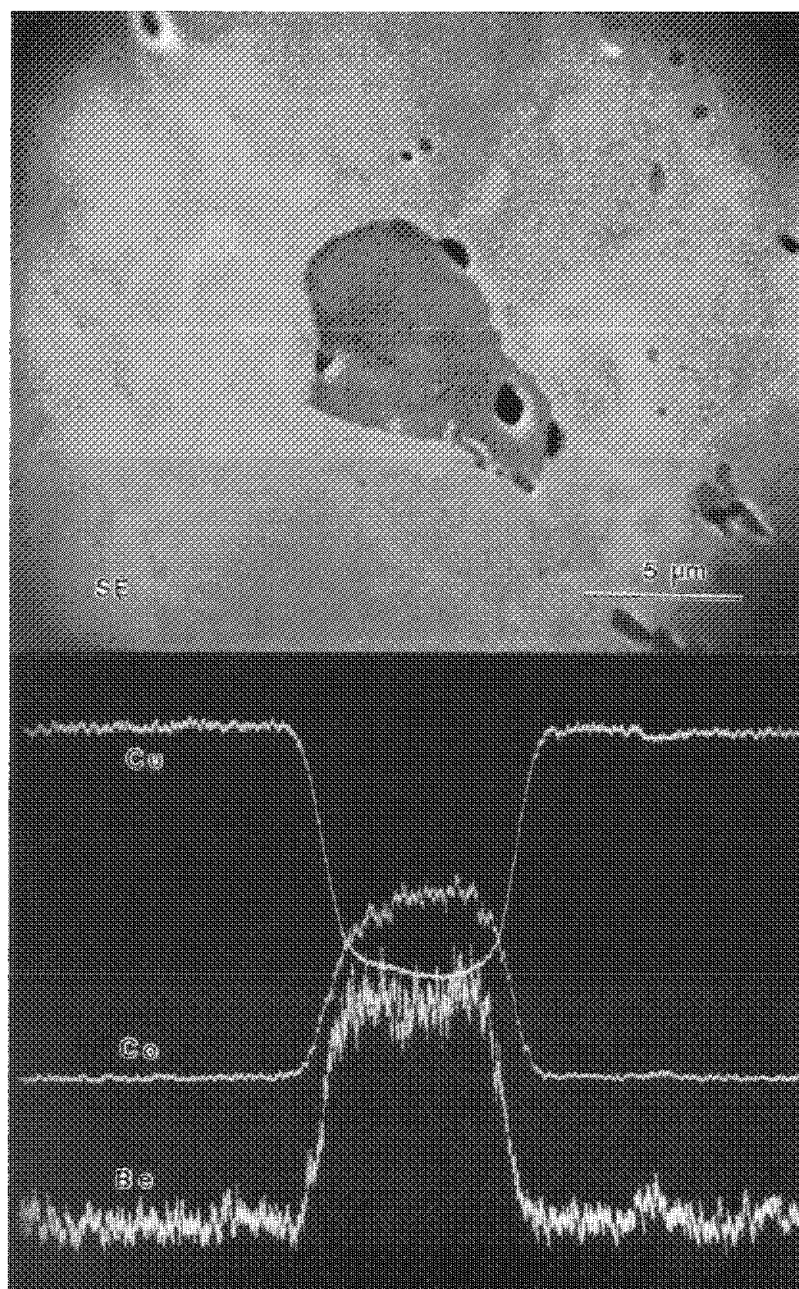


FIG. 3.--Secondary-electron image of precipitated cobalt beryllides (top) and corresponding elemental linescans for beryllium, cobalt, and copper.

TABLE 1.--Beryllium  $K\alpha$  peak and background intensities for beryllium metal, beryllium oxide, beryllium carbide, and copper-cobalt beryllide.

Be $K\alpha$ Intensities			
Specimen	Peak (counts/s)	Background (counts/s)	P/B
Be	5711.20	107.60	53.07
Be <sub>2</sub> C	1391.20	33.46	41.57
BeO	187.87	39.85	4.71
Co <sub>x</sub> Be <sub>y</sub>	110.28	12.38	8.91



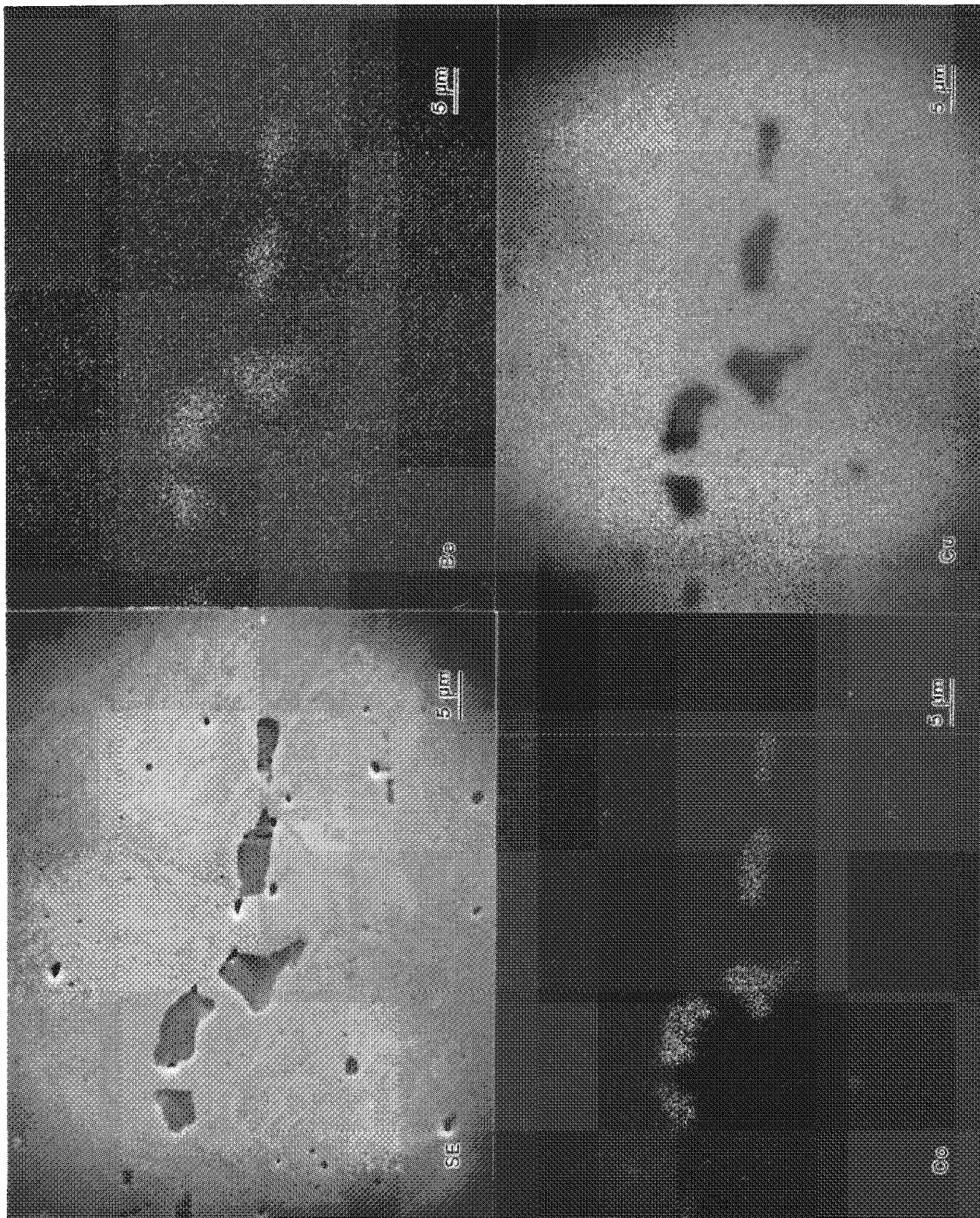


FIG. 4.--Secondary-electron image of precipitated cobalt beryllide and corresponding beryllium, copper, and cobalt elemental distribution images.

## HYDROGEN DETECTABILITY IN URANIUM BY U $N_{VI}O_{IV}$ PEAK SHIFT

K. A. Thompson and L. R. Walker

A distinct shift in the uranium  $N_{VI}O_{IV}$  x-ray line has been observed for several light elements (including hydrogen) bonded to uranium. Elements above beryllium in atomic number can be directly detected from their own x-ray emission lines, whereas hydrogen can only be detected indirectly by secondary effects. This development makes for a promising method of detecting hydrogen in materials with soft x-ray lines from orbitals that are involved in chemical bonding. Other effects, such as crystal orientation, purity of standards, and spectrometer reproducibility, also must be considered; each of these considerations will be discussed in more detail.

Of the many microanalytical techniques available, only a few can detect hydrogen: the nuclear microprobe,<sup>1</sup> the laser microprobe,<sup>2</sup> secondary ion mass spectroscopy (SIMS), and electron-stimulated desorption microscopy,<sup>3</sup> and possibly some others. Only the first method is easily quantitative, but it is also fairly expensive and not readily available. The other techniques are commercially available but have large ranges of elemental sensitivities with high matrix dependencies, which makes quantitative results more difficult to obtain. If these techniques are not available, another possible method to detect hydrogen is to study secondary effects, such as a reduced average atomic number in the backscattered electron signal from a scanning electron microscope, or (by use of an electron microprobe) observation of a possible soft-x-ray peak shift caused by chemical bonding.

Some commercially available backscattered electron detectors can be calibrated, but other contrast mechanisms may interfere with this calibration, such as grain orientation. Yet even with this difficulty, the backscattered-electron signal is very useful in finding areas of interest, which can then be studied in more detail. Other contrast mechanisms that may interfere include directional effects, such as blocking--especially a problem on rough surfaces--and magnetic contrast.

X-ray shifts have been noted previously for several elements, usually with atomic numbers below 20.<sup>4</sup> In most cases, these elements have only one primary x-ray emission line that involves electron orbitals directly influenced by chemical bonding. Boron, carbon, oxygen, and fluorine have all been studied as to the peak shape and shifts.<sup>5</sup> These investigations

were concerned with finding a method of quantification, complicated because of these effects. Aspect ratios were used to overcome this problem, but in many cases bring on other problems such as crystal orientation. Even with these added difficulties, quantitative results can be obtained with due care for details.

All the peak shifts mentioned thus far are small enough so that high-resolution spectrometers (WDS) with appropriate crystals with energy resolutions of the order of one eV must be used. In fact, if the main goal is to do quantitative elemental analysis, it may be more appropriate to use a crystal with moderate resolution in order to diffuse any peak shifts. A particularly good example is aluminum oxide, in which the calculated composition varied nearly 20% for a high-resolution crystal, but <5% for a moderate-resolution crystal.<sup>4</sup>

In addition to the light-element peak shifts, some heavier elements also exhibit similar phenomena. One such case is the Fe  $L\beta$  and  $L\gamma$  peak shifts that have been reported for  $Fe^{+3}$  and  $Fe^{+2}$  coordination species.<sup>6</sup> For this case, the peak shift allowed the coordination number for Fe to be determined for several compounds, some of them containing elements that would otherwise be difficult to quantify with the WDS. This type of example shows that one might detect elements that lack x-ray emission lines with energies that can be studied with the usual WDSs. By study of subtle differences in soft-x-ray shapes and peak positions of heavier elements as related to chemical bonding, more information may be available than otherwise possible. But this method also requires more care in choosing specific standards similar to the unknown to be studied; moreover, interference effects must also be considered.

### *Results and Discussion*

In the study of uranium and uranium alloys, it is not uncommon to find inclusions of uranium along with oxygen, nitrogen, and/or carbon, which can all be detected by the electron microprobe. By use of a Lead Stearate (LSD) crystal with a lattice spacing of 50 Å, all these elements are easily detectable, with a slight interference of the C  $K\alpha$  peak with the uranium  $N_{VI}O_{IV}$  peak, separated by 7 eV, which does not normally cause too much trouble. Other alloying materials can also be studied with relative ease, but a problem exists if elements below boron are present. These light elements may show up in the backscattered elec-

---

Authors Thompson and Walker are at the Plant Laboratory of the Oak Ridge Y-12 Plant, Martin Marietta Energy Systems, Inc., Oak Ridge, TN 37831, operated for the U.S. Department of Energy under contract DE-AC05-84OR21400.

tron image, but a question still exists whether this is a real compositional change, a crystal orientation effect, or some other artifact. A possible solution is to study the effects of these light elements on the uranium  $N_{VI}O_{IV}$  peak. As a direct application, the detectability of hydrogen was studied with regard to this U  $N_{VI}O_{IV}$  peak shift.

Figure 1 shows an U  $N_{VI}O_{IV}$  overlay for pure uranium and the hydride. These spectra were obtained in  $\sim 20$  min, with an electron-beam current of 200 nA at 10 kV, focused to a  $4\mu m^2$  spot. Carbon contamination from the electron beam caused a shoulder to build up on the low-energy side of the peak and was minimized by use of a cold finger and an air jet above the sample.

In addition to this precaution, an entire spectrum could be accumulated in  $< 2$  min with adequate statistics to find the centroid. The samples were freshly polished shortly before each study to insure a minimum amount of oxidation, verified by study of the O  $K\alpha$  x-ray line. The hydride peak was found to be shifted by 0.14 eV to the low-energy side, with a reproducibility of 0.02 eV for different samples and different areas on the sample. Since the peak position did not vary for different areas on the sample, crystal orientation must not be an important variable within the reproducibility of the spectrometer positioning.

Similar spectra for the oxides, carbides, and nitrides also showed the same shift of 0.14 eV toward lower energies (carbon C  $K\alpha$  interferes, so that a deconvolution procedure must be used to remove its contribution to the uranium  $N_{VI}O_{IV}$  transition). Unfortunately, no peak shape differences were noted among any of these compounds; therefore, the presence of each of the other elements and possibly other heavier elements as well must be checked before a shift can be definitely ascribed to hydrogen interaction. The elements with Z numbers between hydrogen and carbon were not investigated at this time, and their effects are not known; thus, their lack of presence must be verified by some other technique (bulk analysis, possibly) before hydrogen presence

can be determined by the peak-shift method.

Other effects besides chemical bonding were observed to cause an apparent peak shift. Room temperature changes caused the peak to shift  $\sim 0.05$  eV in an overnight run. (Evidently the temperature drops a couple of degrees overnight, an effect normally handled by recalibration.) Changing from the LSD crystal to some other crystal and then returning to the original also changes the apparent peak position by as much as 0.1 eV. Moving the electron beam away from the spectrometer plane of focus also causes a peak shift; therefore, an inclined spectrometer was used to minimize height restrictions, and the beam was aligned optically to keep this effect below 0.01 eV. All these effects could be minimized with due care, but they show the importance of studying the system completely and finding any other possible causes for a peak shift before attributing the shift to a chemical effect.

#### References

1. C. J. F. Legge, "Proton microscopy," *Microbeam Analysis--1986*, 170; F. Xiong, F. Rauch, C. Shu, R. P. Livi, and T. A. Tombrello, "Comparison of several nuclear reactions techniques for hydrogen depth profiling in solids," *ibid.*, 85.
2. V. L. Koller, A. Harris, and E. R. Wallach, "Light-element analysis by LIMA," *ibid.*, 467.
3. G. Gillen and P. Williams, "Electron-stimulated desorption microscopy," *ibid.*, 109.
4. K. F. J. Heinrich, *Electron Beam X-ray Microanalysis*, New York: Van Nostrand Reinhold, 1981, 69-71, 351-352.
5. G. F. Bastin and J. J. M. Heijligers, "Quantitative electron-probe microanalysis of very light elements," *Microbeam Analysis--1985*, 1: G. F. Bastin and J. J. M. Heijligers, "Quantitative electron-probe microanalysis of boron in some binary borides," *Microbeam Analysis--1986*, 285; T. N. Solberg, "Fluorine electron microprobe analysis: Variations of x-ray peak shape," *Microbeam Analysis--1982*, 148.
6. A. L. Albe and A. A. Chodos, *Amer. Mineralogist* 55: 491, 1970.

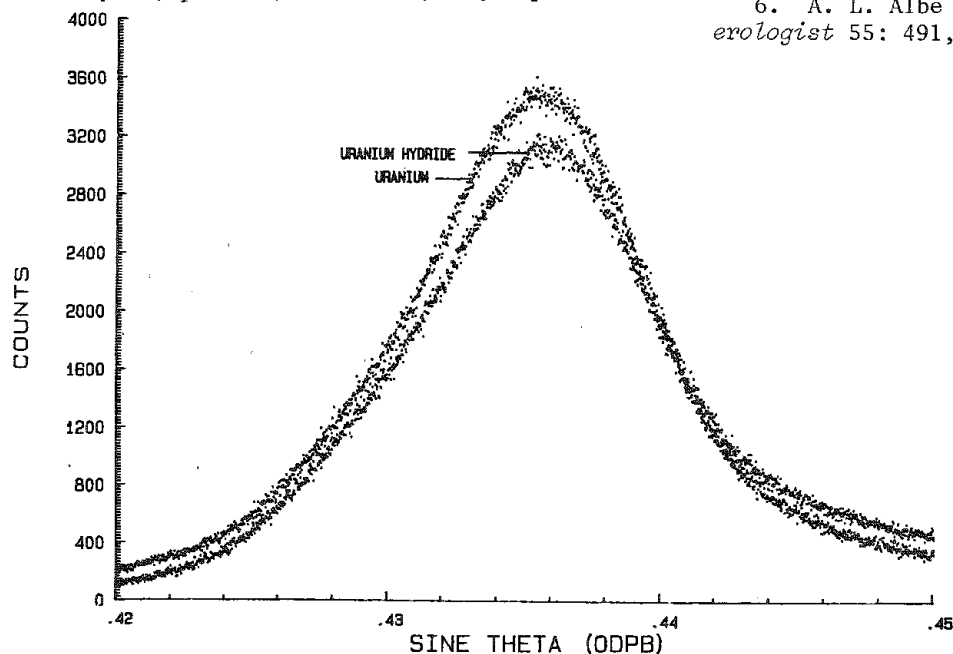


FIG. 1.--Effect of hydrogen bonding to uranium  $N_{VI}O_{IV}$ .

### 3A. SEM: Low Voltage

#### HIGH-RESOLUTION LOW-VOLTAGE SCANNING ELECTRON MICROSCOPY OF UNCOATED BIOLOGICAL SPECIMENS FIXED BY THE FREEZE SUBSTITUTION FIXATION METHOD

Masako Osumi and Takashi Nagatani

Previously we employed a high accelerating voltage (HV) (20–25 kV) for scanning electron microscopy (SEM) in order to obtain as high resolution as possible.<sup>1,2</sup> SEM usually requires coating of the specimen because biological specimens have no conductivity. We have tried a variety of methods to achieve the thinnest and finest coating possible to minimize granularity of the metal. One of the methods was the production of a 2nm-thick platinum-carbon film by electron beam evaporation.<sup>3</sup> However, we concluded that HVSEM images of these specimens present a problem: the specimen is artificially coated no matter how thin or fine the coating film is, or how high the image resolution is. To avoid this problem, low accelerating voltage (LV) was employed because the electron beam will not penetrate deeply into a biological specimen at an accelerating voltage lower than 3 kV. Therefore, an LVSEM image will represent a more accurate surface profile than an HV one does.

In this study, high-fidelity SEM images of uncoated biological specimens were produced with the SEM operating below 2 kV. Fortunately, we have succeeded in the freeze substitution (FS) fixation of yeast cells. It has enabled both ultrathin sectioning and SEM observation,<sup>4–6</sup> because the specimens obtained by FS fixation have good conductivity. After this treatment the yeast cells were surveyed with an ultrahigh-resolution that SEM comprises a cold-cathode field-emission gun and an in-lens system for specimens at 0.6–2 kV. The images were compared with those obtained by conventional HVSEM and by transmission electron microscopy (TEM) of ultrathin-sectioned specimens. Thus, we obtained more dynamical three-dimensional images than those of freeze fracturing of yeast cells.<sup>7,8</sup>

#### Experimental

Cells of the hydrocarbon-utilizing yeast *Candida tropicalis*, the methanol-utilizing yeast *C. boidinii*, their fusants, and *Saccharomyces cerevisiae* were used. The cells were sandwiched between two copper platelets (grids), which were then plunged into liquid nitrogen cooled Freon 23 as rapidly as possible and transferred to liquid nitrogen. Subsequently, the two copper platelets were separated and soaked in freeze substitution fluid, 4% osmium tetroxide in absolute acetone, at 80 °C for 48 h. After a gradual return to room temperature, the specimens (on one grid) were dehydrated, subjected to critical-point drying, and observed with a Hitachi ultrahigh-resolution FESEM (the S-900) at 0.6–2 kV. The other grid was prepared for the TEM observa-

tion. Thus, one development in our FS fixation method is that specimens attached to one copper disk (or grid) can be used for SEM and those on the other grid can be used for TEM (Fig. 1).

The fine structure of uncoated yeast cells was found to be preserved in an extremely good condition within an accelerating voltage of 0.6–1.2 kV when they were examined with the S-800 SEM.<sup>9</sup> Although the images formed at an accelerating voltage of 0.8–0.9 kV accurately represented the structure, a voltage between 1.0 and 1.2 kV can be considered to offer optimum image quality. In the ultrahigh-resolution S-900 SEM, the cells show higher resolution and a higher-fidelity image<sup>10</sup> (Fig. 2a). The outermost cell surface can be seen to consist of fine filaments, which present quite a different image from that of the coated cells and their HVSEM images.<sup>10</sup> This cell is growing in methanol as the sole carbon source. The nucleus N, mitochondrion M, and microbody Mb are clearly seen in the cytoplasm of the fractured cell. In addition, the ribosomes (indicated by the arrow) are identified. These images correspond to those of intracellular organelles in the TEM image (Fig. 2b).

Figure 3 shows images of the yeast cell surface. In the PF (Fig. 3a) and EF (Fig. 3b) faces of the cell membrane, membrane invagination (CMI) can be observed. Furthermore, as a gratifying result, intramembranous particles (IMP) were detected. In the higher-magnification image (Fig. 4), there are many particles distributed homogeneously. The diameter of these intramembranous particles is not homogeneous; the smallest one is about 10 nm and the largest about 20 nm. The particles present a more three-dimensional image than is seen in freeze replica images.<sup>7</sup> We believe this is the first identification of intramembranous particles by SEM. These images correspond to freeze replica images. However, the number of these intramembranous particles in the EF face (Fig. 4b) appeared to be the same as those of the particles in the PF face (Fig. 4a), which usually has more than the EF face.

Figures 4(c) and (d) are the images of the PF face of the cell membrane treated with the antifungal agents rimoprogin and sulconazole nitrate, respectively. The images are quite different from that of the normal cell membrane (Fig. 4a).

#### Conclusion

High fidelity SEM images were produced by application of low accelerating voltage to uncoated biological specimens fixed by the freeze substitution method. In addition to several intracellular organelles, free ribosomes in the cytoplasm and intramembranous particles of the cell membrane were identified.

The authors are at the Department of Biology, Japan Women's University, and Application Laboratory, Naka Works, Hitachi Ltd., Japan.



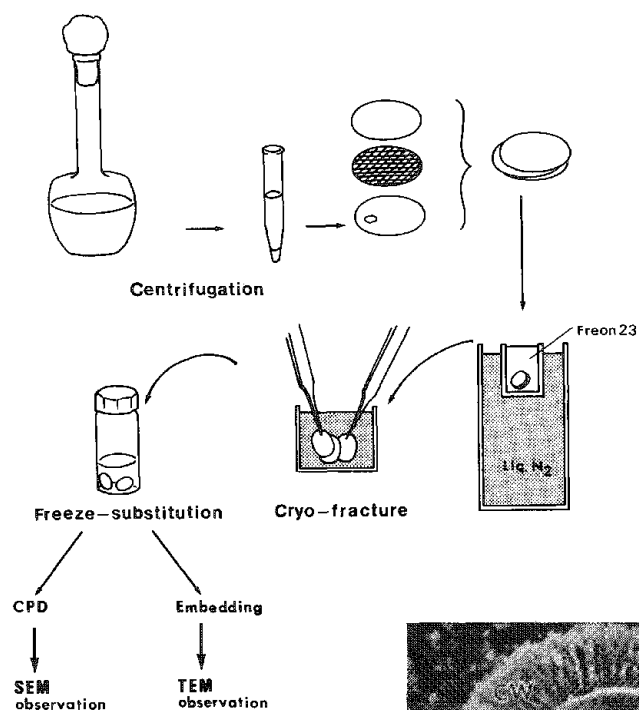


FIG. 1.--Procedure of freeze-substitution fixation method for SEM and TEM observations. (CPD: critical-point drying.)

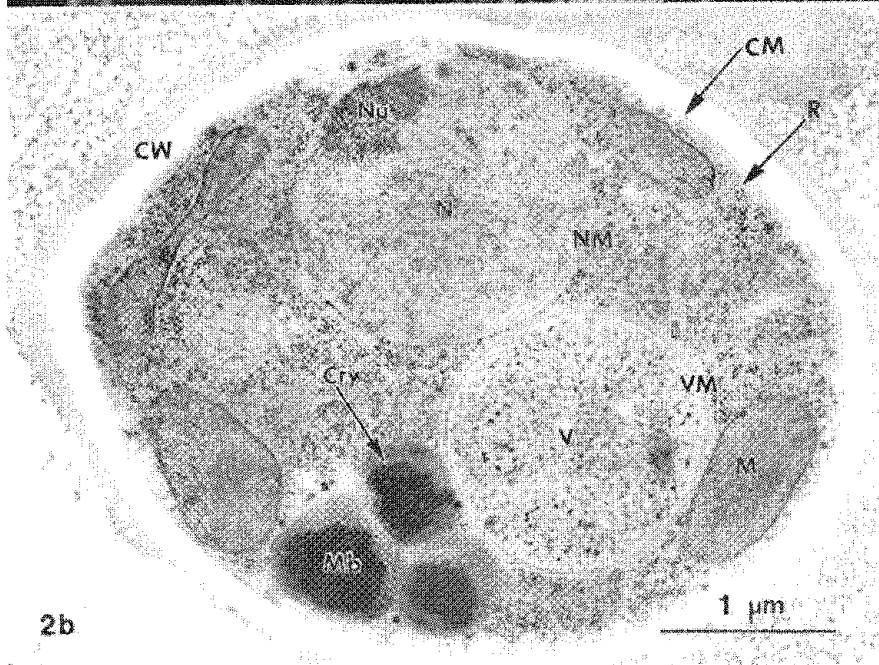
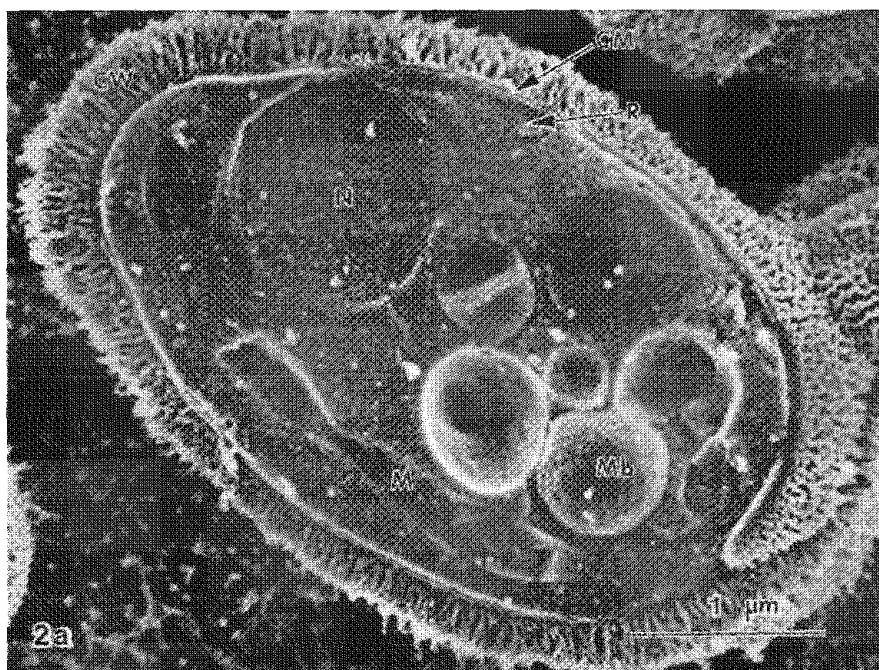


FIG. 2.--(a) SEM and (b) TEM images of fusant FUS-5 and *Candida boidinii* cells, respectively, grown in methanol. Cells were fixed by freeze-substitution method. (a) 25 800 $\times$ , (b) 23 000 $\times$ .



The SEM image of fractured yeasts revealed a more undulated topography than the TEM images obtained by freeze-replica. With this new information the previous model of a yeast cell<sup>11</sup> was modified as shown in Fig. 5.<sup>4</sup>

Needless to say, optimum freezing is an essential condition. Future subjects for study include (1) development of a better method of preparing enhanced conductivity of biological specimens and (2) achievement of higher resolution at LV. Then we should be able to identify several organelles in the cell by SEM, such as ribosomes attached to the nuclear membrane, microtubules in the nucleus, the Golgi apparatus, and actin filaments.

#### Abbreviations

BA	Bud scar	M	Mitochondrion
CM	Cell membrane	Mb	Microbody
CMI	Invagination of cell membrane	MT	Microtubule
Cry	Crystalloid	N	Nucleus
CW	Cell wall	NE	Nuclear envelope
rER	Rough endoplasmic reticulum	NP	Nuclear pore
sER	Smooth endoplasmic reticulum	Nu	Nucleolus
F	Filament	P	Polyphosphate
G	Golgi apparatus	R	Ribosome
Gly	Glycogen	SPB	Spindle pole body
L	Lipid	V	Vacuole
		Ves	Vesicle
		VM	Vacuolar membrane

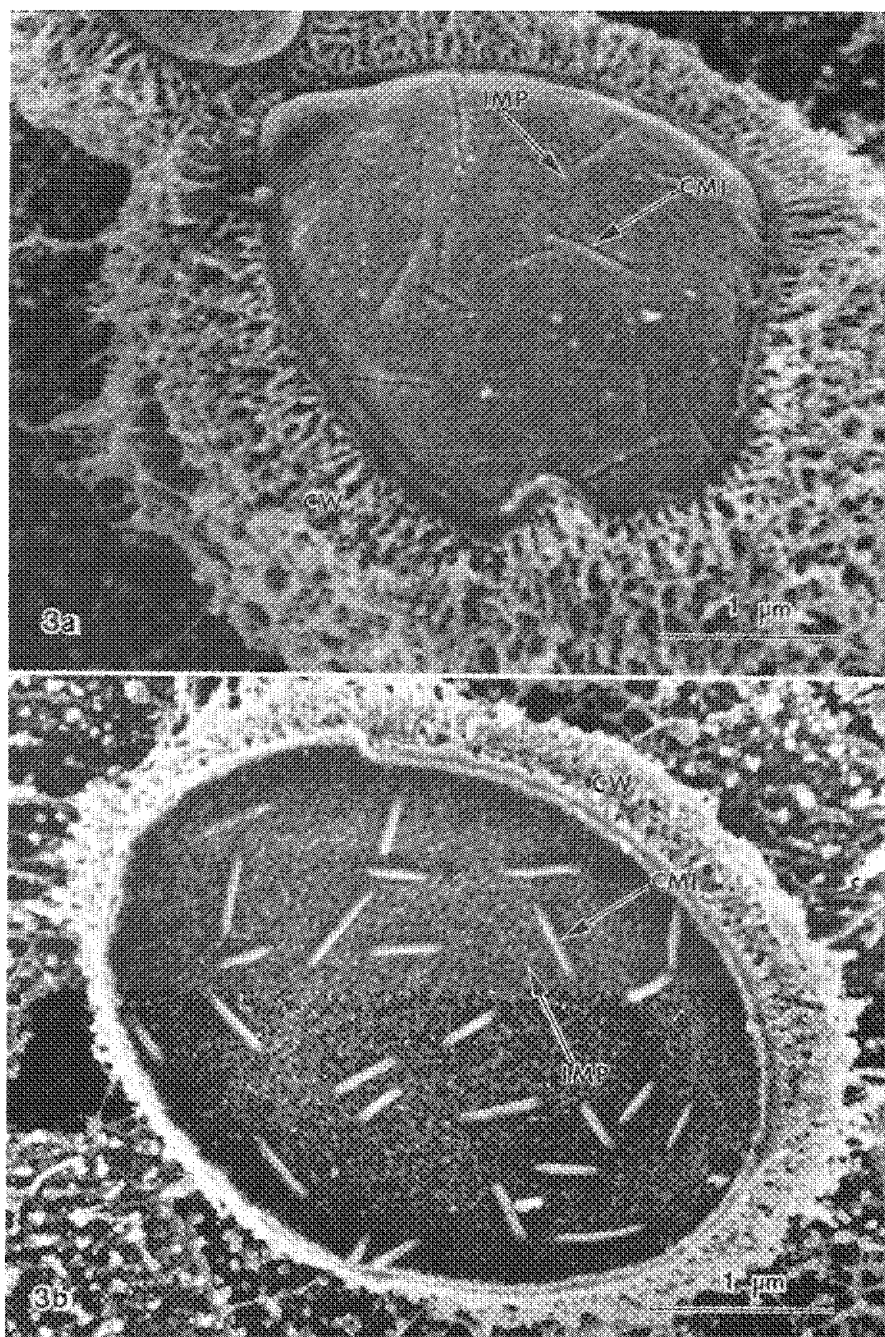


FIG. 3.--(a) PF and (b) EF faces of cell membrane of whole cells (same specimen as in Fig. 2a).  
24 500x.

## References

1. Masako Osumi et al., "Ultrastructure of hydrocarbon utilizing yeast cells," *Proc. 6th Intern. Congr. Electron Microsc.* 1974, (II), 578-579.
2. Masako Osumi and Saki Torigata, "Surface structure of microbodies isolated from yeast cells," *SEM/1977*, II, 617-622.
3. Masako Osumi et al., "Three-dimensional observation of prolamellar bodies in etio-plasts of squash *Cucurbita moschata*," *SEM/1984 I*, 11-119.
4. Misuzu Baba and Masako Osumi, "Transmission and scanning electron microscopic examination of intracellular organelles in freeze-substituted *Loeckera* and *Saccharomyces* yeast cells," *J. Electron Microscopy Technique* 5: 249-261, 1987.
5. Misuzu Baba and Masako Osumi, "Freeze-substitution method for the observation of the ultrastructure of yeast cells," *J. Electron Microsc.* 33: 303, 1984.
6. Misuzu Baba and Masako Osumi, "An application of the freeze-substitution fixation method for an observation of yeast intracellular structures," *J. Electron Microsc.* 34: 222, 1985.
7. Masako Osumi, *Anatomy of Yeast Cells*, Naohiko Yanagishima, Yasuharu Oshima, and

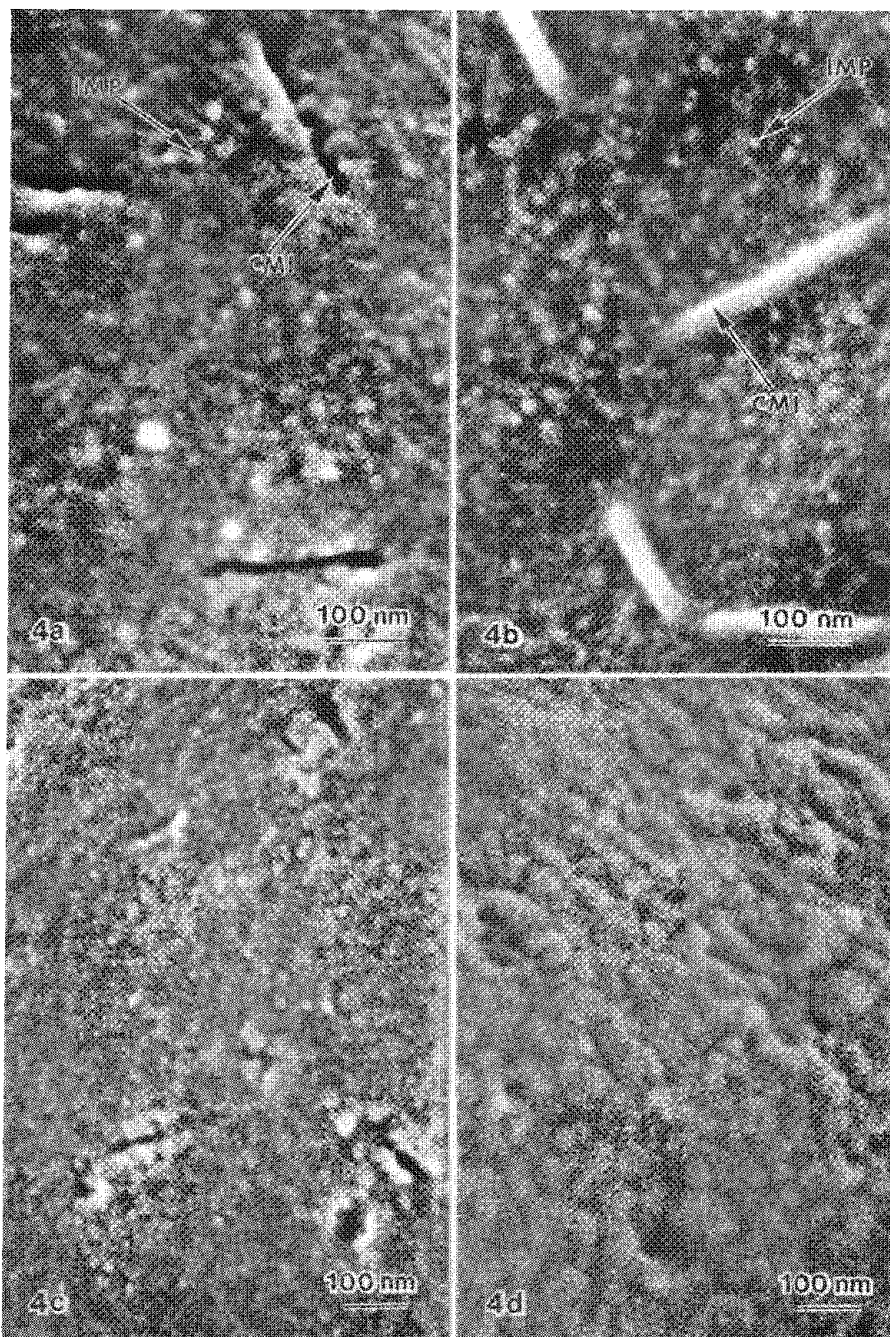


FIG. 4.--Higher-magnification images of cell membrane. (a) PF and (b) EF faces of cell membrane of untreated control fusant cell. Freeze-substituted fractured PF faces of cells treated with (c) rimoprogin and (d) sulconazole nitrate, respectively. (a) and (b) 109 000 $\times$ , (c) and (d) 83 000 $\times$ .

Masako Osumi, Eds., Tokyo: Kodansha Scientific, 1981, 4-16.

8. Misuzu Nagano et al., "Filamentous structure in yeast mitochondria by freeze-etching of replica combined with rapid freezing," *J. Electron Microsc.* 31: 268-272, 1982.

9. Masako Osumi et al., "Low accelerating voltage and high fidelity observation of yeast

cells with high resolution scanning electron microscope," *Biomedical SEM* 14: 47-51, 1985.

10. Masako Osumi, "High resolution, low accelerating voltage scanning electron microscopy of uncoated cells by applying the freeze substitution fixation method," *Proc. 11th Intern. Congr. Electron Microsc.* 1986, 2089-2092.

11. Masako Osumi, Ref. 7, p. 5.

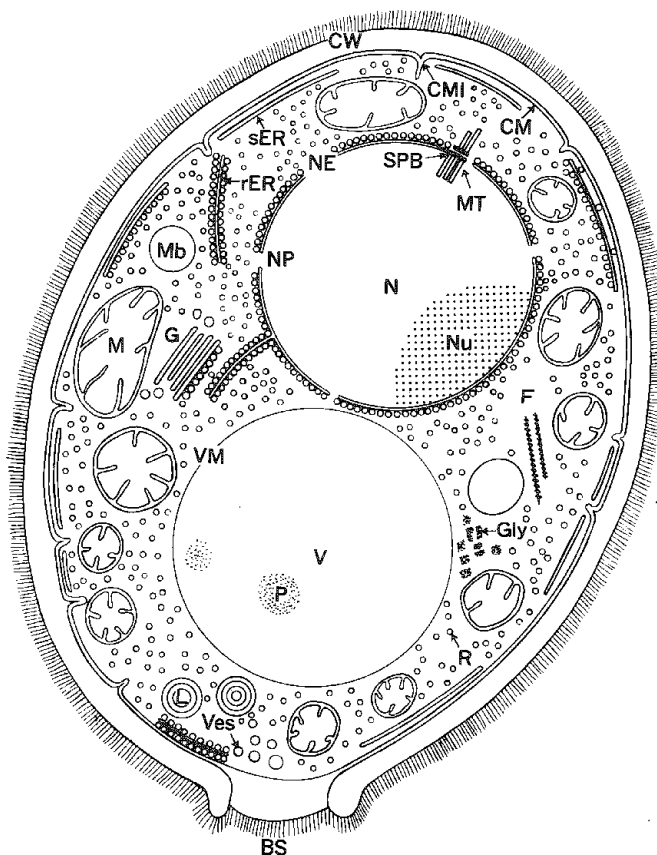


FIG. 5.--Ultrastructure model of yeast cell.<sup>4</sup>

## LOW-LOSS ELECTRON IMAGES OF UNCOATED NONCONDUCTING SAMPLES IN THE SCANNING ELECTRON MICROSCOPE

Oliver C. Wells

The way in which nonconducting samples become charged under electron irradiation in the scanning electron microscope (SEM) was investigated theoretically and practically by Knoll.<sup>1</sup> He showed that one could essentially eliminate charging by operating with a beam energy  $E_0$  at the "second crossover" potential, where the combined secondary electron (SE) and backscattered electron (BSE) coefficients is unity. Thornley and Cartz used this idea to obtain SE images from uncoated ceramics in the SEM.<sup>2</sup> At the present time, this method is used routinely for the examination of uncoated microelectronic samples such as patterns in photoresist.

We can also reduce charging artifacts by working with the BSE image.<sup>3</sup> This method is successful when the charging is serious enough to affect the SE, but not so bad as either to deflect the incident beam or to affect the BSE. During these early investigations, the BSE were collected with a scintillator-light-pipe-photomultiplier system in which an aluminum scintillator is brought close to the specimen to subtend a large collecting solid angle.<sup>3-8</sup>

In one version of the BSE image, a retarding-field energy filter rejects electrons that have lost more than a chosen energy  $E_{\text{loss}}$  to give a low-loss electron (LLE) image. This scheme, which is based on an idea proposed by McMullan<sup>9</sup> and which was demonstrated by Wells,<sup>10</sup> works well in showing topographic and electron channeling contrast, and has a shallow information depth. The LLE image gives clear images from a nonconducting sample such as uncoated photoresist under conditions when the SE image shows serious charging artifacts.<sup>11</sup> A bibliography on LLE imaging techniques has been published by Wells.<sup>12</sup>

The energy-filtering detector used in this work is shown in Fig. 1. The specimen is mounted at a glancing angle of  $30^\circ$  to the incident electron beam. The retarding field is accurately aligned with the scattered electrons by concentric spherical grids. Electrons that pass through the second (filter) grid are collected by a scintillator-lightpipe-photomultiplier collector system.

The energy resolution of an energy filter becomes worse as the acceptance solid angle is increased. With the present detector, the acceptance angle is a cone with semi-angle  $30^\circ$  at an angle of  $50^\circ$  from the axis of the SEM. This arrangement is needed to collect the LLE signal. Palmberg<sup>13</sup> improved the voltage resolution of a retarding-field energy filter with a similar acceptance solid angle by using two filter grids connected together, which was also done here. Palmberg obtained a voltage resolution of 2 eV with  $E_0 = 1$  keV. There is therefore no fundamental problem in designing

a detector with an energy resolution of 0.2%. Thus, if  $E_0 = 5$  keV, the resolution of the energy filter can in principle be as good as 10 eV. This detector would reject electrons that have suffered a single inelastic event. (With the present unit, the voltage resolution is  $\sim 1\%$ .)

In the present work, SE images were obtained with the usual SEM detector. In earlier work, SE were collected by the LLE detector with both grids at +200 V and the scintillator at +12 kV. The charge potential on the specimen was measured with the LLE detector used as an energy filter.

For LLE work, the input grid is grounded. The filter grid is at typically +200 V relative to the SEM cathode. The scintillator is at +12 kV relative to the filter grid. This second condition insures that the LLE (which emerge with a low energy through the filter grid) are collected over the entire mesh area, and that they enter the scintillator with a high enough energy for noise-free detection.

The LLE detector was mounted on the left of the specimen chamber of a Cambridge Instruments S-250 MK III. The specimen was tilted to the left so as to face toward the collector. An ion gauge was mounted (with a light trap) onto the specimen chamber. The ion-gauge control unit was set to cut off the power to the LLE detector supplies if the vacuum rose above  $5 \times 10^{-6}$  Torr. The scintillator potential was +12 kV minus the accelerating potential; thus, if  $E_0 = 5$  keV, a scintillator potential of +7 kV is appropriate.

The uncoated photoresist samples shown in Figs. 2, 3, 5, and 6 were provided by M. Hatzakis, who writes: "The pattern was exposed in 3 $\mu$ m-thick photoresist by contact printing using a Hg arc source. The photoresist was AZ-1350J and the developer was AZ developer. These are registered trademarks of the Azoplate Division of American Hoechst Corp., Somerville, NJ 08876. The material was supplied by Shipley Co., Newton, Mass." The photoresist shown in Fig. 4 was from a reject sample.

The LLE micrographs shown here were all obtained with a glancing angle of incidence of  $30^\circ$  and with  $E_{\text{loss}} = 200$  eV. The recording time was 30 s for the low-magnification micrographs, and 60 s for the high. (A single slow scan for recording the image is satisfactory for a sample such as photoresist that does not charge very badly. For more serious charging, a repetitive fast scan with the image integrated by an image store will probably be needed. This problem is discussed below.)

The beam energy  $E_0$  while Figs 2 and 3 were recorded was 2.5 keV, which is above the second crossover and thus gives rise to specimen charging that seriously degrades the SE image (Fig. 2). An LLE image from the same sample does not show any charging (Fig. 3). The charge potential was measured with the detector operated as an energy filter for SE, and was

The author is at the IBM Thomas J. Watson Research Center, Box 218, Yorktown Heights, NY 10598.

found to be less than 10 V. The charging artifacts in the SE image can therefore be attributed to the sensitivity of this type of image to potentials on the specimen, which is much less serious if the faster electrons are collected.

The LLE image (from a different uncoated photoresist sample) with  $E_0 = 1.6$  keV shows topographic details much more clearly than is the case for the SE image (Fig. 4). (This comparison pair also shows that parts of the surface that face away from the detector cannot be seen in the LLE image.)

If  $E_0 = 10$  keV, the charging with the SE image becomes so bad that it is impossible to record a proper image with a 60s scan (Fig. 5a). The LLE image is still satisfactory (Fig. 5b). Images taken from the developed edge of the photoresist show that the LLE image is better than the SE image for showing surface details under these conditions (Fig. 6).

Preliminary experiments with more massive nonconducting samples have run into difficulties caused by the deflection of the incident electron beam. It is believed that this deflection is caused by the use of a slow recording scan rate; preparations are being made to record images with a faster scan rate and an image store. This work is continuing.

#### References

1. M. Knoll, "Aufladenpotential und Sekundäremission elektronenbestrahlter Körper," *Z. tech. Phys.* 11: 467-475, 1935.
2. R. F. M. Thornley and L. Cartz, "Direct examination of ceramic surfaces with the scanning electron microscope," *J. Am. Ceramic Soc.* 45: 425-428, 1962.
3. O. C. Wells, *The Construction of a Scanning Electron Microscope and Its Application to the Study of Fibres*, Ph.D. dissertation, Cambridge University, 1957.
4. K. C. A. Smith, *The Scanning Electron Microscope and Its Fields of Application*, Ph.D. dissertation, Cambridge University, 1956.
5. T. E. Everhart, *Contrast Formation in the Scanning Electron Microscope*, Ph.D. dissertation, Cambridge University, 1958.
6. T. E. Everhart, O. C. Wells, and C. W. Oatley, "Factors affecting contrast and resolution in the scanning electron microscope," *J. Electronics Control* 7: 97-111, 1959.
7. O. C. Wells, "New contrast mechanism for scanning electron microscope," *Appl. Phys. Lett.* 16: 151-153, 1970.
8. T. E. Everhart and R. F. M. Thornley, "Wide-band detector for micro-microampere low-energy electron currents," *J. Sci. Instr.* 37: 246-248, 1960.
9. D. McMullan, "An improved scanning electron microscope for opaque specimens," *Proc. IEE* 100(Pt. II): 245-259, 1953.
10. O. C. Wells, "Low-loss image for scanning electron microscope," *Appl. Phys. Lett.* 19: 232-235, 1971.
11. O. C. Wells, "Low-loss electron images of uncoated photoresist in the scanning electron microscope," *Appl. Phys. Lett.* 49: 764-766, 1986.
12. O. C. Wells, "Low-loss electron image in the SEM," *Proc. Ann. Meet. EMSA* 41: 2-5, 1983.
13. P. W. Palmberg, "Optimization of Auger electron spectroscopy in LEED systems," *Appl. Phys. Lett.* 13: 183-185, 1968.

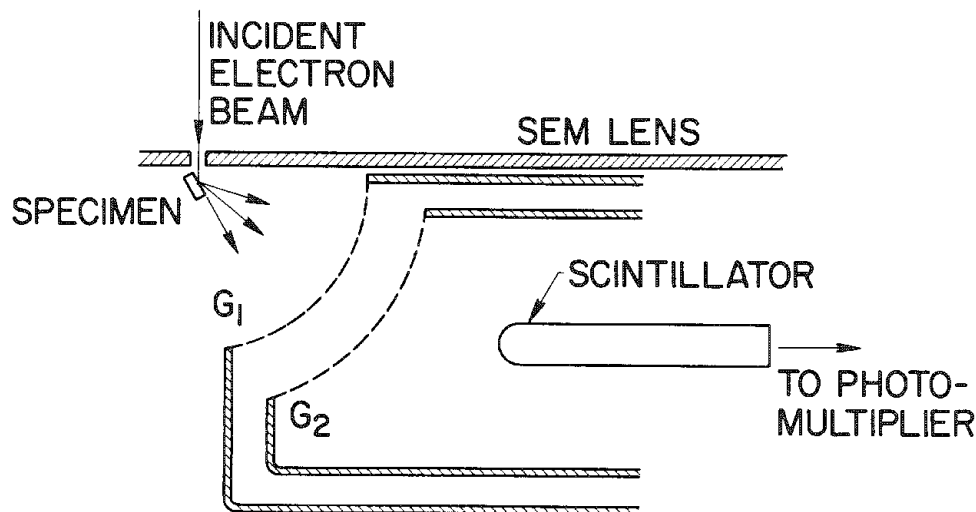


FIG. 1.--Energy-filtering low-loss electron detector.<sup>10</sup>



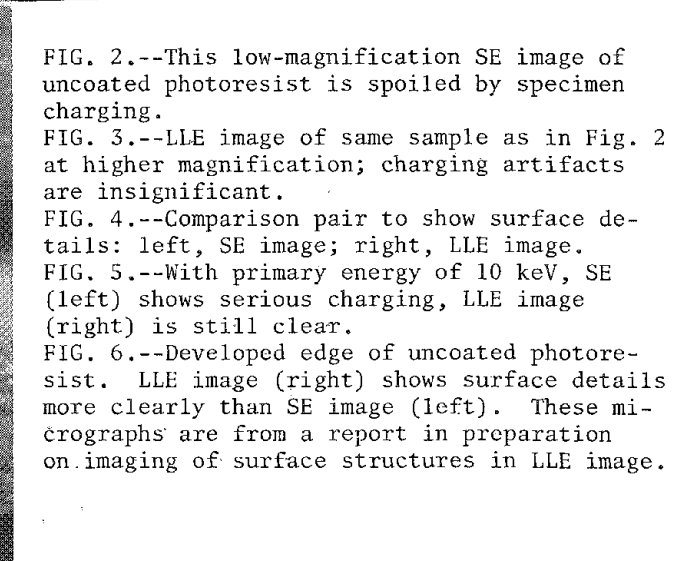
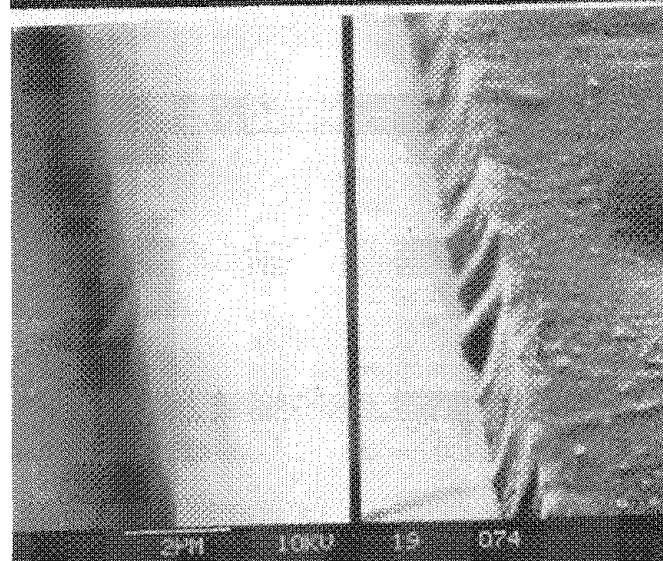
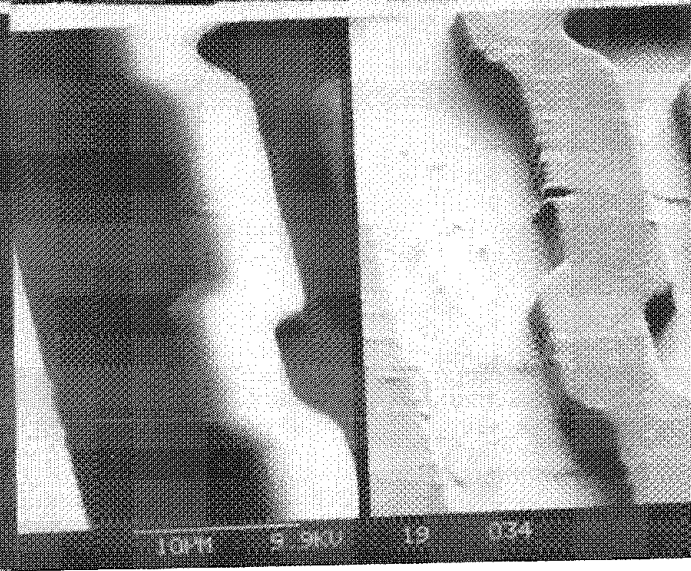
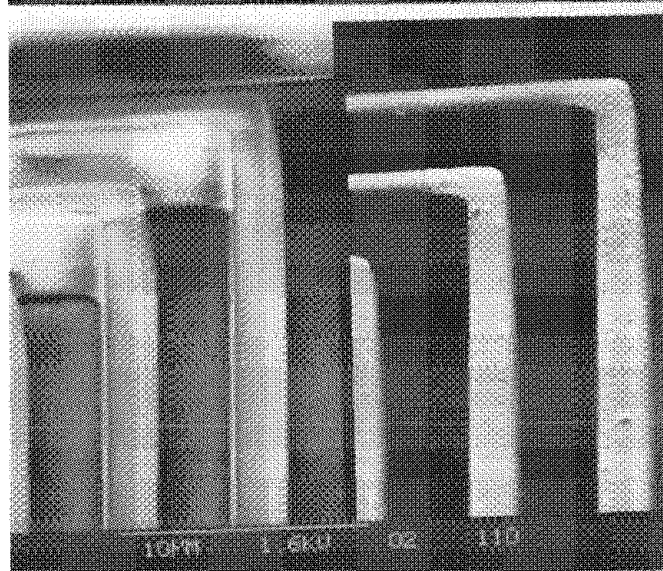
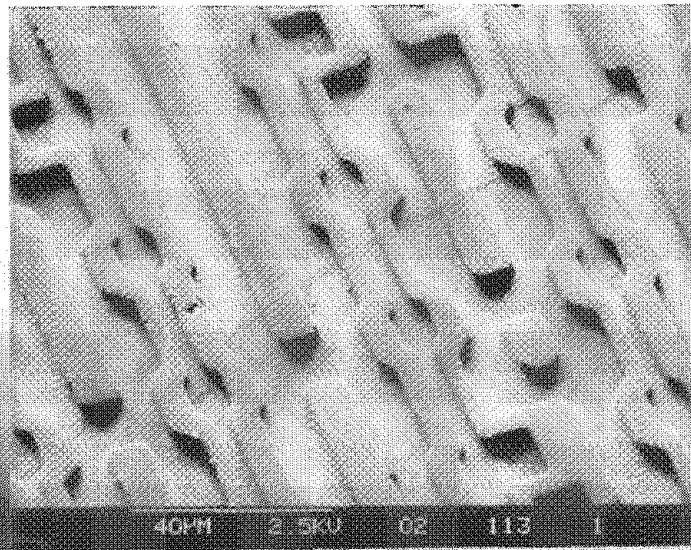
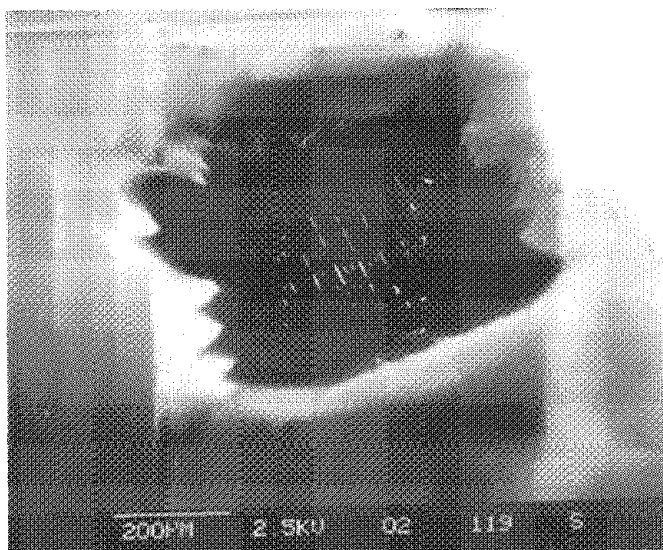


FIG. 2.--This low-magnification SE image of uncoated photoresist is spoiled by specimen charging.

FIG. 3.--LLE image of same sample as in Fig. 2 at higher magnification; charging artifacts are insignificant.

FIG. 4.--Comparison pair to show surface details: left, SE image; right, LLE image.

FIG. 5.--With primary energy of 10 keV, SE (left) shows serious charging, LLE image (right) is still clear.

FIG. 6.--Developed edge of uncoated photoresist. LLE image (right) shows surface details more clearly than SE image (left). These micrographs are from a report in preparation on imaging of surface structures in LLE image.

## VOLTAGE CONTRAST MECHANISM OF SEM IMAGES OVER PASSIVATED DEVICES

N. Sugiyama, S. Ikeda, and Y. Uchikawa

Inspection of microelectronic devices by a scanning electron microscope (SEM) is very promising. The SEM provides a high spatial resolution with a large depth of focus, which results in a wide area of view at a time. These characteristics are very favorable for device inspection. Furthermore, the SEM can visualize a voltage profile of electrodes under passivation as a contrast in the secondary electron (SE) images of the passivated devices. The contrast is often referred to as voltage contrast, since it has been believed that the contrast originates from local variation of the SE signal caused by the voltage distribution over the passivation surface. The contrast undergoes different variations with observation depending on the imaging conditions, which has made a consistent interpretation of the contrast mechanism difficult. In the present paper, we first review our previous work on SE images of the passivation surface<sup>1,2</sup> and then describe an experiment to investigate the contrast mechanism. We also show that the result obtained can be explained by the physical model we have proposed previously.

### *Previous Work*

We first summarize our previous work on the contrast mechanism.

1. A conventional, nonenergy-selective (Everhart-Thornley) SE detector is used.
2. We can classify the contrast variations induced by electron-beam (EB) irradiation over the passivation into two qualitatively distinguishable processes: reversible or irreversible.
3. We discovered that at a low primary electron energy ( $E_p = 1$  keV) the voltage contrast over the passivation undergoes a regular course of variation (Fig. 1). That is, when a different voltage is applied to electrodes, the voltage contrast appears in the first frame of imaging and disappears gradually as the imaging advances shown in the 3rd (b) and 10th (c) frames. The voltage contrast does not recover as long as the EB irradiation continues. But as soon as the applied voltages are turned off, the contrast of polarities opposite to that in (a) appears as in the first frame (d). This contrast also disappears as the imaging continues through the 3rd (e) and the 10th (f) frames. One can reproducibly repeat the whole process of the contrast variation by turning on and off the applied voltages to the electrodes.
4. The micrograph of Fig. 2 shows a typi-

Authors Sugiyama and Uchikawa are at the Faculty of Engineering, Nagoya University, Furo-cho, Chikusa, Nagoya, 464 Japan; author Ikeda is at the Faculty of Science and Technology, Meijo University, Yagoto-urayama, Tempaku, Nagoya, 468 Japan.

cal frame of the irreversible imaging process of contrast variation observed at  $E_p = 2$  keV. As shown, bright negative charge clouds swarm along with the EB irradiation. This process is irreversible in the sense that the contrast never disappears throughout the observation and does not change its polarity even when the applied voltages to the electrodes are turned on or off.

5. One can clearly distinguish the two processes of contrast variations by observing whether the contrast over the electrodes reverses its polarity when the applied voltages are turned on and off.

6. There is a clear threshold of imaging conditions  $E_p$  and  $\phi_p$ , the incident angle of primaries with respect to the surface normal of sample, between the two processes of the contrast variations (Table 1). The angles  $\phi_p$  listed in the table are the threshold values below which the irreversible process takes place for each value of  $E_p$ . We found that the product  $E_p \cos^2 \phi_p$  ( $\equiv E_n$ ) becomes constant,  $E_c \approx 2$  keV, at the threshold imaging conditions and does not depend on the other parameters of imaging such as magnification, primary beam current  $I_p$ , and scanning time  $t_s$ .

7.  $E_n$  denotes the component of the velocity of primaries (in eV) normal to the specimen surface and should be related to the normal penetration depth of the primaries from the specimen surface. Therefore, it is quite reasonable to consider that the above results indicate that the irreversible contrast variation (i.e., negative charge accumulation) takes place when the primaries penetrate beyond a definite depth from the surface.

8. It is hardly possible to explain these experimental results by the effect of the surface potential distribution resulting in the local variation of the emission yield<sup>3</sup> and/or the signal detection efficiency<sup>4</sup> of the secondaries.

9. We postulated the existence of an anomalous surface layer within the passivation (Fig. 3), and explained that the contrast arises from the internal electric field produced across the surface layer. One can also successfully explain the reversible contrast variation by taking into account the carrier mobility within the surface layer. Thus we proposed an interpretation of an "internal electric field contrast" based on a postulated "anomalous surface layer model."

### *Experimental*

To examine our contrast model, we carried out another experiment with cover glass slips as a specimen prepared as follows (Fig. 4). Aluminum electrodes were evaporated onto the bottom surface to simulate actual passivated devices. Half of the top surface was coated by a carbon layer 8 nm thick and was connected to the ground potential. We adjusted the SEM

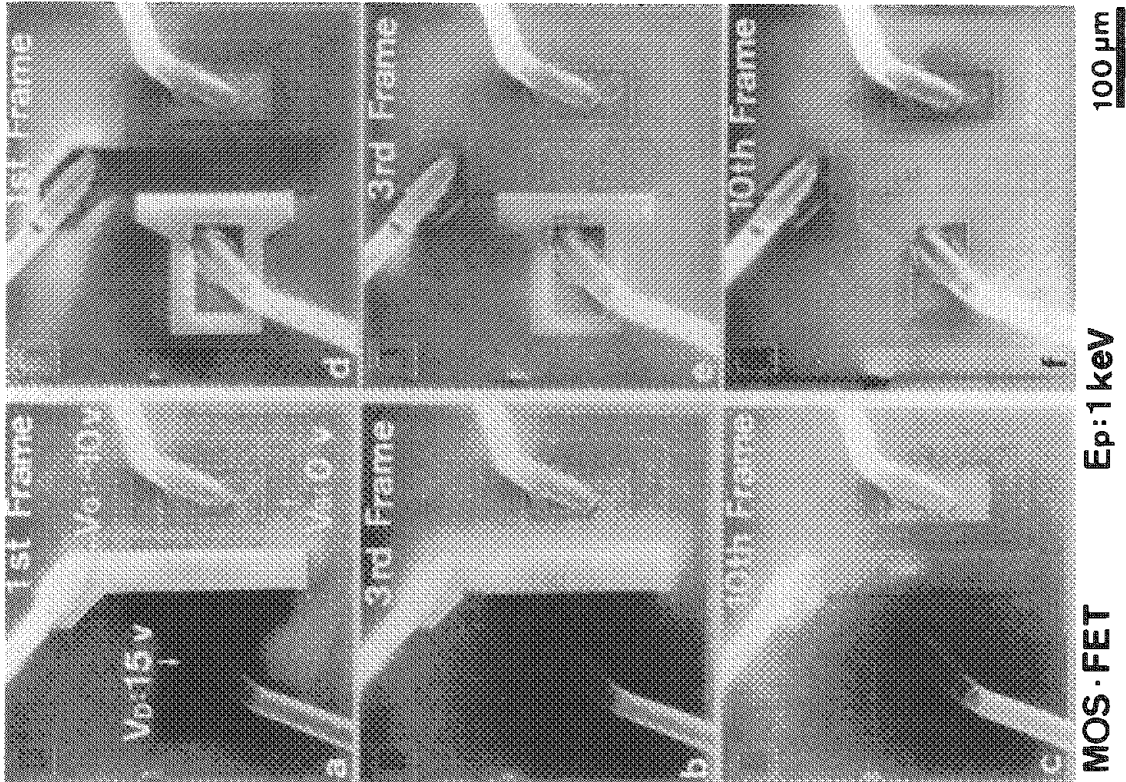


FIG. 1.--Reversible contrast variation over passivation of MOSFET:  $\phi_p = 0^\circ$ ,  $I_p = 10^{-11}$  A,  $t_s = 10$  s.

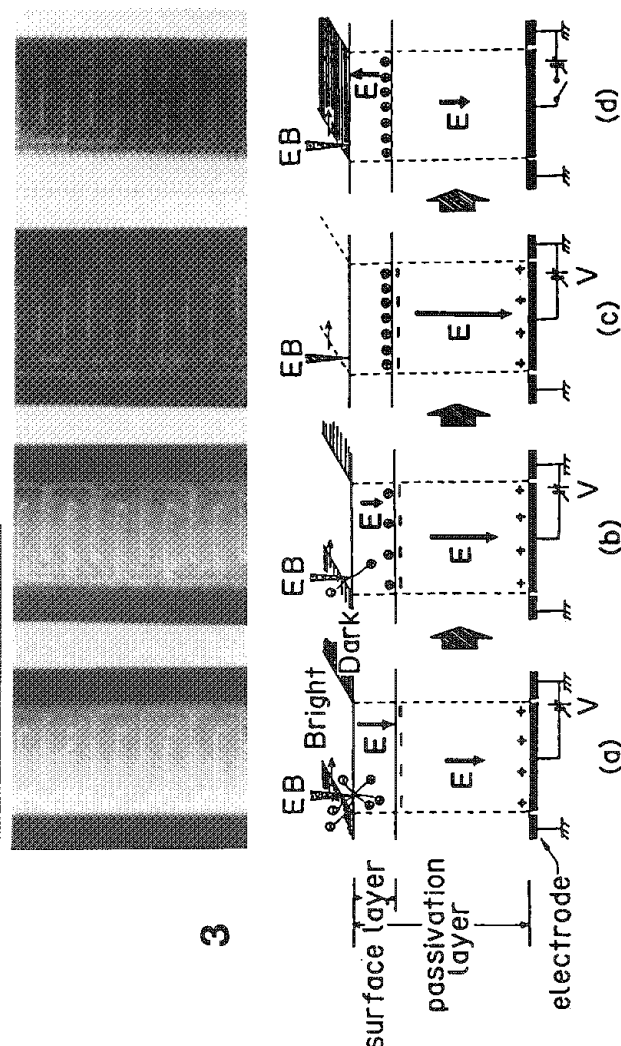
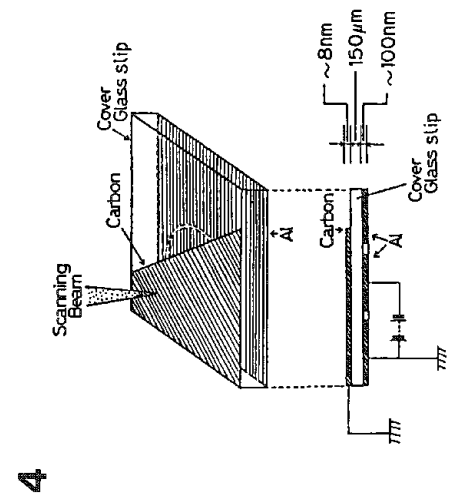
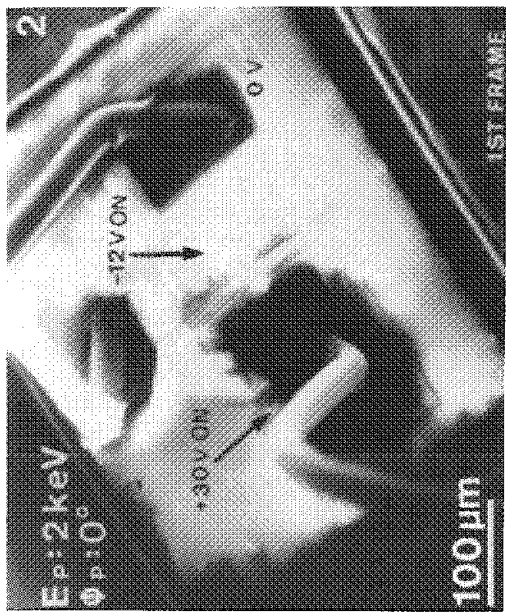


FIG. 2.--Irreversible contrast variation of same device (same imaging conditions as in Fig. 1).

FIG. 3.--Internal electric field contrast based on anomalous surface layer model.

FIG. 4.--Schematic of specimen.



so that both the carbon-coated and the uncoated areas of the glass surface come into view at the same time.

At first, we selected the primary electron energy at  $E_p = 5$  keV with the Al electrodes connected to the ground potential (Fig. 5a). Bright clouds appear flooding over the uncoated surface (right half) showing immediate charge accumulation over that area. A flat contrast over the carbon-coated area (left half) remains unchanged (disregarding frames of imaging). Clearly, the carbon-coated surface is free from charge accumulation. Therefore, we can conclude that the carbon-coated area is conductive enough to be equipotential.

Next, we observed the same area of view at  $E_p = 1$  keV, by applying a negative voltage of -80 V to the central electrode (Fig. 5b). We can observe a bright contrast corresponding to the negative voltage. The contrast appears over the uncoated area as well as over the carbon-coated area. Since the carbon-coated area is equipotential, we concluded that the contrast must arise from some physical origin and not the surface potential difference.

#### Discussion and Conclusions

We selected the thickness of the carbon layer carefully. The 8nm-thick carbon layer is thin enough for the primaries to penetrate through it into the anomalous surface layer.

Since the electric field acts within the anomalous surface layer, the secondaries excited by the primaries in the anomalous surface layer are forced outward by the field. Again, the carbon layer is thin enough for the secondaries to travel across so that more secondaries emit over the negatively biased area than over the grounded area.

Increasing the carbon thickness to 10 nm or more, we found that the bright contrast does not appear at all. Below 5 nm, bright clouds due to charge accumulation were observed over the carbon area at  $E_p = 5$  keV. The circular fringe outside the bright disk over the uncoated area has yet to be explained.

#### References

1. N. Sugiyama et al., "Low voltage SEM inspection of microelectronic devices," *J. Electron Microsc.* 35: 9-18, 1986.
2. Y. Uchikawa and S. Ikeda, "Inspection of micro devices over the passivation top-layer surface using the low-voltage SEM," *Jpn. J. Appl. Phys.* 22: L645-647, 1983.
3. P. R. Thornton, *Scanning Electron Microscopy*, London: Chapman and Hall, 1968.
4. S. Görlich et al., "Basic investigations of capacitive coupling voltage contrast," in A. Heuberger and H. Beneking, Eds., *Microcircuit Engineering 84*, New York: Academic Press, 1985, 451-460.

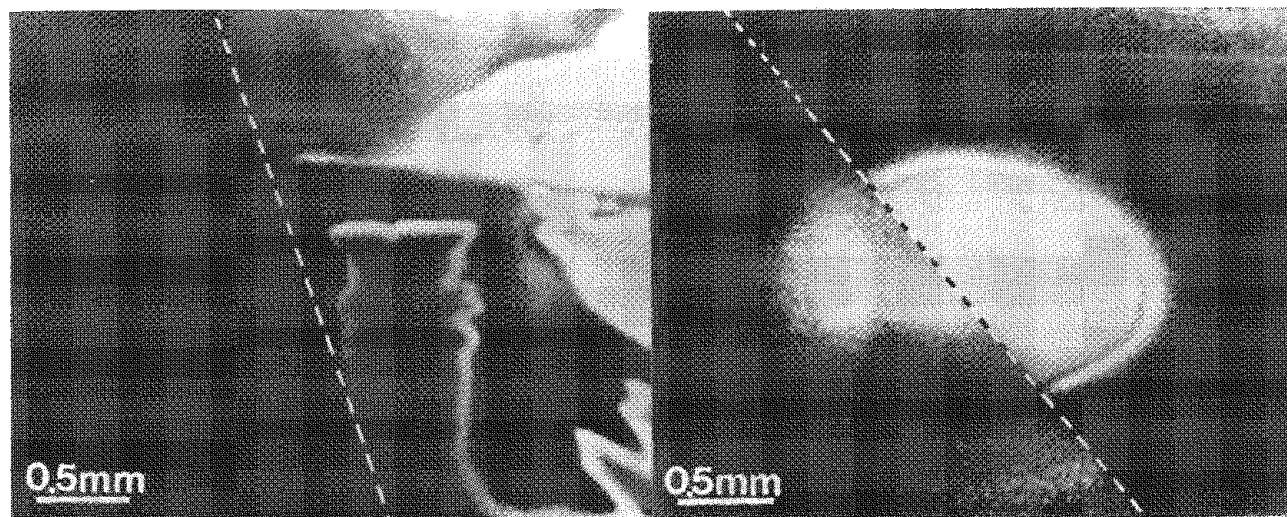


FIG. 5.--(a) SEM image at  $E_p = 5$  keV with bottom electrodes grounded ( $I_p = 10^{-11}$  A,  $\phi_p = 0^\circ$ ,  $t_s = 1.0$  s); left side is carbon-coated area; dotted lines are drawn to indicate boundary between carbon-coated and uncoated areas over glass surface. (b) SE image at  $E_p = 1$  keV with -80 V applied to central electrode under same imaging conditions as in (a).

TABLE 1.--Reversible (O) or irreversible (X) contrast variation and threshold conditions.

$E_p$ (keV)	$0^\circ$	$5^\circ$	$35^\circ$	$45^\circ$
1	O	O	O	O
2	X	O	O	O
3	X	X	O	O
4	X	X	X	O

$E_p$ (keV)	$\phi_p$ ( $\pm 1^\circ$ )	$E_p \cdot \cos^2 \phi_p$
1	0	—
2	5	1.98
3	35	2.01
4	45	2.00

The present study was undertaken as part of a program to apply low-voltage electron beams to information storage systems. They are also important tools for the inspection, programming, and testing of integrated circuits. There are potential applications in low-voltage lithography and selected area annealing as well.

In the conventional approach to generating low-voltage beams, the extraction and landing energies are equal. The attainable current density is severely limited by lens aberrations and space-charge spatial broadening.<sup>1</sup> An alternative approach to the generation of low-voltage beams was pioneered by Zworykin, Hillier, and Snyder, who decelerated a high-voltage beam by a retarding field at the sample.<sup>2</sup> Recently Yau, Pease, et al. have shown lens aberrations are sharply reduced in decelerating probes.<sup>3</sup> The purpose of the present study has been to determine whether the retarding-field design of low-voltage probes is also effective in reducing space-charge spatial broadening effects. Improved performance was expected since electrons travel through most of the length of the column at the full extraction voltage, moving slowly only in a region very close to the target. In addition, the large convergence angle at the target should reduce the electron density in the critical low-voltage region.

#### Experimental Procedures

The basic design of the electron optical column (Fig. 1), without retarding field, is due to J. E. Wolfe.<sup>3</sup> Electrons are extracted from a zirconiated tungsten cathode operated in the Schottky emission mode. The electrons are then collimated by lens 1 and focused onto the sample by lens 2. Deceleration is accomplished by the application of a retarding bias voltage to the sample stage (B in Fig. 1). A ceramic stand-off A insulates the stage from the grounded deceleration tube C. The video signal is derived from the sample current through an isolation capacitor.

#### Results

The column was operated with a 7 kV extraction voltage and 6 kV of deceleration, a net landing energy of 1 keV. The beam current was 320 nA. The beam profile was measured by scanning across a sharp edge on a thin gold film. The beam profile agreed very well with a Gaussian beam shape with 20 nm standard deviation. The peak current density was  $1.3 \times 10^4$  A/cm<sup>2</sup>.

#### Discussion

The work reported here was performed to determine the extent of space charge broadening in high-current density, low-voltage, retarding-field probes. We showed that spot size

stayed a constant 40 nm with or without deceleration, which in turn demonstrates that broadening is not a limiting factor even for current densities up to  $1.3 \times 10^4$  A/cm<sup>2</sup> at a landing energy of 1 keV.

#### Future Work

A significant problem for the application of retarding-field probe designs to low-voltage microscopy is secondary-electron collection. These electrons are accelerated by the retarding field and focused by the objective lens into a high-voltage return beam which can be separated from the primary beam only with difficulty. One possible approach to separating the secondary-electron return beam is to place a double deflection system in the column, which would displace the primary and secondary beams in opposite directions. This approach is currently being investigated.

#### References

1. T. Groves, D. L. Hammond, and H. Kuo, *J. Vac. Sci. Technol.* 16: 1680-1685, 1979.
2. V. K. Zworykin, J. Hillier, and R. L. Snyder, "A scanning electron microscope," *ASTM Bull.* 117: 15-23, 1942.
3. Y. W. Yau, R. F. W. Pease, A. A. Iranmenesh, and K. J. Polasko, *J. Vac. Sci. Technol.* 19: 1048-1052, 1981.
4. J. E. Wolfe, *ibid.* 12: 1169, 1975.

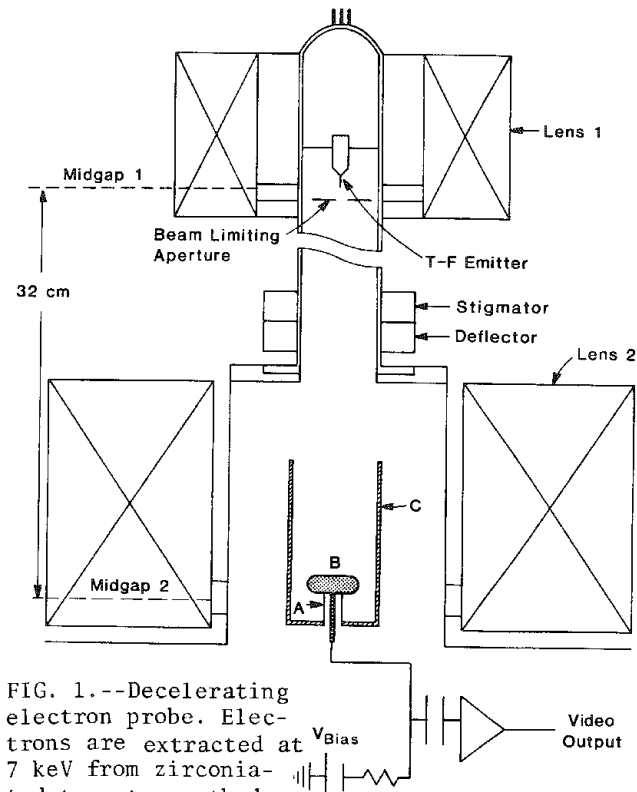


FIG. 1.--Decelerating electron probe. Electrons are extracted at 7 keV from zirconiated tungsten cathode, collimated by lens 1, and focused onto sample by lens 2. Beam is decelerated when sample stub B is biased with respect to grounded cylinder C. Insulating stand-off A supports stub.

## LOW-VOLTAGE SCANNING ELECTRON MICROSCOPY

J. B. Pawley

There are two reasons for the renewed interest in using the SEM at beam voltages  $V_0$  around 1 kV (LVSEM). The most common one arises from applications in the semiconductor industry and emphasizes the reduction in charging artifacts and in subsurface beam damage. The second reason is founded on the belief that increased contrast in the topographic component of the secondary-electron signal will permit an important improvement in topographic spatial resolution if only a sufficiently small probe diameter can be obtained at low  $V_0$ .<sup>1</sup> We shall treat these two areas separately and then describe recent progress in optimizing a modern FE SEM for low-voltage operation.

### *LVSEM in Semiconductor Research*

Surfaces are very important in the manufacture of modern semiconductor devices. The ability of the electron probe to induce current flow (EBIC), to detect variations in surface and subsurface electronic potential, and to excite characteristic x rays, in addition to its ability to image topography in an easily understandable way, has guaranteed the SEM a major role in programs of semiconductor development and failure analysis.<sup>2-4</sup> However, observations of uncoated electronically active ICs are plagued by two problems: charging and beam-induced damage to the specimen.

Large areas of a modern semiconductor consist of insulating materials such as silicon and metal oxides. If such samples are coated with a conductive layer to permit viewing in the SEM without charging artifacts, the conductive layer suppresses voltage contrast and degrades or destroys the device's electronic performance. Similar limitations apply to SEM observations of the uncoated photoresist used to mask part of the silicon substrate during specific steps in the production process. Clearly, observations of such uncoated insulating specimens are subject to charging artifacts.

Beam-induced damage is associated with the fact that some of the beam electrons impinging on an insulator remain trapped within the material. For example, if the insulating oxide is part of a metal oxide-silicon (MOS) device, the potential distribution in the device will be altered and it will not work properly.<sup>5</sup> Similar constraints hold for other solid-state devices.

Both these problems are reduced at low  $V_0$ . Charging is less as the total secondary electron coefficient approaches unity, and trapped charge is confined much nearer to the surface because beam penetration is proportional to

$V_0^{1.75}$ . The sampling depth is also less, and this makes LVSEM an appropriate adjunct to a wide variety of surface analysis techniques such as LEEDs and Auger microscopy.<sup>6</sup>

### *LVSEM and the Topographic Image*

Although early commercial SEMs had poor electron optical performance at low  $V_0$ , early workers still stressed the utility of using  $V_0 = 3$ -10 kV to increase topographic contrast<sup>7,8</sup> (i.e., contrast that varies with the cosecant of the incidence angle). It is well known that the so-called 'secondary electron' signal derived from a standard Everhart-Thornley detector is a function of many variables ( $Z$ ,  $V_s$ , surface contamination, polepiece material, etc.) aside from topography. However, when our attention is caught by a micrograph of an insect head, it is the topography that interests us. Unfortunately, as magnification increases, the simple topographic coding of local surface angle on the object to pixel brightness in the image breaks down: the spines between the insect's eye segments appear to glow white because the probing beam passes through them and produces even more collectable secondaries from the lower surface than from the upper one. Fortunately, the shape of the spines still seems interpretable and in this case we are not perplexed by the anomalous brightness.

However, the bright hairs are a caution that all brightness variations cannot be decoded in terms of local surface angle and that the relationship is likely to break down as either the size of the pixel on the sample or the thickness of the sample approaches the beam penetration volume. Manufacturers have been aware of this feature for years and have routinely demonstrated the performance of their instruments using test samples, such as gold islands on a thin carbon film, that depend on atomic number rather than topographic contrast, and that measure only probe diameter and not the limiting size of visible topographic surface details.

Fundamentally, the problem is one of contrast. In order to image topographically a  $10 \times 10$  nm protuberance on a flat surface of homogeneous, solid material, one must be able to detect an increase in signal at least five times the shot noise in the detected signal when the probe passes over each edge of the bump. Because beam penetration at 20-30 kV in a low-density, low- $Z$  biological sample may be tens of microns and because collectable electrons excited from anywhere in the sample more than 5 nm away from the beam impact point produce a noise background signal, it is clear that the slight change in signal caused by the protuberance will be lost in this noise. In fact, such a protuberance will only be seen at all if it is coated with a heavy metal and if topographic variations in the effective thickness of this coat (the distance that the beam

---

The author is with the NIH Integrated Microscopy Facility for Biomedical Research at the University of Wisconsin, Madison, WI 53706. This work was supported by NIH grant RR00570.

travels through the metal, which varies with surface angle) give rise to Z contrast. Unfortunately, the coating thickness must be reduced if smaller details are not to be obscured, and the reduction reduces the topographic Z contrast. There is only one way to increase high resolution topographical contrast without thick coating; reduce the beam penetration by reducing  $V_0$ .<sup>10</sup>

#### *Problems of LVSEM*

Although the advantages of LVSEM are widely appreciated, it is only recently that there has been any concerted effort to overcome the technical difficulties involved. Below  $V_0 = 10$  kV, SEM probe size is limited by source brightness and chromatic aberration. According to the Langmuir equation, theoretical brightness is proportional to  $V_0$ ; but at voltages around 1 kV, space charge in a thermionic gun often degrades this brightness by an additional factor of 2 to 3. As a result, a larger aperture angle  $\alpha$  must be used if sufficient signal is to be produced. Chromatic aberration enlarges the focused spot to a diameter  $d_c = C_c \alpha \Delta V_0 / V_0$ , where  $C_c$  is the chromatic aberration and  $\Delta V_0$  is the energy spread in the beam. Clearly,  $d$  gets larger with  $\alpha$  and with  $V_0$ .<sup>-1</sup> These problems in forming a small probe are compounded by the fact that, because of its low energy, this beam is very susceptible to distortion or displacement by a signal collection fields or stray electromagnetic fields.<sup>11</sup> As a result, until recently, performance below 100 nm at 1 kV has been rare.

#### *Design Modifications to Improve LVSEM Performance*

Because of the large potential market, most SEM manufacturers have produced instruments geared to the semiconductor field, where 10-20 nm at 1 kV is sufficient. Problems with stray fields have been attacked directly by more extensive use of magnetic shielding materials but reduction of the deleterious effect of the signal collection field has proved to be more complicated. The problem is acute, because reducing  $C_c$  implies a short working distance, which in turn complicates the extraction of the secondary electron signal. The responses have been (1) to use a steeply conical lower lens polepiece to permit a large, flat sample to be tilted at a steep angle while preserving access to the collection field; (2) to place the sample in the lens gap and to collect only secondaries that spiral up the field lines to a collector above<sup>2,12</sup> (an alternative that has the advantage of a lower  $C_c$  but a constraint against the use of magnetic samples); (3) to use a rotationally symmetric microchannel plate detector mounted on the lower polepiece;<sup>13</sup> (4) to employ a compensating magnetic field at right angles to the collection field to cancel out the effect of the latter on electrons having an energy of  $eV_0$ ,<sup>14</sup> or (5) to employ two opposing detectors, adjusted so that their fields cancel out on the EO axis.<sup>1,15</sup>

The problem of low brightness has been

tackled in three ways: (1) by use of  $\text{LaB}_6$  cathodes, which are about 10 times brighter than tungsten and which can produce a smaller  $\Delta V_0$  because they operate at a lower temperature; (2) by addition of a second extraction anode operating positive to ground or reduction of the Wehnelt/anode spacing in order to reduce the problem of space charge; and (3) by use of a cold field-emission (FE) cathode, which has a low  $\Delta V_0$  of 0.17 eV. Only Fe has sufficient brightness to permit operation limited by diffraction rather than by shot noise in the beam. By use of various mixes of these strategies, 20 nm at 1 kV is sometimes attainable in instruments with the normal configuration, whereas instruments that locate the sample in the lens field show about 10 nm with  $\text{LaB}_6$  and <5 nm with cold FE.<sup>16</sup> The Hitachi S-900 is the first instrument to be introduced in the latter category and is discussed below.

#### *Optimizing the Hitachi S-900 for Low-voltage Use*

The first commercial SEM to embody most of the basic design features necessary for optimal performance in the secondary electron mode at low  $V_0$  is the Hitachi S-900.<sup>17</sup> This instrument combines a computer-monitored, cold FE source of proven reliability and performance with a short focal length final lens ( $C_c = 1.9$  and  $C_s = 1.6$  mm) to yield a beam diameter of 3 nm at 1 kV (if the quantum-mechanical formulation of Crewe is used<sup>18</sup>) The sample is mounted on a TEM-type eucentric goniometer stage, which provides far greater stability than the normal SEM stage and also greatly simplifies the production of stereo pairs. The defining aperture is mounted above the scan coils and is projected into the objective lens by an intermediate lens, a feature that simplifies the eventual development of a deflection system to make stereo images produced by electronic tilt of the raster approach angle.<sup>19</sup>

The first production instrument of this type was installed at the Madison Integrated Microscopy Resource in October 1986. The following is a description of our early efforts to optimize this instrument further for  $V_0$  operation. Our efforts so far have concentrated on three areas: contamination, alignment, and resolution.

#### *Contamination*

Contamination, in the form of deposition of beam-polymerized hydrocarbons on the surface of the sample, has been noted in even the most stringently dry-pumped systems.<sup>20</sup> Under these conditions, the hydrocarbons evolve from the sample itself and the only successful approach to avoiding the problem has been to cool the sample and its surroundings to about -120 C.

*Vacuum system.* Although the S-900 does not yet approach this vacuum level, its vacuum system is markedly superior to that of the average SEM. Viton and crushable metal O-rings are used throughout the specimen area, the airlock is differentially pumped, the magnetic bearing turbo is very clean, and backstreaming from the mechanical pumps is reduced

with molecular sieve traps. The result at present is  $4 \times 10^{-8}$  mBar (measured in the vacuum manifold).

Although this performance is acceptable for 30kV operation, where the deposition rate is slower and the resulting deposit less visible in the SE image, several modifications have been made to improve the system further for low-voltage use (Fig. 1). The mechanical pump on the airlock has been replaced by a sorption pump to eliminate completely mechanical pump oil from the airlock. A Gatan retractable two-leaf anticontaminator has been added to surround the specimen rod. The mechanical pump backing the turbo has been replaced by a new type of oil-free mechanical pump called a molecular drag pump (MDP; Alcatel, Danielson Assoc., Lisle, IL 60532). The MDP operates somewhat like a turbo in which opposing screw threads replace the turbine blades. It requires a fore-pressure of 75 mBar, which is maintained by a diaphragm pump.

Finally, the inner seal of the differentially pumped airlock has been redesigned. The original Viton O-ring in the stage nosepiece required that the outer surface of the stage rod be greased. This O-ring is now being replaced with a grease-free teflon one mounted on the rod itself. Teflon O-rings wear quickly and this arrangement will simplify replacement.

*Specimen Preparation.* In the absence of a cold stage, contamination rate depends intimately on specimen preparation. For instance, when a test sample of Au/Pd on solid carbon has been cleaned in organic solvent, it contaminates severely, regardless of the vacuum, unless it has first been vacuum-baked to a high temperature to drive out the absorbed solvent. Fortunately, critical-point-dried biological samples seem to be relatively free from low-molecular-weight hydrocarbons, probably because molecules of this type are removed by the solvent action of the intermediate and transition liquids (acetone or ethanol and  $\text{CO}_2$ ).

*Coating.* Low vacuum diode sputter coating with metal has not been very satisfactory, probably because roughing pump oil is deposited onto the sample during the procedure. Conventional carbon and Pt-C coating in a  $\text{LN}_2$ -trapped, diffusion-pumped system has produced better results, but the best results are at present obtained from Argon ion-beam-sputtered Pt or Cr,<sup>21</sup> deposited in a system pumped with a 63mm Diffstack (Edwards High Vacuum). We are just beginning experiments with an ion-pumped evaporator.

*Mounting.* Attachment of the dried biological sample to the specimen planchet is considerably more complicated when hydrocarbon-based adhesives must be avoided so as not to introduce contamination. Most samples are either mounted on EM grids, for correlative HVEM studies, or on rectangular segments of polished Si wafers, which may be Au-coated to improve cell adherence. The latter are held to the specimen rod by a spring arrangement bearing on the top surface of the wafer. Glass coverslips are too large readily to adhere to these sub-

strates, we have experimented with mechanical attachments (screws, folded-grids) and, more recently (at the suggestion of R. Albrecht), with low-melting-point alloys such as Woods metal. The dried sample is sprinkled on the surface of the alloy, which is then heated enough (45 C) to permit the sample particles to indent the surface.

### Alignment

The asymmetric nature of the SE collection field complicates the alignment of the S-900 column. An objective lens current wobbler is a great assistance and the SE detector retracts for low- $V_0$  work; however, alignment of the final aperture at low  $V_0$  is still a compromise between the axial position and the paraxial angle of the transmitted beam. Recently, the design and operation of a Wien filter system, which uses a magnetic field at right angles to the collection field to cancel out the effect of the latter on the probe, was described.<sup>14</sup> A system of this type, or a symmetrical microchannel-plate detector,<sup>13</sup> is currently being developed.

### Resolution

The problems associated with the measurement of EM resolution are well known. For the TEM, the contrast transfer of an image of a thin amorphous film is now a widely accepted standard, but unfortunately no similar test sample exists for the SEM. The work by Oho and others on computer-analyzed quasi-STEM images is a start,<sup>22</sup> but it does not really account for the delocalizing effects of the SE production event.<sup>18</sup> To fill this void, we have begun to analyze our photographic SEM images of test samples using a TV-based digital image-processing system originally designed for LM images. We are trying to correlate recorded contrast and linescan measurements to determine the absolute contrast in the SE signal from the microscope. This information, and measures of the noise content of the image, will be used to define a threshold contrast at which "resolution" will be defined. The process is unfortunately still very sample dependent, but it is a start.<sup>23</sup>

### References

1. J. B. Pawley, "Low voltage SEM," *J. Microsc.* 136: 45-68, 1984; and "SEM at low beam voltage," *Proc. EMSA* 42: 440-444, 1984.
2. E. Menzel and R. Buchanán, "Some recent developments in low voltage E-beam testing of ICs," *J. Microsc.* 140: 331-349, 1985.
3. K. Ura, "Electron beam testing in electronics," in T. Imura, S. Maruse and T. Suzuki, Eds., *Proc. 11th Intl. Cong. Electron Microsc.*, Tokyo, 1986, 173-176.
4. H. Todokoro, S. Yonedá, K. Yamaguchi, S. Fukuhara, and T. Komoda, "Stroboscopic testing of LSIs with LVSEM," *J. Microsc.* 140: 313-322, 1985.
5. W. J. Keery, K. O. Leedy, and K. F. Galloway, "Electron beam effects on microelectronic devices," *SEM/1976*, 507-514.
6. T. Ichinokawa, Y. Ishikawa, M. Kemmochi, N. Iida, and Y. Hosokawa, "Low energy scan-

ning electron microscopy combined with low-energy electron diffraction," *Surface Sci.* 176: 397-414, 1986.

7. R. F. M. Thornley, "Recent developments in SEM," in A. L. Houwink and B. J. Split, Eds., *EM 1960*, Delft, 173-176.

8. D. C. Joy, "Resolution in low-voltage scanning electron microscopy," *J. Micros.* 140: 283-292, 1985.

9. T. E. Everhart, O. C. Wells and C. W. Oatley, "Factors affecting contrast and resolution in the SEM," *J. Electron Control* 7: 97ff, 1959.

10. M. Osumi, "High resolution, LVSEM of uncoated cells by applying the freeze substitution fixation method," in Ref. 3, pp. 2089-2092.

11. J. B. Pawley, "Strategy for locating and eliminating sources of mains frequency stray magnetic fields," *Scanning* 7: 43-46, 1985.

12. H. Koike, K. Ueno, and M. Suzuki, "Scanning device combined with conventional electron microscope," *Proc. Ann. Meeting EMSA* 29: 28-29, 1971.

13. P. E. Russell and J. F. Mancuso, "Microchannel plate detector for LVSEM," *J. Micros.* 140: 323-330, 1985.

14. J. Zach and H. Rose, "Efficient detection of secondary electrons in LVSEM," *Scanning* 8: 285-293, 1986; and R. Schmid and M. Brunner, "Design and application of a quadrupole detector for LVSEM," *Scanning* 8: 294-299, 1986.

15. L. Reimer and M. Riepenhausen, "Detector strategy for secondary and backscattered electrons using multiple detector systems," *Scanning* 7: 221-238, 1985.

16. J. B. Pawley and W. R. Scala, "LVSEM

update," *Proc. Ann. Meeting EMSA* 44: 654-658, 1986.

17. T. Nagatani and S. Saito, "Instrumentation for ultra high resolution scanning electron microscopy," in Ref. 3, pp. 2101-2194.

18. A. V. Crewe, "Is there a limit to the resolving power of the SEM?" in Ref. 3, pp. 2105-2108.

19. J. B. Pawley, "Design and performance of presently available TV-rate stereo SEM systems," *SEM/1978* I, 157-166.

20. J. Wall, "Contamination in the STEM at ultrahigh vacuum," *SEM/1980*I, 157-166.

21. A. C. Evans and J. Franks, "Specimen coating for high resolution scanning electron microscopy," *Scanning* 4: 169-174, 1981; and K.-R. Peters, "Metal coating thickness and image quality in scanning electron microscopy," *Proc. EMSA* 44: 664-667, 1986; and K.-R. Peters, "Progress in biological field emission SEM with new metal coating procedures: Imaging individual immunoadsorbed IgG on cell membranes," in Ref. 3, pp. 2093-2096.

22. E. Oho, M. Kobayashi, T. Sasaki, K. Adachi, and K. Kanaya, "Automatic measurement of scanning beam diameter using an on-line digital computer," *J. Electron Microsc. Tech.* 3: 159-167, 1986.

23. The instrumentation at IMR is available to qualified biological users who document need. For information, call 608-263-3147.

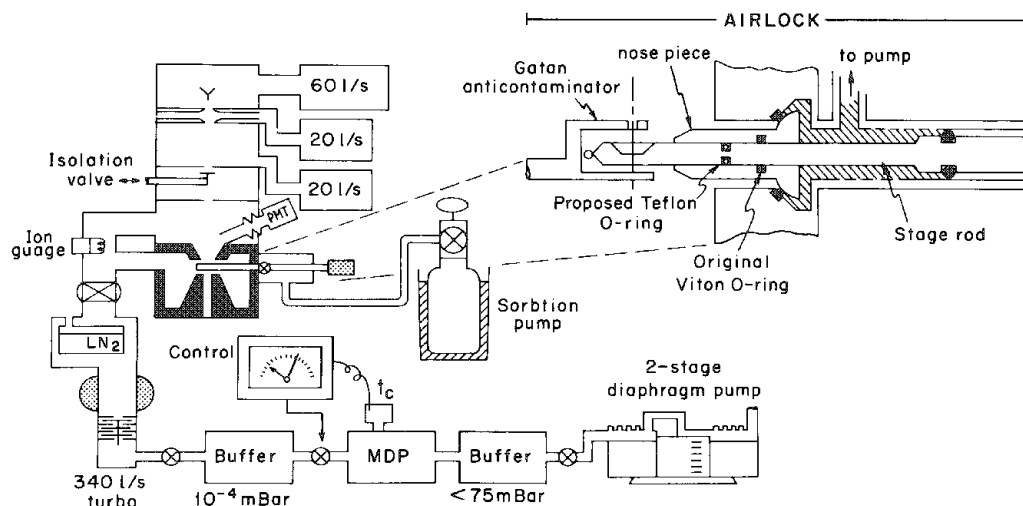


FIG. 1.--S900 vacuum modification.

### 3B. SEM: Applications

#### APPLICATION OF SCANNING ELECTRON MICROSCOPE CATHODOLUMINESCENCE TO THE STUDY OF GALLIUM ARSENIDE ON SILICON

G. A. Reid, K. Nauka, S. J. Rosner, and S. S. Laderman

In this first report on SEM cathodoluminescence (CL) studies of GaAs/Si, we compare the data with the electrical and structural properties of these films. The results show that CL intensity is related to doping concentrations, annealing, growth temperature, and film thickness. On beveled or etched samples, CL can provide information on the electrical quality of the film as a function of film thickness. CL of GaAs/Si is a relatively simple technique to use which we show, by comparison with EBIC data, provides information on the spatial distribution of minority carrier lifetimes.

#### *Introduction*

Interest in gallium arsenide on silicon (GaAs/Si) as a material in which to build devices such as MESFETs, LEDs, lasers, photoconductive detectors, and MODFETs continues to grow. To produce material with the electrical and structural quality required for minority carrier devices and high yield in majority carrier devices, characterization and correlation of the electrical and structural changes caused by variations in the growth process is required.

We describe results obtained by the liquid-nitrogen-temperature total-light CL examination of GaAs/Si grown by molecular beam epitaxy (MBE), and compare them with results obtained from deep-level transient spectroscopy (DLTS), electron-beam-induced current (EBIC), Rutherford backscattering spectrometry (RBS), and x-ray rocking curve measurements.

#### *Experimental*

The samples were grown on (100) substrates tilted toward (110) by amounts varying from approximately 1° to 4°, with buffer layers 25 to 100 nm thick grown at 250 or 405 C. All samples except one had ~2000nm-thick Si-doped GaAs films. Two had mid-growth anneals. The samples cited in this study along with their various growth parameters are listed in Table 1.

For CL, the sample is mounted on an Oxford Instruments liquid nitrogen cold stage in a JEOL 35CF SEM. The CL signal is collected by a silicon diode detector and amplified by a GW Electronics backscatter detector/amplifier.<sup>1</sup> One determines the relative intensity of the CL signal by measuring the voltage output of the constant-amplification preamplifier by

switching the signal from the SEM to an HP 3466A voltmeter or HP 7090A plotter. The average light output from the sample can be measured by rapid scanning of the sample and reading the voltage on the voltmeter, or one can obtain a detailed measurement by plotting the intensity of the CL signal versus the time required for one scan of the SEM screen, thereby maintaining a constant ratio between the magnification of the SEM image and the plot. The average intensity is used for comparison among samples; the intensity of a linescan across the sample is used to measure the difference between the light and dark areas on a single sample. Care is taken to insure that the SEM accelerating voltage, beam current, and magnification remain constant during each measurement, since a change in any of these parameters affects the magnitude of the CL signal.

Both the surface and subsurface of these GaAs/Si films were examined to compare the features revealed by CL and the changes in intensity of the CL signal as a function of depth. The subsurface was exposed by either angle lapping at an angle of 2° or by etching the samples with an isotropic etchant consisting of H<sub>2</sub>PO<sub>4</sub>, H<sub>2</sub>O<sub>2</sub>, and H<sub>2</sub>O.

Once the CL data were recorded, they were compared with electrical data obtained from DLTS, C-V measurements, and EBIC. They were also compared with chemical data from SIMS, and with structural data from RBS and x-ray diffraction.

DLTS information on deep electron traps was acquired by use of aluminum or gold Schottky barriers and gallium/indium or germanium/gold/nickel ohmic contacts. The DLTS signal was measured in the temperature range of 80 to 400 K with a 4-160μs time window.

EBIC images were obtained by use of the Schottky barriers deposited for DLTS measurements. These barriers were thin enough to allow the escape of the CL signal, which enabled us to make a one-to-one comparison of EBIC and CL images.

The crystalline quality of each GaAs film was measured both by channeling RBS and by x-ray rocking curve half-widths. RBS measured the crystalline quality near the surface of the film; rocking curves provided an average of the crystalline quality of the full film thickness. As the quality of the surface of the film improved, the RBS X<sub>min</sub> percentage approached the GaAs homoepitaxial value, obtained with the same experimental conditions, of approximately 3%. Narrower x-ray rocking curve half-widths indicated better crystalline quality throughout the film.

#### *Results and Discussion*

The value of CL for examining GaAs/Si was immediately apparent when we compared CL and EBIC micrographs taken from the same area

---

The authors are at the Hewlett-Packard Laboratories, 3500 Deer Creek Rd., Palo Alto, CA 94304. They wish to express their gratitude to R. Smith and A. Nel for their help with the x-ray data, to M. Juanitas for sample preparation, to S. M. Koch and J. S. Harris Jr. of Stanford University and D. Mars for the GaAs/Si material, and to M. Scott, R. Hull, P. Luscher, and J. Amano for their helpful comments and encouragement.



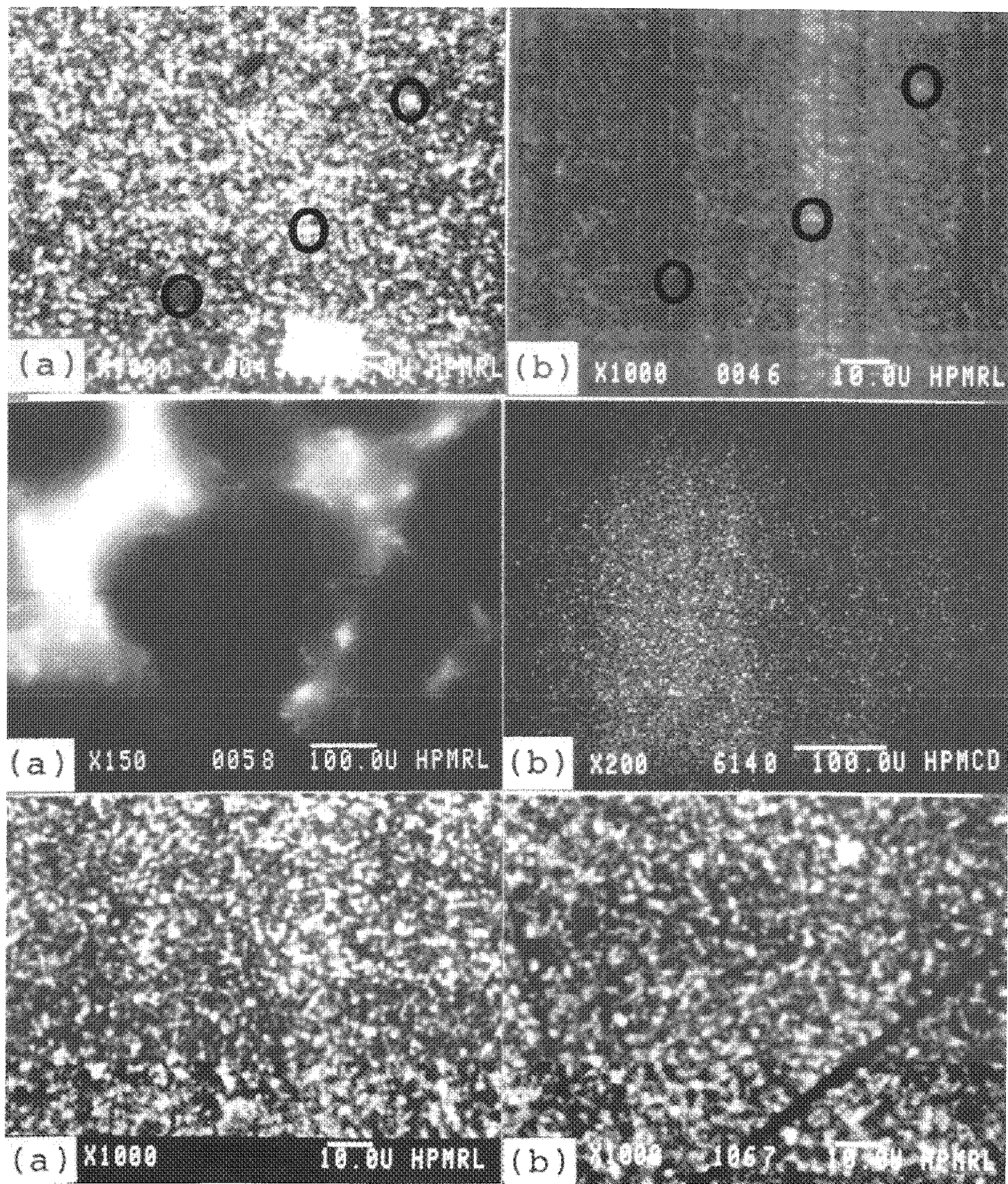


FIG. 1.--(a) EBIC, (b) CL micrographs, showing correspondence of features.

FIG. 2.--(a) LEC GaAs, (b) GaAs/Si CL micrographs showing difference in CL distribution.

FIG. 3.--CL micrographs of (a) sample A and (b) sample D illustrating common speckled appearance in samples with different growth parameters.



(Fig. 1). There was a one-to-one correspondence between the bright and dark areas seen in CL and the bright and dark areas seen in EBIC. This result indicated that areas with a large number of nonradiative recombination centers coincided with areas in which generated nonequilibrium electron/hole pairs had shorter lifetimes.

Also apparent was the difference between the spatial distribution of light emitted by the CL process in GaAs/Si and that emitted by bulk LEC GaAs (Fig. 2). Small radiative spots were uniformly scattered over the GaAs/Si surface, whereas in bulk LEC samples CL was concentrated in regions called cell walls. This concentration was probably caused by point defect gettering by dislocations in the cell walls.<sup>2</sup> Every GaAs/Si film that was examined, regardless of growth parameters, had this speckled appearance even though there were large variations in average CL intensity from sample to sample (Fig. 3).

Two of the samples in this study were etched back to provide CL information on light intensity below the sample surface (Table 2). The results of etching showed that in these Si doped samples the CL emission decreased as the sample was etched closer to the GaAs/Si interface (Fig. 4). This effect could have been caused by either (or a combination) of two mechanisms: a change in the Si level or in the number of nonradiative recombination centers. If the level of Si doping decreased with depth, the CL intensity should also have decreased. We believe that the number of non-radiative recombination centers was increasing with depth, an explanation substantiated by an increase in deep-level traps as determined by DLTS.<sup>3</sup>

Plotting the CL intensity across the interface of the beveled samples provided information on how quickly the number of nonradiative recombination sites is reduced with film thickness. The plot of sample B (Fig. 5), which is typical of plots of the first three samples, shows that the slope of the brightness curve near the interface is much greater than that in the plot of sample F (typical of the succeeding three samples).

### Summary

The major reason for undertaking this work was to investigate the possibility of using SEM CL as a simple tool to provide information on the electrical quality of GaAs/Si films. Two unique features of the GaAs/Si heteroepitaxial system could be observed by SEM CL. First, the distribution of microscopic nonradiative recombination centers, corresponded (as we showed by combining CL and EBIC data) with regions of short electron/hole pair lifetimes and weak CL. Second, we could observe changes in electrical quality as a function of depth by noting the decrease in average CL intensity and comparing this decrease with DLTS data on the increase in deep level traps as the region near the interface was probed.

Si doping affected the intensity of the CL signal more than any other parameter measured, but the effects of mid-growth annealing, higher buffer layer growth temperature, and thicker

GaAs films, at fixed Si concentrations, appeared to be important parameters enhancing CL intensity. We are currently preparing to study the correlation of average CL intensity with average crystal quality as a function of process temperature. For this experiment we shall be using fixed film thicknesses and Si concentrations to reduce the number of experimental variables.

Finally, we have shown that MBE films with a 100nm-thick buffer layer grown at 405 C exhibit maximum CL levels more quickly than 25nm layers grown at 250 C. It is probable that this rapid increase in brightness was the result of better confinement of defects emanating from the GaAs/Si interface.

### References

1. J. Marek, R. Geiss, L. Glassman, and M. Scott, *JECS* 132: 1502, 1985.
2. C. A. Warwick, S. S. Gill, P. J. Wright, and A. G. Cullis, *Inst. Physics Conf. Ser.* 76: 1985.
3. K. Nauka, G. A. Reid, S. J. Rosner, S. M. Koch, and J. S. Harris Jr., *MRS Symp. Proc.* (in preparation).

TABLE 1.--Growth parameters of GaAs/Si samples used in this study.

SAMPLE	GROWTH METHOD	ANNEAL	SI DOPED	TILT	BUFFER	FILM THICKNESS
A	MBE	none	7 E17	4°	405° 100 nm	-2 um
B	MBE	none	8 E17	4°	405° 100 nm doping SL	-2 um
C	MBE	none	8 E17	1°	405° 100 nm	-2 um
D	MBE	none	8 E17	1°	250° 25 nm	-3 um
E	MBE	mid-growth	1 E18	1°	250° 25 nm	-2 um
F	MBE	mid-growth	2 E18	1°	400° 25 nm	-2 um
G	MBE	none	no	4°	400° 30 nm	-2 um

TABLE 2.--Characterization results from the samples used in this study.

SAMPLE	SURFACE BRIGHTNESS (arb. units)	120nm BELOW SURFACE (arb. units)	1 um BELOW SURFACE (arb. units)	RBS X-MIN	X-RAY ROCKING CURVE
A	0.72	0.62	0.26	4.4%	450 arc-sec
B	0.33	-	-	4.0%	360 arc-sec
C	0.13	-	-	4.1%	400 arc-sec
D	0.59	0.50	0.16	4.5%	450 arc-sec
E	0.26	-	-	5.6%	1015 arc-sec
F	0.40	-	-	4.3%	720 arc-sec
G	0.10	0.10	-	3.7%	330 arc-sec

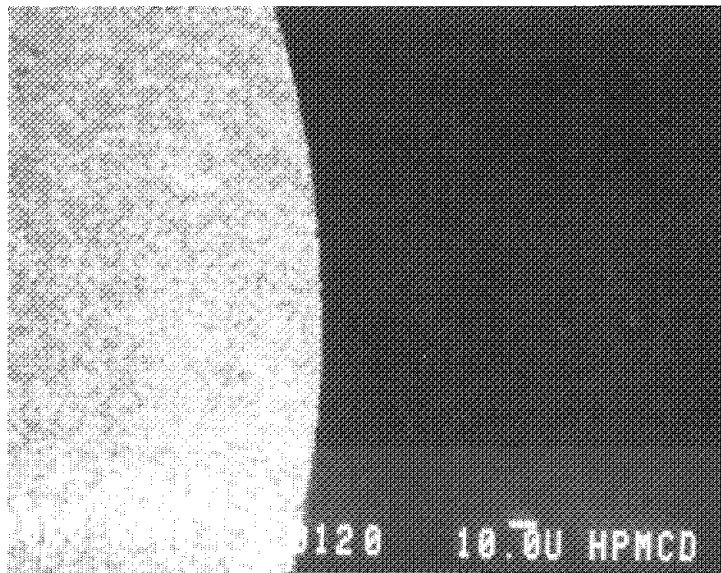


FIG. 4.--CL micrograph of sample A showing decrease in CL intensity in Si-doped GaAs/Si after sample had been etched to depth of  $\sim 1000$  nm. Bright region on left is original surface.

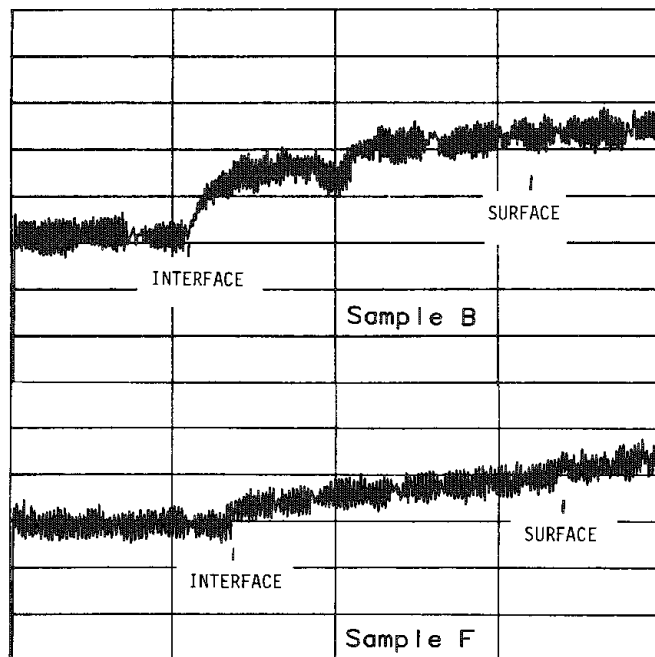


FIG. 5.--CL intensity plots across GaAs/Si interface revealed by  $2^\circ$  angle lap. Sample B (top curve) shows a rapid increase in brightness with film thickness; sample F (bottom curve), which has thinner and lower temperature buffer layer, shows more gradual increase.

## LINE-SAMPLING STROBOSCOPY WITH SEM

T. Ikuta, H. Mase, and R. Shimizu

Dynamic observation of periodic phenomena by scanning electron microscopy is usually achieved by the use of stroboscopic techniques. Many papers have been based on this stroboscopy.<sup>1-4</sup> Although the two approaches are different, primary-beam chopping<sup>1-3</sup> and video-signal gating<sup>4</sup> can both be used for the strobing. Such stroboscopy should be classified as point-sampling stroboscopy, since only one pixel is detected during one period of the driving signal. In point-sampling stroboscopy, the stroboscopic observation at low frequencies (such as line frequency) is difficult in practice because the image acquisition time is proportional to the product of the number of total pixels and the period of the repetition phenomena. As a simple example, the image acquisition time with  $1000 \times 1000$  pixels at a 60Hz drive takes about 4.6 h for just one phase value of the drive. The practical lower limit of the drive frequency is about 1 kHz, as previously reported by two of us.<sup>4</sup>

Recently, the present authors have proposed a new stroboscopy based on a different sampling technique suitable to periodic phenomena at or near line frequencies (50/60 Hz).<sup>5-7</sup> The main application of this stroboscopy is observation of the dynamics when the ferromagnetic domains are excited at line frequency, which is of great importance in core materials of power electric systems, such as silicon steels. Accordingly, our early studies were on silicon steels.<sup>5-7</sup> The application of this technique to other materials is usually restricted by the lower magnetic contrast and the larger surface topographical contrast. This paper describes both the analysis of the topographical contrast and its reduction by use of an image subtraction technique, with some examples of dynamic observations on ferromagnetic amorphous samples.

### *Line-sampling Multiframe Stroboscopy*

In the new stroboscopy near line frequencies, a fast horizontal scan synchronized with the specified drive phase is applied to get total image information on this scan line within one drive phase; that is why it is called line-sampling stroboscopy. The operation of this new stroboscopy is compared with conventional point-sampling stroboscopy in Fig. 1. We see that the new stroboscopy can yield much more information corresponding to the total pixels in one scan-line than the previous point-sampling stroboscopy; the image acquisition time can be reduced to a mere 17 s under the same situation as described above.

---

Author Ikuta is with the Department of Applied Electronics, Osaka Electro-Communication University, Neyagawa, Osaka, Japan; authors Mase and Shimizu are with the Department of Applied Physics, Osaka University, Suita, Osaka, Japan.

The total acquisition time for several phase images can be also reduced by use of a multiframe-mode operation. In this acquisition mode, 2-8 different phase images can be obtained at same time on the same monitor scope by multiple line sampling within one period of the drive cycle. This operation is described in Fig. 2 for the case of a mode of 8 frames.

In the line-sampling method, only video signal strobing and no primary-beam strobing is used. The use of primary-beam strobing during the line sampling may result in a strong transient response in the detector of backscattered electrons. It causes unavoidable saturation effects at the start positions of each sampled scan line. Although very fast operation of the stroboscopic SEM has been achieved by use of beam strobing,<sup>2,3</sup> it is sufficient to use the video signal strobing at the frequency regions at which the present line-sampling stroboscopy is aimed. A remaining problem of the video-signal strobing method is sample contamination. However, this problem is largely removed by use of the multiframe mode operation for its high signal-detection efficiency. For example, the signal detection efficiency of the 8-frame mode operation amounts to about 50%; the efficiencies of the usual point-sampling stroboscopy are limited to 1-2%, to avoid motional blurring. This high efficiency with the signal detection make the contamination problem less important.

### *Surface Topographical Contrast*

Topographical contrast of the surface projection is often observed in the backscattered-electron signal, such as the magnetic contrast. The existence of the topographical contrast often makes the observation of the magnetic contrast very difficult. Fortunately Type II magnetic contrast caused by backscattered electrons increases approximately as the  $3/2$  power of the primary beam energy; therefore, higher beam energy is recommended for good image quality. For the silicon steel samples, the magnetic contrast is only a few per cent under 200kV acceleration. This contrast value results in a fairly good image for the silicon steels, even for a surface-processed sample.

On the other hand, this difficulty remains a problem in new magnetic core materials (such as the amorphous ferromagnetic materials) that contain many holes made by the quenching process and have smaller magnetization. Both approaches to reductions of the topographical contrast, based on the detection system and postimage processing, are thus highly recommended in such observations.

As to the former approach, one of us has reported the condition with the detector position where the topographical contrast disappeared.<sup>8</sup> The origin of this topographical

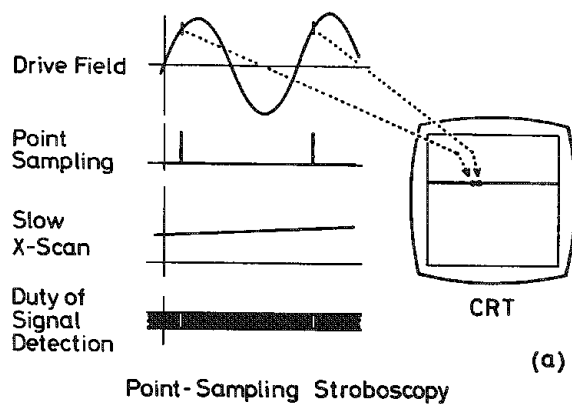


FIG. 1.--Schematic diagrams of (a) conventional point-sampling stroboscopy and (b) line-sampling stroboscopy in scanning electron microscope.

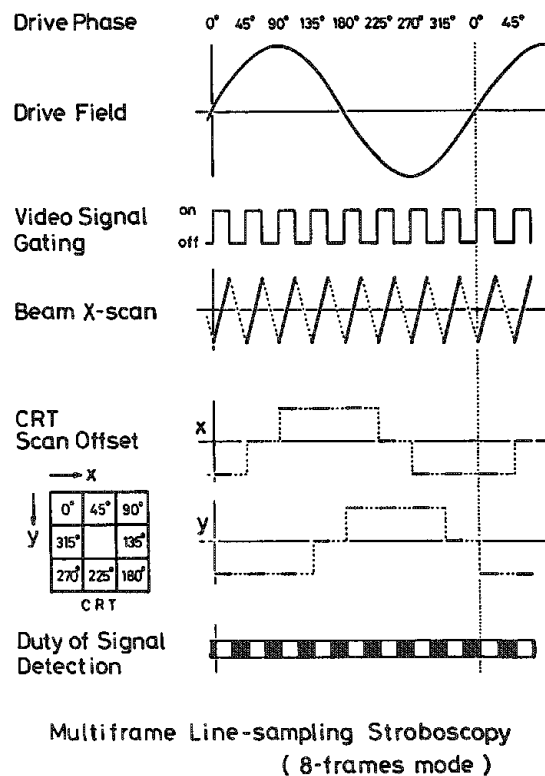


FIG. 2.--Schematic diagrams of multiframe display technique combined to line-sampling stroboscopy shown in Fig. 1(b). (Case of 8-frame mode operation.)

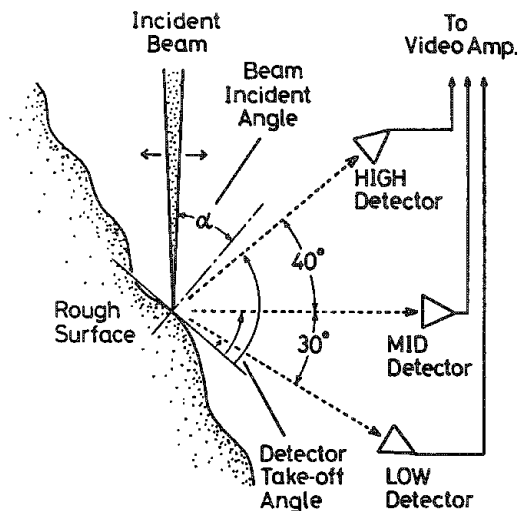


FIG. 3.--Definitions with beam incident angle and detector take-off angle.

contrast is the alteration of the beam incident angle and the dependence of the detector take-off angle on surface roughness. Figure 3 defines the beam incident angle and detector positions used in the Monte Carlo simulation,<sup>9</sup> which assumes Fe samples and 15-90keV acceleration. The results of the simulation are shown in Fig. 4(a), which shows the detection yield of the backscattered electrons as function of the incident beam angle for the three fixed detectors shown in Fig. 3. These results show that the relations between detection yield and the incident angle are almost the same when acceleration is varied from 15 to 90 keV, as are the incident angles for maximum yield. At these beam incident angles, one expects a compensation of the variation in detection yield between the increase in total yield with the increase in incident angle, and the decrease in the backward-scattered yield with the corresponding increase of the effective take-off angle.

If the period of sample roughness is large compared with the beam diffusion area, and the variation in effective incident angle due to the roughness is small, topographical contrast disappears at these optimum incident angles. As shown in Fig. 4(a), the change in these optimum incident angles with acceleration energy is very small. Therefore, almost constant values of the optimum incident angle can be extrapolated up to about 200 keV acceleration.

Figures 4(b) and (c) show the change in detection yields from the samples with different Z number under 30keV acceleration. Although the maximum value of the detection yield is increased as Z increases, the optimum incident angle remains almost same. Hence we conclude that the selection of the optimum incident angle is very effective in reducing topographical contrast with the detection of low-contrast backscattered-electrons over a wide range of samples and acceleration.

#### *Image Subtraction Technique*

If the sample roughness is great and the compensation is insufficient even when the optimum incident angle is selected, the difficulty with the topographical contrast becomes important. As described above, amorphous ferromagnetic materials are corresponding to this situation. As in the technique with the rejection of large background, it is effective to subtract an image from another one if each has same background. This subtraction technique has been already applied to the domain observation by the Keer magneto-optical method.<sup>10</sup> As a preliminary approach, we have also attempted to use this technique for the SEM magnetic domain observation using the off-line method.

In the present experiment, the observed stroboscopic images are first recorded on the photographic medium (Polaroid 667 film). Next, one of the stroboscopic images is stored in a frame integrator (Nippon Avionics, Image-Σ) by use of a CCD camera. Then another stroboscopic image used as a reference image is stored with opposite polarity. Critical positioning between the two images is needed.

This positioning is manually achieved, by use of the real-time subtraction function of the frame integrator.

The example of the image subtraction experiment is shown in Figs. 5 and 6. The observation shown in these figures were made with a commercial 200kV electron microscope (JEOL, 200CX) at 100keV acceleration, in the scanning mode. The sample used is an amorphous ferromagnetic ribbon (Allied Chemical Co., METGLAS 2605SC), and excited by a 60Hz drive field on a specially designed sample stage with magnetizing yoke.

Figure 5 shows an original stroboscopic observation of this sample. The values in each photograph indicate the respective drive phase. In these photographs, the magnetic domain is not clear for the strong topographical contrast from the surface roughness. In Fig. 6, the results of the image subtraction are demonstrated. Figures 6(a), (b), and (c) show (225° - 225°), (225° - 315°), and (225° - 0°) subtracted images, respectively. In these subtract experiments, the 225° image is used as a reference image, since the sample is considered to be magnetically saturated in this phase. Figure 6(a) is shown to indicate that manual positioning has been successfully achieved. Figure 6(c) shows clear magnetic domain images unlike in Fig. 6(b). This result suggests that a sudden magnetic reversal has occurred between 31.5° and 0°.

In Fig. 6(b), one may find some domain-like patterns. However, they are mostly not true domains but the differentiated topographical images caused by spatial distortion due to the leakage drive field on the primary beam path. The influence of the leakage flux may cause the deflection of the primary beam. In the zeroth-order approximation, this effect results in image translation, which is easily compensated for by the manual positioning between the two images. However, it results in complex distortion under the higher-order influence. In these experiments, higher-order distortion is slight but observable (Fig. 6b).

Although the present image-subtraction experiment by use of photographic films as an intermediate recording medium is a preliminary one, it is very effective in removing topographical contrast and revealing the clear domain response. It seems very easy to improve this technique into a real-time one by use of digital electronics. This approach is also effective in removing the effects caused by the nonlinearity of the recording media.

#### *Conclusions*

A new stroboscopic technique line-sampling multiframe stroboscopy and related problems with the practical application are discussed. The main application of this technique is the dynamic domain observation of ferromagnetic materials used in power electric systems. The main difficulty in the stroboscopic observation is topographical contrast due to the sample surface roughness. This paper suggests the selection of the optimum beam incident angle (which is determined by the detector position) to reduce the topographical contrast. The paper also indicates that the introduction

of the image subtraction technique is very useful, especially with ferromagnetic materials having lower magnetization and rough surfaces, such as amorphous ferromagnetic materials.

#### References

1. G. S. Plows and W. C. Nixon, "Stroboscopic scanning electron microscopy," *J. Phys.* E1: 595-600, 1968.
2. N. C. MacDonald, G. Y. Robinson, and R. M. White, "Time-resolved scanning electron microscopy and its application to bulk effect oscillators," *J. Appl. Phys.* 40: 4516-4528, 1969.
3. T. Hosokawa, H. Fujioka, and K. Ura, "Gigahertz stroboscopy with the scanning electron microscope," *Rev. Sci. Instrum.* 49: 1293-1299, 1978.
4. T. Ikuta and R. Shimizu, "A simple technique for the stroboscopic observation of magnetic domain response using scanning electron microscopy," *J. Phys.* E9: 721-724, 1976.
5. R. Shimizu and T. Ikuta, "Line-sampling multiframe stroboscopic technique for dynamic observation of periodic phenomena at low frequencies," *Appl. Phys. Lett.* 44: 811-812, 1984.
6. R. Shimizu et al., "Application of line-sampling multiframe stroboscopy for dynamic observation of magnetic domains in Si steels," *J. Appl. Phys.* 58: 1606-1609, 1985.
7. T. Ikuta, "Stroboscopic technique for dynamic observation of ferromagnetic domains at low frequencies in scanning electron microscopy," *SEM/1985 III*, 973-980.
8. T. Ikuta, "Disappearance of topographical contrast in the backscattered electron image in scanning electron microscopy," *Appl. Phys. Lett.* 42: 533, 534, 1983.
9. R. Shimizu et al., "High contrast observation of magnetic domain with high voltage SEM," *Japan J. Appl. Phys.* 15: 967-981, 1976.
10. K. Shirae and K. Sugiyama, "A CCD image sensor and a microcomputer make magnetic domain observation clear and convenient," *J. Appl. Phys.* 53: 8380-8382, 1982.

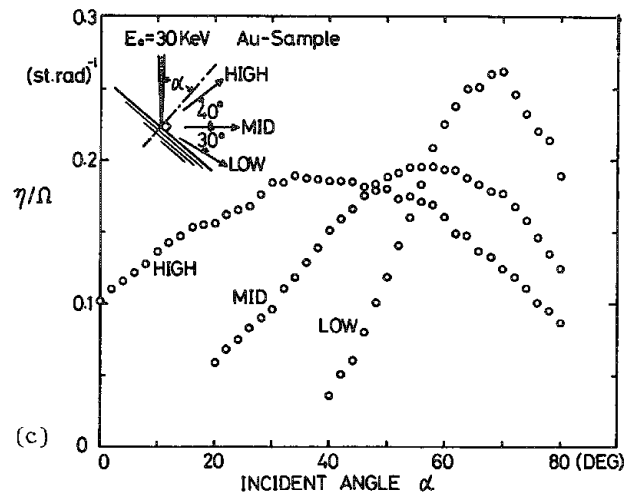
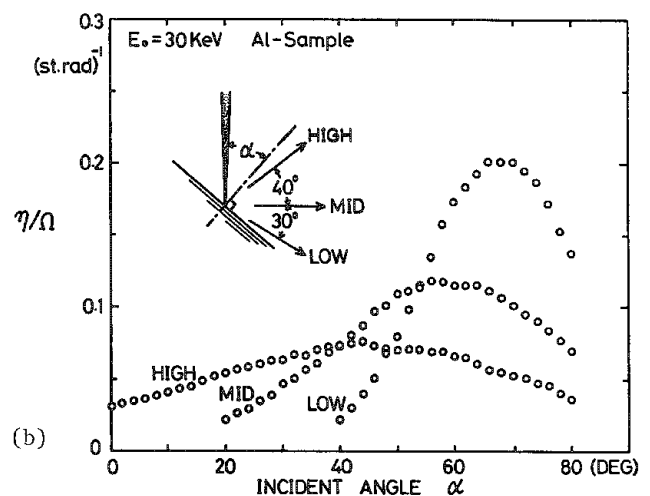
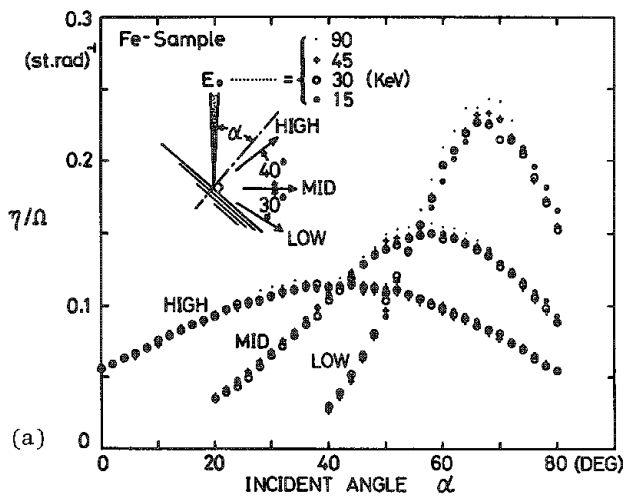


FIG. 4.--Detection yield of backscattered electrons as function of incident beam angle for three fixed position of detectors: (a) Fe ( $Z = 26$ ) at 15-90 keV, (b) Al ( $Z = 13$ ) at 30 keV, (c) Au ( $Z = 79$ ) at 30 keV.

5

# 2605SC

60Hz  
Drive Field

±0.5mm±

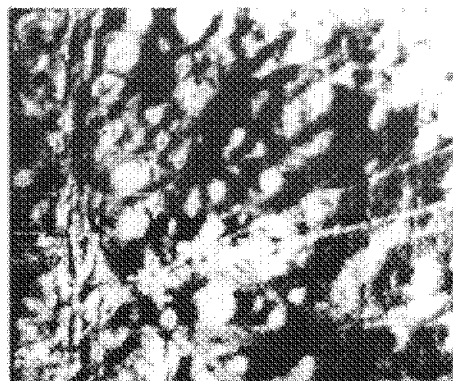
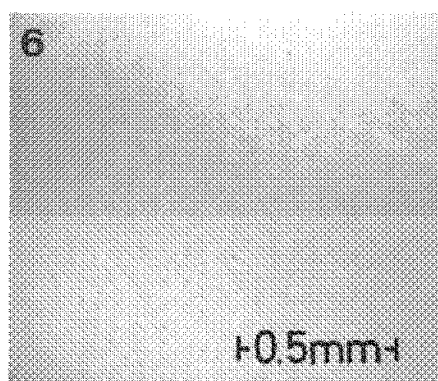
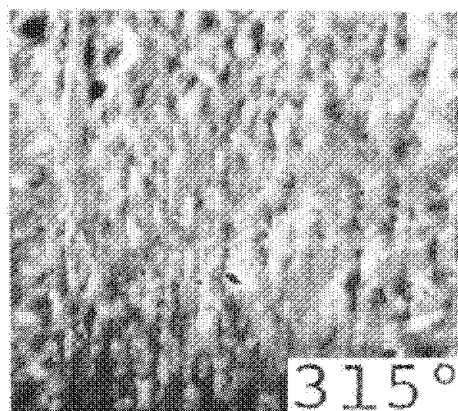
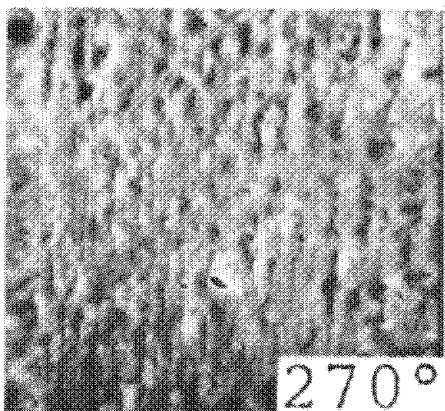
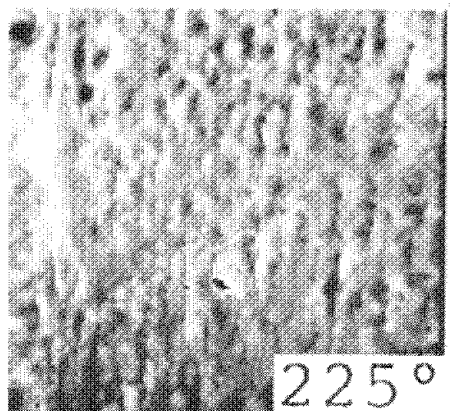
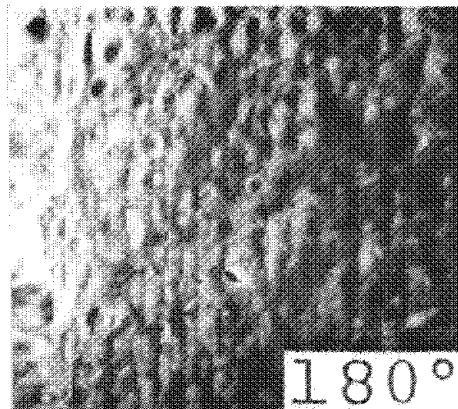
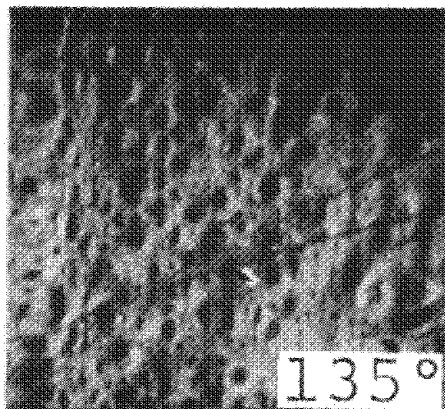
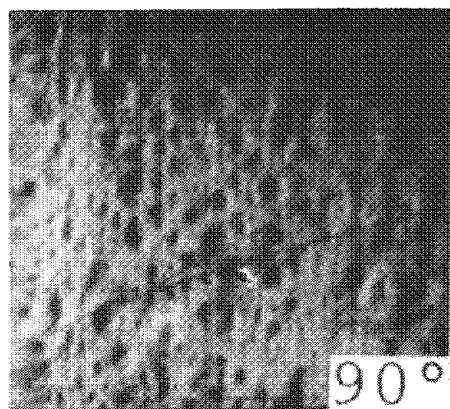
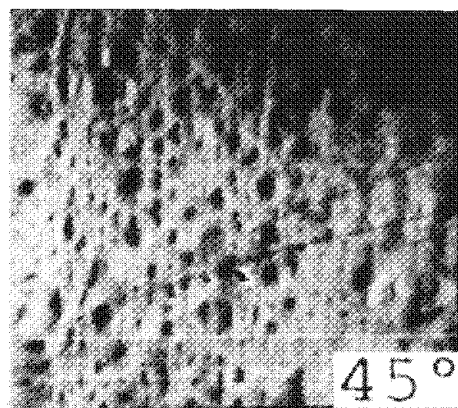
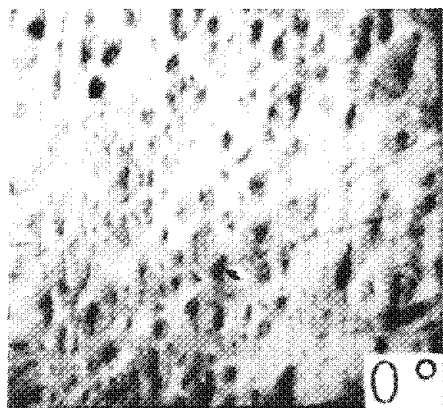


FIG. 5.--Dynamic observation of magnetic domain response in amorphous ribbon (Allied Chemical Co. METGLAS 2605SC) under 60Hz magnetic field. Number indicated on each photograph is drive phase value.

FIG. 6.--Processed images of Fig. 5. (a) 225° - 225°, shown matching at off-line processing; (b) 225° - 315°; (c) 225° - 0°.



## QUANTITATIVE ANALYSIS WITH STANDARDS ON A FIELD-EMISSION MICROSCOPE

J. F. Konopka and M. Shinohara

The field-emission (FE) gun for electron microscopes is unquestionably a boon to electron imaging. Its high brightness produces sharp images at the highest resolutions.<sup>1,2</sup> Until now, however, it has been difficult to use an FE microscope for quantitative x-ray analysis because of the instability of its probe current. Special analytical methods already in practice have mitigated this problem somewhat.<sup>3</sup> In standardless analysis, the probe current need not be known. Use of one multi-element standard for all elements in the unknown and normalization of the result also avoids the need for knowledge of the probe current. However, in many cases these methods do not apply. This paper presents a method for performing full quantitation with standards on FE SEMs.

In x-ray analysis, we need to know the total charge deposited on a sample while x rays are acquired. For quantitative analysis, all x-ray intensities from unknowns are ratioed to intensities from standards, so that only relative values of deposited charge for all unknowns and standards analyzed are needed. Thus, any value proportional to total charge may be used. In x-ray analysis performed with a thermal-emission-gun SEM, the beam current is measured with a Faraday cup and picoammeter before the x-ray data are acquired from the sample. If we assume that the beam current does not fluctuate while data are being acquired, this one-time measurement is proportional to total deposited charge. For the FE gun, this assumption does not hold: emission gradually decreases and may occasionally undergo very rapid fluctuations (Fig. 1).<sup>1</sup> The method described here continuously monitors the beam intensity while x rays are being acquired and so accounts for all fluctuations of beam intensity. This beam-monitor method is a variation of standard techniques used previously to find the correct beam current in a slowly drifting thermal-emission gun. The basic idea is to measure some accessible signal during x-ray acquisition that is linearly proportional to beam current. The average value of beam current is calculated from the average value of the signal and the measured calibration constant. Various signals can be used: backscattered electron intensity, specimen current, or final-aperture current. The easiest to calibrate is the aperture signal, which can be measured at the same time as the true beam current is measured with a Faraday cup. The final-aperture signal has sometimes been used on microprobes as a Faraday cup substitute because once it is calibrated, it provides a fast and convenient method of measuring probe current that avoids the mechan-

ical problems of introducing a Faraday cup for each measurement. Use of the final aperture signal assumes that this signal assumes that this signal is linearly proportional to the beam current while x-ray data are being acquired. Normally, as long as lens currents and other beam shaping factors remain constant, the final aperture may be expected to intercept a constant fraction of the probe current. An uncertainty that arises when this technique is applied to the FE SEM is whether the aperture signal would remain linearly proportional to beam current as the FE gun omission varies.

The SEM used in this work was the Hitachi S800 and the EDS analyzer was the Keves 8000. An electrically isolated final aperture with a buffering amplifier attached is a standard feature of the S800. The Keves system was equipped with a multiplexed, high speed, 12-bit ADC, a picoampere buffer amplifier made by Keves, and some cabling. One channel of the ADC was used to read the aperture signal; a second channel, to read the signal from the Faraday cup as buffered by the special amplifier. The standard Keves quantitative EDS software package, Quantex, was modified as described below to use these signals.

To examine the signals coming from the SEM a Forth program was written to acquire data simultaneously from the final aperture and a Faraday cup and to display these data in graphics. Figure 1 shows about 7 s of data acquired by this tool. The data are plotted in two ways. The two signals are independently plotted versus time and versus each other as a scatter plot. The two straight lines represent two calibration models being tested. This trace shows both a large step as well as smaller variations in the two signals. Note that the same signal variation is reproduced in the Faraday cup signal and the final aperture signal. By use of this tool the correlation of aperture signal and beam current was verified and the appropriate signal processing techniques were developed.

The calibration constant  $k$  relating beam current and aperture signals is  $k = S_b/S_a$ , where  $S_b$  and  $S_a$  are respectively the sums of the beam current and aperture signals measured over some fixed period of time. The effective average beam current is  $I_b = kA$ , where  $A$  is the average value of the aperture signal during the time that x rays were being acquired.

In operation, the aperture signal is calibrated each time a spectrum is acquired. Calibrations are not saved or reused. The modified Quantex software acquires x-ray data in three steps.

1. The user is prompted to move the Faraday cup under the beam. The computer then measures the aperture and Faraday-cup signals for 3 s.

---

Author Konopka is at Kevex Corp., 1101 Chess Drive, Foster City, CA 94404; author Shinohara is at the Naka Works of Hitachi, Ltd., Katsuta, 312 Japan.



2. The user is prompted to remove the Faraday cup and move the sample under the beam. The computer then integrates x rays and aperture signal for desired acquisition time.

3. Again the user is prompted to move the Faraday cup under the beam. The computer then measures the aperture signal and Faraday-cup signal for 3 s and the computer calculates the effective average beam current and stores the result with the acquired x-ray spectrum.

Except for the acquire sequence no other software changes were required for quantitation.

## Results

To show the effectiveness of this method a steel sample (SRM 348) and a mineral, garnet, were analyzed. (The garnet sample and its chemical composition were supplied by Prof. K. Mori of Kyoto University.) Table 1 lists the standards used in all analyses and their respective average probe currents. The values for probe currents are numbers that have not been scaled to standard units, as these numbers are normally used only internally by the software. Table 1 shows the results for the steel. The bottom row labeled  $I_p$  is the average probe current for each spectrum. The data were acquired for 100 s live time at 20 kV and a take-off angle of 47.9°. Although the average beam current in the five analyses varies by 17%, the results for Fe, the dominant element, vary less than 1%, which means that this variation is dominated by counting statistics and not by errors in beam-current measurement. Table 3 shows the results for the garnet sam-

ple. Data were acquired for 200 s live time. Other conditions were the same as for the steel sample. The average beam current varied by 13%, but the results for the dominant element, Si, again varied by less than 1%.

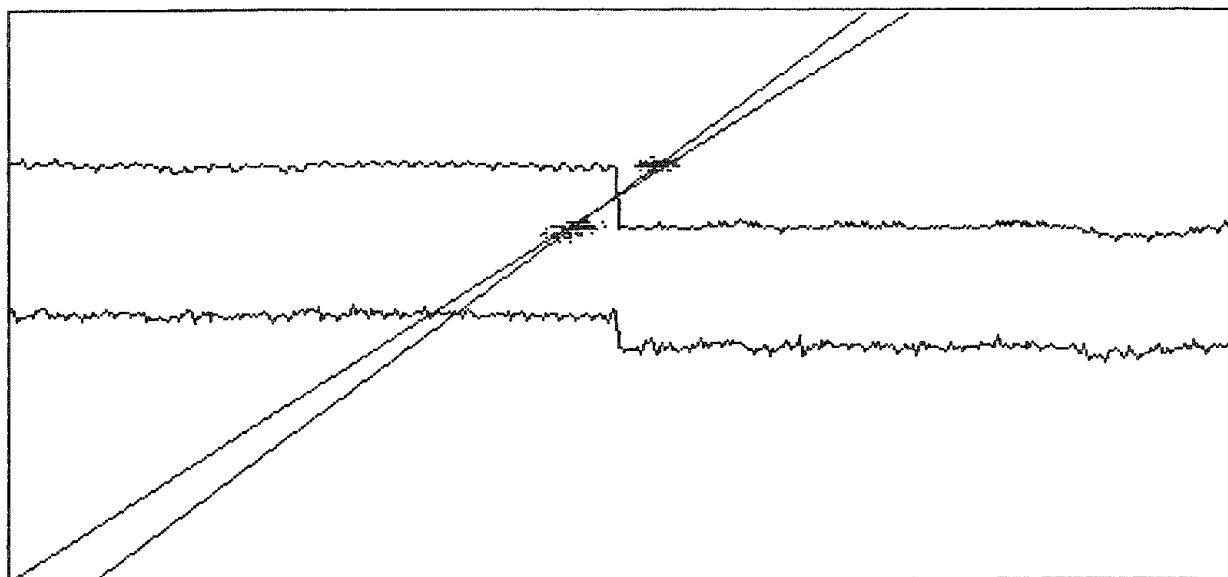
From the quality of the results the following conclusions are drawn. First, within the range of variations encountered, the aperture signal is linearly proportional to beam current. Second, quantitative x-ray analysis with standards may be routinely and reliably performed on FE-gun-equipped SEMs.

## References

1. J. I. Goldstein et al., *Scanning Electron Microscopy and X-ray Microanalysis*, New York: Plenum Press, 1981, 29.
2. M. Sato, Y. Nakaizumi, I. Matsui, and K. Kanda, "Development of the ultrahigh-resolution SEM," *Microbeam Analysis--1986*, 525.
3. Hitachi Technical Data Sheet, SEM No. 30.

TABLE 1. Standards used and relative beam currents for analysis of SRMA38 and garnet.

SRM348		Garnet	
Si	813.7	Mg	MgSiO <sub>3</sub> 88.3
Mo	801.6	Al	Al <sub>2</sub> O <sub>3</sub> 85.5
Ti	674.3	Si	NaAlSiO <sub>3</sub> 94.1
Cr	904.2	Ca	CaSiO <sub>3</sub> 91.4
Mn	938.4	Ti	FeTiO <sub>3</sub> 96.6
Fe	767.6	Mn	(pure) 141.4
Ni	625.0	Fe	Fe <sub>2</sub> O <sub>3</sub> 93.0



Faraday cup average value = 117.819  
 standard deviation = 9.659 = 8.20%  
 Aperture average value = 896.832  
 standard deviation = 61.582 = 6.87%  
 Faraday cup / Aperture = 0.131  
 Fitted slope (LSQ) = 0.153  
 Fitted intercept (LSQ) = -19.752  
 Number of points measured = 459  
 Coefficient of determination = 0.956

FIG. 1.--Plot comparing variation of beam current and aperture signal.

TABLE 2.--Results of analysis of steel sample, SRM348, five times with standards.

FE Gun Data SRM348								
	1	2	3	4	5	Std Dev	Avg. Wet Chem.	
Si	0.60	0.55	0.52	0.51	0.56	6.50%	0.55	0.54
Ti	2.16	2.18	2.06	2.13	2.01	3.38%	2.11	2.24
Cr	14.77	15.02	14.61	14.70	14.69	1.06%	14.76	14.55
Mn	1.88	1.84	1.56	1.70	1.70	7.35%	1.74	1.48
Fe	53.00	53.19	53.46	53.34	53.56	0.41%	53.31	53.30
Ni	24.59	25.43	25.16	25.44	25.51	1.50%	25.23	25.80
Mo	1.17	1.42	1.37	1.27	1.35	7.44%	1.32	1.30
Total	98.17	99.63	98.74	99.09	99.38	0.58%	99.00	99.21
Ib	761.60	747.40	1122.60	992.80	992.10	17.66%	923.30	

TABLE 3.--Results of analysis of garnet, four times with standards.

FE Gun Data Garnet							
	1	2	3	4	Std Dev	Avg. Wet Chem.	
MgO	19.46	18.91	19.08	18.70	1.69%	19.04	18.29
Al2O3	22.45	21.89	22.14	21.90	1.19%	22.10	21.93
SiO2	41.40	41.36	41.29	40.70	0.80%	41.19	40.82
CaO	4.60	4.62	4.76	4.50	2.32%	4.62	4.50
TiO2	0.90	0.88	0.96	0.94	3.97%	0.92	0.85
MnO	0.38	0.41	0.35	0.40	6.87%	0.39	0.35
FeO	12.80	12.72	13.00	12.74	1.00%	12.82	13.10
Total	102.00	100.77	101.59	99.89	0.92%	101.06	99.49
Ib	84.74	86.96	104.77	111.29	13.52%	96.94	

## DYNAMIC STUDIES OF MARTENSITIC TRANSFORMATION ON COPPER SHAPE-MEMORY ALLOYS WITH THE SEM

J. M. Guilemany, B. Mellor, J. R. Miguel, and J. Gil

Observation of the evolution of martensitic transformation on Cu-Al-Zn shape-memory alloys has been realized in a special chamber (heating and cooling stage  $\pm 250$  C) on an SEM with a BSE detector. The potential of this observation system is demonstrated. The conclusions show that the shape-memory effect is not exactly correlated with the structural-memory effect in heating/cooling cycles.

Investigations into  $\beta \rightleftharpoons$  martensite (m) transformations of copper alloys that exhibit the shape-memory effect show discrepancies in characteristics, observed during the transformation, of the evolution of various parameters with temperature (calorimetric signal, acoustic emission, and resistivity variations).<sup>1-3</sup> The possibilities of a device designed for the simultaneous measurement of acoustic emission and calorimetric signal based on an optical microscope were presented earlier.<sup>4</sup> For preliminary results of in situ studies on the SEM, see Ref. 5.

### Methods and Procedures

A backscattered electron (BSE) detector and a heating/cooling stage have been adapted to an SEM of 60Å resolution (Fig. 1) to enable study of the dynamic martensitic transformation on copper shape-memory alloys. The BSE detector makes it possible to obtain images differentiated by their average atomic number due to the different atomic density of the oriented planes of the free surface, a capability that is the more important because martensitic transformations have very poor definition with secondary-emission electronic images.

The heating/cooling stage permits work within the range  $\pm 250$  C and is regulated by a heating resistance and a cooling circuit of N<sub>2</sub> gas refrigerated by liquid nitrogen. A thermocouple of Cu-Const insures control by a precise temperature regulator. A polycrystalline SME alloy (78.23% Cu, 6.28% Al, 15.49% Zn, wt), vacuum melted and thermally treated (10 min at 850 C and water quenched to room temperature) with  $M_s = 15$  C, exhibiting a  $\beta$ -structure, is submitted to heating/cooling cycling within  $\pm 65$  C. Samples are prepared by conventional methods of obtaining polished surfaces.

### Experimental Results

A detailed cycle within the temperature range +62 C to -30 C is shown in Figs. 2-15.

The authors are at the Department of Metallurgy of the University of Barcelona, except author Mellor, who is at the Department of Engineering Materials of the University of Southampton, England. We thank CAICYT (Research project PA-85-0084) and Generalitat de Catalunya for their financial support.

A reference point appears at the right of each picture.

The representative structure of  $\beta$ -phase shown in Fig. 2 (65 C) corresponds to a portion of a  $\beta$ -phase crystal. The BSE image of intracrystalline  $\beta$ -phase shows subgrain boundaries.

Early transformation lines appear at 14 C (Fig. 3) and continue to grow; other lines appear between 14 C and 8 C (Figs. 3,4). Lines show an irregular distribution with orientation angle, even though some of them show some parallelism. Stronger lines with differentiated orientation appear at 4 C (Fig. 5), where some of the earlier lines disappear. The new lines must be produced by high-atomic-density planes, according to the BSE image.

The gradual evolution of the  $\beta \rightarrow$  martensite transformation is shown in Figs. 6 (3 C), 7 (1 C), 8 (-1 C), 9 (-3 C), and 10 (-4 C). In this sequence we can observe that some lines appear and disappear due to the growth of other martensitic crystals (e.g., Figs. 8 and 9).

Martensitic crystallographical orientations exhibit mobility by temperature, as in Figs. 11 (-7 C), 12 (-8 C), 13 (-13 C), and 14 (-19 C)). The final structure is shown in Fig. 15 (-30 C), and 14 (-19 C). This structure is to be compared with the final ones of other cycles.

The transformation martensite  $\rightarrow \beta$  (heating) is very slow, as evident from a comparison of Fig. 16 (0 C) with Fig. 15 (-30 C). Only a small part of the structure has been transformed at a temperature near, but below,  $A_f$ , as seen in Fig. 17 (28 C) but it suddenly evolves within a very narrow range of temperatures. Figure 18 (33 C) shows the completed transformation.

Comparison of Figs. 2 and 18, corresponding to the original and re-heated structure, shows that the structure has been totally regenerated.

Cooling/heating cycling of the same area shows that early lines (Fig. 4, +8 C) present the same orientation but not the same position (Fig. 19, +9 C). Martensitic crystals present the same effect, i.e., the same orientation but different position in relation to the reference point; compare Fig. 20 (+3 C) with Fig. 6 (+3 C), Fig. 21 (+1 C) with Fig. 7 (+1 C), Fig. 22 (-2 C) with Fig. 9 (-3 C), Fig. 23 (-6 C) with Fig. 11 (-7 C), and Fig. 24 (-15 C) with Fig. 13 (-13 C). The final structure in Fig. 25 (-32 C) is very different from Fig. 15 (-30 C).

Hot structures of this cycle (Fig. 26, 39 C), and of other cycles (Fig. 28, 39 C; Fig. 30, 45 C), reproduce the original  $\beta$  structure shown in Fig. 2; cool structures (Fig. 27, -40 C; Fig. 29, -40 C; Fig. 31, -40 C) are different from one another.

Detection of other parameters (acoustic

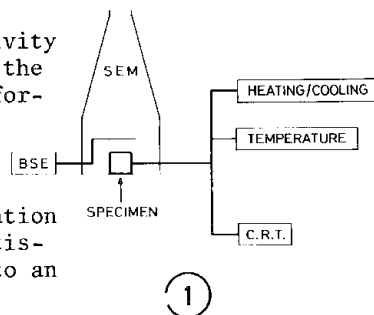
emission, calorimetric signal, and resistivity measures) can be done at the same time as the observation of the evolution of the transformation  $\beta \rightleftharpoons$  martensite.<sup>5</sup>

### Conclusions

The evolution of martensitic transformation on shape-memory alloys can be followed satisfactorily with a special chamber adapted to an SEM ( $\pm 250$  C).

BSE images are an important factor in in situ SEM studies of martensitic transformations on polished samples.

Final martensitic structures obtained in different cycles show pattern differences while maintaining a similar orientation: the material presents a macroscopic shape-memory effect but not a microscopic structural-memory effect.

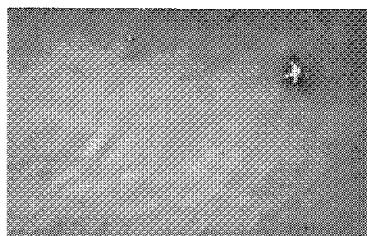


### References

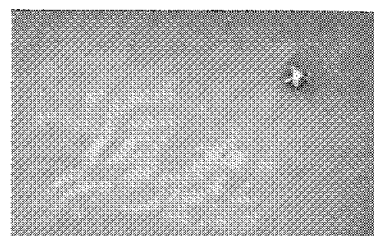
1. A. Planes and J. L. Macqueron, *An. Fis. Ser. B*, 78: 39, 1982.
2. R. Rapacioli et al. *Proc. Jornades Transformacions Termoelastiques*, Col. Conf. Commun 1, University of Palma de Mallorca, 1984.
3. L. Delay et al., *Memory Effect, Superelasticity, and Damping in Cu-Zn-Al Alloys*, Rep. 78R1, Dept. of Metallurgy, Cath. Univ. of Leuven, 1978.
4. V. Torra, J. M. Guilemany, and E. Cesari, *Termochimica Acta* 99: 19-25, 1986.
5. J. M. Guilemany, J. R. Miguel, V. Torra, and E. Cesari, *Rev. Roy. Acad. Sci.* (in press).



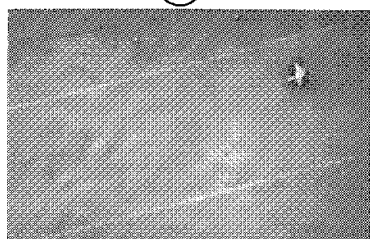
②



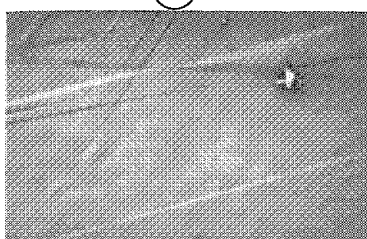
③



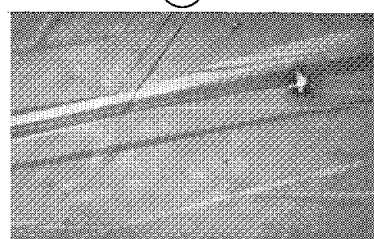
④



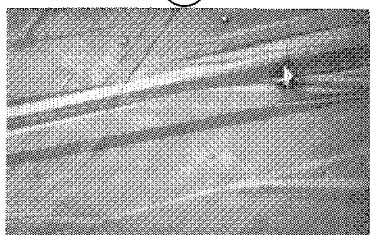
⑤



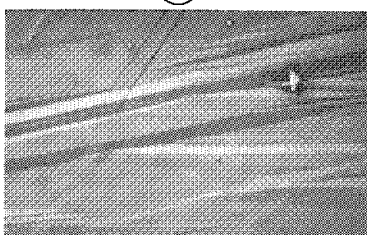
⑥



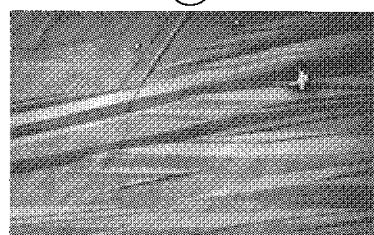
⑦



⑧



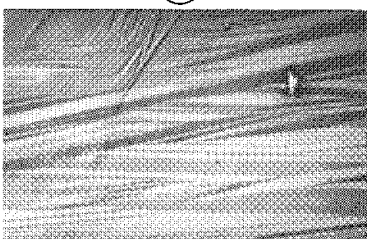
⑨



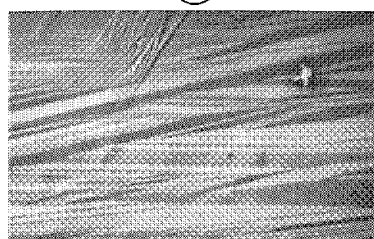
⑩



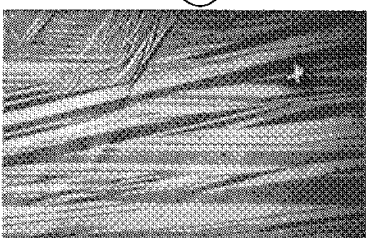
⑪



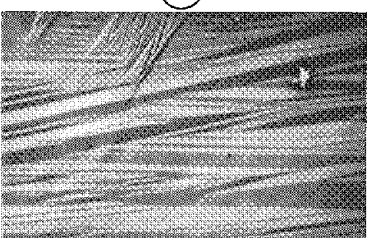
⑫



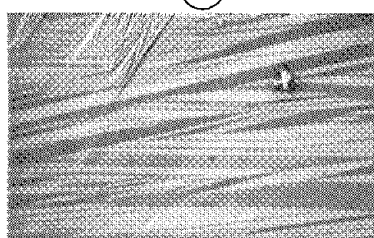
⑬



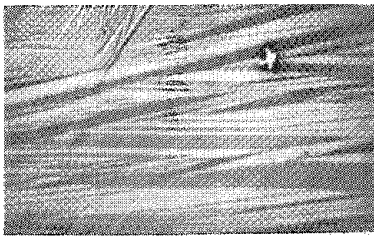
⑭



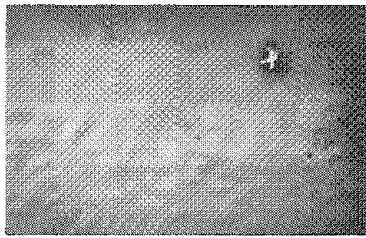
⑮



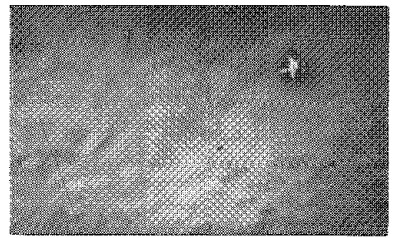
⑯



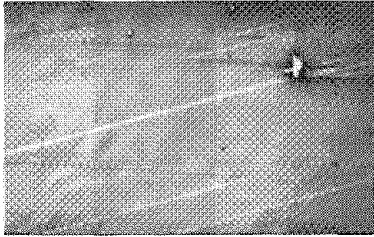
17



18



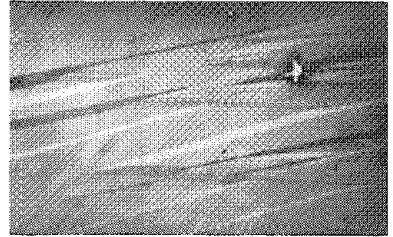
19



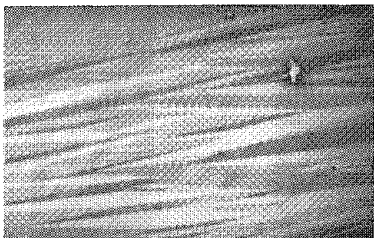
20



21



22



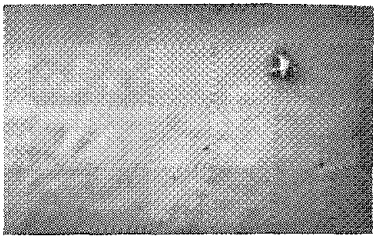
23



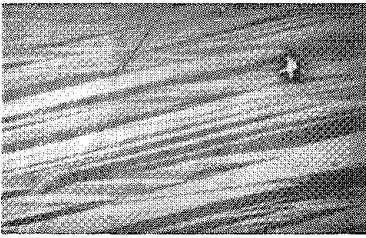
24



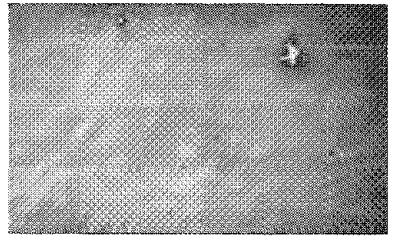
25



26



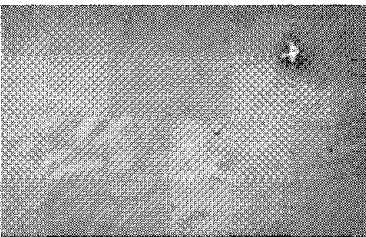
27



28



29



30



31

### 3C. SEM: Image Simulation

#### MONTE CARLO MODELING OF keV ELECTRON SCATTERING IN A CHARGED-UP INSULATOR

Masatoshi Kotera and Hiroshi Suga

If an insulator is bombarded by an electron beam, a positive or a negative charging-up takes place depending on various parameters. The charging-up phenomenon is observed for every insulator in the entire energy region of electron irradiation. It usually causes difficulties in the following analyses and processes. Above 10 keV the charging-up can result in an image distortion in the scanning electron microscope (SEM), a pattern distortion in electron beam lithography, and even an electric breakdown of the specimen. Below 2 keV, the SEM voltage contrast image disappears if the electrodes are covered by an insulating material. Although many papers on charging-up have been published, the analysis of the mechanism remains inadequate, especially in its dynamic process.<sup>1-5</sup>

As the first step of an analysis, we propose a new simulation model of incident-electron behavior, in order to gain a better understanding of some phenomena found at high-energy electron-beam irradiation, by analyzing the electron deposition in the target material and the build-up of an electric potential. A Monte Carlo simulation of incident-electron behavior in solids is well known.<sup>6</sup> Since this simulation is made in three-dimensional space, the boundary condition is flexibly set up.<sup>7</sup> For example, one can explain how the magnetic domain contrast of a ferromagnetic material in the SEM is created by adding the Lorentz force to the simulation. Similarly, one can explain the effects of an electric field in the specimen caused by charging by modifying the simulation. The present study offers a quantitative discussion on the extent of the situation in the electron-penetration depth and the variation in the backscattering coefficient as a function of the charging-up.

##### *Simulation Model*

We make the following assumptions. (1) The insulating specimen is a 1mm-thick PMMA wafer. (2) The electron beam energy is 20 keV. (3) If the behavior of the incident electrons in the virgin specimen is given by a previous Monte Carlo simulation, the distribution of the deposited electrons can be obtained. (4) In accordance with an electron dose, the distribution of (3) is regarded as the accumulated charge-density distribution. (5) We call the doping of a charge to the virgin specimen the "pre-charging" and the electron dose the "pre-charging dose." (6) The charge varies in depth only. (7) From the accumulated charge and the boundary condition of the specimen one can calculate the potential distribution. (8) The incident electron to the specimen undergoes deflection in this electric

field during elastic and inelastic scatterings.

PMMA maintains its insulation up to  $10^7$  V/cm at 0 °C and the relative permittivity is 4.0. The validity of the previous Monte Carlo simulation has been confirmed by an experiment in the electron-beam lithography of a PMMA wafer whose surface has been metallized to avoid the effects of the charging.<sup>8,9</sup> Figure 1 shows a depth distribution of deposited electrons calculated by the previous Monte Carlo simulation. The maximum range of electron penetration is 7.0  $\mu\text{m}$ . We assume only one-dimensional variation in electron deposition for simplicity, as is actually the case for a large-area exposure of the specimen with a defocused broad electron beam. The Monte Carlo simulation gives the probability density of the electron deposition in units of  $\text{cm}^{-1}$  for one electron incidence (Fig. 1). With the precharging dose given in  $\text{C}/\text{cm}^2$ , we obtain the accumulated charge density ( $\text{C}/\text{cm}^3$ ) at any depth. In reality, the accumulated charge may change owing to the electron-beam-induced conduction and the secondary-electron emission during subsequent electron bombardment. We ignore these effects for simplicity.

From the accumulated charge and the geometrical boundary condition of the specimen, we obtain the potential distribution in the PMMA. We assume that the specimen is in the SEM, with a grounded polepiece of the objective lens 10 mm above the specimen surface, and with a grounded specimen holder beneath the specimen. The potential distribution within 10  $\mu\text{m}$  from the specimen surface is calculated by the successive over-relaxation (SOR) method.<sup>10</sup> The calculated potential distributions for various precharging doses (Fig. 2) show that the potential is proportional to the precharging dose. Because the grounded position is established far from the plotted region, the potential changes vary little with depth. This calculation method can be applied to any electron-deposition distribution, to be obtained with more detailed consideration in future.

We next describe the newly constructed electron-scattering model. This model is based on the following assumptions. (1) Angular scattering of an electron due to elastic collision with atoms is calculated from the screened Rutherford equation. (2) Energy loss of an electron due to inelastic collisions is calculated from the modified Bethe equation of Rao Sahib and Wittry.<sup>11</sup> (3) An electron trajectory is expressed stepwise, where the step length equals the elastic scattering mean free path. [Assumptions (1)-(3) are the same as in the previous model.<sup>9</sup>] (4) The electron deflection due to the electric field around the electron is taken into account in every trajectory step. (5) The potential difference between the beginning and the end of each step is converted into electron kinetic energy.

---

The authors are at Osaka Institute of Technology (Department of Electronic Engineering), Omiya, Asahi-ku, Osaka, Japan.

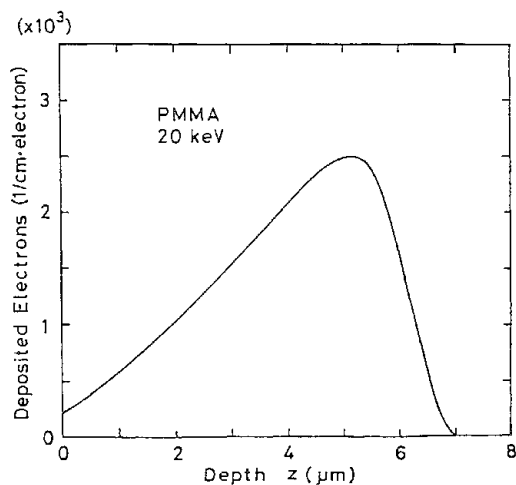


FIG. 1.---Depth distribution of electron deposition in PMMA.

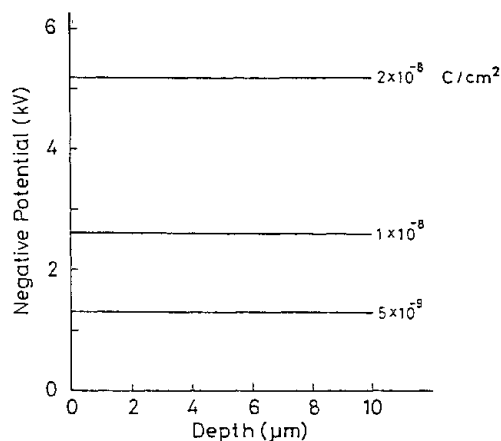


FIG. 2.---Depth distribution of calculated potential.

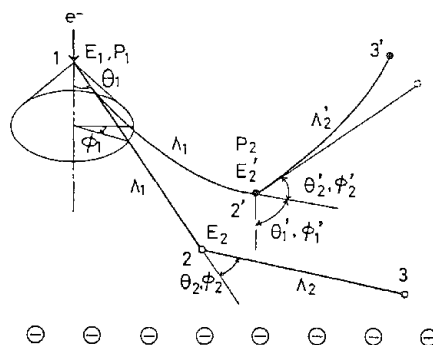


FIG. 3.---Schematic diagram of models for electron scattering.

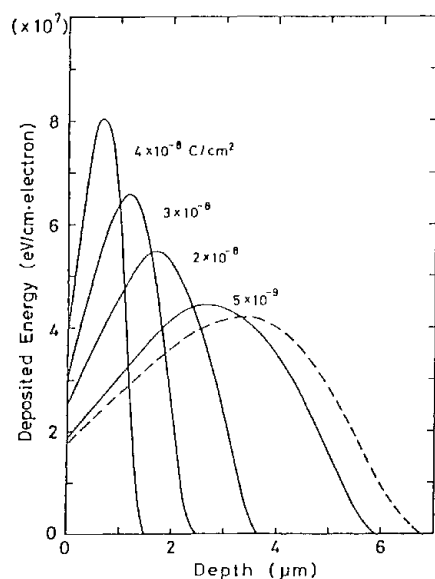


FIG. 4.---Depth distribution of electron energy deposition in charged-up specimen.

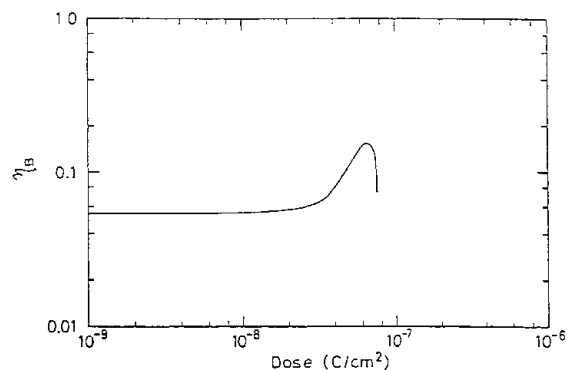


FIG. 5.---Variation of backscattering coefficient in function of precharging dose.



(6) If the kinetic energy drops below 0.1 keV, we regard that electron has stopped.

The present model is based on the previous single-scattering model, but the electron motion in each step is expressed by the equation for electron motion in the electric field. Figure 3 shows one electron trajectory in the present model. The previous model is also shown for comparison. For an electron at position 1 in the figure, the electron scattering is as follows: the electron kinetic energy is  $E_1$ , the potential energy is  $P_1$ , the scattering angle  $\theta_1$  and the azimuthal angle  $\phi_1$  are determined by the screened Rutherford equation and random numbers, and the step length  $\Lambda_1$  equals the elastic scattering mean free path. In the previous model the step ends at position 2 and the electron kinetic energy at 2 is  $E_2 = E_1 - \Delta E_1$ , where  $\Delta E_1 = \Lambda_1 \cdot dE/dx_{E_1}$ , from the modified Bethe equation. In the present model the step ends at 2, where the potential energy is  $P_2$ . The kinetic energy is  $E_2' = E_1 - \Delta E - (P_2 - P_1)$  and the directing angles at 2' are  $\theta_1'$  and  $\phi_1'$ , as shown in the figure. As expressed above, an elastic scattering occurs at 2' and the simulation continues. The validity of assumption (6) can be determined from the difference between the energy lost by inelastic processes and the energy obtained from the surrounding electric field. We have confirmed that an electron will not start moving in the present simulation in an electric field of around  $10^7$  V/cm, which is the electric breakdown field of PMMA.

#### Results and Discussion

In the present study we discuss the influence of the precharging on the penetration depth and on the backscattering coefficient. Figure 4 shows depth distributions of energy deposition for various precharging doses. As shown in Fig. 2, the surface potential increases as the precharging dose increases. Then, the effective incident energy of electrons decreases. When the precharging dose is  $1.8 \times 10^{-8}$  C/cm<sup>2</sup>, the electron penetration is 60% of the electron range for the uncharged specimen. When the precharging dose reaches  $7.7 \times 10^{-8}$  C/cm<sup>2</sup>, the surface voltage is up to the electron-beam accelerating voltage and no

electron can get into the specimen. This electron dose is much smaller than the value commonly used in electron-beam lithography, EPMA, etc. The variation of the backscattering coefficient of electrons in a function of the precharging dose is shown in Fig. 5. The increase of the coefficient with the dose is explained mainly by the decrease of the diffusion depth of incident electrons in the specimen. In that case the escape probability of scattered electrons from the surface increases. Even when no electron can get into the specimen at  $7.7 \times 10^{-8}$  C/cm<sup>2</sup> for the precharging dose, the maximum electric field in the specimen is only  $4.3 \times 10^4$  V/cm. Consequently, the range reduction and the variations found in the backscattering coefficient can be caused only by the potential elevation at the specimen surface. It should be necessary to calculate an electron behavior in the same insulator whose surface is grounded and compare the results with the present data. Future studies should consider the effects of the electron-beam-induced conduction and the secondary-electron emission from the specimen surface for much more precise analyses of the specimen charging.

#### References

1. R. D. Van Veld and T. J. Shaffner, *SEM/1971*, 17-24.
2. B. Gross et al., *J. Appl. Phys.* 44: 2459, 1973.
3. D. M Taylor and A. A. Al-Jassar, *J. Phys. D17*: 1493, 1984.
4. C. Le Gressus et al., *SEM/1984* 1: 41-48.
5. J. Cazaux, *J. Appl. Phys.* 59: 1418, 1986; *Microbeam Analysis--1986*, 527-531.
6. See for example, NBS Spec. Pub. 460, 1976.
7. D. E. Newbury et al., *ibid.*, 151-164.
8. R. Shimizu et al., *J. Appl. Phys.* 46: 1581, 1975.
9. D. F. Kyser and K. Murata, *Electron and Ion Beam Science and Technology*, 1974, 205-223.
10. Details of the calculation will be reported elsewhere.
11. K. Murata et al., *J. Appl. Phys.* 54: 1110, 1983.



## IMAGE SIMULATION FOR THE SEM

D. C. Joy

Computer-simulated micrographs have long been used by high-resolution transmission electron microscopists as an aid to image interpretation; in fact, many microscopists probably spend more time computing images than taking them experimentally. Scanning electron microscopists, on the other hand, mostly analyze and interpret images by relying on the apparent similarity between the way objects appear in the SEM and the way our eyes perceive things in the real world. Although the success of this approach has been a factor in promoting the widespread use of the SEM, with the advent of instruments capable of atomic level resolution and with the current interest in the use of SEMs as a tool for critical-dimension metrology in the semiconductor industry, there is now a need for more rigorous and qualitative models with which to compare images.<sup>1,2</sup>

### *Techniques for Image Simulation*

In order to simulate a line profile from (or the complete image of) some feature we need to be able to calculate the expected backscattered (BS) or secondary electron (SE) signal from the specimen for any given beam position. Three general types of models by which this calculation can be performed have been described. These models differ not only in their level of sophistication but in their area of applicability. The simplest model relies on macroscopic observation that the BS and SE yields both vary as the secant of the angle of incidence of the beam to the specimen surface. If we apply reciprocity (i.e., replace the electron detector with a light source with the eye of the observed), the secant variation is transformed into a cosine variation, which then exactly corresponds to the familiar Lambert cosine law in optics. We can now predict that the SEM image will have the form of the optical image illuminated from the detector position and viewed from above, with surfaces tilted toward the detector bright and surfaces away from detectors dark. It is this model, alluded to earlier, that has formed the basis of most image interpretation in the SEM. At the low-magnification limit of the SEM, where the pixel element size is many microns and thus larger than the electron interaction volume, this model provides an adequate and useful description of the image consistent with the level of information to be expected under these conditions.

At higher magnifications, where the pixel size is comparable with the diameter of the beam interaction volume, a model that incorporates more of the detail of the electron-solid interaction is required. A typical solu-

tion has been the diffusion model, in which the beam interaction is represented as a point source, at half the electron range beneath the surface, from which electrons diffuse toward the surface with some characteristic attenuation length  $L$ .<sup>3,4</sup> Provided that the scale of surface topography is significantly larger than  $L$ , this approach can give a good description of the signal variation with beam position. The technique has the merit that the calculation can usually be performed in a closed analytic form and is therefore very rapid. However, it cannot be accurately applied to features whose size is less than  $L$ , and it is not easily used in multi-component materials. Nor does this model provide a description of the angular or energy distribution of the emitted electrons, and thus the effect of detector configurations on the image cannot be determined.

The third technique for image computation uses Monte Carlo simulation. In this method, random numbers are used as variables in the equations which determine electron scattering and energy loss so that complete electron trajectories can be simulated. By computing a large enough number of such trajectories, one can accurately model the details of the electron-beam interaction with a solid. Provided that the details of the Monte Carlo model are properly set up, such a simulation is useful down to a scale of a few Å while providing full detail on the energy, direction of motion, and position of every electron, both inside the specimen and as it leaves the specimen. Not only can the effect of different detector configurations be investigated, but specimens of arbitrary geometry and complexity can be handled. The Monte Carlo method therefore provides the ideal tool for signal computations in the simulation. The drawbacks of the technique are two-fold. First, considerable computation time is involved in generating sufficient trajectories to produce a statistically accurate result. However, Monte Carlo programs are ideally suited to personal computers, so that the time required is not expensive. The other drawback is that, as described above, the program only provides data about incident and backscattered electrons, whereas for SEM purposes the secondary electron image is of major interest. Although interactions giving rise to the production of secondary electrons can be incorporated, such programs are cumbersome and slow, and of limited validity.<sup>5</sup> However, this problem can be solved if the Monte Carlo simulation is combined with a simple phenomenological model of secondary production, which allows both BS and SE yields to be computed simultaneously. It is this model that forms the basis of the simulations described here.

---

The author is with the EM Facility, Walters Life Sciences Building, University of Tennessee, Knoxville, TN 37996.

A simple procedure for calculating secondary yields was given by Salow and has been subsequently developed by many other workers.<sup>6,7</sup> Consider an incident electron traveling vertically down into the sample (Fig. 1). If its energy is  $E$  at a depth  $z$  beneath the surface, then the number  $N$  of secondary electrons produced is

$$N = -(1/\epsilon) dE/dz \quad (1)$$

where  $\epsilon$  is the energy needed to produce one secondary electron. The secondaries are assumed to diffuse away from their creation point with a characteristic attenuation length  $\lambda$ , so that the probability  $p(s)$  of traveling a distance  $s$  from the source point is

$$p(s) = \exp(-s/\lambda) \quad (2)$$

The overall probability  $p(z)$  of reaching the surface from depth  $z$  is then<sup>8</sup>

$$p(z) = 0.5 \exp(-z/\lambda) \quad (3)$$

Thus the total secondary yield  $\delta$  is

$$\delta = \int Np(z) dz = -(1/2\epsilon) \int \frac{dE}{dz} \exp(-z/\lambda) dz \quad (4)$$

In the original derivation,  $dE/dz$  was estimated from a simple analytical approximation for the electron range, so that the variation of secondary yield with incident energy can be found analytically. Although greatly oversimplified, the Salow model provides a useful approximation to the yield curve.

The model can be improved and generalized if it is incorporated as part of a Monte Carlo simulation.<sup>9,10</sup> The simulation provides the energy loss required in Eq. (1), and because the coordinates of the trajectory of each electron are completely specified, the escape probability to the surface (Eq. 3) can be integrated point by point to give the resultant secondary yield. The variables  $\epsilon$  and  $\lambda$  are found by comparison of computed secondary yields as a function of beam energy with experimental data; e.g., for silicon  $\epsilon$  is 70 eV and  $\lambda$  is 30 Å, and for copper  $\epsilon$  is 125 eV and  $\lambda$  is 25 Å.<sup>10</sup> This simple hybrid model gives excellent results for a wide range of materials and experimental conditions, and provides an ideal foundation for the proposed image modeling because both the secondary and backscattered yields are computed simultaneously. The final step is therefore to see how it can be applied.

### *Modeling a Real Specimen*

The most important decision one must make when preparing to compute an image or a line profile is the spatial resolution of the simulation. That is not simply a matter of matching the spacing of the computation points to the pixel spacing of the experimental micrograph, but also of choosing to use approximations appropriate to the signal mode to be used. The secondary electron signal is usually described as being the sum of three components: SE<sub>I</sub>, the secondaries produced at the incident beam point; SE<sub>II</sub>, the secondaries by exiting backscattered electrons in the sample; and SE<sub>III</sub>, secondaries produced by the impact

of BS electrons on the polepiece and specimen chamber walls of the SEM.<sup>11</sup> Typically only 10-15% of the total SE signal is made up of the SE<sub>I</sub> component, but in an unoptimized instrument 50% or more may be SE<sub>III</sub>. Peters has pointed out that the spatial resolutions of these components (and of the information that they carry) are quite different.<sup>12</sup> The SE<sub>I</sub> signal has a spatial resolution of the order of  $\lambda$  and so is a high-resolution mode. However, in order to make use of this information, the pixel resolution of the image must also be comparable to  $\lambda$ , else the contrast is not visible. Hence SE<sub>I</sub> contrast is only significant at magnifications of typically 20 000× or higher. Below that the signal contrast is carried by SE<sub>II</sub> and SE<sub>III</sub> electrons.

If a high magnification (SE<sub>I</sub>) image is to be simulated, the approximations used in the model must also be on an appropriate scale. Both the SE generation function (i.e., the Monte Carlo simulation used in Eq. 1) and the modeling of the surface and the integration used to determine the escape probability function (Eq. 3) must be carried out by use of numerical techniques with a scale of tens of Å. When simulating a lower-magnification image, where the image contrast is carried by the SE<sub>II</sub> and SE<sub>III</sub> electrons, correspondingly lower-resolution models can be employed. To illustrate these points, let us consider a particular example. Quantitative image simulation is required when the SEM is used to measure the width of a structure such as interconnect line in an integrated circuit. Such Critical Dimension Metrology now forms an important part of the usage of the SEM by the semiconductor industry.<sup>2</sup> Metrology relies on the assumption that it will be possible to deduce, from the form of a suitably positioned SE or BS line, profile information about the physical dimensions of the specimen. To do that, one must clearly be able to predict how the contrast features in the line profile relate to the geometry of the sample. Figure 2 shows the crosssection of a basic example of the type of structure that might be measured, a line of photoresist 1 µm wide by 0.5 µm high, on a substrate of silicon. Experimentally the profile of such structures is scanned with the beam stepping at 100 or 200 Å intervals, and with a probe size of typically 250 Å, which implies that only SE<sub>II</sub> and SE<sub>III</sub> contrast effects will be significant.

Since we are modeling at a relatively low resolution, the specimen can be treated as determined by planar surfaces with no fine structure of their own. The Monte Carlo model, which provides the electron trajectories and hence the generation function for the secondary electrons, also needs only a resolution of a few hundred Å. Such a resolution can be achieved by use of a plural scattering model.<sup>13</sup> In this model, the electron range (determined from the Bethe continuous slowing approximation) is divided into 50 or so steps of equal length. Since electron ranges are of the order of a few microns for incident beam energies of 10-20 keV, the segment steps are a few hundred Å in length and so compatible with the required scale of the simulation. Along each step segment of the trajectory the electron is

assumed to travel in a straight line; at the end of the step the electron is scattered through an angle derived from the screened Rutherford cross section. The parameters in this function are chosen so that the experimentally determined backscattering coefficient for the material is obtained when a sufficiently large number of trajectories are simulated. The energy loss along each step is found from the Bethe expression and the known step length, and then used in Eq. (1) to find the rate of secondary electron generation. This type of model is simple but gives excellent data and runs rapidly (several trajectories per second) even on small computers.

As would be expected, one finds the backscattered signal yield as a function of the incident beam position by tracking each electron and counting the number that leave the specimen. However, since we are attempting to simulate an experimental situation, this simple criterion must be modified so that only backscattered electrons that would actually strike the detector form part of the computed profile. In the examples shown here the backscattered detector is assumed to be an annular device symmetrically placed about the incident beam and effectively subtending a hemisphere at the specimen. However, in a more restricted detector geometry, electrons that missed the detector might still strike the specimen chamber walls and generate SE<sub>III</sub> electrons, and so this number would also be stored. Finally, electrons that leave the structure with a positive component of velocity in the z-direction, that is toward the silicon, will be "re-collected" by the sample. Such electrons must therefore continue to be tracked until they finally lose their energy or are backscattered again.

Secondary electrons are generated throughout the beam interaction volume, but the SE signal actually detected depends on the number that reach the specimen surface; i.e., on the escape probability. In the discussion above use was made of the so-called "straight-line approximation," which treats the secondaries as diffusing away from their generation point without scattering.<sup>14</sup> The probability of finding a secondary at a given distance from its generation source then varies as in Eq. (2). For a point source at a depth z beneath an infinite plane, integration of Eq. (2) yields Eq. (3). If the secondaries are generated at a uniform rate along the trajectory step whose starting z-coordinate is z and whose final z-coordinate is z<sub>n</sub>, the corresponding escape probability is:

$$p(z, z_n) = \frac{\lambda/2}{z - z_n} [\exp(-z/\lambda) - \exp(-z_n/\lambda)] \quad (5)$$

In order to obtain a comparable result for a real specimen, such as that in Fig. 2, which has many surfaces, a solution based on a suggestion by Newbury (private communication) has been adopted. Consider the situation shown in Fig. 3, with the generation point in a volume defined by three surfaces. The perpendicular distances between the start and finish of the trajectory step and each of the three surfaces are calculated by use of the standard results of coordinate geometry. If these distances

are (A, A<sub>1</sub>), (B, B<sub>1</sub>) and (C, C<sub>1</sub>), the escape probability p is

$$p = p(A, A_1) + p(B, B_1) + p(C, C_1) \quad (6)$$

where p(A, A<sub>1</sub>) is the result of Eq. 5 with A, A<sub>1</sub> substituted for z and z<sub>n</sub>, etc. It is clear that this approximation is deficient, not least because the multiplying pre-constant (i.e., 0.5) is not adjusted even at an edge where the solid angle subtended by the plane is reduced. As a result p() is overestimated in such regions. However, because the exponential terms decay rapidly (in a distance of the order λ), the error is confined to a narrow region (one or two pixels) around each edge and so is not a major limitation to the simulation.

The program to implement these procedures is written in PASCAL and run on an AT&T 6300PC. As with any Monte Carlo simulation the precision is inversely proportional to the square root of the number of trajectories; here 5000 or more trajectories are used per pixel to give a 1% precision. Data are calculated at 100 to 1000 Å intervals and then interpolated to produce a profile at uniform 100 Å steps. In order to produce the most general result the computation done on the assumption of a zero-diameter electron probe. The resulting line profile or image is then convoluted with a spread function to give data for a particular probe size.

## Results

Figure 4 shows SE and BS line profiles from the structure of Fig. 2 at 15, 10, 5, and 3 keV and for a Gaussian probe of 250 Å. The rapid variation of the profiles with beam energy demonstrates how dominant the effect of the beam interaction is compared to the influence of the geometry of the structure. At 15 keV, the electron range in both materials is about 3 μm, greater than either the width or height of the line. The SE image produces good definition of the edges, because of the increased escape probability in this region as well as the contribution from BS electrons recollected by the substrate. However, the magnitude of the rise at the edge is too large because of the overestimation of the escape probability. The BS profile is not as well defined because the interaction volume exceeds the line width, so electrons can as easily escape from regions of the feature. At 10 keV, the electron range is reduced to 1.5 μm and the SE profile displays a greater variation across the width of the feature. When the beam is at the center of the feature, fewer incident electrons go close enough to the edges to generate secondaries that can escape, so the yield is reduced. The same effect is seen in the BS profile although the rise at the edge is less marked. Note also the fall in the BS yield outside of the edge. Because the range is comparable with the line width, a significant fraction of the electrons that would be backscattered are stopped by the resist. This feature is also just discernible in the SE profile, since the SE<sub>II</sub> component falls with the BS yield, although the SE<sub>I</sub> component is unaffected.

At 5 keV, with a beam range of about 0.5  $\mu\text{m}$ , the tendencies displayed at 10 keV are more marked. When the beam is in the center of the line, the SE yield falls to the value for the bulk resist, but as the beam approaches the edge more SE can escape and the signal rises. The BS signal in the center of the line is likewise that of bulk resist (i.e.,  $n = 0.06$ ) and so the signal falls below the value recorded on the substrate, where  $n$  is about 0.16. The dip outside the edges is now more pronounced, but narrower because of the lower beam range. Finally, at 3 keV, with a range of 0.2  $\mu\text{m}$ , both profiles retain essentially the same form, but with the transition regions sharpened by the reduction of beam range from that of 5 keV.

Even this purely qualitative use of the simulation, to identify the factors that give rise to variations in the form of the profiles, is valuable--if only because it indicates that the task of metrology is much more complex than might at first appear. However, one can also use these profiles in a quantitative way, by "measuring" them with the various algorithms proposed for metrology and comparing the results with the known geometry that was built into the simulation. The extent to which this method is useful depends of course on the accuracy with which the simulation is capable of matching experimental results. The comparisons made so far indicate that, for situations such as that discussed above, both the shape of the profiles and the absolute predicted contrast levels are in excellent agreement. This agreement shows that the techniques used and the approximations made in the model to represent the electron-solid interaction are suitably chosen. The most significant limitations are due to effects that are, of necessity, difficult to model. Figure 5 shows an experimental profile from resists strips and the comparable computed data. The simulation matches the experimental data well in form and contrast, but whereas the computed data have peaks of equal height and a level baseline, the experimental data have neither. Although the explanation of these effects is straightforward (i.e., the variations in collection efficiency are a function of the feature orientation relative to the detector or to bandwidth and slew-rate limitations in the video chain, and the baseline instability indicates that charging is occurring

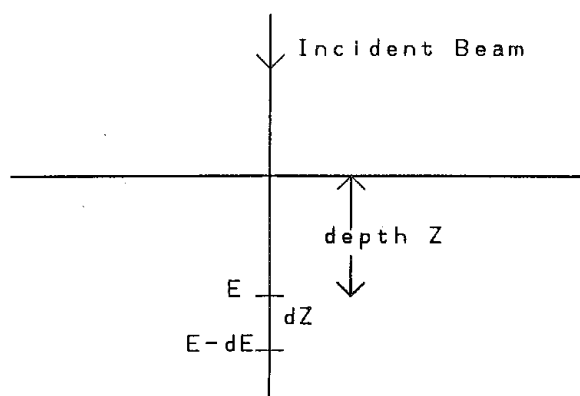


FIG. 1.--Geometry for Salow model of secondary-electron emission.

at many points during the scan), incorporating them into the simulation is a problem that remains to be tackled. Nevertheless, the techniques discussed here now permit simulations for medium resolution images to be carried out with enough accuracy to be quantitatively useful.

#### References

1. K. Kuroda, S. Hosoki, and T. Komoda, "Observation for crystal surface of W <110> field emitter tip by SEM," *J. Electron Microsc.* 34: 179, 1985.
2. M. T. Postek and D. C. Joy, "Micro-electronic dimensional metrology in the SEM," *Solid State Technology* 29(11): 145 and (12): 77, 1986.
3. G. D. Archard, "Backscattering of electrons," *J. Appl. Phys.* 32: 505, 1505, 1961.
4. M. Miyoshi and Y. Yamazaki, "Topographic contrast in linewidth measurement with SEM," *J. Electron Microsc.* 35: 73, 1986.
5. D. C. Joy, "Beam interactions, contrast and resolution in the SEM," *J. Electron Microsc.* 136: 241, 1984.
6. H. Salow, "Sekundärelektronen-emission," *Phys. Z.* 41: 434, 1940.
7. A. J. Dekker, "Secondary electron emission," *Solid State Phys.* 6: 251, 1958.
8. D.B. Wittry and D. F. Kyser, "Cathodoluminescence at p-n junction in GaAs," *J. Appl. Phys.* 36: 1387, 1965.
9. R. Shimizu, "Secondary electron emission with primary electron beam of kilo-electron volts," *J. Appl. Phys.* 45: 2107, 1974.
10. D. C. Joy, "A model for calculating secondary and backscattered electron probes," *J. Microsc.* (in press).
11. H. Drescher, L. Reimer, and H. Seidel, "Rückstreukoeffizient und Sekundärelektronen Ausbeute von 1-100 keV," *Z. angew. Phys.* 29: 331, 1970.
12. K.-R. Peters, "SEM contrast at high magnification," *Microbeam Analysis--1984*, 77.
13. D. C. Joy, "The interpretation of EBIC images using Monte Carlo simulations," *J. Microsc.* 143: 233, 1986.
14. V. M. Dwyer and J. A. D. Matthew, "A comparison of electron transport in AES/PES with neutron transport theory," *Surface Science* 152: 884, 1985.

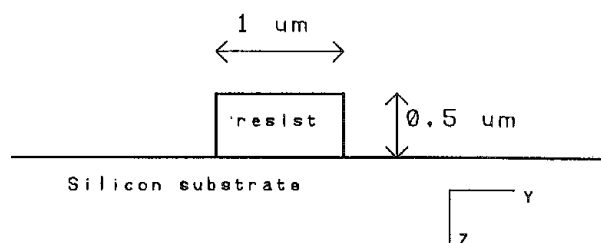


FIG. 2.--Cross section of resist line on silicon substrate.

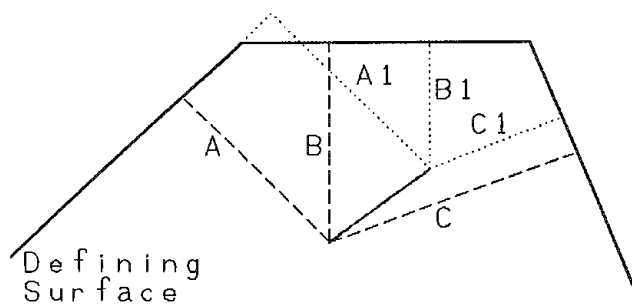


FIG. 3.--Calculation of SE yield from multiple surfaces.

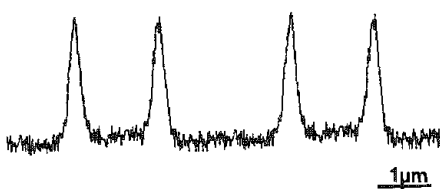
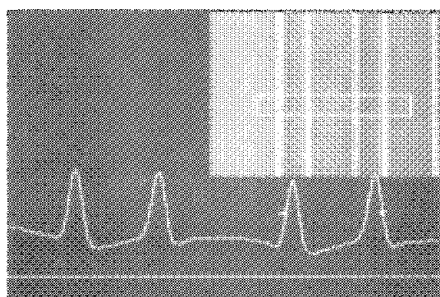


FIG. 5.--Comparison of experimental and computed profiles for resist on substrate. (Experimental data courtesy of S. Spiers, ISI Inc.)

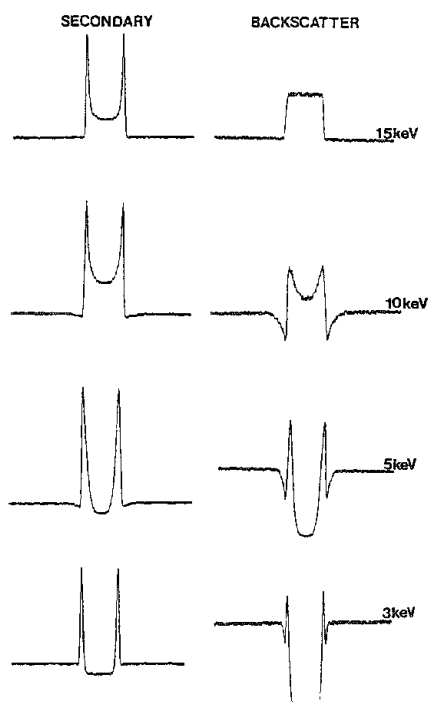


FIG. 4.--SE and BS profiles from 15, 10, 5, and 3 keV from feature of Fig. 2.

# MONTE CARLO ELECTRON TRAJECTORY SIMULATIONS FOR SCANNING ELECTRON MICROSCOPY AND MICROANALYSIS: AN OVERVIEW

Dale E. Newbury

The development of a theoretical description of beam-specimen interactions to aid in the interpretation of images has been a powerful stimulus to several forms of microscopy. The application of diffraction theory to the interpretation of transmission electron microscope images of crystalline materials is an outstanding example.<sup>1</sup> Imaging with the scanning electron microscope has been for the most part a qualitative sort of imaging, with most image interpretation relying on intuitive judgments on the part of the viewer.<sup>2</sup> For example in the important case of imaging topographic features at low to intermediate magnifications (< 10 000×), subjective interpretation is usually adequate. A number of SEM imaging problems go beyond the level of ordinary "look-see" microscopy and require a good understanding of electron beam-specimen interactions for proper image interpretation. These imaging problems include the interpretation of fine topographic structure at high magnifications (> 10 000×), the accurate definition of the positions of interfaces at high resolution, and the interpretation of images which arise by means of the special contrast mechanisms such as magnetic contrast or charge collection microscopy. Moreover, a model is needed that is capable of a numerical description of beam-specimen interactions as an aid to useful quantitative measurements of parameters.

In a related field, quantitative electron probe x-ray microanalysis is based on a good mathematical formulation of electron/x-ray specimen interactions.<sup>2</sup> The complex nature of the matrix correction expressions that have been derived from this formulation has made tractable solutions possible only in the case of flat, semi-infinite solids. Extension to more complex specimen geometries has been limited by the difficulties in introducing finite boundaries and interfaces into the calculations.

The development of the technique of Monte Carlo electron trajectory simulation has provided a tool that is appropriate for modeling electron beam-specimen interactions for SEM imaging and microanalysis calculations.<sup>3,4</sup> This paper presents an overview of the Monte Carlo technique with selected examples to illustrate its capabilities. A full description of a Monte Carlo simulation is beyond the scope of this paper. The interested reader is referred to several published descriptions.<sup>1,5-9</sup>

## Formulation

The basic idea of the Monte Carlo technique

The author is with the Center for Analytical Chemistry, National Bureau of Standards, Gaithersburg, MD 20899.

is to follow the path of an individual beam electron as it undergoes scattering events within the target. Scattering of electrons within solids takes place by means of two distinct mechanisms, elastic and inelastic scattering. Elastic scattering occurs with negligible loss of energy but is responsible for most of the angular deviation the electron suffers. Inelastic scattering is responsible for transferring energy from the beam electron to the target with the subsequent excitation of secondary radiation such as x rays, secondary electrons, etc., but causes negligible angular deviation.

This dichotomy of angular scattering behavior is taken advantage of in the formulation of a Monte Carlo simulation in the following way. The basic, repetitive calculation step of a Monte Carlo simulation is illustrated in Fig. 1. The electron at point  $P_N$  undergoes a scattering event, which causes it to deviate from its incident path (the line connecting path (the line connecting point  $P_N$  to point  $P_{N-1}$ ) by an angle  $\phi$ . It then travels a distance  $S$ , the step length of the calculation, arriving at a point  $P_{N+1}$ , which is located in the base of the scattering cone determined by  $\phi$ ,  $S$ , and the azimuthal angle  $\psi$ . Since inelastic scattering causes a negligible angular deviation, the scattering angle is calculated solely from consideration of elastic scattering. As a consequence, the step length of the calculation is related to the mean free path  $\lambda$  for elastic scattering,

$$\lambda = A/\rho N_A \sigma_E \quad (1)$$

where  $A$  is the atomic weight,  $\rho$  is the density,  $N_A$  is Avogadro's number, and  $\sigma_E$  is the cross section. The mean free path in turn is determined from the total elastic scattering cross section. Various formulations of this cross section are available. Many simple Monte Carlo calculations employ the screened Rutherford cross section for ease of implementing the calculation:

$$\sigma = 5.21 \times 10^{-21} \cdot 4\pi Z^2 / [E^2 \alpha (1 + \alpha)] \quad (2)$$

where  $E$  (keV) is the energy of the electron,  $Z$  is the atomic number of the scattering atom, and  $\alpha$  is a screening factor given by

$$\alpha = 3.4 \times 10^{-3} Z^{0.67} / E \quad (3)$$

A single elastic scattering event can produce an angular deviation ranging from 0 to 180°. A random number is used to select values from this range with an expression, which is derived from the partial cross section and produces the observed angular scattering distribution

$$\cos \phi = 1 - [2\alpha R / (1 + \alpha - R)] \quad (4)$$

The azimuthal angle  $\psi$  in the base of the scattering cone of Fig. 1 is selected by a linearly

distributed random number in the range  
 $0 \leq R \leq 1$ .

Application of Eqs. (1) through (4) in conjunction with equations of analytic geometry for calculation of the coordinates permits simulation of the trajectory of an electron in a stepwise fashion. An example of the simulation of 100 trajectories in a copper target is shown in Fig. 2. No single trajectory is representative of the "average" electron behavior. A statistically significant number of trajectories must be calculated to yield a meaningful result. Thus, if  $n$  trajectories are calculated, the statistical fluctuation is expected to be

$$n^{1/2}/n = n^{-1/2} \quad (5)$$

However, if the particular event of interest does not occur for each trajectory, the fluctuation in that quantity due to statistics are increased. For example, if the backscattering coefficient  $\eta$  is calculated, the precision is given by  $(n\eta)^{-1/2}$ .

Inelastic scattering must be taken into account in order for the electron to have a finite range in the target. It is possible in principle to model each of the inelastic scattering processes discretely, as demonstrated by Shimizu et al.<sup>6</sup> However, because of the difficulty in specifying the numerous inelastic scattering processes with sufficient accuracy, it is much more common in Monte Carlo simulations to employ the Bethe continuous energy loss equation<sup>10</sup>

$$dE/ds = -7.85 \times 10^4 (\rho Z/EA) \ln(1.166E/J) \quad (6)$$

where  $J$  is the mean ionization potential<sup>11</sup>

$$J = (9.76Z + 58.5Z^{0.19}) \times 10^{-3} \text{ (keV)} \quad (7)$$

Since the step length of the Monte Carlo calculation is of the order of a few tens of nanometers, the energy loss along a single step is small and can be conveniently approximated by

$$\Delta E = (dE/ds) * S \quad (8)$$

Although the energy loss from the beam electron due to inelastic scattering is calculated from Eq. (6), individual inelastic processes can still be modeled as needed. As an example, consider characteristic x-ray production. The cross section for inner-shell ionization is the starting point for the calculation.<sup>12</sup>

$$\sigma_i(\text{ionizations/e}/(\text{atom}/\text{cm}^2)) = 6.51 \times 10^{-20} (n^*b/E^*E_c) \ln(c^*E/E_c) \quad (9)$$

where  $n$  is the number of electrons in the atomic shell,  $E_c$  is the critical energy necessary to ionize the shell, and  $b$  and  $c$  are constants for a particular shell. Powell has discussed appropriate values for these constants.<sup>13</sup> The cross section  $\sigma_i$  and the step length  $S$  can be combined in the following way to calculate the x-ray production.

$$\begin{aligned} &\sigma_i(\text{ionizations/e}/(\text{atom}/\text{cm}^2)) * N_A (\text{atoms/mol}) * \\ &(1/A) (\text{mol/g}) * \rho (\text{g}/\text{cm}^3) * S (\text{cm}) * \\ &\omega (\text{x rays/ionization}) = \\ &\sigma_i N_A \rho \omega S / A (\text{x rays/e}) \end{aligned} \quad (10)$$

where  $\omega$  is the ionization yield. Equation (10) permits useful calculations of the x-ray yield as the fractional production per electron. Other secondary radiation products that have been calculated include fast secondary electrons,<sup>14</sup> electron-hole pairs,<sup>15</sup> and slow secondary electrons.<sup>16</sup>

The power of the Monte Carlo technique derives from the variety of information that can be constantly monitored for each trajectory: the sequence of positional coordinates ( $x, y, z$ ), the instantaneous energy, and the direction of travel relative to a set of axes ( $X, Y, Z$ ) fixed to the specimen. Thus, it is possible to generate spatial, angular, and energy distributions for both the primary and secondary radiation. By a comparison of the instantaneous coordinates with the calculated or stored boundary of a specified target shape, beam interactions in complex sample geometries can be calculated, so that the presence of surfaces and interfaces can be taken into account, even when the composition of the specimen changes. These considerations are illustrated by three examples:

*Compositional Contrast with Backscattered Electrons.* An estimate of the compositional contrast which is carried by the backscattered electron signal is usually made on the assumption that the signal  $S$  is proportional to the backscattering coefficient  $\eta$ . The contrast  $\Delta S/S_{\text{max}}$ , where  $S_{\text{max}}$  is the larger of the two signals, is then calculated as

$$\Delta S/S_{\text{max}} = \Delta \eta / \eta_{\text{max}} \quad (11)$$

Equation (11) applies strictly to a detector that is sensitive only to the total number of electrons emitted from the specimen. With the exception of specimen current detection, all other electron detectors that are placed external to the specimen modify the calculated contrast because of the take-off angle and solid angle of the detector, and because of the energy response of the detector. The Monte Carlo calculation can provide this information to make a more accurate estimate of the contrast.

Table 1 gives the results of Monte Carlo calculations for BSE compositional contrast between couples of aluminum, copper, and gold. The contrast has been calculated for four conditions. The total number contrast is the value found with Eq. (11) considering all backscattered electrons with equal weight. We calculated the effect of the energy distribution of the backscattered electrons on the detector response by first forming a histogram of the energy distribution of the backscattered electrons and then convolving that distribution with the function which describes the energy response of the detector, as calculated from the published work of Gedke et al.<sup>17</sup> The increase in contrast that is observed is a consequence of the dependence of the backscattered electron energy distribution on the atomic number. The energy histogram of backscattered electrons also permits simulation of the effect of an energy filter on compositional contrast. The contrast has been calculated for the exclusion of backscattered electrons below 0.5 and 0.8 of the incident energy. These calculations



reveal that a gain in contrast can be realized by excluding the low-energy, multiply scattered electrons.

2. *Type II Magnetic Contrast.* The mechanism of Type II magnetic contrast involves deflection of the beam electrons in the internal magnetic field of a specimen.<sup>18</sup> In order to model the influence of a magnetic field on the scattering process, a "double" Monte Carlo procedure was utilized (Fig. 3).<sup>19</sup> The calculation procedure was identical to that described for Fig. 1, except that after the trajectory segment  $P_N - P_{N+1}$  is calculated, the effect of the acceleration due to the Lorentz force  $F = e \gamma \times B$  is calculated, which brings the electron to a new point,  $P_{N+1}'$ . With this change to the basic Monte Carlo simulation, a wide range of properties of the Type II contrast mechanism can be simulated. An example is the behavior of the contrast as a function of the specimen tilt (Fig. 4a). A good correspondence is found with the experimentally measured tilt dependence (Fig. 4b).

3. *X-ray Production in Films.* The Monte Carlo simulation can be readily adapted to the study of x-ray production in thin foils and films. The thickness of the foil or film is compared to the instantaneous value of the z-coordinate of the electron to determine whether penetration of the finite thickness of the target occurs. In the case of foils, which are unsupported, the electron trajectory is terminated on penetration through the thickness. In the case of a film, a supported structure, on penetration of the film the electron scattering parameters are transferred to those of the substrate. The trajectory is then followed to determine whether re-entry into the film occurs. An example of a calculation of x-ray production in thin gold foils is shown in Fig. 5.<sup>20</sup> The beam energy was 100 keV and the foil was tilted at 45° from the horizontal. The x-ray depth production function, denoted  $\phi(\rho z)$ , is calculated from the intensity generated at a particular depth normalized by the intensity calculated for an infinitesimally thin layer in which there is negligible elastic scattering. Calculations for foils of various thicknesses are shown in Fig. 5. These calculations can be compared to experimental measurements where a thin layer of an element of similar atomic number, in this case hafnium, was placed as a tracer on the exit surface of the foil. The relative intensity of the hafnium tracer is then compared to the relative intensity of gold x-rays calculated at the exit surface. Reasonable agreement is obtained between the calculations and the experimental results.

### Conclusions

Monte Carlo calculations provide a powerful tool for the microscopist and the microanalyst. Several computer codes are now available to provide a foundation for the user to build upon. Considerable efforts often must be expended to adapt the Monte Carlo simulation to a particular set of conditions, but as the examples above indicate, the Monte Carlo simulation is capable of providing insight into many

problems of interest. The development of powerful personal computers in recent years has made it possible to run Monte Carlo simulations at greatly reduced expense. Although these computers are often a factor of 10 or more slower than mainframe systems, their ready access makes them an attractive alternative for Monte Carlo simulation. The publication of working codes for these computers should stimulate the use of Monte Carlo simulations by many microscopists and analysts.

### References

1. P. B. Hirsch, A. Howie, R. B. Nicholson, D. W. Pashley, and M. J. Whelan, *Electron Microscopy of Thin Crystals*, London: Butterworths, 1965.
2. J. I. Goldstein, D. E. Newbury, P. Echlin, D. C. Joy, C. Fiori, and E. Lifshin, *Scanning Electron Microscopy and X-ray Microanalysis*, New York: Plenum, 1981.
3. M. J. Berger, in B. Alder, Ed., *Methods in Computational Physics*, New York: Academic Press, 1963.
4. K. F. J. Heinrich, D. E. Newbury, and H. Yakowitz, Eds., *Use of Monte Carlo Calculations in Electron Probe Microanalysis and Scanning Electron Microscopy*, NBS Special Publication 460, Washington, 1976.
5. D. F. Kyser, and Murata, K., "Quantitative electron microprobe analysis of thin films on substrates," *IBM J. Res. Dev.* 18: 352, 1974.
6. R. Shimizu, Y. Kataoka, T. Ikuta, T. Koshikawa, and H. Hashimoto, "A Monte Carlo approach to the direct simulation of electron penetration in solids," *J. Phys.* D9: 101, 1976.
7. D. E. Newbury, and R. L. Myklebust, "Monte Carlo electron trajectory simulation of beam spreading in thin foil targets," *Ultramicroscopy* 3: 391, 1979.
8. D. E. Newbury, and R. L. Myklebust, "Monte Carlo electron trajectory calculations of electron interactions in samples with special geometries," in *Electron Beam Interactions with Solids*, Chicago: SEM, Inc., 1984, 153.
9. L. Reimer, and D. Stelter, "FORTRAN 77 Monte-Carlo program for minicomputers using Mott cross-sections," *Scanning* 8: 265, 1986.
10. H. A. Bethe, *Handbuch der Physik*, Berlin: Springer, 1924, vol. 24.
11. M. J. Berger, and S. M. Seltzer, National Academy of Science-National Research Council Publ. 1133, Washington, 1964, 205.
12. H. Bethe, *Ann. Physik* 5: 325, 1930.
13. C. J. Powell, "Evaluation of formulas for inner-shell ionization cross sections," Ref. 4, 97.
14. K. Murata, D. F. Kyser, and C. H. Ting, "Monte Carlo simulation of fast secondary electron production in electron beam resists," *J. Appl. Phys.* 52: 4396, 1981.
15. D. C. Joy, "EBIC Simulation," *J. Microsc.* 143: 233, 1986.
16. J. P. Ganachaud, and M. Cailler, "A Monte-Carlo calculation of the secondary electron emission of normal metals," *Surf. Sci.* 83: 498, 1979.
17. D. A. Gedcke, J. B. Ayers, and P. B. DeNee, "A solid state backscattered electron

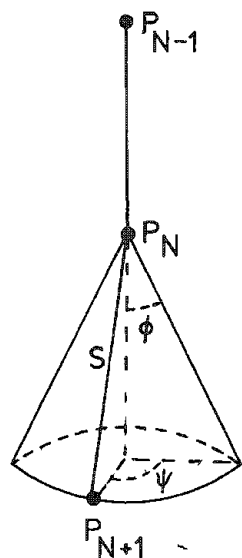


FIG. 1.--Fundamental calculation step in a Monte Carlo simulation: electron is scattered elastically through angle  $\phi$  at point  $P_N$ , travels step length  $S$ , and arrives at point  $P_{N+1}$  in base of cone defined by angle  $\psi$ .

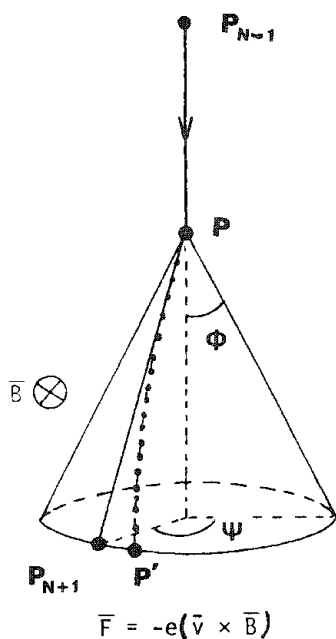


FIG. 3.--Calculation sequence of a "double" Monte Carlo calculation used to simulate Type II magnetic contrast.<sup>19</sup>

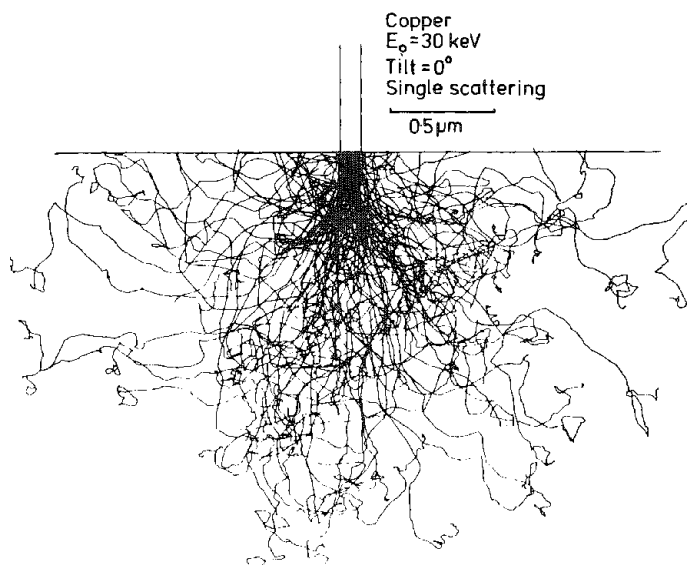


FIG. 2.--Monte Carlo electron trajectory simulation for copper target at beam energy of 30 keV. 100 trajectories were calculated.

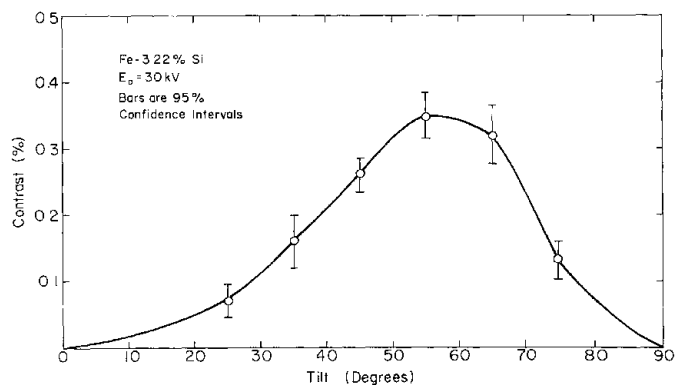
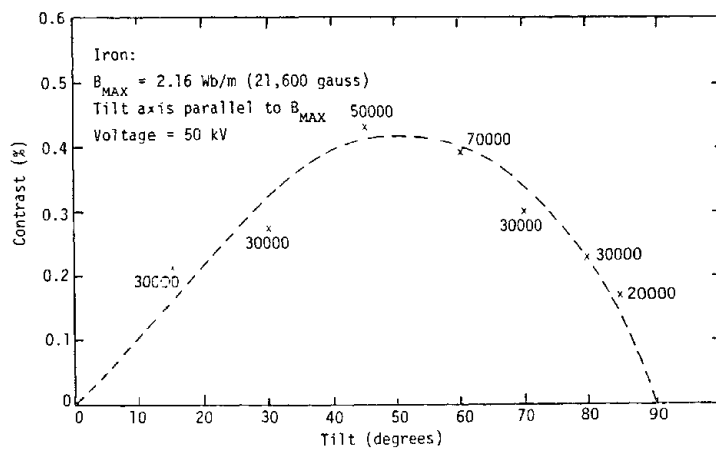


FIG. 4.--The behavior of Type II magnetic contrast as function of tilt: (a) Monte Carlo calculation; (b) direct experimental measurement.<sup>19</sup>

detector capable of operating at TV scan rates," *SEM 1978* I, 581.

18. D. J. Fathers, J. P. Jakubovics, D. C. Joy, D. E. Newbury, and Yakowitz, H., "A new method of observing magnetic domains by scanning electron microscopy: I. Theory of the image contrast," *Phys. Stat. Sol.* 20A: 535, 1973.

19. D. E. Newbury, H. Yakowitz, and R. L. Myklebust, "A study of type II magnetic contrast in the SEM by Monte Carlo electron trajectory simulation," Ref. 4, 151.

20. D. E. Newbury, R. L. Myklebust, A. D. Romig, and K. W. Bieg, "Observations on the determination of  $\phi(\rho z)$  curves for thin films in the analytical electron microscope," *Microbeam Analysis--1983*, 168.

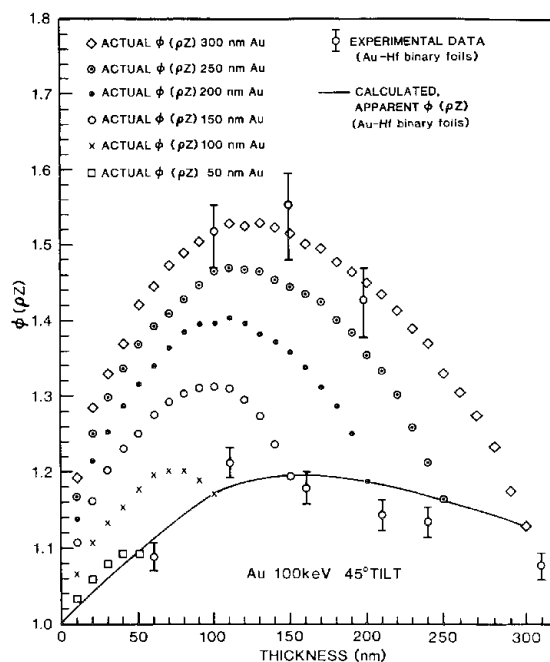


FIG. 5.--Monte Carlo calculations and experimental measurements of x-ray production in foils of gold of various thicknesses tilted at 45° to horizontal for beam energy of 100 keV.<sup>20</sup>

TABLE 1

Couple	Total number contrast	Contrast modified for energy response	Contrast for $E > 0.5 E_0$	Contrast for $E > 0.8 E_0$
Al - Cu	0.465 (3.0%)	0.537	0.544	0.669
Al - Au	0.669 (2.8%)	0.756	0.743	0.885
Cu - Au	0.381 (2.2%)	0.472	0.437	0.652

All calculations are based on 10 000 trajectories. Standard deviations are listed in parentheses.

## SURFACE CHARACTERIZATION BY USE OF AUTOMATED STEREO ANALYSIS AND FRACTALS

K. A. Thompson

This is an initial report of an investigation to determine the practicality of using mini-computers for automated interpretation of stereo pair. The procedure involves the use of autocorrelation procedures to match features from the stereo pairs, determine the height of the feature and repeat for the rest of the image. This is a time-consuming process that requires some simplifying algorithms to limit the area of autocorrelation and possibly the method of autocorrelation. Once topography has been determined, a method is needed to determine the surface roughness analytically; one possibility is the determination of the fractal dimension, if the surface is fractal. This fractality can then be used as a characterization index to compare to other materials or to cross correlate with other experimental techniques.

Electron stereomicroscopy is a method for determining the three-dimensional structure of a material. Due to the large depth of field for the scanning electron microscope (SEM), features at various heights are imaged sharply. If two micrographs of the same area of the sample are imaged with the specimen tilted between each view, different features on one image will be shifted relative to other stereo micrographs by an amount related to the height of the feature. An equation for the height relative to the electron optic axis is

$$h = \frac{p/m}{2 \sin(\theta/2)} \quad (1)$$

in which  $p$  is the shift distance, or parallax, of the feature between images;  $m$  is the magnification; and  $\theta$  is the angle of tilt between micrographs. For other frames of reference, or if the electron beam is not parallel to the optic axis (at low magnification), more complicated formulas are needed.<sup>1</sup> In calculating the height, one must measure the angle from the left to the right image of the stereo pair, in the same manner as the shift is measured; thus, both negative and positive shifts are possible, indicating negative and positive heights. From this equation, the height is inversely related to the angle; therefore, the precision increases as the angle increases. Unfortunately, various features are also hidden if the tilt is increased too much; therefore, a medium tilt of 4-15° is sufficient for most applications.

In order to calculate the topography of a surface from the stereo pair, some algorithm must be formulated to match features between micrographs. Normally, a visual evaluation of the two micrographs determines which features are a match. The human eye is very sensitive

to textural and tonal features, looking at the immediate and surrounding area to find patterns to match. General shapes are easily observed, with little regard to absolute intensities or backgrounds. In addition to the low-frequency patterns, the higher-frequency, short-range features are also easily discernible. Subtle changes from one region to another are visually obvious, but difficult to quantify. Sharp features usually take precedence over other, more subtle features; therefore, a hierarchy to pattern recognition exists. Each of these pattern-recognition capabilities is automatically performed in all directions: horizontally, vertically, and diagonally. Since this process is very complicated, stereo-comparators<sup>1</sup> exist that allow the operator to match features, and the computer stores the data. For the computer to match the features as well, an accurate algorithm must also be able to recognize patterns by similar methods.

A fairly complicated equation results from a similar problem of  $r$  factor analysis<sup>2</sup> for which a set of theoretical curves are matched to experimental figures to find the best fit. This complicated equation can be reformulated for the present stereo pair analysis as follows:

$$r(1) = \frac{1}{1_s} \frac{\left| cI_L'' - I_R'' \right|}{\left| I_R' \right| + \left| I_R' \right|_{\max}} \left| cI_L' - I_R' \right| / \frac{1}{1_s} I_R \quad (2)$$

$$C = \frac{1}{1_s} I_R / \frac{1}{1_s} I_L$$

for which  $1_s$  and  $1_f$  are the positions in the left image of the starting and final pixels to be compared,  $I_L$  and  $I_R$  are the intensities of the pixel for the left and right stereo images, and  $I'$  and  $I''$  are the first and second derivatives of the intensity, respectively. To find the best fit for a particular feature,  $r(1)$  must be minimized for all pixel starting positions in the right stereo image. To be completely accurate, this equation must be used in as many directions as possible: horizontally, vertically, and even diagonally. Another criterion is that  $1_s$  and  $1_f$  must be chosen appropriately so that the area of comparison is long enough to contain features, but short enough that multiple features at different heights are not present.

Equation (2) tries to take into consideration all feature qualities mentioned above, but the resulting equation is very time consuming. One valid simplification is to shorten the area of comparison on the right stereo image. The parallax can only occur perpendicular to the tilt axis; thus, only starting pixels along this direction need be considered. If the parallax is forced to coincide with an image axis, the calculation needs to

The author is at the Plant Laboratory of the Oak Ridge Y-12 Plant, Martin Marietta Energy Systems, Inc., Oak Ridge, TN 37831, operated for the U.S. Department of Energy under contract DE-AC05-84OR21400.

be performed only in that direction. In addition, maximum and minimum height requirements can be set, limiting the number of possible pixel shifts. But even with these simplifications, the time requirement may be prohibitive unless (1) further approximations are made, (2) the dimensions of the image matrix are small, or (3) the speed of the computer is sufficiently fast to handle the computations (for example, if the computer has parallel-processing hardware). Other simplifications may also be possible; if parts of Eq. (2) are fairly constant or small, they may be eliminated. For example, if the brightness and contrast of both images are sufficiently close to each other, the normalizing constant  $c$  would be equal to unity.

Autocorrelation of a series is another similar mathematical treatment that can be applied to this problem. Its formula is as follows:

$$r(t) = \frac{\sum [I(x) - \bar{I}][I(x - t) - \bar{I}]}{\sum [I(x) - \bar{I}]^2} \quad (3)$$

$$\bar{I} = \frac{1}{n} \sum I(x)$$

for which the summations are performed over  $n$  points in the series with an intensity  $I$  at each point  $x$ , displaced by  $t$ . This formula approaches unity as the series correlates. The method in which it could be applied to the present problem is the replacement of the  $I(x - t)$  term by the other half of the stereo pair. Since most features are recognized by a change in intensity as a function of distance, the derivative may be a better choice than the direct intensity. If this substitution is made, this formula begins to resemble Eq. (2) and the similarity of autocorrelation and r-factor analysis becomes more apparent. Equation (2) has the advantage that contrast and brightness variations between the two images need not be the same, but has the disadvantage of amplifying noise variations, which may invalidate this method. For the purpose of this investigation, different combinations and simplifications of these equations are being tested to find the fastest method with sufficient accuracy.

The main purpose of using the stereo images to determine the three-dimensional characteristics of a surface is to determine the actual morphology of the material. For example, if a pit exists on a corroded material, it is often desirable to know the depth and width of the pit. By actually placing dimensions on the feature of interest, comparison with the test sample is facilitated. If some feature can be quantified, identification is much more analytical. Surface roughness is another feature that needs to be quantified. Although other methods have been suggested for quantifying the texture of surfaces, relating the quantification to some physical property is beneficial. Haralick et al. have related the pixel brightness variations to 14 such properties, among them contrast, correlation, and angular second moment, which are properties that refer to texture.<sup>3</sup> Fourier analysis of geometric signature waveforms and the concept of fractal dimensions also help characterize the surface

roughness.<sup>4</sup> Although each of these techniques has its advantages and disadvantages, a more detailed description of the latter method will be given.

Fractal dimensions were first proposed by Mandelbrot.<sup>5</sup> As a first approximation, the rougher a surface is, the higher the fractal dimension. Another fundamental property of true fractal surfaces is that the general appearance of the surface does not change as the magnification varies. The perimeter of fine particles has been shown to be often fractal within certain ranges of resolution,<sup>4</sup> so that it is natural to assume that surfaces will also be fractal within certain magnifications. A method for determining the fractal dimension becomes apparent from the scale dependence of the length found in the Richardson law<sup>5</sup> given as follows:

$$L = N\eta = L_0 \eta^{1-d} \quad (4)$$

for which  $N$  is the count obtained by measurement with a gauge of length  $\eta$ ,  $L_0$  is the characteristic length, and  $d$  is the fractal dimension. If the surface area is calculated as the resolution of the image is degraded or as the magnification of the image is changed, a log-log plot of the gauge length versus surface area should be a straight line. The slope of this line should be equal to  $1 - d$ .

The fractal dimension of a surface can be used as a characterization tool or as a comparison with other experimental techniques. For example, theory relating pore geometry to a fractal dimensionality,<sup>6</sup> using gas adsorption isotherms, is being developed. If the fractal dimension of pores can be calculated by stereo image analysis, a possible method exists to test the new theory. In addition, the surface area can be directly compared by use of both techniques, which is also important in developing new theories, proving old ones, or explaining other phenomena (such as internal surface porosity). More work is necessary in testing the concepts introduced in this paper; the results should be available at a later time.

## References

1. P. G. T. Howell and A. Boyde, "Three-dimensional analysis of surfaces," in P. Echlin, Ed., *Analysis of Organic and Biological Surfaces*, New York: Wiley, 1984, 325-349.
2. E. Zanazzi and F. Jona, "A reliability factor for surface structure determination by low-energy electron diffraction," *Surface Science* 62: 61, 1977.
3. R. M. Haralick, K. Shanmugam, and I. Dinstein, "Textural features for image classification," *IEEE Trans. SMC-3*: 610, 1973.
4. B. H. Kaye, "Fractal dimension and signature waveform characterization of fineparticle shape," *American Laboratory* 18(4): 55, 1986.
5. B. B. Mandelbrot, *The Fractal Geometry of Nature*, New York: Freeman, 1983.
6. E. L. Fuller Jr., Plant Laboratory, Martin Marietta Energy Systems, Inc., Oak Ridge, Tenn.; work in progress in the development of a new theory for gas sorption isotherms.

## A NOTE ON CHARGING IN LOW-VOLTAGE SEM

D. C. Joy

Charging of the specimen under electron-beam irradiation is one of the most common problems in scanning electron microscopy (SEM). Not only does it result in unstable imaging conditions and a loss in resolution due to defocus of the beam, it can even cause permanent changes to the specimen since mobile ions can translocate under the influence of the induced electrostatic field. To minimize problems due to charging, optimized imaging conditions must be chosen. This paper presents some data to aid in this choice.

### *The Physics of Charging*

A detailed model for charging has been supplied by Cazaux.<sup>1</sup> In summary, when incident electrons irradiate an insulator both electrons and holes are produced in the beam interaction volume. The sign of the majority charges is determined by charge conservation.<sup>1</sup> Given a secondary electron (SE) yield of  $\delta$ , and a backscattered (BS) yield of  $\eta$ , and if

$$\delta + \eta < 1 \quad (1)$$

then the net charge is negative; otherwise, it is positive. Figure 1 is a plot of the total electron yield ( $\delta + \eta$ ) for a typical material as a function of incident beam energy  $E$ .<sup>2</sup> This yield is equal to unity at two energies  $E_1$  and  $E_2$ . When  $E > E_2$ , the inequality (1) is satisfied and the sample charges negatively. In principle, positive charging would occur for  $E_1 < E < E_2$  but in practice positive charging leads to the recollection of low-energy secondaries until the yield again falls to unity.

The electrons and holes produced remain stationary for a time  $t$ , the "residence time," and then attempt to drift in the field resulting from the net distribution of charges. If drift can occur then the motion of the charges produces local conductivity and the charge distribution relaxes to some transient equilibrium condition. Otherwise the electric field continues to increase until dielectric breakdown occurs and physically destroys the irradiated region. Since the residence time is short even by comparison with typical pixel times (i.e., tens of microseconds) this cycle of events follows the beam scan position. After a complete scan raster has been scanned, the equilibrium charge distribution will occupy the raster area (or a greater area) and in the absence of some discharging mechanism such as low-energy electron beam irradiation, this distribution may remain stable for periods of days.

The author is with the EM Facility, Walters Life Sciences Building, University of Tennessee, Knoxville, TN 37996.

### *Eliminating Charge-up*

One of the best arguments for low-voltage SEM follows from Eq. (1) and Fig. 1. If the incident beam energy can be sufficiently reduced, then when  $E$  reaches  $E_2$ , ( $\delta + \eta$ ) becomes equal to unity and the net charge deposited is reduced to zero, so that neither positive nor negative charging occurs. The starting point for observing a sample without charging artifacts is therefore to identify the  $E_2$  energy value appropriate to the specimen being examined. Determining  $E_2$  experimentally is not an easy procedure and requires that an electrometer be connected to the sample in the SEM. Consequently very few  $E_2$  values are available in the literature to guide the SEM operator. An alternative approach would be to try to calculate  $E_2$ . A new model has been developed that combines a Monte Carlo trajectory simulation for the incident electrons and a simple diffusion model for secondary-electron production.<sup>2</sup> With this model, the variation in electron yield as a function of beam energy can be computed and the value of  $E_2$  deduced. Table 1 lists  $E_2$  values for a number of common materials computed using this procedure.

Table 1

Material	$E_2$ energy (keV)
HRP resist	0.55
Carbon	0.65
Aluminum	1.05
Silicon	1.15
Teflon	1.9
GaAs	2.6
Quartz	3.0

For some materials the  $E_2$  value is in the energy range of 2-5 keV, which is easily accessible on a modern SEM, but for others  $E_2$  is 1 keV or less, in the regime where only a dedicated low-voltage SEM has adequate performance. When high-quality imaging of an uncoated sample is required, one would therefore want to bring  $E_2$  to a higher value. To do so, we note that when a specimen is tilted, both  $\delta$  and  $\eta$  increase, although raising the beam energy (for  $E > E_2$ ) leads to a fall in  $\delta$ . Hence when a sample is tilted the value of  $E_2$  rises. By use of the Monte Carlo model the variation in electron yield with both beam energy and tilt can be calculated, so the  $E_2$  for any incidence angle can be found. Figure 2 is a plot of this computed variation of  $E_2$  with beam incidence angle for carbon, silicon, and HRP photoresist. The  $E_2$  value rises significantly as the angle increases; the gain is of the order of a factor of 2 for a tilt of 45°. It is also noticeable that all the curves have an approximately similar shape despite the differences in absolute yield.

This type of behavior has been experimentally studied by Sugiyama et al.<sup>3</sup> In their ob-

servations,  $E_2$  was estimated by an experimentally determination of the maximum beam energy  $E_n$  for which a stable image was obtained at normal incidence. This procedure was then repeated to determine the equivalent stable imaging energy  $E_t$  at some angle of incidence  $\phi$ . For quartz their data fitted the relation

$$E_t \cos^2 \phi = E_n \quad (2)$$

Sugiyama et al. explained this result by postulating that there existed a surface layer, equal in depth to the beam penetration at  $E_n$ , within which two-dimensional charge relaxation could occur to stabilize the image. At tilted incidence the normal component of velocity is reduced by  $\cos \phi$ , so that the energy can be increased by a factor of  $\cos^2 \phi$  before the beam has sufficient energy normal to the surface to penetrate below the critical depth.

As shown in Fig. 3, a replot of the data of Fig. 2, again as a function of tilt angle  $\phi$  but with the computed  $E_2$  values multiplied by  $\cos^2 \phi$ , yields almost horizontal lines in each case except at the highest tilt angles, which

indicates that the empirical relationship of Eq. (2) is again satisfied. Since the computed data rely purely on a calculation of the yield, and the "critical depth" model of Sugiyama et al. is not invoked, this result indicates that the relationship of Eq. (2) may in fact be of more general applicability. Thus, given an experimental, or computed, value of  $E_2$  for a material this result provides a criterion for selecting a tilt condition to shift  $E_2$  to a higher and more convenient value.

#### References

1. J. Cazaux, "Some considerations on the electric field induced in insulators by electron bombardment," *J. Appl. Phys.* 59: 1418, 1986.
2. D. C. Joy, "A model for calculating secondary and backscattered electron yields," *J. Microsc.* (in press).
3. N. Sugiyama, S. Ikeda, and Y. Uchikawa, "Low-voltage SEM inspection of microelectronic devices," *J. Electr. Microsc.* 35: 9, 1986.

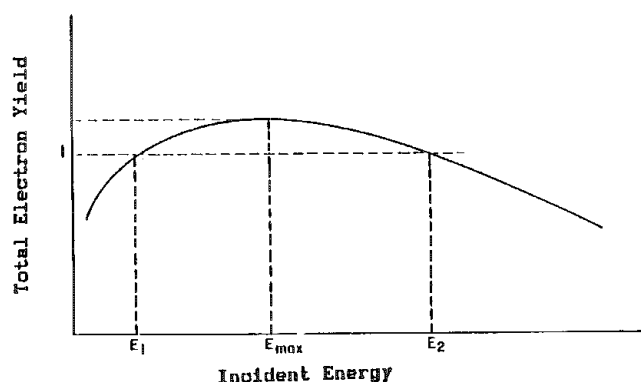


FIG. 1.--Variation of total electron yield with beam energy.

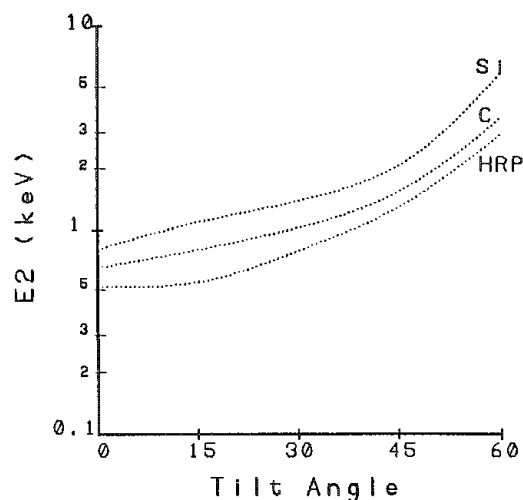


FIG. 2.--Computed plot of  $E_2$  (in keV) as function of tilt.

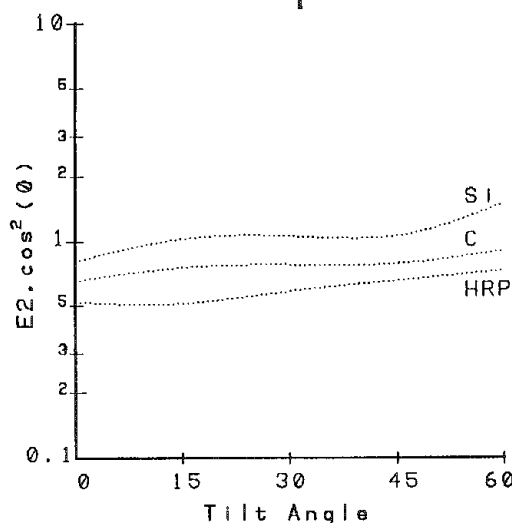


FIG. 3.--Data of Fig. 2 replotted as  $E_2 \cos^2 \phi$  against tilt.



#### 4A. Optical Spectroscopy: Micro-Raman

### EVOLUTION AND PROSPECTS OF RAMAN MICROPROBING TECHNIQUES

Paul Dhamelincourt and Michel Delhayé

From the time of its discovery in 1928 until about ten years ago, Raman scattering has served as a tool for the study of bulk samples of macroscopic dimension providing information about fundamental molecular properties, and in spectrochemical analysis. In principle, the excitation and observation of Raman spectra in the visible region would allow a better spatial resolution. Nevertheless, the entry of Raman spectroscopy into instrumental microanalysis has not been instantaneous and has depended on several major technical advances. In the present paper we try to review the evolution of Raman microprobing techniques, with a special emphasis on future trends of this analytical method.

#### *Raman Microprobing Evolution*

The intensity of the signal delivered by the detector of a spectrometer analyzing a Raman line can be expressed by

$$S \propto I\sigma N\Omega T \quad (1)$$

where  $I$  is the irradiance at the sample,  $\sigma$  the Raman scattering cross section,  $N$  the number of analyzed molecules,  $\Omega$  the solid angle of collection of scattered light, and  $T$  the transmission of the instrument optics.

At the beginning of Raman spectroscopy, when the samples were illuminated by incoherent light sources, all the terms in Eq. (1) could be considered as independent factors. The sole means for obtaining sufficient Raman signal intensity thus was to increase  $N$  by analyzing large volumes of the sample. But with the development of lasers in the early 1960s a new approach was possible.

It was demonstrated quite earlier that  $N$ ,  $I$ , and  $\Omega$  are not independent when coherent-light sources are used<sup>1</sup> and that focusing lasers beams into samples should make lasers useful for microsampling, but some of this potential has been effectively realized only recently. Hirschfeld's prediction that Raman spectra might be observed from a cubic micron<sup>2</sup> was first verified independently at NBS (USA) and at CNRS (University of Lille). Two papers,<sup>3,4</sup> presented in 1974 at the Fourth International Conference on Raman Spectroscopy (ICORS), described the first applications of Raman microprobing with a spatial resolution close to the limit imposed by light diffraction phenomena. More complete calculations made at NBS and by ourselves followed later<sup>5,6</sup> that clearly confirm the potential of Raman microprobing techniques.

In our laboratory, we were more particularly tempted to profit from the excellent analyti-

cal characterization offered by Raman spectra to map out the distribution of chemical substances in a heterogeneous sample. In 1975 we reported the results of the first experiments on "Raman micrography."<sup>7</sup> At approximately the same time, the concept of "Ramanography" was also introduced by Hartley, who proposed to illuminate a gas flow by a flat laser beam and to observe a macroscopic distribution of the species.<sup>8</sup> From the results of initial laboratory experimentation, an industrial prototype was shown at the Fifth ICORS in 1976 which was the outcome of a joint development effort conducted with French industry. The first generation of commercially available Raman microprobes (MOLEs) were constructed under license<sup>9,10</sup> between 1977 and 1980 (Jobin-Yvon ISA). By that time Raman microprobing techniques had matured to the point at which nondestructive molecular microanalysis became entirely practicable for both academic research and industrial purposes, and a large number of applications in various domains were described in the literature.<sup>11,12</sup> Figure 1 shows the evolution of the analyzed sample volume over the past decades. However, one of the limitations of these earlier microprobing techniques using scanning spectrometers with single-channel photodetectors (PMT) resulted from the high irradiance required at the sample (typically  $10^5$  to  $10^6$  kW/cm<sup>2</sup>), which causes degradation of fragile samples during the long exposure time required to record the spectra. One of the most dramatic advances that helped to overcome this difficulty has been achieved through the development of multi-channel photodetectors. As emphasized by Bridoux and coworkers<sup>13</sup> as early as 1973, multi-channel detectors offer significant advantages over conventional scanning techniques; but to obtain the full benefit from the inherent superiority of these detectors, it is not sufficient to replace the photomultiplier at the output of an existing instrument by a multi-channel detector. The entire optical system has to be redesigned to meet the appropriate requirements. Since the first experiments described by Bridoux, great progress has been made in the development of multichannel detectors. Thus, as early as 1980, we developed at Lille, again in close collaboration with French industry (DILOR Company), a second generation of a Raman microprobe employing spectrographic dispersion with an intensified silicon diode array as the detector.<sup>14</sup> Micro-Raman instruments, using commercially available multiplex detection systems and more or less optimized coupling with optics, were developed in laboratories<sup>15,16</sup> and by companies<sup>17</sup> (Spex Industries, Jobin-Yvon ISA, and others).

More than 250 papers have been published up to now, which illustrates the potential of Raman microprobing techniques in a large variety of domains. Moreover, calculations have also been carried out that demonstrate accurate

The authors are at the CNRS Laboratoire de Spectrochimie Infrarouge et Raman, Université des Sciences et Techniques de Lille Flandres Artois, Bat. C5, P-59655 Villeneuve d'Ascq Cedex, France.

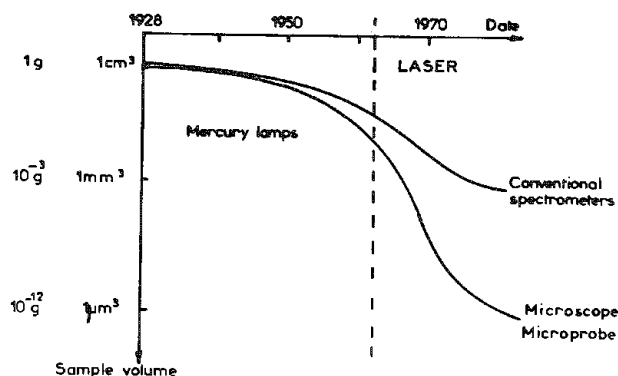


FIG. 1.--Evolution of effective sample volume analyzed in Raman experiments over past decade.

polarization measurements can be achieved.<sup>18</sup>

#### Prospects of Raman Microprobing

Physical limits are now attained for the spatial resolution and detector sensitivity. Fluorescence, the bugbear of Raman spectroscopists, is still by far the greatest problem, though generally less severe than the one encountered with conventional spectrometers, because it is possible to select small non-fluorescent areas in the sample. Nevertheless, it is still hindering a fair number of sample investigations. Future improvements aimed at minimizing this problem may well come about from the use of pulsed lasers in the picosecond range associated with gated detection in order to discriminate Raman features against spectral background. Furthermore, exciting prospects appear on the horizon from the use of FT Raman spectrometers working in the near infrared that will minimize the problems arising from the excitation of sample fluorescence.<sup>19</sup> Indeed, the improved sensitivity of FT spectroscopy should compensate for the weaker Raman signal due to the excitation in the near infrared.

In this case the most critical difficulties to be overcome involve the filtering of the Rayleigh line. One significant breakthrough should certainly come from the recent development of filters based on the Bragg diffraction of light in the optical domain.<sup>20</sup> Another future opportunity for the development of Raman microprobing is to combine, in a single instrument, this technique with other widely used microanalytical methods such as the electron probe and the laser mass spectrometer. Techniques based on coherent anti-stokes emission and nonlinear effects should also develop.<sup>21</sup> At last, improved computer techniques should lead toward the complete automation of the analytical procedure by designing "intelligent spectrometers."

#### References

1. M. Delhay and M. Migeon, *C. r. Acad. Sc. Paris* 262: 1966.
2. T. Hirschfeld, "Raman microprobe: Vibrational spectroscopy in the femtogram range," *J. Opt. Soc. Am.* 63: 476, 1973.
3. G. J. Rosasco et al., "Investigation of the Raman spectra of individual micro-sized particles," *4th ICORS* (Abstracts), 1974.
4. M. Delhay and P. Dhamelincourt, "Laser microprobe and microscope," *ibid.*
5. G. J. Rosasco, "Raman microprobe spectroscopy," in R. J. H. Clark and R. E. Hester, Eds., *Advances in Infrared and Raman Spectroscopy*, London: Heyden, 1980, vol. 7.
6. P. Dhamelincourt, *Etude et réalisation d'une microsonde moléculaire à effet Raman: Quelques exemples d'application*. Thesis, University of Lille I, France, 1979.
7. M. Delhay and P. Dhamelincourt, "Raman microprobe and microscope with laser excitation," *J. Raman Spectrosc.* 3: 33, 1975.
8. D. L. Hartley, in Lapp and Penney, Eds., *Laser Raman Gas Diagnostics*, New York: Plenum, 1974, 311.
9. French Patent ANVAR 2 253 410, 1974.
10. French Patent ANVAR 7 621 539, 1976.
11. *L'Actualité chimique*, Paris: S.F.C., 1980 (No. 4).
12. E. S. Etz and J. J. Blaha, "Scope and limitations of single particle analysis by Raman microprobe spectroscopy," in *Characterization of Particles*, NBS Special Publication 533, Washington: U.S. Government Printing Office, 1980.
13. M. Bridoux et al., "Photographie rapide du spectre Raman," *Pub. GAMS* 4: 309, 1963.
14. M. Delhay et al., "A new generation of laser Raman microspectrometers: Micromars," *Microbeam Analysis--1982*, 275-278.
15. P. Milanovich et al., "The Lawrence Livermore National Laboratory Raman microprobe," *ibid.*, 270-274.
16. W. R. Steinbach et al., "Analytical applications of a multiplex detector laser Raman microprobe," *ibid.*, 279-285.
17. F. J. Purcell and E. S. Etz, "A new spectrograph with a multichannel optical detector for the Raman characterization of microparticles," *ibid.*, 301-306.
18. C. Bremard et al., "The effect of high numerical aperture objectives on polarization measurements in micro-Raman spectrometry," *Appl. Spectrosc.* 39: 6, 1985.
19. B. Chase, "Fluorescence-free Raman spectroscopy," in *Proc. Tenth ICORS*, 1986.
20. R. J. Spry and D. J. Kosan, "Theoretical analysis of the colloidal array filter," *Appl. Spectrosc.* 40: 6, 1986.
21. M. D. Duncan et al., "A scanning CARS microscope," *Optics Letters* 4: 22, 1982.

## TOMAS HIRSCHFELD: REFLECTIONS ON THE LIFE AND WORK OF A 'MICRO' PIONEER

F. P. Milanovich

Tomas Hirschfeld immigrated to the U.S. from Uruguay in 1968. He brought with him a degree in chemical engineering and a dedication to scientific research that would, in his unfortunately short lifetime, raise him to near-legendary stature among his peers.

I first met Tomas at the 1974 International Conference on Raman Spectroscopy in Brunswick, Maine. He was giving a paper on the status of Raman research at Block Engineering. Such talks were to become Tomas's forum. His greatest pleasure in research was in conveying, in his characteristically enthusiastic manner, new ideas to any and all who would listen. The talk in Maine had all the characteristics that I would find in numerous presentations of his that I heard later. The technical content was highly innovative, there was standing room only, and he had more to say than there was time for. (At an internal LLNL symposium, Tomas had a conflict and could not attend. He sent a prerecorded slide show in his place and even that ran over time!)

At Block Engineering, Tomas quickly rose to chief scientist, and at once became the company's major intellectual driving force. His early work concentrated on several significant applications of Raman scattering, including remote atmospheric sensing and a "TV-camera"-based micro-Raman spectrometer. These two efforts were at what was then the forefront of research in the field.

For a scientist to be at the forefront of his field would, for most of us, be a lifetime ambition. To have been there as early, and in as many areas as Tomas, is a true measure of his genius. These fields included remote atmosphere sensing, micro-Raman spectroscopy, FTIR, "hyphenated" instruments, and most recently fiber-optic-based chemical sensors, FT Raman spectroscopy, and microstructures. These endeavors generally encompassed his scientific background in chemistry and spectroscopy. However, if you were to ask Tomas what he considered himself, you would not get the conventional answer of scientist, chemist, or engineer. He used only two words: pioneer and inventor, with emphasis on the latter.

The spirit of invention that Tomas portrayed was fueled by a sort of irreverence that he held for conventional ways of thinking and conventional approaches to problem solving. He was a collector of axioms that reflected his beliefs. One of his favorites was tacked to the bulletin board beside his desk: "Anything can be made smaller--never mind physics." This axiom dominated the later years of his research.

Tomas joined the Lawrence Livermore National Laboratory (LLNL) in 1979. He so impressed

several organizations within LLNL that his first position was jointly with the Biomedical Division, the Chemistry Department, and the Laser Program. In time it became apparent to Tomas that the Chemistry Department, owing to its broad relationship with the entire laboratory, was the best place for a man of his talents. He assumed a full-time position in the Chemistry Department, where he brought his major LLNL accomplishments to fruition.

Many of them were in the development of microstructures. In the major weapons programs at the Laboratory, a significant premium is placed on size and weight. This was an excellent arena for Tomas in which to pursue his fascination with the small. He made numerous contributions to reducing the size of a component while maintaining its performance. None was more ingenious than his "sweat gland." This tiny device was modeled after the human sweat gland. (Tomas derived many of his ideas from biological organisms.) It actively transported water vapor from an enclosure at a savings of better than an order of magnitude weight over other available solutions. Tomas received a prestigious IR-100 award for this accomplishment. He took great pride in these awards, of which he received six in his career, --more than many major U.S. corporations can lay claim to.

Tomas's talents did not rest with his scientific ingenuity alone. After he left industry, his research programs could not follow him; so, in essence, he was starting from scratch when he came to Livermore. He exhibited political skills as he began to establish himself and his programs. These skills were to bring him in a few short years a research budget that approached \$2 million annually and a research group of about 20 individuals.

The best example of his skills was the development of the LLNL micro-Raman spectrometer. Tomas had left the development of a micro-Raman spectrometer at Block Engineering and wanted very much to start a new effort based on some new concepts. It would be an expensive and lengthy development; at that time, circa 1980, there was no proponent of analytical Raman spectroscopy at Livermore (besides myself). Tomas, sensing that a direct approach to procuring funding would likely be futile, invited colleague to give a broad-based lecture on the applications of micro-Raman spectroscopy. In the interim, he contacted key individuals from programs of potential support and invited them to this informative lecture. The idea was to let the potential user come up with the problem and let Tomas provide the solution. The strategy worked and we had a sanctioned program in micro-Raman development that was financed by several potential users.

The project was to be pursued by Tomas, Dave Johnson, and myself. Dave was to commit Tomas's ideas to paper and oversee the machining and construction; I was responsible for

---

The author is a colleague of the late Dr. Tomas B. Hirschfeld, in the Advanced Laser Technology Group, Lawrence Livermore National Laboratory, Box 5508, Livermore, CA 94550.

component breadboarding, system integration, and eventually the operation of the instrument. The device was designed around a bifocal collection ellipsoid. I recall studying the engineering drawings of the ellipsoid and wondering why it was designed at precisely the numerical aperture of 0.28. I raised this question with Tomas and he replied simply that it was the polarization conserving angle of collection. Not to look too ignorant in his presence I answered, "Of course," and then slipped off to the library to refresh my memory on this magic angle. After several days of futile searching I sheepishly returned to Tomas and said that I could find no information about this unique angle. Tomas replied, "Of course not--I haven't published it yet!" It was then that I finally realized the sheer magnitude of his technical productivity. He

introduced me to three filing cabinet drawers titled "Raman Unpublished" and said that the information I needed was in there somewhere. I found the information and much more. Here were dozens of short to intermediate-length technical notes that any of us would proudly include in our curriculum vitae. He simply had no time to publish them. Most of his truly innovative work, though, is in the open literature and will serve many of us for decades to come.

We lost Tomas in April 1986 at the young age of 46. He was as devoted a family man as he was a dedicated scientist. His loss is shared by many. At times like this it is sometimes customary to attempt to quantify a lifetime achievement. However, for his colleagues at Livermore, his greatness is more than adequately measured by the magnitude of his lingering presence.



FIG. 1.--Most recent photograph of Tomas and his group in the Chemistry and Material Science Division of LLNL. Behind Tomas, from left, S. C. Macevicz, W. G. Anderson, F. Miller, N. Thomas, G. R. Haugen, H. H. Miller, W. C. Hui, M. Lewis, J. E. Lane, S. M. Angel; in front, J. L. Hattabaugh, W. Burke, J. N. Roe, D. Olness, R. Steinhaus, W. A. Steele.

## NIR FT-RAMAN OF DERIVATIZED CONTROLLED PORE GLASS

D. D. Archibald and D. E. Honigs

Enzymes, fluorophores, or alkyl chains bound to silica create surfaces that are useful in a variety of analytical methods. The three bonded phases mentioned above are typical of the current generation of surfaces used to distinguish chemical species in solution. In their fundamental form, surface sensors consist of solid substrates with bonded phases that to some extent selectively respond to analytes. These phases generally enhance the spectroscopic, electrochemical, or other response of the analyte over that observed in the absence of the surface interaction.

To understand the mechanisms of surface sensing, and to develop surface sensors, we are currently examining bonded phases of controlled pore glass (CPG). Near Infrared Fourier Transform Raman (NIR FT-Raman) spectroscopy provides several advantages in the characterization of carbon-containing compounds on CPG in an aqueous environment. First, fluorescent interferences from the specimen are absent, which is clearly important for the examination of fluorescent derivatives that are commonly bound to substrates. This advantage is also important in overcoming fluorescent interferences arising from impurities in the CPG. Even if the magnitude of this fluorescence is small, it can be a large interference to the Raman signal of the surface derivative, because of the minute concentration of the derivative. The second advantage is the fact that the polar bonds of the silica and the water are weak Raman scatterers relative to the carbon-silicon, carbon-carbon and carbon-hydrogen bonds of the derivative, which allows one to detect small amounts of the bonded phase in the presence of much larger amounts of water and silica. Furthermore, Raman spectra are highly characteristic of the connectivity and conformation of the bonded molecules.

The geometry of the FT-Raman optics and the techniques used to sample the silica specimens have been established. CPG silanized with 3-aminopropyltriethoxysilane is the focus of initial studies. The detection limit of the hydrolyzed silane in aqueous solution and the effect of the unreacted CPG on the spectrum of the silane are being investigated. These measurements are important in the evaluation of the amount of silane detectable on the silanized CPG. We are also examining the relationship of the silicon-carbon stretch band to the nature of the bonding between the silane molecules and the silica.

### *Prospects for Microprobe FT-Raman Spectroscopy*

Fourier Transform Raman spectroscopy has

The authors are at the University of Washington, Department of Chemistry, BG-10, Seattle, WA 98195. Financial support is from NSF and Perkin-Elmer Corp.

several features that make it attractive as an optical microprobe technique. First, near infrared excitation is a feasible method because of the combination of throughput and multiplex advantages of FT spectroscopy. Despite the decrease in spatial resolution because of the larger diffraction-limited spot size, the use of NIR excitation is often useful because it provides solutions to the problems of specimen fluorescence and photodegradation.<sup>1,2</sup> Use of the near-infrared excitation is also advantageous because of the low molar absorptivity of common materials in this spectral region. Compared to visible photons, more NIR photons can be focused onto a spot of a typical specimen before heating results in damage of the specimen. This advantage is directly opposed by the decreased efficiency of Raman scattering by virtue of using longer-wavelength excitation.

Another feature of FT-Raman spectroscopy that would be useful for microanalysis is the extreme frequency accuracy of an FT spectrometer, which makes for accurate spectral subtractions and comparisons.<sup>3</sup> Although spectral subtractions can be successfully done by dispersive Raman, extreme care is required in order to achieve and maintain sufficient frequency calibration.

In a Raman microprobe instrument, source focusing and spatial filtering is used to reduce the volume from which scattered light is collected. This reduction in sampling volume lends itself quite well to the FT-Raman experiment. The major difficulty with FT-Raman measurements is that after Fourier transformation the noise in the elastically scattered line is essentially spread over the entire Raman spectrum.<sup>4,5</sup> To achieve a decent Raman spectrum, the laser frequency must be attenuated by a factor of  $10^6$  to  $10^{12}$  depending on the stability of the laser, the collection geometry, the particular specimen, and the intensity of the Raman line under observation.<sup>2,3,5,6</sup>

The most useful filters for eliminating elastically scattered light are based on either interference or diffraction phenomena. These devices generally exhibit a sharper cutoff than absorption filters and so less of the Raman spectrum is obscured.<sup>2,7</sup> Interference and dichroic filters function by creating interference between thin and uniform dielectric layers; unlike in absorption filters, the rejection efficiency of dichroic filters shows a marked angular dependence.

Certain crystalline colloidal arrays can Bragg diffract a certain frequency of NIR or visible light, much as crystals can be used to diffract x radiation.<sup>8,9</sup> These filters have not been employed in an FT-Raman instrument, but they have been used to construct dispersive instruments.<sup>10,11</sup> Theoretically the rejection efficiency can be higher than  $10^{16}$  and a rejection of  $10^8$  has been observed in prac-

tice.<sup>9,10</sup> The bandwidth of rejection is of the same order as interference and dichroic filters, but the transmission is higher and more constant across the passband.

Absorption filters are useful for collection of scattered light from a large volume where the light cannot be collimated for filtering by diffraction or interference-based filters. As the sampling volume is decreased through efficient focusing of the excitation laser and through efficient spatial filtering, the ability to collimate the collected light increases. Consequently, interference- and diffraction-based filters become more efficient and the S/N of the Raman spectrum does not decrease as fast as it would in an absorption filtering FT-Raman or for multichannel dispersive Raman instruments.

#### References

1. T. Hirschfeld, "On the nonexistence of nonfluorescent compounds and Raman spectroscopy," *Appl. Spectrosc.* 31: 328, 1977.
2. T. Hirschfeld, "FT-Raman spectroscopy: Development and justification," *Appl. Spectrosc.* 40: 133, 1986.
3. D. B. Chase, "Fourier transform Raman spectroscopy" (in preparation).
4. T. Hirschfeld, "Fellgett's advantage in UV-VIS multiplex spectroscopy," *Appl. Spectrosc.* 30: 68, 1976.
5. G. N. Zhizhin and M. N. Popova, "Application of a Fourier spectrometer for recording the Raman effect," *J. Appl. Spectrosc.* 32: 662, 1980.
6. E. R. Schildkraut and T. Hirschfeld, "Fourier transform Raman spectroscopy," in *Laser Raman Gas Diagnostics*, New York: Plenum, 1974.
7. D. J. Moffatt et al., "Interferometric observation of Raman spectra: Comparison of photomultiplier and avalanche diode detectors," *Appl. Spectrosc.* 40: 1079, 1986.
8. R. J. Carlson and S. A. Asher, "Characterization of optical and crystal structure in monodisperse polystyrene colloids," *Appl. Spectrosc.* 38: 297, 1984.
9. R. J. Spry and D. J. Kosan, "Theoretical analysis of the crystalline colloidal array filter," *Appl. Spectrosc.* 40: 782, 1986.
10. S. A. Asher et al., "Crystalline colloidal Bragg diffraction devices: The basis for a new generation of Raman instrumentation," *Spectrosc.* 1(12): 26, 1986.
11. P. L. Flaugh et al., "Development of a new optical wavelength rejection filter: Demonstration of its utility in Raman spectroscopy," *Appl. Spectrosc.* 38: 847, 1984.

## REAL-TIME RAMAN DETECTION OF MOLECULAR CHANGES IN CERAMICS UNDERGOING SLIDING FRICTION

G. J. Exarhos and M. S. Donley

Time-resolved Raman spectroscopy was used to probe the wear track caused by contact between a rotating ceramic disk (boron nitride or silicon carbide) and either a steel ball bearing or a silicon carbide wedge. The visco-elastic response of the hexagonal phase of boron nitride, which is used as a solid lubricant, was evaluated on a millisecond time scale. Vibrational spectra indicate that this material actually becomes a better lubricant under conditions of increased force between the wear tip and spinning disk. Similar studies involving wear between a silicon carbide disk and silicon carbide wear tip indicated that decomposition and/or segregation of elemental silicon and carbon occurred at high wear rates. The surface temperature near the wear tip was determined from measured vibrational spectra and the temperature profile around the wear track was evaluated. Evidence for oxidation of carbon at the surface was inferred from measured spectra. Application of this laser-based technique to tribological studies provides information relating to localized heating, relaxation dynamics, and phase transformation/decomposition phenomena useful for understanding the fundamental mechanisms of friction and wear.

### *Experimental*

Samples for investigation were fabricated in the shape of 15cm-diameter disks 1.5 cm thick. A 2.5cm-diameter hole was located at the center of each disk to facilitate mounting on a 0.1hp electric motor with an average rotational speed of 1700 rpm. Disks were comprised of either a high-purity grade of the hexagonal phase of boron nitride (BN) or a commercial grade of cubic silicon carbide (SiC) containing an unspecified binder material. A stainless steel bearing (0.5cm-diameter) or silicon carbide wedge (1 cm in length) served as wear tips and were mounted in a spring-loaded jig. A variable load (0-500 g) could be supplied to the wear tip in contact with the spinning disk by means of a calibrated micrometer drive mechanism. In this manner, wear tracks could be cut into the spinning disk at variable distances from the center.

Raman spectra were excited by use of a backscattering geometry. CW radiation from a Spectra Physics 164-09 Ar<sup>+</sup> laser (488 nm) was focused to a spot size between 10 and 50  $\mu\text{m}$

within a wear track of the spinning disk. Scattered radiation was collected at 45° and imaged onto the entrance slits of a 0.85m Spex Model 1403 double monochromator. Dispersed radiation was analyzed using either a conventional photomultiplier detector and associated photon-counting electronics or in a time-resolved manner using a gateable intensified diode array detector (Tracor Northern Model 6133) and associated parallel processing electronics. In the latter case, the spectrometer was operated without intermediate or exit slits, and lower groove density gratings (150 g/mm) were installed to increase the bandwidth. A narrow bandwidth rejection filter (12 nm) centered at the probe laser wavelength was necessary to minimize stray light in the monochromator under these conditions.

### *Results and Discussion*

Traditional friction-and-wear studies are concerned with factors which control the rate of material abrasion, such as atmospheric humidity, not the mechanisms responsible for the process.<sup>1</sup> Often, agreement of experimental results between otherwise seemingly identical measurements is difficult to achieve. Real-time Raman studies can directly probe physical and chemical changes of a material undergoing wear on a molecular level and provide insight for understanding both the mechanistics and kinetics of the process. Initial studies were focused on two contrasting materials.

*Hexagonal Boron Nitride.* Stoichiometric BN can exist in both hexagonal and cubic crystalline modifications. The molecular structure of the soft hexagonal phase (similar to graphite), which is used as a lubricant (Fig. 1), is different from that of graphite in that the atoms are positioned on top of each other (boron on nitrogen) in adjacent layers, rather than skewed with atoms in one layer lying directly above the hexagonal holes in the lower layer. Two vibrational lines are characteristic of hexagonal BN. A strong, sharp high-frequency line at 1366  $\text{cm}^{-1}$  is assigned to intraplanar shear-type rigid layer mode.<sup>2</sup>

Time-resolved Raman spectra were measured from the wear track of a rapidly spinning disk as a function of applied load. Thirty-two spectra acquired over 3.2 s and zero load revealed a curious exponential intensity decrease of the entire spectrum immediately on excitation. At times longer than about 3 s, the intensity showed no further changes. Apparently, surface fluorescence due to adsorbed -OH or organic binder was bleached or removed by the laser excitation, which contributed initially to a large background signal. High-resolution measurements of the intraplanar mode as a function of increasing applied load showed a reversible frequency shift from 1366 to 1368  $\text{cm}^{-1}$  (Fig. 2). The bandwidth also decreased reversibly with increasing load. Ob-

---

Author Exarhos is with Pacific Northwest Laboratory, Box 999, Richland, WA 99352; author Donley is a graduate student in the Department of Materials Science and Engineering, University of Washington, Seattle, WA 98195. Pacific Northwest Laboratory is operated by Battelle Memorial Institute for the U.S. Department of Energy under Contract DE-AC06-76RL0 1830.



served frequency shifts suggest an increase in the strength of intraplanar bonding at increased loads. Additional measurements of the frequency dependence of the low-frequency mode are in progress; current measurements indicate a frequency decrease with increasing load, which suggests a weakening of the interplanar forces. Results suggest that hexagonal BN becomes a better lubricant at higher loads.

**Cubic SiC.** Silicon carbide can exist as a number of crystal polytypes differentiated only by the dimension of the unit cell in the c-direction. This dimension is controlled by the repeat distance of tetrahedrally bonded ( $\text{C-Si}$ ) units in a chain along the c-axis of the unit cell. All polytypes are composed of hexagonal double layers of Si-C, which maintain fourfold coordination of each atom. Second-nearest-neighbor atoms can exist in either a hexagonal or cubic configuration; permutations of this packing sequence determine the crystal polytype. Each polytype exhibits a particular series of folded modes evident in the Raman spectrum that arise from transverse acoustic and transverse optic phonon branches in the c-direction of the unit cell.<sup>3</sup>

Silicon carbide is a hard refractory ceramic used in engines and engine-bearing applications as well as in cutting applications for metal working and drilling. The wear track caused by a silicon carbide wear tip on a rapidly rotating disk of silicon carbide was investigated in real time by Raman spectroscopy. Figure 3 is the Raman spectrum of the spinning disk with no load applied. Lines observed at  $766\text{ cm}^{-1}$ ,  $787\text{ cm}^{-1}$ ,  $796\text{ cm}^{-1}$  (TO), and  $970\text{ cm}^{-1}$  (LO) are characteristic of the 15R polytype which has 15 carbon and 15 silicon atoms along the c-axis of the unit cell. The feature at  $520\text{ cm}^{-1}$  is indicative of crystalline silicon; the weak bands at  $1530$  and  $1580\text{ cm}^{-1}$  can be ascribed to nongraphitic and graphitic carbon, respectively. Under static conditions, the relative band intensities change when the laser probe is moved to a new area indicating composition microheterogeneity. In fact, some regions appear richer in carbon or silicon than silicon carbide. Raman spectra acquired while the disk is spinning represent an average over these inhomogeneous regions.

A representative Raman spectrum acquired at high loads is shown in Fig. 4. Marked intensity changes in regions of the spectrum associated with elemental silicon or carbon species relative to silicon carbide bands are observed. In addition, slight broadening of the SiC lines and a line shift to lower frequencies are observed. Results indicate that friction causes decomposition of SiC and/or surface segregation of elemental Si and C. During wear, carbon is present in both an amorphous phase and as graphite, indicated by features at  $1360$  and  $1580\text{ cm}^{-1}$ , respectively. The low-frequency mode arises from nonplanar microstructural distortions and has been previously assigned.<sup>4</sup>

The broad feature centered at  $1600\text{ cm}^{-1}$  is indicative of the initiation of carbon oxidation and formation of localized  $\text{C=O}$  groups.

Vibrational frequency shifts of ca.  $1.0\text{ cm}^{-1}$  observed for the strong TO phonon line of SiC suggest a surface temperature of  $345\text{ K}$  based on the temperature dependence of SiC vibrational frequencies reported by Cardona and co-workers.<sup>5</sup> The molecular temperature was also determined from both Stokes and anti-Stokes band intensities for the strong TO mode under conditions of high applied load. The intensity ratio is proportional to the Boltzmann factor. Using the procedure advocated by Malyj and Griffiths,<sup>6</sup> we computed the surface temperature to be  $344\text{ K}$ , which is in good agreement with the temperature inferred from the frequency shift data. The temperature of the wear track approximately  $15\text{ ms}$  following contact with the wear tip appears to have equilibrated at  $344\text{ K}$  under these conditions.

### Conclusions

Raman spectroscopy has been used to characterize friction and wear in two contrasting ceramic materials. Reversible physical changes in boron nitride allow the viscoelastic properties of the solid to be followed under conditions where chemical reactions such as oxidation have not yet occurred. Conversely, both chemical changes (decomposition, oxidation) and physical changes (heating) have been observed for silicon carbide under conditions of high applied load. The feasibility for using Raman methods to characterize friction and wear on a molecular level in ceramic materials has been demonstrated and shown to provide fundamental information for modeling the wear process.

### References

1. A. P. Mercer and I. M. Hutchings, "The influence of atmospheric humidity on the abrasive wear of metals," *Wear* 103: 205-215, 1985.
2. T. Kuzuba, K. Era, T. Ishii, and T. Sato, "A low frequency Raman-active vibration of hexagonal boron nitride," *Solid State Commun.* 25: 863-865, 1978.
3. S. Nakashima, H. Katahama, Y. Nakakura, and A. Mitsuishi, "Relative Raman intensities of the folded modes in SiC polytypes," *Phys. Rev.* 33B: 5721-5729, 1986.
4. T. P. Mernagh, R. P. Cooney, and R. A. Johnson, "Raman spectra of Graphon carbon black," *Carbon* 22(1): 39-42, 1984.
5. D. Olego and M. Cardona, "Temperature dependence of the optical phonons and transverse effective charge in 3C-SiC," *Phys. Rev.* 33B: 3889-3896, 1982.
6. M. Malyj and J. E. Griffiths, "Stokes/anti-Stokes Raman vibrational temperatures: Reference materials, standard lamps, and spectrophotometric calibrations," *Appl. Spectrosc.* 37: 315-333, 1983.

# CRYSTAL STRUCTURE OF HEXAGONAL BN

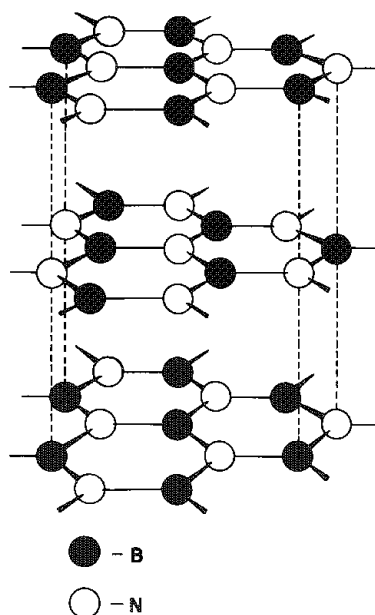


FIG. 1.--Layered graphite-like atomic arrangement in BN.

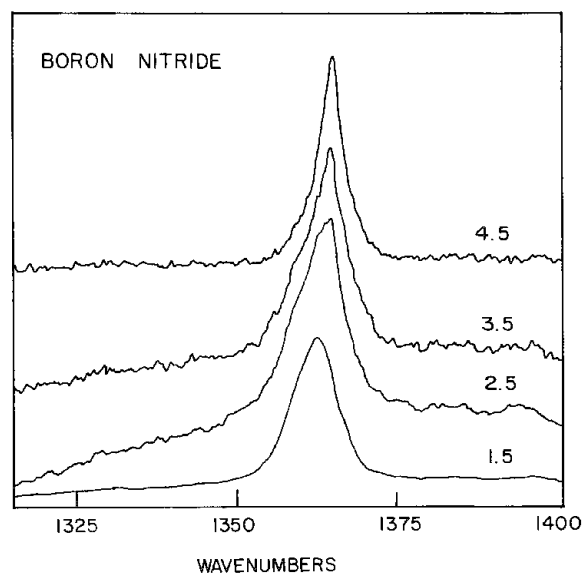


FIG. 2.--Raman spectra from the wear track formed by contact between steel bearing and rapidly spinning BN disk as function of applied load to bearing; numbers refer to hundreds of grams of applied load.

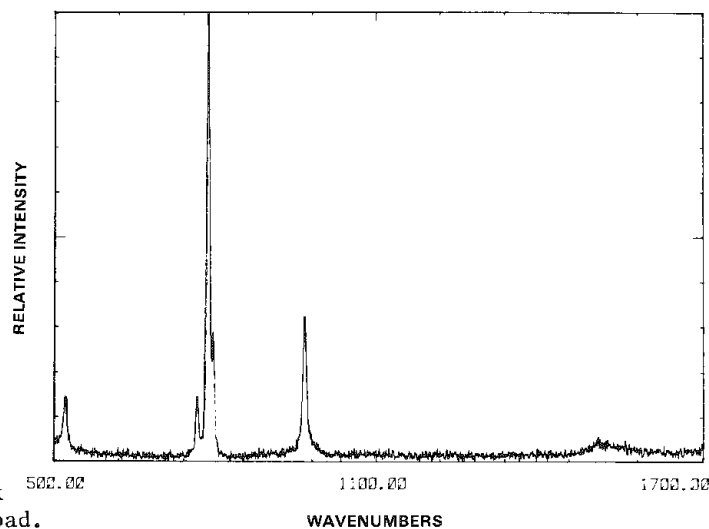


FIG. 3.--Raman spectrum of spinning SiC disk obtained under conditions of zero applied load.

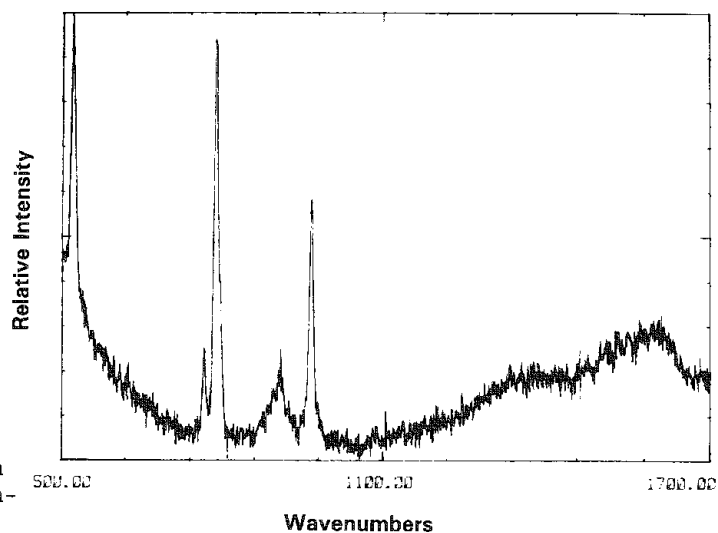


FIG. 4.--Raman spectrum of the wear track in spinning SiC disk induced by SiC wear tip under conditions of high applied load.

## LASER RAMAN MICROPROBE ANALYSIS OF SELECTIVE OXIDATION CATALYSTS

G. L. Schrader and Ümit Ozkan

NiMoO<sub>4</sub> and CoMoO<sub>4</sub> catalysts containing "excess MoO<sub>3</sub>" are active for the selective oxidation of C<sub>4</sub> hydrocarbons to maleic anhydride. Catalysts which contain "excess MoO<sub>3</sub>" are not simple, one-phase oxides; rather, multiphase behavior--as well as other structural and compositional variations--are possible. In this research, extensive characterization of these selective catalysts was performed by use of complementary techniques. However, the crucial compositional and structural identification of the active phase was achieved only with the use of laser Raman microprobe spectroscopy.

Molybdate compounds have been widely studied in previous research because of their catalytic activity for selective oxidation such as ammoxidation and the oxidative dehydrogenation of olefins. An extensive body of literature<sup>1</sup> has reported the characterization and catalytic evaluation of bismuth molybdates, which are a crucial component of catalysts used industrially to produce acrylonitrile via the ammoxidation of propylene. Hartig<sup>2,3</sup> prepared nickel and cobalt molybdate catalysts with "excess MoO<sub>3</sub>" and demonstrated their activity for C<sub>4</sub> to C<sub>10</sub> hydrocarbon conversion to maleic anhydride. Grzybowska et al.<sup>4</sup> demonstrated that the activity of cobalt molybdates for propylene selective oxidation to acrylic acid depended on the amount of "excess MoO<sub>3</sub>" present.

### Experimental

Catalysts were prepared by three methods: precipitation, solid state reaction, and impregnation. Catalytic activity and selectivity measurements were performed by use of a continuous-flow fixed-bed reactor system operated in an integral mode.<sup>5</sup>

Figure 1 shows the activity and selectivity of 1-butene conversion to maleic anhydride. Pure NiMoO<sub>4</sub> and MoO<sub>3</sub> are seen to be completely nonselective for the desired product maleic anhydride. However, catalysts prepared by precipitation involving a stoichiometric excess of molybdenum are more active and yield high amounts of maleic anhydride. Similar behavior is observed for catalysts prepared by solid-state reaction or impregnation and for CoMoO<sub>4</sub> catalysts. Table 1 indicates the stoichiometry of the NiMoO<sub>4</sub> catalysts (which could be controlled by the solution pH) as determined by x-ray fluorescence (and also the surface areas as determined by BET N<sub>2</sub> adsorption).

Author Schrader is at Iowa State University (Department of Chemical Engineering), Ames, IA 50011. Author Ozkan is at Ohio State University (Department of Chemical Engineering), Columbus, OH 43210. Support was from the Ames Laboratory (U.S. Department of Energy) Iowa State University (W-7405-ENG-82).

X-ray powder diffraction was used to investigate the possible occurrence of new phases. Figure 2 compares the x-ray diffraction patterns for pure MoO<sub>3</sub>, a precipitated catalyst prepared at pH 5 (15% "excess MoO<sub>3</sub>"), a catalyst prepared by calcining MoO<sub>3</sub> and NiMoO<sub>4</sub> at 500 C (15% "excess MoO<sub>3</sub>"), and a precipitated catalyst prepared at pH 6 (pure NiMoO<sub>4</sub>). The catalysts with 15% "excess MoO<sub>3</sub>", have diffraction patterns only indicative of NiMoO<sub>4</sub> or MoO<sub>3</sub>: no new compound was observed to be formed. Similar data obtained with a Guinier camera revealed d-spacings due only to NiMoO<sub>4</sub> or MoO<sub>3</sub>. There was no indication of the formation of solid solutions.

Conventional laser Raman spectroscopy techniques were also used to examine these catalysts largely because of the high scattering capabilities of most molybdates. Figure 3 provides the Raman spectra of precipitated NiMoO<sub>4</sub> samples prepared at pH 3, 4, 5, and 6. The spectrum of the sample prepared at pH 6 corresponds to pure NiMoO<sub>4</sub>. As indicated, there are no bands due to any phases other than NiMoO<sub>4</sub> or MoO<sub>3</sub>. Observation of the low wavenumber (<200cm<sup>-1</sup>) region revealed no structural modifications of these phases. The Raman characterization is crucial for these catalysts since the technique can also detect amorphous molybdate phases. The sensitivity for nickel oxide phases is not as high, but x-ray photoelectron spectroscopy was used for these experiments. No new phases were observed.

The results of the experimental work indicated that only NiMoO<sub>4</sub> and MoO<sub>3</sub> were present in the active catalyst but that the pure phases were completely nonselective catalysts. In order to rule out the possibility that the mere coexistence of these phases in the reactor was sufficient for high maleic anhydride selectivity, particles of NiMoO<sub>4</sub> and MoO<sub>3</sub> separated by SiC particles were packed into the reactor. With 15% "excess MoO<sub>3</sub>" in the reactor, no conversion of 1-butene to maleic anhydride was observed.

Laser Raman microprobe spectroscopy provided the key structure characterization of the active phase of these catalysts. It was possible to focus the laser beam on individual catalyst particles or on specific regions of catalyst particles. Hexagonal or needle-like particles were observed that resembled small crystals of MoO<sub>3</sub>--the "excess MoO<sub>3</sub>." The high-surface area, sponge-like particles were identified as NiMoO<sub>4</sub>. The composition of these particles could be analyzed by the Raman microprobe (Fig. 4). When the laser was focused on the sponge-like particles, only the spectrum of NiMoO<sub>4</sub> was obtained. Essentially this phase is nonselective for making maleic anhydride. However, when the laser was focused on the MoO<sub>3</sub> particles, the spectrum revealed the presence of both MoO<sub>3</sub> and NiMoO<sub>4</sub>. Sampling of a large number of particles demonstrated that

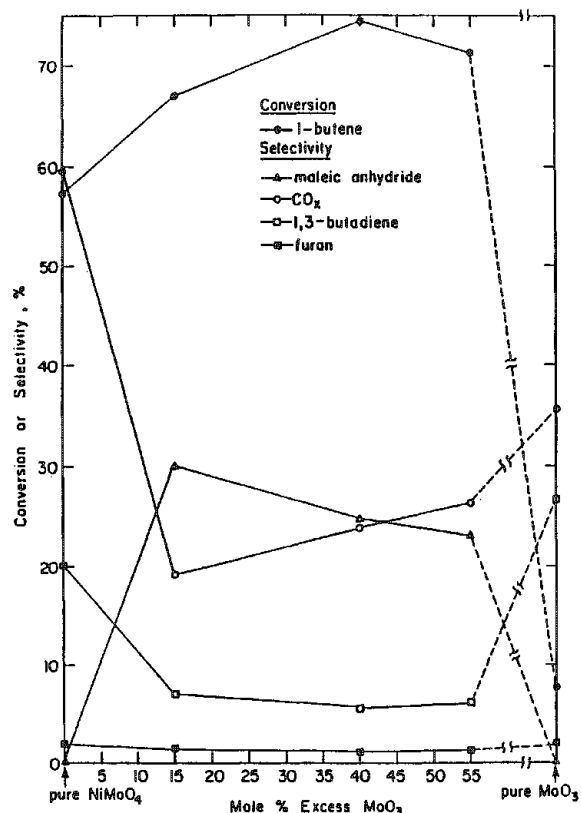


FIG. 1.--Selective oxidation of 1-butene by  $\text{NiMoO}_4$  catalysts related to "excess  $\text{MoO}_3$ " concentration.

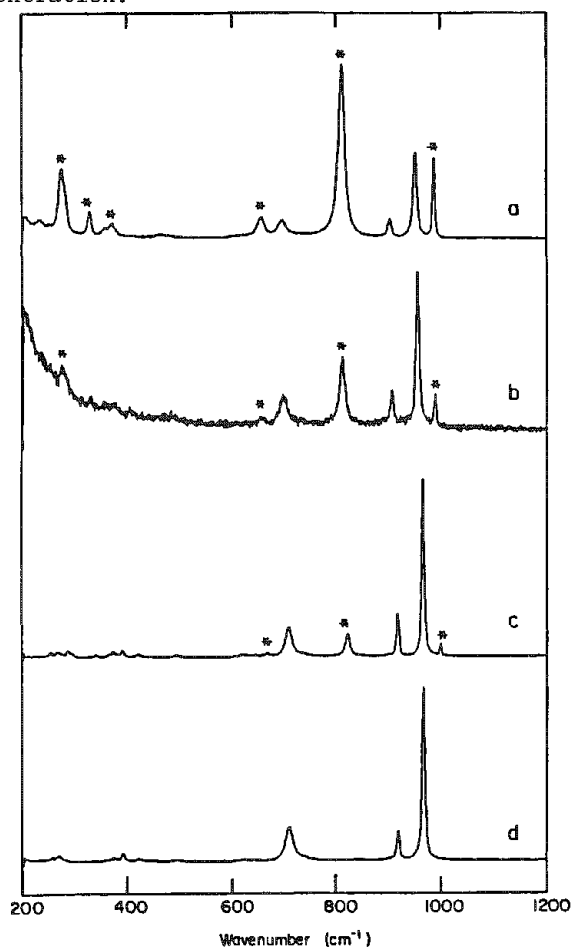


FIG. 3.--Laser Raman spectra of precipitated  $\text{NiMoO}_4$  samples: (a) pH 3, (b) pH 4, (c) pH 5, (d) pH 6. Asterisk identifies  $\text{MoO}_3$  peaks.

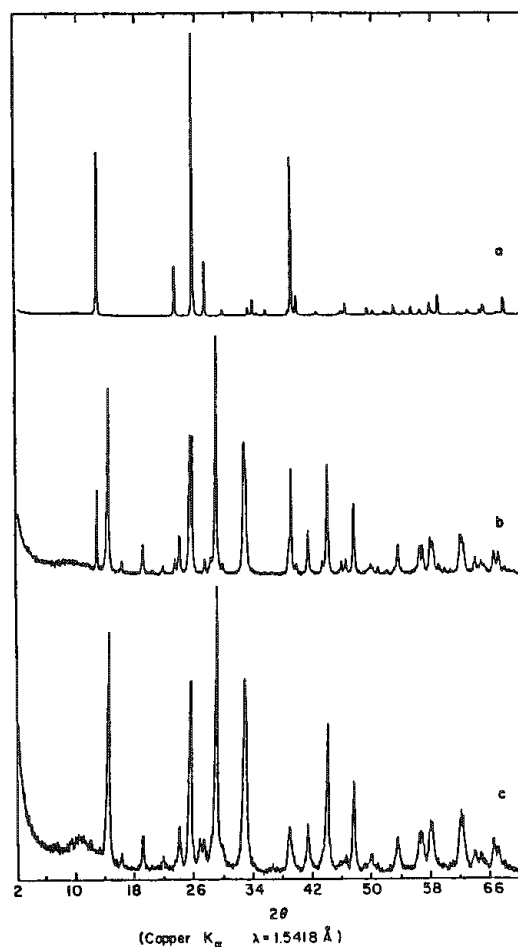


FIG. 2.--X-ray powder diffraction patterns for (a) pure  $\text{MoO}_3$ , (b)  $\text{NiMoO}_4$  with excess  $\text{MoO}_3$  (precipitation or solid state), (c) pure  $\text{NiMoO}_4$ .

TABLE 1.--Stoichiometry and surface areas of precipitated  $\text{NiMoO}_4$  catalysts.

pH during precipitation	pH during aging	Mo/Ni	Surface area ( $\text{m}^2/\text{g}$ )
6	6	1.00	37
5	5.5	1.15	33
4	5.5	1.40	26
3	5.5	1.55	20
$\text{MoO}_3$			3

this unique structure occurred extensively. Studies with  $\text{CoMoO}_4$  also revealed that the  $\text{MoO}_3$  surfaces were "decorated" with the simple molybdate phase. It was also possible to demonstrate by the microprobe technique that alternate structures--such as a "mono-layer" coverage of polymolybdates on  $\text{NiMoO}_4$  or an association of  $\text{MoO}_3$  crystallites on the  $\text{NiMoO}_4$  surfaces--did not exist. The high selectivity of these catalysts for maleic anhydride could be correlated with the existence of  $\text{MoO}_3$  particles with a surface coverage of  $\text{NiMoO}_4$ --the active phase.

#### Conclusions

Industrial selective oxidation catalysts typically consist of a complex mixture of metal oxides. The nature of the interactions between the phases that can possibly occur has

not been widely discussed. Extensive characterization of the catalyst composition and structure is essential. With laser Raman microprobe spectroscopy, it was possible to identify the active phase of catalysts containing "excess  $\text{MoO}_3$ ."

#### References

1. B. C. Gates, J. R. Katzer, and G. C. A. Schuit, *Chemistry of Catalytic Processes*, New York: McGraw-Hill, 1979, 377.
2. M. J. D. Hartig, U.S. Patent 2 625 519, 13 January 1953.
3. M. J. D. Hartig, U.S. Patent 2 691 600, 12 October 1954.
4. B. Grzybowska, J. Haber, and J. Janas, *J. Catal.* 49: 150, 1977.
5. Ü. Ozkan and G. L. Schrader, *J. Catal.* 95: 120, 137, 1985.

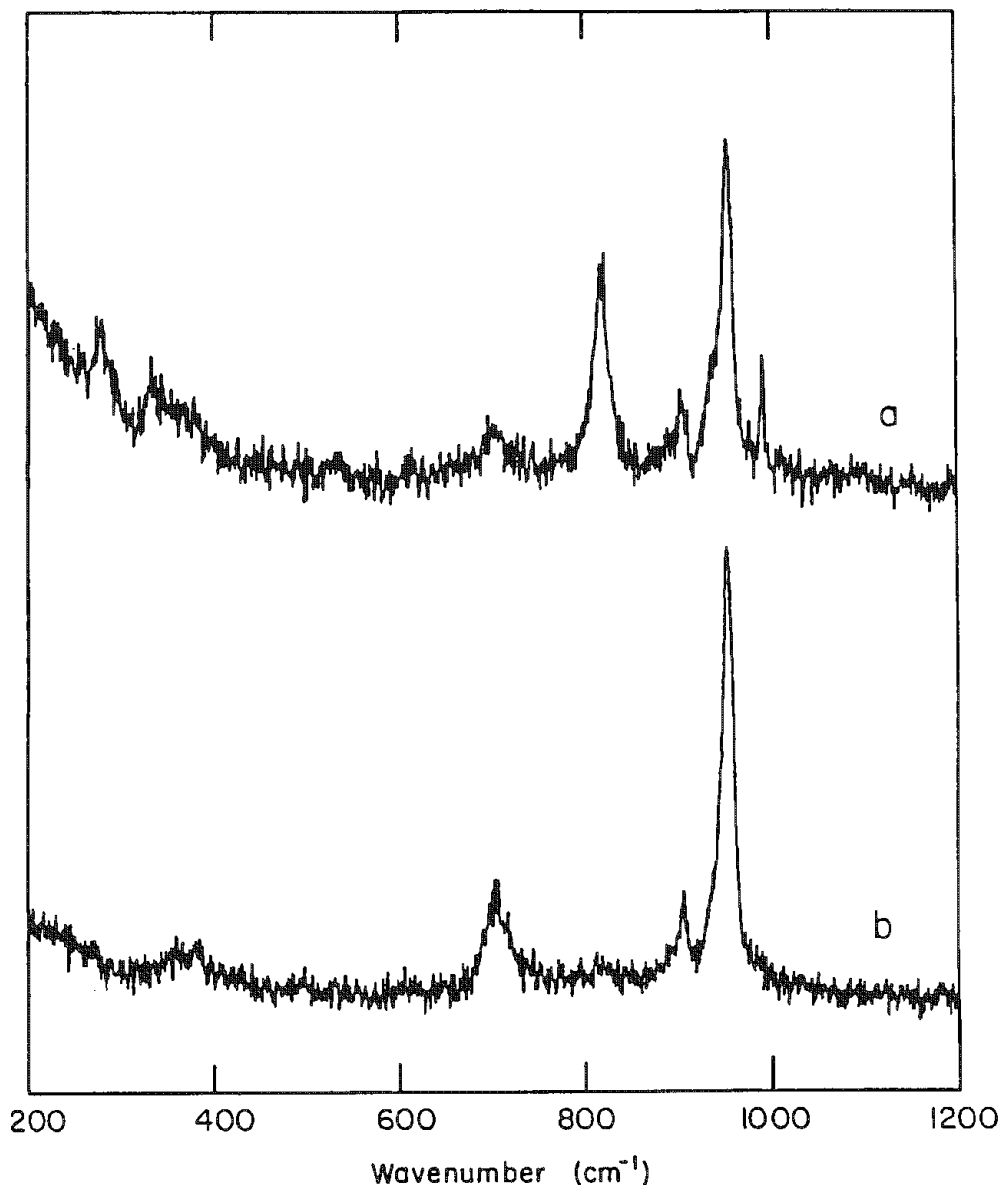


FIG. 4.--Raman microprobe spectra of impregnated  $\text{NiMoO}_4$  catalyst. Laser beam focused on (a) hexagonal particle and (b) sponge-like particle.

## RAMAN MICROSCOPY MAPPING OF HIGH-TEMPERATURE AIR CORROSION PRODUCTS ON IRON CHROMIUM ALLOY

D. J. Gardiner, C. J. Littleton, and Michael Bowden

Raman microscopy has been shown to provide useful information in the identification of corrosion products at localized points on metal surfaces.<sup>1,2</sup> The complex nature and distribution of oxides formed during high-temperature corrosion calls for an analytical technique capable of systematic mapping of chemical species at a microscopic level. In this preliminary paper we report results for one-dimensional (linescan) mapping of the corrosion products formed at high temperatures on iron chromium steel. We have adopted an approach in which the Raman microscope single-point-analysis configuration is used while the sample stage is moved stepwise, and total or partial spectra are accumulated and stored for subsequent analysis.

### Experimental

Coupons of Fe-14%Cr alloy about 10 × 10 mm thick were annealed at 1000 C for 4 h and cooled under vacuum. The samples were then mechanically cleaned, washed in acetone, dried, and corroded in air. A BGSC RMIII Raman microscope was employed in conjunction with a Spex Model 1403 0.85m double monochromator and a Spex Datamate computer and disk drive. This system is fully described elsewhere.<sup>1</sup> The microscope was fitted with a microcomputer-controlled stepper motor-driven stage. When the mapping procedure is initiated, a spectrum from the first location is recorded and stored onto disk. The Datamate then transmits an instruction to the microcomputer, via an RS232 interface, to move to the next sample point. This procedure continues until the complete sets of spectroscopic data from the number of sample points selected have been stored. A 40× microscope objective was used, giving a spot size of around 2 μm.

### Results and Discussion

The results reported here were obtained from the alloy after oxidation at 800 C for 143 h. The surface consisted of a major uniform scale having a granular appearance and a number of regions of thicker scale resulting in raised areas up to 200 μm across and 2-4 μm above the surrounding surface. The 514.5nm line from a Spectra Physics Model 162A-07 air-cooled argon ion laser was used to excite the spectra, with a laser power at the sample of 2 mW. As the system will run unattended, we were able to use long integration times with a spectral band pass of 6 cm<sup>-1</sup> to record complete sets of data overnight.

Figure 1 shows the series of spectra recorded at 10 μm intervals across such a fea-

ture. Four bands can be seen; those at 548 and 612 cm<sup>-1</sup> have been assigned to Cr<sub>2</sub>O<sub>3</sub>; the band at 645 cm<sup>-1</sup> has been assigned to Fe<sub>3</sub>O<sub>4</sub>; and that at 682 cm<sup>-1</sup> to FeCr<sub>2</sub>O<sub>4</sub>, a mixed spinel.<sup>2</sup>

A two-dimensional map of the species present on the surface of a different area of the same sample was also produced. For this experiment a Spectra Physics Model 164-07 Ar<sup>+</sup> laser was used giving ~55 mW at the sample, which allowed a shorter integration time of 6 s to be used. The spectrometer was programmed to measure Raman intensity for the bands due to Cr<sub>2</sub>O<sub>3</sub>, Fe<sub>3</sub>O<sub>4</sub>, and FeCr<sub>2</sub>O<sub>4</sub> along with the baseline on either side of each band. The baseline was subtracted from each band maximum and a linescan of intensity against distance was plotted. The spatial separation of the analysis points on the surface was 2.4 μm and 50 such points were analyzed on each line scan. In all, 350 positions were analyzed on the surface over 8 h. Successive line scans were carried out 10 μm apart to build up two-dimensional Raman maps of the species present on the surface. Two typical sets of linescans across one of the raised areas on the corrosion scale are shown in Fig. 2. The absence of Cr<sub>2</sub>O<sub>3</sub> in the raised portion is clear, as are the variations in Cr<sub>2</sub>O<sub>3</sub> concentration in the major scale. Linescans for Fe<sub>3</sub>O<sub>4</sub> and FeCr<sub>2</sub>O<sub>4</sub> resulted in essentially constant-intensity plots, which indicates the even distribution of these species across the whole surface.

### Conclusions

The results reported here suggest that under the corrosion conditions used, the development of Fe<sub>3</sub>O<sub>4</sub> and FeCr<sub>2</sub>O<sub>4</sub> is fairly uniform across the surface of the alloy. The absence of Cr<sub>2</sub>O<sub>3</sub> in the raised regions is interesting and suggests that in these areas the lack of the retarding effect of Cr<sub>2</sub>O<sub>4</sub> on the diffusion of reacting species has allowed a greater build-up of corrosion scale comprising Fe<sub>3</sub>O<sub>4</sub> and FeCr<sub>2</sub>O<sub>4</sub>.

The mapping approach has been shown to be capable of generating spatial distributions of Raman data from weakly scattering species. The approach is readily adaptable either to the accumulation of complete Raman spectra or to the plotting of the intensity distribution of one or more selected bands. The apparatus described here was constructed as a stage in the development of a more powerful facility, in which scanning will be automated in two perpendicular directions and multichannel detection will be used to increase the rate at which data can be obtained.

### References

The authors are at the School of Chemical and Life Sciences, Newcastle-upon-Tyne Polytechnic, Newcastle-upon-Tyne, England NE1 8ST.

1. D. J. Gardiner et al., "Novel applications of Raman microscopy," *Phil. Trans. Royal Soc.* 320A: 295-306, 1986.

2. D. J. Gardiner et al., "Distribution and characterization of high temperature air corrosion products in iron-chromium alloys by Raman microscopy," *Oxidation of Metals* 27: 59-74, 1987, and references therein.

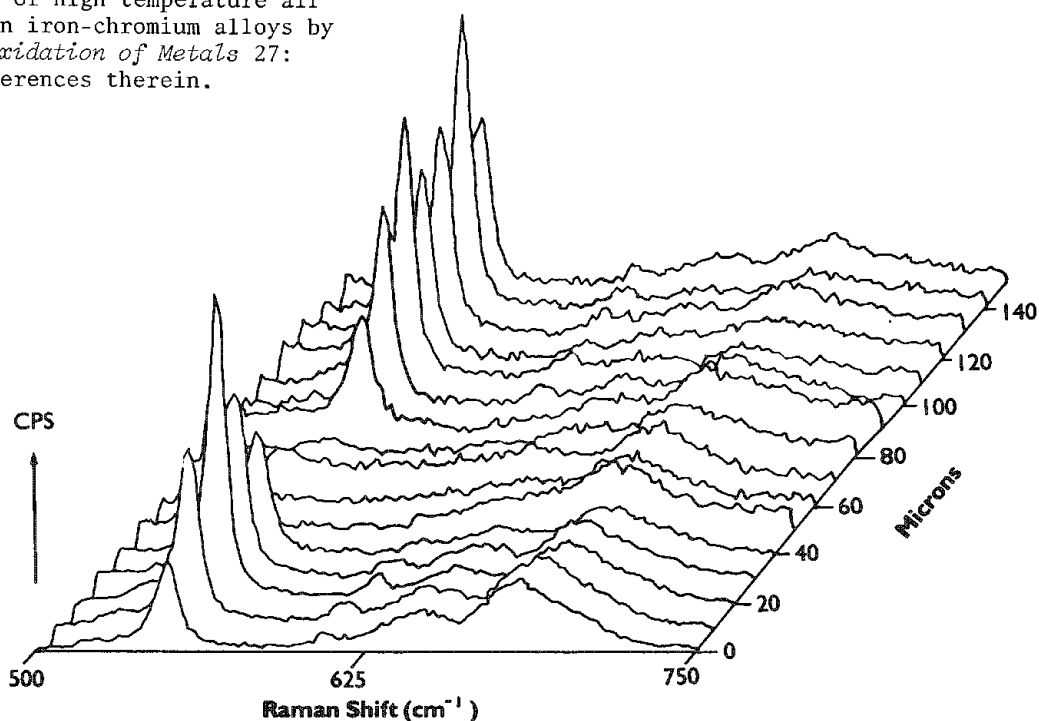


FIG. 1.--Raman spectra at 10 $\mu$ m intervals across raised feature on oxidized iron-chromium alloy.

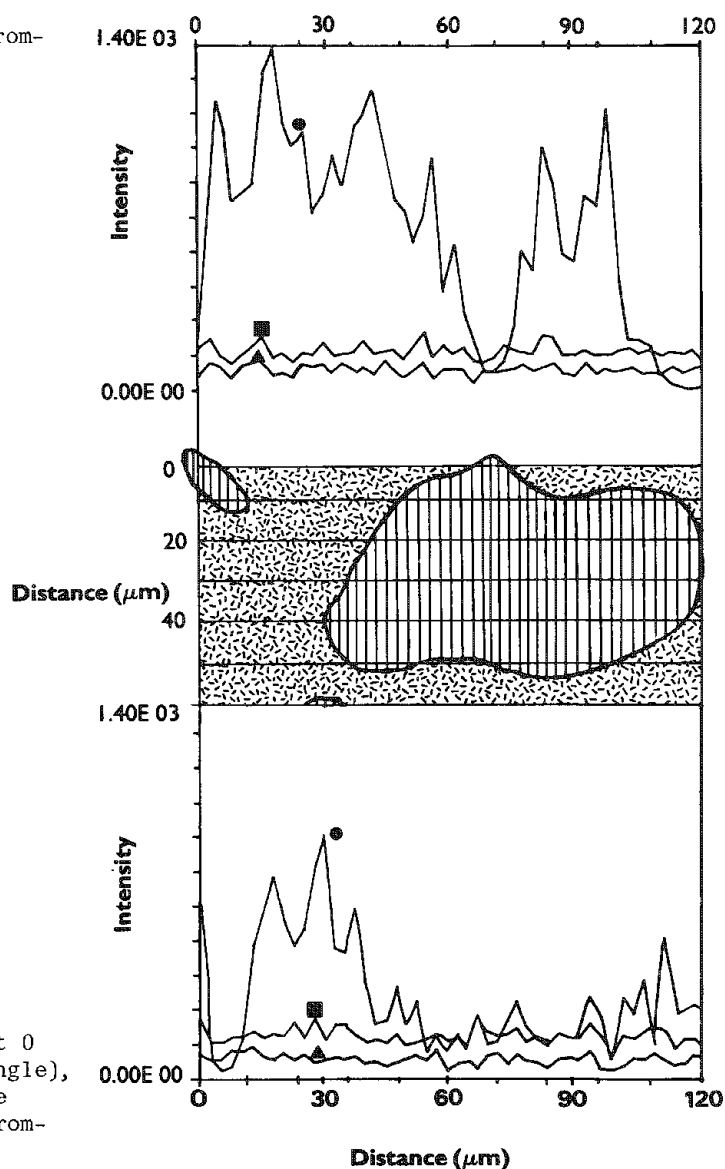


FIG. 2.--Two sets of typical linescans (at 0 and 10  $\mu$ m) for  $\text{Cr}_2\text{O}_3$  (circle),  $\text{Fe}_3\text{O}_4$  (triangle), and  $\text{FeCr}_2\text{O}_4$  (square) across raised feature (shown schematically) on oxidized iron-chromium alloy.



## MICRO-RAMAN SPECTROSCOPIC STUDIES OF MATERIALS AT AMBIENT AND HIGH PRESSURES WITH CW AND PULSED LASERS

Shiv K. Sharma and J. P. Urmos

Micro-Raman spectrophotometry is a recently developed technique<sup>1-6</sup> that can give molecular information on a microscopic scale. The micro-Raman technique most commonly utilizes a continuous-wave (CW) laser as the excitation source and a microscope objective lens for focusing the laser beam and for collecting scattered light in a 180° scattering geometry, useful for the microscopic examination of specimens that are small, inhomogeneous, or colored. However, this geometry is difficult to use with pulsed lasers because of the possibility of sample damage by the tightly focused laser beam.<sup>7</sup> We report here a Raman microscope system used to measure spectra in both the 180° and 135° scattering geometries with a single-channel Raman spectrograph. The 135° scattering geometry is very useful for measuring Raman spectra of selected microvolumes of crystals with CW and pulsed lasers. The micro-Raman system has also been used with a multichannel spectrograph in the 180° scattering geometry for measuring Raman spectra of microscopic samples of transparent or highly colored silicate glasses, and first-order Raman spectra of diamond particles and bulk diamond anvils.

### *Experimental*

The micro-Raman apparatus (Fig. 1), a modified Leitz Ortholux I microscope, was optically coupled either with a Spex double monochromator and a single-channel photomultiplier detector or with a Spex Triplemate triple spectrograph and an optical multichannel detector (OMA III, EG&G Princeton Applied Research) for use in either the 180° or 135° scattering geometry. The microscope was modified to allow a sufficient working distance between the microscope objective and the microscope stage for a 8.25cm-high diamond-anvil cell as designed by Mao and Bell.<sup>8</sup> A long-working-distance 20× objective A focused the 488nm Ar<sup>+</sup> laser beam and also served to collect the scattered Raman signal in the 180° scattering geometry. In the 135° scattering geometry, the laser beam was focused by a long-focal-length 20× objective B, not shown in Fig. 1, mounted at 45° to the optic axis of the microscope. The objectives A and B were mounted so that their foci coincided at

a point along the optic axis of the microscope.<sup>9</sup> This configuration permitted the collection of scattered radiation from a selected sample volume. Radiation collected by the microscope objective was focused on an adjustable aperture ( $\sim 200 \times 200 \mu\text{m}$ ), then reflected by a 90° prism through an achromatic doublet, and focused onto the entrance slit of the spectrograph (Fig. 1).

When using the 532nm exciting line of a frequency-doubled Nd:YAG pulsed laser, we focused the laser beam on the sample in the 135° scattering geometry by a combination of biconcave and biconvex lenses (bottom of Fig. 1). The irradiating laser intensity can be regulated at the sample by adjustment of the focal length of the biconcave lens and its distance from the biconvex lens.<sup>10</sup> The scattered radiation in the 135° scattering geometry was collected, as before, by a long-working-distance 20× objective A. This arrangement permitted the collection of Raman spectra from microvolumes of mineral samples without the laser damage to the sample that would result if the focusing system for the Ar<sup>+</sup> laser were used with the pulsed laser source.

The diamond anvil cell used for high-pressure work has additional ports so that the laser beam can be focused on the sample in both the 180° and 135° scattering geometries.<sup>8</sup> In these experiments the sample chamber was a small cylindrical hole (diameter 0.2 mm and depth 0.1 mm) drilled in a work-hardened stainless-steel gasket. Small ruby crystals ( $\sim 10 \mu\text{m}$ ) were placed in the gasket hole. Solid n-H<sub>2</sub> or a 4:1 methanol-ethanol mixture was used as the pressure transmitting medium in the gasket hole. The pressure shift was determined by measuring the red-shift in wavelength of the R<sub>1</sub> fluorescence line of the ruby crystals.<sup>11</sup>

### *Results and Discussion*

The first-order micro-Raman spectra of diamond particles of various sizes and of a bulk diamond anvil are shown in Fig. 2. These spectra were recorded with a CW laser (10 mW, 488.0 nm Ar<sup>+</sup>) in the 180° scattering geometry and with the multichannel spectrograph. It is evident from Fig. 2 that a decrease in particle size is correlated with a small decrease ( $\sim 2 \text{ cm}^{-1}$  for 1  $\mu\text{m}$  particles) in the frequency of the first-order diamond Raman line at 1333  $\text{cm}^{-1}$  and an increase in the halfwidth ( $\sim 6.6 \text{ cm}^{-1}$  for 1  $\mu\text{m}$  particles). The halfwidth of the first-order diamond line of bulk diamond at room temperature and ambient pressure is 2.8  $\text{cm}^{-1}$ . The width of the 1333  $\text{cm}^{-1}$  line of the diamond anvil in Fig. 2 is larger (4.0  $\text{cm}^{-1}$ ) than the natural halfwidth of the line because the spectral resolution is limited by the pixel width of the optical multichannel analyzer. The halfwidths of the first-order line of 10  $\mu\text{m}$  and 5  $\mu\text{m}$  diamond particles are 5.6

The authors are with the Hawaii Institute of Geophysics, University of Hawaii, Honolulu, HI 96822. Funds for developing the multichannel micro-Raman spectrograph were provided by National Science Foundation grant EAR-8517888 and the University Research Council. We are grateful to Prof. W. A. Bassett of Cornell University for providing samples of diamond particles and to Tom Cooney of the University of Oregon for providing the glass samples used in the present study. Hawaii Institute of Geophysics Contribution No. 1837.

and  $5.8\text{ cm}^{-1}$ , respectively, a difference too small for the spectral resolution of the multichannel spectrograph used in the present work. In the spectrum of  $1\text{ }\mu\text{m}$  diamond particles, the first-order diamond line remains distinct and can be therefore used for analyzing small diamond crystals that may be formed on laser-heating of graphite at high pressures in a diamond anvil cell.

The effect of pressure on the Raman spectra of the diamond anvil (diameter of pressure face  $0.4\text{ mm}$ , height  $2.41\text{ mm}$ ) measured in the  $135^\circ$  and  $180^\circ$  scattering geometries with a single-channel system is shown in Fig. 3. The  $488.0\text{ nm}$   $\text{Ar}^+$  laser beam was focused onto the center of the gasket hole and spectra were measured at sample pressures of 106 and 114 kbar for the  $135^\circ$  to  $180^\circ$  scattering geometries, respectively. The strong diamond line at  $1358\text{ cm}^{-1}$  in the  $135^\circ$  scattering geometry spectrum (Fig. 3a) is at a higher frequency than the diamond line ( $1333\text{ cm}^{-1}$ ) observed at ambient pressure (Fig. 2). When the pressure is increased to 114 kbar, the  $1358\text{ cm}^{-1}$  line shifts to  $1360\text{ cm}^{-1}$  (Fig. 3b). The spectral lines at  $1358\text{ cm}^{-1}$  and  $1360\text{ cm}^{-1}$  originate from the high-pressure region of the diamond anvil in contact with the solid  $\text{n-H}_2$  sample. The weak shoulders at lower frequency in Fig. 3 originate from scattering of the defocused laser beam from regions within the diamond anvil that are at lower pressures than the anvil face. The microvolumes sampled in this example are estimated to be  $\sim 10\text{ }\mu\text{m}$  in diameter and  $50\text{ }\mu\text{m}$  deep. In the spectrum recorded with the  $180^\circ$  scattering geometry (Fig. 3b), the intensity of the low-frequency shoulder is much higher than that of the corresponding shoulder in the spectrum recorded with the  $135^\circ$  scattering geometry (Fig. 3a). Therefore, it appears that the  $135^\circ$  scattering geometry is more suitable for measuring localized stress in the diamond anvil near the sample-diamond interface. Sharma et al.<sup>9</sup> have shown that micro-Raman spectrometry can be used for measuring stress distribution in diamond anvils, and that the diamond line frequency varies linearly with pressure by  $0.237\text{ cm}^{-1}/\text{kbar}$ .

Raman spectra of microsamples of forsterite ( $\text{Mg}_2\text{SiO}_4$ ) and fayalite ( $\text{Fe}_2\text{SiO}_4$ ) crystals and glasses were recorded in the  $180^\circ$  scattering geometry with a CW  $\text{Ar}^+$  laser ( $488\text{ nm}$ ) and a multichannel spectrograph (Fig. 4). These spectra were recorded in less than 6 min (a 1 s integration time and a maximum of 350 scans). Measurements of Raman spectra for fayalite glass with the single-channel spectrograph are very cumbersome, since it would take nearly 60 h to record a spectrum similar in quality to that obtained from the multichannel system. An additional difficulty with fayalite glasses is that they are highly light absorbing and tend to crystallize during long-time exposure to laser radiation. Forsterite glass, on the other hand, is transparent and its Raman spectrum can be measured with a single-channel micro-Raman spectrograph,<sup>12</sup> although it would take from 6 to 12 h to collect a high-quality Raman spectrum. The Raman spectrum of  $\text{Fe}_2\text{SiO}_4$  has not been reported in the literature so far. Our results show that the Raman bands for forsterite glass are rela-

tively broad and that the strong band at  $\sim 865\text{ cm}^{-1}$  corresponds to the  $\nu_s(\text{SiO}_4^{4-})$  symmetrical stretching mode of  $\text{SiO}_4^{4-}$  ions in crystalline forsterite. The close correlation between the spectra of glassy and crystalline forsterite implies a similarity between the structures of forsterite glass and crystal as both contain isolated  $\text{SiO}_4^{4-}$  tetrahedra and  $\text{Mg}^{2+}$  cations in octahedral coordination.

The Raman spectrum of fayalite glass does not show any resemblance to the Raman spectrum of crystalline fayalite (Fig. 4). In the Raman spectrum of fayalite glass the band corresponding to the  $\nu_s(\text{Si-O}^-)$  stretch appears at a higher frequency ( $\sim 965\text{ cm}^{-1}$ ) than the corresponding band at  $815\text{ cm}^{-1}$  in the spectrum of fayalite crystal. In addition, the glass spectrum shows a strong and broad band at  $495 \pm 10\text{ cm}^{-1}$ ; no such band is observed in the spectrum of fayalite crystal although there are a number of weak bands at 364, 507, 523, and  $623\text{ cm}^{-1}$  and bands of medium intensity at 234, 341, and  $123\text{ cm}^{-1}$  (Fig. 4). These differences in the Raman spectra of glassy and crystalline fayalite indicate that fayalite glass is structurally different from fayalite crystal. It is known that polymerization of  $\text{SiO}_4^{4-}$  tetrahedra causes a shifting of the  $\nu_s(\text{Si-O}^-)$  band toward higher frequency.<sup>13,14</sup> Therefore, it appears that  $\text{SiO}_4^{4-}$  tetrahedra are more highly polymerized in the fayalite glass. It is also possible that  $\text{Fe}^{2+}$  might be present in four-fold coordination in the glass in contrast to the six-fold coordination of the  $\text{Fe}^{2+}$  ion in crystalline fayalite. Additional work is needed to clarify these structural differences between glassy and crystalline fayalite.

With the  $532\text{ nm}$  line of a frequency doubled Nd:YAG pulsed laser we have successfully measured the Raman spectrum of crystalline forsterite with the micro-Raman single-channel spectrometer in the  $135^\circ$  scattering geometry. The Raman spectrum of crystalline forsterite recorded with the pulsed laser is identical to the forsterite spectrum recorded with a CW  $\text{Ar}^+$  laser (Fig. 4).

The results of this preliminary investigation have demonstrated the feasibility of obtaining Raman spectra of microsamples with CW and pulsed lasers at ambient and high pressures in the  $135^\circ$  scattering geometry. The multichannel micro-Raman spectrograph is found most suitable for measuring Raman spectra of microsamples of weak Raman scatterers such as  $\text{Fe}_2\text{SiO}_4$  and  $\text{Mg}_2\text{SiO}_4$  glasses. Work is in progress to measure the micro-Raman spectra of small mineral samples at high temperatures with the pulsed laser so that interference from the blackbody radiation in the Raman spectrum will be minimized. The feasibility of measuring the Raman spectra of materials under high pressure and temperature in the diamond cell is being explored.

## References

1. G. J. Rosasco, E. S. Etz, and W. A. Cassatt, "The analysis of discrete fine particles by Raman spectroscopy," *Appl. Spectrosc.* 29: 396, 1975.
2. M. Delhay and P. Dhamelincourt, "Raman microprobe and microscope with laser excita-

tion," *J. Raman Spectrosc.* 3: 33, 1975.

3. G. J. Rosasco, E. Roedder, and J. H. Simmons, "Laser-excited Raman spectroscopy for nondestructive partial analysis of individual fluid inclusions in minerals," *Science* 190: 557, 1975.

4. G. J. Rosasco and E. S. Etz, "The Raman microprobe: A new analytical tool," *Res. Dev.* 28: 20, 1977.

5. B. W. Cook and J. D. Loudon, "A 180° microscope sampling and viewing attachment for a laser Raman spectrometer," *J. Raman Spectrosc.* 8: 249, 1979.

6. D. J. Gardiner, M. Bowden, and P. R. Graves, "Novel applications of Raman microscopy," *Phil. Trans. Royal Soc.* A320: 295, 1986.

7. E. S. Etz and J. J. Blaha, *Scope and Limitations of Single Particle Analysis by Raman Microprobe Spectroscopy*, NBS Special Publication 533: 153, 1980.

8. H. K. Mao and P. M. Bell, "Experiment for in situ high-pressure light-scattering measurements," *Carnegie Inst. Washington Year Book* 79: 411, 1980.

9. S. K. Sharma, H. K. Mao, P. M. Bell,

and J. A. Xu, "Measurement of stress in diamond anvils with micro-Raman spectroscopy," *J. Raman Spectrosc.* 16: 350, 1985.

10. A. Leipertz and M. Fiebig, "Giant pulse laser Raman probe for low gas concentration detection," *Optical Engineering* 20: 599, 1981.

11. H. K. Mao, P. M. Bell, J. Shaner, and D. Steinberg, "Specific volume measurements on Cu, Mo, Pd, and Ag and calibration of the ruby  $R_1$  fluorescence pressure gauge from 0.06 to 1 Mbar," *J. Appl. Phys.* 49: 3276, 1978.

12. P. McMillan, Q. Williams, and T. Cooney, "Vibrational spectra of olivine-composition glasses containing iron, magnesium, and manganese," *Trans. Am. Geophys. Union (EOS)*, 67: 1274, 1986 (Abstract).

13. D. W. Matson, S. K. Sharma, and J. A. Philpotts, "The structure of high-silica alkali silicate glasses: A Raman spectroscopic investigation," *J. Non-cryst. Solids* 58: 323, 1983.

14. S. K. Sharma, B. Simons, and H. S. Yoder Jr., "Raman study of anorthite, calcium Tschermak's pyroxene, and gehlenite in crystalline and glassy states," *Am. Mineral.* 68: 1113, 1983.

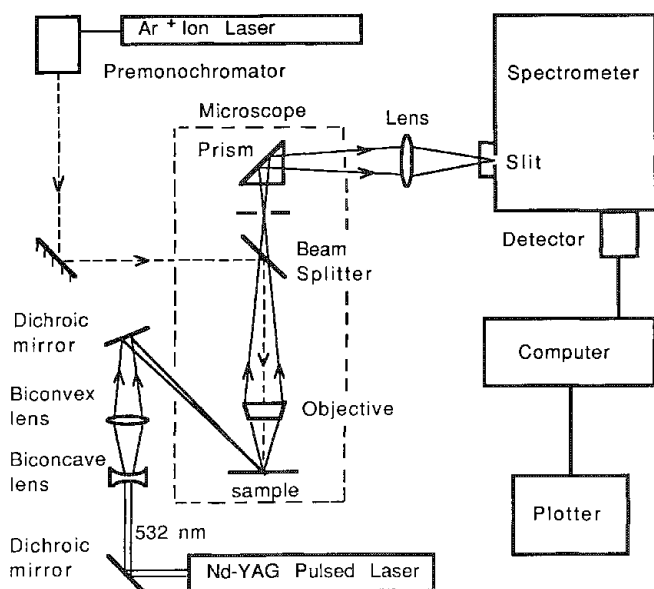


FIG. 1.--Micro-Raman system for use in 135° and 180° scattering geometries with CW Ar<sup>+</sup> and pulsed Nd:YAG lasers, and with single or multichannel spectrograph.

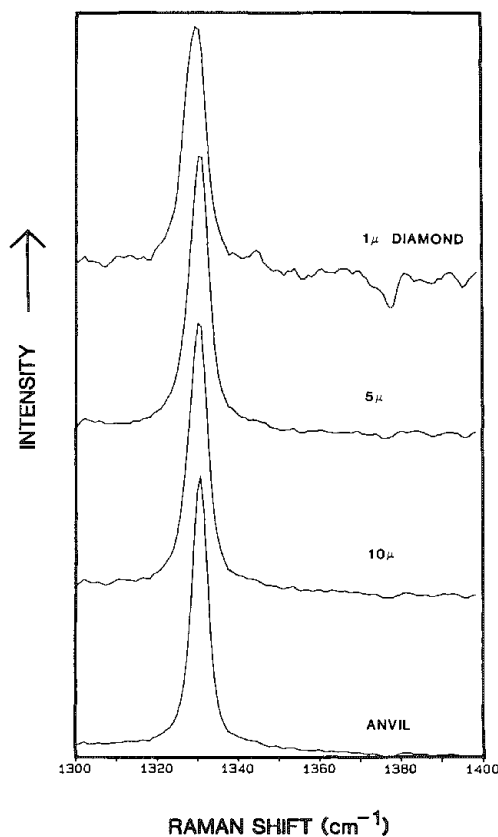


FIG. 2.--First-order micro-Raman spectra of diamond particles and bulk diamond anvil recorded with multichannel micro-Raman spectrograph in 180° scattering geometry.

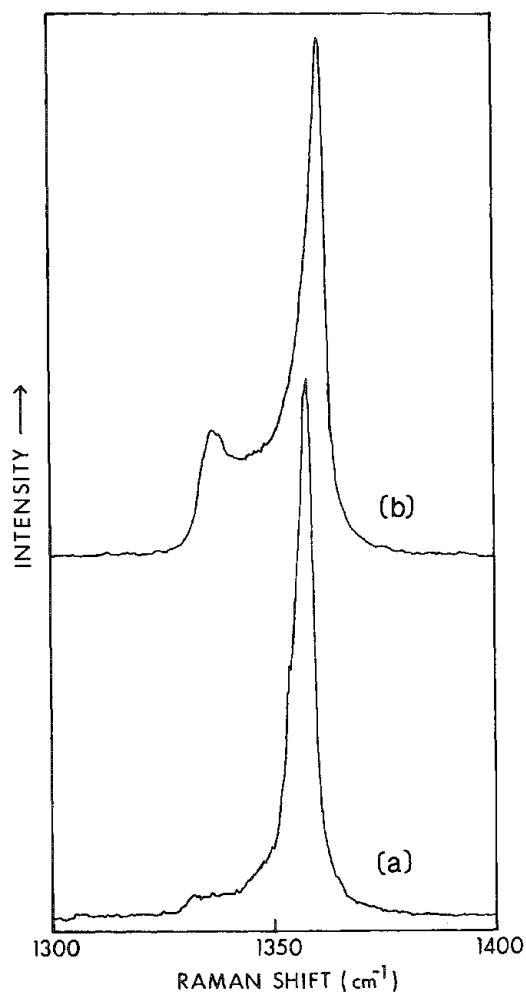


FIG. 3.--Raman spectra of diamond anvil at sample-diamond interface in (a)  $135^\circ$  (sample pressure 106 kbar) and (b)  $180^\circ$  (sample pressure 114 kbar) scattering geometries recorded with single-channel micro-Raman spectrograph.

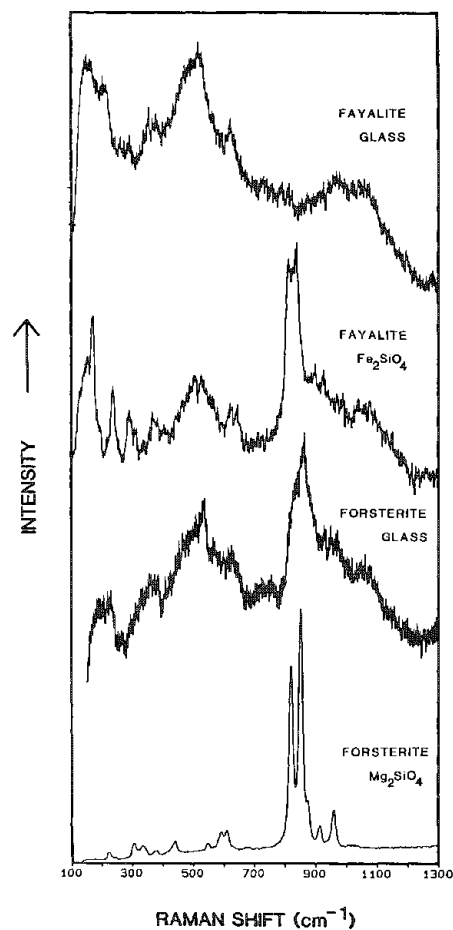


FIG. 4.--Micro-Raman spectra of crystals and glasses of forsterite ( $\text{Mg}_2\text{SiO}_4$ ) and fayalite ( $\text{Fe}_2\text{SiO}_4$ ) compositions recorded with multi-channel micro-Raman spectrograph.

## MICRO-RAMAN SPECTROSCOPY WITH LASER LIGHT TRAPS

W. Kiefer

We report on Raman microprobe techniques where micron-sized solid particles or liquid droplets are trapped in focused laser beams. One such laser light trap is achieved by a vertically directed focused TEM<sub>00</sub>-mode cw gas laser of ~500 mW. As shown by Ashkin,<sup>1</sup> if a particle is hit by the laser beam, it is simultaneously drawn in to the beam axis and accelerated in the direction of the light until the force of radiation pressure is balanced by the gravitational force.<sup>1</sup> We have recently applied this technique in order to trap micron-sized particles to serve as microsamples for Raman spectroscopy.<sup>2</sup>

A true "optical bottle" based on radiation pressure alone can be obtained<sup>1,2</sup> by two opposing equal TEM<sub>00</sub> Gaussian beams with beam waists that are located close together but do not actually coincide spatially. As suggested by us,<sup>2</sup> this light trap allows the observation of inelastically scattered light from very small particles.

Very recently, Ashkin et al. have shown that optical trapping of dielectric particles can be achieved by a single-beam *gradient* force trap.<sup>3</sup> The latter confirms the concept of negative light pressure due to the gradient force. They observed trapping over the entire range of particle size from 10 μm to ~25 nm in water. Use of this new laser light trap extends the size range of macroscopic particles accessible to optical trapping well into the Rayleigh size regime. We have been able to trap stably glass spheres in the size range from ~10 to ~1 μm.<sup>4</sup> However, nonspherical microparticles can be also trapped by this method; as an example, we were successful in trapping single *E. coli* bacteria.<sup>4</sup>

Recently, there has been a good deal of interest in investigations of the light-scattering properties of dielectric spheres. Studies of the wavelength-dependent features of this type of scattering are of particular interest because of the sharp structural resonances that occur as the Mie size parameter  $x = 2\pi a/\lambda$  ( $a$  = radius of sphere,  $\lambda$  = wavelength in the surrounding medium) is varied. These structural resonances have been predicted for incident and/or inelastically scattered spheres. The first observation of morphology-dependent resonances in Raman scattering from dielectric microparticles has been published by Owen et al.<sup>5</sup> The abovementioned trapping techniques are ideal for such studies. We have reported on the observation of such structural resonances in the Raman spectra of single microspheres of glass<sup>6</sup> and liquid droplets<sup>7</sup> applying the technique of optical levitation by radiation pressure. The observed structural resonances in the Raman spectra of dielectric spheres could be assigned by use of the well-known Lorenz-Mie formalism,<sup>8,9</sup> and a good cor-

relation is found between these experimental and theoretically predicted Raman-Mie spectra.

### References

1. A. Ashkin, "Acceleration and trapping of particles by radiation pressure," *Phys. Rev. Lett.* 24: 156-159, 1970.
2. R. Thurn and W. Kiefer, "Raman-microsampling technique applying optical levitation by radiation pressure," *Appl. Spectrosc.* 38: 78-83, 1984.
3. A. Ashkin, J. M. Dziedzic, J. E. Bjorkholm, and S. Chu, "Observation of a single-beam gradient force optical trap for dielectric particles," *Opt. Lett.* 11: 288-290, 1986.
4. M. Marchl, P. Knoll, and W. Kiefer, unpublished.
5. J. F. Owen, P. W. Barber, and R. K. Chang, "Morphology-dependent Raman spectra from microparticles," *Microbeam Analysis--1982*, 255-260.
6. R. Thurn and W. Kiefer, "Observation of structural resonances in the Raman spectra of optically levitated dielectric microspheres," *J. Raman Spectrosc.* 15: 411-413, 1984.
7. R. Thurn and W. Kiefer, "Structural resonances observed in the Raman spectra of optically levitated liquid droplets," *Appl. Opt.* 24: 1515-1519, 1985.
8. M. Kerker, *The Scattering of Light and Other Electromagnetic Radiation*, New York: Academic Press, 1969.
9. P. W. Barber, "Theory of morphology dependent resonances," in W. C. Stawley and M. Lapp, Eds., *Advances in Laser Science: I*, AIP Conf. Proc. 146, New York, 1986, 720-723.

## ABSORPTION AND SCATTERING BY HETEROGENEOUS PARTICLES

Milton Kerker and Ramesh Bhandari

Many particles of great interest contain particulate inclusions, which leads to the question of how to estimate the absorption and scattering by such complex bodies. We are developing a new model in which a Monte Carlo algorithm is used for calculating the absorption and scattering of electromagnetic radiation by a particle containing inclusions that in turn absorb and scatter light.

The host particle is taken to be a sphere containing smaller spherical inclusions. The host sphere must be large enough so that in the absence of the inclusions an accurate description of the scattering and absorption can be obtained by use of (1) ray optics to account for reflections and refractions at the boundary, together with transmissivity within the homogeneous sphere; and (2) Fraunhofer diffraction around the outside of the sphere. The spherical inclusions are large enough to require application of the full Lorenz-Mie formalism, but not so large that the ray-optics-diffraction approach can be applied to the host particle. These inclusions may be located at specific preselected sites, or they may be distributed randomly with the host particle. The condition that the host particle and the inclusions be spheres may be relaxed at a later stage of the study.

A Monte Carlo algorithm is constructed in which the trajectory of a photon is followed from the source beam to termination at detectors located at observation points outside the host particle or at a particular inclusion within the host particle where the photon may be absorbed. The scheme is outlined in Fig. 1, with the incident ray  $S$  along which the photon travels selected randomly. On impact at the boundary  $B$  a decision is made probabilistically (based upon Fresnel's equations) whether the photon is reflected ( $R_1$ ) or refracted ( $R_r$ ). If the photon is refracted, it proceeds to an appropriate detector  $D$ ; otherwise, it follows the path of the refracted ray deterministically until it encounters an inclusion particle  $P$  or the boundary  $B$ . In Fig. 1 a deterministic trajectory is indicated by a full line, a probabilistic by a dashed line.

If the encounter is with an inclusion particle, a probabilistic decision based on the Lorenz-Mie equations is made to determine whether the photon is absorbed ( $A$ ) or scattered into a particular direction  $[S(\theta, \phi)]$ . Absorption terminates this photon ( $T$ ). Scattering leads the particle along a deterministic path either to another inclusion particle or to the boundary where either of the respective probabilistic events recurs.

If the first encounter of the photon within the host particle is with the boundary, a probabilistic decision is made based on Fresnel's equations and leads the photon either to

a detector, or upon reflection along a deterministic ray, which then encounters either an inclusion particle or the boundary.

The process continues until the photon is absorbed or detected. If the host particle is lossy, the photon is attenuated accordingly along its trajectory. The Lorenz-Mie equations are used as if the inclusion particle were irradiated by a plane wave. One can include a factor to account for the divergence of the multiply scattered radiation, but this factor would be incorporated only at a later stage of the study. Consideration of polarization on scattering is also deferred, since that will add considerably to the complexity of the program and the length of the calculation.

The accumulation at the detectors when added to the Fraunhofer diffraction will provide the differential scattering cross section. Integration over all directions gives the total scattering cross section. The total accumulation of photons absorbed at the inclusion particles provides the absorption cross section which when added to the total scattering cross section is the extinction cross section.

Some preliminary results have been obtained that suggest the efficacy of this theoretical model.

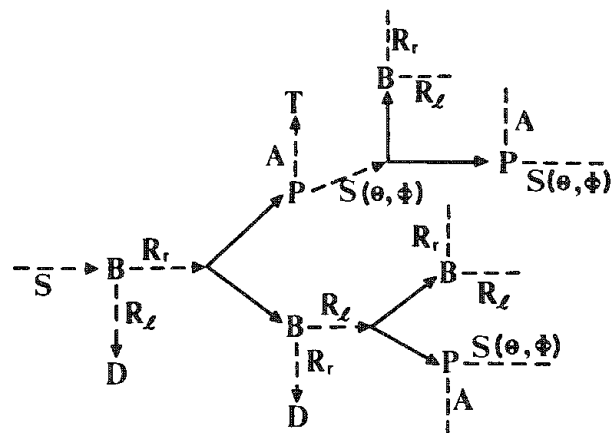


FIG. 1.--Course of photon through heterogeneous particle. Dashed lines represent probabilistic decisions; full line, deterministic decisions. A, absorption; B, boundary; D, detector; P, particle;  $R_1$ , reflection;  $R_r$ , refraction;  $S$ , select incident ray;  $S(\theta, \phi)$ , scattering; T, termination by absorption.

# POLARIZATION MEASUREMENTS IN RAMAN MICROSCOPY

Paul Dhamelincourt, Claude Brémard, Jacky Laureyns, J. C. Merlin, and George Turrell

Raman scattering in gases and liquids, as excited and observed with the use of linearly polarized light, is often employed to distinguish molecular vibrational modes according to their symmetry. Furthermore, such measurements are useful in the determination of crystal orientation, as well as molecular orientation in liquid crystals, model membranes, thin films, polymer fibers, etc.

In Raman microscopy the sample is excited by a laser beam which is focused by a microscope objective. In addition, a beam-splitter is usually used to separate the scattered light from the excitation. As these two optical elements perturb polarization measurements, their effects must be evaluated if quantitative results are to be obtained.<sup>1</sup>

An additional problem arises from the high light intensity produced in the focal region, which often results in destruction of the sample. This difficulty has recently been at least partially alleviated with the development of multichannel detection systems,<sup>2</sup> which permit weaker excitation to be used.

The effects of the beamsplitter can be corrected by application of the method reported previously,<sup>1</sup> and the depolarization introduced by the microscope objective has been calculated in preliminary publications.<sup>1,3</sup> However, the influence of the index of refraction of the sample has not been considered. This aspect of the problem for the case of isotropic samples is summarized in the present communication.

The scattering intensity has been evaluated for the case of a linearly polarized source focused by a large numerical aperture objective and collected by the same objective. If the axis of the cone of light excitation and collection is collinear with the Z axis and the polarization of the excitation is in the X direction, the intensity of the Raman-scattered light is given by<sup>3</sup>

$$I = (\alpha_{XX}^2 A + \alpha_{XY}^2 A + \alpha_{XZ}^2 B)(2C_0 + C_2) + (\alpha_{YX}^2 A + \alpha_{YY}^2 A + \alpha_{YZ}^2 B)C_2 + (\alpha_{ZX}^2 A + \alpha_{ZY}^2 A + \alpha_{ZZ}^2 B)4C_1 \quad (1)$$

The coefficients  $C_0$ ,  $C_1$ , and  $C_2$  associated with the excitation are defined by

$$C_j = 2\pi \int_0^\infty \int_0^\infty |I_j(u,v,n)|^2 v dv du \quad j = 0,1,2 \quad (2)$$

where the integrals  $I_j(u,v,n)$  are functions of the half-angle of acceptance of the objec-

tive, the radial distribution intensity of the excitation, and the index of refraction of the (isotropic) sample. The integrals appearing in Eq. (2) are over the optical coordinates, which are defined by  $u = kZ \sin^2 \theta_m$  and  $v = k\sqrt{X^2 + Y^2} \sin \theta_m$  with  $k = 2\pi/\lambda$  the wave number.

The following expressions are derived in Ref. 4.

$$I_0(u,v,n) = 2 \int_0^{\theta_m} D(\theta) \sin \theta \left( \frac{m}{n^2 \cos \theta + m} + \frac{1}{\cos \theta + m} \right) \cdot \cos \theta J_0 \left( \frac{v \sin \theta}{\sin \theta_m} \right) e^{iu \cos \theta / \sin^2 \theta_m} \cos^{1/2} \theta d\theta \quad (3)$$

$$I_1(u,v,n) = 2 \int_0^{\theta_m} D(\theta) \sin \theta \left( \frac{\sin \theta}{n^2 \cos \theta + m} \right) \cdot \cos \theta J_1 \left( \frac{v \sin \theta}{\sin \theta_m} \right) e^{iu \cos \theta / \sin^2 \theta_m} \cos^{1/2} \theta d\theta \quad (4)$$

$$I_2(u,v,n) = -2 \int_0^{\theta_m} D(\theta) \sin \theta \left( \frac{m}{n^2 \cos \theta + m} + \frac{1}{\cos \theta + m} \right) \cdot \cos \theta J_2 \left( \frac{v \sin \theta}{\sin \theta_m} \right) e^{iu \cos \theta / \sin^2 \theta_m} \cos^{1/2} \theta d\theta \quad (5)$$

where  $\theta$  is the angle of incidence of a given ray of the light excitation and  $D(\theta) = N \csc \theta \cdot \exp(-\sin^2 \theta / \sin^2 \theta_m)$  represents a Gaussian radial distribution in the laser beam and  $N$  is a normalization constant.

The index of refraction of the sample is  $n$ , and  $m = \sqrt{n^2 - \sin^2 \theta_m}$ . The coefficients  $C_0$ ,  $C_1$ , and  $C_2$  were evaluated as functions of  $n$  in Ref. 4. The parameters  $A$  and  $B$ , which are associated with the Raman scattered light, are functions of the numerical aperture of the objective. They are given by<sup>3</sup>

$$A = \pi^2 \int_0^{\theta_m'} (\cos^2 \theta + 1) \sin \theta d\theta = \pi^2 \left( \frac{4}{3} - \cos \theta_m' - \frac{1}{3} \cos^3 \theta_m' \right) \quad (6)$$

$$B = \pi \int_0^{\theta_m'} \sin^3 \theta d\theta = \pi \left( \frac{2}{3} - \cos \theta_m' + \frac{1}{3} \cos^3 \theta_m' \right) \quad (7)$$

where  $\theta_m' = \sin^{-1}[(1/n)\sin \theta_m]$  is the effective angular semi-aperture within the sample.

For randomly oriented molecules, the scattering intensities  $I_{\perp}$  and  $I_{\parallel}$  have been evaluated from Eq. (1) as functions of the invari-

The authors are at the Laboratoire de Spectrochimie Infrarouge et Raman, C.N.R.S. (LP 2641) Université des sciences et Techniques de Lille Flandres Artois, 59655 Villeneuve d'Ascq, Cedex, France.



ants  $\Sigma^0$ ,  $\Sigma^1$  and  $\Sigma^2$  of the polarizability tensor.<sup>5</sup> The depolarization ratio then follows from  $\rho_{\text{cal}} = I_{\perp}/I_{\parallel}$ .

Polarized Raman and resonance-Raman spectra of a variety of isotropic samples (including carbon tetrachloride,  $\beta$ -carotene, and ferrocytochrome c) have been recorded with various numerical-aperture objectives. The experimental depolarization ratio  $\rho_{\text{exp}}$  of some Raman bands are compared with the calculated values in Table 1. The calculated values are within the experimental error range, in good agreement with the experimental values.

For anisotropic samples such as crystals of the cubic system, e.g., diamond,<sup>6</sup> the calculated values obtained from the theoretical expressions based on Eq. (1) are in accordance with the integrated intensities measured from the polarized Raman spectra, providing that the axis of the illumination cone is perpendicular to the surface of the sample. The results are then independent of the depth of focus. In the case of uniaxial crystalline samples such as  $\alpha$ -quartz a significant depolarization is observed, which arises from birefringence,<sup>6,7</sup> when the excitation cone is collinear with the (unique) optical axis. This observation is confirmed by a noted increase in the depolarization leakage with increasing optical path in the sample. When the direction of the electric vector of the excitation is parallel to the nodal lines of the crystal, the depolarization leakage is negligible, again assuming that the axis of illumination is perpendicular to the surface of the crystal.

## References

1. C. Brémard, P. Dhamelincourt, J. Laureyns, and G. Turrell, *Appl. Spectrosc.* 39: 1036, 1985.
2. J. Barbillat and M. Delhaye, *Microbeam Analysis--1983*, 280.
3. G. Turrell, *J. Raman Spectrosc.* 15: 103, 1985.
4. C. Brémard, J. Laureyns, J. C. Merlin, and G. Turrell, *J. Raman Spectrosc.* (in press).
5. O. Sonnich Mortensen and S. Hassing, in R. J. H. Clark and R. E. Hester, Eds., *Advances in Infrared and Raman Spectroscopy*, London: Heyden, 1980, vol. 6, 1.
6. C. Brémard, J. Laureyns, and G. Turrell, *Can. J. Spectrosc.* (in press).
7. M. E. Andersen and J. G. Delly, *Microbeam Analysis--1985*, 33.

TABLE 1.--Experimental and calculated depolarization ratios of Raman bands of typical samples.

$\theta_m$	CCl <sub>4</sub> $\nu_4(F_2), 314 \text{ cm}^{-1}$		$\beta$ -carotene $\nu_1(A_g), 1525 \text{ cm}^{-1}$		ferrocyclochrome c (A <sub>2g</sub> ), 1585 $\text{cm}^{-1}$	
	$\rho_{\text{cal}}$	$\rho_{\text{exp}}$	$\rho_{\text{cal}}$	$\rho_{\text{exp}}$	$\rho_{\text{cal}}$	$\rho_{\text{exp}}$
71.8°	0.770	0.77	0.35	0.36		
64.8°	0.767	0.77	0.34	0.34		
58.2°	0.765	0.76	0.33	0.32		
39.1°	0.758	0.76	0.33	0.32	22	25
20.5°	0.753	0.75	0.33	0.34	58	> 30
10.4°	0.750	0.75	0.33	0.32	227	> 40
5.2°	0.750	0.75	0.33	0.33	848	> 50
~0°	0.750	0.75	0.33	0.33	$\infty$	> 100

## THE SIGNAL-TO-NOISE ADVANTAGES OF MULTICHANNEL DETECTORS ON RAMAN MICROPROBES

Fran Adar, Jeremy Lerner, and Yair Talmi

The multiplex advantage on two Raman microprobes has been demonstrated. It is shown that the size of the image of the source on the entrance slit, the size of the image of the entrance slit on the exit plane, and the size of the elements of the multichannel detector play a role in determining conditions that demonstrate the signal-to-noise improvement with multichannel detectors.

Since the development of high-sensitivity imaging detectors, their application as multichannel detectors on spectrographs has been implemented.<sup>1-8</sup> Fellgett was the first to recognize that one could acquire a spectrum by simultaneous detection of "all" bands in a spectrum much more rapidly than by scanning a monochromator with a photomultiplier tube (PMT) mounted behind the exit slit.<sup>9</sup> However, the experimental measurement of the multiplex advantage is somewhat elusive.

In order to characterize the multiplex advantage, one must examine a sample in *one* system equipped with both monochannel (PMT behind exit slit) and multichannel (diode array) detectors. There is then no question whether the optical throughput is the same for both measurements. However, other considerations affect the measured counting rates that cannot be ignored: the size of the individual elements of a multichannel detector, digitization of the analog signals, differences in interactions between the spectrometer and the detectors, and the line widths of the bands being measured.<sup>2,10</sup> If some or all of these considerations are ignored in casual measurements, a comparison of multichannel with monochannel systems may produce puzzling results.

### Instrumentation

The monochannel/multichannel comparisons that we present were recorded on two different types of optical microprobes. The microscopes and detectors are identical on the two systems, but in one case the spectrometer was a high-resolution double one-meter system (Instruments SA, Inc., Mole® U1000); in the second case the spectrometer was a medium-resolution 640mm spectrometer coupled to a high-luminosity double-subtractive filter (Instruments SA, Inc. Mole® S3000 Triple Spectrograph).

The microscopes are from the Olympus BH series and were optically and mechanically rigidly coupled to the Raman instruments. The laser illumination is provided by a beamsplitter in the epi-illuminator. The spot size at the sample is 1  $\mu\text{m}$ ; the image of this point at the entrance slit is between 75 and 100  $\mu\text{m}$ .

The PMTs (RCA 31034) have GaAs photocathodes that provide high sensitivity out to

900 nm, corresponding to the fundamental electronic gap of the material; the tubes are cooled to -30 C to reduce the thermionic emission.

The multichannel detectors used in this series are intensified diode arrays (DA). The U1000 is equipped with a 3/4-in. image intensifier and a 512-element diode array (IRY 512 from Princeton Instruments, Inc.). The Mole® S3000 is equipped with a 1-in. image intensifier and a 1024-element diode array (Model IRY 1024). Individual diodes are 25  $\mu\text{m}$  wide and 2.5 mm high. The image intensifiers are proximity-focused, which implies that there is no distortion of the spectral field between the photocathode of the image intensifier and the diode array surface. The photocathodes are multialkali and have S20 spectral response. The quantum yields of the detectors are nominally 20% for the PMT and 10% for the DA. The sharpest feature observed by the DA will be 3-4 diodes wide at half maximum.

### Results

Single-crystal silicon was used for the Raman microprobe measurements. With the appropriate orientation of the sample relative to the microprobe and laser polarization, the Raman intensity is reproducible to about  $\pm 10\%$ . Cleavages occur along (110) and ( $\bar{1}\bar{1}0$ ) directions. For axes labeled  $Z = (100)$ ,  $X = (100)$ ,  $Y = (010)$ ,  $X' = (110)$ , and  $Y' = (\bar{1}\bar{1}0)$ , the backscattering Raman tensor has nonvanishing components  $Z(X,Y)\bar{Z}$  and  $Z(X',X')\bar{Z}$  in Porto's notation.<sup>11</sup> The laser polarization coming through the microscope is normally "East/West" (E/W), which connotes the left/right direction when the observer faces the microscope.

Because of significant dichroism of many diffraction gratings, it is usually advisable to choose conditions that produce Raman radiation polarized perpendicular to the slits (which is also perpendicular to the grating grooves) when the excitation wavelength is 514.5 nm, and 1800 g/mm gratings are used. The U1000 has horizontal slits, which dictates orientation of the crystal with its cleavage edges at 45° to the E/W direction in order to utilize the  $Z(X,Y)\bar{Z}$  component of the tensor. The Mole® S3000 has vertical slits, which requires cleavage edges parallel to the microscope raster axes to achieve  $Z(X',X')\bar{Z}$ .

*Mole® U1000.* Figure 1 shows the silicon phonon, as detected by the U1000 microprobe with a 100 $\mu\text{m}$  entrance slit. When scanned with the PMT, the exit slit was also 100  $\mu\text{m}$ . The PMT peak signal ( $\sim 25\,000$  counts/s) is about 70% higher than the DA peak signal ( $\sim 15\,000$  counts/s). The observed full width at half maximum (FWHM) of both spectra is about 5.5  $\text{cm}^{-1}$ , which is significantly larger than the 0.9  $\text{cm}^{-1}$  instrumental resolution for this slit width and corresponds to  $\sim 600$   $\mu\text{m}$  in the focal plane which spans about 24 diodes.

Authors Adar and Lerner are with Instruments SA, 6 Olsen Avenue, Metuchen, NJ 08820; author Talmi is with Princeton Instruments, Box 2318, Princeton, NJ 08540.

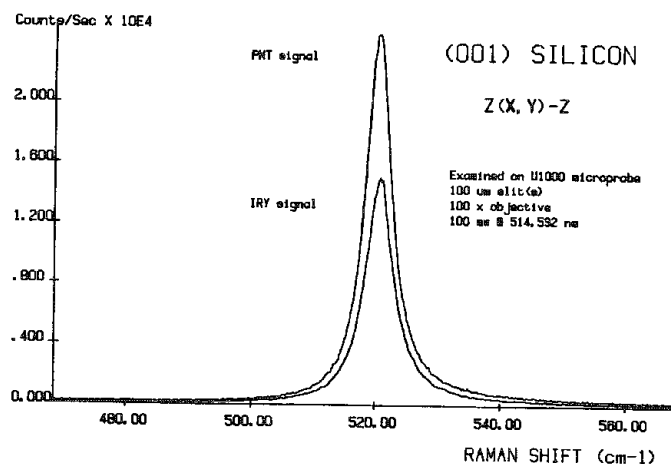


FIG. 1.--Si phonon detected by U1000 microprobe.  $Z(X,Y)\bar{Z}$ ;  $S_1 = 100 \mu\text{m}$ ,  $S_2 = S_3 = 7 \text{ mm}$ ,  $S_4 = 100 \mu\text{m}$  (PMT only). PMT: spectrum scanned with  $1 \text{ s}/0.25 \text{ cm}^{-1}$  per data point. DA (IRY signal): spectrum acquired with one 1s read-out, background subtracted. Laser:  $\lambda - 514.532 \text{ nm}$ ,  $100 \text{ mW}$  entering microscope.

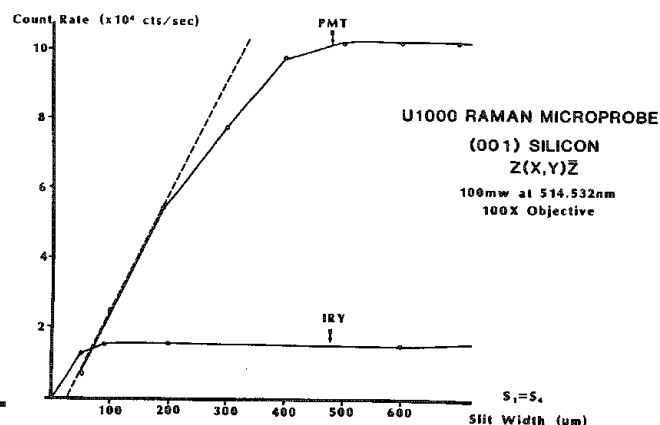


FIG. 2.--Raman signals from (001) Si,  $Z(X,Y)\bar{Z}$ , observed on U1000 microprobe with PMT and DA (IRY signal) detectors, as function of slit width.  $100 \text{ mW}$  at  $514.5 \text{ nm}$  was measured entering the microscope.  $100\times$  objective ( $n.a. = 0.95$ ) was used to focus laser and collect Raman signal.

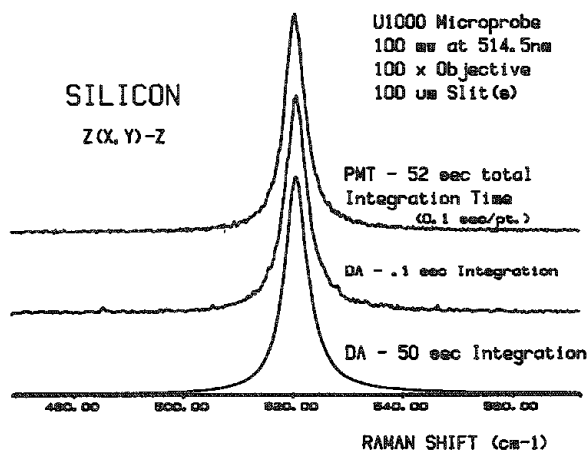


FIG. 3.--Raman signals from (001) Si,  $Z(X,Y)\bar{Z}$  observed on the U1000 microprobe.  $100 \text{ mW}$  at  $514.532 \text{ nm}$  entering the microscope.  $100\times$  objective,  $100 \mu\text{m}$  slits(s). Top: The PMT signal was scanned with  $0.25 \text{ cm}^{-1}/0.1 \text{ s}$  per data point. Middle: DA spectrum acquired with .1s integration. Bottom: DA spectrum acquired with 50s integration

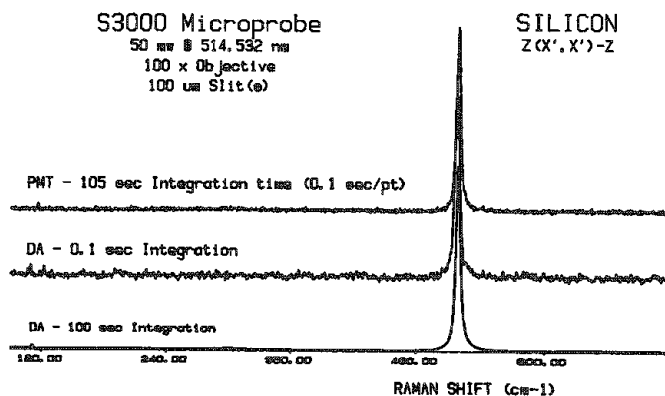


FIG. 4.--Raman signals from (001) Si,  $Z(X',X')\bar{Z}$ , observed on the S3000 microprobe.  $50 \text{ mW}$  at  $514.532 \text{ nm}$  entering microscope;  $100\times$  objective;  $100 \mu\text{m}$  slit(s). Top: The PMT signal was scanned with  $0.6 \text{ cm}^{-1}/0.1 \text{ s}$  per data point. Middle: DA spectrum acquired with 0.1s integration. Bottom: DA spectrum acquired with 100s integration.

Figure 2 illustrates the variation in observed count rates on the DA and PMT as the slit width is changed. At slits smaller than 50  $\mu\text{m}$ , the signals from the DA were higher than from the PMT. When the entrance slit was open to more than 100  $\mu\text{m}$ , no increase in DA signal was observed. In contrast, the PMT signal increased in a close to linear fashion until 500  $\mu\text{m}$ , and then began to plateau. (See also discussion below.)

Figure 3 illustrates the silicon signal on the PMT when scanned with 0.1 s per 0.25  $\text{cm}^{-1}$  per data point. This produces approximately the same number of data points as the diode array integrations (displayed in the same figure) which were acquired with 0.1 s and 52s integration time.

*Mole® S3000.* Figure 4 illustrates the silicon signal detected by the PMT and diode array on the S3000 triple spectrograph. Because of the lower dispersion of this instrument and the larger DA, about 630  $\text{cm}^{-1}$  can be viewed simultaneously by the DA in this region of the spectrum. In order to produce a PMT spectrum with the same number of data points, the spectrum was scanned with 0.6  $\text{cm}^{-1}$  per data point. The PMT integration time was 0.1 s; DA spectra were acquired with 0.1 s and 100s integration times, which corresponded to single-point PMT time and total integration time of the PMT spectrum.

#### Discussion

The dependence of the observed signals on the PMT and the DA as a function of entrance slit width on the U1000 shown in Fig. 2 provide insight into the behavior of these signals. In the case of the DA, the entrance slit is the only slit that limits light through the system. The fact that the DA signal plateaus as the entrance slit is opened indicates that the laser spot at the sample, as it imaged on the entrance slit, is small enough so that further increase in the entrance slit width produces no gain in signal.

In the case of the PMT, the entrance and exit slits are equal in width and the signal does not plateau until much higher slit values are reached. The data from the DA already indicate that for the U1000 entrance slit at 100  $\mu\text{m}$ , no light is gained when this slit is opened further. The increase in signal on the PMT must come then from the effect of the size of the entrance-slit spot as imaged on the exit slit. Since the FWHM of the silicon phonon is  $\sim 5.5 \text{ cm}^{-1}$ , as measured with 100  $\mu\text{m}$  slits on the U1000, the size of the image of the spot in the exit plane of the U1000 is  $\sim 600 \mu\text{m}$  at the half-intensity positions. Therefore, the PMT signal on the U1000 does not increase as the exit slit is opened beyond 500  $\mu\text{m}$ , which corresponds to the plateau in Fig. 2.

We can thus argue that comparison of PMT and DA signals on the U1000 can be done effectively with 100  $\mu\text{m}$  slits. The entrance slit does not block any light. An infinitely sharp Raman line would be imaged on about six diodes. However, because the silicon phonon line is  $\sim 5.5 \text{ cm}^{-1}$  wide, 24 diodes are spanned by the full width at half maximum. The four diodes at the band maximum see signals compa-

table to the signal transmitted by the 100  $\mu\text{m}$  exit slit. Comparison of the PMT to DA spectra from the U1000 in Fig. 3 can now be used to evaluate the multiplex advantage. The signal-to-noise in the top two spectra (acquired with 0.1s integration) on the PMT and DA are comparable; however, the DA spectrum was acquired 500 times faster. The DA spectrum on the bottom of the figure was acquired with the same integration time as the total PMT integration time. It is clear that the added integration time occurring across the entire spectrum produces greatly improved signal-to-noise ratios. Similar comparisons can be made on the PMT and DA scans recorded on the triple Mole® S3000 in Fig. 4. More extensive measurements of the multiplex advantage are continuing so as to enable quantification of the enhancement of signal quality.

#### References

1. Yair Talmi, "TV type multichannel detectors," *Anal. Chem.* 47: 699A-709A, 1975.
2. G. D. Christian, J. B. Callis, and E. R. Davidson, "Array detectors and excitation, emission materials in multicomponent analysis," in E. L. Wehry, Ed., *Modern Fluorescence Spectroscopy*, Chap. 4, Vol. 4, New York: Plenum Press, 1980.
3. M. L. Fultz and R. A. Durst, "Investigation of two multichannel image detectors for use in spectro electrochemistry," *Talanta* 30: 933-939, 1983.
4. Yair Talmi, Ed., *Multichannel Image Detectors*, Vol. 2, ACS Symposium Series #236, American Chemical Society.
5. W. R. Steinbach, C. F. Lohrstorfer, and E. S. Etz, "Analytical applications of a multiplex detector laser Raman microprobe," *Microbeam Analysis--1982*, 279-285.
6. M. Delhaye, M. Bridoux, P. Dhamelin-court, J. Barbillat, E. Da Silva, and B. Rous-sel, "A new generation of laser Raman Micro-spectrometers: Micromars, *ibid.*, 275-278.
7. F. P. Milanovich, T. Hirschfeld, and D. C. Johnson, "The Lawrence Livermore National Laboratory Raman microprobe," *ibid.*, 270-278.
8. F. J. Purcell and E. S. Etz, "A new spectrograph with a multichannel optical detector for the Raman characterization of particles," *ibid.*, 301-306.
9. P. Fellget, Ph.D. thesis, Cambridge University, Cambridge, 1951.
10. Yair Talmi, D. C. Baker, J. R. Jadamec, and W. A. Saner, "Fluorescence spectrometry with optoelectronic image detectors," *Anal. Chem.* 50: 936A-952A, 1978.
11. R. H. Pollak and Raphael Tsu, *Raman Characterization of Semiconductors Revisited*, in SPIE 452, Spectroscopic Techniques for Semiconductor Technology, 26-43, 1983.

## HIGH-SPATIAL-RESOLUTION ANALYSIS OF SEMICONDUCTOR THIN FILMS WITH A RAMAN MICROPROBE

P. M. Fauchet

The Raman microprobe has been used for several years to characterize microsamples. More recently, it has been used to produce line scans of nonuniform semiconductor films, in some cases after laser processing of the surface.<sup>1-3</sup> In fact, two-dimensional maps of such films have been obtained<sup>4</sup> and we have been able to generate three-dimensional maps.<sup>5</sup> We survey our recent contributions to this field and briefly discuss new promising directions of research which we are exploring.

### *One-dimensional Maps of Semiconductor Thin Films*

The general goal of our research is to gain a better understanding of laser-solid interactions. This is a vast field and our contributions have been primarily in two areas. First, we have embarked on a study of laser-induced damage.<sup>6</sup> Such a study is important because damage to optical components limits our ability to obtain high power laser beams. Damage is usually thought to occur at isolated sites associated with the presence of imperfections such as defects or surface roughness.<sup>7</sup> The nature of those imperfections is poorly known, and the inability to observe precursors to damage is puzzling. When exposed to many laser shots (instead of one), most components eventually fail, even if the laser power density is still below the single-shot damage threshold.<sup>8</sup> The incubation period, during which it has not been possible to observe any meaningful precursors to date, is a strong function of the laser power density, and there seems to be a "safe" level<sup>9</sup> that corresponds to power densities so low that no degradation is observed for any practical number of shots.

The second area of interest to us is that of laser annealing, laser recrystallization and formation of metastable phases of matter with short laser pulses. Lasers have now been used for almost ten years to restore crystalline order in ion-implanted semiconductors.<sup>10</sup> Today, lasers and lamps are used to recrystallize polycrystalline or amorphous silicon films grown on insulator, a material of technological importance for thin film transistors.<sup>11</sup> Relatively large single-crystal grains can be produced thanks to the presence of seeds (i.e., uncovered Si islands) in the silicon dioxide film.<sup>12</sup> However, especially with respect to strain and its spatial variations, the effect of laser processing is quite different from that of lamp processing.

The Raman microprobe is an ideal tool to map important material properties that may help us understand the mechanisms at work bet-

ter. The Raman spectrum is sensitive to many parameters. In our work, we have emphasized crystallinity, grain size, and strain or stress.<sup>2,6,13-15</sup> Since the laser beam is focused to a 1  $\mu$ m spot, the Raman maps obtained by scanning the beam have a resolution comparable to what is available from good optical microscopes. Mapping in the third dimension is achieved by tuning of the laser wavelength. The penetration depth of light in semiconductors such as Si, Ge, or GaAs is a strong function of wavelength in the spectral regions covered by an argon or krypton laser.<sup>16</sup> Therefore, one-, two- and three-dimensional maps of crystallinity, grain size, or stress can be generated.

We now discuss briefly two examples from our own work. In the first example, a thin film of polycrystalline silicon grown on silicon dioxide was illuminated by picosecond laser pulses in the visible (532 nm) or in the ultraviolet (355 nm). Melting occurred at the center of the illuminated spot and the surface was rough when observed with an optical microscope. The profile of the surface is sketched in the first entry of Fig. 1. The Raman microprobe was then scanned along a radial line, and the other entries in Fig. 1 show the asymmetry, the width, the shift with respect to the peak of the line before processing, and the intensity of the Raman line of silicon. Those results have been discussed in more detail elsewhere.<sup>15,17</sup> Basically, after 532nm illumination, the central region 1 is made of large grains (>30 nm) under large tensile stress ( $6 \times 10^9$  dyne/cm<sup>2</sup>). In region 2, the stress becomes heterogeneous, which means that the film did not melt thoroughly. In region 3, which appears completely unaffected under optical microscopy, we observe that the grain size is comparable to that in the original film (of the order of 20 nm) but that the stress relaxes over a region of the order of 20  $\mu$ m. Note that the grain size was also measured by Raman scattering as explained in Ref. 18. After 355nm illumination, the central region 1 has similar properties except that the stress is already heterogeneous. In region 2, the average grain size is very small (of the order of 10 nm or less) and the stress relaxes much more slowly than after 532 nm illumination. Note that the grain size is determined by the asymmetry of the Raman line,<sup>18</sup> that the stress is measured from the shift of the peak,<sup>19</sup> and that the heterogeneity is estimated from the width of the line, after the effect of grain size has been accounted for. Finally, we interpret the slow recovery of the line intensity as due to the presence of a thin amorphous layer produced by the ultrafast quenching that follows ultrafast melting.

In the second example, we have compared annealing of thin amorphous silicon films by pulsed or cw lasers, or by lamps. These samples have been obtained from different sources

The author is with Princeton University, Department of Electrical Engineering, Princeton, NJ 08544. The contributions of Ian Campbell and support from NSF are appreciated.

and have undergone widely different processing steps. The geometry of these structures also differ greatly. It is possible at this time to give a crude summary of our findings. In general, the laser processed samples showed residual stress of the order of  $10^9$  to  $10^{10}$  dyne/cm<sup>2</sup>, and this stress relaxed away from the seeds, whereas the lamp-processed samples showed little or no residual stress. Many other factors, for example the details of the sample geometry and the presence of a cap layer, may affect the results. We expect to be able to provide a coherent picture of all our findings in the near future.

#### Two- and Three-dimensional Mapping

Mapping in two dimensions seems like a rather trivial extension of the work described above. However, if we are concerned with a lineshape analysis, it means that a good quality full spectrum must be obtained for each square micron and that the procedure must be repeated many times to cover a macroscopic area. Therefore, in the first two-dimensional mapping of semiconductors of which we are aware the authors took advantage of polarization selection rules to map the strength of the forbidden line.<sup>4</sup> The samples were laser annealed to recrystallize a thin silicon layer. When epitaxy from the substrate was complete, the crystal orientation was nearly perfect and the forbidden line was weak. When epitaxy was incomplete, the grains were more or less randomly oriented and the forbidden line was strong. We have recently obtained two- and three-dimensional maps of the full Raman line in semiconductor heterostructures. The data acquisition time is now greatly increased. It would thus be highly desirable to use an optical multichannel detector array. It is also conceivable that by using proper optical elements, the laser beam can be focused to a line (or at least a high aspect ratio spot) with a width equal to 1-2  $\mu\text{m}$ . The signal coming from the line focus could be analyzed with a two-dimensional detector array. The net gain in data acquisition time might be in excess of 1000 compared to the present capabilities available in our laboratory.

As mentioned before, depth resolution can be achieved by tuning the laser wavelength so that the probe light penetration depth varies. This has been demonstrated with unfocused probe beams on GaAs and InP.<sup>20</sup> We have very recently started to generate three-dimensional

maps of the Raman spectrum in layered structures. With the use of the microprobe and of depth profiling, Raman spectroscopy can now give important structural information on a scale of less than 1  $\mu\text{m}^3$ . Since that can be achieved in a nondestructive manner, we predict a bright future for this technique.

#### References

1. P. Zorabedian and F. Adar, *Appl. Phys. Lett.* 43: 177, 1983.
2. P. M. Fauchet, I. H. Campbell, and F. Adar, *Appl. Phys. Lett.* 47: 479, 1985.
3. J. B. Hopkins and L. A. Farrow, *J. Appl. Phys.* 59: 1103, 1986.
4. S. Nakashima, K. Mizoguchi, Y. Inoue, M. Miyauchi, A. Mitsuishi, T. Nishimura, and Y. Akasaka, *Jpn. J. Appl. Phys.* 25: L222, 1986.
5. P. M. Fauchet, invited presentation at the *Topical Meeting on Lasers in Materials Diagnostics*, Albuquerque, N.M., 1987.
6. P. M. Fauchet, I. H. Campbell, and F. Adar, in *Proc. 17th Ann. Symp. Optical Materials for High-power Lasers*, NBS Special Publication (in press).
7. W. H. Lowdermilk and D. Milam, *IEEE J. QE-17*: 1888, 1981.
8. L. D. Merkle, M. Bass, and R. T. Swimm, *Opt. Eng.* 22: 405, 1983.
9. P. M. Fauchet, *Phys. Lett.* 93A: 155, 1983.
10. S. D. Ferris, H. J. Leamy, and J. M. Poate, Eds., *Laser-solid Interactions and Laser Processing*, New York: AIP, 1979.
11. *Semiconductor on Insulator and Thin Film Transistor Technology*, Mat. Res. Soc. Proc. Series 53, Pittsburgh, 1986.
12. J. M. Gibson, L. N. Pfeiffer, K. W. West, and D. C. Joy, Ref. 11, p. 289.
13. P. M. Fauchet, *IEEE Circuits and Devices Mag.* 2: 37, 1986.
14. P. M. Fauchet, *Mat. Res. Soc. Proc.* 51: 149, 1986.
15. I. H. Campbell, F. Adar, and P. M. Fauchet, Ref. 11, p. 311.
16. E. D. Palik, Ed., *Handbook of Optical Constants of Solids*, New York: Academic Press, 1985.
17. P. M. Fauchet, *SEM/1986 II*, 425.
18. I. H. Campbell and P. M. Fauchet, *Solid State Commun.* 58: 739, 1986.
19. E. Anastassakis, A. Pinczuk, E. Burstein, F. H. Pollak, and M. Cardona, *Solid State Commun.* 8: 133, 1970.
20. H. Shen and F. H. Pollak, *Appl. Phys. Lett.* 45: 692, 1984.

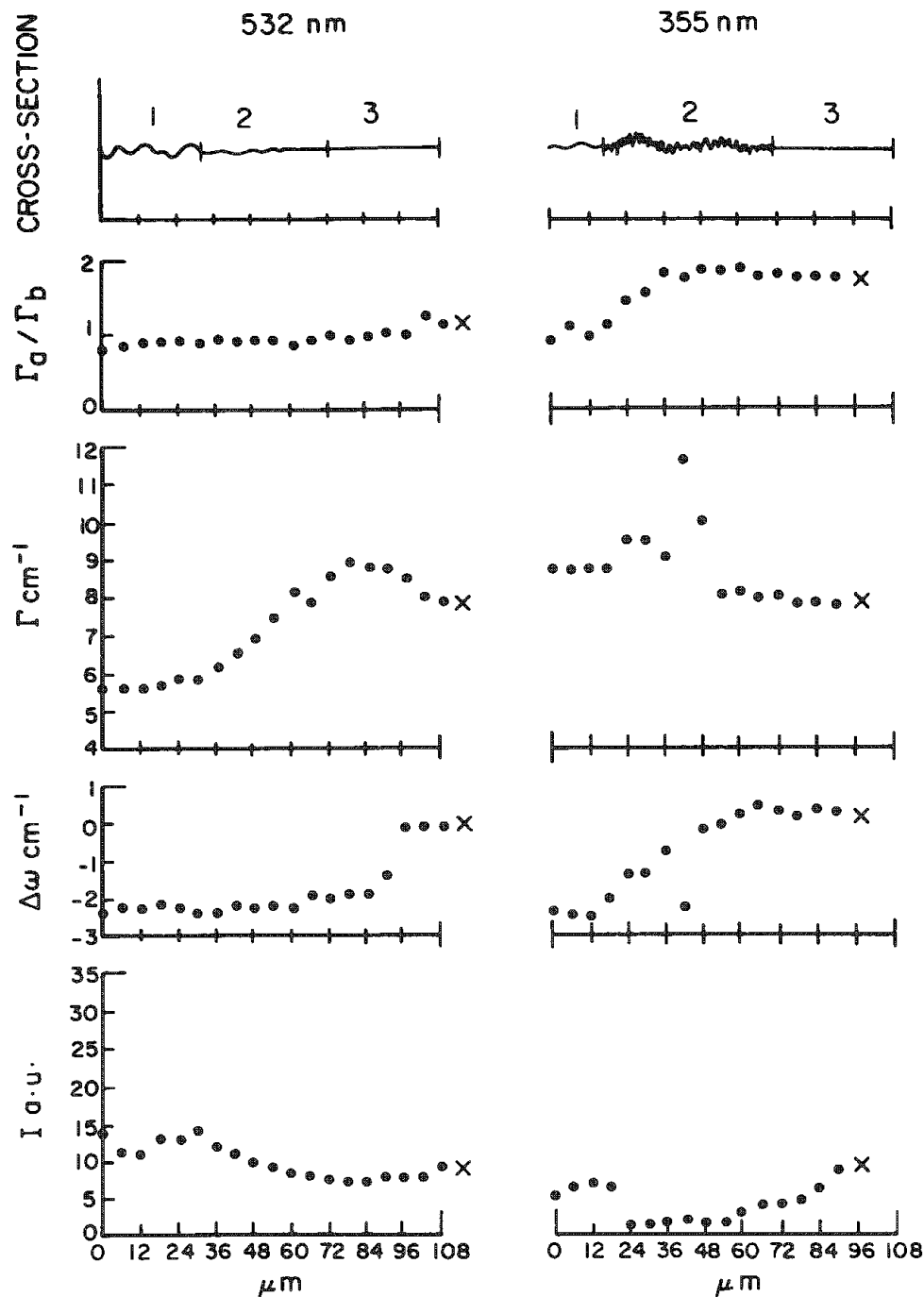


FIG. 1.--Evolution of Raman line of silicon after exposure to picosecond pulses at 532 and 355 nm. Sample is thin polycrystalline Si film grown on silicon dioxide. Top to bottom: surface roughness, asymmetry of line (ratio of low-wavenumber HWHM to high-wavenumber HWHM), full width at half maximum of line, frequency shift with respect to unprocessed material, and peak intensity of line.



## RAMAN MICROPROBE CHARACTERIZATION OF DIELECTRIC FILMS FOLLOWING HIGH-ENERGY PULSED LASER IRRADIATION

G. J. Exarhos and D. M. Friedrich

The interaction of intense laser radiation with thin oxide films often results in degradation of their optical properties through the formation of regions characterized by stress inhomogeneity, phase transformation/recrystallization, or marked material ablation. A Raman microprobe investigation of several sputter-deposited single- and multi-layer films was initiated to study in greater detail the molecular changes induced by high energy irradiation. Catastrophic damage is observed in submillimeter regions whose shape and depth depend upon laser energy, wavelength, and the cumulative number of incident pulses. Spatially resolved Raman spectra acquired with a resolution of a few micrometers have been correlated with a specific damage morphology. In addition to identification of phase inhomogeneity resulting from irradiation, microprobe measurements also reveal non-uniform stress in the coatings inferred from frequency shifts in the sharp  $143\text{ cm}^{-1}$  [ $\nu_6(\text{E}_g)$ ] vibrational phonon mode of the anatase phase. Interpretation of spectra characteristic of the "equilibrium" damage state is based on previous work which demonstrated that Raman spectroscopy is an effective probe of film thickness, phase and stress inhomogeneity, and microcrystallite orientation.<sup>1-3</sup>

### Experimental

Single-layer dielectric films ca.  $1\text{ }\mu\text{m}$  thick and multilayer stacks were prepared by reactively sputtering of Ti or Zr in  $\text{Ar}/\text{O}_2$  atmospheres onto fused silica substrates in an rf diode system.<sup>4</sup> Multilayers consisted of alternating layers of metal oxide and silica and are characterized by sharp wavelength-dependent transmission and reflection bands.<sup>5</sup> Amorphous or polycrystalline films (150nm grain size) of pure or mixed phases could be prepared by variations in the deposition conditions. These coatings were irradiated with a range of 532 or 355nm pulse energies (0-10 mJ) over a spot size diameter of 1 mm or less. Radiation supplied by a Quantel Model 581C Nd:YAG laser had an average pulse width of 7 ns. The equilibrium and time-resolved Raman measurements from these samples have been reported previously.<sup>1</sup> Selected damage regions from these same samples were studied in detail by the Raman microprobe technique.

Raman spectra were excited using the 488.0 or 514.5nm CW lines from a Spectra-Physics

164-09  $\text{Ar}^+$  laser at power levels from 30 to 220 mW into the microscope optics. A Spex Micramate system interfaced to a 0.85m Spex Model 1403 double monochromator equipped with the Datamate photon-counting system was used to analyze backscattered light of samples positioned at the focal point of the 40 $\times$  (0.60 NA) microscope objective, which also focused the excitation onto the sample. Illumination of the sample with white light allowed viewing images from the damaged film areas in reflection or transmission by use of a color video camera. Sample damage regions were photographed from the video screen.

Raman spectra were also recorded in a time-resolved manner by imaging of the dispersed light onto an intensified diode array (Tracor Northern Model 6133). For this measurement, coarse ruled gratings (150 gr/mm) were used in the monochromator to increase the spectral bandpass. A narrow band rejection filter centered at the probe laser wavelength (12nm half bandwidth) was inserted in front of the entrance slits to minimize stray light in the monochromator, which was operated without intermediate slits.

### Raman Measurements of Laser-damaged Coatings

Reactively sputtered oxide coatings on silica substrates are usually found to be under compressional stress owing to the sputtering parameters used during deposition and the difference in thermal properties between coating and substrate. The inherent stress in thin films is determined spectroscopically from measured vibrational frequency shifts relative to bulk crystal frequencies and is one parameter that has been used to characterize laser damage. For example, the pressure dependence of the  $\nu_6(\text{E}_g)$  mode in the anatase phase of  $\text{TiO}_2$  is reported as  $0.312\text{ cm}^{-1}/\text{kbar}$ .<sup>6</sup> Therefore, a frequency shift of this  $143\text{ cm}^{-1}$  mode can be correlated with film stress.

In addition to depth-profiling measurements of laser-damaged regions by measurement of relative vibrational band intensities of the coating material, existence of secondary phases can also be inferred. For example, 532nm pulse irradiation of 0.96 $\mu\text{m}$  anatase coatings leads to material ablation and irreversible transformation of the anatase phase to the more dense rutile phase. Figure 1 shows the three high-frequency Raman lines of the coating before and after irradiation. By use of Raman difference techniques, two lines at 440 and  $605\text{ cm}^{-1}$  (characteristic of the rutile phase) are discerned in the deconvoluted spectrum of the damaged area. Similar results are observed when amorphous coatings (which generally exhibit broad, weak vibrational features) are subjected to pulse laser irradiation. For example, the damage morphology characteristic of 355nm-irradiated amorphous  $\text{ZrO}_2$  coatings

The authors are at Pacific Northwest Laboratory, Box 999, Richland, WA 99352. Pacific Northwest Laboratory is operated by Battelle Memorial Institute for the U.S. Department of Energy under Contract DE-AC06-76RL0 1830. Reported work has been supported in part by the U.S. Department of Energy and the Air Force Weapons Laboratory under Contract P085-037.

(1.2  $\mu\text{m}$  thick) is described by a central damage crater surrounded by regions of surface fracture and pockmarks. Raman microprobe analysis of the cratered region reveals the presence of the monoclinic crystalline form of  $\text{ZrO}_2$ .

A detailed surface profiling investigation of the laser damage region in a multilayer anatase coating following 532nm irradiation is reported and indicates two responses of the coating to the laser pulse. An optical micrograph of the 17-layer  $\text{TiO}_2/\text{SiO}_2$  transmission filter at 514.5 nm following irradiation is shown in Fig. 2(a). To the right of the crater, the coating has fractured into islands of apparently higher reflectivity. Raman scattering from these islands indicates the presence of an unstressed anatase phase ( $\nu_6 = 143 \text{ cm}^{-1}$ ). Around the remainder of the periphery, the undamaged coating shows no cracks. However, Raman spectra acquired near the crater boundary reveal measurable band frequency shifts relative to the undamaged coating as seen for the  $\nu_6$  mode in Fig. 2(b). Closer examination of the irradiated area reveals irregular fingers of lower reflectivity fanning out into the undamaged coating for distances exceeding 150  $\mu\text{m}$ . Figure 2(c) demonstrates regular frequency fluctuations for the mode as a function of distance from the damage crater along one of these darker fingers. Far from the edge, the anatase is unstressed ( $\nu_6 = 143 \text{ cm}^{-1}$ ). As the edge is approached, the frequency increases to a maximum of  $147 \text{ cm}^{-1}$ . (The damage crater itself reveals a decreased quantity of anatase relative to the undamaged coating characterized by a  $\nu_6$  frequency of  $143 \text{ cm}^{-1}$ .) The measured vibrational line shift corresponds to a bulk compressional stress increase in excess of 10 kbar. For coatings subjected to higher pulse irradiation energies, shifts of the  $\nu_6$  frequency to ca.  $149 \text{ cm}^{-1}$  have been observed. At still higher energies, nearly complete ablation of the coating is observed and weak rutile features can be discerned in spectra obtained from the damaged region.

### Results and Discussion

New polycrystalline phases have been identified in pulse laser irradiated dielectric films by Raman microprobe spectroscopy. In addition, irregular regions of stress inhomogeneity, inferred from lattice phonon frequency shifts, were observed radiating outward from irradiated areas of a multilayer anatase film into undamaged regions. This metastable state could result from partial transformation of the film to a higher-density rutile phase with stress concentrating at grain boundaries or from substrate/film relaxation caused by a difference in thermal properties. An extended region of stress fluctuation definitely accompanies catastrophic damage to the film and may be a precursor to such damage through promotion of crystalline phase transformations.

Recrystallization of a metastable amorphous or crystalline phase to a thermodynamically stable phase can occur when a material is subjected to either pressure (stress) or temperature fluctuations. She and coworkers<sup>7</sup> have

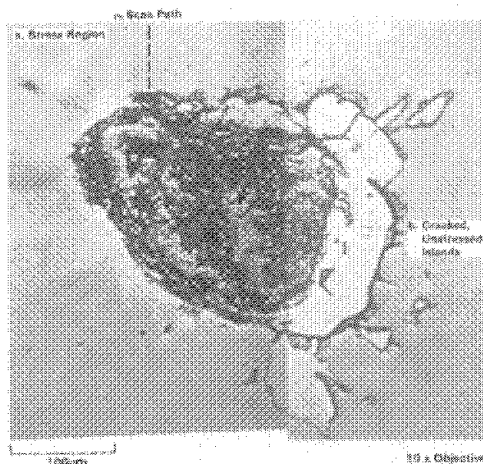
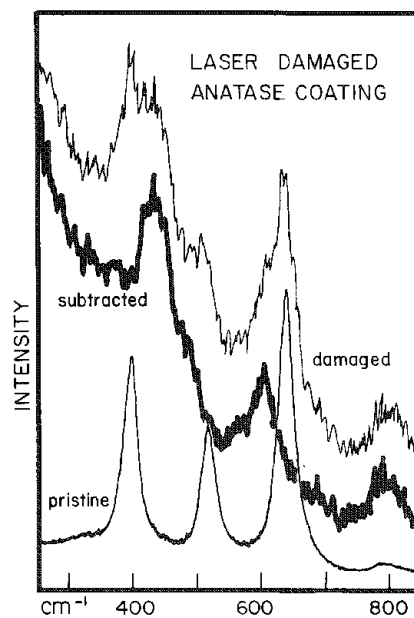
demonstrated that amorphous  $\text{TiO}_2$  films begin to crystallize into anatase, rutile, or mixed phases at temperatures as low as 325 C. Laser absorption during pulsed irradiation of oxide films is capable of producing temperatures well in excess of this value and could promote the observed recrystallization phenomena. Both temperature and stress effects must be considered in the development of a model for the damage process.

Films comprised entirely of the rutile phase of  $\text{TiO}_2$  suffer damage at somewhat higher pulse energies than anatase films of comparable thickness.<sup>8</sup> Recrystallization is observed in grain-ordered coatings following irradiation by polarized Raman measurements, but only a rutile phase can be detected.<sup>2</sup> These results suggest that another mechanism involving multiphoton excitation processes may be responsible for laser damage to rutile films since the rutile phase is stable at very high temperatures and pressures.<sup>1</sup>

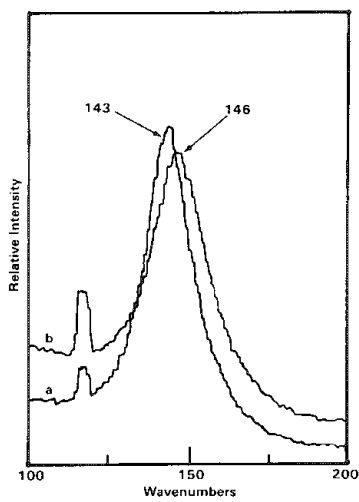
### References

1. G. J. Exarhos and P. L. Morse, "Raman studies of laser damaged single- and multilayer optical coatings," *Proc. Soc. Photo-Opt. Instrum. Eng.* 540: 460-466, 1985.
2. G. J. Exarhos, "Raman studies of phase transformations in pulse laser irradiated dielectric films," in H. Kurz, G. L. Olsen, and J. M. Poate, Eds., *Beam-solid Interactions and Phase Transformations*, Pittsburgh: Materials Research Society, 1985, 51, 179-184.
3. G. J. Exarhos, "Raman determination of molecular structure and physical properties of dielectric coatings," *J. Vac. Sci. Technol.* 4A: 2962-2968, 1986.
4. W. T. Pawlewicz, P. M. Martin, D. D. Hays, and I. B. Mann, "Recent developments in reactively sputtered optical thin films," *Proc. Soc. Photo-Opt. Instrum. Eng.* 325: 105-116, 1982.
5. G. J. Exarhos and W. T. Pawlewicz, "Raman characterization of all-dielectric multilayer  $\text{SiO}_2/\text{TiO}_2$  optical coatings," *Applied Optics* 23: 1986-1988, 1984.
6. T. Ohsaka, S. Yamaoka, and O. Shimomura, "Effect of hydrostatic pressure on the Raman spectrum of anatase ( $\text{TiO}_2$ )," *Solid State Commun.* 30: 345-347, 1979.
7. L. S. Hsu, R. Rujkorakarn, J. R. Sites, and C. Y. She, "Thermally induced crystallization of amorphous-titania films," *J. Appl. Phys.* 59: 3475-3480, 1986.
8. G. J. Exarhos and P. L. Morse, "Time-resolved Raman studies of laser-induced damage in  $\text{TiO}_2$  optical coatings," in H. E. Bennett, A. H. Guenther, D. Milam, and B. E. Newman, Eds., *Laser Induced Damage in Optical Materials: 1984*, Washington: NBS Special Publication 727, 1986, 262-271.

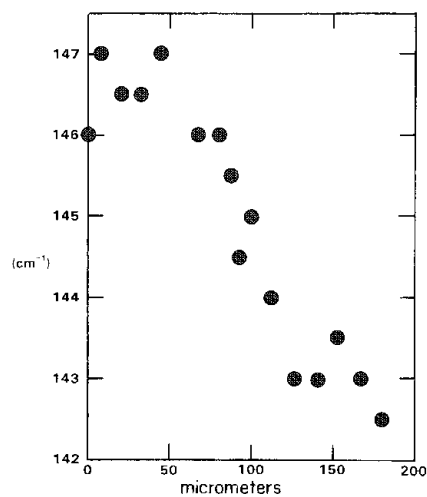
FIG. 1.--Raman spectra of 0.96 $\mu\text{m}$  anatase coating on silica before and after exposure to single 532nm high-energy laser pulse.



(a)



(b)



(c)

FIG. 2.--Surface profiling of laser damage for multilayer anatase film: (a) photomicrograph of damage morphology; (b) expanded trace of  $\nu_6$  lattice phonon mode in unstressed region ( $1\text{fr cm}^{-1}$ ); (c) frequency variation of  $\nu_6$  mode scanning away from damage crater (dashed line).



## CHARACTERIZATION OF QUALITY AND STRAIN IN GALLIUM ARSENIDE SEMICONDUCTORS BY MICRO-RAMAN SPECTROSCOPY

F. J. Purcell

The quality of information characterizing semiconductor materials is one of the most critical factors in designing and manufacturing silicon as well as faster III-V devices. Spectroscopy has emerged as a primary source of information for many reasons, not the least of which is the noncontact and nondestructive nature of spectroscopic techniques. Capable of being fully automated through microprocessor control, spectroscopy also generates a range of data unmatched by other methods.

Raman spectroscopy complements photoluminescence characterization by providing a more comprehensive structural and molecular picture of semiconductor materials. The power of Raman spectroscopy is further enhanced when a research-grade microscope is coupled to the spectrometer and a laser is used as the excitation source. Such a microprobe system permits spatial resolution of the order of 1  $\mu\text{m}$ , facilitating analysis of minute particles within larger samples.

In general, silicon semiconductor devices require an ultrapure, highly crystalline form of this material. Although amorphous silicon is nonconducting, comparatively inexpensive polycrystalline silicon has varying degrees of short-range order and can be employed for certain applications. Raman analysis of peak shifts and bandwidths makes it possible to calculate the length over which a sample is ordered, helping to identify the regions suitable for commercial use.

To obtain desired device characteristics, it is often necessary to "dope" a semiconductor with an excess of a specific type of carrier. Ion implantation is a convenient method of doping at room temperature, but bombarding a crystalline semiconductor with ions destroys the long-range order of the substrate near the surface. To restore order and move the implanted ions to substitutional positions, the wafers are annealed by laser. However, ion damage and crystal regrowth must be carefully monitored for maximum economy. Raman analysis can meet this requirement, in addition to determining the thickness of the implanted region.

Upon doping, the symmetry of III-V semiconductors permits the longitudinal optic (LO) lattice mode of a material such as gallium arsenide to couple with the longitudinal plasmon oscillations of the newly introduced free carriers. The frequencies of these coupled plasmon-LO phonon modes are designated  $W+$  and  $W-$  or  $L+$  and  $L-$ . At concentrations of about  $10^{16} \text{ cm}^{-3}$ , the  $W+$  mode becomes coincident with the LO phonon mode and Raman spectroscopy easily determines the carrier concentration from the position of the  $W+$  mode.

Silicon and III-V wafers are stressed by

processing steps and temperature changes that may cause local deformation and defects in various layers. Furthermore, new techniques to improve isolation between densely packed devices for very large-scale integration (VLSI) can generate strain as well. One such technique involves depositing a layer of ultrapure silicon on an insulator such as sapphire. Whatever the source, though, stress detrimentally affects carrier mobility, and Raman spectroscopy can analyze strain phenomena, even for micron-sized samples.

In the growth of GaAs and other III-V semiconductor materials, both the LO and transverse optic (TO) modes are allowed under certain orientations. However, since most semiconductor devices are constructed along the (100) face of GaAs, symmetry conditions predict that only the LO phonon is allowed in this orientation. Thus, the appearance of the TO phonon in a sample of (100) GaAs would be an indicator of poor crystal quality. The relative position, bandwidth, and lineshape of the LO phonon bank would also be indicative of questionable quality.

To demonstrate the utility of micro-Raman spectroscopy for semiconductor characterization, a gallium arsenide wafer implanted with field-effect transistors (FET) is analyzed with a microprobe Raman system. The analyses were performed on a SPEX Triplemate equipped with Micramate micro-Raman sample chamber.

A 4W argon ion laser (Innova 70-4) with the laser line at 488.0 nm is focused on the spot of interest via a 40 $\times$  objective. The detector is an EG&G PARC 1420 diode array intensified over 700 channels and controlled by an EG&G PARC OMA III console. Instead of acquiring a spectrum point by point, typical of a scanning monochromator coupled to a photomultiplier, a system with a multichannel detector views a spectral bank or even a complete spectrum at any given instant. This feature greatly increases the rate of data acquisition and avoids damage to the sample.

GaAs data will be acquired as a function of distance from the metal interface. Results will be related to the strain induced in the GaAs, as well as to the sample's electrical performance.

---

Author Purcell is with SPEX Industries,  
3880 Park Avenue, Edison, NJ 08820.



## OBSERVATION OF $\text{HSiCl}$ BY LASER-INDUCED MICROFLUORESCENCE DURING DIRECT-LASER WRITING OF SILICON MICROSTRUCTURES

Frank Magnotta

Fluorescence microprobe techniques are used for the first time as a real-time probe during local direct-laser writing. Laser-induced fluorescence (LIF) from the  $\text{HSiCl}$  free radical has been observed during pyrolytic deposition of micron-dimension structures of silicon on germanium from dichlorosilane. The detection of a silicon-containing radical near a localized laser-induced microreaction suggests that gas-phase dynamics are important in pyrolytic silicon deposition from silanes, which may not be merely limited by silane surface kinetics. The use of this microfluorescence technique as a probe for laser gas-surface interactions promises to be a powerful tool in elucidating the dynamics of such interactions.

Conventional chemical vapor deposition (CVD) of silicon from silane and chlorosilanes is commonly used for production of epitaxial films for semiconductor applications. Although the technology of this process is quite mature, the actual physics and chemistry involved in deposition are poorly understood. Recently, this process of pyrolytic deposition has been extended to microfabrication of integrated circuits by direct-laser writing (i.e., laser CVD).<sup>1-3</sup> In this process, focused laser light induces localized heating which results in deposition of material from gas phase precursors or etching of surfaces, aided by gas phase co-reactants. Direct-laser writing has been used to fabricate active devices, as well as to interconnect prefabricated CMOS gate arrays.<sup>4,5</sup> While conventional and laser CVD appear analogous, the conditions under which deposition (or etching) occur are considerably different and result in quite different materials characteristics. Conventional CVD of silicon from silane, for instance, utilizes relatively low temperatures and precursor concentrations and deposition is slow, which results in partially hydrogenated amorphous silicon. On the other hand, pyrolytic laser CVD is carried out at higher pressures and temperatures, and results in deposition of polycrystalline silicon at writing speeds of several millimeters per second.

Various gas phase and surface probes have been used in attempts to elucidate the mechanism leading to thin-film formation in conventional processing.<sup>1</sup> The advantage of coupling similar probes to the laser-CVD process results from the localized nature of the sampled area (usually of the order of several square microns). This also presents the obvious drawback of greatly diminished signal intensity. Recently, the laser Raman microprobe

technique was used for the first time in our laboratory as a real-time probe during local direct-laser writing of silicon microstructures from silane.<sup>6,7</sup> Similarly, micron-dimension structures of germanium-silicon alloys of various compositions were fabricated and analyzed in real time by Raman microprobe spectroscopy.<sup>8</sup> The extension of this surface analysis probe to gas phase detection of reactive free-radical intermediates produced during laser CVD is straightforward.

### *Experimental*

The experimental apparatus is similar to that used for the Raman microprobe experiments mentioned above and is briefly described here (Fig. 1).<sup>6-8</sup> An argon-ion laser (4880 Å) was directed to and focused onto a substrate through an infinity-focus objective, and a vidicon allowed on-line viewing. The focused laser induces pyrolytic microdeposition of silicon from dichlorosilane by local heating of the substrate while exciting a coincidental hot band absorption in  $\text{HSiCl}$ . Fluorescence from the  $\sim 100\mu\text{m}^3$  volume is collected by the objective, prefiltered to remove 4880 Å light, dispersed by a 0.2m polychromator, and detected by a microchannel plate-intensified diode array rapid-scanning spectrometer/signal averager.

### *Results*

Figure 2 shows the emission spectrum obtained during pyrolytic deposition of a silicon line ( $\sim 2\mu\text{m}$  wide by  $\sim 1\mu\text{m}$  high) on a germanium substrate, with an incident laser power of 2.1 W, 162 Torr  $\text{SiH}_2\text{Cl}_2$ , and a cell scanning speed of 0.1 mm/s. Following deposition, the reaction cell was evacuated and the line was rescanned under conditions identical to those used for writing to facilitate background subtraction, which consisted of a large blackbody component. The 4880 Å laser line is in close coincidence with and excites the  $(0,1,0)-(0,1,0)$  hotband  $\tilde{A}(^1A'')-\tilde{X}(^1A')$  transition (bandhead is at 4883.8 Å) of  $\text{HSiCl}$ . Also shown in Fig. 2 are the calculated positions of the vibronic origins from the  $(0,0,0)$  level of the excited state from constants of Ref. 9. The laser Rayleigh line and the  $(0,0,0)-(0,0,0)$  line are completely suppressed. The spectrum was obtained over a 15s integration time; however, reasonable signal-to-noise could be seen in as little as 50 ms. Similarly, pressures as low as 20 Torr (at which point writing becomes thin and erratic) resulted in excellent signal-to-noise. The apparent underlying continuum in Fig. 2 is reproducible and may be due to incomplete background subtraction.

Similar experiments utilizing the 5145 Å laser line resulted in no fluorescence signal in deposition from either silane or dichloro-

---

The author is at the Lawrence Livermore National Laboratory, Livermore, CA 94550. This work was performed by LLNL under the auspices of the U.S. Department of Energy, under contract W-7405-Eng-48.



silane. Defocusing the 4880 Å line slightly to where no visual deposition occurred also resulted in no fluorescence signal. The energetics of dichlorosilane decomposition suggest that  $\text{SiCl}_2$  should be the primary product, since it is the lower-energy product by 32.5 kcal/mole. The observation of the higher-energy product,  $\text{HSiCl}$ , strongly suggests the presence of  $\text{SiCl}_2$ . Future experiments are planned to detect this species.

### Conclusions

The observation of  $\text{HSiCl}$  in localized direct-laser writing of polycrystalline silicon microstructures is a strong indication that gas phase kinetics are involved in the deposition process, in addition to surface kinetics. The highly localized observation region intrinsic to this technique further suggests that this species is produced directly and not as a result of subsequent secondary reactions. Energetic considerations suggest the presence of  $\text{SiCl}_2$ ; however, detection of this species was not attempted. Modification of the apparatus to incorporate a tunable laser would allow a systematic search for other reactive intermediates. Furthermore, the technique of laser-induced microreaction/detection should find widespread use as a powerful spectroscopic probe for studying both photolytic and pyrolytic gas-surface reactions.

### References

1. I. P. Herman, "Direct-laser writing," in K. G. Ibbs and R. M. Osgood, Eds., *Photochemical Materials Processing*, Cambridge: Cambridge University Press (in press).
2. I. P. Herman, in D. Bauerle, Ed., *Laser Processing and Diagnostics-Chemical Physics*, New York: Springer, 1984, vol. 39, 396.
3. D. J. Ehrlich and J. Y. Tsao, in N. Einspruch, Ed., *VLSI Electronics: Microstructure Science*, New York: Academic Press, 1984, vol. 7, 129.
4. B. M. McWilliams et al., in S. Allen, Ed., *Proc. of SPIE/84 Conference*, SPIE, Bellingham, Wash., 1984, vol. 459, 49.
5. J. C. Whitehead et al., *SPIE Proceedings Series*, SPIE, Bellingham, Wash., 1986 (in press).
6. Frank Magnotta and I. P. Herman, "Raman microprobe analysis during direct-laser writing of silicon microstructures," *Appl. Phys. Letters* 48: 195, 1986.
7. I. P. Herman et al., "Direct-laser writing of silicon microstructures: Raman microprobe diagnostics and modeling of nucleation phase of deposition," *J. Vac. Sci. Technol.* A4: 659, 1986.
8. I. P. Herman and Frank Magnotta, "Ge-Si alloy microstructure fabrication by direct-laser writing with analysis by Raman microprobe spectroscopy," *J. Appl. Phys.* (in press).
9. Gerhard Herzberg and R. D. Verma, "Spectra and structures of the free  $\text{HSiCl}$  and  $\text{HSiBr}$  radicals," *Can. J. Phys.* 42: 395, 1964.

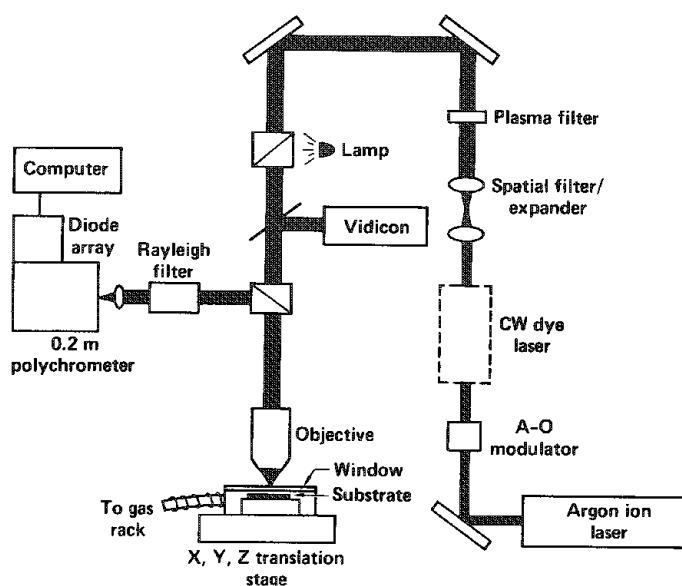


FIG. 1.--Schematic of direct-laser writing microscope/fluorescence microprobe apparatus.

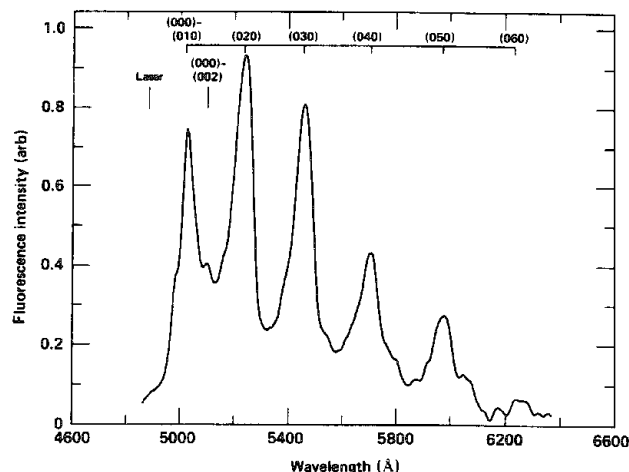


FIG. 2.--Fluorescence emission spectrum of  $\text{HSiCl}$  excited at 4880 Å obtained during direct-laser writing. Line positions, calculated from Ref. 9, are plotted above spectrum ( $v_1', v_2', v_3'$ ) - ( $v_1'', v_2'', v_3''$ ).

## PHOTOTHERMAL MICROSCOPE

N. J. Dovichi and D. S. Burgi

Optical microscopy is an old and venerable field. The simplicity of the compound microscope, along with near universality of optical absorbance, has led to the incorporation of the microscope into many fields of technology. In particular, the development of stains and dyes has produced a wonderful variety of chemical reagents for the determination of many substances within complex, natural matrices. However, the optical microscope suffers from an important limitation: samples must absorb an appreciable amount of light before they can be seen. To be visible, the sample must absorb about 0.3% of the incident light (which corresponds to an absorbance of about 0.001). To image a 1  $\mu\text{m}$ -thick sample, the product of absorptivity with concentration must be at least 10  $\text{cm}^{-1}$ . For a dye with high molar absorptivity (say,  $10^4 \text{ LM}^{-1} \text{cm}^{-1}$ ), the minimum detectable dye concentration is  $10^{-3} \text{ M}$ . Trace analysis with high spatial resolution is not possible with the light microscope. Furthermore, the maximum absorbance that may be studied is in the range of 1-10; the dynamic range of absorbance measurements is slightly greater than three orders of magnitude.

It is possible to study much more weakly absorbing materials with a much higher dynamic range by photothermal (or thermo-optical) techniques. In these techniques, very weak absorbance is detected within a sample not as a decrease in transmitted intensity but rather as a temperature rise within the sample. The temperature rise is indirectly observed as a refractive-index perturbation within the sample; the refractive index of most materials changes with temperature. Photothermal techniques are applicable to most every sample, since an arbitrarily transparent material generally undergoes a measurable temperature rise when illuminated with an arbitrarily powerful light beam.

The high power and excellent spatial coherence of the laser are well suited to photothermal measurements of absorbance. The first photothermal technique to be studied was the thermal lens.<sup>1</sup> Here, a laser beam is focused into a weakly absorbing sample. The sample absorbs the beam and the excited analyte undergoes nonradiative relaxation, heating the sample. Since the beam is most intense in the center and least intense in the wings, a thermal gradient is formed. The resulting refractive-index gradient acts to defocus the laser beam. The laser intensity change is measured with a small-area photodetector centered on the beam profile. By regression analysis of the signal produced when the sample is first illuminated, absorbance detection limits of

$10^{-7}$  have been obtained over a 1 cm path.<sup>2</sup>

The photothermal microscope utilizes the crossed-beam thermal lens to study localized regions within larger, inhomogeneous samples. In this instrument, a second laser beam probes at right angles the heated region produced by a modulated pump beam.<sup>3-4</sup> If the beams are crossed on axis, the photothermal signal is generated only where the two beams intersect. Furthermore, if the beams are very tightly focused, very small volumes may be studied. The technique has demonstrated an improvement of six orders of magnitude in absorbance detection limit compared with Beer's law measurements. Furthermore, a similar improvement in dynamic range appears possible. For example, a crude photothermal detector has been used to study absorbance within neat liquid samples. Absorbance detection limits of  $10^{-9}$  were obtained over a 2  $\mu\text{m}$  path.<sup>5</sup> Within the 0.2 pL probe volume, only 120 analyte molecules were present. The dynamic range of the instrument is limited by sample absorbance since some pump laser light must reach the probe volume. Absorbance in the range of 1 may be studied,<sup>4</sup> provided that the pump laser intensity is decreased to avoid damage to the sample. If the laser intensity can be conveniently decreased, then up to nine orders of magnitude in dynamic range are provided by the technique.

The high sensitivity of the photothermal technique arises from an important property: since the thermal gradient increases as the pump beam is more tightly focused, the sensitivity of the measurement increases as the probe volume decreases.<sup>6</sup> This observation is worth restating in clearer language: the sensitivity of the technique improves simultaneously with spatial resolution. In Beer's law measurements, the opposite is true; decreasing the probe volume by decreasing the path length produces a concomitant degradation of sensitivity. Photothermal techniques offer another interesting property; the phase of the signal is related to the thermal properties of the sample. Materials with high thermal diffusivity quickly reach thermal equilibrium with the laser beam, whereas materials with low thermal diffusivity take a long time to reach thermal equilibrium. It has been shown that regression analysis of the time-resolved crossed-beam thermal lens signal may be used to measure differences in thermal diffusivity of 1%.<sup>6</sup>

An experimental diagram of the current generation photothermal microscope is shown in Fig. 1. A helium-cadmium laser produces a 4 mW pump beam at 442 nm. A helium-neon laser produces a 1 mW probe beam at 632.8 nm. The pump beam is reflected and the probe beam is transmitted by a dichroic filter. The filter and the mirrors (M) are used to align the pump and probe beams parallel and offset by about 5 mm. The beams are directed into a microscope objective equidistant from the central axis of

The authors are at the Department of Chemistry, University of Alberta, Edmonton, Canada T6G 2G2. This work is funded by the Natural Sciences and Engineering Research Council of Canada.

the lens. The lens focuses and crosses the two beams at a point within the sample. After transmission through the sample, the probe beam is filtered to block scattered pump laser light. The pump beam is modulated at 1.3 kHz with a mechanical chopper and a lock-in amplifier is used to estimate both the amplitude and phase of the photothermal signal. The amplitude is divided by the average probe beam intensity to remove artifacts associated with nonphotothermal sources of intensity loss. One generates an image with the microscope by recording the amplitude and phase from the lock-in amplifier as the sample is translated through the intersection region of the laser beams. The sample is moved by use of computer-controlled actuators with 0.1  $\mu\text{m}$  (nominal) resolution. A digital plotter is used to display the image.

This optical configuration represents a significant advance over our first-generation microscope.<sup>7</sup> In the earlier instrument, the pump and probe beams were focused with separate lenses, mounted at 90°. The configuration was cumbersome to align and limited in spatial resolution. It does not appear to be possible to cross two beams of micrometer diameter without having the lenses butt against each other. The current instrument utilizes a single lens and is automatically aligning; as long as the two beams are parallel to the lens and symmetrically located about the lens axis, they cross very near the focus of the lens. In fact 20, 30, 40, and 100 $\times$  objectives are switched without any need for realignment. The only disadvantage of the system is that the beams do not necessarily cross at right angles. However, the great improvement in spatial resolution from use of high-power objectives more than compensates for this disadvantage.

Figure 2 presents images of the amplitude and phase of the photothermal signal of a 15  $\mu\text{m}$ -thick slice of the stem of a 3-year-old plant of *Tilia Americana*. The plant had been stained with both fast green and saffranin. The latter dye preferentially stains lignin and strongly absorbs the helium-cadmium pump laser beam. A 1  $\mu\text{m}$  spacing between data points was used to generate the 100  $\times$  100 pixel image. This image was taken from the xylem portion of the plant. Several cellular features are visible in the images. The small cells near the top right portion of the image correspond to early wood and the large cells correspond to the late wood within the stem. The long, thin cells traversing the image at about 45° form a vascular ray, a portion of the transverse vascular system of the plant. The phase component of the image shows ridges at the cellular boundary and suggests that the cell walls contain material of thermal diffusivity different from the material in the center of the cells. It appears that the phase plot may be used to divide materials into different classes based upon thermal diffusivity.

Figure 3 is an image, again consisting of 100  $\times$  100 pixels at 1.0  $\mu\text{m}$  spacing, of a 6  $\mu\text{m}$ -thick human epidermis section, stained for acid-fast bacteria (AFB). The AFB-stained TB bacteria are red and strongly absorb the pump

laser beam. The phase component of the image is relatively featureless and not presented. A cluster of tuberculosis cells is clearly visible as the annular structure at the bottom left of the image. Other, smaller clusters are scattered throughout the image. Some of the small bumps may be associated with individual bacteria.

In all figures, large changes in signal are observed over the 1  $\mu\text{m}$  step size used in gathering the data. It is particularly interesting that the thermal properties of the sample may be imaged with this resolution. An optical technique is employed to study a nonoptical property of the sample with micrometer or better resolution. The combination of high sensitivity, high dynamic range, high spatial resolution, and combined measurements of absorbance and thermal diffusivity makes the photothermal microscope an interesting tool for a wide range of applications. The spatial resolution demonstrated in these images is not the ultimate produced by the microscope. We have recently employed an oil-immersion objective to study submicrometer features. It is possible to image objects with 0.3  $\mu\text{m}$  resolution. Unfortunately, our current images are limited by the quality of our translation stages; improvements in these components may allow improved resolution.

One last property of the microscope should be mentioned. Since the image is generated only at the intersection region of the two laser beams and not integrated over the optical path of the sample, one can generate a thin section image of a relatively thick sample. The thin-section image is generated simply by translation of the sample in two dimensions through the the tightly focused beams. For example, we have generated the image of a 25  $\mu\text{m}$ -radius fluid inclusion within a 1 mm-thick geological sample.<sup>8</sup> A thin section image should be of value for the study of histopathological materials. Currently, the pathologist requires approximately 24 h to prepare a thin section for visual interpretation. Since images are generated by the photothermal microscope on thick samples, it may be possible to reduce greatly the sample preparation time for improved diagnostic speed.

## References

1. J. R. Whinnery, "Laser measurement of optical absorption in liquids," *Acc. Chem. Res.* 7: 225-231, 1974.
2. N. J. Dovichi and J. M. Harris, "Time-resolved thermal lens calorimetry," *Anal. Chem.* 53: 106-109, 1981.
3. N. J. Dovichi, T. G. Nolan, and W. A. Weimer, "Theory for photothermal refraction," *Anal. Chem.* 56: 1700-1704, 1984.
4. T. G. Nolan, W. A. Weimer, and N. J. Dovichi, "Laser-induced photothermal refraction for small volume absorbance determination," *Anal. Chem.* 56: 1704-1707, 1984.
5. T. G. Nolan and N. J. Dovichi, "Ultra-sensitive analysis with the crossed-beam thermal lens," *IEEE Circuits and Devices Mag.* 2: 54-56, 1986.
6. W. A. Weimer and N. J. Dovichi, "Simple model for the time dependence of the periodi-

cally excited crossed-beam thermal lens," *J. Appl. Phys.* 59: 225-230, 1985.

7. D. S. Burgi, T. O. Nolan, J. A. Risfelt, and N. J. Dovichi, "Photothermal refraction for scanning laser microscopy," *Opt. Eng.* 23: 756-758, 1984.

8. D. S. Burgi and N. J. Dovichi, "Crossed-beam thermal lens as a scanning laser microscope," *AIP Conf. Proc.* (in press).

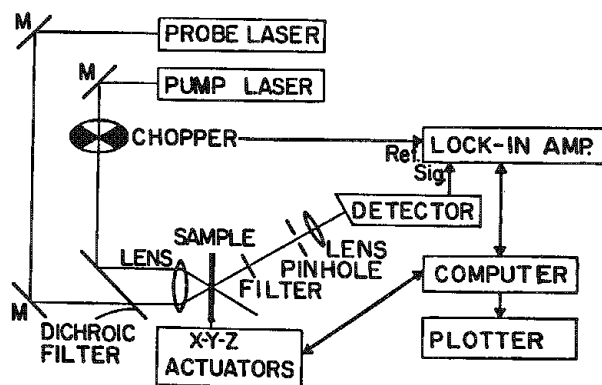


FIG. 1.--Experimental diagram for photothermal microscope.

FIG. 2.--Image of *Tilia Americana*. Length and width of image corresponds to 100  $\mu\text{m}$  in sample. (a) Amplitude component, (b) phase component.

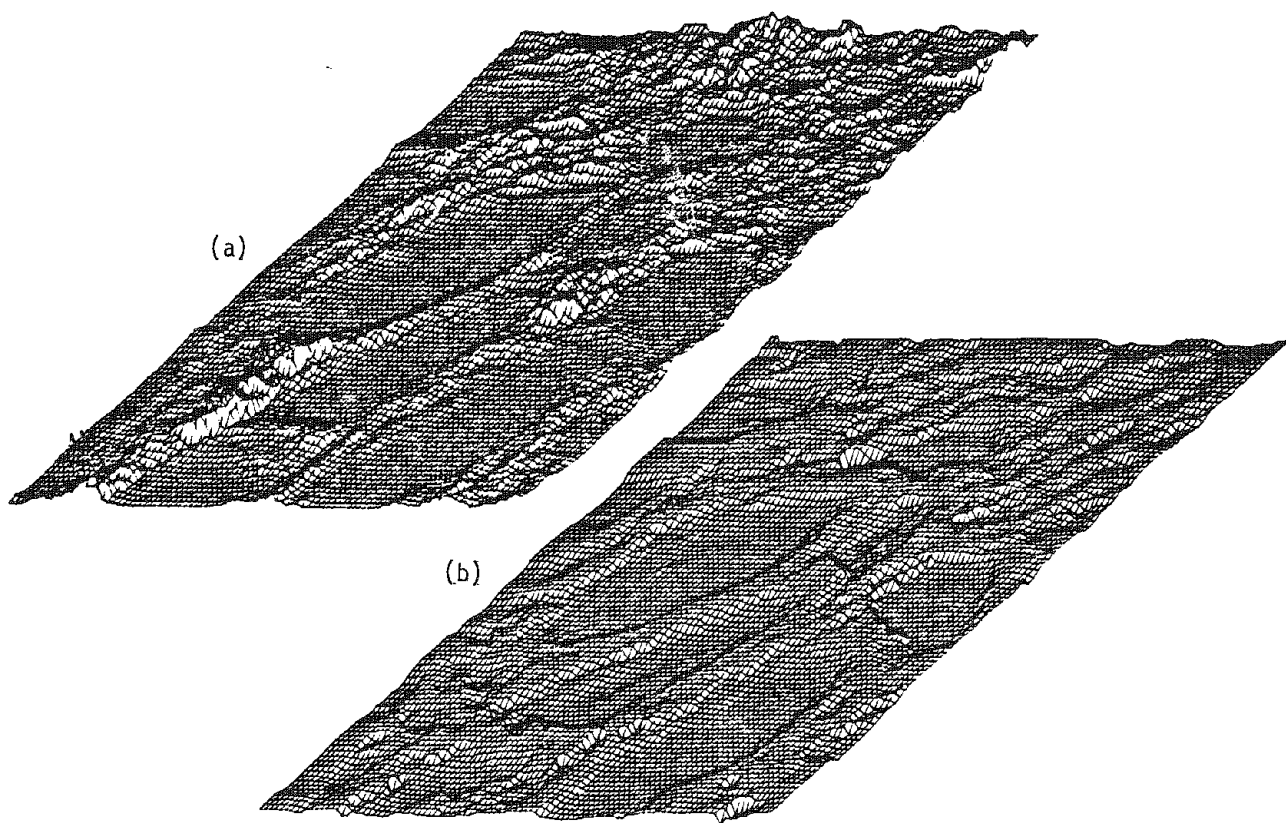
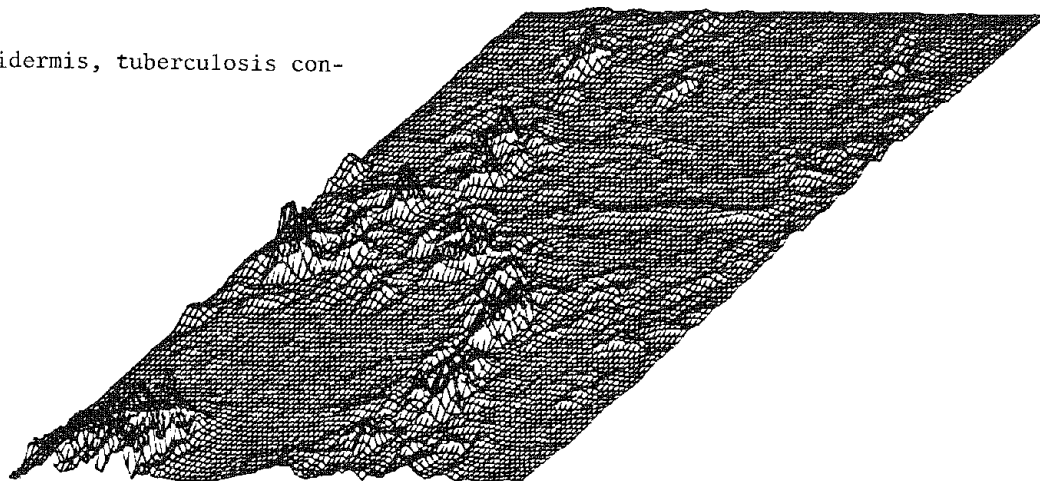


FIG. 3.--Human epidermis, tuberculosis control.



## TRACKING CHEMICAL TRANSFORMATIONS OF PARTICLES IN THE RAMAN MICROPROBE

E. S. Etz

Raman microprobe spectroscopy has become an established technique among other microanalytical methods for the chemical analysis of single particles.<sup>1,2</sup> Several features make Raman spectroscopy attractive for particle characterization, among them the ability to (i) deduce molecular composition; (ii) establish whether the sample is in a crystalline/amorphous, liquid, or gaseous state; and (iii) investigate the specimen under ambient conditions, free from the constraints of an evacuated sample chamber. These attributes, and others, have been thoroughly documented, and Raman microspectroscopy has now been extensively reviewed.<sup>1,3,4</sup>

### *The Analytical Pursuit: Identifying Transient Particle Compositions*

In work with the Raman microprobe, we have on numerous occasions made observations concerning changes in the chemical composition of particles which, had they been investigated by other methods, might have gone entirely undetected.<sup>5-7</sup> In many of these cases, these changes have manifested themselves as chemical transformations (often involving physical, e.g., phase changes) readily detected by diagnostic changes in the pattern of the vibrational fingerprint. Such compositional changes are most often brought on by one of two factors: (1) laser-induced particle modification due to heating or photodecomposition, and (2) particle transformations from sample instability toward ambient atmospheric conditions, mainly moisture, and frequently also ambient levels of CO<sub>2</sub> and NH<sub>3</sub>. These then are the two types of interactions that most often need to be considered when spectral changes indicate transient or variable particle identities.

This paper does not consider chemical transformations of particles brought on by the interaction of the high-intensity, focused laser spot with the sample. Modifications produced by laser irradiation are often difficult to interpret unless something is known about the specific interaction, such as laser-induced thermal oxidation of the sample (e.g., the conversion of W<sub>2</sub>C to WO<sub>3</sub>). Rather we illustrate several types of transformations of particles that are readily tracked by micro-Raman spectroscopy and that involve compositional changes brought on by exposure to reactive components in the air. Examples are

taken from NBS research in (i) the study of sulfate aerosols with relevance to atmospheric reactions, (ii) the characterization of micro-particle transformations in the lithium oxide/hydroxide system, and (iii) the investigation of the long-term stability of uranium oxide reference materials used in the preparation of elemental standards for chemical microanalysis.

### *Instrumentation and Experimental Procedures*

Measurements were performed with the Raman microprobe developed at the National Bureau of Standards.<sup>2,3</sup> The instrument is a conventional Raman spectrometer especially designed in its fore-optical system for single particle analysis. Whenever feasible, the spectra are excited with the 514.5nm line of an argon/krypton laser. When spectral interferences are encountered due to sample fluorescence (e.g., uranyl compounds), the spectra are acquired with 568.2nm radiation. The signal is detected by a cooled photomultiplier tube and processed with conventional photon counting electronics. The Raman microprobe is totally automated in that all of its functions are controlled by a digital computer and its interface modules. The computer interface and associated peripherals have provided the means to develop an extensive spectral library and allow convenient qualitative evaluation and interpretation of the spectra.

Particles are examined individually, generally in particle dispersions supported by either sapphire ( $\alpha$ -Al<sub>2</sub>O<sub>3</sub>; totally inert) or lithium fluoride (LiF; no Raman scatter) substrates. Measurement parameters are in large part determined by the properties and "behavior" of the sample, which govern choice of laser wavelength, incident laser irradiance, signal integration times, and spectrometer scan rates. Conditions generally employed are a variable laser spot size of 6 to 15  $\mu$ m in diameter and laser power (at the sample) varying from 5 to 50 mW, depending on sample tolerance and the rate of sample transformation. Appropriate spectrometer scan rates may then vary from 40 to 100 cm<sup>-1</sup>/min and integration time constants from 2.0 to 0.2 s, respectively. All spectra reported here were acquired with spectral slit widths of either 3 or 5 cm<sup>-1</sup>.

All particle samples were prepared from well-characterized, high-purity chemical reagents (solids), including primary reference standards available from the National Bureau of Standards (NBS Standard Reference Materials, or SRMs) and the New Brunswick Laboratory of the Department of Energy (NBL Certified Reference Materials, or CRMs). These samples were investigated as microparticulate dispersions under ambient laboratory conditions. In other studies of unstable particle dispersions, the microprobe has been at times equipped with a controlled-atmosphere sample chamber.<sup>6</sup>

---

The author is with the Center for Analytical Chemistry at the National Measurement Laboratory, U.S. National Bureau of Standards, Gaithersburg, MD 20899. X-ray diffraction studies of reference samples of uranium oxides were performed by Winnie Wong-Ng of the Institute of Materials Science and Engineering at NBS; this fruitful collaboration is gratefully acknowledged.

**Reactive Sulfate Aerosols.** A particle system receiving much attention is that of reactive sulfate aerosols, since it relates to atmospheric processes and chemistries, with the broader implications of atmospheric pollution and global climatic changes.<sup>6</sup> It has been thoroughly established that atmospheric sulfate may have a number of molecular forms--e.g.,  $\text{H}_2\text{SO}_4$ ,  $(\text{NH}_4)\text{HSO}_4$ ,  $(\text{NH}_4)_2\text{SO}_4$ ,  $\text{MgSO}_4$ ,  $\text{CaSO}_4$ ,  $\text{Na}_2\text{SO}_4$ , etc.--many of which are derived from  $\text{H}_2\text{SO}_4$  mists ("acid rain") and their neutralization products with  $\text{NH}_3$ . Many of these sulfates are hygroscopic substances that form aqueous solution droplets over a wide range of humidities. As deliquescent salts they undergo transitions from the dry crystal to a solution droplet. Certain nitrogen-sulfur compounds have long been suspected as being important in stratospheric reactions, and much evidence points to their physical characteristics as being composed of a volatile slurry mixture of crystalline-like material in a liquid matrix.<sup>9</sup> In work on stratospheric aerosol collections,<sup>6,7</sup> we had a need to examine the properties and behavior of nitrosyl sulfuric acid,  $\text{NOHSO}_4$ , which was postulated as an important aerosol constituent.<sup>9,10</sup> It became relevant to study several simple and complex laboratory-generated sulfate aerosols of various compositions, including binary and ternary systems such as  $\text{H}_2\text{SO}_4$ - $\text{NOHSO}_4$  and  $\text{H}_2\text{SO}_4$ - $(\text{NH}_4)_2\text{SO}_4$ - $\text{NOHSO}_4$ . Because  $\text{NOHSO}_4$  is extremely hygroscopic, ambient moisture is quickly absorbed and the compound is instantly hydrolyzed and decomposes to  $\text{NO}_2$  and  $\text{H}_2\text{SO}_4$  when exposed to air. Measures can be taken to prevent this rapid decomposition of  $\text{NOHSO}_4$ , so that indeed the micro-Raman spectrum of crystalline  $\text{NOHSO}_4$  may be obtained from a particle dispersion, as we have demonstrated.<sup>7</sup> The Raman spectrum of solid  $\text{NOHSO}_4$  exhibits several low-frequency lattice modes and the sharpness of internal vibrational modes characteristic of a crystalline solid. The most pronounced feature is a very strong, sharp band at  $2273\text{ cm}^{-1}$  associated with the N-O symmetric

stretching motion of the nitrosyl ion,  $\text{NO}^+$ , and other bands at  $420$ ,  $578$ ,  $1035$ , and  $1173\text{ cm}^{-1}$  that are assigned to the  $\text{HSO}_4^-$  motions in the molecular solid. In these studies of microparticles of synthetic sulfate aerosols, we have examined the decomposition of  $\text{NOHSO}_4$ , from the initial crystalline state to the decomposition product, a concentrated solution of sulfuric acid. The spectrum of the decomposition product of  $\text{NOHSO}_4$  (Fig. 1) no longer shows any of the features characteristic of the precursor microcrystal.<sup>7</sup> Rather, the bands in the spectrum can all be ascribed to an aqueous solution of sulfuric acid.<sup>11,12</sup> This system constitutes a complex equilibrium mixture involving  $\text{HSO}_4^-$ ,  $\text{SO}_4^{2-}$  ions, and undissociated  $\text{H}_2\text{SO}_4$ , together with ion pairs, and hydrated species (e.g.,  $\text{H}_2\text{SO}_4 \cdot \text{H}_2\text{O}$ ). Whereas the  $\nu_1$  band of  $\text{SO}_4^{2-}$  is expected at  $\sim 980\text{ cm}^{-1}$ , it is frequently not observed, or observed only as a weak shoulder, since the concentration of free  $\text{SO}_4^{2-}$  is very low. Thus, the bands observed in solutions of the  $\text{SO}_4^{2-}/\text{H}_2\text{SO}_4$  system are largely attributed to the bisulfate ion, depending on the degree of dissociation of  $\text{HSO}_4^-$ . The prominent bands in such solutions are centered at Raman shifts  $\sim 425$ ,  $\sim 595$ , and  $\sim 930\text{ cm}^{-1}$ , an intense band at  $\sim 1040\text{ cm}^{-1}$ , and a broader band centered at  $\sim 1200\text{ cm}^{-1}$ .

**Unstable Microparticulate Oxides and Hydroxides.** Numerous classes of compounds, among them oxides and hydroxides, are fully expected to be quite stable on exposure to the ambient atmosphere, so that chemical transformations of any significance are rarely suspected, especially when such substances are considered in bulk form. However, in the finely divided state as powders, these types of materials can undergo slow chemical transformations into new molecular states, often difficult to discern at the single-particle level.

In recent work we have examined several lithium oxides and hydroxides as particle samples since such particulate systems have raised some health concerns in case these compounds are released into the environment as lithium combustion aerosols.<sup>13</sup> Modeling exper-

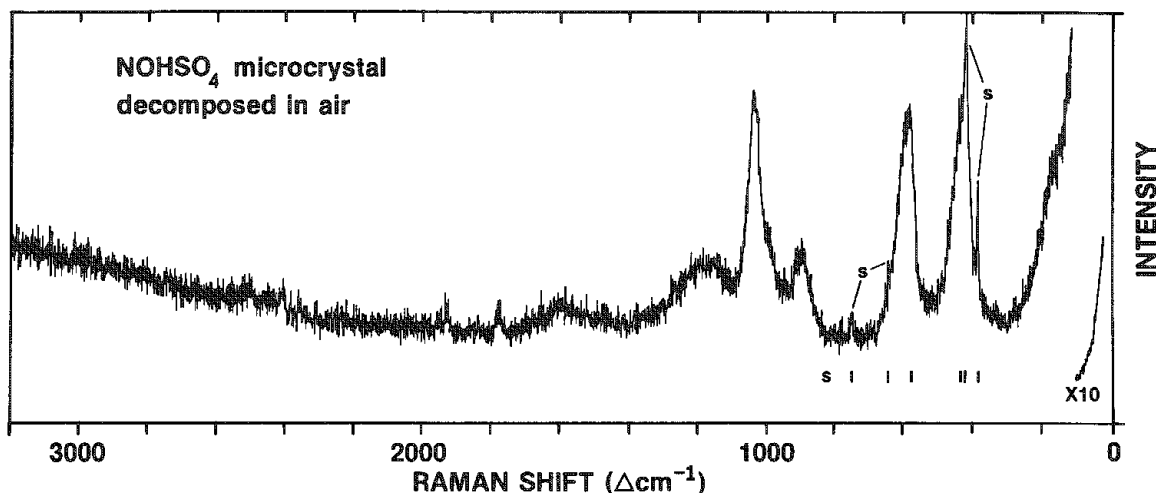


FIG. 1.--Raman microprobe spectrum of decomposed (hydrolyzed in air) microparticle (size,  $\sim 20\text{ }\mu\text{m}$ ) of nitrosyl sulfuric acid. Decomposition residue is droplet of sulfuric acid, supported on sapphire (S) substrate. Excitation at  $514.5\text{ nm}$ ; laser power (at sample)  $80\text{ mW}$  in beam spot  $\sim 12\text{ }\mu\text{m}$  in diameter.

iments have shown that lithium combustion aerosols are composed primarily of lithium monoxide,  $\text{Li}_2\text{O}$ ; lithium hydroxide,  $\text{LiOH}$ ; and lithium carbonate,  $\text{Li}_2\text{CO}_3$  (as well as trace amounts of lithium peroxide,  $\text{Li}_2\text{O}_2$ ). The exact chemical composition of the aerosol is determined by the prevailing concentrations of  $\text{H}_2\text{O}$  and  $\text{CO}_2$ . In moist air, for example, such aerosols consist mostly of  $\text{LiOH}\cdot\text{H}_2\text{O}$ , which is in time converted to  $\text{Li}_2\text{CO}_3$ .

The chemical transformation with time of  $\text{LiOH}$  to  $\text{Li}_2\text{CO}_3$  can be directly studied in the Raman microprobe under the prevailing conditions of the laboratory environment. Reagent-grade  $\text{LiOH}$  is quickly converted to the monohydrate and then, for a typical particle dispersion of  $\text{LiOH}\cdot\text{H}_2\text{O}$ , the slow conversion of the hydroxide to the fully stoichiometric anhydrous carbonate can be followed over a period of days through the uptake of ambient  $\text{CO}_2$ . Results of these measurements are shown in

Fig. 2. The qualitative differences between the two spectra of the same microparticle are readily recognized. The top spectrum was recorded only two hours from the time of preparation of the particle dispersion. While the bands characteristic of hydrated  $\text{LiOH}$  are still predominant at Raman shifts 370, 396, 840 and  $3563\text{ cm}^{-1}$ , partial conversion is already indicated. The latter band in the top spectrum of the hydroxide is sharp and intense and is due to the H-O-H vibrations of the crystallographic waters of hydration.<sup>14</sup> Thus, these initial spectra of the hydroxide show the presence of a detectable (but not quantified) concentration of carbonate as evidenced by the medium-intensity band at  $1091\text{ cm}^{-1}$  ( $\nu_1$  carbonate symmetric stretch vibration). Two days following the preparation of the sample, the spectrum of the hydroxide particle (Fig. 2, bottom) has changed in a remarkable way resulting from the progressive transformation to

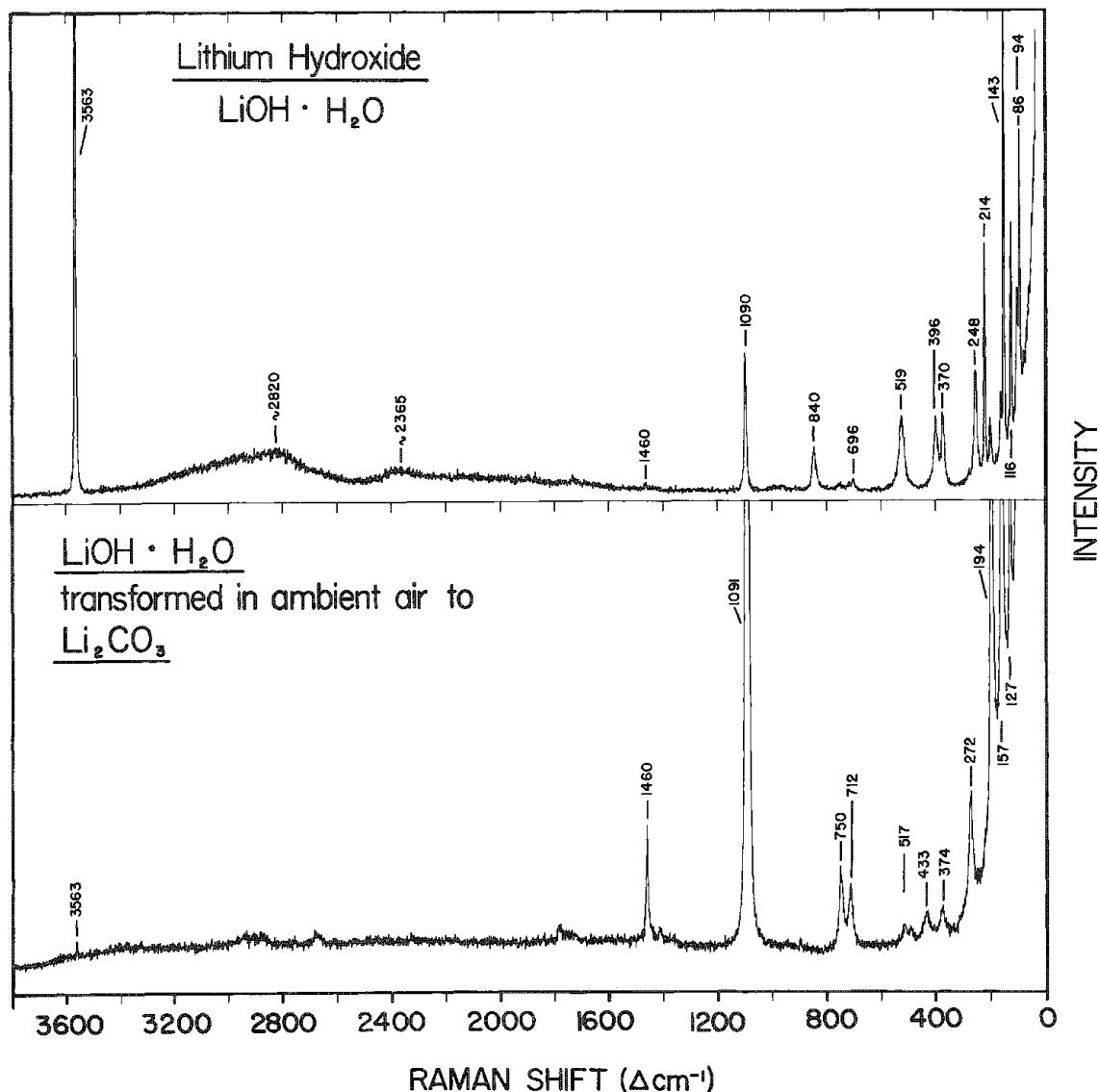


FIG. 2.--Microparticle spectra obtained in study of conversion of lithium hydroxide to lithium carbonate on exposure to atmospheric  $\text{CO}_2$ . Top, spectrum of a microcrystal ( $\sim 15\text{ }\mu\text{m}$  in size) of hydroxide partially converted to carbonate. Bottom, spectrum of the same hydroxide particle nearly completely transformed to lithium carbonate. Excitation at 514.5 nm;  $\text{LiF}$  substrate.

the stoichiometric carbonate,  $\text{Li}_2\text{CO}_3$ . The  $1090\text{ cm}^{-1}$  band is now the dominant feature, and only a weak, remnant band is observed at  $3563\text{ cm}^{-1}$ . In all other respects, the spectrum of the converted particle is consistent with that obtained from a reference sample of lithium carbonate (NBS SRM 924), and is in full accord with the literature Raman data reported for anhydrous polycrystalline  $\text{Li}_2\text{CO}_3$ .<sup>15</sup> Observed are the other characteristic internal carbonate vibrations at shifts 712, 750 and  $1460\text{ cm}^{-1}$ , in addition to the reported lattice vibrations at 95, 127, 157 and  $194\text{ cm}^{-1}$ .

*Long-term Compositional Changes of Uranium Oxide Standards.* In many areas of NBS research it is important to examine the micro-homogeneity of samples, as in the case of source materials (e.g., bulk powders) that are used in the preparation of reference standards. This procedure becomes necessary for source materials whenever there is reason to question the long-term stability and identity of such samples, despite strict adherence to dictated conditions of storage and handling. One particular area where such concerns are of relevance are the steps taken in the preparation of Standard Reference Materials (SRMs) for chemical microanalysis. A specific example is the fabrication and certification of multielement glass SRMs.<sup>16</sup> These glasses consist of various simple and complex compositions, and they are certified with regard to both major and minor elements and are guaranteed to be homogeneous at the microscopic level.

Whenever possible, these certified reference glasses are prepared from high-purity source materials, such as primary reference standards available from NBS or NBL, and are commonly oxides, carbonates, or phosphates. Several of the available silicate and phosphate glass SRMs contain actinides (e.g., Th, U) in certified concentrations, where these elements are introduced into the glass as stoichiometric oxides (e.g., SRMs  $\text{UO}_2$  and  $\text{U}_3\text{O}_8$ ). In conjunction with the preparation of several uranium-bearing glasses, we had reason to examine in the Raman microprobe several of the certified uranium oxide source materials (SRMs and CRMs), to investigate any variabilities in stoichiometry, to determine the specific crystallographic phase, and to examine these powdered oxides for potential compositional modifications resulting from long-term storage. A particularly interesting case are our findings for a sample of Certified Reference Material "Uranium Oxide,  $\text{UO}_3$ " (NBL CRM No. 18) which had been properly stored for several years but was suspected to have undergone a chemical transformation. This material, a finely powdered solid, was examined by micro-Raman spectroscopy, and spectra were obtained from more than a dozen single particles (size range, 5-20  $\mu\text{m}$ ). Because of intense fluorescence emission on excitation at 514.5 nm, the spectra of these particles were acquired with the 568.2nm line. A representative spectrum from these particle measurements is shown in Fig. 3. The principal feature is an intense band centered at  $839\text{ cm}^{-1}$ . This vibration falls into the frequency region 780

to  $900\text{ cm}^{-1}$  characteristic of the symmetric stretching mode of the uranyl ion,  $\text{UO}_2^{2+}$ , reported for a host of uranyl compounds.<sup>14,17,18</sup> Other bands in the spectrum of the sample are consistent with the assignment of a uranyl ion vibrating unit and the identification of the sample as uranyl hydroxide of composition  $\alpha\text{-UO}_2(\text{OH})_2$ , the most prevalent "monohydrate" (i.e.,  $\text{UO}_3\cdot\text{H}_2\text{O}$ ) in the  $\text{UO}_3\text{-H}_2\text{O}$  system.<sup>18</sup> The uranium trioxide-water system is a complicated system for which seven different crystalline polymorphs having three chemical compositions have been identified.<sup>18</sup> These chemical compositions are usually formulated as  $\text{UO}_3\cdot 2\text{H}_2\text{O}$ ,  $\text{UO}_3\cdot\text{H}_2\text{O}$ , and  $\text{UO}_3\cdot 0.5\text{H}_2\text{O}$ , yet still there remain some ambiguities as to the number and identity of the crystal modifications.  $\text{UO}_3\cdot 2\text{H}_2\text{O}$  is considered the only true hydrate in this system. This hydrate may then be written either as  $\text{UO}_2(\text{OH})_2\cdot\text{H}_2\text{O}$  or as  $\text{H}_2\text{UO}_4\cdot\text{H}_2\text{O}$ . Similarly, the compound  $\text{UO}_3\cdot\text{H}_2\text{O}$  may then be more appropriately considered a uranyl compound, which is entirely consistent with the vibrational spectrum, and more exactly formulated as  $\text{UO}_2(\text{OH})_2$ . Four "monohydrate" forms of uranium trioxide have been reported,<sup>18</sup> but only two have been substantiated by rigorous studies, namely the  $\alpha$ - and  $\beta$ -forms of  $\text{UO}_2(\text{OH})_2$ . The  $\alpha$ -phase monohydrate,  $\alpha\text{-UO}_2(\text{OH})_2$ , is reported stable up to temperatures approaching 300 C. However, this phase is said to almost invariably contain less than one water molecule per  $\text{UO}_3$ , i.e.,  $\text{UO}_3\cdot 0.8\text{H}_2\text{O} \pm 0.1\text{H}_2\text{O}$ .

The  $\alpha$ -phase monohydrate identified by micro-Raman spectroscopy was confirmed also by x-ray diffraction studies. A bulk powder sample of CRM No. 18 "Uranium Oxide" yielded an unambiguous x-ray powder pattern identical to that reported for hydrous uranyl oxide,  $\text{UO}_3\cdot\text{H}_2\text{O}$ .<sup>19</sup> Inquiries into the nature and preparation of this NBL Certified Reference Material  $\text{UO}_3$  verified that the material was prepared as  $\gamma\text{-UO}_3$  (fired at 600 C), a pure and relatively stable phase of uranium trioxide.<sup>20</sup> We proceeded to restore this phase by heating the sample at 520 C for 24 h, and re-examined the micro-Raman spectrum of the heated material which produced a spectrum very different from that of  $\alpha\text{-UO}_2(\text{OH})_2$ . We attributed this spectrum to a pure phase of  $\gamma\text{-UO}_3$  showing no traces of any hydrated forms of  $\text{UO}_3$ .

These studies of various uranium oxide reference materials and their potential long-term instability to constancy of stoichiometric composition, or uptake of moisture leading to hydrate formation, illustrate the usefulness of micro-Raman spectroscopy as an investigative tool in diagnostic tracking of compositional changes of critical materials.

## References

1. B. Schrader, "Micro-Raman, fluorescence and scattering spectroscopy of single particles," in K. R. Spurny, Ed., *Physical and Chemical Characterization of Individual Airborne Particles*, New York: Halsted Press, 1986, chap. 19, 358-379.
2. E. S. Etz and J. J. Blaha, "Scope and limitations of single particle analysis by Raman microprobe spectroscopy," in K. F. J.



Heinrich, Ed., *Characterization of Particles*, NBS Special Publication 553, Washington, D.C.: U.S. Government Printing Office, 1980, 153-197.

3. G. J. Rosasco, "Raman microprobe spectroscopy," in R. J. H. Clark and R. E. Hester, Eds., *Advances in Infrared and Raman Spectroscopy*, vol. 7, London: Heyden, 1980, chap. 4, 223.

4. J. G. Graselli, M. K. Snavely, and B. J. Bulkin, *Chemical Applications of Raman Spectroscopy*, New York: Wiley, 1981.

5. J. J. Blaha, G. J. Rosasco, and E. S. Etz, "Raman microprobe characterization of residual carbonaceous material associated with urban airborne particulates," *Appl. Spectrosc.* 32: 292, 1978.

6. W. C. Cunningham, E. S. Etz, and W. H. Zoller, "Raman microprobe characterization of South Pole aerosol," *Microprobe Analysis--1979*, 148.

7. J. J. Blaha and E. S. Etz, "Some experimental problems in the Raman analysis of microsamples," *Microbeam Analysis--1980*, 183.

8. K. A. Rahn, "Progress in Arctic air chemistry, 1980-1984," *Atmos. Environ.* 19: 1987, 1985.

9. N. H. Farlow, K. G. Snetsinger, D. M. Hayes, H. Y. Lem, and B. M. Tooper, "Nitrogen-sulfur compounds in stratospheric aerosols," *J. Geophys. Res.* 83: 6207, 1978.

10. W. H. Schroeder and P. Urone, "Isolation and identification of nitrosonium hydrogen sulfate ( $\text{NOHSO}_4$ ) as a photochemical reaction product in air containing sulfur dioxide and nitrogen dioxide," *Environ. Sci. Technol.* 12: 545, 1978.

11. R. A. Cox, U. L. Haldna, K. L. Idler,

and K. Yates, "Resolution of Raman spectra of aqueous sulfuric acid mixtures using principal factor analysis," *Can. J. Chem.* 59: 2591, 1981.

12. P. Kruus, A. C. Hayes, and W. A. Adams, "Determination of ratios of sulfate to bisulfate ions in aqueous solutions by Raman spectroscopy," *J. Solution Chem.* 14: 117, 1985.

13. M. D. Allen, B. J. Greenspan, J. K. Briant, and M. D. Hoover, "Generation of Li combustion aerosols for animal inhalation studies," *Health Phys.* 51: 117, 1986.

14. S. D. Ross, *Inorganic Infrared and Raman Spectra*, Maidenhead, England: McGraw-Hill, 1972.

15. M. H. Brooker and J. B. Bates, "Raman and infrared spectral studies of anhydrous  $\text{Li}_2\text{CO}_3$  and  $\text{Na}_2\text{CO}_3$ ," *J. Chem. Phys.* 54: 4788, 1971.

16. R. B. Marinenko and D. H. Blackburn, "Glasses for microanalysis: New NBS Standard Reference Materials," *J. de Physique* 45: C2-769, 1984.

17. J. J. Bullock, "Raman and infrared spectroscopic studies of the uranyl ion: The symmetric stretching frequency, force constants and bond lengths," *J. Chem. Soc. (A)*: 781, 1969.

18. H. R. Hoekstra and R. Siegel, "The uranium trioxide-water system," *J. Inorg. Nucl. Chem.* 35: 761, 1973.

19. J. C. Taylor, "The structure of the  $\alpha$ -form of uranyl hydroxide," *Acta Cryst.* B27: 1088, 1971.

20. Communication with Nancy M. Trahey, Safeguards Assessment and Reference Materials Branch, DOE New Brunswick Laboratory, Argonne, Illinois.

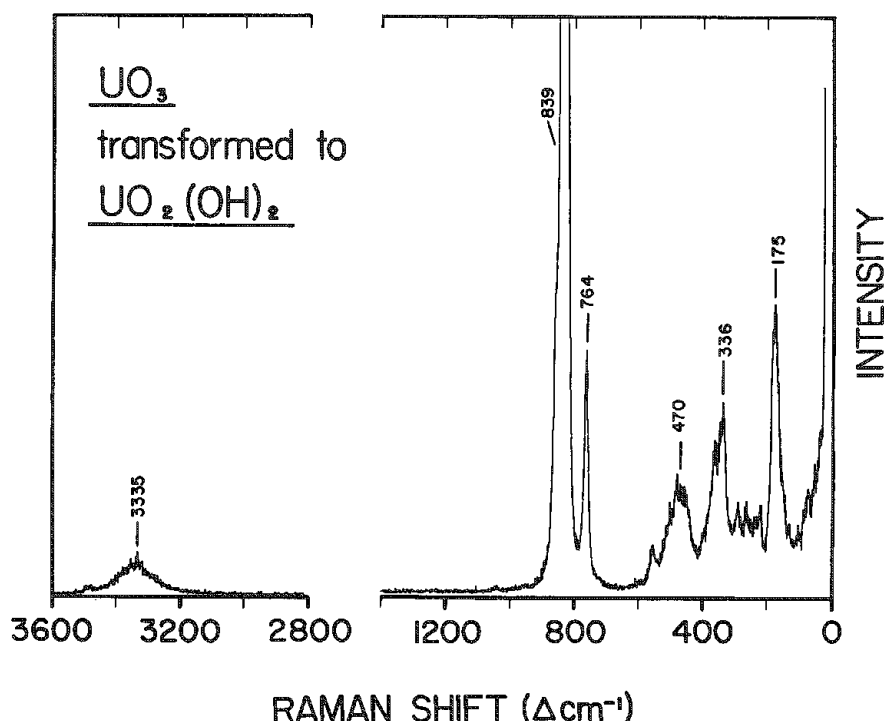


FIG. 3.--Microparticle spectrum of NBL Certified Reference Material "Uranium Oxide,  $\text{UO}_3$ " (NBL CRM No. 18), converted to uranyl hydroxide on long-term storage and handling. Excitation at 568.2 nm; LiF substrate.

## TRANSMISSION ELECTRON MICROSCOPE WITH CASTAING'S ELECTRON X-RAY AND LASER RAMAN PROBES FOR SIMULTANEOUS ELEMENTAL AND MOLECULAR ANALYSIS AT SUBMICROMETRIC SCALE

Michel Truchet and Michel Delhayé

The Raman microprobe<sup>1</sup> is a powerful instrument for molecular microanalysis of micrometric samples. Up to now, numerous applications have dealt with inclusions in polymers or fibers, or in minerals. In biology, mineral and organic secretions precipitated into the cells, or out of them, can be studied by this method. However, the low sensitivity makes it important to analyze pure or locally highly concentrated samples to detect a characteristic signal, even with the new generation of instruments with simultaneous multichannel detection. In biology, concretions larger than 1  $\mu\text{m}$  are seldom made of pure components, and the most common case is that of mixed compositions; therefore, it is not easy to obtain Raman spectra, except in the case of very good Raman scatterers, such as the calcium carbonates or the purinic wastes.<sup>2-4</sup> On the other hand, at the submicrometric scale (0.1-0.5  $\mu\text{m}$ ), concretions and precipitates of biological origin are often more concentrated; in fact, the smaller the size, the greater the concentration of a given component. Unfortunately, submicrometric precipitates cannot be observed with a classical photon microscope. What is needed is a new type of Raman microprobe, with an electron microscope used for the topographic observation, and a system consisting of a laser probe and optical coupling to a photon spectrometer used for molecular Raman analysis. While studying such a new instrument, we have pointed out that it was possible to associate it with an electron probe and x-ray system for simultaneous elemental analysis, as in Castaing's apparatus.<sup>5,6</sup>

Such a system may consist of a Castaing microprobe with an electron microscope device (CAMECA, France) coupled with a multichannel Raman spectrometer (DILOR, France). The original Cassegrain mirror objective of the electron microprobe, previously designed for sample observation, is complemented or replaced by another device for Raman excitation and light collection. In fact, owing to the low density of Raman signals, one must increase the solid angle of light collection, which should ideally reach almost  $4\pi$  steradian. This can be achieved by use of aspherical optical surfaces. However, in practice the available space around the sample is limited by the magnetic lenses. Consequently, the size of the optic for the light collection is very small.

Figures 1 and 2 give a general idea of the system. Other versions of such a compound instrument have been assembled.

### References

1. M. Delhayé and P. Dhamelincourt, "Raman microprobe and microscope with laser excitation," *J. Raman Spectroscopy*, 3: 33-43, 1975.
2. C. Ballan-Dufrançais, M. Truchet, and P. Dhamelincourt, "Interest of Raman laser microprobe (MOLE) for the identification of purinic concretions in histological sections," *Biologie cellulaire* 36: 51058, 1979.
3. M. Martoja and M. Truchet, "Données analytiques sur les concretions du tissu conjonctif de quelques Gastéropodes d'eau douce," *Malacologia* 23: 333-349, 1983.
4. M. Truchet, M. Martoja, R. Martoja, and C. Ballan-Dufrançais, "Applications de la MOLE à l'identification de composés puriques et de sels minéraux sur coupes histologiques," *L'Actualité chimique*, April 1980, 15-18.
5. R. Castaing, *Application des sondes électroniques à une méthode d'analyse ponctuelle, chimique et cristallographique* (Thèse doctorat d'Etat), Paris: ONERA, 1951.
6. R. Castaing and J. Deschamps, "Le dosage des éléments légers par le microanalyseur à sonde électronique," *La Recherche aéronautique* 63: 41-47, 1958.

Author Truchet is at the Laboratoire d'Histophysiologie Fondamentale et Appliquée, UA 680 du CNRS, Université P. et M. Curie, 12 rue Cuvier, F-75005 Paris, France; author Delhayé is at the Laboratoire de Spectrochimie Infra-rouge et Raman, LP CNRS 2631, Université des Sciences et Techniques de Lille-Flandres-Artois, F-59655 Villeneuve d'Ascq Cédex, France.

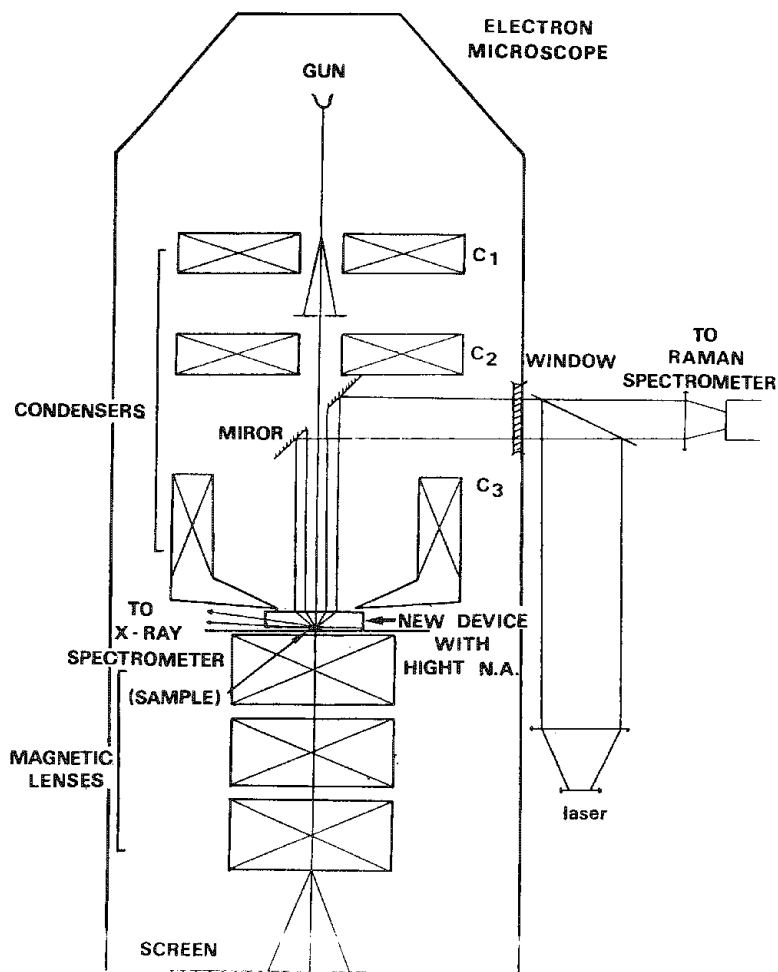


FIG. 1.--Schematic of electron microscope, with devices for elemental x-ray and for molecular Raman microanalysis.

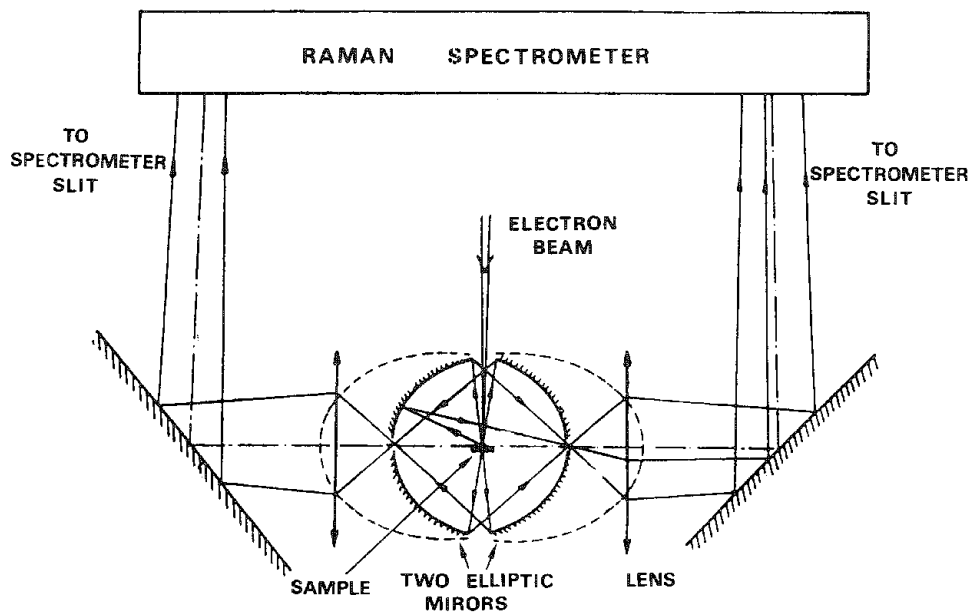


FIG. 2.--Schematic of system allowing light collection in almost  $4\pi$  steradian. It consists of two ellipsoidal mirrors with a common focus, where sample is palced. Light collected by these aspherical surfaces is transmitted to lenses (= objectives) and, with one or several mirrors, to entrance slit of Raman spectrometer. Excitation light is also focused on sample.

# AN IMPROVED ALGORITHM FOR LINEARIZING IN WAVELENGTH OR WAVENUMBER SPECTRAL DATA ACQUIRED WITH A DIODE ARRAY

J. M. Katzenberger, Fran Adar, and J. M. Lerner

We present an improved computational method for converting spectral data acquired with a diode array from diode number to wavelength or wavenumber scales, a process we call linearization. The linearization procedure is based on a method presented by Diem,<sup>1</sup> which we expanded to include a correction for the tilt of the focal plane. An iterative procedure is introduced to determine the true geometric parameters of the spectrograph to which the diode array is attached.

The necessity for accurate linearization of spectral data collected via a diode array/spectrograph detector system has been discussed by Diem.<sup>1</sup> However, the algorithm presented ignores several important considerations. For example, the algorithm assumes that the focal length, groove density, as well as all pertinent angles are known. Even though manufacturers supply this information, the values provided are only the nominal values. The true values, which are a function of the tolerances of the various components used in manufacturing the spectrometer, are usually not known precisely. In addition, the algorithm presented by Diem does not consider a most important parameter--the tilt of the focal plane.

We report here on an algorithm that accounts for this tilt, along with other factors created by an accumulation of geometric "errors." Unfortunately, operating manuals for many Czerny-Turner and Ebert monochromators rarely provide information on tilt. It is left to the user either to determine or ignore this function. Since the tilt, if present, may have a significant effect on the linearization process,<sup>2</sup> we describe a method that aids the user in determining the tilt of the focal plane, and also verifies or determines accurately the other important instrumental parameters required for accurate linearization of diode array spectral data.

Table 1 is included to illustrate the magnitude and type of errors that may result from lack of consideration of tilt. The data presented in Table 1 are for a Czerny-Turner monochromator with an included angle of 24°, groove density of 1200 gr/mm, focal length of 320 mm, and tilt of 2.4°, with a 1024-element diode array. The errors that result are of the order of 0.5 to 1.5 diodes. More important, the errors are larger at one end of the array than at the other.

The combination of correcting for the tilt of the focal plane and determining the instrumental parameters results in accurate linearization to within one-half diode over the width of the diode array.

## References

1. M. Diem, F. Adar, and R. Grayzel, *Computer Enhanced Spectroscopy* 3: 29, 1986.
2. *The Optics of Spectroscopy: A Tutorial*, Instruments S.A., 6 Olsen Avenue, Metuchen, NJ 08820, and Jobin-Yvon Division of Instruments S.A., 16-18 rue du Canal, F-91160 Longjumeau, France.

TABLE 1.--Calculated minimum and maximum wavelength for three central wavelengths with and without correction for tilt.

	Minimum	Wavelength(nm) Center	Maximum
Correct	218.743	250.000	280.889
No Tilt	218.663	250.000	280.865
Error	0.080	0.000	0.024
Correct	470.887	500.000	528.548
No Tilt	470.812	500.000	528.526
Error	0.075	0.000	0.022
Correct	723.930	750.000	775.314
No Tilt	723.863	750.000	775.294
Error	0.067	0.000	0.020

The authors are with Instruments S. A., Inc., 6 Olsen Avenue, Metuchen, NJ 08820.

## CONCENTRATION PROFILES OF METHYL CENTRALITE DETERRENT DIFFUSED INTO A NITROCELLULOSE EXTRUDED MONO-PERFORATED SMALL-ARMS PROPELLANT DETERMINED BY RAMAN MICROSCOPY

J. D. Loudon, B. W. Cook, J. Kelly, and J. Phillipson

The ballistic performance of a propellant is controlled by coating of the granule surface with a deterrent. The deterrent reduces the rate of burning at the surface of the propellant and hence the rate of gas evolution. Knowledge of the concentration profile and penetration depth of the deterrent is important for calculation of ballistic performance.

In this communication a Raman microspectroscopic method is presented for the determination of methyl centralite deterrent diffused into a nitrocellulose matrix.

The concentration of deterrent within the propellant matrix is determined relative to the nitrocellulose by relative intensity measurements of the  $1005\text{cm}^{-1}$  (aromatic ring breathing vibration of methyl centralite) to the  $850\text{cm}^{-1}$   $\text{NO}_2$  deformation or the  $1290\text{cm}^{-1}$   $\text{NO}_2$  symmetric stretch of the nitrocellulose.

Raman measurements were determined at  $5\text{ }\mu\text{m}$  intervals from the external and internal surfaces to a depth of  $50\text{ }\mu\text{m}$  on a microtomed faced-off propellant pellet approximately one-third the way down the pellet.

The external surface profile shows a level concentration of deterrent through a region of

the propellant grain with a steep drop in concentration, which has been ascribed to a diffusion with interaction mechanism.<sup>1</sup> The internal surface profile corresponds to a classical diffusion profile which would initially predict an exponential concentration decrease from the surface inward that would, with time, tend to become level and penetrate through the entire pellet.

### Conclusion

The results show that Raman microspectroscopy is capable of determining concentration profiles and penetration depths of methyl centralite deterrent in a nitrocellulose matrix. Future work will involve the extension of the technique to other deterrent/propellant systems and quantification of the results.

### Reference

1. B. W. Brodman et al., "Autoradiographic determination of the di-n-butyl phthalate concentration profile in a nitrocellulose matrix," *J. Appl. Polym. Sci.* 18: 3739-3744, 1974.

---

Authors Loudon and Cook are at ICI C&P PLC, The Heath, Runcorn, Cheshire, England; authors Kelly and Phillipson, at ICI Nobel's Explosives Co. Ltd., Stevenson, Ayrshire, Scotland. This work has been carried out with the support of the Procurement Executive of the U.K. Ministry of Defence.

## IN SITU MICRO-RAMAN STUDY OF DISCHARGE PRODUCTS OF $\text{Li/SOCl}_2$ CELLS

M. C. Dhamelincourt, P. Dhamelincourt, and F. Wallart

Even though the overall reaction for the thionyl chloride cell is well established now, there continues to be controversy regarding the mechanism and the chemical nature of intermediates of the reaction. Particularly, the pressure generated in  $\text{Li/SOCl}_2$  cells has been found to be significantly lower than that predicted on the basis of the accepted discharge reaction. This finding is believed to be due to the  $\text{SO}_2$  generated being complexed by  $\text{LiAlCl}_4$  and/or absorbed by the carbon cathode.<sup>1,2</sup> Several studies have been carried out on this problem, but no Raman study has been hitherto described in the literature.

Nevertheless, Raman spectroscopy and especially micro-Raman spectroscopy is a technique particularly well adapted to this kind of problem allowing an "in situ" study during the discharge.

### Experimental

The electrolyte was 1.8 M  $\text{LiAlCl}_4$ . It was prepared in a dry nitrogen-filled glove box by dissolving stoichiometric amounts of anhydrous  $\text{LiCl}$  (Carbo-Erba) and  $\text{AlCl}_3$  (Fluka) in  $\text{SOCl}_2$  (Carbo-Erba). The cell is shown in Fig. 1. The anode (b) is a lithium ribbon mechanically attached to the upper end of a stainless-steel rod protected by Teflon coating. The reference (c) and the counter electrode (c) were identical carbon sticks (Carbone-Lorraine) set parallel to each other. The cell was air-tight, sealed by Viton O-rings. The construction and the filling of the cell were carried out in a glove box filled with argon, free of oxygen. The top of the cell, especially made for micro-Raman observations was an optically flat window.

Raman spectra were recorded with a spectral resolution of  $8\text{ cm}^{-1}$  by use of a micro-Raman spectrometer, Microdil 28, DILOR (France). It is equipped with a multichannel detector (intensified reticon linear photodiode array). The Raman spectrometer is coupled to a computer that permits data acquisition and treatment. The excitation was the 514.5nm line of an ionized argon Laser (Spectra-Physics). The power was about 50 mW at the sample. The Raman spectra were recorded with an integration time of 10 s and 10 spectra were sequentially added in order to obtain good signal-to-noise ratio.

A long working distance objective (a) allowed us to record spectra at the surface of the lithium electrode or inside the electrolyte solution. The spatial resolution and the probed volume were  $1\text{ }\mu\text{m}$  and  $10\text{ }\mu\text{m}^3$ , respectively. Data were obtained at room temperature.

### Results and Discussion

The configuration of the cell is such that the ohmic resistance is high, so that we could only observe low discharge rates. Figure 2 shows the spectra of the electrolyte in the spectral range of the S-O vibrational stretching mode. In spectrum (a), recorded before the discharge, the band at  $1230\text{ cm}^{-1}$  were assigned respectively to free  $\text{SOCl}_2$  and to  $\text{SOCl}_2$  molecules bound to the  $\text{Li}^+$  ion.<sup>2</sup> Spectrum (b) was recorded after several hours at low-rate discharge, about  $40\text{ mA/cm}^2$ . We observed the formation of the  $\text{Li}(\text{SOCl}_2)(\text{SO}_2)^+ \text{AlCl}_4^-$  complex characterized by the band appearing at  $1160\text{ cm}^{-1}$ , studied in previous work.<sup>3</sup> These bands have weak intensities because the concentration of the species during the low discharge stays small even after a long time and also because the solution becomes slightly turbid (due to the formation of colloidal particles of sulfur).

Spectrum (c) was obtained when the laser beam was focused at the surface of the lithium electrode, after a discharge at  $90\text{ mA/cm}^2$ . A very broad band is observed at about  $1100\text{ cm}^{-1}$ . This frequency suggests that a complex, most likely  $\text{Li}(\text{SO}_2)_3^+$ , or a charge transfer complex between lithium and  $\text{SO}_2$ , was generated at the surface of the lithium electrode. We cannot observe the formation of lithium chloride because this species has no first-order Raman spectrum.

Under these experimental conditions, free  $\text{SO}_2$  is detected neither in the electrolyte, nor in the gas phase at the top of the cell. Indeed, free  $\text{SO}_2$  in solution or in the gas phase should have exhibited Raman lines at  $1148\text{ cm}^{-1}$  and  $1152\text{ cm}^{-1}$ , respectively. It would be interesting and informative to observe the surface of the carbon electrode. Therefore, we pursued this work by modifying the cell in order to be able to observe the carbon electrode surface, and to verify whether the generated  $\text{SO}_2$  is absorbed or not. We are also constructing a cell that will permit us to observe higher discharge rates in order to increase the concentration of the different species formed during the discharge; experiments are already in progress.

### References

1. K. M. Abraham, L. Pitts, and W. P. Kilroy, *J. Electrochem. Soc.* 132: 2301, 1985.
2. Y. Bedfer, J. Corset, M. C. Dhamelincourt, F. Wallart, and P. Barbier, *J. Power Sources* 9: 267, 1983.
3. M. C. Dhamelincourt, F. Wallart, P. Barbier, G. Mairesse, and P. Descroix, *ibid.*, 14: 77, 1985.

TO THE SPECTROMETER

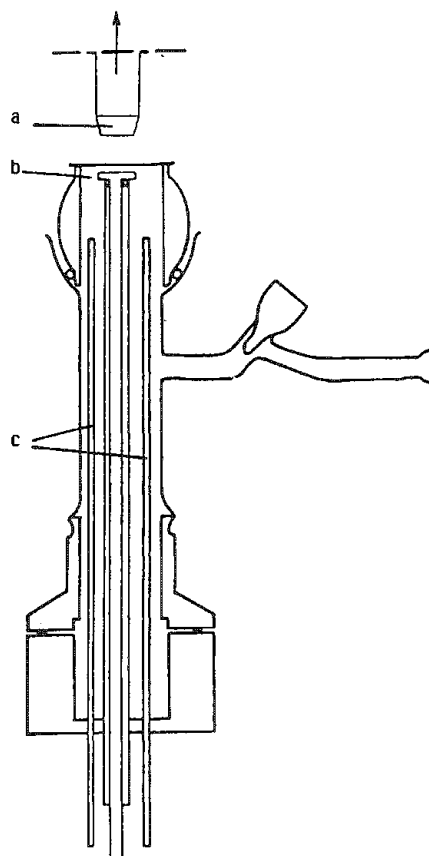


FIG. 1.--Schematic diagram of cell: (a) microscope objective, (b) lithium electrode, (c) graphite electrodes.

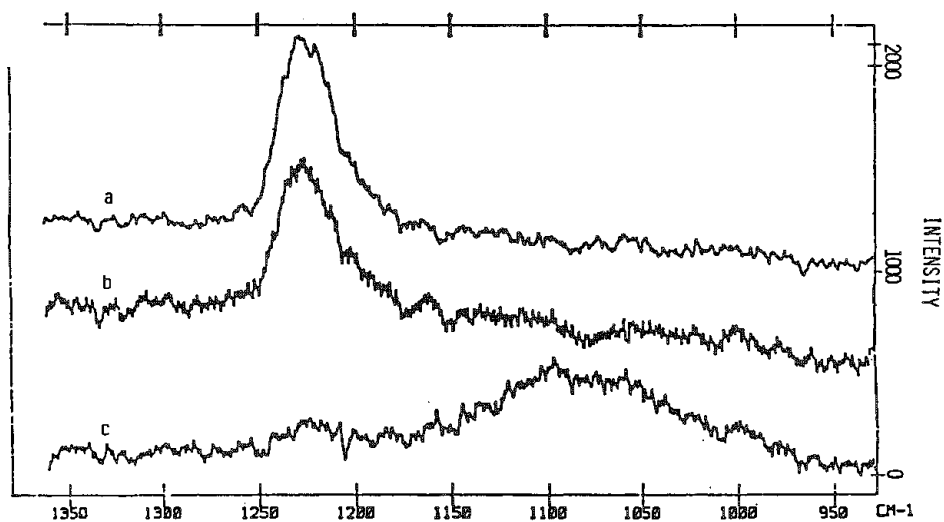


FIG. 2.--Raman spectra (a) before discharge, (b) after several hours at low discharge rate, (c) at lithium electrode surface.

## 4B. Optical Spectroscopy: Micro-IR

### DESIGN AND PERFORMANCE STANDARDS FOR INFRARED MICROSCOPES IN SPECTROSCOPY

R. G. Messerschmidt

The year 1987 is the fortieth the world has had the all-reflecting IR microscope. That is almost as long as we have had infrared spectrometers; indeed, the first combination of the reflecting microscope and infrared spectrometer appears 38 years ago.<sup>1</sup> In the interim, scientists largely did without this combined instrument. The historical development of the use of infrared transmitting microscopes for infrared spectroscopy has been investigated recently and is not recounted here.<sup>2</sup> Why the technique works so well now and is so popular deserves some mention. Therefore, this paper looks at the present-day infrared microscope and investigates its capabilities and limitations through consideration of its inner workings and the theory behind it. Also mentioned is the development of the infrared spectrometer, for it is largely the improvement in spectrometer sensitivity that has made improved microscope performance a worthwhile goal. The infrared microscopes of forty years ago were good enough for dispersive spectrometers; with the introduction of Fourier transform spectrometers, the microscope became the limiter of performance.

In speaking about the performance aspects of the infrared microscope/spectrometer, we must evaluate four criteria. Three are familiar to the spectroscopist and one to the microscopist. The first three are quantitative linearity, qualitative accuracy and signal-to-noise ratio. The fourth criterion, the microscopic figure of merit, is the spatial resolution.<sup>3</sup> What is meant by these four criteria? To begin with, the meaning of spatial resolution in the infrared microscope is slightly different from what it is in microscopes where the eye is the detector.

In an infrared microscope (Fig. 1), the visible optical train is parfocal and colinear with the infrared features that one achieves in setting up the microscope by viewing through a series of small pinholes and then aligning for infrared energy through the same pinholes. In actual use, the area of interest is brought to the center of the field of the microscope under visible (transmitted or reflected) light. Then the area to be analyzed is delineated with high-contrast apertures in the remote image planes of the sample. Preferably these apertures are variable in size so that the area of interest may be "zeroed in on." Since the optical geometry is the same for the visible evaluation and the infrared detection, the diffraction effect is worse for the detection step, because the wavelength is longer. For this reason, we can see the area we want to measure much more easily than we can actually

measure it. For infrared microscope spectrometry, we therefore define spatial resolution as the ability to measure the spectrum from an object delineated by the apertures without impurity radiation from neighboring objects. Since the infrared spectrum is quite complicated, consisting of thousands of data points, it is often difficult to say whether spatial impurity has affected the result. If there is impurity, it can take the form of either a spurious absorption band from a nearby absorber, or stray light from a nearby hole. The Schwarzschild-Villiger effect<sup>4</sup> can then also cause problems. It states that stray radiation affects the strong bands in a spectrum much more than it affects the weak bands, which obviously plays havoc with the quantitative accuracy of the measurement. Both quantitative accuracy and signal to noise may be affected by the ability of a microscope to resolve the specimen spatially.

As an interesting example (Fig. 2), an acrylic fiber 20  $\mu\text{m}$  in diameter is embedded into an acrylic embedding medium and then cross-sectioned to a 10 $\mu\text{m}$  thickness. Three spectra are run, all with the same spectrometer conditions and for the same length of time. In the first spectrum, no particular effort is made to aperture out the surrounding embedding medium. In the second, one variable aperture is used to delineate the fiber. In the third spectrum, two apertures, one in the rear focal plane of the objective and one in the rear focal plane of the condenser, both delineate the same area of the sample. The first spectrum obviously has the best signal-to-noise ratio, but it is predominantly the spectrum of the embedding medium! The singly apertured spectrum shows a much strong  $\nu_{\text{CN}}$  vibration. But the result that best represents the fiber is the third one, even though it is noisier. Since the majority of the spectral absorbances are common between the fiber and the embedding medium, a poorly spatially resolved spectrum appears to be better. But the  $\nu_{\text{CN}}$  band at 2243  $\text{cm}^{-1}$  is attributed to the fiber only. Therefore, the result where this band is strongest, relative to the other bands, is the most accurate result. This aperture redundancy is the heart of a high-performance infrared microscope.

To describe the theory behind the operation of dual remote image masking, we must consider light diffraction. Basically, we ignore the imaging of the specimen in the microscope and consider first the imaging of the sharp-edged high-contrast apertures used to delineate the sample, although the sample can also play an important role in the performance of an infrared microscope. The key to this approach is that the first aperture actually defines the area of the sample that is illuminated: the sample is nonluminous and we "light up" only a small area, not the full field as when we view the sample. Therefore,

The author is with Spectra-Tech, Inc., 652 Glenbrook Rd., Stamford, CT 06906.



we must know the shape of the diffraction-limited image of the aperture in the sample plane. There are very few "exact solutions" in diffraction theory, so it is indeed fortunate that we usually use rectangular apertures to delineate the sample. If we consider each blade of a rectangular aperture separately, the problem becomes that of diffraction at a high-contrast straightedge. This problem has been worked out for us.<sup>5</sup> Figure 3 shows the mathematical relationship between intensity and position for a high-contrast edge which defines the input of energy to the specimen. Also shown is the ideal curve for the imaging of the edge in the absence of diffraction. The energy that exists in the geometrical shadow of the edge is undesirable, since it illuminates an unwanted portion of the specimen. What is left to do is to superimpose a similar output function in the image plane after the specimen. The resultant energy profile at the detector is the product of these two functions (Fig. 3). Of course one can obtain further assurance of spatial purity by overaperturing, i.e., by deliberately closing down the remote-field apertures beyond the desired area of the specimen. However, we are often energy starved in the size limit and cannot afford to throw away energy. In this situation, one does much better by carefully redundantly aperturing to the edges of the area of interest. In some cases, for instance where the surrounding medium is known and can be subtracted, the second aperture may be neglected in the interest of speed.

However, aperture redundancy is only one of many important considerations in the design of a quantitatively and qualitatively accurate, high-sensitivity instrument. Many of the other aspects were adequately addressed in the many papers written about such instruments in the late 1940s and early 1950s.<sup>6-9</sup> Chief among these details is the need for a high-numerical-aperture optical system that is also free of aberrations to below the diffraction limit, over a reasonable field. Numerical aperture is inversely proportional to the extent of the diffraction pattern. A practical limit is reached, though, because as aperture increases, rays impinge on the specimen at steeper angles, which can adversely affect photometric accuracy.

Another often overlooked problem is that the specimen itself acts as an optical element. In the biological microscope, there is a very well defined specimen geometry and most biological microscopes come already corrected for it. That is, the objective is designed with a 0.17mm-thick cover glass expected and required for proper performance. The condenser is similarly corrected for the glass slide. Unfortunately, the specimen is much less well defined in the infrared microspectrometer. The microscope is expected to perform equally well for a cylindrical fiber suspended in the air and a fiber squeezed between 2mm-thick diamonds! The answer lies in the Schwarzschild design<sup>10</sup> of the Cassegrainian microscope objective and condenser. This design has the nice feature that as the separation between the nearly concentric mirrors is decreased, the spherical aberration introduced by the

specimen or support is compensated for (Fig. 4). The chromatic aberration unfortunately remains, so it is still a good idea not to use thick or high-index specimen supports.

### Conclusions

The engineering aspects of the modern infrared microscope/spectrometer have been reviewed so that the reader may understand the apparatus and use its full potential. Redundant Aperturing and Sample Compensation (both are trade names of Spectra-Tech, Inc.) combine to improve the spatial-resolution capabilities of the infrared microscope to the point where the wavelength of light and the numerical aperture of the system are truly the limiters of further gain. Infrared microspectroscopy now stands as the best choice for identification of small amounts of organic materials, and for the measurement of, or correlation with, a number of their physical properties such as dichroic ratio or physical strength.

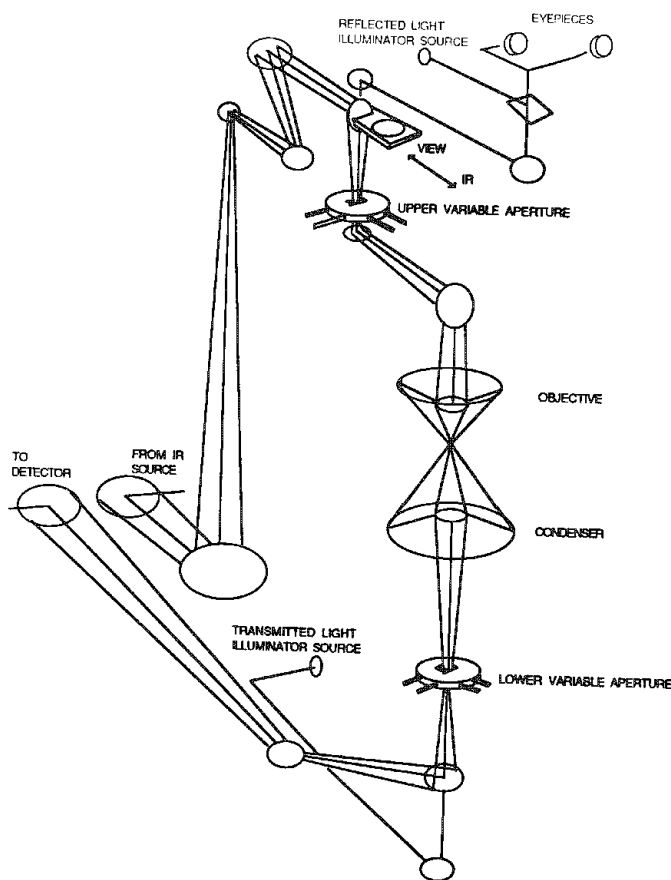


FIG. 1.--Generalized schematic layout of redundantly apertured IR microscope/spectrometer operating in transmission mode. All surfaces in IR beam path are reflecting surfaces. Objective and condenser are Schwarzschild-configuration Cassegrainian microscope objectives.

### References

1. R. Barer, A. R. H. Cole, and H. W. Thompson, "Infra-red spectroscopy with the reflecting microscope in physics, chemistry, and biology," *Nature* 163: 198, 1949.
2. J. A. Reffner, J. P. Coates, and R. G. Messerschmidt, "Chemical microscopy with Fou-

rier transform infrared microspectroscopy," *American Laboratory* 19(No. 4): 86, 1987.

3. R. G. Messerschmidt, J. M. Kwiatkoski, and C. R. Friedman, "Improved microspectrometry and FT-IR sampling," *Intern. Labmate* 11: 1986.

4. K. Schwarzschild and W. Villiger, *Astrophys. J.* 23: 284, 1906.

5. M. Born and E. Wolf, *Principles of Optics*, Oxford and New York: Pergamon Press, 1964.

6. C. R. Burch, *Proc. Phys. Soc.* 59: 47, 1947.

7. R. C. Gore, "Infrared spectrometry of small samples with the reflecting microscope," *Science* 110: 710, 1949.

8. E. R. Blout, G. R. Bird, and D. S. Grey, "Infrared microspectroscopy," *J. Opt. Soc. Amer.* 40: 304, 1950.

9. V. J. Coates, A. Offner, and E. H. Siegler Jr., "Design and performance of an infrared microscope attachment," *J. Opt. Soc. Amer.* 43: 984, 1953.

10. D. S. Grey, "Computed aberrations of spherical Schwarzschild reflecting microscope objectives," *J. Opt. Soc. Amer.* 41: 183, 1951.

#### Non-Apertured Embedded Acrylic Fiber Cross-Section

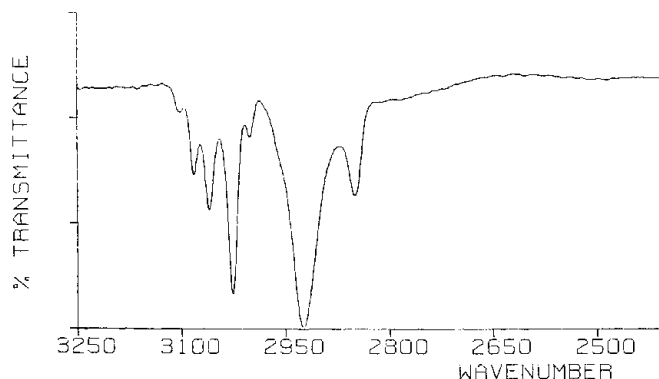
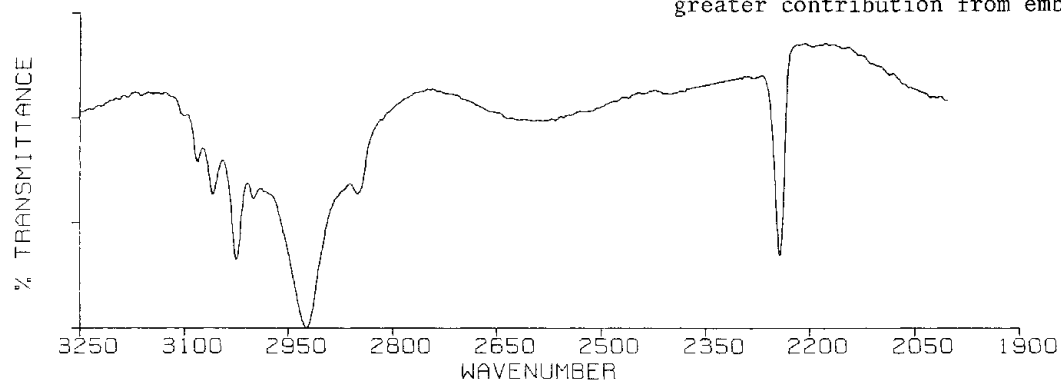
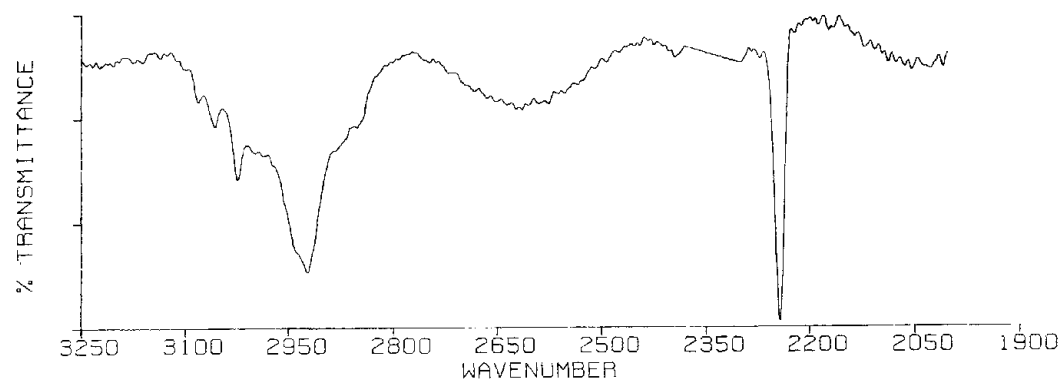


FIG. 2.--Demonstration of importance of second aperture toward spatial purity in IR microspectroscopic measurement. Acrylic fibers are embedded in acrylic resin and cross sectioned. Fiber exhibits strong  $\nu_{CN}$  absorption band, absent in embedding medium. (a) No aperturing, beautiful spectrum, but weakness of  $\nu_{CN}$  band shows spectrum to be predominantly that of embedding medium. (b) Fiber is singly apertured (fiber only visible to eyepiece) and cyanate band is much stronger. (c) Redundantly apertured spectrum shows this band to be even stronger relative to CH-stretching region, which confirms that singly apertured case had greater contribution from embedding medium.

#### Single Apertured Embedded Acrylic Fiber Cross-Section



#### Redundantly Apertured™ Embedded Acrylic Fiber Cross-Section



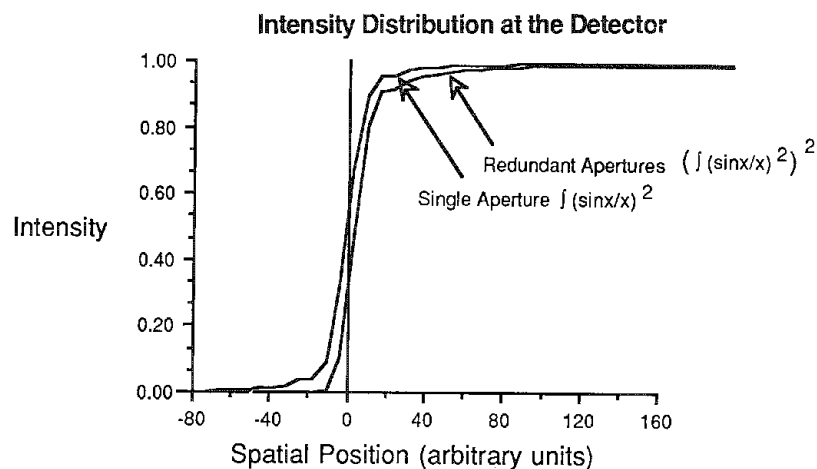


FIG. 3.--Energy distribution at detector for single high-contrast edge in singly apertured microscope. Also shown: energy distribution at detector for two high-contrast aperture blades in remote image planes of specimen (redundantly apertured microscope).

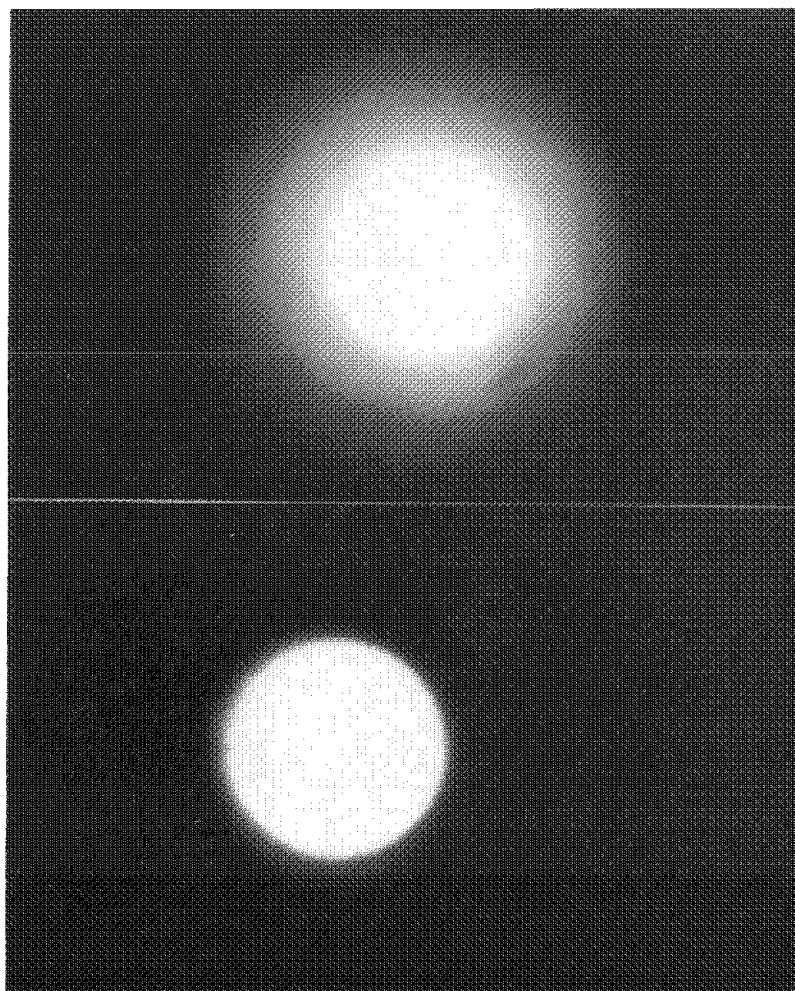


FIG. 4.--Best focus image of 1mm round aperture at lower-aperture position of redundantly apertured microscope, which equates to 100 $\mu$ m image at specimen plane; 2mm-thick barium fluoride window is inserted at specimen plane. top, image of aperture before correction of condenser for spherical aberration introduced by window; below, after adjustment of separation between the two spherical mirrors in condenser assembly (sample compensation).

## COMPOSITIONAL MAPPING WITH THE USE OF FUNCTIONAL GROUP IMAGES OBTAINED BY INFRARED MICROPROBE SPECTROSCOPY

M. A. Harthcock and S. C. Atkin

The use of optical microprobe spectroscopies to map the composition of various materials has recently become the attention of several research efforts.<sup>1-5</sup> For example, the use of spatially resolved Raman spectroscopy (Raman microprobe) has been the topic of numerous papers.<sup>6-8</sup> Recently, surface-enhanced Raman spectroscopic (SERS) techniques have been used to obtain a compositional map (image) of aqueous pyridine on a silver surface by use of the scattering intensity at a particular Raman shift.<sup>1</sup> "Traditional" Raman microprobe techniques have been used to study spatially resolved areas of a material to as small as 1  $\mu\text{m}$ .<sup>6</sup> Recently, infrared microprobe (infrared microspectroscopy, micro-IR, etc.) has begun to grow in application largely due to the advantages offered by Fourier transform infrared technology over conventional dispersive techniques.<sup>9-11</sup>

We have used the advantages of Fourier transform infrared microprobe spectroscopy of spatial resolution to 10-20  $\mu\text{m}$ , high energy throughput, and frequency accuracy coupled with spatial mapping (as small as 10  $\mu\text{m}$ ) to allow compositional mapping of materials. The compositional mapping is accomplished by images (one- or two-dimensions) based on functional group absorption intensities. This paper describes the technique and gives an example demonstrating the technique's capabilities.

### *Functional Group Imaging Instrumentation and Data Analysis*

Figure 1 presents a schematic of the apparatus used for obtaining infrared (IR) spectra at specific x and y spatial dimensions. A Digilab FTS-50 Fourier transform IR spectrophotometer and 3200 data station were used for recording the IR spectra. A Digilab universal microscope accessory equipped with a motorized two-dimensional sample stage was coupled with the spectrophotometer for the microprobe work. The motorized stage was controlled by the 3200 data station, which synchronized the movement of the stage and collection of the IR spectra.

Once the IR spectra have been collected, they are transferred to a personal computer (in our case an IBM PC AT or similar computer) for reduction of the mapping data. The personal computer was interfaced with the 3200 data collection system, which is a multiuser system, so that data transfer and collection can take place simultaneously.

An array of IR spectra (frequency/intensity data), each with a specific x and y value, is then reduced to a single array containing the x position, y position, and the absorption intensity of a vibrational motion that occurs at

a specific frequency. The intensity (absorbance, percent transmittance, relative band intensity, etc.), is a function of several experimental variables, as defined below,

$$I \propto I[\epsilon(\tilde{\nu}), C(a_x, a_y, b), r(R, L), D(s_x, s_y)]$$

where I is the intensity

$\epsilon$  is the absorptivity coefficient (a function of  $\tilde{\nu}$ , the frequency of absorption)

C is the concentration (a function of  $a_x$ , the aperture dimension in the x direction;  $a_y$ , the aperture dimension in the y direction; and b, the path length; these three variables define the volume or absorption cross section from which the infrared spectra are obtained).

r is the increment range for contours in the constructed image and defined as R/L, where R is the range of the appropriate intensity values for the map (R is the absolute value of the difference between the maximum and minimum intensity values, and L is the total number of contour levels that are used in the representation of the image, a variable of most significance when the data from a false color image are being interpreted).

D represents the step sizes in the map and is a function of  $s_x$ , the step size in the x direction; and  $s_y$ , the step size in the y direction.

The D parameter influences the effective enhancement possible in spatial resolution for which specific IR spectra can be obtained. The data (a function of the above variables) are then used to produce the image and hence the compositional map of a material.

### *An Application of a Functional Group Image for Compositional Mapping.*

As in other imaging techniques, use of a given IR absorption frequency to view a material can have many profound effects. For example, optical and electron microscopy techniques by themselves only provide a image that is often subject to the interpretation of the analyst. Use of a chemical functionality that absorbs in the IR spectrum can provide a means of producing a compositional map of a material that is based on the chemical groups present, subject to the condition that in a heterogeneous material the IR absorption due to a specific chemical functional group can be resolved (or deconvoluted) from that of another group. This condition depends on (1) the similarity of functional groups representative of the various phases in a heterogeneous material, and/or (2) the spatial resolution for which the IR spectra can be obtained.

Figure 2 shows the optical micrograph of a polyethylene film, which shows an area that contains a more opaque region than the bulk film. From the micrograph it is difficult, if not impossible, to observe this region. Thus,

The authors are with Analytical and Engineering Sciences, B1218, Texas Applied Science and Technology Laboratories, Dow Chemical U.S.A., Freeport, TX 77541.

in a "standard" IR microprobe experiment, where one would record one spectrum of the bulk phase and one of the area of interest, it would be difficult to distinguish the areas visually to accomplish this. Although not important to this example, several attempts were made to obtain spectra of the above-mentioned two areas, with no success in distinguishing between the regions.

A two-dimensional map of the material was taken so that a compositional map could be obtained. The conditions for the map were: (1) a  $250 \times 250 \mu\text{m}$  aperture that allowed radiation to reach the narrow-band MCT detector, (2)  $250 \mu\text{m}$  steps in the x and y direction made when the stage was moved to collect the spatially specific data, and (3) 32 scans collected at  $8\text{cm}^{-1}$  resolution for signal averaging in obtaining the infrared spectra.

The two-dimensional map provided data that were uniquely representative of the material. A variety of functional group images could be used for studying the material for chemical heterogeneities. Figure 3 shows the results of the two-dimensional map based on the absolute absorbance of a  $1735\text{cm}^{-1}$  carbonyl stretching vibration (the sample thickness was  $0.46\text{mm}$ ). A definite area containing a high concentration of carbonyl functionality is detected. The figure also shows IR spectra representative of the carbonyl containing area versus the average surrounding material. From the IR spectra in the  $2200\text{--}700\text{cm}^{-1}$  region several other differences can be detected. Images based on absorption bands at  $1241$  and  $1016\text{cm}^{-1}$  are shown in Figs. 4 and 5 and are very similar to the image based on the carbonyl stretching absorption. The absorption bands are indicative of ester functionalities and very similar to absorptions in an ethylene/vinyl acetate copolymer or acetate containing material. The three maps complement each other in that essentially the same image is obtained by use of vibrational absorptions that are associated with the same chemical moiety.

From the images based on vibrational absorptions due to an ester group, we see that the polyethylene material contains a contaminant that is in some way contributing to the increased opaqueness of a region of the film. The combined carbonyl-containing areas cover approximately  $1.5 \times 0.75\text{mm}$  of the film in the images shown in Figs. 3-5. This was not the size of the opaque area, but the presence of this material could affect the crystallinity of the bulk polymer, which in turn could result in various degrees of opaqueness in the polymer. To investigate this possibility two additional maps were computed from the spatially specific spectroscopic data.

Figures 6 and 7 show the compositional map of the sample based on absorptions at  $908\text{cm}^{-1}$  (vinyl saturation) and  $1892\text{cm}^{-1}$  (crystalline phase polyethylene band, which is a combination band of Raman active fundamental at  $1168\text{cm}^{-1}$  and the  $730/720\text{cm}^{-1}$  IR  $\text{CH}_2$  rocking modes). The images have been computed by ratioing the absorptions with the  $1365\text{cm}^{-1}$  absorption. From the images it appears, based on the sensitivity of the method, that no differences in the crystallinity or vinyl unsaturation composition are observed as a function of the spa-

tial coordinates.

## Conclusions

The use of IR microprobe techniques has been expanded by use of functional group images in order to obtain compositional information of a material. The technique offers representative sampling of microscopic materials and compositional mapping of heterogeneous materials to assist in interpreting microscopy data or to serve as a chemical visualization technique (within the spatial resolution of approximately  $3\text{--}20\text{ }\mu\text{m}$ ). The example discussed here has demonstrated the usefulness of the technique, whose general utility will prove to be valuable because of the wide applicability of IR spectroscopy for both qualitative and quantitative analysis in such fields as materials and biological sciences. The technique has two main limitations. First, compared to other optical microbeam methods such as Raman and fluorescence, the resolution of the IR technique is only approximately  $3\text{--}10\text{ }\mu\text{m}$  versus approximately  $3500\text{ }\text{\AA}$  for the other methods. Second, data collection and reduction can take as long as  $24\text{--}48\text{ h}$  depending on the material and the experimental conditions and/or data reduction tools necessary for addressing the problem. However, we are investigating methods to improve the resolution and speed of data acquisition for IR microprobe functional group imaging.

## References

1. R. P. Van Duyne, K. L. Haller, and R. I. Altkorn, "Spatially resolved surface enhanced Raman spectroscopy: Feasibility, intensity dependence on sampling area, and attomole mass sensitivity," *Chemical Physics Letters* 126: 190-196, 1986.
2. R. P. Van Duyne, R. I. Altkorn, and K. L. Haller, "Surface Raman spectroscopy as an in-situ probe of laser microchemical processes," *Proc. IEEE* 75: 61-66, 1986.
3. M. A. Harthcock and S. C. Atkin, "Infrared microspectroscopy: Development and applications of imaging capabilities," *Proc. Symp. IR Microspectroscopy*, Federation of Analytical and Spectroscopy Societies 1986 Meeting, paper 436.
4. K. Krishnan, "Characterization of semiconductor silicon using the FT-IR microsampling techniques," *ibid.* paper 517.
5. B. C. McIntosh and S. Bijasiwicz, "The FTIR microprobe," paper 599 at Federation of Analytical and Spectroscopy Societies 1986 Meeting.
6. M. E. Anderson, "Molecular optical laser examiner (MOLE): Application to problems encountered by electron microscopists in the analysis of polymers," in C. D. Craver, Ed., *Polymer Characterization: Spectroscopic, Chromatographic, and Physical Instrumental Methods*, American Chemical Society, 1983, 383-400.
7. F. Adar and H. Noether, "Raman microprobe spectra of spin-oriented and drawn filaments of poly(ethylene terephthalate)," *Polymer* 26: 1935-1943, 1985.
8. R. Grayzel, M. LeClercq, F. Adar, J. Lerner, M. Hutt, and M. Diem, "An automated micro/macro Raman spectrograph system with

multichannel and single-channel detectors in a new molecular/crystalline microprobe," *Microbeam Analysis--1985*, 19.

9. J. E. Katon, G. E. Pacy, and J. F. O'Keefe, "Vibrational molecular microspectroscopy," *Analytical Chemistry* 58: 465A-481A, 1986.

10. M. A. Harthcock, L. A. Lentz, B. L. Davis, and K. Krishnan, "Application of transmittance and reflectance micro/FT-IR to polymeric materials," *Applied Spectroscopy* 40: 210-214, 1986.

11. J. N. Ramsey, "Small area molecular analysis as applied in the microelectronics industry," *J. de Physique C2*: 881-885, 1984.

12. T. Hirschfeld, "Microspectroscopy," *Microbeam Analysis--1982*, 246.

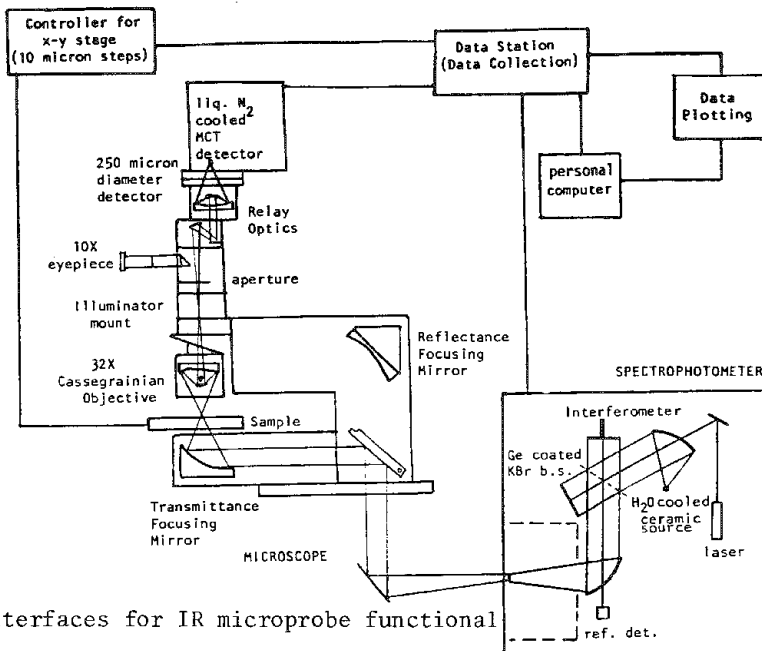


FIG. 1.--Instrumentation and computer interfaces for IR microprobe functional group imaging analyses.

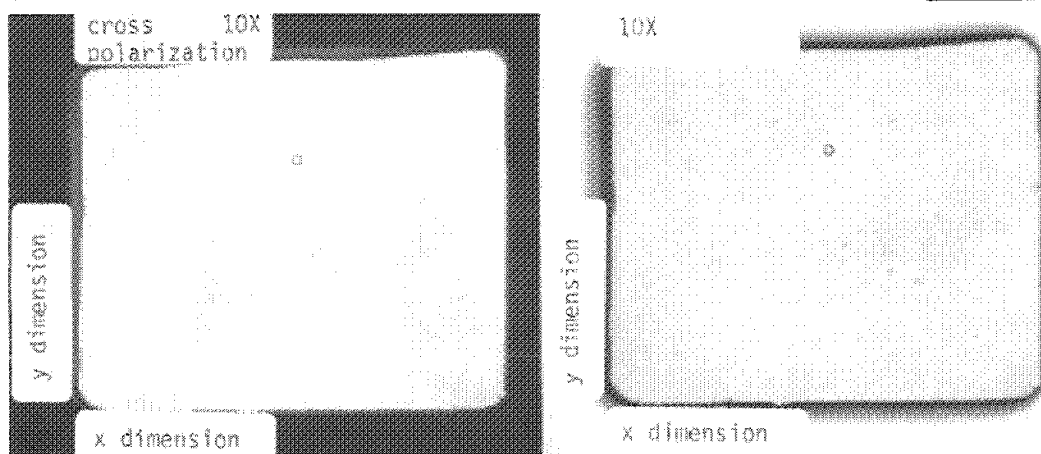


FIG. 2.--Optical micrographs of polyethylene film containing opaque region.

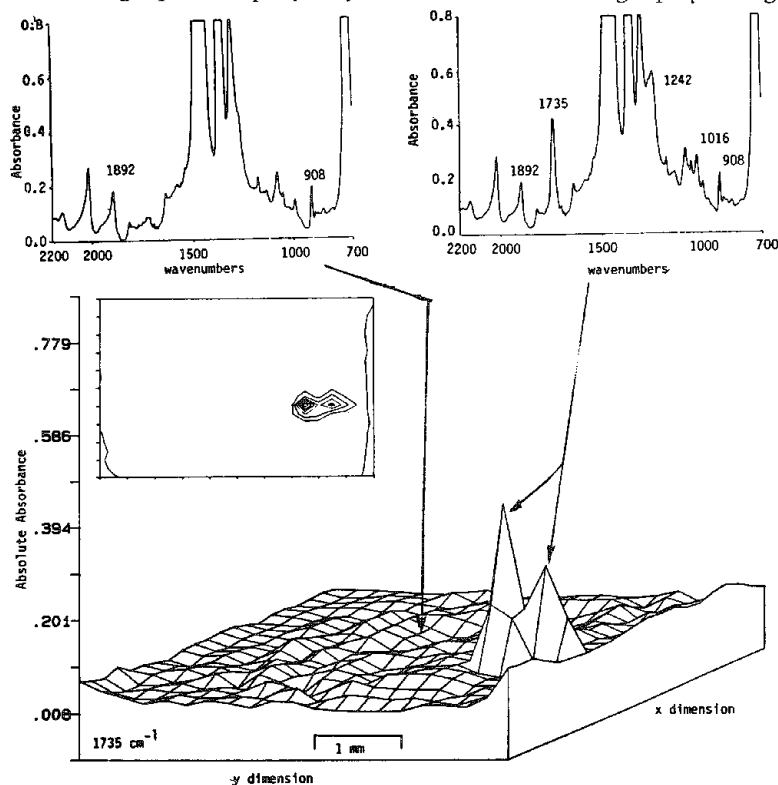
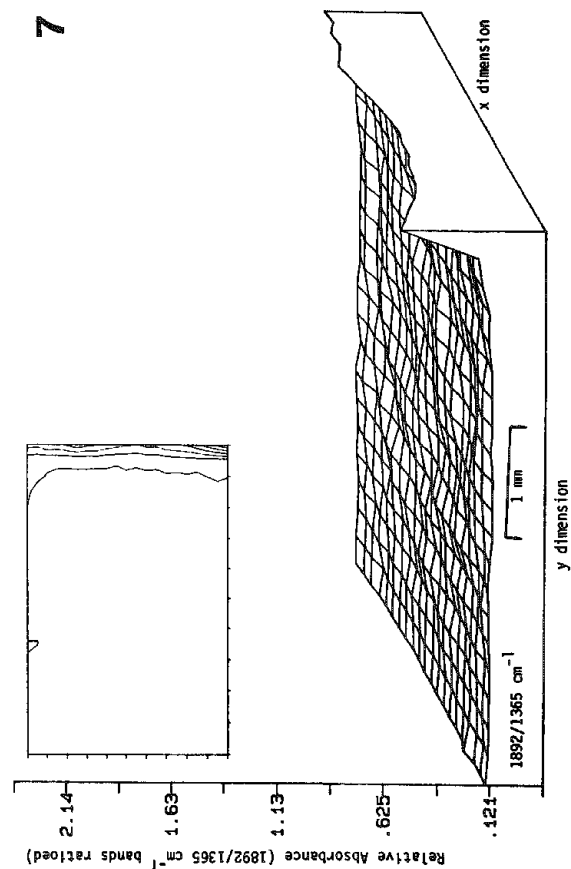
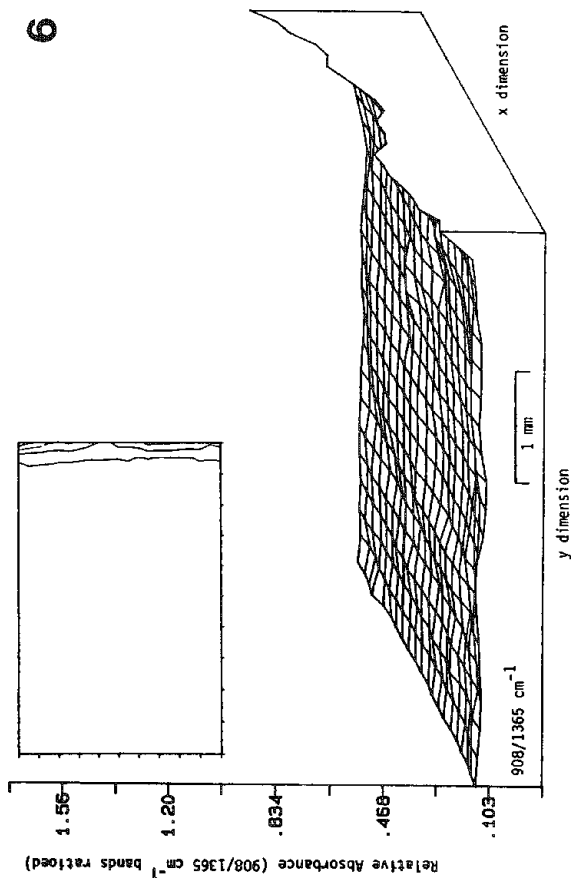
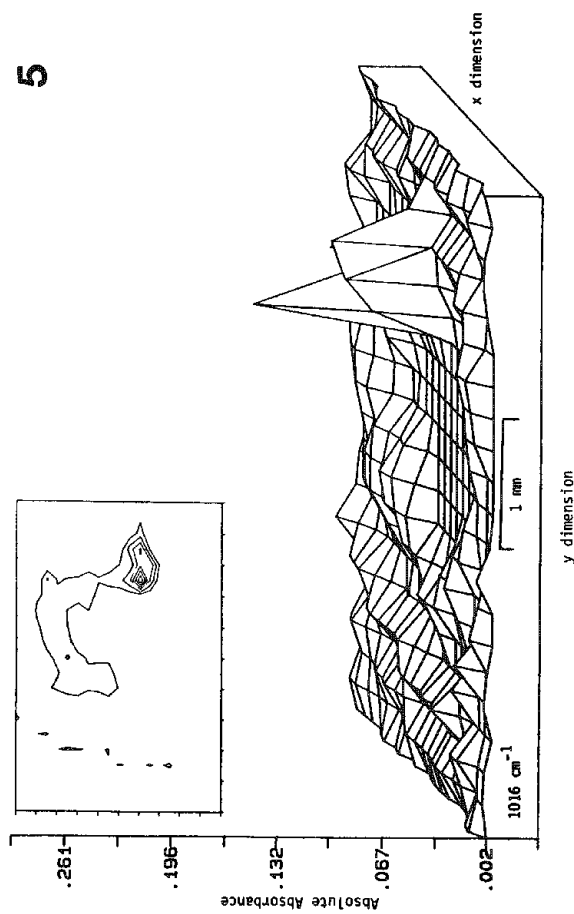
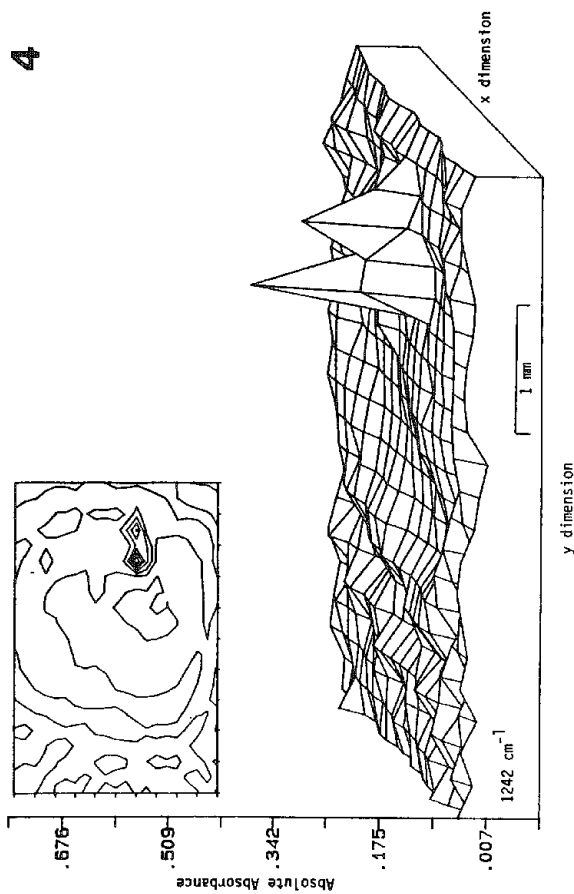


FIG. 3.--IR microprobe functional group image based on  $1735\text{cm}^{-1}$  absorption. Image is represented as axonometric and contour plot (insert). IR spectra corresponding to bulk material and carbonyl absorptions are also inserted.



FIGS. 4-7.--IR microprobe functional group images with contour plot corresponding to axonometric plot inserted. FIG. 4.--Based on 1241 $\text{cm}^{-1}$  absorption. FIG. 5.--Based on 1019 $\text{cm}^{-1}$  absorption. FIG. 6.--Based on 908 $\text{cm}^{-1}$  absorption (vinyl unsaturation linkages in polyethylene). FIG. 7.--Based on 1892 $\text{cm}^{-1}$  absorption (crystalline phase polyethylene band, which is combination of Raman active fundamental at 1168  $\text{cm}^{-1}$  and 730/720 $\text{cm}^{-1}$  IR  $\text{CH}_2$  rocking modes).

THE EFFECT OF METAL SUBSTRATES ON THE PHOTODEGRADATION OF POLYMER FILMS:  
A: FTIR STUDY OF Al-BACKED PVF, PAN, AND PET FILMS

D. M. Smith, W. F. Welch, S. M. Graham, and A. R. Chughtai

Polymer films are used to protect metallic surfaces from exposure to environmental degradation, but such polymer coatings are themselves subject to degradation. How low-cost substrates such as aluminum behave in contact with polymers like polyacrylonitrile (PAN), polyvinyl fluoride (PVF), and polyethylene terephthalate (PET) when exposed to UV radiation remains to be resolved before these polymers can be effectively utilized in solar-energy applications.

Photodegradation and photostabilization of silver-backed polymers (polyacrylonitrile, polycarbonate, and polyethylene terephthalate) have been carried out in this laboratory for the last several years. The effect of various substrates (Al, Cu, Ag, and Au) on the photodegradation of PAN has been recently investigated.<sup>1</sup> Fourier-transform infrared reflection-absorption (FTIR-RA) spectroscopy was found to be a useful nondestructive technique for obtaining information about interfacial reactions.

*FTIR Studies of Metalized and Nonmetalized Polymer Films*

Samples of aluminum-metalized and nonmetalized Tedlar PVF films (Du Pont), PAN film 0.007 in. thick supplied by Mobil Chemical Co., N. Y., and PET (American Hoechst Corp.) were employed for UV exposure.

Two separate techniques of exposure were employed in this photodegradation work. In one, the films were exposed to UV radiation with a Melles-Griot WG305 filter outside the FTS 14B. The spectra were collected by a technique developed in this laboratory,<sup>2</sup> for which no sample preparation is necessary. In the second technique, the exposure of the films was carried out under similar irradiation conditions within a reaction chamber built for the study of in situ reactions.<sup>3</sup> Here preparation of a sample is required, the technique for which is discussed elsewhere.<sup>1</sup>

Before placing the Al/poly film sample into the spectrometer, we mounted it in a reaction chamber that had been purged for several hours. FTIR spectra were collected before and after the exposure at Res = 4, NSS = 100, and ZFF = 2.

*Results and Interpretation*

*Photodegradation of Metalized and Nonmetalized Tedlar PVF Films.* Nonmetalized and Al-backed Tedlar PVF films were individually irradiated for 7 h through a WG305 filter; the subtraction spectra are shown in Fig. 1. For-

The authors are at the University of Denver, Denver, CO 80208. They wish to thank NSF for providing funds for the purchase of Digilab FTS systems (Grant MPS-7506209), for ATM-8300524, and the suppliers of the films.

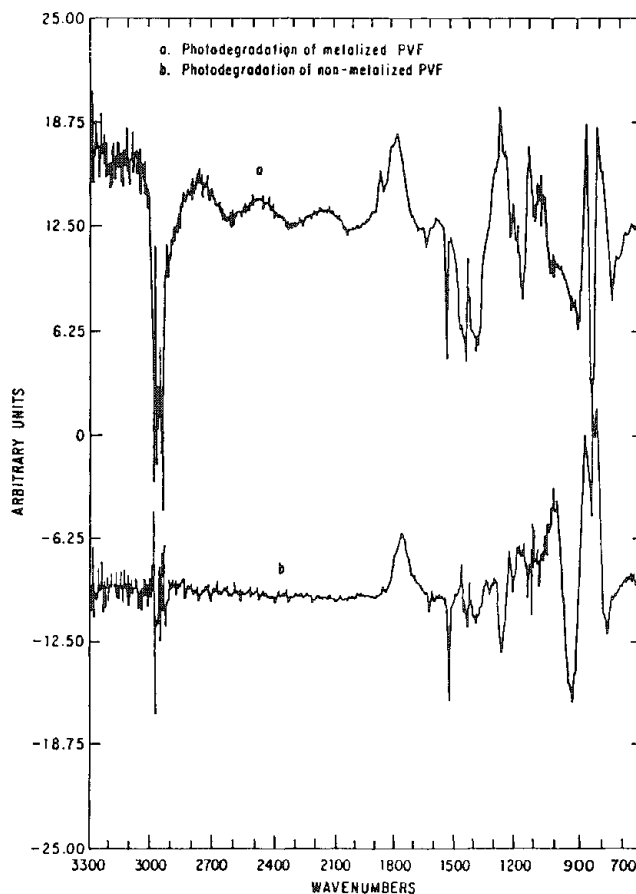


FIG. 1.--Subtraction spectra of exposed Al/PVF and PVF films from unexposed films.

mation bands at 1845, 1785, and 1750  $\text{cm}^{-1}$  are observed as a result of the UV exposure. Loss of band intensity was noticed at 1140, 890, 830, 768, and 720  $\text{cm}^{-1}$ . The three formation bands are due to either C=O or C=CHF functional groups. It is well documented<sup>4,5</sup> that fluorine atoms directly attached to a carbon double bond have the effect of shifting the C=C stretch to higher frequencies. For example, C=CH absorbs at 1690-1665  $\text{cm}^{-1}$ , and  $\text{CF}_2\text{-CF}$  absorbs at 1800-1665  $\text{cm}^{-1}$ . Also, the overtone of the C=C appears at 1850  $\text{cm}^{-1}$ , and C=O absorbs IR radiation around 1750  $\text{cm}^{-1}$ . The subtraction spectra of both metalized and nonmetalized films show a remarkable similarity except that in the case of metalized film, the extent of the photodegradation is almost doubled. Al backing enhances the photodegradation of PVF films.

*Photodegradation of Al/PAN Films.* In order to explore the effect further, another polymer, polyacrylonitrile, which has been the center of investigation in this laboratory for the past several years, was chosen. A set of PAN and Al/PAN samples were subjected to UV irradiation conducted under purge air (con-



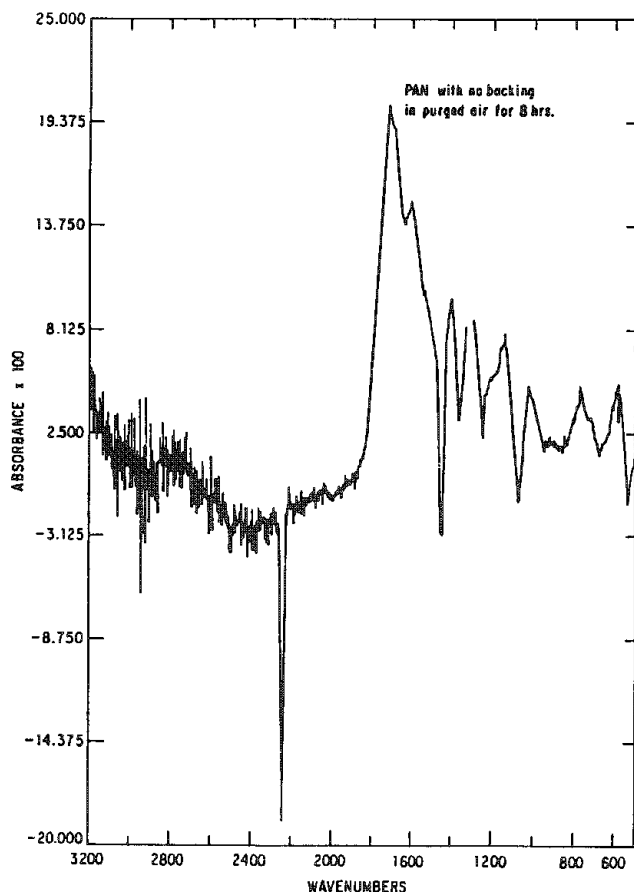


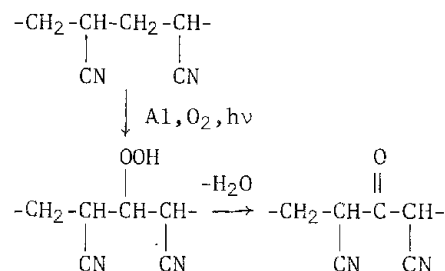
FIG. 2.--Subtraction spectrum of exposed unbacked PAN film.

trolled oxidative conditions; free of  $\text{CO}_2$  and  $\text{H}_2\text{O}$ ) in the controlled-environment chamber fitted in the FTS-14B spectrometer. Under purge air, the photodegradation of unbacked PAN film is more extensive than for the Al/PAN films and of a different nature (Fig. 2).

In the second set of PAN, Al/PAN films, the exposure was conducted under identical conditions. As seen from Fig. 3, the spectrum of the PAN film 0.007 in. thick with Al backing yields a very satisfactory subtraction spectrum. Observations of the photodegradation spectra for PAN, Al/PAN show that the Al-backed PAN film suffers less photodegradation than the nonmetalized PAN film. (Since the quartz retainer prevents external environmental contact, the system behaves as in a vacuum.)

A third set of PAN, Al/PAN samples was subjected to the same treatment, except that degradation was carried out under an atmosphere of  $\text{N}_2$ . The subtraction spectra of these films show photodegradation that is similar to (but not as great as) under oxidative condi-

tions. An explanation for such behavior in the photodegradation of Al/PAN films, under oxidative and nonoxidative conditions, where a carbonyl group is observed, is through the mechanism published earlier.<sup>6</sup>



*Photodegradation of Unbacked and Al/PET Films.* The subtraction spectra of the film after irradiation are shown in Fig. 4. It is obvious that the photodegradation of Al/PET film is similar to that observed with PVF, where Al substrate plays a role in the damage of the polymer coating employed for protection. The Al/PET film became brittle but no coloration was observed.

#### Conclusion

The photodegradation of a polymer must involve the functionalities of the polymer, the nature of the substrate metal, and environmental and UV exposure conditions. In this study, the most suitable polymer for the protection of aluminum surfaces is polyacrylonitrile (PAN); in decreasing order of degradation, Al/PVF  $\gg$  PVF  $\gg$  Al/PET  $\gg$  PET  $\gg$  Al/PAN  $\gg$  PAN.

This study is being extended to other commonly used substrates such as Cu, Ag, and Au.

#### References

1. W. F. Welch, S. M. Graham, A. R. Chughtai, D. M. Smith, and P. Schissel, *Applied Spectroscopy* (in press).
2. C. A. Sergides, A. R. Chughtai, and D. M. Smith, *Applied Spectroscopy* 41: 154-159, 1987.
3. J. D. Webb, P. Schissel, A. W. Czanderna, A. R. Chughtai, and D. M. Smith, *Applied Spectroscopy* 35: 6, 598, 1981.
4. G. Socrates, *Infrared Characteristic Group Frequencies*, New York: Wiley, 1980, 27, 107.
5. B. Ranby and J. F. Rabek, *Photodegradation, Photooxidation, and Photostabilization of Polymers*, New York: Wiley, 1975, 192.
6. C. A. Sergides, A. R. Chughtai, D. M. Smith, and P. Schissel, *Macromolecules* 19: 1448-1453, 1986.

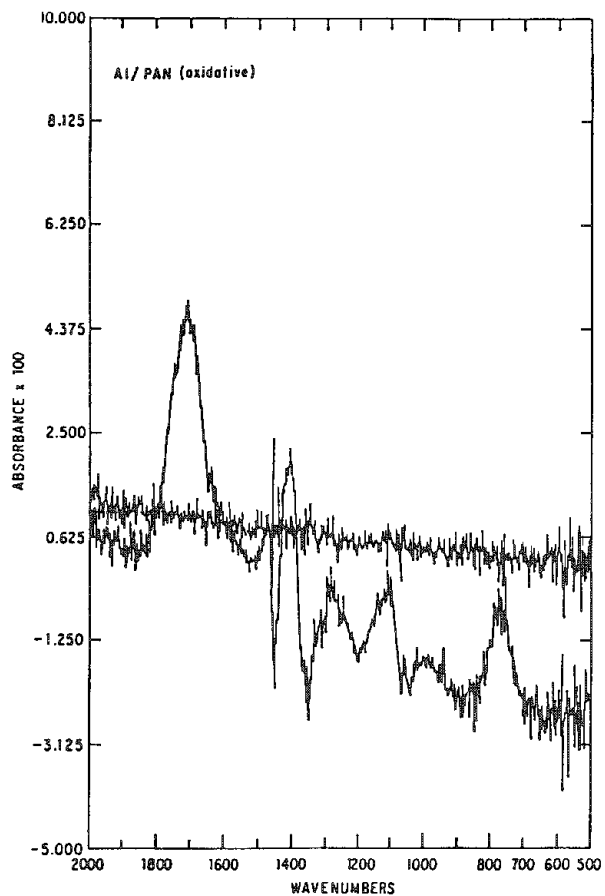


FIG. 3.--Subtraction spectrum of exposed Al/PAN film.

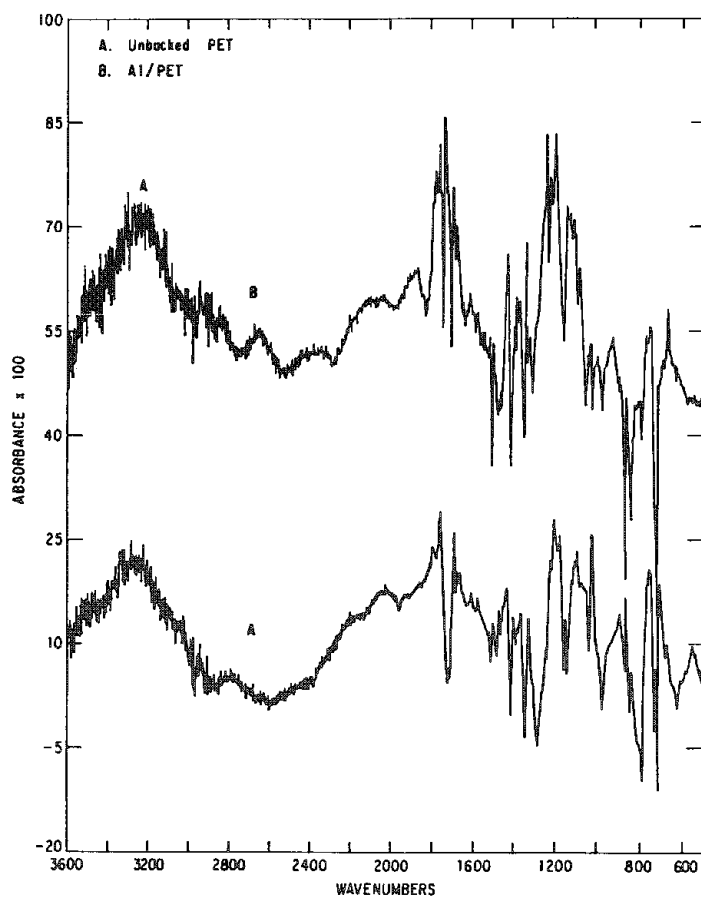


FIG. 4.--Subtraction spectra of exposed unbacked PET film and Al/PET film.

## INFRARED MICROBEAM ANALYSIS

J. A. Reffner, R. G. Messerschmidt, and J. P. Coates

Infrared microbeam analysis can be accomplished by the combination of light microscopy with Fourier transform infrared (FT-IR) spectroscopy. Infrared spectroscopy provides analytical information about the molecular structure; light microscopy is used to define the microscopic area of the sample being analyzed. The microscope for FT-IR microspectroscopy requires IR transmitting optics, variable field apertures, and an optical interface to couple it with the FT-IR spectrometer. One can record FT-IR spectra of a thin film of material, weighing a hundred picograms, by viewing the object and masking the area of the image entering the spectrometer. After reviewing the design of the IR-PLAN<sup>™</sup> microscope and the critical optical constraints of FT-IR microscopy, we demonstrate the microscope's performance for IR microbeam analysis by its analytical applications. Examples from the biological, chemical, forensic, geological materials and pharmaceutical sciences demonstrate this technology's wide range of applications.

For organic materials, IR microspectroscopy is emerging as the most universal technique for microbeam analysis. Of the many reasons for it, the four most important are (1) the advances in FT-IR spectroscopy, (2) the analytical power and extensive data base of IR spectroscopy, (3) the availability of a research microscope with refined reflecting optical systems for light and IR microscopy, and (4) the use of dual remote image plane apertures that minimize the sampling size while improving the photometric accuracy. As the electron beam is a universal reagent for elemental analysis, IR microspectrometry is for molecular microbeam analysis.

Because of the advantages of Fourier transform IR spectrometers, the past decade has seen tremendous advances in the speed, sensitivity and variety of analytical applications of IR spectroscopy. The great improvement in the signal quality and the increased optical throughput are major advantages of FT-IR spectrometry. When these FT-IR advantages were combined with the computer's ability to convert single-beam IR spectral data into background-corrected double-beam spectra, the uniting of IR spectroscopy with microscopy became practical. IR microbeam analysis now a viable analytical technology.

IR spectroscopy is used widely for both quantitative and qualitative analysis of molecular structures. Although the use of IR spectral analysis was reported in 1881, its applications to chemical analysis were not widespread until commercial IR spectrometers became available in the early 1940s.<sup>2</sup> The application of IR spectroscopy for qualitative analysis of organic compounds advanced rapidly with the discovery of the correlations between

absorption spectra and molecular structure.<sup>3</sup> Today this is a mature technology. Several large spectral libraries are available for on-line computer-based search-match analysis in addition to the classical functional group frequency analysis.

The advantages of uniting microscopy and IR spectroscopy were reported in 1949, but use of single-beam dispersive spectrometers for IR microspectrometry proved impractical. With the IR-PLAN<sup>™</sup> microscope coupled with a FT-IR spectrometer, high-quality IR spectra are obtainable from microscopic samples in a few minutes. This union opens a new dimension to IR spectral analysis: IR microbeam analysis.

### *Experimental*

Microbeam analysis implies the ability to analyze small sample volumes and to relate these analyses to the sample's morphological structure. FT-IR microspectrometry performs both functions; it provides a magnified visual image and unique information about the sample's molecular structure. Samples can be solids, liquids, or gases; and no vacuum environment is required for its operation. The IR-PLAN<sup>™</sup> combines coaxial visual light and IR beam paths. The sample is imaged through a 15×, 32×, or 100× reflecting objective, and it is transilluminated by a 0.71 N.A. reflecting condenser. These Schwarzschild-type lenses are totally reflecting optics, transmitting visual and IR radiation without chromatic aberration. The primary image is further magnified by glass refracting lenses for visual light examination. The IR measuring beam is focused on the sample by the objective. When spectra are measured, the condenser lens is the collector and transfers the radiation into the IR spectrometer. When reflection spectra are measured, the objective images the IR beam on the sample and collects the radiation, transferring it to the spectrometer. The visual image records the sample's morphology.

The area selected for spectral analysis is defined by two apertures, one in the primary image plane and the second in the condenser field stop. This combination of apertures, Redundant Aperturing<sup>™</sup>, defines the area that is illuminated and limits the radiation passed to the spectrometer to the selected area. Variable slit apertures are used for most analyses. Figure 1 shows a sample of a nonwoven, print-bonded textile material. Figure 2 shows an area of adhesive masked off to represent the sampling area for spectral analysis. The spectrum of this adhesive is shown in Fig. 3.

At present the practical limit of spatial resolution is about 10  $\mu\text{m}$ . Better stated, an area of 100  $\mu\text{m}^2$  is needed to obtain enough signal for IR spectral analysis. Although

The authors are at Spectra-Tech, Inc., Stamford, CT 06906.

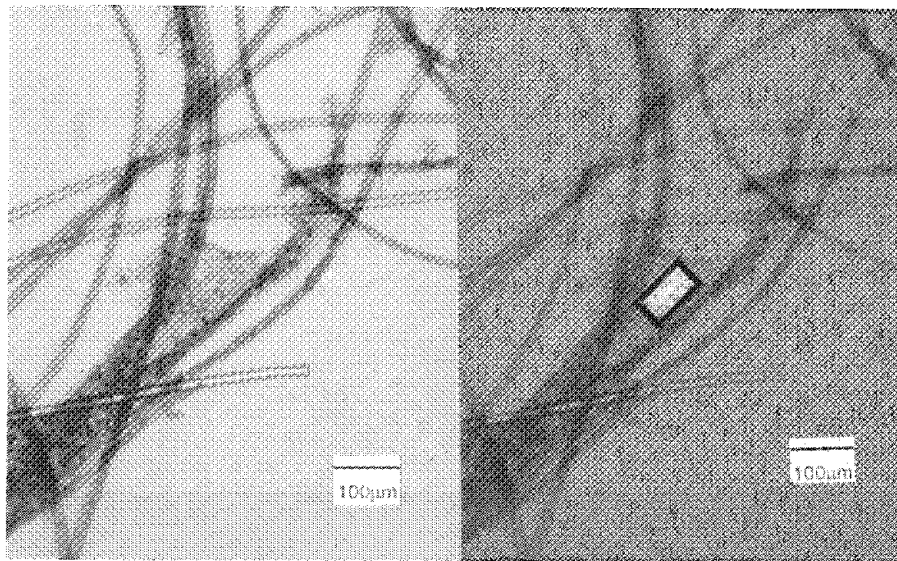


FIG. 1.--Light micrograph of fibers and adhesive from print-bonded nonwoven textile.

FIG. 2.--Same sample as shown in Fig. 1 with shaded area representing masked-off field; unshaded area is sample selected for spectral analysis.

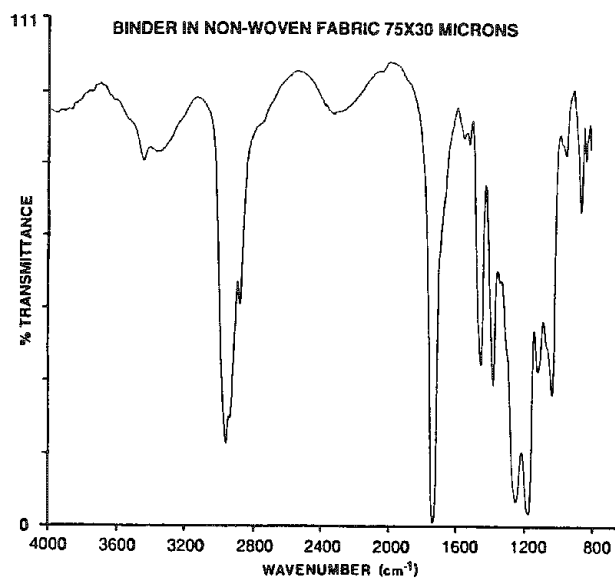


FIG. 3.--Infrared absorption spectrum of adhesive from nonwoven textile.

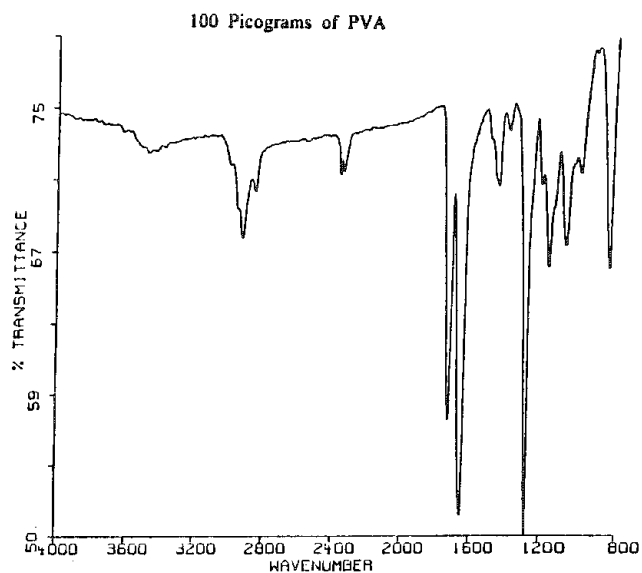


FIG. 5.--IR spectrum obtained from a 0.1µm-thick film of vinyl acetate polymer with sampling area of 1000µm².

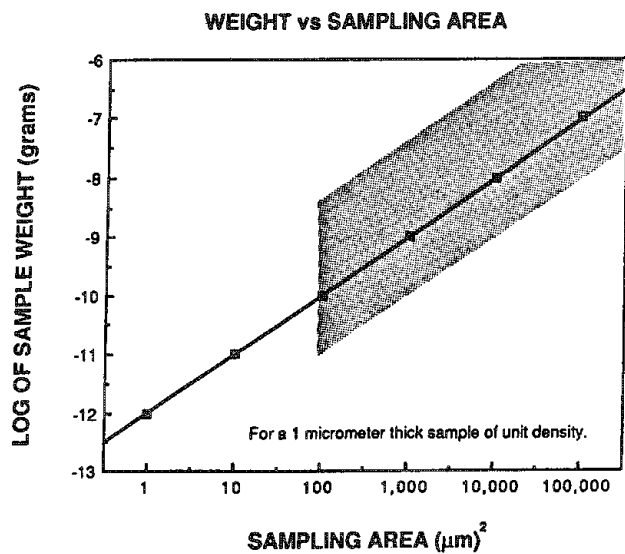


FIG. 4.--Relationship between sample weight and sampling area for 1µm-thick sample of unit density. Shaded area is practical operating range for FT-IR microspectrometry.

this resolution is low by analytical electron microscopy standards, the spectral information provides unique analytical data on systems that cannot be studied by electron microscopy. Polymeric laminates and bicomponent fibers are two examples of complex organic systems directly analyzed by IR microspectrometry.

What is the detection limit of IR spectrometry on a weight basis? That is not easily defined since the detection limit is sample dependent. Figure 4 shows the relationship of sample weight to sample area for a 1 $\mu$ m-thick, unit-density material. The shaded area represents a practical operating range for organic materials with current IR microspectrometry instrumentation in the mid-IR region. Shown in Fig. 5 is the spectrum of a 0.1 $\mu$ m-thick film of a vinyl acetate polymer from a 1000 $\mu$ m<sup>2</sup> area, collected in less than 5 min. There are only 100 pg of polymer in this sampling volume. Since this polymer film extends beyond the boundaries of the remote apertures, diffraction effects would be expected to increase the area of this sample exposed to the IR beam. However, this spectrum clearly demonstrates the subnanogram detection capabilities of IR microspectrometry.

#### Applications

The applications of IR microspectrometry are only emerging, but they appear to extend throughout the chemical, materials, and biological sciences. Only two specific examples are presented here, both analyses of polymeric materials.

*Fiber Analysis.* With FT-IR microspectrometry, the identification of fibers and the measurement of their fundamental spectroscopic parameters is a routine operation. The advantage of IR microbeam analysis is exemplified by the analysis of bicomponent fibers. Bicomponent fibers are formed when two polymeric formulations are extruded simultaneously through the same jet or spinneret orifice. These fibers may consist of two formulations of the same polymer or two different polymer systems. Basically, bicomponent fibers have a laminated structure that can be resolved and analyzed directly by IR microbeam analysis. Figure 6 is a micrograph of Orlon® 21, a bicomponent acrylic fiber. This bilobal fiber has minor differences in the pigment loading and refractive index of each lobe, which suggests that there are composition differences. Morphology and optical properties can distinguish this fiber from other acrylic fibers, but microscopy alone cannot identify the different polymers in this bicomponent fiber. The infrared spectrum of each lobe is presented in Figs. 7 and 8. The sharp band at 2230 cm<sup>-1</sup>, the "fingerprint" regions of these spectra, reveal the minor different polymer composition of each lobe.

The conventional IR techniques for fiber identification<sup>4</sup> cannot detect the microstructural form of a bicomponent fiber. Grinding fibers to form KBr pellets, dissolving fibers and casting films from the solution, or IR reflection techniques destroy the fiber's microstructure. Only when microscopy is combined with spectroscopy can a complete analysis be

made.

*Polymeric Laminates.* Polymeric laminated structures are found in both "high-tech" modern photographic materials and the lowly trash bag, an indication of the increased use that plastic laminates are finding in today's world. Analysis and quality control of these laminates dictates the need to insure that the correct layers are present in the proper sequence and that there are no defects or contaminants. Modern laminates can have several layers, and adhesives are often used to bond the layers together. Chemical separation or physically peeling layers can be complex, incomplete, and impractical. FT-IR microspectrometry provides a direct solution to this analytical problem. After the preparation of laminate cross sections by conventional microtomy, the IR spectral analysis of each layer becomes trivial with the IR-PLAN<sup>™</sup> interfaced to an FT-IR spectrometer. Each layer's infrared spectrum is recorded after it is optically isolated with the microscope's variable apertures. This procedure reduces an intractable analytical separations problem into a simple, direct examination.

Figure 9 is a micrograph of a laminate cross section showing a three-layered, adhesively bonded laminate, which provides five definable layers. Figure 10 shows the IR spectra of each layer of this laminate, polymers and adhesive, obtained directly with the IR-PLAN<sup>™</sup>. These spectra show that each phase was completely isolated "spectroscopically Pure" by the Redunadant Aperturing<sup>™</sup> system (dual remote apertures). Even the spectra of the adhesive layers, which in this case were found to be the same material in both layers (an EVA, and ethylene-vinyl acetate copolymer), were isolated and recorded.

#### Conclusion

FT-IR microspectroscopy has been demonstrated to be a viable microbeam analytical technique. It is possible to isolate optically microscopic areas within complex morphological structures by remote focal plane aperturing, and to perform spectrochemical analysis of the material in these areas by FT-IR spectroscopy. Because IR spectroscopy provides information about the molecular structure, IR microspectrometry is a valuable addition to microbeam analysis.

#### References

1. W. de W. Abney and E. R. Gesting, *Phil. Trans.* 172A: 887, 1881.
2. R. B. Barnes, R. W. Gore, R. W. Stafford, and V. Z. Williams, *Anal. Chem.* 20: 402, 1948.
3. N. B. Colthup, L. H. Daly, and S. E. Wiberly, *Introduction to Infrared and Raman Spectroscopy*, New York: Academic Press, 1975, 2d ed.
4. R. J. Berni and N. M. Morris, in J. W. Weaver, Ed., *Analytical Methods for a Textile Laboratory*, Research Triangle Park, N.C.: AATCC, 1984, 3d ed.

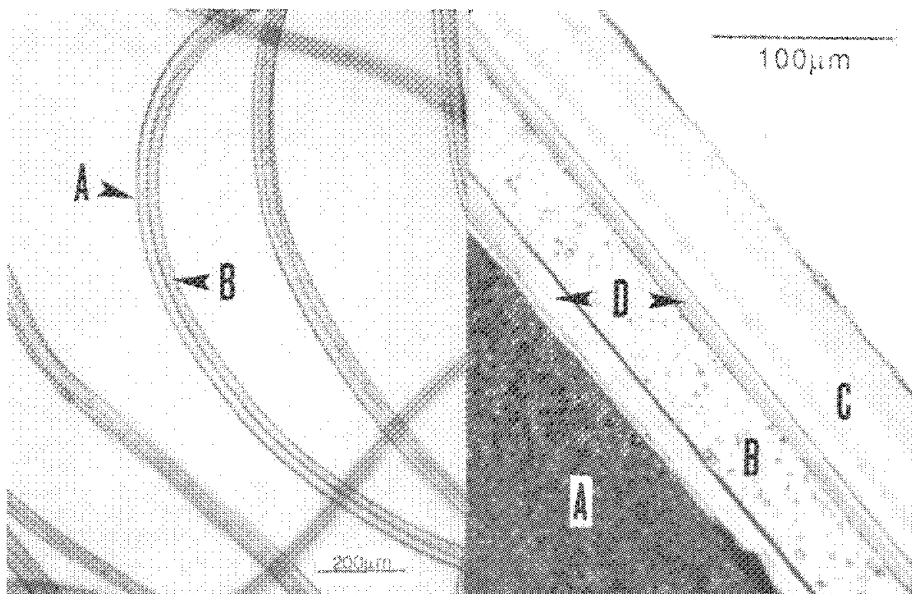


FIG. 6.--Light micrograph of fibers of Orlon® 21, a bicomponent acrylic fiber.

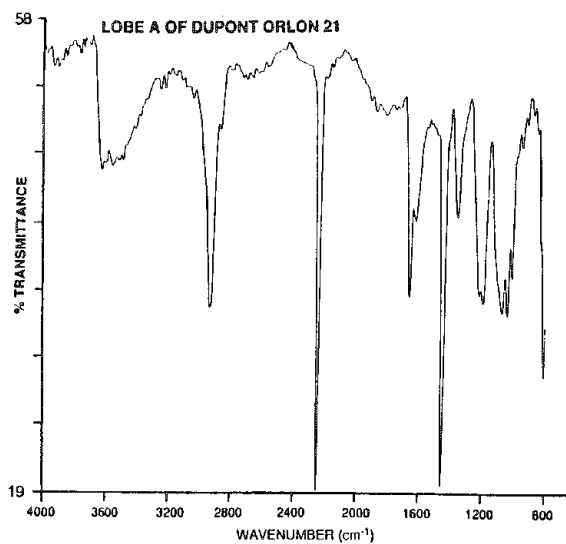


FIG. 7.--IR spectrum of lobe A of bicomponent fiber shown in Fig. 6.

FIG. 9.--Light micrograph of thin cross section of multilayered plastic laminate. Layer A is polystyrene; B, polyvinylidene; C, polyethylene; D, ethylvinylacetate.

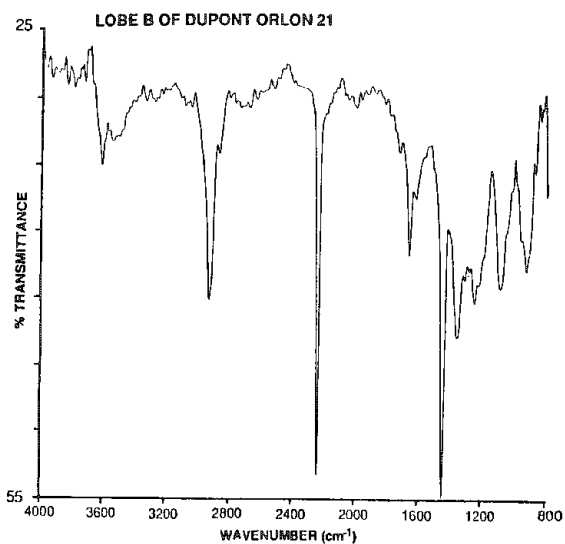


FIG. 8.--IR spectrum of lobe B of bicomponent fiber shown in Fig. 6.

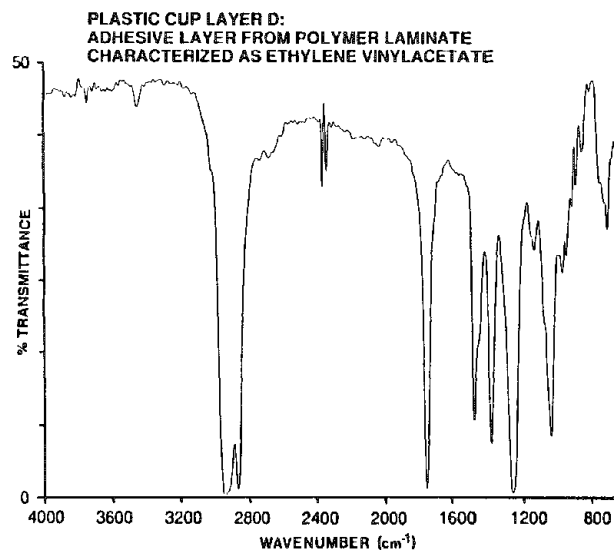
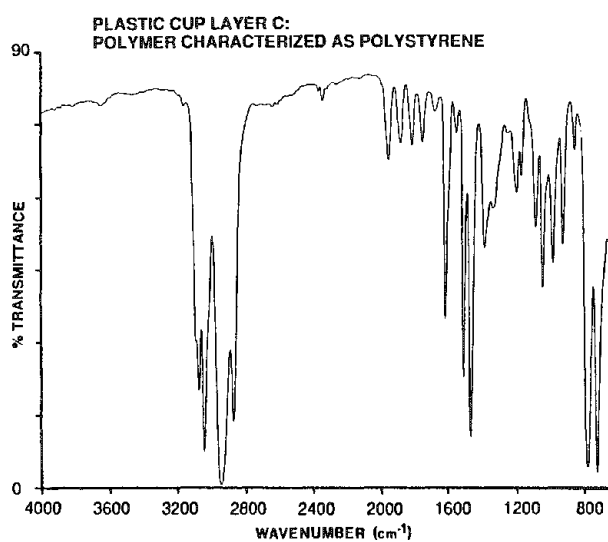
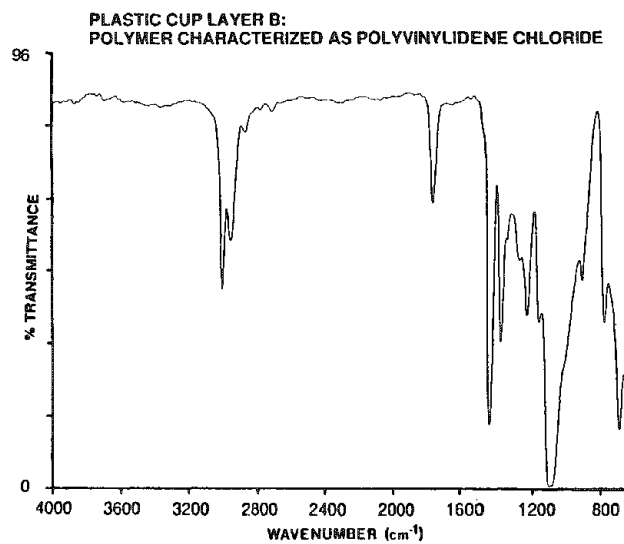
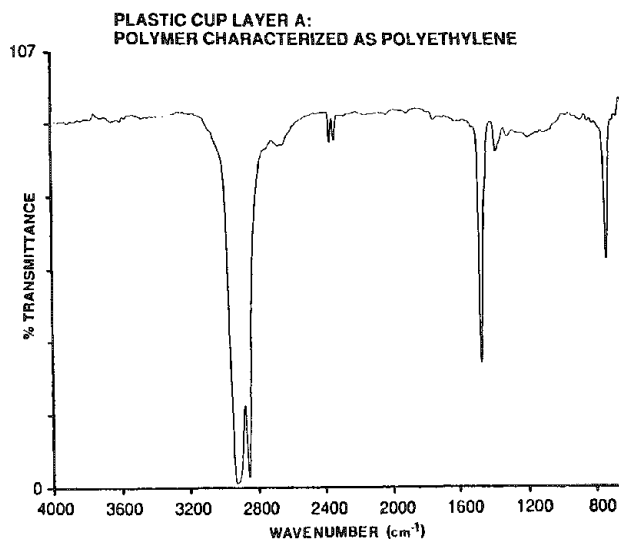


FIG. 10.--Infrared spectra of four polymers found in the laminate of Fig. 9.

## APPLICATIONS OF FTIR MICROSCOPY IN POLYMER ANALYSIS

J. P. Beauchaine and R. J. Rosenthal

Infrared spectroscopy is a common method of polymer analysis. Typically, bulk or surface properties are determined by transmission or reflectance techniques. Often more detailed information is desired, such as the nature of small imperfections ("fish-eyes"), the composition of laminates, or the bonding at interfaces. Traditional methods of infrared analysis are incapable of providing this type of data.

The combination of Fourier transform infrared (FTIR) spectroscopy and microscopy now permits the investigator to obtain this type of information routinely. A most important part of this technique is that many of the attributes of visible microscopy can be employed. Investigators have polarization and aperturing techniques at their disposal to define the area of investigation precisely. Permanent records via micrographs are possible. Scientists are no longer limited to confirming a defect or layer only visually, but can provide identification spectrally.

### Experimental

A Nicolet 5SXC FTIR interfaced to a Nicolet IR Plan microscope was employed in these investigations. The microscope was equipped with a high-sensitivity MCT detector. Each measurement typically consisted of a 1 min scan at 6 wavenumber resolution. The unique redundant aperture system was used in all cases. Typically, the polymer film was microtomed and mounted on a potassium bromide window. This sample was then placed onto the microscopic stage. Library search results were obtained by search of the 2000-element Nicolet Hummel Polymer Library.

### Discussion

In laminates, properties such as permeability, strength, chemical resistance, and light transmission of a polymer can be controlled by proper choice of component layers. The primary interest here is the composition of a complex, three-layer laminate. The microtomed film was examined under crosspolarized light as an aid to distinguishing the boundary areas. Aperturing each layer in succession provided the spectra in Figs. 1-3. The best library search result is shown on the top portion of Figs. 4-6. Two of the layers were positively identified.

Figure 7 shows the spectral overtone features of the outer polymer layer from 6000 to 700  $\text{cm}^{-1}$ .

The 30-micron layer polymer spectrum (Fig. 2) suggests that this material is a combination of two or more compounds. By search of the spectra outside of the CH stretch and

CH bend regions, the best match from the Nicolet/Hummel library is shown to be disodium hydrogen phosphate,  $\text{Na}_2\text{HPO}_4$  (Fig. 5).

The free hydroxyl band at 3642  $\text{cm}^{-1}$  suggests that when disodium hydrogen phosphate is in low concentration and surrounded by a matrix of polypropylene, there is essentially no hydrogen bonding.

Figure 8 shows the best five search results for the 30  $\mu\text{m}$  layer. Layers as thin as 8  $\mu\text{m}$  can be measured and identified, well below what many have thought possible.

### Conclusion

The infrared microscope shows itself to be a valuable tool in polymer analysis. The scientist can provide information on many aspects of polymer design and fabrication. This development represents a major innovation in problem solving.

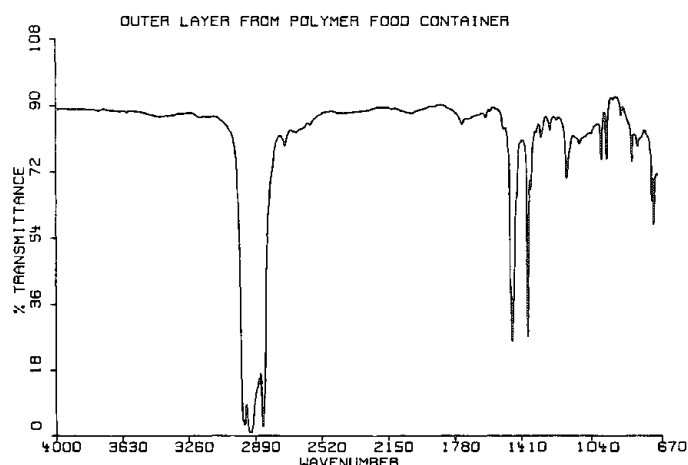


FIG. 1.--Outer layer of multilayer polymer.

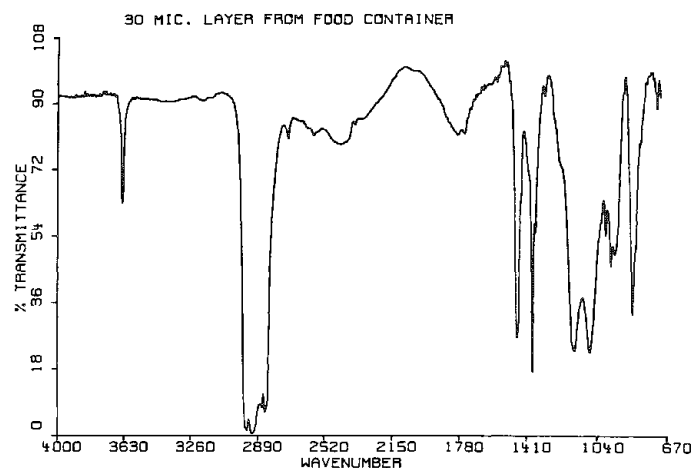


FIG. 2.--30  $\mu\text{m}$  layer.

The authors are located at Nicolet Spectroscopy Research Center, 5225-1 Verona Rd., Madison, WI 53711. (Inquiries to R. J. R.)



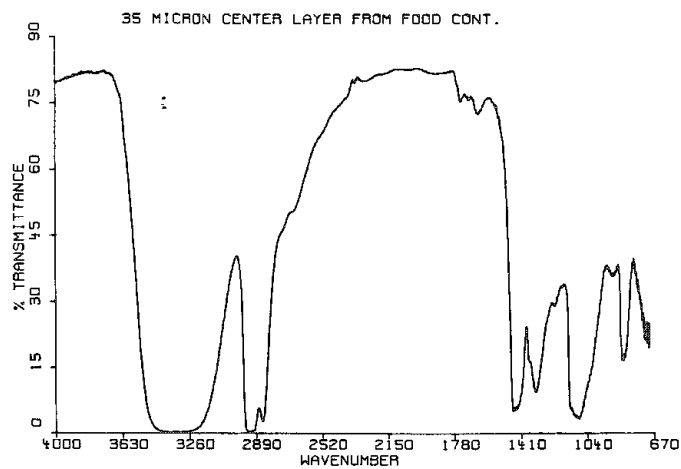


FIG. 3.--35 $\mu$ m center layer.

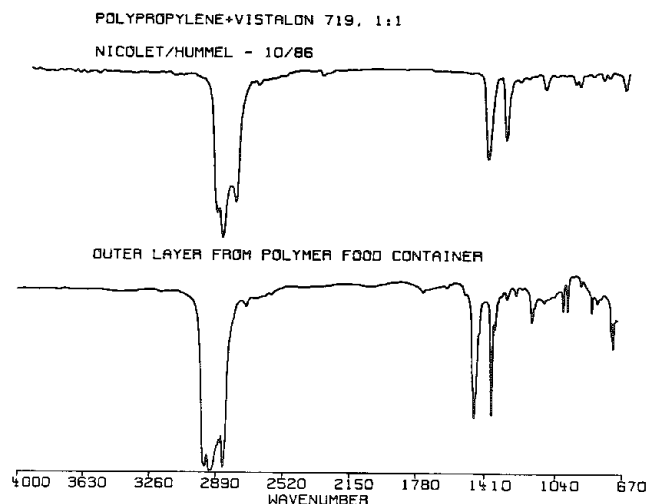


FIG. 4.--Search result of outer layer.

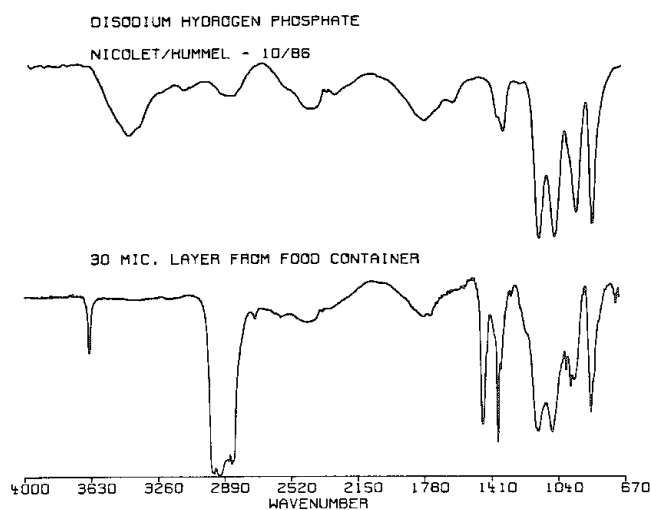


FIG. 5.--Search result for 30 $\mu$ m layer.

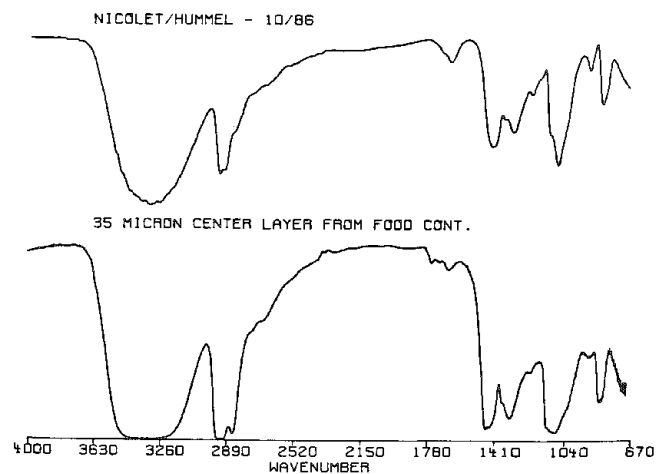


FIG. 6.--Search result for 35 $\mu$ m layer.

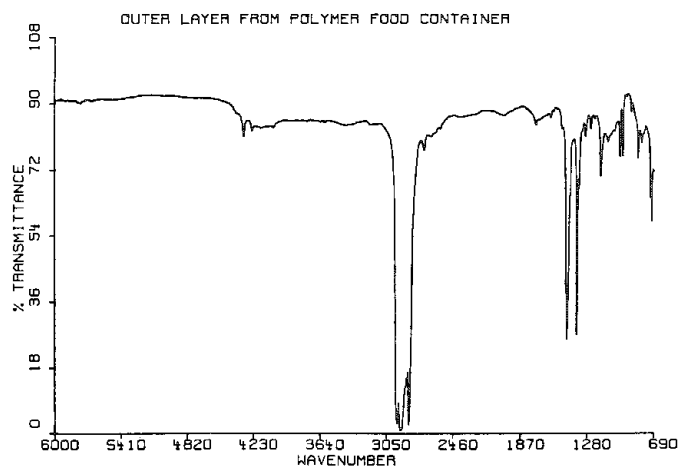


FIG. 7.--6000 to 700  $\text{cm}^{-1}$  spectra of outer layer.

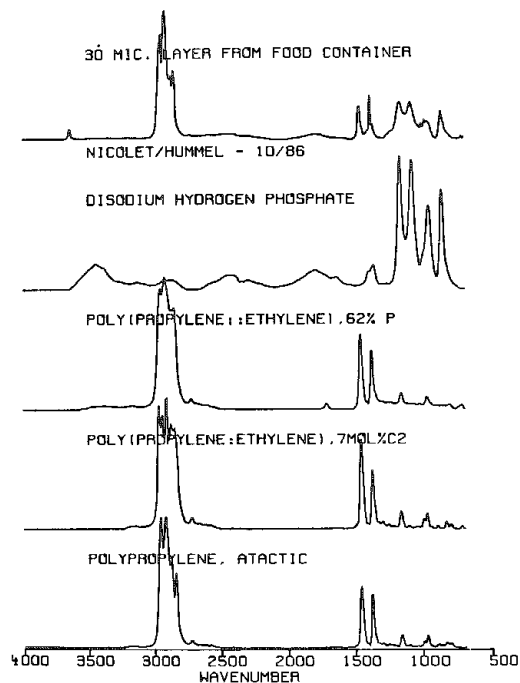


FIG. 8.--Five best search results for 30 $\mu$ m layer.

## APPLICATIONS OF FTIR MICROSCOPY IN FORENSIC ANALYSIS

J. P. Beauchaine, K. D. Kempfert, M. P. Fuller, and R. J. Rosenthal

Forensic analysis is an area of challenge and importance.<sup>1</sup> The analysis of small, often minute samples taxes scientist and instrumentation alike. Materials collected from crime scenes nearly always require special handling. The forensic scientist must provide identifications and evaluations based on spectroscopic methods that will be upheld in courts of law.<sup>2</sup>

Confirmation of the identity or genesis of a powder, liquid, fiber, or chip of paint is required which is nondestructive. The analysis of such materials by infrared spectroscopy provides a unique signature for a given sample.<sup>3</sup> Such spectra can be searched against a database and matched to known reference spectra. Powdered materials are particularly difficult. Ordinarily, a sample would be mixed in a diluent of KBr or mullied in Nujol for infrared analysis. Adequate data could be obtained, but valuable evidence would be lost in the sampling process. Fourier transform infrared (FTIR) spectrometers, with their signal-averaging capability combined with the sampling capabilities of an infrared microscope, permit investigations of these types of samples.

Optical microscopes have been employed for some time in the assessment of materials such as fibers, bullets, and paints. Advantage can be taken of polarization and other enhancements in distinguishing among different components of a powdered mixture or a complex substance. Microscopy provides permanent records in the form of micrographs.

### *Experimental*

A Nicolet 5SXC FTIR interfaced to a Nicolet IR Plan microscope was employed in these investigations. The microscope was equipped with a high-sensitivity MCT detector. Each measurement typically consisted of sixty-four co-added scans at four-wavenumber resolution. The unique redundant-aperture system was used in all cases. Typically, the unknown powder was spread onto an infrared transparent window of potassium bromide and this assembly was mounted on the microscope. No further sample preparation was required.

### *Discussion*

The combination of a visible microscope and infrared microscope allows the forensic scientist to provide positive identifications on amounts of material as small as a single crystal. This feature is noteworthy as most illicit street drugs are not pure substances. The optical characteristics of the microscope and polarization techniques are used for quick

and accurate identification of various crystalline forms.

After components of a mixture have been visually examined, the aperturing system can be used to obtain an infrared spectrum of each constituent, a procedure that obviates time-intensive physical separation. The spectrum presented in Fig. 1 is that of a street sample of a white powder. Under normal illumination the sample appears homogeneous. Under polarized conditions the several components readily become apparent. Figure 2 shows the spectrum of the diluent or cutting agent, inositol, obtained from a single crystal. The library search data are shown in Fig. 3. The other visually identified component, whose spectrum is shown in Fig. 4, is the illicit street drug cocaine. The library search data are shown in Fig. 5. The drug was identified by comparison to the database reference spectrum. Again, database searching provides positive identification. A particularly important aspect of the preceding argument is that single crystals of materials are often too thick in the infrared and result in totally absorbing absorption bands, which unfortunately renders large portions of the data useless. The infrared microscope aperture system can be used to define edge areas (thinner portions) of a crystal for investigation and thus affords excellent data. This technique also requires limited sample preparation.

In another case, a powdery residue was presented for analysis. There was insufficient sample for most forms of infrared identification. IR microscopy permitted the positive identification of a single  $20 \times 15 \mu\text{m}$  speck (Fig. 6) as PCP-hydrochloride [1-(1-phenylcyclohexyl)piperidine]. This type of sample, a salt, can be troublesome when analyzed by traditional techniques. This is a very critical aspect in conventional analysis of typical street drugs: the salt form is identified, followed by extraction of the sample to separate excipient and drug, which irreversibly changes the sample. The technique employed here allows the drug and diluents in their original form to be identified in a nondestructive manner.

### *Conclusion*

The ease of use and the high quality of data obtained recommend this method for routine use in the forensic laboratory. The infrared microscope lessens sample handling, both in preparation and analysis time. The excellent quality of data and the identification possible with the FTIR-microscope combination are significant attributes.

### *References*

The authors are at Nicolet Spectroscopy Research Center, 5225-I Verona Rd., Madison, WI 53711. (Inquiries to R. J. R.)

1. S. M. Gerber, Ed., *Chemistry and Crime*, American Chemical Society, 1983.

2. Geoffrey Davies, Ed., *Forensic Science*, American Chemical Society, 1975.

3. W. R. Lowry and R. J. Rosenthal, "Ef-

fects of sampling methodologies on FTIR database searching," *Mikrochimica Acta* (in press).

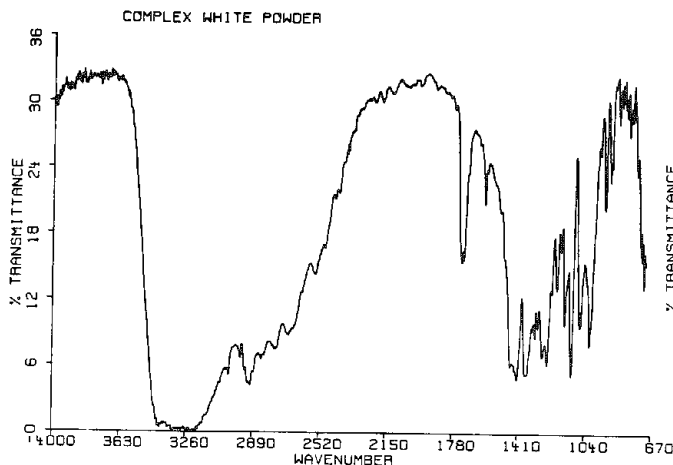


FIG. 1.--Spectrum of complex white powder.

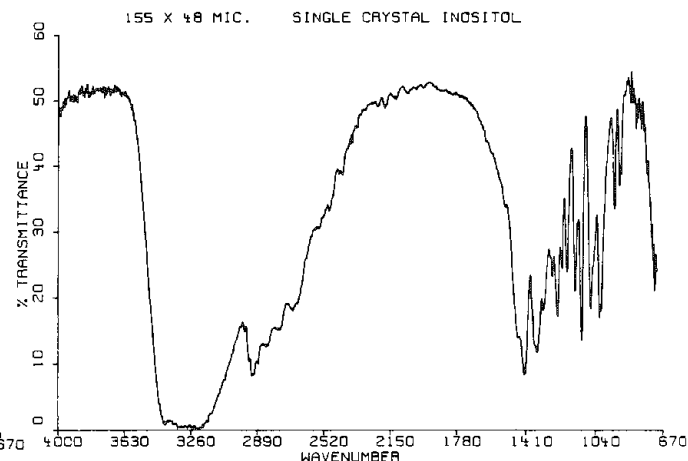


FIG. 2.--Spectrum obtained from single crystal of diluent (Inositol).

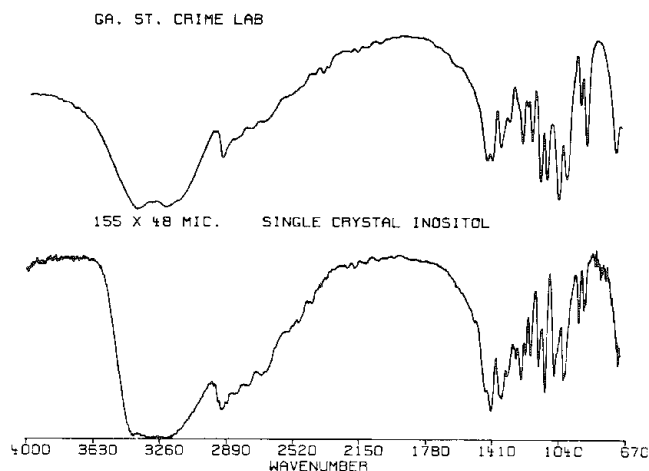


FIG. 3.--Library search result obtained from spectrum in Fig. 2. Top spectrum is best search result from Nicolet-Georgia State Forensic Library.

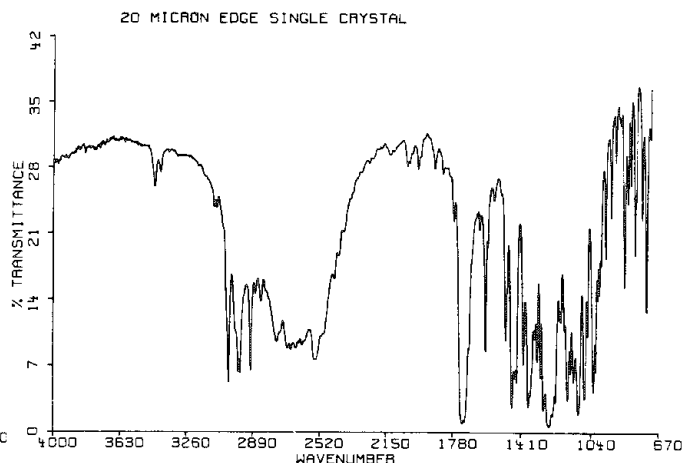


FIG. 4.--Spectrum obtained from single crystal of drug sample (cocaine).

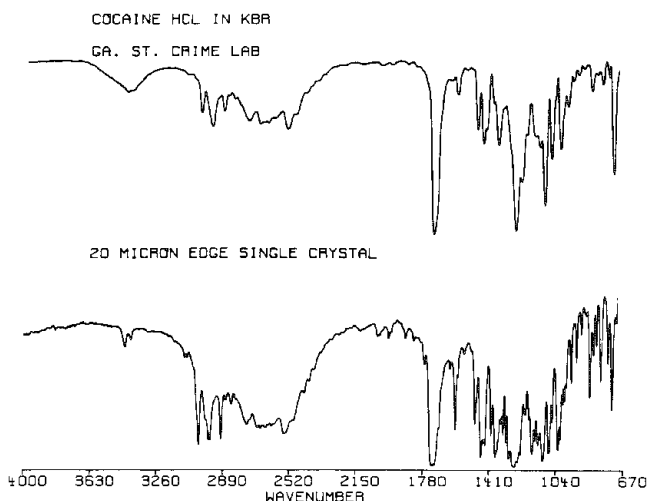


FIG. 5.--Library search result obtained from spectrum in Fig. 4. Top spectrum is best search from Nicolet-Georgia State Forensics Library.

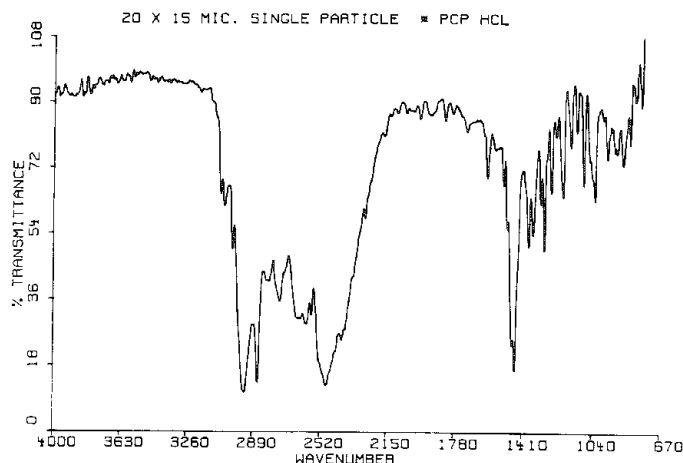


FIG. 6.--PCP-hydrochloride spectrum, measured from single  $20 \times 15\mu\text{m}$  particle.

## RAMAN MICROPROBE AND FOURIER TRANSFORM-INFRARED MICROSAMPLING STUDIES OF THE MICROSTRUCTURE OF GALLSTONES: II. CALCIUM PHOSPHATE STONE AND FATTY ACID CALCIUM-SALT STONE

H. Ishida, Y. Ozaki, R. Kamoto, A. Ishitani, K. Iriyama, I. Takagi,  
E. Tsukie, K. Shibata, F. Ishihara, and H. Kameda

The mechanism of gallstone formation is not always fully understood, although the classification of gallstones has been fairly well established.<sup>1</sup> Gallstones often consist of many components and show complicated microstructure resulting from their formation history. Identification of the constituents of a gallstone is very important for understanding of the mechanism of gallstone formation. Various physico-chemical techniques such as gas chromatography, x-ray diffraction, and IR spectroscopy have been extensively applied for the analysis of gallstone structure. Those techniques have individual advantages, but none of them is perfect for the above purpose. We have recently introduced the Raman microprobe method for the studies of microstructure of gallstones,<sup>2</sup> and Zheng and Tu<sup>3</sup> have studied a bilirubin type gallstone by using a conventional Raman spectrometer. Raman spectroscopy has the following advantages for gallstone research (i) it is a nondestructive analytical tool; (ii) it provides structural information; (iii) sample preparation is very easy. Besides these advantages, the Raman microprobe technique is potentially capable of the simultaneous determination of chemical identification and distribution of gallstone constituents.

In our previous study three kinds of gallstones (a typical cholesterol gallstone, a pigment gallstone, and a mixed stone belonging to a subgroup of cholesterol gallstone) were investigated by laser Raman microprobe and Fourier transform-infrared (FT-IR) spectroscopy combined with a microsampling technique. It was demonstrated that the combination of the Raman microprobe and FT-IR spectroscopy furnishes a detailed picture of the microstructure of gallstones. In the present investigation we have expanded our Raman microprobe and FT-IR microsampling study to a calcium phosphate stone and a fatty acid calcium-salt stone. The observed Raman and IR spectra have revealed that the calcium phosphate stone is composed of  $\alpha$ - $\text{Ca}_3(\text{PO}_4)_2$  and the fatty acid calcium stone includes at least two kinds of fatty acid salts, bilirubin, and very small amounts of cholesterol.

### Experimental

The gallstones investigated in the present study were obtained from human patients at the Jikei University Hospital.

The apparatus used for Raman microprobe analysis of gallstones is a MOLE (Instruments S.A. Division of Jobin-Yvon). The excitation

wavelength employed was 514.5 nm from a Coherent CR-3 Ar laser. All Raman microprobe measurements were carried out under dry nitrogen flow with the laser power less than a few milliwatts at the samples. The spot diameter of the laser beam was a few microns. The IR spectra were recorded by a Bruker IFS-85 FT-IR spectrometer equipped with an IR microscope.

### Results and Discussion

The calcium phosphate stone showed a yellowish white color and consisted of a central part and an outer layer. The FT-IR spectra were measured for trace amounts of samples scraped by the microsampling technique from several small areas of the central part and the outer layer. The observed spectra were almost identical to each other and in good agreement with that of calcium phosphate,<sup>4</sup> which suggests that the stone belonged to the pure calcium phosphate type.

Raman spectroscopy can distinguish clearly between two types of crystalline calcium phosphate,  $\alpha$ - $\text{Ca}_3(\text{PO}_4)_2$  and  $\beta$ - $\text{Ca}_3(\text{PO}_4)_2$ ; the former shows a single intense band at  $968\text{ cm}^{-1}$  due to a PO symmetric stretching mode, and the latter gives rise to an intense doublet at 971 and  $948\text{ cm}^{-1}$  due to the same mode.<sup>4</sup> Figure 1 shows the Raman spectrum measured in situ of the outer layer of the calcium phosphate stone. A Raman spectrum was also obtained for the central part (not shown). Both spectra exhibited an intense band at  $965\text{ cm}^{-1}$  characteristic of  $\alpha$ - $\text{Ca}_3(\text{PO}_4)_2$ , which shows that crystalline calcium phosphate included in the stone is  $\alpha$ -type. Biological calcium phosphate often incorporates carbonate. However, the recorded spectra did not exhibit the characteristic bands of carbonate,<sup>5,6</sup> which suggests that the stone is composed of a nearly pure phase of  $\alpha$ - $\text{Ca}_3(\text{PO}_4)_2$ .

The fatty acid calcium-salt stone showed very complicated fine structure. IR and Raman spectra were measured for five small areas: area a, white lump; area b, large white crystal; area c, white crystal; area d, brown-colored area; area d-1, small white particle included in area d. Figure 2 compares the IR spectra of area a and area b. The spectrum of area b is in good agreement with that of calcium palmitate reported by Henichart et al.<sup>7</sup> Its vibrational assignment is as follows: two sharp peaks at  $2920$  and  $2850\text{ cm}^{-1}$ , anti-symmetric and symmetric stretching modes of methylene group; two intense bands at  $1580$  and  $1542\text{ cm}^{-1}$ , asymmetric stretching mode of calcium carboxylate; an intermediate band at  $1472\text{ cm}^{-1}$ , bending mode characteristic of a long methylene chain; two weak bands at  $1440$  and  $1425\text{ cm}^{-1}$ , symmetric stretching modes of calcium carboxylate. The IR spectra of area c and d-1 are also in good agreement with that

Authors Ishida, Kamoto, and Ishitani are at Toray Research Center, Inc., Otsu, Shiga 520, Japan; the others are at the Jikei University School of Medicine, Minato-ku, Tokyo 105, Japan.

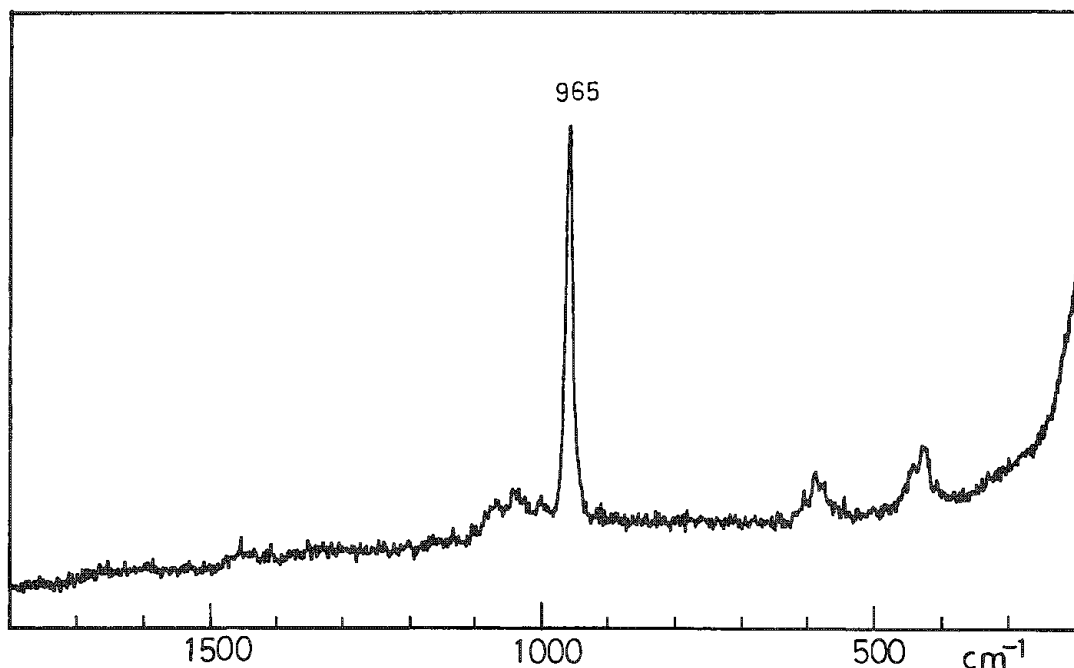


FIG. 1.--Raman spectrum of outer layer of calcium phosphate stone measured by laser Raman microprobe.

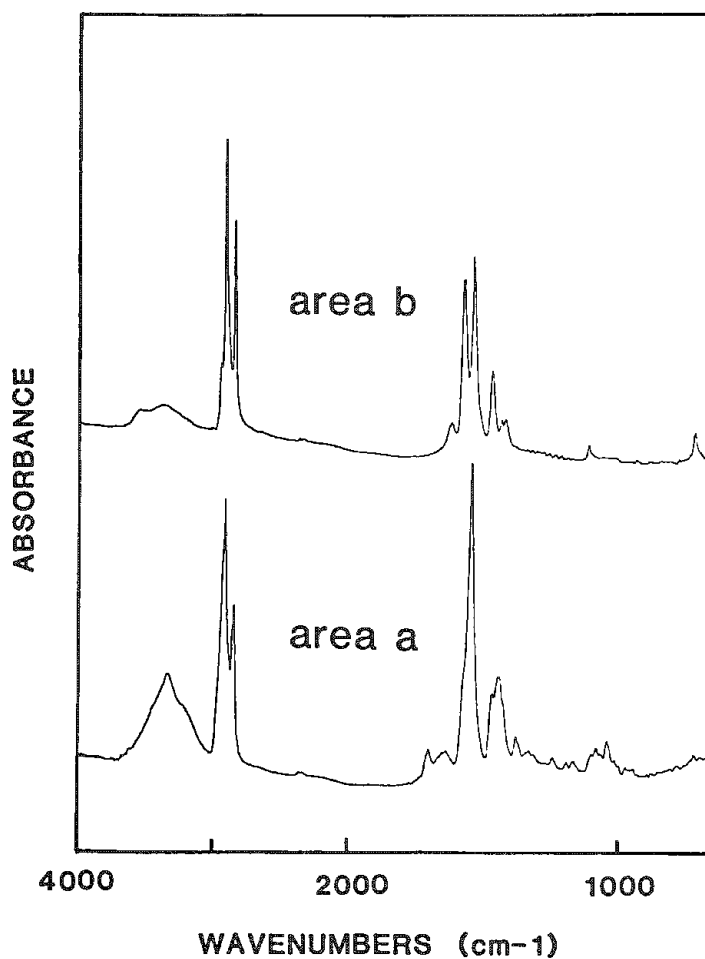


FIG. 2.--Infrared spectra of areas a and b of fatty acid calcium stone obtained by FT-IR microscope.

of calcium palmitate. Therefore, it can be concluded that the stone includes large amounts of calcium palmitate. The IR spectrum of area a is somewhat different from that of area b (Fig. 2), although the former also has characteristics of metal salt of a fatty acid. This observation reveals that the stone contains not only calcium palmitate but also other metal salt of a fatty acid. The identification of the metal salt is now under investigation.

Laser Raman microprobe measurement has provided further information about area c. Figure 3 shows the Raman spectrum measured in situ of a white transparent crystal included in area c. The size of the crystal was ca 10  $\mu\text{m}$ . The spectrum in Figure 3 is very similar to that of cholesterol reported by Zheng and Tu,<sup>3</sup> which suggests that the crystal is composed of cholesterol.

The IR spectrum of area d has an appearance typical of a bilirubin spectrum (not shown)<sup>2,3,7</sup> observed bands at 3410 and 1705  $\text{cm}^{-1}$  were assigned to OH and C=O stretching modes of the acid form of bilirubin, respectively; whereas bands at 1175, 1105, 1050, and 995  $\text{cm}^{-1}$  were due to its calcium salt. This observation has revealed coexistence of the acid form and the calcium salt.

The present study, together with our previous study has demonstrated that the combined Raman microprobe-FT-IR microscope method is very powerful for studying the microstructure of various gallstones.

## References

1. W. A. D. Anderson, *Pathology*, St. Louis: C. V. Mosby, 1977.
2. H. Ishida, R. Kamoto, S. Uchida, A. Ishitani, Y. Ozaki, K. Iriyama, E. Tsukie, K. Shibata, F. Ishihara, and H. Kameda, "Raman microprobe and fourier transform-infrared microsampling studies of the microstructure of gallstones," *Appl. Spectrosc.* 41: 407-412, 1987.
3. S. Zheng and A. T. Tu, "Raman spectroscopic identification of bilirubin type gallstones," *Appl. Spectrosc.* 40: 1099-1103, 1986.
4. A. Bertoluzza, M. A. Battaglia, R. Simoni, and D. A. Long, "Vibrational spectroscopic studies of a new class of oligophosphate glasses of biological interest: 2," *J. Raman Spectrosc.* 14: 178-183, 1983.
5. M. Nishino, S. Yamashita, T. Aoba, M. Okazaki, and Y. Moriwaki, "Laser-Raman spectroscopic studies on human enamel and precipitated carbonate-containing apatites," *J. Dent. Res.* 60: 751-755, 1981.
6. E. S. Etz, B. B. Tomazic, and W. E. Brown, "Micro-Raman characterization of atherosclerotic and bioprosthetic calcification," *Microbeam Analysis--1986*, 39-46.
7. J. P. Henichart, J. L. Bernier, M. Roman, and P. Roussel, "Identification of calcium palmitate in gallstones by infra-red spectroscopy," *Clin. Chim. Acta* 118: 279-287, 1982.

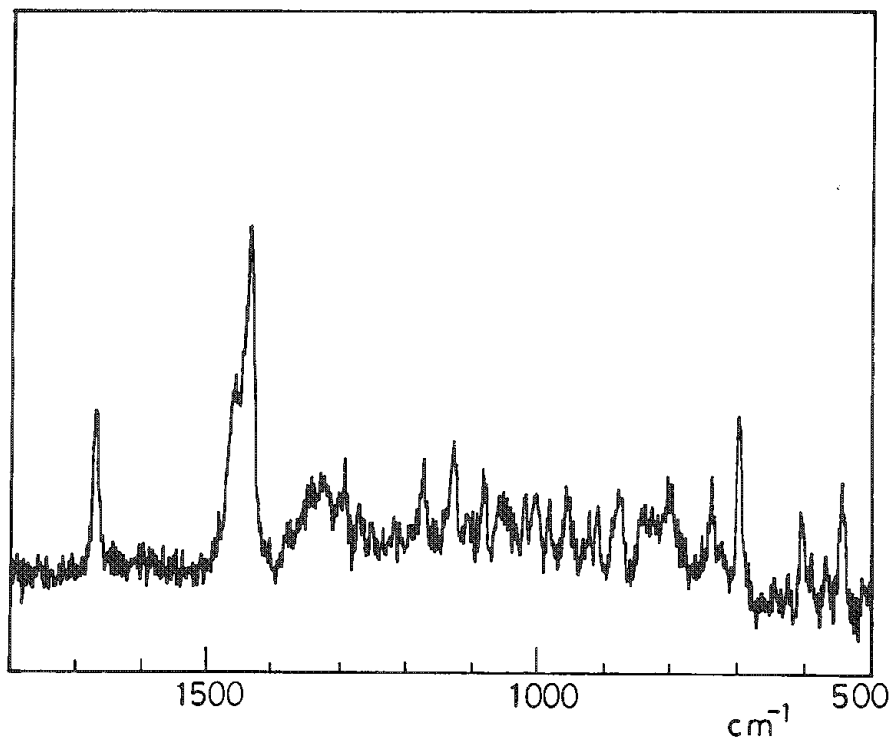


FIG. 3.--Raman spectrum of area c of fatty acid calcium stone measured by laser Raman microprobe.

#### 4C. Optical Spectroscopy: Micro-Raman Fluorescence

##### MICROSPECTROFLUOROMETRIC STUDY OF CELL STRUCTURE AND FUNCTION

Elli Kohen, J. G. Hirschberg, Marek Fried, Cahide Kohen, René Santus, J. P. Reyftmann, Patrice Morlière, D. O. Schachtschabel, W. F. Mangel, B. L. Shapiro, and Jeffrey Prince

If the tremendous progress in molecular biology and genetic manipulation of the prokaryotes and eukaryotes is to be placed in the actual context of the intact living cell, one will require a commensurate understanding of the metabolic control mechanisms involved.<sup>1</sup> Recently there has been a concern that many areas of biotechnology are directly concerned with the study or engineering of cells capable of mass producing metabolites for a certain desired use or application: yet the methods applied must remain semi-empirical unless the control of biochemical mechanisms in the "producer" organism are fully understood. There is an obvious need for knowledge of the exact way in which living cells control the flux of substrates through metabolic pathways of interest. A typical example is the search for a more effective way to circumvent normal metabolic controls which will lead ultimately to the maximum production of a particular metabolite.<sup>1</sup> The above example illustrates the crucial importance of understanding the organization of cell metabolism<sup>2,3</sup> at the single-cell level.

In the late summer of 1985 our plans to unravel the spatiotemporal organization of cell metabolism were reviewed in considerable detail at a NATO Advanced Study Workshop in Hanstholm, Denmark.<sup>4</sup> The focus of the meeting was on metabolic channeling and compartmentation. A consensus definition of metabolic channeling was reached according to which "a substrate is channeled between two or more enzymes if it is diffusionally constrained from the bulk phase of the cell."

In the *in situ* study of metabolic compartmentation at high structural and temporal resolution the microspectrofluorometric method is definitely advantageous. It allows, by topo-

graphic and spectral probing, a structural and functional study of metabolic activity as well as organelle interactions throughout the entire territory of a single living cell. Beyond single cell metabolism,<sup>2,3</sup> metabolic control<sup>5,6</sup> and cell-to-cell interactions<sup>7,8</sup> throughout a multicellular territory, with possibilities of synchronous behavior or local metabolic inhomogeneities,<sup>7</sup> are now open to study.

##### *The Microspectrofluorometer*

The microspectrofluorometer itself has been described previously.<sup>7,9</sup> Its key components are an inverted microscope with Ploemopak illuminator blocks for epi-illumination of cell samples, a high-numerical-aperture, long-working-distance phase condenser permitting the insertion of microinstruments for cell manipulations, intermediate optics, and an optical multichannel detector (OMA). The apparatus is operated in two modes: topographic and spectral. The linear OMA detector provides topographic scanning along a unilinear array of adjacent cell regions or spectral scanning from a single cell region. A new two-dimensional OMA unit allows for a topographic scan of a whole cell or simultaneous spectral scans from an unilinear strip of adjacent cell regions. The theoretical number of cell regions that can then be scanned simultaneously varies from  $2 \times 512$  to  $512 \times 512$ . The shortest scan time for  $512 \times 512$  resolution elements would be about 2 s. However, for the average mammalian cell in culture ( $20 \times 15 \mu\text{m}$ ), in order to obtain a satisfactory signal-to-noise ratio, there would be no significant advantage in attempting to resolve more than 1200 structural elements.

##### *Spatiotemporal Organization of Cell Metabolism*

Authors E. Kohen, C. Kohen, and Prince are at the Department of Biology and authors Hirschberg and Fried at the Department of Physics, University of Miami, Coral Gables, Fla.; authors Santus and Reyftmann are at the Muséum National d'Histoire Naturelle, Laboratoire de Physico-Chimie de l'Adaptation Biologique, Paris; author P. Morlière is at the Hôpital Henri Mondor, Laboratoire de Dermatologie Expérimentale, Créteil, France; author Schachtschabel is at the Institute für Physiologische Chemie II der Medizinischen Fakultät der Philipps Universität, Marburg/Lahn, Fed. Rep. of Germany; author Shapiro is at the Department of Oral Biology and Laboratory Medicine and Oral Pathology, University of Minnesota, Minneapolis; and author Mangel is at the Department of Biology, Brookhaven National Laboratory, Upton, N.Y. Thanks are due to Dr. P. D. Derwan at Caltech for his generous donation of methidium-propyl-EDTA; and to Betty Belman for the art work. This work was supported by National Science Foundation grant DMB-8303691 and Cystic Fibrosis Foundation grant G105 7/01,02.

The  $\text{NAD(P)} \rightleftharpoons \text{NAD(P)H}$  reduction-reoxidation transients<sup>2,3,10</sup> obtained in response to microinjected bioenergetic substrates (e.g., glucose-6-P, 6-phosphogluconate, malate) reveal the metabolic behavior of the cells studied (mouse L cells, human fibroblasts, human melanoma cells, and liver cells). The observed metabolic behavior is at the same time expressive of the cell's individuality and the cell's ability to function reproducibly under standardized steady state. In spite of the complexity of intracellular multienzyme processes, we can progress beyond the phenomenological stage. The cell's metabolic controls require an interpretation in the context of the systemic approach proposed for functionally integrated multienzyme pathways.<sup>5,6</sup> Consideration is also due to the structural correlation of metabolic pathways. It is in this framework that paradoxical metabolic responses (e.g., potentiation of  $\text{NAD(P)}$  redox transients to injected substrate despite high oxidative

activity in fibroblasts pretreated with uncoupler)<sup>11</sup> or metabolic inhomogeneities (e.g., coexistence of localized NAD(P) reductive or oxidative responses to the same injected substrate in various regions of a single cell, or in adjacent cells) can be understood.

The metabolic control theory developed by Kacser,<sup>5</sup> Burns, and Heinrich and Rapoport<sup>6</sup> provides a rational and quantitative basis for the description and interpretation of the above processes. It is unrealistic to attempt the resolution of intracellular metabolic processes from individual enzyme kinetics. A systematic approach is required that can account for (1) the share of control attributable to a change in a single enzyme with all other enzymes kept constant; and (2) the change in the rate of one "isolated" enzyme step, when one metabolite level is changed while all the other metabolites remain constant.

The intact living cell becomes the *in situ* testing ground for the metabolic control theory, which now requires the consideration of one more concept: the structural organization of metabolic activity in terms of compartmentation and organelle interactions.<sup>5</sup> Using drugs active on mitochondrial structure and function (dinitrophenol, the antipsoriatic anthralin,<sup>11</sup> rhodamine 123,<sup>12</sup> porphyrin photosensitizers,<sup>13</sup> and the antimelanoma azelaic acid<sup>14,15</sup>), it becomes rapidly apparent that considerable metabolic upheaval (both mitochondrial and extramitochondrial) accompanies structural alterations of mitochondria. It seems that mitochondria maintain a tight control on cell metabolism. Unless one of the above-cited conditions or ATP traps is used, in the cell with well-coupled electron transport and oxidative phosphorylation, responses to injected mitochondrial or extramitochondrial substrates are restricted to local foci of metabolic activity. A widespread deregulation and amplification of mitochondrial and extramitochondrial transient NAD(P)H responses to injected substrates is observed under conditions where structural damage of mitochondria can be demonstrated by use of vital fluorescent probes such as dimethylaminoethylmethylpyridinium-iodine<sup>16</sup> and rhodamine 123<sup>12</sup> (Fig. 1a). Culture up to one week in the presence of azelaic acid leads to considerable degeneration of mitochondria (Figs. 1b and c). If such mitochondria are then stained with rhodamine 123, the fluorochrome is soon retrieved in the lysosomes due to autodigestion of degenerated mitochondria.

A puzzling aspect is the localization in fibroblasts and human melanoma cells of the metabolic response to injected 6-phosphogluconate and malate at the level of the nucleus. The possibility that the response is in supra- or infranuclear areas seems less plausible in view of the lack of response in juxtannuclear regions of the cytoplasm, although metabolic activity in the nuclear membrane or perinuclear energy metabolism,<sup>17,18</sup> correlated to nucleic acid synthesis, remains open. Upon imposition of a functional load to the cell, e.g., xenobiotic (carcinogens, barbiturate) detoxification, a generalized extramitochondrial (and mitochondrial) response to the same

substrate is observed, possibly of the kind that may be of interest to the biotechnologist in gaining a way to circumventing metabolic controls.

The NAD(P) reduction and reoxidation rate constants can be used as sensitive monitors of reductive and oxidative flux, in the presence of agents added, as described above to the cell environment or following injections of allosteric modifiers, as well as various substrate or modified ratios that can alter the cell's oxidation or phosphorylation potential. The fine tuning of reductive and oxidative fluxes under such circumstances can help to unravel, discrete metabolic differences. An application has been initiated to identify metabolic characteristics of normal vs cystic fibrosis (CF) fibroblasts. First studies suggest a possible deregulation of mitochondria in CF cells,<sup>19</sup> which may be easier to destabilize in the presence of mitochondria active drugs.

#### *Studies in Lysosomes*

New fluorogenic probes such as rhodamine bipeptides<sup>20</sup> can be used to probe lysosomal hydrolases and lysosomal membrane stability. Porphyrin-loaded, low-density lipid LDL<sup>21</sup> is used for intracellular internalization and lysosomal targeting of protoporphyrin or photofrin 2. Upon irradiation at 365 or 436 nm, triplet-triplet energy transfer from the porphyrin to molecular oxygen triggers the following reaction chain<sup>22,23</sup>: formation of singlet oxygen → lipid peroxidation → rupture of lysosomal membranes → release of hydrolases → splitting of rhodamine probe → rhodamine emission as a result of hydrolase action.

#### *Peroxidative Processes*

Porphyrin sensitization also results in formation of a lipid peroxidation end product, malonaldehyde, which then interacts with amines or amino groups to yield blue fluorescent Schiff bases.<sup>22-24</sup> Higher accumulation of such pigment in late passage fibroblasts can represent an expression of cellular senescence. Since the same Schiff bases are known to be deposited spontaneously in quiescent or senescent cells, their accumulation at a much faster rate in photosensitized cells seems to indicate a kind of accelerated "photo-aging." The accumulation of Schiff bases is strikingly prevented in the presence of 10mM glutathione (Fig. 2), a known scavenger of oxidizing equivalents.

#### *Detoxification of Xenobiotics*

In the same way that recent models of intracellular enzyme organization suggest the possibility of transient multienzyme or enzyme-membrane complexes, we have recently obtained possible indications that under circumstances requiring such activity (e.g., detoxification processes) transient multienzyme complexes are also formed.<sup>25</sup> In cells incubated from 1 h to several days in the presence of quinacrine or benzo(a)pyrene, the high resolution of fluorescence microscopy permits the identification of these molecules within lyso-



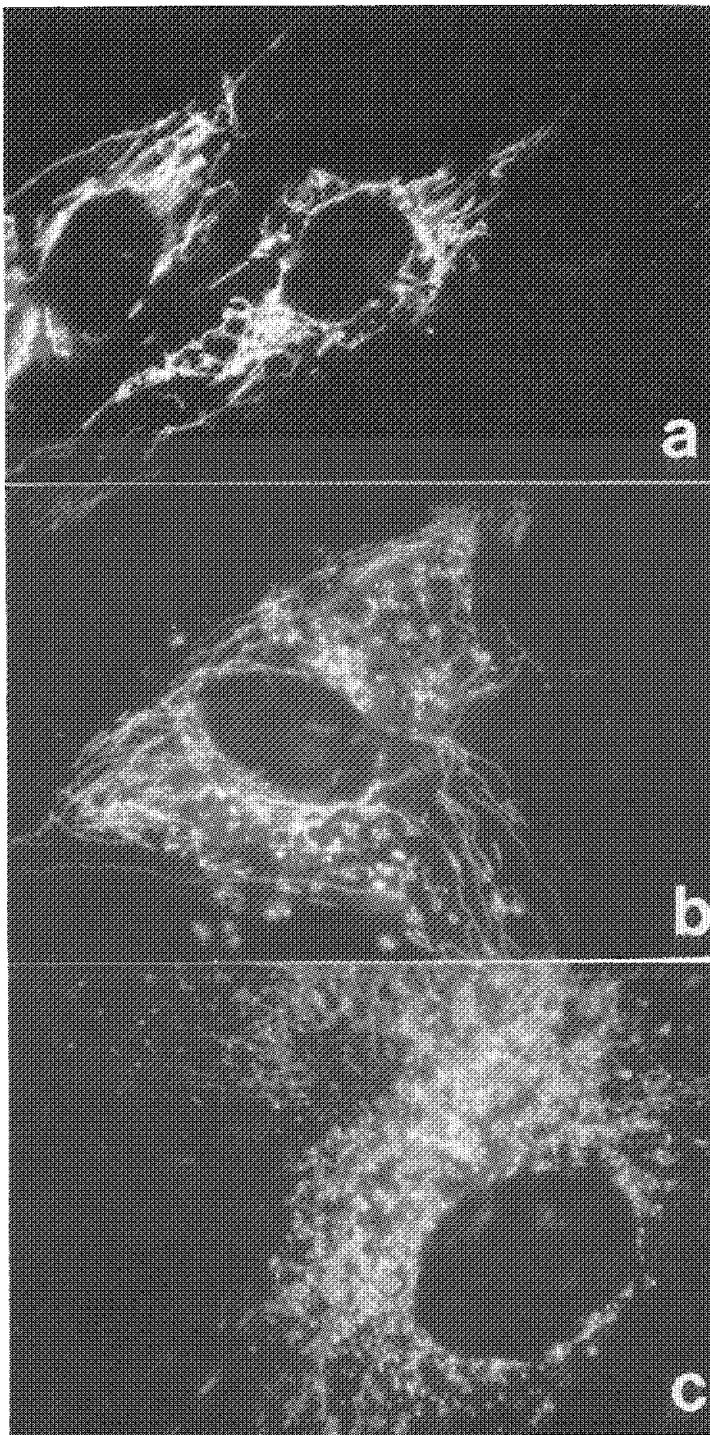


FIG. 1.--(a) Human fibroblasts stained with vital fluorescent probe of mitochondria in situ, rhodamine 123 (10  $\mu$ g/ml for 15 min and then washed). Mitochondria are long and filamentous, with slightly coiled worm-like appearance. Fibroblasts obtained from B. L. Shapiro, University of Minnesota (Department of Oral Biology). (b) Same fibroblasts maintained 3 days in presence of 30 mM azelaic acid in Eagle's MEM medium with 10% calf serum. Several mitochondria are still filamentous but there is some structural damage (apparent fragmentation and clumping, and bead-like forms, also described for human fibroblasts treated by cyanide by Goldstein et al., *J. Cell Biol.* 91: 392, 1981). (c) Same as (b) but after 7 days. Mitochondrial damage has considerably progressed, with near total disruption of filamentous form. Rhodamine 123 is now partly retrieved within lysosome-like cytoplasmic granules.

Experiment numbers: (a) 52-8, (b) 142-18d, (c) 143-20d.

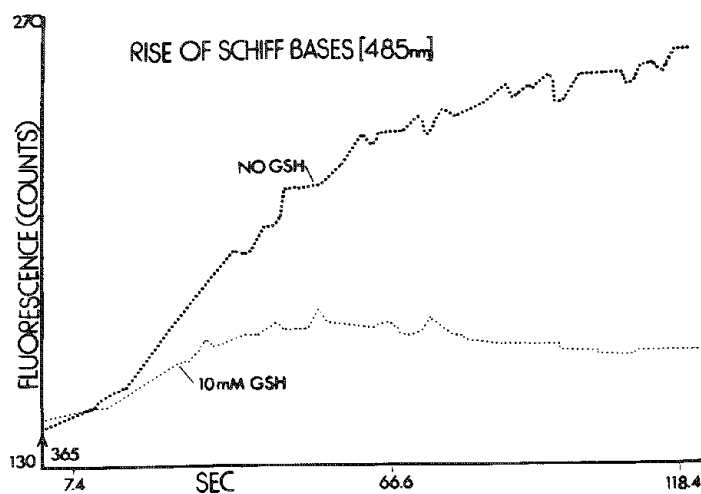


FIG. 2.--Kinetic curves (time plots) of human fibroblast fluorescence recorded at 485 nm show the protective effect of 10 mM reduced glutathione (GSH) from photosensitized lipid peroxidation. Abscissa = time; ordinate = fluorescence intensity (counts). Fibroblasts preincubated with 0.01% hematoporphyrin were irradiated at 365 nm in presence and absence of GSH. Under these conditions fluorescence due to cell's coenzyme fluorochromes (NAD(P)H) is contained in initial baseline left of curves. Since no substrates or metabolic intermediates are added to cell medium or microinjected into fibroblasts, fluorescence increase observed during photosensitization is not due to NAD(P)H but to iminopropenes (Schiff bases), as is further demonstrated by recording of fluorescence spectrum, which shows rise of fluorescence observed in kinetic curves to be accompanied by shift of emission maximum toward longer wavelengths than characteristic spectra of NAD(P)H emission. Fluorescence spectrum of cell thus changes under photosensitization from typical NAD(P)H pattern to Schiff-base pattern. Accumulation of Schiff bases proceeds much slower and reaches much lower plateau in presence of GSH than in untreated fibroblasts.

somes and also a paranuclear multichannel network (Fig. 3). There is some evidence for transient association of different organelles including lysosomes, endoplasmic reticulum (ER), Golgi apparatus, and nuclear membrane into a "multiorganelle deontixification complex."

Very recently an attempt has been initiated to identify further the multichannel structures observed by fluorescence microscopy with ultrastructural studies by electron microscopy. Fibroblasts in culture were incubated with a molecule which is fluorescent and electron-opaque at the same time (e.g., methidiumpropyl-EDTA-Fe<sup>2+</sup>).<sup>26</sup> High-magnification electron microscopy studies are in progress to determine whether the channels observed in fluorescence studies can be visualized as electron opaque areas in unstained preparations.

Fluorescence-emission spectra recorded from various sites of the suspected multiorganelle complex reveal blue or red shifts that might correspond to various metabolites, detoxification products or intracellular interactions of the xenobiotics. The spectra obtained at these sites could represent sum spectra of various fluorochromes. The emission spectra were therefore recorded at several excitation wavelengths,<sup>27</sup> since in this case multivariate statistical methods<sup>28-30</sup> can be used to analyze the data. The large set of individual measurements can be arranged into an emission-excitation matrix, which makes it possible to apply algebraic methods with simple computer implementations. If the concentrations of the fluorochromes are low, the recorded spectra can be represented as sum spectra of the species present, and the number of these species is equal to the "essential" rank of the data matrix. The estimate of this rank is obtained by statistical methods that employ eigenanalysis of the covariance matrix formed from the experimental data matrix. Successive low-rank approximations are then constructed and the distribution of the elements of the data matrix is compared with those of the approximations, with chi-square statistics used as the criterion for the goodness-of-fit. From 1 to 3 components have been identified by the matrix approach in cells incubated with benzo(a)pyrene from minutes to several days. However, further studies are required (e.g., comparison with spectra of individual metabolites in mixtures of different proportions) before actual knowledge of component spectra is possible.

### Conclusions

Microspectrofluorometry permits a structural and functional mapping of living cells (Fig. 4). Studies of the spatiotemporal organization of cell metabolism are not only essential to the development of an in situ biochemistry, they are also crucial to progress in cellular pharmacology and pathology. The strength of the method resides in its ability to detect, within a living cell (where the microarchitecture is in a state of perpetual flux), rapid transient processes expressive of the metabolic controls in operation.

### References

1. D. B. Kell et al., "Metabolic control theory: Its role in microbiology and biotechnology," *FEMS Microbiol. Rev.* 39: 305-320, 1986.
2. E. Kohen et al., "Metabolic control and compartmentation in single living cells," *Cell Biochem. Funct.* 1: 3-16, 1983.
3. E. Kohen et al., "Experimental analysis of spatiotemporal organization of metabolism in intact cells: The enigma of 'metabolic channeling' and 'metabolic compartmentation,'" in G. R. Welch and J. S. Clegg, Eds., *The Organization of Cell Metabolism*, New York: Plenum, 1987.
4. H. V. Westerhoff, "Cell metabolism: Organization in the cell soup," *Nature* 106: 318-319, 1985.
5. H. Kacser et al., "The control of flux, in rate control of biological processes," in D. D. Davies, Ed., *Symp. Soc. Exp. Biol.*, vol. 27, Cambridge: Cambridge University Press, 1973, 65-104.
6. R. Heinrich and T. A. Rapoport, "A linear steady-state treatment of enzymatic chains: General properties, control and effector strength," *Eur. J. Biochem.* 42: 89-95, 1974.
7. E. Kohen et al., "Examination of single cells by microspectrophotometry and microfluorometry," in P. F. Baker, Ed., *Techniques in the Life Sciences. Physiology*, New York: Elsevier, 1983, 103/1-28.
8. P. Meda et al., "Direct communication of homologous and heterologous endocrine islet cells in culture," *J. Cell Biol.* 92: 221-226, 1982.
9. J. G. Hirschberg et al., "A high resolution grating microspectrofluorometer with topographic option for studies in living cells," in Y. Talmi, Ed., *Multichannel Image Detectors*, Washington: ACS Symposium Series, 1979, vol. 102, 263-289.
10. B. Chance, "The identification of enzyme-substrate compounds," in E. S. Guzman Barron, Ed., *Modern Trends in Physiology and Biochemistry*, New York: Academic Press, 1952, 25-46.
11. E. Kohen et al., "A microspectrofluorometric study of the effect of anthralin, an antipsoriatic drug, on cellular structures and metabolism," *Cell Biochem. Funct.* 4: 157-168, 1986.
12. L. B. Chen et al., "Probing mitochondria in living cells with rhodamine 123," *Cold Spring Harbor Symp. Quant. Biol.* 46: 141-155, 1984.
13. E. Kohen et al., "A microspectrofluorometric study of prophylin-photosensitized single living cells: Part II. Metabolic alterations," *Photochem. Photobiol.* 44: 471-475, 1986.
14. A. S. Breathnach, "Azelaic acid," *Brit. J. Dermatol.* 111: 1150-120, 1984.
15. F. Hu et al., "Effect of dicarboxylic acids on normal and malignant melanocytes in culture," *Brit. J. Dermatol.* 114: 115-120, 1986.
16. J. Bereiter-Hahn, "Dimethylaminoethylmethylpyridiniumiodine (DASPMI) as a fluorescent probe for mitochondria in situ," *Biochim. Biophys. Acta* 423: 1-14, 1976.

17. E. Kohen et al., "Metabolism of reduced pyridine nucleotides in ascites cell nuclei," *Histochemie* 3: 552-560, 1964.
18. T. E. Conover et al., "On the occurrence of respiratory components in rat liver nuclei," *Biochim. Biophys. Acta* 99: 1-12, 1965.
19. B. L. Shapiro et al., "Mitochondrial NADH dehydrogenase in cystic fibrosis: Enzyme kinetics in cultured fibroblasts," *Am. J. Human Genet.* 34: 846-852, 1982.
20. S. P. Leytus et al., "Theory and experimental method for determining individual kinetic constants of fast-acting, irreversible protease inhibitors," *Biochim. Biophys. Acta* 788: 74-86, 1984.
21. J. L. Goldstein et al., "Coated pits, coated vesicles and receptor-mediated endocytosis," *Nature* 279: 679-685, 1979.
22. J. P. Reyftmann et al., "A microspectrofluorometric study of porphyrin-photosensitized single living cells: Part I. Membrane alterations," *Photochem. Photobiol.* 44: 461-469, 1986.
23. J. P. Reyftmann, *Contribution à l'étude de l'action photodynamique des porphyrines cellulaires*, Thesis, Université Pierre et Marie Curie, Paris VI.
24. A. L. Tappel, "Measurement of and protection from in vivo lipid peroxidation," in W. A. Pryor, Ed., *Free Radicals in Biology*, New York: Academic Press, 1980, vol. 4, 2-47.
25. E. Kohen, in C. Parkanyi, Ed., *Molecular Toxicology*, 1987 (in press).
26. M. W. Van Dyke et al., "Map of distamycin, netropsin, and actinomycin binding sites on heterogenous DNA: DNA cleavage-inhibition patterns with methidiumpropyl-EDTA-Fe(II)," *Proc. Natl. Acad. Sci. USA* 79: 5470-5474, 1982.
27. G. Weber, "Enumeration of components in complex systems by fluorescence spectrophotometry," *Nature* 190: 27, 29, 1961.
28. I. M. Warner et al., "Analysis of multicomponent fluorescence data," *Anal. Chem.* 49: 564, 1977.
29. E. R. Malinowski, "Theory of error in factor analysis," *Anal. Chem.* 49: 606, 1977.
30. M. Fried, *Statistical Methods for the Determination of the Number of Independent Fluorescent Emitters in Living Cells*, Thesis, Dept. Physics, Univ. of Florida, Coral Gables.

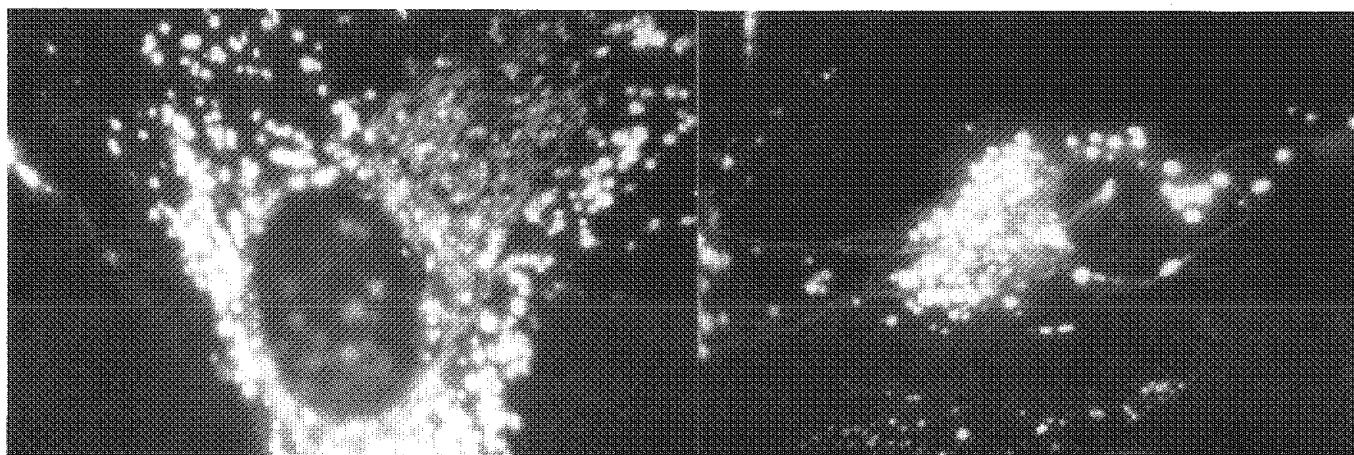
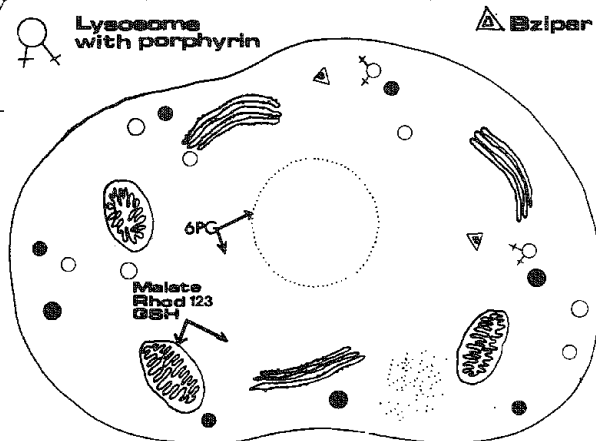


FIG. 3.--(a) Human fibroblast incubated with  $2.8 \times 10^{-6}$  M quinacrine for 2 h, then washed. Fluorochrome is observed within lysosomes and extensive paranuclear multichannel network. (b) As above fluorochrome is found within lysosomes and network of thin meandering channels. Some channels seem to establish connections with lysosome-like vesicles. Experiments: (a) 118-7a, (b) 118-34a.

FIG. 4.--Fluorescence mapping of metabolic activity and organelle functions in fibroblast, showing various intracellular processes that can be probed by microspectrofluorometry: ● residual bodies accumulating in quiescent or senescent cells, ○ functional lysosomes. Mitochondrial and extramitochondrial dehydrogenase pathways are probed by microinjections of malate. Mitochondrial NAD(P)H response to this substrate may be delayed 1-7 s in relation to extramitochondrial response (so that delay due to mitochondrial membrane barrier might be measured by this approach). Hexose monophosphate shunt is monitored via NADPH response to 6PG (6-phosphogluconate) injection. This response in fibroblasts and other cells (thyroid, human melanoma, rhabdomyosarcoma) appears largely confined to nuclear region, but a concomitant extramitochondrial response is observed in ATP-depleted cells, or whenever functional load (such as xenobiotic detoxification) is imposed. Arrows indicate these two response patterns: one points to nucleus, other to cytoplasm. Addition of rhodamine 123 or reduce glutathione to cell medium alters reduction and reoxidation kinetics of NADPH transients triggered by injection of 6-PG. Fluorogenic lysosomal probe BZIPAR (▲) is (CBZ-Ile-Pro-Arg-NH)<sub>2</sub>-rhodamine, a bipeptide of rhodamine. Fluorescence of rhodamine is released only following action of hydrolase, which is liberated following porphyrin-mediated photosensitization. Another result of photosensitization is lipid peroxidation with accumulation of end product, Schiff bases (cf. also Fig. 2), shown here as dots in localized accumulation, although topographic fluorescence scan reveals accumulation throughout.



## MICROBEAM RAMAN/FLUORESCENCE ANALYSIS OF EYE LENS

Nai-Teng Yu, Ming-Zhi Cai, Deborah J.-Y. Ho, F. L. Thompson, and J. F. R. Kuck

We report the design and performance of a new automated laser micro-Raman/fluorescence spectroscopic scanning system for obtaining two-dimensional concentration profiles of protein constituents and various cataract-related fluorophors in the eye lens. Our microprobe system is capable of (1) automated acquisition of "position-defined" Raman/fluorescence spectra from gridded points (1-8  $\mu$ m diameter) of a lens section, (2) storage of intensity data of up to six spectral lines (or integrated intensities) from each point, (3) six-color graphic map indicating regions of different intensity intervals, and (4) plotting of contours intersecting the intensity data with constant-height planes. The instrumentation consists of (1) a modified Zeiss microscope with a video camera and two computer-controlled actuators, (2) a modified Spex 1877 Triplemate, (3) a multichannel detector (PAR model 1420 Intensified Reticon), and (4) an IBM XT computer with home-built interface boards for controlling the detector, a programmed electronic shutter, and the X-Y stage translator. Available lasers are He-Cd, Ar<sup>+</sup>, Kr<sup>+</sup>, and N<sub>2</sub>. This system is expected to be useful for obtaining relevant information pertaining to the modes of fluorophor production and the mechanisms of cataract formation. The method is applicable to any lenses (human/animal; normal/cataractous).

### *Experimental*

Human lenses were obtained from the Atlanta Lions Eye Bank. Before preparation of a flat lens surface for X-Y data collection, the lens was frozen (at  $\sim$ -80 C) in an aluminum rectangular trough whose depth and width are equal to the equatorial radius, optical axis length, and equatorial diameter, respectively. The lens was so positioned that its optical axis was horizontal and one-half of the lens was above the top surface of the aluminum block. The entire aluminum block with a frozen lens in its trough was then transferred to the thermoelectric cold plate (-50 C) affixed to the X-Y translation stage. After the upper half of the lens was shaved away by a knife, the lower half with a flat surface was covered by a layer of glycerol and a thin microscopic slide. Dry nitrogen gas was then channeled into the surrounding of the frozen lens surface via a circular glass apparatus that enclosed the cold plate and the aluminum block, but still allows the microscope objective lens to approach the sample surface.

Authors Yu, Cai, Ho, and Thompson are at Georgia Institute of Technology (Department of Chemistry), Atlanta, GA 30332; author Kuck is at Emory University (Department of Ophthalmology), Atlanta, GA 30332. National Eye Institute support (EY01746 and EY00260) is acknowledged.

A typical laser scanning path on the lens section is shown in Fig. 1. The scanning domain is  $\sim$ 11  $\times$  6 mm, which is somewhat larger than the rectangular trough. A total of 1200 data points (30  $\times$  40) from a lens section were routinely obtained. To obtain a better resolution, a total of 2000 data points (40  $\times$  50) were obtained. The anterior side has less curvature than the posterior side.

### *Results and Discussion*

We report here the testing of the performance of our automated laser microprobe scanning system on a 26-year-old human lens. It is well known that the human lens contains numerous fluorophors, depending on age and pathological state.<sup>1</sup> In the present study, we monitored the fluorophor that exhibits an emission maximum of  $\sim$ 520 nm when excited at 441.6 nm (He-Cd laser). The spatial distribution of this fluorophor on the lens section is shown in Fig. 2. Near the optical axis there is a lower concentration of fluorophor toward the anterior side (Fig. 2a), and there is a saddle-shaped central minimum when one views the graph along the optical axis. Figure 2(b) exhibits a 3-dimensional perspective of the green fluorophor distribution; Fig. 2(c) shows the perspective with a sectioning along the optical axis; and Fig. 2(d) displays the perspective with a sectioning along the equatorial axis.

Studies of fluorophor distributions in the eye lens are important because of the popular belief that they are generated by photocatalyzed reactions, which may be the initiating event for the formation of nuclear senile cataract.<sup>2-4</sup> The hypothesis that the lens may be affected adversely by the radiation it absorbs is a reasonable one, although evidence in favor of such a relationship is only circumstantial. Studies of the epidemiology of this type of cataract always cite the elevated incidence in Tibet (China), India, and Pakistan as perhaps being due primarily to the high intensity of light reaching the eye in a tropical population. Retrospective studies on human cataract offer little hope of proving the hypothesis, and results of experimental studies on animals subject to near ultraviolet (UV) radiation are difficult to correlate with human cataracts for lack of suitable models.

If human nuclear cataract (brunescant type) is caused by light, the pigments (or fluorophors) accumulation should have certain geometrical characteristics that result from this mode of production. First, since near UV light strikes the anterior part of the nucleus first and is absorbed there in all but very young lenses, the pigmented zone should expand anteriorly but not posteriorly. The shape of the pigmented nucleus in an older person should then be asymmetrical along the optical (visual) axis. Second, because of the action of the

pupillary system in regulating the light allowed to enter the eye, the more intense the light, the more the beam is restricted to a pathway coincident with the optical axis. Thus, viewed at the anterior pole along the optical axis, the pigmented zone should be darker at the center. Such an effect is not noticeable because it is indistinguishable from the apparent greater central absorption due entirely to the fact that the optical axis passes through the thickest part of the lens, which interposes more pigments in the light path. Third, since the outer anterior zone of the nucleus protects the inner anterior zone from the effect of the light, pigment concentration should exhibit little increase as one goes toward the center of the nucleus.

These conclusions, arrived at intuitively, can hardly be verified by observing the whole lens in vitro. The proof may come from determinations of the detailed spatial distribution

of various fluorophors. At present, the distribution patterns shown in Fig. 2 indicate that the green fluorophor (520nm emission/441.6nm excitation) is not likely to be generated by the ambient UV light. We are now extending our studies to include more lenses, especially those from Beijing and Tibet, with longer excitation wavelengths (450-700 nm).

#### References

1. N.-T. Yu, M. Bando and J. F. R. Kuck, *Invest. Ophthalmol. Vis. Sci.* 26: 97-101, 1985.
2. A. Pirie, *Invest. Ophthalmol.* 7: 634-650, 1968.
3. R. F. Borkman, A. Dalrymple, and S. Lerman, *Photochem. Photobiol.* 26: 129-132, 1977.
4. R. C. Augusteyn, *Jpn. J. Ophthalmol.* 18: 127-134, 1974.

FIG. 1.--Ocular lens section confined in 11×6mm rectangular domain for two-dimensional grid data collection. Raman/fluorescence signals are obtained from 1200 points (~8μm diameter); laser scanning path is indicated by arrows.

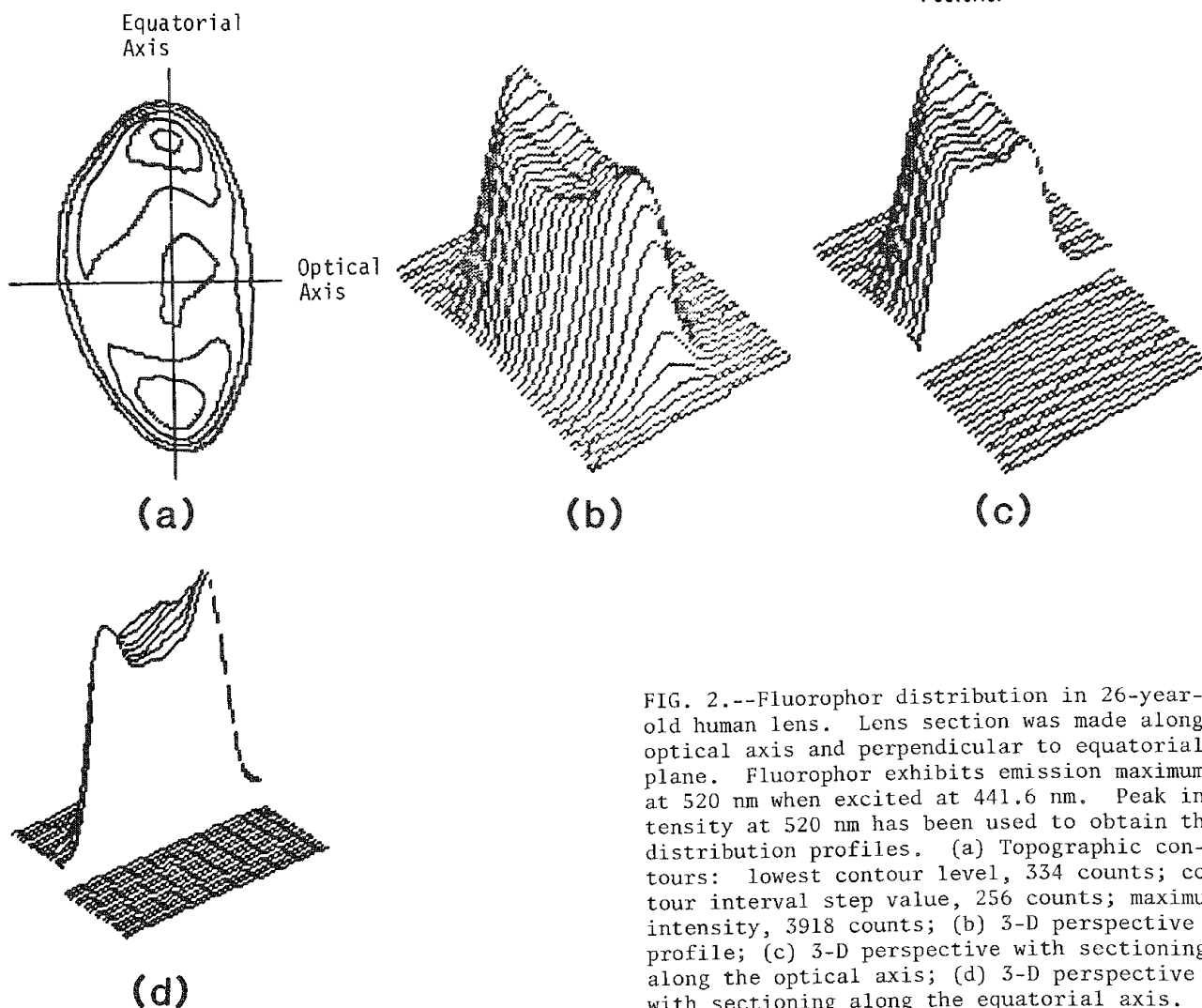


FIG. 2.--Fluorophor distribution in 26-year-old human lens. Lens section was made along optical axis and perpendicular to equatorial plane. Fluorophor exhibits emission maximum at 520 nm when excited at 441.6 nm. Peak intensity at 520 nm has been used to obtain the distribution profiles. (a) Topographic contours: lowest contour level, 334 counts; contour interval step value, 256 counts; maximum intensity, 3918 counts; (b) 3-D perspective profile; (c) 3-D perspective with sectioning along the optical axis; (d) 3-D perspective with sectioning along the equatorial axis.

## LASER RAMAN OPTICAL DISSECTION STUDY OF AN INTACT LENS: COMPARISON AMONG HORIZONTAL AXIS PROFILES OF LENS WATER, SULFHYDRYL, AND DISULFIDE CONTENTS

Aritake Mizuno, Elza Hitomi Takata-Kanematsu, Hiroko Nozawa,  
Yukihiro Ozaki, Keiji Iriyama, and Teruki Ikeda

An ocular lens can be divided into two portions, nucleus and cortex, and both portions consist of many lens fibers. The predominant dry components of a mammalian lens are three structural proteins named  $\alpha$ -,  $\beta$ -, and  $\gamma$ -crystallins and their combined weight accounts for approximately 33% of the total weight of the lens.<sup>1</sup> Lens aging and cataract result from the formation of protein aggregates, which disturbs the supramolecular organization of the crystallins.<sup>1</sup> Microbeam analysis of the lens is particularly important for two reasons. One is that lens water/protein ratio, relative concentrations of the three lens proteins, and microenvironments of their amino acid residues alter along the visual and horizontal axes of the lens; the other is that cataract often starts from microscopic opacification.

Raman spectroscopic technique has been used extensively in lens research as an excellent nondestructive structural probe.<sup>2-4</sup> Raman spectra of an intact lens furnish in situ information about lens hydration or dehydration, relative concentration and secondary structure of the lens proteins, microenvironments of tyrosine and tryptophan residues, and 2SH  $\rightarrow$  S-S conversion of the lens proteins.<sup>2-4</sup> Raman signals can be obtained from an extremely small volume of the lens (typically,  $10^{-3}$   $\mu$ l for a conventional Raman spectrometer and  $10^{-7}$   $\mu$ l for a Raman microprobe<sup>5</sup>), so that the distribution of a constituent may be investigated.

Laser Raman optical dissection technique was first applied by Yu et al.<sup>6-8</sup> to lens research. So far visual axis sulfhydryl profiles have been investigated in considerable detail, but the data on profiles of other amino acid residues and lens water/protein ratio are very limited<sup>6-8</sup> and there has been no report for the profiles along the horizontal axis. Therefore, we have recently started a systematic study on profiles of various amino acid residues and lens water/protein ratio along both axes. In the present paper we report that sulfhydryl and disulfide profiles along the horizontal axis of a rat lens are, respectively, directly and inversely proportional to the corresponding lens water/protein ratio profile.

### Experimental

A normal lens from a 10-month-old SD-strain rat was employed in the present experiments. The excised lens was placed on a cuvette cell

bottom and covered with a tris(hydroxymethyl)aminomethane (Tris) buffered balanced salt solution containing 5.5 mM glucose. The osmolality of the solution was 291 mosM.

Raman measurements were made by a Jasco NR-1000 Raman spectrometer equipped with an HTV 649 photomultiplier tube. The excitation wavelength employed was 514.5 nm from an argon laser (NEC GLG 3200), and the laser power at the sample position was 100 mW. Peak frequencies were calibrated by measuring the spectrum of indene. The lens was illuminated by the laser beam from the bottom of the cell, and the scattered light was collected at 90° to the incident beam. Raman signals were obtained from a microscopic cylindrical volume (50  $\mu$ m in diameter and 0.28 mm height;  $5.5 \times 10^{-4}$   $\mu$ l) of several points along the horizontal axis of the lens; the size of the lens was 4.4 mm in diameter and the points investigated (points a-g) are illustrated in Fig. 1. The boundary between the nucleus and cortex is located near point e.

### Results and Discussion

Figure 1 compares Raman spectra in the 3800-2800 $\text{cm}^{-1}$  region taken at two different points (points a and g) of a 10-month-old SD-strain rat lens. Points a and g belong to the nucleus center and cortical portion near equator, respectively. A broad band near 3390  $\text{cm}^{-1}$  is assignable to an OH stretching mode of water included in the lens; a weak feature at 3064  $\text{cm}^{-1}$  and overlapped bands at and near 2935  $\text{cm}^{-1}$  are due to CH stretching modes of the lens proteins.<sup>9,10</sup> We previously proposed that lens dehydration and hydration can be probed nondestructively and locally by a comparison of the peak heights of two Raman bands at 3390 and 2935  $\text{cm}^{-1}$  ( $I_{3390}/I_{2935}$ ; lens water/protein ratio).<sup>9,10</sup> Note that the intensity ratio ( $I_{3390}/I_{2935}$ ) changes dramatically from point a to point g. Trace (A) in Fig. 2 shows the profile of the intensity ratio along the horizontal axis of the lens. Relative content of lens water to the lens proteins increases gradually along the axis; in other words, protein concentrations decrease.

Trace (B) in Fig. 2 illustrates the profile of the intensity ratio of two Raman bands at 2579 and 2731  $\text{cm}^{-1}$  ( $I_{2579}/I_{2731}$ ) along the horizontal axis of the same lens as for Trace (A). The band at 2579  $\text{cm}^{-1}$  (not shown) is assigned to a SH stretching mode of sulfhydryl groups of the lens proteins.<sup>2-4</sup> The assignment of the 2731 $\text{cm}^{-1}$  band is still uncertain, but its intensity has been used as an internal standard for estimating the relative intensity of the 2579 $\text{cm}^{-1}$  band.<sup>6,8,10</sup> Trace (B) is fairly similar to the visual axis sulfhydryl profile for a 7.5-month old rat lens reported

Authors Mizuno, Takata-Kanematsu, Nozawa, Ozaki, and Iriyama are at The Jikei University School of Medicine, Minato-ku, Tokyo 105, Japan; author Ikeda is at Japan Spectroscopic Co., Ltd., Hachioji, Tokyo 192, Japan.

by Askren et al.<sup>6</sup> Trace (C) in the same figure represents the corresponding profile of the intensity ratio of two bands at 510 and 495  $\text{cm}^{-1}$  ( $I_{510}/I_{495}$ ). The band at 510  $\text{cm}^{-1}$  (not shown) is due to a S-S stretching mode of disulfide bridges in the lens proteins.<sup>2-4</sup> The band at 495  $\text{cm}^{-1}$  arises from the peptide backbone and its intensity has served as an internal standard.<sup>8</sup>

Particularly striking in Fig. 2 is that the sulfhydryl profile is inversely and directly proportional to the disulfide and the lens water/protein ratio profiles, respectively, in the nuclear portion. The correlation between the sulfhydryl and disulfide profiles clearly shows that the decrease of SH content in the nucleus means the formation of S-S linkages. Similar correlation was observed for mouse lenses.<sup>9</sup> With regard to the relation between SH content and lens water/protein ratio, we previously found that age-dependent profile of the SH-stretching mode of nucleus center parallels that of its OH stretching mode; SH content in the nucleus center decreases as lens dehydration proceeds with aging.<sup>10</sup> This observation was interpreted to mean that lens dehydration concentrates the proteins and so facilitates the conversion of SH groups to disulfide bonds.<sup>10</sup> The similarity between the sulfhydryl (Trace B) and the lens water/protein ratio (Trace A) profiles in the nuclear portion may be also interpreted by the same argument. Both SH and S-S contents decrease in the cortex, probably because protein concentrations themselves decrease there.

The present study has clearly demonstrated that the relative content of water to the lens proteins, and that of SH groups, changed markedly along the horizontal axis of a lens and further suggested that the  $2\text{SH} \rightarrow \text{S-S}$  conversion is closely related to lens dehydration. This sort of microbeam analytical study provides basic information for studying microscopic cataractous changes. First cataractous signature is often recognized as a spotlike opacity by optical microscopic observation. In such cases the Raman microprobe method may be more useful.

## References

1. E. Cotlier, "The lens," in R. A. Moses, Ed., *Adler's Physiology of the Eye*, St. Louis: Mosby, 1981, 277-303.
2. Y. Ozaki, A. Mizuno, K. Itoh, and K. Iriyama, "Potential clinical application of laser Raman spectroscopy for cataract diagnosis," *Innov. Tech. Biol. Med.* 5: 269-286, 1984.
3. Y. Ozaki, A. Mizuno, K. Itoh, and K. Iriyama, "Structure and function of the lens proteins studied by Raman spectroscopy," in J. Twardowski, Ed., *Spectroscopic and Structural Studies of Biomedical Materials*, Cheshire: Sigma Press, 1987 (in press).
4. N.-T. Yu, "Ocular lenses," in T. G. Spiro, Ed., *Biological Applications of Raman Spectroscopy*, New York: Wiley, 1987 (in press).
5. G. Gijsbers, G. Vrensen, B. Willekens, D. Maatman, F. De Mul and J. Greve, "Raman microspectroscopic investigations of human eye lenses," in V. Prosser, Ed., *Laser Scattering Spectroscopy of Biological Objects*, Amsterdam: Elsevier, 1987 (in press).
6. C. C. Askren, N.-T. Yu, J. F. R. Ruck Jr., "Variation of the concentration of sulfhydryl along the visual axis of aging lenses by laser Raman optical dissection technique," *Exp. Eye Res.* 29: 647-654, 1979.
7. N.-T. Yu, M. Bando, and J. F. R. Ruck Jr., "Fluorescence/Raman intensity ratio for monitoring the pathologic state of human lens," *Invest. Ophthalmol. Vis. Sci.* 26: 97-101, 1985.
8. N.-T. Yu, D. C. DeNagel, P. L. Pruett, and J. F. R. Ruck Jr., "Disulfide bond formation in the eye lens," *Proc. Natl. Acad. Sci. USA* 82: 7965-7968, 1985.
9. K. Iriyama, A. Mizuno, Y. Ozaki, K. Itoh, and H. Matsuzaki, "An application of laser Raman spectroscopy to the study of a hereditary cataractous lens: On the Raman band for a diagnostic marker of cataractous signatures," *Curr. Eye Res.* 2: 489-492, 1983.
10. Y. Ozaki, A. Mizuno, K. Itoh, M. Yoshimura, T. Iwamoto, and K. Iriyama, "Raman spectroscopic study of age-related structural changes in the lens proteins of an intact mouse lens," *Biochemistry* 22: 6254-6259, 1983.



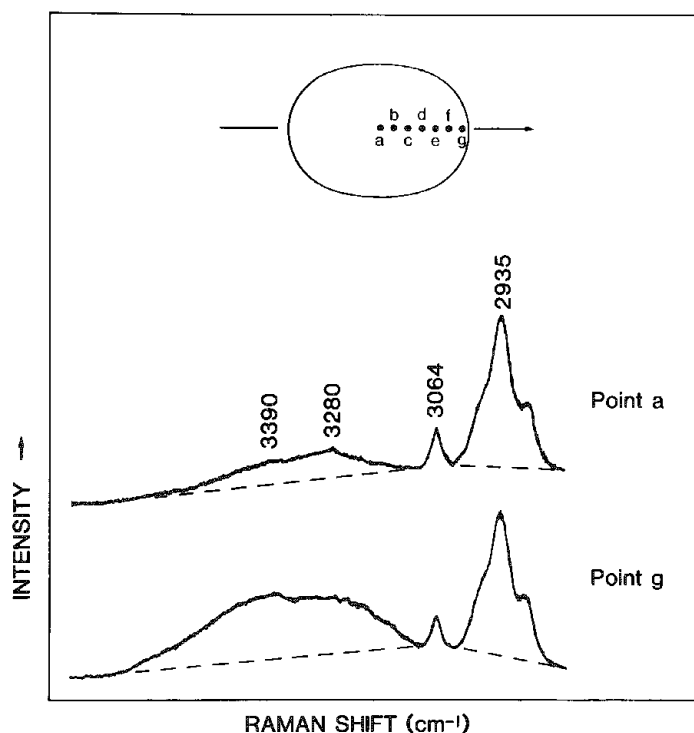


FIG. 1.--Raman spectra in  $3800\text{--}2800\text{cm}^{-1}$  region of point a and point g of 10-month-old rat lens. Raman spectra were measured for points a-g which are located at various distances from geometric center of lens: point a, 0; point b, 0.3 mm; point c, 0.6 mm; point d, 0.9 mm; point e, 1.2 mm; point f, 1.5 mm; point g, 1.8 mm.

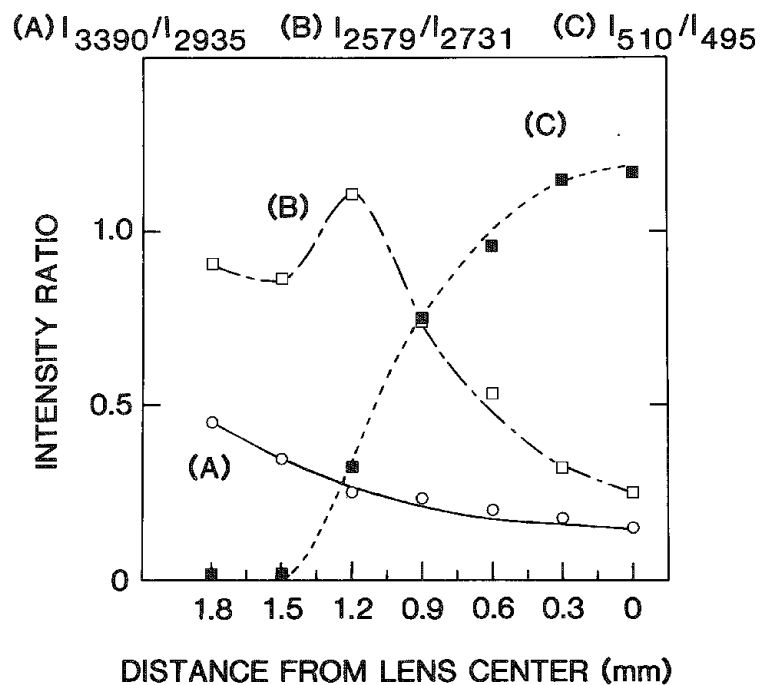


FIG. 2.--Horizontal axis profiles of lens water/protein ratio (A:  $I_{3390}/I_{2935}$ ), sulfhydryl (B:  $I_{2579}/I_{2731}$ ), and disulfide (C:  $I_{510}/I_{495}$ ) for 10-month-old rat lens.



## A FLUORESCENCE TECHNIQUE FOR DETERMINING THE POROSITY OF GEOLOGIC CORE SAMPLES ON A MACRO- AND MICROSCALE

R. A. Velapoldi and Norvald Gjelsvik

The porosity of reservoir rocks is important in estimating reservoir potential, size, and production performance as well as in basin modeling.<sup>1</sup> Generally, porosity has been measured on core samples by use of adsorption of gases or liquids including helium, water, and mercury. However, these measurements provide a measurement of bulk or average porosity of a 1-2cm<sup>3</sup> sample or a crushed sample of similar original size.

Fluorescence microscopy has been used to yield enhanced carbonate petrography including previously uninterpretable depositional facies, diagenetic fabrics, and porosity relationships in highly dolomitized or recrystallized limestones<sup>2</sup>; and to recognize microporosity in sedimentary rocks.<sup>3</sup> Our interest has focused recently on being able to determine the porosity of core samples with a micrometer spatial resolution, so that changes in porosity could be measured on a more local scale with a more realistic view of the porosity gradients within a bulk sample. We present here a method for quantitatively measuring porosity of reservoir rocks on a spatial scale of a few micrometers using fluorescence microscopy. The procedure includes automated scanning of sandstone core thin sections from the North Sea and could be extended to other core rock types examined by geologists.

### Experimental

*Thin Sections.* Thin sections were prepared in the usual manner from sandstone cores chosen for their wide porosity values, ranging from 7 to 30% as determined by He adsorption measurements. Blocks of cores (normal size, 2 × 2 cm; large size, 8 × 15 cm) were cut. The small-size thin sections were prepared from cores that suggested relatively homogeneous porosities under examination; the large-size thin section was selected from a core that suggested variable porosity under microscopic examination as a function of x,y location. These cores were impregnated with the clear epoxy normally used in thin-section production, attached to glass slides, and ground to a nominal 30 μm on a lapping machine. A fluorescing naphthylimide-type dye (Fluorol 755, Day-Glo Color Corp., Cleveland, Ohio) rather than the normal blue visible dye was dissolved in the epoxy to give varying dye concentrations (0.03-10 g/kg). The varying concentrations were used to test two types of measurement conditions: (1) optically dense solutions to give essentially "quantum counter" thin sections for surface fluorescence only, and

(2) optically thin solutions to give thin sections for volume fluorescence measurements.<sup>4,5</sup> The former were not suitable for this study; the latter were used with absorbance values through the thin section measured to be less than 0.05 absorbance units per 30 μm to reduce fluorescence measurement errors.<sup>6</sup>

The 2 × 2cm thin sections were prepared with a strip of fluorophor-doped epoxy on one end to serve as an internal standard, with fluorescence flux corresponding to 100% porosity; the large 8 × 15cm thin section had 6 slots (0.5 × 1 cm) cut into the edge of the thin section to provide the internal standard consisting of only fluorophor-doped epoxy.

*Fluorescence Measurements.* Fluorescence microscopic measurements were made on a Leitz MPV 3 microscope photometer equipped with a Ploem illuminator for incident excitation and scanning stage, monochromator, or mirror, all under computer control. A Ploemopak "D" cube was used giving an excitation band from 355 to 425 nm (wavelengths for 50% transmittance). Dry objectives of 2× or 40× were used and gave nominal magnifications of 25× and 500×, respectively. For most of the measurements, the measuring aperture was 20 μm × 1.1 mm (2× objective). The excitation aperture was set just slightly larger than the measuring aperture to assure that excitation radiation fell on the sample only during the short time when measurements were being made to reduce fluorophor fading. The matrix size for the small thin section measurements, usually 150 × 6, yielded a total of 900 fluorescence flux measurements covering an area of approximately 1.1 × 1.8 cm; the matrix for the large thin section was 525 × 8 and yielded a total of 4400 measurements covering an area of approximately 6 × 2 cm (see raster A in Fig. 1). A smaller matrix of 300 × 20 was also used for the large thin section with the measuring aperture 5 × 10 μm, which gave 6000 measurements covering an area of 3750 by 250 μm (raster B in Fig. 1).

Fluorescence flux values for the internal standard corresponding to 100% porosity were measured in three repetitive 150 × 1 raster movements, followed by 3 to 5 repetitive raster movements on each thin section. (The scanning stage returns to the starting x,y location after each raster movement is completed.) Fluorescence flux values at each x,y location usually had a coefficient of variation (CV) of less than 1% for the standards and generally less than 2% for the thin sections. The total variation of fluorescence flux for the strip of standard covering approximately 1.1 cm ranged from about 1% to as much as 8%. No major variation could be observed in the thin section thickness. (Variations were about 1 μm or less, which would give rise to expected variations in fluores-

Both authors were at Norsk Hydro Research Centre, Bergen, Norway, when work was done; author Velapoldi is at present at the National Bureau of Standards (Center for Analytical Chemistry, Gaithersburg, MD 20899).

cence flux measurements of about 3%. The 100% porosity values derived from each x location in the standard strip were used to calculate the porosity values at the corresponding x locations in the thin section. For the large thin section, the 100% porosity values were measured at 5 of the 6 slots and were averaged. The measured fluorescence flux values within any slot varied by less than 1%; the measured values for all the slots gave a CV of 2.2%.

Blank readings were made and subtracted from the standard and thin section fluorescence flux values. We calculated the percent porosities for each x,y location in the matrix by dividing the thin section corrected fluorescence flux values by fluorescence flux values from the standard and multiplying by 100, and determined average porosities for the thin sections by summing the individual porosity values and dividing by the total number of x,y elements in the matrix for that thin section.

### Results and Discussion

The overall porosities measured by helium adsorption and fluorescence microscopy are summarized in Table 1. Sandstone cores, especially from the North Sea region, contain clays such as kaolinite. Helium porosity values are generally higher by 2 to 5% (and sometimes as much as 15%) than porosities determined by (for example) point counting; in general, the more clay a sample contains, the larger the differences. Considering these facts, excellent agreement between the porosity values for the two techniques is observed, with the values for fluorescence microscopy on an average approximately 3% lower than the He values. The individual porosity values calculated for each x,y location in the small thin sections are represented by the plots of Fig. 2. The average data from Table 1 show the agreement with other techniques, and the figures and porosity values for each x,y location demonstrate the real porosity variations in thin sections that appeared homogeneous. In Fig. 2(b), for example, low porosities are noted for one side of the thin section and higher porosities are noted for the opposite edge, which suggests flow or channeling characteristics not recognized from visual inspection.

The large thin section was also measured in this fashion and gave an average porosity of 11.6%. From Fig. 3, differences in porosity as a function of core depth (X axis) are observable, with the porosity changing from values of approximately 17% at the right and left sides of the thin section to a porosity approaching 8% in the center of the thin section. Although this determination could be made with multiple samples (every 1 cm) when bulk porosities are measured, 8 to 10 times the effort would be required. In addition porosities at individual x,y locations range from 3.4 to 94%; these data, measured every 50  $\mu\text{m}$ , simply would not be available if bulk porosity measurements were made.

The data for the large and small thin sections were obtained by use of a measurement aperture that was 20  $\mu\text{m}$   $\times$  1.1 mm, so that it

does not really give porosities on a micrometer scale in both the x and y directions. Thus, porosities were determined with a measuring aperture 5  $\times$  10  $\mu\text{m}$  (smallest used was 5  $\times$  5  $\mu\text{m}$  with 500 $\times$  magnification). As can be seen from Fig. 1, the large thin section was fractured down the center. Porosity values were obtained by traversing the fracture in a 300  $\times$  20 matrix (raster B in Fig. 1), which gave 6000 data points (matrix elements) that covered a rectangle 3750  $\times$  250  $\mu\text{m}$ , from which Fig. 4 was constructed. The fracture in the center of the thin section (porosities vary from 15 to 75%) is easily observed; porosities from various 5  $\times$  10  $\mu\text{m}$  areas of the thin section range from 0.3 to 100%, not unexpected at those small measurement areas. Thus, Fig. 4 represents porosity data on a micrometer scale in both x and y directions.

### Conclusions

We have developed a fluorescence procedure that can be used to determine the porosity of geologic thin sections on a macro- or micro-scale and that provides excellent agreement with porosities determined by other procedures. This information complements data obtained by other micro techniques used to determine chemical or physical properties; e.g., it could provide insight in assessing accurate element concentrations determined by microprobe techniques.

### References

1. R. M. Sneider et al., "Methods for detection and characterization of reservoir rock, deep basin gas area, western Canada," *J. Pet. Tech.* 1725-1734, September 1983.
2. J. J. Dravis and D. A. Yurewicz, "Enhanced carbonate petrography using fluorescence microscopy," *J. Sed. Petrology* 55: 795-804, 1985.
3. J. E. Yanguas and J. J. Dravis, "Blue fluorescent dye technique for recognition of microporosity in sedimentary rocks," *J. Sed. Petrology* 55: 600-602, 1985.
4. R. A. Velapoldi et al., "Inorganic ion-doped glass fibres as microspectrofluorimetric standards," *J. Microscopy* 103: 293-303, 1976.
5. R. A. Velapoldi and N. Gjelsvik (in preparation).
6. C. A. Parker, *Photoluminescence of Solutions*, New York: Elsevier, 1968, 20.

TABLE 1.--Porosity of sandstone core thin sections measured by He adsorption and fluorescence microscopy.

He	Porosity, %		
	Fluorescence Microscopy		
	0.1 g/kg <sup>a</sup>	1.0 g/kg <sup>a</sup>	Avg. $\Delta$
7.0	3.3	3.8	-3.4
14.0	11.2	12.5	-2.1
20.0	16.3	16.8	-3.4
26.0	23.6	21.8	-3.3
30.0	28.5	27.2	-2.2

<sup>a</sup>fluorophor concentration

FIG. 1.--Portion of large-size thin section showing raster A covering  $6 \times 2$  cm and raster B covering  $3750 \times 250 \mu\text{m}$ .

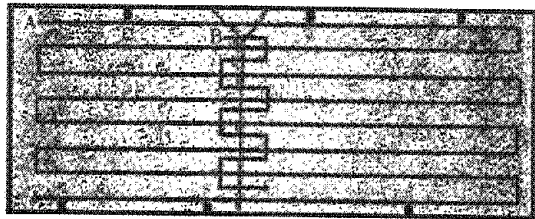


FIG. 2.--Five small sandstone core thin sections with porosities measured by fluorescence microscopy: (a) 3.3%; (b) 11.2%; (c) 16.3%; (d) 23.6%; and (e) 28.5%. Fluorophor concentration, 0.1 g/kg; measurement aperture,  $20 \mu\text{m} \times 1.1 \text{ mm}$ ; data points, 900.

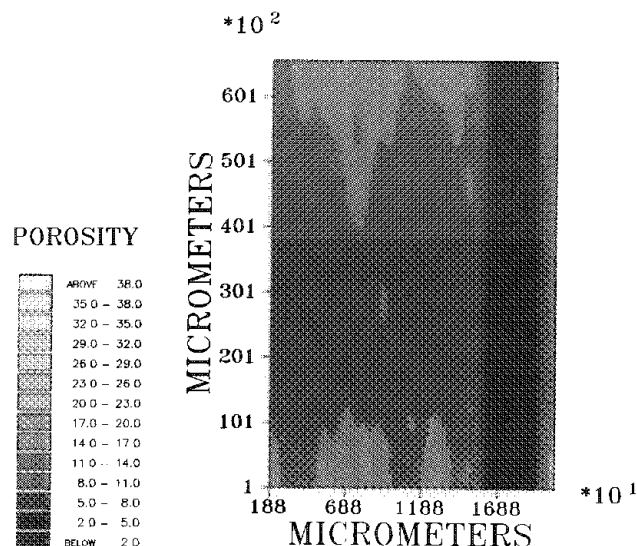
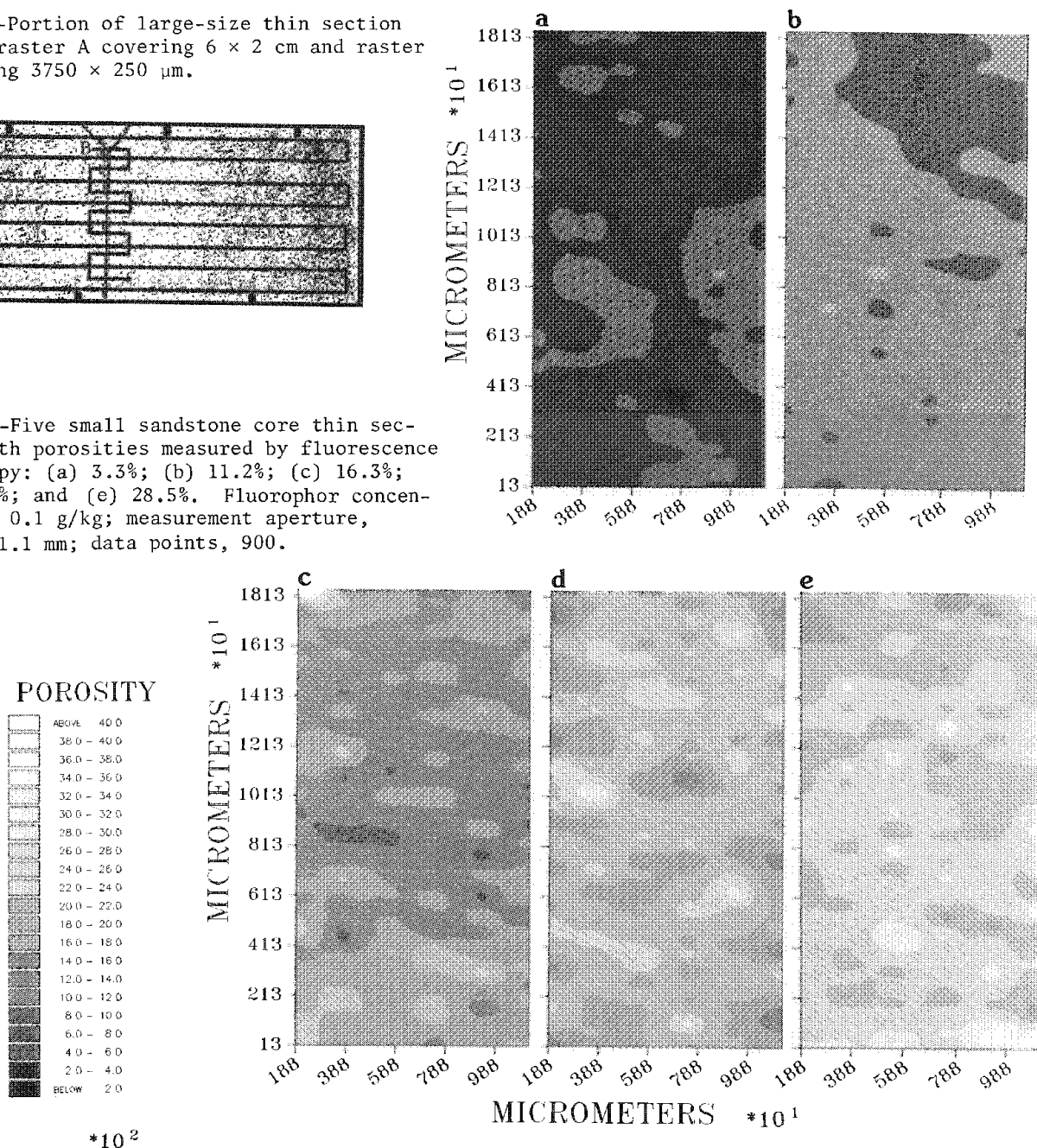


FIG. 3. Porosity variations of large thin section represented by raster A in Fig. 1; fluorophor concentration, 0.1 g/kg; measurement aperture,  $20 \mu\text{m} \times 1.1 \text{ mm}$ ; data points, 4400.

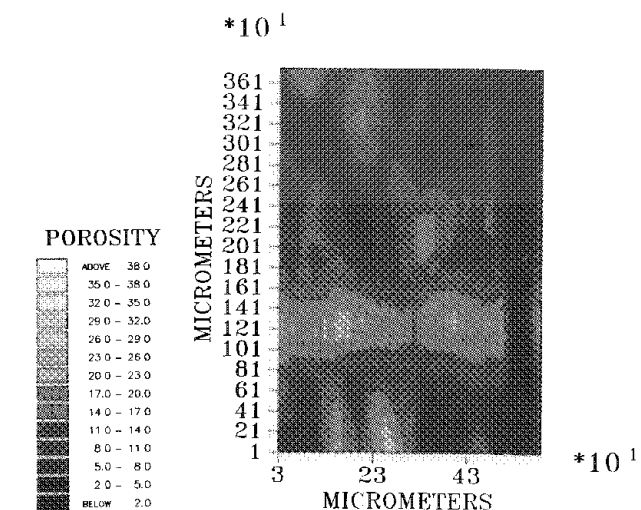


FIG. 4.--Porosity variations of large thin section represented by raster B in Fig. 1; fluorophor concentration, 0.1 g/kg; measurement aperture,  $5 \times 10 \mu\text{m}$ ; data points, 6000.

## USE OF A LASER RAMAN MICROPROBE TO TRACE GEOLOGICAL REACTIONS

J. D. Pasteris and Brigitte Wopenka

Geologists frequently want to monitor the progress and process of reactions in minerals. Before a reaction has gone to completion, the reaction zone commonly consists of thin bands of (or finely intergrown) secondary mineral phases that are replacing the primary phase(s). Identification of these secondary phases, whether they constitute an equilibrium or disequilibrium assemblage, is necessary in order to determine the reaction mechanism and reaction path. Laser Raman microprobe (LRM) spectroscopy provides a means by which the geologist can simultaneously view a reaction front and analyze the mineral and fluid phases on a microscopic scale in a rock chip. The following are preliminary results from studies in our laboratory concerning mafic and ultramafic igneous rocks.

### *Experimental*

Our instrument is a RAMANOR U-1000 (Instruments SA) laser Raman microprobe single-channel analyzer. We operate with the 514nm line of a SW Ar<sup>+</sup> laser. Typical analytical conditions are approximately 10 mW of laser power at the sample surface, spectral counting time of 10 s per point, stepping intervals of either 1 cm<sup>-1</sup> (e.g., for serpentines or graphite) or 0.5 cm<sup>-1</sup> (for volatiles and carbonates), and a spectral resolution of about 5 cm<sup>-1</sup>. Under these analytical conditions, fluid inclusions as small as 2 μm in diameter give strong Raman peaks for CO<sub>2</sub>. The preferred samples are doubly polished unmounted wafers of rock. However, geological samples frequently are only available as doubly polished thin sections, which are less desirable because of the fluorescence that is commonly induced by the laser beam in the epoxy mounting medium. The microscope objectives used are 40× (N.A. = 0.75), 80× (N.A. = 0.90), and 160× (N.A. = 0.95). Depending on the objective used, the beam spot can be as small as 1 μm.

The authors are in the Department of Earth and Planetary Sciences and the McDonnell Center for the Space Sciences at Washington University, Box 1169, St. Louis, MO 63130. They thank their colleague T. A. Abrajano for initiating the analyses to demonstrate the possible usefulness of Raman spectroscopy in distinguishing among the serpentine phases. They also thank the Smithsonian Institution and F. R. Boyd for the loan of the Kao kimberlite sample (USNM #1846) and R. G. Coleman of the U.S. Geological Survey for providing the serpentine standards. The work was supported in part by NSF grant EAR-8408004. JDP gratefully acknowledges the funds provided by Instruments SA, Inc., which helped to make it possible to present this paper at the Conference.

### *Fluid and Solid Inclusions in Mantle Xenoliths and Kimberlites*

When basaltic and kimberlitic igneous rocks explosively erupt, they frequently bring to the surface xenoliths of rock from the earth's upper mantle. Many of the silicate grains in the xenoliths, for instance olivine, contain trails of fluid inclusions. The latter most likely represent episodes in which the solid olivine grains were fractured at depth and then rehealed, capturing some of the ambient fluid. Studies have shown this fluid to be mostly CO<sub>2</sub>, which is believed to reflect processes that the original C-O-H mantle volatiles have undergone during their rise and chemical interactions with surrounding materials as reviewed by Roedder<sup>1</sup> and Pasteris.<sup>2</sup> However, small amounts of CO were detected by LRM analysis in one case.<sup>3</sup>

We have used the LRM to monitor possible changes in these CO<sub>2</sub>-dominant fluids due to late-stage processes as their host rocks neared the surface. The volatiles CO<sub>2</sub>, CO, H<sub>2</sub>S, and CH<sub>4</sub> were analyzed for in fluid inclusions in mantle xenoliths from the San Carlos volcanic field in Arizona and from Kilbourne Hole in New Mexico. In the larger (>10 μm) inclusions in the xenolith olivines, only CO<sub>2</sub> was detected, confirming previous findings.<sup>2</sup> Additional experiments were done to determine whether there was any detectable change in fluid composition in the following cases in which secondary reactions might be expected: (1) fluid inclusions along fractures that also are lined with glass (injected basaltic melt), (2) fluid inclusion trails in xenolith olivines that are in direct contact with the host basalt, and (3) trails of minute inclusions that appear to represent bursting of larger inclusions (during rapid rise and depressurization of the xenoliths) with subsequent recapture of the fluids. In all three cases, CO<sub>2</sub> was the only species that could be detected. This lack of change in fluid composition suggests very similar oxygen fugacity conditions in the basaltic melt that transported the xenoliths and in that portion of the upper mantle where the majority of xenolith fluid inclusions last equilibrated.

In contrast to the above, there are cases in which previously CO<sub>2</sub>-filled inclusions in xenoliths and other rocks record the results of subsequent fluid and fluid-solid re-equilibration. We used the LRM to monitor such changes in an olivine grain in a kimberlite from the Kao kimberlite pipe in Lesotho. The sample shows progressive serpentinization of the olivine grains, accompanied by apparently simultaneous precipitation of extremely fine graphite. The latter produces black rims around the olivine remnants<sup>4</sup> (Fig. 1a). The inclusions in this sample (Figs. 1b,c,d) do not give Raman signals for any of the volatiles listed above, in spite of the fact that

CO<sub>2</sub>-filled fluid inclusions are ubiquitous in kimberlite olivines. Although the inclusions in this sample apparently do not (no longer?) contain volatiles, both colorless anisotropic

grains and a black opaque material (separately or together) are observed partially to fill many of them.

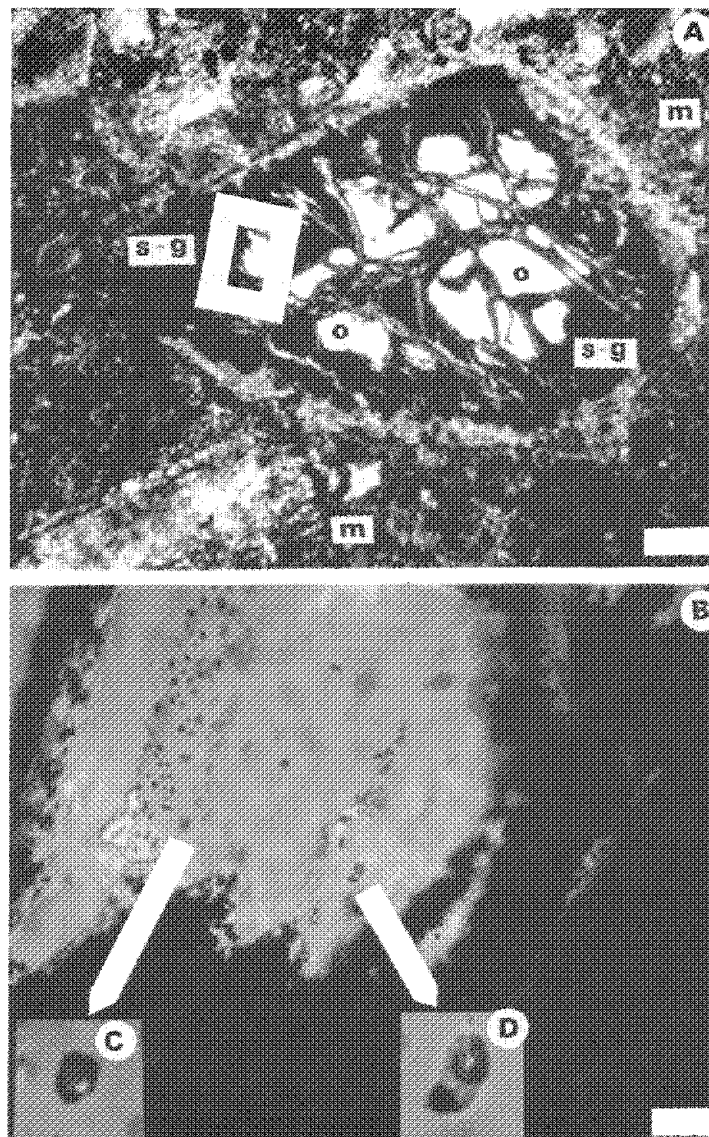


FIG. 1.--(A) Serpentinized, graphitized (s-g) olivine (o) in kimberlite matrix (m) from Kao, Lesotho; scale bar = 200  $\mu$ m. (B) Enlarged view of part of Fig. 1(A) (white rectangle), showing trails of fluid inclusions; scale bar = 25  $\mu$ m. (C) Type-1 inclusion analyzed in this study. (D) Type-2 inclusion analyzed in this study.

Two types of the black material are optically distinguishable by their texture. Type-1 inclusions (Fig. 1c) have a gray coating on their inside, presumably from dispersed, very fine-grained ( $<1\mu\text{m}$ ) opaque material. Type-2 inclusions (Fig. 1d) are optically much clearer, and frequently have a small ( $\sim 1.5\mu\text{m}$ ), distinct black grain on their rim. In spite of their distinctly different appearances, both types of black material show LRM spectra for well-ordered graphite (Fig. 2); i.e., there is a well-developed peak around  $1600\text{ cm}^{-1}$ , but no feature at about  $1350\text{ cm}^{-1}$ .<sup>5,6</sup> Although graphite precipitates have been identified before in mantle rocks and some possible mechanisms for their production have been discussed,<sup>4,7-8</sup> this is the first report to our knowledge of its identification and characterization by Raman spectroscopy. The association of these graphite-bearing inclusions with the graphite-serpentine front that is consuming the olivines suggests that the graphite (at least in the inclusions) may have precipitated from pre-existing  $\text{CO}_2$  during the serpentinization. If hydrogen that probably was released during serpentinization<sup>9-10</sup> reacted with the  $\text{CO}_2$ , the bulk composition of the fluid could have entered the field of stability of graphite. If this was the mechanism of graphite precipitation in our sample, it is interesting that none of the inclusions show the presence of  $\text{CH}_4$ , for which we estimate our detection limit to be about 1 bar partial pressure for inclusions of the size shown in Fig. 1.<sup>11</sup>

For Type-1 graphite-coated inclusions, the lack of detection of any volatiles may be an optical problem. We have done experiments to simulate the thickness of fine-grained graphite coating necessary to block the Raman signal of a volatile species. A carbon-coater was used to sputter layers of carbon of known thickness onto a polished silicon wafer. A  $600\text{\AA}$  coating of carbon reduces the count rate to 10% of that for an uncoated silicon wafer. Thus, it may be very difficult to obtain Raman spectra of any volatiles present in Type-1 inclusions.

The colorless, anisotropic solids ( $\sim 2\mu\text{m}$ ) that occur in both Type-1 and Type-2 inclusions also were analyzed by LRM spectroscopy. In each case, a strong carbonate band was detected, but the peak positions for individual grains vary greatly, suggesting a large variation in the Ca:Mg ratio.<sup>12</sup> Magnesian carbonates were identified previously by electron microbeam techniques as small inclusions in mantle rocks.<sup>13-15</sup> Magnesite and dolomite are inferred to be the stable  $\text{CO}_2$ -bearing phases over a wide range of depths in the upper mantle.<sup>16-18</sup>

From our LRM analyses, there appears to be a correlation of magnesian carbonates (magnesite or dolomite) with the graphite-coated Type-1 inclusions and of calcite with the Type-2 clear inclusions that have graphite on their rims. The reasons for these associations are unclear. Dependence on oxygen fugacity seems unlikely, since iron does not appear to be present. Recrystallization could be important if an original Ca-Mg carbonate exsolved into a more calcic and a more magne-

sian phase. However, there is no evidence seen in this sample for coexistence of two different carbonates in the same inclusion. In contrast, in similar inclusions in a serpentinized but ungraphitized kimberlite sample (DTP-5) from the Dutoitspan kimberlite pipe in South Africa, we identified (also by LRM spectroscopy) minute magnesite and calcite grains that occur together in inclusions in olivines. This finding suggests that some of the calcite and magnesite inclusions in xenoliths may have the same origin.

#### *Tracing the Progressive Serpentinization of Kimberlites*

Serpentinization is a hydration reaction that occurs in many olivine-bearing igneous rocks below about  $500\text{ C}$ . Documentation of this reaction is useful in characterizing the influx of water and the molar proportion of water compared to other volatile species. Because there are three major recognized serpentine phases, each with an individual field of stability, identification of the specific phase can provide additional information on intensive parameters such as temperature.<sup>19-21</sup>

In many kimberlites and some mantle xenoliths, there are serpentines of different colors and textures, which in some cases show a zonal pattern that is suggestive of multiple episodes of serpentinization. In an earlier study,<sup>22</sup> 1mm-wide serpentinized rims on olivine grains in samples from the De Beers kimberlite from South Africa were removed with a dental drill and analyzed by x-ray diffractometry. From peak widths and positions, all that could be inferred is that the material is a very poorly crystallized serpentine. Furthermore, for the multiple thinner zones of serpentine that in many cases occur in kimberlites, a microbeam technique such as LRM spectroscopy is necessary to distinguish the intergrown phases.

To obtain reliable Raman spectra for reference, we acquired one well-characterized powdered sample each of antigorite, lizardite, and chrysotile from Dr. R. G. Coleman of the U.S. Geological Survey.<sup>23</sup> Our preliminary analyses on these samples (Fig. 3) indicate that the major differences among the serpentines occur in the bands at about  $690\text{ cm}^{-1}$  (single peak for chrysotile and lizardite, peak with shoulders for antigorite) and in the OH-stretch region of about  $3660$  to  $3720\text{ cm}^{-1}$  (single peak or peak with shoulder for chrysotile and lizardite, well-resolved double peak for antigorite). Antigorite also shows a strong band at about  $1050\text{ cm}^{-1}$ , which does not appear in the spectra for the other serpentine phases. Additional standards are being obtained to confirm these observations.

In the partially serpentinized kimberlite DTP-5 described above, there are optically distinct zones of fibrous alteration rimming the olivine grains. The Raman spectrum of the outermost rim (Fig. 3) shares spectral features with all the serpentine standards. The innermost zone of bladed material shows no spectral features for olivine, only weak features where two of the strongest serpentine bands occur ( $\sim 390$ ,  $690\text{ cm}^{-1}$ ), a distinctly re-

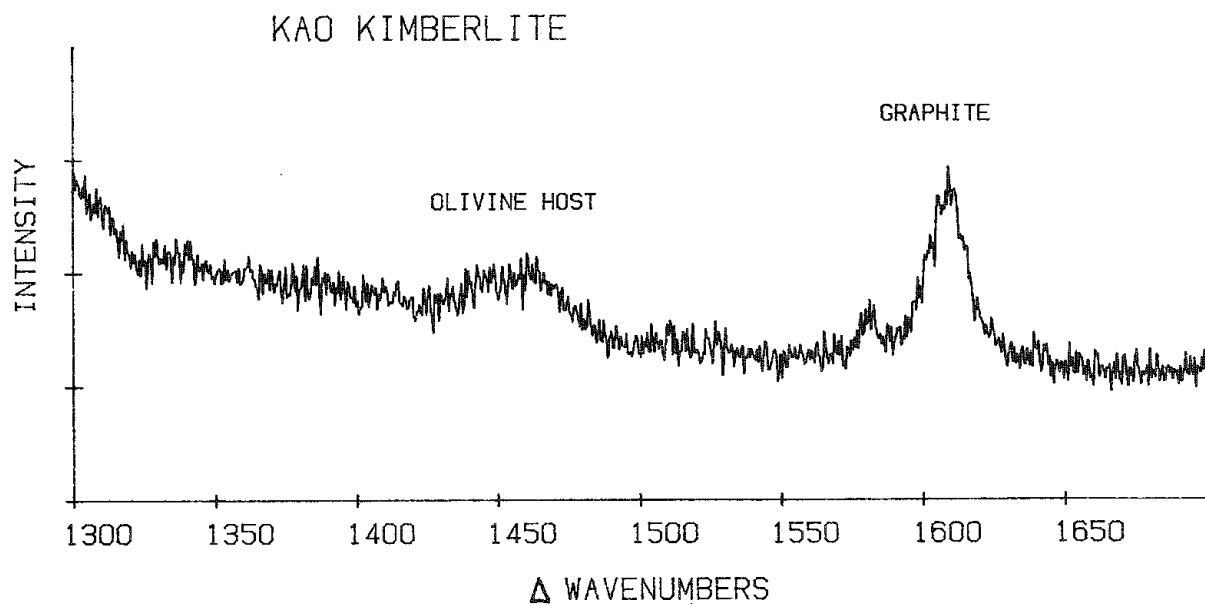


FIG. 2.--Raman spectrum of black coating in Type-1 inclusion as shown in Fig. 1(C).

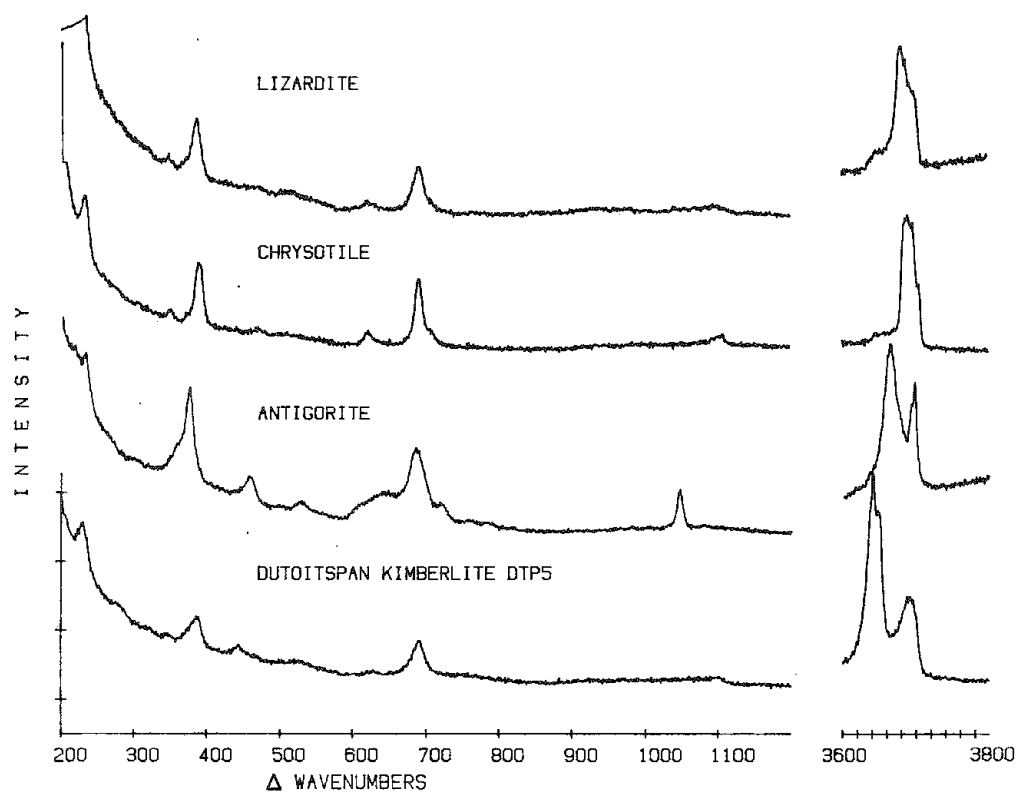


FIG. 3.--Raman spectra of three serpentine standards and one kimberlite sample.



solved double peak in the OH-stretch region ( $3600\text{--}3800\text{ cm}^{-1}$ ), and an additional broad feature at about  $535\text{ cm}^{-1}$ . This material may not yet have fully converted to serpentine. The optically clear, apparently unaltered olivine core in this sample showed an unusual Raman spectrum: in addition to the bands due to olivine, we detected a weak but clearly recognizable double peak or single peak with a shoulder in the OH-stretch region. However, a totally fresh olivine from the Benfontein sill kimberlite in South Africa showed only olivine bands and no OH-stretch. Thus, the LRM had demonstrated the capability to detect incipient hydration in an olivine core that is not visibly altered.

The fully serpentinized De Beers kimberlite, in which the serpentine appears structurally featureless both optically and by XRD analysis, gives a Raman spectrum interpreted to be that of poorly crystallized lizardite or chrysotile. The peaks are broad and weak compared to those in the standards, and the OH-stretch is represented by a single broad peak.

### Conclusion

Our ongoing studies have demonstrated the ability of the LRM spatially to distinguish and identify individual phases that represent either original unaltered material in a rock or the products of mineral and mineral-fluid reactions. Unlike techniques involving bulk extraction and analysis of volatiles, the LRM permits analysis of individual inclusions at measured distances to a reaction front. We have further shown the powerful capability of the LRM to distinguish, in situ, "pseudopolymorphs" (serpentine phases) and minute individual phases in a solid solution series (carbonate phases), which is difficult by any other technique. In summary, the LRM can provide unique information that may be essential in the determination of the actual reaction mechanisms in geological materials.

### References

1. E. Roedder, *Fluid Inclusions*, Washington, D.C.: Mineralogical Society of America, 1984.
2. J. D. Pasteris, "Fluid inclusions in mantle xenoliths," in P. H. Nixon, Ed., *Mantle Xenoliths*, New York: Wiley, 1987 (in press).
3. S. C. Bergman and J. Dubessy, "CO-CO<sub>2</sub> fluid inclusions in a composite peridotite xenolith: Implications for oxygen barometry," *Contrib. Mineral. Petrol.* 85: 1-13, 1984.
4. J. D. Pasteris, "Occurrence of graphite in serpentinized olivines in kimberlite," *Geology* 9: 356-359, 1981.
5. P. Tuinstra and J. L. Koenig, "Raman spectrum of graphite," *J. Chem. Phys.* 53: 1126-1130, 1970.
6. C. Beny-Bassez et al., "First applications of the Raman microprobe MOLE to the study of a series of coals," *Comptes rendus Acad. Sci. Paris* 293(ser.II): 509-512, 1981.
7. E. A. Mathez and J. R. Delaney, "The nature and distribution of carbon in submarine basalts and peridotite nodules," *Earth and Plan. Sci. Lett.* 56: 217-232, 1981.
8. E. A. Mathez et al., "The geochemistry of carbon in mantle peridotites," *Geochim. Cosmochim. Acta* 48: 1849-1859, 1984.
9. P. Ramdohr, "A widespread mineral association connected with serpentinization," *Neues Jb. Mineral., Abhand.* 107: 241-265, 1967.
10. B. R. Frost, "On the stability of sulfides, oxides, and native metals in serpentinite," *J. Petrol.* 26: 31-63, 1985.
11. B. Wopenka and J. D. Pasteris, "Raman intensities and detection limits of geochemically relevant gas mixtures: Empirical calibration of a laser Raman microprobe," *Anal. Chem.* (submitted).
12. W. D. Bischoff, S. K. Sharma, and F. T. Mackenzie, "Carbonate ion disorder in synthetic and biogenic magnesian calcites: A Raman spectral study," *Amer. Mineral.* 70: 581-589, 1985.
13. T. R. McGetchin and J. R. Besancon, "Carbonate inclusions in mantle-derived pyropes," *Earth and Plan. Sci. Lett.* 18: 408-410, 1973.
14. M. R. Roedder and E. A. Mathez, "Magnetite and other minerals in fluid inclusions in a lherzolite xenolith from an alkali basalt," *Terra Cognita* 2: 229, 1982.
15. T. Andersen et al., "The trapped fluid phase in upper mantle xenoliths from Victoria, Australia: Implications for mantle metasomatism," *Contrib. Mineral. Petrol.* 88: 72-85, 1984.
16. D. H. Eggler, "The effect of CO<sub>2</sub> upon partial melting of peridotite in the system Na<sub>2</sub>O-CaO-Al<sub>2</sub>O<sub>3</sub>-MgO-SiO<sub>2</sub>-CO<sub>2</sub> to 35 kb, with an analysis of melting in a peridotite-H<sub>2</sub>O-CO<sub>2</sub> system," *Amer. J. Sci.* 278: 305-343, 1978.
17. P. J. Wyllie, "Magmas and volatile components," *Amer. Mineral.* 64: 469-500, 1979.
18. M. Olafsson and D. H. Eggler, "Phase relations of amphibole, amphibole-carbonate, and phlogopite-carbonate peridotite: Petrologic constraints on the asthenosphere," *Earth Plan. Sci. Lett.* 64: 305-315, 1983.
19. B. W. Evans et al., "Stability of chrysotile and antigorite in the serpentine multisystem," *Schweiz. mineral. petrogr. Mitt.* 56: 79-93, 1976.
20. B. W. Evans, "Metamorphism of Alpine peridotite and serpentinite," *Annual Rev. Earth Plan. Sci.* 5: 397-447, 1977.
21. L. J. Caruso and J. V. Chernosky, "The stability of lizardite," *Can. Mineral.* 17: 713-717, 1979.
22. J. D. Pasteris, *Opaque Oxide Phases of the De Beers Pipe Kimberlite (Kimberley, South Africa) and Their Petrologic Significance*, Ph.D. thesis, Yale University, New Haven, Conn., 1980.
23. N. J. Page and R. G. Coleman, *Serpentine Mineral Analyses and Physical Properties*, U.S. Geological Survey Prof. Paper 575-B, B103-B107, 1967.

NOTE ADDED IN PROOF. Additional LRM analyses on serpentine standards from F. J. Wicks of the Royal Ontario Museum suggest that it is very difficult to distinguish lizardite from chrysotile by Raman spectroscopy. However, the Raman spectrum of antigorite seems to be distinct from those of the other two phases.



## MULTICHANNEL MICROFLUOROMETER WITH LASER EXCITATION

J. Barbillat, P. Dhamelin-court, J. P. Cornard, and B. Lenain

With lasers as sources of excitation of Raman scattering and fluorescence emission and the ongoing developments of instrumentation for optical spectroscopy, microprobing techniques have matured to the point at which nondestructive microanalysis has now become routinely practicable.<sup>1,2</sup> The laser sources present unquestionable advantages in terms of excitation efficiency and spatial resolution because they can be focused onto a spot whose size is only limited by diffraction. This size can be as small as 0.5  $\mu\text{m}$  when high numerical aperture objectives are used.

However, these intense sources must be used very carefully when fragile materials are analyzed because high irradiances induce generally rapid modification of the probed area of the sample. Most of the time studies of fragile materials thus require recording times as short as possible with low laser power at the sample. That is why microprobes that employ spectrographic dispersion with a very sensitive multichannel detector are now being developed and are especially designed to allow both Raman and fluorescence experiments on the same sample.

At the 1985 MAS meeting we introduced a microfluorometer with  $\text{Ar}^+$  laser excitation and multichannel diode array detection based on the technology we developed a few years ago for micro-Raman instrumentation.<sup>3</sup> This instrument has clearly demonstrated the advantage of multichannel detection to improve the sensitivity while maintaining the input laser power far below the damage threshold of the sample. Since this first prototype, many improvements have been implemented in order to increase the straylight rejection and to extend the capability of the instrument by use of UV excitation to biological samples.

This instrument consists of (1) a UV laser (He-Cd Omnichrome) emitting a few milliwatts at 325 nm; (2) a microscope (Olympus BH-2) with a reflected light fluorescence attachment and UV optics, which permits the observation of the sample by conventional microscopy, as well as focusing of the laser beam onto the sample and collection of the fluorescence or Raman radiations; (3) a fully reflective coupling optics between the microscope and the spectrograph, which allows one to analyze any point of the sample located in the field of view of the microscope without moving the sample (spatial resolution: about 1  $\mu\text{m}$ );<sup>4</sup> and (4) a triple spectrograph divided into two sections, a zero-dispersion premonochromator and a spectrograph, a configuration based on three identical Czerny-Turner monochromators that includes two sets of dispersors: three identical gratings (1800 gr/mm) and three prisms (SF 55 glass) all mounted on the same shaft,

which has the advantage that the detector always receives the band pass determined by the prefilter stage whatever the wavelength setting, and that spectral resolution and band pass can be chosen by positioning the proper dispersor (low resolution); prism; higher resolution; gratings), switching from the prisms to the gratings accomplished simply by translation of the shaft.

The premonochromator is used to reject the high-intensity exciting line with a better efficiency than colored glass or notch filters. The gratings used in the prefilter stage result in a dispersion of 61  $\text{cm}^{-1}/\text{mm}$  at 400 nm. Under these conditions, the fixed intermediate slit width (12 mm) determines a spectral coverage of 770  $\text{cm}^{-1}$ . With the prisms, almost all the visible radiations are transmitted through the intermediate slit. The final dispersion of the light is achieved by the spectrograph stage, which focuses the spectrum onto the multichannel detector, and consists of (a) a multichannel intensified array detector previously described elsewhere,<sup>5</sup> and (b) a microcomputer (IBM AT) for total system control: wavelength setting, laser positioning on the sample, data acquisition, and treatment.

There are potential applications of this instrument in intracellular fluorescence of single cells.

### References

1. P. Dhamelin-court, J. Barbillat, and M. Delhay, "Laser Raman microprobing techniques," *J. de Physique* (Colloque C.2) 45: 1984.
2. E. S. Etz and J. J. Blaha, *Scope and Limitations of Single-particle Analysis by Raman Microprobe Analysis*, NBS Special Publication, Washington, D.C.: 1980, 533.
3. J. Barbillat et al., "Nondestructive microprobing by means of a new generation of instruments for Raman and fluorescence spectroscopy," *Microbeam Analysis--1985*, 15-18.
4. M. Delhay et al., "Device optimizing the coupling of two optical systems for the observation and analysis of objects," U.S. Patent 4 523 799, 1985.
5. M. Delhay et al., "A new generation of laser Raman microspectrometers: Micromars," *Microbeam Analysis--1982*, 275-278.

## MICRO-RAMAN SPECTROSCOPIC MEASUREMENT OF CARBON IN METEORITES AND INTERPLANETARY DUST PARTICLES

John Macklin, Don Brownlee, Sherwood Chang, and Ted Bunch

The most direct indication of the structure and distribution of carbon in material from which the solar system was formed is likely to be found in extraterrestrial debris, especially chondritic porous (CP) interplanetary dust particles (IDPs) that may be of cometary origin. Consequently, the study of carbon in extraterrestrial materials can lead to important information about the chemistry of carbon formation in the cosmos and is directly relevant to the distribution and structure of carbon on the primitive, prebiotic Earth. Among the many techniques used to study these materials, Raman spectroscopy has been demonstrated to be a useful, nondestructive probe of structural characteristics of carbon.<sup>1-4</sup> Moreover, Raman spectra of carbon in a number of chondritic meteorites have been reported.<sup>5</sup> The micro-Raman technique affords a means of extending these measurements to CP-IDP fragments that are 1  $\mu\text{m}$  or larger in size. In this paper some Raman measurements of carbonaceous IDPs are reported and compared with spectra of glassy carbon and the carbon in the Murchison and Allende meteorites.

### Experimental

Samples of the Murchison and Allende meteorites were obtained from Ted Bunch and Sherwood Chang at the NASA Ames Research Center. Polyvinylidene chloride (PVDC) was carbonized by George Yuen and Sherwood Chang following the procedure described in Ref. 6. Glassy carbon samples were obtained from Dave Fishbach. They are isotropic, highly disordered materials obtained from commercial sources and heat treated at 2000 C.<sup>2</sup>

The IDPs were collected from the stratosphere at an altitude of 20 km by impaction onto silicone-oil-coated plates mounted on D-2 aircraft operated by the Airborne Science Division of the NASA Ames Research Center. The samples were located on the collection plates and removed under an optical microscope, washed with solvents, and prepared for measurement by Don Brownlee. The details of sample collection and preparation are described in Ref. 7.

The Raman spectra were measured primarily by use of the 488.0nm line of a Spectra Physics 165 argon ion laser. Spectra were also recorded with 457.9 and 514.5nm excitation. The laser power was usually 10-20 mW and the spectrometer slit width was 200  $\mu\text{m}$ . The scat-

tered radiation was dispersed with a SPEX Industries 1477B Triplemate spectrometer equipped with a SPEX Micramate microsampling system based around a modified Zeiss microscope. Both diode array and photomultiplier detection were used to obtain the spectra. Integration times on the diode array ranged from 0.5 to 2 s for 20 collections. Data acquisition and storage were accomplished by use of two coupled Terak minicomputers. Samples were held on microscope slides and radiation collected by backscattering from the opaque materials.

### Results and Discussion

Typical Raman spectra of the Allende and Murchison meteorites, a PVDC carbon prepared at 800 C, glassy carbon, and a CP-IDP (SP-718) are compared in Fig. 1. The spectra include those most commonly measured bands at about 1360 and 1580  $\text{cm}^{-1}$  in the Raman spectra of various materials that contain elemental carbon. They are generally similar but the bands differ in details of width, shape, relative intensity, and frequency. The spectrum of highly ordered graphite consists of a single band at 1580  $\text{cm}^{-1}$  along with several overtones above 2000  $\text{cm}^{-1}$ . The intensity of bands at 1360 and 1620  $\text{cm}^{-1}$  and decreased intensity of the overtones in spectra of poorly graphitized materials is attributed to destruction of the  $D_{6h}$  symmetry of graphite and subsequent relaxation of selection rules.<sup>1-4</sup>

If similar Raman spectra can be taken to indicate similar structure, the comparisons in Fig. 1 suggest that the carbon in the IDP is structurally much like that in the Murchison meteorite, which is likely to be very poorly developed glassy carbon,  $d_{002} = 4.0 \text{ \AA}$ . The carbon in Allende is known to be more fully developed glassy carbon,  $d_{002} = 3.45 \text{ \AA}$ , described as entangled ribbons of graphitic carbon.<sup>8</sup> The Allende measurement is much like that of the well-developed glassy carbon in Fig. 1(e).

The 1360 $\text{cm}^{-1}$  band is generally more intense than that at 1580  $\text{cm}^{-1}$  in the Raman spectrum of glassy carbons.<sup>9</sup> It is unlikely that particle size is the most important factor in lowering the local symmetry in this material. This observation suggests that particle size approximations based upon the relative intensities of the 1360 and 1580 $\text{cm}^{-1}$  lines in the graphite spectrum<sup>4</sup> are not useful for glassy carbons and natural materials that include turbostratic carbon.<sup>5</sup> Furthermore, just as for well-developed crystalline graphite, the overtone at 2700  $\text{cm}^{-1}$  is clearly observed in the Raman spectrum of glassy carbon and the Allende meteorite but is not apparent in Raman spectra of microcrystalline graphite or poorly developed glassy carbon. Another reason for caution in applying the particle-size calcula-

Authors Macklin and Brownlee are at the University of Washington, Seattle, WA 98198; authors Chang and Bunch are at the NASA Ames Research Center, Moffett Field, CA 94035. Thanks are due to Prof. Dave Fishbach for supplying the glassy carbon samples and we gratefully acknowledge the support of NASA Grant NCC2-268.

tion is that the  $1580/1360\text{cm}^{-1}$  intensity ratio differs considerably with different excitation frequencies and the extent of this variation depends on the material, which shows the effect that the electronic character has on varying the resonance enhancement of the two bands.

The materials that are described as poorly developed glassy carbons can be further graphitized by heating. For example, after heating the Murchison material at 1500 C in Ar for 0.5 h, the Raman spectrum is nearly identical to that measured for the Allende material, including the overtone at  $2700\text{cm}^{-1}$ . The same 1500 C temperature treatment of the Allende sample led to very little change in the Raman spectrum. These observations suggest that a major difference in the development of carbon in the materials studied is the temperature that they have experienced and support the surmise that the carbon in the Allende meteorite has experienced a much higher temperature than that in Murchison. The effects of temperature treatments for given time periods on the Raman spectra of carbonaceous extraterrestrial materials can indicate the maximum temperature experienced by that material.

The Raman spectrum of the IDP included in Fig. 1 can be included in the classification by Walker et al.,<sup>10</sup> as type b, equally intense  $1360$  and  $1580\text{cm}^{-1}$  bands. They have identified their Essex, classified as an olivine particle, as included in this category. It is interesting that the major mineral identified in the Raman spectrum in Fig. 1(a) is olivine.

Micro-Raman measurements are clearly useful

for characterizing carbon in IDPs. We have measured Raman spectra of a large number of materials containing carbon in order to correlate with known structural characteristics of the materials and extend the utility of Raman measurements for obtaining structural information about carbon in IDPs.

#### References

1. R. J. Nemanich and S. A. Solin, *Physical Review* 20B: 392, 1979.
2. R. Vidano and D. B. Fishbach, *J. Am. Ceramic Soc.* 67: 13, 1978; Ext. Abs., 15th Carbon Conf., Philadelphia, 1981, 468; D. B. Fishbach and M. Couzi, *Carbon* 24: 365, 1986.
3. T. P. Mernagh et al., *Carbon* 22: 39, 1984.
4. F. Tuinstra and J. L. Koenig, *J. Chem. Phys.* 53: 1126, 1970; *J. Composite Mater.* 4: 492, 1970.
5. A. Lautie et al., *Nature* 292: 321, 1981; *Meteorites* 16: 301, 1981.
6. H. Marsh et al., *J. Appl. Cryst.* 8: 269, 1975; H. Marsh and W. F. K. Wynne-Jones, *Carbon* 1: 269, 1964.
7. D. E. Brownlee, in J. A. M. McDonnell, Ed., *Cosmic Dust*, New York: Wiley, 1978, 295-336.
8. P. P. K. Smith and P. R. Buseck, *Science* 212: 322, 1981.
9. M. I. Nathan et al., *J. Appl. Phys.* 45: 2370, 1974.
10. R. M. Walker et al., *Meteorites* 19: 269, 1984.

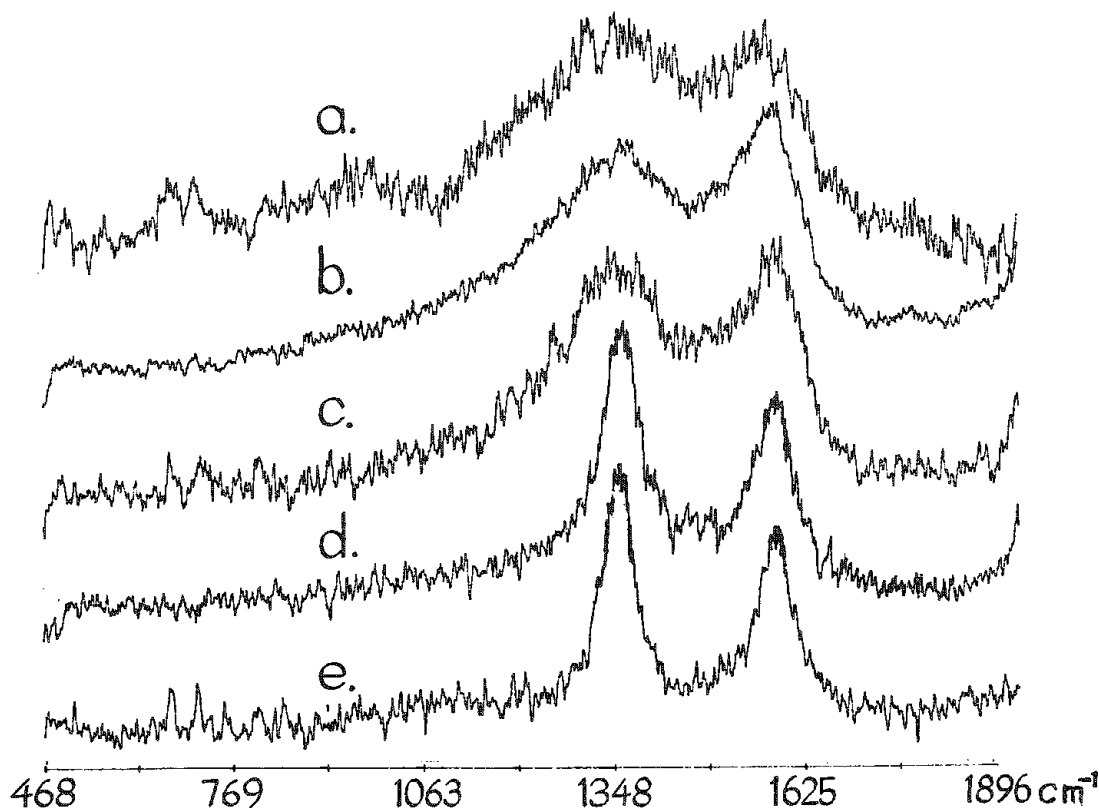


FIG. 1.--Typical Raman spectra: (a) IDP SP-71 $\beta$ , (b) Murchison meteorite, (c) 600 C PVDC carbon, (d) Allende meteorite, (e) glassy carbon.

## LASER RAMAN SPECTROSCOPIC STUDY OF THE OCULAR LENS IN RATS

Yu-Ling Chen, Shu-Ling Chang, and Shu-Tin Ma

In this paper we describe mainly the conformational changes of lens proteins in galactose cataracts by laser Raman spectroscopy.

Eye lens consists of water-soluble protein and water-insoluble protein.<sup>1, 2</sup> Normal lens has a well-developed water-protein construction that efficiently transmits the visible light. When the water-protein structures undergo destruction, the lens degrades in opacification and undergoes interference in vision. That is the cataract. Laser Raman spectroscopy has been used as a nondestructive probe to determine the conformational changes of lens protein during opacification. We have obtained Raman spectra in normal and cataract Wistar rats. Due to the galactose metabolism, lens protein is subject to biochemical changes. Raman spectra obtained show no difference between normal and opaque lens in the 900-1700 $\text{cm}^{-1}$  spectral region. They show the structural changes of lens protein during cataract formation.

### Materials and Methods

Wistar rats weighing about 100 g were injected with a 50% galactose solution in the abdominal cavity twice a day. After 21 days of galactose injection, the lens underwent opacification. The lenses were removed from the eyeball in both normal and cataract cases and were immersed in a physiological saline solution and examined by laser Raman spectroscopy. The laser Raman spectrometer consists of a Spex 1403 double monochromator, a RCA type C-31034 photomultiplier tube, photon-counting electronics, and a Spex Datamate (microprocessor). All spectra were recorded at a scan speed of 4  $\text{cm}^{-1}/\text{s}$  with 900  $\mu\text{m}$  slit width and 2cm slit height, scan range 450-3200  $\text{cm}^{-1}$ . The excitation wavelength at 514.5 nm (150 MW) was provided by a Spectra-Physics Model 2020 argon-ion laser.

### Conclusion

Laser Raman spectroscopy has many advantages for the study of the mechanism of lens opacification at the molecular level. First, Raman spectroscopy enables us to study structural changes in the lens under normal physiological conditions. Second, almost the entire vibrational spectral region lends itself to the analysis of the aqueous lens. Detailed information about lens proteins can be obtained simultaneously from a single scan spectrum in the 400-3200 $\text{cm}^{-1}$  region. Third, Raman spectral bands of relatively high intensity can be obtained for the protein subgroups which reveal structural modification of the lens proteins during opacification. Biologists have undertaken a number of successful investigations in this research area.<sup>1-4</sup>

The authors are in the Institute of Biophysics, Academia Sinica, Beijing, China.

Figure 1 shows the Raman spectra of the normal and the cataract lens. Figure 2 compares the Raman spectra of the normal lens with those of lenses of differing capacity. In the vibrational spectra of the region 900-1700  $\text{cm}^{-1}$ , the amide I band at 1670  $\text{cm}^{-1}$  and the amide III band at 1240  $\text{cm}^{-1}$  show that the peptide backbones of lens protein in Wistar rats are in the antiparallel  $\beta$ -sheet conformation. We can observe that the vibrational frequencies and band shapes in this spectral region do not exhibit any difference between the normal and the opacity lens. The intensity ratios  $I_{850}/I_{830}$  indicate the tyrosine doublet and  $I_{880}/I_{760}$  indicates the change in the tryptophan doublet with increasing opacification in the 700-900 $\text{cm}^{-1}$  region. Thus, Raman features have been used as a probe in studying the microenvironment changes of the tryptophan and tyrosine molecules. In addition, the changes of  $I_{644}/I_{622}$  indicate tyrosine/phenylalanine residues and  $I_{2578}/I_{2731}$  from -SH seem to be correlated with the change of -S-S bonds in the 450-500 $\text{cm}^{-1}$  region. Therefore, these results show that lens opacification is not associated with major conformational changes of protein secondary structure. The process of protein aggregation is not accompanied by major conformational changes of polypeptide. Instead, the protein aggregation causes microenvironmental changes of tyrosine and tryptophan residues. The conformational changes of the subgroups -SH and -S-S-correlate with the modification of protein. Other intense Raman bands in the spectrum at 1006  $\text{cm}^{-1}$  (Phe), 1031  $\text{cm}^{-1}$  (Phe), 1209  $\text{cm}^{-1}$  (Tyr), 1447  $\text{cm}^{-1}$  ( $\text{CH}_2$  deformation), and 1547  $\text{cm}^{-1}$  (Trp) are insensitive to environmental changes.<sup>2-4</sup> So if we want to monitor the cause of cataract formation, we must closely notice these microenvironmental changes of the side chains of lens protein. We have also observed that the fluorescence background is increased with the occurrence of opacification, we attribute to the light scattering from various metabolism products.

### References

1. Y. Ozaki, A. Mizuno, et al., "Raman spectroscopic study of age-related structural changes in the lens protein of an intact mouse lens," *Biochemistry* 22: 6254-6258, 1983.
2. Nai-Teng Yu and E. J. East, "Laser Raman spectroscopic studies of ocular lens and its isolated protein fractions," *J. Biol. Chem.* 250: 2196, 1975.
3. Koichi Itoh, Yukihiro Ozaki, et al., "Structural changes in the lens proteins of hereditary cataracts monitored by Raman spectroscopy," *Biochemistry* 22: 1773-1778, 1983.
4. Emily East, R. C. C. Chang, and N.-T Yu, "Raman spectroscopic measurement of total sulfhydryl in intact lens as affected by aging and ultraviolet irradiation," *J. Biol. Chem.* 253: 1436-1441, 1978.

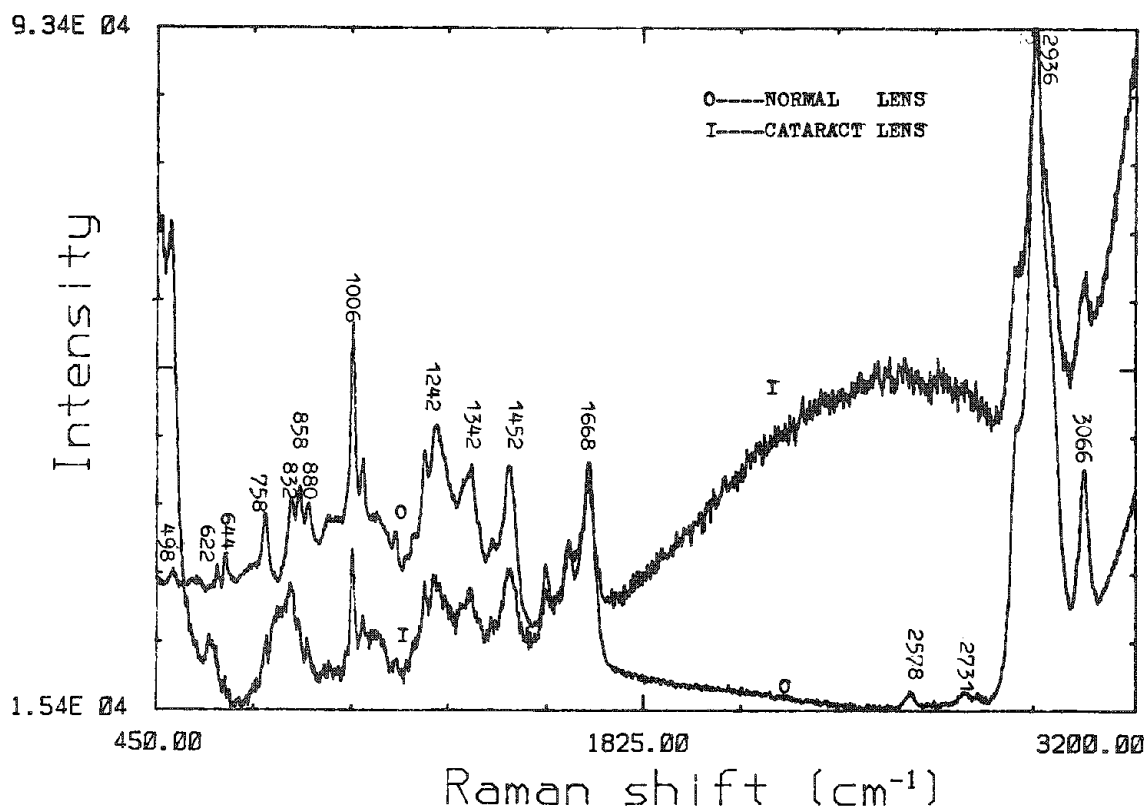


FIG. 1.--Raman spectra of normal and cataractous lens (in rat).

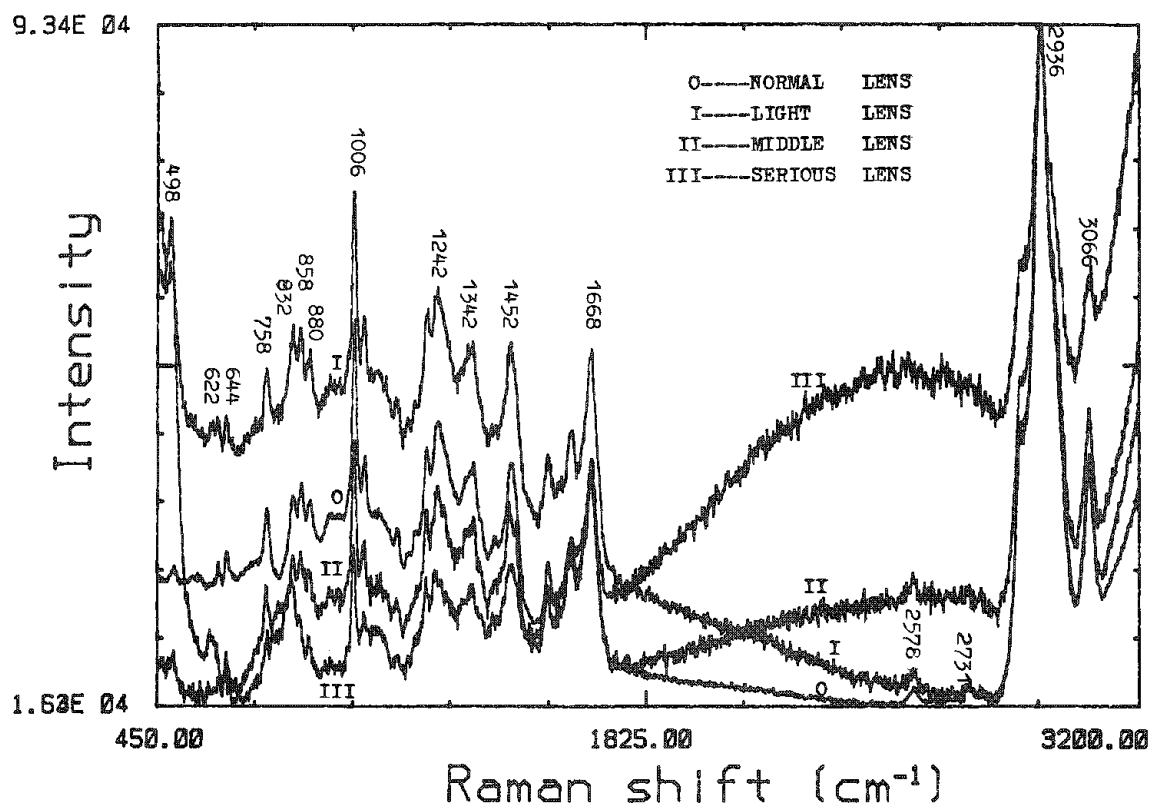


FIG. 2.--Raman spectra comparing normal rat lens with lenses of various degrees of opacity.

## 5A. Materials Science: Ceramics

### ELECTRON MICROSCOPY STUDIES OF SOME METASTABLE CERAMIC PHASES

T. E. Mitchell, P. Pirouz, and A. H. Heuer

Metastable phases are ubiquitous in ceramics, even in the so-called advanced ceramics being developed for such demanding applications as structural materials, electronic devices, and operation in hostile environments (or combinations of the three). Examples of such metastable phases include the following:

(a)  $\beta$ -SiC. This metastable form of SiC has the cubic sphalerite structure and forms commonly in gas-phase reactions. The stable form is  $\alpha$ -SiC, which is a mixture of hexagonal and rhombohedral polytypes based on stacking sequences of Si-C tetrahedra.

(b) Tetragonal  $\text{ZrO}_2$ .  $t$ - $\text{ZrO}_2$  is the metastable phase in the partially stabilized  $\text{ZrO}_2$ 's (PSZs), where  $\text{ZrO}_2$  is alloyed with such oxides as MgO, CaO, or  $\text{Y}_2\text{O}_3$ ; the other phase has cubic symmetry ( $c$ - $\text{ZrO}_2$ ). The stable low-temperature phase has monoclinic symmetry ( $m$ - $\text{ZrO}_2$ ).

(c)  $\gamma$ - $\text{Al}_2\text{O}_3$ . This form generally refers to a variety of  $\text{Al}_2\text{O}_3$  polymorphs which are spinel-related structures based on fcc anion packing with various cation occupancies.  $\gamma$ - $\text{Al}_2\text{O}_3$  is formed by heating of Al hydroxides and oxyhydroxides or by oxidization of Al-containing alloys. The stable form is rhombohedral  $\alpha$ - $\text{Al}_2\text{O}_3$ , which is based on hcp anion packing.

(d)  $\alpha$ - $\text{Si}_3\text{N}_4$ . This metastable trigonal form of  $\text{Si}_3\text{N}_4$  commonly occurs during reaction processing. It converts to stable rhombohedral  $\beta$ - $\text{Si}_3\text{N}_4$  during high-temperature exposure.

There are many other examples. We describe examples of the first three, emphasizing particularly the ways in which analytical and high-resolution electron microscopy have aided in understanding the influence of microstructure on the stability of the various phases.

#### *$\beta$ -SiC Grown Epitaxially on Si by CVD*

Aside from the attractive mechanical properties of silicon carbide, this material also is interesting for its electronic properties. It has a high saturated drift velocity, good thermal conductivity, low dielectric constant, high temperature stability, and a large band gap, from  $\sim 2.3$  to  $\sim 3$  eV depending on the polytype, which implies that semiconductor devices made from this material could be operated at high temperatures. However, a major problem arises in the growth of bulk SiC single crystals for semiconducting purposes, due to the very low stacking fault energy of SiC and the resulting uncontrolled mixture of polytypes which is detrimental to the electronic proper-

ties of the material. However, Nishino et al.<sup>1,2</sup> have succeeded in growing single crystals of  $\beta$ -SiC epitaxially on silicon substrates by chemical vapor deposition (CVD). The thickness is limited to about 50  $\mu\text{m}$ , above which the epilayer starts cracking. We have recently been investigating the quality of the  $\beta$ -SiC grown by this technique at NASA-Lewis in Cleveland.

Figure 1 is a low-magnification plan-view micrograph of a typical specimen grown by the CVD technique. A high density of stacking faults is observed, all lying on  $\{111\}$ . The stacking faults are generally of two types. The majority are much wider than the equilibrium width and grow wider with increasing distance from the Si/SiC interface. It is rare to see isolated stacking faults because, during growth, as their width increases, they intersect and produce stair-rod dislocations.<sup>3</sup> Thus the wide stacking faults are often bounded on one side by a stair rod and on the other side by a Shockley partial. A second type of stacking fault is also observed, which is of the equilibrium width. These faults arise from the dissociation of threading dislocations produced at the interface by the stresses due to the large lattice mismatch.

Cross-sectional HREM has also been used to study the interface;<sup>4,5</sup> an example is shown in Fig. 2. A rough, irregular interface, misfit dislocations, and a high density of twins are the general features observed by this technique. The lattice mismatch between the Si substrate and  $\beta$ -SiC is 20%, which implies that, on geometrical grounds, there should be one misfit dislocation at every fourth lattice plane of the Si substrate. Over certain regions, this is indeed the case, although the regularity is soon broken down by the occurrence of twinning.<sup>4</sup>

In the deposition of a compound semiconductor, such as SiC, over (001) Si substrates, there are two ways in which the nuclei may deposit. The first deposited atoms could be Si or they could be C. Islands grown from two such nuclei give rise to domains of different polarity and when two such islands meet, antiphase domain boundaries (APBs) are produced. Chemical etching or thermal oxidation of  $\beta$ -SiC brings out the antiphase boundaries (Fig. 3). In the TEM, the APBs appear as irregular planar defects, which show fringe contrast (Fig. 4). The different polarity of the neighboring domains has been demonstrated by the convergent-beam technique, by a method due to Taftø.<sup>6</sup> This effect is shown in Fig. 5, where the two CBED patterns from the two sides of an APB are presented. The intersecting Kikuchi lines in the 200 disk have opposite contrast, which indicates that the polarity has reversed when the boundary is crossed.<sup>7</sup>

The authors are at the Department of Metallurgy and Materials Science, Case Western Reserve University, Cleveland, OH 44106. This research was supported variously by NASA, DOE, and AFOSR. The assistance of V. Lanteri, C. Chorey, and J. K. Doychak is gratefully acknowledged.



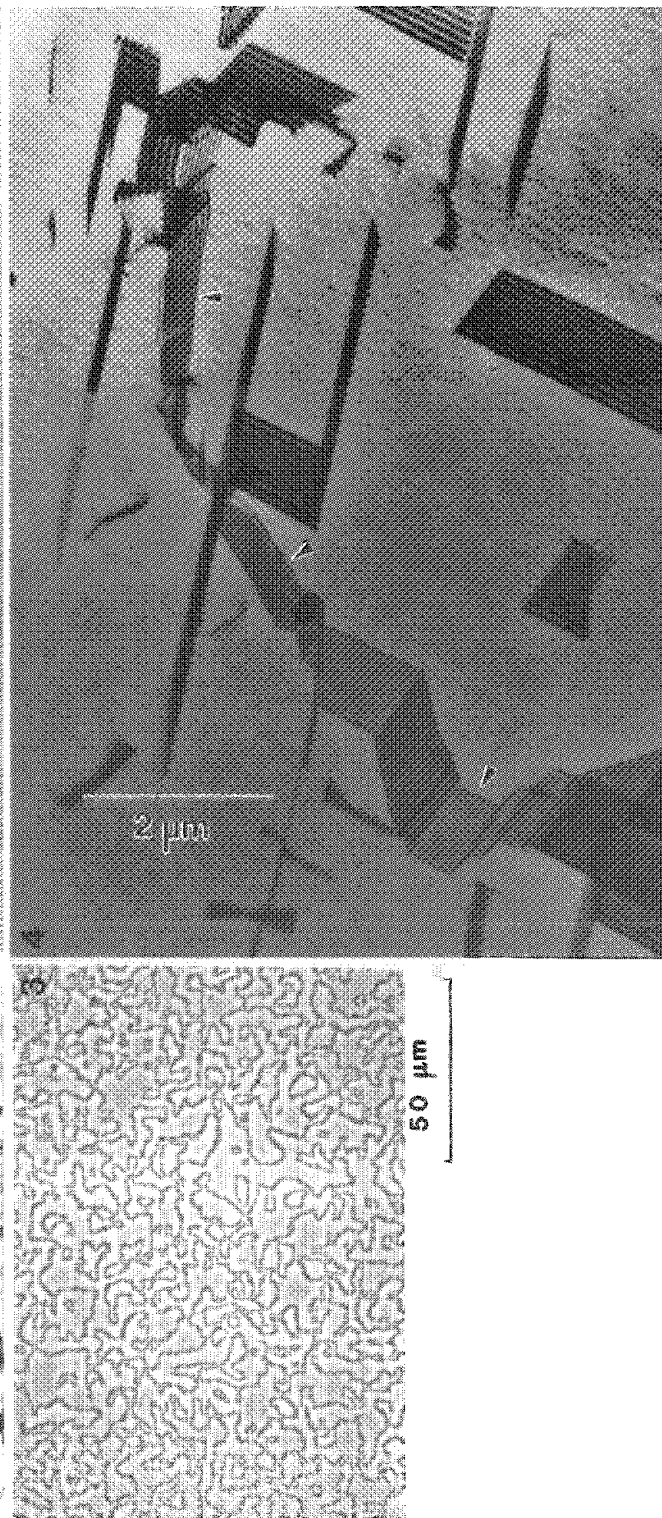
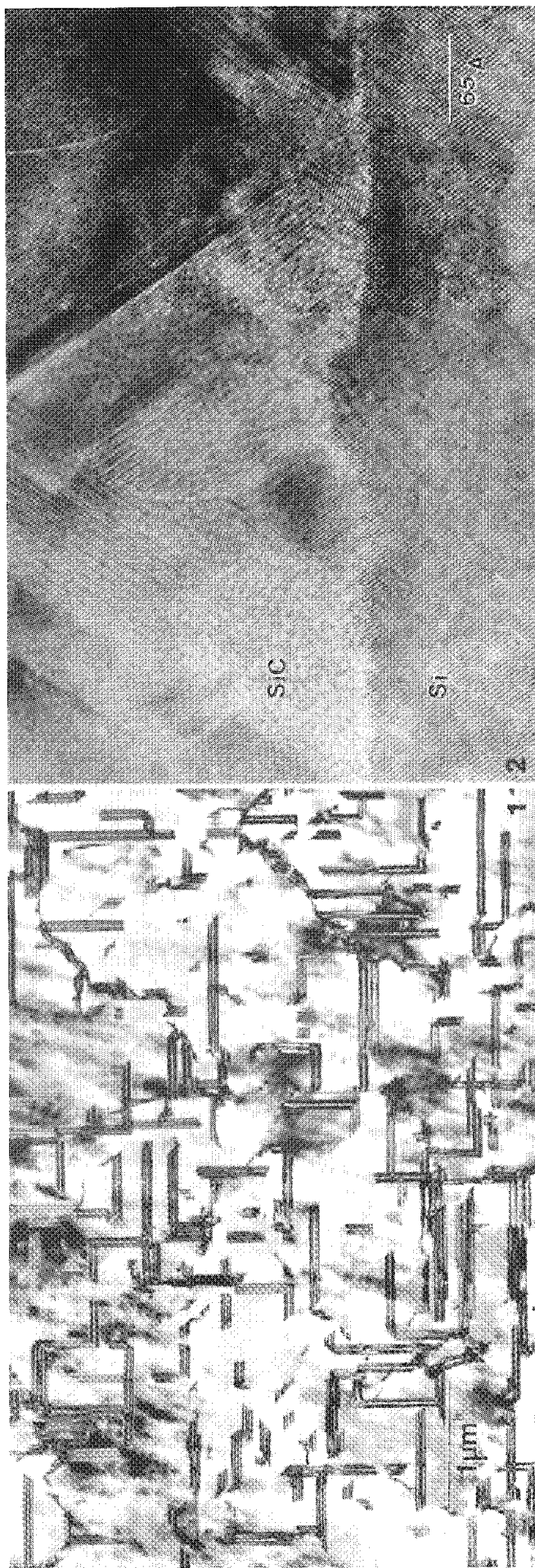


FIG. 1.--Low-magnification plan-view micrograph of  $\beta$ -SiC epilayer.  
 FIG. 2.--Cross-sectional HREM micrograph of Si/SiC interface.  
 FIG. 3.--SEM (backscattered electrons) plan view of  $\beta$ -SiC epilayer chemically etched to bring out APBs.  
 FIG. 4.--Cross-sectional TEM view of APB (arrows) in  $\beta$ -SiC epilayer.

The transformation of  $t$ -ZrO<sub>2</sub> to  $m$ -ZrO<sub>2</sub> is martensitic in nature and is accompanied by a volume increase of about 3%. It is detrimental to the physical integrity of ZrO<sub>2</sub>-containing ceramics but the addition of oxides such as MgO, CaO, or Y<sub>2</sub>O<sub>3</sub> is efficient in reducing  $M_s$  below room temperature. The behavior of such materials depends critically on the microstructure. In this section we describe some observations on Y-PSZ, which has many commercial applications ranging from thermal barrier coatings (TBCs) to solid electrolytes (oxygen sensors, high-temperature fuel cells, etc.).

Figure 6 shows the ZrO<sub>2</sub>-rich portion of the phase diagram.<sup>8</sup> The region in which we are interested, the  $c + t$  field (i.e., 4 to 13 wt% Y<sub>2</sub>O<sub>3</sub>), has been studied by energy-dispersive x-ray analysis (EDS)<sup>9</sup> and the phase relationships were found to be in good agreement with the results of Scott.<sup>8</sup> Scott also pointed out that alloys in the range of 4-12 wt%, when quenched from high temperature, have a fully tetragonal microstructure instead of a mixture of  $t$ -ZrO<sub>2</sub> precipitates in a  $c$ -ZrO<sub>2</sub> matrix, as predicted by the phase diagram. Figure 7 shows the characteristic microstructure of an alloy (11.5 wt% Y<sub>2</sub>O<sub>3</sub>) annealed at 1600 C in the cubic field for 20 h and then air-quenched. The grain shown in the figure is entirely tetragonal but with a composition of 11.5 wt% (determined by EDS), which leads us to conclude that at the annealing temperature, the microstructure is cubic and transforms upon cooling, by a displacive transformation, to a tetragonal solid solution ( $t'$ -ZrO<sub>2</sub>) with the same composition as the original cubic phase. Two features, characteristic of the  $t$ -ZrO<sub>2</sub> phase, are readily visible on Fig. 7: (i) antiphase domain boundaries, which are due to the loss of symmetry resulting from the  $c \rightarrow t$  transformation;<sup>10</sup> and (ii) deformation twins, formed to relieve the strains due to the transformation.<sup>11</sup>

When the same specimen is slowly cooled to room temperature ( $\sim 24$  h) a quite different microstructure results (Fig. 8). The microstructure is composed of small  $t$ -ZrO<sub>2</sub> precipitates in a cubic matrix, which have a tendency to align along  $\langle 101 \rangle$ . (Note that three variants are generated with  $\bar{c}$  axes along the  $\langle 001 \rangle$  cube directions.) With long annealing times in the two-phase field, the equilibrium microstructure is developed (Figs. 9 and 10), consisting of large colonies of twin-related variants ( $\bar{c}$  axes at 90° sharing the same  $\{101\}$  habit plane). This colony microstructure is very effective in reducing the overall elastic strain energy.<sup>12</sup> The difference in the matrix microstructure results from the difference in cooling rate between the specimens of Figs. 9 and 10. The slowly cooled specimen of Fig. 9 has the same matrix microstructure as the specimen of Fig. 8, whereas in the quenched specimen (Fig. 10) the matrix, which was cubic at the annealing temperature, has transformed to  $t'$ -ZrO<sub>2</sub> upon cooling, with the formation of APBs.

Figure 11 shows a high-resolution micrograph near Scherzer defocus of the interface

region between a colony and matrix. Both the cubic-tetragonal and tetragonal-tetragonal (twin) interfaces are coherent. This feature, along with the low strain energy of the colony configuration, are important factors in the "stability" of these metastable structures.

#### $\gamma$ -Al<sub>2</sub>O<sub>3</sub> Formed by the Oxidation of $\beta$ -NiAl

The formation of  $\gamma$ -Al<sub>2</sub>O<sub>3</sub> and its transformation to  $\alpha$ -Al<sub>2</sub>O<sub>3</sub> has been studied by the oxidation of cubic  $\beta$ -NiAl at 800 C and 1100 C.  $\gamma$ -Al<sub>2</sub>O<sub>3</sub> is ideally written as Al<sub>8/3</sub>□<sub>1/3</sub>O<sub>4</sub> where □ represents a cation vacancy in the M<sub>3</sub>O<sub>4</sub> spinel structure; 2/3 of the cations are on octahedral sites, 1/3 are on tetrahedral sites, and the vacancies are distributed at random. In  $\delta$ -Al<sub>2</sub>O<sub>3</sub>, there is some ordering of the cations and vacancies to form a tetragonal structure consisting of three spinel unit cells. In  $\theta$ -Al<sub>2</sub>O<sub>3</sub>, there is distinct ordering such that the cations are distributed equally on the octahedral and tetrahedral sites and the resulting structure is monoclinic. The rhombohedral  $\alpha$ -Al<sub>2</sub>O<sub>3</sub> is completely different, with hcp anion stacking and only octahedral cation occupancy. In addition, the  $\gamma \rightarrow \alpha$  transformation is accompanied by a 15% reduction in volume.

The initial formation of  $\gamma$ -Al<sub>2</sub>O<sub>3</sub> at 800 C is epitaxial. In the example shown in Fig. 12, the original (001)  $\beta$ -NiAl substrate has been back-thinned away, leaving an oxide with a 10nm "domain" size. The fringes in Fig. 12 are due to moiré effects between domains, and to faulting. The corresponding SAD is shown in Fig. 13; its complexity is due to the many variants of  $\gamma$ -Al<sub>2</sub>O<sub>3</sub> present and to the fact that cation ordering has occurred (e.g., the  $\gamma \rightarrow \delta$  transformation). This feature has been demonstrated by microdiffraction from single domains; the example in Fig. 14 can be interpreted as  $\delta$ -Al<sub>2</sub>O<sub>3</sub> but other examples appear to show additional ordering.<sup>13</sup>

With increasing oxidation time, further ordering occurs and  $\theta$ -Al<sub>2</sub>O<sub>3</sub> becomes evident, not only in the diffraction pattern but also because of its plate-like morphology. This ordering is particularly dramatic in the early stages of oxidation at higher temperatures (1100 C), as shown in the SEM picture in Fig. 15.  $\alpha$ -Al<sub>2</sub>O<sub>3</sub> does not form at 800 C; even at 1100 C, it is only observed after the alloy is completely covered with  $\theta$ -Al<sub>2</sub>O<sub>3</sub>. The resulting microstructure is shown in the SEM picture 16, which has been described as "lacey."<sup>14</sup> It might more properly be called a "cobweb" structure, since it has radiating arms and peripheral ridges and clearly forms by a nucleation and growth process. The nature of the transformation is shown in the STEM picture in Fig. 17 and the TEM picture in Fig. 18. These and other observations indicate that the  $\theta \rightarrow \alpha$  nucleates at widely spaced positions in the oxide; the volume decrease causes radial cracks, which then heal with formation of polycrystalline  $\alpha$ -Al<sub>2</sub>O<sub>3</sub> to form the radial ridges. The transformation spreads out radially, sweeping the impurities into the peripheral ridges of the oxide film. The high density of voids, dislocations, and low-angle boundaries in Fig. 18 are a result of the 15% volume decrease.<sup>15</sup>

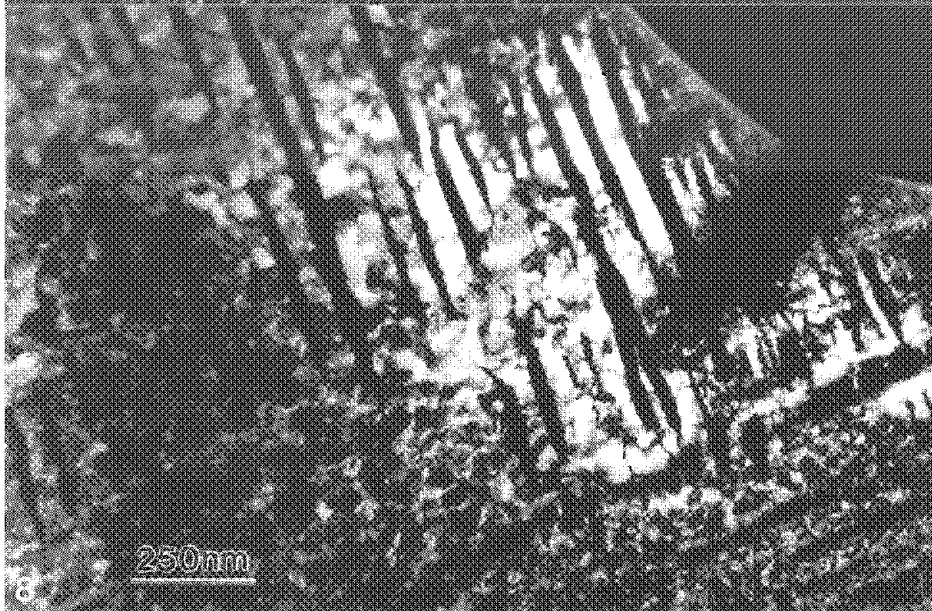
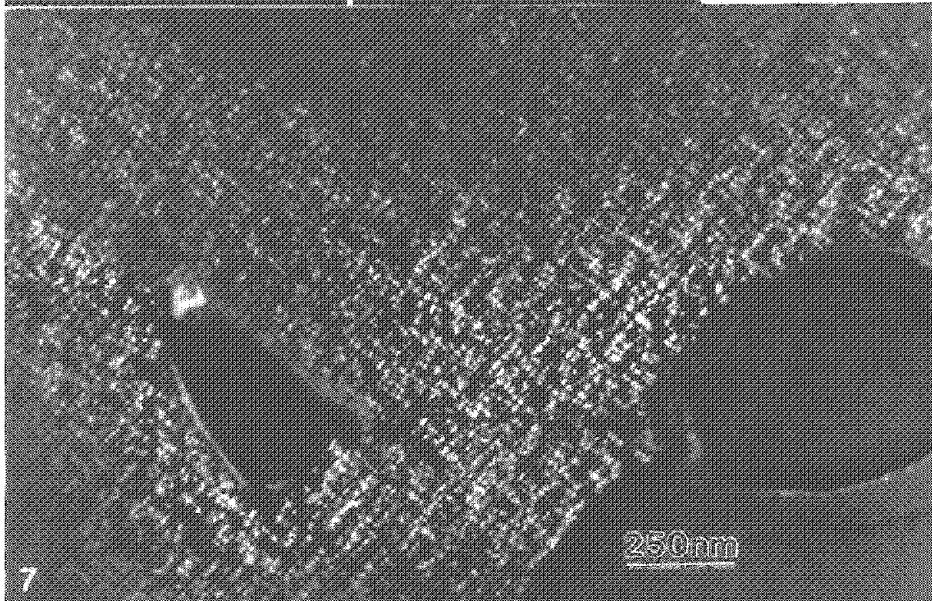
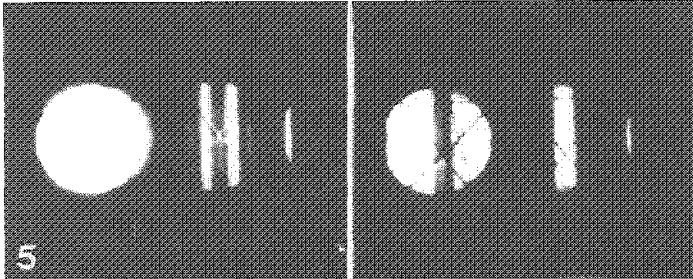
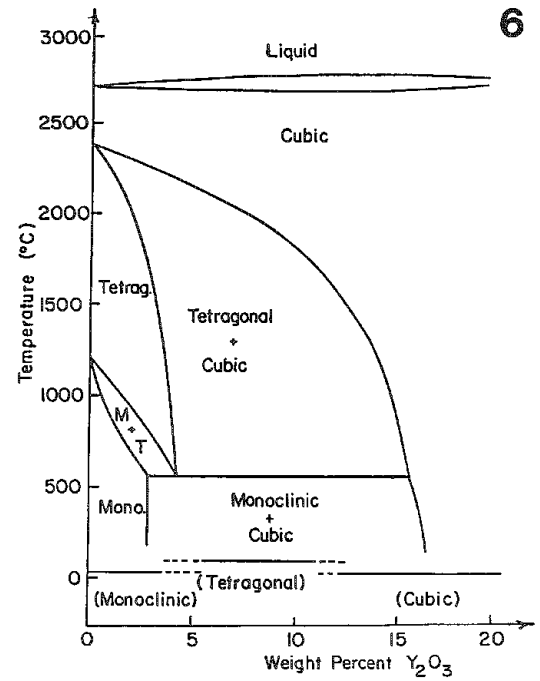


FIG. 5.--CBED patterns from two sides of APB in  $\beta$ -SiC. Note contrast reversal of intersecting Kikuchi lines in 200 disk.

FIG. 6.--ZrO<sub>2</sub>-rich portion of ZrO<sub>2</sub>-Y<sub>2</sub>O<sub>3</sub> phase diagram.<sup>8</sup>

FIG. 7.--Dark-field micrograph using a tetragonal reflection of a 11.5 wt% Y<sub>2</sub>O<sub>3</sub> specimen, annealed at 1600 C for 20 h and then quenched.

FIG. 8.--Dark-field micrograph of same specimen as Fig. 7 but slowly cooled to room temperature ( $\sim 24$  h).



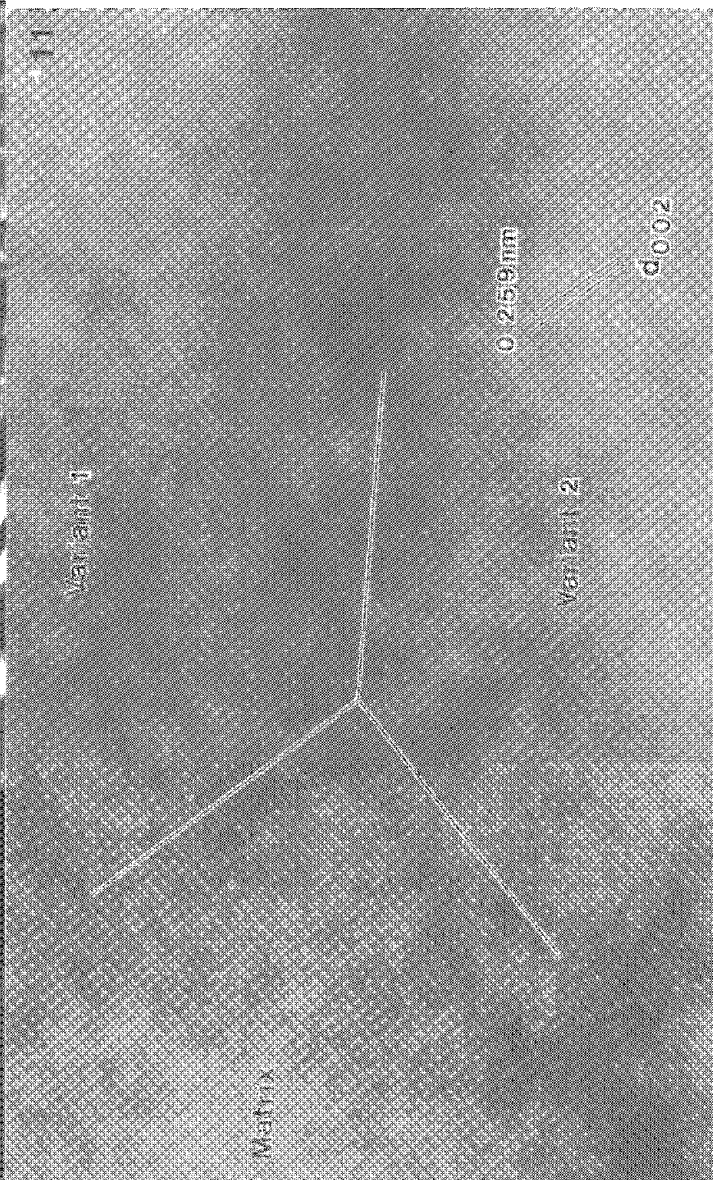
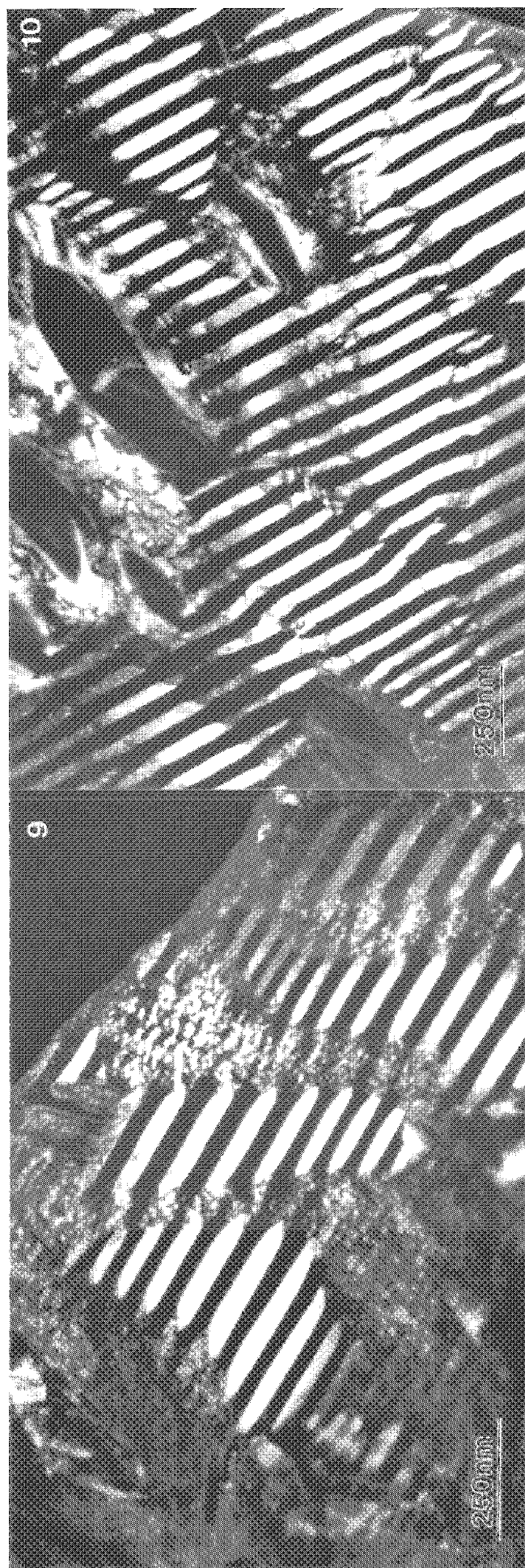


FIG. 9.--Dark-field micrographs of "colony" microstructure in 8 wt%  $Y_2O_3$  skull-melted single crystal annealed for 50 h at 1600 C and slowly cooled.  
 FIG. 10.--Dark-field micrographs of "colony" microstructure in 8 wt%  $Y_2O_3$  skull-melted single crystal annealed for 100 h at 1600 C and quenched.  
 FIG. 11.--[010] high-resolution electron micrograph of 8 wt%  $Y_2O_3$  skull-melted single crystal annealed for 50 h at 1600 C.

## References

1. S. Nishino, Y. Hazuki, H. Matsunami, and T. Tanaka, *J. Electrochem. Soc.* 127: 2674, 1980.
2. S. Nishino, J. A. Powell, and H. A. Will, *Appl. Phys. Lett.* 42: 460, 1983.
3. C. M. Chorey, P. Pirouz, J. A. Powell, and T. E. Mitchell, in M. L. Green et al., Eds., *Semiconductor-based Heterostructures: Interfacial Structure and Stability*, TMS Publications 1986, 115.
4. P. Pirouz and C. M. Chorey, *Proc. 5th Intern. Congress on Structure and Properties of Dislocations in Semiconductors*, Moscow, 1986; *Bull. Acad. Sci. USSR* (in press).
5. S. R. Nutt, D. J. Smith, H. J. Kim, and R. F. Davis, *Appl. Phys. Lett.* 50: 203, 1987.
6. J. Taftø, *Proc. 39th Ann. Meeting EMSA*, 1979, 154.
7. P. Pirouz, C. M. Chorey, and J. A. Powell, *Appl. Phys. Lett.* 50: 223, 1987.
8. H. G. Scott, "Phase relationships in the zirconia-yttria system," *J. Mater. Sci.* 10: 1527, 1975.
9. V. Lanteri, *The Tetragonal Phase in Y-PSZ*, Ph.D. Thesis, Case Western Reserve University, Cleveland, 1986.
10. A. H. Heuer and M. Ruhle, in N. Clausen et al., Eds., *The Science and Technology of Zirconia II* (Advances in Ceramics, vol. 12), Columbus, Ohio: American Ceramic Society, 1984, 1-13.
11. A. H. Heuer, R. Chaim, and V. Lanteri, "Displacive cubic  $\rightarrow$  tetragonal transformation in the  $ZrO_2$ - $Y_2O_3$  system," *Acta Metall.* 35: 661, 1987.
12. V. Lanteri, T. E. Mitchell, and A. H. Heuer, "Morphology of tetragonal precipitates in partially stabilized  $ZrO_2$ ," *J. Am. Ceram. Soc.* 69: 564, 1986.
13. J. K. Doychak, T. E. Mitchell, and J. L. Smialek, *MRS Symposium Proc.* 39: 475, 1985.
14. J. L. Smialek, *Met. Trans.* 9A: 309, 1978.
15. J. K. Doychak, Ph.D. Dissertation, Case Western Reserve University, 1986.

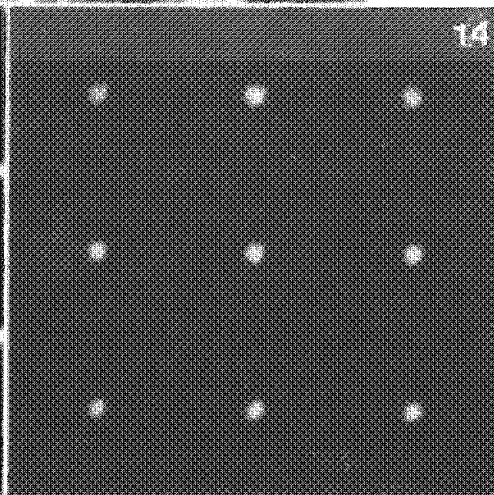
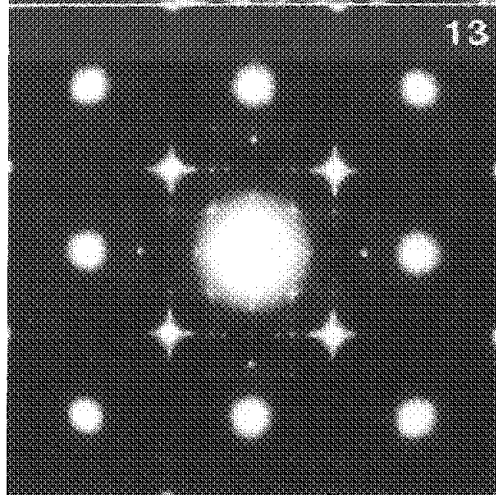
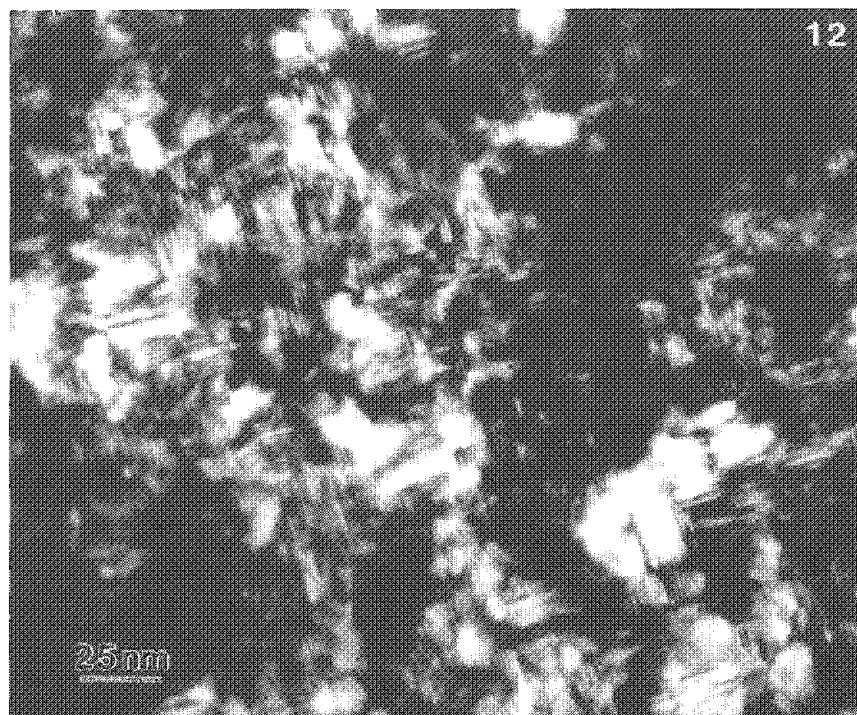


FIG. 12.--Dark-field image of  $Al_2O_3$  scale back-thinned from  $\beta$ -NiAl substrate after oxidation for 1 h at 800 C.

FIG. 13.--SAD pattern of general area of Fig. 12.

FIG. 14.--Microdiffraction pattern from single domain in Fig. 13.



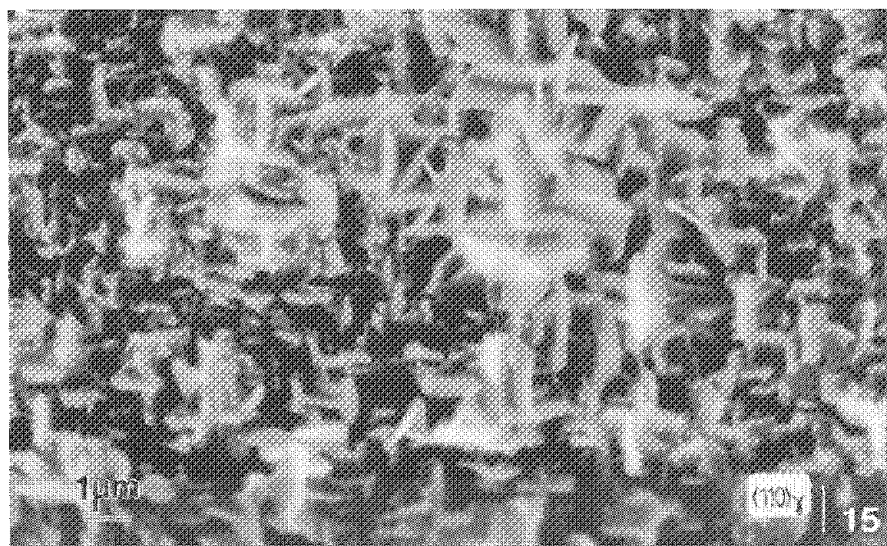
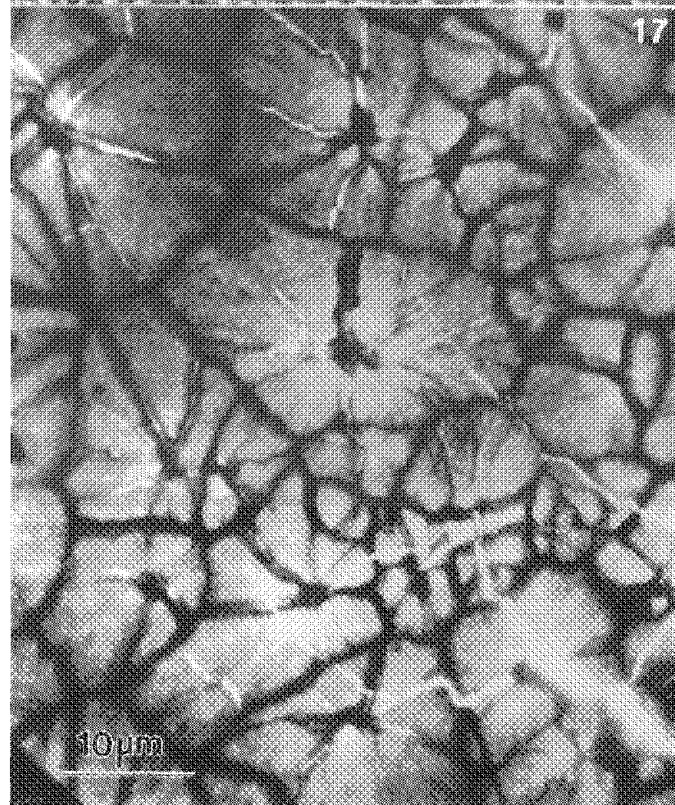
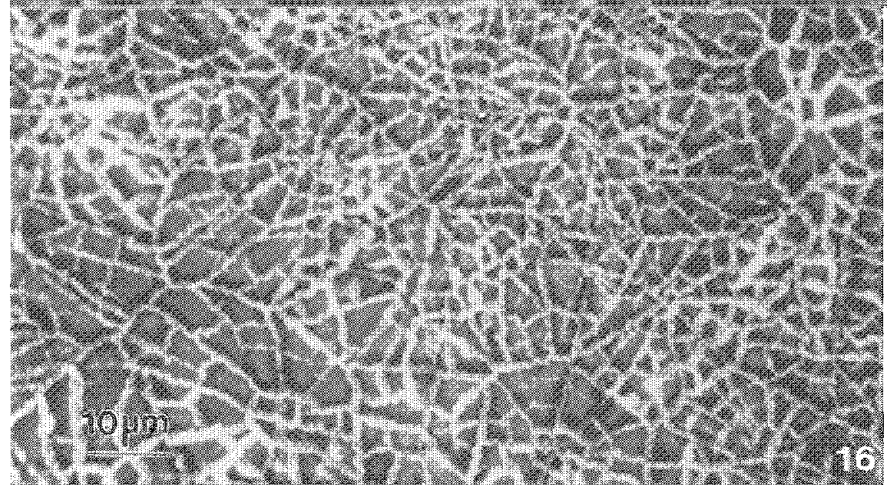


FIG. 15.--SEM image of  $\theta$ - $\text{Al}_2\text{O}_3$  plates grown on  $\beta$ -NiAl oxidized for 1 h at 1100 C.

FIG. 16.--SEM image of "lacey"  $\alpha$ - $\text{Al}_2\text{O}_3$  scale grown on  $\beta$ -NiAl oxidized for 100 h at 1000 C.

FIG. 17.--STEM BF image of back-thinned specimen of Fig. 16.

FIG. 18.--TEM BF image of same specimen as Fig. 17, showing radial texture emanating from transformation center at top left.



## MICROANALYSIS OF POLYTYPOID CERAMICS BY IMAGING, DIFFRACTION, AND SPECTROSCOPY

K. M. Krishnan and G. Thomas

Combined atomic resolution imaging, microdiffraction, and energy dispersive x-ray microanalysis suggest that the 32H polytypoid in the  $\text{AlN-Al}_2\text{O}_3$  pseudobinary system is in fact a 7:9 periodic intergrowth of the 21R and 27R polytypoids. Furthermore, these combined techniques verify that the cation/anion ratio is 16/17 and that this ratio defines the polytypoid precisely.

The processing of structural ceramics generally involves additions that modify the structures, their interfaces, or both. Well-known examples are oxide additives to sintered or hot-pressed  $\text{Si}_3\text{N}_4$ , which produces intergranular glassy and/or crystalline phases. The avoidance of glassy phases is necessary for optimum refractory performance.<sup>1</sup> On the other hand, it has been shown that a variety of compositions in the  $\text{Al}_2\text{O}_3$ -AlN pseudobinary system can be successfully processed to almost theoretical densities without the use of additives.<sup>2</sup> In addition to the fact that the end members of the above composition-tie line are, independently, potential candidates for advanced structural applications, the system is of fundamental importance because the various microstructures are largely anion controlled.<sup>3</sup> However, at either end of the phase diagram, small additions of the other end member result in a variety of modulated structures based on the wurtzite (AlN-rich end) structure<sup>4</sup> and having anisotropic grain shapes elongated parallel to the (0001) fault plane in the above structure ( $\text{P6}_3\text{mc}$ ).

An assortment of modulated structures at the AlN-rich end of the  $\text{Al}_2\text{O}_3$ -AlN phase diagram, called compositional polytypes or polytypoids, including  $\text{SiO}_2$  sintered AlN<sup>5</sup> have been reported.<sup>4-7</sup> It has been argued that the structures of all these polytypoids are strictly determined by their composition and a specific cation/anion ratio can be associated with each structure. However, the compositions identified with a particular structure are contradictory<sup>4,8</sup> and the experimental confirmations are often incomplete.<sup>7</sup>

Recent studies of the  $\text{AlN-Al}_2\text{O}_3$  system produced by reaction sintering resolved a new polytype, 32H.<sup>6</sup> This paper reports a further study by high-resolution imaging, microdiffraction, and energy-dispersive x-ray spectroscopy made in order to understand this sys-

tem and to probe directly whether the predicted cation/anion ratio of 16/17 for the 32H structure--which assumes ideal charge balance in the absence of point defects--is in fact valid.

### *Experimental Procedure*

Samples of a nominal starting composition of 95 mol% AlN (rest  $\text{Al}_2\text{O}_3$ ) and an actual composition of 85 mol% AlN were prepared by a reaction-sintering process.<sup>2</sup> The starting powders were ball-milled with an ethanol fluid medium for 24 h, isostatically pressed at 25 000 psi, and prereacted at 1200 C for 24 h in gas-tight flowing nitrogen before final sintering. Final reaction sintering was then carried out at temperatures of 1950-2100 C for 1 h in an inductively heated graphite furnace with flowing nitrogen.

We prepared TEM specimens by cutting thin slices of the ceramic with a diamond saw, grinding and polishing to form 40 $\mu\text{m}$ -thick slices, and ion-milling to perforation by use of argon ions accelerated through a potential of 5 kV. The specimens were coated with a thin layer of evaporated carbon to avoid surface charging. They were then examined in a JEOL 200CX TEM operating at 200 kV by conventional SAD, CBED, and phase-contrast-imaging techniques. Optical microdiffraction was carried out from small regions of the photographic negative with a He-Ne laser. The microanalysis was carried out on another dedicated JEOL 200CX analytical electron microscope fitted with an ultrathin-window detector (resolution,  $\text{FWHM} \approx 109 \text{ eV}$  for  $\text{F K}_\alpha$  x rays). EELS was also studied but the x-ray data proved to be superior. The k-factors required for the microanalysis were all determined experimentally.<sup>9</sup> Finally, structure images were obtained by use of the JEM Atomic Resolution Microscope operating at 1000 kV, with a demonstrated point-to-point resolution of 0.16 nm.

### *Results*

Figure 1 shows a selected area diffraction pattern, conventional lattice image, and an optical diffractogram from a region of the sample of a 32H polytypoid structure. The position of the 010 spot with respect to the transmitted beam in the SAD (Fig. 1a) confirms the hexagonal stacking sequence. From the diffraction pattern, the repeat distance along the c-axis can be calculated to be 8.3 nm for this polytypoid. However, the lattice image (Fig. 1b) and the accompanying optical diffractogram (Fig. 1c) both show a spacing of 4.3 nm. The discrepancy is not surprising, for the nH polytypoids in this system normally consist of two blocks of n/2 layers related by a c-glide plane,<sup>4</sup> as verified in Fig. 2, which shows a CBD pattern oriented such that the c-axis is

Authors Krishnan and Thomas are at National Center for Electron Microscopy, Lawrence Berkeley Laboratory, University of California, Berkeley, CA 94720. They wish to thank Dr. J. W. McCauley for the sample, Dr. R. S. Rai for help in high resolution imaging, C. J. Echer for assistance on the 200CX/AEM, and Ms. W. Smith for specimen preparation. This work was supported by the U.S. Department of Energy under Contract DE-AC03-76SF00098.

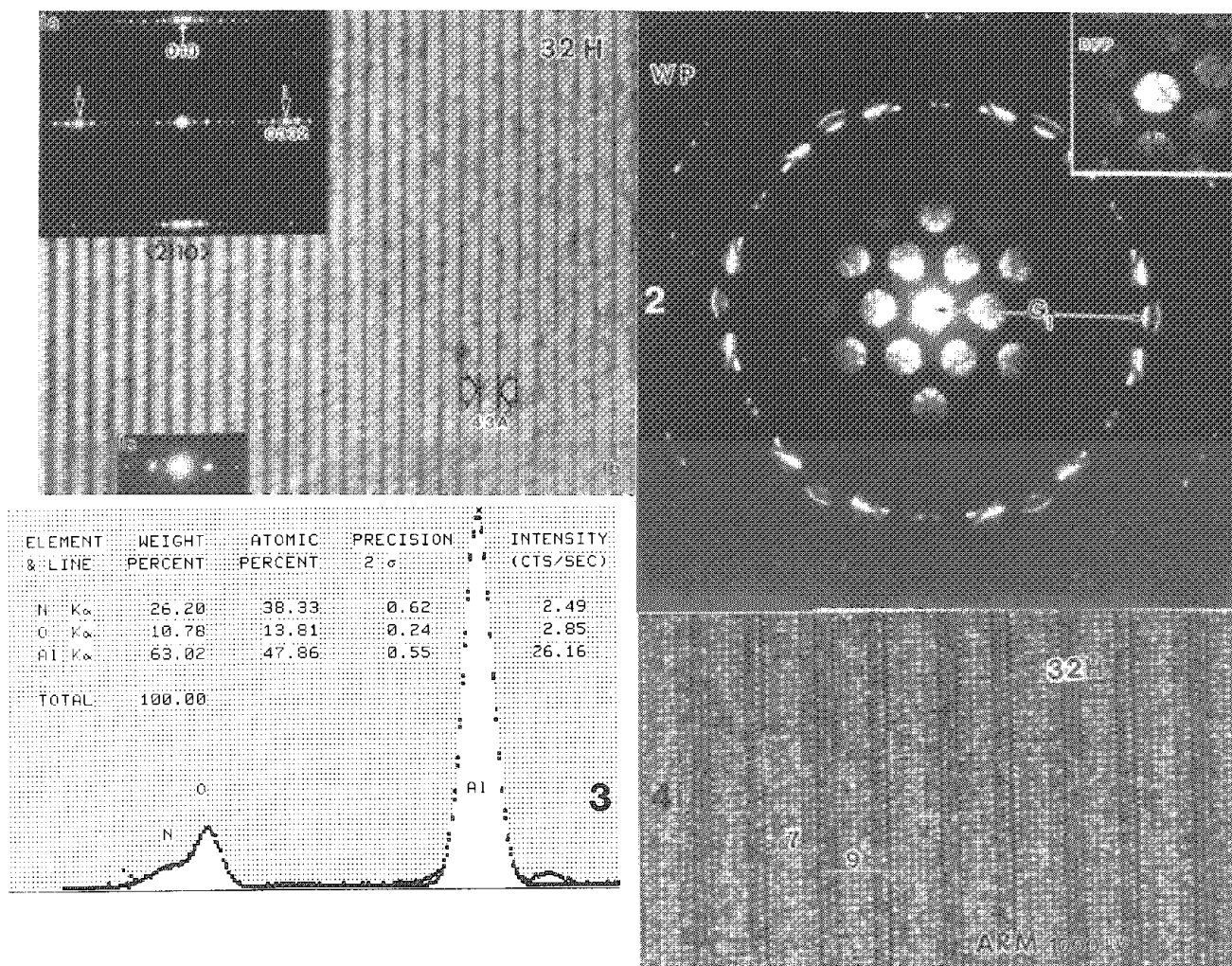


FIG. 1.--(a) SAD pattern of 32H polytypoid structure taken such that c-axis is perpendicular to incident beam. Reflections corresponding to 00.32 reflection indicate that  $c = 8.3$  nm. (b,c) Lattice image and corresponding optical diffractogram from same region of specimen: 4.3nm fringes corresponding to half unit cell reveal presence of c-glide plane.

FIG. 2.--CBED pattern taken with incident beam parallel to c-axis; diameter of FOLZ ring confirms a c-repeat of 4.24 nm.

FIG. 3.--Typical EDX spectra acquired with KEVEX UTW detector. Accompanying microanalysis based on experimentally determined k-factors confirms cation/anion ratio of 16/17.

FIG. 4.--Atomic resolution image of 32H polytypoid at 1000 kV: 32H structure is actually due to parallel intergrowth of 21R and 27R polytypoid structures.

parallel to the incident beam. Based on the radius of the FOLZ ring,  $G$ , the periodicity along the  $c$ -axis is calculated to be 4.2 nm, which confirms the above structural predictions. However, this CBD pattern was obtained with a 60nm-diameter probe and hence the information obtained is averaged over a much larger area than that of a unit of the 32H structure. When direct imaging with atomic resolution is used (Fig. 3), a periodicity is resolved that can be sequenced as alternate [7:9:7:9] repeats. This result can be interpreted as parallel intergrowths of the 27R ( $c = 7.2$  nm) and 21R ( $c = 5.7$  nm) polytypoids. Clearly adjacent units of 27R plus 21R add up to the 32H repeat unit. A detailed interpretation of these images would require simulations for a predicted structure of the unit cells. Image calculations by use of the multislice method<sup>10</sup> are currently in process. Similar intergrowths have also been observed in the SiC polytype structures.<sup>10</sup>

For further analysis, one must measure the cation/anion ratio. A typical EDS spectrum obtained from a 32H region of the sample is shown in Fig. 4. The analysis, carried out with carefully determined experimental  $k$ -factors,<sup>9</sup> suggests a composition of 47.9 at.% Al, 13.8 at.% O and 38.3 at.% N. Within experimental error ( $\pm 3\%$  in the microanalysis) the anion/cation ratio measured (1.08) is in agreement with the theoretically predicted ratio ( $17/16 = 1.06$ ). Unlike previous erroneous attempts,<sup>7</sup> in which a combination of EELS (with approximately 30% error in analysis) for the study of anions and EDXS for the study of the

cations was used, this evidence conclusively supports the view that the ratio defines the polytypoid. In addition, direct atomic resolution imaging indicates that the structure is not a new 32H phase but periodic 7:9 intergrowths of 21R and 27R.

#### References

1. See, for example, a review by G. Thomas in J. Pask, Ed., *Ceramic Microstructures*, Berkeley, 1986 (in press).
2. J. W. McCauley and N. D. Corbin, *J. Am. Cer. Soc.* 62: 476, 1979.
3. J. W. McCauley, K. M. Krishnan, R. S. Rai, G. Thomas, A. Zangrill, R. W. Doser and N. D. Corgin in Ref. 1.
4. K. H. Jack, *J. Materials Science* 11: 1135, 1976.
5. G. van Tendeloo, K. T. Faber, and G. Thomas, *J. Mater. Sci.* 18: 525, 1983.
6. K. M. Krishnan, R. S. Rai, G. Thomas, N. D. Corbin, and J. W. McCauley, *MRS Proc.* 60: 211, 1986.
7. Y. Bando, M. Mitomo, Y. Kitami, and F. Izumi, *J. Micros.* 142: 235, 1986.
8. L. J. Gauckler, H. L. Lukas, and K. G. Petzow, *J. Am. Cer. Soc.* 58: 346, 1975.
9. K. M. Krishnan and C. J. Echer, this proceedings.
10. M. A. O'Keefe, in J. J. Hren, F. A. Lenz, E. Munro, and P. B. Sewell, Eds., *Electron Optical Systems*, AMF O'Hare, Ill.: SEM Inc., 1984, 209.
11. S. R. Singh, G. Singh and G. van Tendeloo, *Phys. Stat. Sol.* 67A: 625, 1981.

## OXYGEN BUBBLE FORMATION IN NUCLEAR WASTE GLASSES BY GAMMA IRRADIATION

J. P. Heuer and D. G. Howitt

The formation of oxygen bubbles in nuclear waste glass by irradiation is well documented and has been shown to be induced predominantly by ionization damage which produces free oxygen. However, there is a large discrepancy between the fluxes (dose rates) used in these initial experiments<sup>1,2</sup> and those characteristic of actual nuclear waste glasses. In this paper, we present some results of the gamma irradiation of these glasses at dose rates comparable to those expected in the actual waste glasses.

### *Experimental*

The glasses used in these experiments were borosilicate glasses of the type proposed for the containment of defense wastes. The glasses were prepared at the Savannah River Laboratories; their particular compositions are shown in Table 1. Four different glasses were evaluated and specimens of each type of glass were irradiated at a common flux to various fluences. The glass samples were prepared for irradiation by cutting of thin sections from the bulk, with a diamond saw and glycerol used as a cutting medium. These sections were polished to a thickness of 100  $\mu\text{m}$  by 600 grit paper. The samples were then reduced to 40  $\mu\text{m}$  by a dimpling machine. At this stage, the samples could be ion milled to perforation for evaluation by transmission electron microscopy. The samples were irradiated both as 40  $\mu\text{m}$  disks and as ion milled thin specimens. The glasses were irradiated to five different fluences ranging from  $2 \times 10^6$  to  $1.3 \times 10^9$  rad at a dose rate of  $2.5 \times 10^6$  rad/h. This rate was measured by thin-film radiochromic dosimeters.<sup>3</sup> The temperature in the gamma pond was  $100 \pm 2$  C, as measured by a thermocouple. The glasses that were irradiated as thin specimens were heavily contaminated even at the lowest fluence ( $2 \times 10^6$  rad) and had to be ion milled for approximately 30 min for the structure of the glass to be revealed. The specimens were carbon coated prior to evaluation in the electron microscope to facilitate charge dissipation. The transmission electron microscopy of these specimens was performed at minimal electron dose to the specimens to distinguish the early stages of oxygen bubble formation. All the micrographs were taken at doses substantially lower than that which could induce bubbles by electron damage in the unirradiated foils.

### *Results*

The micrograph of Fig. 1 shows the micro-

The authors are at the University of California (Department of Mechanical Engineering), Davis, CA 95616. Work is supported by U.S. Department of Energy Contract DE-AC09-76SR00001. They thank Dr. N. E. Bibler at the Savannah River Laboratories for conducting the gamma irradiations.

structure of the Hi Al glass irradiated to a dose of  $5 \times 10^8$  rad at  $2.5 \times 10^6$  rad/h. This microstructure is similar to that observed in all four glasses. The bubble distribution from gamma radiolysis is clearly much finer and more uniform than the microstructure induced by the in situ electron irradiation of these glasses in the electron microscope (Fig. 2). This difference can be attributed to the uniformity of the gamma radiation and the absence of surface effects, which permit the bubble distribution to extend to the edge of the foil. This is not the case in electron radiation.<sup>4</sup>

Because the microstructure is so uniform for the gamma irradiations, it is possible to determine from the micrographs the threshold dose and saturation dose for the formation of bubbles. Figure 3 shows the bubble density as a function of the total dose received at a constant flux. These fluences are  $10^5$  times lower than those associated with electron irradiation.<sup>5</sup>

### *Discussion*

As can be seen from Fig. 3, the four glasses showed similar response to the gamma irradiations and no substantial effect could be attributed to the composition variation. It is apparent that as the dose rate of the irradiation approaches the values that are anticipated for nuclear waste containment, the glasses appear to be more sensitive to irradiation and form oxygen bubbles more reproducibly than from the more accelerated electron irradiations. Furthermore, since the microstructures of these glasses were all similarly altered, it would seem that slight modifications to the glass composition to not give rise to dramatic increases in sensitivity.

The difference in bubble formation efficiency correlates well with the decrease in the energy deposition rate when compared to the electron and ion irradiation studies that have already been done. For example, DeNatale and Howitt<sup>1</sup> found the oxygen bubble formation threshold to be  $6 \times 10^{13}$  rad at a flux of  $10^{15}$  rad/h in the electron case, where our studies show the threshold to be approximately  $3 \times 10^8$  rad at  $2.5 \times 10^6$  rad/h. It is likely that this difference in efficiency is in part due to the reduced amount of defect recombination at the low dose rates, since the defect annihilation is proportional to the concentration of defects present.

Previous studies of the composite nuclear waste glass have shown that gamma irradiation<sup>6</sup> does not substantially affect its durability. The fluences in those studies were  $8 \times 10^{10}$  rad and leach tests were performed on irradiated and unirradiated samples. The results indicated that the change in leach rate was less than a factor of 2. However, the microstructure of those glasses were not evaluated and we are currently irradiating samples large



enough to be leached and also examined for bubble formation.

#### Summary

From our studies it is apparent that for a fixed irradiation dose the efficiency of oxygen bubble formation increases substantially as the dose rate is reduced. It is also clear that the composition variations of these types of glasses are less significant at the lower dose rates, so that it should be possible to predict the irradiation sensitivity of nuclear waste glasses with reasonable certainty.

#### References

1. J. F. DeNatale and D. G. Howitt, *Nuclear Instruments and Methods in Physics Research* B1: 489-497, 1984.
2. G. W. Arnold, *Radiation Effects* 65: 17-30, 1982.
3. N. E. Bibler, *USERDA Report DP-1414*, Aiken, S.C.: Savannah River Laboratory, E. I. du Pont de Nemours and Co., 1977.
4. J. F. DeNatale and D. G. Howitt, *Radiation Effects* 91: 89-96, 1985.
5. J. F. DeNatale, D. G. Howitt, and G. W. Arnold, *Radiation Effects in Insulators* 3: 1, 229-236.
6. N. E. Bibler in S. V. Topp, Ed., *The Scientific Basis for Nuclear Waste Management*, New York: Elsevier, 1982.

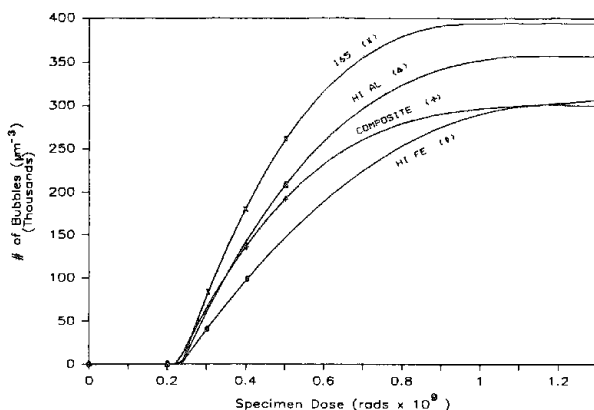
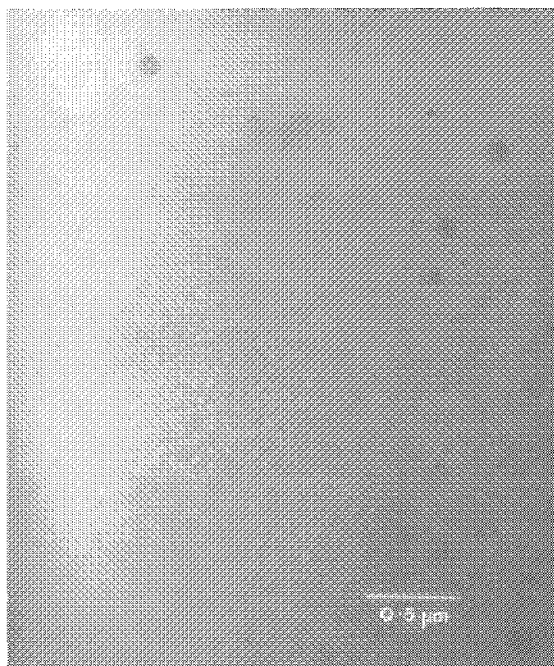


FIG. 1.--Oxygen bubbles formed by gamma irradiation.

FIG. 2.--Oxygen bubbles formed by in situ electron irradiation.

FIG. 3.--Oxygen-bubble formation as function of total gamma radiation dose received.

TABLE 1.--Chemical composition of the simulated nuclear wastes used in this study.

COMPONENT	AMOUNT (WT%)			
	165	HI AL	COMPOSITE	HI FE
Fe <sub>2</sub> O <sub>3</sub>	12.30	3.96	12.64	17.61
Al <sub>2</sub> O <sub>3</sub>	4.10	14.15	4.65	0.42
MnO <sub>2</sub>	2.90	3.24	3.52	1.19
NiO	0.90	0.57	1.07	3.01
SiO <sub>2</sub>	55.10	49.77	50.43	48.60
CaO	1.50	0.26	1.50	1.19
Na <sub>2</sub> O	10.30	10.70	9.02	10.89
B <sub>2</sub> O <sub>3</sub>	6.80	7.13	6.94	7.02
MgO	0.80	0.71	0.69	0.70
Li <sub>2</sub> O		4.99	4.86	4.91
Zeolite		2.93	2.05	2.89
Coal		0.66	0.31	0.63
Na <sub>2</sub> SO <sub>4</sub>		0.20	0.12	0.24
U <sub>3</sub> O <sub>8</sub>	4.60			
ZrO <sub>2</sub>	1.20			
Na <sub>2</sub> CO <sub>3</sub>			1.50	

## THE MICROSTRUCTURE OF EXPLOSIVELY DEFORMED ALUMINA

D. G. Howitt, J. P. Heuer, P. V. Kelsey, and J. E. Flynn

The explosive shock loading of materials can produce very large hydrostatic pressures in an extremely short period of time. This very high strain rate deformation is capable of inducing intense defect microstructures. For example, it is apparent that metals can be hardened by shock loading to three or four times the levels that can be otherwise achieved.<sup>1</sup> It is also apparent that these high rates of strain are associated with substantial temperature variations; the formation of shear bands (local regions of particularly high slip) is frequently observed.

In metals it has been shown that dislocation arrays, stacking faults, and twins can all contribute to this residual strengthening and that there is a correspondence between the stacking fault energy and the type of microstructure that forms.<sup>2</sup> Dislocation cell structures, for example, seem to be favored when the stacking fault energy is high (60 mJm<sup>-2</sup> for Cu and Ni) and planar dislocation arrays and twins are favored, at least in FCC metals, when the stacking fault energy decreases.

The types of defect that form in metals are quite similar to those induced at more conventional strain rates; however, the morphology is different, as is particularly noticeable in the intense dislocation activity that results in the formation of shear bands. This local slip plane activity, which produces extremely high shear strains, is sufficient to induce plastic instability. The presence of these shear bands has been generally attributed to a thermal softening of the material caused by the heat generation during plastic deformation. This conversion of mechanical energy to heat is probably very rapid and is generally regarded as an adiabatic effect. The local deformation could be conceivably self-perpetuating for the particular slip system,<sup>3</sup> although it is also likely that the thermal energy is derived from an alternative mechanical effect.

Experimental observations of the microstructure of explosively compacted alumina<sup>4</sup> has shown that dislocation arrays, similar in some respects to the shear bands observed in metals and twins, are present in the microstructure of compacted bodies that have achieved a density of about 90% of theoretical. The experimental observations presented here are of the microstructure that is produced by the explosive shock loading of an alumina monolith. In this case the material is reduced to a powder. It is the microstructure of these remnants that has been evaluated.

### Experimental

A monolith of fine-grained alumina (ALCOA RD99) was explosively shock loaded by a flyer-plate technique in the manner described by Murr.<sup>2</sup> The shock pressure was recorded as 20 Gpa for 4  $\mu$ s and the resulting powder was evaluated by transmission electron microscopy. The fine powder was examined by evaporation of an alcohol suspension onto a thin carbon film, which directly provided regions of sufficient electron transparency. Larger fragments were cut and polished into thin sections and then ion milled to electron transparency.

### Results

The microstructure of the residual alumina powder contained a high density of dislocations and twins. A substantial proportion of the deformation was concentrated in planar dislocation arrays similar to those observed in low stacking fault energy alloys. The majority of these arrays were in the basal plane (Fig. 1), but there was evidence of the formation of cellular dislocation structures and twins (Fig. 2). The twin structures were also similar to those observed in metals, and both these features, as well as fine microcracks (Fig. 3), were similar to the microstructure of the compacted alumina observed by Yust and Harris.<sup>4</sup>

The microstructure of the undeformed alumina was particularly uniform, composed of equiaxed grains of about 1  $\mu$ m in diameter with almost no detectable glass phase or defects (Fig. 4). This result is in sharp contrast to the microstructure of the explosively deformed structure, which showed a substantial variation in grain size and a fairly high proportion of glass phase.

### Discussion

The microstructure observed in the explosively loaded monolith is similar in many respects to the residual microstructure of the compacted powder observed by Yust and Harris.<sup>4</sup> This is specifically true of the shear band activity, which we observed in both the fine powder residue and in the interior of the large fragments. The substantial differences between the grain sizes of these fragments and the original material and the increased proportion of glass phase suggest that substantial temperature increases have been induced during the deformation of the monolith.

### References

1. L. E. Murr and D. Kuhlmann-Wilsdorf, *Acta Met* 26: 847, 1978.
2. L. E. Murr, in M. A. Meyer and L. E. Murr, Eds., *Shock Waves and High Strain Rate Phenomena in Metals*, New York: Plenum, 1981, 607.
3. C. Zener and J. H. Hollomon, *J. Appl.*

Authors Howitt and Heuer are at the Department of Mechanical Engineering, University of California, Davis, CA 95616; author Kelsey is at the Alcoa Technical Center in Pittsburgh, Pa.; and author Flynn is at the Idaho National Engineering Laboratory, Idaho Falls, ID 83415.

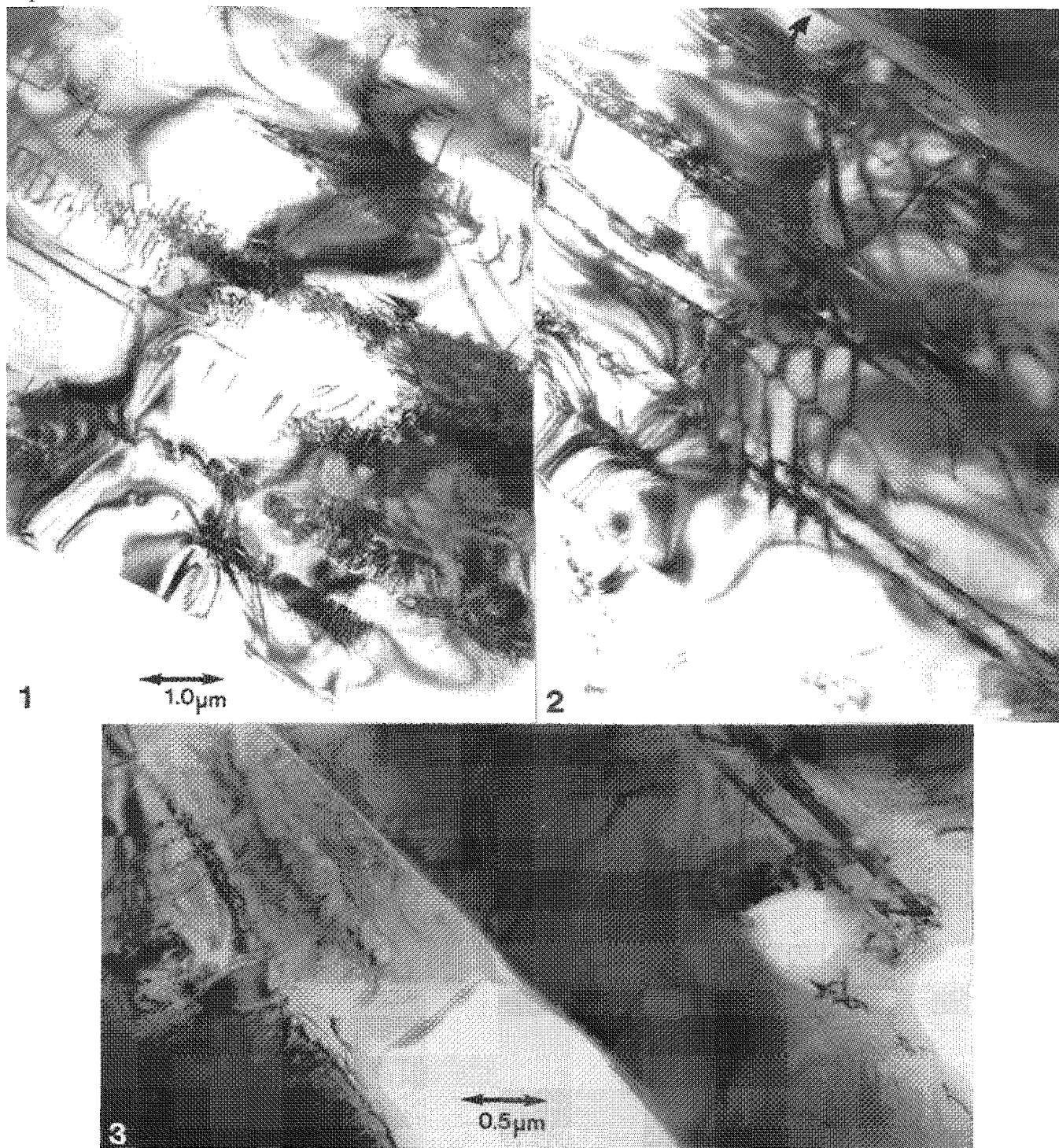


FIG. 1.--Bright-field micrograph showing shear bands in basal plane of alumina. Slip plane is inclined  $\sim 15^\circ$ ; dislocations are closely stacked and form shear bands. Diffraction vector is  $(3\bar{3}00)$ .

FIG. 2.--Bright-field micrograph of same region as in Fig. 1 but in  $(2\bar{1}\bar{1}3)$  reflection, with shear bands oriented normal to foil plane. Shear bands and contrast from dislocation array in the prismatic plane are clearly visible. Glass phase separating alumina grains is also more clearly visible (arrow).

FIG. 3.--Bright-field micrograph of microcrack which traverses an alumina grain.

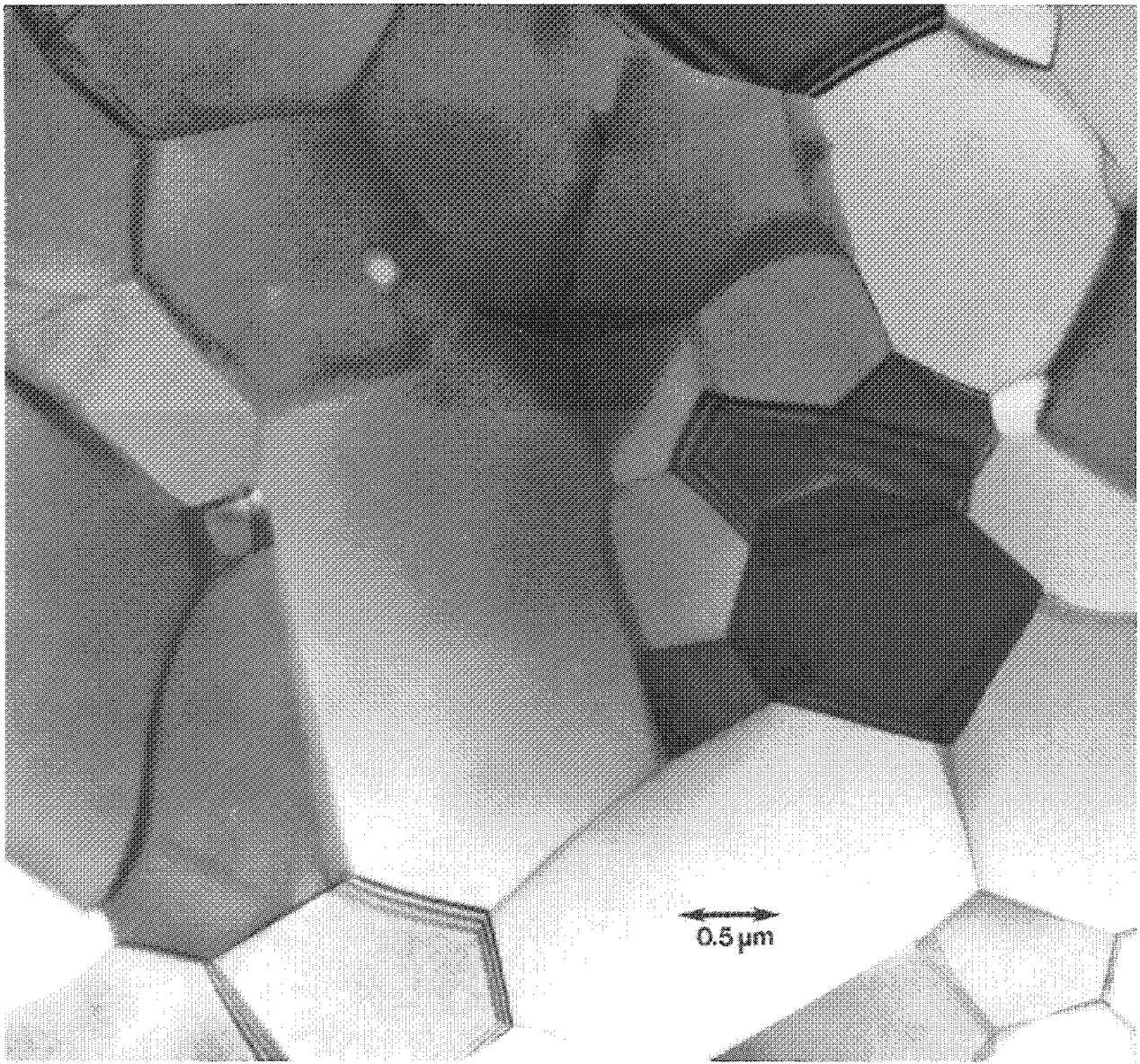


FIG. 4.--Bright-field micrograph of grain structure of alumina prior to deformation.

## CRYSTALLINE PHASES OF THE SIMULATED ICPP NUCLEAR WASTES

H. W. Chan, D. G. Howitt, and A. B. Harker

The principal factors in the consolidation of high-level nuclear waste (HLW) are the processed volume and the waste loading of the final consolidated form. The glass waste forms that have been identified for the storage of defense and commercial wastes are limited to practical loadings of about 33 wt% with a maximum density equal to 3 g/cm<sup>3</sup>. Polyphase ceramic waste forms, on the other hand, have been reported to offer up to 65 wt% waste loading with densities as high as 4 g/cm<sup>3</sup>. The waste form described here is a combination of both ceramic and glass which can accommodate up to 80 wt% of the HLW from the Idaho Chemical Processing Plant (ICPP). The composition of the final waste form is shown in Table 1; it has a consolidated density of 3.6 g/cm<sup>3</sup>, which includes the inert phases such as CaF<sub>2</sub>.<sup>1</sup> These wastes have been prepared with two different frits, silica-Y<sub>2</sub>O<sub>3</sub> and silica-Li<sub>2</sub>O, and samples of both final waste forms have been examined by electron microscopy.

### Experimental

Simulated ICPP waste was prepared with nitrates of the individual components combined with inert CaF<sub>2</sub> powder. The mixture was then calcined and hot pressed isostatically (HIPped) in Ar at a temperature of 1000 C and a pressure of 20 ksi. The specimens were sectioned and polished to 3 mm round disks and ion milled to perforation to use as electron microscopy specimens. These thin specimens were carbon coated to enhance charge dissipation and examined in the microscopes at 100 and 1500 keV.

### Microstructures

The microstructures of both the silica-Y<sub>2</sub>O<sub>3</sub> and silica-Li<sub>2</sub>O based waste forms contain a high-silica glass and various ceramic phases. The principal crystalline phases of the silica-Y<sub>2</sub>O<sub>3</sub> waste are cubic calcium fluoride (CaF<sub>2</sub>) and monoclinic zirconia (ZrO<sub>2</sub>). There are some other minor phases which include cubic zirconia and zirconium suboxides that have been reported in the ASTM card file. The amorphous phase has not yet been optimized and is principally single phased. The Li<sub>2</sub>O waste has a similar microstructure, but the phase-separated glass has not been found, and there is a substantial amount of zircon (ZrSiO<sub>4</sub>) which depletes silica from the glass phases.

The most abundant component in both ICPP

waste forms is cubic CaF<sub>2</sub> (Fig. 1). In this particular case, it is adjacent to a glassy region which does not exhibit any diffraction contrast. The CaF<sub>2</sub> phase can exist in one of two forms. It is present as the original CaF<sub>2</sub> powder, which remains as large spherical particles, or it can also recrystallize, in which case it invariably contains zirconia particles.<sup>2</sup>

Figure 2 illustrates the microstructure of the CaF<sub>2</sub> phase found in a melter waste glass based on the same calcine.<sup>3</sup> The melter glass is just a waste glass consolidated by melting the frit with the calcined waste followed by slow cooling. Obviously, the CaF<sub>2</sub> in the waste glass is still partially in solid solution with the glass phase and is not a single phase as it is after HIPping (Fig. 2). This behavior is consistent with phase stability predictions of the nuclear waste system;<sup>1</sup> i.e., the CaF<sub>2</sub> is expected to be found in solid solution as well as a single phase depending on the temperature of processing and the waste loadings.

Under the HIPping conditions used to prepare these ceramics, monoclinic zirconia is in fact the favored form rather than the cubic one.<sup>1</sup> Figure 3 shows the various morphologies of the monoclinic ZrO<sub>2</sub> in both waste forms with the corresponding selected-area diffraction patterns. Indexing of these patterns shows that some of the reflections correspond to the hexagonal Zr<sub>3</sub>O as well as the monoclinic ZrO<sub>2</sub> (Fig. 4), although the existence of the hexagonal form is rather doubtful. In addition, there are tweed and twin type microstructures present in the ZrO<sub>2</sub> particles which suggest that a transformation from the cubic to the tetragonal and monoclinic polymorphs occurs during cooling.<sup>4-6</sup>

The cubic form of ZrO<sub>2</sub> exists in the yttria-based waste forms as fine crystallites distributed in the other major phases such as CaF<sub>2</sub> (Fig. 5). The corresponding diffraction pattern from a large number of such cubic crystals can be straightforwardly identified. Moreover, other similar diffraction patterns show the coexistence of the tetragonal and cubic polymorphs. According to Heuer et al., bulk cubic zirconia is stable only from the melting point of 2680 to 3740 C when the tetragonal phase usually forms.<sup>6</sup> During cooling, the tetragonal polymorph precipitates from the cubic fluorite positions along the <100> directions.<sup>4</sup> The cubic phase is well known to be stabilized by the addition of Y<sub>2</sub>O<sub>3</sub>,<sup>1,7</sup> which in turns reduces the transformation temperature. Nonetheless, at room temperature, the monoclinic form is thermodynamically stable, and the cubic form transforms to the monoclinic one when the Y<sub>2</sub>O<sub>3</sub> concentration drops below 8 mole %.<sup>5</sup> We have not been able to identify the cubic zirconia in the silica-Li<sub>2</sub>O frit ICPP waste, but the x-ray powder diffraction pattern suggests that a small amount of this

Authors Chan and Howitt are at the University of California (Department of Mechanical Engineering), Davis, CA 95616; author Harker is at Rockwell International Corporation, Thousand Oaks, CA 91360. This work was supported by the U.S. Department of Energy, Idaho Operations Office.



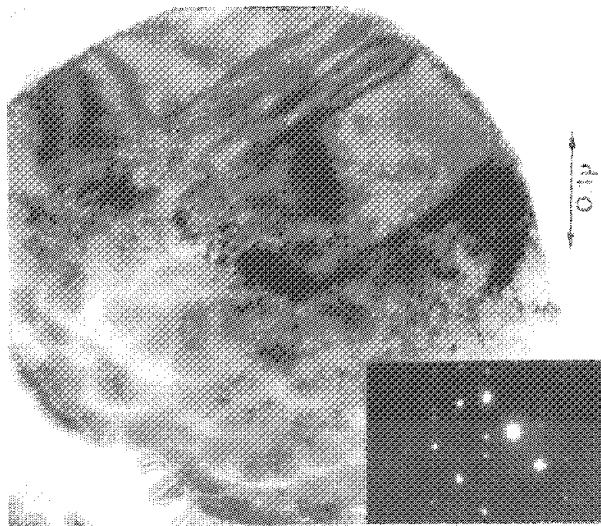
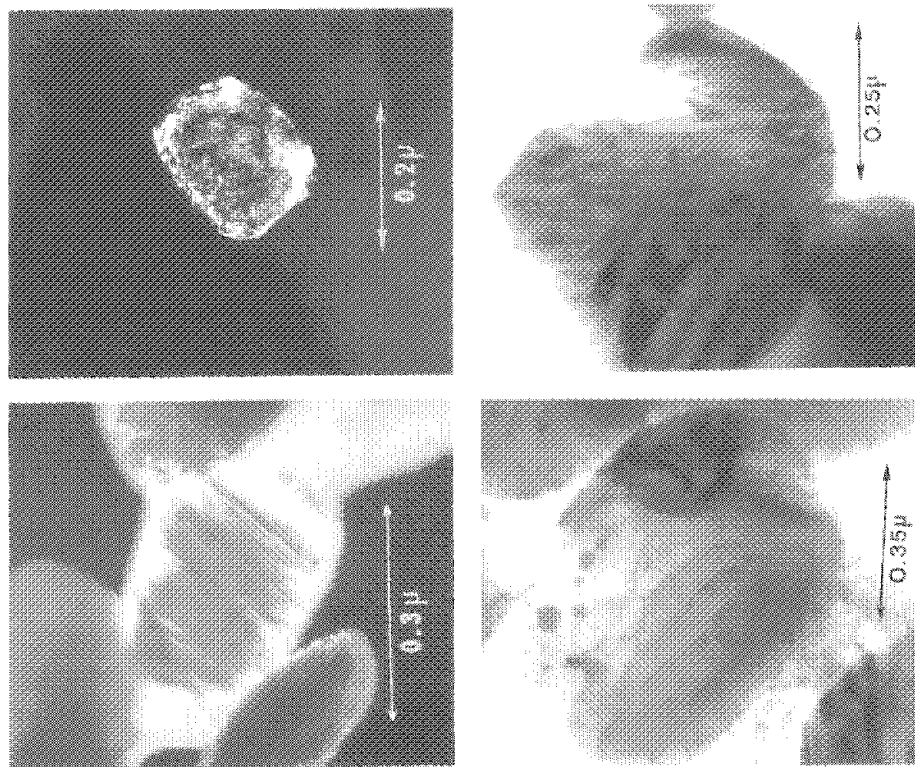
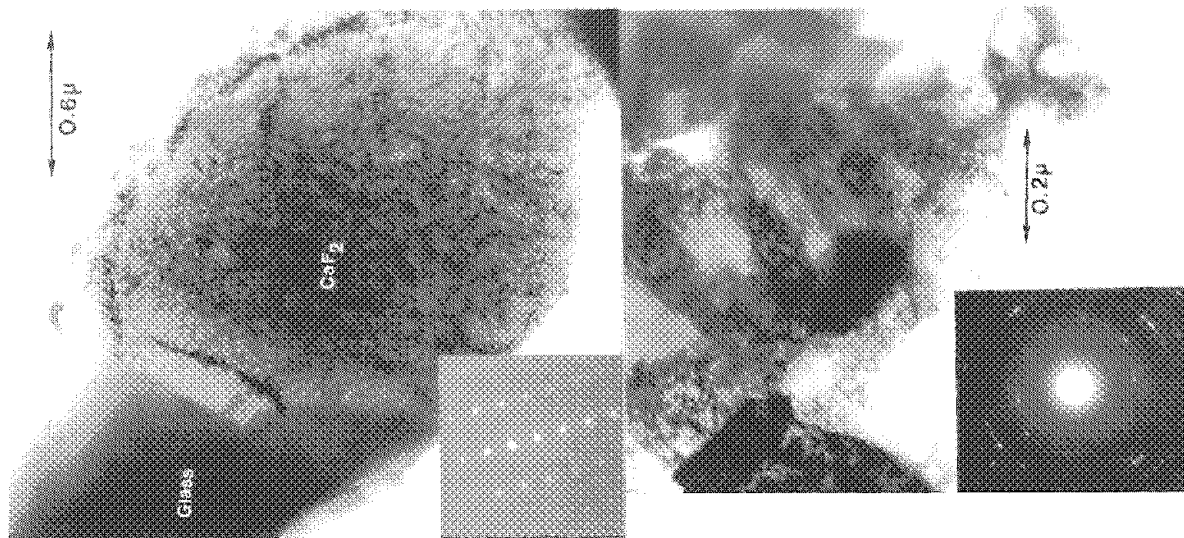


FIG. 1.-- $\text{CaF}_2$  phase from silica-yttria based waste.

FIG. 2.-- $\text{CaF}_2$  phase from melter waste glass. Note that ring-type diffraction suggests that  $\text{CaF}_2$  exists in small crystallites.

FIG. 3.--(a) Bright and (b) dark field micrographs of zirconia particles. Attached diffraction pattern from Fig. 3(b) is analyzed in Fig. 4.

phase is present. However, the major difference between the two forms is the presence of zircon in the  $\text{Li}_2\text{O}$  frit waste. Under the SEM, this phase appears as a large single crystal with a rectangular morphology; its TEM micrograph is shown in Fig. 6.

#### Summary

TEM analysis of simulated ICPP high level waste shows that the silica-yttria frit-based waste contains cubic  $\text{CaF}_2$ , monoclinic  $\text{ZrO}_2$ , and different glass phases. There are also minor phases such as cubic  $\text{ZrO}_2$  and suboxides of Zr and Cr. The silica- $\text{Li}_2\text{O}$  frit-based waste has the same basic microstructure except that the glass does not appear to phase separate, and there is a substantial amount of zircon,  $\text{ZrSiO}_4$ .

#### References

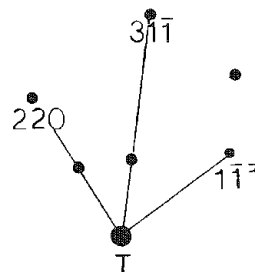
1. A. Harker and J. Flintoff, "Crystalline phase formation in hot isostatic pressing of nuclear waste ceramics with high zirconia content," *J. Am. Ceram. Soc.* 68[3]: 159-165, 1985.
2. A. Harker and J. Flintoff, "Polyphase ceramics and glass ceramic forms for immobilizing ICPP high-level nuclear waste," *Mat. Res. Soc. Symp. Proc.* 26: 513-520, 1984.
3. B. A. Staples et al., *Property of Formula 127 Glass Prepared with Radioactive Zirconia Calcine*, Report ENICO-1120, 1982.
4. R. Ingel and D. Lewis III, "Lattice parameters and density for  $\text{Y}_2\text{O}_3$ -stabilized  $\text{ZrO}_2$ ," *J. Am. Ceram. Soc.* 69[4]: 325-332, 1986.
5. R. Chaim, M. Rühle, and A. H. Heuer, "Microstructural evolution in a  $\text{ZrO}_2$ -12wt%  $\text{Y}_2\text{O}_3$  ceramic," *J. Am. Ceram. Soc.* 68[8]: 427-431, 1985.
6. S. Block, J. A. DaJornada, and G. J. Piermarini, "Pressure-temperature phase diagram of zirconia," *J. Am. Ceram. Soc.* 68[9]: 497-499, 1985.

7. A. H. Heuer and M. Rühle, "Phase transformation in  $\text{ZrO}_2$  containing ceramics," *Advances in Ceramics* (Science and Technology of Zirconia II) 12: 1-5, 1984.

TABLE 1.--Reference compositions for ICPP waste ceramics.

	80 wt% Waste 20% $\text{Y}_2\text{O}_3$ Frit	80 wt% Waste 20% $\text{Li}_2\text{O}$ Frit
$\text{ZrO}_2$	17.13	17.13
$\text{CaF}_2$	41.77	41.77
$\text{Al}_2\text{O}_3$	5.71	5.71
$\text{CaSO}_4$	0.81	0.81
$\text{CaO}$	4.46	4.46
$\text{B}_2\text{O}_3$	3.32	3.32
$\text{Na}_2\text{O}$	3.01	3.01
$\text{CaO}$	2.06	2.06
$\text{K}_2\text{O}$	0.44	0.44
$\text{Ce}_2\text{O}_3$	1.20	1.20
$\text{U}_3\text{O}_8$		
$\text{Cs}_2\text{O}$		
$\text{SrO}$		
$\text{Fe}_2\text{O}_3$	0.09	0.09
$\text{SiO}_2$	16.72	$\text{SiO}_2$ 18.38
$\text{Y}_2\text{O}_3$	3.28	$\text{Li}_2\text{O}$ 1.62

Material: ICPP  
Phase: Monoclinic  $\text{ZrO}_2$   
Zone axis:  $[\bar{1}\bar{1}2]$



Material: ICPP  
Phase: Hexagonal  $\text{Zr}_3\text{O}$   
Zone axis:  $[\bar{1}2\bar{1}0]$

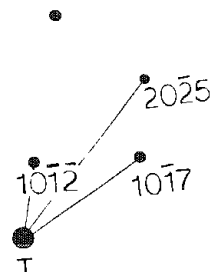


FIG. 4.--Analysis of diffraction pattern from Fig. 3(b).

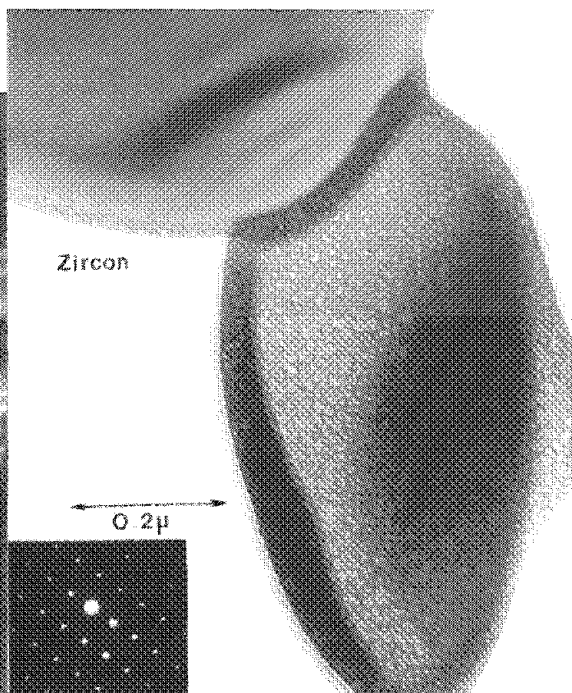
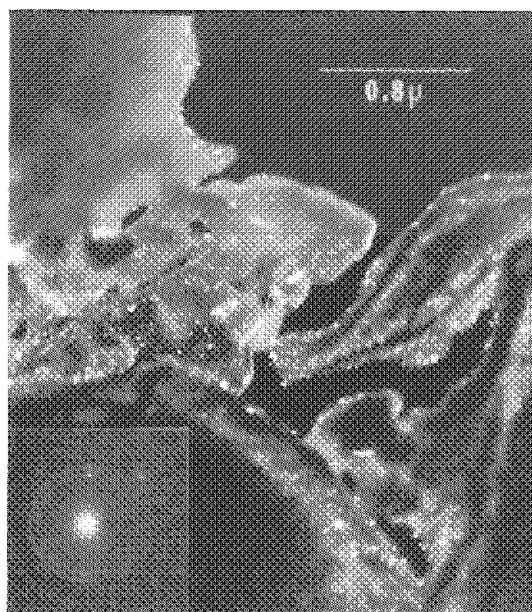


FIG. 5.--Cubic  $\text{ZrO}_2$  from yttria-based waste form. FIG. 6.--Zircon from lithia-based waste form.

## A MICROSTRUCTURAL STUDY OF ALUMINUM- $\delta$ -ALUMINA COMPOSITES

W. J. Clegg, I. Horsfall, and N. A. Briscoe

In this paper we describe the microstructure of aluminum-base matrix composites containing  $\delta$ - $\text{Al}_2\text{O}_3$  fibers and prepared by squeeze infiltration. We show that the melt around the fibers solidifies last, so that the interfacial region around them is rich in solute. For specific solutes, such as magnesium, this sequence can lead to changes in the interfacial strength. Electron microscopy shows that magnesium can be absorbed into the surface layers of the fiber without the formation of continuous interfacial phases.

That metal matrix composites are now attracting considerable interest as structural materials of high specific stiffness and strength is due to the development both of new, cheap reinforcing materials such as  $\text{Al}_2\text{O}_3$  fibers and SiC whiskers, and of suitable fabrication methods that yield composites free from gross flaws, with intimate contact between the fiber and the matrix. Of these methods perhaps the simplest and most economically attractive is that of infiltrating a suitable mat of fibers, or preform, with liquid metal.

Despite the technological interest in this process, very little work has been carried out to determine how the microstructure of such a composite is developed during fabrication. In this paper we have studied the microstructure of aluminum alloy matrix composites containing fibers of  $\delta$ - $\text{Al}_2\text{O}_3$  and prepared by squeeze infiltration. We have emphasized the role of the fibers in determining the solidification of the matrix and the effects it has on the interfacial region between the matrix and fiber in terms of chemical composition and properties.

### *Experimental*

Composites were prepared by squeeze infiltrating preforms of "Saffil" RF-grade fibers ( $\delta$ - $\text{Al}_2\text{O}_3$  fibers from ICI) with liquid metal. The fibers are about 3 mm in diameter and are chopped and milled to give a length of about 500  $\mu\text{m}$ . The composition is a  $\delta$ - $\text{Al}_2\text{O}_3$  containing about 5%  $\text{SiO}_2$ , uniformly distributed throughout the fiber. The fibers are then arranged in a planar random array, with a silica binder used to give the preform some handling strength.

The melt was superheated by about 200 C before being infiltrated into the preform under a pressure of about 20 MPa. The details are described elsewhere.<sup>1</sup> Microstructural analysis was carried out on polished sections by both optical microscopy and SEM and by TEM on thin foils prepared by grinding to about 70  $\mu\text{m}$  and then ion milling.

### *Results and Discussion*

The fiber distribution in the composite is similar to that in the preform; the planar random nature is quite clearly seen in Fig. 1, showing polished sections both parallel and perpendicular to the fiber plane for an Al-2.5 wt% Mg matrix. Figure 2 shows a squeeze cast section of some of the unreinforced material. The most striking feature is the considerable grain refinement that occurs in the fiber-containing material. At first we thought the cause was that fibers acted as nucleating sites for the matrix grains.<sup>2</sup> Further work on a material containing only 0.05 volume fraction of fibers showed that this was not the case. As shown in Fig. 3, there is a transition from fine-grained to coarse-grained material within the fiber-containing region of the composite. This transition suggests that the differences in grain structure arise from differences in the undercooling of the melt down the composite; i.e., we assume that the fibers absorb heat very rapidly from the liquid metal as the melt front passes through the preform. The part of the melt that passes through the preform first (and finishes up at the bottom of the preform) has a greater undercooling than that which passes through the preform slightly later on, as the fibers through which it passes are now preheated by the initial melt. The grain size is therefore smaller as one proceeds from the bottom to the top of the composite. That the fibers do absorb heat rapidly has been confirmed by the calculations of Clyne and Mason,<sup>3</sup> who showed that the fibers reached the melt temperature in microseconds.

This result is also consistent with the observation that the transition from a small to a large grain size occurs closer to the bottom of the preform containing a 0.05 volume fraction of fibers than in one where the volume fraction is higher at 0.18. However, the most convincing evidence that it is heat flow that determines the grain size is the observation that the grain size begins to decrease again as one moves toward the top face of the billet in the fiber-free region due to absorption of heat by the ram.

That solidification of the melt takes place in this way has a significant effect on the fiber-matrix interface region: rather than being the first region of the matrix to solidify, it is the last, so that the fibers become surrounded by solute rich liquid. This result is clearly seen in Fig. 4, which shows the copper-rich phases formed by the rejection of solute ahead of the growing dendrite in an Al 2024 alloy.

For some solutes, such as magnesium, this effect can lead to changes in the properties of the fiber-matrix interface, as shown in Fig. 5, which shows the fracture surfaces of an Al-2.5 wt% Mg matrix and 99.97% pure Al matrix containing 0.18 volume fraction of fibers.

---

The authors are at Imperial Chemical Industries, Runcorn, England.



In the former, the fracture surface consists of ductile dimples, each of which contains a fiber that has been broken by the growing crack. (That the fibers were indeed broken, rather than the dimples growing from the ends of the fibers, was confirmed by examination of mating halves of the fracture surface.) However, in the pure-aluminum matrix there is a complete change, in that final crack growth takes place by the decohesion of fibers parallel to the fracture surface. These observations suggest that magnesium raises the interfacial strength of Al- $\delta$ -Al<sub>2</sub>O<sub>3</sub> composites.

Electron probe microanalysis in the SEM indicates that the magnesium is almost always associated with silicon (Fig. 6). The silicon appears to originate from the silica binder and leads to the formation of particles at the interface. These particles could hardly be expected to raise the interfacial strength; indeed, fracture surfaces of a commercial purity aluminium showed that they tended to act as nuclei for cavities (Fig. 7).

TEM of the interfacial region shows that magnesium is observed into the very surface layer of the fiber to the depth of about a single crystallite about 5 nm (Fig. 8). Only magnesium appears to be absorbed in this fashion. The exact mechanism by which this

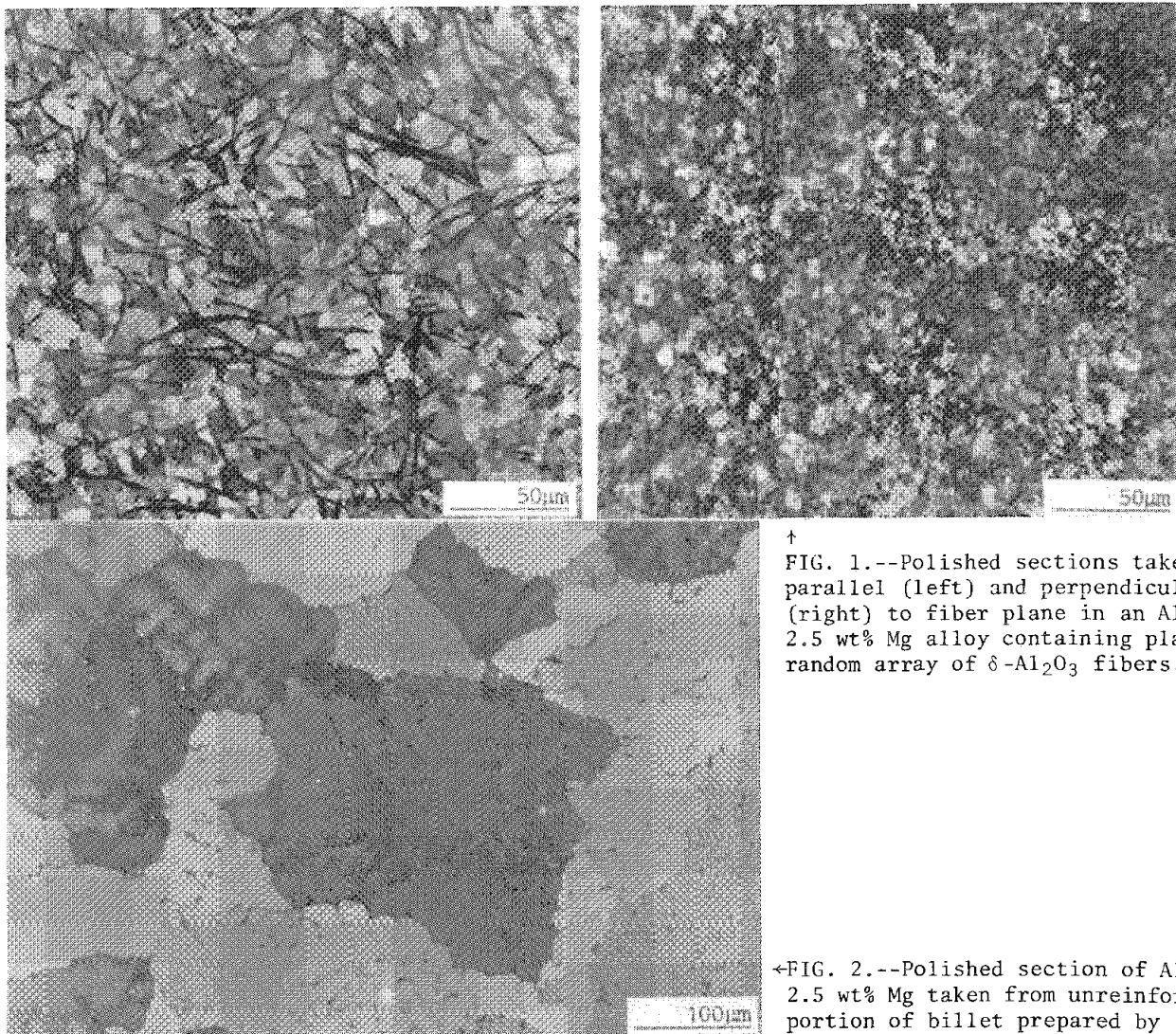
process leads to an increase in the interfacial strength is not yet clear, but it does allow some measure of control over the interfacial properties of Al- $\delta$ -Al<sub>2</sub>O<sub>3</sub>.

### Conclusions

The grain structure of squeeze-infiltrated composites is determined by the effect of fibers on the undercooling of the melt rather than the fibers acting as nucleation sites for grains. This process leads to the melt surrounding the fiber that is the last to freeze, so that the particle/matrix interface is rich in solute. That can lead to the precipitation of excess solute at the interface, which may have deleterious effects. However, in the case of magnesium the excess solute can be absorbed into the interface and increase the interfacial strength.

### References

1. T. W. Clyne and M. G. Bader, *Proc. ICCM AIME*, 1985, V, 775.
2. M. G. Bader, T. W. Clyne, C. R. Cappleman, and P. A. Hubert, *Composite Science and Technology* 23: 1985.
3. T. W. Clyne and J. F. Mason (in preparation).



↑  
FIG. 1.--Polished sections taken parallel (left) and perpendicular (right) to fiber plane in an Al-2.5 wt% Mg alloy containing planar random array of  $\delta$ -Al<sub>2</sub>O<sub>3</sub> fibers.

←FIG. 2.--Polished section of Al-2.5 wt% Mg taken from unreinforced portion of billet prepared by squeeze infiltration.

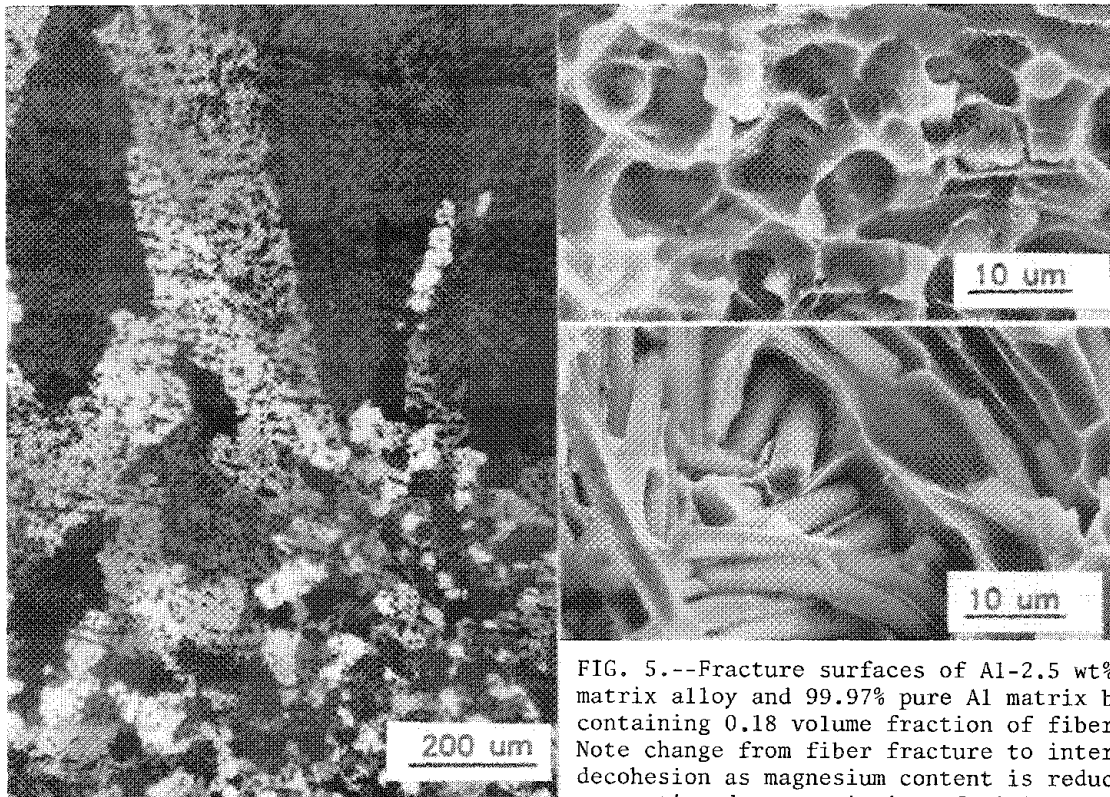


FIG. 3.--Polished section of Al-2.5 wt% Mg alloy containing 0.05 volume fraction of  $\delta$ -Al<sub>2</sub>O<sub>3</sub> fibers, transverse to fiber plane. Note sudden increase in grain size in reinforced portion of billet.

FIG. 5.--Fracture surfaces of Al-2.5 wt% Mg matrix alloy and 99.97% pure Al matrix both containing 0.18 volume fraction of fibers. Note change from fiber fracture to interfacial decohesion as magnesium content is reduced, suggesting decrease in interfacial strength.

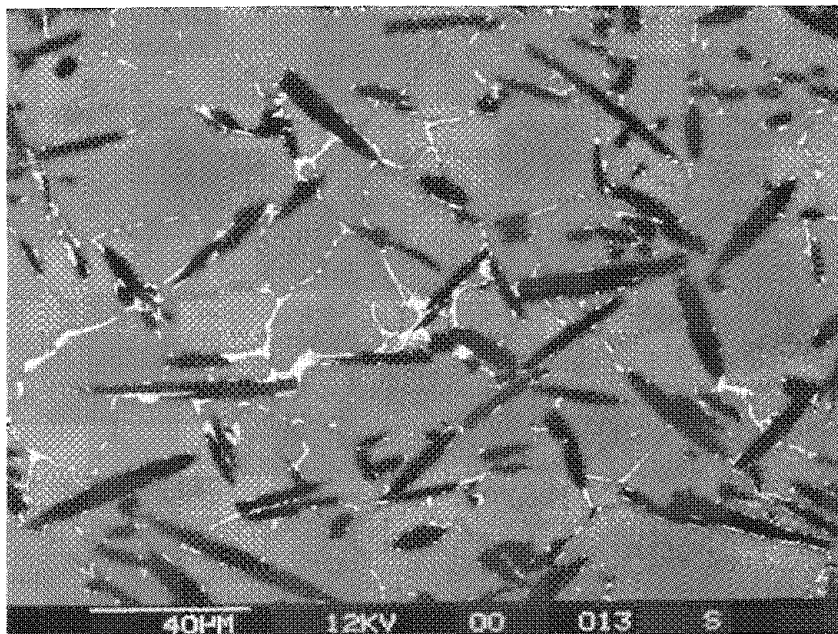


FIG. 4.--Polished section in fiber plane Al-2024 matrix composite containing 0.18 volume fraction of fibers. Interfacial phases present at the fiber-matrix interface are thus due to rejection of solute from growing dendrite.

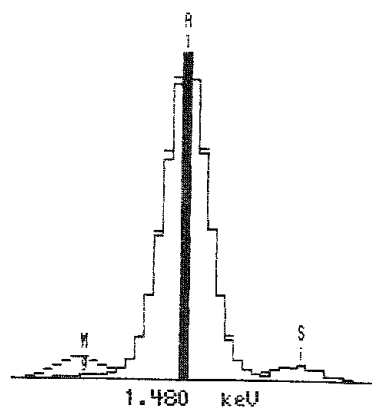
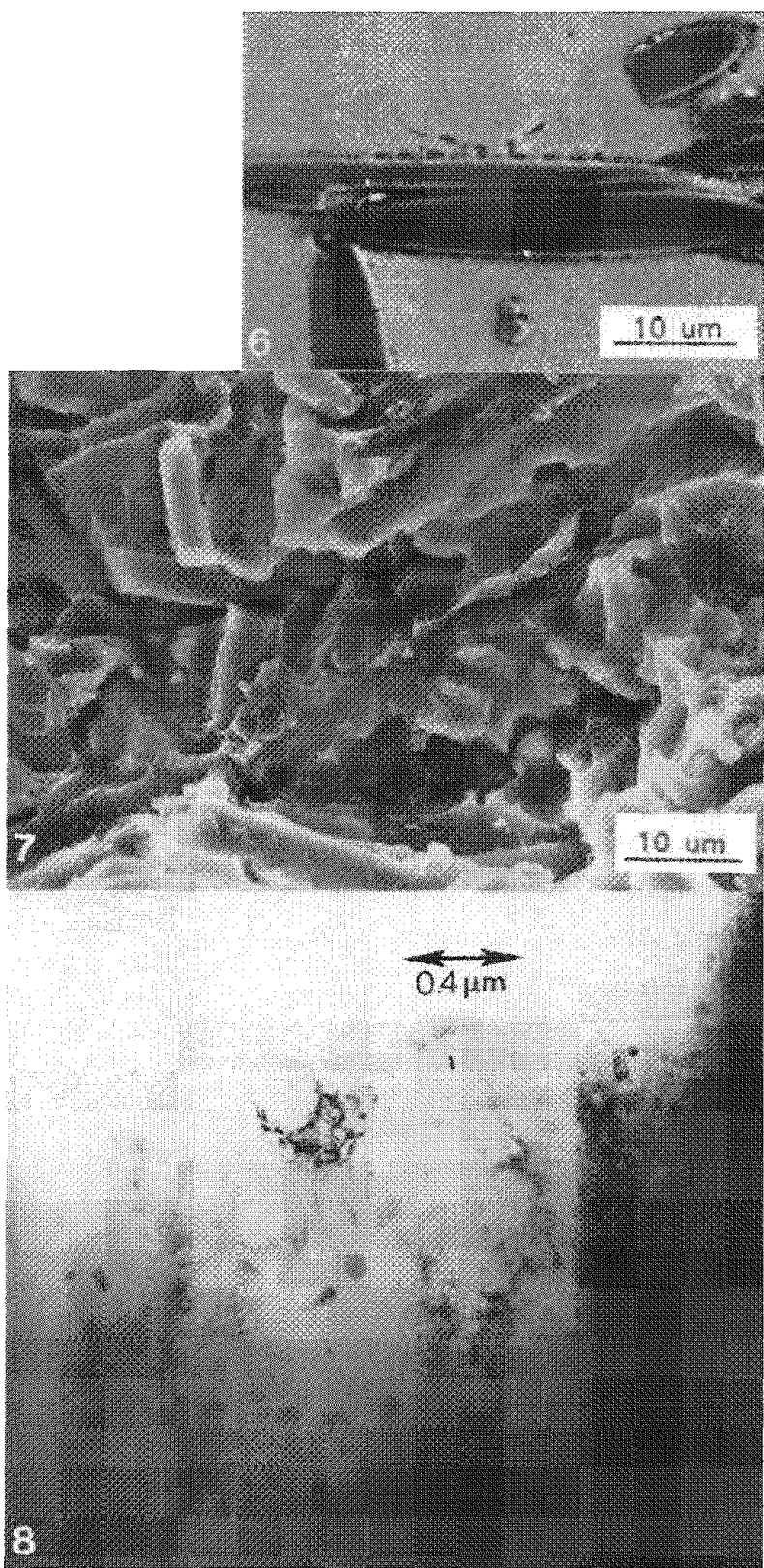


FIG. 6.--EDMA shows that particles at particle/matrix interface consist of magnesium and silicon and are presumably Mg,Si.  
 FIG. 7.--Fracture surface of commercial purity aluminium matrix containing 0.18 volume fraction of fibers. Note particles acting as nuclei for cavities at fiber matrix surfaces.  
 FIG. 8.--Magnesium-rich layer in surface crystallites of a fiber in aluminium alloy containing magnesium.



## SAMPLE PREPARATION OF RAPIDLY SOLIDIFIED POWDER PARTICLES FOR ANALYTICAL ELECTRON MICROSCOPY

R. E. Omlor, P. F. Lloyd, R. D. Brodecki, and A. G. Jackson

In aerospace applications today there is great interest in rapid solidification technology (RST). One method of achieving RST is through powder metallurgy (PM). The physical properties of the end products made from PM depend on the microstructure and chemical composition of these powders. The preparation of these individual particles of rapidly quenched pre-alloyed powders for study in the STEM presents a real challenge. The information obtained by study of these individual particles can lend insight into the optimization of the powder-producing techniques as well as the interrelationships between the as-produced powder, densification processes, and the properties of the end product. This paper describes valid techniques for preparing thin foils from aluminum and titanium pre-alloyed powder with the use of conventional electropolishing techniques.

### Procedure

In the past, thin foils have been made from pre-alloyed powders by electropolishing, ion milling, and microtoming techniques; each of these techniques was effective in specific cases. To be successful in ion milling the powder type must possess a sputtering rate comparable to or faster than that of the substrate material. The microtome procedure involves embedding the powder in an epoxy substrate of comparable hardness. Each of these methods involves many hours of sample preparation time. Jet acid thinning (electropolishing) was then chosen as the most suitable method for sample preparation. With the wide range of particle size, 5 to 200  $\mu\text{m}$  (Fig. 1), and the wide variety of shapes (Fig. 2), the powder particles must be embedded in a metal matrix that can be handled like a conventional foil.

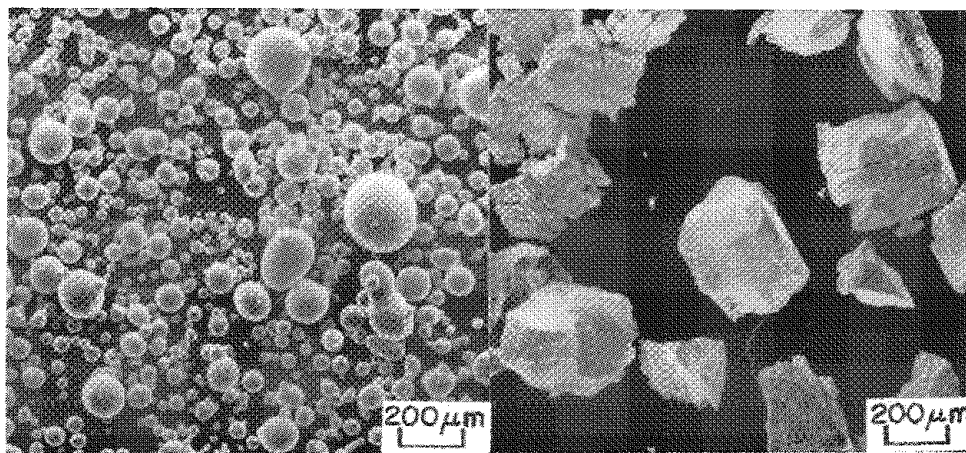


FIG. 1.--SEM micrograph of as-received pre-alloyed aluminum powder.

A nickel-plating technique was chosen as the method to produce a workable metal matrix. The Ni-plating equipment is shown in Figs. 3 and 4.

The powder is placed on a wet (methanol) stainless-steel cathode and placed in the Ni-sulfamate plating solution. The solution is heated to +60 C with *no* stirring; a 1A current is applied for 15 h to accomplish the plating. When plating is completed, the Ni-plated powder particles are mechanically polished to a thickness of 0.003-0.005 in. before removal from the stainless steel cathode. Standard 3mm foils are then punched. The foils are electropolished in a solution of 5%  $\text{H}_2\text{SO}_4$  in methanol at -50 C.

### Results

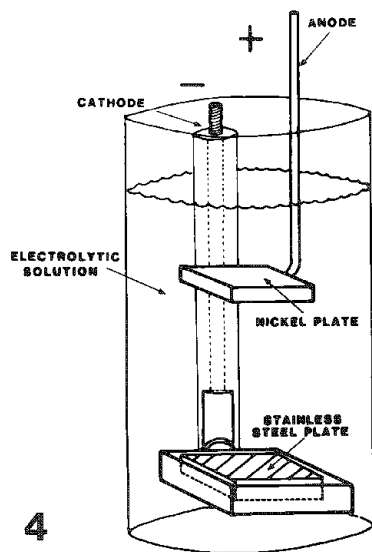
Ni-plating and electropolishing parameters have been established for both aluminum and titanium pre-alloyed RST powders. Figures 5 through 7 show results obtained by these procedures. With this development, complete analytical microscopy can be performed on the as-received pre-alloyed powders.

### References

1. T. E. Tietz and I. G. Palmer, "Advanced P/M alloys," *Advances in Powder Technology*, 189-224, 1981.
2. M. J. Couper and R. F. Singer, "Rapidly solidified aluminum alloy powder produced by optimization of the gas atomization technique," *Proc. 5th Intern. Conf. on Rapidly Quenched Metals*, Würzburg, Federal Republic of Germany, 1984.
3. D. Schechtman and E. Gutmanar, "Transmission electron microscopy of metallic powders," *Praktische Metallographie* 18: 587-593, 1981.

FIG. 2.--SEM micrograph of as-received pre-alloyed titanium powder.

The authors are at Systems Research Laboratories, Inc., 2800 Indian Ripple Rd., Dayton, OH 45440. This research was done under Government Contract F-33615-86-C-5073.



4. L. E. Matson and R. E. Omlor, "Thin-foil preparation of prealloyed metal powders," in R. Mehrabian, B. H. Kear, and M. Cohen, Eds., *Rapid Solidification Processing*, 1980, 135-140.

5. G. S. Morris, "Transmission electron microscope study of aluminum powder," *Powder Metallurgy* 4: 208-209, 1979.

6. D. Schechtman, *Supersaturated Aluminum Alloy Powders*, EOARD-TR-80-6, November 1979.

7. M. J. Couper, "Microstructure of rapidly solidified aluminum alloy powders," *Proc. PM Aerospace Materials Conf.*, Berne, 1984.

8. R. Baumann and M. J. Couper, "Microstructure of rapidly cooled aluminum powders," *Practical Metallography* 3: 140-148, 1986.

9. Private conversation with S. Kirchoff and Lt. J. Adkins, AFWAL/MLLS.

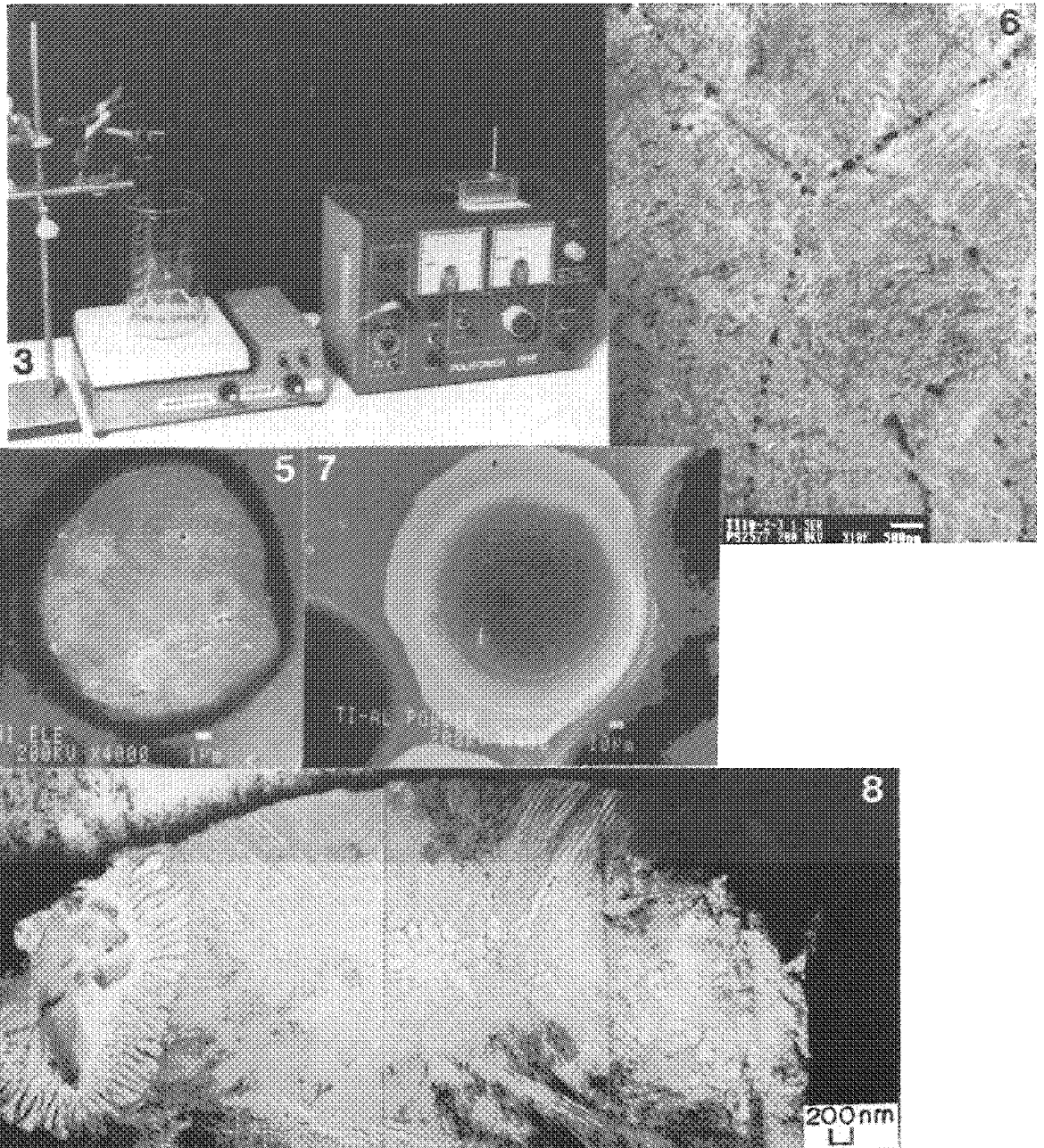


FIG. 3.--Standard Ni-plating equipment.

FIG. 4.--Schematic of Ni-plating bath.

FIG. 5.--SEM micrograph (JEOL 2000-FX STEM) of

perforation in center of Ni-plated Ti-Al powder particle.

FIG. 6.--TEM image of Ti-10-2-3

1.5 Er showing Er in grain boundaries.

FIG. 7.--SEM micrograph (JEOL 2000-FX STEM) of

two Al-Fe-Ni nickel-plated powder particles.

FIG. 8.--TEM montage showing complete Al-Fe-Ni

powder particle.

## DIFFUSION IN SHOCK-ACTIVATED Be-Al INTERFACES

N. E. Elliott, K. P. Staudhammer, and K. A. Johnson

Over the past decade, several studies have shown significant shock effects on materials.<sup>1-3</sup> Shock activation has been successfully employed as an aid in hot pressing hard to consolidate powdered material, with concomitant decrease of temperature and/or time required for sintering.<sup>4,5</sup> Mechanisms for this beneficial effect are not understood in detail at present. However, the effect depends strongly on the degree of introduction of atomic-level defects, such as dislocations, in the material during shock.<sup>6</sup> The objective of this study was to obtain initial information on a related effect, the diffusion of solid aluminum-clad beryllium subjected to an explosive-shock loading environment. The postshock elemental concentration profiles were evaluated as a function of time and temperature. An experimental approach allows the routine and convenient observation of effects of shock pressures from roughly 1 to 170 GPa in a single sample. The exact pressures achieved depend on the material being shocked. In this investigation the maximum estimated pressure was 40 GPa with associated local strains of less than 8%. The shock design and parameters allowing the routine recovery of specimens has been given elsewhere.<sup>7</sup>

The Al-Be system is reported as a simple eutectic with low solid solubilities for each element.<sup>8</sup> The enhancement of Al diffusion in Be by shock was postulated because defects in microstructure can enhance diffusion, particularly if the homologous temperature of the second element is significantly lower than that of the matrix containing the defects. This is the case in the Al-Be system: Al has a melting point 0.6 that of Be, which implies that the defects in Be are not appreciably annealed out at the temperatures required for Al diffusion. The concept was that increased solubility of Al would result in bonds of higher strength during subsequent solid-state bonding of Be parts with an Al intermediate layer.<sup>8-10</sup>

### Experimental

A Be rod 3.0 mm in diameter was vacuum vapor deposited with Al on the outer circumference to a thickness of approximately 10  $\mu\text{m}$ . This rod was then inserted into an 1100 Al sleeve with an outer diameter of 9.5 mm, which was in turn inserted into a 304 stainless-steel holder (Fig. 1). High explosive detonated around the outside of this assembly produced shock pressures from roughly 4 to 40 GPa in the Be and associated strain of 0% to 8% at the low- and high-pressure ends. The post-shock samples were heated and the distribution of Al in the Be was measured by energy- and

wavelength-dispersive spectroscopy in a scanning electron microscope. The heat treat temperatures used in this investigation were 640 C (solid state) and 680 C (Al melt). The Al solubility was expected to be greatest in the portion of the sample with the highest defect density as a result of pressure and strain. Figure 2 shows the Be-Al interface region with the beam path and Al x-ray profile superimposed. The concentration gradient is shown in more detail in Fig. 3. The average measured concentration of Al away from the interface is 0.05 wt% for sample areas shocked at 40 GPa and only 0.02 wt% for the sample areas shocked at 4 GPa. These measured concentrations of Al in Be seem to exceed levels predicted by the equilibrium phase diagram. This portion of the phase diagram has widely varying reported solubility of Al in Be ranging from 0 to 4 or 5 wt% per cent near 630 C.<sup>8</sup> It is even possible that the Al-Be system may be immiscible.<sup>11</sup> This variability is also found in other Be binary systems and a variety of possible explanations exist. The relative changes in Al solubility we have measured are significant (Fig. 4). The data are the result of repeated measurements with a  $\pm 10\%$  relative variation. Most of this variation appears correlated to morphology of the Be. The actual value thus depended on where the measurement was made. The preferential concentration of Al near Be grain boundaries may indicate that the Al was "injected" into the Be via the shockwave at the grain boundaries. Alternately, the heat treatment may act to exsolve the Al and return the system to the equilibrium state. The estimated residual shock temperature of highly strained Be at 40 GPa is 288 C.<sup>12</sup> The lower strain of this experiment should reduce this temperature. We do not feel that this temperature affects the observed results.

If the existing equilibrium phase diagram for Al-Be can indeed be considered a reliable indicator, we can only speculate on quasi or nonequilibrium shock effects. At 40 GPa in Be the estimated adiabatic temperature is 700 C.<sup>12</sup> Under these combined extreme conditions material could be "carried" considerably further into the Be than what would be expected with only a single variable (time or temperature) being applied.

### Conclusion

Aluminum solubility in Be can be enhanced in a single, uniform specimen by shock activation. The absolute solubility and detailed nature of this enhancement remain to be determined.

### References

1. M. A. Meyers and L. E. Murr, *Shock Waves and High Strain-rate Phenomena in Metals*, New York: Plenum, 1981.
2. L. E. Murr et al., *Metallurgical*

The authors are at the Los Alamos National Laboratory (Materials Science and Technology Division), Los Alamos, NM 87545.

*Applications of Shock-Wave and High Strain-rate Phenomena*, New York: Marcel Dekker, 1986.

3. Y. M. Gupta, *Shock Waves in Condensed Matter*, New York: Plenum, 1986.

4. R. A. Prummer, "Das Explosivscheissen," *J. Mat. Tech.* 3: 306-310, 1972.

5. S. Soga et al., in T. R. Asay et al., Eds., *Shock Waves in Condensed Matter*, Amsterdam: Elsevier Science Publishing Co., 1983, 375-478.

6. K. P. Staudhammer, K. A. Johnson, and B. W. Olinger, *Third APS Topical Conference on Shock in Condensed Matter*, 1983, 419-422.

7. K. P. Staudhammer and K. A. Johnson, in C. M. Cheng et al., Eds., *Proc. Intern. Symp. on Intense Dynamic Loading and Its Effects*,

Beijing: Science Press, 1986, 759-764.

8. R. P. Elliott, *Constitution of Binary Alloys*, New York: McGraw-Hill, 1985.

9. L. A. Jacobsen, *Joining Methods for Beryllium: A Survey*, UCID-20750, 1986.

10. D. Hauser, D. G. Howden, and R. E. Monroe, *Technical Management Report on Diffusion Welding of Beryllium*, Columbus, Ohio: Battelle Memorial Institute, 1970.

11. W. J. Boettinger and J. H. Perepexko, in S. K. Das, Ed., "Fundamentals of rapid solidification," *Rapidly Solidified Crystalline Alloys*, New York: Metallurgical Society, 1985, 29.

12. M. A. Meyers and L. E. Murr, Ref. 1, App. B.

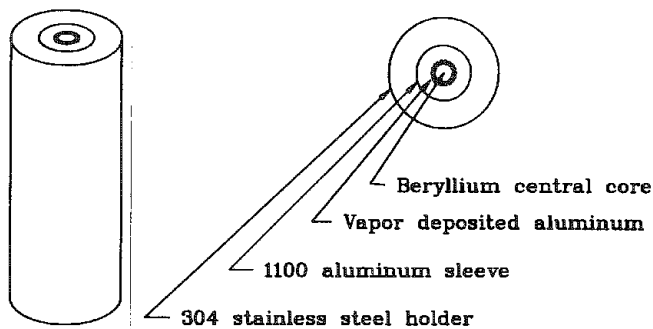


FIG. 1.--Shock-loading assembly showing configuration used for aluminum-clad beryllium.

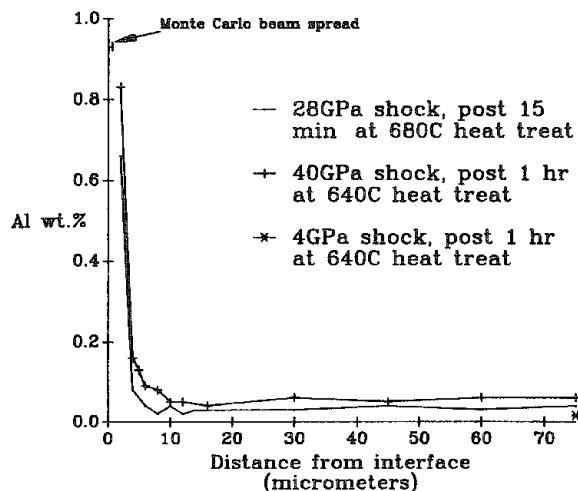


FIG. 3.--More detailed Al profile across Al/Be interface with result of Monte Carlo beam-spread calculation.

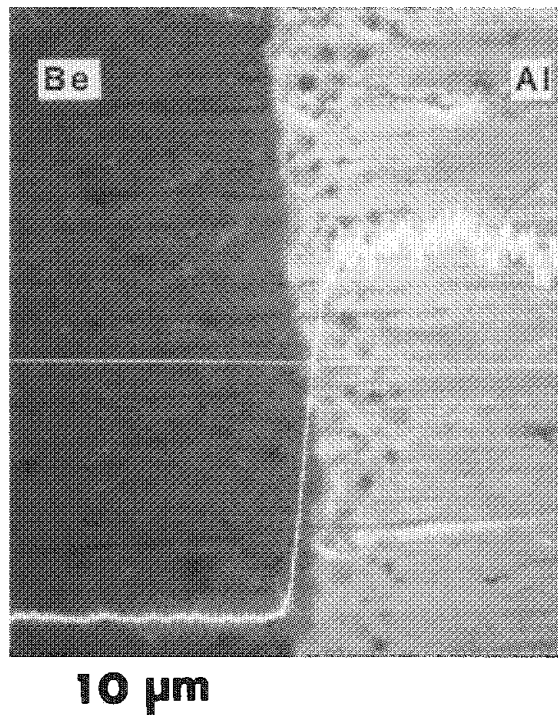


FIG. 2.--Backscattered electron image of Al/Be interface. Background-subtracted Al x-ray profile shows major Al diffusion (electron spread estimated at 0.7  $\mu\text{m}$ ).

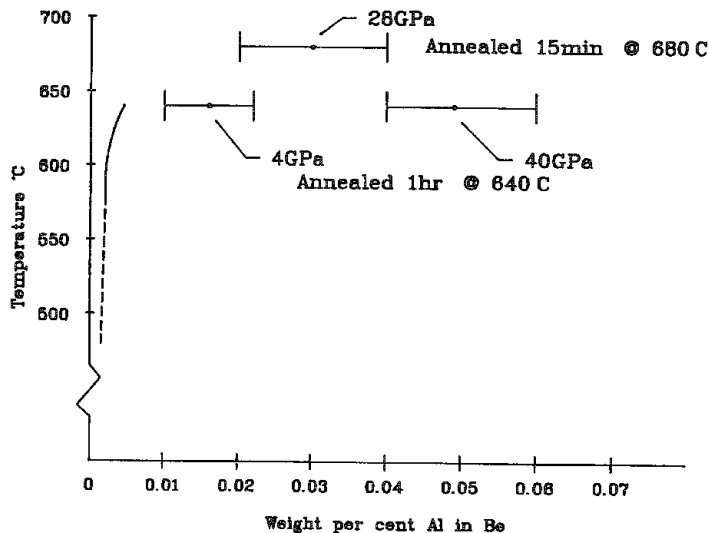


FIG. 4.--Measured Al solubilities (this study) and published equilibrium solubility.



## 5B. Materials Science: Thin Films

### TRANSFORMATION BEHAVIOR IN AMORPHOUS THIN FILMS

J. F. DeNatale and A. B. Harker

Crystallization behavior and microstructural development have been studied in thin films of titanium and vanadium oxides. Several common mechanisms of nucleation, consolidation, and stress accommodation along with orientation phenomena have been observed in free-standing and substrate-supported films by transmission electron microscopy, and their qualitative effects on thin-film microstructures are illustrated.

The microstructural development of crystalline thin films is a complex function of their specific deposition and annealing conditions. This development has in general a correspondingly strong influence on the electrical, optical, and physical properties of these films. In the study of the relationships between physical properties and film microstructures in the oxides of titanium and vanadium, a number of distinct microstructures associated with the mechanisms of nucleation, stress accommodation, grain consolidation, and crystal orientation have been observed. These structures and transformation mechanisms are typical of those found in both oxide and nonoxide materials, and qualitatively illustrate the effects of various deposition, film, and substrate parameters that influence the crystallization behavior of thin films in general.

#### *Experimental*

The thin films in this study were prepared by reactive ion beam deposition, with a single Kaufman-type source and a background pressure of oxygen. Sputtering targets included both metallic and ceramic materials. The substrate was heated from room temperature to 550 C, which resulted in either initially amorphous or crystalline films. Films were deposited onto single crystal NaCl and floated onto TEM grids for free-standing films, and deposited onto electron transparent foils of various substrate materials for supported films. Postdeposition annealing was conducted both in controlled atmosphere tube furnaces and in the ultrahigh-vacuum deposition chamber itself.

#### *Results and Discussion*

Although the factors affecting thin film transformations are highly interrelated, their influence on the ultimate film microstructure can be divided into factors affecting nucleation and those affecting growth and consolidation.

Factors related to nucleation and early-stage growth

1. *Preferred crystallographic growth modes, e.g., needles, laths, oblate spheroids.* This factor is similar to that affecting bulk

nucleation behavior; however, the influence of the thin-film geometry can alter the magnitude and direction of the strain contributions to free energy, as can the interfacial forces generated by the supporting substrate. In  $\text{TiO}_2$ , for instance, nuclei consistently adopted an oblate configuration, whereas in  $\text{VO}_2$  needle-like structures were the most common (Fig. 1).

2. *Substrate symmetry and crystallography.* The symmetry of the substrate and scale of the surface lattice plane can affect both the local and global orientation of the nuclei with respect to the substrate. The presence of a favorably matched lattice plane in the substrate can constrain film transformation along preferred crystal axes, inducing both one- and two-dimensional grain orientation. In addition, the directionality of the interfacial stresses can influence nucleation geometry and can be retained in amorphous films even after removal from the substrates. An example of this retained stress effect is shown in Fig. 2 for a free-standing vanadium oxide film in which orthogonal nucleation orientations are occurring beyond the advancing growth front due to the influence of the original cubic substrate.

Factors related to consolidation and later-stage growth

1. *Nuclei orientation.* The ability to form large-grained structures in thin films often depends on the consolidation of crystallites oriented in equivalent crystallographic directions (Fig. 3). This is the primary means for generation near-single crystal films, as has been demonstrated previously in  $\text{TiO}_2$  (Fig. 4).<sup>1</sup>

2. *Nucleation rate.* The effect of nucleation rate in thin-film transformation is identical to that in bulk-nucleation behavior and merely influences the degree to which other factors specific to thin-film geometries affect the microstructural development. Because of the limited scale of crystallite orientation often accompanying rapid nucleation, films may show poor consolidation (Fig. 5).

3. *Film thickness.* The thickness of the film is a major factor in the ultimate microstructure that can be achieved. It constrains the degree of two-dimensional orientation of crystallites as they consolidate, and the vacancy transport to the surfaces during densification. Film thickness in  $\text{TiO}_2$  is crucial to the development of large-grained, oriented microstructures. This effect is illustrated in Fig. 6, near the edge of a titania film of varying thickness. The gradation of film integrity, grain development, and porosity accommodation with increasing thickness is clearly visible.

4. *Accommodation of density differences during crystallization.* This affects the retention of film integrity, the manner in which

The authors are at the Rockwell International Science Center, Thousand Oaks, CA 91360.

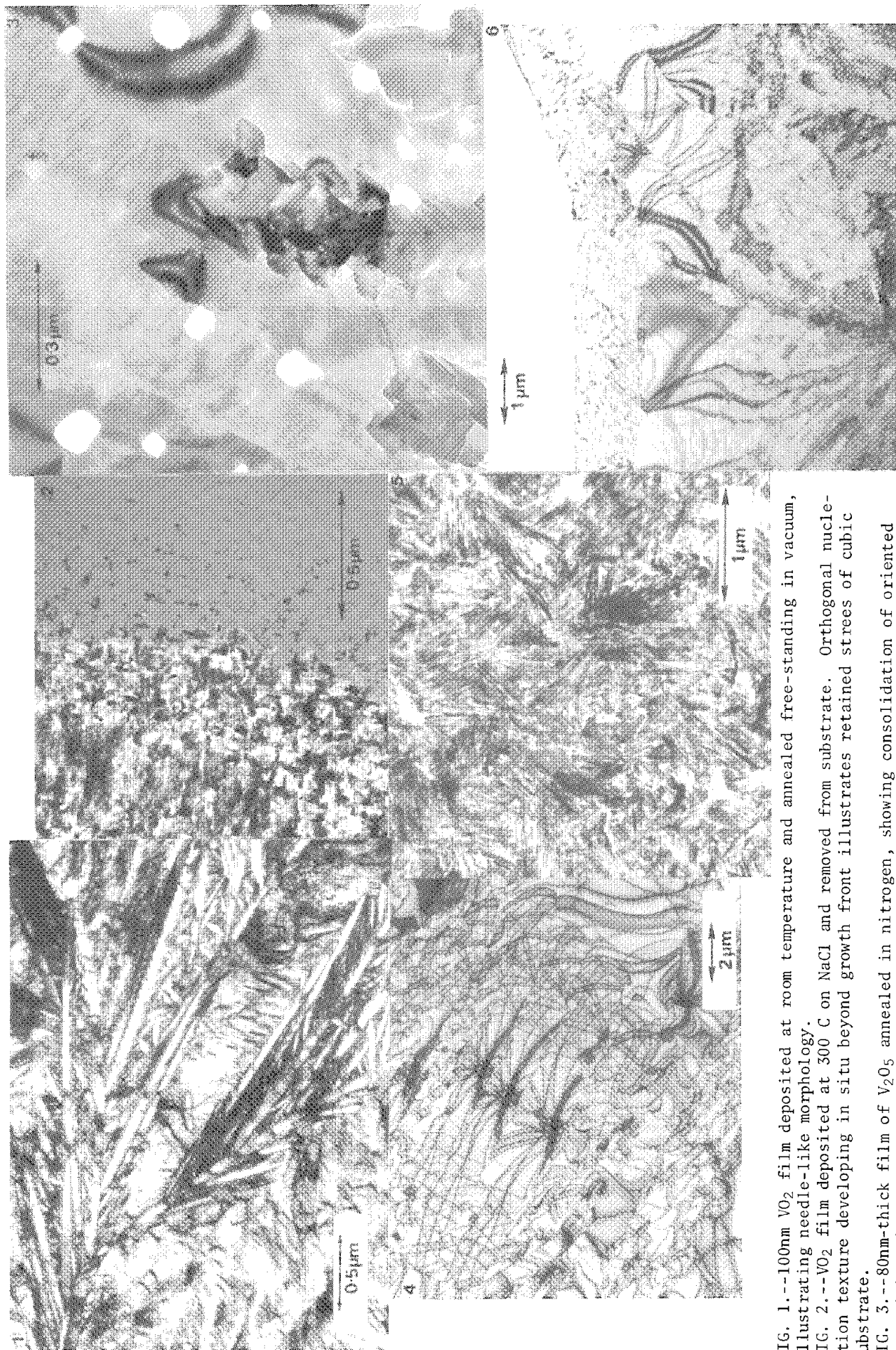


FIG. 1.--100nm  $\text{VO}_2$  film deposited at room temperature and annealed free-standing in vacuum, illustrating needle-like morphology.

FIG. 2.-- $\text{VO}_2$  film deposited at 300 C on NaCl and removed from substrate. Orthogonal nucleation texture developing in situ beyond growth front illustrates retained stresses of cubic substrate.

FIG. 3.--80nm-thick film of  $\text{V}_2\text{O}_5$  annealed in nitrogen, showing consolidation of oriented crystallites into large grains.

FIG. 4.--Annealed film of  $\text{TiO}_2$ , illustrating formation of large oriented grains.

FIG. 5.--Nucleation-dominated microstructure in thick (300nm)  $\text{VO}_2$  film.

FIG. 6.--Gradation of microstructural development in  $\text{TiO}_2$  film of varying thickness.

porosity is accommodated, and the nature of the growth front as it propagates. In very thin films deposited at room temperature, the large density differences accompanying the transformation can in some instances lead to loss of film integrity (Fig. 7) or impart large amounts of inter- or intra-granular porosity into the crystalline film (Fig. 8).

5. *Substrate crystallography.* As noted in regard to nucleation, the presence of oriented crystallites greatly enhances consolidation and large-grain formation. Studies in  $\text{VO}_2$  show a dramatic difference in the nature of grain development and bulk properties for films deposited on different planes of the same substrate material. The degree of lattice matching and symmetry relations between film and substrate can have a major influence on intergranular orientation, registry, and stress.

The quantitative interaction between these factors is strongly material dependent. In  $\text{TiO}_2$ , for example, the microstructural development is primarily determined by the film thickness and is quite insensitive to the nature of the substrate. Not only are these thickness effects important in the oxides of vanadium, but the stresses and crystallography of the substrate also have a major influence on the porosity accommodation and the grain development of the films. This difference in substrate dependence is believed to be due to the energetics of the transformation. In the terminal oxide  $\text{TiO}_2$ , the free energy of the transformation is large and likely overshadows any contribution from the degree of substrate interaction. In the intermediate oxide  $\text{VO}_2$ , these interaction energies are of sufficiently similar magnitude for the substrate to influence the geometry of the transformation. The establishment of these and other controlling factors in any given system provides a great advantage for tailoring the microstructure of the film to its intended application.

## References

1. A. B. Harker, D. G. Howitt, P. J. Hood, and P. Kobrin, "Electron microscopy of ion deposited thin films of the oxides of titanium," *Proc. 1985 MRS Symp. on Materials Problem Solving with the Transmission Electron Microscope*, vol. 62, 1986.

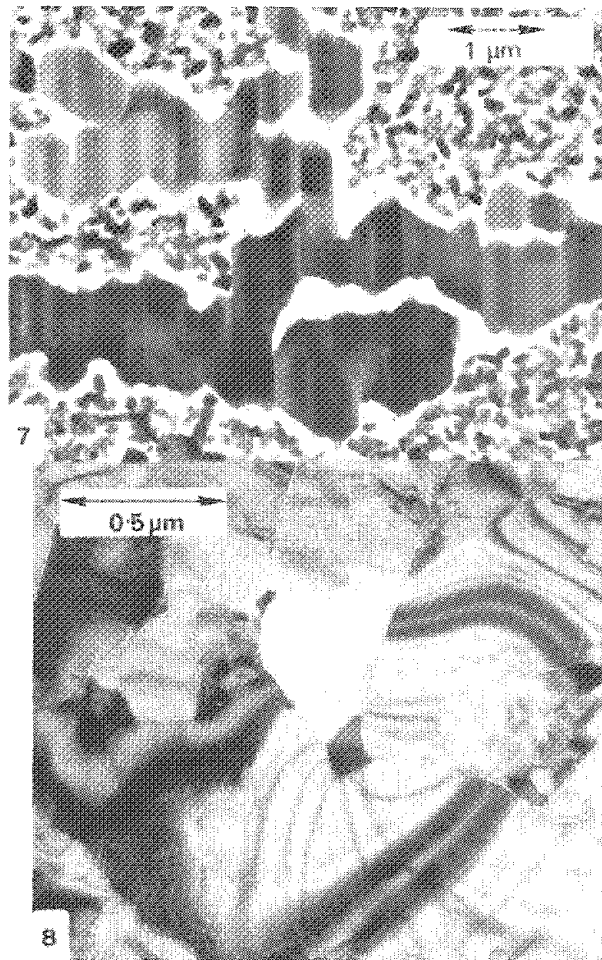


FIG. 7.--Loss of film integrity upon annealing in  $\text{V}_2\text{O}_5$  film.

FIG. 8. Inter- and intragranular accommodation of porosity in annealed  $\text{VO}_2$  film.

## SUBSTRATE EFFECTS IN THE MICROSTRUCTURE AND PHASE TRANSFORMATION OF VANADIUM DIOXIDE

A. B. Harker and J. F. DeNatale

The conductivity change during the semiconductor-to-metal thermal transition in thin-film  $\text{VO}_2$  has been studied as a function of film microstructure on a number of substrates including sapphire, germanium, silicon, quartz, and fused silica. Substrate effects dominate both the texture development in the films and the changes in electric properties occurring during thermal transition. Conductivity measurements made on films deposited on the basal and prismatic faces of sapphire also demonstrate that stress in the films can lower the temperature of the thermal transition.

It is well known that vanadium dioxide undergoes a semiconductor-to-metal transition upon heating at or near 68 C.<sup>1</sup> This transition involves a crystal lattice distortion in which low-temperature monoclinic form ( $a = 0.575173$  nm,  $c = 0.538326$  nm at 298 K) is converted to a tetragonal structure ( $a = 0.455349$  nm,  $c = 0.284944$  nm at 338.5 K).<sup>2</sup> In the high-temperature rutile structure the vanadium cations are equidistant along the  $c$ -axis; in the monoclinic form the cations are alternately separated by internuclear distances of 0.316 and 0.262 nm along the  $a$ -axis. In the monoclinic form the alternate vanadium cations are also displaced off-axis, which shortens one of the V-O bonds and causes an anti-ferroelectric distortion.<sup>3</sup> The first-order transition, which is nearly reversible in thin films, occurs over a 0.1 K temperature range in single crystal  $\text{VO}_2$  with only a small unit cell volume change, 0.044%.<sup>2</sup>

The electrical and optical property changes that occur in thin-film  $\text{VO}_2$  during the thermal transition are a strong function of stoichiometry, grain development, and stress. The multiple oxidation states of vanadium and the existence of  $\text{VO}_x$  Magneli phases require that fine control be achieved in film preparation to achieve the correct stoichiometry,  $\text{O}/\text{V} = 2.00000 + 0.00005$ , without secondary phase formation.<sup>4</sup> In addition, a beta monoclinic form of stoichiometric  $\text{VO}_2$  exists that forms from the reduction of  $\text{V}_2\text{O}_5$  through a crystallographic shear<sup>5</sup> and that does not exhibit the semiconductor-to-metal transition. Typically, the change in resistivity of  $\text{VO}_2$  thin films reported in the literature is of the order of 100 to 1000,<sup>6</sup> whereas single-crystal data have shown that resistance changes of the order of 50 000 to 100 000 are intrinsically possible.<sup>7</sup> A major factor in the lower resistivity change in many thin films is a decrease in the resistivity of the semiconducting state through the formation of suboxides.<sup>7</sup>

In this work, it has been demonstrated that near-single-crystal thin films of  $\text{VO}_2$  can be formed by reactive ion beam deposition with postdeposition annealing and that the texture

development in such films is highly substrate dependent. The films formed by this technique exhibit transition properties similar to those reported for single crystal material, except that it has been demonstrated that stress effects in the films can affect the transition temperature.

### Experimental

The thin films were grown in a custom copper gasketed ultrahigh-vacuum deposition chamber with a turbopumped base vacuum of  $1 \times 10^{-8}$  Torr, a single Kaufman ion source with a vanadium metal target and oxygen as a background gas was used. The ion source was typically operated at 1 keV and 20 mA with both target and substrate being ion beam cleaned before film deposition. The substrates were mounted on a heated substrate holder, with deposition carried out at temperatures from 20 to 550 C. After deposition, the films were annealed in the deposition chamber with controlled oxygen pressure. Phase identification and film microstructure determination were carried out by transmission electron microscopy and electron diffraction. Film thickness and index of refraction were determined by ellipsometry. Resistance measurements were made as a function of temperature by standard 4-point probe techniques.

### Results and Discussion

Free-standing and initially amorphous films of vanadium oxide, floated from NaCl and suspended on Ni TEM grids, were annealed to form  $\text{VO}_2$  to provide a substrate-free microstructure. The crystallization processes in these films during transformation strongly affects the microstructural development, as observed previously with titanium oxide films.<sup>8-9</sup> In thinner films or films with significant enclosed porosity, the nucleation of submicron needle-shaped grains dominated; further consolidation under annealing eventually produced supermicron grain development. In thicker and more dense films, initial nucleation produced lath-like grain development characterized by cellular growth along a preferred crystalline axis, and led to local orientation in supermicron grains (Fig. 1).  $\text{VO}_2$  films transformed on substrates showed substantially different microstructures.

Films produced on single-crystal 100 silicon, fused silica, and Z-quartz all had randomly oriented fine-grain microstructures. Films deposited on basal and prismatic sapphire substrates had a much higher degree of orientation and grain development. The films formed on the prismatic face (110 plane) have a global one-dimensional orientation, with lath-like 2 to 3  $\mu\text{m}$  grains (Fig. 2). The films deposited on the basal sapphire (001 plane) had near-single-crystal structure, with two-dimensional orientation and significant

The authors are at the Rockwell International Science Center, Thousand Oaks, CA 91360.



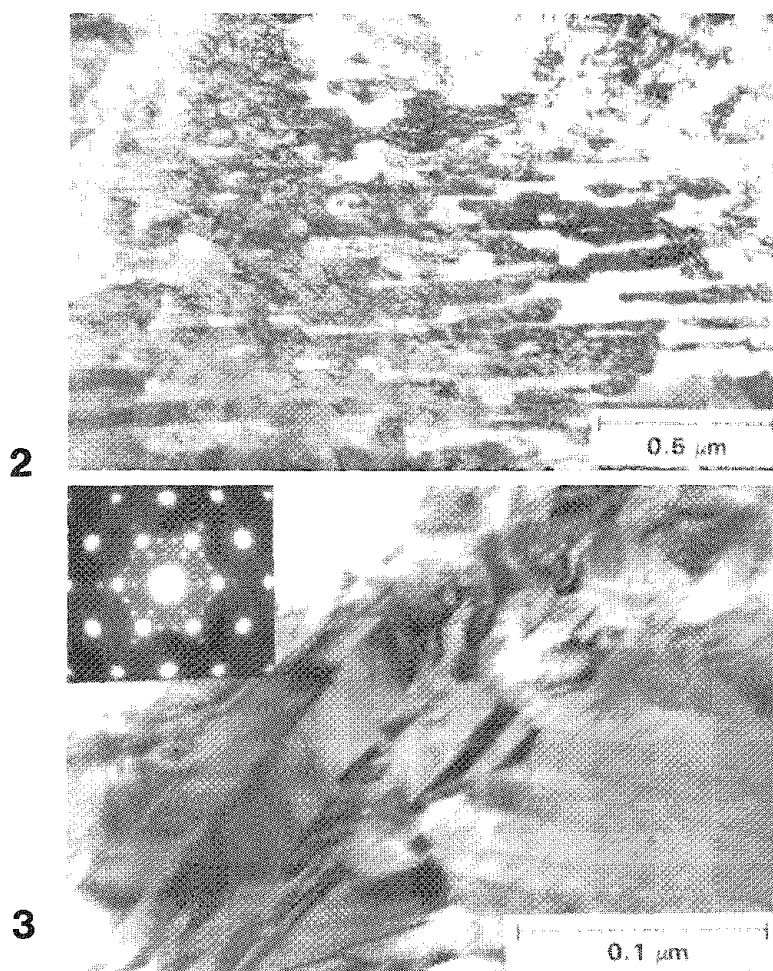
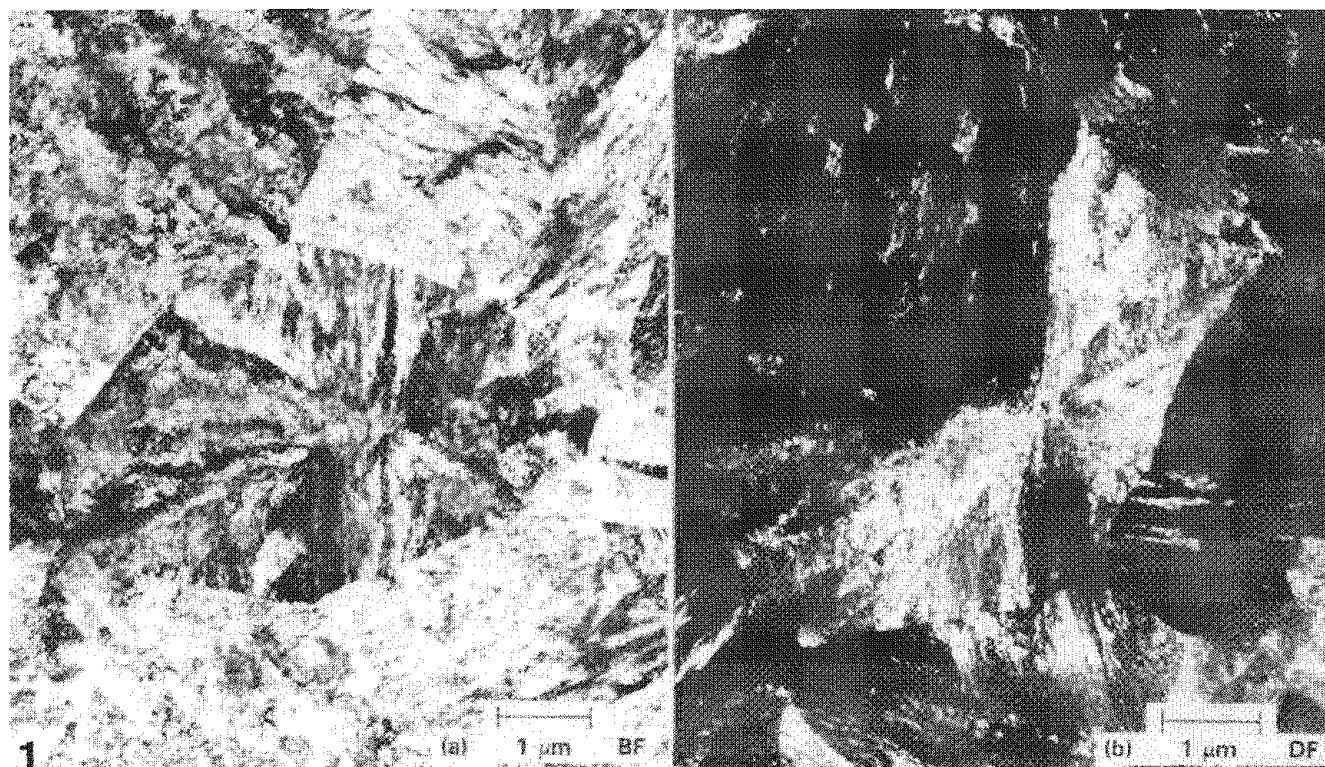


FIG. 1.--(a) Bright-field and (b) dark-field TEM micrographs showing supermicron grain development and local orientation effects in annealed free-standing thin film of  $\text{VO}_2$ .  
 FIG. 2.--Bright-field TEM micrograph of microstructure of  $\text{VO}_2$  thin film formed on 110 prismatic plane of sapphire.  
 FIG. 3.--Bright-field TEM micrograph and SAD pattern of  $\text{VO}_2$  thin film formed on 001 basal plane of sapphire.

twinning (Fig. 3). The electron diffraction pattern from the films match that of the thin foil sapphire substrate within 2%, as can be seen in Fig. 3. The twinning boundaries of the  $\text{VO}_2$  films occur on a submicron scale, with the high degree of orientation severely constraining intergranular mismatch.

The changes in the electronic properties of the  $\text{VO}_2$  films reflect the degree of grain development on the various substrates. The randomly oriented fine-structured grains showed resistivity changes of only 10 to 1000 in the vicinity of 68 C, with the high temperature form significantly less metallic than single-crystal  $\text{VO}_2$ . The  $\text{VO}_2$  films formed on sapphire showed near-single-crystal resistivity changes (Fig. 4), with the prismatic plane films exhibiting the transition at 57 C as compared to 67 C for the two-dimensionally oriented  $\text{VO}_2$  film on the basal sapphire.

### Conclusions

The number of nonstoichiometric vanadium oxide phases that can form at grain boundaries makes the lattice match between the substrate and the high-temperature rutile  $\text{VO}_2$  structure critical to microstructural development in thin films. In addition, fine-grain-structure films show limited electrical property changes during thermal transformation, presumably due to the high concentration of nonstoichiometric material at the grain boundaries and poor intergranular registry. Single-crystal thermal transformation behavior can be obtained with both one- and two-dimensionally oriented films with large grain development, although film stresses can affect the transformation temperature.

### References

1. F. Morin, "Oxides which show a metal-to-transition at the NEEL temperature," *Phys. Rev. Lett.* 3: 34, 1959.
2. D. Kucharczyk and T. Niklewski, "Accurate x-ray determinations of the lattice parameters and the thermal expansion coefficients of  $\text{VO}_2$  near the transition temperature," *J. Appl. Cryst.* 12: 370, 1979.
3. F. Pintchovski, W. S. Glaunsinger, and A. Navrotsky, "Experimental study of the electronic and lattice contributions to the  $\text{VO}_2$  transition," *J. Phys. Chem. Solids* 39: 941, 1978.
4. J. F. Marucco, B. Poumellic, and F. Lagnel, "Stoichiometry of vanadium dioxide," *J. Mat. Sci. Lett.* 5: 99, 1986.
5. F. Theobald, R. Cabala, and J. Bernard, "Essai sur la structure de  $\text{VO}_2(\text{B})$ ," *J. Solid State Chem.* 17: 431, 1976.
6. C. H. Griffiths and H. K. Eastwood, "Influence of stoichiometry on the metal-semiconductor transition in vanadium dioxide," *J. Appl. Phys.* 45: 2201, 1974.
7. W. Brukner, W. Moldenhauer, H. Wich, E. Wolf, H. Oppeermann, U. Gerlach, and W. Reichelt, "The range of homogeneity of  $\text{VO}_2$  and the influence on the composition on the physical properties," *Phys. Stat Sol.* 29: 63, 1975.
8. A. B. Harker, D. G. Howitt, and P. Kobrin, "Crystallization processes by electron microscopy," *Proc. Symp. on Solving Problems by Electron Microscopy*, Materials Research Society Fall Meeting, 1985 (in press).
9. D. G. Howitt and A. B. Harker, oriented growth of anatase in thin films of amorphous titania," *J. Mat. Res.* (in press).

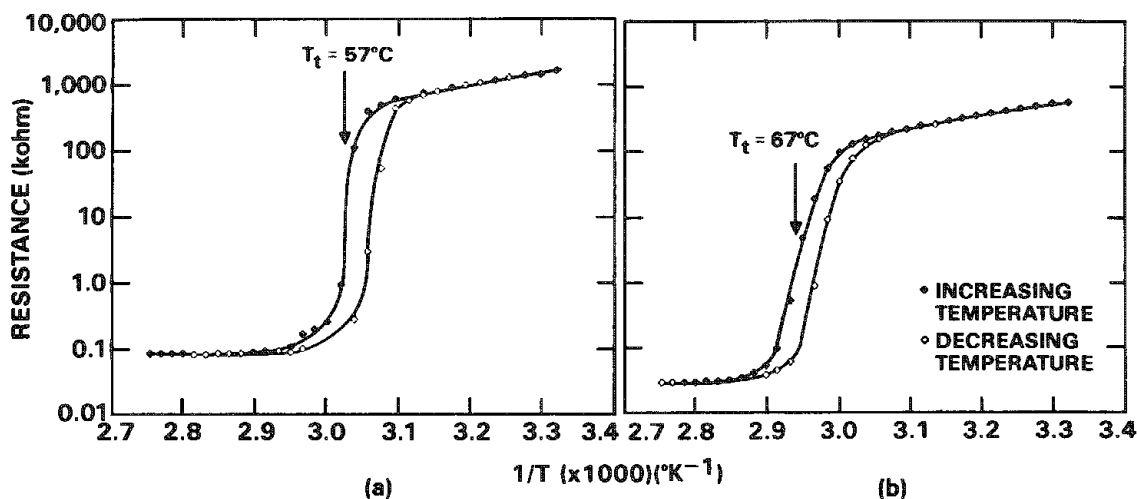


FIG. 4.--Resistance change as function of  $1/T$  ( $^{\circ}\text{K}$ ) through semiconductor-to-metal transition in  $\text{VO}_2$  thin films formed of (a) prismatic sapphire, (b) basal sapphire.

## MICROSTRUCTURE-PROPERTY RELATIONS IN OPTICAL THIN FILMS

J. F. DeNatale, H. Sankur, and W. J. Gunning

The relation between microstructure and intrinsic stress in  $\text{MgF}_2$ -Ge thin films was investigated as a function of film thickness, composition, and method of mixing. Dramatic differences were observed between films mixed by co-evaporation and those prepared by sequential deposition of the pure components. Microstructural analysis reveals a corresponding difference in the grain structure of the films, which suggests that differences in stress arise from grain-boundary interactions between like and unlike components.

The preparation of thin-film optical coatings and devices requires the generation of controlled optical density gradients within the film. Generation of such arbitrary gradients in the refractive index is commonly achieved by two distinct methods, analog and digital. Analog preparation employs codeposition to tailor the film index to the desired local value.<sup>1</sup> Digital preparation uses controlled sequencing of distinct materials in a prescribed manner to generate a given average index over a small number of layers.<sup>2</sup> The use of these techniques to implement certain optical designs may require preparation of comparatively thick films, often in excess of 100  $\mu\text{m}$ . In these regimes, the issues of intrinsic stress generation and delamination become significant. The aim of this study was to investigate the dependence of intrinsic stress on the method of mixing in the  $\text{MgF}_2$ -Ge system, and to establish the microstructural origins of these differences.

### *Experimental*

Films were prepared in an UHV deposition system, with a cw  $\text{CO}_2$  laser used to evaporate the  $\text{MgF}_2$ . The Ge was independently evaporated from an alumina-coated tungsten boat. Composition and thickness monitoring was performed in situ with quartz crystal monitors; the compositional data were confirmed in the final films by energy-dispersive x-ray spectroscopy. Quantitative measurements of film stress were made from the bending of thin cantilevered glass substrates.

Films were deposited onto cleaved single-crystal NaCl substrates by both analog and digital techniques, and then floated onto fine-mesh grids for microstructural analysis by transmission electron microscopy (TEM). Films were grown to varying total thicknesses to determine the evolution of stress and microstructure with increasing thickness.

### *Results*

The composition dependence of intrinsic stress for both analog and digitally mixed  $\text{MgF}_2$ -Ge films is shown in Fig. 1. The stress

in the digital films was found to exhibit a well-behaved dependence on composition, varying linearly between the two extreme compositions and remaining tensile over the entire range. However, the behavior of the codeposited films was quite different. In these films, a rapid reduction in the tensile stress was observed that became low and compressive over the intermediate composition range (18-61 wt% Ge). A similar deviation in stress has been observed in other mixed film systems, which often exhibit quite complex behavior.<sup>3</sup>

A distinct microstructural evolution was observed in these analog films as a function of composition (Fig. 2). Coarsening of both the  $\text{MgF}_2$  and Ge grains occurred with increasing Ge additions, with the Ge exhibiting a larger degree of growth. The digital films, on the other hand, showed little microstructural change with composition (Fig. 3). Electron diffraction was in all cases consistent with the pure constituents and showed no evidence for the formation of mixed phases.

Measurement of the evolution of the intrinsic stress with progressively increasing film thickness revealed a distinctly nonlinear behavior. The incremental stress generated by each additional thickness of film is shown in Fig. 4; clearly most of the stress is generated in the initial few hundred Å of the film. The microstructures of these analog films were also found to vary with film thickness (Fig. 5), although this dependence was less pronounced in the low-Ge films than in the midcomposition range.

### *Discussion*

The behavior of the  $\text{MgF}_2$ -Ge analog mixed films shows promise for generation of low-stress optical devices. The index of refraction in these films corresponding to the low-stress regime ranges from 1.8 to 3.3, which provides a great deal of flexibility in the design of gradient index films.

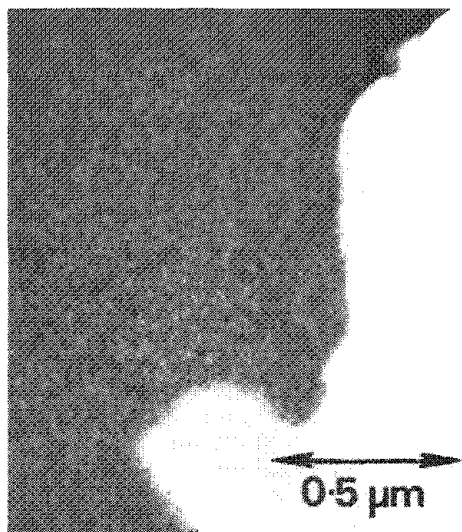
Microstructural analysis shows a consistent association between the measured stress in these films and the grain structure. Films showing large stress values, both in analog and digital cases, have been associated with fine-grained microstructures. But in the intermediate compositions exhibiting low intrinsic stress, coarser-grained structures prevailed. A similar trend was observed in the thickness dependence for the midcomposition analog films, in which the thinner films corresponding to the higher incremental stress values exhibited finer textures, coarsening as the film thickness increased.

The shape of the intrinsic stress curve for the analog films (Fig. 1) and the observed microstructural dependence suggest that the stress reduction is related to the total grain-boundary energy of the system. Electrostatic interaction at the grain boundaries is

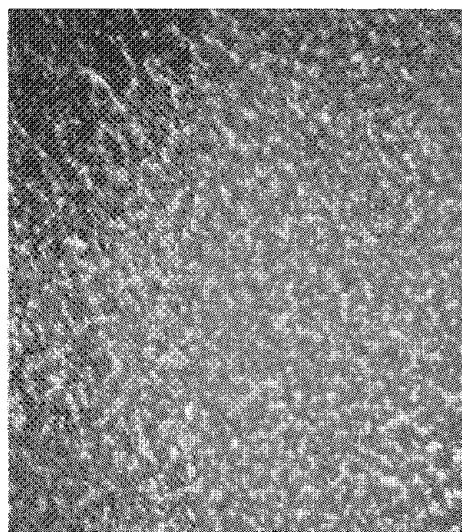
---

The authors are at the Rockwell International Science Center, Thousand Oaks, CA 91360.

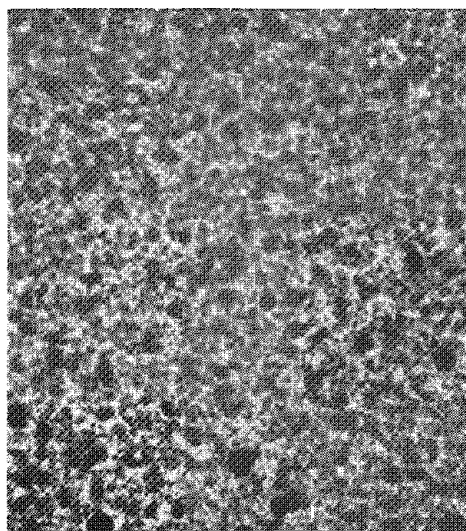




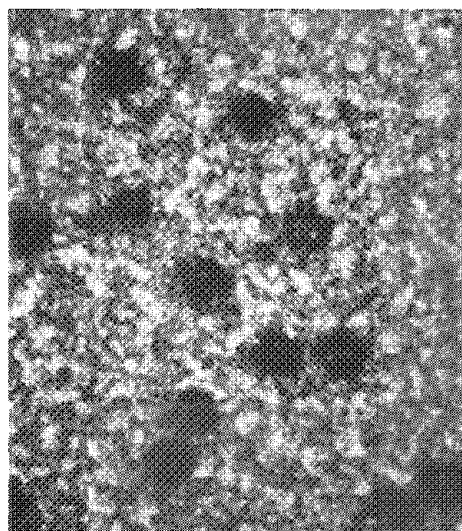
**a**



**b**

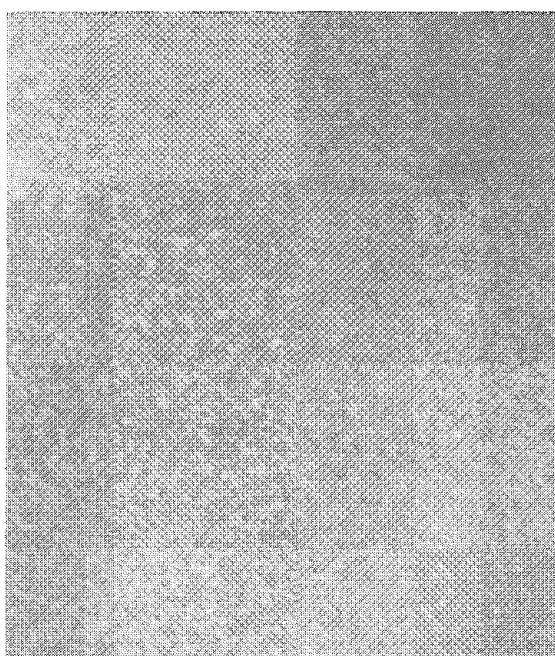


**c**

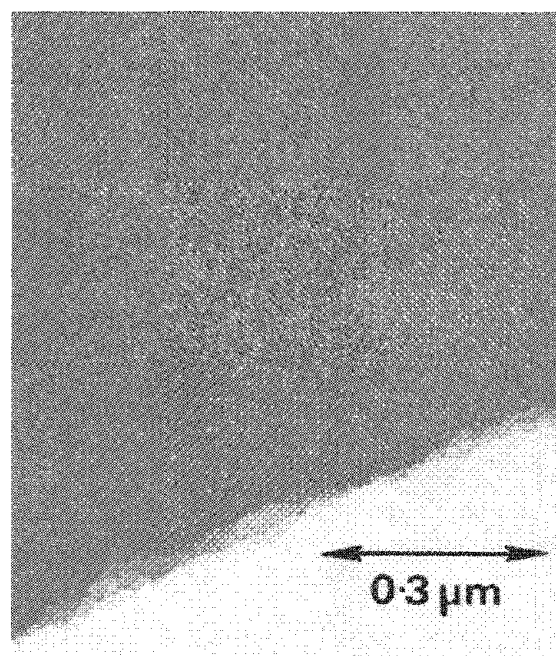


**d**

**2**



**a**



**b**

**3**

FIG. 2.--Variation of film microstructure with composition in analog  $\text{MgF}_2$ -Ge films: (a)  $\text{MgF}_2$ , (b) 14% Ge, (c) 26% Ge, (d) 71% Ge.  
FIG. 3.--Digital  $\text{MgF}_2$ -Ge films: (a) 15% Ge, (b) 50% Ge.

a commonly accepted mechanism for stress generation in crystalline thin films; hence a variation in the total grain boundary area and its distribution could potentially affect the stress of the film. The qualitative similarity between the shape of the stress curve and the enthalpy of a mixed system derived from the quasichemical theory<sup>4</sup> suggests that the stress reduction arises from the mixing of grains with different interaction energies associated with like and unlike neighbors. In this manner, the total grain boundary interaction energy would depend on the grain size, which affects the total grain boundary volume; and on the distribution of components, which affects the balance of like and unlike interactions in the total summation. Thus, both coarsening and mixing effects will contribute to the intrinsic stress generation in the films. With this approach, even complex stress behavior as observed in ZnS mixed films could be explained qualitatively.<sup>3</sup>

### Conclusions

The intrinsic stress in  $\text{MgF}_2$ -Ge mixed films has been analyzed and compared to the microstructural development. The codeposited films show significant stress reduction as compared to sequentially deposited layers, a result that could be useful for generation of low-stress optical devices. Moreover, the close correlation between the stress and the grain structure suggests a mechanism associated with the grain size and intergranular distribution of the components. Such a mechanism has been proposed, based on differences in intergranular interaction energies between like and unlike grains.

### References

1. J. F. DeNatale and A. B. Harker, "Mixed cation optical thin films from tailored composition targets," *Proc. 1986 Mat. Res. Soc. Fall Meeting, Symposium on Interfaces, Superlattices, and Thin Films* (in press).
2. R. H. Hall, W. H. Southwell, and W. J. Gunning, "Fabrication of arbitrary index profiles," presented at OSA Meeting, Seattle, 1986.
3. H. Sankur, J. F. DeNatale, and W. J. Gunning, "Intrinsic stress and structure in mixed composition thin films," in Ref. 1.
4. P. G. Shewmon, *Transformations in Metals*, New York: McGraw-Hill, 1969, 138.

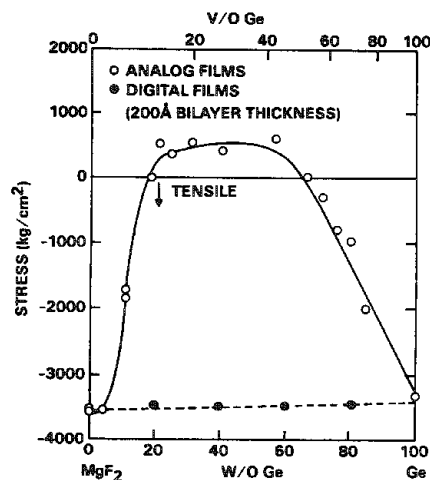


FIG. 1.--Intrinsic stress vs composition for analog and digital mixed  $\text{MgF}_2$ -Ge films.

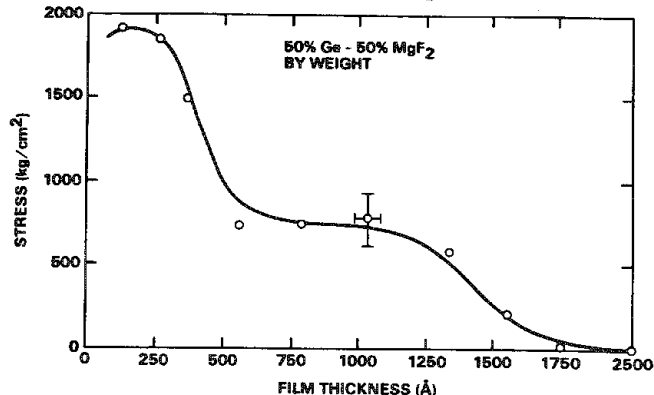
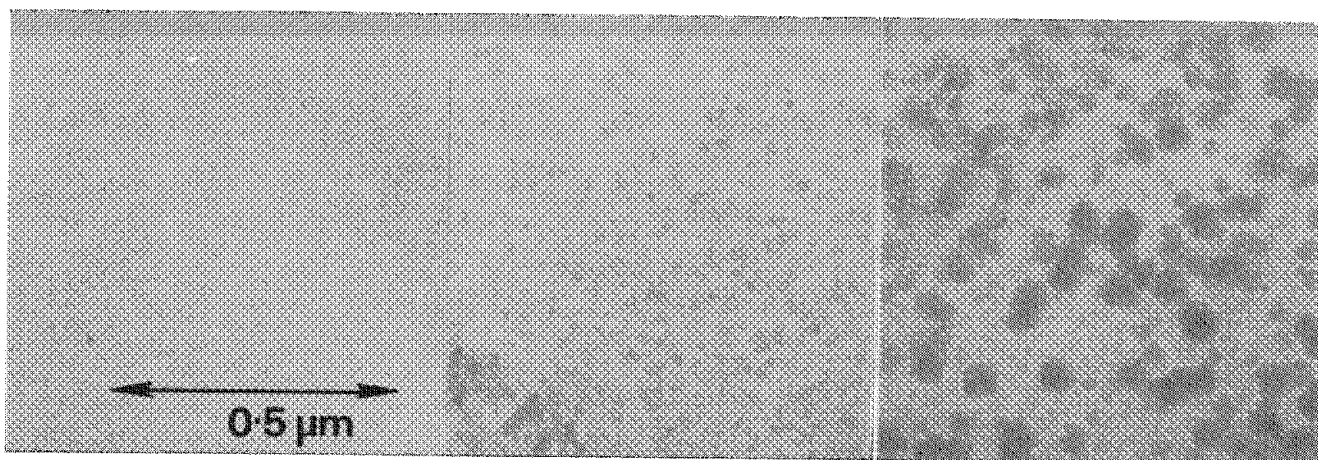


FIG. 4.--Incremental stress vs film thickness for  $\text{MgF}_2$ -Ge mixed film.

FIG. 5.--Variation of microstructure with thickness for 50% Ge analog mixed film: left to right, 600, 1000, and 1500 Å.



## INTERFACE STUDIES OF AlGaAs/InGaAs PSEUDOMORPHIC MODULATION DOPED FIELD-EFFECT TRANSISTORS WITH p-DOPED SURFACE LAYERS

D. R. Kitchen, T. E. McLaughlin, R. E. Omlor, P. F. Lloyd, and R. D. Brodecki

Since the introduction of the transistor in 1948, there has been a continuing comprehensive effort to improve the switching speed of this device. The modulation-doped field-effect transistor (MODFET) is the latest transistor to appear in the evolutionary cycle. It is a GaAs/AlGaAs heterostructure device that switches on or off in only slightly more than 10 ps. It operates not only as a digital switch, but can also serve as an analog amplifier at frequencies up to about 60 GHz.<sup>1,2</sup> This device is the fastest known operating device, with the possible exception of the Josephson junction. The novel interface structure of the device allows for its fast operation that greatly surpasses that of the MESFET at microwave frequencies. It is based on the fact that electrons move very rapidly in undoped gallium arsenide.<sup>3</sup> This unique feature is a result of the properties of the heterostructure, where charge-carrying electrons are confined to a thin, very-high-mobility quantum well. The device also accepts and releases considerable amounts of charge rapidly, and dissipates little energy in so doing.<sup>1</sup> Despite its very high switching speeds, the MODFET suffers from problems associated with a persistent photoconductivity effect at reduced temperatures<sup>4</sup> and an inability to support gate voltages larger than the gate barrier height. Also, current studies have indicated that MODFETs can be extremely noisy. It has been shown previously<sup>5,6</sup> that these problems can be solved with the formation of a heterostructure based on the InGaAs/GaAs system. However, the InGaAs layer must be very thin, approximately 200 Å. This new device is called the pseudomorphic MODFET. The purpose of this paper is to discuss ongoing studies at the Air Force Institute of Technology and the Air Force Wright Aeronautical Laboratories (both located at Wright-Patterson AFB, Ohio) to examine the dc and frequency response in addition to the noise performance of the pseudomorphic MODFET device. In this work, devices were built with 1.35-1.5 µm gate lengths and highly p-doped surface layers incorporated under the gate contact. However, these devices exhibited problems attributed to strain in the InGaAs layer. X-ray maps were taken to characterize the surface topology of the device. Transmission electron microscopy was also used to delineate the layered interface structure.

Authors Kitchen, McLaughlin, and Omlor are at the Air Force Institute of Technology, School of Engineering, Wright-Patterson AFB, OH 45433; authors Lloyd and Brodecki, at Systems Research Laboratories, Inc., 2800 Indian Ripple Rd., Dayton, OH 45440. They wish to acknowledge the aid of C. W. Litton of the U.S. Avionics Laboratory for technical support, and Dr. H. Morkoc of the University of Illinois for providing the substrate materials.

### *Experimental Procedures*

Samples for these experiments were In<sub>0.15</sub>Ga<sub>0.85</sub>As/Al<sub>0.15</sub>Ga<sub>0.85</sub>As heterostructures grown by MBE on semi-insulating GaAs substrates. Figure 1 shows a typical structure consisting of a 20-period GaAs/AlAs superlattice. This structure is followed by a 0.5 µm unintentionally doped GaAs buffer layer and a 200 Å quantum well of strained, undoped In<sub>0.15</sub>Ga<sub>0.85</sub>As. Finally, a 30 Å undoped setback layer, a 350 Å n-Al<sub>0.15</sub>Ga<sub>0.85</sub>As layer doped with  $2 \times 10^{18}$ /cm<sup>3</sup> Si, and a 100 Å Be-doped GaAs cap layer to enhance the Schottky barrier gate contact is grown. Active device regions were defined by use of standard photolithographic and etching techniques. Alloying of AuGe/Ni/Au to the source and drain regions of the device in a hydrogen atmosphere at 500 °C produced ohmic contacts. The gate metal contact used was either Al or Cr/Pd/Au. Fabricated wafers were then scribed into individual devices and mounted for dc and microwave measurements. Samples were inspected with a Tracor Northern x-ray analyzer to map the surface topography. Devices examined by a TEM were first electrolytically plated with nickel to allow handling and then mechanically polished with a 600-grit paper. A dimpler was used to reduce the cross section of the specimen to 0.003 in. The devices were then placed in an argon ion mill with a 1 mA beam current for final thinning prior to the TEM inspection.

### *Experimental Results*

Devices were dc characterized by a HP4145 semiconductor parameter analyzer at 300 K. Typical current-voltage curves for the pseudomorphic structure are shown in Fig. 2. The curves show excellent saturation and pinch-off characteristics. These devices exhibited transconductance as high as 230 mS/mm at room temperature, which is unsurpassed for devices with 1.35-1.5 µm gate lengths. The normalized contact resistances of the ohmic contacts were also measured. The average value observed was 0.70 Ω-mm; the lowest value was 0.002 Ω-mm. Our experiments indicate that changing the gate structure alters the noise and frequency response of the device. With a Be dopant under the gate, pseudomorphic devices were constructed that revealed an increase in noise resistance over that of the standard MODFET. Detailed RF measurements revealed cutoff frequencies of approximately 15-17 GHz. This is a significant result, considering that the gate lengths were 1.35-1.5 µm. The surface topology of these devices was mapped with an EDS spectrometer. Figure 3 shows the resultant video image of the device with the elements Au, Al, and Ti individually accentuated. Figure 4 illustrates the EDS spectra. The source, drain, and gate contacts are clearly

100 Å $p^+$ - GaAs
350 Å $n$ - $Al_{0.15}Ga_{0.85}As$
30 Å Undoped $Al_{0.15}Ga_{0.85}As$
200 Å $In_{0.15}Ga_{0.85}As$
0.5 $\mu m$ Unintentionally Doped GaAs
20 Period GaAs/AlAs Superlattice
1 $\mu m$ Unintentionally Doped GaAs

Structure for Pseudomorph Device

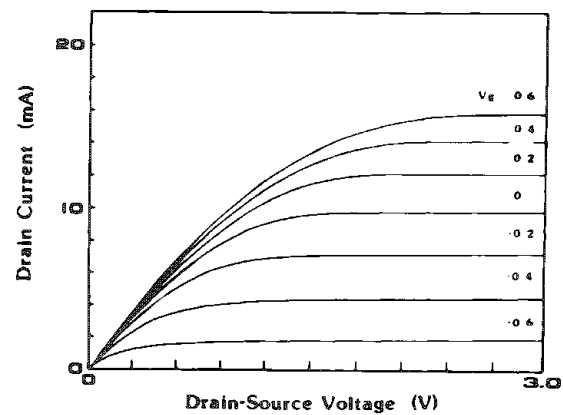


FIG. 2.--Current-voltage characteristics of pseudomorphic MODFET.

### X-RAY MAP OF PSEUDOMORPH CHIP

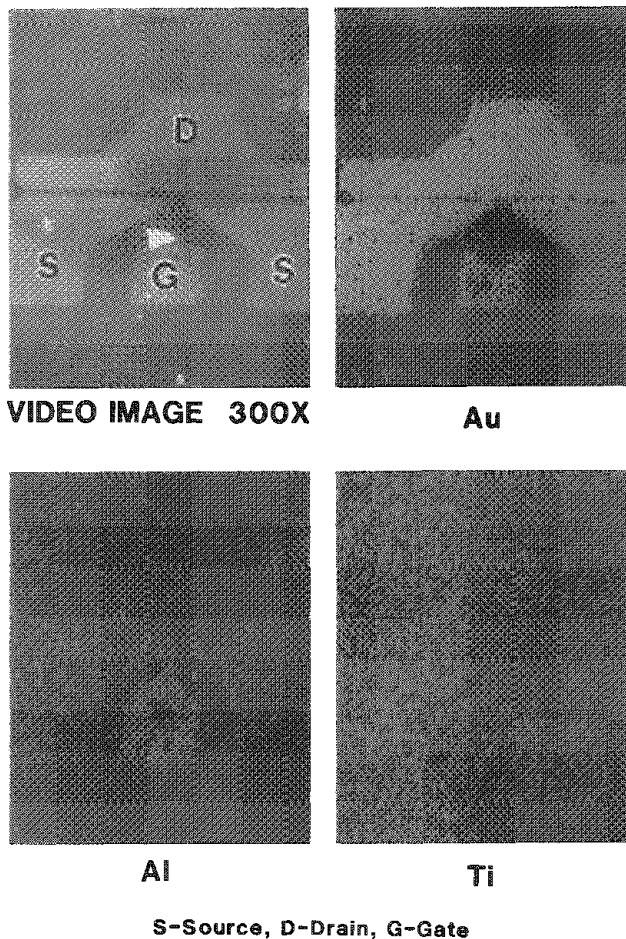


FIG. 3.--X-ray map of pseudomorphic device showing video image. Elements Au, Al, and Ti are mapped out individually.

visible. The image also reveals the presence of Ti throughout the structure. A thick Ti/Au film is used as an overlay metallization to cover the Al gate contact. The deposit is used to form the bond pad for the gate region only. Apparently the Ti was not removed in the source and drain regions adequately during fabrication. However, the electrical characteristics of the device were not affected. Lattice imaging of the cross section of the device to examine the heterostructure have been only recently started. A big problem has been in the preparation of a thin structure suitable for the TEM showing the interface structure of the device. Preliminary results indicate a typical lattice structure of GaAs. But the expected lattice mismatch associated with the InGaAs/AlGaAs interface is not yet clear.

### Conclusions

Pseudomorphic MODFET devices were successfully fabricated from MBE grown wafers. Devices revealed excellent dc characteristics and microwave responses. Indeed, the RF cut-off frequencies for these devices were 15-17 GHz for 1.35-1.5  $\mu\text{m}$  gate lengths. Devices also exhibited extremely low contact resistances and high transconductance values. EDS imaging

was used to examine the source, drain, and gate contacts. A TEM study of the interface structure is still in progress.

### References

1. H. Morkoc and P. Solomon, "The HEMT: A superfast transistor," *IEEE Spectrum* 21: 28-35, February 1984.
2. T. J. Drummond et al., "Modulation-doped GaAs/(Al,Ga)As heterojunction field-effect transistors: MODFETs," *Proc. IEEE* 74: 773-816, 1986.
3. P. Solomon and H. Morkoc, "Modulation-doped GaAs/AlGaAs heterojunction field-effect transistors (MODFETs), ultrahigh-speed devices for supercomputers," *IEEE Trans. ED-31*: 1015-1027, 1984.
4. T. J. Drummond et al., "Photoconductivity effect in extremely high mobility modulation doped (Al,Ga)As/GaAs heterostructures," *J. Appl. Phys.* 53: 1238, February 1982.
5. A. A. Ketterson et al., "Characterization of InGaAs/AlGaAs pseudomorphic modulation-doped field effect transistors," *IEEE Trans. ED-33*: 564-571, 1986.
6. J. J. Rosenberg et al., "An  $\text{In}_{0.15}\text{Ga}_{0.85}\text{As}$ /GaAs pseudomorphic single quantum well HEMT," *IEEE Trans. EDL-6*: 491-493, 1985.

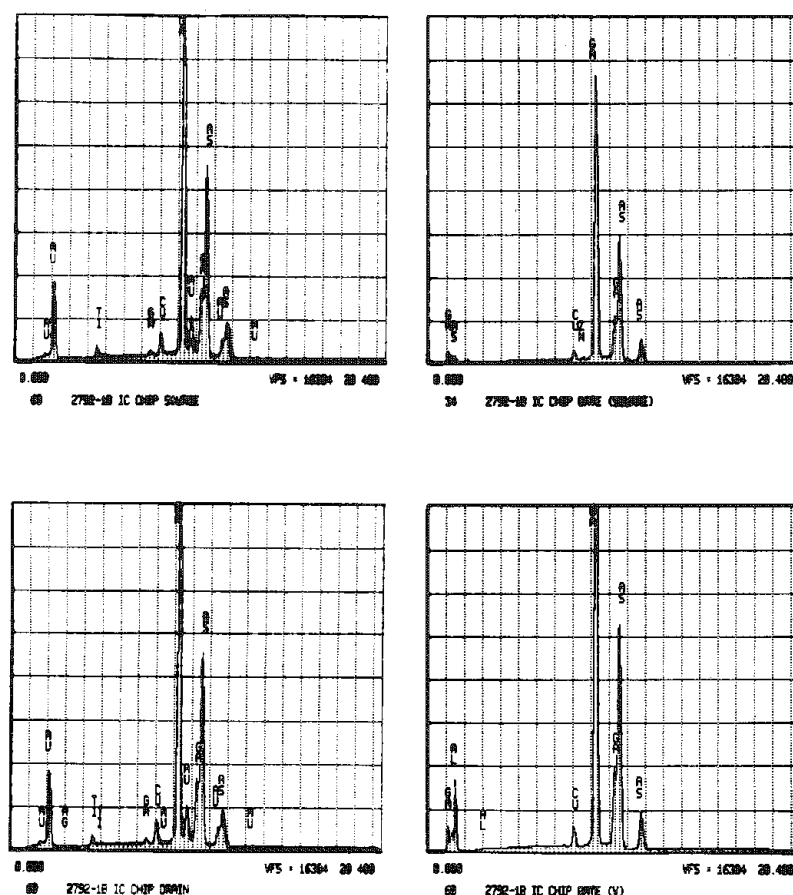


FIG. 4. EDS spectra generated from source, drain, and gate areas of pseudomorphic MODFET.



## AN INVESTIGATION OF THE FERRITE-MAGNESIUM OXIDE INTERFACE

A. G. Fitzgerald, P. A. Moir, and B. E. Storey

The structure and composition of ferrimagnetic films is an important parameter in device efficiency. The choice of a suitable substrate that will not produce strain leading to crystal defects at the film-substrate interface and will not interact chemically with the film is important in preserving the magnetic properties. Single-crystal magnesium oxide is believed to be a suitable substrate for epitaxial growth of single-crystal ferrite films, and (100) ferrite films have been grown on the (100) faces of MgO single crystals.<sup>1,2</sup> For most ferrites the (100) interplanar spacing is almost exactly twice the (100) spacing in MgO; however, the misfit<sup>3</sup>  $f$  between ferrites and MgO has been shown to be of a magnitude that in most cases results in its accommodation by interfacial dislocations.<sup>4</sup> Detailed studies have been made of the microstructure of ferrite thin films grown on MgO and some preliminary qualitative studies of the composition of these films has been made by energy-dispersive x-ray microanalysis in the transmission electron microscope.

The objective of this paper is to present the results of a detailed analysis of the influence of the MgO substrate on film composition and the MgO-ferrite interface.

### *Experimental*

The majority of ferrite films were prepared by chemical vapor deposition using a T-reactor system.<sup>1</sup> The effects of oxidation of sputtered films and of alloy films deposited onto MgO from an electron-beam source were also investigated. The single-crystal magnesium oxide substrates were polished prior to film deposition by means of the procedure described by Fitzgerald and Engin.<sup>5</sup>

*Transmission Electron Microscopy and Diffraction.* Previous transmission electron microscope studies of films grown by chemical vapor deposition on magnesium oxide substrates have shown that ferrite films grow with extensive arrays of stacking faults.<sup>6</sup> Films deposited from an electron beam source onto MgO and oxidized at 1000 C were found to consist of small inclusions with the ferrite crystal structure within a magnesium oxide matrix (Fig. 1). Similar inclusions were observed in sputtered films annealed in air at a similar temperature.

*Auger Electron Spectroscopy and X-ray Photoelectron Spectroscopy.* Auger electron spectra have been obtained from  $\text{NiFe}_2$  and  $\text{CoFe}_2$  films oxidized on the single-crystal magnesium oxide substrates. Figure 2 shows Auger electron spectra obtained from a  $\text{CoFe}_2$  film before and after oxidation. The cobalt, iron, and

oxygen present on the surface before oxidation have been replaced by magnesium and oxygen with traces of iron. Similar Auger electron spectra (AES) have been obtained from sputtered films (Fig. 3). X-ray photoelectron spectroscopy (XPS) observations taken from the surface after oxidation confirm these results. These observations suggest that there is considerable diffusion of the constituents of a ferrite film into the magnesium oxide substrate at high oxidation temperatures. Chemical vapor deposition of ferrite films onto magnesium oxide substrates occurs at temperatures above 1000 C and most likely similar diffusion effects occur during deposition. Figure 4 shows a series of Auger electron spectra obtained from a cobalt ferrite film prepared by chemical vapor deposition after argon ion etching for increased periods of time. It is clear that magnesium is detected with cobalt, iron, and oxygen on the surface of the film and is present, with these elements, through the thickness of the complete film. Magnesium has also been detected in lithium ferrite, nickel ferrite, manganese ferrite, and magnetite films grown by chemical vapor deposition. Figure 5 shows an x-ray photoelectron spectrum taken from the surface of a lithium ferrite film grown on MgO; magnesium photoelectron peaks are present and confirm the presence of magnesium on the surface.

*X-ray Microanalysis.* Energy-dispersive x-ray microanalysis spectra (EDX) have been obtained in the SEM and in the TEM from films prepared by chemical vapor deposition. These spectra were found to contain magnesium peaks (Fig. 6). In previous investigations the appearance of these peaks had been attributed to a contribution from the underlying magnesium oxide substrate.<sup>4</sup> To confirm that the magnesium detected by EDX originates completely from the ferrite film, the substrate and film have been examined in cross section in a JEOL T300 SEM (Fig. 7). The majority of films were found to be thicker than 5  $\mu\text{m}$ . For films of this thickness all the magnesium x rays detected originate from the film and the concentration of magnesium in each of the ferrite films studied can be determined. The composition of each film has been obtained by use of the MAGIC IV x-ray microanalysis program<sup>7</sup> (Table 1).

### *Conclusions*

The nature of the oxides formed on the surface after annealing films prepared by sputtering and by electron-beam source has been examined by Auger electron spectroscopy and x-ray photoelectron spectroscopy. These measurements show that the metal constituents of the ferrite diffuse into the magnesium oxide substrate. These results are supported by transmission electron microscope observations

The authors are at the Carnegie Laboratory of Physics, University of Dundee, Dundee, Great Britain, DD1 4HN.

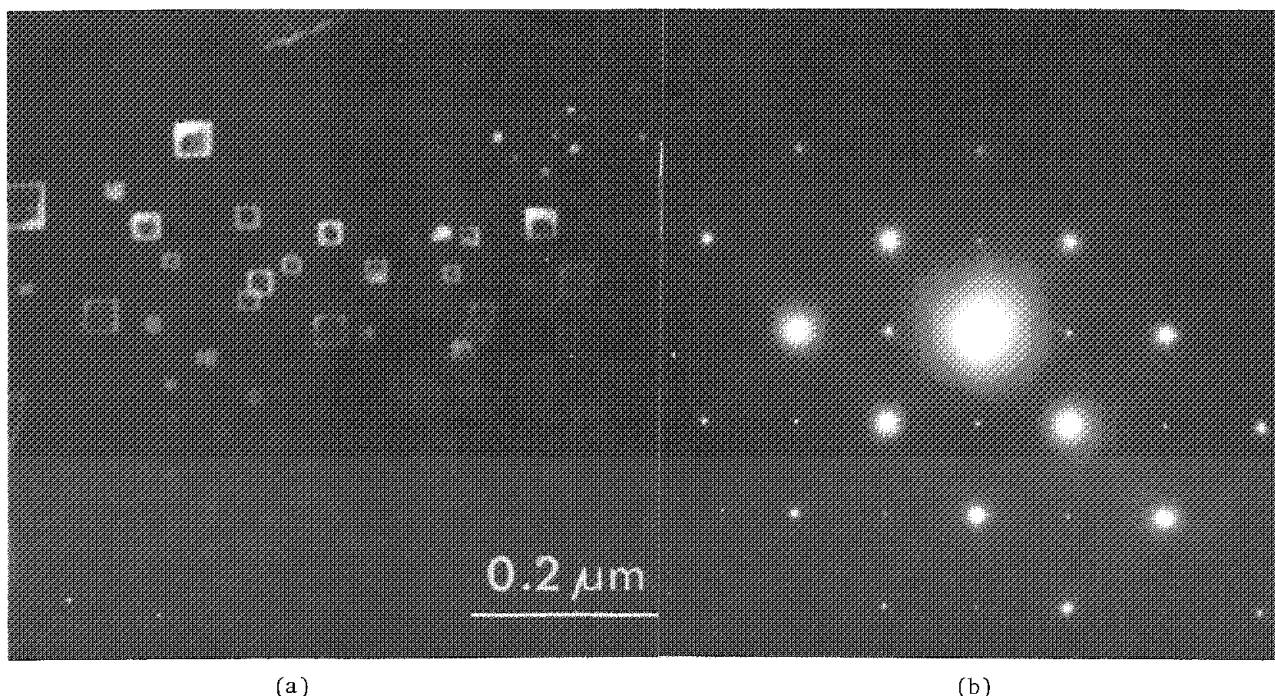


FIG. 1.--(a) Dark-field electron micrograph of ferrite precipitates in magnesium oxide single crystal obtained with (220) ferrite reflection. Material prepared by oxidation of  $\text{NiFe}_2$  film deposited on MgO. (b) Electron diffraction pattern from area shown in (a); fainter spots are associated with ferrite inclusions. MgO and ferrite inclusions are in (100) orientation.

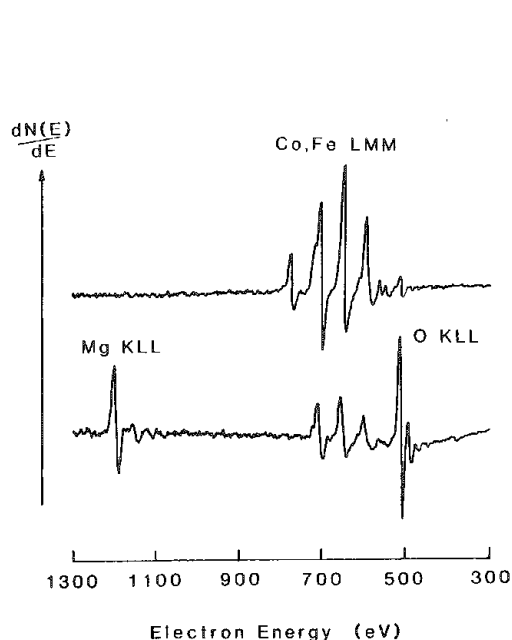


FIG. 2.--Auger electron spectra from  $\text{CoFe}_2$  film deposited onto single crystal MgO by electron beam source. Top spectrum, immediately after deposition; bottom, after annealing for 24 h at 1000 C.

TABLE 1.--Elements (at.%) in ferrites studied.

	Mg	Ni	Co	Mn	Fe	O
Nickel ferrite/MgO	7.7	5.9	-	-	26.6	59.8
Manganese ferrite/MgO	15.5	-	-	3.6	15.3	65.6
Cobalt ferrite/MgO	9.7	-	9.51	-	30.3	50.5
Magnetite/MgO	13.1	-	-	-	27.4	59.5

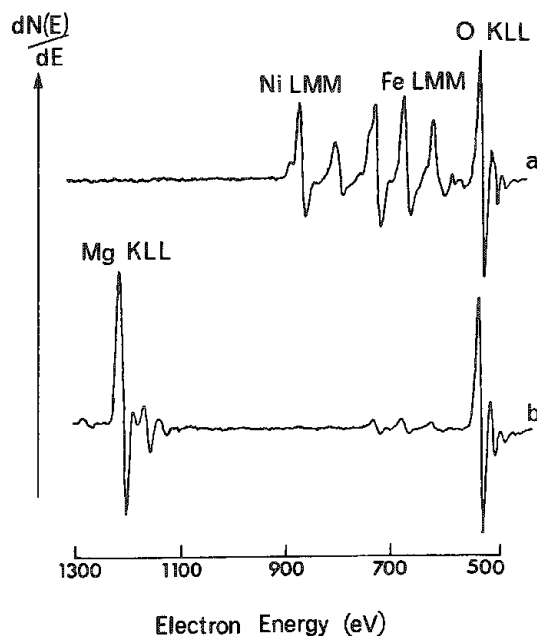


FIG. 3.--Auger electron spectra obtained from film sputtered in argon from nickel ferrite cathode and deposited onto single crystal MgO: (a) immediately after deposition, (b) after annealing in air for 24 h.

TABLE 2.--Lattice parameters of materials studied.

Material	$\bar{a}$
Magnesium oxide	4.21
Magnesium ferrite	8.397
Manganese ferrite	8.517
Nickel ferrite	8.337
Cobalt ferrite	8.38
Magnetite	8.397



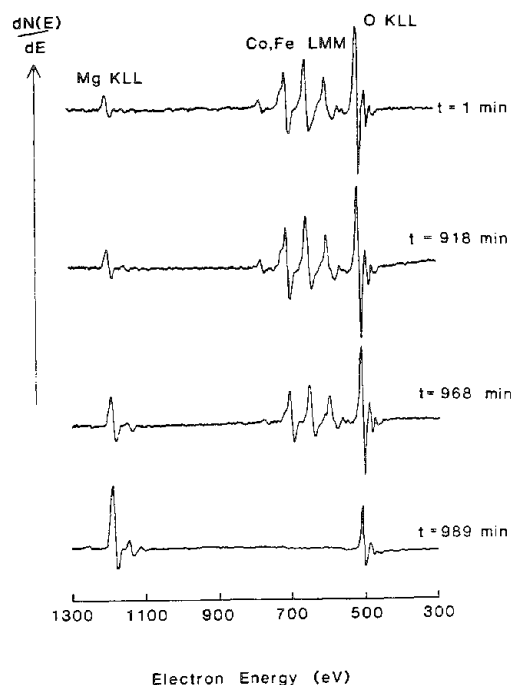


FIG. 4.--Auger electron spectra obtained from cobalt ferrite film prepared by chemical vapor deposition, as-deposited and after argon ion etching for periods of time indicated.

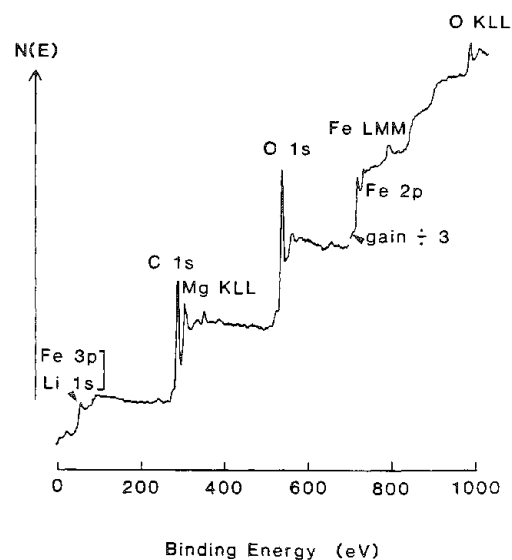


FIG. 5.--X-ray photoelectron spectrum taken from surface of lithium ferrite film prepared by chemical vapor deposition.

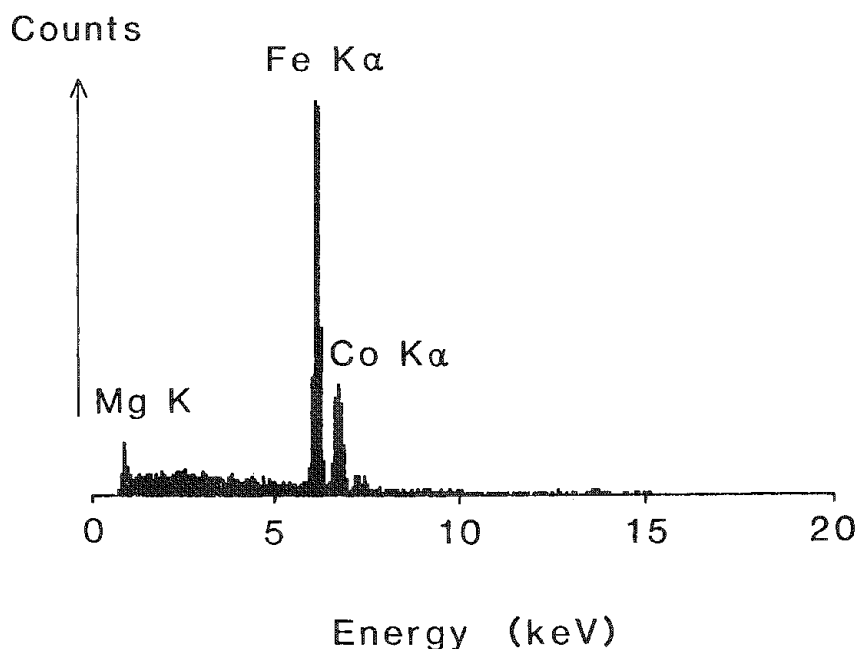


FIG. 6.--X-ray microanalysis spectrum from cobalt ferrite chemical vapor deposited on MgO, obtained in JEOL T300 SEM operated at 20 kV.

of oxidized films on magnesium oxide. Ferrite inclusions have been detected.

Chemical vapor deposited films have been identified as having the ferrite crystal structure and are found to grow epitaxially on the MgO substrate. The surface constituents of these films have also been identified by AES and XPS. Each of the ferrite films studied contained a considerable amount of magnesium.

The composition distribution with depth in these chemical vapor deposited films has been studied by AES in conjunction with argon ion etching. It is found that magnesium is distributed uniformly through the ferrite films with a higher concentration of magnesium very close to the ferrite-MgO interface.

EDX spectra obtained from these chemical vapor deposited films were also found to contain magnesium peaks; the exact composition of each ferrite has been determined. It is possible that the incorporation of magnesium from the substrate into chemical vapor deposited films leads to a lower misfit between film and substrate. The epitaxy of each ferrite on MgO occurs at about 1200 C; however, since both ferrites and MgO have almost similar expansivities, the misfit between ferrite and MgO substrate depends only on the lattice parameters of both materials. Table 1 shows that only in two systems, magnetite-MgO and nickel ferrite-MgO are true ferrites formed with chemical formula  $\text{MeFe}_2\text{O}_4$ . For the nickel ferrite-MgO system the incorporation of magnesium leads to a smaller misfit with the MgO substrate. The lattice parameters of magnetite and magnesium ferrite (Table 2) are identical and there is no misfit reduction on the inclusion of magnesium in the film; however, there appears to be a wide range of quoted values for the lattice parameter of magnesium ferrite<sup>8</sup> from  $a = 8.377$  to  $8.402 \text{ \AA}$  and it is possible that a misfit reduction also occurs in the magnetite-MgO system. Analysis of the films formed in the cobalt ferrite-MgO system indicated that these films are oxygen deficient with respect to standard ferrite material, whereas in the manganese ferrite-MgO films the films contained an oxygen excess. It is difficult to compare the composition of these

materials with data on the variation of lattice parameter with addition of magnesium in ferrites in the standard form,  $\text{CoFe}_2\text{O}_4$  and  $\text{MnFe}_2\text{O}_4$ . In these materials the addition of magnesium leads to a lattice parameter that reduces misfit with MgO.

It is clear that there is considerable interdiffusion of metal ions between ferrite films and magnesium oxide substrates when these films are deposited or annealed at high temperatures. These effects must be taken into account in any thin film device applications of ferrite films grown on MgO substrates.

## References

1. G. R. Pulliam et al., "Localized doping of epitaxial ferrite films," *J. Appl. Phys.* 5: 2192, 1967.
2. A. G. Fitzgerald and T. G. May, "Defects in epitaxial ferrite films grown by chemical vapour deposition," *Thin Solid Films*, 35: 201, 1979.
3. J. H. Van der Merwe and N. G. Berg, "Misfit dislocation energy in epitaxial overgrowths of finite thickness," *Surface Science* 32: 1, 1972.
4. A. G. Fitzgerald, "Growth defects in epitaxial ferrite films," in A. P. Cracknell and R. A. Vaughan, Eds., *Magnetism in Solids*, Proc. 22nd Scottish Universities Summer School in Physics, SUSSP Publications, 1981, 181.
5. A. G. Fitzgerald and R. Engin, "Surface preparation of MgO single crystal substrates," *J. Mater. Sci.* 9: 339, 1974.
6. A. G. Fitzgerald and R. Engin, "Defects in nickel ferrite thin films grown by chemical vapour deposition," *Thin Solid Films* 20: 317, 1974.
7. J. W. Colby, "Quantitative microprobe analysis of thin insulating films," *Advances in X-ray Analysis* 11: 287, 1968.
8. C. J. Kriessman and A. P. Grier, in K. H. Hellwege and A. M. Hellewege, Eds., *Magnetic Oxides and Related Compounds*, Landolt-Bornstein, Vol. 4b, Berlin: Springer, 1970.
9. P. J. M. van der Straten and R. Metseelaar, "Liquid phase epitaxial growth of indium substituted magnesium ferrite films," *Mat. Res. Bull.* 12: 707, 1977.

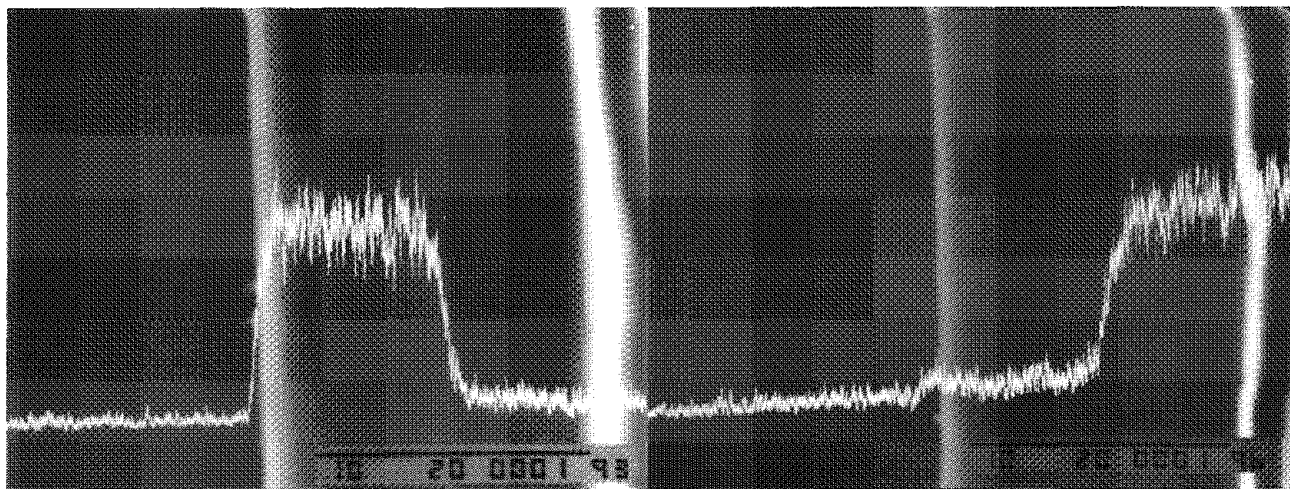


FIG. 7.--Secondary-electron images from cross section of magnetite film deposited by chemical vapor deposition onto MgO, showing x-ray linescans from (a) iron, (b) magnesium. Scale mark 10  $\mu\text{m}$ .

## CHARACTERIZATION OF A GRAPHITE-OFHC COPPER BRAZE JOINT

F. M. Hosking, R. E. Semarge, and C. R. Hills

Fabrication of actively cooled limiter blades for magnetic confinement fusion devices requires joining graphite tiles to copper substrates. Brazing graphite to copper with active braze alloys is a promising approach since it reduces the number of steps necessary to make the assembly. The subsequent braze structure and reaction phase at the graphite/braze interface is of special interest and is discussed in this study.

### Background

The potential for sustaining net energy with a magnetic confinement fusion device<sup>1</sup> has stimulated international interest in the scientific and engineering communities. However, there are significant hurdles that must be overcome to achieve fusion energy at a commercially available level. Not only must the deuterium-tritium fuel be heated to  $10^8$  C, but the resulting ionized gas or plasma must be confined such that more energy is released than consumed. Stabilization of the plasma is accomplished with magnetic fields.

One of the critical components in the vessel is the pump limiter.<sup>2,3</sup> The limiter defines the plasma edge and removes neutral particles and impurities. The current design uses graphite as the limiter surface. Since these limiters are being built for long-pulse, high-power fusion devices, the graphite tiles must be actively cooled. This cooling can be achieved by brazing of the graphite to a cooling substrate. For example, a proposed design has Poco AXF-5Q graphite attached to a water-cooled copper plate.<sup>4</sup>

Brazing graphite directly to copper presents a real engineering challenge.<sup>5-7</sup> Besides the thermal-expansion differences that exist between the two materials, graphite cannot be easily wet by most commercial brazing alloys. Several active braze alloys have been developed with some success. They generally contain Ta, Mo, Zr, or Ti and are suspected of forming a carbide reaction layer. An especially attractive choice comes from the Ag-Cu-Ti system.

The specific alloy studied here has a Ag-27 wt% Cu-5 wt% Ti composition. It not only has a relatively low brazing temperature (850 to 870 C), but it also has a reasonably low Ti content which should minimize the TiC reaction layer. The purpose of this investigation, then, was to evaluate brazing graphite to copper with the Ag-27 Cu-5 Ti alloy. A variety of microanalytical techniques was used to identify the braze structure and composition and

determine the effectiveness of the Ti component on wetting graphite.

### Experimental

**Brazing.** Poco AXF-5Q graphite and oxygen-free high-conductivity (OFHC) copper were used for the study. The filler was a clad foil, 0.075 mm thick, with a nominal composition of Ag-27 Cu-5 Ti as discussed above. Sample size was a 20mm disk. All parts were ground flat and given a final surface abrasion with a 400-grit paper. They were then ultrasonically cleaned in alcohol and rinsed in deionized water. The graphite disks were also vacuum baked at 300 C for 4 h before brazing.

The braze samples were joined in vacuum, 6.7 mPA ( $5 \times 10^{-5}$  Torr), at 870 C. Time at temperature was 5 min, followed by a programmed slow cool of 3 C/min.

**Microanalysis.** Metallographic specimens were removed along two radii perpendicular to each other. These specimens were examined with a JEOL 35C scanning electron microscope (SEM) for braze structure and initial elemental analysis. A CAMECA MBX electron probe microanalysis (EPMA) with a Sandia Task8 automation system<sup>8</sup> was used to quantify the elemental components present in the braze joint and at the graphite interface. EMPA analyses were performed at 15 kV, 20 nA, and a 20s maximum count time with a 1µm effective beam diameter. A set of photomicrographs, including secondary electron (SE), compositional backscattered electron (BSE), and elemental distribution (EDPM), was taken of the Cu/braze, bulk braze, and braze/graphite regions. Additional specimens were taken from the remaining sample and ion thinned for transmission electron microscope (TEM) and energy-dispersive spectroscopy (EDS) analyses. TEM samples were prepared by slicing perpendicular to the braze with a low-speed diamond saw. The slice was mechanically ground through 1µm diamond paste to a final thickness of approximately 75 µm. Disks centered about the braze joint were then mechanically punched from the thinned section. Sample size was 3 mm. Electron transparent foils were examined with a JEM 200CX at 200 kV. EDS analysis was done at 100 kV with a JEM 100C equipped with a conventional Si(Li) x-ray detector. Electron diffraction was also performed on selected regions near the graphite/braze interface to determine the crystal structure of the phases present.

### Results and Discussion

Initial SEM analysis revealed excellent wetting of the graphite and Cu surfaces (Fig. 1). Poco AXF-5Q graphite is a porous material and up to 50 µm of capillary infiltration by the Ag-27 Cu-5 Ti alloy into the graphite was observed. The braze structure was composed primarily of a Ag-rich eutectic surrounding discontinuous proeutectic Cu-rich

---

The authors are with Sandia National Laboratories, Albuquerque, NM 87185. They acknowledge the help of A. A. Netz for brazing support and N. A. Creager for SEM analysis. This work was supported by the U.S. Department of Energy under contract DE-AC04-76DP09789.

FIG. 1.--BSE micrograph of Poco AXF-5Q graphite-to-OFHC Cu braze made with Ag-27 Cu-5 Ti filler metal.

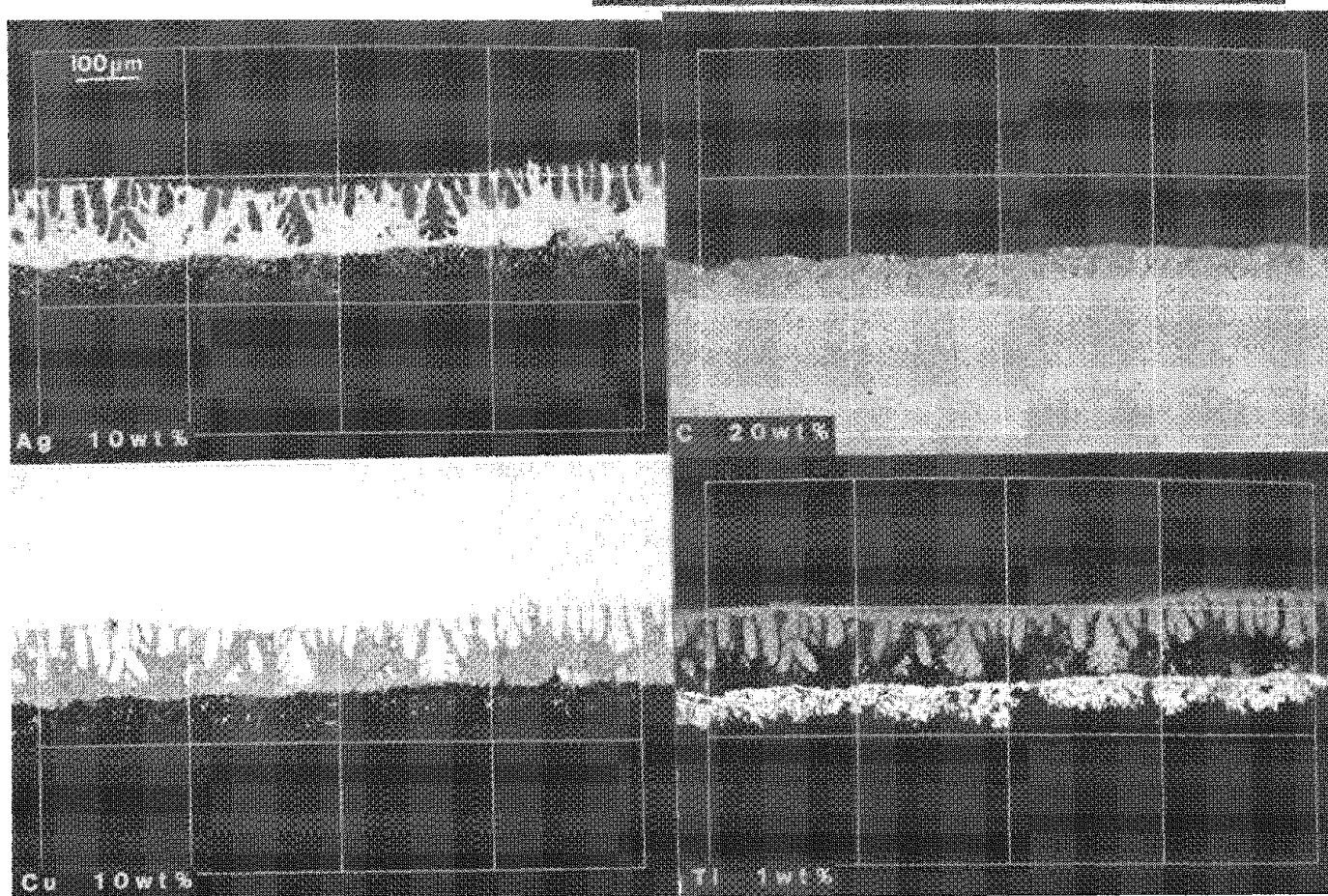
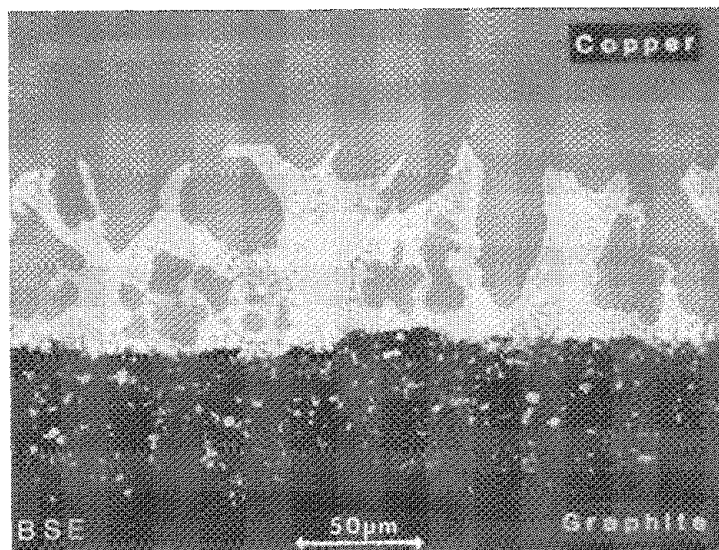


FIG. 2.--Ag, C, Cu, and Ti x-ray EDPMs of typical graphite-Cu braze made with Ag-27 Cu-5 Ti filler metal.

clusters. On the OFHC Cu side of the braze joint, a Cu-rich phase extended from the Cu base into the eutectic region.

Table 1 lists quantitative compositional results from the EPMA analysis. X-ray EDPs of Ag, C, Cu, and Ti are shown in Fig. 2. Both Cu-rich regions were found to have a nominal composition of 8.5 wt% Ag, 3.0 wt% Ti, with the balance Cu. This composition compared well to the solidus line of the Cu-rich side of the Ag-Cu binary phase diagram.<sup>9</sup> Dissolution of the OFHC Cu base by the liquid braze provided excess Cu that mixed with the bulk alloy and resulted in this proeutectic structure.

The Ag-rich microconstituent was generally lean in Ti, <0.3 wt%, with a near eutectic bulk composition of 28 wt% Cu and balance Ag. Close examination of the braze that infiltrated the porous graphite region showed the centers of these areas to be eutectic (Ag-Cu) in nature with the reaction layer at the graphite/metal interface enriched in Ti. Although the reaction layer was too small to analyze quantitatively within the microprobe's x-ray spatial resolution, the relative ratio of Ti to other braze elements (1:1) was significantly higher than found in the bulk braze composition. A very thin reaction layer of TiC was suspected.

TEM and electron diffraction analyses were next used to identify the phase at the graphite/braze interface. This reaction zone was determined to have an approximate thickness of 0.35  $\mu\text{m}$  (Fig. 3). Electron diffraction patterns of the zone confirmed the formation of a TiC layer (Fig. 4). It is the formation of the carbide that promotes wetting of the graphite surface.

EDS analysis supported the microprobe results of the bulk braze. Ti was detected at a significant level in the Cu-rich regions. These areas were also more complex than shown by the EPMA. TEM analysis of the Cu-rich areas revealed a composite structure consisting of an elemental Cu matrix with fine precipitates (Fig. 5). Electron diffraction patterns identified one of the precipitates as elemental Ag. A Cu-rich, Cu-Ti precipitate was also found, although not positively identified. These precipitates were nearly coherent with the Cu matrix. Particle size of the Ag and Cu-Ti precipitates was 0.1 to 0.25  $\mu\text{m}$  and 0.5  $\mu\text{m}$ , respectively. The shape of the Cu-Ti particles was irregular. There were also some larger Ag particles ranging in size up to 0.8  $\mu\text{m}$  with a platelike morphology.

TEM of the Ag-rich, eutectic structure revealed fine precipitates in the Ag phase (Fig. 6). The precipitates were identified by electron diffraction as elemental Cu. Their formation would be similar to the precipitation of Cu in the binary Ag-Cu eutectic as it cools from the eutectic temperature. The solid solubility of Cu in Ag decreases from 8.8 wt% at 779 C to <0.2 wt% at room temperature.<sup>9</sup> Particle size was 0.1 to 0.2  $\mu\text{m}$ . EDS analysis showed negligible Ti in the Ag-rich constituent.

## Conclusion

SEM, EPMA, TEM, EDS, and electron diffraction patterns were used to characterize a Poco AXF-5Q graphite-to-OFHC Cu braze made with Ag-Cu-Ti filler metal. The braze joint was composed of proeutectic Cu-rich and eutectic Ag-rich regions. The Cu-rich region was a composite of an elemental Cu matrix with fine precipitates of Ag and a Cu-Ti intermetallic. The Ag-rich region was near eutectic with a bulk composition of 28 wt% Cu, a trace of Ti, and balance Ag. Fine precipitates of elemental Cu were detected in the Ag phase. The reaction layer at the graphite and braze interface was verified as TiC. Wetting of the graphite surface was promoted by the formation of this carbide zone.

## References

1. *Fusion Power*, Information Bulletin NT-1, Princeton University (Plasma Physics Laboratory), 1982.
2. R. W. Conn, "Tokamak advanced pump limiter experiments and analysis," *Proc. 9th Intern. Vacuum Congress and 5th Inter. Conf. Solid Surfaces*, 1983, 568.
3. P. Deschamps, A. Grosman, M. Lipa, and A. Samain, "Power exhaust and plasma-surface interaction control in Tore Supra," *J. Nuclear Materials*, 38: 128-129, 1984.
4. J. B. Whitley (Project Leader), *SNLA Tore Supra Pump Limiter Baseline Study*, Sandia National Laboratories Tokamak Design Review, 1985.
5. H. E. Pattee, R. M. Evans, and R. E. Moore, *Joining Ceramics and Graphite to Other Materials*, NASA SP-5052, 1968, 71.
6. L. O. Lindquist, and R. Mah, *Graphite-to-metal Bonding Techniques*, Los Alamos National Laboratories Report LA-6928-MS, 1977.
7. D. E. Schechter, C. C. Tsai, F. Sluss, W. R. Becraft, and D. J. Hoffman, "Erosion tests of materials by energetic particle beams," *Fusion Technology* 8: 559, 1985.
8. W. F. Chambers, *SANDIA TASKS8: A Sub-routed Electron Microprobe Automation System*, Sandia National Laboratories Report SAND85-2037, 1985.
9. M. Hansen and K. Anderko, *Constitution of Binary Alloys*, New York: Genium, 1985, 18.

TABLE 1.--Bulk composition (wt%) of primary braze phases.

	Ag	Cu	Ti
Cu-rich phase	8.5	bal.	3.0
Ag-rich eutectic	72.0	27.0	<0.3



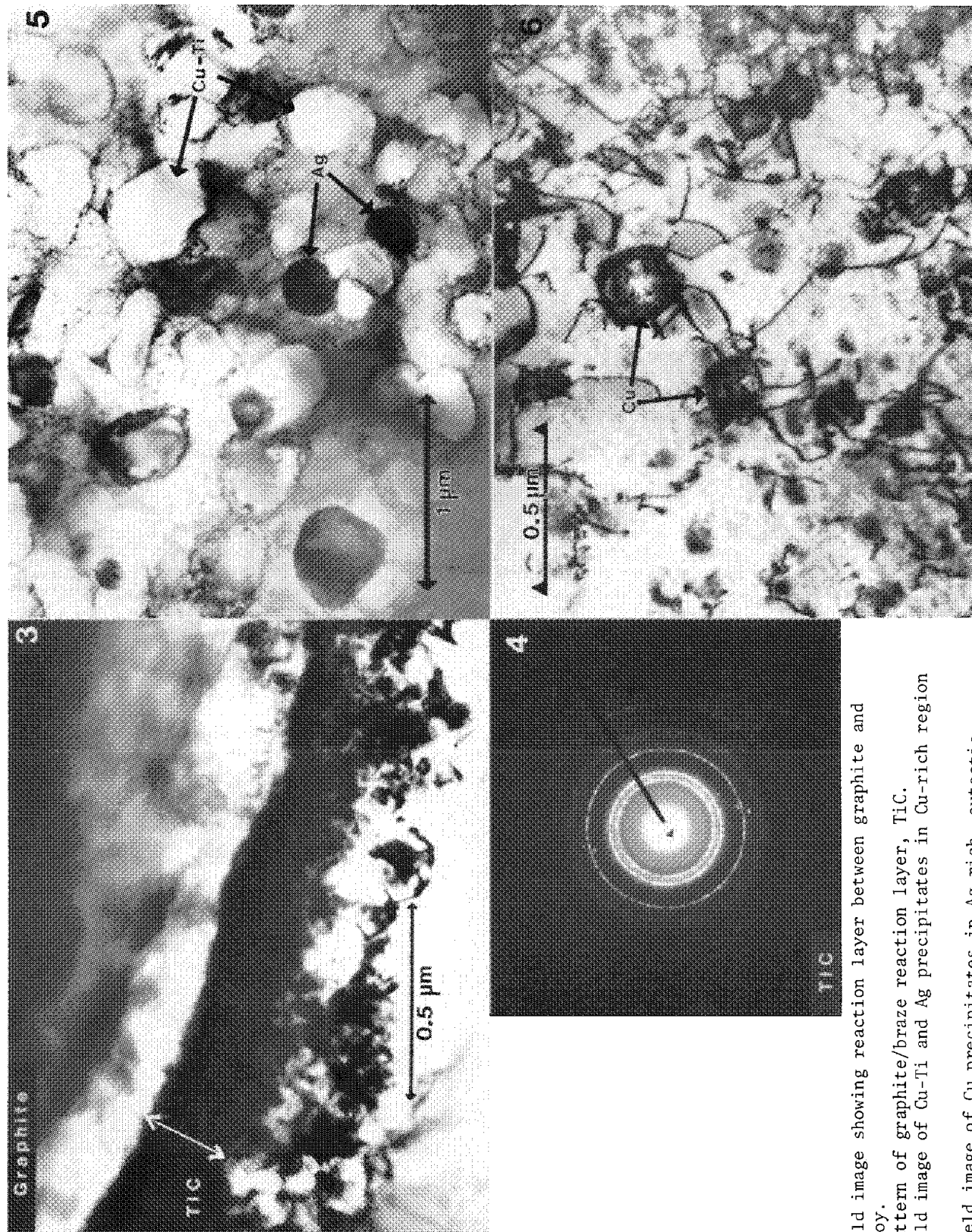


FIG. 3.--TEM bright-field image showing reaction layer between graphite and AG-27 Cu-5 Ti braze alloy.  
 FIG. 4.--Diffraction pattern of graphite/braze reaction layer, TiC.  
 FIG. 5.--TEM bright-field image of Cu-Ti and Ag precipitates in Cu-rich region of braze.  
 FIG. 6.--TEM bright-field image of Cu precipitates in Ag-rich, eutectic region of braze.

## 6. Biological Applications

### ION PROBE MICROANALYSIS OF Li- AND Be-TREATED HEPATOCYTE CULTURES

A. R. Crooker, E. W. Sod, M. C. Myers, K. P. Baran, and G. H. Morrison

The light element lithium (Li,  $Z = 3$ ) has been studied in biological systems by a variety of microscopy techniques;<sup>1-5</sup> the toxic element beryllium (Be,  $Z = 4$ ) has been less extensively investigated.<sup>6-9</sup> In nearly all cases, conventional chemical fixation has been utilized for specimen preparation. These techniques cause the loss and redistribution of exogenous and endogenous elements and physiologically important ions unless the elements are covalently bound or are present as discrete granules. Only cryotechniques can faithfully preserve elemental and ion distributions for biological microanalysis.

Ion microscopy, based on secondary ion mass spectrometry (SIMS), can detect all elements and isotopes from hydrogen through uranium with sensitivities typically in the ppm range. The greater sensitivity of ion microscopy compared with analytical electron microscopy, the inability of x-ray microanalysis to detect Li and Be in biological specimens effectively and the need for ultrathin cryosections of appropriate thickness ( $< 50$  nm) for electron energy loss spectrometry make this technique particularly attractive.

The present investigation utilizes freeze-fracture cryotechniques and ion probe microanalysis to examine the intracellular distribution of Li and Be in primary monolayers of adult rat hepatocytes. The effects these light elements may have on intracellular Na, K, Ca, and Mg were also examined.

#### *Experimental*

Freshly dissociated adult rat hepatocytes were seeded on the polished side of collagen-coated  $1\text{cm}^2$  pieces of semiconductor grade N-type Si wafers (General Diode) placed in the bottom of culture dishes. The resulting primary monolayers were maintained in Dulbecco's Modified Eagles Medium at 310 K in 90% air/10%  $\text{CO}_2$ . After 16-20 h the growth medium was replaced with new medium containing  $10\mu\text{M}$  polystyrene beads. These beads served as spacers to help control the fracture plane during sample preparation. At this time, the appropriate volume of dosing solution was added to each culture, and cells were incubated for 24 h with 0 (control), 625, 1250, 2500, 5000, 10 000, and 15 000  $\mu\text{M}$  lithium carbonate ( $\text{Li}_2\text{CO}_3$ , Aldrich Chemical Co.) and 0 (control), 125, 250, 500, 1000, and 2000  $\mu\text{M}$  beryllium sulfate tetrahydrate ( $\text{BeSO}_4 \cdot 4\text{H}_2\text{O}$ , Aldrich

Chemical Co.).

Sample preparation follows that of Chandra, Morrison, and Wolcott,<sup>10</sup> except that specimens were frozen in liquid propane/isopentane instead of nitrogen slush or freon. Briefly, the technique involves removing an Si wafer from the culture dish, blotting excess media from the wafer, and then placing the polished side of another wafer atop the cells on the bottom wafer to form a wafer-cell-wafer sandwich. The sandwich was quench-frozen in liquid propane/isopentane (70:30) cooled with liquid nitrogen to 83 K, then fractured apart under liquid nitrogen to reveal the interior of the cell, so that interference from the surrounding culture medium was eliminated. Following freeze-drying, the sandwich halves were transferred to a dry box and mounted on Al disks with silver paste. Mounted samples were stored in a nitrogen atmosphere over desiccant.

A Cameca IMS-3f ion microscope operating with a 10.5keV  $\text{O}^{2+}$  primary beam and monitoring positive secondary ions was used for the study. A primary beam of 100 nA (Li) and 250 nA (Be) was rastered over an area  $50 \times 50 \mu\text{m}$ . Only cells fractured through the apical surface were analyzed. The ion images were recorded on Kodak Tri-X film with a 35mm camera.

Leakage of the cytoplasmic enzyme lactate dehydrogenase (LDH) from the cells into the culture medium was used as an index of cytotoxicity.<sup>11</sup>

#### *Results and Discussion*

Lithium images obtained from cells at all concentrations revealed that Li is distributed homogeneously throughout the nucleus and cytoplasm (Fig. 1). Images frequently indicated a higher concentration of Li in the nucleus than the cytoplasm (image brightness is an indicator of secondary ion emission). The findings are not unexpected since Li is thought to be transported through ion carrying channels<sup>12</sup> and may be found free in the cell, sequestered in organelles,<sup>3</sup> or bound at sites normally occupied by Ca or Mg.<sup>13</sup> Lithium might also be expected to accumulate in nucleotide-rich environments, since it displays a relatively high affinity for ATP and ADP.<sup>13</sup> A distinct cytoplasmic compartmentalization of Li was not seen.

Lithium is known to interfere with Na and K balance, primarily in *in vivo* situations.<sup>12</sup> Under the conditions of the present study, an effect on the quantity and distribution of these ions was not seen. However, some cells did show higher Na and K in the nucleus (Fig. 1). At concentrations up to 10 000  $\mu\text{M}$ , Na/K ratios remained similar to those of the controls. At 15 000  $\mu\text{M}$ , a high intracellular Na/K ratio indicative of dead or injured cells was seen. LDH leakage studies (Table 1) indicated that minimal cytotoxicity was occurring

Authors Crooker, Myers, and Baran are with Norwich Eaton Pharmaceuticals, Inc., Box 191, Norwich, NY 13815; authors Sod and Morrison are at the Department of Chemistry, Cornell University, Ithaca, NY 14853. This work was supported by the National Institutes of Health (G.H.M.). The authors thank J. Micklas, Norwich Eaton Pharmaceuticals, for his assistance with the preparation of hepatocyte cultures.



## ULTRASTRUCTURAL CHANGES IN THE GLOMERULUS OF A HIBERNATOR BY SCANNING AND TRANSMISSION ELECTRON MICROSCOPY

D. G. Anderson, S. D. Brazal, M. O. Natividad, and G. A. Lopez

Electron microscopic comparisons of kidneys from nonhibernating (normothermic) and hibernating (hypothermic) squirrels have shown numerous differences in glomerular morphology.<sup>1</sup> These glomerular changes appear to be related to cellular hydration and sodium retention for purposes of water balance during the inactive period of hibernation, when the nephron (the filtration unit of the kidney) is essentially nonfunctional.

These changes were also found to be similar to those observed in various human renal nephrotic syndromes, which suggest the existence of common, altered renal mechanisms, mediating glomerular function in two widely dissimilar physiological states. These observations leave open the attractive possibility of using the inactive hypothermic hibernator as a unique animal model to study human renal glomerular disease.

The striking glomerular changes observed in this preliminary study between the active normothermic squirrel *Spermophilus lateralis* and its hibernating hypothermic counterpart were made possible by the use of scanning electron microscopy (SEM), which has revealed cellular components not previously reported in the hibernator. Transmission electron microscopy (TEM) further confirmed these findings, and has supported other previously reported cellular changes in this species.

### Materials and Methods

Active, male, normothermic golden-mantled ground squirrels, *Spermophilus lateralis*, captured in the wild, were fed a standard Purina Chow diet with unlimited access to water. These animals were kept individually in cages in a room maintained at a constant temperature (25 C) and a 12h light and dark cycle. Body weight changes were monitored weekly. When the animals reached 300 g in bodyweight, they were transferred to a cold room (5 C), where hibernation bouts began to occur naturally. Animals were sacrificed in weight-matched pairs, beginning at midsummer. Active normothermic squirrels weighed 200-250 g. Hibernating animals weighting 240-250 g were housed in the cold room for 3 months before being sacrificed by decapitation after light anesthesia. Their kidneys were then rapidly removed and their renal cortical region was minced with a razor blade to 1 mm<sup>3</sup> and immersed in room-temperature fixative (2.5% glutaraldehyde, 2.0% paraformaldehyde in 0.1M

cacodylate buffer, pH 7.4) for 1 h. Tissue blocks were then washed and postfixed in 1% osmium tetroxide for transmission electron microscopy. The tissues were dehydrated in graded steps of acetone and embedded in Araldite 502 (Pelco); 1µm sections were cut on a LKB Ultratome III with glass knives (LKB Sweden) and stained with toluidine blue for glomerular orientation. Thin sections were cut with a diamond knife, placed on uncoated grids, and stained with 2% uranyl acetate and bismuth subnitrate.<sup>2</sup> The sections were examined with a Zeiss 109 TEM.

In the SEM study, tissue blocks fixed in the previously described fixative were not postfixed, but dehydrated in graded steps of acetone and allowed to air dry. These tissues were mounted on glass coverslips with colloidal silver paste (Pelco). Glomerular orientation was aided by use of a dissecting microscope during mounting. The tissue was kept under dessication until double evaporation coating with carbon and gold-palladium. The tissue was examined with a Cambridge Stereoscan MK-3 at 20kV accelerating voltage by secondary electron imaging.

Glomerular basement membrane width was measured in 10-20 areas chosen randomly on five TEM micrographs from each sample. Endothelial pores were measured in 10-20 areas from each sample where pores could be found. Podocytic processes, microprojections, foot processes, glomerular basement membrane, and mesangial cell renal elements were compared between normothermic active and hibernating inactive animals.

### Observations

*Scanning Electron Microscopy of the Glomerulus of Nonhibernating Squirrels.* The glomerular surface of the normothermic squirrel is illustrated in Fig. 1. The Bowman's capsule was cut open in this view. Podocyte cell bodies and their processes covered all of the outer surfaces of the capillary loops. One of the capillary loops is enlarged in Fig. 2. Each podocyte consists of a centrally nucleated cell body from which arm-like processes arise and wrap around underlying glomerular capillary loops. These major processes, which arise from one podocyte, may fuse with each other and are often irregular in shape.<sup>3</sup> At right angles from the major processes were smaller projections termed pedicels. Pedicels from one cell always interdigitated with pedicels from another cell, as reported by Andrews.<sup>3</sup> A sparse population of microprojections arose from the free surfaces of cell bodies, major processes, and pedicels. Podocytic pedicels varied in size and exhibited bulbous and stubby ends. Slit pores were seen between pedicels through which glomerular filtrate is forced into Bowman's capsular space. At a low magnification (Fig. 1), the glomerulus had an overall smooth surface appearance

The authors are at the Department of Biology, California State University, Los Angeles, CA 90032. They gratefully acknowledge the SEM technical assistance of Steve Dowell of the Los Angeles County Medical Examiner's office. This work was supported by an NIH grant 5-S06-RR08101.

with few blebs or microprojections. The processes and pedicels were flat against the capillary loops. At a higher magnification (Fig. 2), cell processes and pedicels with their smooth surfaces were seen. Small nodules were noticed on the surface of major processes. In some areas cell bodies appeared round, but with few surface irregularities.

*Transmission Electron Microscopy of the Glomerulus of Normothermic and Hibernating Squirrels.* A normothermic podocytic cell body with major processes, secondary processes, and pedicels lying along the glomerular basement membrane is shown in Fig. 3. The smooth surface of the cell body is apparent. Few microprojections were noted in the normothermic glomerulus. The pedicels with foot processes were anchored on the basement membrane. Usually, pedicels originated from major or secondary cell processes and very seldom from cell bodies directly.

Endothelial fenestrations were obvious in Fig. 3. Many fenestrations were revealed by TEM. The glomerular basement membrane was found to be uniform in thickness in the normothermic animal.

In the hibernating squirrel, numerous microprojections were seen originating from cell bodies, major processes, and secondary processes. These microprojections in most cases, did not terminate on the capillary loop as foot processes. Endothelial fenestrations had decreased in number. The endothelium was observed to be thicker in the hibernating animal. Pinocytotic vesicles were found in the parietal epithelium of Bowman's capsule. The glomerular basement membrane of the hibernator was approximately twice as thick and irregular in width, which agrees with the observations of Zimny et al.<sup>1</sup>

Heavy osmiophilic staining was observed along podocytic plasma membranes in the hibernator. In some areas, microvilli similar to a brush border were found on the parietal epithelium. Mesangial cells showed an increase in dense bodies. Vacuoles were observed in podocytes as previously reported by Zimny et al.<sup>1</sup>

### Discussion

Normal and pathogenic glomerular structure was initially described by Arakawa<sup>4</sup> in 1970, using SEM. Only through SEM could such a striking three-dimensional image of the visceral epithelial cells (i.e., podocytes) be obtained, providing us with this view of the altered kidney during hibernation. By comparing this three-dimensional surface image with the two-dimensional interior view obtained by TEM, the numerous glomerular structural modifications that this animal has developed to cope with drastic changes in its environment can be appreciated.

It is now generally accepted, for several species of rodents, that minimal urine formation takes place while the animal is at very low body temperature during hibernation.<sup>5</sup> However, significant urine production occurs during periodic arousal during hibernation, as the animal's body temperature increases and normal blood flow is restored to the renal

system.<sup>5</sup>

The hydrostatic pressure gradient between the glomerular capillary vessels and Bowman's space is the primary driving force for filtration in the kidney. During hibernation there is a 90% reduction in blood perfusion of the kidney and 55% to 60% reduction in mean arterial pressure. This would explain the practically negligible extent of glomerular filtration.<sup>6</sup> The normothermic kidney receives 16% of the cardiac output; hibernating kidneys receive only 10%. Plasma volume decreases by 35% during hibernation. Blood flow to the heart, lung, diaphragm, and brown fat increases; flow to the visceral organs decreases.<sup>6</sup> The renal medullary osmotic gradient is not present when the animal is at low body temperature, so that even if some urine is formed, it could not be concentrated; and it is hypertonic to plasma.<sup>5</sup> During periodic arousal, every 10-14 days, sodium and urea gradients are simultaneously and rapidly restored to normal.<sup>7</sup>

The low or nonfunctional glomerulus during hibernation has structural characteristics similar to those found in human congenital nephrotic syndrome and epithelial cell disease.<sup>8</sup> Epithelial cell disease shows foot process obliteration and the basement membrane is covered by sheets of podocytic cytoplasm. Visceral epithelial cells show prominent intracytoplasmic organelles, which suggests increased cytoplasmic activity. Microvillous hyperplasia and vacuolated podocytes are seen in these pathological states.<sup>8</sup> Podocytic microprojections are not uncommonly seen by TEM in many other nephrotic diseases. These observations during diseased renal states are strikingly similar to those seen in the kidney of the inactive hibernating ground squirrel in this study.

The glomerular basement thickening found in the present study may be explained by a previous observation of an increase in acid mucopolysaccharide content in this membrane during hibernation.<sup>9</sup> The glomerular basement membrane in the hibernator stained positively with ruthenium red, indicating acid mucopolysaccharide.<sup>9</sup> Zimny suggests this polyamionic acid mucopolysaccharide could act as a resin for the exchange of cations between the capillary and urinary space. This increased quantity of anionic material may allow more sites for exchange of cations, more attraction for water, and a greater concentration of protein, all of which would increase water and electrolyte balance during hibernation.<sup>9</sup>

Clearly, further studies are needed to elucidate the reason for the presence of this villous hyperplasia in a nonfunctioning but healthy nephron unit, and to determine whether there is a correlation with the villous hyperplasia seen in human renal nephrotic disorders. It is conceivable that the use of the hibernating ground squirrel as an animal model to study human renal disease may provide us with valuable insight into the specific physiological alterations which lead to renal pathological function. The results of this preliminary study are consistent with this possibility.

## References

1. M. L. Zimny and E. Rigamer, "Glomerular ultrastructure in the kidney of hibernating animal," *Anat. Rec.* 154: 87-94, 1966.
2. S. K. Ainsworth and M. J. Karnovsky, "An ultrastructural staining method for enhancing the size and electron opacity of ferritin in thin sections," *J. Histochem. Cytochem.* 20: 225, 1972.
3. P. M. Andrews, "The urinary system: Kidney," in G. M. Hodges, Ed., *Biomedical Research Applications of Scanning Electron Microscopy*, New York: Academic Press, 1979, 273-306.
4. M. Arakawa, "A scanning electron microscopy of the glomerulus of normal and nephrotic rats," *Lab. Invest.* 33: 489-496, 1970.
5. A. E. Muchlinski and A. L. Carlisle, "Urine concentration by an undisturbed naturally arousing hibernator (*Spermophilus lateralis*): Water balance implications," *J. Mamm.* 63: 510-512, 1982.
6. G. E. Tempel et al., "Mechanisms responsible for decreased glomerular filtration and hypothermic," *J. Appl. Physiol.* 42: 420-425, 1977.
7. R. M. Moy, "Renal function in the hibernating ground squirrel *Spermophilus columbicus*," *Amer. J. Physiol.* 220: 747-753, 1977.
8. B. Spargo et al., *Renal Biopsy Pathology*, New York: Wiley, 1980.
9. M. L. Zimny, "Mucopolysaccharide in the glomerular basement membrane of a hibernator," *Am. J. Anat.* 138: 121-125, 1973.

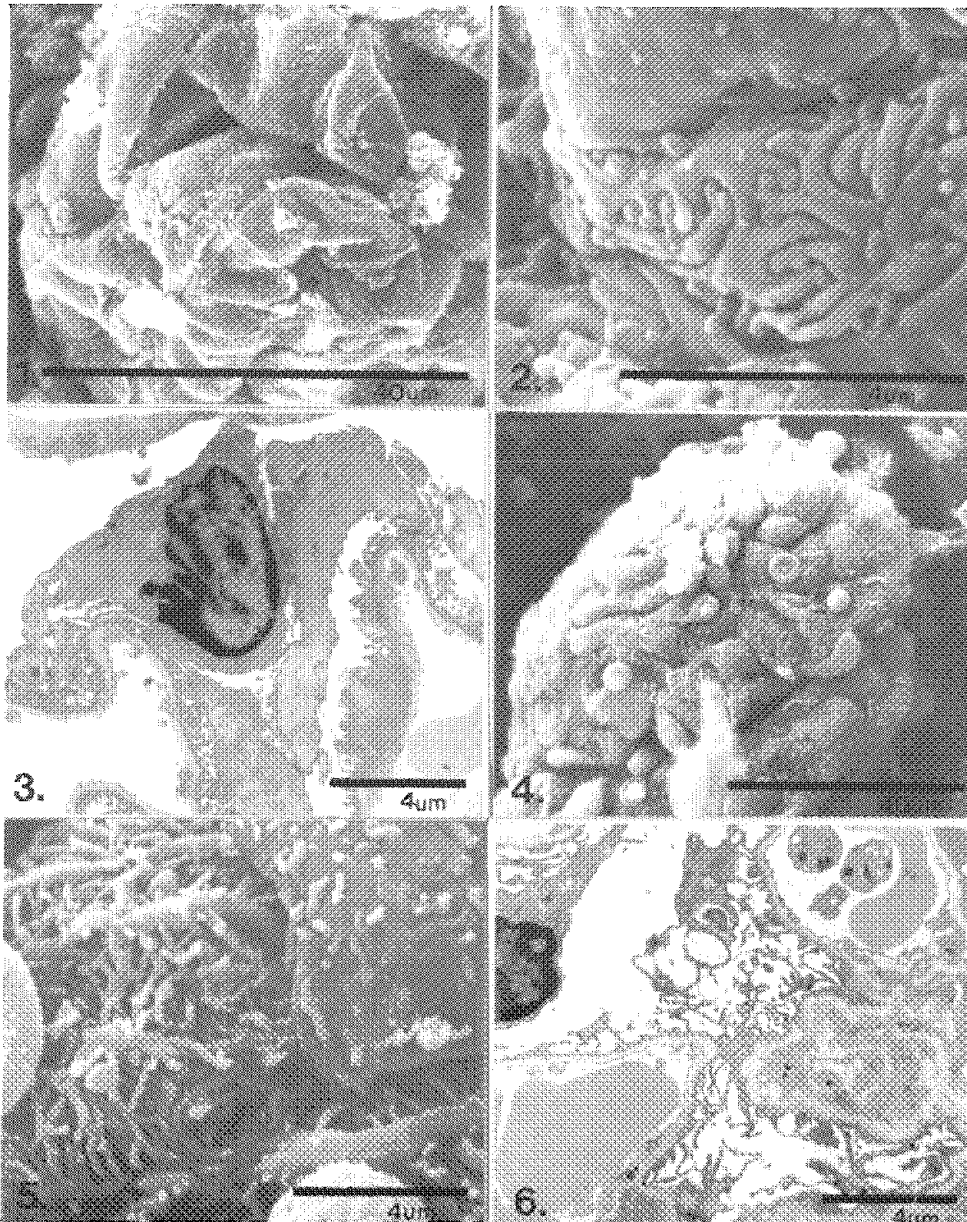


FIG. 1.--Low-magnification SEM micrograph of normothermic squirrel's glomerulus. Winding capillary loops are covered by podocytes. Interdigitating processes are visible at top of micrograph.

FIG. 2.--Higher-magnification view of podocytic interdigitating processes over capillary loop. Processes and pedicels are flat against capillary loops in normothermic squirrel.

FIG. 3.--TEM of normothermic podocytic cell body, major processes, and foot processes anchored on basement membrane of capillary loop. Few microprojections are present.

FIG. 4.--Low-magnification SEM micrograph of hibernating squirrel's glomerulus. Capillary loops are covered by microvillus podocytic processes. Glomerulus has overall "hairy" appearance.

FIG. 5.--Higher-magnification SEM micrograph of podocyte cell body and secondary processes covered by microprojections. Cell body is viewed at right. From glomerulus of hibernating squirrel.

FIG. 6.--TEM micrograph from hibernating squirrel. Microprojections are cut in cross section and longitudinal. Foot processes anchor on basement membrane.

## Na-Ca COMPARTMENTATION IN CULTURED HEART CELLS

Ann LeFurgey, L. A. Hawkey, Melvyn Lieberman, and Peter Ingram

Recent investigations in our laboratory of sodium-calcium exchange in cultured chick heart cells have demonstrated that during Na-free incubation total cell calcium ( $Ca_t$ ) rises by  $\sim 1.4$ – $2.8$  mM (5–10 nmol/mg protein or 7.7–15.4 mmol/kg dry wt), and cytoplasmic free calcium ( $Ca_f$ ) increases from  $\sim 60$  nM to only 165 nM.<sup>1</sup> These data suggest that Ca is being sequestered intracellularly. In addition when cells are preloaded with Na (by incubation with ouabain in a nominally Ca-free solution)  $Ca_f$  rises to  $\sim 1$   $\mu$ M, a level six times greater than during Na-free incubation alone. This latter difference suggests that during Na-free incubation Ca may be sequestered in an organelle of limited uptake capacity (e.g., sarcoplasmic reticulum) rather than in a high-capacity store (e.g., mitochondria). Electron probe x-ray microanalysis (EPXMA) is the best currently available technique for determining the sites and quantitative amounts of Ca sequestered by perturbing the sodium-calcium transport system. We used EPXMA, in conjunction with correlative biochemical techniques for measuring  $Ca_t$  and  $Ca_f$ , to define whether or not changes in cellular Na and Ca content and compartmentation are consistent with a sarcolemmal Na-Ca exchange and/or with the presence of a sarcolemmal Ca-ATPase.

### Methods

*Cell Culture, Manipulation, and Cryopreservation.* Aggregates of cardiac muscle cells were grown as described by Ebihara et al.<sup>2</sup> Briefly, muscle-enriched cells from 11-day-old embryonic chick hearts were used to seed agar-coated culture dishes containing small openings (20  $\mu$ m). The cultures were incubated at 37 C in a humidified chamber containing 4% CO<sub>2</sub> and 96% air. On day 3 or 4 spontaneously contracting aggregates were rinsed free of growth media and transferred for 20 min to either modified Earle's balanced salt solution (MEBSS) or MEBSS in which all sodium was replaced with trimethyl-ammonium Cl and choline HCO<sub>3</sub>. Immediately following the incubation period cells were rapidly frozen in liquid propane and cryosectioned as previously described,<sup>3</sup> and only specimens with overall ice crystal sizes smaller than regions to be probed (as monitored by parallel freeze-substitution from the same specimen) were used.

*X-ray Microanalysis.* All analyses were

performed on freeze-dried cryosections  $\leq 1000$  Å thick in a transmission electron microscope (JEOL 1200EX TEMSCAN) equipped with a scanning device, additional hard x-ray aperture, collimated 30mm<sup>2</sup> Si(Li) energy-dispersive x-ray detector and microanalysis system (Tracor Northern 5500), and liquid nitrogen-cooled low-background cryotransfer stage (Gatan 626). X-ray spectra were obtained for 500 s per area from selected cell compartments at  $-110$  C by use of a small square raster (0.1–0.06  $\mu$ m<sup>2</sup>) at 100 000 to 150 000 magnification with specimen tilt of 35°, accelerating voltage, 80 kV and beam current of  $\sim 1$  nA. All spectral data were transferred directly from the x-ray analyzer to a VAX 11/750 computer for quantitative analysis by the Hall continuum normalization method<sup>4</sup> with the peak centroid shift and broadening corrections of Kitazawa et al.,<sup>5</sup> using the programs developed by and provided to us by Somlyo and colleagues. Standards were prepared according to the methods of Shuman et al.<sup>6</sup> Specimen mass changes due to the electron beam or to shift during probing were monitored every 50 s. The microscope and stage were baked out periodically and the stage was left in the instrument when not in use to minimize residual contamination in the region of the specimen. Following initial mass loss<sup>7</sup> at the high doses used, which is assumed to be the same for standards and sample, further mass changes were always  $\leq 1\%$ . This result also indicated that the anticontamination trap on the microscope was colder than the stage (specimen).

### Results and Discussion

Preliminary quantitative EPXMA analyses for nucleus, cytoplasm including regions of sarcoplasmic reticulum, and mitochondria are enumerated in Table 1 for heart-cell aggregates frozen after incubation for 20 min in either a control medium (MEBBS) or sodium-free MEBBS. Relative to control, primary changes occurred during Na-free treatment in Na and Ca content and compartmentation (Figs. 1 and 2); Cl content decreased in all compartments. K, P, and S content changed variably in each compartment and Mg exhibited no large percentage changes. The decreases in sodium content observed after ONa incubation were statistically significant for all cell compartments analyzed (Fig. 1). In cytoplasm + SR and in mitochondria, sodium decreased nominally to zero. In parallel measurements of total cell ion content by atomic absorption spectrometry<sup>1</sup> Na was about 13.4 mmol/kg dry wt (control, about 194 mmol/kg dry wt); the EPXMA data suggest that approximately one-third of this amount remained compartmentalized within the nucleus.

Significant increases in Ca content were detectable in cytoplasmic regions (Fig. 2). Cytoplasmic probes invariably included regions of sarcoplasmic reticulum. The SR is abundant

Authors LeFurgey, Hawkey, and Lieberman are with the Department of Physiology, Duke University Medical Center, Durham, NC 27710; author Ingram is with the Research Triangle Institute, Chemistry and Life Sciences Division, Research Triangle Park, NC 27709. Supported by NIH HL 07101, 17670, and 27105, BRSH S07 RR05405.

and randomly distributed but rather small in these embryonic cells; the quality of freezing did not allow us to visualize unambiguously SR in all sections. Organized myofibrils were identifiable within the cytoplasm but were not probed. Mitochondria showed a marginally significant ( $0.1 > p > 0.05$ ) increase in Ca content after 20 min in ONa. Nuclear Ca content decreased in comparison with control but the decrease again was not statistically significant given the limited number of measurements performed to date. These data are consistent with independent measurements of  $Ca_i$  and  $Ca_f$  under identical conditions of Na depletion, which show that the increase in  $Ca_i$  cannot be fully accounted for by increased  $Ca_f$  and thus suggest that Ca is sequestered.<sup>1</sup> The relatively small increase in mitochondrial Ca, compared to the increase observed in cytoplasm + SR, demonstrates that under these conditions mitochondria do not serve as a major Ca storage site. Because the measurements were made following 20 min in Na-free media, the possibility exists that at some earlier time point mitochondria function as an intermediate store for Ca. Similar APXMA results demonstrating low Ca in mitochondria have been observed by Wheeler-Clark and Tormey in rabbit ventricular muscle bathed in low external Na.<sup>8</sup> These investigators also documented increased Ca in the junctional sarcoplasmic reticulum and decreased Cl in all compartments analyzed. The interesting observation of a trend toward decreasing nuclear Ca with concomitant decreasing nuclear Na may

suggest that the nucleus is also a source of Ca movement into the cytoplasm-SR complex.

#### References

1. E. Murphy et al., "Coupled sodium-calcium transport in cultured chick heart cells," *Am. J. Physiol.* 250: C442-452, 1986.
2. L. Ebihara et al., "The initial inward current in spherical clusters of chick embryonic heart cells," *J. Gen. Physiol.* 75: 437-456, 1980.
3. A. LeFurgey et al., "Quantitating elemental characterization of cultured heart cells by electron probe x-ray microanalysis and ion-selective electrodes," *Microbeam Analysis--1986*, 205-208.
4. T. Hall, "Biological x-ray microanalysis," *J. Microscopy* 117: 145-163, 1979.
5. T. Kitazawa et al., "Quantitative electron probe analysis: Problems and solutions," *Ultramicroscopy* 11: 251-262, 1983.
6. H. Shuman et al., "Quantitative electron probe microanalysis of biological thin sections: Methods and validity," *Ultramicroscopy* 11: 317-339, 1976.
7. M. E. Cantino et al., "Beam induced mass loss in high resolution biological microanalysis," *J. Microsc.* 144: 317-327, 1986.
8. E. S. Wheeler-Clark et al., "Redistribution of subcellular electrolytes accompanying the increased myocardial contractility produced by low Na," *Microbeam Analysis--1985*, 116-118.

TABLE 1.--Elemental content in nucleus, cytoplasm + sarcoplasmic reticulum (SR), and mitochondria as determined by EPXMA. (Negative Na values have no biological significance, but do reflect statistical variations, and thus the need for long counting times for low-Na quantification.)

	n	mmol/kg dry wt						
		Na	Mg	P	S	Cl	K	Ca
		Control, 20 min						
Nucleus	6	136 ± 7	50 ± 5	373 ± 22	218 ± 8	106 ± 8	421 ± 23	5.0 ± 3.0
Cytoplasm+ SR	37	120 ± 14	64 ± 6	518 ± 26	223 ± 16	131 ± 19	923 ± 73	6.0 ± 2.0
Mitochondria	36	79 ± 9	42 ± 2	434 ± 15	228 ± 7	114 ± 14	698 ± 45	2.9 ± 1.0
		ONa, 20 min						
Nucleus	10	4 ± 14	62 ± 7	531 ± 41	337 ± 28	77 ± 11	568 ± 29	-1.9 ± 5.1
Cytoplasm + SR	10	-16 ± 15	76 ± 10	601 ± 52	386 ± 30	106 ± 18	646 ± 50	17.3 ± 6.8
Mitochondria	10	-8 ± 12	34 ± 7	341 ± 22	266 ± 20	35 ± 7	348 ± 24	7.2 ± 3.1

n = number of raster probes (500s) obtained from each region; values are mean ± S.E.M.

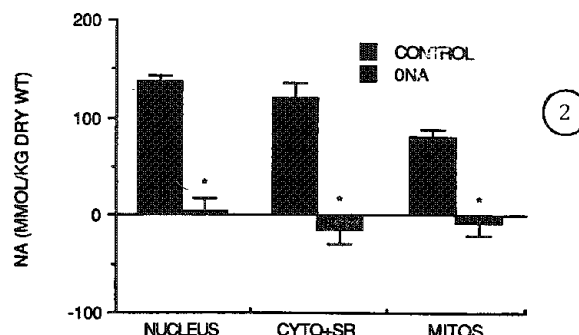
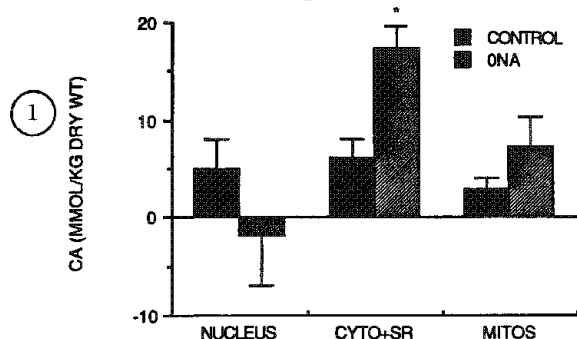


FIG. 1.--Sodium content ( $\pm$ SEM) in control and ONa-treated heart cells for nucleus, cytoplasm + sarcoplasmic reticulum, and mitochondria. Asterisk denotes values significantly different from control by Student's t-test ( $p < 0.001$ ).

FIG. 2.--Calcium content ( $\pm$ SEM) in control and ONa-treated heart cells for nucleus, cytoplasm + sarcoplasmic reticulum, and mitochondria. Asterisk denotes values significantly different from control by Student's t-test ( $p < 0.05$ ).

## QUANTITATIVE PROCEDURES FOR BULK FROZEN-HYDRATED BIOLOGICAL SAMPLES BASED ON $\phi(\rho z)$ CURVES

A. T. Marshall and R. J. Condrón

The quantitative analysis of frozen-hydrated bulk biological samples can be carried out by use of  $\phi(\rho z)$  curves and inorganic standards. The ionization function or  $\phi(\rho z)$  curve has been modeled by two sets of empirical equations.<sup>1,2</sup> More recently a Gaussian expression has been used.<sup>3,4</sup> The  $\phi(\rho z)$  curve models x-ray generation with depth in a solid target and provides a measure of the total generated and emitted x rays. The latter provides the atomic number and absorption corrections.

The  $\phi(\rho z)$  curve absorption correction for frozen-hydrated biological bulk samples has been described previously,<sup>5</sup> the full correction procedure is validated here. The method can also be used to obtain oxygen concentrations in frozen-hydrated samples which can then be used to estimate dry weight fractions.

### Experimental

It is assumed that the cell matrix is modeled reasonably well by a protein solution.<sup>5</sup> Mean values for absorption and atomic number corrections can be used for elements except Na and Mg over the usual biological concentration range, since the corrections vary little in a frozen-hydrated matrix with changes in protein and element concentration. The corrections for Na and Mg can be obtained from linear regressions of correction factors on protein concentrations. Oxygen concentrations can be converted to dry weight fractions in biological systems on the basis of the linear relationship between O and protein concentration in a protein solution.<sup>5</sup>

The accuracy of the procedure was assessed by analysis of organic and inorganic samples (sodium nitroprusside, sodium acetate, sodium citrate, sodium fumarate, sodium gluconate, potassium phosphate and potassium sulphate) and gelatine gels (12 and 16% w/v) containing Na, K, and Cl at 10, 100, and 110 mmol kg<sup>-1</sup> of solvent (water). Standards of NaCl, KCl, quartz, and ice were used. Samples were coated with 10nm Be and analyzed at 15 kV and 101 K.

Analytical results are shown in Tables 1 and 2. Considering the difficulties (absorption or loss of water and radiation damage) of formulating biological systems, there is a reasonable correspondence between measured and theoretical results.

### Conclusions

The absorption and atomic number corrections obtainable from empirically calculated  $\phi(\rho z)$  curves provide reasonably accurate quantitative analyses of biological models. An estimate of

the dry weight fraction of frozen-hydrated biological samples can be obtained from the O concentration. Recent examples of the application of this method are shown in Table 3.

### References

1. L. Parobek and J. D. Brown. "The atomic number and absorption corrections in electron microprobe analysis at low electron energies," *X-Ray Spectrom.* 7: 26-30, 1978.
2. J. D. Brown and W. H. Robinson, "Quantitative analysis by  $\phi(\rho z)$  curves," *Microbeam Analysis--1979*, 238-240.
3. R. H. Packwood and J. D. Brown, "A Gaussian expression to describe  $\phi(\rho z)$  curves for quantitative electron-probe microanalysis," *X-Ray Spectrom.* 10: 138-146, 1981.
4. G. F. Bastin et al., "An evaluation of the use of Gaussian  $\phi(\rho z)$  curves in quantitative electron probe microanalysis: A new optimization," *X-Ray Spectrom.* 13: 91-97, 1984.
5. A. T. Marshall, "Application of  $\phi(\rho z)$  curves and a windowless detector to the quantitative X-ray microanalysis of frozen-hydrated bulk biological specimens," *SEM/1982 I*, 243-260.

---

The authors are at the Analytical Electron Microscopy Laboratory, Department of Zoology, La Trobe University, Bundoora (Melbourne), Victoria 3083, Australia. ARGS support is acknowledged.

TABLE 1.--X-ray microanalysis of inorganic and organic salts.

Sample	Na, K g%		O g%	
	Theoret.	Measured	Theoret.	Measured
Na citrate	23.5	23.5±0.5	49.0	50.8±3.6
Na acetate	28.0	25.1±2.2	39.0	36.2±5.1
Na fumarate	28.7	28.4±0.5	45.4	41.9±2.2
K phosphate	28.7	27.6±0.1	47.0	49.5±1.2
K sulphate	44.9	42.5±0.4	36.7	44.3±1.2

Mean ± SD, n = 5

TABLE 2.--X-ray microanalysis of gelatine gels containing NaCl and KCl.

	Protein g%		Na		Cl		K	
			mmol/l					
Theoretical	12	16	10	10	110	110	100	100
Measured	13	16	8±11	13±16	114±5	113±2	99±5	100±6

Mean ± SD, n = 5

TABLE 3.--Biological applications of  $\phi(\rho z)$  curve corrections.

	Dry Wt. g%	Na	Cl	K	Mg	Ca
		mmol/l			mmol/kg	
Secretory tubule cells of duck salt gland	23	47	54	113	14	8
Secretory tubule cells of green sea turtle salt gland	15	43	71	146	15	9
Proximal tubule cells of chicken kidney	17	48	34	102	26	10



## IN VIVO AND IN VITRO ANALYSIS OF A POLYMER DRUG-DELIVERY SYSTEM

G. E. Visscher, R. L. Robison, and G. J. Argentieri

The use of sustained drug delivery systems has attracted considerable attention in recent years. Slow release mechanisms allow for the continuous administration of various medicinal agents.<sup>1</sup> Some forms of such devices include sheets, rods, pellets, and films that are surgically implanted.<sup>2</sup> Our recent research efforts have focused on the biodegradation of and tissue response to injectable microcapsules produced from various biodegradable polymers.<sup>3,4</sup>

### Experimental

The production of microcapsules from the copolymer 50:50 poly(DL-lactide-co-glycolide) (DL-PLGA) was by a phase separation process. In vivo and in vitro biodegradation of microcapsules was analyzed by scanning electron microscopy (SEM). Analysis of the tissue response to injected microcapsules was by light microscopic and transmission electron microscopic techniques. For in vitro analysis, microcapsules were placed in a pH 7.4 phosphate buffer and rotated at 37 C in a water bath; samples were removed at various time periods for SEM survey. Further in vitro analysis of microcapsules was performed by loss of molecular-weight data obtained by gel permeation chromatography (GPC).

### Results

Microscopic survey of injected microcapsules in muscle revealed an initial sharply localized acute myositis at the injection site, which gradually changed to a minimal foreign body giant cell and connective tissue response by day 20. By 60 days post injection only a small amount of mature connective tissue was evident in the area of injected microcapsules.

In vivo degradation of DL-PLGA microcapsules was first observed by SEM approximately 30 to 40 days post injection. An erosion and increased porosity of the internal matrix of the microcapsules was evident (Fig. 1). By 60 days post injection, microcapsules were extensively eroded and occupied by cells.

Correlation of GPC data with SEM of in vitro degradation of microcapsules has shown a close correlation. A structural deterioration consisting of increased porosity and internal erosion of microcapsules was seen over the first 20 days of treatment (Fig. 2). After day 20 only collapsed, porous pieces of microcapsules were seen. GPC data revealed a rapid decline in microcapsule molecular weight until day 20, followed by a gradual loss until the termination of the study.

### Conclusion

The tissue reaction we have observed in response to injected microcapsules was an initial mild, sharply localized inflammatory and foreign body giant cell tissue reaction which gradually evolved to a minimal connective tissue response. Microcapsules produced from the copolymer DL-PLGA are almost completely eroded and resolved by 60 days post injection. In vitro correlation of SEM and GPC data shows a simultaneous, rapid decline in microcapsule structure and molecular weight during the first 20 days of treatment, after which a gradual loss of molecular weight was seen.

### References

1. T. M. S. Chang, "Biodegradable semipermeable microcapsules containing enzymes, hormones, vaccines and other biologicals," *J. Bioengineering*, 1976, 25-32.
2. D. A. Wood, "Biodegradable drug delivery systems," *Intern. J. Pharmaceuticals*, 1980, 1-18.
3. G. E. Visscher et al., "Biodegradation of and tissue reaction to 50:50 poly (DL-lactide-co-glycolide) microcapsules," *J. Biomed. Materials Res.*, 1985, 349-365.
4. G. E. Visscher et al., "Note: Biodegradation of and tissue reaction to poly (DL-lactide) microcapsules," *ibid.*, 1986, 667-676.

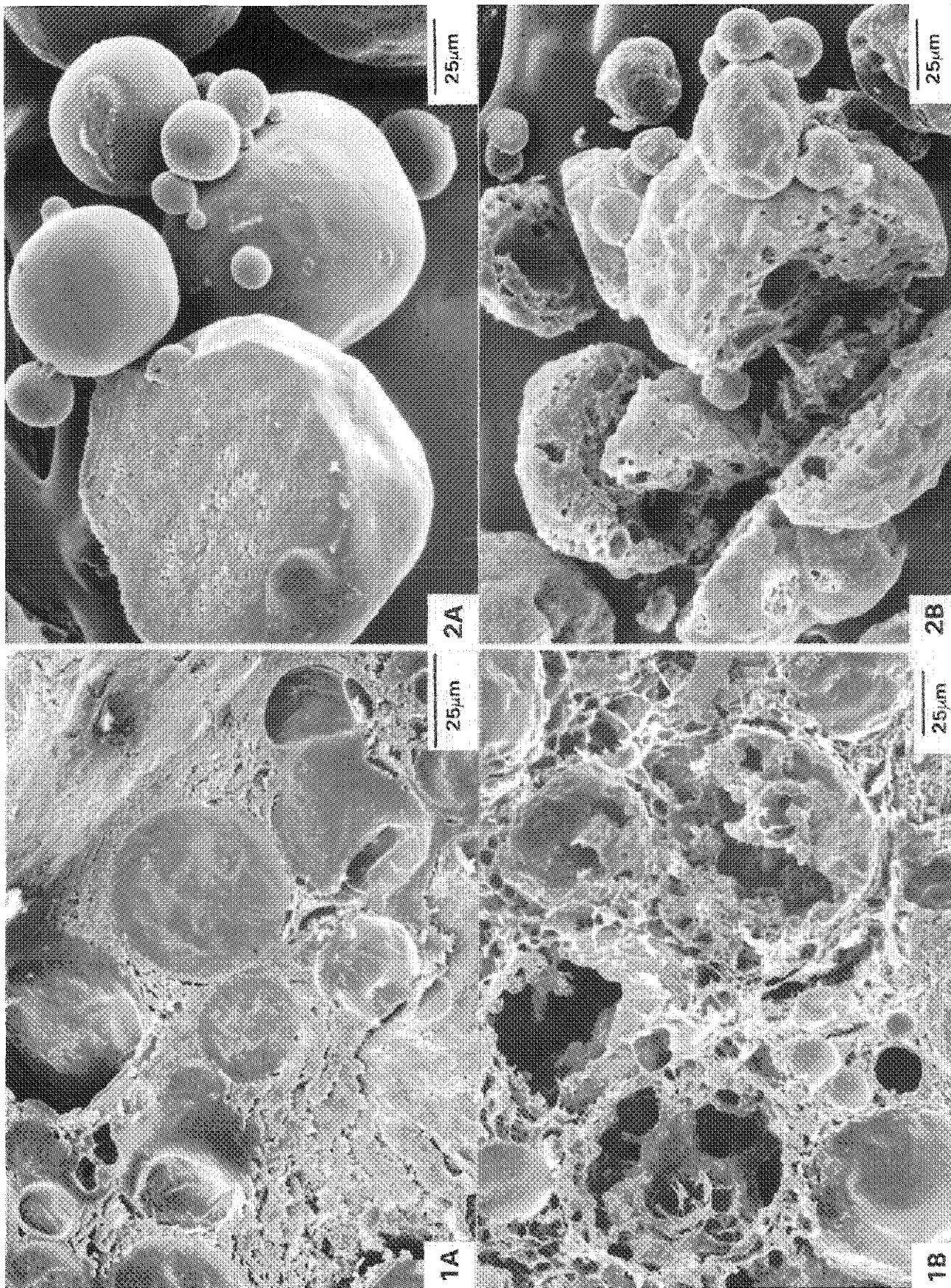


FIG. 1.--(A) Solid microcapsules 1 day after in vivo injection; (b) after 40 days, microcapsules are extensively eroded.

FIG. 2.--(A) Microcapsules appear relatively smooth with slight porosity of their internal matrix before in vitro treatment; (B) after 20 days of treatment microcapsules are eroded internally and porous on their external surface.

# REMOVAL OF PLURAL INELASTIC SCATTERING IN ELECTRON ENERGY LOSS SPECTRA FROM ORGANIC SAMPLES: A NEW APPROACH

R. D. Leapman and C. R. Swyt

A new method for removing plural inelastic scattering from energy loss core edge spectra has been developed for use with organic or biological samples. The method relies on fitting the measured core edge spectrum with a set of reference spectra. The first member of this set is the measured spectrum from a thin sample; the second is derived from the first by convolution with the low-loss spectrum and thus represents a core plus one valence electron excitation; the third is derived from the second by a further convolution with the low-loss spectrum, and so on. These references are fitted to the measured spectrum by means of a multiple linear least-squares algorithm similar to that used to fit x-ray peaks in quantitation of energy-dispersive x-ray spectra.<sup>1,2</sup> The method has several advantages over the conventional Fourier ratio or Fourier logarithmic deconvolution techniques. First, the low-loss spectrum need not be recorded for each spectrum that is processed. Second, the method does not assume uniform sample thickness within the analytical volume. Third, the procedure is very fast and mathematically well behaved.

## Method

The method that we describe here to solve the plural scattering problem is not intended to be generally applicable but is intended to be used in certain special, although important, situations. In particular, we are interested in removing plural scattering from core edge spectra occurring at a few hundred electron volts of energy loss in organic samples where the general shape of the single-scattering low-loss spectrum is well known. We are concerned with the spectrum above the carbon K edge at 284 eV that includes, for example, the potassium  $L_{23}$  edge at 294 eV, the calcium  $L_{23}$  edge at 346 eV, and the nitrogen K edge at 401 eV. Quantitation of these elements tends to be severely complicated by edge overlap and by plural scattering, which distorts the spectral shape and inhibits accurate background estimation.<sup>3</sup> A problem with conventional deconvolution procedures for removing plural scattering is the difficulty in measuring the low-loss and core-loss spectrum simultaneously. Even if such a measurement is possible, there is often some uncertainty about the linearity of the spectrum because of the high counting rates in the zero-loss peak. Furthermore, with the development of parallel detection systems, edges with much smaller peak/background ratios can now be detected<sup>4</sup> (e.g.,  $P/B < 0.001$ ), which involves a demand-

ing precision in the analysis. In fact, Shuman et al.<sup>5</sup> have already discussed the use of standard spectra to fit parallel recorded energy loss spectra. Here we extend this approach to deal with plural scattering.

Let us assume that the background intensity under the major core edge (i.e., carbon K) can be successfully subtracted over a limited energy range of, say, 100 or 200 eV shows threshold by means of the well-known inverse power law extrapolation.<sup>6</sup> This procedure leaves us with the core edge intensity  $I_X(E)$  for a group of elements consisting of carbon as a major component and several other elements as minor components. Since the cross section for these core excitations is very small compared with the total inelastic cross section  $I_X(E)$  is given to a good approximation by

$$I_X(E) = I(E) * S_X(E) \quad (1)$$

where  $I(E)$  is the entire energy loss spectrum including the zero-loss and low-loss (valence electron or plasmon excitation), and  $S_X(E)$  is the single-scattering core-edge distribution that is the quantity we wish to derive.<sup>7</sup>  $I(E)$  is given by the Poisson distribution for plural scattering and contains zero, single, double, etc. scattering events described by a sum of  $n$ -fold self-convolutions of the single scattering distribution  $S(E)$  weighted with constants  $k_n$ :

$$I(E) = k_0 \delta(E) + k_1 S(E) + k_2 S(E) * S(E) \dots \quad (2)$$

Therefore by combining Eqs. (1) and (2) we obtain

$$\begin{aligned} I_X(E) = & k_0 S_a(E) + k_1 S(E) * S_a(E) \\ & + k_2 S(E) * S_a(E) + \dots \\ & + F_b I(E) * S_b(E) + F_c I(E) * S_c(E) + \dots \quad (3) \end{aligned}$$

In the present method each of these terms represents a reference spectrum. Typically the first term can be obtained experimentally by measuring the core edge spectrum from a thin evaporated carbon film. The second term is computed by convolution of the first term with the measured low-loss spectrum (excluding the zero-loss peak) obtained from a very thin sample of similar composition as the unknown; a thin carbon film may suffice for this purpose. The third term is computed by convolution of the second term with the low-loss spectrum again. If necessary this procedure can be repeated to allow for higher-order scattering events. The last two terms in Eq. (3) correspond to other minor elements in the spectrum such as calcium and nitrogen.  $S_b(E)$  and  $S_c(E)$  represent the single scattering core edges for elements  $b$  and  $c$  and may be obtained experimentally by recording of spectra from thin layers of pure compounds such as a calcium salt. In practice, because the carbon K edge is the dominant feature in the spectrum, we can first derive a reasonable

The authors are with the Biomedical Engineering and Instrumentation Branch, DRS, National Institutes of Health, Bethesda, MD 20892.

estimate of the coefficients  $k_n$  by fitting just the carbon K edge terms. When these coefficients have been determined, we have an estimate for  $I(E)$  in Eq. (1). Thus the plural scattering that occurs at the weak core edges of the minor elements is constrained by the plural scattering observed at the strong carbon edge. Therefore, when the fitting procedure is reapplied to the original data, only one extra coefficient is required for each minor element that is believed to be present; these coefficients are denoted by  $F_b$  and  $F_c$  in Eq. (3). If necessary the fitting procedure can be iterated to refine further the coefficients  $k_n$  and to regenerate the reference spectra for the minor elements.

The single-scattering core edge spectra must be acquired with good counting statistics in order to insure a satisfactory fit to the raw data. The derived reference spectra are fitted by means of a multiple linear least-squares algorithm incorporated into a FORTRAN program. It does not matter if the 'single-scattering' core edge reference spectrum contains a small double-scattering contribution; that will affect the coefficients  $k_n$  but should still provide a satisfactory fit.

## Results

Electron energy loss spectra were collected at 100keV beam energy with a Gatan model 607 EELS spectrometer mounted below the camera chamber of a Hitachi H700H analytical electron microscope operated in the TEM mode. Spectra were acquired with a Kevex 7000 multichannel analyzer and were transferred into a Digital Equipment Corporation PDP 11-60 computer for processing.

To illustrate the application of the least-square/plural-scattering method to a biological sample we consider the spectrum from a thin section of immature mineralizing tooth enamel (Fig. 1). The area analyzed was approximately 1  $\mu$ m in diameter and contained protein matrix, embedding plastic and enamel crystallites. A reference spectrum was recorded from a carbon film with thickness  $t = 0.38 \lambda_1$ , as estimated from the low-loss region,<sup>8</sup> where  $\lambda_1$  is the total inelastic mean free path ( $\lambda_1 \sim 50$  nm at 100keV beam energy). The solidline in Fig. 2 is this 'zero-plasmon' C K reference spectrum after background subtraction; the dashed lines are obtained by successive convolution with the low-loss (plasmon) spectrum and represent the other carbon reference spectra that are needed to take account of plural scattering. The 'zero-plasmon' reference spectrum for the calcium  $L_{23}$  edge was recorded from a thin layer of calcium chloride deposited on a carbon film ( $t/\lambda_1 = 0.35$ ) and is shown in Fig. 3 after background subtraction. Figure 4 shows the result of fitting the reference spectra in Figs. 2 and 3 to the data in Fig. 1. Although there is significant plural scattering ( $t/\lambda_1 > 1$ ), the fit is satisfactory. Discrepancies at 285 eV and from 300 to 325 eV may be due to (i) small differences in near-edge fine structure between the reference and the unknown, (ii) the neglect of the potassium  $L_{23}$  edge that may be present, (iii) possible errors in removing the unscattered/elastic peak from the

low-loss spectrum, and (iv) error introduced by failure to use the exact single-scattering distribution as reference spectra.

## Discussion and Conclusions

Let us consider the advantages of the method described here. It removes plural inelastic scattering from some important core edges found in organic and biological samples. At the same time the method yields the background under each edge and a quantitative measure of the integrated core edge signal. Unlike the conventional Fourier deconvolution techniques, the method does not assume constant sample thickness within the analytical volume and therefore is applicable to a wider range of samples. That is so because the measured core edge spectrum must always have the same form as the scattering terms in Eq. (3) regardless of thickness variations. However, the coefficients need not be uniquely related to each other by the Poisson distribution as they are when the thickness is uniform. In our experience,<sup>9</sup> Fourier methods can sometimes fail drastically because of sample nonuniformity. Another advantage is that the low-loss spectrum  $I(E)$  need not be measured for each spectrum to be processed; instead  $I(E)$  is itself determined from the core edge spectrum alone. The fitting procedure can be applied to a limited range of energy losses provided the reference spectra have been generated over that range. On the other hand, Fourier deconvolution methods require an extended range of energy losses for the data to be analyzed, otherwise truncation effects tend to arise. The multiple linear least-squares procedure can be computed very rapidly (typically in 1 s), whereas the Fourier methods take longer (typically 10 s) on our computer.

Despite these significant advantages, the least-squares fitting procedure does depend on certain assumptions, which we shall now examine. It has been assumed that the core edge spectra from the reference samples and from the unknown are identical. In fact, small differences are likely to occur due to differences in chemical bonding that are evident as changes in near-edge and extended fine structure.<sup>10</sup> Such differences may sometimes present a problem, but spectra from biological samples often exhibit similar C, N, and O edges, at least at a resolution of 2 eV and at the radiation doses commonly used for analytical electron microscopy. Similarly, K and Ca have quite constant  $L_{23}$  edge shapes in biological samples. It has also been assumed that we know the shape of the low-loss spectrum  $S(E)$ ; small variations in this region of the spectrum may create small errors in generating the plural scattering terms in Eq. (3). Nevertheless, the low-loss spectra from a range of different biological samples are experimentally similar, at least at high dose. Care must be taken to align the energy scales of the reference spectra and the unknown spectrum. A fraction of an eV error here may result in a large carbon residual superimposed on a minor edge like calcium when the degree of fit is tested. However, it may be possible to correct for small shifts in energy loss calibration or energy resolution by

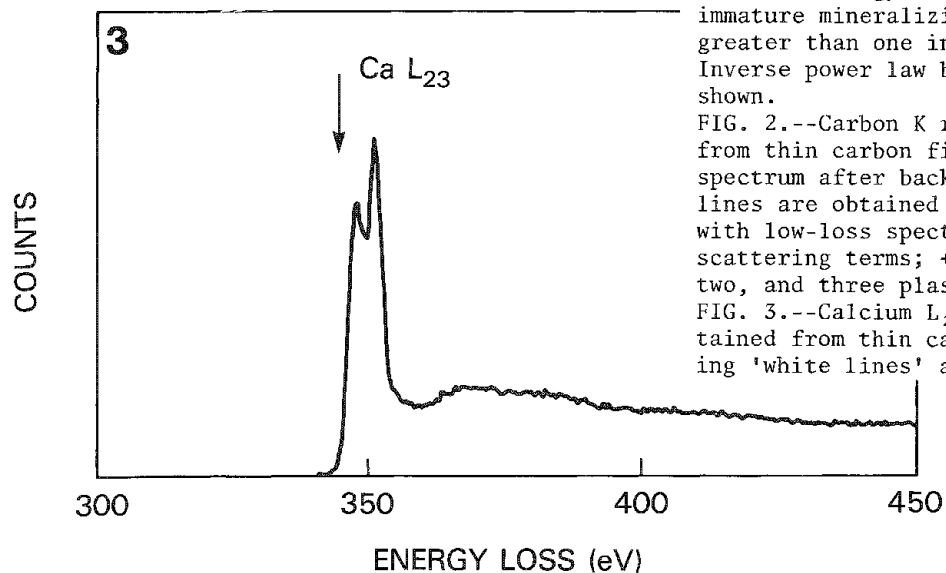
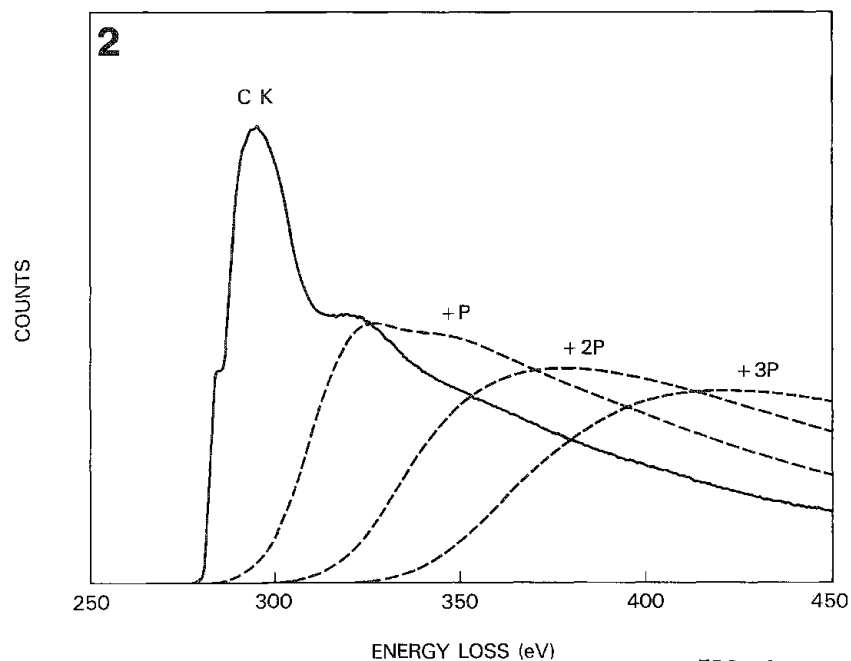
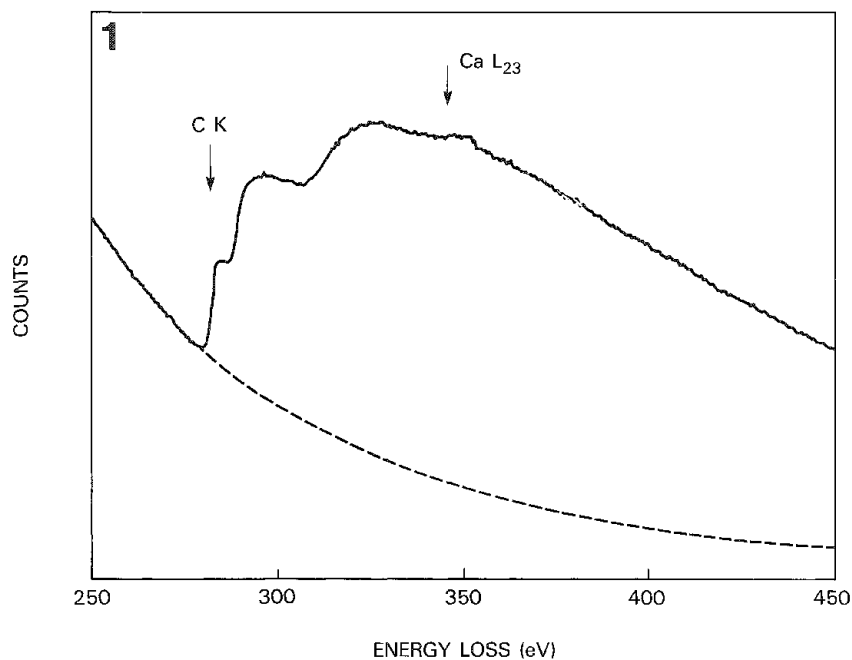


FIG. 1.--Energy loss spectrum from sample of immature mineralizing enamel with thickness greater than one inelastic mean free path. Inverse power law background extrapolation is shown.

FIG. 2.--Carbon K reference spectra obtained from thin carbon film. Solid line is raw spectrum after background subtraction. Dashed lines are obtained by successive convolutions with low-loss spectrum and represent plural scattering terms; +P, +2P, +3P refer to one, two, and three plasmons, respectively.

FIG. 3.--Calcium  $L_{23}$  reference spectrum obtained from thin calcium chloride sample showing 'white lines' at threshold.

following the approach of Kitazawa et al.,<sup>11</sup> which was developed for x-ray spectra; in the case of EELS this method would involve adding the first and second derivatives of the carbon reference spectrum. Care must also be taken to measure the reference spectra and the unknown spectrum under the same electron optical conditions. For example, changes in collection angle alter the spectral shape and such differences cannot be accommodated in the fitting procedure.

Finally, we mention that the core edge fitting procedure described here may be useful for applying 'EELS Atlas' data<sup>12</sup> to quantitative microanalysis. It could eventually permit this type of digitally stored database to be treated as reference spectra, since plural scattering is taken into account.

#### References

1. H. Shuman, A. V. Somlyo, and A. P. Somlyo, "Quantitative electron probe microanalysis of biological thin sections: Methods and validity," *Ultramicroscopy* 1: 317-339, 1976.
2. F. H. Schamber, "A new technique for deconvolution of complex x-ray spectra," in *Proc. 8th Nat. Conf. Electron Probe Analysis*, 1973, 85A-C.
3. R. D. Leapman and R. L. Ornberg, "Quantitative electron energy loss spectroscopy in biology," *Ultramicroscopy* (in press).
4. H. Shuman and P. Kruit, "Quantitative

data processing of parallel recorded electron energy loss spectra with low signal to background," *Rev. Sci. Instr.* 56: 231-239, 1985.

5. H. Shuman, P. Kruit, and A. P. Somlyo, "Quantitative electron energy loss spectroscopy of low concentrations of calcium in carbon containing matrices," *Microbeam Analysis--1983*, 247-251.

6. R. F. Egerton, "Inelastic scattering of 80 keV electrons in amorphous carbon," *Phil. Mag.* 31: 199-215, 1975.

7. R. D. Leapman and C. R. Swyt, "Electron energy loss spectroscopy under conditions of plural scattering," *Analytical Electron Microscopy--1981*, 164-172.

8. R. D. Leapman, C. E. Fiori, and C. R. Swyt, "Mass thickness determination by electron energy loss for quantitative x-ray microanalysis in biology," *J. Microsc.* 133: 239-253, 1984.

9. C. R. Swyt and R. D. Leapman, "Removal of plural scattering in EELS: Practical considerations," *Microbeam Analysis--1984*, 45-48.

10. R. F. Egerton, in *Electron Energy Loss Spectroscopy in the Electron Microscopy*, New York: Plenum Press, 1986.

11. T. Kitazawa, H. Shuman, and A. P. Somlyo, "Quantitative electron probe analysis: Problems and solutions," *Ultramicroscopy* 11: 251-262, 1983.

12. C. C. Ahn and O. L. Krivanek, *EELS Atlas*, ASU Center for Solid State Science, Tempe, Ariz., and Gatan Inc., Warrendale, Pa.

#### NOTE ADDED IN PROOF

After this paper was submitted for publication, an article by H. Shuman and A. P. Somlyo that uses a similar approach appeared in *Ultramicroscopy* 21: 23-32, 1987, entitled "Electron energy loss analysis of near-trace-element concentrations of calcium."

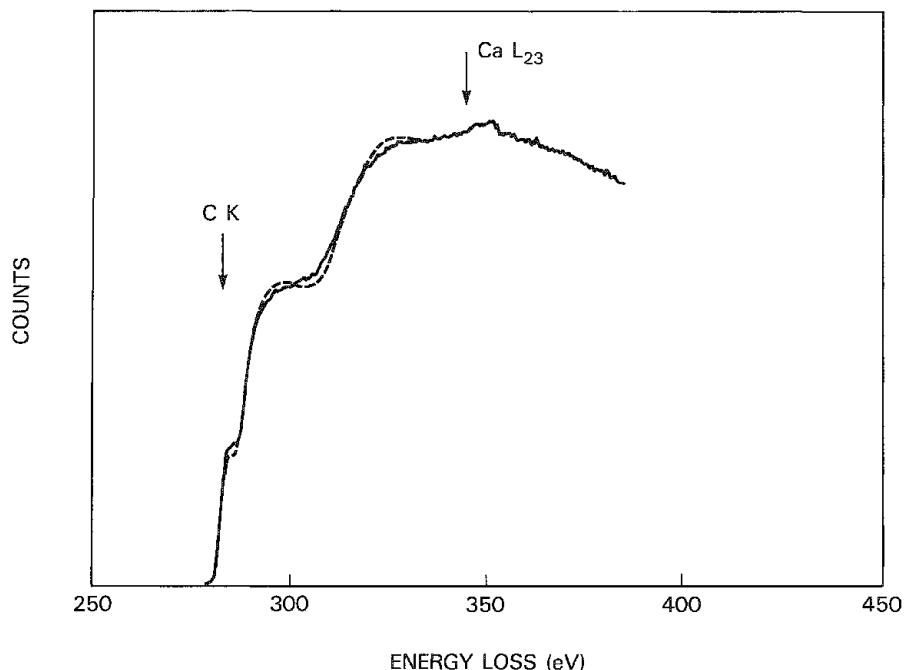


FIG. 4.--Comparison between core edges from immature mineralizing enamel from Fig. 1 (solid line), and sum of fitted reference spectra from Figs. 2 and 3 (dashed line). Agreement is good, especially in region of  $\text{Ca L}_{23}$  edge.



## 7. Computer-aided Imaging and Simulation

### TEACHING COMPUTERS TO SEE

J. Christian Russ and John C. Russ

#### *"Conventional" Image Analysis*

Computer image analysis is the process of extracting useful information, usually in the form of a small number of measurement parameters, from one or more digitized two-dimensional images. The development of the hardware to acquire these images from raster-scan sources such as video cameras and scanning electron microscopes has flourished in the past few years. The development of the software needed to process, discriminate, measure, and interpret the images is still very much in progress.

It will help to define a few terms. Image processing is a collection of techniques that begin with a two-dimensional image, as an array of pixels in which each has a brightness and perhaps color or other information. The processing may either take place in the spatial domain in which pixels are compared to or combined with neighbors, or in the frequency domain (e.g., Fourier space) in which the variations between pixel values as a function of their spacing are used. In either case, after the process is complete, the result is again an image.<sup>1,2</sup> In most cases, the location of pixels in the final image is identical to that in the original, but the values are altered to emphasize some particular aspect of the signal at the expense of other information originally present.

A simple example is a high-pass filter that suppresses gradual changes in brightness while amplifying local contrast (edges, etc.). This process can be achieved in the frequency domain by aperturing, or in the spatial domain by a Laplacian operator that replaces each pixel with the difference between it and its neighbors. Another class of image processing operations involves geometrical transformations such as stretching and rotation, and is most often used to remove projection distortion from spacecraft images of the curved surfaces of planets.<sup>3</sup>

Image discrimination is the reduction of a gray-scale image in which each pixel has a brightness value (which may be simply image brightness or may have been altered by prior image processing steps) to one in which each pixel is either "on" or "off" depending on whether it is or is not part of the features in the image that are of interest. In its simplest mode, discrimination consists of selecting a range of brightnesses that correspond to the phase, objects, etc. to be studied. With appropriate processing, the pixel brightness can be made proportional to other properties of the original image, such as tex-

ture.<sup>4</sup> Manual setting of discriminators with the human eye used as a judge of correctness can be replaced with various algorithms that give improved consistency and accuracy.<sup>5</sup>

The more general term for this reduction from the gray-scale image to a binary representation of objects is "segmentation" and there are ways to accomplish it other than simple discrimination. For instance, it is possible to locate and then follow an edge or to start with arbitrary points within objects in the image and then expand them by comparing each neighbor point and deciding whether it should or should not be made part of the object.<sup>6</sup> These methods are much slower than discrimination, and equivalent results can be obtained with appropriate image processing beforehand to produce derived gray-scale images in which the pixel values describe some neighbor property.

The discriminated or "binary" image may be further edited by the performance of logical combinations (and, or, not, etc.) of several such images of the same area, obtained by the use of different discriminator settings or differently processed gray images, to select specific objects. There is also a powerful class of operations that smooth outlines, separate touching features, determine the skeletons of objects, and perform certain types of counting and measurements based on the patterns of neighbors present around each pixel.<sup>7,8</sup>

Once discrimination has been performed, each object in the image is defined as a contiguous group of pixels. Depending on whether the image is a planar cut through a structure, a projected image through a slice of finite thickness, or some other known configuration, it is possible to relate the dimensions of objects seen in the image to their three-dimensional nature, by use of the principles of stereology.<sup>9</sup> The measurement parameters that can be obtained fall into four classes.

a. measures of size, such as area, perimeter, length, breadth, etc., and the derived three-dimensional estimates such as volume, surface area, equivalent spherical diameter, etc.;

b. measures of shape, such as the number of internal voids, the fractal dimension of the outline, and a variety of dimensionless shape descriptors such as aspect ratio (length/breadth), formfactor ( $4\pi\text{Area}/\text{perimeter}^2$ ), convexity (convex perimeter/perimeter), solidity (area/convex area), etc.;

c. measures of location and orientation, such as the coordinates of the centroid of the object, the angle of its line of minimum moment or longest chord, and derived parameters such as the nearest neighbor distance; and

d. measures of brightness, such as the mean brightness of pixels in the original image (related to object density), and the contrast and texture that describe variations of brightness

---

Author J. Christian Russ is at the University of Michigan, Ann Arbor; author John C. Russ is with the Materials Science and Engineering Department, North Carolina State University, Box 7916, Raleigh, NC 27695.



within the object.<sup>10,11</sup>

In most typical computer-based image analyzers, some 20-30 such parameters are readily determined for all the objects in a discriminated image. They may then be studied by use of various statistical analysis routines to plot distribution histograms, search for correlations, compare to preset acceptance criteria, and so forth.

Although these data are often useful in research and quality control situations, they do not represent all the information present in the image, and the procedures used by computer-based systems to obtain them are quite different from the methods that the human visual system employs to extract meaning from images. In order to extend the computer-based equipment to have a deeper level of scene understanding (for instance, as employed in robotic vision), or to deal with three-dimensional images (either in the form of a series of 2-D "slices" as encountered in serial section microscopy, or in the form of a stereo pair of images whose parallax gives depth information), or to be able to learn to recognize objects in context (which falls within the broad range of "artificial intelligence" and may more narrowly result in the image computer operating as an expert system), a better understanding of how humans accomplish these same tasks seems important.

#### *The Human Visual System*

It may not always be practical or necessary to duplicate the methods used in the human visual system, which depend to an extreme degree on the "hardware" organization of our neurons, but rather to emulate them in the software. A typical modern image-analysis computer system, whether a dedicated microcomputer<sup>12</sup> or minicomputer, or a task sharing the resources of a mainframe, has a computational capacity of perhaps 1-5 MIPS (million instructions per second) with megabytes of storage. (One should not confound MIPS with MFLOPS, which are millions of floating point instructions per second; without special hardware coprocessors one gets much fewer MFLOPS, but most image analysis deals with integer values, and often with single bytes, so that MIPS is a more relevant measure of performance.) Images fundamentally eat up storage quickly, so that the gigabytes offered by optical disk technology may be highly appropriate. The operations that will be described below would require of the order of 100 MIPS to achieve results in times that could be considered "interactive" (still well short of "real time"). At these speeds, conventional computers reach limits based on the speed of electrons in circuits.

Yet the human neural system is very slow, with signal propagation rates measured in feet per second. How then does the eye/brain combination perform its amazing feats of image interpretation so quickly? The answer lies primarily in the distributed nature of the computation. Within the image sensor itself (the retina) there are wiring patterns among the neurons (Fig. 1) that select particular image features so that much less raw data need to be transmitted to higher levels of inter-

pretation. This feature is particularly important considering that the human eye contains more than 150 million receptors, whereas many computer-based image analyzers employ only 250 000 pixels. Also, the visual system may devote as many as a quarter-million cells, each capable of proportional logic response (by varying the rate of pulses produced) to various combinations of other cell outputs, and all operating at once, for each local feature in the image.

At each higher level of processing, there is a further synthesis and "data reduction" until only a few "important" parameters are passed up to the conscious or interpretive level. Evolution has taught us which parameters are important (especially edges and corners, and anything that moves, especially if it moves toward us!). Many of these interconnections specifically employ the time delays in the neural connections to select particular pieces of higher-order information from the various lower level information, and for "memory".<sup>13</sup>

Similarly, for object recognition the brain proceeds in parallel. Rather than measuring objects in our visual field and comparing the dimensions to a sequential list of everything we have ever seen, we find that we can recognize Aunt Hazel's face almost immediately, even if most of the cues that we would consciously select are obscured, or if encountered in a situation where we would not expect to meet her. The simplest explanation is that we have trained an "Aunt Hazel" detector (among many others) that constantly scans all parts of each image to find something to match, and reports to conscious levels if matching occurs.

It is worthwhile to develop simulations of these processes for several reasons. One, of course, is better understanding of the visual system itself. A second is to develop computer hardware and programming techniques that can achieve some of the "massively parallel" efficiencies. The third is to develop image-analysis algorithms that work and that will become practical to implement as computer power increases. That will certainly continue to happen; the only question is how soon we shall have affordable and practical access to 100 MIPS computers with gigabytes of storage on our desks, in our pocket calculators, and (one suspects) in our digital watches.

#### *Simulating the Human Visual System with a Computer*

The four specific goals we have been pursuing are:

1. To develop an object recognition system that can be easily "trained" with a small number of objects of each of several classes, will automatically select those parameters which distinguish the classes, and will then be able to select those objects from complex fields of different objects. This expert system also continues to learn from each successful identification, so that even if the training objects are not identical to (or an unbiased sample of) the objects in context, a continuous and gradual refinement of the system's

knowledge will take place.

2. To develop methods to deal with stereo pairs. The first step is to provide an automatic detection of the "important" features in each pair of images, and then to fuse them so their parallax can be determined. This process produces an array of points (X, Y, Z coordinates) that describe a surface or some internal objects within a transparent section. The second step is then to interpolate the rest of the surfaces, and to refine and simplify this description until the surface or objects can be characterized and measured.

3. To deal with a three-dimensional stack of discrete images. Most often these images will consist of planes of focus achieved by sequentially polishing or cutting a surface; or focusing light, electrons, or sound waves at various depths in a body. The methods are equally applicable to stacks in which the different planes are different elemental x-ray maps, different energies of electrons or colors of light, or a time sequence of images of the same surface or scene.

4. To understand the mechanics of optical illusion, in which the image processing and feature extraction tools of the human visual system misfire and produce an incorrect qualitative or quantitative result. By duplicating these errors with computer algorithms, we can hope to discover the algorithms that mimic the human visual system in its more successful operations as well, and find efficient and powerful tools to extract useful information.

In order to perform these types of operations in a reasonable length of time, and with a minimal investment in equipment, we use some unconventional computer systems. The typical CPU-Memory-I/O architecture suffers from a severe bottleneck when all information must pass, one byte or word at a time, through the same communication bus and the same CPU. Array processors, often used with two-dimensional images, can offload a portion of the computation from the main CPU, but they suffer from many limitations (inflexible programming, difficulty in dealing with three- or higher-dimensional arrays, requirements for vast amounts of intermediate storage).

A more promising approach is available in the Processor Array or Cosmic Cube type of architectures, with a large number of identical, individually rather simple processors, each with a modest amount of memory and their own, often identical programs. Each processor is given a portion of the image or other processors working on neighboring regions, and higher-order dimensions are readily implemented by the nature of the interconnects. The processor array, which we are using, retains a slightly greater degree of flexibility at the expense of speed. Each slave computer is connected to a single master processor, which allocates the tasks, monitors the progress of each slave, and acts as a mailman to pass data between regions.

### *Object Recognition*

We are forced to make the initial assumption that the parameters which we can measure on objects in the image(s) available include

parameters that can distinguish the objects into various classes. There may be some measurement parameters available to the human visual system that are not covered by the list of parameters we can measure, but evidence suggests that the reverse is more likely to be true: that the list includes parameters which the human visual system has decided to ignore (because they are rarely useful) and that people actually use only a rather small number of "wired-in" parameters to characterize objects.

A brute-force approach to classification would simply require measuring a large number of objects in each of several known classes, for all the available measurement parameters. These measurements then allow frequency plots (probability distribution functions or "pdf's") to be made for each class of object, for each parameter (Fig. 2). Subsequent measurements on "unknown" objects can be compared to each of these distributions, and a probability assigned to the likelihood that the unknown is a member of the standardized population of each class.

This procedure would be quite straightforward if the various pdf's were Gaussian or Poisson curves, which can be simply parametrized by mean and standard deviation. Unfortunately, this situation is only rarely encountered, and well-known statistical tests such as analysis of variance are of little use. Consequently, the entire pdf must be saved, usually in the form of a frequency histogram.

The pdf's constitute an *a priori* knowledge of the objects. If the measurement on the unknown is simply compared to the various classes, we may be able to decide to which one it belongs. Bayesian estimation carries this process one step further, by allowing us to combine the *a priori* probabilities of class membership and the current measurement, to compute for each class the probability that the new data point belongs to the class. This is an *a posteriori* method known as a maximum likelihood classifier, and it can be shown that it minimizes the risk of misclassification of an object.

One difficulty with the method as described is that it operates in an  $n$ -dimensional space of very high order (the number of measured parameters), and not all  $n$  are truly orthogonal. For instance, some of the shape descriptors such as aspect ratio or formfactor are powerful classification tools, but they depend on other parameters (length, breadth, area, etc.) that are also used. There may also be other correlations between parameters, such as some measure of size and density. These correlations present mathematical problems in dealing with the matrices of data. The pairwise covariance of each set of measurement parameters can be calculated for each class of objects; if the magnitude is high, one or the other can be eliminated. This procedure also reduces the dimensionality of the  $n$ -space, which is helpful.

Besides parameters that may be highly correlated with others, we would also like to eliminate any that do not contribute significantly to distinguishing the classes. Experience suggests that in each context, only a few parameters are important. They may involve

shape, size, density, or some combination of these discrete measurements. Of course, in another context entirely different parameters may be important so that we cannot decide beforehand what not to measure. But we can look at the data from a representative number of objects in two (or more) classes to determine whether each of the  $n$  variables can be eliminated. If the frequency distributions for each class were normal, an analysis of a variance test could be used to determine the probability that the classes were different in the selected parameter. However, few real pdf's are Gaussian.

Instead, a Wilcoxon or similar test can sometimes be employed. This test is sensitive to the rank order of objects, and can be visualized as a deck of cards marked with the value of some parameter (e.g., length) and sorted into order. In addition, the cards are colored red or blue depending on whether the object is of Class A or B. The binomial theorem gives the probability that a particular sequence of red and blue cards will arise from random shuffling of cards, and hence allows us to estimate whether the two classes are distinct or not. Parameters that do not show a significant (usually 90 or 95%) probability of being different by this test are discarded, and the original  $n$  dimensions are reduced to  $m$  important parameters. Generally,  $m$  is much less than  $n$ .

Within the final  $m$ -space plot of points from each measured object in the training suite, there are clusters of points corresponding to each class. We can now define a pseudo-parameter, a linear combination of the measured, quasi-orthogonal measurements that gives the maximum separation between each pair of classes. Figure 3 shows how this pseudo-parameter can be visualized as a rotated axis that passes parallel to the line connecting the centers of the clusters.<sup>3</sup> Projection of each point (object parameters) onto the line produces new pdf's that have the maximum separation between the classes.

The line can be determined if we find the direction that maximizes the moment of the point distribution. This line, or pseudo-variable, then defines the context in which these classes of objects will be discriminated. All that is required is to measure the  $m$  parameters for an unknown object, calculate a linear combination of the values using the direction cosines of the context line, and compare the value to a decision threshold taken as the minimum point separating the two normalized class pdf's. Normalization is necessary if the classes have different numbers of objects used in the training operation.

This training is established by measuring tens or hundreds of representative objects. It is not necessary for the human to specify what the important parameters for distinguishing classes are, or even to know how he or she actually recognizes them as distinct. This point is a potentially very important one, and is one of the criteria by which the system can now be referred to as a self-learning expert system. The heuristic for learning is built in, and the system extracts the important information from that supplied by the operator.

Because in many situations, even skilled operators may use subtle or unconscious cues to recognize objects, which may not always be evident in individual images, the performance of this recognition system often exceeds that of the operator who trained it.

This system for object classification is also capable of continuing to learn. This feature may be important if the training objects were not exactly representative of the populations actually encountered in context. Once the context itself (the linear pseudo-variable axis) has been established, and the pdf's of the classes been established, subsequent measurements that are classified in one class or the other can be added to the respective pdf's to update them continuously. This approach in effect adapts the original knowledge of the classes, obtained from the training objects, to the real unknown samples. It is related to the Bayesian *a posteriori* approach, using all knowledge available up to the time of measurement.

The potential problems with this approach are basically ones of nonlinearity. Two kinds of nonlinearity can develop, and either can be overcome mathematically, given enough data. As mentioned, the measurement parameters may not be entirely orthogonal, which means that the context line may not be linear in  $m$ -space. In principle, it is not necessary to restrict the fitting of the context line to be a linear combination of the individual measurement parameters, but other regression equations (polynomial, logarithmic, etc.) cannot generally be chosen beforehand as being preferred. Nonlinear regression methods are available that can evaluate these functions if enough data points (the number of objects in the training set) are available and the proper point weighting is used. Although time consuming, this is still a one-time operation that forms part of the initial training, and once the context line is established the classification of unknowns is not affected.

It is also possible that the difference between the training objects and the real ones is great enough so that the decision point along the context line may move significantly. If that happens, it would be preferable to recompute the pdf's with different, perhaps nonlinear histogram spacing. That can be done periodically during measurement of unknowns, but only if the actual values for each measured object are saved, rather than just being added to the pdf for its class. This method is perhaps best implemented at present in conjunction with the ability of the operator to overrule an object classification made by the computer, which would then signal the need to replot and renormalize the pdf's on the basis of all stored information to date.

It is instructive to compare this method to a very simple classification scheme sometimes employed for the identification of metal alloys based on their chemical composition, which is also multidimensional based on the number of elements present. Each alloy composition has a finite permitted range (known *a priori*), which occupies a polygonal volume in space. Each unknown analysis represents a point in space, which is expanded into an ellipsoid

whose axes are defined by the expected measurement accuracy. Identification is achieved if the ellipsoid intersects a polygon. If not, then the vector distance to the nearest polygon identifies the "most similar" alloy. This method does not work well for our problem of object classification because the class regions are not well defined, either in terms of shape or of having a sharp boundary. Also, the various axes are not of equal or linear importance.

### *Stereoscopy, Fusion, and Simplification*

Most humans can perceive depth information in stereo pair images, but not all: there are people (with two eyes) who cannot fuse stereo images, just as there are colorblind individuals. It is also common to overestimate the extent to which we use stereoscopy in everyday life; most judgments of distance are based on relative size, brightness, or precedence (one object partially obscuring another). A number of optical illusions take advantage of these cues to trick the human observer into mistaking object distance or size. Nonetheless, stereoscopy is a powerful tool that can be used to determine the three-dimensional location of surfaces or internal features in a transparent medium.

When we "look at" a stereo pair, the process by which we achieve "fusion" of the two images in our mind is complex and only partially understood. Key points are located on one or both images in some kind of order based on their significance in the individual images (i.e., corners, edges, and other points of interest are chosen). They are then compared between the images, based both on their neighborhood (relationship to other cues in the images) and their parallax (points are rejected for fusion if they lead to a bizarre interpretation of the viewed surface).

Given a pair of images, we can mimic the visual system's method for choosing interesting features by using image processing. Various derivatives of the original gray-scale image can be obtained by use of a Laplacian operator, or the maxima or other combinations of directional derivatives. These derivatives emphasize to varying degrees the edges, points, lines, and line ends in the image. Their X-Y position in the images can be noted, and it is these features one must then compare to figure out how to pair them up.

There is a practical limit to how many points can be extracted from a pair of photos. Tests with random-dot stereograms (apparently random arrays of dots which the human visual system readily fuses into a single image) suggest that a few thousand points are enough to represent a rather complex surface.<sup>14</sup> That is probably more points than can easily be found in a typical  $512 \times 512$  pixel gray image, especially if the interesting points are not uniformly spaced. If an "interesting feature" is defined as a group of a minimum of 9 pixels (a central pixel and its neighbors), which needs to be separated from other interesting features by a similar dimension to its width (which amounts to surrounding the central nine pixels with another 72 pixels), then the total

number of regularly spaced interesting points possible would be about 3000. In real images where regions devoid of interesting points are present, finding 500 such points may be a realistic goal.

The points can be found by use of either of the pair of images, since points present in only one will not be useful. The image can be processed to produce a derived image in which the pixel brightness value corresponds to how interesting it is, and then thresholding can be used to locate the desired number of points, rejecting less interesting ones that are too close to interesting ones. The list of X-Y coordinates is obtained at the same time.

To match the points from the first image to the second image, and thereby achieve "fusion" in the computer's understanding of the images, we use the local texture in the original image. The difference in brightness between the central pixel and its neighbors is compared, point by point, to pixels in the second image. This technique is called crosscorrelation, and one carries it out by multiplying together the values for each pixel (in this case, the difference between its brightness and the central pixel) in the pair of images, and adding the total up over the local neighborhood.<sup>15</sup> When the points match, the crosscorrelation sum is very high, whereas otherwise it is not. The location of the pixel whose sum produced a maximum in the second image gives the parallax for the point, and its elevation is then readily calculated.

In most cases, the crosscorrelation can be carried out over a rather restricted range of the second image. In a valid stereo pair, the parallax is mostly lateral (corresponding image points are displayed normal to the tilt axis, which is the perpendicular bisector of the line between the two eyepoints). Further, there is a maximum amount of displacement that can be tolerated, depending on the maximum amount of relief that can be expected, and on the limitations in the visual system for imaging objects with too great a disparity. This restriction usually means that the search needs to be carried out over only 1% or less of the total image area, in a stripe of narrow height and finite width. Even greater efficiency is possible if the crosscorrelation is performed only against a similar list of interesting points found in the second image.

The use of brightness differences in the crosscorrelation relaxes the dependence on image illumination, which mimics the human visual system's ability to compensate for great changes or unevenness in lighting. That is especially important in SEM images obtained by tilting the specimen, because doing so usually also changes the image brightness and contrast.

Parallax calculations yield the spatial X, Y, Z coordinates of each of the matched points, which then define the surface. To reconstruct the entire surface from these points, interpolating between them, we can construct a Voronoi tessellation of triangles using the irregularly distributed points as vertices. Each triangular facet represents a portion of the surface which we assume to be planar. This is not a bad assumption, because if the surface were locally irregular, it should have produced an

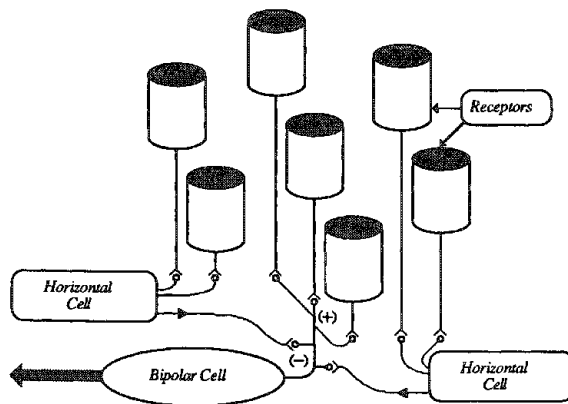


FIG. 1.--Simple line detector formed by lateral inhibition between neighboring receptors.

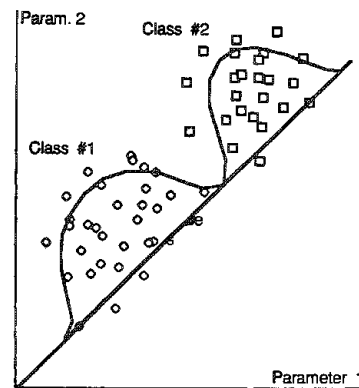


FIG. 3.--Rotation of pseudo-variable axis in two dimensions, with resulting pdf's.

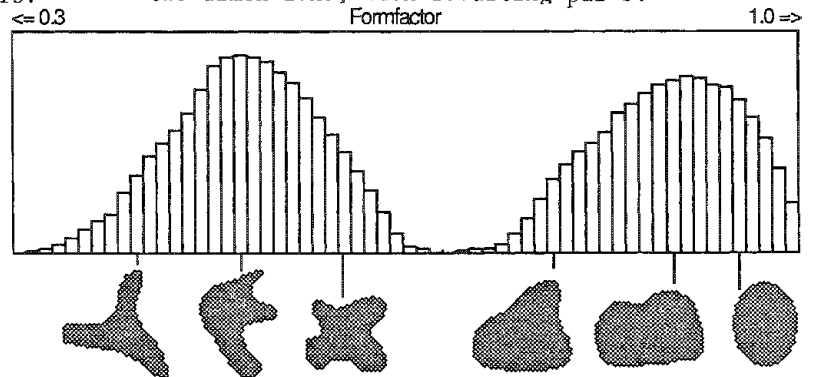


FIG. 2.--Example of two classes of objects based on shape factor, and their pdf's.

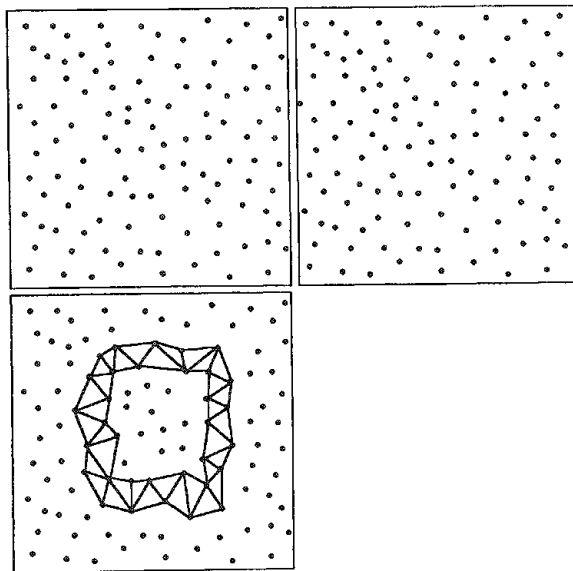


FIG. 4.--Random dot stereogram with raised central plateau. Tessellation of cliff area shown is perceived as square with vertical sides.

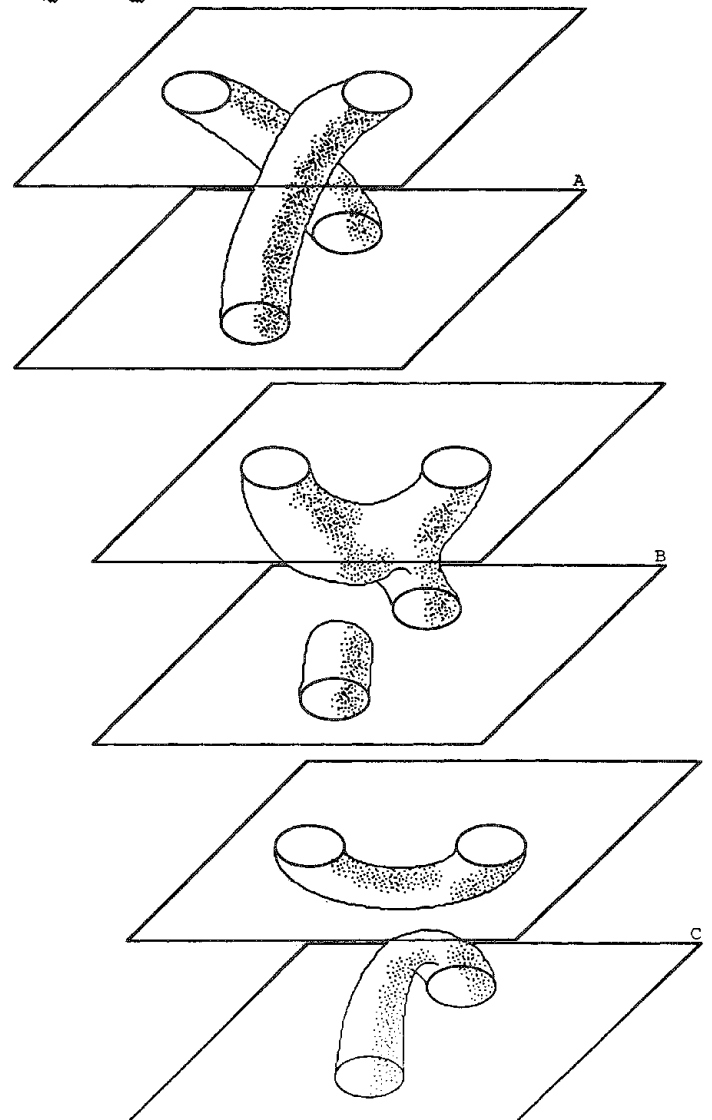


FIG. 5.--Three possible interpolations of ambiguous serial section data.

"interesting point" which would have subdivided the triangle. From these triangles one can straightforwardly perform measurements of elevation profiles, drawings of contour maps, and integration of volume and surface area.<sup>16</sup>

When the human visual system looks at a random dot stereogram (Fig. 4) that is basically similar to our array of interesting points, it applies some further rules to simplify the surfaces. Boundaries between surfaces of small orientation differences are not seen as edges; instead, a smooth curve is interpolated. Furthermore, the irregular boundary between groups of facets that lie at quite different orientations is simplified to a single fold line.<sup>17</sup>

There is also a strong preference on the part of the human viewer for simple curves and straight lines, for angles between lines and surfaces that are simple angles (e.g., 90°, 60°, or 44°), and for orientations that correspond to up, down, left, and right as the image is viewed. These may be incorrect biases on our part, especially when looking at microscopic images of natural surfaces rather than macroscopic man-made objects. Still, our stated goal was to duplicate the visual system's preferences and constraints.

We can do it by weighting each triangle edge by the surface angle across it, and then selecting only those lines with a large value. These lines can be furthermore linked together by a weighted regression, which averages the line orientations and positions with weighting that prefers multiples of 30° or 45°. The result is to interpolate simplified boundaries that may correspond to object outlines, within which three-dimensional measurements of size and shape can be performed just as for two-dimensional images. In the figure, the small disparity among points on the base plane and on the raised plateau is ignored, which produces the illusion of a raised central plane. Further, although the actual cliff is irregular, visual simplification imposes a square shape. We "see" a cube on a flat surface.

#### *Multiple Image Planes*

In general, a series of image planes is different from a three-dimensional array of pixels. In some cases, such as the ion microprobe, it is possible to build up a three-dimensional array of pixels in which each represents a cubical point in space, just as a pixel represents a small square in a 2-D image. Even in this case there are problems with interpreting the voxels as cubes, because the depth dimension may be quite different from the lateral spacing, and the depth of pixels in a plane may not be the same because of non-uniform rates of specimen erosion. However, the pixels are contiguous in the depth direction just as they are laterally.

For most stacks of images, the individual image planes are separated from each other by a distance much greater than the spacing of the pixels laterally, and no information is available from the intervening space. That means that information is missing between the planes and must be inferred from what can be seen, usually by interpolation and probabilis-

tic decisions (Fig. 5). If similar features are seen in two adjacent planes, it may be reasonable to interpolate the same object between them, with a smoothly linear set of lines and Euclidean surfaces of minimum energy, or with lines or surfaces having the same degree of irregularity as seen in the planar sections. Certainly there is no reason to expect sudden changes of size or direction between the visible planes, and in fact the spacing of the sampling planes must be sufficiently small to prevent missing this kind of interesting behavior.

Sometimes, crossing or branching of objects does occur. In this case, we may be able to estimate where the point occurs, either by linear interpolation or nonlinear fitting through feature traces in several adjacent planes. However, there are some configurations of 2-D images that are indeterminate and it is only possible to estimate the relative probabilities of different structures between the planes based on the frequency with which similar structures are observed in the 2-D images. The logic to decide on the contiguity relationships between objects in adjacent planes is therefore a bit different from the logic of connecting touching pixels together in a 2-D image.

One thing that can be learned from a serial section image stack is a three-dimensional reconstruction of the object(s), by one of two rather different approaches. The first is to construct two outline images of the individual sections, viewed from slightly different locations to produce a stereo pair; the second is to model the surfaces between these outlines to show a solid body representation of the object. Both methods have advantages and disadvantages. The presentation methods are similar to those used for tomographic reconstruction, but the image data are obtained in a different way. Tomograms use a synthesis of multiple 1- or 2-D projections to form a 2- or 3-D image of the inaccessible interior of a sample.

The outline method for presentation relies on the abilities of the human visual system to understand the image. Measurement of volume is possible by addition of the areas of the sections, and the "wire frame" drawing allows us to see internal structure. However, it is difficult to see the behavior of the object in the "depth" direction perpendicular to the planes of section, and determination of surface area and shape are difficult or inaccurate.

Solid modeling obscures internal details, and most important requires significant amounts of computation. However, the resulting objects are relatively easy for most viewers to understand and interpret, and three-dimensional measurements of shape and surface area can be carried out directly. Fortunately, the use of micro- and minicomputers for computer-aided design/computer-aided manufacture (CAD/CAM) applications has led to the availability of software that does this kind of modeling, complete with color coding or shading of surfaces and the ability to rotate objects in space for viewing purposes (although perhaps not in "real time"). It is usually only necessary to pass the X, Y, Z coordinates of points

on the surface to the display program to generate these kinds of images, which are at least attractive and may also help to transmit real understanding of three-dimensional objects.

However the three-dimensional objects may be viewed, it is important to be able to measure them. Just as for 2-D features, a variety of parameters may be of interest for measurement, description, comparison and classification. Size is relatively straightforward, and includes such parameters as volume, surface area, maximum projected length, etc. Likewise, the location, orientation, integrated density, and other parameters are straightforward extensions of the 2-D case.

Shape is a more subtle and perplexing quality. Besides the use of dimensionless ratios of size parameters, analogous to the 2-D case, it is possible to describe the actual topology of an object from its three-dimensional representation. The principal topological parameter of importance is the connectivity (the genus, or number of holes within the object). From the skeleton of the object, the connectivity can be determined along with counts of the number of branches, number of nodes, and number of end points in the skeleton. These describe the shape independent of size or orientation, and are often powerful classifiers of three-dimensional objects.

### *Illusion*

One of the simplest and most common illusions (Fig. 6a) is that two lines of equal length appear unequal if their ends are joined to lines that extend outward or inward. Similarly, curvature or orientation or different thicknesses or densities of the lines can make them appear unequal. It is easy to write a computer program that is not fooled by this illusion, and returns accurate measurements of line length. But why is the human visual system fooled?

There are two slightly different reasons that combine in these cases.<sup>14</sup> For one thing, humans see entire objects, consisting of all of the connected portions of lines. Even when one is trying to select the principal line for estimation, the line segments connected to the ends of the line act to weight the position of the end points, resulting in the illusion.

Similarly, there is a weighting of orientation, of density, and of angles. We impose Euclidean geometry on the things we see, and prefer to have corners be right angles, or at least multiples of 45° or 60°. In Fig. 6(b) the weighting of orientation by the short vertical and horizontal lines makes the diagonal lines appear to be not parallel. This illusion is accomplished in the visual system by an inhibition mechanism not between adjacent pixels, as mentioned before, but between cells that detect orientation. The vertical bars, for instance, produce an output from cells that detect them, which in turn inhibits the output of vertical sensing cells for the diagonal line, making it appear to be rotated to a more horizontal orientation (and *mutatis mutandi*, for the diagonal line with horizontal bars).

How can we make the computer measure these

images in the same way? An operator that mimics the human visual system in this case is the Hough transform, which can assign to each point in the image an orientation vector that is the distance-weighted average of all edges present. This transform tends to extend lines or contract them, depending on the line segments at the end, as in Fig. 6(a). It also weights the line orientations in Fig. 6(b) so that they appear not to be parallel.

What good is such a foolish transform? Well, another thing that the human visual system does rather well is to supply missing lines (see Fig. 6c). We can use the Hough transform to supply missing lines such as grain boundaries, to find linear patterns in noisy data, and to refine jagged boundaries into simplified, smooth object outlines.<sup>6</sup> When images are incomplete or noisy, this may be an important tool. Similar operators are used to find corners, which are even more strongly selected by the human visual system.

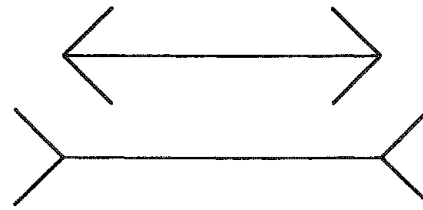
Inhibition in the human visual system is both lateral (the key to locating edges and corners) and temporal. Temporal inhibition or saturation is easily demonstrated by negative afterimages. View a brightly illuminated shape, especially one in color, and then look at a plain gray card. The image will appear in the complementary color. Temporal inhibitions are easily modeled by use of multiple image planes to contain a time sequence of images, and of weighted subtraction or Boolean logic to combine the images. This process makes it possible to follow objects as a function of time, and to interpolate in time just as the human visual system does when watching a movie. It is especially powerful as a motion sensor. It is not surprising, then, that we see moving edges before anything else in an image.

If we knew more about how the eye encodes information on edges and corners, and their relationship to each other, and the visual system's rules by which nearby or similar features are connected together to form objects, we would advance significantly on the road to recognition of simple objects such as handwritten letters and numerals, which are recognizable to a small child even when written in a variety of styles in ways that intentionally violate all the conventions that might logically be selected to define the pattern. We shall also be able to find better ways to present information to the viewer, especially the sort of multidimensional data often encountered in image analysis.<sup>18</sup>

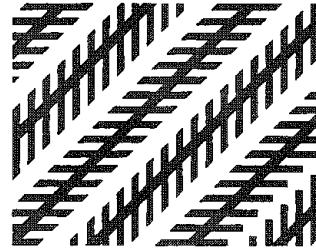
A final example of illusion is brightness aliasing (Fig. 7). In the Mach bands, we perceive a variation in brightness near each boundary that increases the magnitude of the actual step. When such a variation is actually present, as in the Craik-Cornsweet-O'Brien illusion, the visual system treats it as an edge and overcompensates, so that the equal brightness areas away from the boundary are judged to be different.

Because of its interest in edges, the visual system preserves or expands brightness changes across discontinuities. But it fills in intervening areas and does not see gradual changes of brightness as indicating edges.

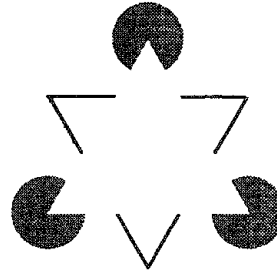




A: Müller-Lyer lines: the horizontal lines actually have the same length.



B: Zöllner lines: the oblique lines are actually parallel.



C: Kanizsa' triangle has illusory boundaries and a brightness greater than its surroundings.

FIG. 6.--Three illusions.

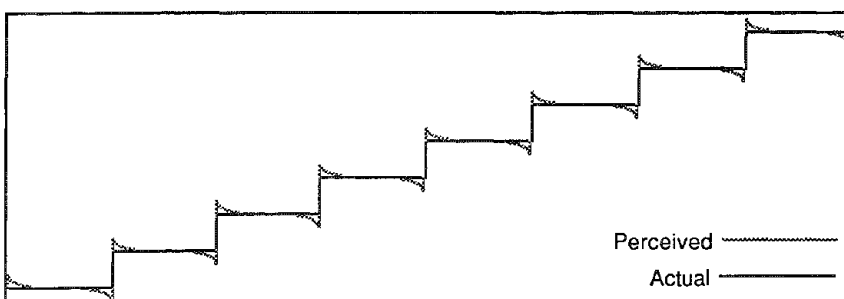
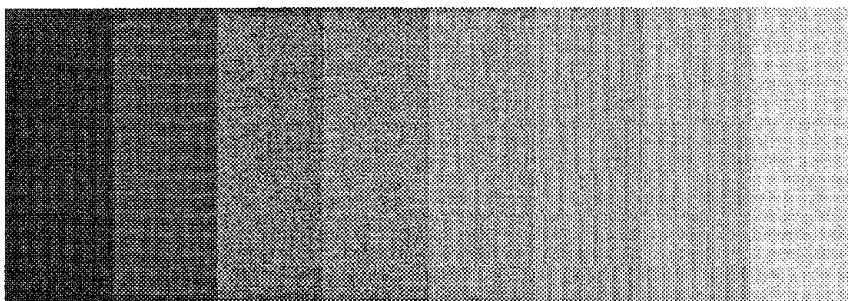
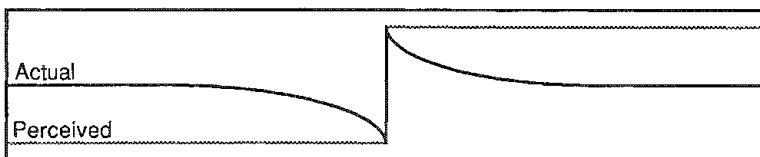
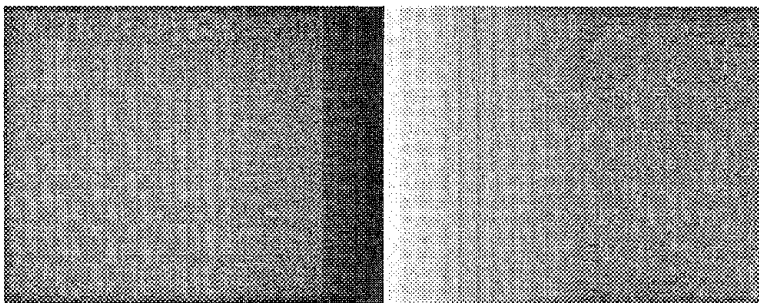


FIG. 7.--Craik-Cornsweet-O'Brien contrast illusion (top) and Mach bands (bottom) show response of visual system to edge contrast and its ability to affect uniform regions.

This allows us to see objects even in the presence of nonuniform illumination and (together with the ability to normalize for local or overall changes in absolute brightness) to see things under quite nonideal conditions of lighting. The mechanism is based on lateral inhibition, and can be modeled directly using Laplacian or derivative operators.

There are many other illusions, some well known, that can be explained and modeled by simple computer algorithms, and many more that cannot yet be fully explained. Attempting to understand them may present us with additional image processing, recognition, and measurement tools.

### Conclusions

Work by computer scientists, neuroanatomists, electronics and device experts, and (not least) image analysts is contributing steady growth to our basic knowledge of human visual processes. They are heavily parallel, hierarchical, and probabilistic. They are also marked by extreme economy: very few individual pieces of information are extracted from millions of pixels at the retinal level and communicated to higher levels in the brain, yet they are usually adequate for object identification and scene interpretation. The organization of this information is by feature or object rather than by pixel.

Consideration of these results leads to the selection of a number of useful algorithms for image processing (e.g., spatial domain operators) which can pick out boundaries based on subtle characteristics such as texture, join incomplete boundaries, and simplify irregular ones. Measurement parameters for object size and location are much more accurate with simple computer algorithms than any visual estimate, but shape is much more difficult to quantify. Efforts are still under way to develop algorithms that extract those characteristics of object shape to which the human visual system responds. That is especially true for three-dimensional structures, in which some information is either hidden by foreground objects or must be interpolated between successive image planes, and orientation-invariant shape estimators are required.

It is practical now to create expert systems for object recognition and selection. They can be readily trained with small suites of archetypical objects (which by virtue of their human selection may not represent the real world), and will continue to learn from subsequent use. They are quite capable of outperforming the human trainer, and by virtue of yielding results that are subtle and not always obvious to the observer, can be considered to exhibit some degree of artificial intelligence. More powerful computer architectures are especially important in dealing with images, which place severe burdens on conventional systems. Massive parallelism is especially suitable for image handling, but it is not easy to take advantage of it with existing programming languages. Considerable progress in all these areas of computer "seeing" is being made, but few final answers can yet be glimpsed. Developments of software algorithms

and hardware architecture can be expected to proceed hand in hand into the foreseeable future.

### References

1. W. K. Pratt, *Digital Image Processing*, New York: Wiley, 1978.
2. A. Rosenfeld and A. C. Kak, *Digital Picture Processing*, London: Academic Press, 1982.
3. K. R. Castelman, *Digital Image Processing*, Englewood Cliffs, N.J.: Prentice Hall, 1979.
4. J. Ch. Russ and J. C. Russ, "Image processing for the location and isolation of features," *Microbeam Analysis--1986*, 501.
5. J. C. Russ and J. Ch. Russ, "Automatic discrimination of gray scale images," *J. Microscopy* (in press).
6. D. H. Ballard and C. M. Brown, *Computer Vision*, Englewood Cliffs, N.J.: Prentice Hall, 1982.
7. J. Serra, *Image Analysis and Mathematical Morphology*, London: Academic Press, 1982.
8. J. C. Russ and J. Ch. Russ, "Automatic editing of binary images for feature isolation and measurement," in Ref. 4, p. 505.
9. J. C. Russ, *Practical Stereology*, New York: Plenum Press, 1986.
10. J. Ch. Russ and J. C. Russ, "Shape and surface roughness characterization for particles and surfaces viewed in SEM," in Ref. 4, p. 509.
11. J. C. Russ and J. Ch. Russ, "Feature-specific measurement of surface roughness in SEM images," *Particle Characterization* (in press).
12. J. C. Russ and J. Ch. Russ, "Image processing in a general-purpose microcomputer," *J. Microscopy* 135: 89, 1985.
13. V. Braitenberg, *Vehicles: Experiments in Synthetic Psychology*, Cambridge, Mass.: MIT Press, 1984.
14. J. Frisby, *Vision: Illusion, Brain and Mind*, Oxford: Oxford University Press, 1980.
15. H. Mehlo, "Der Einsatz von Grauwertbildspeichern bei der quantitativen Bildanalyse von Werkstoffgefügen," Dissertation, University of Stuttgart, 1983.
16. J. C. Russ, T. M. Hare, R. P. Christensen, T. K. Hare, and J. Ch. Russ, "SEM low magnification stereoscopic technique for mapping surface contours," *J. Microscopy* 144: 329, 1986.
17. D. Marr, *Vision*, San Francisco: W. M. Freeman, 1982.
18. E. R. Tufte, *The Visual Display of Quantitative Information*, Cheshire, Conn.: Graphics Press, 1983.

## COMPUTER COMPARISON OF DIGITAL IMAGES

R. B. Mott

Digital acquisition and processing has become a routine analytical tool for electron images, light microscope images, and two-dimensional x-ray composition maps. Fiori et al. have given a concise summary of desirable features in an interactive digital image display system, including zoom/pan under hardware control and the ability to overlay text and histograms.<sup>1</sup> Techniques such as pseudo-coloring, digital filtering to suppress noise or enhance edges, and gray-level histogram stretching for improved contrast allow the operator great flexibility in modifying the original image to emphasize features of interest.<sup>1,2</sup> Besides visual enhancement, digitization of images permits precise, controllable comparison between them. Small computers cannot do these comparisons rapidly in software; new comparison and display hardware in the PGT System 4+ performs video-rate interactive comparison on two digital images stored in independent frame buffers. This paper defines desirable system features for digital image comparison, and explores the considerations involved in making such comparisons valid and displaying the results effectively.

### *Why Image Comparison?*

We perceive images by relating them to other images we have seen before, so in that sense we are always doing image comparison. More specifically, we are often interested in the differences or similarities between pairs or sequences of images. Many examples can be taken from the semiconductor industry, such as comparing failed parts against good ones by voltage-contrast techniques, or time-sequence tracing of fault propagation in integrated circuits.<sup>3,4</sup> Images of the same sample from different signals, such as x rays and back-scattered electrons, are also likely candidates for comparison. Indeed, we may wish to compare the same digital image before and after a series of processing operations.

The traditional presentation of side-by-side images can give a visual impression that something has changed, but determining exactly what it is may not be easy. If our interest is in minor changes of detail in a reasonably complex image, side-by-side inspection is either quite tedious or fails altogether. The comparison result must be presented as a single image in order to engage the eye's feature recognition capacity.

Three problems are associated with image comparison. First, the images must be brought

into spatial registration so that corresponding points are superimposed. Second, the images must be normalized for contrast and brightness or differences in digitization parameters. Finally, an image comparison operator must be selected and the results mapped onto the display.

### *Spatial Registration*

The general linear transformations in the plane are scaling (zoom, magnification), translation (offset in x and y), and rotation. Often translation alone will suffice; if two integrated circuits (ICs) are aligned the same way in the microscope stage, an attempt to digitize the same region of the two ICs at the same magnification is likely to differ only by a simple offset. The display hardware should allow pan and zoom of the two images independently relative to each other, with comparison performed between pixels superimposed on the screen regardless of their relative positions in the two frame buffers. The zoom function should be nearly continuous, so that small magnification differences can be corrected--a feature that is also useful for images of differing resolutions. X-ray element maps are often collected at coarse resolution relative to electron images, due to the lengthy dwell time per point for usable statistics. An x-ray map can be zoomed up and matched against the electron image; since many low-resolution x-ray maps will fit in a single frame buffer, maps for multiple elements can be rapidly overlaid in sequence.

Of course, in many cases the simple transformations available in display hardware are not adequate. The images may be rotated with respect to each other. Images of flat samples taken at different tilt angles, or rotated and tilted, have different apparent aspect ratios between the image axes. Bright describes a comparison between a transmission and back-scatter image in which nonlinear distortion occurs that cannot be corrected by linear operations.<sup>5</sup>

Geometric correction algorithms originally developed for use on Viking Mars Lander images and in satellite cartography can be readily adapted to handle even the nonlinear cases if the user is willing to specify tie points in both images.<sup>6</sup> However, if the samples are very rough and the images taken at different tilt angles, there will be areas where registration is impossible because the signal is obscured in one image or the other.

### *Brightness and Contrast Normalization*

When the images to be compared represent actual counts at each pixel, such as the number of characteristic x-ray photons detected for a given element in a given length of time, the mapping of those counts onto the gray levels of

---

The author is at Princeton Gamma-Tech (PGT), Princeton, NJ 08540. He wishes to acknowledge D. C. Dailey of PGT for inspiration; J. J. Friel and M. C. Mott, also of PGT, for help with the perspiration; and the memory of John von Neumann, without whom none of this would be possible.

the two frame buffers can be adjusted arbitrarily to suit the analyst's convenience, and quantitative comparison is well defined.

If the signals that formed the two images have no obvious numeric relationship, as in x-ray counts and backscattered electrons, the comparison operations are more likely to be qualitative (simple overlay) or logical--masking the electron image by the presence or absence of various combinations of elements. Normalization of brightness and contrast is reduced to a matter of taste in the electron image and thresholding in the x-ray image(s).

When two electron images are to be compared, the first issue is the selection of the contrast mechanism appropriate to the analytical problem from the possibilities tabulated by Newbury.<sup>7</sup> Then the SEM and digitizing parameters are chosen to minimize contributions from other contrast sources. Also, we must assume that any gradual spatial variations in brightness and contrast within the individual images (for example, due to uneven illumination) have been digitally corrected. Bright and Steel list some methods for such corrections.<sup>8</sup>

The remaining variations in brightness and contrast between the images can arise from two sources. One is real information representing differences that we wish to observe; the other is a global difference in the digitization mapping of the analog signal into the (typically 256) digital gray levels. This last manifests itself as a shift or stretch (which may not be linear) in the gray-level histogram of the digitized image. In fact, if the digitizing dynamic range is chosen incorrectly, information may be lost due to clipping at the high or low end of the digital gray scale.

A histogram transformation can be performed, but the choice of transform function will be somewhat arbitrary unless a reasonable calibration of gray level to some physical quantity exists, such as voltage in voltage contrast images or average atomic number in backscatter images. If the images have distinct phases that result in sharp peaks in the gray-level histogram, the normalizing transform can be defined by matching of the corresponding histogram peaks via software.

#### *Arithmetic Comparison Operators*

Many operations can be performed on the corresponding pixel pairs from the two images once the appropriate spatial and intensity normalizations are made. The familiar arithmetic functions add, subtract, multiply, and divide can be used, but certain constraints apply when the results are mapped back onto the display.

The problem arises because the results of arithmetic operations on N-bit numbers have a dynamic range greater than N bits, so that some scaling function must be applied to compress the results back into an N-bit display. Subtraction is particularly messy because the results may contain negative values. Possible approaches include clipping negative results to zero; folding about zero (displaying the absolute value of the difference); and setting zero to be medium gray (128 in an 8-bit image),

with positive differences extending toward white and negative differences extending toward black. The last method is confusing in gray scale but useful when the gray levels representing positive and negative values are pseudo-colored differently.

The results of addition may also be clipped at the maximum intensity for sums that exceed 8 bits, or the two original images may be pre-scaled to half intensity. If the latter solution is adopted, the images are effectively averaged.

Addition and subtraction can only generate 9 bits of dynamic range from 8-bit images, but multiplication and division can generate 16 bits (65 536 levels) of dynamic range, which presents a much more serious problem in selecting an appropriate mapping of results to the display. An arbitrary fixed mapping is very likely to compress the information of interest into a very few gray levels. The ability to adjust the mapping interactively is preferable.

The capacity for high-speed arithmetic operations on the individual images before comparisons are made is also useful. In addition to contrast enhancement by gray-level scaling or shifting, higher-order functions such as logarithms, powers, and roots may be of interest. These functions cannot be completed in one frame time, but response time well under 1 s seems reasonable.

Once again, the results must be scaled into the 8 bits of the frame buffers, but within that limitation the analyst can generate complex combinations of point and comparison operations, such as the ratio of the logarithms of two images. In general the scaling cannot be inverted to restore the gray levels to their state prior to the last operation; therefore, the original gray-level images should be preserved to allow the analyst to "undo" undesirable results. Such preservation also permits rapid application of several comparison operators to find the one that performs best.

#### *Boolean Logic Comparison Operators*

The Boolean logic operations such as AND, OR, and XOR are commonly thought of as single-bit functions defined on binary images.<sup>9</sup> One can readily extend them to 8-bit gray-level images by performing the operation bitwise on the corresponding bits of the two input pixels to generate an 8-bit result. There are no difficulties with dynamic range, since the result has the same number of bits as the inputs. However, 8-bit logic operations can be counterintuitive; consider a pair of pixels having adjacent gray levels (Table 1).

TABLE 1.--Worst-case results of 8-bit logic operations

127 (decimal)	01111111 (binary)
128	10000000
0	00000000 (result of AND)
255	11111111 (result of OR)
255	11111111 (result of XOR)

Our sense of Boolean logic leads us to expect that something ANDed or ORed with itself

should produce itself, and that something XORed with itself should produce zero. Two adjacent gray levels would be almost indistinguishable in an image; yet the logical AND produces zero; the logical OR produces a pixel roughly twice as bright as the input pixels, and the logical XOR produces the opposite of the expected result. Less dramatic but similar problems occur near any major bit transition.

Even fairly homogeneous regions of an image have local fluctuations of a few gray levels. Therefore, the bitwise logical operations are not very useful if performed directly on the gray levels of the image. However, one would like to extend these operations beyond the simple binary cases to multiple-phase images, voltage-contrast images, or multiple-element x-ray maps.

#### *Combining Pseudo-color with Comparison Operations*

Consider the properties of the Boolean logic operations in general terms. The AND function detects a match between two quantities; the OR blends them; and the XOR detects differences. Pseudo-coloring has three very interesting properties in this context: first, data reduction by grouping related gray levels into a single entity; second, data enhancement by increasing contrast between nearby gray levels; and third, correction for brightness and contrast differences by painting different gray-level groups in the two images with the same color. If the raw gray levels are transformed into codes representing their assigned pseudo-color, the problems discussed above in applying Boolean logic to gray-scale images disappear. Painting an image in pseudo-color is a familiar and simple interactive process for setting thresholds on the gray scale.

Consider Miller's color-coding scheme for voltage-contrast images.<sup>3</sup> If two such images are color-coded consistently, regardless of differences in their gray-level histograms, they are directly comparable on the basis of color. An XOR between images of a good and a failed part cancels everywhere the colors match, leaving only color mismatches--regions where the parts behave differently.

#### *Comparing an Image Against Itself*

Surprisingly useful results can be obtained by storing the same image into both frame buffers. If each frame buffer is loaded with multiple low-resolution x-ray element maps, rapid pairwise element comparisons can be made. One can do crude but very fast and non-destructive smoothing or edge detection on a gray-level image by loading it into both buffers, panning the images slightly relative to each other, and invoking the averaging or subtraction comparison operators, respectively. Then, if an edge finding filter is used on one copy of the image, the detected edges can be thresholded in white and superimposed on the original image with the OR operator.

#### *Conclusions*

Many vendors and authors have discussed digital image processing techniques as a data-enhancement tool, but few have considered in detail the problem of comparison between digitized images. The importance of rapid, dynamic interaction with the analyst is emphasized;<sup>1</sup> such interaction requires hardware support for an effective rate of arithmetic operations on gray-scale images two to three orders of magnitude faster than software running on general-purpose laboratory minicomputers. The hardware should also be able to perform arithmetic point operations at high speed on the individual images prior to comparison.

It is desirable to preserve the original gray-level data so that many comparisons can be made in sequence without accumulating the errors inherent in scaling the point operation and comparison results back to an 8-bit display.

Bitwise extensions of Boolean logic operators do not work well for gray-level images; however, useful results can be obtained for images with multiple well-defined phases or other groupings of gray levels, as in voltage contrast, by applying the Boolean operators to pseudo-colors assigned to the gray-level groups.

#### *References*

1. C. E. Fiori et al. "Computer-aided compositional mapping in scanning electron column devices." *Microbeam Analysis--1985*, 219-226.
2. J. C. Russ and J. C. Russ, "Enhancement and combination of x-ray maps and electron images," *Microbeam Analysis--1984*, 161-163.
3. E. L. Miller, "Digital processing and color coding of voltage contrast images," *Proc. Intern. Symp. on Testing and Failure Analysis*, 1985, 63-71.
4. T. C. May et al., "Dynamic fault imaging of VLSI random logic devices," *IEEE Intern. Reliability Physics Symp.*, 1984, 95-108.
5. D. S. Bright, "Computer matching two different images of the same particle field," *Microbeam Analysis--1984*, 173-174.
6. K. R. Castleman, *Digital Image Processing*, Englewood Cliffs, N.J.: Prentice-Hall, 1979.
7. D. E. Newbury, "Strategy for interpretation of contrast mechanisms in scanning electron microscopy: A tutorial," *Microbeam Analysis--1986*, 1-5.
8. D. S. Bright and E. B. Steel, "Bright-field image correction with various image-processing tools," *Microbeam Analysis--1986*, 517-520.
9. J. C. Russ and J. C. Russ, "Automatic editing of binary images for feature isolation and measurement," *Microbeam Analysis--1986*, 505-508.

## AN OBJECT FINDER BASED ON MULTIPLE THRESHOLDS, CONNECTIVITY, AND INTERNAL STRUCTURE

D. S. Bright

This paper describes a robust algorithm, called the Blob splitting algorithm, for finding simple objects in digital images that have variable backgrounds. Locating objects in digital images with computer algorithms is difficult where there is a large background (compared with the brightness of the objects), where the objects are of various sizes (and shapes) and have fuzzy edges, or where the objects are not clearly separated. More conventional means that have been unsatisfactory in such cases are simply setting the threshold,<sup>1</sup> finding edges first via the gradient of the image,<sup>2</sup> or using gated filters such as the top hat filter.<sup>3</sup> The algorithm here may seem similar to the erosion operation for binary images,<sup>1,4</sup> except that obtaining a binary image in the first place requires setting the threshold—a step that this algorithm avoids by working at multiple thresholds. Morphological operations such as erosion are being applied to gray-scale images, but the work is still under development.<sup>5</sup>

As an example of the inadequacy of simply taking the threshold, Fig. 1 shows a mesh plot of part of an image of particles taken with an ion microscope. Figure 2 is a hand-drawn schematic contour plot of the four particles in Fig. 1. A simple threshold (i.e., a horizontal slice through the surface of Fig. 1) either misses particle B (Fig. 2, at intensity 50), or does not resolve particles C and D (Fig. 2, at intensity 40).

### *Object-finding Algorithm*

For simplicity, we assume dark-field images throughout the following discussion.

The algorithm can be thought of in terms of the relationships of contour plot isophotes,<sup>6</sup> which we will just call 'contours' or lines of constant intensity. A contour is said to split when it encloses more than one contour of equal intensity. For example, the outermost contour of intensity 10 in Fig. 2 splits into three contours of intensity 20. As the intensity increases (typically in increments of  $H_{\min}$ , to be defined later), objects are defined as contours that have just resulted from a split and that do not themselves split with subsequent values of the threshold. The solid contours in Fig. 2 represent objects defined in this way.

For implementing the algorithm on a computer, it is easier to think in terms of groups of pixels. If a threshold is set for a given gray-level image, a binary image results, consisting of pixels with intensity greater than or equal to the threshold. Such pixels may be grouped by connectivity. A group of pixels in which every pixel is adjacent to at least one

other of the group is called a blob.<sup>7</sup> In this particular case, all pixels of the group are also brighter than the given threshold.

Objects are chosen from the blobs during the process of incrementally raising the threshold from the lower to the upper limit. Objects are blobs that have just split from a larger blob as the threshold is raised and that do not split for any subsequent threshold increments. The algorithm is therefore called the blob splitting algorithm.

With noisy images, a blob often splits into a smaller blob and single pixels or small groups of pixels. Therefore, the blob splitting algorithm requires a definition of  $A_{\min}$ , the minimum area (number of pixels) for a blob to be considered an object. Noise may also appear as small undulations in an otherwise level background. The algorithm also requires a definition of  $H_{\min}$ , the minimum blob height (regardless of area) for a blob to be considered an object. The blob height is the maximum pixel intensity of the blob less the minimum, or threshold, blob intensity. Neither  $H_{\min}$  nor  $A_{\min}$  are critical to the performance of the algorithm, and each can be approximated if the nature of the image to be analyzed is known.

### *The Blob-splitting Algorithm*

The algorithm uses two lists of blobs for input and output: a working list and an object list. Initially, the object list is empty and the working list consists of the image-filling blob at the minimum threshold. The algorithm repeats steps 1 and 2 below until the working list is empty and then gives the object list as the result.

1. Select a blob B from the working list. Set the current working threshold  $T_w$  to the threshold originally used to get blob B.
2. Set  $T_w$  to  $T_w + H_{\min}$  and make a temporary list T of the resulting blobs. Discard any blobs with area less than  $A_{\min}$  or height less than  $H_{\min}$ .
  - a. If the list T has one blob, repeat step 2.
  - b. If list T has no blobs, put blob B on the object list.
  - c. Otherwise, list T has two or more blobs and splitting has occurred. Put the blobs in list T into the working list.

### *Results*

The algorithm has been used in the laboratory in the analysis of several types of images. One type is spots in electron-diffraction patterns taken on an analytical electron microscope in the diffraction mode; the other images of particles taken with an ion microscope.

Figure 3 shows an electron diffraction pattern. In many cases, the top-hat filter<sup>3</sup>

The author is at the Center for Analytical Chemistry, National Bureau of Standards, Gaithersburg, MD 20899.

isolates the diffraction spots, but in this case the diameter of the larger spots is greater than the separation of the smaller spots and the top-hat filter will not work. The rectangles in Fig. 3 are the bounding rectangles of the blobs found by the blob-splitting algorithm.

Figure 4 shows a barium image of particles taken with the ion microscope. The logarithm of the intensity has been photographed to show the dimmer particles. The intensity profile taken along the line A-B illustrates the same sort of problem as in Fig. 1. Also, though not visible from the photograph, the background varies enough to make finding the dimmer particles difficult. Figure 5 shows the results of the splitting algorithm, where most of the particles are resolved and even the dim particles are located.

### Conclusions

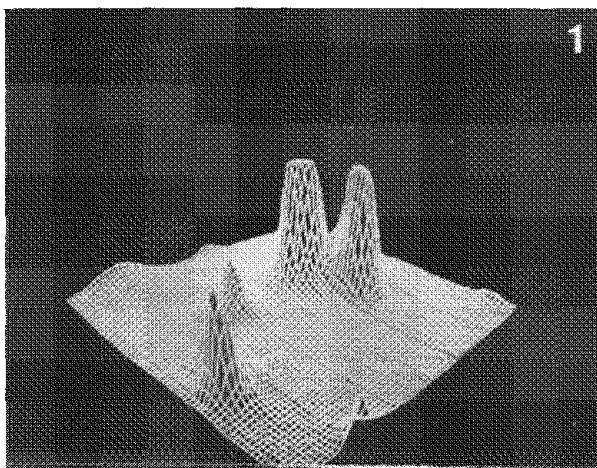
An algorithm is presented for locating objects in digital images. The blob-splitting algorithm is not sensitive to object shape or size, but rather to intensities relative to a local surround and to internal bright spots which potentially are objects themselves. Although computationally intensive, the algorithm is robust and is used routinely in our

laboratory. Examples of its use include particle locations in ion microscope images and spot location in electron diffraction patterns.

### References

1. J. C. Russ, *Practical Stereology*, New York: Plenum Press, 1986, 80,81.
2. V. Berzins, "Accuracy of Laplacian edge detectors," *Computer Vision, Graphics and Image Processing* 27: 195-210, 1984.
3. D. S. Bright and E. B. Steel, "Two dimensional top hat filter for extracting spots and spheres from digital images," *J. Microsc.* (in press).
4. J. Serra, *Image Analysis and Mathematical Morphology*, New York: Academic Press, 1982.
5. S. R. Sternberg, "Esoteric iterative algorithms," in S. Levialdi, Ed., *Digital Image Analysis*, London: Pitman, 1985, 60-68.
6. H. P. Meinzer and U. Engelmann, "The interpreter PIC: A tool in the field of image processing," *Med. Inform.* 9: 93-102, 1984.
7. R. A. Kirsch, "Computer determination of the constituent structure of biological images," *Computers and Biomedical Research* 4: 315-328, 1971.





2

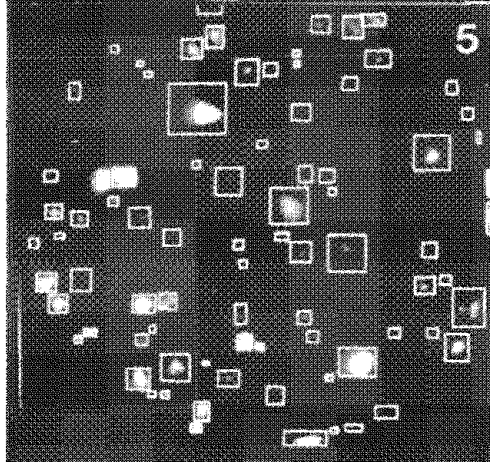
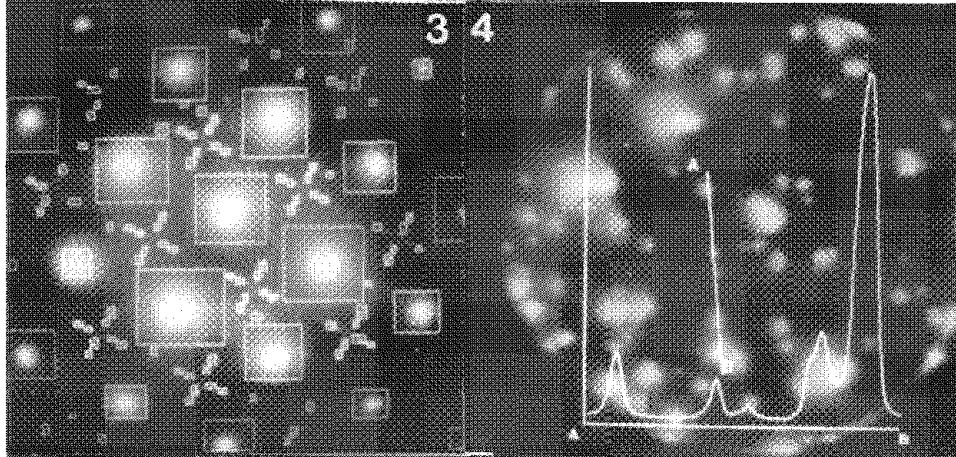
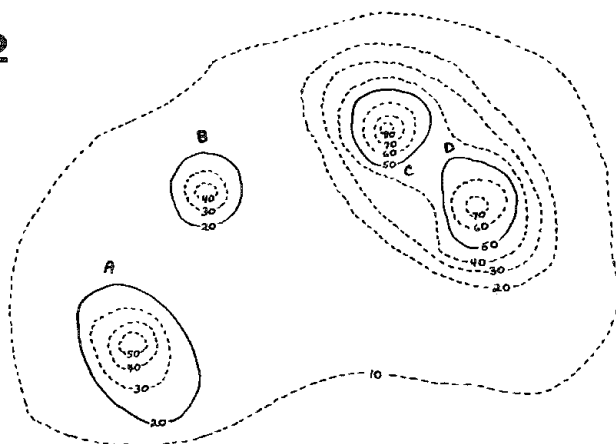


FIG. 1.--Mesh plot of portion of image of particles taken with ion microscope. Smallest peak is lower than saddle between two largest peaks.

FIG. 2.--Schematic hand-drawn contour isophotes for four peaks of Fig. 1. Intensities for each contour are also for illustrative purposes only. Objects found by the blob-splitting algorithm are represented by solid contours.

FIG. 3.--Electron diffraction pattern where spots of interest vary greatly in size as well as intensity. Rectangles represent single spot locations as found by blob-splitting algorithm.

FIG. 4.--Barium image of field of particles taken with ion microscope. Log of intensity is displayed. Intensity profile taken on line A-B.

FIG. 5.--Same field as Fig. 4, along with rectangles that show particle locations as determined by blob-splitting algorithm. Intensity displayed linearly.

## INTERACTIVE SOFTWARE FOR SIMULATION OF HIGH-RESOLUTION TEM IMAGES

Roar Kilaas

A new highly interactive and user-friendly software package for simulation and processing of high-resolution transmission electron micrographs has been developed at the National Center for Electron Microscopy (NCEM) at the Lawrence Berkeley Laboratory. Designed to be used by scientific visitors to the Center, the software is completely menu driven from a graphics terminal with a mouse and requires almost no computer knowledge for proper usage. Although the software is written to insure maximum performance with hardware available at the NCEM, hardware-dependent code is kept in separate modules that are easily modified. The new software package combines an unparalleled ease of use with the latest theory in the field of simulation of high-resolution transmission electron micrographs.

There has been a tremendous improvement in computer hardware in recent years. Only a few years ago, image simulations of high-resolution electron micrographs were mostly done on large mainframes and often overnight. Images were printed out the next day in the form of overprinted characters on computer paper. Today it is possible to purchase a micro/mini-computer such as a MicroVax or a Sun, connect it to a small array processor and a framestore, and compute images faster than it is possible on a computer costing millions of dollars--and all at a cost of less than \$100K. Interactive software is gaining popularity at the expense of software written to run in batch mode. With almost instantaneous results available in most cases, the user often requires the capability of immediate change of input and output parameters. That is the case at the NCEM at Berkeley, where a new dedicated facility for computer processing and simulation of electron micrographs has been a major project for the past two years. Hand in hand with acquisition of hardware there has also been a major effort in software development. Experience with previous software had shown that there are many factors beyond the ability to solve certain equations that determine the usefulness of a set of programs. Some of the more important factors are listed below.

1. *The user interface.* Apart from the ability to produce correct results, the user interface is the most important feature of any type of software and is likely to be overlooked,

---

Author Kilaas is at the National Center for Electron Microscopy, Lawrence Berkeley Laboratory, University of California, Berkeley, CA 94720. He thanks Dr. M. A. O'Keefe for assistance in planning screen outlays and suggesting useful options and ways to make the programs run more efficiently. Dr. O'Keefe's own SHRLI programs provided at all times useful checks as to the accuracy of CEMPAS. This work was supported by DOE under Contract DE-AC03-76SF00098.

particularly in the scientific community. It determines how accessible programs are to others than the author and how quickly new problems can be tackled. There are numerous examples of powerful software packages that are never used to their potential because of the time it takes the user to become familiar with commands and options. It is also essential that some form of help is available other than through manuals.

2. *Flexibility.* Beyond memory and speed considerations there should be no limit on the size and shape of the calculation that could be performed. Most existing software is built around fixed array dimensions, which are often of a wrong size and shape for many image calculations. Calculations of defects especially require array sizes that can be varied independently in the two image dimensions and that can be made large enough to minimize boundary effects when employing periodic continuation.<sup>1</sup>

3. *Expansion possibilities.* Earlier software packages were often written with tight constraints on computer memory and modularity of the software was often compromised. Modification of these packages so as to take advantage of recent developments in hardware is then made more difficult. Hardware-dependent code should be confined to a set of primitives that can be easily modified.

Each of the above factors had to be addressed during the design of the new software. (They are further discussed below.) The goal was to create a set of programs that was simple to use and yet sophisticated enough to allow growth in the future. The culmination of this effort is called CEMPAS (Center for Electron Microscopy Processing and Simulation), which at this stage is primarily a simulation software package. A limited number of processing is currently being handled by the SEMPER software package,<sup>2</sup> but an integration of CEMPAS and SEMPER is also being investigated.

### *Design Implementation*

*The User Interface.* The choice of a user interface depends on the ultimate user of the software; unfortunately there are no easy answers. The most common interface is the command language interpreter (CLI), where the program executes functions according to commands typed at the keyboard. Parameters associated with a given command are provided with default values that need only be specified if different values are to be used. Commands are thus quickly entered and executed. The advantage of this approach is speed; the fingers never need to leave the keyboard. The disadvantage is the time it takes for new users to learn the commands and options to take full advantage of the software.

A different approach is to provide input through the keyboard via menus. Users respond to prompts by entering their choice of command.

The advantage is that the user need not remember any of the commands; the disadvantages are that updating menus takes time and the user must be prompted for any parameters.

The interface chosen for CEMPAS makes extensive use of menus, but instead of typing a response from the keyboard, the user responds by moving the cursor to a region associated with the command and presses one of the buttons on a mouse. The keyboard is used for input of data. The advantage is that the time required to learn to run the software is reduced to almost zero and the graphics screen used with the menus can be used for drawing curves, crystalline unit cells, etc., providing a very pleasing environment. The disadvantage is that experienced users might find it easier and faster to input data from the keyboard.

Another problem not related to how commands are input, is determining what information to display, what kind of commands to build into the program, etc. Unfortunately, new users always find they need features that are not included and thus the software is always changing.

*Flexibility.* Some simulation software restricts users to using arrays of fixed dimensions in their calculations. Typical dimension is a  $128 \times 128$ -point array. The largest dimension in a calculation is then limited to  $32 \text{ \AA}$ , if the potential is to be sampled every  $0.25 \text{ \AA}$ . To avoid aliasing, the propagator should only extend as far as  $1/2$  the phase-grating, which results in a calculation that only includes diffracted beams out to  $1 \text{ \AA}^{-1}$ . Instead of fixed dimensions, CEMPAS uses variable array dimensions that are limited only by the amount of memory available. Thus if the unit cell is  $16 \times 120 \text{ \AA}$ , the program might choose an array of  $64 \times 512$  points. At present the maximum array dimensions are determined by the product of the two dimensions and cannot exceed 256K ( $512 \times 512$ ,  $256 \times 1024$ , etc.).

*Expansion Possibilities.* It is to be expected that more efficient and accurate algorithms will be developed in the future and that progress in hardware development will continue to reduce computation times further. Given sufficient money new hardware can be quickly acquired; however, development of software takes time, and changes in hardware should preferably only require minor modifications to a program. CEMPAS is written such that every menu option has a subroutine associated with it, so that only subroutines need to be modified when algorithms change. Likewise, device-dependent code is limited to a set of primitives and only the codes required to draw a line between two points, to read the cursor position, etc., need to be modified in case of a change in the display hardware. The penalty in overhead associated with transfer in and out of subroutines is offset by the ease of maintenance.

*Accuracy of the Calculations.* CEMPAS has been written to include recent development in imaging theory to insure accuracy. At present most dynamical scattering calculations employ

Fourier transforms, although there has been some research into newer algorithms.<sup>3,4</sup> However these new algorithms do not offer a practical alternative to the use of Fourier transforms at present.<sup>5,6</sup> CEMPAS uses a method originally published by Ishizuka and Uyeda,<sup>7</sup> with the addition of the option to include potential eccentricity.<sup>5</sup> For accurate subslicing of the unit cell, the program automatically incorporates upper Laue layer interactions.<sup>8</sup> In the formation of the image, second-order imaging effects are included to insure more accurate results.<sup>9</sup>

*Description of the Hardware.* The hardware at NCEM will be described in detail in a forthcoming paper; only the part that is relevant to the operation of CEMPAS is presented below. A complete diagram of the system is given in Fig. 1.

The heart of the system is a MicroVas with 7 MB of memory, soon to be expanded to 13 MB. Intensive vector operations, such as operations on large arrays, are performed in the CSPI MM+4 array processor. The CSPI MM+4 consists of four array processors that can be run in parallel to give a performance enhancement over the stand-alone MicroVax of a factor of 20 to 80, depending on the number of array processors that are employed in the calculation. Images are displayed on TV monitors connected to a dual user GOULD 9527 image processor; hardcopy is provided on the Apple Laserwriter. Images are stored on a 500MB formatted Fujitsu Eagle II Winchester disk drive. Archiving and backup is onto 6250bpi magnetic tape in a Kennedy tape drive.

*Description of CEMPAS.* CEMPAS consists at present of about 14 000 lines of computer code and is continually being improved and expanded as enhancements are needed. Approximately 35% is written in FORTRAN, 64% in C, and 1% in VAX11 MACRO. The user interface is written entirely in C; most of the number-crunching routines are written in FORTRAN. A few routines were written in ASSEMBLER to increase speed.

As previously mentioned, the use of menus and a pointing device makes CEMPAS extremely easy to use. Several users of the NCEM facilities have already made use of the software without having had to consult a manual. The use of menus eliminates the need to remember commands, and displays all options in plain view. To obtain help on a specific command, the user need only point at the command and press "h" on the keyboard to produce a help message. Input is simplified by the fact that scattering factors for the first 98 elements and crystallographic data on all 230 space groups are stored in the program, and the user is being prompted for any other necessary information. The program automatically creates the proper input files such that the user is not required to learn how to edit files. All parameters needed in a calculation are visible to the user and can be changed immediately. To insure that the program has the correct data, there are several ways of drawing the unit cell with the atomic content. Images, diffraction patterns, "optical" diffractograms,

Pendellösung plots, Contrast Transfer Function plots, etc. are easily calculated and promptly displayed. Images can be zoomed in or out, histogram equalized, Fourier transformed, intensity transformed, filtered and compared, again all with the use of the mouse. The list below gives some of the more important features of CEMPAS.

- Input of crystallographic data facilitated by a database of the 230 crystallographic spacegroups and/or the use of any supplied set of symmetry operators. In addition there are menu-driven operations that can expand an existing unit cell in any particular direction to create a large supercell and to create defects such as interstitials or vacancies or vacancies. Atoms can be visually moved around in the unit cell and deposited anywhere. Further facilities for creating defects, such as shearing of subsections, twinning about a given plane, etc., are being added.

- Viewing of the crystallographic cell from any direction, both with or without perspective view. In addition, the structure can be viewed from a given direction with a specified field of view with options of measuring distances between atoms, marking 2D or 3D unit cell, highlighting of specific atoms, specifying lighting conditions, etc.

- Automatic calculation of a projected 2D or true 3D unit cell perpendicular to the incoming electron beam direction for use in the image simulation program, viewable with or without perspective.

- Automatic selection of correct array dimensions for the specified model to use in the multislice calculation up to  $x \times y = 256K$ . The ability to vary the array dimensions independently is invaluable for simulating defects such as grain boundaries, which often has a short periodicity along the boundary, e.g., though a  $16\ 384 \times 16$ -point calculation.

- Visual compositional display of the specimen when creating a structure that varies in the direction of the electron beam is being created. Compositional layers are easily inserted, deposited, and deleted from the structure.

- Display of projected potentials and Fourier coefficients (structure factors).

- Computation and display of simulated high-resolution EM images.

- Choice of output ranging from the graphic terminal screen to one of three framestores or the laser printer.

- Provision for inclusion of upper-Laue-layer interactions though proper subslicing of the unit cell potential. Automatic subslicing of the unit cell potential if the periodicity along the incident beam direction is too large.

- Inclusion of second-order effects in the image formation.

- Computation and display of dynamical diffraction patterns. Options include indexing of patterns and modification of the convergence angle and the camera constant.

- Plotting of amplitudes/intensities and phases vs thickness of any number of selected beams.

- Plotting of Electron Microscope Contrast

Transfer Functions.

- Positive or negative interpolative zoom of images, histogram equalization, histogram calculation and specification, and contrast and brightness adjustments.

- Fourier transforms of images or diffractograms, high- and low-pass filters, and specification of frequency windows.

- Multislice calculations involving 64K beams with 256K interactions in  $\sim 2$  s/slice.

### Examples

The use of CEMPAS is best demonstrated by a subset of the available screens and menus to which the user has access. Figures 3-15 show a typical session with CEMPAS where a simulation of a limited through-focus thickness set of images has been calculated for orthorhombic  $ZrO_2$ . In addition, two screens that aid the user in creating structures with defects are shown in Figs. 14 and 15. Figure 13 shows the quality of images available from the terminal screen in the absence of a frame store.

### References

1. P. G. Self et al., "Practical computation of amplitudes and phases in electron diffraction," *Ultramicroscopy* 11: 35-52, 1983.
2. W. O. Saxton et al., "Digital image processing: The SEMPER system," *Ultramicroscopy* 4: 343-354, 1979.
3. D. Van Dyck, "Fast computational procedures for the simulation of structure images in complex or disordered crystals: A new approach," *J. Microscopy* 119: 141-152, 1980.
4. D. Van Dyck, "High-speed computation techniques for the simulation of high resolution electron micrographs," *J. Microscopy* 132: 31-42, 1983.
5. R. Kilaas and R. Gronsky, "Real space image simulation in high resolution electron microscopy," *Ultramicroscopy* 11: 289-298, 1983.
6. R. Kilaas, "On the improved phase-grating method," *Ultramicroscopy* 19: 23-31, 1986.
7. K. Ishizuka and N. Uyeda, "A new theoretical and practical approach to the multislice method," *Acta Crystallographica* A33: 740-749, 1977.
8. R. Kilaas et al., "On the inclusion of upper Laue layers in computational methods in high resolution transmission electron microscopy," *Ultramicroscopy* 21: 47-62, 1987.
9. M. A. O'Keefe, "Resolution-damping functions in non-linear images," *EMSA/1979*, 556-557.

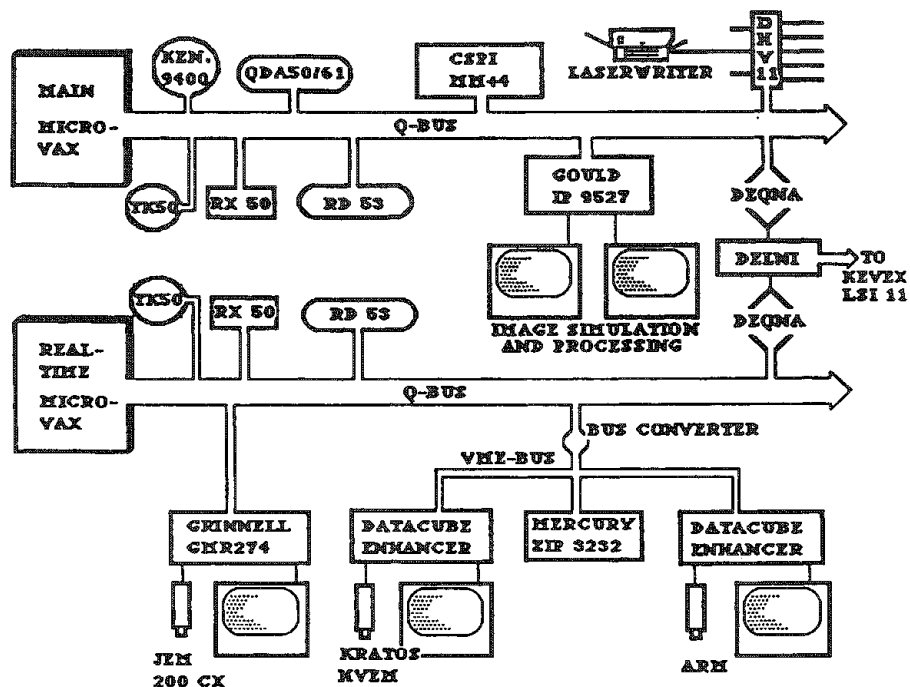


FIG. 1.--NCEM computer system for simulation and processing of transmission electron micrographs. TK50: 95 MB cartridge tape; RX50: dual floppy disk drives; RD53: 71 MB fixed disk; QDA50/61: controller with 503 MB formatted capacity Winchester disk; CSPI MM+4: 4 individual array processors; Gould IP9527: dual user image processor. Second MicroVax is used in real time data acquisition.

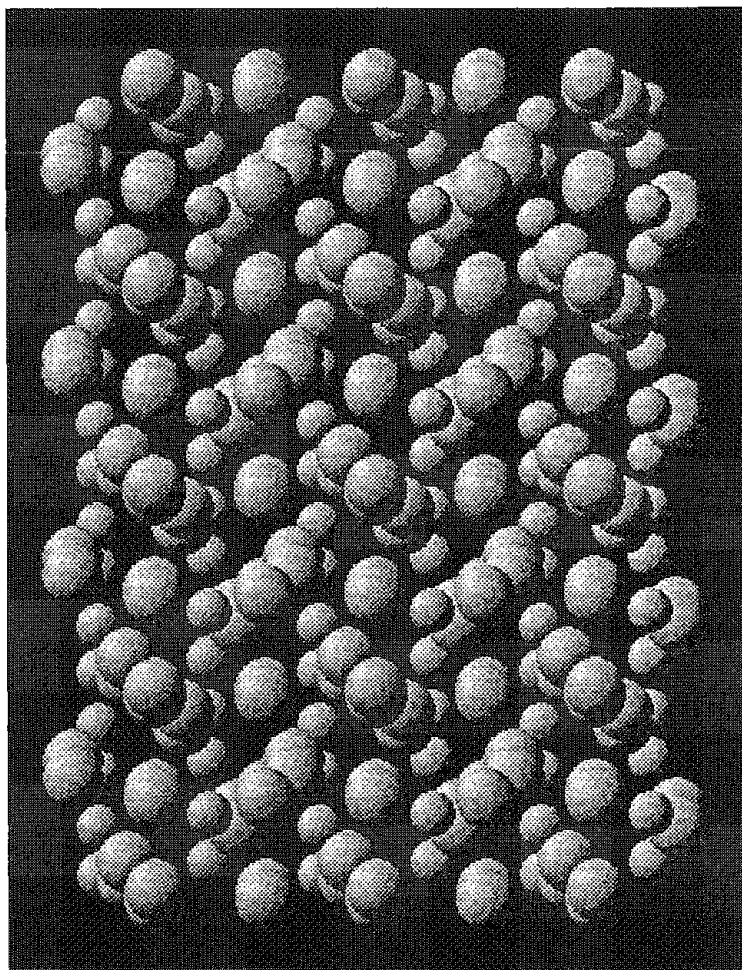


FIG. 2.--Display of section of orthorhombic  $\text{ZrO}_2$  structure viewed along 110 direction. Output routine courtesy of W. O. Saxton. This is the atomic model used in calculation of images in Fig. 3.



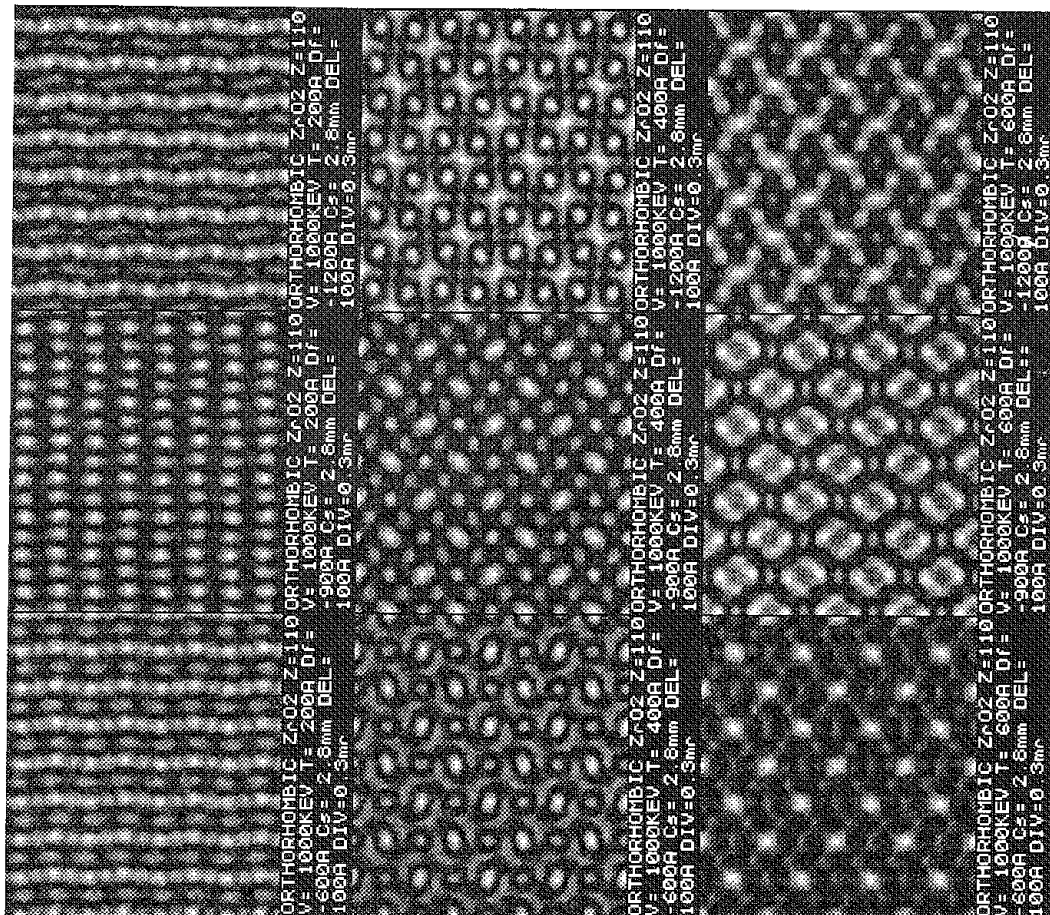


FIG. 3.--Limited through-focus/through-thickness series of computed images of orthorhombic phase of ZrO<sub>2</sub>. Images were first displayed on Gould framestore and subsequently printed on Apple LaserWriter.

PERSONAL	COMMON	NEXT PAGE	PREV. PAGE	DCL
AL203	AL3LI	AL3LVAC	ALUMINUM	
ANATESE	BAT1205	BAT103	BITE	
BITE4	BTEL1	BTEL4	BTEK	
BTEKNEW	COTE	C02S104	COPPER	
CUBE	CUBE121	C02S104	CULARGE	
CUT12	D100	DOLM	FAUJ001	
FAUJ110	FAUJPT	GALAS	GARS	
GENBO	GOLD	INP	INTERFACE	
INTERFACE1	LASRCU04	LAYER1	LAYER2	
MAGNESIUM	MOLYBDENUM	MZR	MZRO2	
OCTAHEDRON	PLATINUM	QU	QULARGE	
RUTILE	S13N4	S13N41FC	SICBETA	
SILICON	S102	S102EXT2	SPINEL	
SPINEL4	STACY	TEST	T102B	
ZIRCON	Z5H5			

USE DISPLAYED FILE

CREATE NEW FILE

RETURN

FIG. 4.--CENPAS menu showing existing structure files belonging to a user. Additional structures are available from space marked COMMON. These are Center files made available to all users.

INPUT FOR : ORTHORHOMBIC ZR02

DCL

SPACE GROUP # 61

ALPHA = 90.00

BETA = 90.00

GAMMA = 90.00

ZONE AXIS : 1 1 0

NO. OF SYMMETRY OPERATORS : 8

NO. OF SLICES PER UNIT CELL : 1

NO. OF ATOMS IN THE BASIS : 3

NO. OF DIFFERENT ATOMS : 2

MICROSCOPE : ARM

CS = 2.00

FOIL THICKNESS : 600.00

DEL = 100.00

AMPLIT. OUTPUT FOR PLOTTING : YES

TH. = 0.30

THE INDICES ARE : H K L

VOLT. = 1000.00

CENT. OF LAUE CIRCLE: H = 0.00

K = 0.00

OBJ. LENS DEFOCUS : -1200.00

APERTURE RADIUS : 0.70

CENT. OF OBJ. APRT. : H = 0.00

K = 0.00

CENT. OF OPTIC AXIS : H = 0.00

K = 0.00

CHANGE

SHOW BASIS

PHSORT

IMAGE

DISPLAY

CTF

RUN

SHOW ATOMS

MSLICE

AMPLIT

VIEW FILE

RETURN

FIG. 5.--CENPAS menu showing pertinent information regarding simulation of particular structure. Most important structural data, together with microscope data, are displayed in this menu. Multislice calculations are run from here.

#	TYPE	NAME	X	Y	Z	DW	OCC	
1	1	ZR	0.1340	0.0334	0.2500	0.2000	1.00	DCL
2	1	ZR	0.0340	0.4666	0.7500	0.2000	1.00	PAGE +
3	1	ZR	0.0660	0.5334	0.2500	0.2000	1.00	PAGE -
4	1	ZR	0.0660	0.9666	0.7500	0.2000	1.00	PAGE #
5	1	ZR	0.0660	0.9666	0.7500	0.2000	1.00	
6	1	ZR	0.0660	0.5334	0.2500	0.2000	1.00	
7	1	ZR	0.1340	0.4666	0.7500	0.2000	1.00	
8	1	ZR	0.0340	0.0334	0.2500	0.2000	1.00	
9	2	O	0.0411	0.3750	0.1292	0.2000	1.00	
10	2	O	0.5411	0.1250	0.6705	0.2000	1.00	
11	2	O	0.9589	0.0750	0.3705	0.2000	1.00	
12	2	O	0.4589	0.6250	0.6292	0.2000	1.00	
13	2	O	0.9589	0.6250	0.0705	0.2000	1.00	
14	2	O	0.4589	0.0750	0.1292	0.2000	1.00	
15	2	O	0.0411	0.1250	0.6292	0.2000	1.00	
16	2	O	0.5411	0.3750	0.3705	0.2000	1.00	
17	2	O	0.2280	0.7500	0.5000	0.2000	1.00	
18	2	O	0.7280	0.7500	0.5000	0.2000	1.00	
19	2	O	0.7720	0.2500	0.0000	0.2000	1.00	
20	2	O	0.2720	0.2500	0.0000	0.2000	1.00	RETURN

FIG. 6.--Display of atom positions generated by application of symmetry operators to basis atoms. Orthorhombic phase of  $ZrO_2$ .

#	SYMMETRY OPERATOR	#	SYMMETRY OPERATOR	
1	X,Y,Z	21	1/3+Y-X,2/3+Y,1/6+Z	DCL
2	-Y,X-Y,Z	22	1/3+Y,2/3+X,1/6-Z	PAGE +
3	Y-X,-X,Z	23	1/3-X,2/3+Y-X,1/6-Z	PAGE -
4	-X,-Y,-Z	24	1/3+X-Y,2/3-Y,1/6-Z	
5	Y,Y-X,-Z	25	2/3+X,1/3+Y,1/3+Z	
6	X-Y,X,-Z	26	2/3-Y,1/3+X-Y,1/3+Z	
7	-Y,-X,1/2+Z	27	2/3+Y-X,1/3-X,1/3+Z	
8	X,X-Y,1/2+Z	28	2/3-X,1/3-Y,1/3-Z	
9	Y-X,Y,1/2+Z	29	2/3+Y,1/3+Y-X,1/3-Z	
10	Y,X,1/2-Z	30	2/3+X-Y,1/3+X,1/3-Z	
11	-X,Y-X,1/2-Z	31	2/3-Y,1/3-X,5/6+Z	
12	X-Y,-Y,1/2-Z	32	2/3+X,1/3+X-Y,5/6+Z	
13	1/3+X,2/3+Y,2/3+Z	33	2/3+Y-X,1/3+Y,5/6+Z	
14	1/3-Y,2/3+X-Y,2/3+Z	34	2/3+Y,1/3+X,5/6-Z	
15	1/3+Y-X,2/3-X,2/3+Z	35	2/3-X,1/3+Y-X,5/6-Z	
16	1/3-X,2/3-Y,2/3-Z	36	2/3+X-Y,1/3-Y,5/6-Z	
17	1/3+Y,2/3+Y-X,2/3-Z			
18	1/3+X-Y,2/3+X,2/3-Z			
19	1/3-Y,2/3-X,1/6+Z			
20	1/3+X,2/3+X-Y,1/6+Z			

FIG. 7.--Display of symmetry operators associated with particular space group. These symmetry operators are maintained in database that provides information on all 230 space groups. Symmetry operators are easily customized from menu.

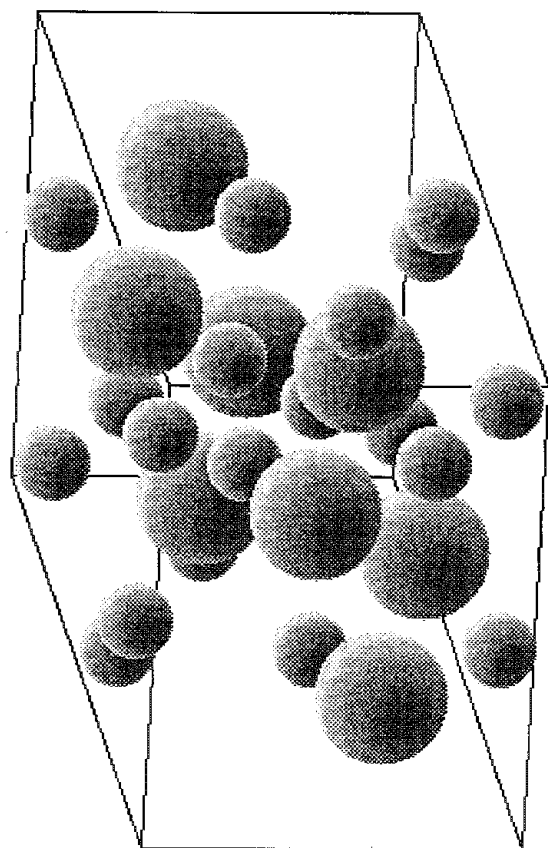


FIG. 8.--Display of  $ZrO_2$  unit cell viewed from 542 direction. Small spheres represent oxygen atoms.

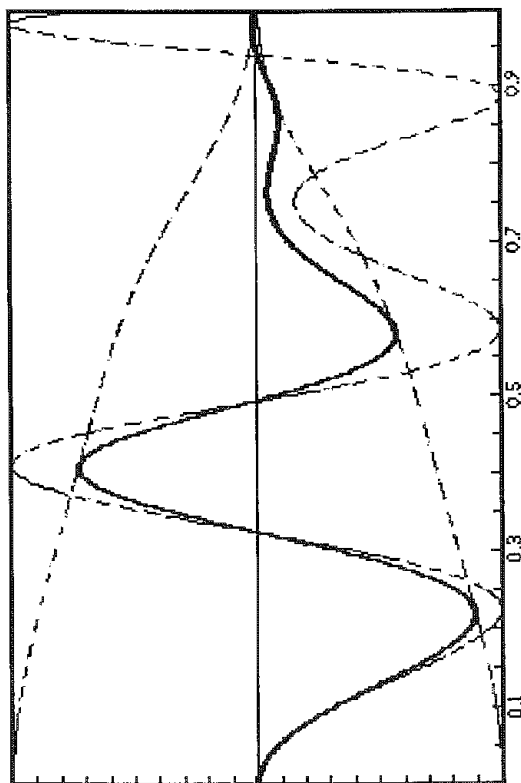


FIG. 9.--Contrast transfer function with and without damping.

Scattering Vector [  $\text{\AA}^{-1}$  ]

Accel.Voltage = 1000.0 kV  
Spher. Abber. = 2.8 mm  
Obj. Lens Def. = -1200.  $\text{\AA}$   
Delta = 100.  $\text{\AA}$   
Div. Angle [Half] = 0.30 mrad



IP9527-0	IP9527-1	GRINNELL	TERMINAL
MANIPULATE THE IMAGE PROCESSOR			
POTENTIAL	HISTOGR	CORREL	#UN.CLS
EXIT-WF	HIST.EQ.	ADJ.CNT	ZOOM IN
DIFFR.PAT.	EXPAND	FILTER	ZOOM OUT
IMAGE	REDUCE	FFT	DISPLAY
EXP. IMAGE	ROTATE	INV.FFT	LASER
DCL			
EXECUTE			
SAVE			
CANCEL			
RETURN			

FIG. 10.--CEMPAS menu indicating how user can choose to select sequence of operations to be performed on selected source, image, diffraction-pattern, etc., and display result.

SET BLACK-WHITE	WHITE	BLACK	INPUT	WHITE
	0	1	0.5	1
	BRIGHTNESS			
DECR.	INCR.			
CONTRAST				
1.0				
DOWN				
UP				
RETURN				

FIG. 11.--Menu showing current setting of image brightness and contrast with options to change these settings.

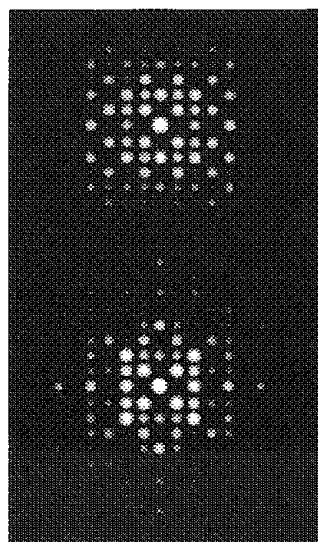


FIG. 12.--Computed dynamical diffraction pattern (left) and computed power spectrum of corresponding image (Fig. 13).

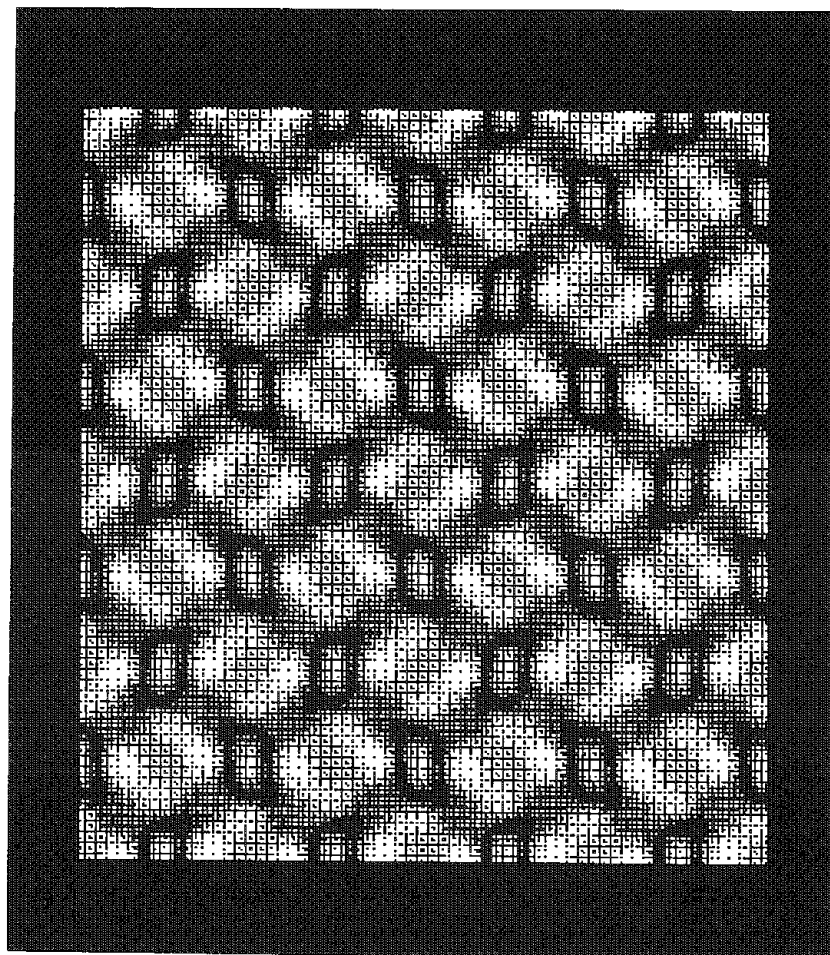


FIG. 13.--Print of terminal screen showing halftone image; each image-point is represented by square of 5 x 5 pixels.

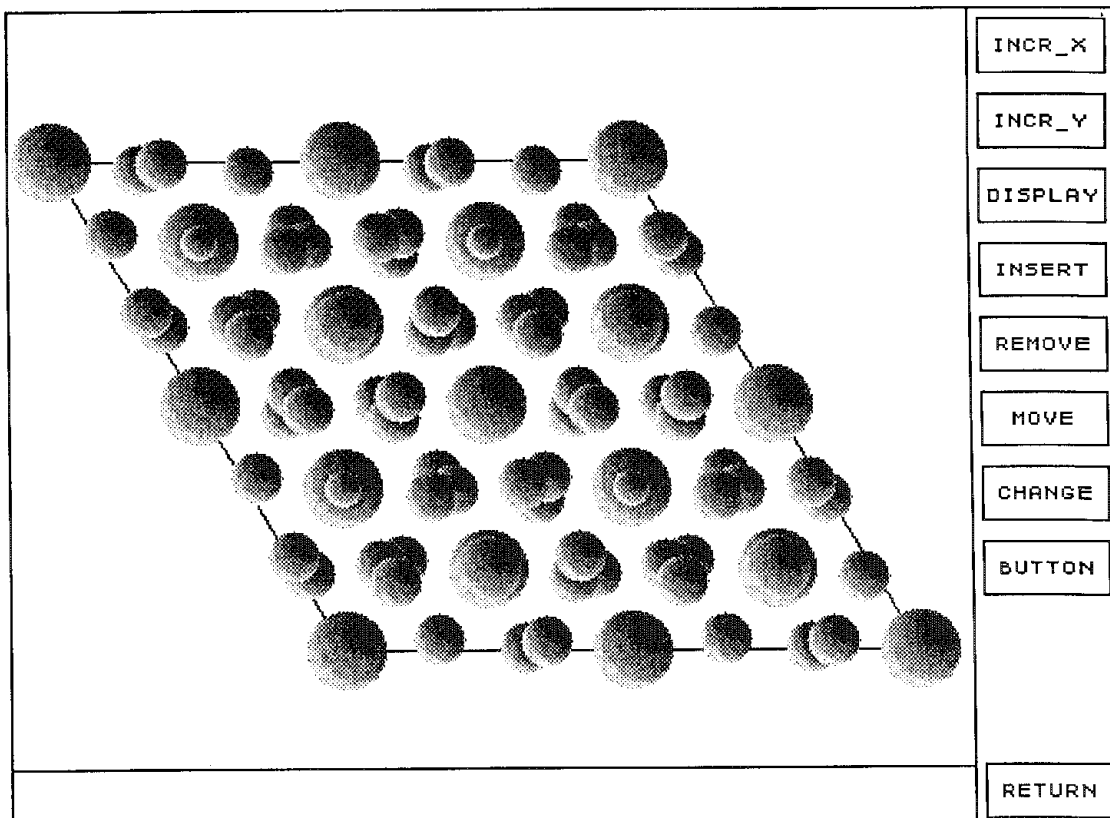


FIG. 14.--CEMPAS menu indicating how user can construct unit cell for use in image calculation.

\*\*\*\*\* CONSTRUCT PHASE-GRATING SEQUENCE \*\*\*\*\*

LAYER #	NAME	UNIT CELL THICKNESS
1	LAYER1	3.00
2	LAYER2	3.00
3	LAYER3	3.00

TOP - 0.00 A

16.00

57.00

81.00

BOTTOM - 81.00 A

RESET

REMOVE

DEF LAY

DEL LAY

DEPOSIT

INSERT

REPEAT

PHASE-GRATING SEQUENCE :

1 1 1 1 1 2 2 2 2 2 2 2 2 2 2 2 3 3 3 3 3

3 3

RETURN

FIG. 15.--Menu used to construct specimen where composition varies along incident-beam direction.

## TECHNIQUES FOR COMPUTER-AIDED IMAGING IN SEM AND STEM

J. J. McCarthy, D. A. Christenson, and J. C. Seymour

Digital control of image collection from scanning instruments such as the SEM and STEM has led to a new generation of image analysis equipment. New modes of image collection coupled with digital image enhancement can minimize sample exposure to the electron beam and still provide acceptable or superior images. In addition, the investigator can also collect, analyze, and correlate analytical data (for example, chemistry and mean atomic number) with morphological data extracted from the stored image. The analytical data simplify feature analysis problems that are difficult to solve by gray-level segmentation techniques alone. The additional analytical parameters also complicate feature classification and have led to the development of more complex sorting schemes.

This paper describes some of the techniques for computer-aided imaging currently available and their use in several applications. A specific instrumental configuration (TN-5700) is briefly described.

### *System Description*

The system used in this work consists of an integrated image processor and microanalysis system. The major components of the image processor (TN-5700) are a 12.5MHz 68010 (CPU), disk interface and associated I/O controllers, a pipelined image processor (PIP), two variable-size image memories (up to  $1024 \times 1024 \times 16$  bits each), an image display controller ( $640 \times 480$  pixels, 8 image bits plus 3 overlay bits) and an integrated microanalysis system (TN-5500) with its own processors. Data acquisition interfaces include a video camera digitizer, a passive digitizer that synchronizes to external scan signals, and a high-performance digital scan generator (HPDSG). The operator controls include an ASCII keyboard with softkeys, a touchpad for dedicated functions, and a mouse. Analytical data are exchanged between processors over high-speed parallel and serial ports.

The HPDSG and the PIP have been designed to enhance image collection from the electron microscope (EM). The HPDSG can digitize signals from four video inputs simultaneously at programmable scan sizes and rates up to a maximum of  $1024^2$  pixels at 5 frames/s. Image data can be averaged on a frame-by-frame basis by the PIP during collection. An additional dedicated high-speed interface from the TN-5500 to the image processor allows x-ray images to be collected and averaged at video scan rates.

---

The authors are at Tracor Northern, Inc., 2551 West Beltline Highway, Middleton, WI 53562. They wish to thank J. Walker and G. Fritz of Tracor Northern for their assistance in developing the Locked-Liberated Analysis procedure.

### *Application Examples*

*Image Noise Reduction by Kalman Frame Averaging.* In general, TV rate EM images have a poor signal-to-noise ratio (SNR) due to the small number of electrons collected at each pixel. A poor SNR obscures detail in the image and makes fine adjustment of the microscope difficult. Image quality at slower scan rates can also be noise limited when extremely low beam currents are required to obtain high resolution or to prevent damage to the specimen. One can address the problem of poor SNR in images by averaging the video signal to reduce noise. A traditional method by which one can improve SNR is to average the video signal by slowing down the raster speed and recording the image on film. This type of averaging has the disadvantages that long exposure time is required, and the image cannot be viewed until the exposed film has been developed. These disadvantages can be overcome by use of a digital image processor that is capable of digital frame averaging. Many image processors employ some form of temporal digital filtering to average input signals. The averaging filter (frame integration) and first-order recursive filters (exponential frame averaging) have been widely used. An alternative technique, Kalman filtering, has been shown to produce optimal frame averaging.<sup>1</sup> Kalman filtering requires specialized hardware and software beyond that required for frame integration or exponential averaging. All three techniques have been implemented in this system.

Figure 1 contrasts the SNR improvement of the three techniques and illustrates why the Kalman filter is optimal. The vertical axis plots the improvement in the SNR (in dB) after averaging compared to the SNR of a single frame. The horizontal axis is the number of frames averaged. The diagonal solid line is the maximum theoretical improvement of SNR that could be obtained. Frame integration and Kalman averaging give SNR improvements close to the theoretical result. However, the Kalman average can be viewed on a frame-by-frame basis during acquisition (5 frames/s), whereas the result of frame integration cannot. The slight deviation of the experimental Kalman curve from the theoretical curve after a high number of frames is due to image shift after a long time and not to a failure of the averaging technique. The final curve shows the results of exponential averaging for one choice of filter constants. This type of filter never provides the SNR improvements of the other methods and soon reaches a steady-state SNR that depends on the filter constant. In any event, the SNR improvement is never as good as by frame integration or Kalman filtering.

To summarize, in contrast to other types of frame averaging, Kalman filtering provides both optimal SNR improvement and the ability

to see the image on a continuous frame-by-frame basis.

*Image Enhancement by On-line FFT Processing.* In a series of papers, Hashimoto and his coworkers<sup>2</sup> have described the use of FFT processing for image enhancement and for measurement of imaging parameters in high-resolution EM. Similar applications of the FFT have been reported for SEM images.<sup>3</sup> The TN-5700 can perform a complex 2-D FFT on a  $512^2$  pixel image in 15 s. We have used this capability to remove artifacts in images (such as 60Hz noise) and to enhance the visibility of structures in low-dose, high-resolution images.

Figure 2 illustrates the use of the 2-D FFT to remove periodic artifacts from an image. Figure 2(a) is the original secondary-electron image of a semiconductor chip with 60Hz noise. The transform of the image (Fig. 2b) has a central region with two spots above and two spots below it. These spots were edited out of the transform by use of a mask function (Fig. 2c) and the inverse transform was performed. The result is the final enhanced image (Fig. 2d).

Figure 3(a) is a low-dose, high-resolution image of a faujasite ([111] axis), a type of zeolite. The image is very noisy, so that it is difficult to see any structure. The image was transformed (Fig. 3b) and multiplied by a mask function (Fig. 3c). The inverse Fourier transform of this image is shown in Fig. 3(d). The zeolite microstructure is clearly visible in the enhanced image.

*X-ray Mapping at Video Scan Rates.* Traditional x-ray dot mapping suffers from several drawbacks. Since x-ray counting rates are inherently much slower than video signal collection, long scan times are required to obtain a highly detailed x-ray dot map. The final result is not known until the entire process is complete and recorded on film for viewing. At faster scan rates, the amount of data collected is insufficient to determine which areas produce characteristic x rays versus background x rays, except in the rather trivial case of high elemental concentrations. Point-by-point digital x-ray mapping is a partial solution to these difficulties. Background subtraction is easily accomplished during the mapping acquisition and dwell times can be adjusted to obtain good mapping results for small concentrations. The disadvantage of point digital mapping is that it often takes even longer to collect a map than a traditional dot map. The longer dwell times per point and the line-by-line collection can be a problem during map collection on beam-sensitive materials. Again, the final result is not known until the last line of data is collected.

The image processing system we have used can acquire x-ray maps at video scan rates (video rate x-ray mapping, or VRXM), a decided advantage over other types of digital mapping despite the long overall collection time. In the VRXM mode, the image processor (TN-5700) accepts x-ray counts from the EDS system (TN-5500) at maximum rates. The TN-5700 correlates the X and Y location of each x-ray event as it occurs, even at near video scan rates. As the TN-5500 continues to accept valid x-ray events,

the TN-5700 updates the x-ray map in its memory. The result is an x-ray image of the entire area being scanned. As frame after frame is collected, the image is continually integrated and improves in clarity. In addition, rapid scanning minimizes beam damage on sensitive materials. VRXM images can be collected simultaneously with video images of the same area and at the same resolution, so that immediate comparison with specific features of interest is provided. After a few frames, the operator can often assess the entire map being built up and decide to alter collection conditions and start again. Once satisfied that the conditions are optimum for the desired map results, a long-term, many-frame map can be acquired for the best statistical result.

In an illustration of VRXM (Fig. 4), the display has been divided into quadrants each presenting a  $256 \times 256$  pixel image. Three of the images are 16-bit x-ray maps for Au, Cu, and Fe; the fourth image is the averaged backscattered electron signal. The sample contains NBS Au-Cu SRMs in the form of wires embedded in epoxy mounted in a stainless-steel holder. Figure 4(a) was taken after only a few seconds of x-ray image acquisition; although some features are defined, it is difficult to discern any detail. Figure 4(b) was taken after several minutes of collection; variations in elemental concentration are shown quite clearly.

*Analysis of Locked Versus Liberated Mineral Phases.* The combination of x-ray images with the normal gray-level image can be applied to analysis problems difficult to solve by use of video signals only. An example is the determination of mineral particle liberation in an ore-beneficiation process. Traditional approaches rely on the contrast present in the backscattered electron (BSE) signals to separate the various ore phases from the gangue. This separation is quite difficult, if not impossible, in samples that contain phases with very similar average atomic numbers and thus produce nearly equal BSE intensities; e.g., cubanite ( $\text{CuFe}_2\text{S}_3$ ) and chalcopyrite ( $\text{CuFeS}_2$ ), which differs by only 0.003 mean backscatter coefficient at 20 kV.

The first step in the locked-liberated analysis is to obtain both BSE and x-ray images of the field of interest. The BSE image can be used to prepare a binary image of all the mineral particles (locked, liberated, and gangue). A binary image is then prepared for each phase to be measured, based on segmentation of up to 16 individual x-ray images or additional BSE images. All these phase images are later combined into a single composite phase image. As each mineral particle in the primary BSE image is measured, data from each included phase are obtained from the analysis of the intersection of the image of the measured feature with the composite phase image.

This type of analysis is illustrated in Figs. 5 and 6. The upper half of Fig. 5 is a portion of the primary BSE image of the specimen; the lower half shows the 8 x-ray images used in the construction of the composite phase image. Data were obtained from a number of fields, and stored for use by a database

program which allows sorting of data, plotting results, and calculation of computed results. A typical result is a histogram of the type shown in Fig. 6. The x-axis of the histogram is the parentage area that this particular included phase represents in each mineral particle. The y-axis is the area fraction that each x-axis bin represents of the total mineral present.

#### References

1. S. J. Erasmus, *J. Microsc.* 127: 29, 1982.
2. H. Hashimoto, *Electron Microscopy Technique* 2: 1, 1986.
3. S. J. Erasmus, D. M. Holburn, and K. C. A. Smith, *Scanning* 3/4: 273, 1980.

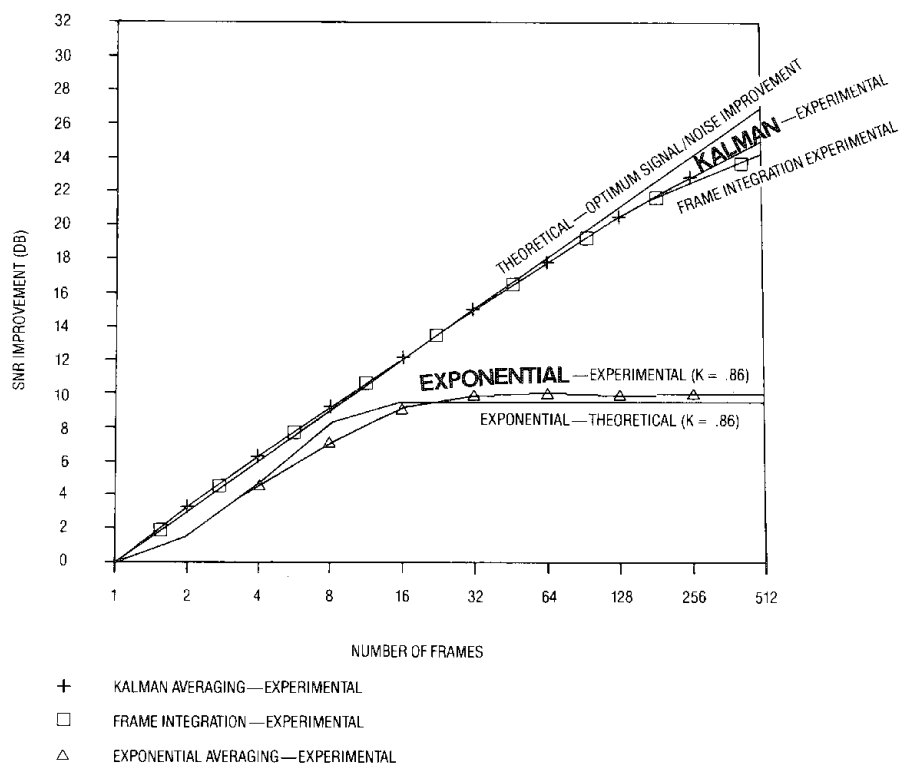


FIG. 1.--Signal-to-noise ratio improvement versus number of frames averaged. Solid lines are theoretical calculation.

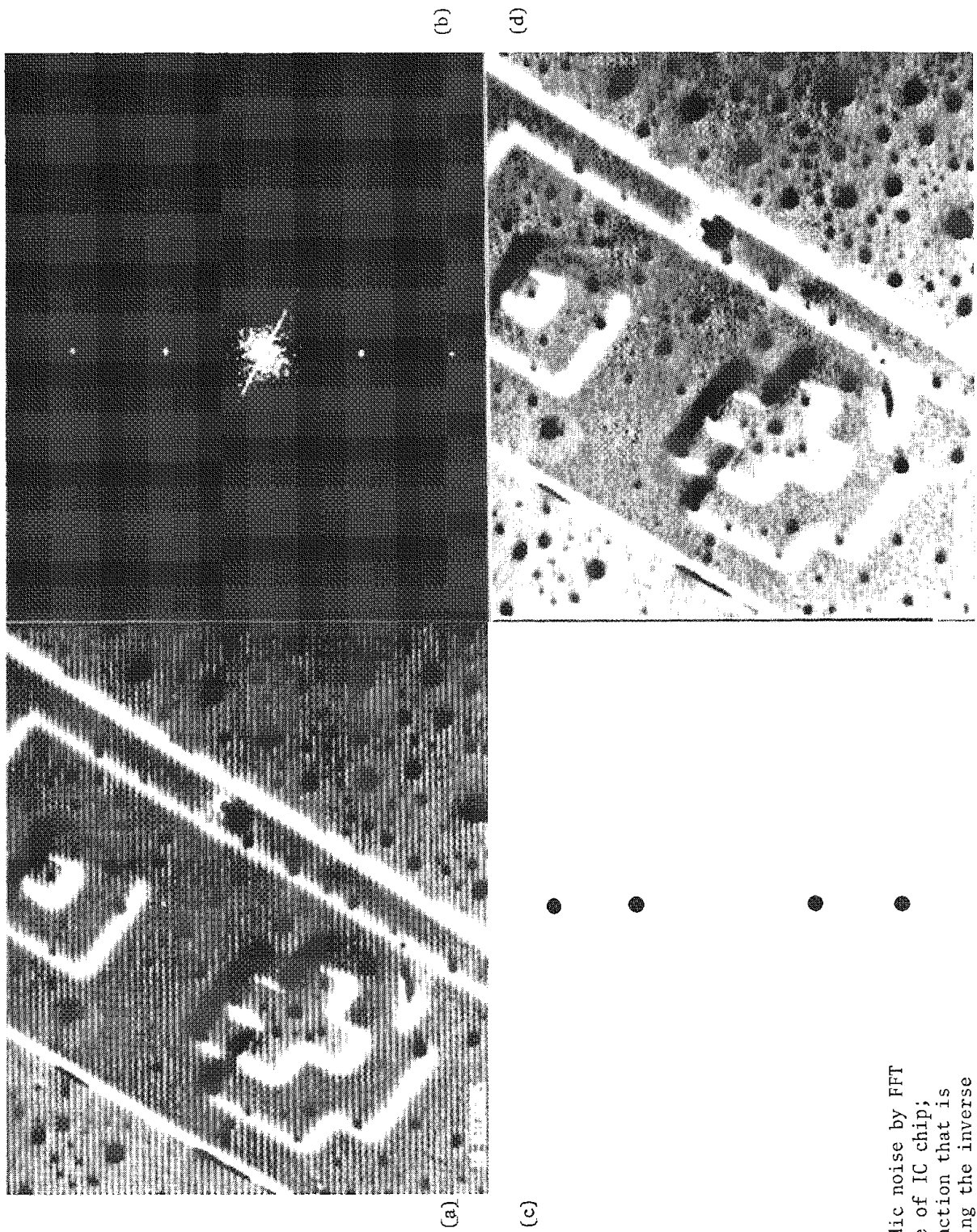


FIG. 2.--Elimination of periodic noise by FFT processing: 2a) original image of IC chip; 2b) 2-D FFT of 2a; 2c) mask function that is applied to 2-D FFT before taking the inverse transform; and 2d) final image, the inverse 2-D FFT of 2c.

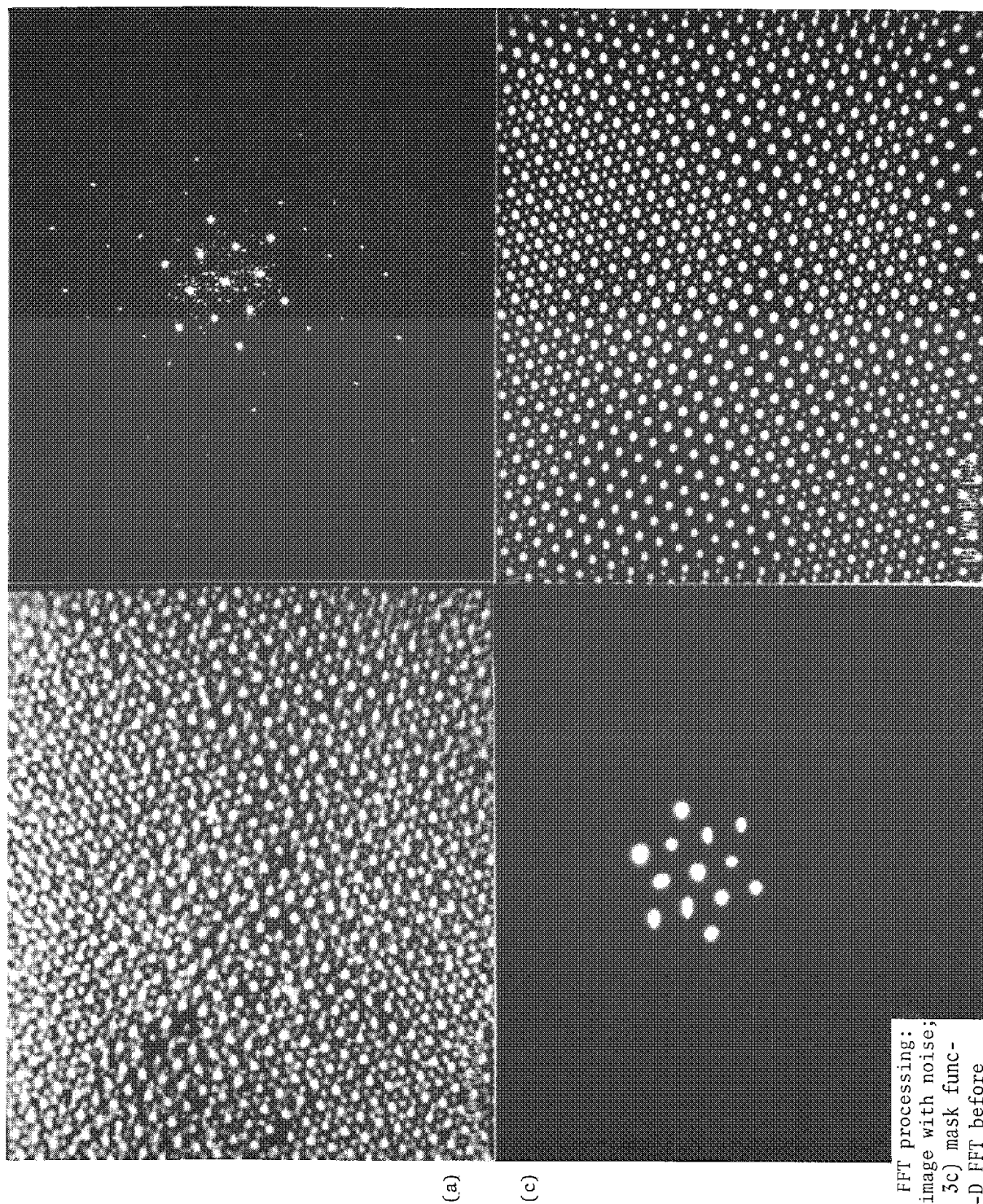


FIG. 3.--Image enhancement by FFT processing: 3a) original low dose xcolite image with noise; 3b) 2-D FFT of original image; 3c) mask function that is applied to the 2-D FFT before taking inverse transform; and 3d) final enhancing image.



FIG. 4.--X-ray mapping at video scan rates. Sample is NBS Au-Cu SRM wires mounted in epoxy in stainless-steel mount. (a) Three x-ray images and BSE image after collection time of a few seconds. (b) Same images after collection time of several minutes. Differences in concentration levels are now quite clear.

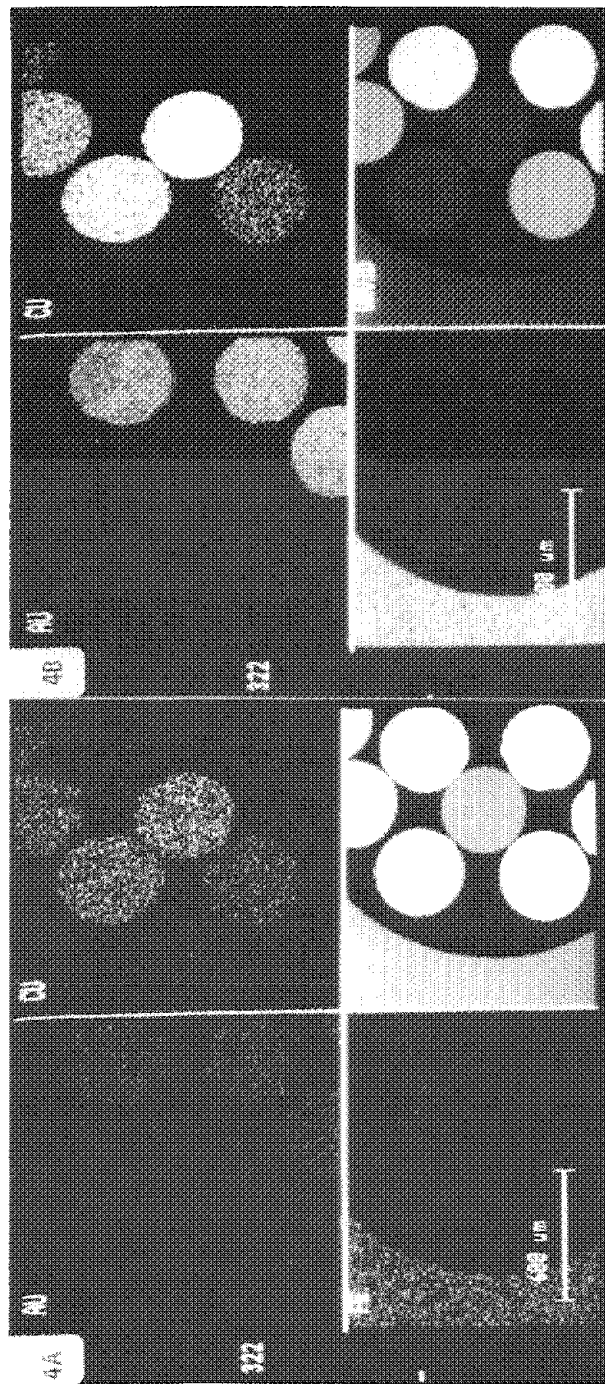
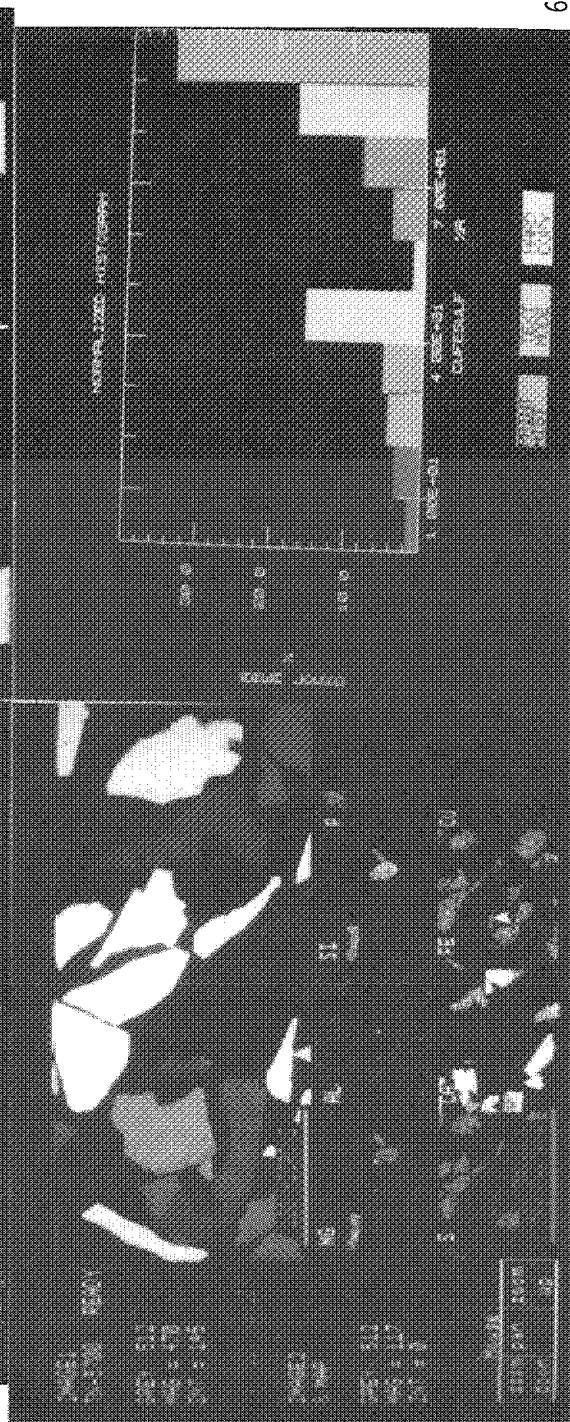


FIG. 5.--Images analyzed for mineral liberation study. Upper half is BSE image of specimen and shows some included ore phases. Lower half is x-ray images for eight elements used to discriminate specific phases.

FIG. 6.--Histogram of results from liberation analysis. Contents of each bin are area fraction of this (chalcopryite) phase relative to total mineral area measured. Bins are plotted as function of area of this locked phase computed as percent of gangue particle that contains it.



## COMPUTER-GENERATED THREE-DIMENSIONAL MICROSTRUCTURES

M. Lakshminarasimha and P. F. Johnson

Microstructure evolution during phase transformations has been modeled by several authors<sup>1-5</sup> in two dimensions, and for situations involving 100% transformation. In this paper, we discuss microstructure modeling in three dimensions that includes incomplete (i.e., 100%) transformation in addition to the more traditional space-filling case. The geometry and topology of the microstructures and their distributions have been calculated in three dimensions at progressive stages of growth. The calculated microstructural features take into account the effects of impingement between grains. Some of the features are compared with those obtained from real microstructures.

Computer modeling of microstructures has several uses. The impingement behavior of grains can be studied only by computer modeling. Microstructural modeling in three dimensions can serve as a potential tool for establishing more realistic and accurate microstructure-physical property relationships. Sintering behavior may also be studied from this kind of a model.<sup>6</sup>

### Computer Simulation Procedure

The parent phase, called  $\alpha$  phase throughout, is modeled as a cube of side 256 units in which a new phase  $\beta$  is nucleated randomly and grown. Any type of nucleation--simultaneous (cell-model),<sup>7</sup> constant, or decreasing rate--may be the input. The  $\beta$  grains are assumed to grow isotropically. Since we are primarily concerned with effects that result from the geometry of the microstructure during its evolution, the assumption of any nucleation or growth mechanism is not crucial to any of the conclusions that can be drawn, and could be modified if necessary. While growth is taking place, the microstructure is analyzed at progressive times  $t$  corresponding to different times during the transformation process. The  $\beta$  volume,  $\alpha\beta$  interface area,  $\beta\beta$  interface area, total surface area ( $\alpha\beta + \beta\beta$ ), and average radius of each grain are calculated in spherical coordinates.

Each element tested is either a volume, area, edge, or a corner element of the microstructure. If an element is reached *earliest* by only one growing grain, it is a  $\beta$  volume element. If it is reached by two growing grains simultaneously, it is a  $\beta\beta$  interfacial (grain boundary) area element. Similarly, three and four or more grains reaching an element simultaneously form respectively the edges and the corners of  $\beta$  grains. If an element has not been included in a  $\beta$  grain, it belongs to the parent  $\alpha$  phase. Once a tested element is assigned to a grain, it always

remains in that grain; that is, grain growth following impingement has not been incorporated into the model.

As shown in Fig. 1, a point X that falls on the boundary of a grain is first located at a distance  $R(\theta, \phi)$ . Similarly, points Z, Y, and W on the boundary at  $R(\theta + \delta\theta, \phi)$ ,  $R(\theta, \phi + \delta\phi)$ ,  $R(\theta + \delta\theta, \phi + \delta\phi)$  are found. The volume contained within the grain is calculated from the formula for the volume element  $dV$  in spherical coordinates,  $dV = r^2 \sin \theta d\theta d\phi dr$ , which leads to

$$\Delta V = \frac{R^3(\theta, \phi) \sin \theta \Delta \theta \Delta \phi}{3}$$

The volume element  $\Delta V$  is summed over all  $\theta$  and  $\phi$  to yield the volume of the grain  $V$ :

$$V = \frac{\sum_{\phi=0}^{2\pi} \sum_{\theta=0}^{\pi} R^3(\theta, \phi) \sin \theta \Delta \theta \Delta \phi}{3}$$

The element of surface area  $XYWZ$  on the boundary of the grain is calculated from Fig. 1 as:

$$\begin{aligned} \Delta A &= YX \times XZ \\ &= \sqrt{[R(\theta, \phi) \sin \theta \delta \phi]^2 + [R(\theta, \phi + \delta \phi) - R(\theta, \phi)]^2} \\ &\times \sqrt{[R(\theta + \delta \theta, \phi) - R(\theta, \phi)]^2 + [R(\theta, \phi) \delta \theta]^2} \end{aligned}$$

The total grain boundary area  $A$  associated with a grain is similarly obtained by summation over all  $\theta$ 's and  $\phi$ 's:

$$A = \sum_{\phi=0}^{2\pi} \sum_{\theta=0}^{\pi} \Delta A$$

The average radius  $R_{av}$  of each grain is calculated by averaging of the radius vector to the boundary  $R_b$  over all  $\phi$  and  $\theta$ .

$$R_{av} = \frac{\sum_{\phi=0}^{2\pi} \sum_{\theta=0}^{\pi} R_b(\theta, \phi)}{(2\pi/\Delta \phi)(\pi/\Delta \theta)}$$

The above procedure is repeated for all grains in the volume at progressive times of evolution of microstructure, which yields the distributions of geometric properties and their variation with time. When growth proceeds to 100% transformation into  $\beta$ , the whole region of space is occupied (space-filled case). For this situation the distributions of topological properties such as faces, edge lengths, and average number of sides/face are computed and compared to their average values calculated by Meijering.<sup>7</sup> These distributions may be determined from Euler's law, according to which each grain is a polyhedron in three dimensions with  $f$  faces,  $e$  edges, and  $c$  corners that satisfy the relation  $f + c - e = 2$ .

The authors are with the College of Ceramics of Alfred University, Alfred, NY 14802.

In three dimensions, each corner is an intersection of a minimum of four edges. Even in reality the occurrence of more than four edges at a corner, as suggested by Smith,<sup>8</sup> is very rare. It is therefore assumed that every corner in the computed microstructure is an intersection of only four edges. Of these four, only three belong to a polyhedron and each edge terminates in two corners. Therefore for each polyhedron,  $3e = 2c$  and  $f - (c/2) = 2$ . By knowing the number of corners belonging to each polyhedron, one can calculate the number of faces on each grain from the above formula. Each corner of a grain is equidistant from at least four closest grain centers. The corner is therefore the center of an irregular tetrahedron formed by the closest four grain centers, which was easily calculated from coordinate geometry and vector algebra. (A more detailed discussion of the derivation of the model as well as the computer code in FORTRAN 77 is available on request.)

### Results

Microstructural evolution was studied for the cell model with random simultaneous nucleation of 2000, 1000, and 400  $\beta$  sites in a cube of  $\alpha$  phase with edge length equal to 256 units. The microstructure was analyzed in three dimensions from the instant of nucleation of the  $\beta$  phase to 100% transformation of  $\alpha$  phase to  $\beta$  phase. Growth velocity of the  $\beta$  phase was isotropic. The volumes, areas, and average radius were calculated by the program at progressive stages of microstructural evolution. To eliminate effects at the boundary of the cube, all nuclei that grew and eventually intersected the faces of the cube were ignored. Two-dimensional sections were taken from the three-dimensional computer-generated microstructure by selection of a random plane and plotted (Fig. 2).

The computer-calculated surface areas and edge lengths for the 100% transformation (space-filling) case are compared with the average values predicted by Meijering<sup>7</sup> in Tables 1 and 2. A good agreement of the computer-calculated average values with those predicted by Meijering's cell model is apparent, so that the correctness of the computer calculations is verified.

Figure 3 shows an Avrami plot<sup>9</sup> of the volume fraction transformed with time for 400, 1000, and 2000 sites. The transformed fraction  $V_v$  follows the Avrami equation;

$$V_v = 1 - \exp(-kt)^n$$

A straight-line behavior with a constant Avrami exponent  $n$  of 3.0 is shown for all three predicted structures.

The geometric properties of the microstructure are analyzed in terms of the growth path,<sup>10</sup> for grains falling in five different size classes ranging from 10 to 90 cumulative per cent finer than (CPFT) size. This classification was found to be necessary because one cannot plot the growth path for every grain, even though the computer program keeps track of them. The same size class can be used for all times because a grain bigger than another at any time always remains so as growth takes

place. For these five classes of grain, grain volume and various surface areas are plotted as functions of time of evolution of the microstructure, in Fig. 4. These five classes represent the growth path behavior of the average grain in each size class. Figure 4(a) shows that at small times the volume of all grains increase rapidly because of relatively few impingements. As time goes by, the smaller grains (CPFT 10-50) increase less in volume (lower slope) than the larger grains (CPFT 70-90). This result is expected, since all grains have the same size soon after nucleation and as growth proceeds, the grains that grow less are the ones that have more impingements. Therefore growth retardation is greater for smaller grains than for larger grains. Figure 4(b) shows a similar growth path for  $\beta\beta$  and the total surface area, but the  $\alpha\beta$  growth path is somewhat different. At small times, when only a few grains are impinging, the  $\alpha\beta$  interface area increases, but with time the  $\alpha\beta$  area is consumed because of more impingement between neighboring grains. As a result the  $\alpha\beta$  area reaches a maximum after a certain time and starts decreasing. Again, the bigger grains (CPFT 70-90) have a maximum area at longer times than the smaller grains. This effect is shown in Fig. 4(b), where the maximum  $\alpha\beta$  area is reached at time  $t < 10$  units for smaller grains (CPFT 10-50) and the maximum is not reached until  $t = 10-12$  units for larger grains (CPFT 70-90).

Information about faces, edges, and corners of grains can be used to model grain growth after 100% transformation; therefore, the topological properties were analyzed for complete space filling (100% transformation) obtained after simultaneous nucleation of 2000 sites in a cube of  $256 \times 256 \times 256$  and growth to space filling. Again, to handle the boundary effects, the grains that intersect the boundaries of the cube were ignored. Thus, all topological properties described below were calculated for 1275 inner grains out of a total of 2000. Table 3 compares the mean topological properties of a grain calculated by Meijering for the cell model with those calculated by computer simulation for the situation described above. The good agreement confirms the correctness of the model.

The program calculates the distributions of these topological parameters, which cannot be done by use of the Meijering analysis. The results are described in Fig. 5, which shows the distribution of the number of faces on a grain for the calculated structure compared with the equivalent structure obtained experimentally by Williams and Smith for 91 grains.<sup>11</sup> Experimentally more grains with 10 faces were obtained, whereas the computer calculated more grains with 13-15 faces. The experimentally obtained distribution is different owing to grain growth that results in the disappearance of smaller grains. As growth proceeds, the faces with fewer sides disappear. Therefore grain growth after 100% transformation results in an overall decrease in the number of faces. That is why the experimentally observed distribution of number of faces shows more grains with smaller number of faces than those found by the computer

simulation, which does not consider the effects of grain growth after 100% transformation. The fact that grains with faces with fewer than four sides disappear during growth after 100% transformation is shown in Fig. 6. The experimental results show a very small fraction of three-sided faces while those calculated by the computer simulation show a substantially higher fraction of faces with three sides.

### Discussion

The cell model can be used as a good approximation of the microstructure resulting from phase transformations such as nucleation and growth and recrystallization. Many glass-ceramics systems have been observed to follow the Avrami equation,<sup>12</sup> which is a consequence of site saturation nucleation and growth. The results of the simulation give rise to an interesting impingement behavior. When all grains nucleate at the same time and grow isotropically, the smaller grains are shown to suffer more impingements. That means only that the impingement volume is greater for the smaller grains, not that the smaller grains have more neighbors. In fact it is seen from Fig. 7 that the smaller grains have a smaller number of faces and hence have fewer neighbors than the larger grains. This observation is well substantiated by experiments and theory.<sup>13-14</sup> A greater impingement area does not mean more neighbors.

Only site saturation nucleation (Meijering or Voronoi model) has been analyzed. The computer model also incorporates constant-rate nucleation (Johnson-Mehl model). A detailed discussion of the results of analysis of that model is in preparation.<sup>16</sup> Nucleation in which the rate changes with time can also be modeled but has not been analyzed.

### Conclusions

Three-dimensional microstructure has been modeled for site saturation nucleation and growth to impingement. The geometric properties and their distributions have been calculated in three dimensions and their mean values compared with those predicted. There is a good agreement between the computer-calculated mean values and those predicted by theory, so that the correctness of computer calculations in three dimension is confirmed. Comparison with experimentally observed microstructural parameters have been performed. Better agreement with experimentally determined results may be obtained if the effects of grain growth are incorporated into the model; that is to be the subject of future work. The present three-dimensional microstructure simulation will be extended to model sintering, grain growth after complete transformation, and correlation of microstructure with physical properties.

### References

1. K. W. Mahin, K. Hanson, and J. W. Morris Jr., *Acta metall.* 28: 443, 1980.
2. T. O. Saetre, O. Hunderi, and E. Nes, *Acta metall.* 34: 981, 1986.

3. H. J. Frost and C. V. Thompson, D. J. Srolovitz, Ed., in *Computer Simulation of Microstructural Evolution*, Toronto: Metallurgical Society, 1985, 33.
4. M. P. Anderson, G. S. Grest, and D. J. Srolovitz in Ref. 3, p. 77.
5. J. W. Ross, W. A. Miller, and G. C. Weatherly, *Acta metall.* 30: 203, 1982.
6. R. L. Coble, *J. Appl. Phys.* 32: 787, 1961.
7. J. L. Meijering, *Philips Res. Rep.* 8: 270, 1953.
8. C. S. Smith, *A Search for Structure*, Cambridge, Mass.: MIT Press, 1981.
9. M. Avrami, *J. Chem. Phys.* 7: 1103, 1939.
10. R. T. DeHoff, *Met. Trans.* 2: 521, 1971.
11. W. M. Williams and C. S. Smith, *Trans. AIME*, p. 755, 1952; *J. Metals*, July 1952.
12. N. P. Bansal, R. H. Doremus, A. J. Bruce, and C. T. Moynihan, *J. Am. Cer. Soc.* 66: 233, 1983.
13. F. N. Rhines and B. R. Patterson, *Met. Trans.* 13A: 985, 1982.
14. R. T. DeHoff and G. Q. Liu, *Met. Trans.* 16A: 2007, 1985.
15. E. N. Gilbert, *Ann. Math. Statistics* 33: 958, 1962.
16. M. Lakshminarasimha and P. F. Johnson (in preparation).

TABLE 1.--Computer-calculated geometric properties.

number of grains(N)	Total Volume (V)	Total Surface Area (S)	Total edge length (L)	number density (N <sub>v</sub> )
1275	10381468	1518412	149549	$1.228 \times 10^{-4}$
565	9141031	1056364	82713	$6.1809 \times 10^{-5}$
184	7255005	620843		$2.536 \times 10^{-5}$

TABLE 2.--Comparison between computer-calculated mean values and Meijering's calculations. N is number of grains completely surrounded by other grains. 2000, 1000, and 400 nuclei were found to yield the results shown. Total volume and surface area of 1275, 565, and 184 grains were used to obtain S<sub>p</sub>, so that boundary errors were avoided. CV is coefficient of variation as predicted by Gilbert<sup>15</sup> for cell model.

N	S <sub>p</sub>	S/N	L <sub>v</sub>	L/N	CV	
1275	.145	2381	$1.442 \times 10^{-2}$	349.9	.4228	Computer
	.146	2356	$1.4419 \times 10^{-2}$	351.9	.42	cell model
565	.1155	3739	$9.05 \times 10^{-3}$	146.4	.4321	Computer
	.1151	3723	$9.12 \times 10^{-3}$	147.5	.42	cell model
184	.008557	6748	—	—	.4366	Computer
	.008557	6742	—	—	.42	Cell model

TABLE 3.--Mean topological properties for single grain.

Quantity	Cell model <sup>7</sup>	Computer calculated
Number of faces	15.54	15.09
Number of edges	40.61	39.28
Number of corners	27.07	26.17

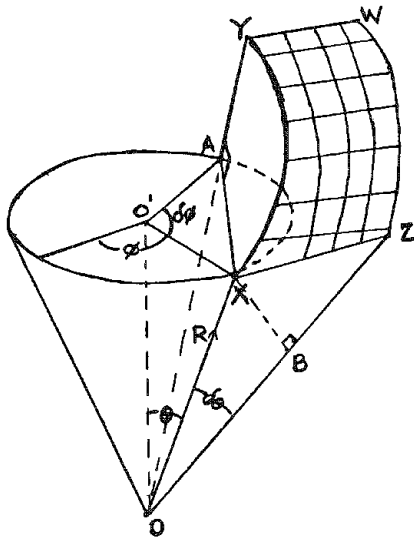


FIG. 1.--Analysis method of computer-calculated microstructure in spherical coordinates. O is grain origin (randomly selected nucleation site), cross-hatched area is grain-boundary element. After point X belonging to two grains is found, points W, Y, and Z are determined. Distance of these points from nucleation site of grain is  $OX = R(\theta, \phi)$ ,  $OY = R(\theta, \phi + \delta\phi)$ ,  $OZ = R(\theta + \delta\theta, \phi)$ ,  $OW = R(\theta + \delta\theta, \phi + \delta\phi)$ .

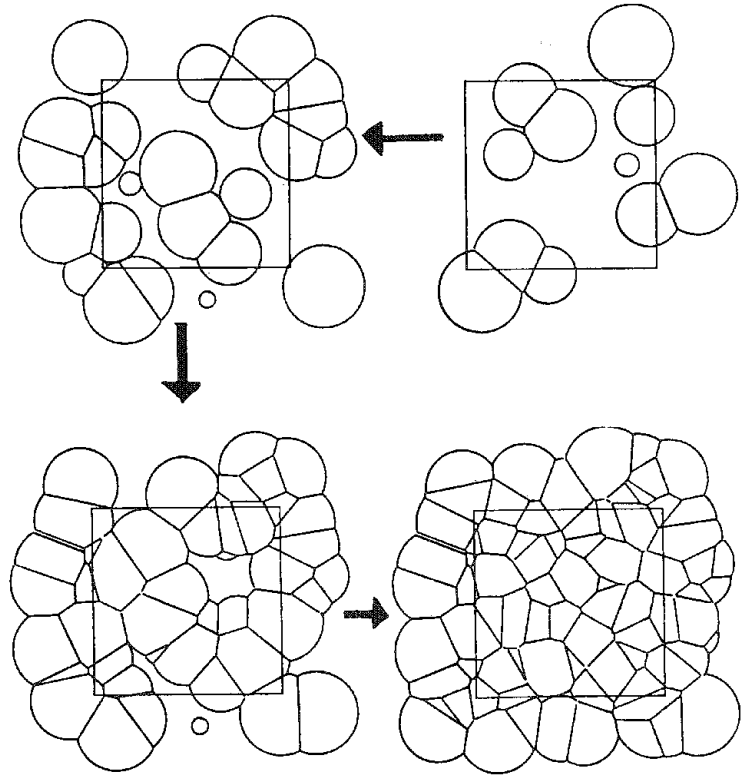


FIG. 2.--Two-dimensional sections taken from cell of size  $256 \times 256 \times 256$ , in which 2000 sites were burst nucleated and grown to space filling. Sequence of evolution at progressive times of growth is shown. All boundaries are straight because site-saturated nucleation was used.

FIG. 3.--Avrami plot of volume fraction of  $\alpha$  phase transformed to  $\beta$  phase at progressive times of growth for various numbers of nucleation sites. Only grains that do not intersect cube faces are included in total volume. Total volume used for volume fraction calculation is total volume of grains after complete impingement. Cell size is  $256 \times 256 \times 256$  units in which 400, 1000, and 2000 sites are burst nucleated and grown to space filling.

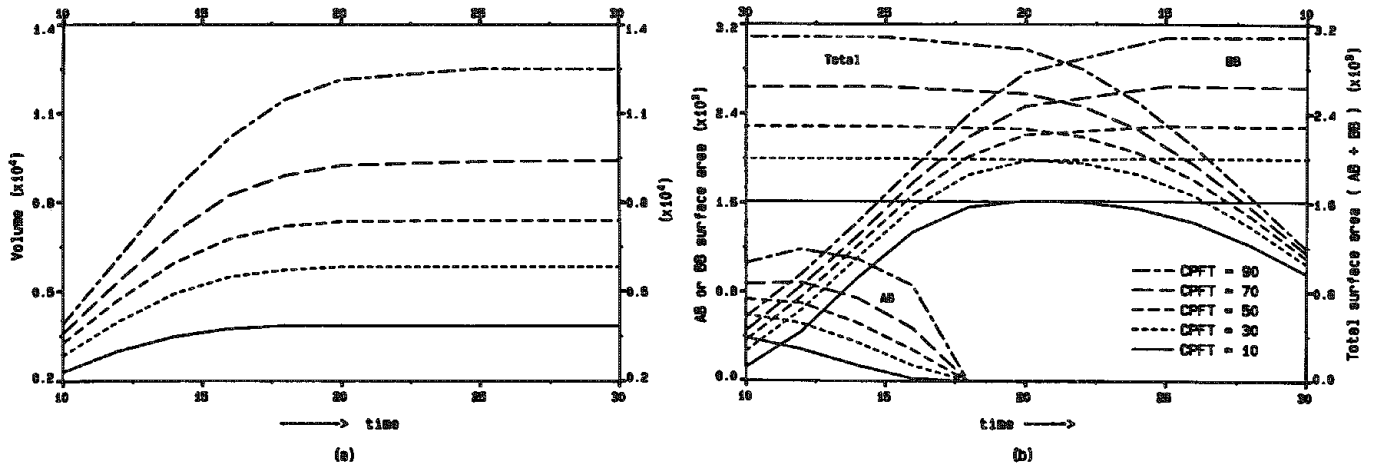
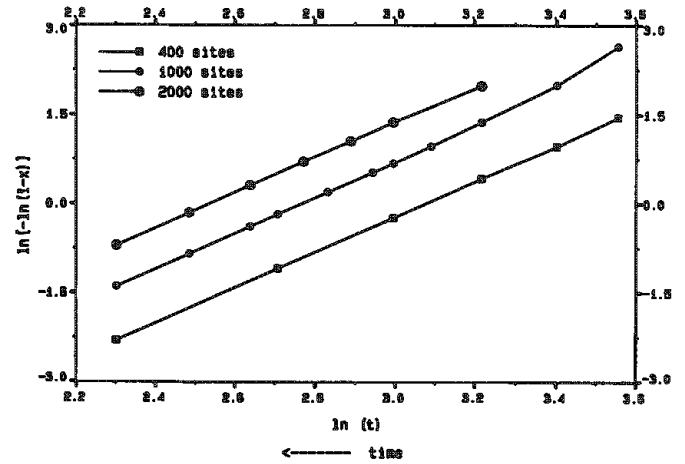


FIG. 4.--Growth path of (a) volume, (b)  $\alpha\beta$ (AB),  $\beta\beta$ (BB), and the total surface area for grains of five size classes (CPFT 10-90).

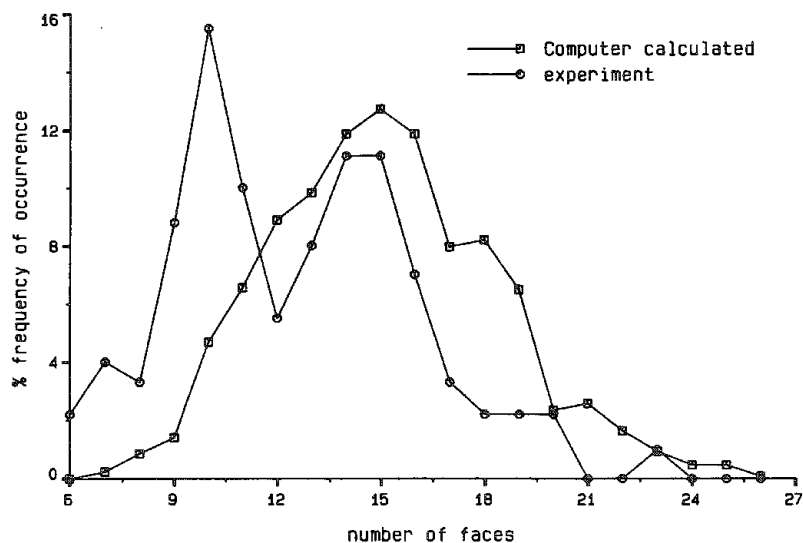


FIG. 5.--Comparison between experimentally obtained distribution of number of faces<sup>11</sup> and computer-calculated distribution.

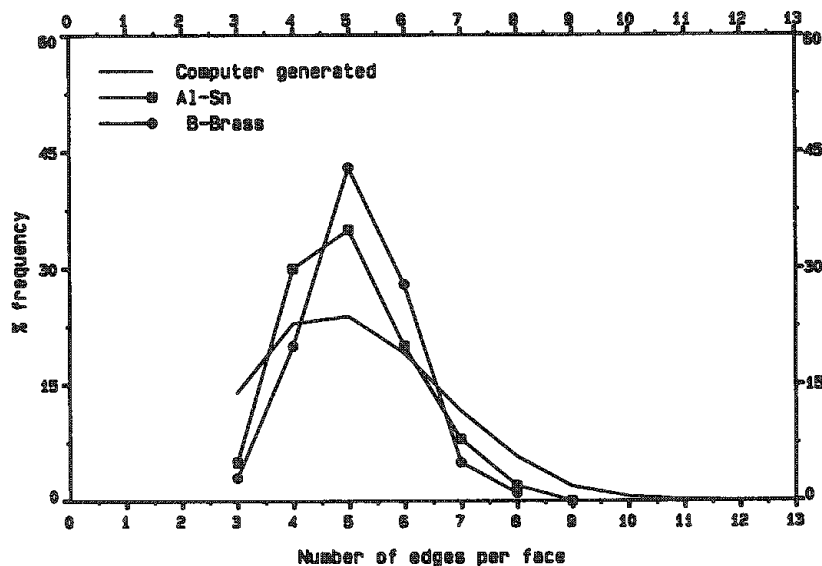


FIG. 6.--Distribution of number of edges per face obtained by experiments<sup>6</sup> and by computer simulation.

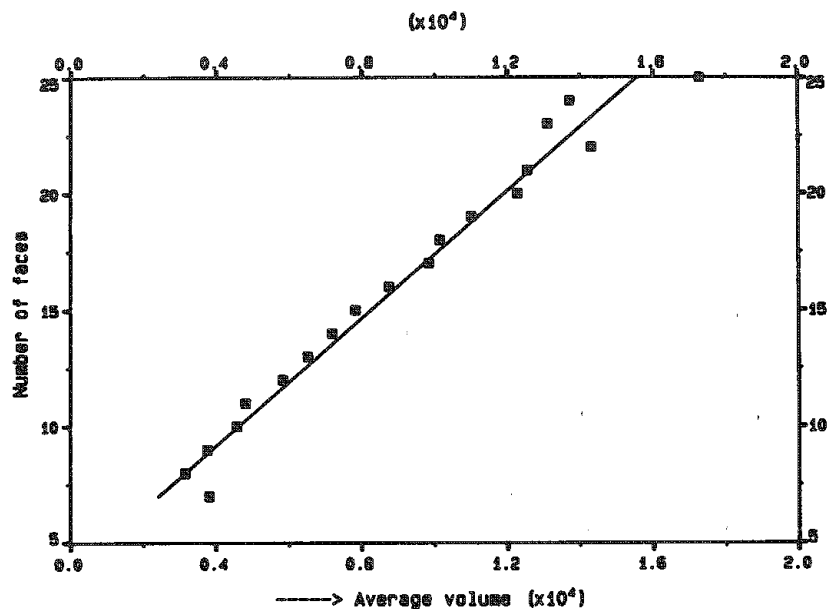


FIG. 7.--Variation of number of faces with volume of grains.

## 8. Geological Applications

### THE USE OF THE ELECTRON MICROPROBE IN THE SMITHSONIAN INSTITUTION MUSEUMS

Eugene Jarosewich

The availability of modern instruments in the contemporary museum environment is important to research, to the identification of specimens, and to the restoration and conservation of various objects. The wealth of material in museum collections used as reference specimens, educational material, or exhibit objects frequently requires detailed study. These studies may include historical, scientific, and curatorial endeavors.

Most major museums have their own laboratories for these purposes; some are equipped with modest instrumentation such as conservation and preparation equipment, others with more advanced instruments such as x-ray diffraction units, SEMs, electron microprobes, mass spectrometers, and others. Museums that are not as well equipped draw on the expertise of other museum laboratories or seek the assistance of academic or other research institutions.

The present contribution deals primarily with the use of the microprobe in the Smithsonian Institution museum environment. Following is a brief historical introduction to the Institution.

The Smithsonian Institution consists of museums and research facilities in the USA and abroad. Ten museums are located in Washington, D.C., and one, the Cooper Hewitt Museum, in New York City. Some of the other major Bureaus are the Smithsonian Astrophysical Observatory, Cambridge, Mass.; Fort Pierce, a marine facility in Florida; and a Smithsonian Tropical Research Institute in Panama.

The Smithsonian was established 1846 as a result of a bequest from James Smithson (1765-1829), an English natural philosopher, "to found at Washington, under the name of the Smithsonian Institution, an establishment for the increase & diffusion of knowledge among men." At first the Congress was reluctant to accept the money from a foreigner and the funds were channeled to other projects. Eight years later Congress had a change of heart and restored the funds, establishing the Smithsonian Institution in the original spirit of Smithson's will.

At first, the Institution was viewed as a center for intellectual activities and as providing assistance for original research. The present image of the Smithsonian, primarily as museums, is in large part due to the interests of Spencer F. Baird, who first served as the assistant to the first Secretary, Joseph Henry, and then as second Secretary of the Institution (1878-1887). As a naturalist, he had a strong interest in collections and research. Smithson, who was himself a chemist by training, with an interest in minerals, had a re-

markable collection of geologic materials which was left to the Institution. Unfortunately, most of his collection perished in a fire in 1865. These original collections could be considered as the nucleus of the collections in the Institution.

The establishment of a chemical laboratory was mandated by Congress, as were other functions of the Institution. This mandate was a natural consequence of Smithson's interest and the needs of the Institution and of the U.S. Geological Survey, which at that time was closely associated with the Museum of Natural History. At the present time, in addition to specialized departmental laboratories, there is a Conservation and Analytical Laboratory for Smithsonian-wide needs, which is also responsible for training students from other museums in the art of conservation.

The Department of Mineral Sciences, by nature of its activity, has a laboratory for classical chemical analyses, and is equipped with x-ray diffraction units, SEM, and an electron microprobe. The microprobe is used by most of the staff and those who participate in collaborative projects with some of the staff.

Since the microprobe is being used in numerous museum applications, several examples are listed below.

1. Petrologic, mineralogic, and meteoritic research.
2. Identifications of geologic specimens (gems, minerals, meteorites).
3. Study of archaeological objects (glasses, pottery, bones, metals, ancient bronzes).
4. Identification of pigments from paintings.
5. Numismatic identifications.
6. Biological applications.
7. Work with other Federal agencies.

One of the most difficult problems in any of the work with museum specimens is the restrictions on sampling. Frequently, curatorial decisions must be based on the uniqueness or value of the specimen and on judgments in what manner the sampling would affect the integrity of the sample. Ingenuity in sampling and in obtaining as much information as possible from a limited sample requires close interaction between curatorial and scientific personnel.

---

The author is with the Department of Mineral Sciences, Museum of Natural History, Smithsonian Institution, Washington, DC 20560.



## MICROPROBE ANALYSIS OF TETRAHEDRITE IN THE COEUR d'ALENE MINING DISTRICT, IDAHO

Charles R. Knowles

An electron microprobe study was made on fifty-four ore samples from ten mines in the Coeur d'Alene mining district. This district covers region of approximately 325 km<sup>2</sup> (125 mi<sup>2</sup>) in the panhandle of northern Idaho in the Bitterroot mountains. Mining began in the district in 1884; however, silver mining started to boom in the 1920s and one billion ounces of silver have been mined to date. The region produces approximately half the silver in the USA and is also a producer of lead, zinc, antimony, and copper.<sup>1</sup> Only a few mines are still in production between Wallace and Kellogg, Idaho. These active mines (Lucky Friday, Galena, Coeur, and Sunshine) produce mostly silver, with lead, zinc, cadmium, antimony, copper, and gold as byproducts and coproducts. These mines are among the deepest in the world, with shafts of over 2400 m (8000 ft). Because of high operating costs and poor market prices, two mines (Bunker Hill and Star-Morning) have closed permanently since the samples were collected and two (Sunshine and Lucky Friday) are on standby-by status until silver prices stabilize.

Ore samples were collected from nine of these mines (Sunshine, Bunker Hill, Star-Morning, Lucky Friday, Galena, Page, Crescent, Snowstorm, Royal Apex, and Atlas) and from core samples in the Capital Silver property. Samples were collected from diverse regions within the mines, both vertically and laterally. The sample numbers in Table 1 show the depth (e.g., SM7700-106 is from the 7700ft level of the Star-Morning Mine). The Page mine and Atlas mine have been closed for years; a single sample of each was obtained from an ore sample collection belonging to Stan Huff at the Galena mine. The Snowstorm mine sample was taken from the mine's ore dump. Core samples were collected from the Capital Silver property during exploration. A single sample was taken from the inactive tunnel workings of the Royal Apex mine.

Geologists have believed that silver is present in solid solution with galena (PbS) in a relationship of 1% Pb correlated to 1 oz/ton (34 ppm) of Ag. If 1 oz/ton as Ag is in solid solution, a silver value of 0.3% mixed with galena would be expected (e.g., 86.6% Pb in galena corresponds to 0.29% Ag). To test this hypothesis, samples of inclusion-free "pure" galena were examined with an ARL and a CAMECA electron microprobe to measure the quantity of Ag in the galena matrix. Both microprobes have a detection limit better than 0.1% Ag.

The origin of the silver-rich ore has been open to conjecture. One popular idea is that the original sediments were deposited with silver minerals within them (stratabound).<sup>2</sup> The silver was subsequently remobilized into

silver veins. Several samples of stratabound type ore were collected throughout the district to test this hypothesis.

### *Experimental Procedure*

The ore samples were cut into lin blocks, mounted in room-temperature-polymerizing epoxy resin, polished to less than 1  $\mu$ m relief with diamond paste, and coated with approximately 100 Å of carbon. In one sample, four single crystals from the Sunshine Mine were extracted from a vug, placed on a glass slide with epoxy, and polished flat and smooth.

An ARL-EMX-SM electron microprobe was used operating at 15 kV and 0.1  $\mu$ A reference current (approximately 1nA sample current). Pure metals (>99.9% purity) and reference minerals were used as standards. Background, deadtime, and ZAF corrections were made.

To analyze the silver content it was necessary to find a silver-rich area on the polished section. We accomplished that by tuning a crystal (wavelength-dispersive) spectrometer to the silver x-ray line, traversing around the sample until the ratemeter indicated high intensity, and then analyzing that area.

To determine whether Ag was present in the galena matrix, very careful off-peak background measurements over a long period (100 s) were used to compare with the peak position, also measured for 100 s. This procedure was also followed with a CAMECA microprobe at the Washington State University geology department in addition to the ARL instrument. The sensitivity on both instruments at long counting times is better than 0.1% for silver.

### *Results*

Table 1 gives the analysis of the silver minerals found in the ore samples and core samples from the ten mining regions. These data show that four silver minerals were present. The most abundant mineral is argentiferous tetrahedrite. Miargyrite and polybasite were present in samples from the Galena Mine. Pyrargyrite was seen in only one sample from the Lucky Friday Mine. No silver minerals were found in some of the samples analyzed. The core samples from the Capitol Silver project and the samples of stratabound ore showed no silver.

The Capitol Silver core samples were from stratabound type rock and several samples from the Star-Morning, Lucky Friday, and Galena mines were identified as stratabound. These samples were carefully analyzed for any silver minerals. Only the Snowstorm Mine sample had any detectable silver minerals.

This sample from the Snowstorm Mine had sparse grains of miargyrite and abundant galena. It is the only stratabound sample listed in Table 1. The other stratabound samples were galena rich with no Ag in the galena matrix. One sample from the Star-Morning Mine

The author is at the Idaho Geological Survey, Moscow, ID 83843.

was stratabound with sphalerite and galena. No Ag was present in this sample.

The Galena Mine samples showed two coexisting silver-rich minerals in some of the samples. One of the samples contained tetrahedrite and miargyrite (G4300-164EB). Three other samples had two tetrahedrite minerals with different chemistry coexisting in the same sample. These samples showed a large percentage of Ag vs a small amount of Cu in one case and the opposite in the other. One sample (G 2800-16) has 34.1% Ag. This is the largest percentage of Ag in tetrahedrite in these ore samples.

### Conclusions

No Ag from any of the fifty-four samples could be detected in solid solution with galena. However, silver was present in most of the ore samples as discrete mineral grains. The most common mineral is argentiferous tetrahedrite,  $(\text{Cu}, \text{Ag})_{12}\text{Sb}_4\text{S}_{13}$ , with some small inclusions of polybasite,  $\text{Ag}_{16}\text{Sb}_2\text{S}_{11}$ , pyrrargyrite,  $\text{Ag}_6\text{Sb}_2\text{S}_6$ , and miargyrite,  $\text{AgSbS}_2$ . X-ray scan photographs show that in these silver-rich regions the tetrahedrite commonly forms a rim around sphalerite ( $\text{ZnS}$ ) grains. The silver minerals are generally very small and, in some samples, less than 1  $\mu\text{m}$  in size; thus, only the larger inclusions could be quantitatively analyzed.

If any silver is present in the galena matrix in solid solution, it is less than 0.1%.

Although the data are sparse, the Star-Morning samples have the highest amount of silver in the tetrahedrite; the Sunshine Mine, Galena Mine, and the Lucky Friday Mine the least amount. More samples would be necessary to verify a regional trend.

The stratabound ore samples contained very low silver-rich minerals. They were predominantly galena with one sample of sphalerite. It is plausible that the galena-rich veins may have been derived from these stratabound sediments and later infused with silver minerals that possibly were emplaced hydrothermally.

### References

1. U.S. Bureau of Mines, *Minerals Yearbook 1980*, Washington, D. C.: U.S. Government Printing Office, 1982, vol. 2, 157-170.
2. V. M. Ramalingaswamy and E. S. Cheney, in R. R. Reid and G. W. Williams, Eds., *Society of Economic Geologists' Coeur d'Alene Field Conference, Idaho-1977*, Idaho Bureau of Mines and Geology Bulletin 24, 1982.
3. B. J. Skinner et al., "Studies of the sulfosalts of copper: III. Phases and phase relations in the system Cu-Sb-S," *Economic Geology* 67: 924, 1972.

TABLE 1.--Microprobe analysis of silver minerals.

Sample	Cu	Ag	Fe	Zn	Sb	As	S
Snowstorm Mine		35.2			34.7		30.1*
LF 3450-88	34.9	4.0	2.1	7.5	26.6	1.6	23.3
LF 4250-AL	32.8	8.8	1.6	3.9	27.3	1.2	22.8
LF 4250-94WB	37.6	4.2	2.3	3.4	29.2	0.7	23.7
LF 4250-94W	35.4	7.0	3.1	3.1	28.1	1.0	22.3
LF 4660-94WQ	34.4	4.8	2.5	5.6	28.2	1.0	23.5
LF 4660-94E	34.4	7.9	1.8	5.5	22.2	5.0	23.8
LF 4660-96 1st	16.3	29.4	5.0	1.1	25.5	0.2	21.5
2nd		62.4			17.9		19.7**
LF 4660-98	13.8	29.6	4.2	5.0	31.0	0.3	15.8
G 110		35.3			31.6		33.1*
G 750		36.2			35.8		28.0*
G 215		35.8			33.9		30.3*
G 2800-B		71.4			13.1		15.5***
G 2800-S		35.2			32.1		32.7*
G 2800-16 1st	25.2	19.5	2.0	3.4	25.4	1.8	22.7
2nd	18.6	34.1	4.5	1.9	18.4	0	22.3
G 3400-7 1st	28.3	14.6	5.2	1.2	26.4	1.5	23.3
2nd	34.0	6.3	6.2	2.3	27.5	1.9	24.0
G 4000-94	27.1	14.2	1.6	5.7	25.9	0.7	23.4
G 4000-104	35.7	3.1	3.3	4.1	26.8	1.2	24.7
G 4300-164EB1st	33.9	6.2	1.9	5.7	27.0	1.0	24.7
G 4300-164EE2nd		34.7			31.2		34.1*
G 4600-164 1st	35.1	4.7	4.4	2.8	27.0	1.2	24.8
2nd	24.9	18.6	1.1	6.2	24.9	1.2	23.3
G 4900-MB	35.1	4.5	4.6	2.6	26.1	1.5	24.8
G 4900-77	34.9	6.8	5.0	1.2	25.7	2.4	22.9
SM 5900-121	24.7	17.1	5.3	3.4	25.7	0.1	22.5
SM 6500-122	25.1	14.2	5.3	2.6	25.8	0.3	22.3
SM 6500-125	22.7	20.0	3.2	4.0	24.1	0.5	22.6
Royal Apex Mine	36.3	5.5	0.5	4.4	25.9	2.7	23.8
Crescent Mine	32.9	8.3	4.7	2.0	24.8	2.1	24.7
S 4100-625	28.5	13.3	4.1	2.8	26.3	0.7	23.6
S 4300-625	29.9	11.1	4.5	2.4	26.2	1.0	23.9
S 4500-625	31.6	8.9	4.7	2.1	26.7	1.0	24.2
S 5200-13	33.7	7.3	4.8	2.3	25.5	1.9	24.8

\*--Miargyrite,  $\text{AgSbS}_2$ ; \*\*\*--Pyrrargyrite,  $\text{Ag}_6\text{Sb}_2\text{S}_6$ ;   
 \*\*\*--Polybasite,  $\text{Ag}_{16}\text{Sb}_2\text{S}_{11}$

LF--Lucky Friday Mine; G--Galena Mine; SM--Star-Morning Mine;

TABLE 2.--Microprobe analysis of tetrahedrite crystals from the Sunshine Mine.

Crystal	Cu	Ag	Fe	Zn	Sb	As	S
#1	32.7%	8.9%	4.5%	2.3%	26.7%	2.2%	23.7%
#2	34.6	6.5	4.7	2.4	26.8	2.4	23.9
#3	31.7	9.5	5.1	1.6	26.9	1.6	23.8
#4	34.0	8.2	4.7	2.5	26.8	1.7	23.7
Average	33.2	8.3	4.7	2.2	26.8	2.0	23.8

Formula Analyzed  $(\text{Cu}_{9.4}\text{Fe}_{1.5}\text{Zn}_{0.6}\text{Ag}_{1.4})(\text{Sb}_{3.9}\text{As}_{0.5})\text{S}_{13}$   
 Idealized Formula  $3\text{Cu}_{12-x}\text{Sb}_4+y\text{S}_{13}$  where  $0 < x < 1.92$  and  $-0.02 < y < 0.27$

# MICROPROBE ANALYSIS OF "RESET" ZIRCONS FROM THE BREVARD ZONE, NEAR ROSMAN, N.C.

D. M. Wayne, T. N. Solberg, and A. K. Sinha

Total loss of radiogenic Pb from zircons during low- to medium-grade regional metamorphism is rarely observed. However, U-Pb ages may be completely reset during prograde mylonitization where zircon crystals undergo fracturing and grain size reduction in a fluid-rich environment. To investigate the chemical trends accompanying Pb loss/U gain within a mylonite zone, we have analyzed a suite of zircons from relatively undeformed Henderson gneiss (Hgn) and "reset" zircons from a mylonite zone within the Henderson gneiss (samples B8A, B8B, and B8C of Ref. 1). Microprobe data indicate that trace-element-rich overgrowths developed during mylonitization.

Zircons were analyzed with an automated ARL-SEM9 9-channel microprobe at the Department of Geological Sciences, V.P.I. & S.U. Instrumental conditions, counting times, and peak and background standards are listed in Table 1 and further described in Ref. 2. Whole grain (rim-core-rim) traverses consist of 5 to 17 analysis points (depending on zircon size), directed parallel or perpendicular to [001] or [100] (depending on orientation).

Restandardization was necessary only once over the two-week analysis period. We monitored instrumental drift by traversing the synthetic ZrSiO<sub>4</sub> standard periodically. Table 2 lists the results from a pair of standard traverses over a three-day interval. Of the nineteen elements included in our analytical scheme, only Zr, Si, Hf, P, U, Yb, Ca, and Fe were above detection limits in most of the samples. We have since added Th, Dy, and Ti to our analytical scheme.

Electron microprobe traverses revealed the presence of metamorphic overgrowths on zircons from the mylonitized Henderson gneiss. Trace element abundances in zircon overgrowths from the entire range of mylonitic fabric types (i.e., protomylonite, blastomylonite, ultramylonite) are strikingly similar (Table 3). Zircon cores, by contrast, show wide variations in trace element abundances. X-ray maps of Ca and U on selected zircons (Fig. 1) illustrate the redistribution of trace elements within the zircons with increasing strain. The thickness of the zircon overgrowths is correlated with increasing deformation and increasing fluid activity of the host rock. A significant portion of the zircons from the ultramylonite are totally recrystallized and show no relict zoning. Microprobe data from isotopically reset zircons from the most intensely mylonitized zone, within the Henderson gneiss suggest that fracturing and grain-size reduction accelerated the rate of Pb loss in a fluid-rich environment. The formation of overgrowths on these zircons indicates that typically "immobile" elements (e.g., Zr, Hf,

Y, P, and U) may undergo solution transport as complexed, aqueous species during mylonitization at amphibolite facies.

## References

1. A. K. Sinha and L. Glover III, "U/Pb systematics of zircons during dynamic metamorphism: A study from the Brevard fault zone," *Contrib. Min. Pet.* 66: 305-310, 1978.
2. T. N. Solberg and J. A. Speer, "Q-ALL: A 16-element analytical scheme for efficient petrologic work on an automated ARL-SEM9: Application to mica reference samples," *Microbeam Analysis--1982*, 422-426.

TABLE 1.--Analytical conditions, counting times, and peak and background standards for the analysis of zircons. Beam width ~1  $\mu$ m at 15 kV, sample current 50 nA (on ZrSiO<sub>4</sub>).

Element	Count time(s)	Peak std.	Bk. std.
Zr	200	ZrSiO <sub>4</sub> syn.	YAG
Si	1000	ZrSiO <sub>4</sub> syn.	YAG
Hf	200	HfSiO <sub>4</sub> syn.	ZrSiO <sub>4</sub> syn.
Y	200	YAG	ZrSiO <sub>4</sub> syn.
P	200	Apatite	ZrSiO <sub>4</sub> syn.
U	400	UO <sub>2</sub> syn.	ZrSiO <sub>4</sub> syn.
Ca	1000	Hornblende	ZrSiO <sub>4</sub> syn.
Fe	1000	Hornblende	ZrSiO <sub>4</sub> syn.

TABLE 2.--Analyses of synthetic zircon standard, over a 3-day interval.

Oxide	Average of 5		Drift/day
	Start	After 73 h	
ZrO <sub>2</sub>	67.931 (0.517)	67.562 (0.549)	0.123
SiO <sub>2</sub>	32.736 (0.087)	31.935 (0.199)	0.267
HfO <sub>2</sub>	0.036 (0.016)	-0.002 (0.015)	0.013
Y <sub>2</sub> O <sub>3</sub>	0.003 (0.006)	-0.005 (0.005)	0.003
P <sub>2</sub> O <sub>5</sub>	-0.004 (0.010)	-0.017 (0.013)	0.004
UO <sub>2</sub>	0.010 (0.003)	0.002 (0.008)	0.003
CaO	0.006 (0.002)	0.002 (0.006)	0.002
FeO	0.013 (0.002)	0.003 (0.005)	0.004
Total	100.734	99.480	

TABLE 3.--Trace element abundances (in wt.% oxide) from zircon cores and overgrowths formed during prograde mylonitization.

	Overgrowth	Core
HfO <sub>2</sub>	1.39 - 1.69	1.03 - 1.76
Y <sub>2</sub> O <sub>3</sub>	0.19 - 0.45	0.05 - 1.14
P <sub>2</sub> O <sub>5</sub>	0.11 - 0.20	0.00 - 0.37
UO <sub>2</sub>	0.08 - 0.22	0.00 - 0.34
Zr/Hf	34.98 - 40.72	32.22 - 57.59

Authors are at the Department of Geological Sciences, V.P.I. & S.U., Blacksburg, VA 24061-0796. NSF funding is acknowledged.

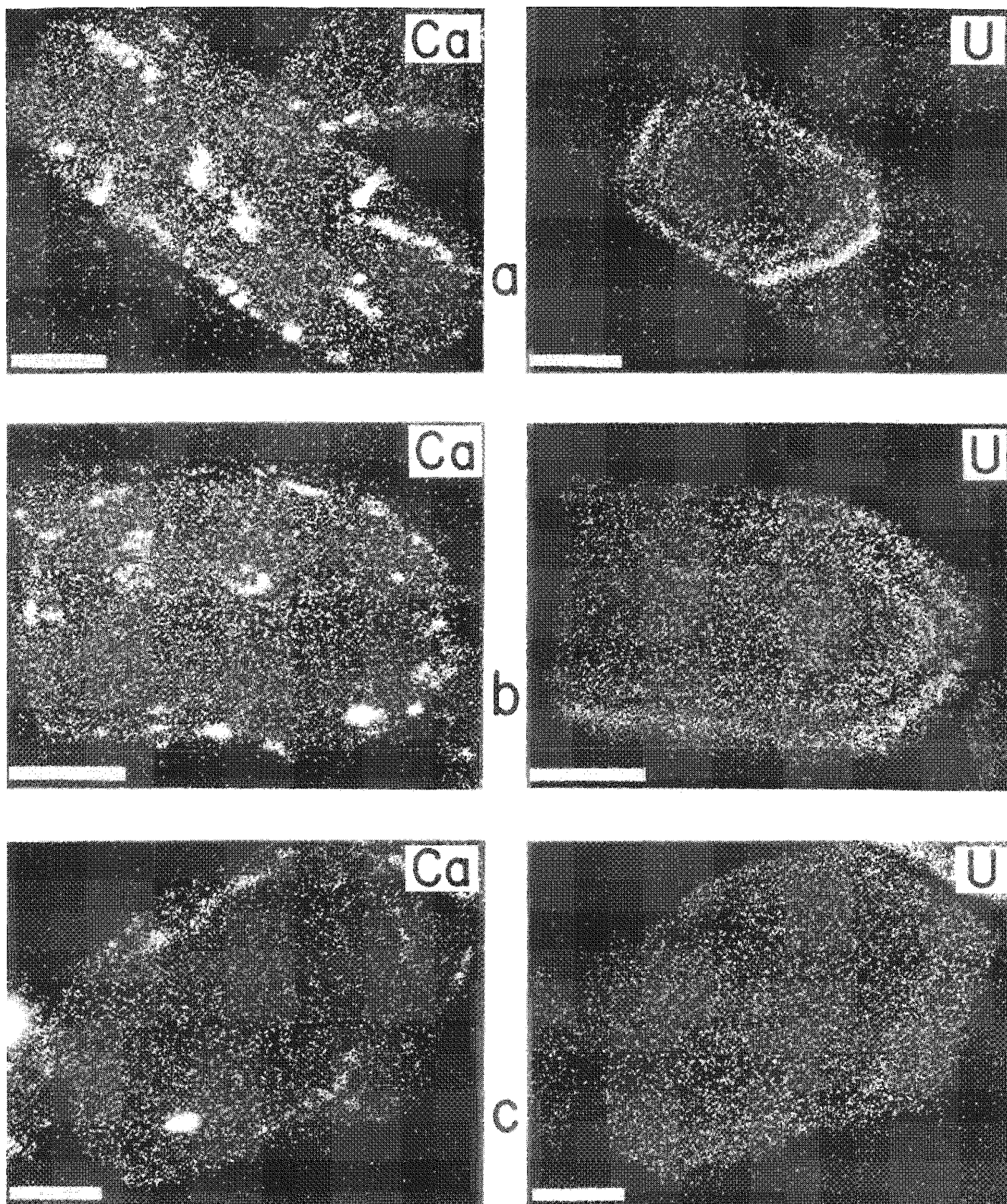


FIG. 1.--X-ray maps depicting trace element distributions in zircons from (a) Henderson gneiss, (b) protomylonite, (c) blastomylonite. Bar = 30  $\mu$ m.

## COLOR AND CHEMISTRY OF GEM GARNETS

Carol Stockton

One of the notable features of garnets that makes them especially appealing as gemstones is the broad range of colors in which they occur—every spectral hue except blue. This feature is largely due to the variety of transition metal elements that can be incorporated into the garnet structure. Although about fifteen or so garnet species occur naturally,<sup>1</sup> most gem garnets have compositions that can be at least 99% accounted for by the five end members pyrope, almandine, spessartine, grossular, and andradite; it is the origin of color in these garnets that is discussed in this article.

### *Experimental*

As part of a general study of transparent gem garnets,<sup>2</sup> we analyzed about 500 garnets (mostly faceted gemstones) by microprobe on a MAC automated microprobe (courtesy of the California Institute of Technology), with corrections according to the Ultimate program.<sup>3</sup> Oxides determined were  $\text{SiO}_2$ ,  $\text{TiO}_2$ ,  $\text{Al}_2\text{O}_3$ ,  $\text{V}_2\text{O}_3$ ,  $\text{Cr}_2\text{O}_3$ ,  $\text{CaO}$ ,  $\text{MgO}$ ,  $\text{MnO}$ , and  $\text{FeO}$ . Some atoms, especially Fe and Ti, can go into more than one site in the garnet structure. Since valence states and site occupancies could not be determined directly, we determined a redistribution of oxides according to stoichiometry, similar to that done by Rickwood,<sup>4</sup> from which we were able to determine end-member compositions for our sample garnets. These calculations, though not ideal, provided us with very good indications of likely chromogens when correlated with variability in color and other physical properties. CIE color coordinates were determined for the study garnets; Fig. 1 shows a representative sample of the garnets on a chromaticity diagram. The variability in color is readily apparent.

### *Results and Discussion*

Andradite garnet, the simplest case, exhibits very little chemical variability; all specimens consist of more than 97 wt% andradite,<sup>5</sup> and it is known that andradite is intrinsically yellow-green from  $\text{Fe}^{3+}$  in the octahedral site. The only other potential chromogens were  $\text{Cr}^{3+}$  (<0.6 wt%  $\text{Cr}_2\text{O}_3$ ), Ti (<0.1 wt%  $\text{Ti}_2\text{O}_3$ ), and  $\text{Mn}^{2+}$  (<0.1 wt%  $\text{MnO}$ ). The color range of the samples included slightly orangy yellow to very slightly yellowish green. The more intense greens highly desired by gemstone collectors clearly correlate with increasing amounts of chromium, as has long been established.<sup>6</sup> The orangy yellow color was not clearly related to any chromogen, and our limited sample (one specimen) is too small to invite speculation. Both Ti and

Mn have been related to yellow and brown color in andradites.<sup>7</sup>

Grossular garnets show considerable color variability, from colorless to yellow, orange, and green.<sup>8</sup> Figure 2 is a partial ternary diagram that shows that, in spite of this broad color range, grossular garnets have somewhat limited compositional variability. Virtually pure grossulars do occur, from which a trend extends along the join with andradite. However, a large group of grossulars contain no andradite, but instead have variable amounts of other end-member components. Potential chromogens among them include  $\text{Fe}^{2+}$ ,  $\text{Mn}^{2+}$ ,  $\text{Cr}^{3+}$ ,  $\text{V}^{3+}$ , and Ti. Mn and Ti exhibit no correlation with color, although  $\text{Mn}^{2+}$  has been observed as a chromogen in nongem grossulars.<sup>7</sup> Figure 3 shows the distribution of a representative sample of grossular garnets on a CIE chromaticity diagram. Two color trends can be distinguished: colorless through yellow to orange, and colorless to green. If regarded for analytical purposes as linear, these two trends can be used to compare the amounts of green and orange to potential chromogens. The results are interesting (Fig. 4). There is a clear correlation between  $\text{Fe}^{3+}$  and yellow-to-orange color. The  $\text{Fe}^{2+}$  pattern confirms our limited ability to determine valence states and site coordination by stoichiometry. As to green, both  $\text{V}_2\text{O}_3$  and  $\text{Cr}_2\text{O}_3$  correlate with color, though the latter in lesser amounts. There are also green grossulars that are colored solely by  $\text{Cr}^{3+}$ , but they are seldom large enough to be cut as gemstones.<sup>9</sup>

Figure 5 shows the distribution of a representative sample of garnets composed primarily of pyrope, almandine, and spessartine components on a ternary diagram bounded by those same end members. These garnets are generally quite low in grossular content, although a few have been observed to contain as much as 25 wt%; none contains more than 4 wt% andradite. Obviously, many more of these specimens are of mixed composition than of a composition approaching any one end member. Specimens along the pyrope-almandine join vary from medium to very dark orangy red to red-purple; those in the almandine-spessartine series range from light-medium to dark yellowish orange to orange-red; pyrope-spessartine garnets exhibit even more variability with light to dark greenish yellow through purple.

In addition to the chromogens intrinsic to spessartine and almandine ( $\text{Mn}^{2+}$  and  $\text{Fe}^{2+}$ , respectively),  $\text{Cr}^{3+}$ ,  $\text{V}^{3+}$ ,  $\text{Fe}^{3+}$ , and Ti are present to various extents.  $\text{Fe}^{3+}$  and Ti are present in such small amounts that the presence (or absence) of correlation must call into question the accuracy of the microprobe and correction procedures themselves; moreover, for  $\text{Fe}^{3+}$ , we cannot rely on stoichiometric calculations that involve small quantities. That leaves us with  $\text{Mn}^{2+}$ ,  $\text{Fe}^{2+}$ ,  $\text{Cr}^{3+}$ , and  $\text{V}^{3+}$

The author is at the Gemological Institute of America (Research Department), Santa Monica, CA 90404.

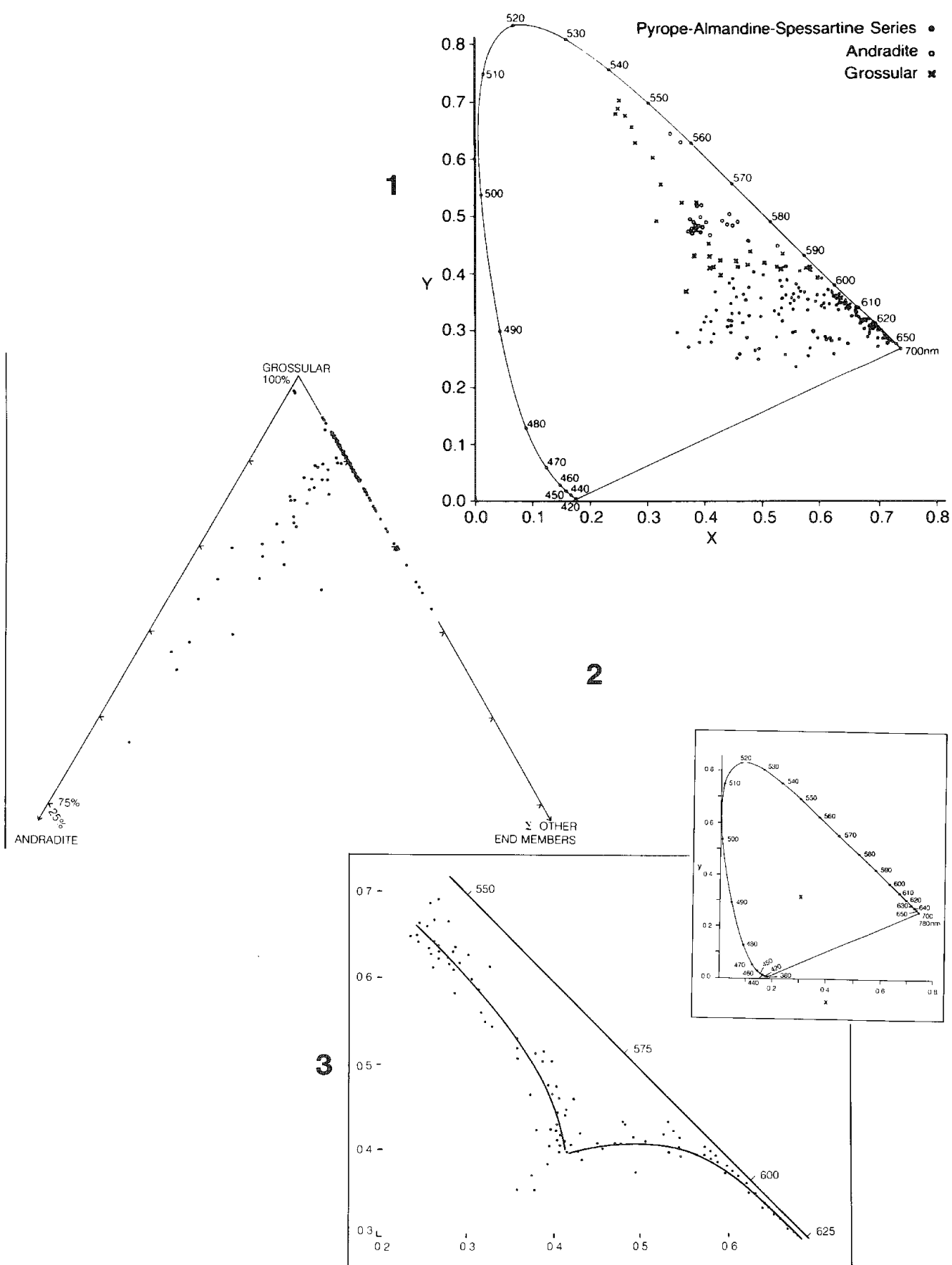


FIG. 1.--CIE chromaticity diagram with coordinate points for representative sample of 202 garnets. Range of hues extends from green to purple.

FIG. 2.--105 grossular garnets in relation to major end-member components. Stones along grossular-andradite join are predominantly yellow or orange; remaining grossulars range from colorless to green (see Fig. 3).

FIG. 3.--CIE chromaticity diagram with color coordinate points for 105 grossulars. Color trend lines are superimposed for use in calculating Fig. 4.



for purposes of explaining color variabilities. Quantities of all these chromogens below our detection limits can affect color, yet  $\text{Fe}^{3+}$  and Ti are not notorious for strongly affecting color except when involved in charge-transfer processes.<sup>10-11</sup> But  $\text{Cr}^{3+}$  and  $\text{V}^{3+}$  can have considerable effects at low levels.<sup>12</sup>

With that in mind, what are the general trends? Among specimens along the pyrope-almandine join, those with little or no chromogens other than  $\text{Fe}^{2+}$  exhibit a purplish red to brownish red when  $\text{Fe}^{2+}$  content is high (i.e., toward pure almandine) and an orange color when  $\text{Fe}^{2+}$  is low (i.e., high in pyrope). Increasing  $\text{Mn}^{2+}$  in the high- $\text{Fe}^{2+}$  stones has little perceptible effect, but when  $\text{Fe}^{2+}$  content is low, a more purplish hue occurs. Whether this color is actually due to Mn, or is related to traces of  $\text{Cr}^{3+}$ , remains a question. As  $\text{Cr}^{3+}$  increases in a low- $\text{Fe}^{2+}$ , low- $\text{Mn}^{2+}$  stone, we see an increasingly dark blood-red color (a typical "chrome pyrope"); extremely high  $\text{Cr}^{3+}$  content yields a green-red color change, but no gem-size specimens have been encountered.  $\text{Cr}^{3+}$ , though detected only in amounts below 2 wt%  $\text{Cr}_2\text{O}_3$  in high  $\text{Fe}^{2+}$  stones, appears to contribute a purplish component in higher-almandine garnets.

Almandine-spessartine garnets are as uncomplicated as they are abundant: high- $\text{Mn}^{2+}$  content yields a more orange hue and  $\text{Fe}^{2+}$  generates a more reddish color. Since these chromogens are intrinsic, the color is invariably of medium to dark tone. No other chromogens were detected in significant amounts.

Finally, the recently discovered pyrope-spessartine series yields a veritable Pandora's box of color and chemical variability. In the near absence of other chromogens, it can be observed that intrinsic  $\text{Mn}^{2+}$  adds orange color, as we might expect. When  $\text{Mn}^{2+}$  is low,  $\text{Cr}^{3+}$  adds red color. For example, 2 wt%  $\text{Cr}_2\text{O}_3$  with 9 wt%  $\text{MnO}$ , 5 wt%  $\text{FeO}$ , and 19 wt%  $\text{MgO}$  provides a pink color; such a stone would be classified as a pink pyrope. A stone with no  $\text{Cr}_2\text{O}_3$ , no  $\text{MnO}$ , 21 wt%  $\text{MgO}$ , and 9.5 wt%  $\text{FeO}$  is light orange. The pink color thus derives from the presence of  $\text{Cr}^{3+}$ . With higher  $\text{Mn}^{2+}$  content,  $\text{Cr}^{3+}$  and  $\text{V}^{3+}$  (both are invariably present in these stones) add a red overtone to the intrinsic orange hue and, in slightly higher amounts, produce a color-change phenomenon due to the balance of absorption created in the blue ( $\text{Mn}^{2+}$ ) and in the yellow ( $\text{Cr}^{3+}$  plus  $\text{V}^{3+}$ ). The exact hues produced depend on the complex ratio  $\text{Mn}^{2+}:\text{Cr}^{3+}:\text{V}^{3+}:\text{Fe}^{2+}$ ; the last generally contributes a reddish hue. It is also likely that  $\text{Fe}^{3+}$  may occur in these garnets and doubtless affects hue. Considerable amounts of  $\text{Ca}^{2+}$  related to a grossular component, as well as that associated with  $\text{Cr}^{3+}$  and  $\text{V}^{3+}$  end members, also affect the garnet lattice and certainly create additional variability.

### Conclusion

Our review of garnet colors and chemistry shows that the microprobe work done to date provides us with a point of departure for further investigations. Since the specimens used for this

type of study are gem materials, nondestructive analysis is imperative. A means to determine valence states and site occupancies is required. Spectral studies have provided some of this information<sup>13-17</sup> and will continue to do so. Further, trace-level microprobe analysis could provide additional information that, coupled with visible and infrared spectrophotometry, would answer many of the questions that remain about color origin in gem garnets.

### References

1. M. Fleischer, *Glossary of Mineral Species*, Tucson, Ariz.: Mineralogical Record, 1983, 4th ed.
2. C. M. Stockton and D. V. Manson, "A proposed new classification for gem-quality garnets," *Gems & Gemology* 21: 205-218, 1985.
3. A. A. Chodos, A. L. Albee, A. J. Garcarz, and J. Laird, "Optimization of computer-controlled quantitative analysis of minerals," *Proc. 8th Intern. Conf. Electron Probe Microanalysis*, 1973.
4. P. C. Rickwood, "On recasting analyses of garnet into end-member molecules," *Contributions to Mineralogy and Petrology*, 18: 175-198, 1968.
5. C. M. Stockton and D. V. Manson, "Gem andradite garnets," *Gems & Gemology* 19: 202-208, 1983.
6. B. W. Anderson and C. J. Payne, "The spectroscope and its applications to gemology," Part 17. Absorption spectrum of demantoid garnet," *The Gemmologist* 24: 5-8, 1955.
7. W. A. Deer, R. A. Howie, and J. Zussman, *Rock-forming Minerals (vol. 1A: Orthosilicates)*, London: Longman, 1982.
8. D. V. Manson and C. M. Stockton, "Gem-quality grossular garnets," *Gems & Gemology* 18: 204-213, 1982.
9. W. Wight and J. D. Grice, "Grossular garnet from the Jeffrey Mine, Asbestos, Quebec, Canada," *J. Gemmology* 18: 126-130, 1982.
10. R. K. Moore and W. B. White, "Intervalence electron transfer effects in the spectra of the melanite garnets," *Am. Mineralogist* 56: 826-840, 1971.
11. S. M. Mattson and G. R. Rossman, "Identifying characteristics of charge transfer transitions in minerals," *Physics and Chemistry of Minerals* 14: 94-99, 1987.
12. K. Schmetzer and J. Ottemann, "Kristall- und Farbe Vanadium-haltiger Granate," *Neues Jahrbuch für Mineralogie: Abhandlungen* 136: 146-168, 1979.
13. S. P. Clark, "Absorption spectra of some silicates in the visible and near infrared," *Am. Mineralogist* 42: 732-742, 1957.
14. P. C. Manning, "The optical absorption spectra of the garnets almandine-pyrope, pyrope and spessartine and some structural interpretations of mineralogical significance," *Canadian Mineralogist* 9: 237-251, 1967.
15. G. A. Slack and R. M. Chrenko, "Optical absorption of natural garnets from 1000 to 30 000 wavenumbers," *J. Optical Soc. Am.* 61: 1325-1329, 1971.
16. K. R. Frentrup and K. Langer, " $\text{Mn}^{3+}$  in garnets: Optical absorption spectrum of a synthetic  $\text{Mn}^{3+}$  bearing silicate garnet," *Neues Jahrbuch für Mineralogie: Monatshefte* 6:



245-256, 1981.

17. K. R. Frentrop and K. Langer, "Microscope absorption spectrometry of silicate microcrystals in the range 40 000-5000  $\text{cm}^{-1}$

and its application to garnet end members synthesized at high pressures," in W. Schreyer, Ed., *High-pressure Researches in Geoscience*, 1982, 247-258.

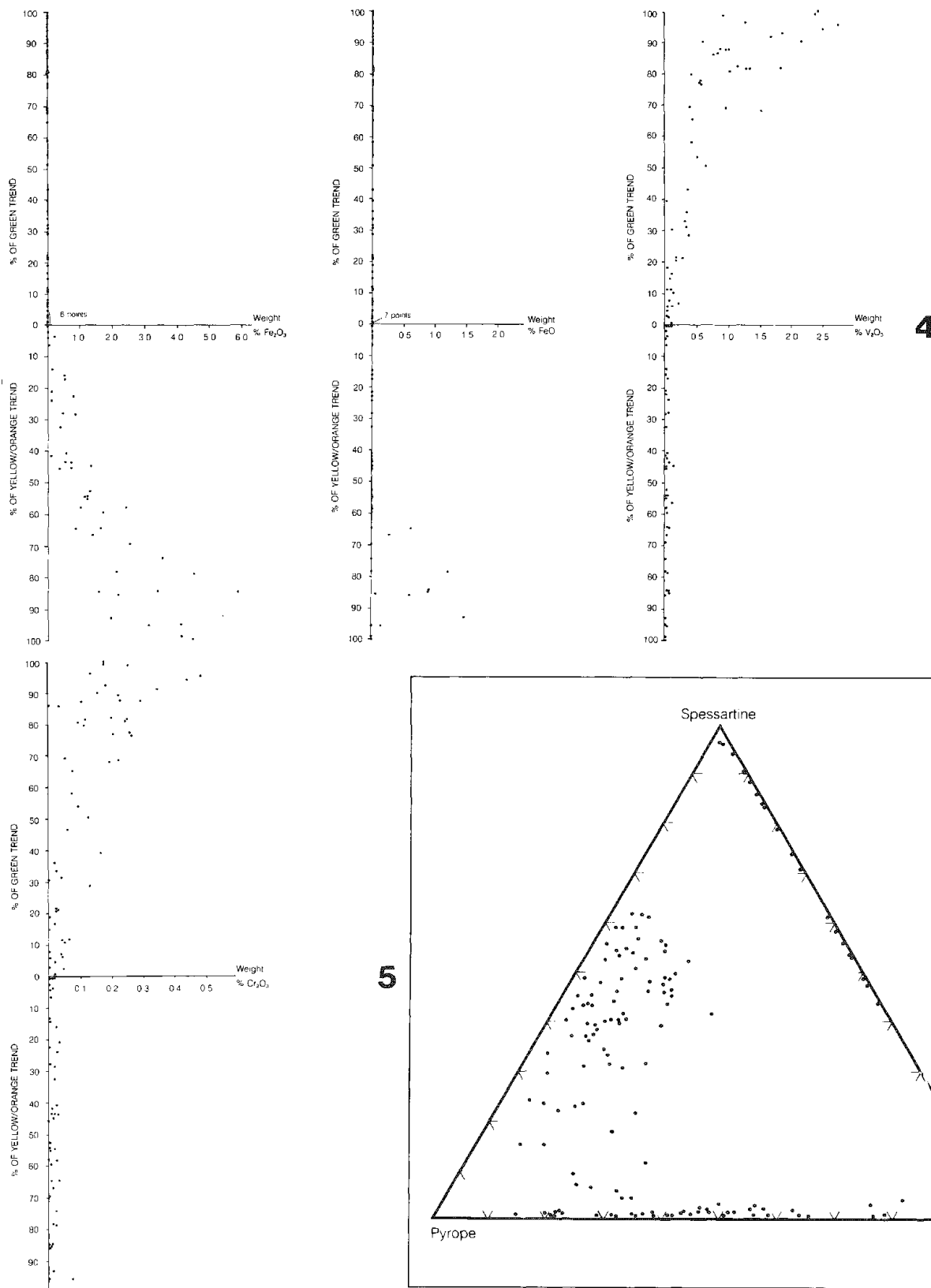


FIG. 4.--Weight percentages of  $\text{Fe}_2\text{O}_3$ ,  $\text{FeO}$ ,  $\text{V}_2\text{O}_5$ , and  $\text{Cr}_2\text{O}_3$  plotted against increasing depth of yellow/orange and green color exhibit correlation of  $\text{Fe}_2\text{O}_3$  with former colors, and both  $\text{V}_2\text{O}_5$  and  $\text{Cr}_2\text{O}_3$  with latter.

FIG. 5.--Compositional distribution of 139 garnets composed predominantly of pyrope, almandine, and/or spessartine end-member components, in weight percent. None of these stones contains more than 25 wt% grossular, and most have considerably less.

## ELECTRON AND ION MICROPROBE INVESTIGATION OF PLAGIOCLASE PHENOCRYSTS IN THE FRENCHMAN SPRINGS AND ROZA MEMBERS OF THE COLUMBIA RIVER BASALTS

J. R. Hinthorne and R. D. Bentley

Plagioclase phenocrysts in thin section of lava flows from the Frenchman Springs and Roza Members of the Columbia River Basalts, Central Oregon and Washington, were analyzed in detail with the electron microprobe (35 samples) and ion microprobe (8 samples) to test the hypothesis that detailed chemical distributions in these crystals might yield information useful for correlating individual lava flows across the Columbia Plateau that have proved to be difficult to correlate by more conventional methods. Some useful correlations have proved to be possible; e.g., the recognition of two of the Roza flows some tens of miles farther south in Oregon than previously suspected. The most useful kind of data seems to be detailed electron probe line scans (400-700 points per line with 2-5  $\mu\text{m}$  point spacing) for the Ca component ( $\text{CaAl}_2\text{Si}_2\text{O}_8$  = anorthite) in the phenocrysts. It was also found that two successive flows in Oregon contain plagioclase phenocrysts with much higher Ca content than previously reported for the Columbia River Basalts: 85-90% anorthite (An) component (compared with 55-65% An for all other flows). Ion-microprobe data on seven trace elements seem to provide limited additional information, but support the conclusions drawn from the electron-probe data. The compositions of Ca-rich and Ca-poor pyroxenes found in a melt inclusion in a plagioclase phenocryst indicate a minimum equilibration (eruption?) temperature of about 1130 C for one of the Frenchman Springs flows.

In the Columbia Plateau geologic province of Oregon, Washington, and Idaho, extraordinarily voluminous basaltic lava flows (some more than 100 cubic km) erupted from about 17 million years before present (mybp) to about 13.5 mybp, with smaller eruptions continuing until about 6 mybp. Crustal deformation during and after the eruptive period has resulted in large-amplitude folds and numerous faults with displacements of up to one mile.

The Hanford nuclear facility, including present and possible future nuclear power plants and waste storage sites, is located near the center of the area covered by the Columbia River Basalt (CRB) flows. Since 1972 major efforts have been under way by many organizations and investigators to characterize the rock

The authors are in the Department of Geology, Central Washington University, Ellensburg, WA 98926. They wish to thank Jack Powell for helping collect and tentatively identify most of the samples, the Office of Graduate Studies and Research at CWU for financial support, Floyd Hodges of Battelle PNL, for the electron probe time (through a NORCUS fellowship to JRH), and Nicholas Marquez of Aerospace Corp. for the ion microprobe time and operational assistance.

materials themselves and to decipher the history of deformation in the Columbia Plateau in order to gain a better understanding of the general geology of the area and to improve the assessment of risk associated with the nuclear facilities.

Accurate correlation of individual flows from point to point throughout the plateau is one of the factors crucial to the proper interpretation of the timing and intensity of structural deformation in the area. This microprobe study was undertaken as a pilot project to determine whether detailed mineral chemistry, and chemical zonation patterns of phenocrysts in particular (as indicators of conditions and processes in the magma chambers prior to eruptions), could be of value in the identification of individual lava flows. Other field and laboratory techniques have not been entirely successful in answering the correlation questions because the appearance, mineralogy, bulk chemistry, and magnetic character of many of the flows are extremely similar.

### *Samples and Experimental Methods*

Samples of basalt were collected specifically for this study from exposed sequences of basalt flows previously mapped in detail and assigned to the Frenchman Springs or Roza Members of the Wanapum Basalt Formation of the Columbia River Basalt Group. The localities collected are geographically distributed from Vantage, on the Columbia River in Central Washington, south to the Hanford area in Washington, southwest to near Maupin on the Deschutes River in north-central Oregon and west to Portland. Because phenocrysts are quite rare in some of the flows (e.g., less than one per 10  $\text{m}^2$  of surface exposure), large samples were sometimes needed and numerous saw cuts required to find appropriate phenocrysts for analysis. When an appropriate crystal was located on a sawed face, a polished thin section of that portion of the rock was prepared by a commercial thin-section service. No attempt was made to achieve consistent crystallographic orientation of the minerals analyzed.

After carbon coating, the phenocrysts were documented by photomicrography on a polarized-light microscope. The photographic documentation was critical to locating the most appropriate areas for microanalysis because the chemical zonation patterns are qualitatively shown in transmitted-light photomicrographs.

The electron microprobe used for this work is a JEOL 733 Superprobe with three scanning spectrometers, Tracor Northern automation system, and Sandia TASK software. The analytical standards used were Lake County labradorite for Si, Al, Ca, and Na, and other well-known mineral standards for the minor elements K, Fe, and Mg. An electron beam of 15 kV, 20 nA,

focused to about 1  $\mu\text{m}$ , was used for all analyses. Na and K were always measured first to minimize any possible effects of volatilization. Standards were checked and/or remeasured at the beginning and end of every working session or every 12-24 h during long periods of continuous operation (up to 100 h). Each point analysis was normalized to constant probe current by a Faraday cup measurement. The Sandia TASK software incremented the stage position during line traverses, controlled the data acquisition, computed concentrations (alpha factor method) and mineral formulas, and reported the data as individual analyses and in tabular summary form. Analyses of other phases (ilmenite, magnetite, pyroxene, olivine, and glass) in the basalts for 6-10 elements were conducted using the same beam conditions and appropriate groups of mineral standards.

The ion microprobe, an ARL IMMA, was used to analyze some of the same crystals in the same polished and carbon-coated thin sections. The analytical conditions were: 0- beam, 20 kV, 4-6 nA, 20  $\mu\text{m}$  diameter. Secondary ions peaks were counted for 10 s.

Table 1 gives the chemistry of typical grains of the three main silicate mineral phases in the basalts, plagioclase, pyroxene, and olivine (sometimes absent).  $\text{Cr}_2\text{O}_3$  was sought, and found to be less than 0.02% in the pyroxene and olivine.

## Results

*Plagioclase.* Representative results from the microprobe line traverses are shown in Fig. 1. The three lower traces represent three major flow units of the Frenchman Springs (FS) Member; the upper trace (SQ-4) is from the Roza Member overlying the FS. Note the very similar patterns for the SQ-1, SQ-2, and SQ-3 phenocrysts: uniform composition for most of the distance from the center toward the edge of the crystal, a somewhat erratic behavior and slight increase of 2-3% An as the edge is approached, a decrease to approximately 58% An, and a final narrow-edge zone with rapidly decreasing An contents. The collective features of these three patterns are found in the analyzed phenocrysts in samples of the thick FS flows collected throughout the study area. We believe the pattern is a fairly reliable "fingerprint" for recognition of the main FS flows. The data from several locations suggest that the phenocrysts in the oldest (lowest) FS flow (e.g., SQ-1) consistently have slightly lower An contents in the central portions of the crystals, 57-59% An, compared with the younger FS flows, 61-63% An (e.g., SQ-2 and SQ-3); confirmation of this small difference on more samples would establish a microchemical fingerprint for this single flow.

The plagioclase phenocryst zoning pattern for the Roza Member flow (SQ-4) in Fig. 1 differs considerably from the FS patterns. The central region has a relatively high An content (65-68%) and there is no extended central region of uniform composition. Instead, the composition changes gradually to lower An toward the edge with a couple of major pertur-

bations. This pattern was observed in samples from two other localities (including a drill-core sample from near Hanford) and seems to be a dependable characteristic or phenocrysts contained in the lowest flow of the Roza Member. Figure 2 shows the similarity of the drill-core sample (RZ-12-2) and sample SQ-4; both have been identified by other workers to be the lowest Roza flow. Though of lower spatial resolution, the pattern for sample MP-24 (from Maupin, Oregon) is indistinguishable from the other two, and we therefore assign that sample to the lowest flow of the Roza Member. This is the first recognition of Roza flows so far south, near the southernmost exposures of the CRBs. A different zoning pattern, with several distinctive characteristics, obtained from a younger Roza flow (unlabeled in Fig. 3) compares quite well with the flow (MP-25; Fig. 3) found just above MP-24 near Maupin, and helps confirm the presence of the Roza Member at this location. We tentatively conclude that two of the Roza flows have been "fingerprinted" by microchemical analysis.

*Pyroxene.* Pyroxene phenocrysts were found to be almost entirely absent from the FS and Roza flows sampled. Compositions of a few microphenocrysts and the abundant groundmass pyroxene probably depend to a large extent on factors such as flow thickness and local cooling rate, which makes the chemistry generally less useful for correlation purposes. However, two FS flows (MP-16 and MP-17) from Maupin, Oregon, have relatively large, thin, bladed plagioclase phenocrysts with very unusual compositions in the core regions of 80-90% An, and narrow rims with 58-63% An (like normal FS phenocryst cores). Several pockets of trapped magma are found as rounded blebs in the cores of these phenocrysts; most have devitrified to "clay," but in one in MP-16 the isolated magma crystallized small grains of two pyroxene compositions. The compositions are plotted in Fig. 3, along with typical groundmass pyroxenes. The tight clustering of the two groups of pyroxene grains suggests that equilibrium was attained and that the pair of compositions could be useful as a geothermometer. Experimental petrology studies (summarized by Huebner<sup>1</sup>) on pyroxene pairs similar in average composition to the pair measured here can be used to estimate the minimum temperature of equilibration for the pair. This temperature is about 1130 C and is interpreted to be the temperature at which slow cooling ceased, followed by eruption and rapid cooling. It is probably the temperature at which the plagioclase phenocryst rim (50% An) crystallized, rather than the core.

*Trace Elements.* A total of 14 ion microprobe analyses were done on phenocrysts in 8 selected samples. The elements Li, B, F, Rb, Sr, Y, and Ba were detectable in each analysis and data were recorded by measurement of the positive secondary-ion intensity for the main isotope of each. For intercomparison of samples, the data were ratioed to Si to remove most of the instrument drift and ion yield problems. Generally, no clearcut trends are apparent in this data set that would significantly add to

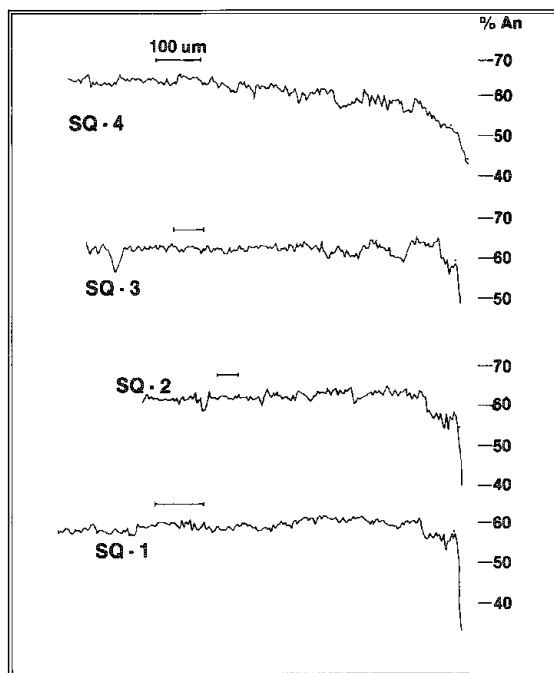


FIG. 1.--Plots of anorthite contents (An) vs distance along traverses from centers of plagioclase phenocrysts to edges (zoning patterns). Samples were collected from well-exposed section at Squaw Creek, between Ellensburg and Yakima, Washington. Scale bar for each represents 100  $\mu\text{m}$ .

TABLE 1.--Representative analyses of Frenchman Springs basalt silicate phases. All are from sample SQ-3b collected between Ellensburg and Yakima, Washington. (Values in wt%; n.a. = not analyzed, assumed to be very low abundance.)

	Plagioclase	Pyroxene	Olivine
$\text{SiO}_2$	54.77	50.22	36.13
$\text{Al}_2\text{O}_3$	27.85	1.88	0.03
$\text{TiO}_2$	n.a.	1.09	0.03
$\text{FeO}$	0.57	14.16	28.76
$\text{MnO}$	n.a.	0.36	0.34
$\text{MgO}$	0.14	14.25	33.54
$\text{CaO}$	12.15	18.41	0.23
$\text{Na}_2\text{O}$	4.30	0.28	n.a.
$\text{K}_2\text{O}$	0.41	0.03	n.a.
Total	100.19	100.68	99.06

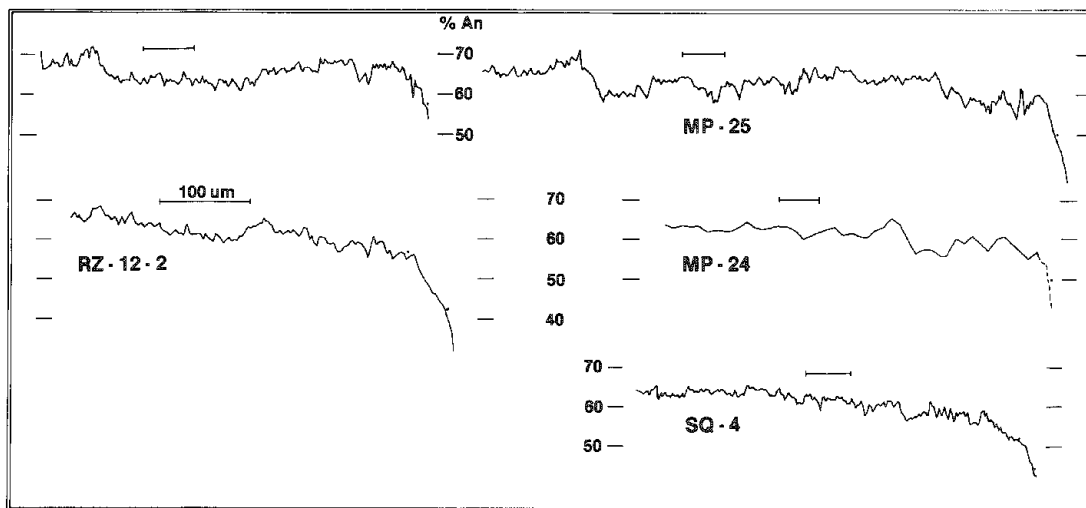


FIG. 2.--Comparison of zoning patterns for plagioclase phenocrysts from known and proposed Roza Member flows. Samples are from Hanford (drill core; RZ and unlabeled), Maupin, Oregon (MP), and Squaw Creek (SQ).

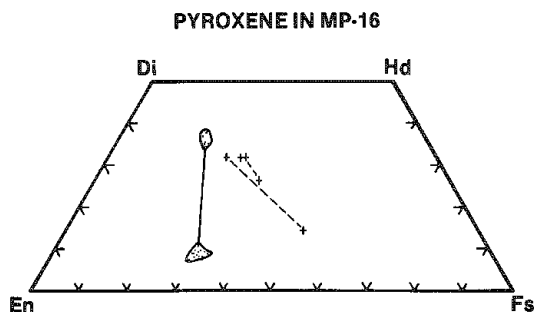


FIG. 3.--Pyroxene composition diagram showing typical zoning trends in groundmass pyroxenes (+ symbols), and coexisting Ca-rich and Ca-poor pairs (groups joined by solid tie line) found enclosed in plagioclase phenocryst from Maupin, Oregon, Frenchman Springs Member section. En =  $\text{MgSiO}_3$ ; Fs =  $\text{FeSiO}_3$ ; top corner of triangle (not shown) =  $\text{CaSiO}_3$ .

or change the conclusions based on the major-element electron-probe data, perhaps because the precision of analysis (10-20%) exceeds the trace element variability between most of the samples and so suggests they all had a similar origin and history.

Li, Sr, and Ba appear to have the most potential use. Table 2 shows the data for these elements. The Li, Ba, and Sr (minor) enrichment in the rims of MP-16 and MP-17 shows possible contamination of the magma while resident in the crust prior to eruption. Note the similarity of Sr and Ba in three samples proposed (on the basis of zonation patterns) to be from the same flow (RZ-12-2, SQ-4, and MP-24; see Fig. 2).

#### *Summary*

Of the 35 samples in which phenocryst zonation patterns were analyzed, collected from 10

localities throughout the Columbia River plateau, about half have provided useful microchemical data to assist in making correlations of individual lava flows or of relatively small groups of lava flows. This technique probably can be expanded to many other flows in the CRB Group with good results. Careful sampling and accurate, high-precision microprobe analyses of hundreds of points per crystal are needed because the chemical variation within and among the phenocrysts is generally small.

#### *References*

1. J. S. Huebner, "Pyroxene phase equilibria at low pressure," in C. T. Prewitt, Ed., *Reviews in Mineralogy: Pyroxenes*, Washington, D.C.: Mineralogical Society of America, vol. 7.

TABLE 2.--Ion microprobe data for Li, Sr, and Ba from selected phenocrysts. (All values are count rates  $\times 10\ 000$ , ratioed to  $\text{Si}^+$ .)

	MP-16		MP-17		RZ-12-2	SQ-4	MP-24
	core	rim	core	rim	core	core	core
Li+	1.8	3.4	1.2	1.6	2.0	4.9	3.4
Sr+	31.	36.	22.	23.	26.	26.	30.
Ba+	1.3	7.1	1.0	2.8	3.5	3.3	3.8

## COMPUTER-AIDED IMAGING OF BASALTIC GLASS

J. J. Friel

The feasibility of isolating nuclear waste by burying it underground has spurred extensive study of the composition and properties of various rock types and of their geochemical reactions.<sup>1</sup> In the case of basalt, a significant amount of intersertal silicate glass is present which is metastable with respect to crystalline phases of different composition. Inasmuch as geochemical stability is crucial for nuclear-waste isolation, the glass phase assumes an important role. Glass compositions are usually variable even in the same sample both within and between individual glass pools. Furthermore, it is often not clear whether or not this variability merely represents continuous variation of late liquid composition or the presence of more than one discrete phase formed either by liquid immiscibility or subsolidus exsolution. Computer-aided imaging of the energy-dispersive x-ray signal can disclose the internal texture of the volcanic glass and reveal local inhomogeneities, which in turn could affect the dissolution kinetics of the rapidly dissolving glass phase.

### Method

The intersertal glass of two basalt samples was examined both optically and in the SEM. One sample was a Columbia Plateau basalt from the Cohasset flow (53 wt% SiO<sub>2</sub>);<sup>2</sup> the other was from the Krafla flow (49 wt% SiO<sub>2</sub>) in northeastern Iceland.<sup>3,4</sup> Contrast mechanisms such as secondary electrons, backscattered electrons, and transmitted and reflected light do not clearly show the texture within intersertal pools of glass because of the fine grain size, small differences in average atomic number, and dark color of the Fe-rich glass. As a consequence of this difficulty, quantitative analysis of individual points produces haphazard results, as the beam often falls on more than one phase. Sodium loss is also a problem at moderate beam dwell times. However, x-ray mapping with dwell times of a few tenths of a second per point and adequate x-ray spatial resolution begins to reveal the texture. The resolution is of course controlled by the x-ray range, which is in turn affected only by the overvoltage and the density of the sample. For example, at 10 kV accelerating voltage, the x-ray resolution possible in the glass phase is about 1  $\mu$ m.<sup>5</sup> At 500 $\times$  magnification, a typical digital imaging resolution of 128  $\times$  100 beam steps results in 1.6  $\mu$ m/pixel, calculated from  $n = L/MR$ , where  $n$  = the number of pixels in one direction needed to match the x-ray resolu-

tion,  $L$  = length of the test line digitized on the CRT,  $M$  = magnification, and  $R$  = x-ray range, all in the same units of length. Since the number of digital steps available is usually selected from a fixed list of possibilities, pixel resolution is actually  $L/n'M$ , where  $n'$  is the number of digital beam steps; i.e., 128. In this case,  $10\text{cm}/(128 \times 500) = 1.6 \mu\text{m}/\text{pixel}$ .

Inasmuch as 1.6  $\mu$ m is larger than the x-ray-excited area (1.0  $\mu$ m), resolution is inadequate. However, a raster of 256  $\times$  200 beam steps results in 0.8  $\mu$ m/pixel, which is smaller than the x-ray-excited area and is therefore suitable for this magnification. At higher magnifications, fewer pixels would be required. Accordingly, a true, live-time-corrected, background-subtracted x-ray intensity map is capable of revealing submicrometer texture. The precision of the data is of course limited by the number of x-ray counts that can be collected in the dwell time. However, the large number of points sampled and the lack of significant Na loss make it possible to see textures that would otherwise be concealed.

For the samples of volcanic glass, an ISI SS-40 SEM was operated at 10 kV and a beam current of 2.0 nA. Takeoff angle was 44°, and the PGT EDS detector was used in either the windowless or ultrathin window mode to enhance the collection of Na x rays. Glass-rich regions of each sample were mapped for Na, K, Al, Si, Ca, Mg, Fe, and Ti, and sometimes O, by use of a PGT microanalysis system. After the maps were collected and stored, the computer screened the intensity at each pixel for each element of interest in accordance with the instructions of the analyst. At all points where the specified ranges of intensity were met, the computer drew those parts of the SE or BSE image. Various subimages thus generated were compared logically to find areas that were different. Each point in two subimages created by screening the x-ray data must either have identical intensities (i.e., corresponding pixels both illuminated or both off) or they must be completely different (one on and one off). One of these conditions must be true at each pixel, because parts of the same SE or BSE image are being compared. The EXCLUSIVE OR logical operation proved informative in this work because it showed only areas that were different.

### Results

To screen x-ray maps of glass-rich regions of the samples, we had the computer display only regions high in Si, so as to show only glass. In like manner, high-Na or high-K conditions were imposed to discriminate different glass compositions. Specifically, areas containing Si at more than 65% of its intensity range .AND. Na or K at more than 40% of

---

The author is with Princeton Gamma-Tech, 1200 State Rd., Princeton, NJ 08540. The samples were provided by G. H. Kacandes, D. E. Grandstaff, and G. C. Ulmer of Temple University. Assistance with the analyses provided by Ted Juzwak and John Weakliem's review of the manuscript are gratefully acknowledged.

theirs were defined as either high-Na glass or high-K glass. Figure 1 shows maps of the raw data for Na, K, Si, and O along with the BSE image and the computed images of Na- and K-glass. The ranges used to define Na- and K-glass were determined interactively and led to the observation of two distinct glass compositions within the same intersertal pools in both the Icelandic and the Columbia Plateau basalts. On the basis of this discovery, quantitative EDS analyses were performed at various points on each type of glass; the average compositions are reported in Table 1. It was evident that Na and Ca were positively correlated within the glass, as were K and Si. Na and K were negatively correlated.

In the Icelandic sample, the .EXCLUSIVE OR. logical comparison showed that two glass compositions formed a fine intergrowth in most intersertal pools and nearly all analyses clearly fell into either the high-Na or high-K category. In contrast, the Columbia Plateau sample was characterized by fewer regions of K-glass and they contained significant Na<sub>2</sub>O. Regions that were rich in K<sub>2</sub>O were typically less than about 2  $\mu$ m and of uniform composition; K<sub>2</sub>O was also present in the rest of the glass, but generally at less than one half the Na<sub>2</sub>O concentration. In both basalts, K-glass was often associated with Fe-Ti-Oxides. Computer-aided imaging greatly facilitated finding the regions of different composition, particularly the less abundant K-glass in the Columbia Plateau sample.

### Conclusions

Computer-aided imaging led to the discovery of at least two distinct glass compositions in basaltic glass. The ability to screen x-ray images interactively based on the intensity of selected elements provides a powerful tool with which to discover and quantify chemical associations. Furthermore, the use of logical comparisons between selected areas can lead to an even greater understanding of the microstructure. Consequently, x-ray maps are at least as useful for gathering information as they are for displaying it. Further work will be necessary to ascertain whether more than one distinct glass phase is present in other basalts, and how the glass phases behave under the conditions of nuclear-waste isolation.

TABLE 1.--Composition of bulk rock and glass phases.

	Cohasset (31% glass) <sup>a</sup>			Krafla (12% glass) <sup>a</sup>		
	Bulk comp <sup>2</sup>	Na-glass	K-glass	Bulk comp <sup>4</sup>	Na-glass	K-glass
SiO <sub>2</sub>	52.95	68.08	72.71	49.28	71.92	80.67
TiO <sub>2</sub>	1.69	0.70	0.66	0.80	na	na
Al <sub>2</sub> O <sub>3</sub>	15.08	14.34	13.41	16.75	16.25	11.50
FeO <sup>3</sup>	11.84	5.25	2.76	8.89	2.47	2.56
MnO	0.20	na	na	0.17	na	na
MgO	5.27	0.20	0.80	8.98	0.15	0.09
CaO	9.03	2.76	0.70	12.48	3.81	1.79
Na <sub>2</sub> O	2.55	4.82	2.36	2.27	4.00	0.70
K <sub>2</sub> O	0.94	2.06	4.06	0.09	0.73	2.50
P <sub>2</sub> O <sub>5</sub>	0.25	na	na	0.07	na	na
TOTAL	99.80	98.21	97.46	99.78	99.33	99.81

na = not analyzed

### References

1. K. B. Krauskopf, "Aqueous geochemistry of radioactive waste disposal," *Applied Geochemistry* 1: 15-23, 1986.
2. C. C. Allen, *Characterization of Reference Umtanum and Cohasset Basalt*, RHO-BWI-DP-053, Richland, Wash.: Rockwell Hanford Operations, 1985.
3. G. C. Ulmer et al., "Icelandic geothermal fields as an analog for nuclear waste disposal in basalt," *Advances in Ceramics*, vol. 20 (in press).
4. G. H. Kacandes, personal communication.
5. C. A. Andersen and M. F. Hasler, "Extension of electron microprobe techniques to biochemistry by the use of long-wavelength x-rays," in R. Castaing et al., Eds., *4th Intl. Cong. on X-ray Optics and Microanalysis*, Paris: Hermann, 1966, 310-327.

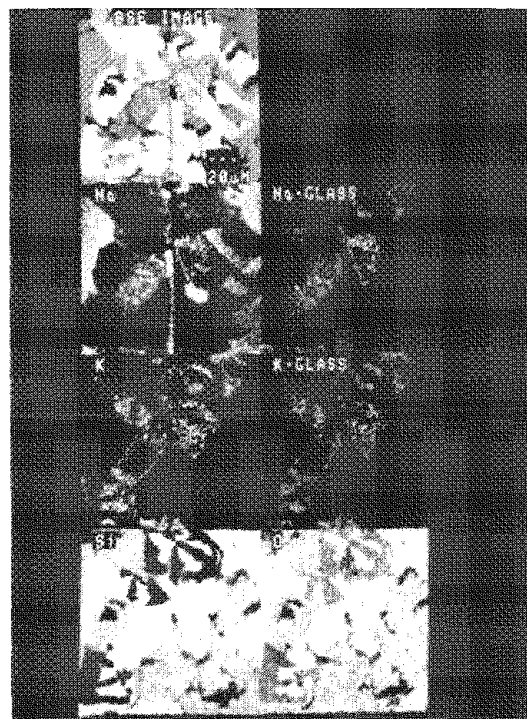


FIG. 1.--BSE image of Icelandic basalt with x-ray maps of Na, K, Si, and O. Parts of the BSE image showing different glass compositions are labeled Na-glass and K-glass.



## ANALYSIS OF MICROPOROSITY IN RESERVOIR ROCKS BY COMBINED SCANNING ELECTRON MICROSCOPY AND DIGITAL IMAGE ANALYSIS

C. J. Stuart, C. L. Vavra, and T. H. Levesque

Combined Scanning Electron Microscopy (SEM) and Digital Image Analysis (DIA) techniques can provide critical information on the amount, location, and size distribution of micropores in petroleum reservoir rocks. Micropore size, abundance, and location control porosity (storage capacity), permeability (flow capacity), hydrocarbon saturation, and the amount and type of fluids produced in hydrocarbon reservoirs. Previous techniques such as mercury injection or thin-section analysis were limited in that they could not determine micropore abundance, geometry, and size distribution on the same sample. In contrast, combined SEM and DIA can rapidly provide this information on an identical population of micropores in a standard polished thin section or rock slab.

A rock chip was pressure impregnated with blue epoxy and a polished 30  $\mu\text{m}$  thin section was prepared. The thin-section was coated with 300 Å of carbon. Backscatter electron imaging (BSE) was used for pore imaging because BSE provided optimum gray-level contrast between micropores and rock matrix (Fig. 1). Samples were examined at a variety of magnification. For this work, a magnification of 2000 $\times$  was chosen to optimize the sample analysis area and pixel resolution with respect to pore size distribution and sample complexity. This procedure provided high resolution and contrast between pore and rock matrix, and optimum data acquisition time, and also resolve most micropores, so that an increase in magnification resulted in no increase in the microporosity values.

BSE video images were acquired with a Tracor Northern TN5700 Image Analysis System on a ISI WB-6 SEM equipped with a Robinson Backscatter Detector. All images were collected at 15 kV in a 512  $\times$  512 pixel format. The best contrast image for later analysis was obtained by averaging 25 frames, with use of the Kalman frame-averaging technique. Acquisition time was under 30 s per image. These images were digitized to 256 gray levels and stored on disk. A binary image (Fig. 2) was created by an interactive segmentation technique used on a image histogram. The binary image was visually verified by overlaying it with the original digitized BSE video image. When present, artifacts of the segmentation process were removed by processing of the binary image with erosion and dilation. This processed image was compared to the original video image in order to insure correlation of the actual pore areas. Individual feature analysis was then carried out by a technique of rotating diame-

ter, whereby twenty diameters were rotated, with chord lengths measured every 18°. Area was determined by summation of the number of pixels comprising an individual pore. Initial data reduction and statistical analysis were made with the Tracor Northern Techcalc program. These data were then transferred to an IBM PC. Data processing and plotting (Fig. 3) were completed on the IBM PC with in-house statistical and graphics software.

An image field representing approximately 30  $\times$  30  $\mu\text{m}$  of the sample surface could be acquired and analyzed in under 5 min. The field data were automatically stored to disk, which allowed later retrieval or linking with data from other image fields. Linked data from multiple-image fields in each sample were then analyzed statistically to characterize the entire sample.

The SEM-DIA combination can rapidly provide critical data on the amount, location, and size of micropores in petroleum reservoir rocks. This is an important improvement over prior techniques because all measurements can be made on the same group of pores in the rock.

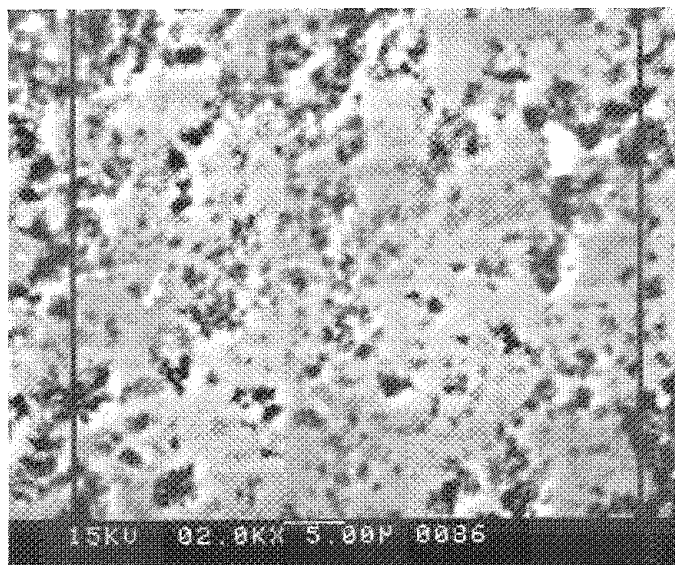


FIG. 1.--Backscatter electron image of polished thin-section illustrating gray-level contrast between micropores (black) and rock matrix (white). Black vertical lines are right and left boundaries of Fig. 2.

Authors Stuart and Vavra are at ARCO Oil and Gas Co., 2300 W. Plano Parkway, Plano, TX 75075; author Levesque is at Tracor Northern Inc., 4270 Kellway Circle, Dallas, TX 75244.

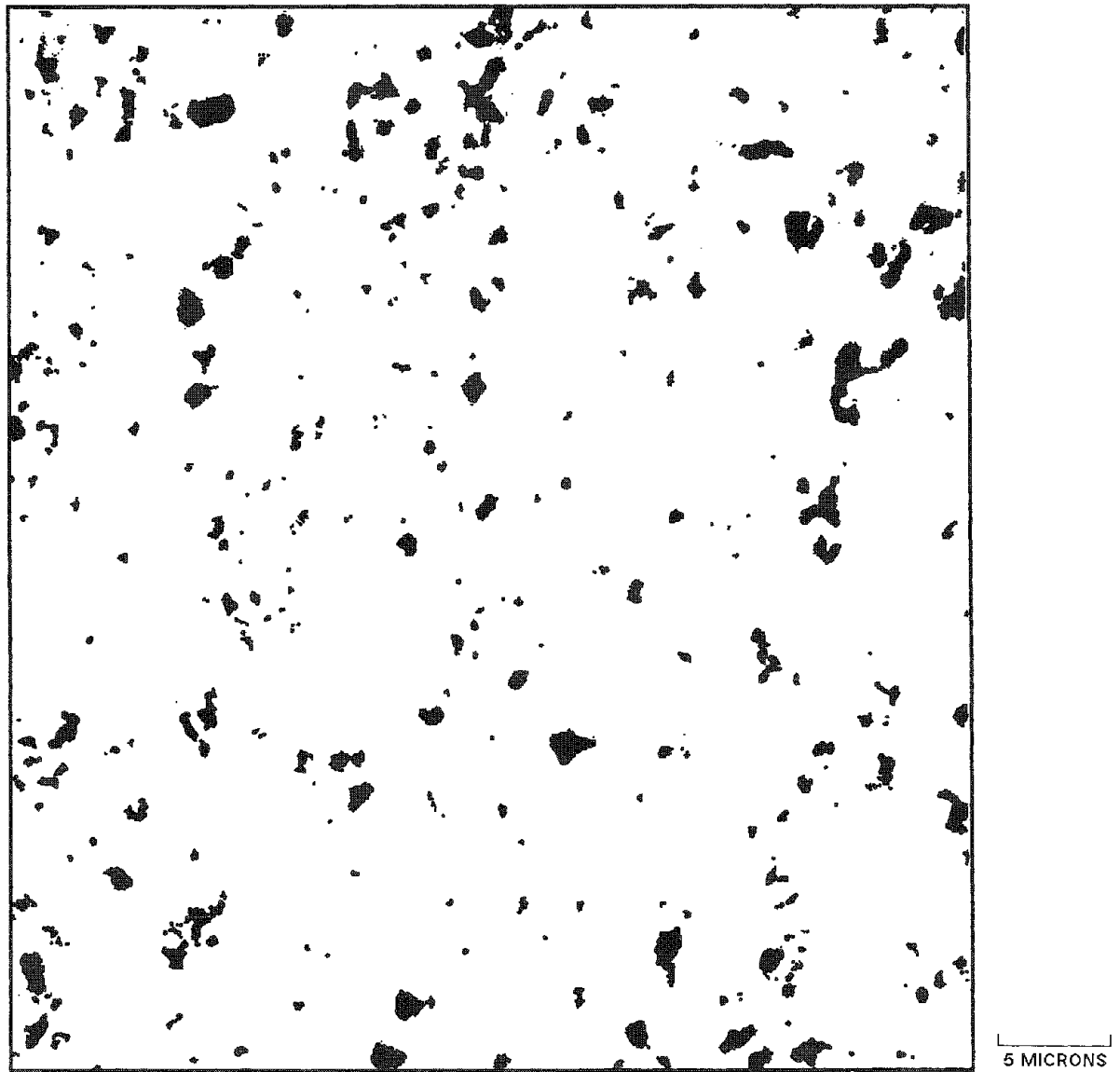


FIG. 2.--Processed binary image of a region of Fig. 1. Micropores are black, rock matrix is white.

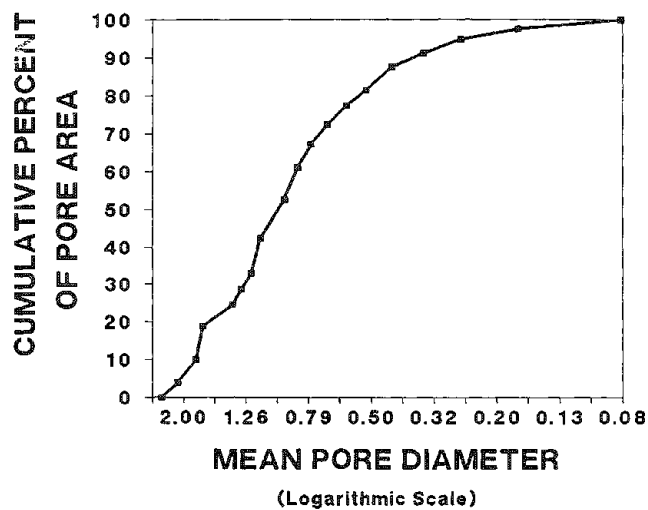


FIG. 3.--Plot of cumulative percent of pore area versus mean pore diameter. Pore diameter (in micrometers) was measured by rotating diameters; pore area was determined by calibration of area of an individual pixel and then integration of number of pixels in each pore.

## USE OF MICROBEAM METHODS IN THE STUDY OF DISSEMINATED GOLD DEPOSITS: PROSPECTING, 1980s STYLE

J. A. Minkin, E. C. T. Chao, J. M. Back, and J. R. Chen

For more than 20 years, mineralogists, petrologists and metallurgists have been trying to determine and understand the precise nature of the occurrence of the generally "invisible" gold in Carlin-type sediment-hosted, disseminated precious-metal deposits. The name "Carlin type" is derived from the Carlin gold deposit in north central Nevada, in the Lynn mining district near the crest of the Tuscarora Mountains.<sup>1</sup> Production at the Carlin mine began in 1965; the estimated gold reserves were approximately 11 million tons, averaging 0.32 oz of gold per ton.<sup>2</sup> Carlin-type deposits, currently the major U.S. commercial source of gold, are found mainly in Nevada, although examples are found elsewhere, e.g., in Mercur, Utah.<sup>3</sup> The geological characteristics of the Carlin gold deposit have been described by Hausen and Kerr<sup>2</sup> and Radtke.<sup>1</sup> A comprehensive review of the characteristics of Carlin-type deposits has been prepared by Bagby and Berger.<sup>5</sup>

### *Previous Studies*

Two main sequences of mineralization were postulated at Carlin by Hausen and Park.<sup>4</sup> They suggested an early (Cretaceous-Jurassic) base-metal mineralization associated with quartz-barite-calcite veins and igneous intrusions at a depth of about 6 km. The intrusive bodies included felsic dikes and stocks. Later (Tertiary) low-temperature introduction of Au, Hg, As, Sb, and Tl was related to shallow-level epithermal and thermal-spring activity. In addition, Bagby and Berger<sup>5</sup> suggested that oxidation of the ore, caused by weathering, probably occurred in the late Miocene to early Pliocene. Gold ore in Carlin-type deposits comes unoxidized and oxidized. Gold can be extracted from oxidized ore by simple cyanidization; for unoxidized ore, grinding and more complex chemical procedures are required.<sup>4</sup>

Observation of gold by direct methods in Carlin-type samples has proved to be most elusive. In field examination usually no distinction can be made between barren rock and ore.<sup>3</sup> Particulate gold has rarely been observed in unoxidized samples, even at magnifications up to 15 000 $\times$  in the scanning electron microscope (SEM). Wells and Mullens<sup>5</sup> concluded, on the basis of electron microprobe study (EPMA) of a limited number of samples from two locations, that gold in unoxidized ores is mostly associated with pyrite. Radtke<sup>1</sup> expanded the suite of samples analyzed to represent a better sampling of the entire Carlin

ore body and found six modes of gold occurrence in unoxidized Carlin ore: (1) as coatings or thin films on pyrite, (2) sporadically distributed on the surfaces of amorphous carbon grains, (3) in association with organic acid(s) as a gold-organic compound, (4) as metallic gold, (5) dispersed in realgar in solid solution or as metallic gold particles, and (6) in solid solution in sparse grains of elemental arsenic. Hausen and co-workers<sup>6</sup> prepared flotation and gravity concentrates of carbonate-dominated, siliceous, and argillaceous types of unoxidized ore from the Carlin deposit. Optical and SEM investigation of the prepared separates showed gold particles mainly associated with illitic agglomerations. Although most of these agglomerations were formed during the flotation process, the authors concluded that primary gold occurrence in illite was a strong possibility because separation products of high gold grades consistently coincided with high illite concentrations. Hausen et al. therefore suggested further investigation of this association. They found very little evidence of gold association with coarse pyrite (>30 $\mu$ m grain size), especially euhedral pyrite.

In oxidized ore samples, gold is more readily observed, at least at magnifications available with the SEM. According to Radtke,<sup>1</sup> gold is observed in oxidized ores as (1) fine metallic particles in seams and patches of silica, (2) particles on and near the borders of oxidized pyrite grains (that have been altered to iron oxides), (3) dispersed through iron oxide-rich patches in the matrix of the rock, (4) associated with clay minerals in the matrix, and (5) as randomly dispersed particles <5  $\mu$ m in size.

Wells and Mullens<sup>5</sup> were satisfied that their EPMA data on gold in pyrite accounted for almost all the gold indicated in the bulk chemical analyses of their samples. However, for all other investigations we have found in the literature, the amount of gold detected by optical/SEM/EPMA methods in any given sample, oxidized or unoxidized, has fallen short of the amount indicated by bulk chemical assays. This shortfall may be attributed mainly to two factors: first, that one cannot examine in a reasonable time enough of the surface of a sample at the magnifications needed to resolve the predominantly extremely fine gold particles; and second, the indication that most of the gold may exist in particle sizes finer (<0.1  $\mu$ m) than can generally be observed and identified by SEM augmented with energy-dispersive x-ray analysis (EDX). Transmission electron microscope (TEM) study by Hochella et al.<sup>7</sup> has shown that gold in the 0.01-0.04 $\mu$ m particle size range is associated with clays in an oxidized Carlin-type ore sample (M. F. Hochella, oral communication).

### *Strategy for the Present Study*

To extend the ability to determine the

Authors Minkin, Chao, and Back are at the U.S. Geological Survey National Center, Reston, VA 22092. Author Chen is at the Department of Physics at the SUNY College at Genesee, NY 14454. The authors thank A. L. Hanson, S. R. Sutton, K. W. Jones, and M. L. Rivers for use of the SXRF microprobe at Brookhaven National Laboratory, and W. C. Bagby and C. A. Kuehn for supplying the samples for this study.

precise modes of occurrence of gold in Carlin-type ore samples, we localize areas of significant gold concentration by combining micro-optical examination with synchrotron radiation fluorescence (SXRF) microprobe analysis, a quantitative, nondestructive technique with minimum detection limits (MDLs) for gold at the ppm level.<sup>8-10</sup> The SXRF microprobe at the National Synchrotron Light Source (NSLS) at Brookhaven National Laboratory has a spatial resolution of about 20  $\mu\text{m}$ ; analysis of a given area requires about 15 min. Use of the combined optical/SXRF procedure should substantially reduce the time required to locate and identify gold and its associations at electron microscope magnifications.

#### *Procedure*

Doubly polished thin sections are prepared on high-purity fused silica wafers to avoid the possibility of trace-element contamination of SXRF analyses by the substrate. Such sections permit petrographic examination by optical microscopy before selection of areas for SXRF analysis. After SXRF analysis the sample is reexamined with the optical microscope for further characterization of the areas in which gold was detected by SXRF, and differentiation from those in which no gold was found. EPMA and/or SEM analyses are then conducted to "home in" on the modes of gold occurrence indicated by SXRF. Several iterations are required to refine the observations and draw definite conclusions.

#### *Result of Preliminary Study*

This methodology has been applied to the study of doubly polished thin sections prepared from three samples identified as gold-bearing on the basis of bulk chemical analysis. The samples are: (1) a carbonaceous microbreccia (33 ppm Au); (2) a laminated, carbonaceous, partially silicified, de-calcitized sample (48 ppm Au); and (3) an oxidized, partially decarbonatized sample (74 ppm Au). Detailed results will be described elsewhere.<sup>11</sup> The following information is presented here to show how areas were chosen for EPMA and SEM investigation.

*Sample 1.* Highest amounts of gold detected by SXRF measurements were associated with certain siliceous areas in the matrix. Gold was not detected, with an incident synchrotron radiation beam diameter of 30  $\mu\text{m}$ , in detrital quartz grains, euhedral pyrite (grain size  $>30$   $\mu\text{m}$ ), or carbon-rich areas in this sample.<sup>8-10</sup>

*Sample 2.* Highest amounts of gold detected by SXRF appear to be associated with particular bands in this sample. Small amounts of quartz are present in these bands, as well as some scattered euhedral pyrite grains, mostly smaller than 10  $\mu\text{m}$ .

*Sample 3.* Gold was detected by SXRF principally in boundary zones between areas where carbonates have been leached or removed, and where the carbonate grains still remained.

Prior to SXRF study, EPMA (beam diameter 3  $\mu\text{m}$ , MDL for gold = 0.08 wt%) analysis of pyrite grains ranging in size from  $>30$  to  $<10$   $\mu\text{m}$  failed to detect any gold. Following SXRF

analysis, EPMA was used to analyze the gold-bearing areas in Samples 1 and 2 indicated by SXRF; no gold was detected by EPMA. Sample 3 has not yet been studied with the electron microprobe.

SEM study of gold-rich areas in these three samples has produced the following results so far.

*Sample 1.* Detailed scrutiny of the siliceous areas indicated as gold-rich by SXRF analysis revealed only four free gold particles (Fig. 1) that were identified by EDX. All four were found next to silica grains but not on or in them. Particle size ranged from 0.2 to 0.5  $\mu\text{m}$ . Other smaller particles of high contrast were observed in the SEM in the backscattered mode, but an EDX spectrum could not be obtained for them. Besides direct SEM examination, x-ray maps were generated with SEM-EDX for areas in the fine-grained siliceous matrix. The maps were obtained at 3000 $\times$  for 256 $\times$ 256 picture points, i.e., a step size of 0.15  $\mu\text{m}$  between points. Counts were taken for 0.6 s at each picture point, so that with a dead time of about 20%, generation of such a map required approximately 13 h. The minimum particle size of identifiable gold in these x-ray maps was found to be about 0.5  $\mu\text{m}$ .

*Sample 2.* No gold was observed with the SEM in this sample.

*Sample 3.* Like other investigators, we found gold much more in evidence in the oxidized sample. SEM examination of areas identified by SXRF analyses as gold-rich, found particulate gold, mostly in the 0.2- $\mu\text{m}$  size range, in much greater abundance than in Sample 1. Gold particles were associated with the borders of iron oxide pseudomorphs after pyrite (Fig. 2), adjoining calcite grains, dispersed within silica grains, and randomly dispersed in the matrix of the rock.

#### *Discussion and Conclusions*

The variations observed in the three samples show that the modes of occurrence of gold in Carlin-type ores are multiple and complex; a full understanding of paragenesis, implications for exploration, etc., will require careful study of many samples collected with appropriate geologic controls. Since so many samples must be studied, the use of rapid, sensitive analytical methods for locating the gold-bearing areas in each sample is important. That is why SXRF is valuable: it limits the time-consuming number and extent of the areas that must be examined with high-magnification techniques.

However, SEM examination of SXRF-pinpointed gold-bearing areas is not without problems. The penetration of the incident synchrotron radiation beam causes characteristic x rays to be emitted from as far as 30  $\mu\text{m}$  below the sample surface. Thus SEM-EDX, with a penetration of only 1-2  $\mu\text{m}$  at 25 kV, may be unable to detect much of the gold indicated by SXRF analyses. Furthermore, the geometry of the NSLS SXRF microprobe positions the target at an angle of 45 $^\circ$  to the incident beam, so that a small difference in focusing can result in a shift of the beam by as much as tens of micrometers along the target surface, which

means that the area examined in the SEM may not correspond to the gold-bearing area indicated by the SXRF analysis.

The greatest remaining problem is that only a small percentage of the gold present has been detected in the SXRF analyses, and a much smaller amount has been observed with the SEM. SXRF analysis would be enhanced if lower MDLs were attainable and smaller beam diameters were feasible. The imminent installation at NSLS of new insertion devices for the x-ray storage ring is expected to advance the achievement of both these objectives. The very small percentage of gold identified with the SEM emphasizes the desirability of extending these studies through the use of the TEM to evaluate the presence and associations of gold particles smaller than 0.1  $\mu\text{m}$ .

#### References

1. A. S. Radtke, "Geology of the Carlin gold deposit, Nevada," U.S. Geological Survey professional paper 1267, Washington, D.C.: Government Printing Office, 1985.
2. D. M. Hausen and P. F. Kerr, "Fine gold occurrence at Carlin, Nevada," in J. D. Ridge, Ed., *Ore Deposits of the United States, 1933-1967*, New York: AIME, 1968, 908-940.
3. W. C. Bagby and B. R. Berger, "Geologic characteristics of sediment-hosted, disseminated precious-metal deposits in the western United States," in B. R. Berger and P. M. Bethke, Eds., *Geology and Geochemistry of Epithermal Systems*, El Paso, Tex.: Economic Geology Publishing Co., 1986, 169-199.
4. D. M. Hausen and W. C. Park, "Observations on the association of gold mineralization with organic matter in Carlin-type ores," in W. E. Dean, Ed., *Proc. Denver Region Exploration Geologists Soc. Symp. on Organics and Ore Deposits, Wheat Ridge, Colo.*, 1986, 119-136.
5. J. D. Wells and T. E. Mullens, "Gold-bearing arsenian pyrite determined by microprobe analysis, Cortez and Carlin gold mines, Nevada," *Economic Geology*, 68: 187-201, 1973.
6. D. M. Hausen, J. W. Ahlrichs, W. Mueller, and W. C. Park, "Particulate gold occurrences in three Carlin carbonaceous ore types," *Process Mineralogy* (in press).
7. M. F. Hochella, B. M. Bakken, A. F. Marshall, D. W. Harris, and A. M. Turner, "Scanning Auger and transmission electron microscopy of pyrite grains in carbonaceous ore concentrates," *Abstr. AIME 116th Ann. Meeting*, Denver, 1987, 37.
8. J. R. Chen, E. C. T. Chao, J. A. Minkin, J. M. Back, W. C. Bagby, M. L. Rivers, S. R. Sutton, B. M. Gordon, A. L. Hanson, and K. W. Jones, "Determination of the occurrence of gold in an unoxidized Carlin-type ore sample using synchrotron radiation," *Nuclear Instruments and Methods* (in press).
9. E. C. T. Chao, J. A. Minkin, J. M. Back, J. R. Chen, W. C. Bagby, M. L. Rivers, S. R. Sutton, A. L. Hanson, B. M. Gordon, and K. W. Jones, "Occurrence of gold in an unoxidized Carlin-type ore sample: A preliminary synchrotron and micro-optical restudy," *Abstracts GSA Ann. Meeting*, San Antonio, 1986, 562.
10. E. C. T. Chao, J. A. Minkin, J. M. Back, W. C. Bagby, C. A. Kuehn, J. R. Chen, K. W. Jones, and A. L. Hanson, "Synchrotron and micro-optical studies of gold in five Carlin-type ore samples," *Abstr. AIME 116th Ann. Meeting*, Denver, 1987, 37.
11. E. C. T. Chao (in preparation).

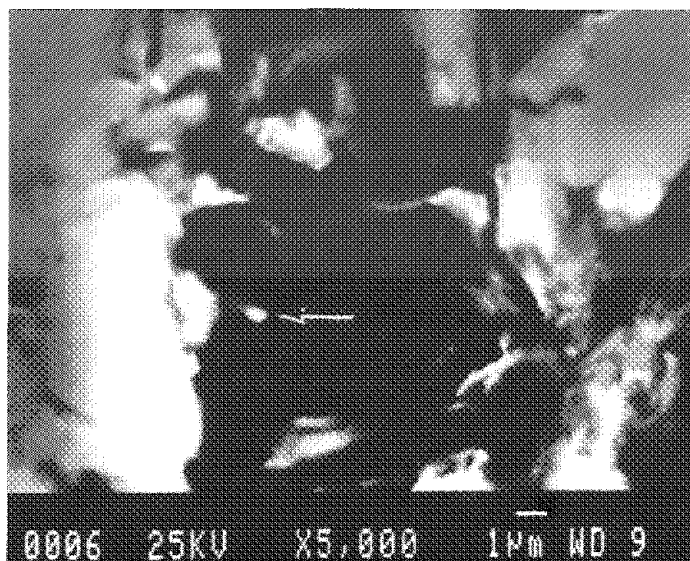


FIG. 1.--Secondary electron micrograph of part of area of fine-grained fragments in Sample 1, showing free gold particle (arrow) in void adjoining silica grain.

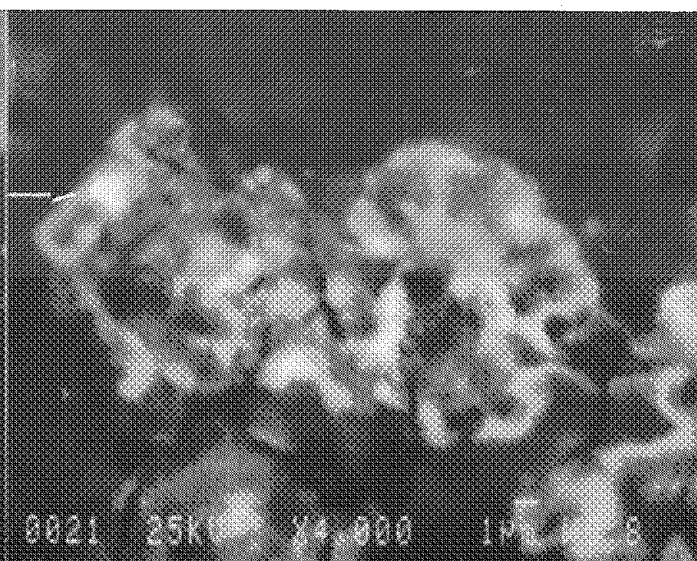


FIG. 2.--Backscattered electron micrograph showing gold particle (arrow) associated with rim of oxidized euhedral pyrite grain that has been altered to iron oxide in Sample 3.

## MICROANALYSIS OF CLAYS AT LOW TEMPERATURE

I. D. R. Mackinnon and S. A. Kaser

Accurate thin-film energy dispersive spectroscopic (EDS) analyses of clays with low-atomic-number (low Z) elements (e.g., Na, Al, Si), presents a challenge to the microscopist not only because of the spatial resolution required, but also because of their susceptibility to electron beam-induced radiation damage<sup>1</sup> and very low x-ray count rates. Most common clays, such as kaolinite, smectite, and illite, occur as submicrometer crystallites with varying degrees of structural order in at least two directions<sup>2</sup> and may have dimensions as small as one or two unit cells along the basal direction.<sup>3</sup> Thus, even clays with relatively large a-b dimensions (e.g., 100 × 100 nm) may be <5 nm in the c-axis direction. For typical conditions in an analytical electron microscope (AEM), this sample thickness gives rise to very poor count rates (<200 cps) and necessitates long counting times (>300 s) in order to obtain satisfactory statistical precision. Unfortunately, beam damage rates for the common clays are very rapid (<10 s in imaging mode)<sup>1</sup> between 100 and 200 kV. With a focused probe for elemental analyses, the damage rate is exacerbated by a high current density and may result in loss of low-Z elements during data collection and consequent loss of analytical accuracy.

In a study of element loss in feldspars under typical analytical conditions, Mackinnon et al. showed that both Na and Al loss could be reduced by cooling of the sample to low temperatures during analysis.<sup>4</sup> At -150 C, averaged  $k_{\text{AlSi}}$  and  $k_{\text{NaSi}}$  values showed no significant variation with collection time for periods up to 300 s, whereas averaged k-factors increased considerably with collection time for analyses at 20 C. In practice, this result suggests that it may be possible to obtain accurate chemical analyses of fine-grained, beam-sensitive samples by use of techniques at the scale of the individual mineral grains. This possibility is important for many areas of clay mineralogy, not least those dealing with mineral diagenesis in both terrestrial and extraterrestrial environments (see, for example, Ref. 5). In order to test the utility of this approach for minerals more difficult than albite, thin-film analyses over a range of temperatures to -150 C have been obtained from well-characterized clays. In addition, further data on albite k-factors at a higher beam current density than reported in Ref. 4 are provided.

### Experimental

Analyses were obtained via a JEOL 2000FX

The authors performed this work at the Electron Microbeam Analysis Facility in the Department of Geology, University of New Mexico, Albuquerque, NM 87131. Partially supported by NASA grant NAG9-160.

AEM at an accelerating voltage of 200 kV with an attached Tracor-Northern TN-5500 EDS, with nominal resolution of 143 eV (column test, Mo K $\alpha$  FWHM) and take-off angle of 72°. Particular care is taken to insure that excessive backscattered radiation to the detector is reduced during all microscope operations in order to maintain detector performance over long time periods. This care includes a protective shutter, which is used on all occasions other than data collection, a low-magnification interlock with motor-drive, and no use of objective apertures when the detector is inserted for analysis. All samples were dispersed on holey carbon films on 150-mesh Be grids and housed in Gatan low-background, double-tilt holders during analysis. Beam currents at the sample were measured with a simple Faraday cup and picoammeter attached to the double-tilt holders and ranged from 0.25 to 1.05 nA, depending on selected lens configurations and electron sources. For all analyses, column vacuum was  $<1.5 \times 10^{-5}$  Pa. Further details on data collection conditions are given in Mackinnon et al.<sup>4</sup> Clay samples are from the Source Clays repository of the Clay Minerals Society in Indiana and are described by Van Olphen and Fripiat.<sup>6</sup>

### Observations

In the previous study of *Amelia albite*,<sup>4</sup> a W hairpin filament was used for all spectra collection and provided a beam current of <0.2 nA at the sample for a nominal beam diameter (FWTM) of 35 nm.<sup>7</sup> More recent data for *Amelia albite* at -150 C (at a higher current density, from an LaB<sub>6</sub> filament) are plotted in Fig. 1, along with k-factors obtained with a W hairpin filament. Again, a significant improvement in the behavior of both  $k_{\text{NaSi}}$  and  $k_{\text{AlSi}}$  with collection time can be observed for low-temperature analyses. However, the influence of a higher beam current density on element loss at low temperature is apparent for collection times >200 s as both k-factors deviate significantly from the linear trend shown for W filament data.

Well-crystallized Georgia kaolinite (Sample No. KGa-1 of the Source Clays) has an Al/Si ratio of 1.04 (bulk analysis)<sup>6</sup> and a data point at the high end of a  $\text{Ca}_{\text{Al}}/\text{CSi}$  vs  $\text{I}_{\text{Al}}/\text{I}_{\text{Si}}$  plot. Figure 2 shows the variation of  $k_{\text{AlSi}}$  for kaolinite with irradiation time at -150 C. At least 15 separate spectra were collected and averaged for each time point shown in Fig. 2. Standard deviations are Students' t-test-weighted values.<sup>8</sup> For collection times <100 s, k-factors show little or no significant deviation and suggest that element loss is minimized at -150 C. However, an increase in  $k_{\text{AlSi}}$  values is evident for collection times >100 s and corresponds with a general loss of higher order reflections in microdiffraction patterns obtained from similar grains. This rise of the

k-factor curve indicates that element loss may become significant for kaolinite samples at collection times of 200 s or more. The slight minima in this k-factor curve (Fig. 2) at 100 s is probably due to better counting statistics compared with that obtained for the 25 and 50 s data.

The Wyoming montmorillonite (Sample No. SWY-1 from the Source Clays) is a fine-grained (<50nm) sample with minor amounts of Na, Mg, Fe, Ca, and K according to bulk analyses,<sup>6</sup> as shown in Table 1. A total of 30 analyses of this sample were obtained at -150 C for two different collection times and beam current values. All 30 analyses were reduced to normalized oxide weight percent values with k-factors previously determined for these instrumental conditions.<sup>4</sup> Table 2 contains the k-factors used for this data reduction along with relevant correlation coefficients and sample size. The reduced oxide weight percent values for SWY-1 are shown in Table 1 for comparison with the normalized bulk analysis from wet chemical techniques.<sup>6</sup> Such a comparison with bulk chemical analyses is subject to some uncertainty owing to the unavoidable inclusion of impurity minerals (such as quartz and carbonates) during collection and processing.<sup>6</sup> However, within the limitations of the technique, it appears that analyses showing consistent trends can be obtained from beam-sensitive clay minerals. Table 1 indicates that all low-Z elements (except Si) show a general decrease in relative value as the beam current and collection time increase. This variation in smectite analyses with beam current and irradiation time is consistent with a loss of low-Z elements during data collection, even at low temperature (-150 C).

#### Summary

Element loss during thin-film analyses of silicate minerals prone to electron-beam-in-

duced irradiation damage can be reduced by collection of data at low temperatures (e.g., -150 C) and for relatively short counting times (<200 s). For high beam current densities from LaB<sub>6</sub> filaments, this reduction of element loss is not as effective at the same temperature as for lower current densities from a W filament.

#### References

1. R. E. Klimentidis and I. D. R. Mackinnon, "High resolution imaging of ordered mixed-layer clays," *Clays and Clay Minerals* 34: 155-164, 1986.
2. G. W. Brindley and G. Brown, *Crystal Structures of Minerals and their X-ray Identification*, London: Mineralogical Society, 1980.
3. P. H. Nadeau et al., "Interstratified XRD characteristics of physical mixtures of elementary clay particles," *Clay and Clay Minerals* 19: 67-76 1984; I. D. R. Mackinnon, *Clays and Clay Minerals* 34: 356-358, 1986.
4. I. D. R. Mackinnon et al., "Thin-film analyses of silicate standards at 200 kV: The effect of temperature on element loss," *Microbeam Analysis--1986*, 451-454.
5. J. H. Ahn and D. R. Peacor, "Transmission and analytical electron microscopy of the smectite-to-illite transition," *Clays and Clay Minerals* 34: 165-179, 1986; F. J. M. Rietmeijer and I. D. R. Mackinnon, "Layer silicates in a chondritic porous interplanetary dust particle," *J. Geophys. Res.* 90: D149-155, 1985.
6. H. van Olphen and J. J. Fripiat, *Data Handbook for Clay Materials and other Non-metallic Minerals*, New York: Pergamon Press, 1979.
7. D. B. Williams, "Standardized definitions of x-ray analysis performance criteria in the AEM," *Microbeam Analysis--1986*, 443-448.
8. D. B. Williams, *Practical Analytical Electron Microscopy in Materials Science*, Mahwah, N.J.: Philips Electronic Instruments.

TABLE 1.--Smectite (SWY-1) analyses.†

	Time:	200s	200s	600s	Bulk*
	i <sub>b</sub> :	0.24nA	1.05nA	1.05nA	n.a.
SiO <sub>2</sub>		67.31(2.75)	72.16(3.77)	76.23(3.61)	67.60
Al <sub>2</sub> O <sub>3</sub>		24.36(0.81)	22.65(2.31)	19.67(2.72)	21.06
TiO <sub>2</sub>		0.03(0.08)	0.01(0.02)	n.d.	0.10
FeO		2.95(0.82)	2.11(0.59)	1.79(0.48)	1.96
MgO		3.87(1.01)	2.59(0.90)	1.97(0.42)	3.28
CaO		0.31(0.29)	0.14(0.16)	0.10(0.48)	1.81
Na <sub>2</sub> O		0.99(0.88)	0.30(0.46)	0.23(0.11)	1.64
K <sub>2</sub> O		0.18(0.19)	0.03(0.10)	0.02(0.02)	0.57

†All analyses normalized to 100%; standard deviations (in parentheses) for n = 10.

\*Bulk analysis from van Olphen and Fripiat.<sup>6</sup>



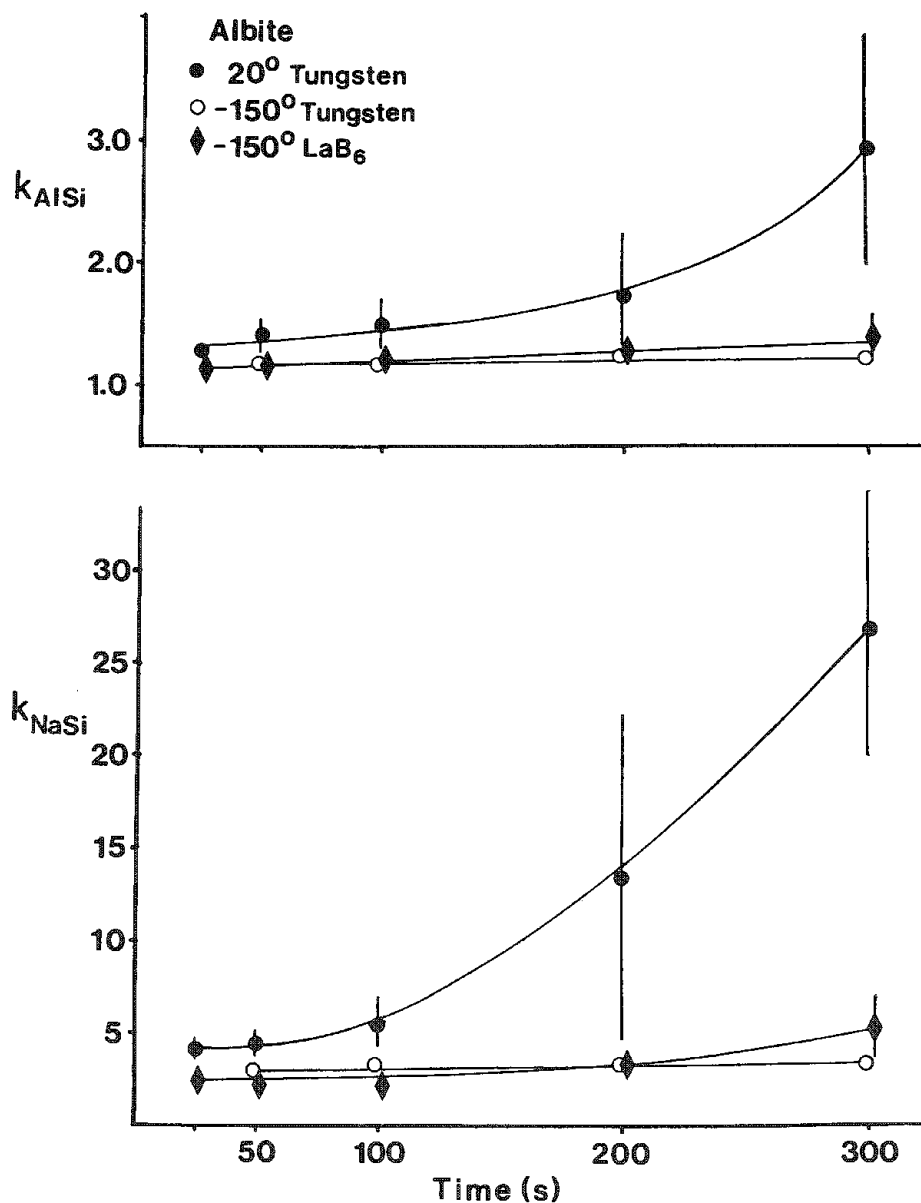


FIG. 1.--Comparison of k-factor plots for Amelia albite at -150 C and 20 C with W and LaB<sub>6</sub> filaments. W filament data are from earlier work;<sup>4</sup> error bars are one standard deviation.

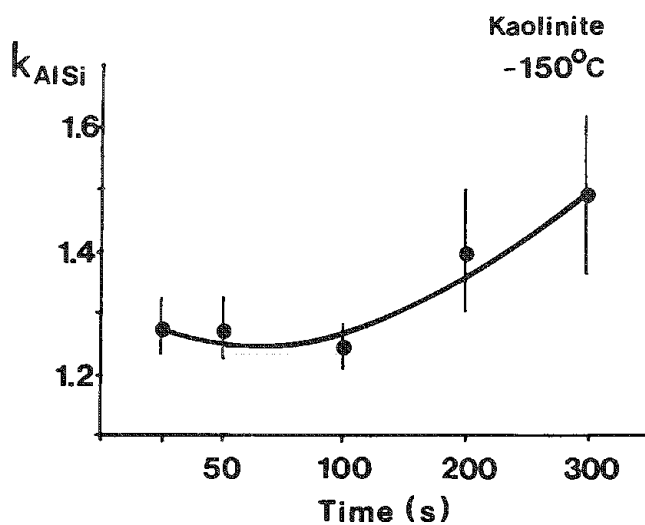


FIG. 2.--Plot of  $k_{AlSi}$  vs collection time for well-crystallized Georgia kaolinite at -150 C. Error bars are one standard deviation.

TABLE 2

Element	$k_{ZSi}$	$r^*$	$N^+$
Na	2.96	0.98	5
Mg	1.60	0.99	5
Al	1.27	0.99	8
K	1.35	0.99	3
Ca	1.09	0.99	6
Fe	1.12	0.99	5

\* Correlation coefficient for  $C_{Z/C_{Si}}$  vs.  $I_{Z/I_{Si}}$  plots.

+ No. of mineral standards used.

## ANALYTICAL ELECTRON MICROSCOPY OF EXTRATERRESTRIAL MATERIALS: RESULTS FROM MICROTOME SECTIONS OF CARBONACEOUS CHONDRITES AND INTERPLANETARY DUST PARTICLES

D. F. Blake, A. J. Mardinly, and T. E. Bunch

With the exception of samples returned from the moon during the Apollo program, the only materials available for direct laboratory study that are of extraterrestrial origin are meteorites and interplanetary dust particles (IDPs). IDPs are a relatively new class of extraterrestrial materials, which are collected by high-flying aircraft in the stratosphere.<sup>1-5</sup> These particles, 1-50  $\mu\text{m}$  in size, enter the earth's atmosphere at ballistic velocities, but are sufficiently small to be decelerated without burning up. IDPs commonly have chondritic elemental abundances, and so, like chondrite meteorites, are thought to have undergone very little differentiation since the formation of the solar system.<sup>5,6</sup> Furthermore, IDPs contain many of the phases and commonly exhibit phase relationships that have been proposed for pre-solar system material. One class of IDPs, the chondritic porous variety, is comprised of loosely aggregated grains of high-temperature phases such as olivines and pyroxenes, mantled in carbon which appears to have been deposited directly from the gaseous state. However, other IDPs are comprised of layer lattice silicates and thus appear to be secondary products of hydrothermal processing in a parent body of some kind. Carbonaceous chondrites, once thought to be pristine remnants of the solar nebula, have proved to be in almost all cases, extensively hydrothermally altered samples from the regolith of planetoids.<sup>7</sup> Despite being extensively altered, some components of carbonaceous chondrites clearly have retained vestiges of their pre-solar system origin, largely in the form of trapped noble gases in some carbonaceous phases.<sup>8</sup>

Many questions remain concerning the origin of carbonaceous chondrites and IDPs, their relationships one to the other, and the significance of the phases they contain. Progress has been hindered in the elucidation of phase relationships primarily due to the fine-grained nature of the individual grains. In IDPs, phases commonly range from 0.1  $\mu\text{m}$  to 1.0  $\mu\text{m}$ . Larger phases (1.0-5.0  $\mu\text{m}$ ) occur in carbonaceous chondrites, but many matrix phases, particularly in extensively altered material, are in the submicrometer size range. Modern

analytical electron microscopes are well suited to the task of analyzing and imaging phases in this size range. However, because of the fine-grained and heterogeneous nature of the materials, conventional specimen preparation techniques are inadequate.

Until recently, most AEM results from IDPs were obtained from lightly crushed material dispersed on holey carbon support films. This specimen preparation technique has yielded nearly all the high-resolution analytical information to date.<sup>5,9-11</sup> For carbonaceous chondrites, for which a greater amount of material is available, a number of approaches have been used, including crushed-grain mounts of separates, and high-voltage and conventional TEM observation of ion-thinned foils.<sup>12-14</sup> Recently, ultramicrotomy has been successfully applied to the study of IDPs.<sup>15</sup> This technique has proved invaluable in a variety of materials science applications, including high-resolution structure imaging of particulate catalysts in an HVEM.<sup>16</sup>

We describe here a method we have found useful for embedding, sectioning, and observing two types of extraterrestrial materials: hydrated interplanetary dust particles, and carbonaceous chondrite meteorites. The petrology of each is discussed and compared.

### Methods

We prepared meteorite samples by embedding a small piece of material in the tip of an acrylic rod 2 in. long and 5/16 in. in diameter. A shallow hole is drilled in the center of one end of the rod, a small piece of meteorite is placed in the hole, and the remaining volume is filled with LR White "hard" grade resin.<sup>17</sup> The assemblage is then placed in a vacuum oven and heat-cured at 90 C for 1 h.<sup>18</sup> Before the resin sets, the oven is evacuated and brought back to atmosphere to insure that no air-filled voids remain within the material. After curing, the acrylic rod is placed in a specially made fixture (Fig. 1) which is used to grind a pyramidal shape on the end of the rod that contains the sample. The result is a 45° four-sided pyramid whose apex is the meteorite sample itself (Fig. 2). In this way, microtome sections can be made from the very point of the block, which results in an extremely tiny block face. Small block faces are essential when microtoming hard materials, to minimize potential diamond knife damage, and to reduce artifacts in the sectioned material. In addition, a small block face insures that a large number of serial sections can be placed on the same grid, which permits three-dimensional interpretations to be made of grains that occur in more than one section.

IDPs are prepared in a slightly different fashion. Initially, the end of a 2 in. piece of acrylic rod is fashioned into a pyramidal

---

Authors Blake and Bunch are with the Planetary Biology Branch, NASA/Ames Research Center, Moffett Field, CA 94035; author Mardinly is with Lockheed Missiles and Space Co., Sunnyvale, CA 94086. Support through the Exobiology Division of NASA to TEB and the National Research Council to DFB is gratefully acknowledged. The authors wish to thank Hitachi Scientific Instruments for providing instrument time on a Hitachi S-900 FESEM (used for Fig. 8), and Dr. Delbert Philpott, for providing facilities for the microtomy.

shape, as above. Next, a tiny flat is ground on the pyramid tip. A tiny drop of resin is placed on the flat block face and cured until tacky, and an IDP is transferred to the block using a glass fiber. (This technique has been previously described in detail by Bradley and Brownlee<sup>17</sup> and Bradley.<sup>18</sup>) A second coat of resin is placed on the particle and heat cured in a vacuum oven, as above.

Sample blocks prepared as above were placed in a Porter Blum MT-2 microtome for sectioning. Sectioning was performed at very slow speed, to minimize the potential for knife damage, and to reduce sectioning artifacts. The sections were floated onto holey C support films on 3mm EM grids. After carbon coating, the specimens were observed in an Hitachi H-500 TEM operated at 100 keV. STEM microanalytical work was performed on a JEM 2000FX equipped with a Kevex detector and Microanalyst 8000 system. Semiquantitative standardless analyses were performed using the Kevex supplied data reduction program FOIL.

## Results

*IDP Ames-DEC86-11.* Figure 3 shows a low-magnification view of a microtomed section of Ames-DEC86-11, which is a hydrated particle (or CF).<sup>19</sup> The particle consists of a relatively nonporous aggregate of fine-grained layer lattice silicates which appear to have been in situ hydrous alteration products of pre-existing grains (Fig. 4). The layer lattice silicates have a bimodal size distribution in which matrix phyllosilicates have a grain size of 30-100 nm, and those which have pseudomorphically replaced pre-existing grains have a crystallite size of  $<10.0$  nm. Both appear to be smectites with compositions (assuming 20% water) of MgO, 8.5%; Al<sub>2</sub>O<sub>3</sub>, 5.3%; SiO<sub>2</sub>, 47.9%; and FeO, 18.3% (matrix phyllosilicate), and MgO, 5.9%; Al<sub>2</sub>O<sub>3</sub>, 6.1%; SiO<sub>2</sub>, 47.2%; and FeO, 20.6% (grain). Powder diffraction patterns with major spacings of 5.2, 4.42, 2.53, 1.93, 1.65, and 1.51 Å are supportive of an identification of smectite. The preservation of the delicate replacement fabric and the retention of phase relationships at the sub-10nm scale demonstrate the usefulness of the microtome technique.

*Murchison Carbonaceous Chondrite Matrix.* A micrograph of microtomed Murchison carbonaceous chondrite matrix is shown in Fig. 5. Large areas of suitably thin material are commonly obtained from highly altered CM type meteorites such as Murchison. Figure 6 shows a lattice fringe image of one of the commonly occurring layer lattice silicates in the Murchison matrix.

*Allende Dark Inclusion.* Figure 7 shows a low-magnification image of a microtome section of Allende, a less highly altered C3 carbonaceous chondrite. The mineral grains present in the micrograph are predominantly olivine. The morphology of the grains, and the apparent grain size reduction relative to that determined in ultrathin optical and microprobe sections, led us to realize that significant artifacts were present in the section. Nevertheless, many of the grains, although shat-

tered, are still in situ and some petrologic interpretations are possible. Figure 8 shows a low-voltage SEM micrograph of the uncoated surface of the microtome block, which indicates (in particular, on the olivine grain) significant chipping and artifactual damage. This type of damage is often found in microtomed thin sections, and should be kept in mind when micrographs are interpreted.

## Discussion and Conclusions

*Advantages of the Technique.* There are numerous advantages to the use of microtomy in the preparation of TEM samples of extraterrestrial materials. Unlike the crushed-grain technique, it is clearly possible to maintain delicate interfaces, boundaries, and phase relationships between grains. This preservation allows for the possibility of detailed petrologic examination of phases. The technique produces large thin areas suitable for both high-resolution imaging and thin-film microanalysis. Because phases are held in place, layer lattice silicates and other minerals with strong preferred orientations can be viewed in any orientation, including that normal to their basal planes. A number of serial sections can be placed on the same EM grid, allowing one to get a notion of the 3-D nature of the sample. Lastly, the remaining material in the resin block, or additional serial sections from the same block, can be used for complimentary techniques, such as ion microprobe, Auger microanalysis, scanning electron microscopy, etc.

*Disadvantages of the Technique.* As with any specimen preparation technique, microtomy produces artifacts that must be separated from original features of the sample. Particularly in hard materials, artifacts such as chattering (Fig. 8), reduction in grain size, etc., are problems that must be routinely dealt with. Where possible, it is always advisable to characterize a feature of interest in samples prepared by more than one technique. The embedding resin poses additional problems: a number of techniques of analysis are rendered difficult or impossible, including TEM analysis or identification of noncrystalline phases in the section, quantitative or even qualitative analysis for carbon, and isotopic analysis for various elements present in both the resin and the sample material. Because the sections are commonly floated off the knife into distilled water, layer lattice silicates such as smectite may swell or expand during sample preparation. Finally, for careful EDS microanalytical work, a very clean sample is necessary in order to avoid the buildup of contamination during an analysis. Maintaining the necessary degree of cleanliness on the sample is particularly difficult during microtomy.

Despite the difficulties, microtomy appears to have advantages that far outweigh its disadvantages. In many cases, data can be obtained from microtomed samples that would be impossible to collect by any other technique.

## References

1. D. E. Brownlee et al., "The physical

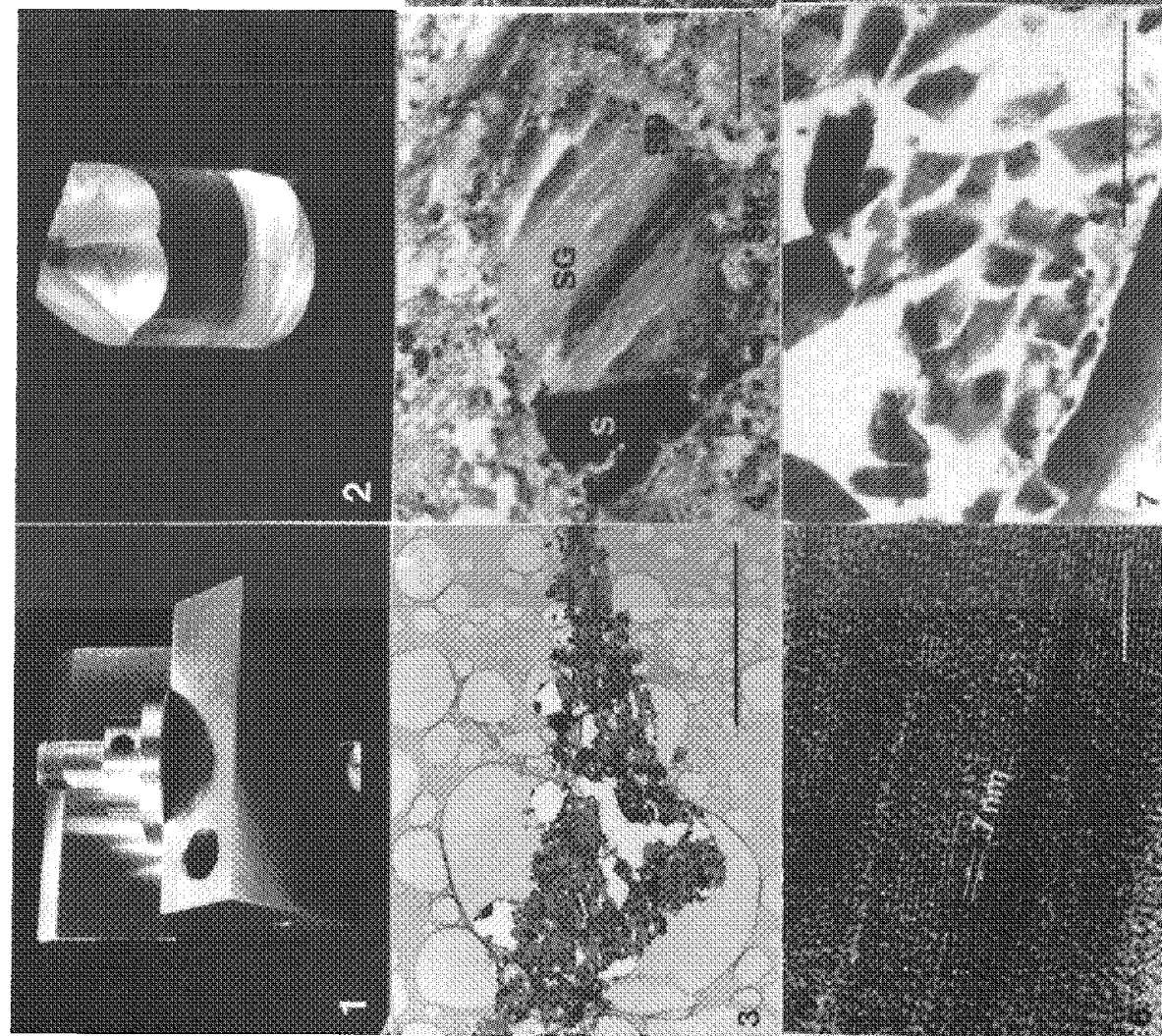


FIG. 1.--Sanding fixture used to prepare microtome blocks, with sample installed.

FIG. 2.--Finished microtome block of a meteorite, ready for sectioning.

FIG. 3.--Low-magnification bright-field image of a hydrated IDP, AMES-Dec86-11. Scale bar = 10  $\mu$ m.

FIG. 4.--Bright-field TEM micrograph of partially replaced grain in IDP AMES-Dec86-11. SG = smectite replacing grain, SM = smectite replacing matrix, SD = sulfide decorating grain, S = sulfide relict phase, M = magnetite in matrix. Scale bar = 200 nm.

FIG. 5.--Low-magnification bright-field micrograph of Murchison matrix. Scale bar = 1  $\mu$ m.

FIG. 6.--High-resolution image of layer lattice silicate in Murchison matrix. Scale bar = 10 nm.

FIG. 7.--Low-magnification bright-field image of Allende dark inclusion. Note "shattered" appearance of crystalline phases. Scale bar = 1  $\mu$ m.

FIG. 8.--LVSEM image of microtome block face of Allende dark inclusion. Shattering marks on large olivine grain are clearly visible. Scale bar = 1  $\mu$ m.

- nature of interplanetary dust as inferred by particles collected at 35 km," in C. L. Hemenway, P. M. Millman, and A. F. Cook, Eds., *Evolutionary and Physical Properties of Meteoroids*, NASA SP-319, U.S. Government Printing Office, 1973, 291-295.
2. D. E. Brownlee, "Interplanetary dust: Possible implication for comets and presolar interstellar grains," in T. Gehrels, Ed.), *Protostars and Planets*, 1978, 134-150.
3. D. E. Brownlee, "Interplanetary dust," *Rev. Geophysics Space Physics* 17: 1735-1742, 1979.
4. D. E. Brownlee, "Terrestrial and extra-terrestrial pollution in the stratosphere," *Microbeam Analysis--1980*, 199-202.
5. I. D. R. Mackinnon and F. J. M. Rietmeijer, "Mineralogy of chondritic interplanetary dust particles," *Reviews of Geophysics* (in press).
6. D. E. Brownlee et al., "Elemental abundances in interplanetary dust," *Nature* 252: 667-669, 1974.
7. T. Bunch and S. Chang, "Carbonaceous chondrite phyllosilicates and light element geochemistry as indicators of parent body processes and surface conditions," *Geochim. Cosmochim. Acta* 44: 1543-1577, 1980.
8. U. Ott et al., "Noble-gas rich separates from the Allende meteorite," *Geochim. Cosmochim. Acta* 45: 1751-1788, 1981.
9. J. P. Bradley and D. E. Brownlee, "Analytical SEM/STEM studies of individual grains of disaggregated CP interplanetary dust," *Lunar Planet. Sci.* 13: 65-66, 1982.
10. J. P. Bradley and D. E. Brownlee, "Microanalysis of dispersed interplanetary dust particles," *Microbeam Analysis--1983*, 187-190.
11. P. Fraundorf, "Interplanetary dust in the transmission electron microscope: Diverse materials from the early solar system," *Geochim. Cosmochim. Acta* 45: 915-943, 1981.
12. H. W. Green et al., "Allende meteorite: A high voltage electron petrographic study," *Science* 172: 936-939, 1971.
13. D. J. Barber, "Matrix phyllosilicates and associated minerals in C2M carbonaceous chondrites," *Geochim. Cosmochim. Acta* 45: 945-970, 1981.
14. D. J. Barber, "Phyllosilicates and other layered-structure materials in stony meteorites," *Clay Minerals* 20: 415-454, 1985.
15. J. P. Bradley and D. E. Brownlee, "Cometary particles: Thin sectioning and electron beam analysis," *Science* 231: 1542-1544, 1986.
16. R. Csencsits et al., "An improved method for thin-sectioning of particulate catalysts," *J. EM Tech.* 2: 643-644, 1985.
17. L. R. White Resin Co., London. (Available from SPI and other EM suppliers.)
18. J. P. Bradley et al., "Microtomed thin-sections of individual interplanetary dust particles: New insight regarding textures and petrographic associations," *Meteoritics* 20: 614-615, 1986.
19. D. E. Brownlee et al., "A working taxonomy for micrometeorites," *Lunar Planet. Sci.* 13: 71-72, 1982.

## COMBINED CATHODOLUMINESCENCE/BACKSCATTERED ELECTRON IMAGING AND TRACE ELEMENT ANALYSIS WITH THE ELECTRON MICROPROBE: APPLICATIONS TO GEOLOGICAL MATERIALS

D. J. Henry and J. B. Toney

Over the past 25 years cathodoluminescence (CL) has been used in geology primarily as a qualitative tool to enhance textural features not readily visible with optical microscopy.<sup>1</sup> In geological materials CL can result from a variety of processes in several minerals (Table 1). The traditional method for making CL observations in geological studies is to utilize a petrographic microscope equipped with a small chamber under vacuum ( $\sim 10$   $\mu$ m pressure) and an electron gun. The luminescence image can be recorded with color film. This approach has revealed many valuable textural features (especially in carbonate cements in sedimentary rocks) that have contributed to the understanding of sedimentary rock petrogenesis.<sup>2</sup> However, this technique has several disadvantages, including the difficulty of maintaining constant operating conditions during and between observations (e.g., vacuum levels, accelerating potential, sample current, etc.); the variable intensity and color sensitivity of color films; the generally poor resolution of images; and the low CL intensity of many geologically important minerals (especially quartz).

In order to overcome these problems, we have employed an imaging technique that uses a high-resolution electron microprobe equipped with a backscattered electron (BSE) detector and a cathodoluminescence (CL) detector with spectrometer. By combining the BSE and CL images one can reveal textural features that cannot be resolved with optical or traditional CL microscopy or BSE imaging by themselves. Furthermore, with these images as guides, detailed electron microprobe analysis of trace elements can establish their distribution in minerals. Consequently, there are several advantages to this technique, including: (1) high imaging resolution ( $< 5$   $\mu$ m); (2) constant, strictly controlled operating conditions; (3) spectral analysis of the CL signal; and (4) the ability to utilize controlled electron-beam damage to enhance textural features. In this paper we highlight application of this technique to several geologic problems.

### *Instrumentation and Techniques*

For our investigation we have employed a Cameca MBX electron microprobe equipped with three wavelength-dispersive spectrometers, secondary-electron detector, BSE and CL detector, and spectrometer (with a range of 400-900 nm). This configuration is particularly useful because (1) CL images can be obtained at any given wavelength within the spectral

range or for total CL luminescence, (2) signals from the BSE and CL detectors can be imaged separately or electronically mixed, and (3) CL spectra can be obtained for small regions.

Imaging was obtained with a focused, rastered beam with an accelerating potential of 15 kV and sample currents of 50-100 nA. Total CL luminescence was generally used for imaging. CL and BSE signals were mixed (with the BSE signal as the subordinate signal) to enhance surficial fractures and grain edges (primarily from the BSE signal) so that CL luminescence due to secondary surface features can be readily distinguished from primary features. For comparative purposes, spectra were obtained with a defocused electron beam of fixed diameter (generally 10 or 20  $\mu$ m). It was found that in several minerals a decrease in the beam diameter (i.e., a greater electron flux per unit area) produced a significant enhancement of the intensity of the red portion of the spectrum. Polished thin sections with a 250 Å carbon coating were used.

Various geologically important minerals undergo variable degrees of beam damage under the experimental conditions outlined above. For example, carbonate minerals typically develop severe damage, so that much of the useful information is lost. Quartz undergoes a mild degree of beam damage: the intensity of the luminescence increases irreversibly with continued exposure to the rastered electron beam. Because portions of quartz grains may contain various trace element levels (and susceptibility to beam damage), the relative beam damage may actually be used to enhance textural features.

### *Applications*

#### *Diagenesis in Quartzose Clastic Rocks.*

With traditional CL techniques, quartz generally has a low CL intensity, especially in the diagenetic quartz overgrowths that can develop on detrital quartz grains in clastic sedimentary rocks. With the approach outlined above, we can readily observe subtle features that have generally not been previously discerned. For example, Fig. 1(b) shows that we can easily observe the proportion of overgrowth relating to detrital quartz as well as the fine oscillatory zoning patterns developed in the overgrowth. Furthermore, detailed trace-element analyses from the overgrowth and the detrital portion of the quartz (Fig. 2) establish that the overgrowths are relatively Al-rich and that there is an inverse relation between Al contents and CL intensity. This type of approach enables one to evaluate the subtle structures within detrital grains, development of pressure solution and overgrowth, style of zoning of the overgrowths, patterns of fracturing and brecciation in quartz, and possible provenance of the detrital quartz grains.<sup>3</sup>

---

Author Henry is with Louisiana State University, Department of Geology, Baton Rouge, LA 70803; author Toney is with ARCO Oil and Gas Company, 2300 West Plano Parkway, Plano, TX 75075.



TABLE 1.

A. Common factors affecting CL response in minerals relevant to geologic studies.

1. Enhanced CL response develops in minerals that contain:
  - (a) cations that act as activators to CL (especially  $Mn^{+2}$  and rare earth elements)
  - (b) cations that serve as sensitizers to CL (e.g.,  $Pb^{+2}$  or  $Ce^{+3}$ )
  - (c) lattice vacancies
  - (d) structural distortions resulting from mosaic or intergrown crystals.

2. Inhibited CL response develops in minerals that contain:

- (a) significant amounts of cations that quench the CL (especially  $Fe^{+2}$ )

B. Typical minerals that display CL.

1. Common rock-forming minerals:

Quartz, feldspar, pyroxenes (low Fe), olivine (low Fe), amphiboles (low Fe), mica (low Fe),  $Al_2SiO_5$  polymorphs calcite

2. Accessory or minor phases:

Apatite, zircon, monazite, tourmaline (low Fe)

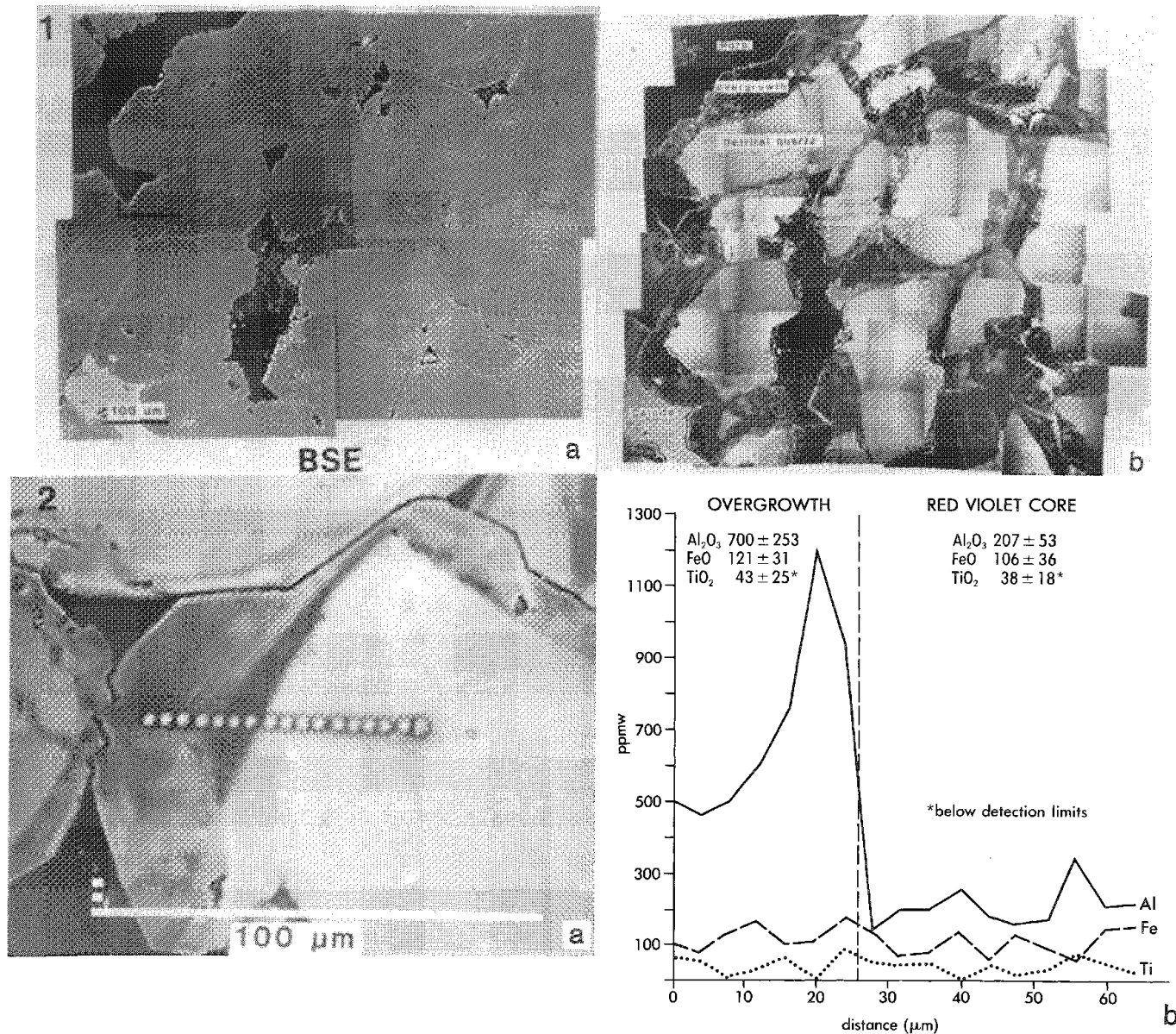


FIG. 1.--(a) BSE image and (b) combined CL/BSE image of quartz sandstone. Note dramatic differences in CL intensity of detrital relative to overgrowth portion of quartz grains in (b). Furthermore, oscillatory zoning in overgrowths become apparent.

FIG. 2.--(a) CL/BSE image and (b) trace element traverse in quartz grain with well-developed overgrowth from quartz arenite. Analytical points are indicated by contamination spots. Overgrowth luminescence is dull red whereas detrital core luminescence is bright red-violet. Note inverse relation between CL intensity and Al content in overgrowth.



**Zircon and U-Pb Isotope Analysis.** Zircon is a widespread refractory mineral that occurs in a wide variety of sedimentary, igneous, and metamorphic rocks. The minor and trace element composition of a given zircon grain can reflect the geologic environment of the host rock as well as earlier stages in its crystallization history. The evaluation of the zircon prehistory is especially important since U-Pb isotopes are commonly utilized for age dating. With the technique outlined above, it is possible to observe features such as growth zoning, resorption, metamict or alteration textures, and overgrowths developed on inherited zircon grains (Fig. 3). In addition, detailed quantitative analyses can establish the quantitative distributions of trace and minor elements such as P, Hf, etc. (Fig. 3b). The interpretation of the U-Pb isotopic systematics in zircon can therefore be refined and we suggest BSE-CL imaging as a necessary step in the routine U-Pb isotope analysis of zircons.<sup>4</sup>

**Apatite and the Role of Rare Earth Elements (REE).** REE contents in apatite have been used in petrology to infer processes such as the degree of fractionation of coexisting magmas.<sup>5</sup>

However, interpretations are somewhat limited if the nature of the REE distribution is unknown. Because small REE concentrations (<1-10 ppb) in apatite can produce high intensity CL signals, the CL imaging technique can easily detail REE distributions (Fig. 4).

**Other Applications.** The nucleation and growth history of minerals are generally difficult to evaluate in many silicate and oxide minerals. However, in silicates displaying CL, minor variations in trace elements (and the resulting CL) can reveal useful information on grain growth. For example, the early growth history of sillimanite, a mineral that generally appears homogeneous in optical microscopy, can be readily observed with CL (Fig. 5).

### Conclusions

We have described only a few possible applications of the newly proposed BSE-CL technique. Many other applications are possible and improvements to the hardware as well as to the proposed techniques will extend these applications even further.

### References

1. E. Nickel, "The present status of cathode luminescence as a tool in sedimentology," *Minerals Science Engineering* 10: 73-100, 1978.
2. H. Machel, "Cathodoluminescence in calcite and dolomite and its chemical interpretation," *Geoscience Canada* 12: 139-147, 1985.

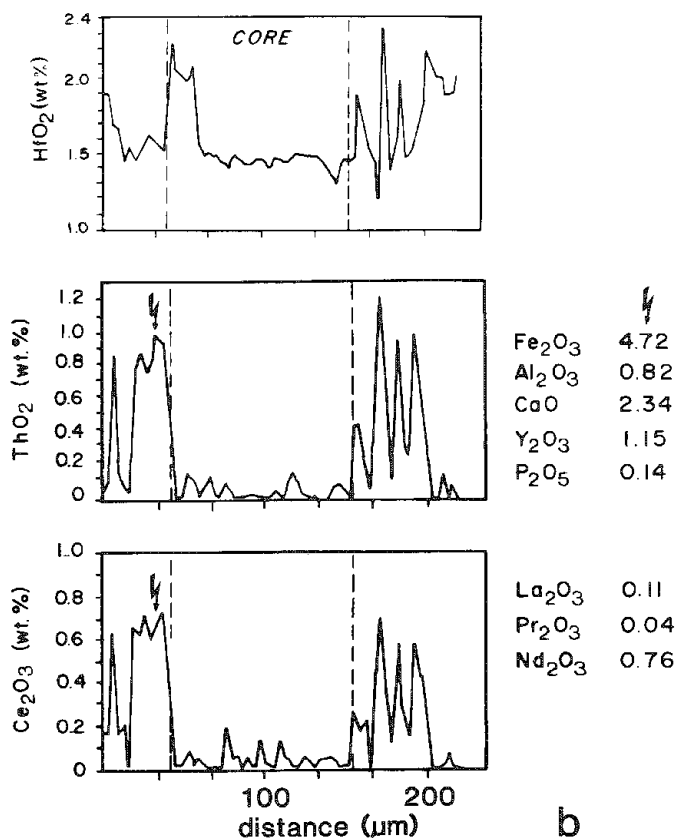
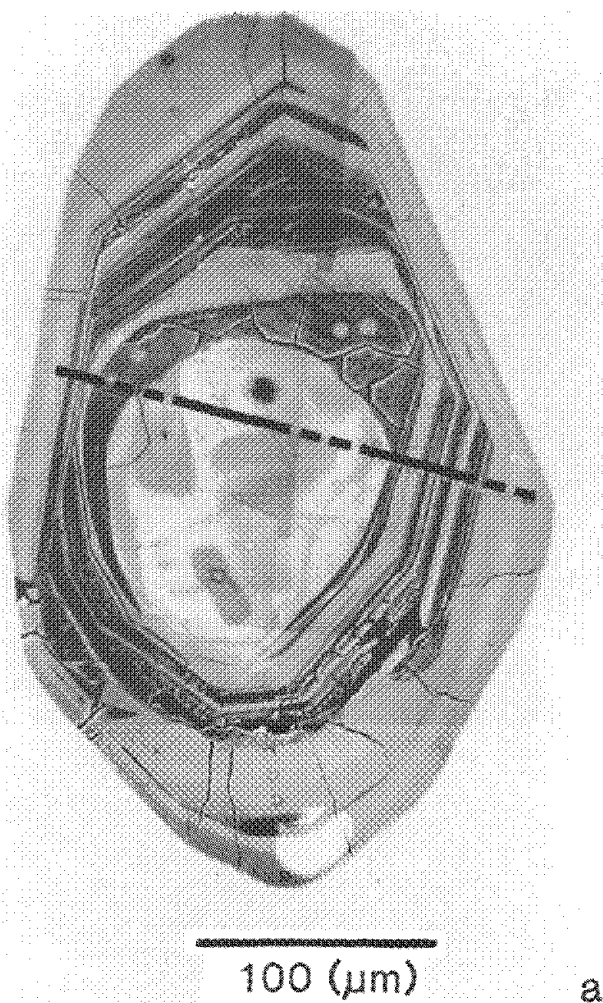


FIG. 3.--(a) CL/BSE image and (b) compositional profile of minor and trace elements in zircon grain from granite. Rounded core with high CL intensity is relict zircon grain. This core is surrounded by alternating metamict/alteration zones (dark) and normal zircon zones (light). Arrow represents a typical analysis of zircon composition within metamict/alteration zone.

3. D. J. Henry, J. B. Toney, R. K. Suchecki, and S. Bloch, "Development of quartz overgrowths and pressure solution in quartz sandstones: Evidence from cathodoluminescence/backscattered electron imaging and trace element analysis on the electron microprobe," *Geol. Soc. Am. (Abstracts with Program)* 18: 365, 1986.

4. D. J. Henry, P. A. Mueller, and J. B. Toney, "Zircon mineral chemistry and cathodo-

luminescence/backscattered imaging: Evidence for the development of age discordance," *Terra Cognita* 6: 156, 1986.

5. E. B. Watson and T. H. Green, "Apatite/liquid partition coefficients for the rare earth elements and strontium," *Earth and Planetary Sci. Letters* 56: 405-421, 1981

6. D. Huaxin, "Cathodoluminescence study of apatite," *Geochimica* 4: 368-374, 1980.

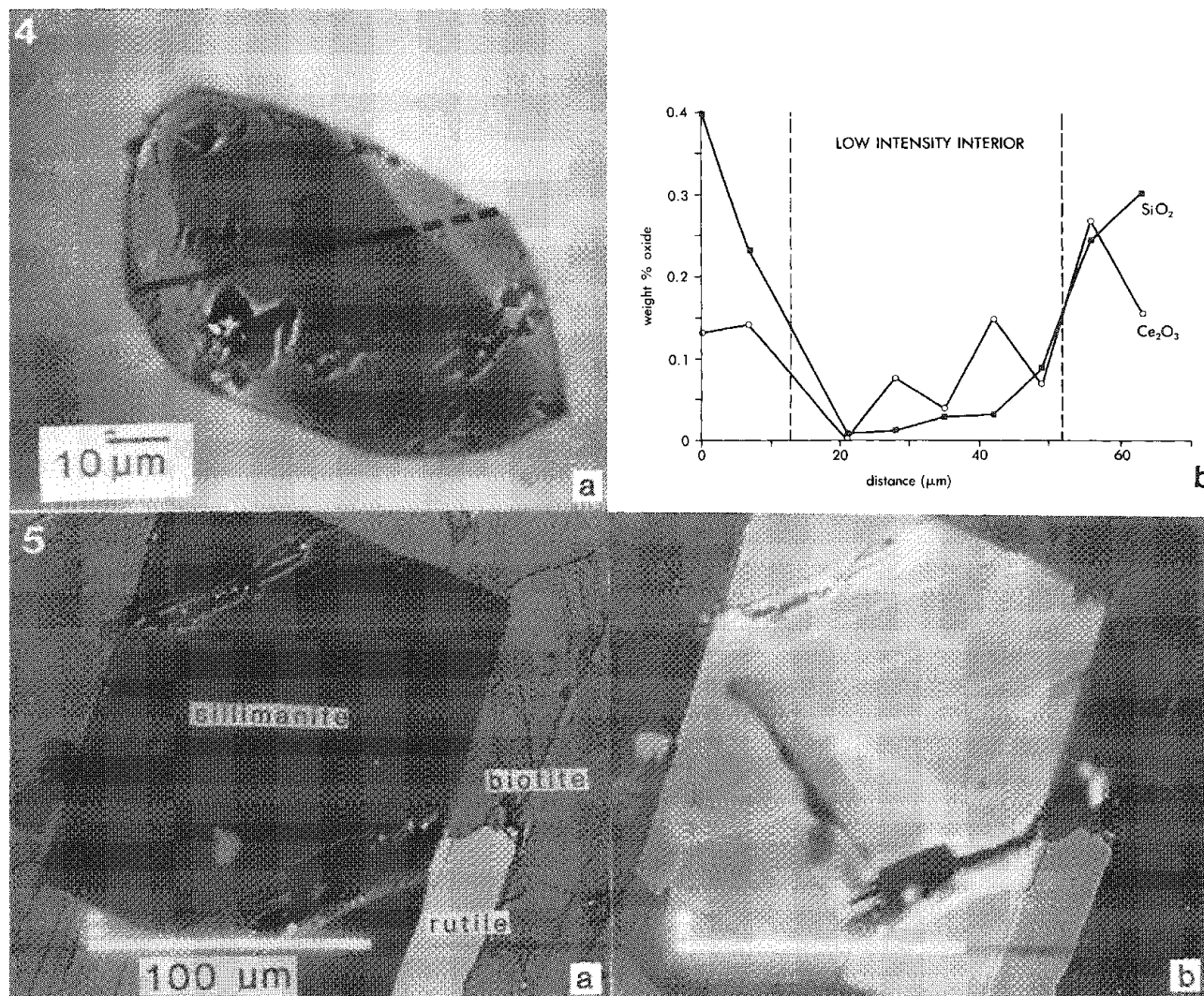


FIG. 4.--(a) CL/BSE image and (b) partial trace element traverse in apatite from high-grade ironstone. High-intensity CL zones correspond to zones enhanced in REE and SiO<sub>2</sub>. Ce is representative of all REE. Note traverse line in (a).

FIG. 5.--(a) BSE image and (b) CL/BSE image of euhedral sillimanite from pelitic schist. Surface fractures develop enhanced CL but are easily distinguished from primary dark CL feature that represents early growth feature in (b).

## INDIVIDUAL PARTICLE ANALYSIS BY AUTOMATED EPMA FOR THE IMPROVEMENT OF SOURCE APPORTIONMENT STUDIES FOR REMOTE AEROSOLS

Hedwig Storms, Paulo Artaxo, Frank Bruynseels, and René Van Grieken

As part of the Global Tropospheric Experiment (GTE), the Amazon Boundary Layer Experiment (ABLE-2A) was designed to study the processes of aerosol and gas emissions by the forest and to assess the chemical mechanisms occurring in the Amazon Basin atmosphere. In the context of this study, aerosols were collected at two ground stations. At one sampling location, Duke Reserve, located 25 km from Manaus, samples were collected 1.5 m above ground level. At the other site, Bacia Modelo Tower, situated at about 75 km north of Manaus, aerosol samples were collected at a tower 45 m above ground level, 15 m above the canopy. The locations were selected so that anthropogenic contributions were minimized. The fine and coarse mode aerosols were collected with stacked filter units. Particles with aerodynamic diameters  $1.5\mu\text{m} \leq d_p \leq 15\mu\text{m}$  were collected on an 8 $\mu\text{m}$  pore-size Nuclepore filter, and the fine particles ( $d_p < 1.5\mu\text{m}$ ) on a 0.4 $\mu\text{m}$  filter. Their loadings were optimized for single-particle analysis by automated Electron Probe x-ray Microanalysis (EPMA).

### Data Treatment

The x-ray intensities obtained from the EPMA analysis of the individual particles are converted into weight concentrations by the application of a spherical particle ZAF-correction as described by Armstrong and Buseck.<sup>1</sup> A nonhierarchical nearest-centroid sorting is carried out to classify the particles into chemically similar groups.<sup>2,3</sup> For this approach a set of training vectors is required that are obtained in two steps. First, a hierarchical cluster analysis using the Ward's error sum approach is performed on the data set of each sample analyzed, resulting in the average elemental composition of each group of particles for each sample. Subsequently a cluster analysis is performed on the average compositional data for all particle types in all samples. The result is a set of training vectors that are representative for the whole data set. Once the training vectors have been obtained, a nearest-centroid sorting is performed in which each particle is classified to the nearest centroid of the training vectors.

### Results

For the fine-mode particles, a total of 3321 individual particles were analyzed for 7 different samples. Fourteen elements were detected and the x-ray intensities and the morphological information was stored for all par-

ticles. We found 914 particles (27.5%) showing no detectable elements with  $Z > 10$ . ZAF-corrections were applied to the remaining 2407 particles, which showed at least one detectable element. The ZAF-corrected data set was submitted to clustering procedures in order to obtain the average elemental composition of the particle groups and to classify the various clusters of particles.

In addition to the microanalysis, bulk trace element measurements were performed on all the samples. Twenty elements with detection limits around 0.1 ng/m<sup>3</sup> were measured by Proton Induced X-ray Emission (PIXE). The PIXE data were interpreted with the help of three receptor models: chemical mass balance, stepwise multiple regression, and absolute principal factor analysis, in order to obtain quantitative source apportionment results for the Amazon Basin aerosols.<sup>4</sup> The results for the bulk measurements were published elsewhere.<sup>5</sup>

Fourteen particle types were obtained from the application of hierarchical and nonhierarchical clustering. The mean value of the 14 particle types are listed in Table 1. The elemental concentrations, expressed in weight percent, are listed in brackets. The concentration of the elements was calculated for their occurrence in their most common oxide form; the oxygen contribution is not listed. Only particles containing elements detectable with EPMA ( $Z > 10$ ) were included in the cluster analysis. Most of the particle types can be related to two prevalent local sources. The major elements present in soil dust are Al, Si, Ti, and Fe. Three particle types, as can be seen in Table 1, are composed of a combination of these elements and represent 30% of the total aerosol load.

The particle types containing mainly S, K, and P, or a combination of those elements, can be related to the emission of aerosols by the vegetation. From Table 1, three particle types can be assigned to these sources and account for 57% of the particles. The most abundant group shows only S as detectable element, in an organic matrix, as can be deduced from the high spectrum background. This particle type is not identified as ammonium sulfate, but consists of organic material (mainly C, O) with a minor contribution of S. The particle type containing mainly Zn and S, with an abundance of 6.6%, can also be related to the forest emissions. Indeed, the release of Zn by vegetation has been measured by Beauford et al.<sup>6</sup> Hence, 95% of the fine mode aerosol fraction can be related to these two local sources.

Table 2 shows the set of training vectors, obtained as described above, that can be used to classify the particles in each sample.

From the results listed in Table 3 it is possible to investigate the variability of

---

Authors Bruynseels, Storms and Van Grieken are at the Department of Chemistry, University of Antwerp-U1A, Antwerp, Belgium; author Artaxo is at the Instituto de Fisica, Universidade de Sao Paulo, Sao Paulo, Brazil.

the contribution of the different particle types as a function of sampling and weather conditions, but no significant influences can be observed from those factors. That means that the contribution of the two major sources of the aerosols is insensitive to the variations mentioned above, and that the fine particles in the Amazon Basin have a homogeneous spatial distribution. The bulk analysis result shows that the aerosols related to the vegetation account for 70% and the soil dust accounts for 30% of the total airborne aerosol concentration.<sup>5</sup> Only 3 factors can explain 85% of the variability of the trace elemental concentrations, and two of them are clearly related to aerosols emitted by the vegetation.

### Conclusion

This orienting study of the fine mode aerosol fraction collected in the Amazon Basin shows that the combination of individual particle analysis and clustering techniques constitutes a powerful method in the study of aerosol sources and their contribution to the environment. It offers the possibility of diversifying the different particle types originating from the same source. For instance, five particle types could be identified as originating from the vegetation. The soil dust is differentiated into three types. It would be difficult to discriminate the small differences between these particle types by the application of source apportionment models to bulk analysis results.

### References

1. J. T. Armstrong and P. R. Buseck, "Quantitative chemical analysis of individual microparticles using the electron microprobe: Theoretical," *Anal. Chem.* 47: 2178-2192, 1975.

2. D. L. Massart and L. Kaufman, *The Interpretation of Analytical Data by the Use of Cluster Analysis*, New York: Wiley, 1983.

3. P. C. Bernard et al., "Classification of estuarine particles using automated microprobe analysis and multivariate techniques," *Environ. Sci. Technol.* 20: 467-473, 1986.

4. P. Artaxo and C. Orsini, "The emission of aerosol by plants as revealed by three receptor models," in G. Israel, Ed., *Aerosols: Formation and Reactivity*, 2nd Intern. Aerosol Conf. (Berlin), London: Pergamon Journals, 1986, 148-151.

5. P. Artaxo et al., "Composition and sources of aerosols from the Amazon Basin," *J. Geophys. Res.* (in press).

6. W. Beauford et al., "Release of particles containing metals from vegetation into the atmosphere," *Science* 195: 571-573, 1976.

TABLE 1.--Results of nearest-centroid sorting for total data set. Values between brackets are weight percent of detected elements calculated as their common oxides. Oxygen contribution is not included.

Particle type	Abundance (in %)
S[39]	24.0
S[28], K[24]	22.1
Al[21], Si[20]	19.9
P[12], S[24]	9.3
Si[41]	7.1
S[18], Zn[39]	6.6
Fe[55], Si[5]	3.5
S[16], Ca[30]	2.7
K[82]	2.1
Ca[68]	1.5
Cl[100]	0.9
Cr[68]	0.6
Cl[25], Cu[64]	0.36
Na[48], S[10]	0.17

TABLE 2.--List of concentrations of groups representative for whole data set (training vectors). Weight concentrations are calculated according to most common oxidation state of elements present.

Group number	Composition (in %)						
	Na	Mg	Al	Si	P	S	Cl
1	-	-	-	0.1	0.3	39.0	-
2	0.2	0.5	0.1	0.9	9.4	25.5	0.4
3	0.2	0.3	0.2	0.2	0.2	28.1	-
4	-	-	0.4	0.4	-	1.9	-
5	-	0.7	0.9	0.9	-	15.4	-
6	52.4	-	-	-	-	9.4	2.0
7	0.1	0.1	18.6	18.6	0.1	2.6	0.01
8	0.04	0.4	42.1	42.1	-	1.8	-
9	-	-	-	-	-	-	-
10	2.5	-	0.6	0.6	-	10.0	-
11	-	-	-	-	-	-	21.5
12	-	-	-	-	-	-	100.0
13	0.2	0.04	3.4	3.9	-	1.2	-
14	-	0.2	-	-	-	0.1	-

Group number	Composition (in %)						
	K	Ca	Ti	Cr	Fe	Cu	Zn
1	1.0	-	-	0.02	0.1	-	-
2	3.1	2.0	0.2	0.5	0.6	-	-
3	22.9	0.3	0.01	-	0.04	-	0.07
4	0.5	66.9	-	-	-	-	-
5	8.1	34.3	0.03	-	0.1	-	-
6	3.6	-	-	-	-	-	-
7	2.3	0.7	1.3	-	7.7	-	0.4
8	0.9	0.6	0.04	-	0.9	-	-
9	-	-	-	68.4	0.0	-	-
10	3.9	1.3	-	0.4	5.7	-	44.8
11	-	-	-	-	-	-	-
12	-	-	-	-	-	66.6	-
13	3.6	3.4	0.1	0.2	58.7	-	0.8
14	82.0	-	-	-	-	-	-

TABLE 3.--Abundance of particle types for fine-mode aerosol samples collected in Amazon Basin.

Particle type	Sample number						
	1	2	3	4	5	6	7
1	31.0	22.7	35.0	11.4	19.1	12.7	36.0
2	5.7	4.1	16.3	2.9	11.6	2.4	22.0
3	2.2	1.6	15.7	30.8	20.0	63.7	20.8
4	0.0	5.7	1.4	1.9	0.2	0.3	0.7
5	0.4	2.4	2.1	5.3	3.7	2.4	2.2
6	0.0	0.0	0.2	0.5	0.0	0.0	0.5
7	9.3	44.7	15.7	27.4	27.7	6.2	8.1
8	7.0	8.9	4.8	7.0	10.0	5.8	5.9
9	0.0	4.0	0.0	0.0	0.0	0.0	0.0
10	38.9	2.4	1.7	1.9	0.9	0.7	0.0
11	0.9	1.6	0.0	0.0	0.0	0.0	0.0
12	0.4	0.0	0.2	0.0	0.0	0.0	0.0
13	3.5	1.6	6.2	4.8	5.8	0.7	2.2
14	0.4	0.0	0.6	5.8	0.9	5.1	1.5

## MINQUANT I: A QUANTITATIVE ANALYSIS SCHEDULE FOR TRACOR NORTHERN TASK5

S. I. Recca, D. E. Lange, and T. L. Grove

MINQUANT I (MINQ) is a program code segment written in Tracor Northern TASK5<sup>1</sup> schedule format for a TN-5500/TN-5600 electron microprobe automation system. MINQ is designed to provide a simplified method for quantitative analysis of geologic or other materials (silicates, oxides, sulfides, metals, etc.). MINQ allows occasional operators to obtain quantitative analyses without extensive knowledge of the TASK operating program. In design, the MINQ schedule is similar to other user-oriented analysis programs, like ULTIMATE<sup>2</sup> and QUANT.<sup>3</sup>

Within the TASK operating environment MINQ utilizes the TN-5500 color-coded soft keys to provide the operator with a set of user-selectable analytical options, referred to as mineral codes. Each mineral code selects an autonomous schedule designed to analyze a specific material (rock-forming minerals, glasses, metals, etc.). MINQ soft keys and TN-5600 PAC (Program Automation Control) function keys allow the user to control instrument operations that are commonly used in the course of identifying minerals or materials, selecting analytical conditions, and storing analytical data. The MINQ schedule is written so that it is transparent to the TASK operating environment, which allows experienced users to control analytical conditions and implement stage automation control routines (e.g., points tables and traces) directly through TASK commands.

Quantitative mineral/material analysis is performed by an autonomous schedule, which may be run independently under TASK. Each analysis schedule specifies the elements to be analyzed; the order of analysis; and, for each element the reference standards to be used, maximum counting time and whether peak searching is enabled or disabled. Either Bence-Albee<sup>4</sup> or ZAF<sup>5</sup> data reduction procedures may be selected. A structural formula is calculated by use of the appropriate number of oxygen and cation units for the selected mineral and reported in the analysis output, and mineral end member calculations are provided.

MINQ is divided into two functionally and logically distinct sections: an initialization section and a data acquisition and reduction section (Fig. 1). These two sections are driven by color-coded soft keys and screen dialog, which request simple keyboard responses from the operator.

---

Authors Recca and Grove are at the MIT Department of Earth, Atmospheric, and Planetary Sciences, Cambridge, MA 02139; author Lange is at the Harvard Department of Earth and Planetary Sciences, Cambridge, MA 02138. They wish to thank JEOL (USA) and especially C. H. Nielsen for support and assistance in developing MINQUANT.

### *Initialization*

The initial display of MINQ provides the user with the options; ANALYZE, DEFINE MINCODE, DEFINE DRIVES, DEFINE FILES, a Bence-Albee/ZAF correction routine toggle, and EXIT TO TASK. A user-definable set of default parameters (drives, mincodes, files, and correction routine) is stored within the schedule, but they can be altered with the initialization soft keys. ANALYZE enables the next level of soft keys, and is used to begin the material analysis section of MINQ. The DEFINE MINCODE soft key allows the user to set up the mineral codes to be displayed in the analysis section of MINQ. Seven character identifiers are used as mineral codes and correspond to the names of common rock-forming minerals or other materials of interest. The desired mineral codes can be selected interactively from a list of up to 250 options. DEFINE DRIVES allows the user to specify the storage device (disk drive, RAM memory) to be used for each of the following file types: system files and programs (e.g., correction routines), element tables, standard tables, Bence-Albee and ZAF definition files and analysis schedules, background files, data (analysis output as saved by Bence-Albee or ZAF), and external data save which sets a flag enabling echoing of output over one of the auxiliary RS232 lines of the TN-5500 for off-line storage. COR RTN (correction routine) toggles between the Bence-Albee and ZAF correction procedures, selects the appropriate set of mineral codes, including defaults, and automatically loads the appropriate element and standard files for the selected correction procedure (as specified in DEFINE FILES). DEFINE FILES specifies the TASK element and standard files to be loaded for the Bence-Albee or ZAF correction routines. EXIT TO TASK or CANCEL exits from MINQ and returns to the TASK operating environment.

### *Analysis*

The second program level is accessed through the ANALYZE soft key. At the ANALYZE level five user-selected mineral codes are displayed on the first five color-coded soft keys. An arrow appears below the currently active mineral code, which on entering ANALYZE is the leftmost soft key. The sixth soft key, designated OTHER, is used to reset any of the first 5 soft keys to access any of the available mineral codes available for the selected correction routine. The CANCEL soft key returns control to the INITIALIZE level.

In the ANALYZE mode the PAC function keys, and single key-strokes on the TN-5500 keyboard provide additional program control. The PAC function keys (F1-F5) are used to start an analysis with the currently selected mineral code (F1), acquire an EDS spectrum (F2), toggle the cup (beam flag) in and out (F3), toggle the background switch on and off (F4), and

delete the last acquired analysis from a running average (F5). On the TN-5500 keyboard the following character keys are enabled: C, input a comment label to be printed before each analysis is output (Fig. 2); A, average analyses performed since the last time average was invoked or since the last change in mineral code selection occurred; R, recalculate structural formula with a new cation and/or oxygen base and/or end member formula; and L, list any or all of the available mineral analysis and their associated definitions files.

When a new mineral code is selected, MINQ loads several files from the storage devices selected through DEFINE DRIVES. A schedule (ANALYZE) is loaded which contains the TASK commands which select elements for analysis, maximum counting time for each element, peak search options, and the order of analysis. A separate file contains the background intensities for each element; this file is updated each time an analysis is performed with the background switch set to on. A separate Bence-Albee or ZAF definition file is loaded for each mineral group.

Commands within TASK allow the ANALYSIS schedules and definition files to be changed to suit users' specific needs.

#### References

1. N. F. Wodke, *TN-5500 Automation System TASK Wave-dispersive Spectrometer and Stage Automation Program*, Tracor Northern, 1984.
2. A. A. Chodos, A. L. Albee, A. C. Gancarz, and J. Laird, "Optimization of computer-controlled quantitative analysis of minerals," *Proc. 8th Conf. on Electron Microprobe Analysis*, 1973, 45A-45C.
3. W. F. Chambers and J. H. Doyle, "A user-oriented software system for electron microprobes," *Microbeam Analysis--1979*, 279-280.
4. N. Wodke and J. McCarthy, *TN-2121 Bence-Albee Matrix Correction Program: Operation and Program Description*, Tracor Northern, 1982.
5. F. Schamber, N. Wodke, and J. McCarthy, *TN2120 ZAF Matrix Correction Procedure for Bulk Samples: Operation and Program Description*, Tracor Northern, 1981.

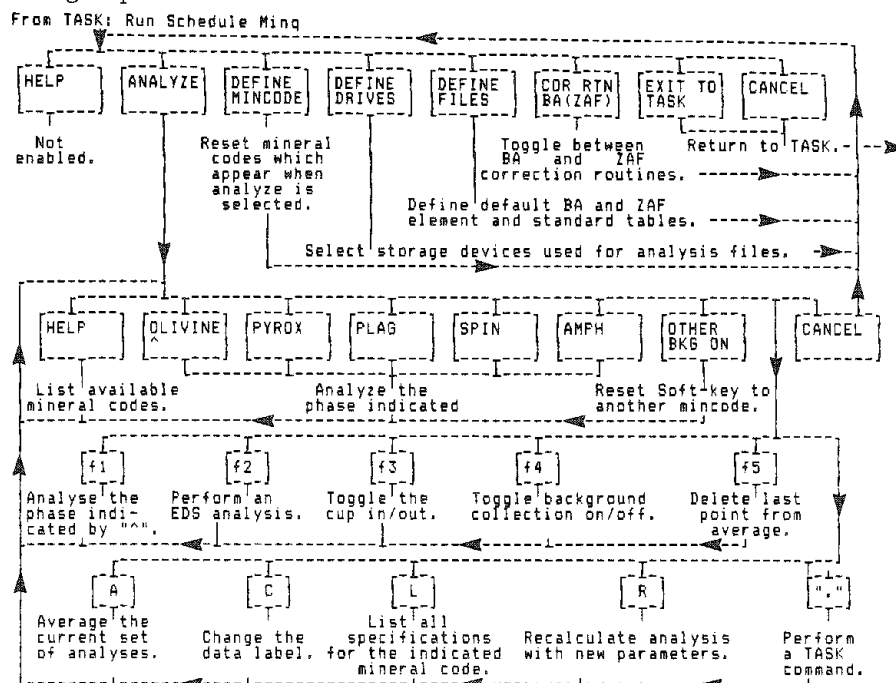


FIG. 1.--Schematic diagram of program flow in Minquant I.

```

BKG ON
X= 15.971 Y= 34.397 Z= 11.334          -- FLAG
29-JAN-87 13:15:57
(CLEAR LAKE LABRADORITE (THIS IS THE ANALYSIS LABEL))

REF.8 WDS:NA1 WDS:MG2 WDS:AL2 WDS:SI2 WDS:CA2 WDS:FE3 WDS:K3

BENCE-ALBEE ANALYSIS 100.1462 99.8848 99.9275
OXIDE  K-RATIO  BETA  CALC'D WT % FORMULA BASE= 8.0  5 CAT
NA2O   0.0248  1.4169   3.52   NA  0.3106  0.3107
MgO    0.0004  1.1510   0.05   MG  0.0034  0.0034
AL2O3  0.2872  1.0731  30.82   AL  1.6536  1.6553
SiO2   0.4340  1.1844  51.41   SI  2.3403  2.3426
CaO    0.1260  1.0703  13.49   CA  0.6577  0.6584
FeO    0.0036  1.1424   0.41   FE  0.0156  0.0156
K2O    0.0021  1.1163   0.23   K   0.0136  0.0136
TOTAL=                99.93                4.9947  8.0076

NORMALIZED  CA  0.663  NA  0.330  K  0.007
AL FRACTION  0.651

```

FIG. 2.--Sample Minquant output using Bence-Albee correction.



## MINQUANT II: A MINERAL CODE SOFT KEY PROGRAM FOR SANDIA TASK8

D. E. Lange and S. I. Recca

MINQUANT II is an on-line quantitative analysis procedure that allows mineral code selection through the use of the soft keys on a Tracor Northern 5500 series system. Each mineral code controls data acquisition through a linked matrix correction definition and provides control over counting parameters and structural formula and end member calculations. MINQUANT II is written as a series of FLEXTRAN<sup>1</sup> subroutines for use with Sandia TASK8<sup>2</sup> and may be used with any matrix correction program suitably adapted.

MINQUANT I<sup>3</sup> was developed for use with TASK5<sup>4</sup> but has limitations imposed by TASK5 of little control over counting parameters for individual elements or mineral codes and is constrained in the number of references available by the small element table available with TASK5. Sandia TASK8 provides much more flexibility and uses an element table of up to 100 references. QUANT,<sup>5</sup> a quantitative analysis schedule, is available for Sandia TASKS8 but only allows a single definition available at any time. A mineral code capability is available for BA85<sup>5</sup> but is limited and did not completely meet our needs.

MINQUANT II was developed with the following goals in mind:

1. Mineral code selection via a single keystroke.
2. Easy to set up and use in a university environment that has many occasional users.
3. Complete control of counting parameters for individual elements and individual mineral codes.
4. Background intensities saved and recalled for each mineral code.
5. Mineral code calculations and control would work with various matrix correction programs.

Each mineral code has the following definable: seven character name, kV, beam current, structural formula calculation information, and an end-member calculation subroutine. The number of elements is limited to the number allowed within the matrix correction program (for example, 45 for BA85). Within a mineral code, each element has the following definable: minimum and maximum counting times, peak search and background measurement ON/OFF flags, desired standard deviation, minimum peak-to-background ratio for maximum time, and priority.

On entering MINQUANT the user is provided with a list of available mineral codes based on current kV and matrix correction procedure desired. The available mineral code

files are copied to ramdisk for fast access. The soft keys are then set up as the operator desires with up to two sets of five available; the sixth soft key selects the other set. The currently selected soft key is indicated with an "^" below the mineral code name; a "B" follows the "^" if backgrounds are to be run for the next point. An analysis is started by selection of a mineral code via its soft key or, if the current selection is desired, by the f1(TN-5600) or #1(TN-1310) button on the joystick box. The background flag is toggled on/off with the "B" key. Once the soft keys are set up, MINQUANT may be exited and reentered without the soft keys being set up. Most TASK commands are available within MINQUANT through the "." interrupt.

The soft key selections may be edited at any time but exit from MINQUANT is required to set up a new mineral code or to edit an existing one. To set up a mineral code, a matrix correction definition must first be set up or an existing one loaded. Several mineral codes may use the same matrix correction definition as long as the elements and references are the same.

Mineral codes may also be used with a points table. The SET POINT command calls a mineral code setup routine if the MVAR MINCODE variable is on. The soft keys are first assigned mineral codes as in the joystick mode; then the pressing of a soft key assigns the selected mineral code to the point and advances the point counter by one. From the joystick box, f1 or #1 will do a jog, f2 or #2 will accept the point assigning the last-used mineral code, and the pointer is advanced by one.

### References

1. F. H. Schamber, *FLEXTRAN*, Tracor Northern Report TN-1800M, 1975.
2. W. F. Chambers, *Sandia TASK8: A Subroutinized Electron Microprobe Automation System*, Sandia Report SAND85-2037, 1985.
3. S. I. Recca, D. E. Lange, and T. L. Grove, "MINQUANT I: A quantitative analysis schedule for Tracor Northern TASK5," (this volume).
4. N. F. Wodke, *TN-5600 Automation System TASK Wave-dispersive Spectrometer and Stage Automation Program*, Tracor Northern Software Department, 1984.
5. Ref. 2 and personal communication.

Author Lange is with the Department of Earth and Planetary Sciences, Harvard University, Cambridge, MA 02138; author Recca, with the Department of Earth, Atmospheric, and Planetary Sciences, Massachusetts Institute of Technology, Cambridge, MA 02139.

## SEM-BSE MICROSTRUCTURE OF Pb-Zn ORE FROM NAVALMEDIO, CIUDAD REAL, SPAIN

F. A. Calvo, J. M. Guilemany, J. M. Gómez de Salazar, and A. Ureña

The Pb-Zn ore from Navalmedio (Ciudad Real, Spain) is situated 25 km from the famous mercury mine of Almadén.<sup>1</sup> This ore is in process of exploitation; the preparatory work (mine well, galleries, and adjacent installations) has been completed. The estimated reserves for this ore are 4 million tonnes, with 4% Pb and 2.5% Zn. The ore also contains 80-120 ppm Ag and 0.2% Hg.

We have made SEM measurements on representative samples of the ore, in order to learn the disposition, distribution, and microstructure of the phases present and to determine the metallic elements in solid solution. As a result of this study we propose a genesis for this ore and a justification of the physical-chemical process for its treatment.

### Experimental

Previous to the SEM study, we have identified the following phases by x-ray diffraction: galena, sphalerite, quartz, pyrite, and aluminosilicates. Analysis by spectrographic emission shows as majority element Al, Si, Zn, and Pb; minority elements Mg, V, Cr, Cu, and Sn; and as trace elements Ti, Co, Ni, Ag, and Hg.

The SEM-BSE studies on mineral samples, prepared on polished or broken surfaces, were made with a JEOL JSM 35C scanning electron microscope with a Kevex 7077 microanalyzer and a ZAF-Magic V data correction. The work conditions were 25 kV, work distances of 15 and 39 mm, preset 100 s, reference current 380-440  $\mu$ A, and take-off angle 35°. Johnson Matthey mineral samples were used as analysis standards.

### Results

The majority economic phases present in Navalmedio ore are galena and sphalerite. These mineral phases allotriomorphically refill the siliceous phases that constitute the host rock (metamorphic rock). Figure 1 shows the joint mineralization of galena (G) and sphalerite (Sh) on oolitic quartz (Q), siderite (C), and aluminosilicates phases (A). The sphalerite phase frequently appears in idiomorphic form. In Fig. 2 the galena phase (G) allotriomorphically refills the oolitic quartz crystals (Q), which occasionally exhibit intracrystalline inclusions of galena, with a marked idiomorphic character (hexagonal, as shown in Fig. 3, a detail of Fig. 2). When we observe broken surfaces (brittled in liquid air), oolitic quartz crystals appear, formed (constituted) by a determinate number of idiomorphic crystals that grow freely and exhibit

high porosity that permits the access of PbS to the interior (Fig. 4).

The idiomorphic siderite phase is associated with quartz and aluminosilicates phases and shows Mn and Ca in solid solution (Figs. 5 and 6). The mean concentration detected in siderite is Ca 2% and Mn 7.3%. Broken surfaces show a clear fibrous-lamellar character for this phase (Fig. 7).

Both galena and sphalerite show laminar fracture surfaces (100 planes in galena), which gives this ore a high delezability (Figs. 8 and 9). EDS microanalysis on the sphalerite phase shows the presence of Fe, Co, and Ni in solid solution: the Fe concentration in sphalerite is between 4.5% and 9.8% (Fig. 10).

Cubic crystals (twinning) of the mineral-phase galena are observed growing preferentially on free surfaces (pores and veins) (Fig. 11). If we compare these structures (natural ore) with those obtained by synthesis tests (magmatic way), we verify a high degree of similarity (Figs. 12 and 13); and the same is true when we compare natural ore and synthetic ore (Figs. 14 and 15). We can deduce that the Navalmedio ore was formed by injection of a magmatic melt that contained S, Zn, and Pb, and that during its cooling the galena and sphalerite phases were stabilized. Other mineral phases detected in Navalmedio ore (minorities) are pyrite, which appears idiomorphic (Fig. 16); chalcopyrite (Ch), with silver in solid solution (Figs. 17 and 18); and the minerals covellite-chalcocite, associated to tetrahedrite (Fig. 19). Silver in solid solution is frequently detected in these minerals (Figs. 20 and 21). The mean concentration of this element in copper sulfides is 16.2 wt%.<sup>2</sup>

### Conclusions

1. Navalmedio ore is formed by galena and sphalerite as economic mineral phases.
2. Silver elements have been detected in chalcopyrite, covellite-chalcocite, and tetrahedrite minerals.
3. We have not detected mercury in solid solution.
4. We propose as genesis the injection of a magmatic melt with S, Zn, and Pb as majority constituents, which during its cooling (solidification) stabilized the most thermodynamic stable phases (galena and sphalerite).<sup>3,4</sup>
5. We suggest that this ore should be benefited by grinding and global flotation of sulfur phases, and that all economic elements of interest (Zn, Pb, and Ag) be obtained by hydrometallurgical processes.

### References

The authors are at the Department of Materials and Metallurgical Engineering, Complutense University of Madrid, except author Guilemany, who is at the Department of Metallurgy, University of Barcelona, Spain.

1. Mapa Geológico de España 1:200.000 (Almadén), IGME.
2. F. A. Calvo et al., "EDS microanalysis

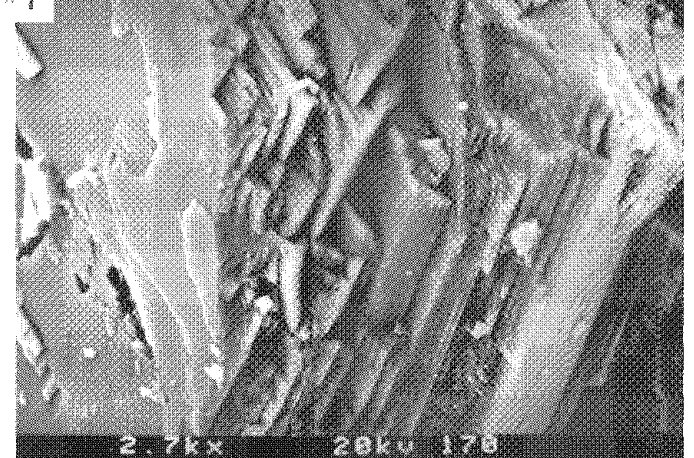
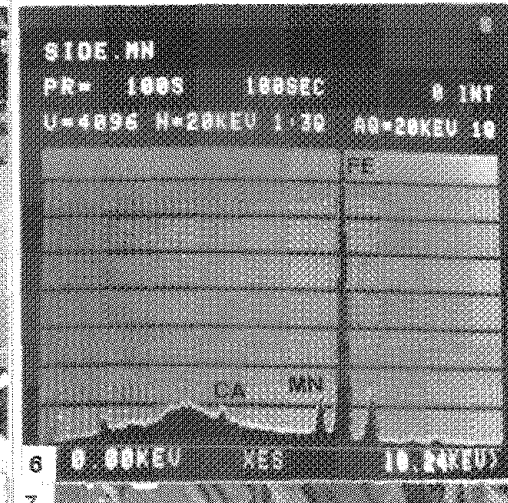
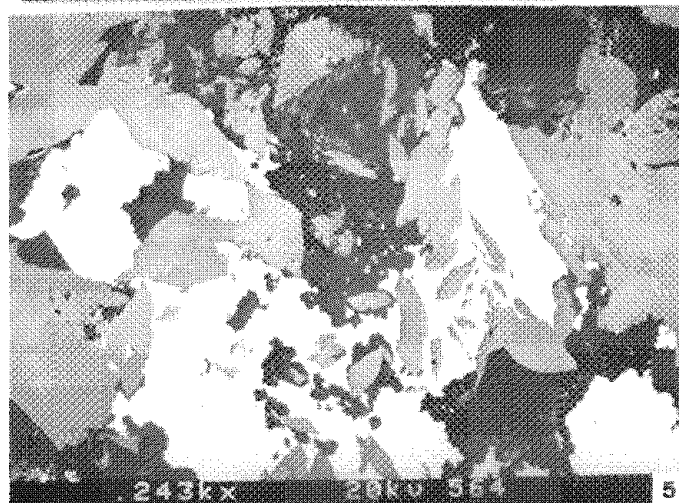
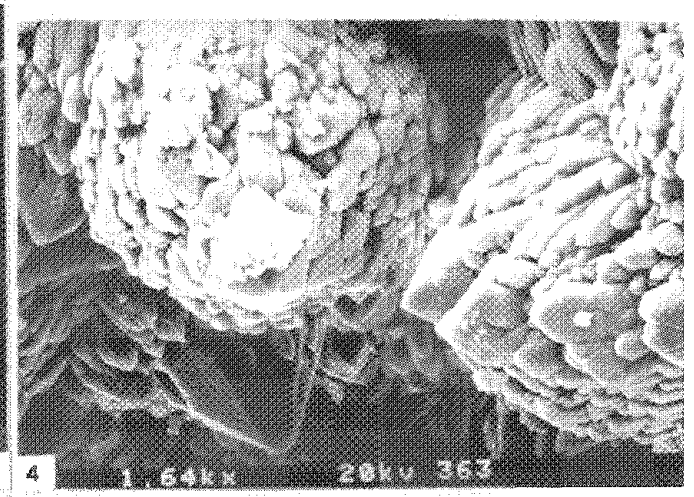
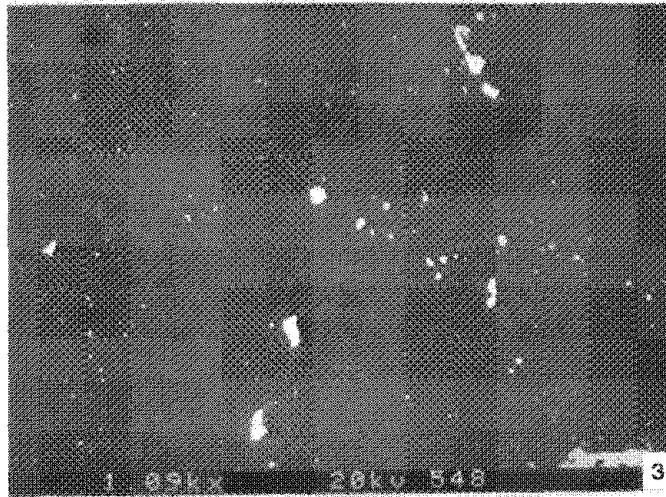
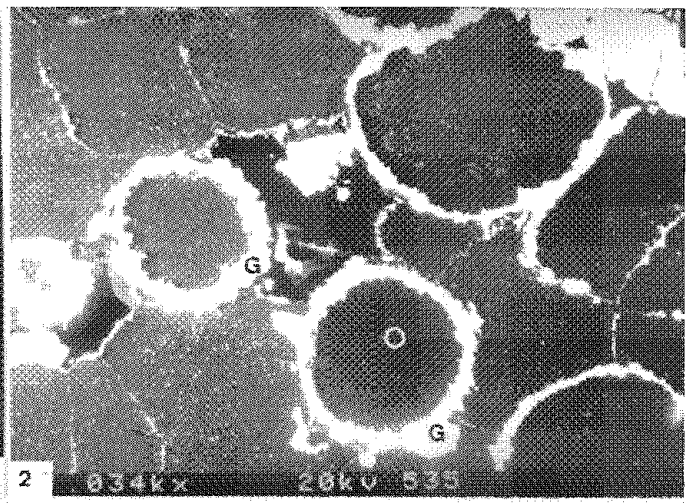
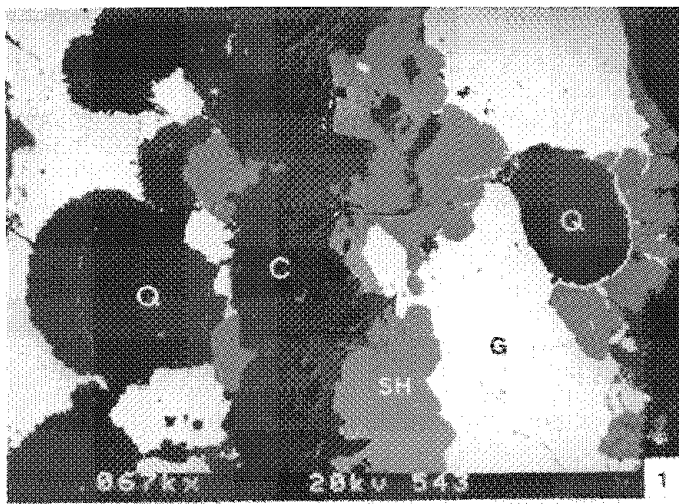


FIG. 1.--Galena (G) and sphalerite (Sh) re-fill idiomorphic siderite (C) and oolitic quarts (Q). BSI.  
 FIG. 2.--Oolitic quartz crystals mineralized by PbS (G). BSI.  
 FIG. 3.--Intracrystalline galena in quartz (detail of Fig. 2). BSI.  
 FIG. 4.--Idiomorphic quartz crystals growing freely in oolitic form. SEI.  
 FIG. 5.--Idiomorphic siderite with Ca and Mn in solid solution. BSI.  
 FIG. 6.--EDS image of siderite with Ca and Mn in solid solution.  
 FIG. 7.--Fibrous-laminar structure of siderite phase. SEI.



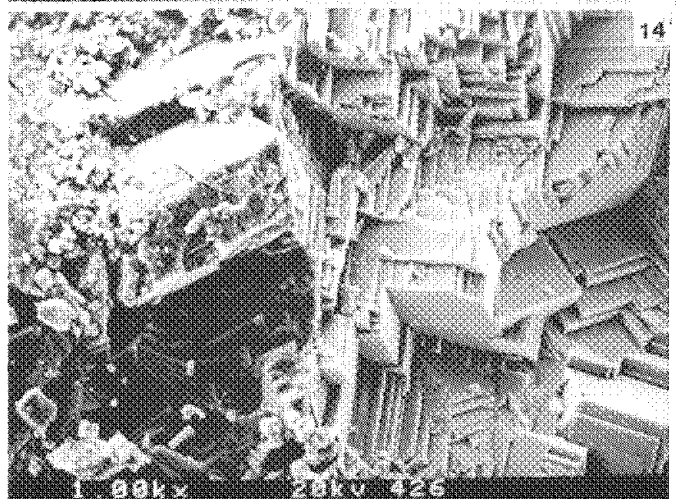
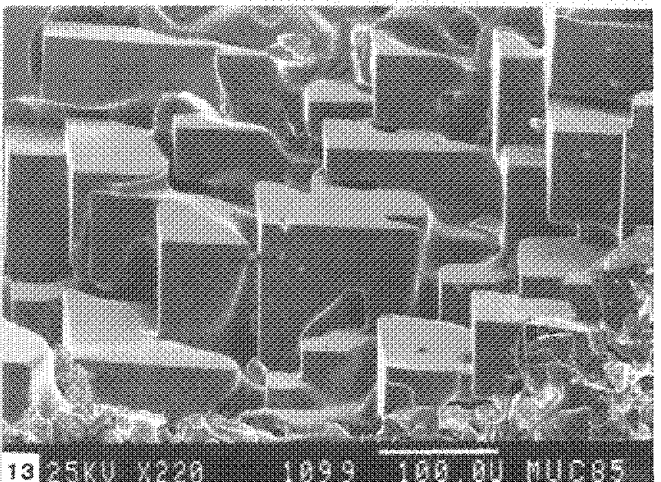
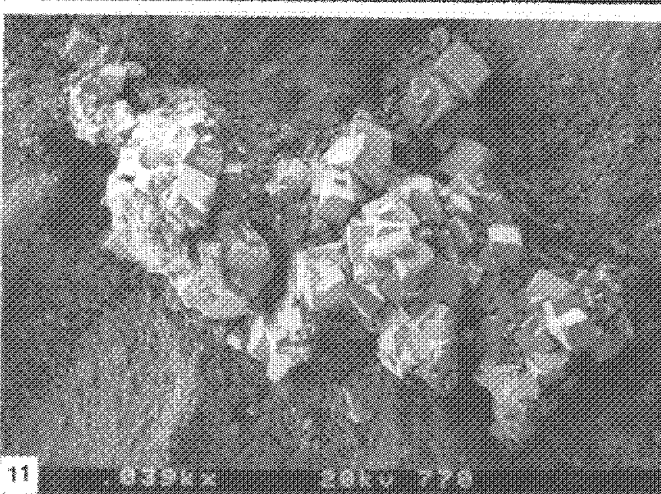
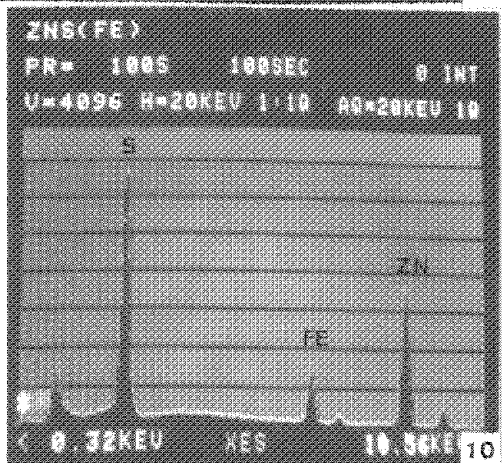
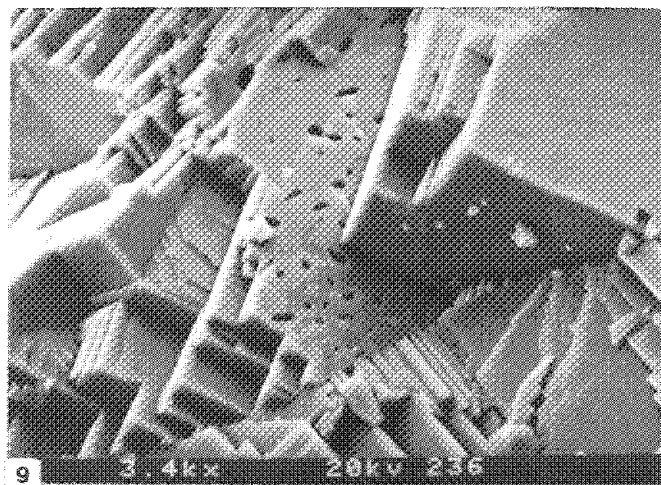
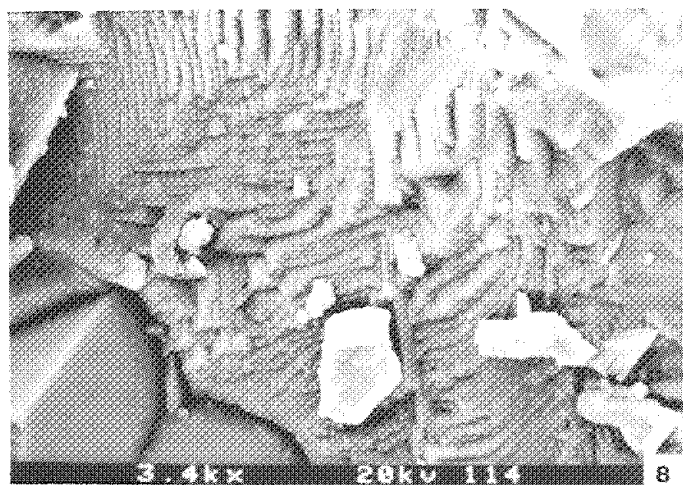


FIG. 8.--Broken surface of sphalerite. SEI.  
 FIG. 9.--Basal fracture of galena in 100 planes. SEI.  
 FIG. 10.--EDS image of sphalerite with Fe, Co, and Ni in solid solution.  
 FIG. 11.--Cubic crystals of galena (twinning). SEI.  
 FIG. 12.--Cubic crystals of galena detected in natural ore. SEI.  
 FIG. 13.--Cubic crystals of galena obtained by synthesis test. SEI.  
 FIG. 14.--Details of natural ore (galena and sphalerite). SEI.

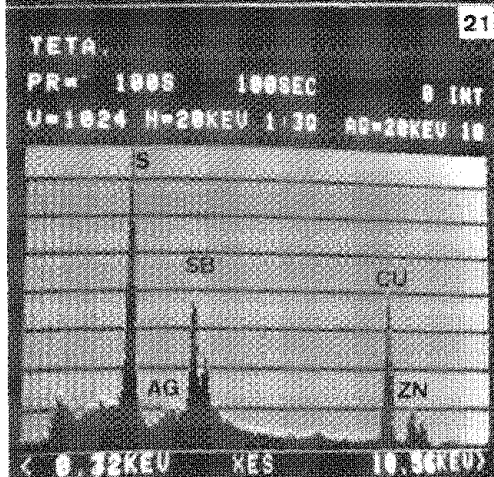
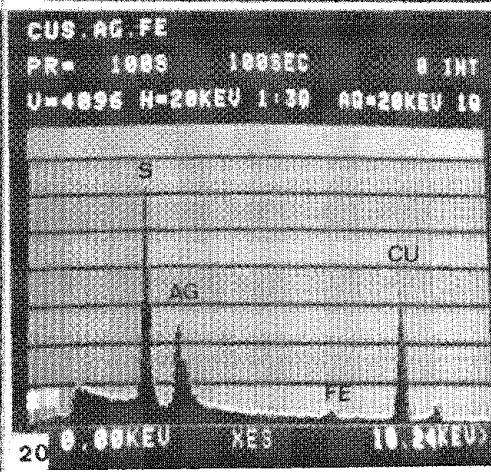
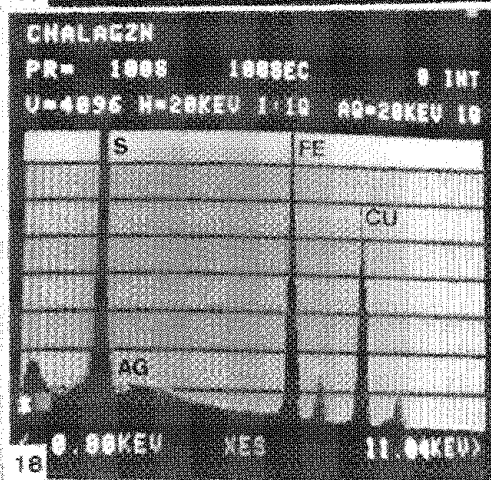
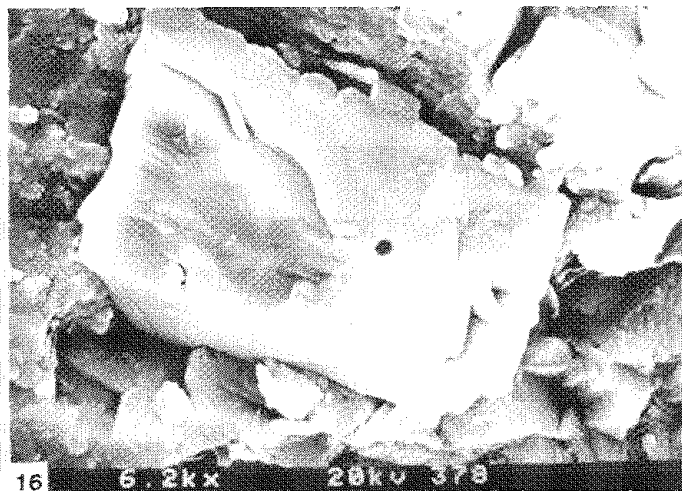


FIG. 15.--Details of synthetic ore (galena & sphalerite). SEI.  
FIG. 16.--Idiomorphic pyrite present in natural ore. SEI.  
FIG. 17.--Chalcopyrite (Ch) with Ag in solid solution. BSI.  
FIG. 18.--EDS image of chalcopyrite.  
FIG. 19.--Covellite-chalcosite phases associated with  
tetrahydrite phase.  
FIG. 20.--EDS image of covellite-chalcosite phases with Ag  
in solid solution.  
FIG. 21.--EDS image of tetrahydrite showing presence of Ag  
in solid solution.

### References (Cont'd)

applied to the study of pyrite complex ore from Rio Tinto Huelva (Spain)," *Microbeam Analysis--1986*, 164-166.

3. F. A. Calvo et al., "Morfologías al SEM de sulfuros polimetálicos obtenidos por síntesis magmática," 14 reunión bienal Soc. Española de Microscopía Electrónica, 1986, 92.

4. E. G. Ehlers, *The Interpretation of Geological Phase Diagrams*, San Francisco: Freeman, 1972.

## 9. Laser Microprobe Analysis

### LAMMA AS A TOOL IN MICROBIOLOGY

Ulrich Seydel and B. Lindner

The two commercially available laser microprobes LAMMA (Leybold-Heraeus, Federal Republic of Germany) and LIMA (Cambridge MS, Great Britain) work on the same principle: a high-power pulse laser is focused through a microscope objective onto the sample, and evaporates and partially ionizes a small volume; the produced ions are analyzed in a time-of-flight (TOF) mass analyzer. This design results in specific analytical features, which differ from some of those of other microprobe systems: (i) the lateral resolution is relatively poor due to the limitation set by the optical resolution of the focusing system, (ii) the detection limits for elements, even for low  $Z$ , are extremely low, (iii) the mass spectrometric analysis makes it possible to register molecular ions and isotopes, and (iv) the utilization of a laser as ionization source allows an application of such instruments for laser desorption mass spectrometry (LDMS) of complex, thermolabile nonvolatile biomolecules in the higher mass region.

For the analysis of biological specimens (thin sections, cells, cell components, bacteria) the application of a transmission type of instrument--laser-sample-TOF arranged linearly--is most favorable. For our purposes we use the LAMMA 500. However, the use of a TOF analyzer in combination with the laser ionization brings about some restrictions with regard to the mass resolution ( $\sim 700$ ) which often cause difficulties in separating molecular from atomic ions; e.g.,  $^{41}\text{K}^+$  from  $(\text{C}_3\text{H}_5)^+$ .

Advantages of this technique for solving problems in microbiology arise particularly out of its two features, high sensitivity and lateral resolution, which allow the analysis of single bacterial cells. In that way, questions can be answered that are not accessible to the normally applied integral methods. The two most obvious applications to be emphasized in this connection are the possibility of establishing distributions of (for example) elemental concentrations within a bacterial population, and of correlations between certain measured characteristics of a bacterium with its morphology.

The mass spectrum of a single bacterial cell contains information on its intracellular cation contents as well as on the organic matrix. In particular, the relation between the sodium and potassium contents can serve as a criterion of the physiological state of a cell, and thus of its viability. The information from the organic matrix can be extracted

from the complex spectra of fragment ions produced by the interaction of the laser with the cell. The large number of fragment ions cannot be assigned to particular chemical structures of the cell, but they can be evaluated by multivariate analytical procedures as mass fingerprints and thus yield additional information.

In this contribution we give examples that demonstrate the capability and limitations of this single-cell mass analytical tool in microbiology.

#### Experimental

A detailed description of the LAMMA 500 instrument is given elsewhere.<sup>1</sup> For single-cell mass analysis, the bacteria are harvested from the growth medium in the case of cultivable cells, or isolated from infected tissue in the case of *Mycobacterium leprae*, which does not multiply in artificial culture media. The bacteria are then washed in distilled water to remove extracellular contaminations, with care being taken that alterations in the intracellular concentrations are avoided. The bacteria are then brought onto pioloform-coated copper meshes in a widespread distribution, so that laser evaporation of a single cell at a time is made possible.<sup>2,3</sup>

Although one can determine the absolute intracellular contents of sodium and potassium of a single cell,<sup>4</sup> which are by orders of magnitude higher than the absolute detection limits of the LAMMA instrument ( $2 \times 10^{-20}$  and  $1 \times 10^{-20}$  g, respectively), for the determination of the physiological state it is sufficient to measure their ratio. This way, many problems which are inevitably connected with absolute measurements can be excluded. Because of overlapping contributions of atomic and molecular ions at mass  $m/z$  41, the determination of the sodium to potassium ratio ( $\text{Na}^+/\text{K}^+$  ratio) is related to the potassium isotope  $^{39}\text{K}$ . To establish a distribution of this ratio for a bacterial sample, data of 600 cells are collected.

For fingerprinting, 120 spectra are typically evaluated from each sample. For establishing similarity relationships among various samples by cluster analysis, the experimental conditions concerning growth medium, isolation procedure, sample preparation, and instrumental settings must be identical. Furthermore, all spectra have to be normalized to total intensity to minimize variations in the ion intensities from shot to shot due to varying laser-sample interactions. Details of the applied cluster analysis are described elsewhere.<sup>5</sup>

#### Results

In Fig. 1 an example is given for the application of the single-cell analysis to the determination of variations in the physiological state within bacterial populations. It demon-

The authors are with Forschungsinstitut Borstel, Division of Biophysics, D-2061 Borstel, Federal Republic of Germany. This project was financially supported by the Federal Ministry for Research and Technology under grant 038667/1 and the German Leprosy Relief Association. The responsibility for the content of this publication rests solely with the authors.



strates differences in the relative cumulative distributions of the  $\text{Na}^+/\text{K}^+$  ratios for *Mycobacterium smegmatis* prepared from a culture medium (A) and *M. leprae* isolated from an infected armadillo liver (B). From microbiological viability tests it is known that approximately 90% of all *M. smeg.* cells are viable under the particular growth conditions applied here. The 90% value of the  $\text{Na}^+/\text{K}^+$  ratios is 0.4 in this case. However, only about 50% of all cells lie below this value in curve (A). Under certain assumptions, which cannot be discussed here, it can be concluded from this comparison that this *M. leprae* population contained only a reduced number of viable cells. In this way it is possible to determine the number of viable cells of noncultivable bacteria, a task that can be otherwise performed only unsatisfactorily in animal tests.

Figure 2 shows the mass spectra of two microscopically identical morphological structures, both from the same *M. leprae* preparation of a human biopsy: (a) a pattern found to be characteristic for mycobacteria, and (b) a spectrum that leads to a completely different mass fingerprint. This example shows the feasibility of judging the homogeneity of a bacterial sample, and of achieving a correlation between different morphological structures and the related mass spectrometric data. For example, one could examine in this way the assumption that a relation exists in leprosy between the morphological appearance of a cell and its physiological state; i.e., a high degree of granulation expresses a loss of viability.

Another field of application of the mass fingerprinting is shown in Fig. 3: the 3-di-

mensional nonlinear map of the similarity relationships among 34 *M. leprae* samples isolated from patient biopsies before and after several months of a monotherapy with a chemotherapeutic. Each point represents the average over 120 single-cell mass spectra of one sample. Obviously, these averaged spectra are separated into two groups, untreated and treated. The two points A3' and B4' represent bacteria from patients under therapy who did not respond to the treatment, as was deduced from the intracellular  $\text{Na}^+/\text{K}^+$  ratios.<sup>6</sup>

Beyond the pure application of LAMMA as a microprobe, the instrument can be also utilized as a laser desorption mass spectrometer and thus give additional information for structural elucidation of biomolecules isolated from bacteria in a mass region up to about 3000 amu.<sup>7</sup>

#### References

1. H. Vogt, H. J. Heinen, S. Meier, and R. Wechsungen, *Fresenius Z. anal. Chem.* 308: 195-200, 1981.
2. B. Lindner and U. Seydel, *J. Gen. Microbiol.* 129: 51-55, 1983.
3. B. Lindner and U. Seydel, *Microbeam Analysis--1983*, 106-108.
4. U. Seydel and B. Lindner, *Fresenius Z. anal. Chem.* 308: 253-257, 1981.
5. B. Lindner and U. Seydel, *J. Phys. Colloq. (France)* 45(C-2): 565-568, 1984.
6. U. Seydel, B. Lindner, and A. M. Dhople, *Int. J. Leprosy* 53: 365-372, 1985.
7. U. Seydel et al., *Eur. J. Biochem.* 145: 505-509, 1984.

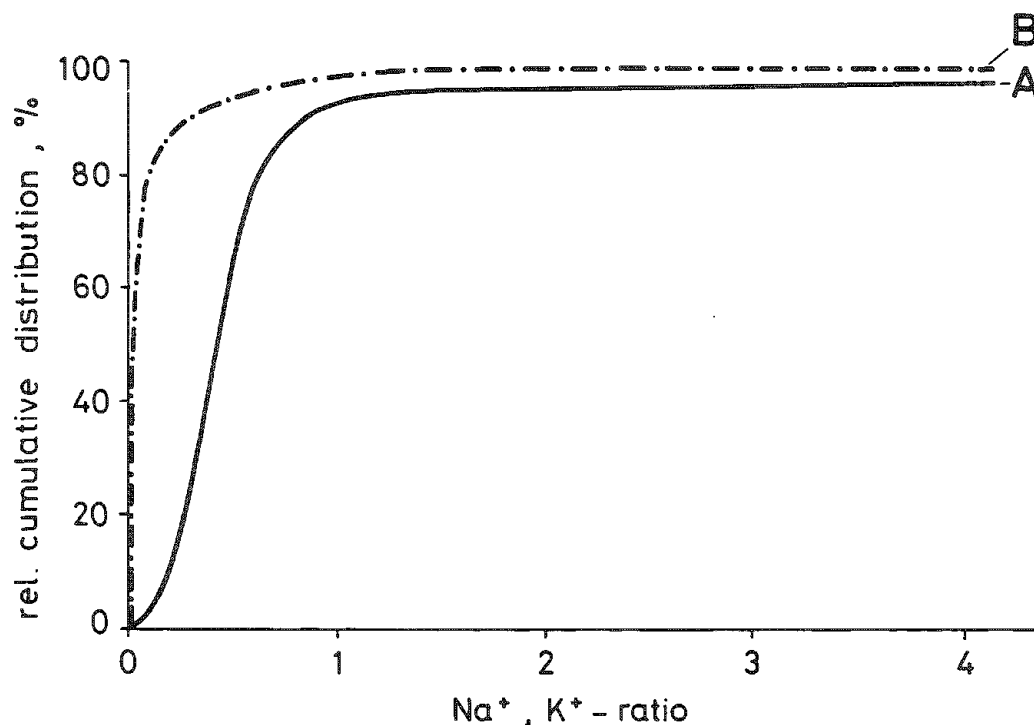


FIG. 1.--Relative cumulative distributions of  $\text{Na}^+/\text{K}^+$  ratios of 600 single cells, in each case for two bacterial populations: (A) *M. leprae* isolated from armadillo liver, (B) *M. smegmatis* prepared from growth medium.



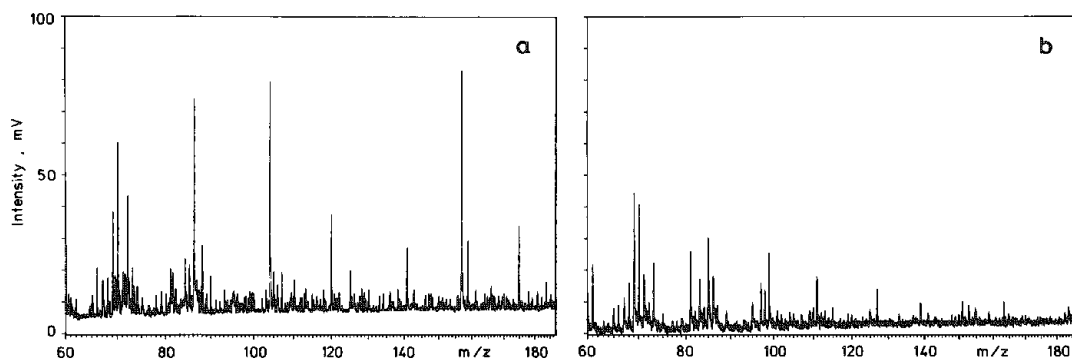


FIG. 2.--LAMMA fingerprint spectra of two microscopically identical structures: (a) typical fingerprint of one mycobacterium, (b) fingerprint of artifact.

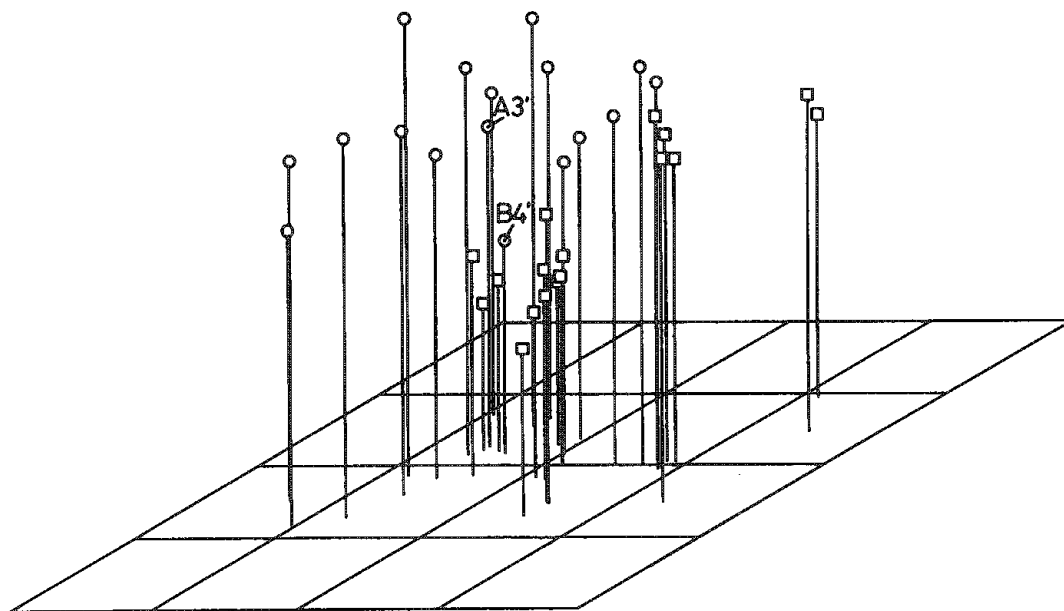


FIG. 3.--3-dimensional nonlinear map of similarity relationships among 34 bacterial samples. Each point represents averaged fingerprint of 120 single-cell analyses.  $\square$  fingerprints from cells of untreated patients,  $\circ$  fingerprints from cells of patients under therapy.

## LAMMA STUDY OF AEROSOL SAMPLES COLLECTED IN THE AMAZON BASIN

F. J. Bruynseels, P. Artaxo, H. M. Storms, and R. E. Van Grieken

Aerosol samples collected in the Amazon Basin with a 10-stage cascade impactor were analyzed in the laser microprobe mass analyzer (LAMMA-500). Because of the high organic content of the aerosols and the current interest in the enrichment of trace metals in biogenic aerosol emissions, the application of LAMMA in this field of atmospheric research can provide interesting results. Individual aerosol particle analysis was performed with a view to studying the usefulness of LAMMA in aerosol source identification for plant-related aerosol emissions.

### *Sampling and Analysis*

Aerosol sampling was carried out both from ground-based stations and by aircraft flights during the Amazon Boundary Layer Experiment (ABLE-2A) as a part of the Global Tropospheric Experiment (GTE). The aerosols were collected with a 10-stage Batelle-type cascade impactor (cutoff diameters of 16, 8, 4, 2, 1, 0.5, 0.25, 0.12, and 0.06  $\mu\text{m}$  and a backup filter), operated at a flow rate of 1 l/min. Formvar-coated electron microscope grids were mounted on each stage. The sampling campaign was carried out from 11 July to 5 August 1985. One impactor sample for LAMMA analysis discussed below was sampled on 13 July 1985 from 11:58 a.m. to 12:13 p.m. at a site named Bacia Modelo Tower, situated in a reservation park about 70 km north of the city of Manaus, Brazil. The sampling equipment was installed on top of a 45m high tower, at about 15 m above the forest canopy. The sampling area is very difficult to access, so that almost no local anthropogenic contributions are to be expected, as was also evident from proton-induced x-ray emission measurements on the bulk samples.<sup>1</sup> The second aerosol sample was collected on 19 July 1985, during a flight with the NASA Electra aircraft from Manaus to Belem. Details of the sampling procedures and sites can be found elsewhere.<sup>1</sup> The particle size was checked by optical observations in the microscope, because variations in altitude during the flight changed the cutoff characteristics of the impactor.

The loaded electron microscope grids were analyzed in the LAMMA instrument for the determination of the chemical composition of the individual aerosol particles. For the impactor sampled at Bacia Modelo Tower, 150 spectra of individual particles were recorded. For the aerosol sample collected during the aircraft flight, 100 submicron aerosol particles were analyzed.

### *Results and Discussion*

*Sample Collected at Bacia Modelo Tower.* In the cascade impactor collected in Bacia Modelo Tower, at least seven types of particles could be detected. In the coarse-mode aerosol, large particles were found that are possibly released by mechanical abrasion of the leaves due to wind action.<sup>2</sup> The numerous mass peaks in the positive mode mass spectra originating from the organic material show the following systematic structure:

$(\text{C}_n\text{H}_{2n-1})^+$  at  $m/z = 27, 41, 55, 69, 83, 97, \dots$   
 $(\text{C}_n\text{H}_{2n+1})^+$  at  $m/z = 29, 43, 57, 71, 85, 99, \dots$   
 $(\text{C}_n\text{H}_{2n+1}\text{O})^+$  at  $m/z = 31, 45, 59, 73, 87, 101, \dots$

In the negative ion mode spectra the following series of peaks were identified:

$(\text{C}_n\text{H}_{2n-1})^-$  at  $m/z = 41, 55, 69, 83, 97, 111, 115, \dots$   
 $(\text{C}_n\text{H}_{2n-1}\text{O})^-$  at  $m/z = 43, 57, 71, 85, 99, 113, 127, \dots$   
 $(\text{C}_n\text{H}_{2n+1}\text{O})^-$  at  $m/z = 45, 59, 73, 87, 101, 115, 129, \dots$

These mass peaks are the result of the fragmentation of hydrocarbons and terpenes, and the oxygen-containing ions are formed by the fragmentation of oxygenated compounds (e.g., alcohols, esters, etc.). Since the spectrum is a superposition of many organic compounds, and because of the complex fragmentation behavior of long-chain hydrocarbons, a detailed structural interpretation of the spectra is not possible. Besides the organics, inorganic elements such as Na, Mg, K, Ca, and Cu could be also identified.

The second and most abundant particle type accounts for about 50% of the particles. The mass spectrum was compared with reference spectra of  $\text{K}_3\text{PO}_4$ ,  $\text{K}_2\text{HPO}_4$ , and  $\text{KH}_2\text{PO}_4$ . The positive mode peaks at  $m/z = 141, 157, 175$ , and 213 were identified as  $\text{K}_2\text{PO}_3^+$ ,  $\text{K}_2\text{PO}_4^+$ , and  $\text{K}_3\text{HPO}_4^+$ , respectively. In the negative ion mode, the mass peaks at  $m/z = 63$  ( $\text{PO}_2^-$ ),  $m/z = 79$  ( $\text{PO}_3^-$ ) were detected for all reference compounds, but the  $\text{H}_2\text{PO}_4^-$  cluster was only observed for  $\text{KH}_2\text{PO}_4$ . The positive mode clusters, seen in the spectra of the reference salts, were also recorded in the spectra of the ambient aerosols. Although the relative intensities of the clusters most closely correlate with the  $\text{KH}_2\text{PO}_4$  fingerprint, the spectra are not identical. This result permits the assumption that the phosphate group in the unknown sample is probably linked to an organic chain (e.g., in phospholipids). The presence of an organic fraction is clearly indicated by clusters such as  $\text{C}_3\text{H}_7^-$  ( $m/z = 43$ ),  $\text{C}_2\text{H}_5\text{O}^-$  ( $m/z = 45$ ),  $\text{C}_5\text{H}_{11}^-$  ( $m/z = 71$ ), etc. The presence of K and P in aerosol samples collected above forested areas has been assigned to aerosol emission by plants.<sup>2</sup>

The third important particle type was identified as a mixture of several salts including sulfates, carbonates, and chlorides, and it also contained an organic fraction. The major mass peaks can be classified as follows:

Authors Bruynseels, Storms, and Van Grieken are at Department of Chemistry, University of Antwerp-UIA, Antwerp, Belgium; author Artaxo is at Instituto de Fisica, Universidade de Sao Paulo, Sao Paulo, Brazil.

$M_2^+$	at $m/z = 46, 62, 78$ with $M = Na, K$
$M_2CN^+$	at $m/z = 72, 88, 104$
$M_2C_3H_7^+$	at $m/z = 89, 105, 121$
$M_2O^+$	at $m/z = 62, 78, 94$
$M_2OH^+$	at $m/z = 63, 79, 95$
$M_2Cl^+$	at $m/z = 81, 97, 113$
$M_3SO_4^+$	at $m/z = 165, 181, 197, 213$
$M_3CO_3^+$	at $m/z = 129, 145, 161$

Inorganic elements such as Na, Mg, K, and Ca are abundantly present. These aerosols are thus most likely related to the emissions by plants. The appearance of nutrient elements like Na, Mg, K, Ca, Cl, and  $SO_4^{2-}$  is attributed to the emission of aerosols during plant transpiration and these elements could be emitted simultaneously with the plant wax.<sup>3,4</sup> The migration of salts into the atmosphere during crop plant transpiration was studied by Nemeruyk, who measured the transpiration of  $Ca^{2+}$ ,  $SO_4^{2+}$ ,  $Cl^-$ ,  $K^+$ ,  $Mg^{2+}$ , and  $Na^+$  from plants in ambient air.<sup>5</sup>

The fourth type of aerosols yielded fingerprint spectra such as shown in Fig. 1(a) and (b) for the positive and negative mode, respectively. Their major component was tentatively interpreted as a sulfate salt of an organic nitrogen compound, namely an amine. From the elemental composition of the mass peak at  $m/z = 112$  ( $C_7H_{14}N^+$ ) a molecular weight of 113 daltons is proposed for the amine. An additional mass peak at  $m/z = 95$  can be attributed to a  $CH_3SO_3^-$  anion. This cluster was found to be typical for a sulfonate species as was inferred from reference spectra of  $NaCH_3SO_3$ . The negative mass peaks at  $m/z = 141$  and 155 are interpreted as a combination of the  $HSO_4^-$  cluster with the  $C_2H_6N$  and  $C_3H_8N$  fragments, respectively. The origin of vanadium, found to be present as a trace element in these particles, is unknown.

The organic fractions frequently detected in biogenic airborne organic matter are hydrocarbons (wax and terpenes), carboxylic acids, ketones, and alcohols.<sup>6</sup> Data about amino compounds in aerosols are very scarce, but amines, amides, and amino acids have been identified in dry and wet deposition samples, so that their occurrence in the atmosphere is obvious.<sup>7</sup> The formation of organic ammonium salts could be important for the neutralization of the airborne sulfuric acid in addition to the neutralization by ammonia. The detection of the methane sulfonic acid species is consistent with the finding that also land plants can produce dimethylsulfide (DMS).<sup>8</sup> The reaction pathway for the oxidation of DMS by OH and  $NO_3$  radicals results in the formation of dimethylsulfoxide ( $CH_3SOCH_3$ ) methane-sulfonic acid ( $CH_3SO_3H$ ) and sulfur dioxide ( $SO_2$ ). If methanesulfonic acid exhibits the same behavior as  $H_2SO_4$  formed by  $SO_2$  oxidation, it will take part in the formation of the fine mode sulfate aerosol (excess sulfate), which is in agreement with the LAMMA data.

*The Sample Collected on Board the Electra Aircraft.* About 80% of the fine-mode aerosols detected in the aircraft sample contained sulfates, chlorides, carbonates, and organic material. Figure 2(a) shows a typical spectrum

of this type of particle, similar to those of the particles found in the ground sample. However, in addition to these salts, trace elements such as Pb and Cr were also detected in some of these aerosols. In fact, about 25% of the fine-mode aerosols contained Pb as a trace element, not associated specifically with one particle type, which could point to a gas-phase condensation formation mechanism that is not specifically selective for a certain particle type. A minor fraction of these aerosols also contained nitrogen-oxy-salts. Other aerosols contained Cu but also Zn and Pb (Fig. 2b) in agreement with the results of Beauford et al.<sup>9</sup> In addition to these elements, Cr could be detected in the same particles.

The K- and P-rich phosphate particles shown in Fig. 3, similar to the most abundant particle type for the ground-based sampling, revealed some molecular fragment peaks that point to the molecular species  $C_4H_9NO_2$ . The fragmentation pattern is consistent with an organic molecule having both a carboxyl group and an amine function, which points to an aminobutyric acid as being the most plausible identification for the unknown molecule.<sup>10</sup>

### Conclusion

The results clearly demonstrate the power of LAMMA for the simultaneous detection of trace elements and the fingerprinting of organic molecules, together with the speciation of the matrix composition of the individual aerosol particulates. Since one spectrum is a superposition of the fingerprints of many individual chemical identities, the interpretation of the spectra is not always straightforward. Nevertheless, the results of the LAMMA measurements form an important supplement to the electron probe x-ray microanalysis (EPMA) data. The application of individual particle analysis techniques can very advantageously support the interpretation of trace element bulk analysis.

Interesting data about the correlation of plant related material with trace elements such as Cr, Cu, Zn, and Pb have been found and the detection of some organic molecules on the micrometer-size level became feasible. Also, the detection of particles consisting of plant nutrients provides a direct indication for the release of these chemical species by plant transpiration.

### References

1. P. Artaxo et al., "Composition and sources of aerosols from the Amazon Basin," *J. Geophys. Res.* (in preparation).
2. W. Beauford et al., "Release of particles containing metals from vegetation into the atmosphere," *Science* 195: 571-573, 1977.
3. E. R. J. Wils et al., "The occurrence of plant wax constituents in airborne particulate matter in an urbanized area," *Chemosphere* 11: 1087-1096, 1982.
4. B. R. T. Simoneit, "Application of molecular marker analysis to reconcile sources of carbonaceous particulates in tropospheric aerosols," *Sci. Tot. Environ.* 36: 61-72, 1984.
5. G. E. Nemeruyk, "Migration of salts

into the atmosphere during transpiration," *Soviet Plant Physiol.* 17: 560-566, 1970.

6. B. R. T. Simoneit and M. A. Mazurek, "Air pollution: The organic component," *CRC Critical Reviews in Environmental Control* 11: 219-276, 1981.

7. M. A. Mazurek and B. R. T. Simoneit, "Organic components in bulk and wet-only precipitation," *CRC Critical Reviews in Environmental Control* 16: 1-140, 1986.

8. M. O. Andreae, "The ocean as a source for atmospheric sulfur compounds," in P. Buat-Menard, Ed., *The Role of Air-sea Exchange in Geochemical Cycling*, Dordrecht: Reidel, 1986.

9. W. Beauford et al., "Heavy metal release from plants into the atmosphere," *Nature* 256: 35, 1975.

10. C. D. Parker and D. M. Hercules, "Laser mass spectra of simple aliphatic and aromatic amino acids," *Anal. Chem.* 57: 698-704, 1985.

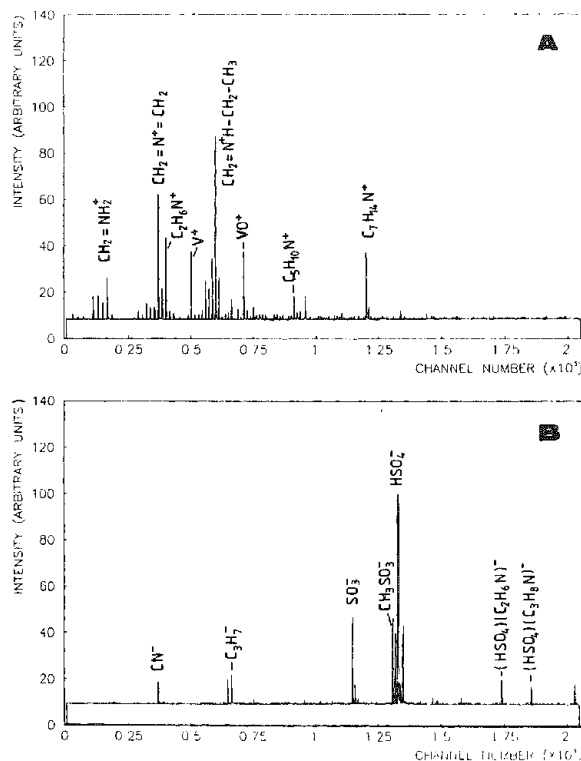


FIG. 1.--(a) Positive and (b) negative mode LAMMA spectra of a particle type assigned to a sulfate and sulfonate salt of an amine.

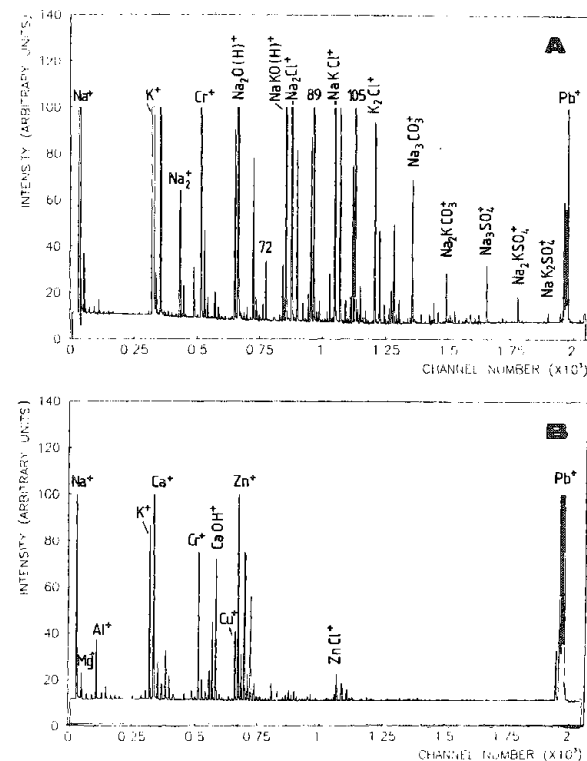


FIG. 2.--Positive-mode LAMMA spectra illustrating presence of elements such as Cr, Pb, Cu, and Zn in Amazon Basin aerosol.

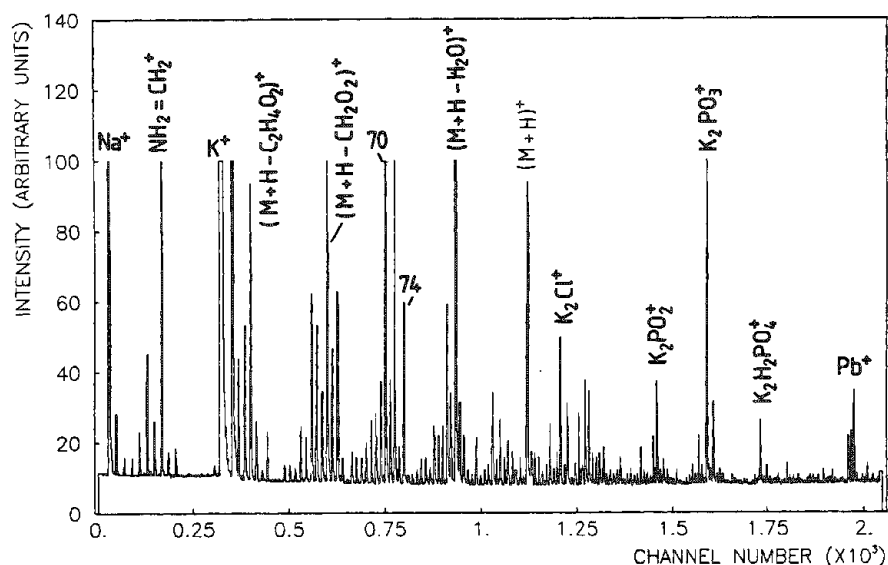


FIG. 3.--Positive-mode LAMMA spectrum of K- and P-rich particles, which also point to presence of  $C_4H_9NO_2$ -molecule.

## MULTI-ISOTOPE MULTI-ELEMENT LABELING IN MICROBEAM ANALYSIS OF BIOLOGICAL TISSUES

W. H. Schröder, Angela Einerhand, Jürgen Lauer, Hans Eschweiler,  
Ruth Langner, G. L. Fain, and Josef Bauch

The study of cellular compartmentization is of major importance in cell biology. Conventional microbeam analysis techniques can yield important information on the distribution of cellular material at a given time. However, as the cell is constantly changing and responding to outside stimuli, a static image does not give sufficient information on the actual dynamic processes. Analysis of time kinetics by conventional microbeam technique is faced with the problem (not always recognized) that uptake and release of material may balance out, so that even rapidly exchanging systems appear to the observer as static systems without any change.

In following the goal of studying dynamic processes, we developed a labeling system for microbeam analysis of cells and tissues based on the LAMMA microprobe technique and the use of stable isotopes.

The LAMMA instrument uses a focused laser beam selectively to vaporize small areas of sections and introduces the resulting ions into the beam of a time-of-flight mass spectrometer. This procedure permits isotope analysis with a local resolution better than 1  $\mu\text{m}$ .

One of the most interesting elements for studies on compartmentization and how cells use compartments to regulate cellular processes is Ca, since the Ca ion is known to be involved in many regulatory processes. The free  $\text{Ca}^{2+}$  concentration in the cytoplasm is probably very low in most cells but most likely very high in some internal pools (enclosed compartments).

### *Isotope Labeling to Study Ca Uptake*

In the first experiments to demonstrate the feasibility of isotope labeling we analyzed the uptake of Ca into pigment granules in arthropod photoreceptor cells, which we suspect to be large, slowly exchanging Ca pools.

In these experiments the retinas were isolated and then incubated in media that contained as the only Ca source  $^{44}\text{Ca}$ , 98% enriched. After the incubation for various times we analyzed the pigment granules (for  $^{40}\text{Ca}$  and  $^{44}\text{Ca}$ ) and were able to measure a time kinetics of  $^{40}\text{Ca}$  originally present, as well uptake of  $^{44}\text{Ca}$  from the medium. The combination of the isotope ratios from LAMMA measurements and the absolute Ca amount from EDX analysis permitted quantitative analysis for

each of the isotopes.

### *Labeling Uptake from Various Sources*

Just as uptake from the incubation medium can be monitored by incubation in labeled media, we can study uptake from both sides of a tissue or transport across a tissue by incubating a planar tissue with different isotopes on either side. This procedure is of particular interest in the study of epithelia.

We incubated preparations of isolated (retinal) pigment epithelium-choroid tissue in a two-chambered dish (such as is frequently used for physiological studies) with media containing  $^{42}\text{Ca}$  on one side and  $^{44}\text{Ca}$  on the other. We then used the time kinetics from LAMMA measurements of the original 40, the label 42, and  $^{44}\text{Ca}$  to trace simultaneously the uptake of Ca from the two sides of epithelium. Differences in uptake could be clearly demonstrated.

### *Pulse Chase Labeling*

Once the uptake of Ca is demonstrated it is interesting to see whether Ca pooling occurs and to analyze the transfer rates between pools. That can be done using pulse chase labeling in analogy to radio-tracer labeling for autoradiography. In pulse chase labeling the label is not applied constantly but only for a brief time and then the label is washed out. This procedure makes it possible to follow how the label moves in and out of pools. An elaborate extension of pulse chase labeling is the use of a different isotope (different from the one originally present and from the label) for the chase.

One system for which the analysis of the movement of Ca in and out of internal stores is of special interest as a model system is the vertebrate photoreceptor. A specific question is whether, in the outer segment of rods, a fraction of Ca may be sequestered in membrane vesicles, the disks. Here we incubated the isolated retina first in  $^{42}\text{Ca}$  and allowed for a considerable uptake of  $^{42}\text{Ca}$ . Later we exchanged the incubation medium for one containing  $^{44}\text{Ca}$ . In LAMMA analysis we could monitor first the uptake of  $^{42}\text{Ca}$  in the first labeling solution but little release of the  $^{40}\text{Ca}$  already present. After the switch to the  $^{44}\text{Ca}$  solution we observed a very rapid exchange of the first label ( $^{42}\text{Ca}$ ) with the second label ( $^{44}\text{Ca}$ ), but very slow exchange of the original  $^{40}\text{Ca}$ . We took that to indicate that there are at least two pools of Ca, one rapidly exchanging with the outside and one with very slow exchange, presumably within the membrane enclosed compartment, the disks.

### *Multi-element Multi-isotope Labeling*

The labeling procedures presented here for Ca can of course be applied to all elements

The authors are at the Institut für Biologische Informationsverarbeitung der Kernforschungsanlage Jülich, D-5170 Jülich, Federal Republic of Germany, except G. L. Fain, who is at the Jules Stein Eye Institute, UCLA School of Medicine, Los Angeles, CA 90024; and J. Bauch, who is at University of Hamburg (Holzbiologie).

with two or more stable isotopes. Our first application to the labeling of several elements is the study of nutrient uptake in plant root cells.

Very little is known about the molecular and cellular mechanisms of the nutrient uptake in roots of plants. Besides the severe technical problems in the specimen preparation of plant tissue it is evident, especially in this case, that no changes in the amount of any element taken up will be seen in (healthy) steady-state conditions if conventional microprobe techniques are used. We have incubated roots from intact spruce plants in laboratory and field studies with  $^{25}\text{Mg}$ ,  $^{41}\text{K}$ , and  $^{44}\text{Ca}$  and have monitored the effects of various environmental factors (e.g., low pH and high  $[\text{Al}]$ ) on the ion exchange properties of the cell walls of the root cells, and have followed the label into the stem of the plants to study transport kinetics.

## FINGERPRINTING OF CHEMICAL SPECIES IN MICROPARTICLES: CORRELATIVE LASER AND ELECTRON MICROPROBE STUDIES

I. H. Musselman, J. T. Rickman, and R. W. Linton

Laser microprobe mass spectrometry (LAMMS) has been shown to differentiate among particles of nickel metal and various nickel compounds ( $\text{NiO}$ ,  $\text{NiSO}_4 \cdot 7\text{H}_2\text{O}$ ,  $\text{NiS}$ , and  $\text{Ni}_3\text{S}_2$ ), by use of their characteristic cluster ion mass spectra.<sup>1</sup> However, the identification of compounds such as these nickel species and their distribution between, or within, individual environmental particles by LAMMS alone is complicated by both inherent particle heterogeneity and the limitations of the LAMMS technique (changes in spectral intensity due to variations in laser energy from shot to shot, limited dynamic range, and complexities of cluster ion formation). These difficulties may be addressed by use of the complementary technique of scanning electron microscopy coupled to energy dispersive x-ray spectroscopy, SEM/EDS.<sup>2</sup> The imaging capabilities of the SEM may be used to establish particle morphology and size prior to chemical analysis by EDS and LAMMS. A qualitative survey of the major and minor elements in the sample as well as quantitative x-ray intensity information may be obtained by EDS. Unlike SEM/EDS, which is unable to detect x rays generated from elements with  $Z < 11$  with the conventional thin beryllium window lithium-drifted silicon [Si(Li)] detector, LAMMS permits the detection of all elements and their isotopes. In addition, the formation and detection of cluster ions (an ion which consists of a group of atoms, not necessarily a multiple of the molecular ion) by LAMMS may make the differentiation of closely related compounds possible.<sup>1,3-6</sup> In comparison, x-ray line shapes in conventional EDS studies generally provide little direct chemical speciation information.

In this study we compare data taken by combined SEM/EDS and LAMMS from identical particles in the micrometer size range produced by

a fluidized bed roaster (FBR) in a nickel refinery. The goal is to assign molecular structures to the nickel-containing compounds in the particles. The FBR dust serves as a useful environmental sample for analytical technique development in that it has a very high total nickel content (about 50 wt%) and is known from wet chemical analyses to have several classes of nickel compounds (e.g., oxides, sulfides, sulfates) with varying biological impacts.

### *Experimental*

*Sample Preparation.* The nickel reference samples ( $\text{Ni}^0$ ,  $\text{NiO}$ ,  $\text{NiSO}_4 \cdot 7\text{H}_2\text{O}$ ,  $\text{NiS}$ , and  $\text{Ni}_3\text{S}_2$ ) were mounted dry on Formvar-coated transmission electron microscope (TEM) grids for SEM and LAMMS analysis. The FBR dust sample was dispersed in freon in an ultrasonic bath to form a homogeneous distribution of particles. A drop of the freon/particle mixture was placed on a TEM grid and allowed to dry under a heat lamp. All samples prepared for SEM/EDS analysis were subsequently coated with carbon to minimize charging during measurements.

*Correlative Procedure.* Spectra from nickel metal and the nickel compounds were obtained by both SEM/EDS and LAMMS to use as references for the spectra collected from the FBR particles. For SEM/EDS, the S/Ni ratios of the nickel samples, calculated from the  $K\alpha$  x-ray peak areas, served as the references. For LAMMS, the references were the characteristic positive cluster ion mass spectra of each of the nickel samples.

The FBR dust sample was analyzed first by the SEM. The grid squares of the sample mount were chosen randomly and eliminated only if particle loading was too heavy or if substantial portions of the Formvar film were damaged. All particles in each suitable grid square were analyzed by SEM/EDS unless the particle was too small or too close to adjacent particles. Following x-ray analysis, the same FBR particles were analyzed destructively by LAMMS.

*Instrumentation and Analysis.* The SEM/EDS measurements were made in an ISI DS-130 Scanning Electron Microscope equipped with an energy-dispersive Si(Li) detector. The microscope is automated with a Tracor Northern TN-5500 Digital Imaging System, which includes a particle recognition and characterization (PRC) program. This program uses digital beam control to locate, size, and obtain x-ray spectra from the particles. The EDS measurements were obtained with a 15keV electron beam and a collection time of 99 s per particle. EDS spectra were obtained from about 50 particles of each nickel reference sample, and from 172 FBR particles. Background-corrected x-ray intensity ratios of S/Ni were obtained from the  $K\alpha$  lines of each spectrum. The majority of particles analyzed for the reference and

Author Linton is in the Department of Chemistry at the University of North Carolina, Chapel Hill, NC 27514; authors Musselman (currently at the National Bureau of Standards, Gaithersburg, MD 20899) and Rickman are graduate students at UNC. Certain commercial equipment, instruments, or materials are identified in this paper. Such identification does not imply recommendation or endorsement by NBS, nor does it imply that the materials or equipment are necessarily the best available for the purpose. Support of this research under U.S. Environmental Protection Agency cooperative agreement CR-812908-01-1 is gratefully acknowledged. Although funded in part by EPA, the research has not been subjected to EPA review and so does not necessarily reflect the EPA's view; no official endorsement should be inferred. The authors gratefully acknowledge the assistance of S. D. Leigh of the NBS Center for Applied Mathematics in the preparation of this manuscript.



FBR particle samples were within the 1-2 $\mu$ m-diameter range. However, since the S and Ni K $\alpha$  x rays are of considerably different energy (2.31 keV and 7.48 keV, respectively), and the particles are not highly spherical, size effects may be particularly significant even in this narrow range. No corrections have yet been made for particle size effects.

The laser microprobe measurements were made with a Laser Microprobe Mass Analyzer, LAMMA-500, coupled to two Biomation model 8100 transient recorders.<sup>7-9</sup> The chosen laser wavelength for analysis was 266 nm and the average energy delivered to the sample was 0.97  $\mu$ J. The laser and spectrometer conditions allowed for complete ablation of each particle and were chosen to maximize the production and detection of positive cluster ions<sup>10-12</sup> to facilitate differentiation of the nickel reference samples.<sup>1</sup> Five positive ion mass spectra were obtained from 1-2 $\mu$ m-diameter particles from each of the nickel reference samples. The same FBR particles analyzed by SEM were analyzed subsequently by LAMMS.

### Results and Discussion

By use of only a few select atomic and cluster ions in the positive ion LAMMS spectra obtained from the nickel reference samples Ni<sup>o</sup>, NiO, NiSO<sub>4</sub>·7H<sub>2</sub>O, NiS, and Ni<sub>3</sub>S<sub>2</sub>, four of the five nickel species are differentiated, as shown previously.<sup>1</sup> In the former study, NiS (sulfide) and Ni<sub>3</sub>S<sub>2</sub> (subsulfide) have qualitatively identical spectra, both exhibiting peaks for the NiS<sup>+</sup>, Ni<sub>2</sub><sup>+</sup>, NiS<sub>2</sub><sup>+</sup>, Ni<sub>2</sub>S<sup>+</sup>, and Ni<sub>3</sub>S<sup>+</sup> cluster ions. The variation in cluster ion peak intensities obtained from multiple analyses of the two sulfide compounds is too large to enable their distinction. Representative positive ion LAMMS spectra of four of the reference samples are shown in Fig. 1.

LAMMS data were obtained from 120 of the 172 FBR particles analyzed by SEM/EDS. Spectra of the remaining 52 particles were not taken due to breakage of the formvar film, to particle loss during transport, or to imprecise laser alignment during the ablation step. Fifty-seven of the 120 particles (48%) analyzed by LAMMS exhibit nickel-containing cluster ions in the positive ion mass spectra. The LAMMS results for the remaining particles exhibit ions only for atomic species or for clusters containing other elements. The absence of cluster ions in some spectra is attributed to inadequate coupling of the laser pulse energy with the particle due to inherent fluctuations in the laser energy from pulse to pulse, to variations in laser focus, and to the imprecise lateral positioning of the laser beam on the particle.

The procedure by which the SEM/EDS (172 spectra) and LAMMS (120 spectra) data are correlated is summarized in a flow chart in Fig. 2. The data are first divided according to the presence or absence of nickel-containing cluster ions in the LAMMS positive ion mass spectrum. Specific species assignments are not possible for particles without LAMMS data exhibiting nickel-containing cluster ions. Based solely on the LAMMS cluster ion spectra, the particles are divided into two categories:

(1) particles whose LAMMS spectra resemble the reference sample of nickel oxide or nickel sulfate, i.e., the presence of the NiO<sup>+</sup> and Ni<sub>2</sub>O<sup>+</sup> cluster ions (Fig. 3A), and (2) particles whose LAMMS spectra resemble that of nickel sulfide or nickel subsulfide, i.e., the presence of the NiS<sup>+</sup>, NiS<sub>2</sub><sup>+</sup>, and Ni<sub>2</sub>S<sup>+</sup> cluster ions (Fig. 3B). The intensities of the cluster ions from the FBR dust sample are generally smaller than for the nickel reference samples, probably due to the heterogeneous nature of the dust particles. For this reason, the small Ni<sub>2</sub>O<sub>2</sub><sup>+</sup>/Ni<sub>2</sub>S<sup>+</sup> peak in the spectra of NiSO<sub>4</sub>·7H<sub>2</sub>O (but not NiO) is rarely seen in the spectra of the FBR particles. Atomic sulfur, because of its high ionization potential (10.36 eV) is often not present in positive ion LAMMS spectra and therefore is not used to differentiate nickel sulfate from nickel oxide. Of the 57 particles whose positive ion mass spectra exhibit nickel-containing cluster ions, 43 are classified as containing nickel oxide and/or nickel sulfate and the remaining 14 are classified as containing nickel sulfide and/or nickel subsulfide. Although the spectra of some of the FBR particles contain peaks for the nickel atomic ion Ni<sup>+</sup> and the cluster ion Ni<sub>2</sub><sup>+</sup>, as observed in the spectra of nickel metal, the EDS spectra of these same particles often exhibit major peaks for sulfur. Since the intensities of the Ni<sub>2</sub><sup>+</sup> peak in these spectra are small, other cluster ions that should be present are probably not detected. This group of particles is treated as exhibiting no nickel cluster ions.

The FBR particles, whose LAMMS spectra exhibit nickel-containing cluster ions, can be divided further by examination of their x-ray spectra. The criteria used to classify these particles are indicated in the flow chart. Of the 43 particles classified by LAMMS as containing nickel oxide and/or nickel sulfate, 17 exist as nickel oxide as determined by low S/Ni x-ray intensity ratios, <0.2. The S/Ni ratios of 9 of the 43 particles are within  $\pm 1\sigma$ , 1.5-2.6, of the average ratio obtained from 51 particles of the nickel reference sample nickel sulfate. For the remaining 17 particles, the S/Ni ratios are skewed, all outside of the lower  $1\sigma$  limit, <1.51. It is possible that these particles exist as nickel sulfate, but more probably they exist as mixtures of nickel sulfate and nickel oxide.

The S/Ni normal distributions of the Ni<sub>3</sub>S<sub>2</sub> and NiS reference samples (obtained from 49 and 40 particles, respectively) are shown in Fig. 4. The distributions are different enough to allow for discrimination between the sulfides, although care must be taken in the region of overlap. The distinction between Ni<sub>3</sub>S<sub>2</sub> and NiS is based on  $\pm 1\sigma$  (Ni<sub>3</sub>S<sub>2</sub>: 1.2-1.5, NiS: 1.9-2.5). The particles whose S/Ni ratios are outside of the  $1\sigma$  limit, away from the region of overlap, are also differentiated as Ni<sub>3</sub>S<sub>2</sub> or NiS, based on the assumption that elemental Ni or S is not present to alter the x-ray ratios. Of the 14 particles classified by LAMMS as containing nickel sulfide and/or nickel subsulfide, 6 exist as Ni<sub>3</sub>S<sub>2</sub> and 4 as NiS. The S/Ni ratios of the remaining 4 particles, which lie in the region of overlap, may exist as either NiS or Ni<sub>3</sub>S<sub>2</sub> or as a mix-

FIG. 1.--Representative positive ion LAMMS spectra for  $\text{Ni}^0$ ,  $\text{NiO}$ ,  $\text{NiSO}_4 \cdot 7\text{H}_2\text{O}$ , and  $\text{NiS}$ .

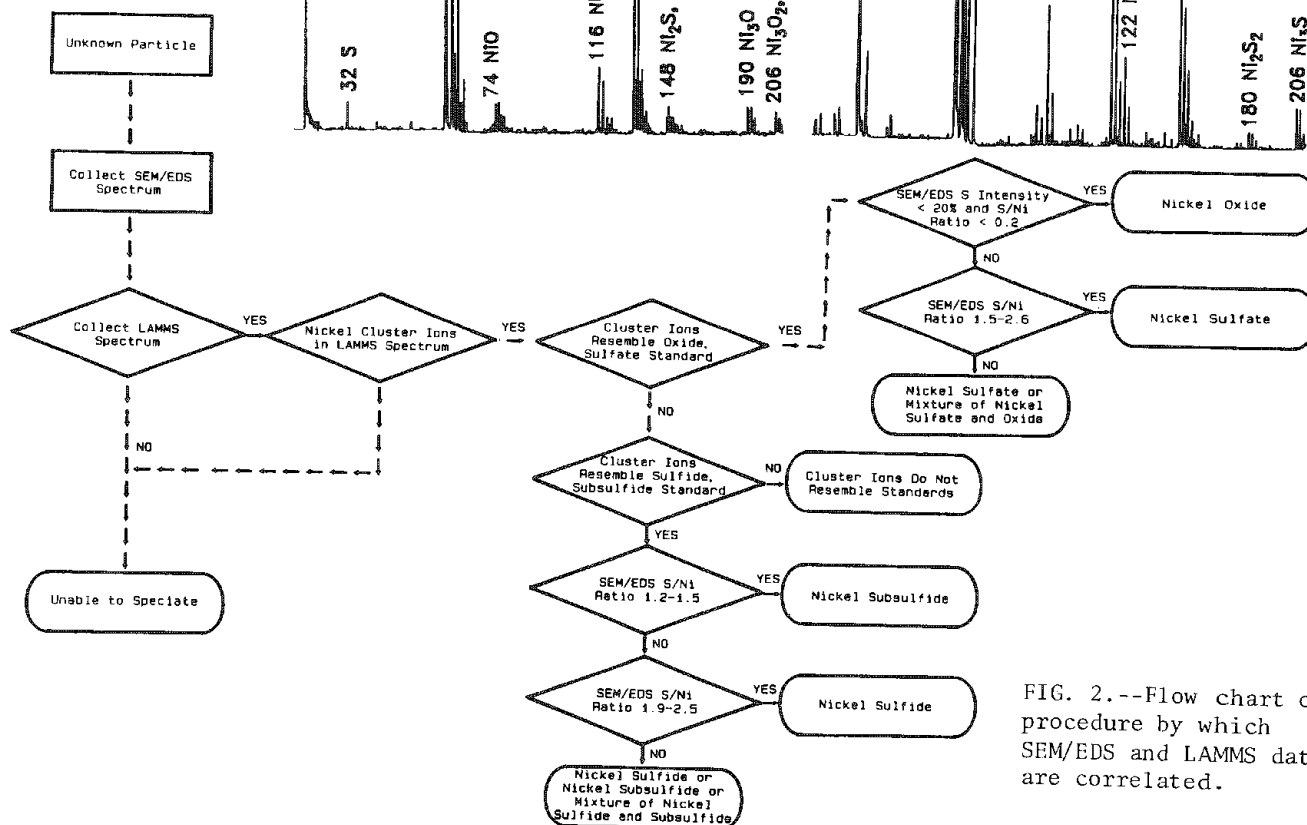
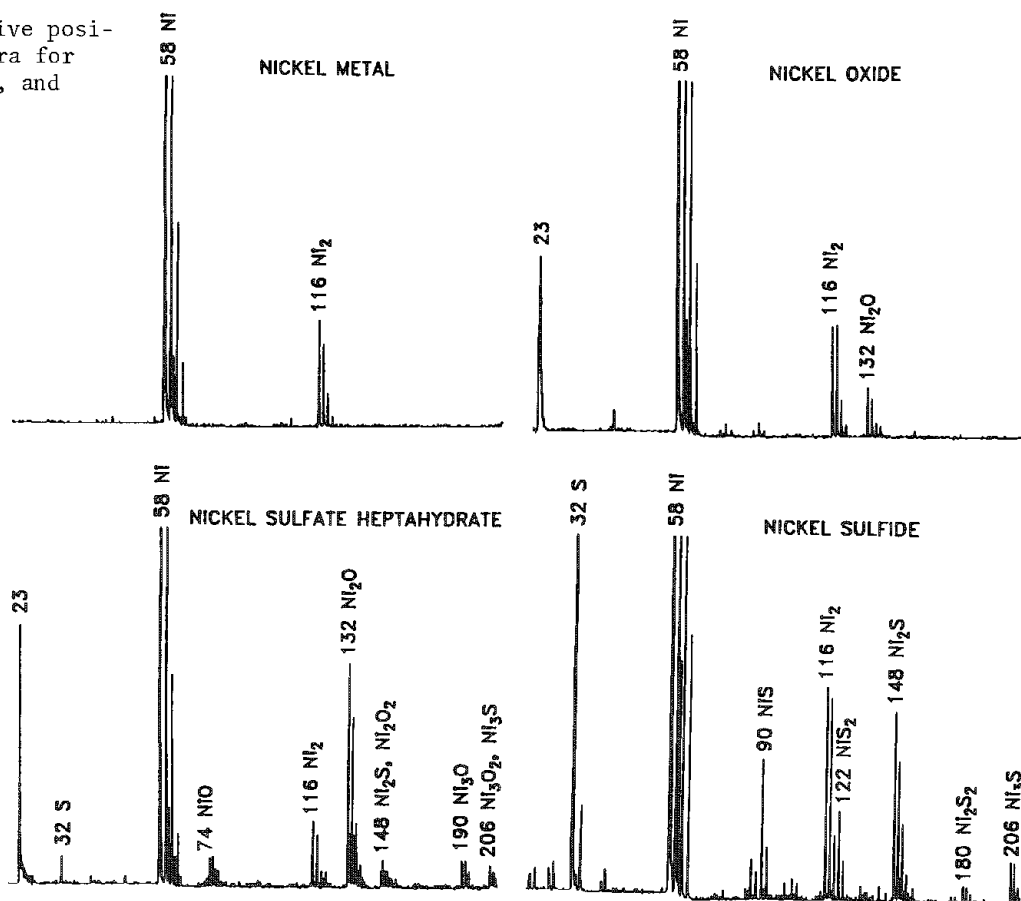
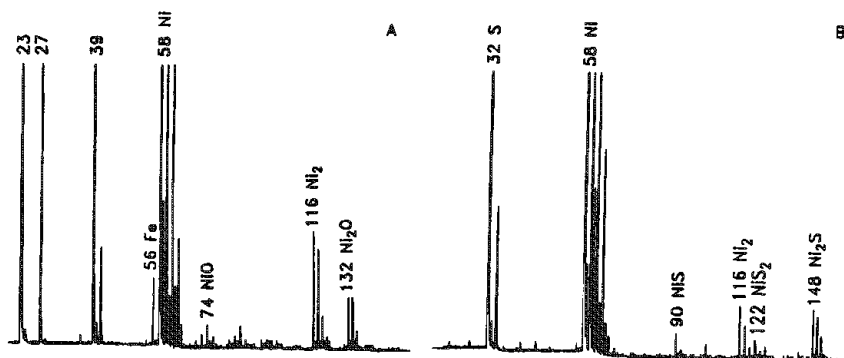


FIG. 2.--Flow chart of procedure by which SEM/EDS and LAMMS data are correlated.

FIG. 3.--Representative positive ion mass spectra obtained from FBR particles: (A) resembles that of nickel oxide or nickel sulfate sample, (B) resembles that of nickel sulfide or nickel subsulfide reference sample.



ture of NiS and Ni<sub>3</sub>S<sub>2</sub>. Particle classifications are listed with the corresponding number of particles assigned to each class in Table 1.

LAMMS has been shown to differentiate among particles of various nickel reference samples.<sup>1</sup> However, environmental samples, such as these FBR particles, complicate the LAMMS spectra making nickel compound identification difficult by LAMMS alone. LAMMS, in this study, was able to distinguish between two distinct particle types: NiO/NiSO<sub>4</sub>·7H<sub>2</sub>O and NiS/Ni<sub>3</sub>S<sub>2</sub>. Using the complementary techniques of LAMMS and SEM/EDS, however, we have shown that molecular structures may be assigned to four nickel-containing compounds (NiO, NiSO<sub>4</sub>·7H<sub>2</sub>O, NiS, and Ni<sub>3</sub>S<sub>2</sub>) in the FBR particles. With proposed corrections for particle size effects, it may be possible to remove some of the ambiguity surrounding the identification of the particles currently classified as mixtures of nickel compounds. Direct supporting evidence for intraparticle heterogeneity has been obtained recently by cross-sectional imaging studies involving techniques including light microscopy and SEM/EDS.<sup>13</sup> Many of the x-ray spectra obtained from FBR single particles probably reflect both the effects of particle size and the actual presence of mixtures of nickel species.

#### Reference

1. I. H. Musselman, R. W. Linton, and D. S. Simons, "The use of laser microprobe mass analysis for nickel speciation in individual particles of micrometer size," *Microbeam Analysis--1985*, 337-341.
2. E. B. Steel, D. S. Simons, J. A. Small, and D. E. Newbury, "Analysis of submicrometer particles by sequential AEM and LAMMA," *Microbeam Analysis--1984*, 27-29.
3. E. Michiels and R. Gijbels, "Fingerprint spectra in laser microprobe mass analysis of titanium oxides of different stoichiometry," *Spectrochimica Acta* 38B: 1347-1354, 1983.
4. F. J. Bruynseels and R. E. Van Grieken, "Laser microprobe mass spectrometric identification of sulfur species in single micrometer-size particles," *Anal. Chem.* 56: 871-873, 1984.
5. J. Marien and E. De Pauw, "On the identification of the sulfur oxidation state in inorganic sodium sulfoxy salts by laser microprobe mass analysis and secondary ion mass spectrometry," *Anal. Chem.* 57: 361-362, 1985.
6. F. J. Bruynseels and R. E. Van Grieken, "Molecular ion distributions in laser microprobe mass spectrometry of calcium oxide and calcium salts," *Spectrochimica Acta* 38B: 853-858, 1983.
7. H. Vogt, H. J. Heinen, S. Meier, and R. Wechsung, "LAMMA 500 principle and technical description of the instrument," *Fresenius Z. Anal. Chem.* 308: 195-200, 1981.
8. E. Denoyer, R. Van Grieken, F. Adams, and D. F. S. Natusch, "Laser microprobe mass spectrometry: 1. Basic principles and performance characteristics," *Anal. Chem.* 26A-32A, 1982.
9. R. Kaufmann and P. Wieser, "Laser microprobe mass analysis in particle analysis,"

in J. Beddow, Ed., *Particle Characterization in Technology*, Boca Raton, Fla.: CBC Press, 1984, 21-57.

10. T. Mauney and F. Adams, "Ion kinetic energy measurements on laser induced plasmas in laser microprobe mass analysis (LAMMA): Part 1. Methodology," *Int. J. Mass Spectrom. Ion Proc.* 59: 103-119, 1984.

11. E. Michiels, T. Mauney, F. Adams, and R. Gijbels, "Ion kinetic energy measurements on laser induced plasmas in laser microprobe mass analysis (LAMMA): Part 2. Titanium dioxide," *Int. J. Mass Spectrom. Ion Proc.* 61: 231-246, 1984.

12. E. Michiels, M. De Wolf, and R. Gijbels, "Ion discrimination effects in the laser microprobe mass analyzer," *SEM/1985 III*, 947-958.

13. J. Mullis, J. Rickman, and R. Linton (in preparation).

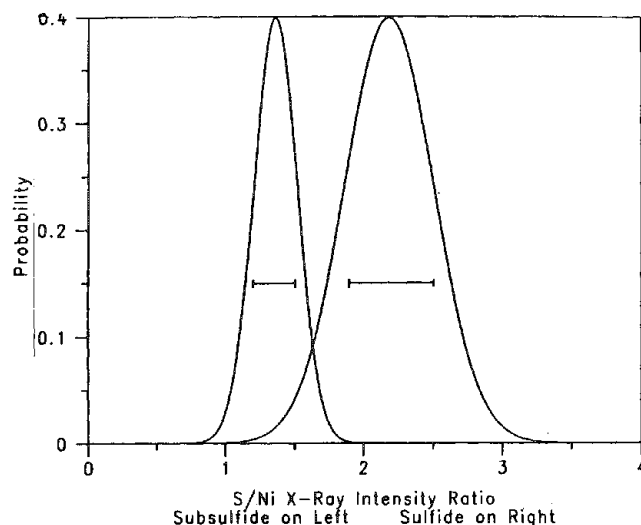


FIG. 4.--S/Ni normal distributions of nickel subsulfide (left) and nickel sulfide (right) reference samples obtained from 49 and 40 particles, respectively. Markers indicate  $\pm 1\sigma$  confidence limits.

TABLE 1.--Nickel refinery particle classifications.

1. Nickel oxide	17
2. Nickel sulfate	9
3. Nickel sulfate or mixture including nickel sulfate and nickel oxide	17
4. Nickel subsulfide	6
5. Nickel sulfide	4
6. Nickel sulfide, nickel subsulfide, or mixture of the two	4
	<hr/> 57
7. Unable to speciate, no LAMMS data containing nickel cluster ions	+115
	Total = 172

NOTE: Particle classes 1-6 are from correlative LAMMS and SEM/EDS data.

## INORGANIC CLUSTER ION FORMATION IN THE LASER MICROPROBE

R. W. Linton, I. H. Musselman, Frank Bruynseels, and D. S. Simons

One of the analytically important features of laser microprobe mass spectrometry (LAMMS) is the observation of abundant cluster ion signals in a unique "fingerprint" pattern that may be characteristic of compound structure and stoichiometry. Thus, the spectra may constitute a valuable empirical approach to the determination of chemical species within microvolumes of solid materials. One illustration is our LAMMS study of various nickel compounds present in environmental particulate matter.<sup>1-3</sup> A much more difficult issue is the establishment of mechanisms by which the above cluster ion patterns are produced, including the influences of instrumental parameters.

It is generally impossible to predict *a priori* the nature of cluster ions generated from various compounds. It is complicated by the sensitivity of the clusters to various sample characteristics (e.g., particle size, shape, orientation) and to various instrumental parameters (e.g., laser energy, laser power density, ion kinetic energy discrimination, transient digitizer dynamic range). Cluster ion formation reflects not only the direct emission of charged species during pulsed laser beam irradiation that mirror the molecular structure of the solid, but also recombination reactions of ionized and neutral species in the laser-induced plasma. The latter process obviously complicates the relationship between the cluster ions detected and the original molecular characteristics of the sample.

As an initial demonstration that recombination of cluster ions from nickel compounds, micrometer-size NiS particles were mounted on an isotopically enriched <sup>34</sup>S film. The transmission geometry of the LAMMS instrumentation used in this study requires laser penetration

through the sample thickness and ion extraction from the sample side facing the extraction lens of the time-of-flight (TOF) mass spectrometer. This geometry insures that both the NiS particles and the <sup>34</sup>S film underneath them are included in the analytical volume vaporized by a single laser pulse. Substantial recombination, as reflected in <sup>34</sup>S enrichments in the various Ni<sub>x</sub>S<sub>y</sub> cluster ions, was observed.<sup>4</sup>

Although the above experimental system provides unequivocal evidence of recombination, it is limited by the effects of variations in particle physical characteristics (size, shape) on spectral reproducibility, and by the fact that all clusters may reflect contributions by both direct and recombination formation mechanisms. To circumvent these complications, a multilayer "sandwich" film sample preparation was developed (Fig. 1). The Au film between the Ni and S layers assures that any Ni<sub>x</sub>S<sub>y</sub> ions observed must form by mechanisms involving recombination, i.e., no bonding of Ni and S is possible in the solid state. However, for other ions observed, such as Ni<sub>x</sub> or S<sub>y</sub>, clusters may form by direct emission or by fragmentation of larger metastable species, as well as by recombination reactions. The sandwich films are sufficiently uniform to provide the necessary spectral reproducibility for a systematic evaluation of the effects of LAMMS instrumental parameters on cluster ion formation. Preliminary studies of positive ion spectra as a function of sample geometry, laser power density, and ion extraction lens potential are described below. A more detailed investigation, including negative ion spectra and ion kinetic energy distributions derived from the energy cutoff property of the ion reflector, is the subject of a subsequent study.<sup>5</sup>

Author Linton is at the University of North Carolina, Chapel Hill, NC 27514; some of his work was done at the University of Antwerp in 1986 under a grant from the Belgian National Science Foundation. Author Musselman is a UNC graduate student, currently at the National Bureau of Standards. Author Bruynseels is at the University of Antwerp Department of Chemistry, B-2610 Wilrijk, Belgium. Author Simons is at the NBS Center for Analytical Chemistry, Gaithersburg, MD 20899. Certain commercial equipment, instruments, or materials are identified in this paper. Such identification does not imply recommendation or endorsement by NBS nor does it imply that the materials or equipment are necessarily the best available for the purpose. Support of this research under U.S. Environmental Protection Agency cooperative agreement CR-8129-8-01-1 with UNC is gratefully acknowledged. Although funded in part by EPA, the research has not been subjected to EPA review and so does not necessarily reflect EPA's view; no official endorsement should be inferred.

### Experimental

**Sample Preparation.** High-purity elemental S or Ni powders were secured by double-stick tape on a stainless-steel mount. The powders were sputtered with Ar in a Gatan Dual Ion Mill (2.5 kV, 0.25 mA gun discharge current, 40° angle of incidence). Sputtered material was deposited as a film on Formvar-coated transmission electron microscope (TEM) grids. Deposition times of 1-1.5 h for each layer were optimal. Shorter times (0.5 h) created films of inadequate thickness to produce detectable cluster ions; longer times (> 2 h) produced films that were too difficult to perforate with the maximum laser power density available. Contaminants (Fe, Cr) were observed in the spectra of the films, probably originating from the stainless-steel mount. However, these species did not interfere significantly with the detection of the cluster ions of interest. Thin Au films between the Ni and S layers were deposited for 4 min by means of a

Technics Hummer Sputter Coater and a Au target (7 or 8 kV, 10 mA discharge current). Some Al contamination was observed in the Au film, probably originating from the target holder in the coater. The Al impurity did not pose problems in the study of the  $\text{Ni}_x\text{S}_y$  clusters.

Two sequences for film depositions were used (Fig. 1). LAMMS data were obtained after each step of this multilayer deposition scheme, which assured that samples were fabricated according to design and that signals corresponding to the  $\text{Ni}_x\text{S}_y$  cluster ions of interest appeared only after the deposition of both the Ni and S layers. Initial LAMMS experiments indicated problems in the stability of the films, specifically when the S layer was deposited on the Formvar film directly adjacent to TEM grids made of Cu (Fig. 1a). Mass spectra taken over several weeks were increasingly dominated by Cu and  $\text{Cu}_x\text{S}_y$  clusters, rather than the intended  $\text{Ni}_x\text{S}_y$  species. These artifacts were eliminated by use of Au TEM grids and by storage of the sandwich films under Ar.

**LAMMS Instrumentation.** The LAMMS measurements were obtained with a Laser Microprobe Mass Analyzer, LAMMA-500 (Leybold Heraeus). A frequency-quadrupled Nd-YAG laser ( $\lambda = 266$  nm,  $\tau = 15$  ns, maximum power density ca  $10^{10}$  W/cm<sup>2</sup>) was focused on the specimen with the aid of a He-Ne pilot laser. Studies of cluster ion intensity as a function of laser power density were performed by incremental shifts in the axial position of the 32 $\times$  objective lens, which focuses the laser beam according to procedures described previously by Wurster et al.<sup>6</sup> Spectra were taken as a function of increasing defocus; i.e., the laser was focused at increasingly greater distances away from the time-of-flight (TOF) mass spectrometer. Corresponding objective lens shifts from the focus condition are described as +5, +10, and +20  $\mu\text{m}$ . Negative shifts (<0  $\mu\text{m}$ ) or shifts >25  $\mu\text{m}$  produced minimal  $\text{Ni}_x\text{S}_y$  cluster ion signals in most instances. The size (diameter and area) of the laser-induced perforations was measured subsequently by a scanning electron microscope (ISI Model DS-130) and a digital imaging system (Tracor Northern Model 5500).

The ions generated by the laser pulse in the LAMMA-500 are extracted at 180° relative to the incident laser (transmission geometry) and analyzed in a TOF mass spectrometer. For the studies described in the preceding paragraph, the ion focusing lens potential was optimized for maximum  $\text{Ni}_x\text{S}_y$  cluster ion intensities at approximately -1125 V. Significantly different intensity dependences of atomic vs cluster ions are generally observed as a function of ion lens potential. This result is attributed to chromatic aberrations, which lead to different transmissions of various ions having different kinetic-energy distributions.<sup>7</sup> Studies of cluster ion intensity as a function of ion lens potential were performed on the sandwich films over a total range of -750 to -1350 V in a random sequence of 25-50V increments.

For all the experiments described above, a average of 10 spectra (each obtained from a fresh surface) was used for each distinct setting of laser focus (objective lens shift) and

ion lens potential. This procedure helped to reduce the effects of variations in laser energy (typically 15% S.D.) or focus from shot to shot. A LeCroy transient digitizer (Model TR 8818-MM8103/8 coupled to an IBM PC-AT Computer) was used to collect and process the spectra as described by Van Espen et al.<sup>8</sup> The integrated peak areas for the atomic Ni and  $\text{Ni}_x\text{S}_y$  ion clusters of interest covered a range of about 100:1 for any given setting of laser focus or ion lens potential. For all conditions, the most intense Ni-containing ion used for quantitative purposes was  $^{60}\text{Ni}^+$ . Comparison of its intensity to the much less abundant  $^{62}\text{Ni}^+$  isotope was used to confirm that detector saturation or other nonlinear processes did not substantially affect ion signals of interest.

## Results and Discussion

**Effects of Sample Geometry.** Examples of qualitative spectra for the sandwich films are shown in Fig. 2. Figures 2(a) and 2(b) correspond to the sample geometries shown in Figs. 1(a) and 1(b), respectively. In both cases, sample orientation was such that the Formvar-coated grid was facing toward the ion extraction lens, and thus away from the direction of laser incidence. Clearly, the orientation with the S layer closer to the ion extraction lens provides better  $\text{Ni}_x\text{S}_y$  cluster ion signals (Figs. 1a and 2a). Orientation of sample A in the LAMMA sample holder such that the Ni layer faced the ion lens produced spectra comparable to that of Fig. 2(b). Similarly, orientation of sample B such that the S layer faced the ion lens produced spectra more comparable to that of Fig. 2(a), although the absolute intensities of atomic Ni and  $\text{Ni}_x\text{S}_y$  clusters were usually not as high. This finding probably reflects the fact that the laser pulse must dissipate some energy in penetrating the Formvar film before reaching the sandwich structure. Hence, in all subsequent studies the sample A geometry was used with the Formvar layer closest to the ion lens of the mass spectrometer.

**Effects of Laser Power Density.** Data for the studies of selected ion intensities and perforation sizes as a function of objective lens shift are summarized in Table 1. Although not shown, values for a 0 $\mu\text{m}$  shift were similar to the +5 $\mu\text{m}$  position. Shifts outside of the 0 to +20 $\mu\text{m}$  range produced  $\text{Ni}_x\text{S}_y$  cluster intensities below detection limits in most cases.

The ratio of intensity to perforation volume is a rough measure of the relative ionization probability (IP). The signal intensity is a function both of the laser power density and the elemental ionization potential. The atomic ion signals ( $\text{Ni}^+$  or  $\text{Au}^+$ ) exhibit a decrease in intensity with increasing laser defocusing (decreasing laser power density). For the  $^{60}\text{Ni}^+$  signal, the ratio of IP at the +5  $\mu\text{m}$  vs +20  $\mu\text{m}$  objective lens shift is about 21:1. For  $^{197}\text{Au}^+$ , the corresponding IP ratio is about 110:1. Atomic S, because of its very high ionization potential (10.36 eV), was not present reproducibly in the positive ion spectra and could not be compared to other atomic ion data.

As expected, the cluster ion intensities are highest at a more defocused condition

(+10 $\mu$ m shift) reflecting lower laser power densities more typical of a laser desorption mode. However, some of the recombination cluster ions ( $\text{Ni}_x\text{S}_y$ ) are similar in abundance to intensities of the clusters originating from only one of the films ( $^{116}\text{Ni}_2^+$  or  $^{64}\text{S}_2^+$ ). The dimer ions also may be formed by recombination in addition to direct emission from the solid via laser desorption. The above results are comparable to those observed by Wurster et al. for Cu/Ag sandwich films.<sup>6</sup>

Figure 3 illustrates the trends in ion intensities as a function of laser focus. The most intense signal for each ion among the three focus conditions is normalized to 100 to facilitate a direct comparison of the various ions. All the  $\text{Ni}_x\text{S}_y$  clusters show the same qualitative trend with a peak in intensity at the +10 $\mu$ m objective shift. The exception is  $^{90}\text{NiS}^+$ , which peaks at the most focused condition (+5 $\mu$ m shift) and shows a decrease with defocusing similar to those of the atomic  $^{60}\text{Ni}^+$  and  $^{197}\text{Au}^+$  ions.

Based on the above results involving both sample geometry and laser focus, it is possible to speculate on some of the ion recombination mechanisms responsible for  $\text{Ni}_x\text{S}_y$  cluster ion formation. One likely contributor is gas phase ion molecule reactions involving  $\text{Ni}^+$  or  $\text{Ni}_2^+$  cationization of neutral  $\text{S}_x$  clusters ( $\text{S}, \text{S}_2, \text{S}_3$ ) produced from the S film. A laser power density that is too high in the S layer may decrease the abundance of  $\text{S}_x$  neutral clusters, produced by either laser desorption or recombination, that are available for Ni cationization reactions. Correspondingly, a somewhat higher laser power density may be desirable in the Ni layer to assure substantial production of Ni ions ( $\text{Ni}^+, \text{Ni}_2^+$ ) available for subsequent reaction with  $\text{S}_x$  clusters. Indeed, the preferred sample orientation is such that the full laser energy is available only to the Ni film. Furthermore, the laser energy used was within about a factor of 3 of the minimum required for perforation of the sample. Laser power densities close to the threshold of perforation have been known to promote preferential ion extraction from the sample side facing the ion extraction lens.<sup>6,9</sup> Thus, the LAMMA spectra also would be expected to show a preferential contribution from S-containing ions since the S film is closer to the ion lens.

*Effects of Ion Extraction Lens Potential.* Ion discrimination effects in the LAMMA-500 have been described previously.<sup>7</sup> The discrimination effects of the einzel lens used for ion focusing can be attributed to chromatic aberration if the different types of ions have different kinetic energy distributions. The kinetic energy distributions of positive atomic or diatomic ions tend to be broader and peak at less negative ion lens potentials relative to more complex clusters, as observed previously in LAMMA studies of a  $\text{TiO}_2$  film.<sup>7</sup> Lower-energy ions are transmitted in the range between about -1350 and -1050 V; higher-energy ions are detected between -1050 and -750 V.

Results from our Ni/Au/S sandwich films are very consistent with the results described previously for  $\text{TiO}_2$ .<sup>7</sup> Plots of ion intensity

vs lens potential are given in Fig. 4. Atomic ions ( $\text{Ni}^+, \text{Au}^+$ ) have a broad distribution with a peak at -1075 V. This result is consistent with atomic ion formation at high thermal energies followed by transfer of some energy to other species in the plasma. Increasingly complex cluster ions ( $\text{Ni}_x\text{S}_y$ ) have progressively narrower energy distributions. Peak intensities also occur at lens potentials about 25 to 50 V more negative than for the atomic ions. This is the likely result of incomplete ion acceleration reflecting the locus of ion formation.<sup>10,11</sup> The  $\text{Ni}_x\text{S}_y$  clusters form by recombination after some expansion of the vaporized plasma. For example, a negative shift in median energy of 25 eV relative to atomic ions would imply formation of the clusters after a plasma vapor expansion of about 50  $\mu$ m following the laser pulse.<sup>7</sup> (This value is based on an estimated field strength of 0.5 V/ $\mu$ m in the ion source.) Other experiments consider the ion kinetic energy distributions in more detail using the energy cutoff property of the ion reflector.<sup>5</sup>

### Conclusions

The results for the Ni/Au/S sandwich films demonstrate that the observation of cluster ions in the LAMMA spectrum is a sensitive function of (1) sample geometry and orientation, (2) laser power density, and (3) ion focusing lens potential. With appropriate selection of these parameters, extensive ion recombination is observed involving  $\text{Ni}_x\text{S}_y$  clusters. The kinetic energy distributions of these cluster ions are narrower and peak at lower energy in comparison to atomic ions. All these factors complicate the relationship between the laser microprobe spectrum and the inherent molecular structure of the solid sample.

### References

1. I. H. Musselman, R. W. Linton, and D. S. Simons, "The use of laser microprobe mass analysis for nickel speciation in individual particles of micrometer size," *Microbeam Analysis--1985*, 337-341.
2. I. H. Musselman, J. T. Rickman, and R. W. Linton, "Fingerprinting of chemical species in microparticles: Correlative laser and electron microprobe studies," this volume.
3. I. H. Musselman, J. T. Rickman, R. W. Linton, "Correlation of microprobe analysis data for individual particle speciation: Nickel compounds from stationary sources," *Environ. Sci. Technol.* (submitted).
4. I. H. Musselman, R. W. Linton, and D. S. Simons, "Cluster ion formation under laser bombardment: Studies of recombination using isotope labeling," *Anal. Chem.* (submitted).
5. F. Bruynseels, T. Mauney, I. H. Musselman, and R. W. Linton (in preparation).
6. R. Wurster, U. Haas, and P. Wieser, "Electron microscopical investigations of laser irradiated foils and particles," *Fresenius Z. anal. Chem.* 308: 206-211, 1981.
7. E. Michiels, M. DeWolf, and R. Gijbels, "Ion discrimination effects in the laser microprobe mass analyzer," *SEM/1985 III*, 947-958.

8. P. Van Espen, L. Van Vaeck, and F. Adams, "Transient recorders: A key element in laser microprobe mass spectrometer instrumentation," *Proc. 3d Intern. Laser Microprobe Mass Spectrometry Workshop*, 1986, 195-197.

9. F. Bruynseels and R. Van Grieken, "Recombination reactions and geometry effects in laser microprobe mass analysis studied with  $^{12}\text{C}/^{13}\text{C}$  bilayers," *Intern. J. Mass Spectrom. Ion Proc.* 74: 161-177, 1986.

10. T. Mauney and F. Adams, "Ion kinetic energy measurements on laser-induced plasmas in laser microprobe mass analysis (LAMMA): Part 1. Methodology," *Intern. J. Mass Spectrom. Ion Proc.*, 59: 103-119, 1984.

11. T. Mauney and F. Adams, "Interpretation of ion kinetic energy distributions in laser microprobe mass analysis," *Microbeam Analysis --1984*, 19-22.

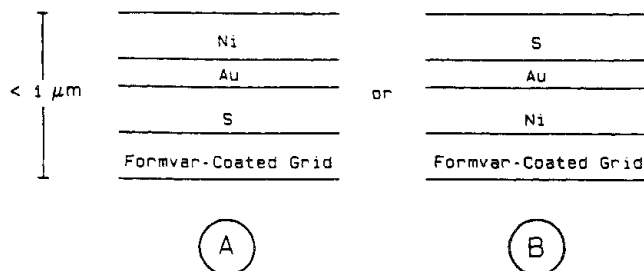


FIG. 1.--Ni/Au/S sandwich film samples.

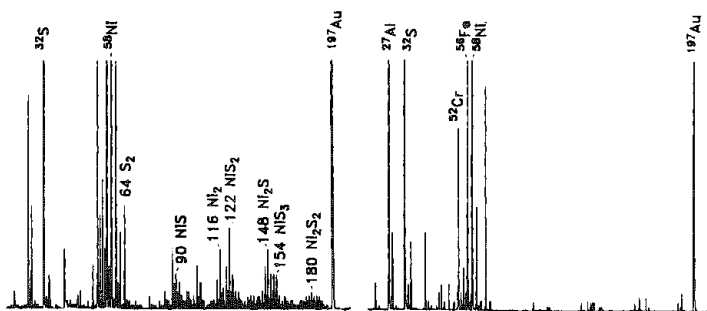


FIG. 2.--LAMMA spectra of sandwich films, with Formvar-coated grid facing ion extraction lens. Left, as in Fig. 1A; right, as in Fig. 1B.

TABLE 1.--Mean integral ion intensities (arbitrary units) as function of laser power density varied by axial shifts in the objective lens position.

Ion	Objective Lens Shift ( $\mu\text{m}$ )		
	+5	+10	+20
$^{60}\text{Ni}^+$	934	758	310
$^{62}\text{Ni}^+$	139	116	51
$^{90}\text{NiS}^+$	79	58	<10
$^{116}\text{Ni}_2^+$	113	217	100
$^{122}\text{NiS}_2^+$	85	137	49
$^{148}\text{Ni}_2\text{S}^+$	80	186	108
$^{154}\text{NiS}_3^+$	<10	41	<10
$^{180}\text{Ni}_2\text{S}_2^+$	<10	26	<10
$^{197}\text{Au}^+$	1441	1265	91

**Perforation Sizes**

Avg. Radius ( $\mu\text{m}$ )	1.35 (.25) <sup>a</sup>	2.04 (.77) <sup>a</sup>	3.58 (.95) <sup>a</sup>
Avg. Area ( $\mu\text{m}^2$ )	6.33 (2.43) <sup>a</sup>	15.3 (10.3) <sup>a</sup>	44.8 (21.7) <sup>a</sup>

<sup>a</sup>Relative standard deviation for -10 spectra shown in parentheses.

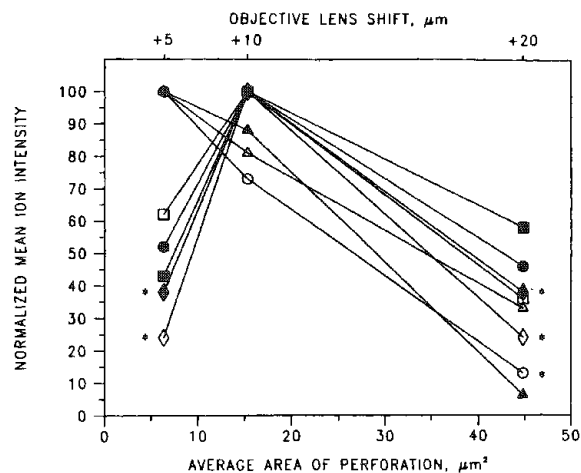


FIG. 3.--Normalized mean ion intensities as function of objective lens shifts and corresponding areas of perforation. Asterisks indicate detection limit values. (Ion signals were not observed.)

$\triangle = ^{60}\text{Ni}^+$  1 atom  
 $\blacktriangle = ^{197}\text{Au}^+$  1 atom  
 $\circ = ^{90}\text{NiS}^+$  2 atom  
 $\bullet = ^{116}\text{Ni}_2^+$  2 atom  
 $\square = ^{122}\text{NiS}_2^+$  3 atom  
 $\blacksquare = ^{148}\text{Ni}_2\text{S}^+$  3 atom  
 $\diamond = ^{154}\text{NiS}_3^+$  4 atom  
 $\blacklozenge = ^{180}\text{Ni}_2\text{S}_2^+$  4 atom

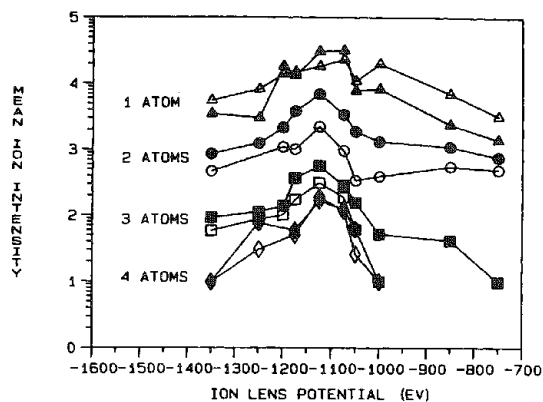


FIG. 4.--Mean ion intensities (arbitrary units) as function of ion lens potential. Ion identities are as in Fig. 3. Detection limits for ions correspond to mean ion intensity of  $\sim 1$  on log scale.



## OBSERVATIONS DERIVED FROM THE APPLICATION OF PRINCIPAL-COMPONENT ANALYSIS TO LASER MICROPROBE MASS SPECTROMETRY

R. A. Fletcher and L. A. Currie

Laser Microprobe Mass Spectrometry (LAMMS) provides a unique means of obtaining mass spectral information from nonvolatile organic compounds. With such information one has the potential to infer the structure and identification of compounds, and origins of micro-particles. Because of the relatively low mass resolution of the spectrometer, fragment ion and hence chemical identification is often difficult. We are therefore exploring a range of powerful multivariate and pattern-recognition approaches such as principal-component analysis (PCA) to aid in LAMMS experiment design and spectrum interpretation. A new sample-mounting technique is also presented.

Pattern recognition has already been employed to analyze pyrolysis mass spectra,<sup>1,2</sup> and some work has been done to implement a fingerprinting procedure for LAMMS.<sup>3</sup> In our work, a laser microprobe mass spectrometer (LAMMA 500)<sup>4</sup> is the source of numerous mass spectra to which PCA has been applied. The most important step in our data reduction is a filtering process or feature selection (Fig. 1) to distinguish important or relevant information. For PCA, the peak areas of each computer-archived spectrum are first found and then normalized by use of a common peak area selected on the basis of its chemical significance and measurement reliability. Normalization is desirable to focus attention on differences in patterns. The normalized areas are then filtered by computer (with human supervision and intervention) for features that contain the most useful pattern recognition information. "Filtering" in this context refers to the automatic selection of masses (peaks) exhibiting sufficient "characteristicity,"<sup>1</sup> adequate discriminating power based on inter- (in contrast to intra-) component variance. In the expression,  $m_1$  and  $m_2$  refer to means of corresponding features (for set 1 and 2; i.e., compound 1 or 2) and  $SD_1$  and  $SD_2$  are their standard deviations. A data matrix composed of the more relevant features (peaks) is then used to extract the eigenvectors that best describe the data. The first few eigenvectors (principal components) typically contain most of the information and are conveniently displayed as a PCA map.

When the data are plotted in terms of principal components, like qualities appear in the form of clusters in principal-component space. If the features are quite similar, the clusters overlap. When significant differences appear, the clusters are separated in principal-component space. An interesting property of PCA as used here (nonscaled) is that the

diameter of the clusters indicates the level of precision in the data. Malinowski<sup>5</sup> provides an extensive explanation of PCA and target factor analysis.

We have analyzed by LAMMS/PCA two closely related polymeric materials being employed in a biotechnology study at NBS, poly(4-vinylpyridine) and poly(2-vinylpyridine). In Fig. 2 the two materials, though very much alike structurally, have been resolved through PCA of their fragment ion patterns. The materials are in the form of microbeads and are ablated by the laser microprobe by grazing or striking the edge of the bead with the radiation. This grazing technique may diminish reproducibility of the spectra due to the variable amount of particle irradiance and to the way the radiation is coupled into the particle. An interesting observation provided by the plot of the first two principal components is that there is a large variance in the P2VP spectra that does not appear in the P4VP data. Since both are in the form of polymer beads, we would expect similar cluster diameters (hence variances). We are currently seeking an explanation. Most important, this example shows that a *single* spectrum (if properly selected in the manner mentioned above) does contain enough information to permit PCA. For certain applications, including those discussed below, only limited numbers of spectra can be obtained.

Some of the other areas to which we apply the multivariate techniques are qualitative (ID) plus semiquantitative analysis of multi-component mixtures, and separation or recognition of airborne particulate pollutant sources. In multicomponent analysis, the simplest case is a two-component (hypothetical) mixture of compound A and B (Fig. 3). Ideally, in principal-component space, one would expect the 2/3 A to 1/3 B mixture clusters ( $A_2B$ ) and 1/3 A to 2/3 B mixture ( $AB_2$ ) to relate to the pure component clusters A and B, as shown in the figure. This technique is well known in target-factor analysis.<sup>5</sup>

As an experimental multicomponent test case, we studied the two-component mixture of the amino acids tyrosine (MW 181) and phenylalanine (MW 165). These two compounds were chosen because of the considerable previously reported work done on them with LAMMS.<sup>6</sup> Figure 4(a) shows the results for single-particle spectra in a plot of PC1 vs PC2, with the pure phenylalanine (P) cluster at the right and the pure tyrosine (T) cluster at the far left. The mixtures fall in between, but not in the expected order. Figure 4(b) shows the cluster orientation for summed spectra. For each point, 6 to 10 spectra were summed together for the given mixture or compound. Data reduction was performed on the summed spectra instead of the single spectra in Fig. 4(a). As can be seen, the summing process generally

The authors are at the Center for Analytical Chemistry, National Bureau of Standards, Gaithersburg, MD 20899. They thank A. Fatiadi for the amino acids and G. Mulholland for the carbon soot.

reduces the variance within a cluster and thus increases the significance of the separation between clusters. The trends in the mixed-component clusters are essentially the same. The mixed-component clusters, by their proximity to P, show that the features of phenylalanine tend to dominate those of tyrosine. This early result is very promising in that it does confirm the possibility of PCA in LAMMS of two component mixtures. The unexpected orientations of the clusters is intriguing and is currently under investigation.

For the goal of individual particle analysis, we have realized the ability to do PCA on single spectra, as is necessary for particulate work by LAMMS. To establish some background information concerning carbon particles, we have obtained sets of mass spectra for carbon particulate soot generated from controlled burning of four different materials. The carbon particles were caught on high-purity quartz fiber filters that had been heat treated to drive off pre-existing organic compounds. The quartz fibers provide an excellent support matrix material for microprobe analysis in the LAMMA 500 because entire fibers containing the particles of interest can be easily transferred to a transmission electron microscope mounting grid. This procedure minimizes contamination of the particles, since they never leave the filter fiber that collected them. Also, the fibers are long enough to lay unsupported across grid squares and thus do not come in contact with any other surface. The quartz fibers are of high purity and low in carbon contamination due to the heat treatment. Lastly, quartz is optically transparent to the laser radiation at its normal operating wavelength, 266 nm. For these reasons, the use of quartz fibers is an ideal

method for mounting of particles, especially carbon-containing particles.

In summary, PCA offers a way of uncovering hidden similarities in mass spectral data from the laser microprobe. We have demonstrated the utility for analysis of single mass spectra, useful for particulate studies; and we have reported some preliminary results from a study of binary mixtures. We are currently analyzing the carbon soot data and working on extending the effort to collect ambient airborne carbon particulates. Classification of airborne carbon particulates by PCA is useful for source identification of the pollutants.

#### References

1. W. Eshuis, P. G. Kistemaker, and H. L. C. Meuzelarr, in C. E. R. Jones and C. A. Cramers, Eds., *Analytical Pyrolysis*, Amsterdam: Elsevier, 1977, 151-166.
2. K. J. Voorhees, S. M. Kunen, S. L. Durfee, L. A. Currie, and G. A. Klouda, *Anal. Chem.* 53: 463, 1981.
3. U. Seydel and B. Lindner, *Proc. LAMMA Workshop at Forschungsinstitute Borstel--1983*, 1984, p. 111.
4. Certain commercial equipment, instruments, or materials are identified in this paper to specify adequately the experimental procedures. Such identification does not imply recommendation or endorsement by the National Bureau of Standards, nor does it imply that the materials or equipment identified are necessarily the best available for the purpose.
5. E. Malinowski, *Factor Analysis in Chemistry*, New York: Wiley, 1980.
6. M. Karas, D. Bachmann, and F. Hillenkamp, *Anal. Chem.* 57: 2935, 1985.

#### DATA REDUCTION

Raw Data ----> Normalize----> Filter----> PCA ----> PC Plots

Integrated Mass Peaks	To Selected Mass Peak	ml+m2 ----- (SD1 + SD2)	Principal Component Analysis
	Not Normalized		
	to Sum		

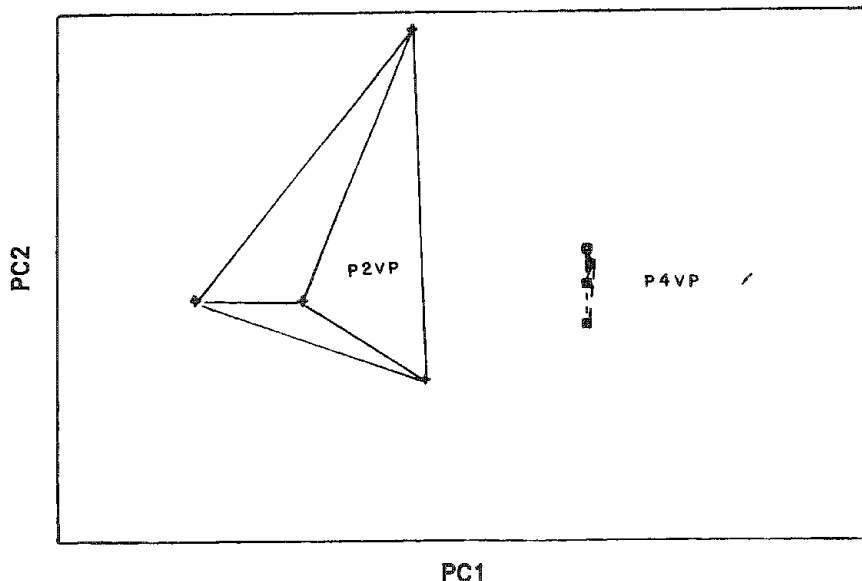


FIG. 1.--Flow chart of data-reduction process. Left to right, raw data (peak areas) are normalized by selected mass feature, filtered by examination of characteristicity<sup>1</sup> for each feature, then analyzed by PCA following Malinowski.<sup>5</sup>

FIG. 2.--Eigenvector [PCA] plot of poly(4-vinylpyridine) (P4VP) and poly(2-vinylpyridine) (P2VP). Each point represents individual particle (bead).

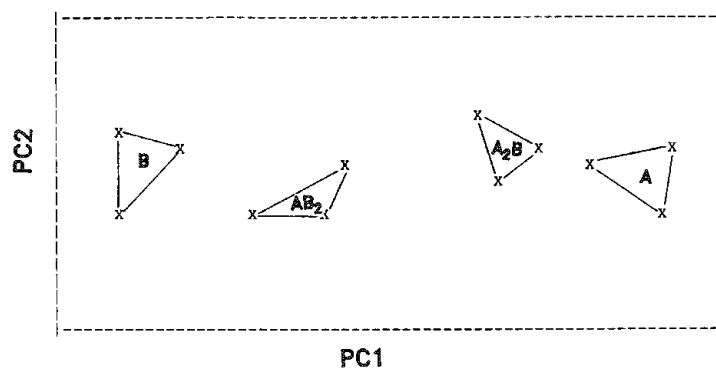


FIG. 3.--Hypothetical of two-component plotted in PC space.

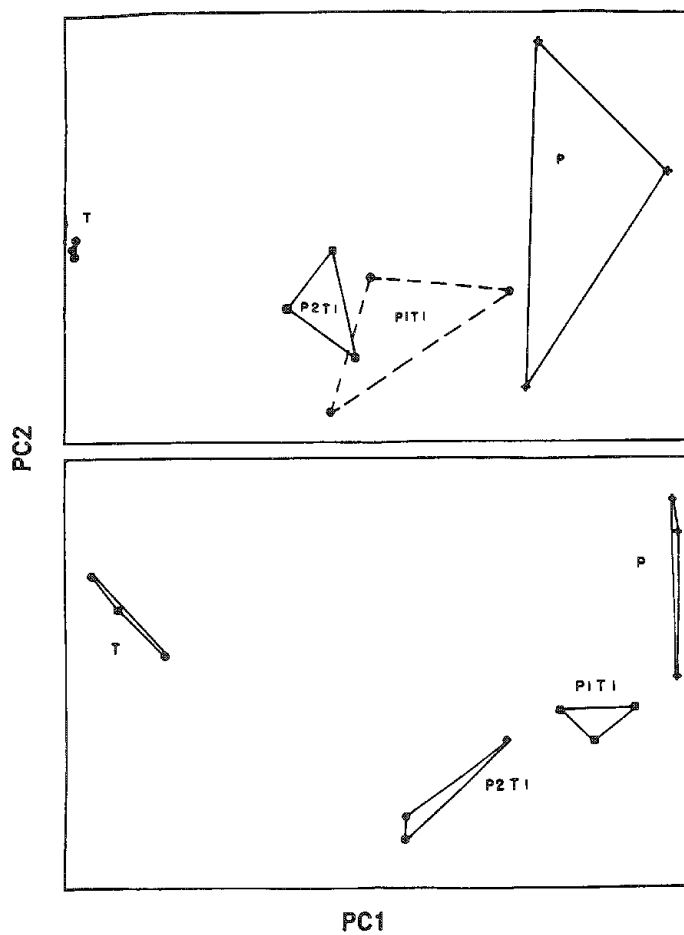


FIG. 4.--(a) PC plot of pure and mixed tyrosine (T) and phenylalanine (P); data reduced from single-particle spectra. (b) Same chemical system with 6 to 10 single spectra summed.



## Author Index

- Adar, F., 141, 165  
 Anderson, D. G., 264  
 Archibald, D. D., 123  
 Argentieri, G. J., 271  
 Artaxo, P., 343, 356  
 Atkin, S. C., 173  
 Back, J. M., 329  
 Baran, K. P., 261  
 Barbillat, J., 210  
 Bauch, J., 359  
 Beauchaine, J., 185, 187  
 Bentley, R. D., 321  
 Bhandari, R., 138  
 Blake, D. F., 335  
 Bowden, M., 131  
 Brazal, S. D., 264  
 Brémard, C., 139  
 Bright, D., 25, 40, 290  
 Briscoe, N. A., 233  
 Brodecki, R. D., 237, 250  
 Brownlee, D., 211  
 Bruynseels, F., 343, 356, 365  
 Bunch, T. E., 211, 335  
 Burgi, D. S., 155  
 Cai, M. Z., 197  
 Calvo, F. A., 349  
 Carpenter, P. K., 29  
 Chambers, W. F., 15  
 Chan, H. W., 230  
 Chang, S., 211  
 Chang, S.-L., 213  
 Chao, E. C. T., 329  
 Chen, J. R., 329  
 Chen, Y.-L., 213  
 Christenson, D. A., 301  
 Chughtai, A. R., 177  
 Clegg, W. J., 233  
 Coates, J. P., 180  
 Cook, B. W., 166  
 Condron, R. J., 269  
 Cornard, J. P., 210  
 Crooker, A. R., 261  
 Curie, L. A., 369  
 Delhay, M., 119, 163  
 DeNatale, J. D., 241, 244, 247  
 Dhamelincourt, M. C., 167  
 Dhamelincourt, P., 119, 139, 167, 210  
 Donley, M. S., 125  
 Dovichi, N. J., 155  
 Einerhand, A., 359  
 Elliott, N. E., 239  
 Eschweiler, H., 359  
 Etz, E. S., 158  
 Exarhos, G. J., 125, 147  
 Fain, G., 359  
 Fauchet, P. M., 144  
 Fitzgerald, A. G., 253  
 Fletcher, R. A., 369  
 Flynn, J. E., 227  
 Fried, M., 192  
 Friedrich, D. M., 147  
 Friel, J. J., 325  
 Fuller, M. P., 187  
 Gardiner, D. J., 131  
 Gil, J., 99  
 Gjelsvik, N., 202  
 Golijanin, D. M., 51, 54  
 Gómez de Salazar, J. M., 349  
 Graham, S. M., 177  
 Grove, T. L., 346  
 Guilemany, J. M., 99, 349  
 Gunning, W. J., 247  
 Harker, A. B., 230, 241, 244  
 Harthcock, M. A., 173  
 Hawkey, L. A., 267  
 Heinrich, K. F. J., 23, 24  
 Heitur, H. I., 65  
 Henry, D. J., 339  
 Heuer, A. H., 215, 225, 227  
 Hills, C. R., 257  
 Hinthorne, J. R., 321  
 Hirschberg, J. C., 192  
 Hlava, P. F., 15  
 Ho, Y., 197  
 Honigs, D. E., 123  
 Horsfall, I., 233  
 Hosking, F. M., 257  
 Howitt, D. G., 225, 227, 230  
 Ikeda, S., 79  
 Ikeda, T., 199  
 Ikuta, T., 91  
 Ingram, P., 267  
 Iriyama, K., 189, 199  
 Ishida, H., 189  
 Ishihara, F., 189  
 Ishitani, A., 189  
 Jackson, A. G., 237  
 Jarosevich, E., 312  
 Johnson, K. A., 239  
 Johnson, P. F., 307  
 Joy, D. C., 105, 117  
 Kajikawa, T., 37  
 Kameda, H., 189  
 Kamoto, R., 189  
 Kaser, S. A., 332  
 Katzenberger, J. M., 165  
 Kelly, J., 166  
 Kelsey, P. V., 227  
 Kempfert, K. D., 187  
 Kerker, M., 138  
 Kiefer, W., 137  
 Kilaas, R., 293  
 Kinalidis, C., 82  
 Kitchen, C. R., 313  
 Kohara, K., 37, 192  
 Kohen, C., 192  
 Kohen, E., 192  
 Konopka, J. F., 43, 96  
 Kotera, M., 102  
 Krishnan, K. M., 222  
 Kuck, J. F. R., 197  
 Laderman, S. S., 87  
 Lakshminarasimha, M., 307  
 Lange, D. E., 346, 348  
 Langner, R., 359  
 Lauer, J., 359  
 Laureyns, J., 139  
 Leapman, R. D., 273  
 LeFurgey, A., 267  
 Lenain, B., 210  
 Lerner, J., 141, 165  
 Levesque, T. H., 327  
 Lieberman, M., 267  
 Lindner, B., 353

Linton, R. W., 361, 365  
 Littleton, C. J., 131  
 Lloyd, P. F., 237, 250  
 Lopez, G. A., 264  
 Loudon, J. D., 166  
 Ma, S.-T., 213  
 McCarthy, J. J., 301  
 McCoy, D. D., 46  
 Mackinnon, I. D. R., 332  
 Macklin, J., 211  
 McLaughlin, T. E., 250  
 Magnotta, F., 153  
 Mangel, W. F., 192  
 Marinenko, R., 25, 40  
 Mardinly, A. J., 335  
 Marshall, A. T., 269  
 Mase, H., 91  
 Mellor, B., 99  
 Merlin, J., 139  
 Messerschmidt, R. G., 169, 180  
 Miguel, J. R., 99  
 Milanovich, F. P., 121  
 Minkin, J. A., 329  
 Mitchell, T. E., 215  
 Miyokawa, T., 57  
 Mizuno, A., 199  
 Moir, P. A., 253  
 Morrison, G. H., 261  
 Morlière, P., 192  
 Mott, R. B., 287  
 Musselman, I. H., 361, 365  
 Myers, M. C., 261  
 Myklebust, R. L., 20, 25, 40  
 Nagatani, T., 71  
 Nagatsuka, Y., 57  
 Natividad, M. O., 264  
 Nauka, K., 87  
 Newbury, D. E., 20, 25, 33, 40, 110  
 Nockolds, C. E., 9  
 Nozawa, H., 199  
 Omlor, R. E., 237, 250  
 Osumi, M., 71  
 Otsuki, M., 57  
 Ozaki, Y., 189, 199  
 Ozkan, U., 128  
 Pasteris, J. D., 205  
 Pawley, J. B., 83  
 Phillipson, J., 166  
 Pirouz, P., 215  
 Prince, J., 192  
 Purcell, F., 151  
 Recca, S. I., 346, 348  
 Reffner, J. A., 180  
 Reid, G. A., 87  
 Reyftman, J., 192  
 Rickman, J. T., 361  
 Robison, R. L., 271  
 Romig, A. D., Jr., 15  
 Rosenthal, R. J., 185, 187  
 Rosner, S. J., 87  
 Russ, J. C., 277  
 Russ, J. Ch., 277  
 Sankur, H., 247  
 Santus, R., 192  
 Schachtschabel, D. O., 192  
 Schrader, G. L., 128  
 Schröder, W. H., 359  
 Semarge, R. E., 257  
 Sentner, D. A., 65  
 Seydel, U., 353  
 Seymour, J. C., 301  
 Shapiro, B. L., 192  
 Sharma, S. K., 133  
 Shibata, K., 189  
 Shimizu, R., 91  
 Shinohara, M., 96  
 Simons, D. S., 365  
 Sinha, A. K., 315  
 Small, J. A., 20  
 Smith, D. G. W., 12  
 Smith, D. M., 177  
 Sod, E. W., 261  
 Soezima, H., 37  
 Solberg, T. N., 315  
 Staudhammer, K. P., 239  
 Stockton, C. M., 317  
 Storey, B. E., 253  
 Storms, J., 343, 356  
 Stuart, C. J., 327  
 Suga, H., 102  
 Sugiyama, N., 79  
 Suzumi, J., 57  
 Swyt, C. R., 273  
 Tagata, S., 57  
 Takagi, I., 189  
 Takata-Kanematsu, E. H., 199  
 Talmi, Y., 222  
 Thomas, G., 222  
 Thompson, F. L., 197  
 Thompson, K. A., 69, 115  
 Toney, J. B., 339  
 Truchet, M., 163  
 Tsukie, E., 189  
 Turrell, G., 139  
 Uchikawa, Y., 79  
 Ureña, A., 349  
 Urmos, J. P., 133  
 Van Grieken, R., 343, 356  
 Vavra, C. L., 327  
 Velapoldi, R., 202  
 Visscher, G. E., 271  
 Walker, L. R., 69  
 Wallart, F., 167  
 Ware, N. G., 62  
 Watanabe, T., 57  
 Wayne, D. M., 315  
 Welch, W. F., 177  
 Wells, O. C., 1, 76  
 Wittry, D. B., 51  
 Wolfe, J. C., 82  
 Wopenka, B., 295  
 Wynne, D. A., 12  
 Yu, N. T., 197  
 Zenitani, F., 37

## Notes



# Notes